Transactions of the ASME®

Journal of Heat Transfer

Published Quarterly by The American Society of Mechanical Engineers

VOLUME 114 • NUMBER 4 • NOVEMBER 1992

HEAT TRANSFER DIVISION
Chairman, J. B. KITTO, JR.
Secretary, O. A. PLUMB
Technical Editor, R. VISKANTA (1995)
Associate Technical Editors,
Y. BAYAZITOGLU (1995)
R. O. BUCKIUS (1993)
W. A. FIVELAND (1994)
L. S. FLETCHER (1994)
W. L. GROSSHANDLER (1995)
C. E. HICKOX, JR. (1995)
F. P. INCROPERA (1993)
J. H. KIM (1993)
J. R. LLOYD (1995)
T. W. SIMON (1995)
R. J. SIMONEAU (1993)
L. C. WITTE (1994)

BOARD ON COMMUNICATIONS
Chairman and Vice President
R. D. ROCKE

Members-at-Large
T. BARLOW, W. BEGELL, T. F. CONRY,
T. DEAR, J. KITTO, R. MATES,
W. MORGAN, E. M. PATTON,
S. PATULSKI, R. E. REDER,
A. VAN DER SLUYS, F. M. WHITE

President, J. A. FALCON
Executive Director,
D. L. BELDEN
Treasurer,
ROBERT A. BENNETT

PUBLISHING STAFF
Mng. Dir., Publ.,
CHARLES W. BEARDSLEY
Managing Editor,
CORNELIA MONAHAN
Sr. Production Editor,
VALERIE WINTERS
Production Assistant,
MARISOL ANDINO

Transactions of the ASME, Journal of Heat Transfer (ISSN 0022-1481) is published quarterly (Feb., May, Aug., Nov.) for $165.00 per year by The American Society of Mechanical Engineers, 345 East 47th Street, New York, NY 10017. Second class postage paid at New York, NY and additional mailing offices. POSTMASTER: Send address changes to Transactions of the ASME, Journal of Heat Transfer, c/o THE AMERICAN SOCIETY OF MECHANICAL ENGINEERS, 22 Law Drive, Box 2300, Fairfield, NJ 07007-2300.
CHANGES OF ADDRESS must be received at Society headquarters seven weeks before they are to be effective. Please send old label and new address.
PRICES: To members, $40.00, annually: to nonmembers, $165.00.
Add $24.00 for postage to countries outside the United States and Canada.
STATEMENT from By-Laws. The Society shall not be responsible for statements or opinions advanced in papers or . . . printed in its publications (B7.1, para. 3).
COPYRIGHT © 1992 by The American Society of Mechanical Engineers. Authorization to photocopy material for internal or personal use under circumstances not falling within the fair use provisions of the Copyright Act is granted by ASME to libraries and other users registered with the Copyright Clearance Center (CCC) Transactional Reporting Service provided that the base fee of $3.00 per article plus $.30 per page is paid directly to CCC, 27 Congress St., Salem, MA 01970. Request for special permission or bulk copying should be addressed to Reprints/Permission Department.
INDEXED by Applied Mechanics Reviews and Engineering Information, Inc. Canadian Goods & Services Tax Registration #126148048.

ANNOUNCEMENTS

810 Change of address form for subscribers

1071 Author Index: Volume 114, 1992

1076 Call for papers: 1993 Winter Annual Meeting

1079 Information for authors

TECHNICAL PAPERS

796 Optimization of Multiprobe Cryosurgery
R. G. Keanini and B. Rubinsky

802 Effect of Surface Deformations on Contact Conductance
M. Williamson and A. Majumdar

811 Thermal Constriction Resistance of Phase-Mixed Metallic Coatings
K. C. Chung, J. W. Sheffield, and H. J. Sauer, Jr.

819 Visualization and Analysis of Flow in an Offset Channel
J. A. Walter and C.-J. Chen

827 Heat Transfer With Very High Free-Stream Turbulence: Part I—Experimental Data
P. K. Maciejewski and R. J. Moffat

834 Heat Transfer With Very High Free-Stream Turbulence: Part II—Analysis of Results
P. K. Maciejewski and R. J. Moffat

840 Turbulent Heat Transport in a Boundary Layer Behind a Junction of a Streamlined Cylinder and a Wall
D. E. Wroblewski and P. A. Eibeck

850 Effect of Uneven Wall Temperature on Local Heat Transfer in a Rotating Square Channel With Smooth Walls and Radial Outward Flow
J.-C. Han and Y. M. Zhang

859 Hot Wire/Film Behavior in Low-Temperature Gases
E. Y. Kwack, P. Shakkottai, T. S. Luchik, K. M. Aaron, G. Fabris, and L. H. Back

866 Heat and Momentum Transport in Self-Sustained Oscillatory Viscous Flows
D. Majumdar and C. H. Amon

874 Effect of Nozzle Configuration on Transport in the Stagnation Zone of Axisymmetric, Impinging Free-Surface Liquid Jets: Part 1—Turbulent Flow Structure
J. Stevens, Y. Pan, and B. W. Webb

880 Effect of Nozzle Configuration on Transport in the Stagnation Zone of Axisymmetric, Impinging Free-Surface Liquid Jets: Part 2—Local Heat Transfer
Y. Pan, J. Stevens, and B. W. Webb

887 Analysis of a Screen Heat Exchanger
G. F. Jones and F. C. Prenger

893 Prediction of Heat Transfer and Friction for the Louver Fin Geometry
A. Sahnoun and R. L. Webb

901 Experiment on Spatio-Temporal Turbulent Structures of a Natural Convection Boundary Layer
T. Tsuji, Y. Nagano, and M. Tagawa

909 Linearization of Natural Convection From a Vertical Plate With Arbitrary Heat-Flux Distributions
S. Lee and M. M. Yovanovich

917 Natural Convection Heat Transfer From an Isothermal Vertical Surface to a Stable Thermally Stratified Fluid
D. Angirasa and J. Srinivasan

924 Three-Dimensional Natural Convection in a Vertical Porous Layer With a Hexagonal Honeycomb Core
Y. Asako, H. Nakamura, Y. Yamaguchi, and M. Faghri

928 Reversed Flow Structure and Heat Transfer Measurements for Buoyancy-Assisted Convection in a Heated Vertical Duct
C. Gau, K. A. Yih, and W. Aung

936 Effects of Buoyancy on Laminar Flow in Curved Elliptic Ducts
Z. F. Dong and M. A. Ebadian

944 Holographic Interferometry Temperature Measurements in Liquids for Pool Fires Supported on Water
A. Ito, K. Saito, and T. Inamura

Downloaded 04 Feb 2011 to 194.85.80.107. Redistribution subject to ASME license or copyright; see http://www.asme.org/terms/Terms_Use.cfm

(Contents continued)

950 Radiative Properties of Interacting Particles
M. A. Al-Nimr and V. S. Arpaci

958 Radiative Properties of Y-Ba-Cu-O Films With Variable Oxygen Content
B. I. Choi, Z. M. Zhang, M. I. Flik, and T. Siegrist

965 Evaporation of Single Drops of *n*-Pentane/*n*-Hexane Mixtures in Water
H. Shimaoka and Y. H. Mori

972 Unifying the Controlling Mechanisms for the Critical Heat Flux and Quenching: The Ability of Liquid to Contact the Hot Surface
C. Unal, V. Daw, and R. A. Nelson

983 Modeling of Transient Stratified Flow in Vertical Tube Assemblies
P. F. Peterson and A. Akbarzadeh

990 Transient Natural Convection in a Horizontal Concentric Annulus Filled With a Porous Medium
I. Pop, D. B. Ingham, and P. Cheng

998 A Two-Wavelength Holographic Interferometry Study on the Solidification of a Binary Alloy Around a Horizontal Pipe
T. L. Spatz and D. Poulikakos

1011 Condensation in a Porous Region Bounded by a Cold Vertical Surface
J. N. Chung, O. A. Plumb, and W. C Lee

1019 A Study of Thermal Energy Storage Systems With Conjugate Turbulent Forced Convection
Y. Cao and A. Faghri

1028 Closed-Form Analytical Solutions of High-Temperature Heat Pipe Startup and Frozen Startup Limitation
Y. Cao and A. Faghri

1036 Freezing Flow in a Subcooled Permeable Medium
S. K. Griffiths and R. H. Nilson

TECHNICAL NOTES

1042 Experimental Evidence for the Temperature Waves Around a Rapidly Propagating Crack Tip
D. Y. Tzou

1045 The Effect of Interstitial Fluid on Thermal Constriction Resistance
A. K. Das and S. S. Sadhal

1048 Nonlinear Steady-State Inverse Heat Conduction Problem With Space-Variable Boundary Conditions
J. Taler

1051 Effects of Axial and Radial-Gap Spacing on the Local Heat Transfer of a Shrouded Rotor-Stator System
M. K. Chyu and D. J. Bizzak

1054 Measurement of the Free Convection Heat Transfer Coefficient for a Rough Horizontal Nonisothermal Cylinder in Ambient Air by Infrared Scanning
M. S. Farid and C. K. Hsieh

1057 Measurements of Laminar Mixed Convection Adjacent to a Vertical Plate—Uniform Wall Heat Flux Case
H. I. Abu-Mulaweh, B. F. Armaly, and T. S. Chen

1060 Identification of the Temperature Profile in an Absorbing, Emitting, and Isotropically Scattering Medium by Inverse Analysis
H. Y. Li and M. N. Özişik

1063 The Effect of Variable Viscosity on Forced Convection Over a Flat Plate Submersed in a Porous Medium
J. X. Ling and A. Dybbs

1065 Analytical Solution of Steady Natural Convection in an Annular Porous Medium Evaluated With a Symbolic Algebra Code
A. Mojtabi and M. C. Charrier-Mojtabi

1068 Thermocapillary Convection During Solid-Liquid Phase Change
T. E. Voth, A. Liu, and T. L. Bergman

Downloaded 04 Feb 2011 to 194.85.80.107. Redistribution subject to ASME license or copyright; see http://www.asme.org/terms/Terms_Use.cfm

Optimization of Multiprobe Cryosurgery

R. G. Keanini

B. Rubinsky

University of California,
Department of Mechanical Engineering,
Berkeley, CA 94720

This paper describes a general technique for optimizing cryosurgical procedures. The method, which is based on the simplex minimization algorithm, minimizes unnecessary freezing by optimizing various surgical parameters. The optimization procedure is illustrated using a simplified model of prostatic cryosurgery. In this illustrative case, the function to be minimized, F, defined as the volume of healthy tissue destroyed during complete freezing of the prostate, is assumed to depend on three parameters: the number of cryoprobes used, the freezing length per cryoprobe, and the cryoprobe diameter. Using an iterative procedure, the optimization algorithm first alters these parameters, then calculates F by solving a three-dimensional bioheat transfer model of multiprobe cryosurgery, and finally determines whether F is minimized. The iterative procedure continues until unnecessary freezing is minimized. For the model considered here, the optimization code indicates that unnecessary freezing during cryoprostatectomy is minimized using approximately 5 cryoprobes, each 7.5 mm in length and 4 mm in diameter.

Introduction

Cryosurgery utilizes freezing to destroy diseased tissue. Freezing is induced using a cryoprobe, a small, typically nitrogen-perfused hollow cylinder (diameters typically range from 2 to 10 mm), which is insulated everywhere, save the tip. Due to the cryoprobe's diminutive size, freezing is highly localized, and when directly monitored, is readily controlled. Cryosurgical procedures can use one or several probes, the number being determined by both the size of the diseased region and by the patient's ability to withstand surgical trauma. Cryosurgery has been used to treat a range of illnesses, both cancerous and benign (Flocks et al., 1972; Gage, 1982; Rubinsky et al., 1987; Onik, 1991; Onik et al., 1991a; Bischoff et al., 1992), and is generally of greatest utility in cases of local, nondiffuse pathological growth.

Since the introduction of cryosurgical techniques in human patients (Cooper and Lee, 1961), however, unintended perioperative destruction of healthy tissue has been a vexing problem that has, in many cases, limited the technique's application. Such unnecessary freezing can lead to a host of lethal or chronic complications (Debruyne and Kirkels, 1983). Generally, detrimental freezing is of concern when: (1) the diseased region is located close to critical organs or structures, and (2) when freezing cannot be accurately monitored.

At present, cryosurgical planning, i.e., selecting the number, size, location, and spatial orientation of the cryoprobes used in the procedure, is left to a surgeon's judgment. The planning phase is important first, for the reasons outlined above, and second, in high-risk cases where the patient for example, has a heart condition, is in a weakened state, has hemophilia, or is of advanced age. Visualization techniques, in particular ultrasonic monitoring (Onik, 1991; Onik et al., 1991a) allow relatively accurate control of freezing, and effectively widen the surgeon's margin for error during the planning phase. Nevertheless, since monitoring provides only two-dimensional information on an inherently three-dimensional process, and since cryoprobe movement is impossible once freezing has begun, unnecessary tissue destruction continues to be a problem.

Solving the problem of detrimental freezing, or at least *minimizing* healthy tissue destruction, clearly requires more than surgical judgment or reliance on visual monitoring. In this paper, we describe a method for planning cryosurgical procedures. The technique, which essentially quantifies the planning phase, minimizes unnecessary freezing by optimizing the number and size of cryoprobes used in the procedure.

The paper's purpose is to introduce and illustrate the optimization technique. Although the optimization procedure presented here is based on the multidimensional simplex minimization algorithm (Spendly et al., 1962), other minimization techniques may be more suitable in other applications. Similarly, the choice of surgical parameters to be optimized is not limited to those treated here. Rather, clinical applications will likely require that probe locations and orientations also be optimized. These points will be elaborated upon below. The optimization technique is illustrated using a simplified model of multiprobe *prostatic* cryosurgery.

Prostatic Cryosurgery. We choose prostatic cryosurgery for illustration since this procedure is widely used and since it provides a compelling example of the need for quantitatively based cryosurgical planning. We will focus on radical cryoprostatectomy in which the prostate is completely frozen.

In brief, prostatic diseases are either cancerous or benign, and primarily afflict middle-aged and elderly males. Prostate cancer, in various stages of development, is very prevalent, being found in approximately 30 percent of all males over 50 and over 90 percent of males over the age of 85 (Franks, 1977). Complications often include partial to complete blockage of the urinary tract and/or anal canal, pain during urination or bowel movement, and chronic pain in the pelvic and/or spinal regions. Benign prostatic hyperplasia is a related disease, characterized by nonmalignant enlargement of the prostrate, and having symptoms similar to prostate cancer.

Although cryosurgery has been used to treat prostatic diseases, the procedure has not been completely accepted, largely due to difficulties in monitoring the extent of freezing (Onik, 1991). In particular, the surgeon must ensure that both the urethra and the rectum are not damaged, since a number of postoperative complications can otherwise result (e.g., urinary incontinence, urinary tract infection, urethral stenosis, rectal fistula, sphincter damage, and death). As noted above, even relatively accurate visualization techniques do not solve the problem, since it is difficult to monitor the complete three-dimensional freezing front.

Prior Work. A limited number of studies have applied optimization and/or minimization techniques to biological heat transfer problems. For example, Rubinsky and Shitzer (1978)

Contributed by the Heat Transfer Division for publication in the JOURNAL OF HEAT TRANSFER. Manuscript received by the Heat Transfer Division October 1991; revision received April 1992. Keywords: Conduction, Moving Boundaries, Phase-Change Phenomena. Technical Editor: R. Viskanta.

Copyright © 1992 by ASME
Downloaded 13 Dec 2010 to 193.140.21.150. Redistribution subject to ASME license or copyright; see http://www.asme.org/terms/Terms_Use.cfm

solved a one-dimensional inverse Stefan problem, which determined the boundary heat flux leading to maximum tissue destruction during cryosurgery. Dulikravich and Hayes (1988) reported a technique in which tissue survival during cryopreservation was maximized by optimizing exterior cooling rates. Clegg et al. (1988) reported recent work on an inverse method for predicting three-dimensional temperature distributions during hyperthermic treatments. The method simultaneously determined an unknown blood perfusion distribution and the temperature field by minimizing the total difference between known and iteratively calculated temperatures. Although related studies have been carried out in the above areas (Madison et al., 1987; Clegg and Roemer, 1989), it appears that no work has been reported on optimizing multiple probe cryosurgery or on minimizing unnecessary freezing during cryosurgery.

Since the present optimization program utilizes a three-dimensional simulation of multiprobe cryosurgery, it is of interest to discuss briefly prior analytical and numerical simulations of cryosurgical freezing. A number of one- and two-dimensional models of cryoprobe-induced freezing have been reported. For example, Cooper and Trezek (1970, 1971) used one-dimensional analytical models to examine the effect of probe shape on the freezing process. Budman et al. (1986) employed both analytical and numerical models in order to compare predicted freezing characteristics with freezing observed experimentally. Bischoff et al. (1992) developed a one-dimensional numerical model of lung tumor cryosurgery. Other analytical and numerical investigations of cryosurgical heat transfer include those of Staub and Storey (1967) and Comini and Del Giudice (1976). It appears that no three-dimensional simulations of multiple probe cryosurgical freezing have been reported.

Simplex Technique

In this section we first describe the simplex algorithm and then apply it to optimize cryosurgery. The multidimensional downhill simplex method (Spendly et al., 1962; Nelder and Mead, 1965), is a direct search minimization technique that utilizes simple geometric concepts to determine function minima.

Given a function, F, of K variables, p_i $(i=1, 2, \ldots, K)$, we seek a local minimum of F in K-space. The minimization process begins with the construction of a K-dimensional simplex (where for example, a simplex in two dimensions is a triangle, or in three dimensions, a tetrahedron). This initial construction is accomplished by evaluating F at $K+1$ points, $x_1, x_2, \ldots, x_{K+1}$, where each point, $x(p_1, p_2, \ldots, p_K)$, corresponds to a different set of independent variables. We imagine that each point x corresponds to a vertex, and that the set of all $K+1$ vertices defines a K-dimensional simplex. Once the simplex is thus constructed, the values of F at all $K+1$ vertices are compared. The vertices v_h and v_s, at which F assumes its largest and smallest values, $F_{\max}$ and $F_{\min}$, respectively, are then identified. The crux of the simplex method is to displace v_h to a new point, $x^*(p_1, p_2, \ldots, p_K)$, such that

$$F(x^*) < F_{\max} \tag{1}$$

Once x^* is found, a new vertex, v^*, is placed there, and the simplex is reconstructed using the K unchanged vertices and v^*.

Displacement of v_h can occur in one of three ways: reflection, contraction, or expansion. Following Nelder and Mead (1965), a reflection projects v_h to a point x^* such that

$$x^* = (1+\alpha)x^o - \alpha x^h \tag{2}$$

where $x^h(p_1, p_2, \ldots, p_K)$ is the point defining v_h, $x^o(p_1, p_2, \ldots, p_K)$ is the centroid of all remaining vertices (not including v_h), and α is a positive constant called the reflection coefficient. To illustrate, in a three-dimensional space, in which the simplex is a tetrahedron, a reflection would project v_h through the centroid of the opposing tetrahedral face. The new simplex in this case would be a somewhat inverted image of the original tetrahedron. If a reflection results in $F_{\min} < F(x^*) < F_{\max}$, then x^* is taken as the new vertex, and the simplex is reconstructed. In the event that $F(x^*) < F_{\min}$, then we have happened onto a region of decreasing F, and thus attempt an *expansion* to a new point $x^{**}(p_1, p_2, \ldots, p_K)$, where x^{**} is given by

Nomenclature

c = specific heat, W s/(kg K)
d_p = probe diameter, mm
$F = F(n_p, l_p, d_p)$ = volume of healthy tissue frozen, mm^3
$F*$ = (volume of extraprostatic tissue frozen)/(volume of prostate) * 100 percent
h = heat transfer coefficient, W/(m^{2}K)
k = thermal conductivity, W/(mK)
l_p = probe heat transfer length, mm
n_p = number of probes
p = variable in the minimization problem
Q = metabolic heat source term, W/m^3
t = time, s
t_o^c, t_o^f = time required to completely freeze prostate on $25\times25\times25$ and $49\times49\times49$ node grids, respectively
T = temperature, K
T_i = initial temperature of prostate and extraprostatic tissue, K
v = coordinate point of a vertex on a K-dimensional simplex
w = blood perfusion, ml/(g min)
x, y, z = Cartesian coordinates, m
x = coordinate point in K-space
α = thermal diffusivity, m^2/s; also reflection coefficient
β = contraction coefficient
γ = expansion coefficient
ϵ = minimization convergence tolerance
ρ = density, kg/m^3

Subscripts

a = arterial
b = blood
f = frozen
h = high value
i, j, k = grid indices for x, y, and z directions; also index for optimization variables
ln = liquid nitrogen
max = maximum
min = minimum
p = probe
s = small value
u = unfrozen
∂ = denotes boundary

Superscripts

c = coarse grid
f = fine grid
h = high value
I = iteration number
o = centroid
s = small value
$'$ = primary test point
$**$ = secondary test point

Downloaded 13 Dec 2010 to 193.140.21.150. Redistribution subject to ASME license or copyright; see http://www.asme.org/terms/Terms_Use.cfm

$$x^{**} = (1-\gamma)x^o + \gamma x^h \tag{3}$$

Here, γ, the expansion coefficient, is greater than 1. If $F(x^{**}) < F_{\min}$, then the expansion is successful and a new simplex is constructed using x^{**}. However, if $F(x^{**}) > F_{\min}$, then the expansion is not taken, and the new simplex is constructed using x^*.

It may happen that reflection of x^h to x^* simply leads to another function maximum, i.e.,

$$F(x^*) > F(x_i)$$

where x_i denotes either the set of all vertex points or the set of all vertex points, save x^h. In either case, a *contraction* is called for. A contraction begins by first comparing $F(x^*)$ with $F(x^h)$ $(=F_{\max})$. If $F(x^*) < F_{\max}$, then a new vertex is placed at x^*, while no change is made if $F(x^*) > F_{\max}$. Given this new temporary simplex, x^h is then displaced to x^{**}, where

$$x^{**} = (1-\beta)x^o + \beta x^h \tag{4}$$

Here, β, the contraction coefficient, satisfies $0 < \beta < 1$. The contraction is successful and x^{**} is taken as a new vertex if $F(x^{**}) < \min(F_{\max}, F(x^*))$. Otherwise, we have to construct a completely new simplex by contracting all vertices around the current minimum point at $x^s(p_1, p_2, \ldots, p_K)$ (where $F(x^s) = F_{\min}$). This latter procedure is accomplished by moving each vertex point, x_1, to the point $(x_i + x^s)/2$.

Through this process of reflection, expansion, and contraction, the simplex method eventually drives the simplex to a region of K-space, where F has a local minimum. As the minimum is approached, the vertices begin to approach one another and a criterion can be employed to signal convergence. Here, convergence is assumed to occur if the following condition holds (Press et al., 1981):

$$|F_{\max} - F_{\min}| / |F_{\max} + F_{\min}| < \epsilon \tag{5}$$

where ϵ is a specified tolerance.

Optimizing Cryosurgery. For our illustration, the function to be minimized, F, is the volume of healthy extraprostatic tissue destroyed during the freezing process:

F = volume of healthy tissue destroyed during cryosurgery

We assume that this function depends on three independent variables ($K=3$): the number of probes (n_p), the probe diameter (d_p), and the probe active length (l_p), or

$$F = F(n_p, l_p, d_p) \tag{6}$$

As explained below, we fix the location and orientation of all n_p cryoprobes rather than determining these parameters through minimization. This latter simplification greatly reduces the problem's scope, shrinking the parameter space from $6n_p + 3$ to three dimensions (where the $6n_p + 3$ dimensions correspond to 3 n_p coordinates fixing n_p reference points on n_p probes, 3 n_p corresponding direction cosines, and 3 probe parameters, n_p, l_p, d_p).

Following Nelder and Mead (1965) α, γ, and β are given the values 1.0, 2.0, and 0.5.

Heat Transfer Model

Heat transfer within a blood perfused tissue is modeled by the bioheat transfer equation (Pennes, 1948):

$$\rho c_p \frac{\partial T}{\partial t} = \nabla \cdot [k \nabla T] - \rho_b \cdot w c_b (T - T_a) + Q \tag{7}$$

where ρ is the tissue density, c_p is the tissue specific heat, k is the tissue thermal conductivity, w is the blood perfusion, c_b is the blood specific heat, ρ_b is the blood density, T_a is the arterial blood temperature, and Q is the metabolic heat generation. Although the validity of this model has recently been questioned by several investigators (see, e.g., Chen, 1980), it nevertheless predicts heat transfer well within first and second-generation vascular regions, and captures temperature profiles within third-generation vascular regions, which agree reasonably well with comprehensive theoretical predictions (Charny et al., 1990).

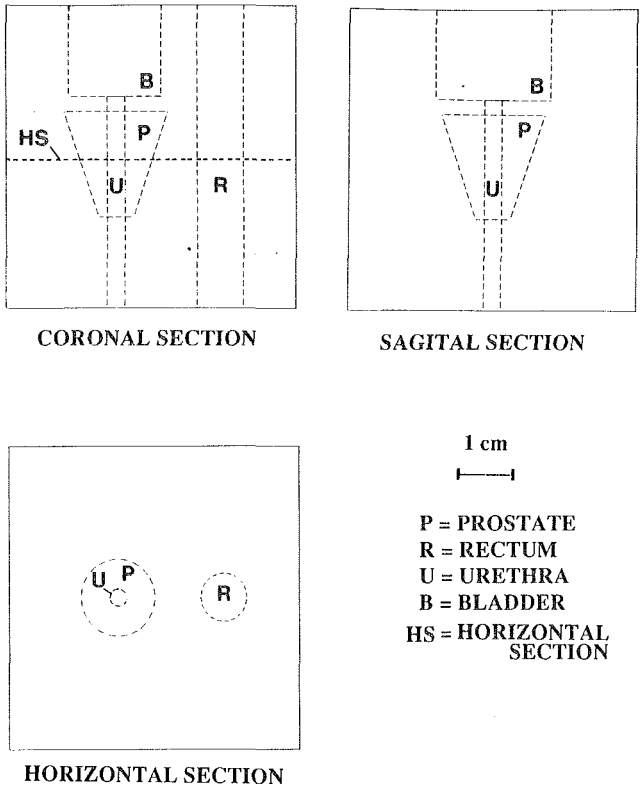

Fig. 1 Geometry of prostate region; horizontal plane bisects the tissue domain

The boundary conditions and initial condition for the problem are as follows. At the surface of each cryoprobe, the normal flux is given as

$$k \frac{\partial T}{\partial n} = h_p (T - T_p) \tag{8a}$$

The tissue temperature at the boundary of the problem domain is fixed at a constant value:

$$T_\partial = T_o \tag{8b}$$

while the initial temperature within the domain is given as a function of position:

$$T(x, y, z, t=0) = G(x, y, z) \tag{8c}$$

Assumptions

Since this work is designed to illustrate a cryosurgical optimization technique, simplified heat transfer and physiological models are used. The assumptions are as follows:

1 The shapes of the major structures lying within the problem domain are simplified. Specifically, we idealize the three-dimensional bounding surfaces of the prostrate, urethra, bladder, and rectum as being composed of intersecting circular cylinders, circular conic sections, and planes. Refer to Fig. 1. Likewise, cryoprobes are idealized as simple circular cylinders.

2 Differences in tissue thermophysical properties are not accounted for, and all properties, save thermal conductivity, are assumed to be temperature independent. Thermal conductivity assumes one constant value in the frozen phase, and another constant value in the unfrozen phase. These simplifications neglect tissue density variations and the temperature dependence of various properties (e.g., specific heat, thermal

Downloaded 13 Dec 2010 to 193.140.21.150. Redistribution subject to ASME license or copyright; see http://www.asme.org/terms/Terms_Use.cfm

conductivity). A simulation that accurately accounts for tissue geometry, property inhomogeneities, and temperature dependencies will require a much larger computational effort.

3 Due to the overwhelming influence of the cryoprobes on tissue heat transfer (Anderson et al., 1988), metabolic heat release is neglected.

4 During prostatic cryosurgery, the bladder is flushed with warm solution in order to prevent bladder freezing. This procedure is simulated by maintaining the bladder at 310 K.

5 In order to simulate a recently developed technique in which a heated fluid is introduced into the urethra through the urinary tract (Onik et al., 1991a), we assume that the temperature on the centerline of the urethra is fixed at a characteristic temperature of 310 K. All other temperatures within the urethra are allowed to vary, and are determined as part of the overall solution.

6 For the initial condition, the operating area, save the bladder and the urethra, is precooled to 285 K. The urethra's initial temperature and the bladder's fixed temperature are 310 K.

Following Clegg et al. (1988), we employ approximate representative tissue properties in the calculations. Property and parameter values are as follows (Vanderby et al., 1988; Bischoff et al., 1992): $c_p = c_b = 4300$ W s/(kgK), $\rho = \rho_b = 1000$ kg/m^3, $w = 100$ ml/(100 g min), $k_f = 2.25$ W/(m/K), $k_u = 0.63$ W/(mK), $T_a = 310$ K, $T_p = 83$ K, $h_p = 500$ W/(m^{2}K).

Optimization Study Simplifications

The program begins by incrementing the number of cryoprobes from some initial number (e.g., 0). For n_p cryoprobes, the prostrate is divided into n_p equiangular subregions about a given reference axis. In order to reduce the scope of the minimization problem, we specify the position and orientation of all n_p probes by placing each cryoprobe (of given radius and length) at the centroid of each subregion, with its long axis parallel to the urethra's long axis (see Fig. 1). The latter simplification is consistent with the fact that the preferred orientation for cryoprobe application during most operations is somewhat parallel to the urethra. The former simplification should provide spatially uniform freezing since our idealized prostate is symmetric about the urethra. In general, when the object to be frozen lacks symmetry, then probe placement may have to be determined through minimization.

Numerical Method

Three-Dimensional Freezing Simulation. The optimization algorithm requires that the three-dimensional heat transfer problem defined by Eqs. (7) and (8) be solved every time n_p, l_p, or d_p is altered during minimization. A number of techniques exist for treating unsteady phase change problems (see, e.g., Crank, 1984). Here, we employ the finite difference enthalpy method (Lunardini, 1981) with an Euler forward integration scheme. The problem domain corresponds to a cubic volume 5 cm on a side, slightly offset from the center of the prostate. A mesh of 43 nodes in each coordinate direction (79507 total nodes) is employed for the calculations discussed here. The three-dimensional freezing simulation was checked for grid independence by comparing solutions on $25 \times 25 \times 25$ and $49 \times 49 \times 49$ node meshes. A comparison of temperature fields at the time of complete prostatic freezing, t_o, indicated a maximum relative temperature difference, Δ, of 4.2 percent, where

$$\Delta = \max\left(\frac{|T_i^f - T_I^c|}{T_i^f}\right)$$

Here, T_i^f and T_I^c denote corresponding nodal temperatures on the fine and coarse grids, respectively. (Note, the indices i and I have different values in each mesh but refer to the temperature at the same location within the problem domain. The comparison was carried out using the parameter combination $(n_p, l_p, d_p) = (5, 6.0$ mm, 2.5 mm).) The relative difference in freezing times for this comparison case,

$$\frac{|t_o^f - t_o^c|}{t_o^f}$$

was 3.4 percent. The time step used with the $43 \times 43 \times 43$ mesh was 0.005 s.

Optimization Algorithm. At the beginning of the program, an initial simplex is constructed by guessing four different combinations of (n_p, l_p, d_p). The associated F's are determined by executing the three-dimensional freezing simulation four times. Once the initial simplex is constructed, the optimization program uses the following iterative procedure to minimize F:

1 The current simplex is altered by displacing v_h to a new point in parameter space such that $F_{\max}$ becomes smaller. As described above, movement of v_h is accomplished by (*i*) reflection, (*ii*) reflection followed by expansion, (*iii*) contraction, or (*iv*) complete contraction around the current minimum.

2 Each time v_h is moved to a candidate point in parameter space, the corresponding F is calculated by inputing the $n_p l_p d_p$ coordinates of the candidate point into the freezing simulation. (The simulation is capable of modeling freezing due to variable numbers of probes, each of variable length and diameter.) Thus, each *permanent* displacement of v_h requires at least one simulation run (in the case of a reflection), and as many as three runs (in the case of a complete contraction). Note that the simplex procedure generally displaces v_h to points in parameter space where n_p is nonintegral. Thus, once the simplex procedure determines a candidate point, then the corresponding value of n_p is rounded to the nearest integer prior to use in the freezing simulation. Similarly, the l_p and d_p values determined by each v_h displacement are altered to coincide with the nearest gridlines prior to use in the simulation.

The simplex is iteratively altered until a local minimum in F is located, as indicated by the inequality in Eq. (5).

Results and Discussion

Freezing Characteristics. The qualitative features of the freezing process are depicted in Figs. 2–4, in the case when $n_p = 5$, $l_p = 6.0$ mm, and $d_p = 2.5$ mm. The location of the freezing front is shown in the coronal, sagittal, and horizontal planes at various stages of freezing. The iceballs propagate preferentially in the radial direction and gradually grow into one another as the prostate approaches complete freezing. Although the sagittal isotherm maps appear to show complete freezing within the urethra, the coronal and horizontal sections reveal that this is not the case. Instead, freezing within the urethra occurs predominantly on its distal edges and is inhibited in the central region due to the imposed constant temperature boundary condition on the centerline (see assumption 5 above). Freezing is also inhibited near the constant-temperature bladder (assumption 4), and consistent with clinical observations, freezing remains confined to the immediate vicinity of the probes. Prostatic freezing decreases at an approximately exponential rate under the above conditions ($n_p = 5$, $l_p = 6.0$ mm, $d_p = 2.5$ mm), with a time constant on the order of 0.05 s^{-1}. Note that in Fig. 4, the cryoprobes appear to be square due to the coarseness of the grid. Note too that the horizontal plane shown in Fig. 4 bisects the tissue domain as shown in Fig. 1.

Results of Optimization Procedure. For the purpose of illustration, and due to the computational expense (on the order of 10 to 20 min cpu time on the Cray X-MP), we only consider two different sets of initial parameter combinations. The results from the two optimization runs are given in Tables 1 and 2. As shown in the tables, ϵ equals 0.1 in the first test case

Downloaded 13 Dec 2010 to 193.140.21.150. Redistribution subject to ASME license or copyright; see http://www.asme.org/terms/Terms_Use.cfm

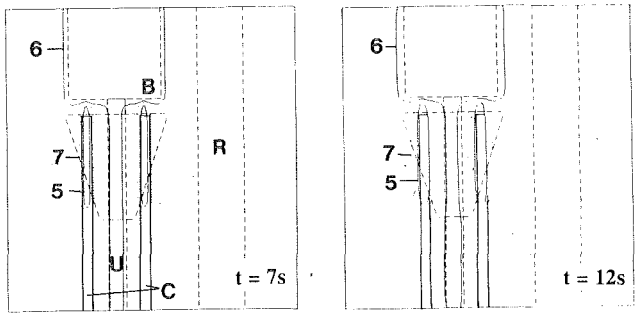

Fig. 2 Isotherms in coronal plane when $n_p = 5$ probes, $l_p = 6.0$ mm, $d_p = 2.5$ mm; isotherm spacing = 40 K

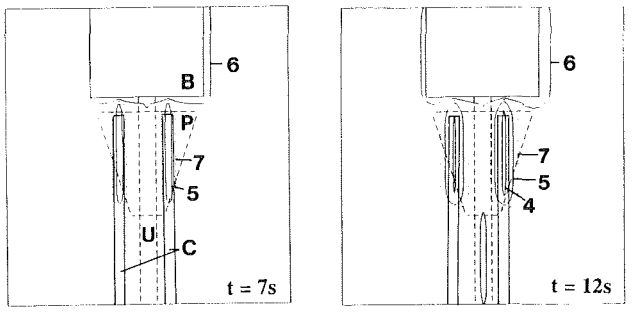

Fig. 3 Isotherms in sagittal plane when $n_p = 5$ probes, $l_p = 6.0$ mm, $d_p = 2.5$ mm; isothermal spacing = 40 K

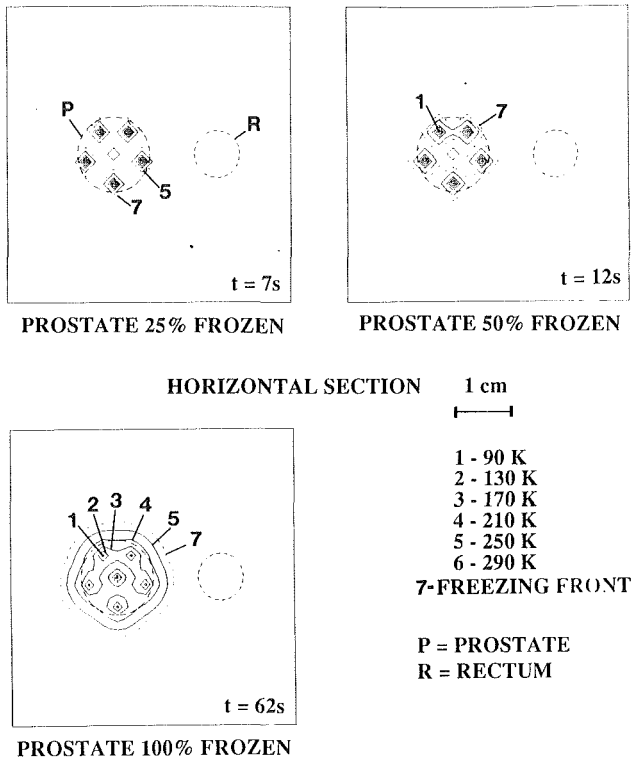

Fig. 4 Isotherms in horizontal plane (as defined in Fig. 1) when $n_p = 5$ probes, $l_p = 6.0$ mm, $d_p = 2.5$ mm; isotherm spacing = 40 K

and 0.01 in the second. Following construction of the initial simplex, the first test required three subsequent adjustments of the simplex to achieve convergence, while the second required 10 subsequent iterations. Note that in the tables, F^* is the volume of frozen extra-prostatic tissue divided by the volume of the prostate, determined at the time of complete prostatic freezing.

From the tables, we see that convergence occurs approximately at the point where n_p, l_p, and d_p equal 5 probes, 7.5 mm, and 4.0 mm, respectively. We thus take this combination of probe parameters as the one that leads to minimal extra prostatic freezing. Interestingly, this point appears to be the approximate minimum for a fairly large region within n_p, l_p, d_p space, since a wide range of initial parameter combinations approach it.

Extension of Present Technique. In closing this section, we outline some of the general features associated with optimization problems and note possible modifications to the present application:

1 Other minimization techniques that appear to be suitable for the present problem include Powell's direct search method (Powell, 1964) and the simulated annealing technique (Press et al., 1986). In contrast, techniques requiring derivative calculations of F (e.g., the Davidon–Fletcher–Powell variable metric method and the Polak–Ribiere conjugate gradient method), may be inefficient.

2 Defining the function to be minimized is problem specific. For example, in the area of prostatic cryosurgery, it is sometimes important to minimize freeze damage to the seminal vesicles. In this case, the function to be minimized would be the amount of seminal vesicle freezing produced during cryosurgery.

3 Once a function is defined, all of the parameters on which it depends should be identified.

4 In order to reduce the scope of the minimization problem, some of these parameters might have to be specified in some way other than minimization. For example, in the problem treated here, we specified probe placement and probe orientation.

Downloaded 13 Dec 2010 to 193.140.21.150. Redistribution subject to ASME license or copyright; see http://www.asme.org/terms/Terms_Use.cfm

Table 1(*a*) Initial parameter values—Case 1 ($\epsilon = 0.1$)

Point	No. of Probes	Probe Dia. (mm)	Probe Length (mm)
1	3	2.80	6.50
2	4	3.20	7.00
3	5	3.60	7.50
4	6	4.00	8.00

Table 1(*b*) Parameter values and amount of frozen tissue at convergence

Point	No. of Probes	Probe Dia. (mm)	Probe Length (mm)	F^* (%)
1	6	4.06	8.08	71.5
2	5	3.60	7.50	75.5
3	5	3.60	7.50	75.5
4	6	4.00	8.00	71.5

Table 2(*a*) Initial parameter values—Case 2 ($\epsilon = 0.01$)

Point	No. of Probes	Probe Dia. (mm)	Probe Length (mm)
1	5	4.00	7.00
2	7	4.50	9.00
3	9	5.00	7.00
4	8	5.50	5.00

Table 2(*b*) Parameter values and amount of frozen tissue at convergence

Point	No. of Probes	Probe Dia. (mm)	Probe Length (mm)	F^* (%)
1	6	4.10	7.44	71.8
2	5	3.97	8.11	71.4
3	5	3.94	7.50	71.8
4	5	3.81	7.48	71.4

F^* is the volume of extra-prostatic tissue frozen at the time of complete prostatic freezing divided by the volume of the prostate (expressed as a percentage)

Conclusions

This paper presents a method for optimizing cryosurgical procedures. Although the method is illustrated using the particular case of complete cryoprostatectomy, the technique can be specialized to aid in planning other cryosurgical procedures, such as freezing of single or multiple tumors. For the present application, the approximate optimal parameter combination is $n_p = 5$ probes, $l_n = 7.5$ mm, and $d_p = 4.0$ mm.

Clinical application of this technique will require, at minimum, accurate biophysical models of the tissues being frozen, comprehensive bioheat transfer models that accurately account for blood perfusion, and efficient minimization algorithms capable of treating large numbers of parameters. Due to the highly localized nature of cryosurgical freezing, the size of the tissue domain considered could conceivably be reduced to a volume not much larger than the diseased region. This would clearly reduce the scope of the problem.

Acknowledgments

This work was supported by an award from the Whitaker Foundation.

References

Anderson, G. T., Valvano, J. W., Hayes, L. J., and White, C. H., 1988, "The Effect of Perfusion on Self-Heated Thermistors: A Comparison Between Pennes' Equation and an Effective Thermal Conductivity Model," in: *Computational Methods in Bioengineering*, R. L. Spilker and B. R. Simon, eds., ASME, New York, pp. 301–312.

Bischoff, J. B., Bastacky, J., and Rubinsky, B., 1992, "An Analytical Study of Cryosurgery in the Lung," ASME *Journal of Biomechanical Engineering*, in press.

Budman, H., Shitzer, A., and Del Giudice, S., 1986, "Investigation of Temperature Fields Around Embedded Cryoprobes," ASME *Journal of Biomechanical Engineering*, Vol. 108, pp. 42–48.

Charny, C. K., Weinbaum, S., and Levin, R. L., 1990, "An Evaluation of the Weinbaum-Jiji Bioheat Equation for Normal and Hyperthermic Conditions," ASME *Journal of Biomechanical Engineering*, Vol. 112, pp. 80–87.

Chen, M. M., 1980, "Microvascular Contribution to Tissue Heat Transfer," *Annals of the New York Academy of Science*, Vol. 335, pp. 137–150.

Clegg, S. T., Liauh, C. T., and Roemer, R. B., 1988, "Selecting the Optimal Amount of Regularization to Reconstruct Three-Dimensional Temperature Fields From Limited Noisy Temperature Measurements During Hyperthermia," in: *Computational Methods in Bioengineering*, R. L. Spilker and B. R. Simon, eds., ASME, New York, pp. 280–291.

Clegg, S. T., and Roemer, R. B., 1989, "Predictions of Three-Dimensional Temperature Distributions During Hyperthermia Experiments," in: *Bioheat Transfer—Applications in Hyperthermia, Emerging Horizons in Instrumentation and Modeling*, R. B. Roemer, J. J. McGrath, and H. F. Bowman, eds., ASME HTD-Vol. 126, pp. 37–44.

Comini, G., and Del Giudice, S., 1976, "Thermal Aspects of Cryosurgery," ASME JOURNAL OF HEAT TRANSFER, Vol. 98, pp. 543–549.

Connolly, J. G., 1977, "Surgery of the Prostate Gland," in: *Urologic Pathology: The Prostate*, M. Tannenbaum, ed., Lea & Febiger, New York, pp. 283–300.

Cooper, I. S., and Lee, A. S. J., 1961, "Cryothalamectomy—Hypothermic Congelation, Technical Advance in Basal Ganglia Surgery," *Journal of the American Geriatric Society*, Vol. 9, p. 714.

Cooper, T. E., and Trezek, G. J., 1970, "Analytical Prediction of the Temperature Field Emanating From a Cryogenic Surgical Cannula," *Cryobiology*, Vol. 7, p. 79.

Cooper, T. E., and Trezek, G. J., 1971, "Rate of Lesion Growth Around Spherical and Cylindrical Cryoprobes," *Cryobiology*, Vol. 7, pp. 183–190.

Crank, J., 1984, *Free and Moving Boundary Problems*, Clarendon Press, New York.

Debruyne, F. M. J., and Kirkels, W. J., 1983, "Cryosurgery of Prostatic Carcinoma," in: *Cancer of the Prostate and Kidney*, M. Pavone-Macaluso and P. H. Smith, eds., Plenum Press, New York, pp. 269–275.

Dulikravich, G. S., and Hayes, L. J., 1988, "Control of Surface Temperatures to Optimize Survival in Cryopreservation," in: *Computational Methods in Bioengineering*, R. L. Spilker and B. R. Simon, eds., ASME BED-Vol. 9, pp. 255–266.

Flocks, R. H., Nelson, C. M. K., and Boatman, D. L., 1972, "Perineal Cryosurgery for Prostatic Carcinoma," *Journal of Urology*, Vol. 108, p. 933.

Franks, L. M., 1977, "Etiology and Epidemiology of Human Prostatic Disorders," in: *Urologic Pathology: The Prostate*, M. Tannenbaum, ed., Lea & Febiger, New York, pp. 23–32.

Gage, A. A., 1982, "Current Issues in Cryosurgery," *Cryobiology*, Vol. 119, pp. 219–222.

Lunardini, V., 1981, *Heat Transfer in Cold Climates*, Van Nostrand Reinhold Co., New York.

Madison, J. V., Dulikravich, G. S., and Hayes, L. J., 1987, "Optimization of Container Wall Temperature Variation During Transplant Tissue Cooling," *Proceedings, 2nd International Conference on Inverse Design Concepts and Optimization in Engineering Sciences*, G. S. Dulikravich, ed., The Pennsylvania State University, University Park, PA.

Nelder, J. A., and Mead, R., 1965, "A Simplex Method for Function Minimization," *Computer Journal*, Vol. 7, pp. 308–313.

Onik, G., 1991, Personal Communications.

Onik, G., Porterfield, B., Rubinsky, B., and Cohen, J., 1991a, "Percutaneous Transperineal Cryosurgery Using Transrectal Ultrasound Guidance," *Urology*, Vol. 37, pp. 277–281.

Onik, G., Rubinsky, B., Zemel, R., Weaver, L., Diamond, D., Cobb, C., and Porterfield, B., 1991b, "Ultrasound-Guided Hepatic Cryosurgery in the Treatment of Metastatic Colon Carcinoma," *Cancer*, Vol. 67, pp. 901–907.

Pennes, H. H., 1948, "Analysis of Tissue and Arterial Blood Temperature in the Resting Human Forearm," *Journal of Applied Physiology*, Vol. 1, pp. 93–102.

Powell, M. J. D., 1964, "An Efficient Method for Finding the Minimum of a Function of Several Variables Without Calculating Derivatives," *The Computer Journal*, Vol. 7, pp. 155–162.

Press, W. H., Flannery, B. P., Teukolsky, S. A., and Vetterling, W. T., 1981, *Numerical Recipes*, Cambridge University Press, New York, pp. 289–293.

Rubinsky, B., and Shitzer, A., 1978, "Analytical Solutions to the Heat Equation Involving a Moving Boundary With Applications to the Change of Phase Problem (the Inverse Stefan Problem)," ASME JOURNAL OF HEAT TRANSFER, Vol. 100, pp. 300–304.

Rubinsky, B., Lee, C. Y., Bastacky, J., and Hayes, T. L., 1987, "The Mechanism of Freezing in Biological Tissue in the Liver," *Cryoletters*, Vol. 8, pp. 370–381.

Spendly, W., Hext, G. R., and Himsworth, F. R., 1962, "Sequential Application of Simplex Designs in Optimization and Evolutionary Operation," *Technometrics*, Vol. 4, p. 441.

Staub, N. C., and Storey, W. F., 1967, "Relation Between Morphological Events in Lung Studied by Rapid Freezing," *Journal of Applied Physiology*, Vol. 17, pp. 381–390.

Vanderby, R., Paliwal, B. R., Wakai, R. T., Belloi, D. M., Partington, B. P., Steeves, R. A., and Heiner, J. P., 1988, "A Parametric Study of Temperature Distribution in Ferromagnetic Hyperthermia," in: *Computational Methods in Bioengineering*, R. L. Spilker and B. R. Simon, eds., ASME, New York, pp. 291–299.

Downloaded 13 Dec 2010 to 193.140.21.150. Redistribution subject to ASME license or copyright; see http://www.asme.org/terms/Terms_Use.cfm

Effect of Surface Deformations on Contact Conductance

M. Williamson

A. Majumdar[1]

Department of Mechanical and Aerospace Engineering, Arizona State University, Tempe, AZ 85287

This study experimentally investigates the influence of surface deformations on contact conductance when two dissimilar metals are brought into contact. Most relations between the contact conductance and the load use the surface hardness to characterize surface deformations. This inherently assumes that deformations are predominantly plastic. To check the validity of this assumption, five tests were conducted in the contact pressure range of 30 kPa to 4 MPa, with sample combinations of (I) smooth aluminum–rough stainless steel, (II) rough aluminum–smooth stainless steel, (III) rough copper–smooth stainless steel, (IV) smooth copper–rough stainless steel, and (V) smooth aluminum–smooth stainless steel. The experimental results of tests I, II, and IV indicate that the conductance of the first load–unload cycle showed hysteresis, suggesting that the plastic deformation was significant. However, for subsequent load cycles, no conductance hysteresis was observed, implying that elastic deformation was predominant. In contrast, no conductance hysteresis was observed for all load–unload cycles of tests III and V. Therefore, the surface deformation for this combination was always predominantly elastic. In practical applications where plastic deformation is significant for the first loading, mechanical vibrations can produce oscillating loads, which can finally lead to predominance of elastic deformation. Comparison of the results of tests II and V show that even though plastic deformation was significant for the first loading of a rough aluminum surface, elastic deformation was always predominant for the smoother aluminum surface.

Introduction

When two solid materials are brought into contact, the presence of surface roughness leads to contact only at discrete spots. Consequently, the real area of contact is normally a fraction of the apparent cross-sectional area. During heat flow across the interface, the reduction in available area results in a high thermal resistance and a temperature jump, ΔT_j, across the interface. This is qualitatively shown in Fig. 1. The high interface or contact resistance can be very detrimental in applications where heat must be dissipated in an effort to reduce temperatures. With the trends toward higher densities of microelectronic circuitry and its increasing demand on dissipating high thermal loads, contact resistance has become a key issue in thermal management of microelectronic packages (Yovanovich, 1987; Fletcher, 1988).

At the contact interface, there are two channels for heat flow: one through the solid–solid contact spots and the other through the material in the interstitial gap. Most theoretical and experimental studies (Tien, 1968; Cooper et al., 1969; Thomas and Probert, 1970; Mikic, 1974; Yovanovich et al., 1983; Madhusudana and Fletcher, 1983) on solid–solid conductance of nominally flat metal surfaces have related the nondimensional conductance and load as

$$\frac{h\sigma}{\sigma' k} = C\left(\frac{F}{HA_a}\right)^n \tag{1}$$

where h is the contact conductance, σ is the combined standard deviation of the surface heights of the two surfaces $\sigma = \sqrt{\sigma_1^2 + \sigma_2^2}$, σ' is the combined standard deviation of the surface slopes, k is the harmonic mean of the thermal conductivities of the two contacting solids, F is the applied load, H is the microhardness of the softer material, A_a is the apparent cross-sectional area, C is a constant, and n is the load exponent.

Previous investigations have found different values for the load exponent, n, ranging from 0.66 (Malkov, 1970; Madhusudana and Fletcher, 1983) to 0.99 (Cooper et al., 1969). The most commonly used values are $n = 0.95$ and $C = 1.25$ (Yovanovich et al., 1983). Song and Yovanovich (1988) have shown the dependence on the relative contact pressure, F/HA_a, on parameters such as the bulk hardness, H_b, rms height and slope, pressure, F/A_a, indentation diagonal of Vickers microhardness measurements, d_V, and constants for Vickers microhardness correlations. Although Eq. (1) is frequently used for predicting the solid–solid conductance for a given load and material properties, there are several questions about its validity. These concern the load exponent n, mean slope σ', the surface hardness H, and the type of surface deformations.

Since the microhardness, H, is used in Eq. (1), it is inherently assumed that the surface deformation is predominantly plastic. To determine if surfaces in contact deform elastically or plastically, Greenwood and Williamson (1966) introduced a plasticity index, ψ, defined as

$$\psi = \frac{E}{H}\sqrt{\sigma \cdot \sigma''} \tag{2}$$

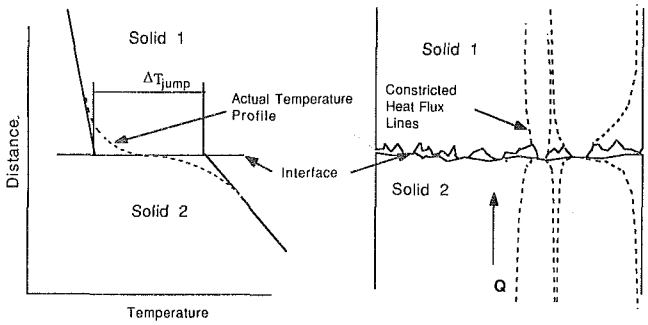

Fig. 1 Schematic diagram of imperfect contact resulting in contact resistance and temperature jump

[1]Current address: Department of Mechanical and Environmental Engineering, University of California, Santa Barbara, CA 93106-5070.

Contributed by the Heat Transfer Division for publication in the JOURNAL OF HEAT TRANSFER. Manuscript received by the Heat Transfer Division November 1991; revision received May 1992. Keywords: Conduction, Thermal Packaging. Associate Technical Editor: L. S. Fletcher.

Copyright © 1992 by ASME
Downloaded 13 Dec 2010 to 193.140.21.150. Redistribution subject to ASME license or copyright; see http://www.asme.org/terms/Terms_Use.cfm

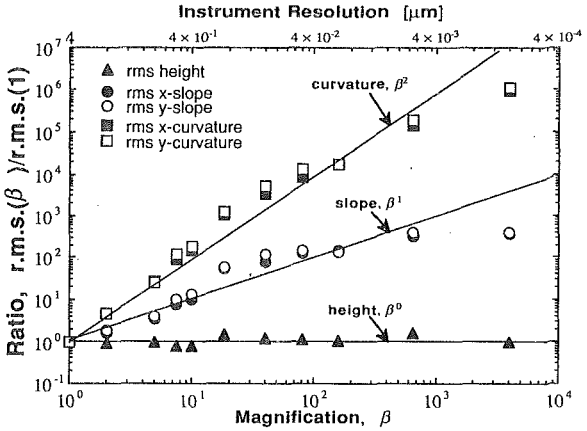

Fig. 2 Variation of rms height, slope, and curvature as a function of instrument resolution (Bhushan et al., 1988); data for $\beta > 40$ were obtained by atomic force microscopy (Oden et al., 1991)

where E is the combined elastic modulus and σ'' is the combined standard deviation of the surface asperity curvatures. They concluded that for $\psi > 1.0$, the surface deformation is predominantly plastic, whereas for $\psi < 0.6$ the surface deformation is predominantly elastic. For most engineering surfaces, they have found that $\psi > 1.0$, suggesting that surface deformations are predominantly plastic. Mikic (1974) used the parameter

$$\gamma = \frac{H}{E\sigma'} \tag{3}$$

to determine if elastic or plastic deformation was dominant. For $\gamma \geq 3$, the deformation is predominantly elastic and for $\gamma \leq 0.33$, the deformation is predominantly plastic. He also developed conductance-load relations for (*a*) plastic deformation, (*b*) plastic deformation considering plastic flow, (*c*) plastic deformation with a correction for elastic displacement, and (*d*) elastic deformation.

Roughness measurements over several decades of length scales have shown that the mean slope, σ', and curvature, σ'', of a rough surface depend on the resolution of the roughness measuring instrument. As an example, observe the dependence of the ratio of rms values at a magnification of β with that at magnification of unity, on the magnification of the surface in Fig. 2. Also provided are the corresponding resolutions of the roughness measuring instrument. The surface considered was that of a commercial magnetic tape. The measurements for $\beta < 40$ were obtained by optical interferometry (Bhushan et al., 1988) and those for $\beta > 40$ corresponding to nanometer-scale resolution were obtained by atomic force microscopy (Oden et al., 1992). It is clear that although the rms height does not depend on the instrument resolution, the rms slope and curvature show a strong dependence. Although the measurements are for a magnetic tape surface, the dependence of the rms slope on instrument resolution has also been shown analytically (Majumdar and Tien, 1991; Majumdar and Bhushan, 1990, 1991). Since different instrument resolutions will yield different values of σ' and σ'' for the same surface, the values of ψ and γ in Eqs. (2) and (3) would be scale-dependent. Therefore, these statistical parameters *cannot* be used to predict whether surface deformations are elastic or plastic. Hence the question of whether surface deformations are elastic or plastic remains open.

To eliminate the scale-dependence problem associated with determining the σ' and σ'', Majumdar and Tien (1991) have characterized surface roughness using scale-independent fractal parameters, such as the fractal dimension of the surface profile, D, which varies between 1 and 2, and a roughness parameter G. These parameters can be found by obtaining the structure function $S(\tau)$ of the profile $z(x)$ of a rough surface, as

$$S(\tau) = \langle (z(x+\tau) - z(x))^2 \rangle \tag{4}$$

where $\langle \ldots \rangle$ implies spatial averaging. Details of how to calculate the structure function can be found from Majumdar et al. (1991) and Majumdar and Tien (1991). For a fractal roughness profile, $S(\tau)$ follows a power law with τ as (Majumdar and Bhushan, 1990)

$$S(\tau) = \xi G^{2(D-1)} \tau^{(4-2D)} \tag{5}$$

where ξ is a constant and is a function of fractal dimension D. The roughness parameter G is a scaling constant that has units of length. An increase or decrease in the value of G implies a proportional increase or decrease of the roughness amplitude over all length scales. Using this fractal analysis, Majumdar and Tien (1991) have theoretically explained the origins of the load-exponent and found it to be equal to $\eta D/2$ where D is the fractal dimension and η is the exponent in the area-load relation $A_r \sim F^{\eta}$, where A_r is the real area of contact.

Based on the fractal characterization, Majumdar and Bhushan (1991) recently developed a model of contact between a rough and a smooth hard surface. They found that for a particular combination of contacting surfaces, there exists a critical length, l_c, of the contact spot lateral size defined as

Nomenclature

a = radius of contact spot, m
A = area, m^2
C = constant defined in Eq. (1)
D = fractal dimension
E = combined elastic modulus of contacting surfaces, Nm^{-2}; $1/E = (1-\nu_1^2)/E_1 + (1-\nu_2^2)/E_2$
F = load, N
G = fractal roughness parameter, m
h = conductance, $Wm^{-2}K^{-1}$
H = microhardness of the softer material, Nm^{-2}
k = harmonic mean of the thermal conductivity, $Wm^{-1}K^{-1}$; $1/k = 1/k_1 + 1/k_2$
l_c = critical contact spot size for plastic–elastic transition
n = load exponent defined in Eq. (1)
F = load on surface, N
q = heat flux, Wm^{-2}
R_a = roughness average, m
$S(\tau)$ = structure function, m^2
T = temperature, K
$z(x)$ = surface height at a lateral position x, m
β = magnification of a surface
γ = plasticity parameter in Eq. (3)
η = load-exponent for area-load relation
ν = Poisson ratio
ξ = constant defined in Eq. (5)
σ = combined standard deviation of height of two surface, m; $[\sqrt{\sigma_1^2 + \sigma_2^2}]$
σ' = combined standard deviation of slope of two surfaces $[\sqrt{\sigma_1'^2 + \sigma_2'^2}]$
σ'' = combined standard deviation of curvature of two surfaces, m^{-1} $[\sqrt{\sigma_1''^2 + \sigma_2''^2}]$
τ = lag parameter used to find structure function, m
ψ = plasticity index, defined in Eq. (2)

Subscripts

1, 2 = refer to the two contacting surfaces
a = apparent area
b = bulk
r = real area of contact
j = jump

Downloaded 13 Dec 2010 to 193.140.21.150. Redistribution subject to ASME license or copyright; see http://www.asme.org/terms/Terms_Use.cfm

$$l_c = \frac{G}{(H/2E)^{1/(D-1)}} \tag{6}$$

All spots smaller than l_c deform plastically, whereas spots larger than l_c deform elastically. Since solid–solid conductance is dominated by larger spots, it is possible that the *elastic* deformation is more relevant for contact conductance. When a surface is made smoother, the value of G decreases, thus making the critical length l_c smaller. This results in a larger fraction of contact spots to be in elastic deformation. Therefore surface smoothening tends to make elastic deformation more dominant.

It is evident for the scale dependence of σ' and σ'' that prediction of elastic or plastic surface deformations by classical theories can lead to errors. The new contact model based on fractal parameters suggests that if the critical size l_c is small compared to the largest contact spot, elastic deformation may be dominant. This paper attempts to answer some of the questions raised in this controversy regarding the type of surface deformations. Experiments using rough and smooth stainless steel, aluminum, and copper samples reveal interesting results on the type of deformations. In a recent study, Stevenson et al. (1991) measured the contact conductance across rough–smooth interfaces of stainless steel and nickel. The aim of their study was to observe the effect of heat flow direction on conductance. In contrast, this present work does not investigate directional effects, but focuses on the contributions of elastic and plastic deformation on conductance by observing the difference in conductance during loading and unloading.

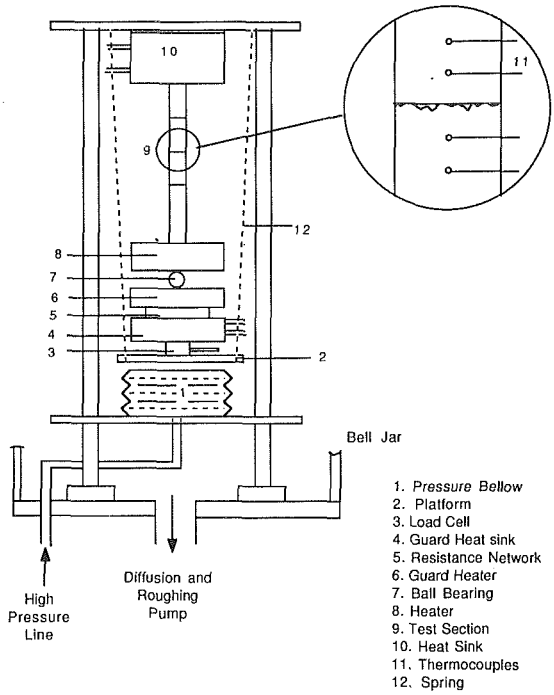

Fig. 3 Schematic diagram of experimental apparatus used for contact conductance tests and thermal conductivity measurements

Experiments

Apparatus. The experimental apparatus consisted of a data acquisition system, vacuum pumps, and a vacuum chamber containing a test column. The test column contained the load application and measurement systems, heat sources and sinks, thermocouples, and an alignment system.

A vacuum environment was required to isolate the solid–solid conductance from the effect of interstitial gas and to reduce natural and forced convection. The vacuum system consisted of a pyrex bell jar, 45.7 cm in diameter and 76.2 cm in height, placed on a stainless steel base plate. The vacuum chamber was evacuated using an oil diffusion pump in conjunction with a mechanical roughing pump. The operating vacuum pressure was less than 5×10^{-5} Torr.

The test column, shown in Fig. 3, was housed on a metal framework inside the vacuum chamber. From bottom to top the column consisted of (1) pressure bellow, (2) platform, (3) load cell, (4) guard cooler, (5) high thermal resistance network, (6) guard heater, (7) ball bearing, (8) heater, (9) test area, and (10) heat sink.

The pressure bellow was used to load the sample and was made of stainless steel. To prevent the top surface from warping during loading, a rigid stainless steel plate was welded onto the bellow. To load the specimens, the test column was first aligned and placed on a support platform. The height of the platform was adjustable such that the test specimens would barely come in contact. A gap was left between the platform and the pressure bellow, which allowed room for expansion of the bellow when the chamber was evacuated. This arrangement prevented any preloading of the sample. The ball bearing assured that the load was distributed evenly throughout the test column. The load was applied from below so that the minimum applied pressure was determined solely by the weight of the top specimen, the resolution of the load cell, and the resolution to which air can be pressurized in the bellow. In contrast, the minimum load by top-loading is determined by the weight of all the fixtures above the specimen interface. The bellow was connected to a high-pressure line and a vacuum line, which were both connected to the building services. The high-pressure line operates at 1.01 MPa, which was monitored with a pressure transducer.

An 80 W electric band heater (8) supplied heat to the test specimens. Heat was removed using a cooling coil (10), or heat sink. Chilled water from building services flowed through the cooling coil. The heating unit was insulated from the rest of the apparatus by a guard heater (6). The insulating effect was created by adjusting the guard heater power so that there was no temperature difference across the ball bearing (7) separating the two heaters. To absorb the downward heat flow from the guard heater, a cooling coil (4) was used. This guard heat sink was attached to the same cooling water supply as that of cooling coil (10). A high thermal resistance network (5) was placed between the guard heater and the guard heat sink. The guard heat sink also kept the load cell (3) at a constant temperature and reduced the time required for thermal equilibrium to be achieved in the apparatus.

Since the heating and the cooling blocks were much larger in diameter than the test samples, radial temperature gradients would exist in the samples. To distribute the heat evenly through the specimens, heat spreaders were used at both the heating and cooling ends of the test column. The heat spreaders were of the same diameter as the test specimens and were made of aluminum. A radiation barrier was placed around the circumference of the test column to reduce radiation losses.

After the specimens were aligned and all the equipment was turned on, the vacuum chamber were attached and evacuated. The test column was allowed to reach equilibrium such that none of the thermocouple readings changed by more than 0.25°C within a twenty minute interval. Pressure was then applied to the bellows to apply load on the samples. The second, and subsequent, data points were recorded after the equilibrium criterion was met. After the last data point was recorded during loading, the load was reduced. Data points were taken during unloading in an identical fashion.

Test Specimens. The test samples are cylindrical in shape, 2.54 cm in diameter and 3.175 cm long. Two types of samples were used: ones with rough surfaces and ones with smooth surfaces. The contact surfaces of the smooth samples were

Downloaded 13 Dec 2010 to 193.140.21.150. Redistribution subject to ASME license or copyright; see http://www.asme.org/terms/Terms_Use.cfm

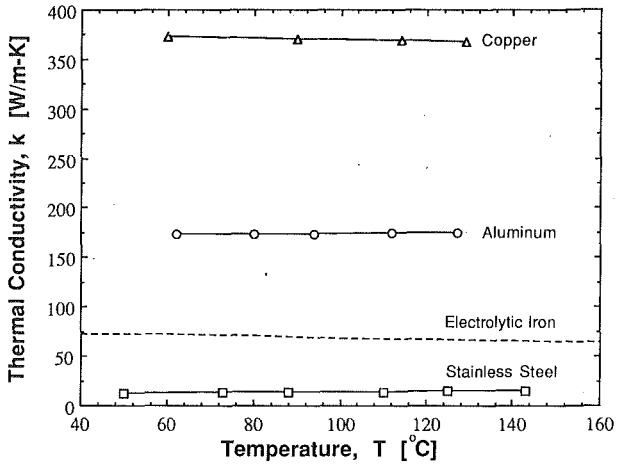

Fig. 4 Measured variation of thermal conductivity for copper, aluminum, and stainless steel samples and electrolytic iron

lapped. The contact surfaces of the rough samples were first lapped, then milled and finally bead blasted. The rough copper samples were annealed previous to milling and bead blasting. The samples were cleaned in degreasing and de-oxidizing agents in an ultrasonic bath. The noncontact surfaces of all the samples were lapped smooth and coated with a high-thermal-conductivity grease. The temperature gradient through the specimens and the subsequent temperature jump across the interface were measured using type-K thermocouples placed along the length of the samples at 0.635 cm intervals. The thermocouples were inserted in holes of diameter 1.092 cm drilled to the axis of the cylindrical specimens. To ensure good contact between the thermocouples and the test specimens, thermal grease was inserted in the thermocouples holes.

Before the experiments were conducted, one additional sample of each material was made from each bar stock. The samples were placed between two heat meters and placed in the apparatus. The heat meters were made of electrolytic iron, for which the thermal conductivity is known as a function of temperature. A thermal gradient was imposed and measured through the samples. The heat flux through the meters and sample were calculated, and the thermal conductivity of each material was determined as a function of temperature as shown in Fig. 4. These measured thermal conductivities were used to obtain the heat flux through the sample in the contact conductance experiments.

The surface microhardness of each sample was measured at room temperature using a Knoop microhardness tester. The test involved penetration of the surface by a silicon carbide indenter where the length of the penetration was correlated to the microhardness. At least four measurements of each sample were taken. For each of the smooth samples, the measured values were within 10 percent of each other. For rough samples, the indentation depth was of the order of the surface roughness. This gave rise to uneven indentation, which led to significant variations in the measured microhardness. It is due to the inaccuracy in the microhardness measurements that no attempt was made to use the data to nondimensionalize the load. Therefore, the errors in the hardness measurements did not appear in the final error analysis of the conductance measurements.

The surface roughness of each sample was measured using a diamond stylus profilometer. The R_a value was provided for the smooth surfaces, which was used to determine the rms value or the standard deviation as (Thomas, 1982)

$$\sigma = \sqrt{\frac{\pi}{2}} R_a \tag{7}$$

Table 1 Roughness and material properties of the rough and smooth copper, aluminum, and stainless steel samples

Sample*	R.m.s. roughness (μm)	Hardness (MPa)	Elastic Modulus (GPa)
Smooth Samples			
Aluminum (I)	0.48	932	68.9
Aluminum (V)	0.47	947	-
Copper (IV)	0.47	1367	107.5
Stainless Steel (II)	0.40	2757	197.2
Stainless Steel (III)	0.41	2653	-
Stainless Steel (V)	0.27	2755	-
Rough Samples			
Aluminum (II)	8.71	564	68.9
Copper (III)	9.30	1073	107.5
Stainless Steel (I)	6.54	2958	197.2
Stainless Steel (IV)	5.66	4207	--

*The roman numbers in parenthesis correspond to the test where the samples were used.

Table 2 Fractal parameters of each material

Specimen Material	Fractal Regime	Fractal Dimension, D	Roughness Parameter, G [m]
Aluminum	first, $\tau < 16\mu m$	1.129	3.30×10^{-12}
	second, $\tau > 16\mu m$	1.734	1.58×10^{-6}
Copper	first, $\tau < 16\mu m$	1.186	1.65×10^{-10}
	second, $\tau > 16\mu m$	1.762	9.00×10^{-7}
Stainless Steel	first, $\tau < 8\mu m$	1.124	6.33×10^{-13}
	second, $\tau > 8\mu m$	1.723	5.47×10^{-7}

by assuming a Gaussian distribution of the surface heights. The profiles of the rough samples were analyzed directly to determine the rms value of the roughness. Table 1 lists the properties of the different samples including the elastic modulus (Burmeister et al., 1978).

One additional rough sample of each material was made from each bar stock in a fashion identical to the rough test samples. Three 1-mm-long profiles of each rough material were taken. These data were used to determine the structure function, $S(\tau)$, of the rough surfaces. These parameters are assumed to be the same for each material, although only one sample of each material was analyzed in this manner. The structure functions taken from one trace of each material are shown in Fig. 5 where it is clear that there are two regimes of fractal structure that join at a length scale of around 20 μm. Although G and D change for the different regimes, they remain constant over the span of length scale in each regime. The length scale of 20 μm is possibly the size of the sand grains used for blasting. The Al surface is rougher at larger length scales, since the Al is softer than the other metals, thereby incurring larger deformations. However, below 20 μm all surfaces appear to the same, thereby suggesting that the lapping and milling process produced the same roughness in all three materials below 20 μm. Table 2 lists the fractal properties of the different sample materials.

Experimental Procedure. Four tests were conducted on the contact of rough and smooth interfaces of dissimilar metals. These were: (I) smooth aluminum in contact with rough stain-

Downloaded 13 Dec 2010 to 193.140.21.150. Redistribution subject to ASME license or copyright; see http://www.asme.org/terms/Terms_Use.cfm

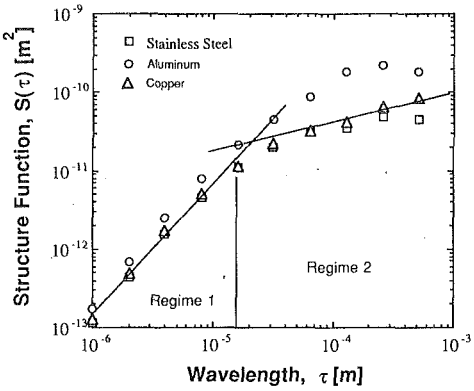

Fig. 5 Structure function of the sandblasted rough surfaces of aluminum, copper, and stainless steel

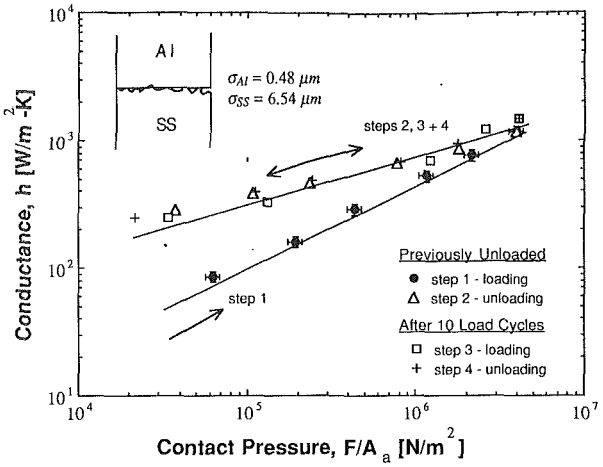

Fig. 6 Conductance as a function of load measured for smooth aluminum surface in contact with a rough stainless steel surface during loading and unloading. Error bars for the conductance and the load are provided for the first loading.

less steel, (II) rough aluminum in contact with smooth stainless steel, (III) rough copper in contact with smooth stainless steel, (IV) smooth copper in contact with rough stainless steel. The final test was: (V) smooth aluminum in contact with smooth stainless steel. The heat flow direction for all tests was from the stainless steel to the other sample. This was done to eliminate any directional effects. Unless noted, the test pairs remained in contact during the entire test.

Since stainless steel is harder than aluminum, the first two tests were aimed at studying the effect of the penetration of stainless steel asperities (test I) as opposed to deformation of aluminum asperities (test II). Tests III and IV were also designed for the same reason with the difference that copper is harder than aluminum and might show interesting deformation behavior. To study the effect of surface roughness on the predominance of elastic or plastic deformation, test V was conducted to compare the results with test II.

To determine whether elastic or plastic deformation was dominant at the surface, the following procedure was adopted. For both types of interface, the first conductance measurements were obtained for *freshly* prepared surfaces, while *increasing* the load. The fresh surfaces were not deformed between the time they were made to the time of the first test, which prevents previous plastic deformation from interfering with the test results. After a maximum load was reached, similar measurements were taken for decreasing load. If plastic deformation of the surface occurs, one would expect to observe an increase in the conductance during unloading over that during initial loading. However, if the surface deformation is predominantly elastic, the increase and decrease of real area of contact during loading and unloading, respectively, are reversible. Hence there would not be any difference in the measured conductance. To ensure that any plastic deformation in the load range is complete after the first load-unload cycle, the interface underwent ten load cycles to the same peak load as the first cycle. Conductance measurements were again made on the same surfaces during the subsequent load cycle.

Results and Discussion

The measured temperature profile in each sample was linear, indicating an absence of transients. The temperature profile was extrapolated to the interface to obtain the temperature difference ΔT_j at the interface. Using the measured thermal conductivities, the heat flux q for each sample in contact was found as $q = -kdT/dz$, where dT/dz is the measured temperature gradient. The heat flux through the two contacting samples differed by only a few percent. The contact conductance, h, was then found by the relation

$$h = \frac{q}{\Delta T_j} \tag{8}$$

where q is the heat flux through the stainless steel sample. The heat flux through the stainless steel was used because the temperature gradient was much larger than that in the other samples, which results in more accurate predictions.

The error in the measured contact conductance was found by performing an error analysis that included errors in the measured temperature gradient, thermal conductivity, and temperature jumps at the interface. The analysis showed that the errors in the contact conductance was no more than 6 percent. The error in the contact pressure was found to be no more than 5.5 percent. For each of the following test results, the error bars for conductance and load are shown for the first loading of the fresh surfaces.

(Test I) Smooth Aluminum–Rough Stainless Steel Interface. The results of this conductance test are shown in Fig. 6. The conductance during the initial unloading (step 2) was greater than that for the initial loading (step 1) for the same applied pressure. This implies that there was a significant amount of plastic deformation during the initial loading. However, since conductance was still a function of load during unloading, elastic recovery (springing back) must be significant. For the surface to spring back during unloading, it must have deformed elastically during the initial loading also. After unloading, the samples underwent ten loading cycles at an elevated temperature[2] of 80°C to the same maximum load as step 1. The subsequent load–unload cycle (steps 3 and 4) resulted in the same conductance-load relationship as the unloading of step 2. The repeatability of these three steps strongly suggests that the dominant mode of surface deformation becomes elastic. The majority of plastic deformation was completed in step 1.

(Test II) Rough Aluminum–Smooth Stainless Steel Interface. The results of this test were very similar to those of the rough stainless steel–smooth aluminum test. Figure 7 shows a significant conductance increase during the first unloading (step 2) from the first loading (step 1). The conductance during unloading was still a function of load. The samples then underwent ten load–unload cycles at an elevated temperature to the same maximum load as the first cycle. The results of the subsequent load–unload cycle (steps 3 and 4) matched those of step 2. This again implies that the surfaces deform elastically for these three steps and that any plastic deformation occurred during step 1.

[2]This elevated temperature is roughly the same as the mean interface temperature during the test load cycles.

Downloaded 13 Dec 2010 to 193.140.21.150. Redistribution subject to ASME license or copyright; see http://www.asme.org/terms/Terms_Use.cfm

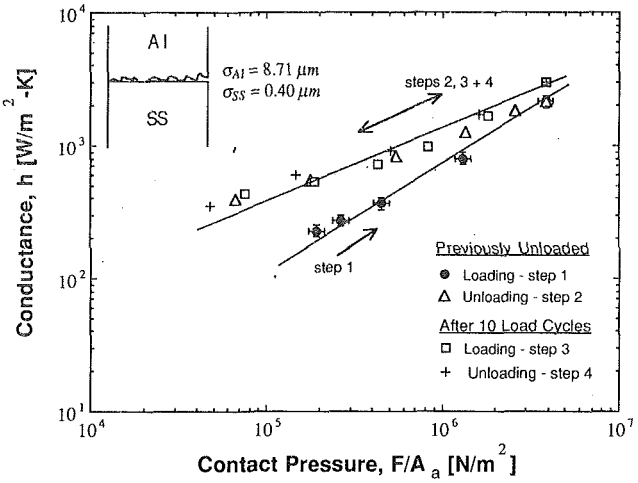

Fig. 7 Conductance as a function of load measured for rough aluminum surface in contact with a smooth stainless steel surface during loading and unloading. Error bars for the conductance and the load are provided for the first loading.

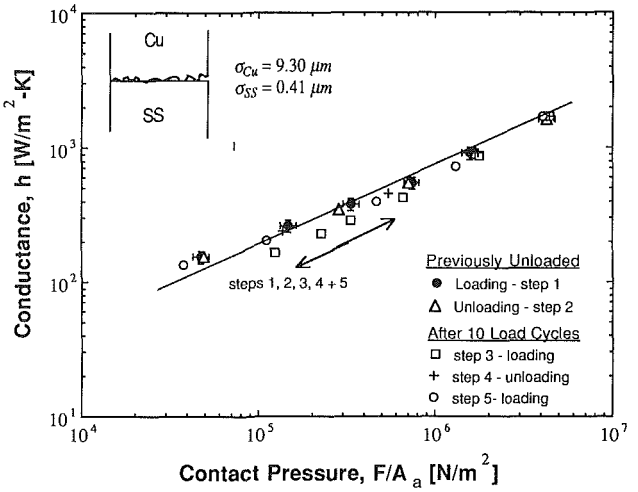

Fig. 8 Conductance as a function of load measured for rough copper surface in contact with a smooth stainless steel surface (test III) during loading and unloading. Error bars for the conductance and the load are provided for the first loading.

There was a slight increase in conductance for steps 3 and 4 over step 2 for high loads. It is possible that one or more of the ten load cycles exceeded the maximum load of step 1. This would result in additional plastic deformation. Since this additional plastic deformation did not manifest itself as higher conductance at lower loads, this suggest that the asperities of lower height were the ones to deform. At the lower loads, the asperities close to the surface were not in contact with the stainless steel and therefore did not enhance the conductance.

(Test III) Rough Copper–Smooth Stainless Steel Interface. Figure 8 shows the conductance measurements for a rough copper surface contacting a smooth stainless steel surface. It is evident that the data for the first loading (step 1) and subsequent unloading (step 2) agreed very well. After unloading, the interface was allowed to stay at the lowest load of 10^4 N/m^2 for about a day. Then, 10 loading–unloading cycles were applied to the interface at room temperature after which the conductance was again measured during both loading and unloading. It was observed that during loading (step 3), the measured conductance at low loads was slightly lower than that obtained earlier. However, the agreement was excellent at higher loads. In addition, the measurements during the subsequent unloading (step 4) were also in agreement with those measured for the first loading–unloading cycle, that is step 1 and step 2. To check whether the disagreement at low loads for step 3 was repeatable, the load was increased again. This time the measured conductance (step 5) was again in good agreement with those of steps 1, 2, and 4.

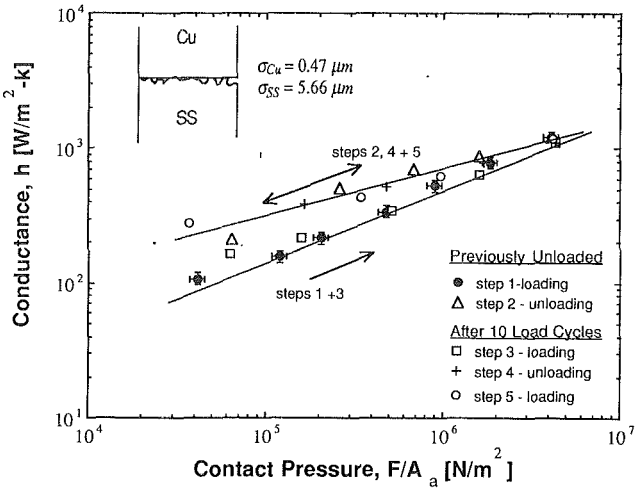

Fig. 9 Conductance as a function of load measured for smooth copper surface in contact with a rough stainless steel surface during loading and unloading. Error bars for the conductance and the load are provided for the first loading.

From these data, it is clear that for the load range in this experiment there is no difference in the measured conductance during loading and unloading. Since the conductance and the real area of contact are uniquely related, the experiments suggest that the increase and decrease of the real area of contact were reversible with load. Therefore, the dominant mode of deformations was *elastic*. However, the reason for the slight disagreement at low loads between step 3 and the other measurements is still unclear.

(Test IV) Rough Stainless Steel–Smooth Copper Interface. The conductance measurements for this sample combination are shown in Fig. 9. It is evident that the conductance during the first unloading (step 2) is greater than that for the initial loading (step 1). This implies that there was some plastic deformation of the surface. After the samples were unloaded (step 2), they were taken apart and the apparatus was shut down. Several days later, the samples were placed back in the apparatus and realigned to roughly the same position. It is important to note that the specimens were not in the exact position as before. The locations of contact spots for the initial load cycle would therefore be different than after they had been realigned. The samples then underwent ten load–unload cycles at room temperature to the same maximum pressure as for step 1. The apparatus was restarted and more data were taken. The results for the next loading (step 3), unloading (step 4), and subsequent loading (step 5) are shown in Fig. 9.

A hysteresis effect was observed between steps 3 and 4. Plastic deformation for this load range was therefore not complete during the ten load–unload cycles at room temperature. Due to the realignment, the plastic deformation of the original load cycle (steps 1 and 2) would not have a significant effect on steps 3, 4, and 5, since different spots would now be in contact. The subsequent load (step 5) followed the same path as that for the previous unloading (step 4). The state of the surface deformation was therefore the same at each load of steps 4 and 5. This suggests that, because the surface during step 4 was being deformed elastically, the surface during step 5 must also have deformed elastically. The plastic deformation was therefore complete for this load cycle.

Downloaded 13 Dec 2010 to 193.140.21.150. Redistribution subject to ASME license or copyright; see http://www.asme.org/terms/Terms_Use.cfm

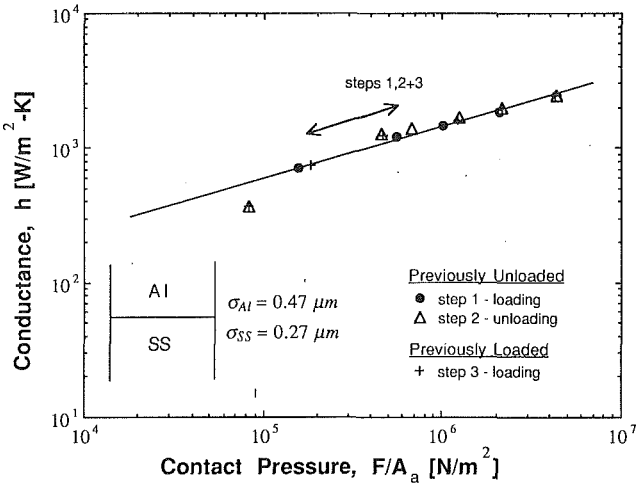

Fig. 10 Conductance as a function of load measured for smooth aluminum surface in contact with a smooth stainless steel surface during loading and unloading

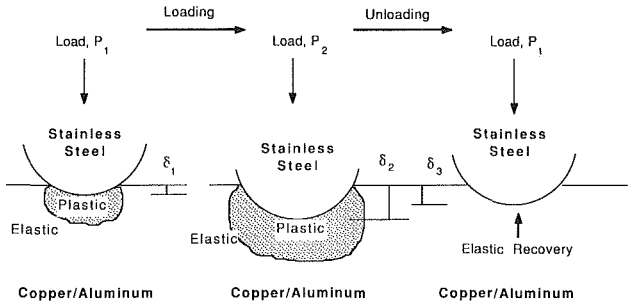

Fig. 11 Schematic diagram of the deformation process during loading and unloading for rough stainless steel surface in contact with smooth copper or aluminum

The question that arises is why was the plastic deformation not complete during the ten load-unload cycles at room temperature? One possible reason for this behavior may be due to the temperatures of the samples during loading. It has been found that even below the recrystallization temperature, the hardness of a monomorphic metal (copper and aluminum are two) reduces as the temperature increases (Savitsky and Sherby, 1957). This has been experimentally shown by Nho (1990) for aluminum, stainless steel, and nickel.

After the initial loading, the samples were taken apart and realigned, which does not guarantee that the same spots were placed back in contact. The new contact spots were then loaded ten times at room temperature ($\approx$24°C). The subsequent loading was done at the elevated temperature of approximately 80°C. The hardness during this loading was reduced, allowing the asperities, which deformed elastically at 24°C, to deform plastically even though the maximum load was not exceeded.

(Test V) Smooth Aluminum–Smooth Stainless Steel. Figure 10 shows the results of the conductance measurements for this sample combination. It is clear that the conductance during the first loading (step 1) and subsequent unloading (step 2) did not show any hysteresis. This suggests that elastic deformation was predominant even for the fresh surface. The load was then increased (step 3) without applying the ten load–unload cycles. The excellent agreement between the measured conductance of step 3 with those of steps 1 and 2 confirms the predominance of elastic deformation in all the steps.

Comparison of Test Results. Since the surface hardness and elastic modulus of copper and aluminum are less than those of stainless steel, the majority of the elastic and plastic deformation occurs in the aluminum or copper when in contact with stainless steel. For the sample combinations of a rough aluminum or copper sample in contact with a smooth stainless steel sample (tests II and III), the aluminum or copper asperities will deform. For the combination of rough stainless steel in contact with copper or aluminum (test I and IV), the stainless steel will penetrate the softer, less rigid surface. Since both stainless steel and aluminum surfaces were smooth in test V, it is difficult to say whether asperity deformation or penetration was dominant in this test.

In tests I, II, and IV, the measured conductance was greater during unloading and repeated loading than during the initial loading (step 1). Mikic (1971) predicted this trend by assuming that during loading the deformation is purely plastic while during unloading the deformation is elastic. An explanation for this behavior is provided in Fig. 11. As the stainless steel asperity penetrates the softer surface in (*a*), the softer material deforms plastically in the region close to the contact spot. Beyond that region the softer material (and to a lesser extent stainless steel) deforms elastically. As the load is increased, the softer material flows plastically to conform to the stainless steel asperities. This increases the actual contact area while increasing the depth of penetration, δ. More asperities then come in contact thereby increasing the conductance. The asperities cease to deform when (*b*) the maximum load is reached. The plastic deformation in (*a*) and (*b*) results in permanent deformation by producing dislocations. During unloading in (*c*), the surface and subsurface stresses relax elastically. However due to the permanent deformation, the contact spot size during unloading (*c*) is greater than during loading (*a*) for the same load. The displacement between mean surfaces is also reduced, resulting in more spots in contact. The larger area of contact at a single spot and the increased number of contact spots result in a higher conductance during unloading. Subsequent loading and unloading creates more subsurface dislocations. Finally the dislocation density increases so much that they lock each other, prohibiting any more permanent deformation. The surface then deforms only elastically as experimentally observed in tests I, II and IV. The hysteresis effect for a soft rough surface in contact with a smooth harder surface can be explained in a similar manner.

Table 3 provides the load exponent found for the initial loading and the final step for each test combination. It can be seen that the load exponents for the asperity deformation process were generally higher than those for the asperity penetration process. This trend is much more evident for the final step, which coincides with elastic deformation. The load exponents found for the initial loadings are significantly lower than those most commonly used in Eq. (1).

Comparing the results of the two sets of tests shows that there is more of a hysteresis effect in the aluminum–stainless steel combinations than in the copper–stainless steel combinations. This is to be expected due to the fact that aluminum is softer than copper. This trend is also qualitatively predicted by the fractal model for the rough aluminum and copper in contact with smooth stainless steel. Using the fractal parameters of each material found from the structure function and provided in Table 2, the critical length, l_c, for elastic deformation was found for both fractal regimes and is provided in Table 4. Since the critical length scales for the first regimes exceed the limits of this regime, it is concluded that all spots falling in the first regime must deform plastically. In the second fractal regime, the critical length scale of the rough copper–smooth stainless steel combination is less than that for the rough aluminum–smooth stainless steel combination. Therefore, it is likely that more copper contact spots will be in elastic deformation than aluminum contact spots. The predominance of elastic deformation in test III is probably a result of this. The critical length for the rough stainless steel asperities pen-

Downloaded 13 Dec 2010 to 193.140.21.150. Redistribution subject to ASME license or copyright; see http://www.asme.org/terms/Terms_Use.cfm

Table 3 Load exponent for initial loading and for repetitive loading; the load exponent for repetitive loading was determined for the final step.

Specimen Combination*	Asperity Behavior	Load Exponent, n†	Loading Cycle
Al s -SS r (I)	Penetration	0.637 (±0.027)	Initial
Al r - SS s (II)	Deformation	0.748 (±0.094)	
Cu r - SS s (III)	Deformation	0.522 (±0.053)	
Cu s -SS r (IV)	Penetration	0.547 (±0.056)	
Al s - SS s (V)	-	0.372 (±0.038)	
Al s -SS r (I)	Penetration	0.331 (±0.049)	Repetitive
Al r - SS s (II)	Deformation	0.445 (±0.069)	
Cu s -SS r (IV)	Penetration	0.376 (±0.116)	
Cu r - SS s (III)	Deformation	0.548 (±0.074)	
Al s - SS s (V)	-	0.36 (±0.052)	

*The roman numbers in parenthesis correspond to the test where the samples were used.

†The load-exponent was obtained by calculating the slope of the least-square straight-line fit of the log-log plot of conductance versus pressure. The numbers in the parenthesis are three times the standard deviation of the slope, calculated from the least-square analysis (Doeblin, 1975).

Table 4 Critical contact spot length for elastic-plastic deformation

Specimen Combination	Fractal Regime	Critical Contact Spot Length, ℓ_c
Al r - SS s (II)	first	3.63×10^6 m
	second	2.18 mm
Cu r - SS s (III)	first	69.34 m
	second	0.618 mm

etrating the smooth copper or aluminum were not determined. This is because the model that is used to determine the critical length of the contact spot is based on a model of asperity deformation (Majumdar and Bhushan, 1991).

Conclusions

This study makes several conclusions, which are described as follows:

1 The conductance during repeated loading for the smooth Cu-rough SS, rough Al-smooth SS, and smooth Al-rough SS sample combinations were greater than the conductance during the initial loading for the same applied pressure in the range of 30 kPa to 4 MPa. Therefore, significant *plastic* deformation of the surface occurred for the fresh surface. During repeated loadings of these sample combinations, the conductance was repeatable and still a function of the load. Therefore, *elastic* deformation contributed significantly to the overall surface deformation. In practical applications, if the plastic deformation is significant for the first loading, mechanical vibrations can induce oscillating loads, which can finally lead to predominantly elastic deformations.

2 The conductance measurements for the rough Cu-smooth SS and the smooth Al-smooth SS combinations were always repeatable during load cycling, for loads between 30 kPa and 4 MPa. The deformation for these combinations was therefore predominantly *elastic*, even for the first load cycle. The commonly used conductance-load relation assumes dominant plastic deformation and therefore cannot be used for such situations.

3 Comparison of results of the rough Al-smooth SS and smooth Al-smooth SS combinations suggests that even for a soft material like Al, the surface deformations are always predominantly *elastic* as the roughness is reduced to optical smoothness.

4 The hysteresis effect can be used to increase contact conductance. By preloading a contact interface beyond the maximum operating load encountered in practical applications, the hysteresis effect (assuming there is one) may increase the conductance through the contact substantially at low loads.

5 In general, the load exponent for the asperity penetration was lower than that for the asperity deformation for both material combinations during the initial and repeated loadings. Therefore, the contact area increases more with load for the asperity deformation than the asperity penetration. The type of deformation (asperity deformation or asperity penetration) is an important factor in determining the conductance-load relation.

Acknowledgments

The authors would like to express their gratitude to Motorola Inc. at Phoenix, IBM at Tucson, and Sloan Technologies at Santa Barbara for roughness measurements. This work was supported in part by the National Science Foundation through Grant No. CTS-9010311 and by the MAE Department of Arizona State University.

References

Bhushan, B., Wyant, J. C., and Meiling, J., 1988, "A New Three-Dimensional Non-contact Digital Optical Profiler," *Wear*, Vol. 122, pp. 301-312.

Burmeister, T., Avallone, E. A., and Burmeister, T., III, 1978, *Mark's Standard Handbook for Mechanical Engineers*, McGraw-Hill, New York.

Cooper, M. G., Mikic, B. B., and Yovanovich, M. M., 1969, "Thermal Contact Conductance," *International Journal of Heat and Mass Transfer*, Vol. 12, pp. 279-300.

Crandall, S. H., Dahl, N. C., and Lardner, T. J., 1978, *An Introduction of the Mechanics of Solids*, 2nd ed., McGraw-Hill, New York.

Doeblin, E. O., 1975, *Measurement Systems*, McGraw-Hill, New York, pp. 55-57.

Fletcher, L. S., 1988, "Recent Developments on Contact Conductance Heat Transfer," ASME JOURNAL OF HEAT TRANSFER, Vol. 110, pp. 1059-1070.

Greenwood, J. A., and Williamson, J. B. P., 1966, "Contact of Nominally Flat Surfaces," *Proceedings of the Royal Society of London*, Vol. A295, pp. 300-319.

Madhusudana, C. V., and Fletcher, L. S., 1983, "Solid Spot Thermal Conductance of Zircaloy-2/Uranium Dioxide Interfaces," *Nuclear Science and Engineering*, Vol. 83, pp. 327-332.

Majumdar, A., and Bhushan, B., 1990, "Role of Fractal Geometry in Roughness Characterization and Contact Mechanics of Surfaces," ASME *Journal of Tribology*, Vol. 112, pp. 205-216.

Majumdar, A., and Tien, C. L., 1990, "Fractal Characterization and Simulation of Rough Surfaces," *Wear*, Vol. 136, pp. 313-327.

Majumdar, A., and Bhushan, B., 1991, "Fractal Model of Contact Between Rough Surfaces," ASME *Journal of Tribology*, Vol. 113, pp. 1-11.

Majumdar, A., and Tien, C. L., 1991, "Fractal Network Model for Contact Conductance," ASME JOURNAL OF HEAT TRANSFER, Vol. 113, pp. 516-525.

Malkov, V. A., 1970, "Thermal Contact Resistance of Machined Metal Surfaces in a Vacuum Environment," *Heat Transfer-Soviet Research*, Vol. 2, pp. 24-33.

Mikic, B. B., 1971, "Analytical Studies of Contact of Nominally Flat Surfaces; Effect of Previous Loading," ASME *Journal of Lubrication Technology*, Vol. 93, pp. 451-456.

Mikic, B. B., 1974, "Thermal Contact Conductance: Theoretical Considerations," *International Journal of Heat and Mass Transfer*, Vol. 17, pp. 205-214.

Nho, K. M., 1990, "Experimental Investigation of Heat Flow Rate and Directional Effect on Contact Conductance of Anisotropic Ground/Lapped Interfaces," Ph.D. thesis, University of Waterloo, Canada.

Oden, P. I., Majumdar, A., Bhushan, B., Padmanabhan, A., and Graham, J. J., 1992, "AFM Imaging, Roughness Analysis and Contact Mechanics of Magnetic Tape and Head Surfaces," ASME *Journal of Tribology*, in press.

Savitsky, E. M., and Sherby, O. D., 1957, *The Influence of Temperature on the Mechanical Properties of Metals and Alloys*, Stanford University Press, Stanford, CA.

Downloaded 13 Dec 2010 to 193.140.21.150. Redistribution subject to ASME license or copyright; see http://www.asme.org/terms/Terms_Use.cfm

Song, S., and Yovanovich, M. M., 1988, "Relative Contact Pressure: Dependance on Surface Roughness and Vickers Microhardness," *J. of Thermophysics and Heat Transfer*, Vol. 2, No.1, pp. 43-47.

Stevenson, P. F., Peterson, G. P., and Fletcher, L. S., 1991, "Thermal Rectification in Similar and Dissimilar Metal Contacts," ASME JOURNAL OF HEAT TRANSFER, Vol. 113, pp. 30-36.

Thomas, T. R., and Probert, S. D., 1970, "Thermal Contact Resistance: The Directional Effect and Other Problems," *International Journal of Heat and Mass Transfer*, Vol. 13, pp. 789-807.

Thomas, T. R., 1970, *Rough Surfaces*, Longman, Inc., New York.

Tien, C. L., 1968, "A Correlation for Thermal Contact Conductance of Nominally-Flat Surfaces in Vacuum," *Proceedings of the 7th Thermal Conductivity Conference*, U.S. Bureau of Standards, pp. 755-759.

Yovanovich, M. M., DeVaal, J., and Hegazy, A. A., 1983, "A Statistical Model to Predict Thermal Gap Conductance Between Conforming Rough Surfaces," AIAA Paper No. 83-0888.

Yovanovich, M. M., 1987, "Theory and Applications of Constriction and Spreading Resistance Concepts for Microelectronic Thermal Management," *Proceedings of the International Symposium on Cooling Technology for Electronic Equipment*, Honolulu, HI.

Downloaded 13 Dec 2010 to 193.140.21.150. Redistribution subject to ASME license or copyright; see http://www.asme.org/terms/Terms_Use.cfm

Thermal Constriction Resistance of Phase-Mixed Metallic Coatings

K. C. Chung

J. W. Sheffield

H. J. Sauer, Jr.

Department of Mechanical and Aerospace Engineering
and Engineering Mechanics,
University of Missouri—Rolla,
Rolla, MO 65401

A phase-mixed coating using plasma-enhanced deposition onto a cold surface can offer excellent characteristics of adhesion of coatings to a wide range of base materials, and very close control of coating thickness. These physical characteristics are of great importance to the control of surface contact situations and in particular to the thermal constriction resistance of contact joints, with many applications in thermal control systems. Analytical expressions were developed for the thermal constriction resistance of cylindrical contact spots in such coatings. The thermal constriction parameter was presented in the dimensionless form as a function of the contact geometry, coating thickness, and thermal conductivity ratio of the two different coating materials. Finally, the results of analytical thermal constriction resistance were compared with experimental investigation using copper–carbon and silver–carbon phase-mixed coating materials. Conclusions on selecting phase-mixed coating materials were based solely on the thermal point of view.

1 Introduction

When two surfaces are brought into contact and heat is transferred across the interface, the thermal contact resistance is defined as the temperature drop across an interface divided by the heat flow rate through the interface. Recently, many research investigations have focused on reducing the thermal contact resistance and enhancing the thermal contact conductance at the interface of two materials. For most junctions, heat is transferred across the interface by conduction through actual contact spots, conduction through the substance in the gaps around the contact spots, radiation across the gaps, or a combination of all three modes of heat transfer. In order to enhance the thermal transfer across a junction, the area of contact spots should be increased or a soft substance should be inserted to increase the total contact area and improve the heat transfer at the junction. The most frequent techniques for reducing the thermal resistance include: (1) the insertion of interstitial materials or soft metallic foils to fill the voids, (2) the insertion of metallic screen material to increase the number and size of contacts, and (3) the use of surface treatments such as anodization and metallic coatings.

To analyze the heat flux across the coated interface, the effect of surface coatings on the thermal constriction resistance must be known. Antonetti and Yovanovich (1985) experimentally verified the theoretical model that was developed for nominally flat, rough contacting surfaces coated with a metallic layer. Under vacuum conditions and with negligible radiation heat flow through discrete contact spots at the interface, smoother bare contacting surfaces had lower thermal constriction resistance. A method was presented to reduce a coated joint to an equivalent bare joint by using the effective microhardness and effective thermal conductivity. O'Callaghan et al. (1983) developed a theoretical analysis to predict the optimal soft-coating thickness to be applied at a bare joint resulting in a minimum thermal contact resistance. An extensive experimental investigation was conducted by Kang et al. (1989). These different coating materials, lead, tin, and indium, were evaluated using four different thicknesses for each coating material. The results demonstrated that the optimum coating thickness achieved a minimum thermal contact resistance for a given contact pressure. A different contact geometry, i.e., a steel sphere in elastic contact with a flat nickel surface coated by a silver layer, was investigated analytically and experimentally by Fisher and Yovanovich (1989). They developed a simple model to predict the effect of a surface layer on the thermal constriction resistance of the sphere/layered flat contact and to verify the model by experimental measurements. Dryden (1983) analyzed the effect of a surface coating on the constriction resistance for a spot on an infinite half-plane. Results indicated that the thermal constriction resistance decreases hyperbolically with respect to the coating thickness when the coating thickness is greater than twice the contact spot radius. Theoretical solutions of thermal constriction resistance of a circular contact spot on a coated half-space were developed by Negus et al. (1988) for both heat flux and temperature-specified boundary conditions on the contact. Results showed that the thermal constriction resistance is based on an average contact temperature. However, the thermal constriction resistance is insensitive to the contact boundary condition for most practical purposes.

An experimental study of phase-mixed coatings by a new metallic coating technique, Transitional Buffering Interface (TBI), was conducted by Chung et al. (1991). The new process appears to offer excellent characteristics of adhesion of coatings to a wide range of base materials, and very close control of coating thickness, flatness, and roughness. These physical characteristics are of great importance to the control of surface contact situations of either metallic or nonmetallic joints. As far as is known to the authors, the influence of phase-mixed coatings on thermal constriction resistance has not been explored. Therefore, the thermal constriction resistance of a mixed coating layer needs to be studied extensively.

Theoretical Analysis

The typical thermal analysis model relating to the metallic coatings was proposed by Antonetti (1983), who verified the model using silver coatings on one contacting side of the paired nickel specimens. The phase-mixed coating model shown in Fig. 1 contains two regions. At the contact interface, heat enters one of many long right circular cylindrical contact spots with radius a. Region 1 is a mixed coating layer so that the thermal conductivity, k_1, is a function of distance along the z axis and the ratio of two different coating materials. Region 2 is a homogeneous substrate with constant thermal conductivity, k_2. An axisymmetric heat flux was prescribed over the contact area with the remainder of the plane defined by $z=0$ taken to be insulated. The other boundaries were also assumed adi-

Contributed by the Heat Transfer Division for publication in the JOURNAL OF HEAT TRANSFER. Manuscript received by the Heat Transfer Division November 1991; revision received April 1992. Keywords: Conduction, Materials Processing and Manufacturing Processes. Associate Technical Editor: L. S. Fletcher.

Copyright © 1992 by ASME
Downloaded 13 Dec 2010 to 193.140.21.150. Redistribution subject to ASME license or copyright; see http://www.asme.org/terms/Terms_Use.cfm

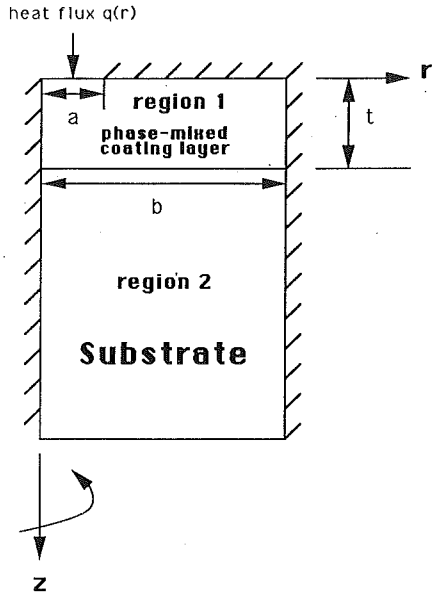

Fig. 1 A circular cylinder model for contact spot analysis

abatic. At a distance in the substrate far from the contact surface, the heat flow is uniform with a constant temperature gradient parallel to the Z axis.

Consider a two-dimensional, steady-state heat conduction problem, with the governing partial differential equations and boundary conditions of two regions as follows:

Region 1:

$$\frac{1}{r}\frac{\partial}{\partial r}\left(k_1 r\frac{\partial T_1}{\partial r}\right)+\frac{\partial}{\partial z}\left(k_1\frac{\partial T_1}{\partial z}\right)=0 \tag{1}$$

$$\frac{\partial T_1}{\partial r}(0, z)=0 \qquad 0\le z\le t \tag{2}$$

$$\frac{\partial T_1}{\partial r}(b, z)=0 \qquad 0\le z\le t \tag{3}$$

$$\frac{\partial T_1}{\partial z}(r, 0)=0 \qquad a<r\le b \tag{4}$$

$$-k_1\frac{\partial T_1}{\partial z}(r, 0)=q(r) \qquad 0\le r\le a \tag{5}$$

Region 2:

$$k_2\frac{1}{r}\frac{\partial}{\partial r}\left(r\frac{\partial T_2}{\partial r}\right)+k_2\frac{\partial}{\partial z}\left(\frac{\partial T_2}{\partial z}\right)=0 \tag{6}$$

$$\frac{\partial T_2}{\partial r}(0, z)=0 \qquad t\le z\le\infty \tag{7}$$

$$\frac{\partial T_2}{\partial r}(b, z)=0 \qquad t\le z\le\infty \tag{8}$$

$$-k_2\frac{\partial T_2}{\partial z}(r, \infty)=\frac{Q}{\pi b^2} \qquad 0\le r\le b \tag{9}$$

where

$$Q=\int_0^a 2\pi r q(r)\,dr$$

In addition to the preceding boundary conditions, both the heat flux and temperature continuity are required at the interface between region 1 and 2.

$$T_1=T_2 \quad z=t, \quad 0\le r\le b \tag{10}$$

$$k_1\frac{\partial T_1}{\partial z}=k_2\frac{\partial T_2}{\partial z} \qquad z=t, \qquad 0\le r\le b. \tag{11}$$

Using separation of variables and superposition techniques and applying the boundary conditions of Eqs. (7)–(9), we can determine the temperature distribution in region 2

$$T_2(r, z)=A_0-\frac{Q_z}{k_2\pi b^2}+\sum_{n=1}^{\infty}A_n J_0(\lambda_n r)e^{-\lambda_n z} \tag{12}$$

where A_0 is a constant and A_n is a series coefficient for temperature distribution in region 2. The boundary condition of Eq. (8) provided that $\lambda_n b$ are the roots of $J_1(\lambda_n b)=0$. The $J_1(\lambda_n b)$ is the Bessel function of the first kind of order one.

Within the phase-mixed coating layer, with no amorphous structure of the coatings and no lattice and oxygen defects in the coatings, the thermal conductivities of two different coating materials are k_h and k_s, respectively. Thus, the thermal conductivity of the phase-mixed coating layer is a function of three parameters, k_h, k_s and z. At the top coating surface ($Z=0$), the thermal conductivity of the TBI coating layer is equal to k_s and at the bottom coating surface ($z=t$), the thermal con-

Nomenclature

a = contact spot radius, m
A_0 = constant for temperature solution of region 2
A_a = apparent contact area, m^2
A_n = series coefficient for temperature solution in region 2
b = radius of heat flux tube, m
B_n = series coefficient for temperature solution in region 1
c = a constant $= tk_h/(k_s-k_h)$
C_n = series coefficient for temperature solution in region 1
E_0 = constant for temperature solution of region 1
F_0 = constant for temperature solution of region 1
H = microhardness, Pa
I_ν = modified Bessel function of the first kind of order ν
J_0 = Bessel function of first kind of order zero
J_1 = Bessel function of first kind of order one
k = thermal conductivity ratio of a substrate to phase-mixed coating layer $= k_2/k_s$
k_1 = variable thermal conductivity of the coating layer, W/mK
k_2 = thermal conductivity of the substrate, W/mK
k_h = thermal conductivity of the hard coating layer, W/mK
k_s = thermal conductivity of the soft coating layer, W/mK
k' = mean thermal conductivity, W/mK
K_ν = modified Bessel function of the second kind of order ν
m = thermal conductivity ratio inside a mixed coating layer $= k_s/k_h$
N = number of contact spots
p = constant in Eq. (19)
P = contact pressure, Pa
q = constant in Eq. (19)
q_0 = uniform heat flux over the contact spot, W/m^2
$q(r)$ = heat flux distribution on the contact spot, W/m^2

Downloaded 13 Dec 2010 to 193.140.21.150. Redistribution subject to ASME license or copyright; see http://www.asme.org/terms/Terms_Use.cfm

ductivity is equl to k_h. Therefore, the thermal conductivity for two different coating materials at the mixed coating layer can be reasonably given by:

$$\frac{1}{k_1}=\frac{1}{k_s}+\frac{z}{t}\left(\frac{1}{k_h}-\frac{1}{k_s}\right) \tag{13}$$

Using the same procedure in solving for the temperature distribution in region 2, two ordinary differential equations of region 1 can be obtained from Eq. (1).

$$\frac{d^2R}{dr^2}+\frac{1}{r}\frac{dR}{dr}+\lambda^2R=0 \tag{14}$$

$$\frac{d^2Z}{dz^2}+\frac{1}{k_1}\frac{dk_1}{dz}\frac{dZ}{dz}-\lambda^2Z=0 \tag{15}$$

First, consider the case where the separation constant, λ, is zero and apply the boundary conditions of Eqs. (2) and (3) leading to the first part of the temperature distribution in region 1

$$T_{1,0}(z)=F_0+\frac{E_0}{k_s}z+\frac{E_0}{2t}\left(\frac{1}{k_h}-\frac{1}{k_s}\right)z^2 \tag{16}$$

where E_0 and F_0 are constants.

If λ is negative, a temperature distribution of region 1 can be obtained. Otherwise, a trivial solution is produced. From Eq. (13), an expression is introduced for the thermal conductivity of region 1 to yield the following:

$$\frac{1}{k_1}\frac{dk_1}{dz}=-\frac{1}{z+\dfrac{tk_h}{k_s-k_h}}=-\frac{1}{z+c}. \tag{17}$$

Substituting Eq. (17) into Eq. (15), the second-order ordinary differential equation can be written as

$$\frac{d^2Z}{dz^2}-\frac{1}{z+c}\frac{dZ}{dz}-\lambda^2Z=0. \tag{18}$$

Introducing a new variable $x=\lambda(z+c)$, a general Bessel function equation form is obtained from Eq. (18).

$$x^2\frac{d^2Z}{dx^2}+px\frac{dZ}{dz}+q^2x^2Z=0 \tag{19}$$

where $p=-1$ and $q=i$.

We introduce the dependent variable change $Z=x^vy$ and rearrange Eq. (19) to give Bessel's equation

$$x\frac{d}{dx}\left(x\frac{dy}{dx}\right)+(q^2x^2-v^2)y=0 \tag{20}$$

Thus the solution of this equation is

$$Z(z)=x^v[B_nI_v(x)+C_nK_v(x)] \tag{21}$$

where I_ν and K_ν are the Modified Bessel functions of the first kind.

From Eq. (16) and a combination of the solutions of Eqs. (14) and (20), a complete temperature distribution of region 1 is given.

$$T_1(r,z)=F_0+\frac{E_0}{k_s}z+\frac{E_0}{2t}\left(\frac{1}{k_h}-\frac{1}{k_s}\right)z^2+\sum_{n=1}^{\infty}\lambda_n(z+c)[B_nI_1(\lambda_n(z+c))+C_nK_1(\lambda_n(z+c))]J_0(\lambda_nr) \tag{22}$$

Either B_n and C_n, an unknown constant, can be eliminated by invoking the perfect contact interface boundary conditions of Eqs. (10) and (11). Applying the boundary conditions of Eqs. (10) and (11), two additional equations were produced:

$$\lambda_n(t+c)[B_nI_1(\lambda_n(t+c))+C_nK_1(\lambda_n(t+c))]-A_ne^{-\lambda_nt}=0 \tag{23}$$

$$\lambda_n(t+c)[B_nI_0(\lambda_n(t+c))-C_nK_0(\lambda_n(t+c))]+A_ne^{-\lambda_nt}=0 \tag{24}$$

Comparing Eq. (23) to Eq. (24), we deduced that

$$B_n=\Theta(\lambda_n)C_n, \tag{25}$$

where

$$\Theta(\lambda_n)=\frac{K_0(\lambda_n(t+c))-K_1(\lambda_n(t+c))}{I_0(\lambda_n(t+c))+I_1(\lambda_n(t+c))}.$$

Hence the temperature distribution of region 1 can be expressed as

$$T_1(r,z)=F_0+\frac{E_0}{k_s}z+\frac{E_0}{2t}\left(\frac{1}{k_h}-\frac{1}{k_s}\right)z^2+\sum_{n=1}^{\infty}\lambda_n(z+c)C_n[K_1(\lambda_n(z+c))+\Theta(\lambda_n)I_1(\lambda_m(z+c))]J_0(\lambda_nr). \tag{26}$$

The final constant C_n can be determined by application of the boundary conditions of Eqs. (4) and (5). By substituting Eq. (26) into Eq. (5), multiplying both sides by $rJ_0(\lambda_nr)$, and

Nomenclature (cont.)

Q = total heat flow rate, W
r = radial coordinate, m
$R(r)$ = separation variable of the temperature distribution
R_c = thermal constriction resistance, K/W
R_t = total thermal constriction resistance, K/W
t = coating layer thickness, m
T_1 = temperature distribution in the coating layer, K
$T_{1,0}$ = temperature distribution in the coating layer for $\lambda=0$, K
T_2 = temperature distribution in the substrate, K
$\overline{T}_a$ = average temperature over the contact spot, K
$\overline{T}_b$ = average temperature over the contacting substrate interface, K
x = transfer axial coordinate $=\lambda(z+c)$, m
z = cylindrical coordinate system, m
$Z(z)$ = separation variable of the temperature distribution
$\Theta(\lambda_n)$ = function defined by Eq. (25)
$\Theta'(\lambda_n)$ = function defined by Eq. (33)
Ψ = dimensionless thermal constriction parameter
Ψ_1 = dimensionless thermal constriction parameter for isothermal boundary condition
Ψ_2 = dimensionless thermal constriction parameter for uniform heat flux boundary condition
ϵ = dimensionless radii ratio $=a/b$
β = dimensionless coating thickness $=t/a$
λ_n = roots for $J_1(\lambda_nb)=0$
ν = order of Bessel equation (=1 in Eq. (21))
μ = defined by Eq. (34)

Subscripts

n = series coefficient
h = hard material
s = soft material
1 = region 1
2 = region 2

Downloaded 13 Dec 2010 to 193.140.21.150. Redistribution subject to ASME license or copyright; see http://www.asme.org/terms/Terms_Use.cfm

then integrating from $r=0$ to $r=b$, one obtains C_n when the orthogonal Bessel functions are applied within the integration.

$$C_n=\frac{2t\int_0^a rJ_0(\lambda_n r)q(r)dr}{ck_1(0)\lambda_n^2 b^2 J_0^2(\lambda_n b)[K_0(\lambda_n c)-\Theta(\lambda_n)I_0(\lambda_n c)]} \tag{27}$$

The thermal constriction resistance R_c is given by

$$R_c=\frac{\overline{T}_a-\overline{T}_b}{Q} \tag{28}$$

where $\overline{T}_a$ is the average temperature over the contact spot, $\overline{T}_b$ is the average temperature over the contacting substrate interface, and Q is total heat flow rate passing through the real contact area.

$$\overline{T}_a=\frac{1}{\pi a^2}\int_0^a T_1(r,0)2\pi r dr \tag{29}$$

$$\overline{T}_b=\frac{1}{\pi b^2}\int_0^b T_1(r,0)2\pi r dr \tag{30}$$

The resulting expression for R_c was found by using Eqs. (26), (27), (28), (29), and (30) as:

$$R_c=\frac{2}{Q}\sum_{n=1}^{\infty}\lambda_n c C_n[K_1(\lambda_n c)+\Theta(\lambda_n)I_1(\lambda_n c)]\frac{J_1(\lambda_n a)}{\lambda_n a} \tag{31}$$

A dimensionless constriction parameter is defined as:

$$\Psi=4k_2 a R_c \tag{32}$$

Thus an expression for the thermal constriction parameter can be obtained by substituting Eq. (31) into Eq. (32) yielding

$$\Psi=\frac{16}{Q}\frac{k_2}{k_1(0)}\sum_{n=1}^{\infty}\frac{J_1(\lambda_n a)\int_0^a rJ_0(\lambda_n r)q(r)dr}{(\lambda_n b)^2 J_0^2(\lambda_n b)}\Theta'(\lambda_n) \tag{33}$$

where

$$\Theta'(\lambda_n)=\frac{K_1(\lambda_n c)+\Theta(\lambda_n)I_1(\lambda_n c)}{K_0(\lambda_n)-\Theta(\lambda_n)I_0(\lambda_n c)}.$$

As part of a further investigation, a general expression was examined for predicting the thermal constriction resistance of a cylindrical contact spot as a function of the prescribed heat flux over the contact area. Yovanovich (1976) showed that the actual heat flux over the symmetric and nonsymmetric, coaxial cylindrical contact area lies between $q(r)=$ const and $q(r)=[1-(r/a)^2]^{-1/2}$. Therefore, a heat flux distribution was presented as

$$q(r)=q_0\left[1-\left(\frac{r}{a}\right)^2\right]^{\mu} \tag{34}$$

Substituting Eq. (34) into Eq. (33), where the integral function of Eq. (33) is given by Gradshteyn and Ryzhik (1980), results in a general expression for the dimensionless thermal constriction parameter

$$\Psi=\frac{16}{\pi\epsilon}\frac{k_2}{k_s}2^{\mu}(1+\mu)\Gamma(1+\mu)\times\sum_{n=1}^{\infty}\frac{J_1(\lambda_n b\epsilon)J_{\mu+1}(\lambda_n b\epsilon)}{(\lambda_n b)^3(\lambda_n b\epsilon)^{\mu}J_0^2(\lambda_n b)}\Theta'(d\lambda_n) \tag{35}$$

where $\Gamma(1+\mu)$ the Gamma function and $J_{\mu+1}$ the Bessel function of the first kind of order $\mu+1$.

Results and Discussion

The special case ($\mu=-1/2$) of an equivalent heat flux applied over the contact was noted to be the exact heat flux distribution for an isothermal contact on a homogeneous half-space. This flux distribution was used to approximate an isothermal boundary condition over the contact interface to avoid directly solving a mixed boundary problem. The expression for the thermal constriction parameter was found to be:

$$\Psi_1=\frac{8}{\pi\epsilon}\frac{k_2}{k_s}\sum_{n=1}^{\infty}\frac{J_1(\lambda_n b\epsilon)\sin(\lambda_n b\epsilon)}{(\lambda_n b)^3 J_0^2(\lambda_n b)}\Theta'(\lambda_n). \tag{36}$$

Another interesting case of the contact surface heat flux was defined for $\mu=0$, which corresponds to the uniform heat flux applied over the contact surface and the expression for the thermal constriction parameter was found to be:

$$\Psi_2=\frac{16}{\pi\epsilon}\frac{k_2}{k_s}\sum_{n=1}^{\infty}\frac{J_1^2(\lambda_n b\epsilon)}{(\lambda_n b)^3 J_0^2(\lambda_n b)}\Theta'(\lambda_n). \tag{37}$$

The thermal constriction parameter were concisely defined by four new parameters. The four dimensionless parameters were defined as a radius ratio, $\epsilon=a/b$; a thermal conductivity ratio inside a mixed coating layer, $m=k_s/k_h$; a relative layer thickness, $\beta=t/a$; and a thermal conductivity ratio of a mixed coating layer to substrate, $k=k_2/k_s$. By using these parameters, some useful dimensionless groups were given as:

$$\lambda_n c=\frac{\lambda_n b\epsilon\beta}{m-1} \tag{38}$$

$$\lambda_n(t+c)=\frac{\lambda_n b\epsilon\beta m}{m-1} \tag{39}$$

The coefficients of Eq. (25), $\Theta(\lambda_n)$, were solved for by using Eq. (39), and the values of $\Theta'(\lambda_n)$ in Eq. (33) were solved for by using Eq. (38). Finally, the thermal constriction parameters were given by Eqs. (36) and (37). To evaluate the effect of the phase-mixed coating layer, the dimensionless constriction parameters were plotted against the dimensionless layer thickness. The effect of the parameter, m, on different coating materials inside the mixed coating layer was also presented.

The dimensionless constriction parameter was defined as the ratio of the thermal constriction parameter with a layer to that without a layer. When the dimensionless constriction parameter is less than 1.0, heat transfer is enhanced. From a thermal point of view, an enhanced effect can be produced if the thermal conductivity of the substrate is less than that of the coating layer. The optimum enhancement of thermal contact conductance should always occur at the coating thickness less than 10 μm (Kang et al., 1989). Increasing the layer thickness greater than 10 μm results in very little additional benefit and can even increase the thermal constriction resistance. Therefore, the value of $\epsilon\beta$ should be controlled to be less than 0.001. When $\epsilon\beta$ is larger than 0.001, it means that for a 1 cm diameter substrate ($b=0.5$ cm), the coating layer thickness is greater than 10 μm.

The results of Ψ_1 from numerical computation are illustrated in Figs. 2–5. These show the plots for six thermal conductivity ratios of a mixed coating layer to substrate, k, and eight thermal conductivity ratios of a mixed coating layer, m. The dimensionless constriction parameter of an isothermal heat flux boundary is plotted against various values of m, k, and the dimensionless thickness β. It was found that the dimensionless constriction parameter required about 250 terms to converge. When the value of m was less than 1, i.e., $k_s<k_h$, the thermal conductivity of the top surface was less than the thermal conductivity at the interface of the coating layer so the slope of the thermal conductivity at region 1, dk_1/dz, was positive, causing a sign change in Eq. (17). Using the same solution procedure, exact solutions of Eqs. (36) and (37) were obtained and yielded different functions of Θ and Θ':

$$\Theta(\lambda_n)=\frac{I_0(\lambda_n(-t-c))-I_1(\lambda_n(-t-c))}{K_0(\lambda_n(-t-c))+K_1(\lambda_n(-t-c))} \tag{40}$$

Downloaded 13 Dec 2010 to 193.140.21.150. Redistribution subject to ASME license or copyright; see http://www.asme.org/terms/Terms_Use.cfm

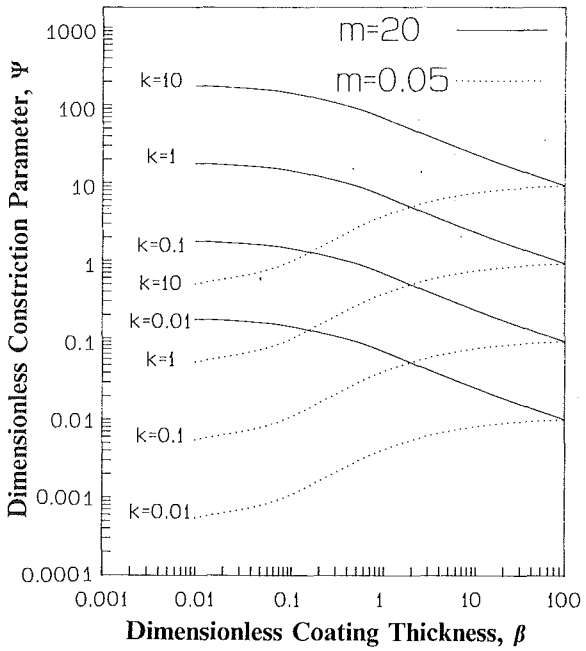

Fig. 2 Dimensionless constriction parameter versus dimensionless coating thickness for $m = 20$ and 0.05 at $\epsilon = 0.01$

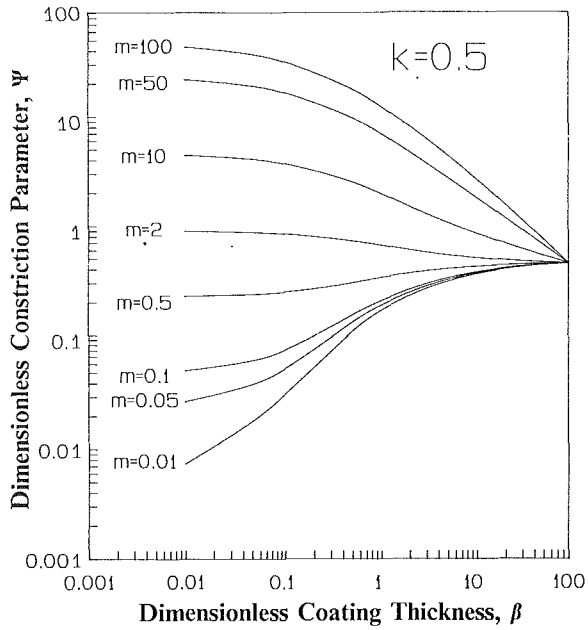

Fig. 3 Dimensionless constriction parameter versus dimensionless coating thickness for $k = 0.5$ at $\epsilon = 0.01$

$$\Theta'(\lambda_n) = \frac{I_1(-\lambda_n c) + \Theta(\lambda_n) K_1(-\lambda_n c)}{I_0(-\lambda_n c) - \Theta(\lambda_n) K_0(-\lambda_n c)} \tag{41}$$

with two dimensionless parameters defined as:

$$-\lambda_n c = \frac{\lambda_n b \epsilon \beta}{1-m} \tag{42}$$

$$-\lambda_n (t+c) = \frac{\lambda_n b \epsilon \beta m}{1-m} \tag{43}$$

Figure 2 shows the relative constriction parameter at four different values of k plotted as a function of the dimensionless coating thickness for two values of m. The dimensionless constriction factor decreases as β increases when $m > 1$ and the dimensionless constriction factor increases as β increases when $m < 1$. However, both cases will converge to the same values of k. When k decreases one order of magnitude, the dimensionless constriction parameter decreases an order of magnitude also. The thermal conductivity of substrate decreases an order of magnitude with a decrease of one order of magnitude in the ratio, k.

As illustrated in Fig. 3, eight different values of m were employed for k equal to 0.5. The results indicated that the dimensionless constriction parameter is less than 1 when m is less than 1. The dimensionless constriction parameter decreases as the dimensionless layer thickness increases when m is greater than 1. However, values of the dimensionless constriction parameter converged to 0.5. Two different thermal conductivity materials were used in the mixed coating layer, resulting in variable conductivity coatings. Consequently, the slope of thermal conductivity of the coating layer between two surfaces will decrease when the dimensionless coating thickness increases. As $\beta \to \infty$, the slope of the thermal conductivity of the coating layer approaches a value of zero and a constant thermal conductivity will be obtained. Hence, an optimum coating thickness exists. It is noted that too thick a coating will not enhance the thermal contact conductance.

Figure 4 shows the variation of m with k for a fixed β. The dimensionless constriction parameter shows a monotonically increasing trend as $k < 1$. It is apparent from Fig. 4, that independent of the value of m, all the dimensionless constriction

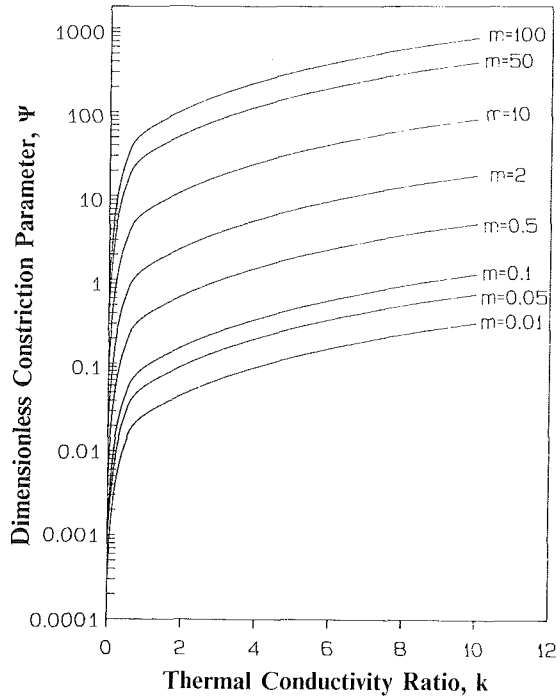

Fig. 4 Dimensionless constriction parameter as a function of k for $\epsilon = 0.01$ and $\beta = 0.05$

parameters increase with increasing values of k when the values of m are in the range $0.01 \le m \le 100$ and $\epsilon\beta = 0.0005$. For a fixed thermal conductivity ratio, k, the dimensionless constriction parameter decreased as m decreased. This is as expected, since placing the high thermal conductivity coating material near the interface can enhance the heat transfer effects. For $k < 1$, the slopes of the curves are much greater than for $k > 1$. The addition of a secondary coating material to the layer plays an important role of conductive heat transfer enhancement for k less than 1. As in the case of k greater than 1, m decreased an order of magnitude, resulting in an order

Downloaded 13 Dec 2010 to 193.140.21.150. Redistribution subject to ASME license or copyright; see http://www.asme.org/terms/Terms_Use.cfm

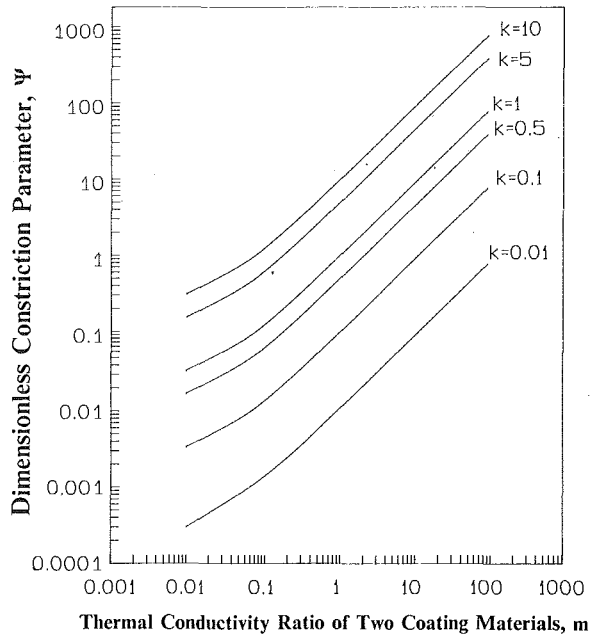

Fig. 5 Dimensionless constriction parameter as a function of m for $\epsilon = 0.01$ and $\beta = 0.05$

Table 1 Test specimen characteristics

Specimens No.	Coating Materials	Coating Thickness (μm)	Surface Roughness (μm)	Asperity Slope (rads)
1A	Cu/C	0.25	0.15	0.025
1B	Cu/C	0.25	0.17	0.019
2A	Cu/C	0.45	0.26	0.046
2B	Cu/C	0.45	0.29	0.048
3A	Cu/C	0.45	1.91	0.270
3B	Cu/C	0.45	1.66	0.200
4A	Cu/C	0.25	2.62	0.378
4B	Cu/C	0.25	2.85	0.395
5A	Ag/C	0.18	0.23	0.032
5B	Ag/C	0.18	0.20	0.031
6A	Ag/C	0.18	0.26	0.033
6B	Ag/C	0.18	0.23	0.030
7A	Ag/C	0.39	1.98	0.287
7B	Ag/C	0.39	2.11	0.291
8A	Ag/C	0.39	2.13	0.395
8B	Ag/C	0.39	2.41	0.435

of magnitude decrease of the dimensionless constriction parameter.

The results from computing the different k values are illustrated in Fig. 5 and show the dimensionless constriction parameter plotted against the thermal conductivity ratio of a mixed coating layer. As can be seen with all the curves, there is an increase in the dimensionless constriction parameter with increasing the thermal conductivity ratio of a mixed coating layer. The dimensionless constriction parameter did not approach constant values for any of the six curves. If the thermal conductivity ratio of a mixed coating layer is increased further, the k_s values are much larger than k_h value and cause higher dimensionless constriction parameter. As shown in the Fig. 5, it is seen that the k values cause a linear effect on the thermal constriction parameter for all values m. When k decreased an order of magnitude, the dimensionless constriction parameter also decreased an order of magnitude.

Two different cases of specified boundary conditions over the contact were investigated. The results for the uniform heat flux boundary condition case are not shown in the figures because the isothermal and uniform heat flux boundary condition cases produced identical curves. The choice of boundary condition had little effect on the theoretically predicted thermal constriction resistance. The maximum difference between the results for the two different cases of specified boundary condition at the contact surface was 7.2 percent.

A total of N circular microcontacts having a radius, a, were assumed to be distributed over the apparent contact area, A_a. The total thermal constriction resistance was defined by Antonetti and Yovanovich (1985) as:

$$R_t = \frac{\Psi}{2aNk'} \tag{44}$$

A simple force balance at the contacting interface was used to determine the total number of microcontacts per unit area as follows:

$$\frac{P}{H} = \frac{N\pi a^2}{A_a} \tag{45}$$

By substituting Eq. (45) into Eq. (44), the expression for the total thermal constriction resistance becomes:

$$R_t = \frac{\pi a}{2A_a}\frac{\Psi}{k'}\frac{H}{P} \tag{46}$$

where k' is a mean thermal conductivity, H is microhardness, and P is the contact pressure.

To verify the present analysis, the experimental test results from Chung (1992) were compared to the theoretical model, given by Eq. (46). All test specimens were fabricated from a single aluminum 6061-T651 rod. Contact surfaces were prepared on the faces of specimens 2.54 cm in diameter by 2.54 long cylindrical. The ends of the specimens were carefully turned to produce smooth and flat surfaces. The specimens were tested in pairs, with both of the pair treated further by four different surface treatments, polished, turned, blasted-smooth and blasted-rough, at one end to a specified roughness. Blasted-smooth and blasted-rough surfaces were producted by a jet of air with entrained glass beads. Two different phase-mixed coating materials, copper-carbon and silver-carbon, were used to produce the coating on aluminum 6061-T651 substrate of each specimen. The experimental error for the total thermal constriction resistance in the test setup was estimated to be ±8 percent. Pertinent test specimen characteristics are shown in Table 1.

Comparisons of the present analysis of the total thermal constriction resistance with experimental results are shown in Figs. 6 and 7. Figure 6 presents a plot of the total thermal constriction resistance versus contact pressure for phase-mixed copper-carbon coating specimens. As expected, the thermal constriction resistance decreases with an increase in contact pressure. It can be seen that the agreement between the experiment and theory is not good for the first point of each set. The measured resistances are considerably lower than the prediction for these first points, but tends toward the theoretical line at the next points. The overall rms percentage difference for all 16 test points was 25.3 percent. The same behavior was observed for different surface textures. Figure 7 demonstrates a comparison between the measured constriction resistance and the predicted values for the silver-carbon coatings pairs. It was observed that the characteristics of the experimental data were quite similar to the copper-carbon test pairs. The deviation between the first data points and the theory was also

Downloaded 13 Dec 2010 to 193.140.21.150. Redistribution subject to ASME license or copyright; see http://www.asme.org/terms/Terms_Use.cfm

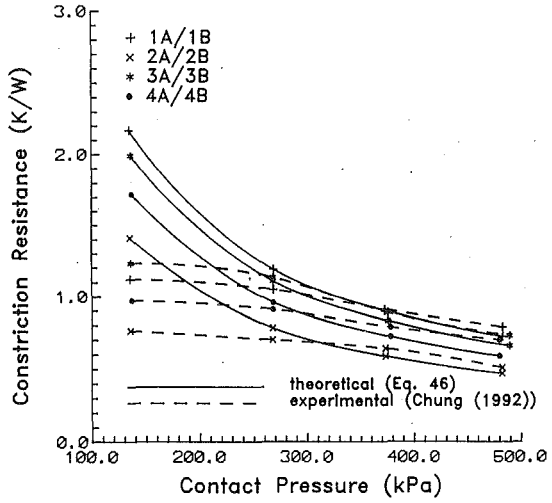

Fig. 6 Comparison between theory and test results for copper-carbon specimens

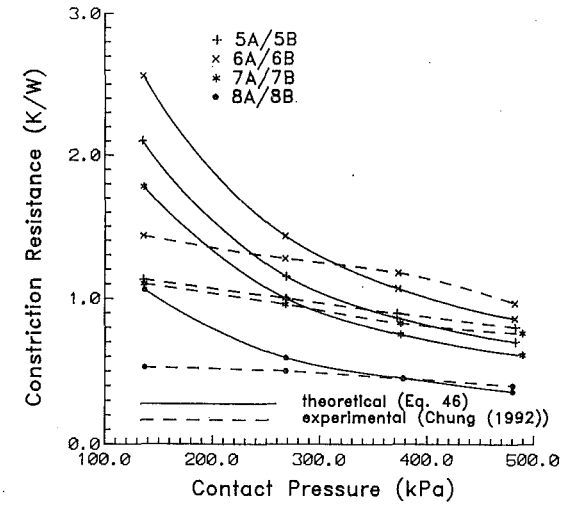

Fig. 7 Comparison between theory and test results for silver-carbon specimens

significantly higher, although this deviation decreases rapidly with increasing applied load. The overall rms percentage difference between the experiment and theory for silver-carbon coating specimens was 26.6 percent.

One of the possible explanations for discrepancies between experimental and predicted results was believed to be the difficulty in controlling the exact gradient of carbon in the phase-mixed coatings. Conceptually, the very low thermal conductivity of carbon should cause some effect on thermal constriction resistance of phase-mixed coatings. However, the deviation between the experiments and the predictions also depends upon the surface characteristics, contact pressure, and thermal flux. Table 2 summarized the results of the parameters involved in the calculation of the thermal constriction resistance for all the specimens tested.

Conclusions

The thermal constriction resistance for a phase-mixed coating layer by a new coating technique, TBI, was presented analytically. An approximate solution for an isothermal contact was obtained by using a linear superposition technique with power series solutions. Both isothermal ($\mu = -1/2$) and uniform heat flux ($\mu = 0$) boundary conditions were applied to compute the dimensionless constriction parameters. Dimensionless parameters were used to evaluate the dimensionless thermal constriction parameter. Based upon the results, the thermal conductivity ratio, m, is a significant parameter to determine the thermal constriction parameter when $k < 1$. The heat transfer was enhanced when the dimensionless constriction parameter was less than 1. Enhancement was also obtained by coating a relatively soft layer whose thermal conductivity was lower than that of the substrate. A coating layer with a sufficiently low microhardness would tend to increase the heat transfer at the interface by increasing the real contact area or the number of contact spots.

The total thermal constriction resistance of a phase-mixed coating layer was developed by combining the previous theoretical model as well as the thermal constriction parameter in this work. Comparison of the predictions with the experimental results from Chung (1992) indicated that the overall rms percentage differences were 25.3 percent and 26.6 percent for copper-carbon and silver-carbon phase mixture coatings, respectively.

Table 2 Summary of calculated parameters and constriction response

Specimen No.	P (kPa)	H (GPa)	$\Psi/k' \times 10^2$ (mK/W)	a (μm)	R_t (K/W)
1A/1B	134.8	1.681	2.55	2.21	0.91
	268.7	1.674	2.67	2.32	1.66
	372.5	1.670	2.74	2.37	2.19
	482.8	1.668	2.80	2.42	2.73
2A/2B	135.5	1.605	2.09	1.84	1.41
	267.7	1.598	2.19	1.93	2.53
	373.4	1.595	2.25	1.98	3.37
	482.6	1.592	2.29	2.02	4.19
3A/3B	136.2	1.365	2.70	2.38	0.99
	268.2	1.359	2.84	2.50	1.78
	375.4	1.356	2.91	2.56	2.38
	489.3	1.354	2.97	2.62	2.98
4A/4B	136.8	1.315	2.59	2.24	1.15
	268.2	1.310	2.72	2.35	2.05
	378.1	1.307	2.79	2.42	2.75
	480.1	1.305	2.84	2.46	3.37
5A/5B	135.1	1.702	2.51	2.16	0.94
	268.2	1.694	2.63	2.26	1.71
	375.5	1.691	2.69	2.32	2.28
	483.3	1.688	2.75	2.36	2.82
6A/6B	136.4	1.682	2.79	2.40	0.77
	266.2	1.675	2.92	2.52	1.38
	373.5	1.671	2.30	2.58	1.85
	481.3	1.668	3.06	2.63	2.29
7A/7B	136.2	1.389	2.54	2.23	1.11
	264.2	1.383	2.67	2.34	1.96
	372.1	1.380	2.74	2.40	2.63
	480.3	1.377	2.79	2.45	3.26
8A/8B	136.8	1.376	1.97	1.73	1.87
	268.2	1.370	2.07	1.81	3.34
	372.1	1.367	2.12	1.86	4.42
	480.1	1.364	2.16	1.90	5.48

References

Antonetti, V. W., 1983, "On the Use of Metallic Coatings to Enhance Thermal Contact Conductance," Ph.D. thesis, University of Waterloo, Ontario, Canada.

Antonetti, V. W., and Yovanovich, M. M., 1985, "Enhancement of Thermal Contact Conductance by Metallic Coatings: Theory and Experiment," ASME JOURNAL OF HEAT TRANSFER, Vol. 107, pp. 513-519.

Chung, K. C., Sheffield, J. W., Sauer, H. J., Jr., O'Keefe, T. J., and Williams, A., 1991, "An Experimental Study of Enhancing Thermal Contact Conductance by Transitional Buffering Interface (TBI)," AIAA Paper No. 91-0490.

Chung, K. C., 1992, "Thermal Contact Conductance of a Phase-Mixed Coating Layer by Transitional Buffering Interface," Ph.D. Dissertation, Department of Mechanical Engineering, University of Missouri—Rolla, Rolla, MO.

Dryden, J. R., 1983, "The Effect of a Surface Coating on the Constriction Resistance of a Spot on an Infinite Half-Plane," ASME JOURNAL OF HEAT TRANSFER, Vol. 105, pp. 408-410.

Downloaded 13 Dec 2010 to 193.140.21.150. Redistribution subject to ASME license or copyright; see http://www.asme.org/terms/Terms_Use.cfm

Fisher, N. J., and Yovanovich, M. M., 1989, "Thermal Constriction Resistance of Sphere/Layered Flat Contacts: Theory and Experiment," ASME JOURNAL OF HEAT TRANSFER, Vol. 111, pp. 249–256.

Gradshteyn, I. S., and Ryzhik, I. M., 1980, *Table of Integrals, Series and Products*, Academic Press, New York.

Kang, T. K., Peterson, G. P., and Fletcher, L. S., 1989, "Enhancing the Thermal Contact Conductance Through the Use of Thin Metallic Coating," ASME Paper No. 89-HT-23.

Negus, K. J., Yovanovich, M. M., and Thompson, J. C., 1988, "Constriction Resistance of Circular Contacts on Coated Surfaces: Effect of Boundary Conditions," *Journal of Thermophysics and Heat Transfer*, Vol. 2, pp. 158–164.

O'Callaghan, P. W., Snaith, B., Probert, S. D., and Al-Astrabadi, F. R., 1983, "Prediction of Interfacial Filler Thickness for Minimum Thermal Contact Resistance," *AIAA Journal*, Vol. 21, pp. 1325–1330.

Yovanovich, M. M., 1976, "General Expressions for Circular Constriction Resistance for Arbitrary Flux Distribution," *Progress in Astronautics and Aeronautics: Radiative Transfer and Thermal Control*, A. M. Smith, ed., Vol. 49, pp. 301–308.

Downloaded 13 Dec 2010 to 193.140.21.150. Redistribution subject to ASME license or copyright; see http://www.asme.org/terms/Terms_Use.cfm

Visualization and Analysis of Flow in an Offset Channel

J. A. Walter
Graduate Research Assistant.
Student Mem. ASME

C.-J. Chen[1]
Senior Research Scientist,
Iowa Institute of Hydraulic Research.
Professor and Chairman.
Fellow ASME

Department of Mechanical Engineering,
The University of Iowa,
Iowa City, IA 52242

This paper investigates flow characteristics for a benchmark experiment that is important for thermal hydraulic phenomena in nuclear power plant design. The flow visualization experiment is carried out for flow in a rectangular offset channel covering both the laminar and turbulent flow regimes. The Reynolds number, based on the inlet velocity and the height of the inlet channel, ranges from 25 to 4600. The offset channel is an idealized thermal hydraulic geometry. Duct flow expands in a rectangular chamber and exits to a duct that is offset from the entrance duct. The offset geometry creates zones of recirculation for thermal-hydraulic mixing. Flow patterns are visualized by a laser light sheet in the symmetry plane of the primary flow direction and in three cross-sectional planes. A charge-coupled device (CCD) images the flow field, simplifying the experimental process and subsequent image analyses. The flow pattern and size of the recirculation zones change dramatically with Reynolds number until the flow is fully turbulent. While the velocity field itself is predominantly two dimensional, it is shown that the walls of the chamber produce a fully three-dimensional flow that could not be predicted properly by a two-dimensional calculation. Quantitative measurements of particle pathlines from several images are superimposed to give a composite view of the velocity field at one of the Reynolds numbers examined.

1 Introduction

Flow in an offset channel shown in Fig. 1 is a fundamental configuration in many practical engineering applications, such as thermal hydraulics in power plant design, heat exchangers, electronic cooling, and reacting chambers. For the design and analysis of a new thermal hydraulic system in nuclear power generation, Ushijima et al. (1985) used this geometry to study the flow patterns and simulation of circulation flows. In addition, the flow through an offset channel can be used as a first step in analysis of flow through turbine combustion chamber walls, engine valves, and in partition walls of underground tunnels (Tulapurkara et al., 1988). It may also be considered as an approximation of shell-side flow through baffles in a shell-and-tube heat exchanger (Berner et al., 1984). The pattern of the flow in the offset channel can provide information regarding the residual time of fluid in the chamber, recirculation pattern, temperature distribution, rate of heat transfer, and diffusion of mass for these applications. The objective of this work is to characterize flow pattern variations for a range of Reynolds numbers, using flow visualization and image analysis. We describe the experimental system first, followed by a discussion of the flow images obtained.

2 Experimental System

2.1 Test Chamber and Circulation System. Figure 1 shows the experimental setup for this investigation. The test section is a rectangular chamber 116 mm long, 111 mm high, and 22 mm deep. The inlet arm at the lower right corner and the outlet arm at the upper left have the same cross sections, 11 mm high and 22 mm deep. The inlet arm is 387 mm long and the outlet arm is 311 mm long. The chamber is made of clear plexiglass for optical access. The working fluid is water. The test section connects to a closed-circuit pumping system by 13 mm plastic hose tapped into the ends of the inlet and outlet arms. Two pumps and two correlated flow meters control and measure the flow rate, depending on the Reynolds number desired. Both flow meters have an accuracy of ±2 percent of the scale reading. The mean inlet velocity is calculated from the measured flow rate and the cross-sectional area of the inlet duct. The Reynolds number is based on the inlet velocity and the height of the inlet arm.

2.2 Illumination System. Figure 1 also shows the optical system used to produce a sheet of light for planar visualization. A 10 mW Uniphase He–Ne laser is used for illumination. The laser beam passes through two rectangular cylindrical lenses (with focal lengths of 6.35 and 19 mm) to produce a light sheet equal to the length of the test section. The light sheet reflects off a plane mirror placed at 45 deg to the test section, as shown in Fig. 1. Most of the visualizations were conducted in the plane of geometric symmetry, shown in Fig. 2. The test section

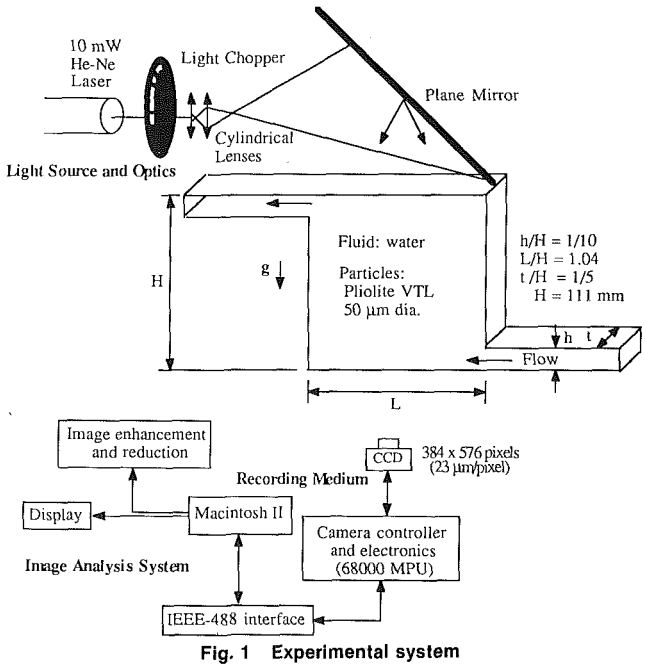

Fig. 1 Experimental system

[1] Present address: Dean, FAMU/FSU, College of Engineering, Tallahassee, FL 32316.

Contributed by the Heat Transfer Division for publication in the JOURNAL OF HEAT TRANSFER. Manuscript received by the Heat Transfer Division March 1991; revision received April 1992. Keywords: Flow Separation, Flow Visualization, Forced Convection. Associate Technical Editor: D. M. McEligot.

Copyright © 1992 by ASME
Downloaded 13 Dec 2010 to 193.140.21.150. Redistribution subject to ASME license or copyright; see http://www.asme.org/terms/Terms_Use.cfm

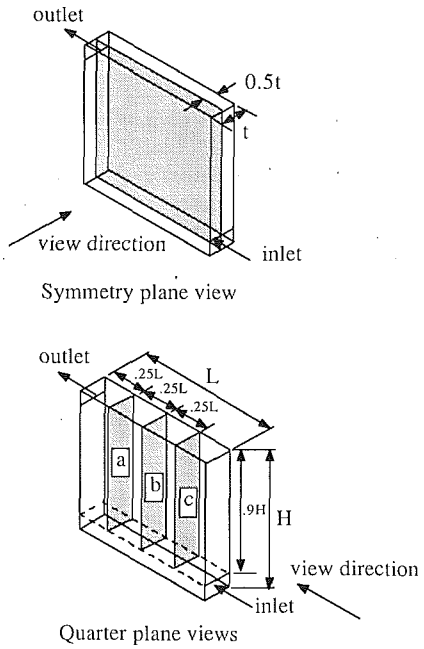

Fig. 2 Domain of flow visualization

was rotated 90 deg so that flow in the quarter plane cross sections shown in Fig. 2 could be visualized as well. In these images, the view is from the inlet side toward the outlet side.

The seed particles used in this study are known by the trade name Pliolite VT, manufactured by Goodyear Tire and Rubber Company. The particles have a specific gravity of 1.03, and may be considered neutrally buoyant. The particles are passed through a wire mesh; only those of nominal diameter less than 50 μm are allowed into the circulation system. The particles used in this study are smaller than the particles used by Agüí and Jiménez (1987) and Utami and Ueno (1987) in water at similar Reynolds numbers, both of whom concluded that the particles tracked the flow sufficiently.

For interpretation of flow visualization images, it is important to know the direction a fluid particle moved during the time it was imaged. If the seed particles are imaged in space, then each particle or group of particles is frozen in successive frames. Several methods have been developed to resolve the direction of the velocity in this case (e.g., Landreth et al., 1988). If the particles are imaged in time, then each particle forms a streak (pathline) of finite length on a single image (e.g., Khalighi, 1989). In this work, the seed particles are imaged in time. Then, similar to Agüí and Jiménez (1987), the laser beam is passed through a rotating aluminum disk shown in Fig. 1. The disk chops the light asymmetrically before it reaches the optics and test section. In this way, light reaching the test section is coded so that the direction the particle moved during the exposure can be deduced. A digital tachometer monitors the angular speed of the chopping disk, which then effectively serves as a camera shutter with known exposure time. A streak pattern is obtained in which a single dot imaged first represents the origin of the velocity vector in the particle streak, and two terminal dots indicate the tail of the vector. For quantitative measurements, a complete code pattern of one dot, a long period, and two final dots is needed to ensure the particle remains within the illuminated section of the test chamber during the exposure.

2.3 Detector and Imaging System. The image detector used is a scientific-grade charge-coupled device (CCD). In the context of flow visualization, the principal advantages of the CCD are its high quantum efficiency and low system noise. These render the CCD very sensitive to optical radiation, allowing use of a less powerful light source than is possible with other photographic media. The CCD also has a large dynamic range. Dynamic range is the ratio of intensities of the brightest object that can be imaged without saturating the analog-to-digital (A/D) converter to the dimmest object that can be imaged. Fast-moving particles have less time in which to scatter light while they form a streak. The sensitivity of CCD makes these streaks visible. The CCD chip is a Thomson model CSF packaged by Photometrics, Ltd. A standard 50 mm camera lens is mounted on the camera head. The CCD chip digitizes to 12 bit (4096 gray level) precision. The low noise level of the system is achieved by thermoelectric cooling of the chip to $-45°C$, minimizing thermally generated noise, and slow-scan signal processing electronics (200 kHz in our system). The Thomson CCD chip is 384×576 pixels with each pixel measuring 23 μm square. Therefore, in the present setting, the area of one pixel in the CCD is approximately equivalent to a 0.08 mm^2 region in the plane of the test section. The spatial resolution of the Thomson CCD is roughly equivalent to a typical video camera.

The entire experimental system is diagrammed in Fig. 1. The CCD is connected to a camera controller based around a Motorola 68000 MPU chip containing the hardware command set for operation of the camera. The camera controller is in turn operated by the user through an IEEE-488 interface to a Macintosh II microcomputer, which sends commands such as exposure time to the CCD via the camera controller. If desired, an image can be displayed immediately so that adjustments of focus, aperture (f#), and exposure time can be made quickly. The number of images that can be stored is limited only by the memory of the host computer.

2.4 Quantitative Measurements and Error Analysis. The exposure time known from the revolution rate of the chopping wheel and the length of each pathline measured from the image allow calculation of the velocity. The velocity magnitude and direction are calculated using an interactive computer program in which mouse clicks on the coded pathlines store the appropriate quantitative information. Using the criteria set forth by Agüí and Jiménez (1987), Walter and Chen (1990) found the total error in the velocity measurement to be about 5 percent of the average particle streak length. This includes errors due to the inability to locate the end points of the particle pathlines precisely, and the instability of the chopping wheel. Error in the exposure interval due to the finite time required to chop the light was neglected, and, as mentioned, the particles were assumed to follow the flow. The error in quantitative visualization is mainly due to the coarse resolution of the CCD. Advanced CCDs with better spatial resolution (500×1000 pixels) than our CCD are now available. These would provide more accurate measurement. The spatial resolution of photographic film currently remains superior to that of electronic mediums (Adrian, 1986). However, film suffers from its own disadvantages, namely, difficulty of use and the need to develop the film.

Complete details of the experimental system and velocity calculation method are given by Walter and Chen (1990).

3 Results and Discussion

3.1 General Remarks. The range of velocity magnitude within the chamber was quite large for most of the Reynolds numbers investigated. The velocity is maximum near the inlet (a sudden expansion), while the secondary recirculating flow is nearly stationary at its core. Consequently, no single exposure time can capture the range of motion satisfactorily. The exposure times chosen in the experiments represented a trade-off between these two extremes.

To ensure that the flow in the system had come to steady state, four images were acquired in succession and stored in

Downloaded 13 Dec 2010 to 193.140.21.150. Redistribution subject to ASME license or copyright; see http://www.asme.org/terms/Terms_Use.cfm

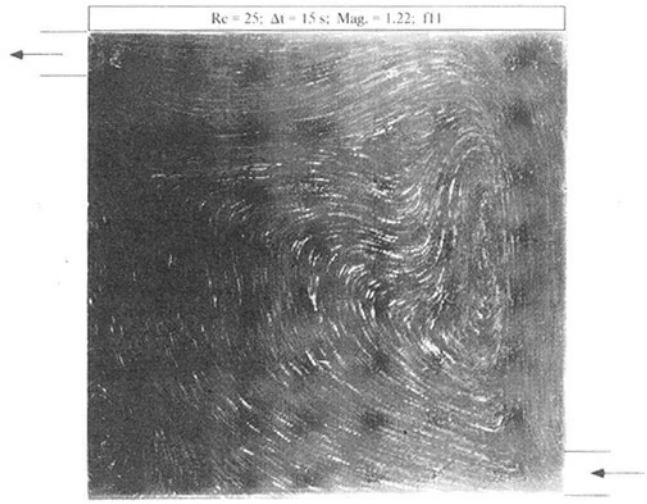

Fig. 3 Symmetry plane visualization for Re = 25

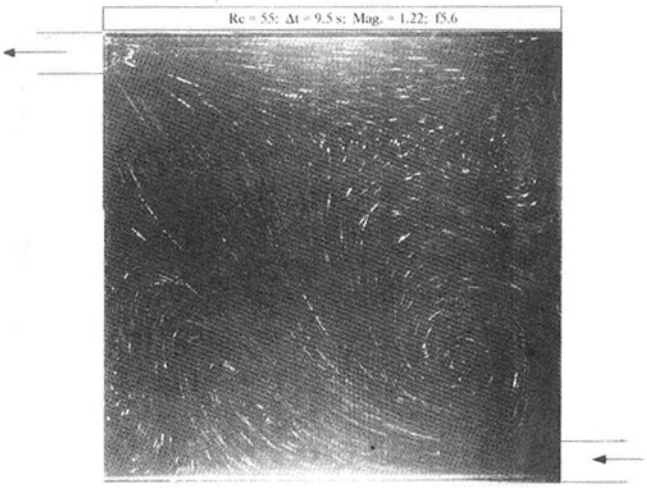

Fig. 4 Symmetry plane visualization for Re = 55

the temporary memory of the camera controller. The images were compared for repeatability. If the flow patterns did not agree qualitatively, this process was repeated until the flow pattern was repeatable. In all cases, the offset channel was situated in a vertical position with respect to gravity, so that the horizontal outlet was above the horizontal inlet.

Figures 3–4 show the flow patterns in the chamber for the eight Reynolds numbers investigated: 25, 55, 105, 205, 435, 625, 910, and 4600. The Reynolds number is defined from the mean inlet velocity, the height of the inlet duct, h, and the kinematic viscosity of water at room temperature. The mean inlet velocity at Re = 105 is 9.5 mm/s. Inlet velocities at other Reynolds numbers may be found by appropriate scaling. For example, the inlet velocity at Re = 435 is 39 mm/s. For each Reynolds number, the side view of the center plane of the test section is shown, as indicated in Fig. 2.

Quarter plane cross-sectional flow patterns of the third dimension are shown in Figs. 5, 9, and 12 for Re = 55, 205, and 625, respectively. The bright horizontal line one-third of the distance down the cross-sectional images is due to a glue joint on the outside of the test section. The dimmer horizontal line above the bright one is the bottom of the outlet arm. The velocity component in the cross-sectional plane was extremely small, and the seeding particles moved mostly in and out of the plane. Since the complete coded streak pattern was rarely found in the cross-sectional plane, the chopping wheel was not used for Figs. 5, 9, and 12. All the images shown were enhanced slightly from their original appearance to increase the visibility of the streaks. For the enhancement, a simple brightness and contrast filter was used.

The critical Reynolds number for two dimensional channel flow is about 800 (White, 1974). If the flow in the inlet duct is turbulent, it is then turbulent in the test section. Thus, the flow at Re = 910 and 4600 is turbulent, and this can be seen in images to be presented. Turbulent fluctuations of the particles were easily observed at these Reynolds numbers during the experiments. The flow at Re = 625 or less is laminar.

3.2 Qualitative Laminar Flow Visualization. Figure 3 shows the flow pattern at Re = 25. The fluid enters the channel from the lower right side and deflects immediately upward where the upper wall turns it horizontally to the left and below the main flow path. The center of the recirculation zone is not located at the center of the chamber but rather closer to the right wall, and the recirculation pattern shows a vertical dumbbell shape. A small recirculation cell also develops in the lower left corner of the chamber. The coded streak pattern of Fig. 3 can be distinguished on many of the streak images, although it should be noted that the exposure of 15 seconds in Fig. 3 is long, so that many of the streaks, especially those in the throughflow, become blurred and indistinguishable from one another. Long exposure times are necessary to create a better qualitative illustration of the flow patterns. However, images with shorter exposure times yield more accurate velocity measurements even though they do not reveal details of the flow patterns. In some cases, the individual streaks are visible, but the coded streak pattern is not. A complete code pattern in the image indicates two-dimensional motion within the depth of the light sheet (1.5 mm), while an incomplete code pattern indicates that the particle has moved out of the plane during the exposure time. In general, one expects the flow to be three dimensional, because the offset channel is three dimensional. On the other hand, because the depth of the channel is less than one-fifth of the channel length, the third velocity component is expected to be small. Also, as the image is taken at the center plane of the channel, the flow there tends to be planar.

Physically, one may expect the fluid coming from the inlet to penetrate the chamber of the offset channel along the bottom wall before moving toward the outlet. For Re = 25, the image shown in Fig. 3 reveals that the flow deflects upward almost immediately. This is because the outlet geometry is such that it tends to extract the fluid along the upper wall horizontally. Thus the fluid near the upper wall may first accelerate toward the outlet. In doing so, the fluid along the right wall is drawn upward to make up for the fluid being withdrawn. While fluid is being withdrawn at the outlet, some deflects downward near the left wall, creating a stagnation point and a higher pressure several centimeters below the outlet. This downward flow creates a recirculating flow that rotates in the counterclockwise direction. In addition, the side walls of the chamber create a three-dimensional effect by imparting a large viscous drag to the fluid. The momentum of the incoming fluid is diffused, preventing further penetration into the chamber.

Figure 3 also shows a stagnation point near the bottom right corner where the incoming fluid and recirculating fluid meet and turn upward. Another stagnation point appears in the upper right corner of the chamber. It is seen in Fig. 3 that the velocity is of a similar magnitude throughout much of the test section, because the streaks are of similar lengths. This is because the flow is at a low Reynolds number, and the strong viscous force diffuses much of the inertia and momentum of the incoming flow to the recirculation flow.

The flow patterns can be described in terms of several recurring parameters. Some are introduced here but described in more detail when all the results have been presented. When the Reynolds number is larger than 25, two recirculation zones

Downloaded 13 Dec 2010 to 193.140.21.150. Redistribution subject to ASME license or copyright; see http://www.asme.org/terms/Terms_Use.cfm

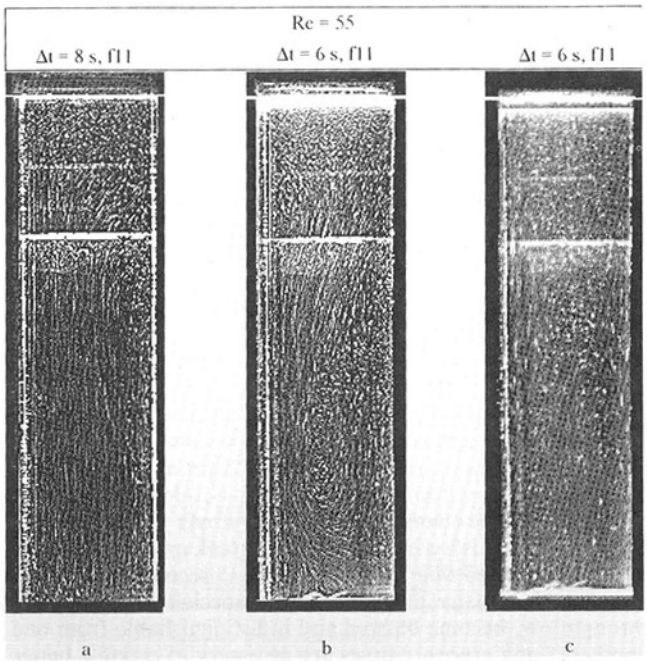

Fig. 5 Quarter plane visualization for Re = 55

form, one on either side of the main flow path. The center of the recirculation zone above and to the right of the main path is called the upper recirculation center (UC). The rotation of the flow in this zone is clockwise. The center of the recirculation zone below and to the left of the main path is called the lower recirculation center (LC); its rotation is counterclockwise, and the size of this zone shrinks with increasing Reynolds number. The recirculation zones are related to stagnation points observed on the walls. For all Reynolds numbers, a lower stagnation point (LS) occurs on the left wall as the flow from the inlet impinges on it. For Reynolds numbers higher than 435, the flow above this stagnation point retains sufficient momentum to impinge on the upper wall and form a stagnation point (US). Without sufficient momentum (i.e., lower Reynolds numbers), the flow is reversed in the chamber, and the US instead forms on the right wall. Several other parameters are introduced and defined as needed in the following discussion. A description in terms of these parameters facilitates a basic overview of the flow field in the offset channel and provide a means of comparing the patterns at different Reynolds numbers.

The flow at Re = 55 is shown in Fig. 4. The major difference from Re = 25 is that the throughflow now proceeds in a diagonal, more direct fashion from inlet to outlet. This is due to the increased momentum of the incoming fluid. The inertia of the fluid causes the main flow path to penetrate deeper into the chamber before deflecting upward. The lower stagnation point (LS) occurs approximately halfway down the left wall, somewhat lower than at Re = 25. Flow separating below this point forms the lower recirculation zone, and flow above it exits the chamber. The upper stagnation point (US) occurs halfway down the right wall. The two recirculation zones in this case are approximately equal in size, with one on either side of the main throughflow. The right recirculation zone moves clockwise, and the left counterclockwise. Flow separating above the upper stagnation point forms a secondary recirculation zone (SC) in the upper right region of the chamber as it moves toward the outlet. The exposure time of 9.5 seconds for Fig. 4 reveals that this region still appears stagnant. On the left side of the secondary recirculation zone a saddle point is observed but is not obvious. A saddle point (S) is a stagnant point where the flow is both converging and diverging at the

Fig. 6 Symmetry plane visualization for Re = 105

point. It will be illustrated more clearly at Re = 105. We refer to flow turned downward from the LS and impinging on the bottom wall as a reverse stagnation point (RV), which can be seen in Fig. 4. Flow to the right of this point is entrained into the throughflow, and flow to the left of it circulates in the lower recirculation zone. Due to the three-dimensional nature of the flow, the fluid initially in the recirculation zones may be entrained in the throughflow and eventually move out of the chamber. Much of the fluid in the recirculation zones is likely comprised of fluid that flows into the plane from adjacent planes. Figure 5 shows the cross-sectional view of the flow for Re = 55. In the inlet and outlet quarter planes, the flow pattern is very much parallel to the vertical wall, indicating little crossflow. In the middle plane the flow is more three dimensional. A circulating pattern is even suggested in the lower center of Fig. 5(*b*), but the small velocity components in this plane make such a conclusion difficult.

3.3 Qualitative and Quantitative Flow Visualization. When the Reynolds number is increased to Re = 105, Fig. 6 shows that the range of velocity in the channel increases dramatically from the previous two Reynolds numbers. The exposure time is reduced appropriately to $\Delta t = 5.5$ s. Now the momentum of the inlet flow creates one dominant flow path, along the lower and left walls. At this higher inlet speed, the fluid penetrates much deeper into the chamber before the lower stagnation point (LS) is created on the left wall. This stagnation point therefore occurs farther down the wall than at Re = 55. If a quasi-steady increase in Reynolds number is imagined between Re = 55 and Re = 105, then the lower recirculation zone in Fig. 4 (Re = 55) shrinks to a small region in the extreme lower left of the chamber in Fig. 6 (Re = 105). On the other hand, the upper recirculation zone in Fig. 4 moves to the left and down because the throughflow path is primarily along the bottom and left walls. The upper stagnation point occurs on the right wall and is lower and closer to the inlet than at Re = 55. The secondary recirculation zone observed at Re = 55 moves to the middle region of the chamber, just above the center. This recirculation zone is more evident than at Re = 55, as well as the saddle point to the left of it. In the present case, flow near the saddle point both converges and diverges, as shown in Fig. 6, and probably involves three-dimensional flow toward or outward from the saddle point, normal to the plane of the image.

Figure 7 shows a quantitative velocity measurement at flow at Re = 105. As a reference, the magnitude of the mean inlet velocity of 9.5 mm/s is provided in the figure caption. It is a composite of 20 images with varying exposure times and aperture settings. Experimentally, this procedure is possible only if the imaging area and magnification are the same for every

Downloaded 13 Dec 2010 to 193.140.21.150. Redistribution subject to ASME license or copyright; see http://www.asme.org/terms/Terms_Use.cfm

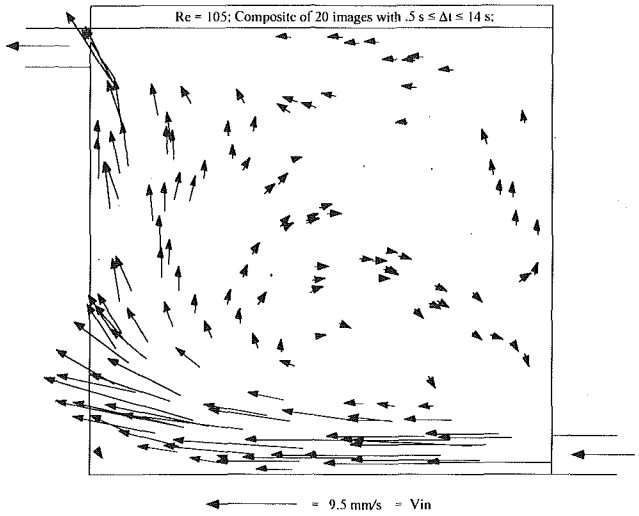

Fig. 7 Velocity vector plot for Re = 105

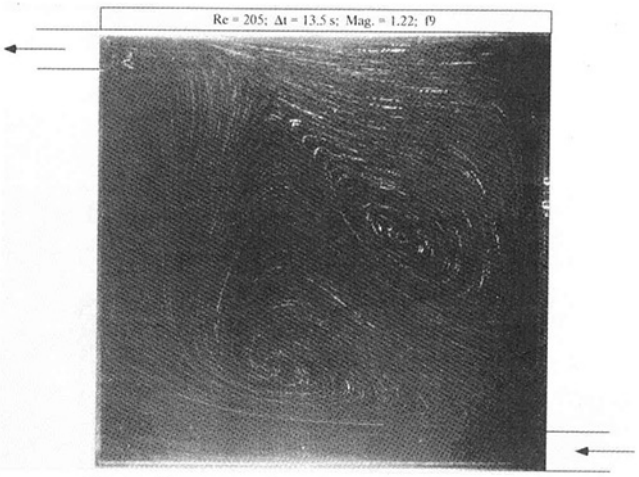

Fig. 8 Symmetry plane visualization for Re = 205

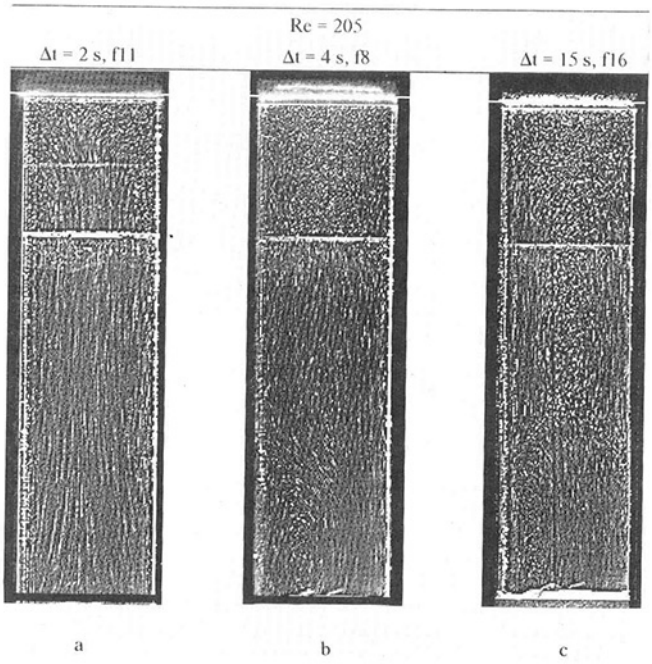

Fig. 9 Quarter plane visualization for Re = 205

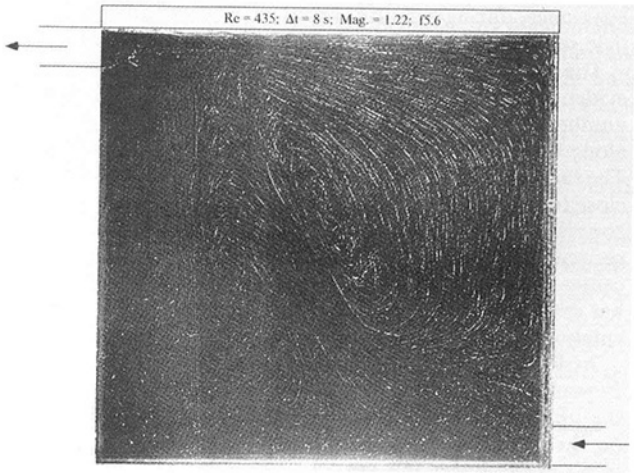

Fig. 10 Symmetry plane visualization for Re = 435

image and if the flow is steady in time and repeatable. A composite image such as this is necessary because of the widely varying velocity magnitudes in the flow field. The dynamic range of velocity magnitude (ratio of maximum to minimum) measured in Fig. 7 is about 50. Exposure times between 0.5 and 1.875 s were required to make velocity measurements in the high-speed main path, whereas longer exposure times between 5.5 and 14 s were required for flow near the recirculation zones. Details of the quantitative measurements are given by Walter and Chen (1990).

At Re = 205, shown in Figs. 8 and 9, the flow pattern remains laminar and is similar to Re = 105. The stronger momentum of the incoming fluid causes the stagnation point on the left wall to move farther down. The lower recirculation center (LC) is barely visible in the lower left corner. The upper recirculation zone, to the right of the main flow, shrinks in size due to the increased speed of the flow above it, and also moves farther to the left. The upper stagnation point (US) moves farther down the right wall from the previous Reynolds number, but its exact location is difficult to pinpoint in the image. The secondary recirculation zone is pushed downward, but the saddle point moves slightly upward, perhaps due to the increased momentum of the main throughflow. Figure 9 shows the outlet quarter plane and indicates that the upward flow for Re = 205 has sufficient momentum such that very near the upper wall the flow is turned sideways. It is seen from Fig. 9 that the flow is basically two-dimensional flow, but slightly asymmetric about the center plane. Figure 9(*b*) shows the cross section in the middle plane. The velocity component in the cross section below the bright horizontal line is downward, and above the bright horizontal line, the flow is essentially stagnant in the plane or moves normal to it. The lower one-fourth of the Fig. 9(*b*) image is not symmetric with respect to the center plane. The right side shows uniform vertical movement while the left side appears stagnant. As discussed above, it is likely that some flow into the center plane in Fig. 8 is from adjacent planes, so that the saddle point in Fig. 8 appears rather like a "source." However, precise conclusions are difficult because the horizontal velocity component in the cross-sectional planes is very small.

3.4 Asymmetric Flow. With increasing Reynolds number beyond Re = 205, repeatability of the flow pattern in the cross-sectional planes became more difficult, showing the beginning instability of symmetric flow in the cross section. However, because the velocity component in the cross section is very small, the side views of the primary flow patterns are, in general, relatively steady and reproducible for Reynolds numbers up to 625.

Downloaded 13 Dec 2010 to 193.140.21.150. Redistribution subject to ASME license or copyright; see http://www.asme.org/terms/Terms_Use.cfm

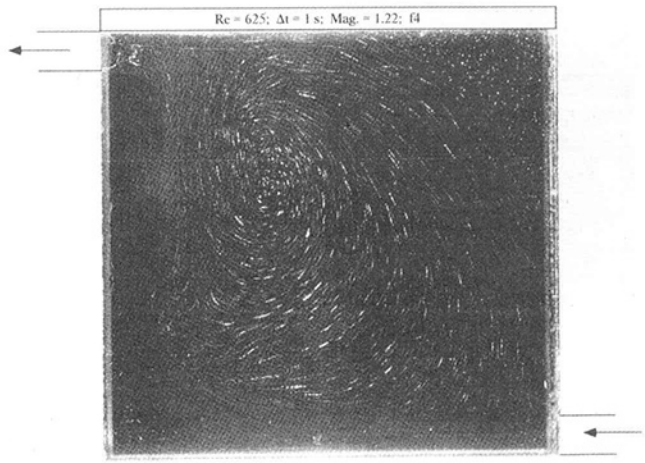

Fig. 11 Symmetry plane visualization for Re = 625

The flow pattern at Re = 435 is shown in Fig. 10. This image and the ones that follow are enhanced with a high-pass filter (in addition to brightness contrasting) in order to enhance the streaks against the dark background, as are all the third-dimension views. This is necessary at higher Reynolds numbers where shorter exposure times are required to distinguish pathlines since, during a shorter exposure time, a fast-moving particle scatters less light into a given area of the image plane.

The evolution of flow patterns from Re = 205 to Re = 435 is evident from a comparison of Figs. 8 and 10. At Reynolds number of 435, the main flow path is now almost moving along the lower and left walls, flowing directly to the outlet. The saddle point observed at the previous two Reynolds is very close to the upper wall near the outlet. The lower recirculation zone in the left corner of the chamber is very small. The upper recirculation zone becomes larger and has moved to the left center region of the chamber. The secondary recirculation zone has grown to approximately the same size as the right recirculation zone, and is located close to the center of the chamber.

At Re = 625 (Fig. 11), the saddle point visible for the lower Reynolds numbers has attached to the upper wall to become the upper stagnation point (US), which previously appeared on the right wall. The lower recirculation zone is again very small in the lower left corner. The upper recirculation zone now encompasses much of the middle section of the test cell and is centered in the upper left region, to the right of the throughflow. The secondary recirculation zone has shrunk and moved to the extreme upper right corner, so flow exits the chamber only through the main path, along the bottom and right walls. Direct observation indicated that the flow along the left wall may be in transition to turbulence due to the amplification of the disturbance created by the inlet jet impinging on the left wall at high speed. This is also indicated by the highly three-dimensional pattern in the cross section of the outlet quarter plane in Fig. 12. The rather disorganized three-dimensional flow pattern in Fig. 12 also suggests that the flow may be in transition to turbulence.

3.5 Turbulent Flow. At Re = 910 (Fig. 13), the flow pattern is predominantly turbulent and reveals more fluctuations in the streak motion, indicating the presence of turbulent flow in the regions of higher speed throughout much of the chamber. As with Re = 625, the upper recirculation zone is much larger than at previous Reynolds numbers, and now includes most of the test section. As a result, the center of the recirculation zone moves to the middle of the test section, but is still above the center. The stagnation point on the upper wall (US) moves farther left toward the outlet due to the high momentum carried by the throughflow.

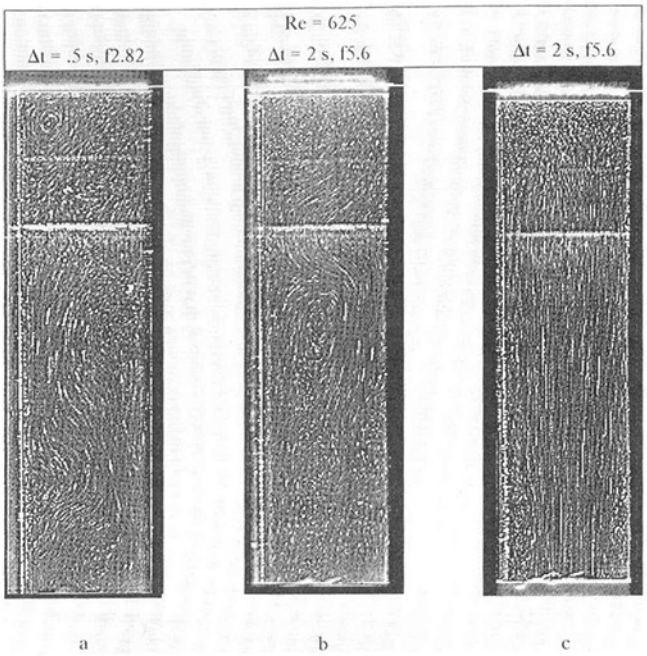

Fig. 12 Quarter plane visualization for Re = 625

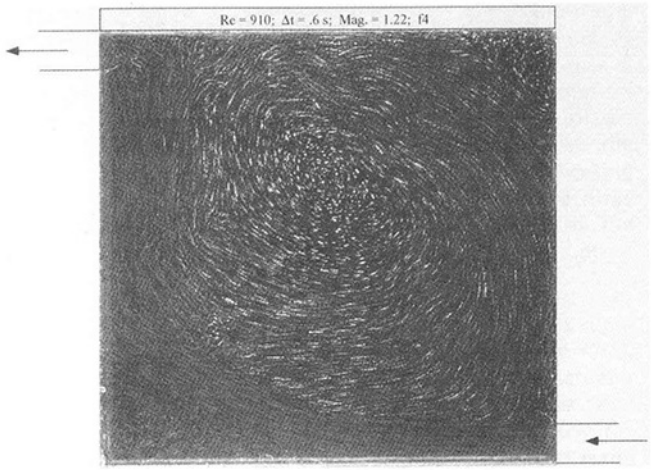

Fig. 13 Symmetry plane visualization for Re = 910

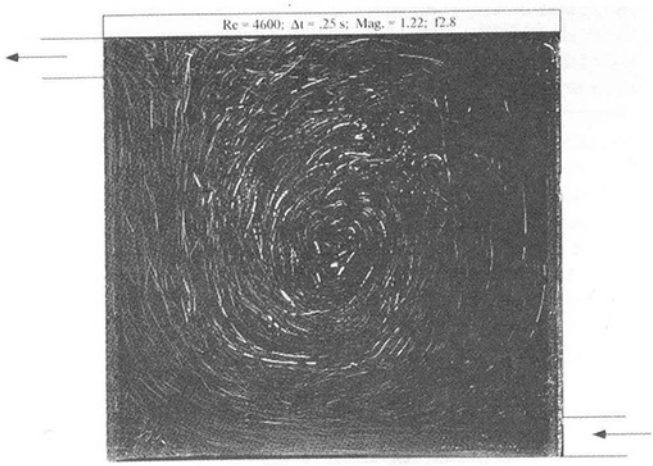

Fig. 14 Symmetry plane visualization for Re = 4600

At Re = 4600 (Fig. 14), the flow in the entire chamber is turbulent. This is because the Reynolds number at the inlet exceeds the critical Reynolds number for laminar channel flow.

Downloaded 13 Dec 2010 to 193.140.21.150. Redistribution subject to ASME license or copyright; see http://www.asme.org/terms/Terms_Use.cfm

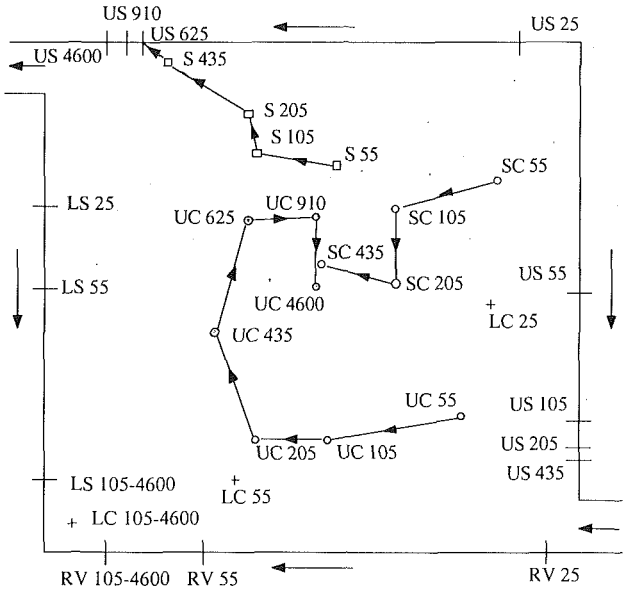

Fig. 15 Summary of flow parameters

Visual inspection also indicates turbulent flow. The flow pattern begins to resemble the well-known driven-cavity flow, where one large recirculation zone forms with its center located at the center of the cavity, as shown in Fig. 14. Because the flow is turbulent, the existence of large turbulent momentum diffusion prevents small separation and isolated recirculation zones from forming at the corners of the chamber. The flow may be more two dimensional than three dimensional, because the viscous diffusion from the two walls normal to the image is small compared with the turbulent diffusion.

3.6 Summary of Flow Parameters. Figure 15 summarizes the main features of the flow patterns in the offset channel at the Reynolds numbers investigated. The main flow path separates at the upper (US) and lower (LS) stagnation points shown. Upper stagnation points (US) are shown on the upper and right walls. The upper stagnation point occurs on the upper wall for Reynolds numbers 25, 635, 910, and 4600. In these cases, flow to the right of the upper stagnation point forms the upper recirculation zone (UC), while flow to the left exits the chamber. The lower stagnation point occurs only on the left wall. Below this point, the lower recirculation zone (LC) forms, and above it, the fluid either exits the chamber or separates at the upper stagnation point. Figure 4 (Re = 55) provides the best illustration of this terminology, because the upper and lower recirculation zones are approximately the same size. The size of the lower recirculation zone shrinks rapidly after Re = 55. The reverse stagnation point (RV) on the bottom wall is the result of flow in the lower recirculation zone impinging on the bottom wall.

When the fluid does not have sufficient momentum to separate at the top wall, a saddle point (S) forms, and the upper stagnation point (US) instead occurs on the right wall. Saddle points are observed at Reynolds numbers 55, 105, 205, and 435. In these cases, flow below the upper stagnation point is entrained back into the main flow path to form the upper recirculation zone, and flow above the upper stagnation point gives rise to the secondary recirculation zone (SC) shown, for example, in Fig. 6 (Re = 105). The location of the center of the upper recirculation zone (UC) correlates roughly with the location of the upper stagnation point and saddle point. For Re = 625 and 910, the upper stagnation point occurs on the top wall, and the upper recirculation zone moves to the upper half of the chamber. When the flow is fully turbulent (Re = 4600), the upper recirculation zone moves downward, to the center of the chamber, suggesting that its location may become independent of the upper stagnation point. The locations of some these parameters are difficult to define and plot precisely. For example, the upper stagnation points for the turbulent Reynolds numbers would require much longer exposure times to determine the precise locations, while shorter exposure times would be necessary for investigation of turbulence structures. The exposure times selected represented a necessary compromise between such extremes.

Conclusions

Flow in an offset channel has been investigated and characterized for a wide range of Reynolds numbers. At Re = 25, one counterclockwise recirculation cell is observed. At Re = 55, two circulation cells are observed, rotating in opposite directions and separated by the diagonal through flow. At higher Reynolds numbers, Re = 105, 205, 435, and 625, the counterclockwise recirculation cell reduces rapidly in size and eventually disappears. Turbulent flow in the chamber is observed at Reynolds numbers of 910 and 4600. The recirculation cell spreads to the entire test section due to strong turbulent mixing, except the primary through flow path, along the bottom and left walls. Between Re = 55 and Re = 435 a saddle point forms in the upper left region of the chamber, rather than a stagnation point on the upper wall near the outlet for the higher Reynolds numbers. This is due to the diffusion of momentum by the side walls, a three-dimensional characteristic of this flow. A larger depth (t/H in Fig. 1) might prevent this phenomenon at all but the lowest of Reynolds numbers. Finally, the flow patterns in the cross-sectional planes normal to the side walls in general were not symmetric with respect to the center plane of the test section, suggesting that asymmetric flow is more stable.

The present experimental study may be useful for verification of numerical flow calculations. In this regard, we emphasize that the flow in this study is fully three dimensional and would not be predicted properly by a two-dimensional simulation. Although the velocity field is largely two dimensional (the component normal to the side walls is very small), the drag induced by the walls at lower Reynolds numbers alters the topology of the flow drastically. Attempts at numerical simulation of this flow are currently under way.

Because the flow patterns are so different in the range of Reynolds numbers studied, properties of practical interest such as temperature distribution and heat transfer rate in a heat exchanger configuration will vary with Reynolds numbers. The present study contributes to a better understanding of the flow field for a range of Reynolds numbers in the laminar and turbulent regimes.

Acknowledgments

The authors would like to thank R. G. Hering, Dean of the College of Engineering at the University of Iowa, for his support of this research. We are also grateful to the reviewers for their constructive comments. Partial support for this work was provided by NSF Grant No. EID-8711681.

References

Adrian, R. J., 1986, "Multi-point Optical Measurements of Simultaneous Vectors in Unsteady Flow—a Review," *International Journal of Heat and Fluid Flow*, Vol. 7, No. 2, pp. 127–145.

Agüí, J. C., and Jiménez, J., 1987, "On the Performance of Particle Tracking," *Journal of Fluid Mechanics*, Vol. 185, pp. 447–468.

Berner, C., Durst, F., and McEligot, D. M., 1984, "Flow Around Baffles," ASME Journal of Heat Transfer, Vol. 106, No. 4, pp. 743–749.

Khalighi, B., 1989, "Quantitative Fluid Velocity Measurements by Automatic

Downloaded 13 Dec 2010 to 193.140.21.150. Redistribution subject to ASME license or copyright; see http://www.asme.org/terms/Terms_Use.cfm

Analysis of Flow Visualization Images," *Journal of Experiments in Fluids*, Vol. 7, No. 2, pp. 142–144.

Landreth, C. C., Adrian, R. J., and Yao, C. S., 1988, "Double Pulsed Particle Image Velocimeter With Directional Resolution for Complex Flows," *Journal of Experiments in Fluids*, Vol. 6, No. 2, pp. 119–128.

Tulapurkara, E. G., Lakshmana Gowda, B. H., and Balachandran, N., 1988, "Laminar Flow Through Slots," *Journal of Fluid Mechanics*, Vol. 190, pp. 179–200.

Ushijima, S., Kato, M., Fujimoto, K., and Moriya, S., 1985, "Application of Some Turbulence Models—Numerical Analyses of Two-Dimensional Circulation Flows," Central Research Institute of the Electric Power Industry (Japan), Civil Engineering Laboratory Report No. 385019, Abiko City, Japan.

Utami, T., and Ueno, T., 1987, "Experimental Study on the Coherent Structure of Turbulent Open-Channel Flow Using Visualization and Picture-Processing," *Journal of Fluid Mechanics*, Vol. 174, pp. 399–440.

Walter, J. A., and Chen, C. J., 1990, "Development of a Quantitative Velocity Measurement System and Its Application to Offset Channel Flow," IIHR Report No. 338, Iowa Institute of Hydraulic Research, The University of Iowa, Iowa City, IA.

White, F. M., 1974, *Viscous Fluid Flow*, McGraw-Hill, New York, Chap. 5.

Downloaded 13 Dec 2010 to 193.140.21.150. Redistribution subject to ASME license or copyright; see http://www.asme.org/terms/Terms_Use.cfm

Heat Transfer With Very High Free-Stream Turbulence: Part I—Experimental Data

P. K. Maciejewski
Mechanical Engineering Department,
University of Pittsburgh,
Pittsburgh, PA 15261

R. J. Moffat
Department of Mechanical Engineering,
Stanford University,
Stanford, CA 94305

The present research investigates boundary layer heat transfer with very high free-stream turbulence, a problem of primary interest in the gas turbine industry where existing boundary layer correlations and codes underpredict local heat transfer rates on first-stage turbine blades and vanes by as much as a factor of three for some engine designs. The problem was studied experimentally by placing a constant-temperature heat transfer surface at various locations in the margin of a turbulent free jet and measuring both the surface heat transfer rate and the turbulence in the free stream. In this experiment, free-stream turbulent fluctuations 20 to 60 percent relative to the mean velocity augment heat transfer 1.8 to 4 times that which would be predicted locally using accepted correlations for turbulent boundary layers at the same Reynolds number.

Introduction

The present research confronts one of the most persistent and difficult problems in the gas turbine industry: predicting the heat transfer to turbine blades and vanes, particularly to the first stages. Not even the most modern, carefully applied heat transfer theory can guarantee to predict the heat transfer to the first-stage blades and vanes of a newly designed gas turbine within a factor of two or three under some engine conditions. Only models "tuned-up" using test data from a geometrically and aerodynamically similar engine can guarantee acceptably accurate results. This state of affairs has persisted for more than 20 years in spite of all the careful heat transfer research performed in industrial and academic laboratories.

The fact that flow fields with aggressive heat transfer characteristics, like those present in gas turbine engine designs, have not been studied and incorporated into predictive models might explain why predictive codes based on extensive laboratory data grossly underpredict heat transfer in an engine environment. Historically, free-stream turbulence has been regarded as a complicating factor rather than a natural accompaniment of high-energy density systems. In fact, one of the hallmarks of careful research has been the "quality" of the flow in the wind tunnel, defined principally by a low level of turbulence, the lower the better. Consequently, low-turbulence flow fields provide all the "benchmark" heat transfer data in the literature. When free-stream turbulence has been studied, the experimental designs employed typically followed a single pattern: establish a flow field with known turbulence properties and measure its effect on heat transfer.

High levels of heat transfer must first be isolated and measured before they can be explained. Simonich and Bradshaw (1978), Pedisius et al. (1979), and Blair (1983a) all report heat transfer augmentation due to free-stream turbulence, but they do not reproduce the range of Stanton numbers experienced in an engine environment. However, these studies were conducted with grid-generated, nearly isotropic turbulence of low to moderate intensity. Meanwhile, gas turbine engines run with turbulence intensities up to 20–30 percent, which is, probably, highly anisotropic and well laced with large coherent structures coming downstream from the combustion chamber. Prior to the present research, little was known about what happens at higher intensity with large-scale, anisotropic turbulence.

This paper describes a flow field with very aggressive heat transfer characteristics. The paper that follows identifies the aspects of the high free-stream turbulence associated with high levels of heat transfer.

Review of Prior Work

The works of Kestin (1966), Kearney (1970), Consigny and Richards (1982), Simonich and Bradshaw (1978), Pedisius et al. (1979), and Blair (1983) give a representative collection of prior experiments on the effects of free-stream turbulence on boundary layer heat transfer. Kestin (1966) found that the principal effect of free-stream turbulence of 3.8 percent was to move the location of transition upstream. He concluded that there was no effect on the fully turbulent boundary layer. Since the work of Kestin (1966), researchers generally concede that turbulence alters the behavior of transition, advancing it to lower Reynolds numbers, but opinions have been divided as to whether or not free-stream turbulence has any effect on the already turbulent boundary layer.

Kearney (1970) reports no effect of free-stream turbulence on either a constant-velocity boundary layer or one with a strong acceleration applied to the flow ($K = 2.5 \times 10^{-6}$) for a grid-generated turbulence level of 4 percent. In order to separate the effect of free-stream turbulence on turbulent boundary layer heat transfer from its effect on the location of transition, Kearney (1970) correlated his data using a Reynolds number based on the local free-stream velocity and enthalpy thickness. In addition, Kearney fitted a numerical model with a turbulence kinetic energy closure and produced results that matched the data: no effect on Stanton number for 4 percent turbulence.

Consigny and Richards (1982) confirm the conclusion of Kestin (1966) and Kearney (1970), that the principal effect of turbulence was to alter the location and extent of transition. Their data show that changes in turbulence intensity from 1 to 3.6 percent shift the transition zone upstream from its original location at x-Reynolds number of 250,000 to a final location at x-Reynolds number of 100,000. This causes dramatic changes in the heat transfer coefficient at locations that were originally laminar and finally turbulent, but do not significantly alter values of h in the already turbulent region.

Simonich and Bradshaw (1978) report as much as a 30 per-

Contributed by the Heat Transfer Division for publication in the JOURNAL OF HEAT TRANSFER. Manuscript received by the Heat Transfer Division April 1991; revision received April 1992. Keywords: Forced Convection, Turbulence. Associate Technical Editor: D. M. McEligot.

Copyright © 1992 by ASME
Downloaded 13 Dec 2010 to 193.140.21.150. Redistribution subject to ASME license or copyright; see http://www.asme.org/terms/Terms_Use.cfm

cent increases in heat transfer due to free-stream turbulence of 6 percent. However, their data for heat transfer coefficient represent average values over a flat plate of relatively large size placed on the centerline of the tunnel. It is possible that increasing the turbulence caused a change in the location of the transition zone on the plate. If this occurred, one would expect high turbulence levels to cause the transition location to move upstream, raising the average heat transfer coefficient on the plate by exposing more of the plate to the turbulent boundary layer. If this had occurred, it would account for the rather large effects observed.

Pedisius et al. (1979) tested over a wider range of turbulence levels (0.5 to 24 percent). In their data, the effect of turbulence level is clearly discernible and orderly, and suggests an effect approaching 40 percent on Stanton number. In addition, their experiments permit local measures of Stanton number to be compared to an existing correlation at the same momentum thickness Reynolds number. These were the first data to suggest unambiguously a significant increase in Stanton number due to high levels of free-stream turbulence.

In a carefully controlled and documented study, Blair (1983a) reports that free-stream turbulence has a significant effect on heat transfer for fully turbulent boundary layer flow. His data clearly show both the effect of free-stream turbulence on the transition location and on the Stanton number distribution in the fully turbulent region. In the fully turbulent region, with free-stream turbulence levels of 4 to 6 percent, Stanton number is significantly higher than the correlation given by Kays and Crawford (1980) for low levels of free-stream turbulence. Blair (1983a) reports increases as much as 20 percent for grid-generated free-stream turbulence of 7 percent.

Prior to the present study it appeared likely that free-stream turbulence levels up to 10 percent caused a proportional increase in heat transfer for turbulent boundary layers. Large effects on average values might result if the turbulence affected the location of transition and if the heat transfer data were compared (with and without turbulence) at constant x-Reynolds numbers or at a fixed position on the surface.

Objectives

The objective of this paper and the one that follows is to document the effects of very high free-stream turbulence on turbulent boundary layer heat transfer. This objective requires that several subordinate goals be met:

1 To identify a flow field that greatly augments heat transfer through a turbulent boundary layer, compared with a turbulent boundary layer with negligible free-stream turbulence at the same enthalpy thickness Reynolds number.

2 To measure the levels of heat transfer augmentation and the turbulence properties of this flow.

3 To document the effects that high free-stream turbulence has on boundary layer mean velocity and mean temperature profiles.

4 To evaluate the usefulness of existing correlations describing the effect of free-stream turbulence on turbulent boundary layer heat transfer.

5 To investigate the sensitivity of the heat transfer augmentation to local values of the free-stream turbulence, Tu, and Λ/Δ_2.

6 To develop a plausible model for the mechanism by which high free-stream turbulence affects heat transfer.

Items (1)–(3) will be treated presently. Items (4)–(6) will be deferred to "Part II: Analysis of Results."

Test Facility

A free turbulent jet offers a simple flow field capable of generating very high local turbulence levels with significant contributions from large-scale, relatively well organized structures. Figure 1, created from the work of Wygnanski and Fiedler (1969), illustrates the features of the free jet that make it attractive. The mean velocity is distributed across the jet, from a maximum on the centerline to zero in the surrounding air. The relative turbulence intensity increases dramatically near the outer edge. Relative turbulence intensities of up to 50 percent based on local mean velocity can easily be found. In addition, integral length scales of the turbulence increase with the distance from the jet exit. In short, a variable velocity free jet facility produces a wide range of local combinations of mean velocity, turbulence intensity, and integral length scale.

The present experiments were conducted by placing a constant-temperature heat transfer surface in the margin of a large diameter turbulent free jet. Figure 2 shows a schematic of the free jet facility with the heat transfer test surface in a representative position, within a few exit diameters off the axis of

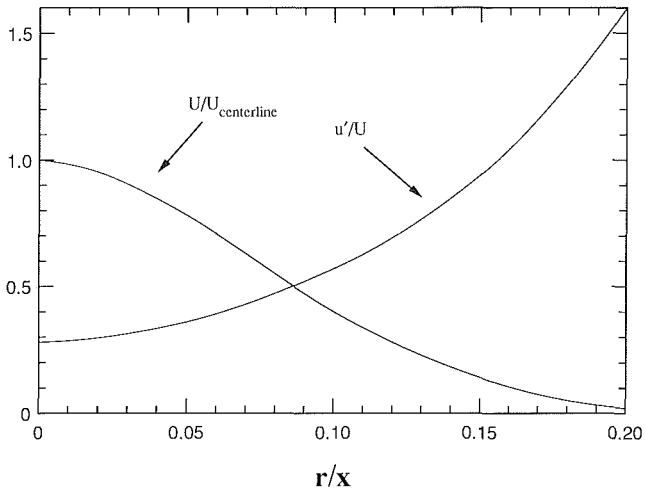

Fig. 1 Characteristics of a round, self-similar free jet

Nomenclature

C_f = skin friction coefficient
Pr = Prandtl number
Pr_t = turbulent Prandtl number
Re_x = Reynolds number based on plate location
$Re_{\Delta 2}$ = Reynolds number based on enthalpy thickness
Re_θ = Reynolds number based on momentum thickness
St = Stanton number
Tu = ratio of rms velocity fluctuation to mean value
U = mean convective velocity
u' = standard deviation in the streamwise component of velocity
v' = standard deviation in the component of velocity normal to the surface
w' = standard deviation in the spanwise component of velocity
t^+ = temperature scaled on inner variables
u^+ = mean velocity scaled on inner variables
y^+ = distance from the wall, scaled on inner variables
Δ_2 = enthalpy thickness
Λ = turbulence integral scale
D = blower exit diameter
K = acceleration parameter
r = radial position coordinate in the free jet
x = streamwise position coordinate in the free jet

Downloaded 13 Dec 2010 to 193.140.21.150. Redistribution subject to ASME license or copyright; see http://www.asme.org/terms/Terms_Use.cfm

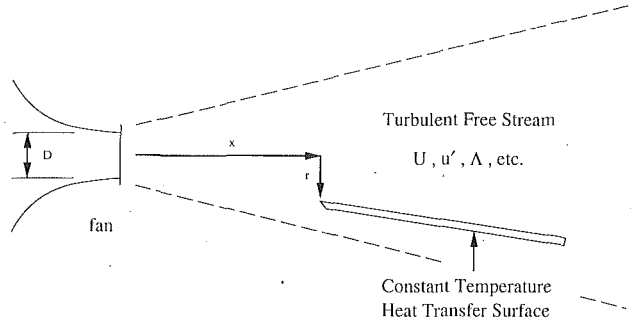

Fig. 2 Schematic of the free jet test facility

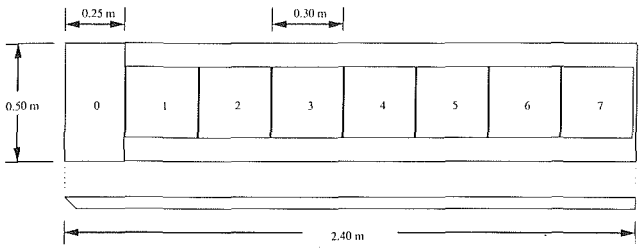

NOTE: only sections 1 through 7 are heated

Fig. 3 Schematic of the heat transfer surface

the jet and several diameters downstream of the jet exit plane. For all the experiments described below, the plate was either aligned with the centerline axis of the jet or set at an angle so that the plane of the test plate intersected the blower exit plane at the centerline axis. Runs were made in the free jet with the test surface at streamwise positions $x/D = 5.7$ and $x/D = 11.4$. Between individual test runs, the radial position of the test surface varied between $r/x = 0.0$ and $r/x = 0.3$.

Blower. A centrifugal fan (0.4 m wheel diameter) dumping to a 0.35-m-dia round exit plane produces the free jet used for this experiment. A slide gate at the fan inlet sets the velocity at the blower exit plane. The fan typically runs off design, making the velocity field in the exit plane nonuniform and highly turbulent. This was entirely consistent with the objectives of the project, and no attempt was made to "clean up" the flow. Adjusting the blower inlet gate changes the character of the velocity field in the fan exit plane, hence each different "buildup" can be considered a qualitatively different flow field. In effect, this widens the parameter space of the study, which is not intended to be a study of heat transfer in a classical, self-similar free turbulent jet, but a survey of heat transfer under highly turbulent flow conditions.

Test Surface. The heat transfer test surface, shown schematically in Fig. 3, is a 2.4-m-long, 0.5-m-wide, aerodynamically smooth, constant-temperature flat plate. To isolate the heated section of the test surface from side wall effects, only the central 60 percent of the surface width is heated. This region consists of 0.01-m-thick aluminum sections each 0.3 m wide. The first of these, section 0, is 0.25 m in length, has a sharp leading edge, and is not heated. The other seven sections, 1 through 7, are each 0.3 m in length. Each of these sections has a resistance "patch" heater (Electrofilm part #113000-910, 12 in. × 12 in., 115 VAC, 10 W/in.^{2}) bonded to its backside, which is then heavily insulated with fiberglass insulation. The sections are also insulated from each other by strips of balsa. Five type J thermocouples are embedded in each of the sections in a cross pattern to measure plate temperature and to check for spanwise and streamwise temperature uniformity. During test runs, side walls are attached to the surface in an attempt to "freeze" the flow over the surface at the conditions found at its leading edge. The power delivered to each section is controlled individually so that at equilibirum all seven heated sections have the same average temperature to ±0.25°C. The plate-to-free-stream temperature difference is nominally 20°C for each run. Conduction losses out the back and sides are typically about 5 percent of the measured input power. Radiative losses are estimated to be less than 1 percent of the input power.

Instrumentation. Heat transfer coefficients for each section of the surface were determined by measuring the power delivered to each section, the average temperature of each section, and the free-stream temperature. The power delivered to each patch heater was measured with a Valhalla Model 2000 Autoranging Digital Watt-Ammeter. The average temperature of each section was measured by reading the thermocouples embedded in each section with an HP 3456A Digital Voltmeter. The free-stream temperature was also measured with a type J thermocouple. Temperature measurements in the thermal boundary layer were made using a 5 mil, butt-welded, type E, thermocouple probe.

Triple wire velocity measurements were made with a DISA 55P91 triaxial probe operated in constant-temperature mode using a TSI Model 1051-G Monitor and Power Supply and a set of three TSI 1050 CTA's. The output from each CTA was first passed through a TSI 1052 Signal Linearizer and then read in burst mode (simultaneous sample and hold ADC on three channels) by a Data Translation Model 2828 Data Acquisition Card running on an IBM AT Computer. Before the triaxial probe was used in the free jet it was first qualified in the Stanford two-dimensional channel. Single wire velocity measurements were made using a normal 5 μm tungsten wire operated in constant-temperature mode using a DISA 55M01 Main Unit and a DISA 55M10 CTA Standard Bridge.

Profile measurements were made by first manually positioning the probe near the wall, then moving the probe under computer control using a probe traversing mechanism. Only the axis normal to the wall was used.

Experimental Uncertainty. The relative uncertainty in each of the measured variables and in each of the derived variables and parameters was determined by the methods described in ANSI/ASME PTC 19.1-1985. The major sources of experimental uncertainty in the heat transfer coefficient, h, were the average surface to free-stream temperature difference, ΔT, which could be estimated to within ±2.5 percent, and the average surface convective heat flux, q'', which could be estimated to within ±1.9 percent. The average relative uncertainty in h for these experiments was ±3.2 percent. The major source of experimental uncertainty in the mean velocity, U, was due to slight drifts of the hot-wire probe off its initial calibration. Hot-wire data for a given run were accepted only if the probe response matched its calibration for velocity to within ±2.0 percent both before and after the run. The average relative uncertainties in U, u', and Λ were ±2.0 percent, ±5.6 percent, and ±5.6 percent, respectively. Uncertainty in the estimates of fluid properties, which were typically less than 1.0 percent, had only a slight effect on the overall uncertainty in the estimates of the relevant nondimensional parameters. The average relative uncertainties in St, Re_x, $\mathrm{Re}_{\Delta 2}$, and Tu were ±3.8 percent, ±2.1 percent, ±3.8 percent, and ±6.0 percent, respectively. The uncertainty in the near-wall parameters u^+, t^+, and y^+ was also significantly affected by the uncertainty in the skin friction coefficient, $C_f/2$, which could be estimated by a Clauser plot method to within ±5.0 percent. The average relative uncertainty in u^+ was ±3.8 percent, the average relative uncertainty in t^+ was ±5.7 percent, and the average relative uncertainty in y^+ ranged from ±6.0 percent near the wall to ±3.2 percent in the outer region of the boundary layer.

Downloaded 13 Dec 2010 to 193.140.21.150. Redistribution subject to ASME license or copyright; see http://www.asme.org/terms/Terms_Use.cfm

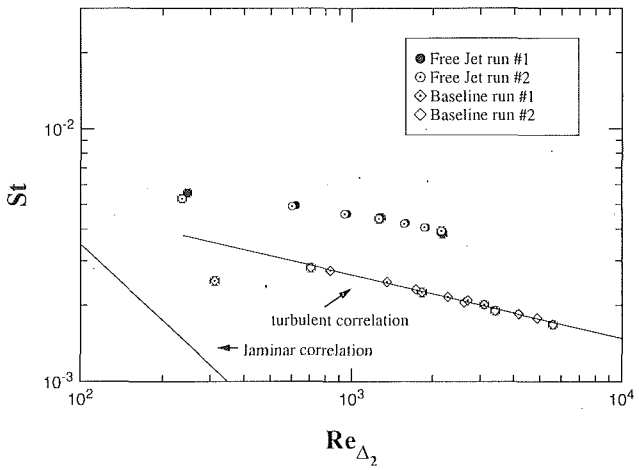

Fig. 4 Qualification of the heat transfer test surface

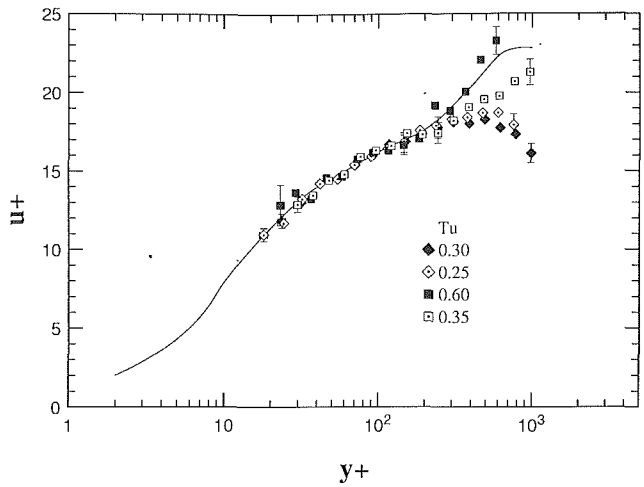

Fig. 5 Mean velocity profiles in the presence of very high free-stream turbulence

The error brackets presented in Figs. 4–9 represent 95 percent confidence intervals for the indicated parameters.

Test Surface Qualification. The heat transfer surface was qualified by installing it in a closed-loop wind tunnel and testing it in a uniform velocity flow with negligible levels of free-stream turbulence. Figure 4 shows Stanton number measurements on the surface for two separate baseline runs. Each run matches an accepted flat plate correlation (Kays and Crawford, 1980, Eq. (12.30)), for normal turbulent boundary layer behavior to within ±2.5 percent. From this test we conclude that the absolute level of the heat transfer coefficient can be measured on this test surface to within ±2.5 percent. Figure 4 also shows the second part of the equilibrium runs—a demonstration of repeatability in the free jet. Stanton number measurements were made on two runs in the free jet, on separate days under identical experimental conditions (i.e., with the plate put into the same position in the flow and with the blower at the same setting). The agreement between these two data sets again lies within ±2.5 percent, establishing that the heat transfer coefficient on the surface in the free jet is repeatable for identical buildups to within the accuracy within which we can measure it absolutely.

Measurements Using the Orthogonal Triple-Wire Probe. Detailed measurements of the free-stream velocity for each run were made using the data interpretation techniques described by Maciejewski and Moffat (1990). Due to the difficulties in the interpretation of the turbulence measurements made with the triple-wire probe in the presence of very high free-stream turbulence, estimates of the correlations between the fluctuating components of velocity will not be presented. Figure 5 presents profiles of mean velocity for locations in the jet with turbulence intensities in the free stream up to 60 percent. The cases at 60 and 35 percent turbulence intensity were measured with the blower at a steep angle (16 deg) relative to the surface. The cases at 25 and 30 percent turbulence were measured with the blower at 0 deg relative to the surface. All four cases show close agreement in the "law of the wall" region, then break off to a mean profile set by the jet itself. The two innermost points for the 60 percent case fall above the "law of the wall" because the relative turbulence intensities at those locations exceed 80 percent, so that even the robust estimates of the mean velocity employed using the techniques described by Maciejewski and Moffat (1990) can be expected to be biased in the direction observed. If the flow in the jet has an effect on Stanton number that is significantly different than its effect on skin friction, the evidence of the effect is not present in the mean velocity profile in the near wall region.

Certain qualitative characteristics of the flow near the heat transfer surface, as determined by measurements with the orthogonal triple wire, allow simplifications in the aerodynamic description of the physical situations under investigation. For the present experiments, $u' \approx w' \approx 0.7v'$, so that the single descriptor u' reasonably characterizes the state of all three components of the turbulent fluctuations in the free stream. One might hypothesize that v' plays a more vital role than u' in determining the surface heat transfer rate. However, this hypothesis cannot be tested by the present data. The nearly linear relationship between u' and v' for the experiment in the jet suggests that one variable might correlate the data as well as the other. For convenience in making subsequent comparisons to other experiments, results will be discussed in terms of u'. In addition, both u' and the integral length scale of the u component of velocity are nearly uniform through the outer region of the boundary layer. Therefore, a single scalar measure of each can be used to characterize the state of the free-stream turbulence over a given location of the heat transfer surface.

Design of the Experiments

The effects of very high turbulence on heat transfer were studied by measuring the heat transfer rates on the test surface when it was placed in the free jet for 12 runs with the blower at various inlet gate settings and at various angles to and axial distances from the plate. While h was measured on all seven heated sections, free-stream turbulence was measured only over sections 2, 4, and 6. Between individual runs, the free-stream mean velocity varied from 1.0 to 3.5 m/s, the turbulence intensity varied from 20 to 60 percent, and the integral scale varied from 8 to 40 cm. In terms of conventional nondimensional aerodynamic parameters, the heat transfer data for high turbulence fall on the domain of $300 < \mathrm{Re}_{\Delta 2} < 3000$, $0.20 < Tu < 0.6$, and $10 < \Lambda/\Delta_2 < 100$.

The heat transfer measurements were made prior to the velocity measurements, sometimes on different days. While less than desirable, the procedure of acquiring heat transfer data on one day and velocity data on another day had to be adopted due to the duration of the measurement procedures. To facilitate the repositioning of the jet for the purpose of making detailed turbulence measurements, triple-wire measurements were made at a single point 10 cm over the center of the surface prior to measuring the heat transfer rate. More extensive triple-wire measurements were later made for each heat transfer run by positioning the blower and matching the measures of free-stream mean velocity and turbulence intensity to within ±5 percent for a single sample of 2500 points. This

Downloaded 13 Dec 2010 to 193.140.21.150. Redistribution subject to ASME license or copyright; see http://www.asme.org/terms/Terms_Use.cfm

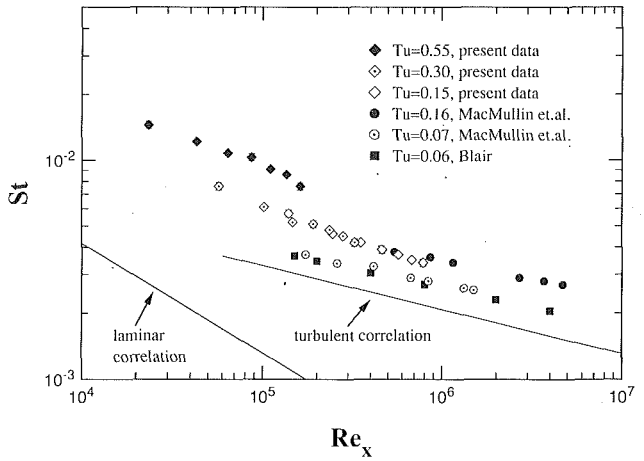

Fig. 6 High turbulence increases Stanton number by as much as a factor of four

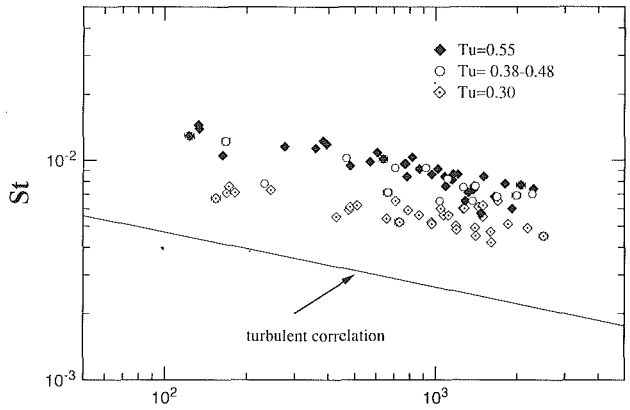

Fig. 7 High turbulence increases Stanton number locally

is within the single sample uncertainty established by multiple samples of 2500 points taken over the period over which the heat transfer is measured.

In addition to the 12 runs devoted to the study of the surface heat transfer rate under very high free-stream turbulence, a separate run was made to investigate the behavior of the profiles of mean velocity and temperature under very high free-stream turbulence. In order to acquire accurate velocity measurements very close to the wall, a single-wire probe was used and the free-stream turbulence level was slightly reduced. The conditions for this run were $U = 5.25$ m/s and $Tu = 0.15$.

Heat Transfer Results

Traditionally, Stanton number and Reynolds number described boundary layer heat transfer. Figure 6 shows a subset of the present data set plotted in terms of St and Re_x, compared with the following textbook correlations for laminar and turbulent boundary layers given by Kays and Crawford (1980):

$$St\ Pr^{2/3} = 0.332\ Re_x^{-1/2} \quad \text{(laminar, Eqs. (9)–(13))}$$

$$St\ Pr^{0.4} = 0.0287\ Re_x^{-0.2} \quad \text{(turbulent, Eqs. (12)–(14))}$$

In the comparison presented in Fig. 6, the present data have been scaled on a global measure of the mean velocity over the heat transfer surface, the value measured over section 4. All the data from the present experiment fall significantly above both correlations. At the low end, the data labeled $Tu = 0.15$ lie 80 percent above the turbulent correlation and 265 percent above the laminar correlation at $Re_x = 50{,}000$. At the high end, the data labeled $Tu = 0.55$ lie 220 percent above the turbulent correlation and 540 percent above the laminar correlation at $Re_x = 50{,}000$. These increases in St are larger than any previously reported in the literature, and in the terms of this comparison no upper limit on the increases in St has been found in the present experiments. Data for a given run lie approximately parallel to the turbulent correlation, even when Re_x falls below 60,000, the value reported by Kays and Crawford (1980) for the lower critical Reynolds number for transition to turbulence. As far as Stanton number is concerned, a boundary layer with very high free-stream turbulence behaves like a fully turbulent boundary layer with no sign of laminar or transitional behavior. Figure 6 also compares the present data to data from Blair (1983a) and MacMullin et al. (1989). The independent study of MacMullin et al. (1989) confirms the observed increases in Stanton number found by Blair (1983b) and in the present experiment, at least over part of the range. The experiment of MacMullin et al. (1989) at $Tu = 7$ percent reproduces the increases in Stanton number found by Blair (1983a) at $Tu = 6$ percent. Similarly, the experiment of MacMullin et al. (1989) at $Tu = 16$ percent reproduces the increases in Stanton number found in the present experiment at $Tu = 15$ percent. The agreement between these three experiments suggest that increases in Stanton number may be a function of Tu, independent of the mechanism used to generate the turbulence in the free stream. This hypothesis will be considered more closely in Part II.

In many situations Stanton number data correlate better using the local thickness of the boundary layer, Δ_2, than on the upstream history of the boundary layer described by the position on the surface, x. In the present case, increases in Stanton number due to high free-stream turbulence can be compared with a correlation for St in terms of $Re_{\Delta 2}$ given by Kays and Crawford, Eqs. (12)–(30). Figure 7 shows a subset of the present data set plotted in those terms. In this comparison, the present data have been scaled using local measures of the mean velocity on each section of the surface, inferred from data measured over sections 2, 4, and 6. Again, all the data from the present experiment fall significantly above the turbulent correlation in these coordinates as well. The increases in Stanton number at constant $Re_{\Delta 2}$ range from 100 percent at $Tu = 0.30$ to 300 percent at $Tu = 0.55$. In the remainder of this paper and in the entirety of Part II, the term "increase in Stanton number" will mean increase in Stanton number as compared to the following equation from Kays and Crawford at the same $Re_{\Delta 2}$:

$$St = 0.0125\ Pr^{-0.5} Re_{\Delta 2}^{-0.25} \quad \text{(turbulent, Eqs. (12)–(30))}$$

Figure 7 displays an apparent ordering of Stanton number with Tu at fixed $Re_{\Delta 2}$. How well the data orders with local measures of free-stream turbulence is the subject of the Part II.

Mean Profiles in Velocity and Temperature

For turbulent boundary layers in flows with Prandtl number near unity, the mean velocity profile and the mean temperature profile exhibit the same functional form. In fact, for a turbulent boundary layer with no free-stream turbulence, the "law of the wall" for a thermal boundary layer for Pr near 1.00 can be derived by the same methods used to derive the "law of the wall" for the momentum boundary layer once the factors Pr and Pr_t are considered (Kays and Crawford, 1980, pp. 207–211). The analogy between the aerodynamic and the thermal behavior make it easy to extend turbulence models to predict heat transfer behavior via Reynolds analogy or Pr_t. If the validity of this analogy can be demonstrated for boundary layers in the presence of very high free-stream turbulence, there is hope that existing computational schemes will continue to predict heat transfer correctly.

The mean velocity profile for a turbulent boundary layer with no free-stream turbulence can be divided into three re-

Downloaded 13 Dec 2010 to 193.140.21.150. Redistribution subject to ASME license or copyright; see http://www.asme.org/terms/Terms_Use.cfm

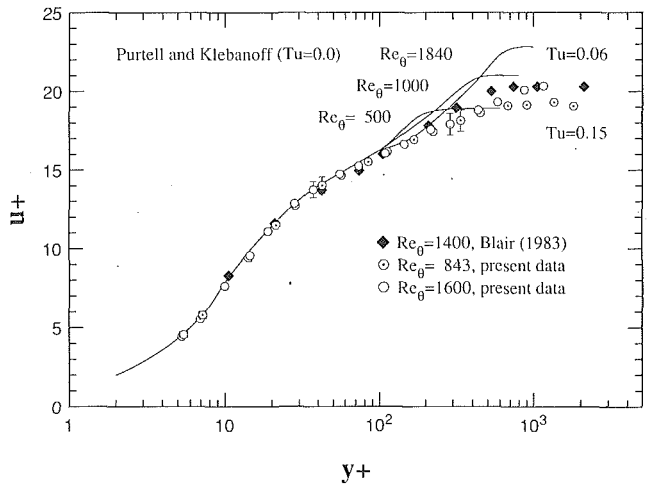

Fig. 8 Mean velocity profiles fit hydrodynamic law of the wall

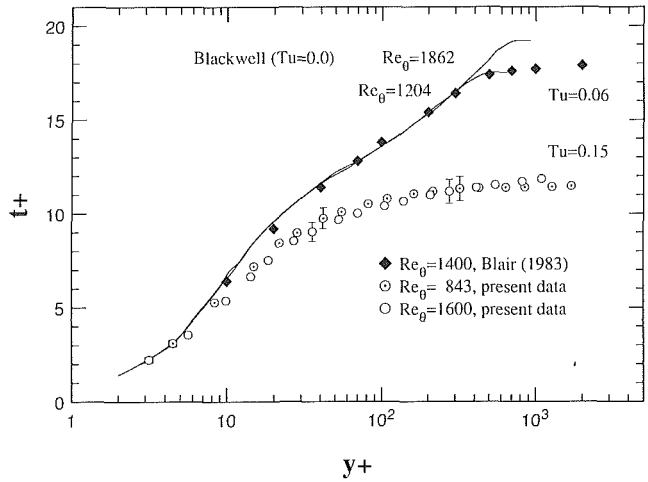

Fig. 9 Mean temperature profiles do not fit temperature law of the wall

gions: (*i*) the inner, or near-wall, region, (*ii*) the logarithmic region, and (*iii*) the wake region. Blair (1983b) finds that for $Tu = 0.06$, the mean velocity profile, when compared to profiles for a turbulent boundary layer with no free-stream turbulence plotted in inner coordinates, is unaffected by free-stream turbulence in the inner and logarithmic regions. In Blair's (1983b) data, the only effect of free-stream turbulence on the mean velocity profile is to suppress the wake region. Figure 8 compares mean velocity profiles for the present experiment at $Tu = 0.15$ to a mean velocity profile from experiment of Blair (1983b) at $Tu = 0.06$. Figure 8 also compares both the present data and the data of Blair (1983b) to mean velocity profiles from the experiments of Purtell and Klebanoff (1981) over a range of Reynolds numbers with $Tu = 0.0$. C_f for the present data was determined using a Clauser plot method. The present data agree with Blair's (1983b) data. Free-stream turbulence of 15 percent suppresses the wake region leaving the inner and logarithmic regions unaffected. The increases in C_f for the data from the present experiment shown in Fig. 8 are 6 and 10 percent, corresponding to Re_θ of 843 and 1600, respectively.

Similarly, the mean temperature profile for a turbulent boundary layer with no free-stream turbulence can be divided into three regions: (*i*) the inner, or near-wall, region, (*ii*) the logarithmic region, and (*iii*) the wake region. Blair (1983b) finds that for $Tu = 0.06$, the mean temperature profile, when compared to profiles for a turbulent boundary layer with no free-stream turbulence plotted in inner coordinates, is unaffected by free-stream turbulence in the inner and logarithmic regions. In Blair's (1983b) data, the only effect of free-stream turbulence on the mean temperature profile is to suppress the wake region. Figure 9 compares mean temperature profiles for the present experiment at $Tu = 0.15$ to a mean temperature profile from experiment of Blair (1983b) at $Tu = 0.06$. Figure 9 also compares both the present data and the data of Blair (1983b) to mean temperature profiles from the experiment of Blackwell (1972) over a range of Reynolds numbers with $Tu = 0.0$. The present data do not agree with either Blair's (1983b) data or Blackwell's (1972) data. Free-stream turbulence of 15 percent affects all three regions of the thermal boundary layer. The increases in St for the data from the present experiment shown in Fig. 9 are 80 and 95 percent, corresponding to Re_θ of 843 and 1600, respectively.

Comparing the profiles of mean velocity and mean temperature shows that the velocity field and the temperature velocity field behave quite differently. For the case presented, the Reynolds analogy factor, $2St/C_f$, is approximately 1.8, and the turbulent Prandtl number is approximately 0.55.

Discussion

The free jet has very aggressive heat transfer characteristics. By studying it experimentally we have extended the range of Stanton numbers that can be experienced in boundary layers due to turbulence by as much as 400 percent. While there is no guarantee that the causes of these elevated Stanton numbers in the present experiments correspond to the causes of high heat transfer in a gas turbine environment, they do reproduce the levels of Stanton number experienced by these engines.

The specific causes of the increases in Stanton number must be attributed to certain aspects of the very high turbulence in the free stream. Since the heat transfer surface produces expected results to within ±2.5 percent in a known physical situation at two operating points, the increases in Stanton number must be due to the flow situation in the free jet. The increases in Stanton number cannot be due to the mean velocity profile. Measurements with the orthogonal triple wire probe indicate that for these experiments the mean velocity profiles in the boundary layer in the vicinity of the wall are similar to that of a turbulent boundary layer in the absence of free-stream turbulence. At the same time, the time-averaged heat transfer coefficient must be determined by the time-averaged aspects of velocity and temperature fields, e.g., through the elements of the Reynolds stress tensor or through a correlation function for the turbulence. For the present experiments, the free-stream turbulence intensity and the integral length scale are nearly uniform throughout the outer region of the boundary layer. The levels of increase in Stanton number witnessed in these experiment cannot be caused by the spatial variation of these measures in the boundary layer. Furthermore, for the present experiments the normal components of the Reynolds stress tensor are nearly linearly related. If the increases in Stanton number are due to the elements of the Reynolds stress tensor and independent of the anisotropic part, then the increases for the present experiment should correlate on u'.

Conclusion

Free-stream turbulence of 20 to 60 percent intensity results in Stanton numbers 1.8 to 4 times those that would be predicted locally using accepted correlations for turbulent boundary layers at the same enthalpy thickness Reynolds number.

Reflection on the experiment in the free jet raises new questions about the field of turbulent convective heat transfer. For example, if there is a factor of 4 variation in Stanton number due to some measure of free-stream turbulence, why bother with a descriptor like the Reynolds number at all, since Stanton number varies only ±20 percent with the momentum thickness Reynolds number over the domain 1000 to 5000?

Downloaded 13 Dec 2010 to 193.140.21.150. Redistribution subject to ASME license or copyright; see http://www.asme.org/terms/Terms_Use.cfm

Acknowledgments

This study was supported by the NASA Hot Section Technology Program as NASA NAG 3-522. The work was initiated under the technical administration of Dr. John Rhode and continued under Dr. Raymond Gaugler, both of the Lewis Research Laboratories.

References

Blackwell, B. F., 1972, "The Turbulent Boundary Layer on a Porous Plate: An Experimental Study of the Heat Transfer Behavior With Adverse Pressure Gradients," Ph.D. Thesis, Stanford University, Stanford, CA.

Blair, M. F., 1983a, "Influence of Free-Stream Turbulence on Turbulent Boundary Layer Heat Transfer and Mean Profile Development, Part I—Experimental Data," ASME JOURNAL OF HEAT TRANSFER, Vol. 105, p. 33.

Blair, M. F., 1983b, "Influence of Free-Stream Turbulence on Turbulent Boundary Layer Heat Transfer and Mean Profile Development, Part II—Analysis of Results," ASME JOURNAL OF HEAT TRANSFER, Vol. 105, p. 41.

Consigny, H., and Richards, B. E., 1982, "Short-Duration Measurements of Heat Transfer Rate to a Gas Turbine Rotor Blade," ASME *Journal of Engineering for Power*, Vol. 4, p. 542.

Kays, W. M., and Crawford, M. E., 1980, *Convective Heat and Mass Transfer*, 2nd ed., McGraw-Hill, New York.

Kearney, D. W., 1970, "The Turbulent Boundary Layer: Experimental Heat Transfer With Strong Favorable Pressure Gradients and Blowing," Ph.D. Thesis, Stanford University, Stanford, CA.

Kestin, J., 1966, "The Effect of Free-Stream Turbulence on Heat Transfer Rates," *Advances in Heat Transfer*, T. F. Irvine and J. P. Harnett, eds., Academic Press, London, Vol. 3, p. 1.

MacMullin, R., Elrod, W., and Rivir, R., 1989, "Free-Stream Turbulence From a Circular Wall Jet on a Flat Plate Heat Transfer and Boundary Layer Flow," ASME *Journal of Turbomachinery*, Vol. 111, p. 78.

Maciejewski, P. K., and Moffat, R. J., 1990, "Heat Transfer With Very High Free Stream Turbulence," Report No. HMT-42, Thermosciences Division of Mechanical Engineering, Stanford University.

Pedisius, A. A., Kazimekas, P.-V. A., and Slanciauskas, A. A., 1979, "Heat Transfer From a Plate to a High-Turbulence Air Flow," *Soviet Research*, Vol. 11, No. 5, p. 125.

Purtell, L. P., and Klebanoff, P. S., 1981, "Turbulent Boundary Layer at Low Reynolds Number," *Phys. Fluids*, Vol. 24, No. 5, p. 802.

Simonich, J. C., and Bradshaw, P., 1978, "Effect of Free-Stream Turbulence on Heat Transfer Through a Turbulent Boundary Layer," ASME JOURNAL OF HEAT TRANSFER, Vol. 100, p. 673.

Wygnanski, I., and Fiedler, H., 1969, "Some Measurements in a Self-Preserving Jet," *J. Fluid Mech.*, Vol. 38, p. 577.

Downloaded 13 Dec 2010 to 193.140.21.150. Redistribution subject to ASME license or copyright; see http://www.asme.org/terms/Terms_Use.cfm

Heat Transfer With Very High Free-Stream Turbulence: Part II—Analysis of Results

P. K. Maciejewski
Mechanical Engineering Department,
University of Pittsburgh,
Pittsburgh, PA 15261

R. J. Moffat
Department of Mechanical Engineering,
Stanford University,
Stanford, CA 94305

Correlations describing the effect of free-stream turbulence on heat transfer have been offered by Simonich and Bradshaw (1978), Pedisius et al. (1983), and Blair (1983a), but they fail to describe the present data. The present data can be represented by a function of St, St/St_o, $Re_{\Delta 2}$, Tu, and Λ/Δ_2 within ±20 percent, but equally well by a simple correlation relating the rms fluctuating velocity in the free stream, u′, to the heat transfer coefficient, h. A new Stanton number, St′, based on u'_{max}, the maximum standard deviation in the streamwise component of velocity found in the wall affected region, collects the data of Blair (1983b), Pedisius et al. (1983), Vogel (1984), MacArthur (1986), and Hollingsworth et al. (1989), as well as the data from the present experiment, all within ±15 percent. The fact that h can be expressed as a function of local u′ alone suggests the possibility of geometry-independent correlations for turbulent heat transfer.

Introduction

The preceding paper establishes the fact that a flat-plate constant-temperature heat transfer surface placed in the margin of a free turbulent jet experiences heat transfer rates 1.8 to 4 times higher than would be predicted by a correlation for a turbulent boundary layer evaluated at the same Reynolds number. Furthermore, that paper argues that the high levels of heat transfer must be attributed to aspects of the turbulence in the free stream. The present paper addresses the question: Which aspects of the free-stream turbulence allow one to predict the heat transfer rate?

The primitive variables that describe the state of the turbulence that are accessible through the measured data for the present experiments are the nine elements of the Reynolds stress tensor and the time correlations for the fluctuating velocity components. However, in the present experiments, the Reynolds normal stresses are not varied independently, the estimates of the Reynolds shear stresses have high relative uncertainties, and only the time correlation in the fluctuating streamwise component offers a simple physical interpretation. Consequently, if there is any hope of correlating h for the present experiments, then h must be capable of being described by the set of variables $\{\Delta_2, U, u', \Lambda\}$. This list of variables is no more restrictive than those for other experiments with isotropic turbulence, and it does allow us to compare the present data to previously proposed correlations describing the effects of free-stream turbulence on heat transfer.

To date, the convention has been to attempt to correlate the heat transfer coefficient expressed as Stanton number with Reynolds number, turbulence intensity, and a ratio of turbulence length scale to the thickness of the boundary layer. How well can the present data be correlated in these terms? Is there another way to look at the data that proves to be more satisfactory?

Evaluation of Experimental Uncertainty

The primary sources of uncertainty in the results of this experiment were presented in "Part I: Experimental Data." The average uncertainties in the estimates of the additional parameters ΔSt, $Tu/(\Lambda/\Delta_2+300)$, and St′ presented in this paper are ±5.4 percent, ±5.7 percent, and ±6.5 percent, respectively. The error brackets presented in Figs. 1–6 represent 95 percent confidence intervals for the indicated parameters.

Comparison to Previous Correlations

The studies of Simonich and Bradshaw (1978), Pedisius et al. (1983), and Blair (1983a), each propose a general correlation to describe the effects of free-stream turbulence on boundary layer heat transfer. Simonich and Bradshaw and Pedisius et al. each present a correlation for increases in Stanton number in terms of a single parameter, Tu, having the functional form

$$\Delta St/St_o = f(Tu)$$

while Blair's correlation for increases in Stanton number with free-stream turbulence attempts to account for both Reynolds number and free-stream turbulence scale effects in addition to describing the effects of turbulence intensity. Blair's correlation has the functional form

$$\Delta St/St_o = f(Re_\theta, Tu, L/\delta)$$

All three correlations choose $\Delta St/St_o$ as the parameter to describe the heat transfer rate. There are two assumptions embedded in this choice. Firstly, it assumes that the variables used to define St are relevant in describing both physical situations, namely, flow over a flat plate with and without free-stream turbulence. Past experience with boundary layers suggests this is a reasonable assumption for the case without free-stream turbulence. Secondly, it assumes the value of St that the boundary layer would have had with no free-stream turbulence, St_o, is a relevant baseline value for describing the increase of St caused by free-stream turbulence. This second assumption follows from the first. Consider the following functional relationship

$$St = f(Re_\theta, Tu, L/\delta)$$

St_o is the value to which $f(Re_\theta, Tu, L/\delta)$ tends as Tu (and L)$\rightarrow 0$.

Both Simonich and Bradshaw and Pedisius et al. describe increases in Stanton number in terms of Tu alone. Simonich and Bradshaw propose the simple linear model

$$\Delta St/St_o = A_\theta Tu$$

where A_θ is a constant approximately equal to five. While this

Contributed by the Heat Transfer Division for publication in the JOURNAL OF HEAT TRANSFER. Manuscript received by the Heat Transfer Division April 1991; revision received April 1992. Keywords: Forced Convection, Turbulence. Associate Technical Editor: D. M. McEligot.

Copyright © 1992 by ASME
Downloaded 13 Dec 2010 to 193.140.21.150. Redistribution subject to ASME license or copyright; see http://www.asme.org/terms/Terms_Use.cfm

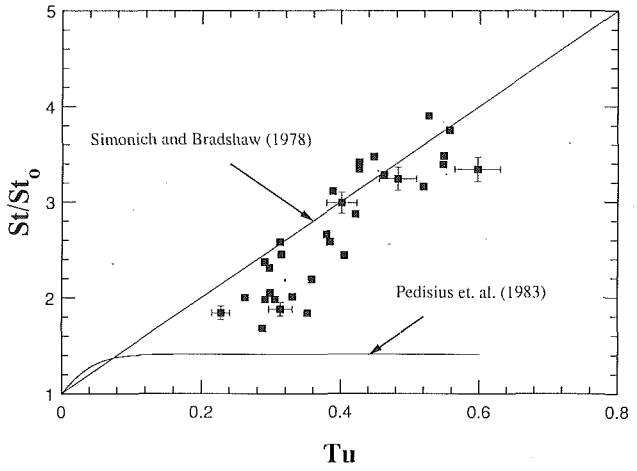

Fig. 1 Comparison to correlations in terms of *Tu* alone

correlation does capture the gross features of their data, the scatter is at least ±25 percent. The authors suggest a possible effect of low Reynolds number or length scale of the free-stream turbulence, although it might be due to an inappropriate choice for $f(Tu)$. This model places no upper limit on increases in Stanton number, a feature confirmed by the present experiments. Pedisius et al. argue that there should be a limiting value as Tu gets large. They propose the model

$$\Delta \mathrm{St}/\mathrm{St}_o = C_1 \tanh(C_2 Tu)$$

where, for air, C_1 and C_2 are constants equal to 0.41 and 20, respectively. This function reaches 95 percent of its limiting value, C_1 at $Tu = 0.092$. Figure 1 compares the present data set to the correlations of Simonich and Bradshaw and Pedisius et al. The data show a strong upward trend with Tu. The correlation of Simonich and Bradshaw does surprisingly well, primarily because the present data show no drop-off in the sensitivity of $\Delta \mathrm{St}/\mathrm{St}_o$ to Tu as Tu gets large. A least-squares linear regression through the present data results in the relationship

$$\mathrm{St}/\mathrm{St}_o = 5.81 Tu + 0.42$$

The intercept for this regression line falls closer to zero than it does to 1, suggesting that there is something wrong with the proposed simple linear model. The scatter about the regression is ±25 percent. The residual variation in the data is independent of Tu, i.e., the scatter in $\mathrm{St}/\mathrm{St}_o$ is ±25 percent for a fixed value of Tu. Therefore, for the present experiment, this is the best model for $\mathrm{St}/\mathrm{St}_o$ based on Tu alone. Furthermore, general models predicting increases in Stanton number based on Tu alone cannot do better than ±25 percent.

Hancock and Bradshaw (1983) describe increases in skin friction coefficient with free-stream turbulence using an empirically based free-stream turbulence parameter, FST, which accounts for the effects of both turbulence intensity and length scale. Their correlation has the form

$$\Delta C_f / C_{fo} = f(\mathrm{FST})$$

where

$$\mathrm{FST} \equiv Tu/(L_e^u/\delta + 2)$$

According to Baskaran et al. (1989), the agreement of their data with this correlation is within ±2 percent. In the context of the general convective heat transfer problem, if the aerodynamic field is completely specified, then one can calculate the temperature field through the energy equation (for fixed temperature initial conditions and boundary conditions). This suggests that a set of variables sufficient to determine the mean near-wall velocity behavior should suffice to determine the mean near-wall thermal behavior.

Assuming a close analogy between the mechanisms by which turbulence transports momentum and heat, the skin friction correlation of Hancock and Bradshaw should predict increases in Stanton number with free-stream turbulence once the correlation is scaled properly. Blair attempts to describe the increases in Stanton number found in his experiment using a slight modification of the empirically based free-stream turbulence parameter suggested by Hancock and Bradshaw to describe increases in skin friction coefficient. Blair uses the form

$$\Delta \mathrm{St}/\mathrm{St}_o = Rf(\mathrm{FST}_{\mathrm{Blair}})$$

where

$$\mathrm{FST}_{\mathrm{Blair}} \equiv Tu/(\alpha\beta)$$

and

$$\alpha = L_e^u/\delta + 2$$
$$\beta = 1 + 3\exp - [\mathrm{Re}_\theta/400]$$

The function f used by Blair is identical to the function f used by Hancock and Bradshaw, so that for high Re_θ

$$\mathrm{FST}_{\mathrm{Blair}} \rightarrow \mathrm{FST}$$

and

$$\Delta \mathrm{St}/\mathrm{St}_o \approx R \Delta C_f / C_{fo}$$

Blair uses the value 1.3 for the Reynolds analogy factor, R. While Blair's data do agree with this correlation, his data cover only a small portion of the domain for FST, not enough to test fully the usefulness of the application of the correlation of Hancock and Bradshaw to describe increases in Stanton number. However, MacMullin et al. (1989) compare their data to the correlation used by Blair. At $\mathrm{FST}_{\mathrm{Blair}} = 2.5$, Blair's correlation on average underestimates their data by 40 percent. In reviewing the usefulness of the FST parameter, Baskaran et al. state that while the distributions of C_f agree with the correlation of Hancock and Bradshaw, the distributions of St do not, even if Blair's adjustment for the Reynolds analogy factor is made.

Nomenclature

C_f = skin friction coefficient
C_{fo} = reference skin friction coefficient
ΔC_f = difference between C_f and C_{fo}
Pr = Prandtl number
R = Reynolds analogy factor
$\mathrm{Re}_{\Delta 2}$ = Reynolds number based on enthalpy thickness
Re_θ = Reynolds number based on momentum thickness
St = Stanton number
St_o = reference Stanton number
$\Delta \mathrm{St}$ = difference between St and St_o
St′ = Stanton number based on u'
Tu = ratio of rms velocity fluctuation to mean value
U = mean convective velocity
u' = standard deviation in U
δ = boundary layer thickness
Δ_2 = enthalpy thickness
L = turbulence scale
Λ = turbulence integral scale
L_e^u = turbulence dissipation length scale
h = heat transfer coefficient
C_p = fluid specific heat
ρ = fluid density

Downloaded 13 Dec 2010 to 193.140.21.150. Redistribution subject to ASME license or copyright; see http://www.asme.org/terms/Terms_Use.cfm

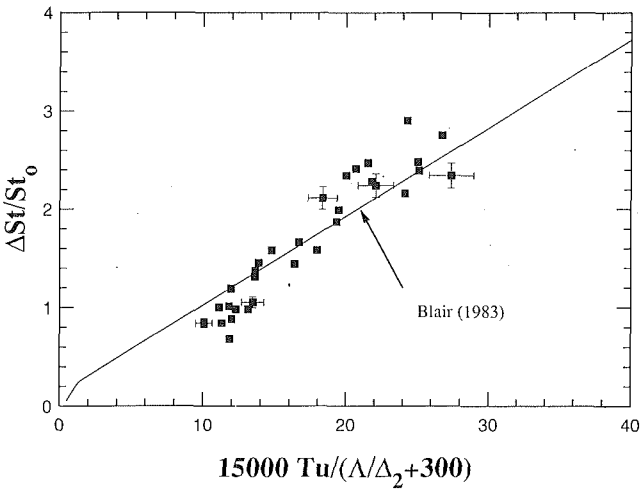

Fig. 2 Comparison to the correlation of Blair (1983a)

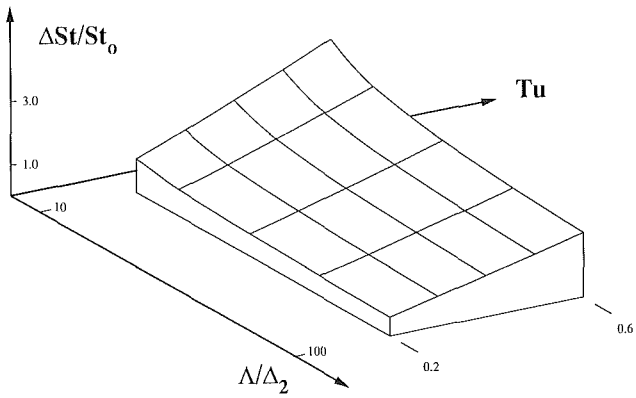

Fig. 3 Response surface for the present experiments

The present work uses Λ/Δ_2 instead of L_e^u/δ to describe the effect of the scale of the free-steam turbulence. In Blair's work, Λ/Δ_2 and L_e^u/δ are related by a scalar, so that the present data can be compared to those of Blair. The relationship between Λ/Δ_2 and L_e^u/δ for Blair's work is described by

$$\Lambda/\Delta_2 \approx 150 L_e^u/\delta$$

Figure 2 compares the present data set to the correlation of Blair. Blair's correlation runs through the center of the present data, but there is considerable scatter in the data. For example, at $FST_{Blair} = 12$, Blair's correlation on average overestimates the present data by 35 percent.

Describing the Present Data Using Conventional Descriptors

The fact that the parameter FST_{Blair} does not adequately describe the present data does not in itself rule out the possibility that the set of parameters $\{Tu, \Lambda/\Delta_2\}$ suffices to describe $\Delta St/St_o$. How well can the present data set be described using these parameters? Consider a model of the form

$$\Delta St/St_o = CTu^a(\Lambda/\Delta_2)^b$$

Clearly, this correlation cannot have the correct behavior for all values of Tu and Λ/Δ_2 for arbitrary a and b. Such a correlation is developed here only to describe the present data, and no comparisons to other experiments will be made. The constants a, b, and C were determined by a least-squares linear regression to be 1.12, -0.25, and 11, respectively.

The description of the present data given by the correlation above can be used to construct a response surface for $\Delta St/St_o$ in terms of Tu and Λ/Δ_2. Figure 3, a graph of the correlation presented above, illustrates the combined effects of intensity and scale on increases in Stanton number with free-stream turbulence for the present experiments. The present data fit this surface to within ± 20 percent. For very large-scale turbulence, $\Lambda/\Delta_2 > 10$, $\Delta St/St_o$ depends primarily on Tu. For $\Lambda/\Delta_2 < 10$, both scale and intensity affect $\Delta St/St_o$. Figure 3 shows the correct limiting behavior for the effect of intensity as $Tu \to 0$ at fixed scale, $\Delta St/St_o \to 0$, but shows no upper limit on $\Delta St/St_o$ as $Tu \to \infty$. Figure 3 shows reasonable limiting behavior for the effect of scale. As $\Lambda/\Delta_2 \to \infty$ at fixed intensity, $\Delta St/St_o \to$ constant, but shows no upper limit on $\Delta St/St_o$ as $\Lambda/\Delta_2 \to 0$. $\Delta St/St_o$ should go to 0 as $\Lambda/\Delta_2 \to 0$, but this cannot be determined from the present data.

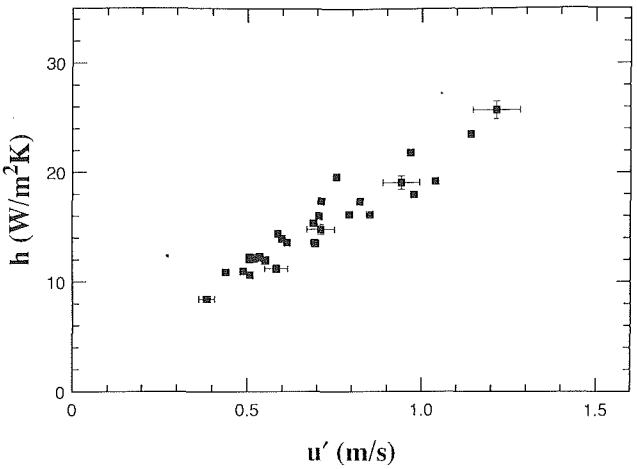

Fig. 4 Relationship between h and u' for the present experiments

A Simple Model

The analysis of the present data given above presumed that the conventional dimensionless parameters St, St_o, $Re_{\Delta 2}$, Tu, and Λ/Δ_2, were appropriate for boundary layer flows with a highly turbulent external stream. The primary result of this analysis, a correlation for $\Delta St/St_o$ in terms of Tu and Λ/Δ_2, appears reasonable but is not the only way to look at the data. There is a simpler way to present the heat transfer data for situations involving high turbulence.

A simple hypothesis for these data would be to propose that the heat transfer coefficient, h, is determined by free-stream turbulence alone. Figure 4 shows the local heat transfer coefficient, h, plotted against the local level of turbulent fluctuations in the free stream, u', for the condition of very high free-stream turbulence. The coherence of the data set is striking, appearing as a linear relationship between h and u', despite the fact that the data points are measured over a wide range of mean velocities, boundary layer thicknesses, and turbulence scales. In fact, a best-fit linear regression through the data in Fig. 4 accounts for 92 percent of the total variation in h for the data set, leaving only 8 percent to be explained by any other process variables and experimental uncertainty.

The linear relationship between h and u' for very high free-stream turbulence can be expressed in the following dimensionless form:

$$h/\rho C_p u' = \text{const}$$

$h/\rho C_p u'$ is the dimensionless parameter offering the simplest collapse of the present data. This relationship is simpler in form, produces less scatter in the data, and is more easily interpreted physically than any of the correlations presented above.

Downloaded 13 Dec 2010 to 193.140.21.150. Redistribution subject to ASME license or copyright; see http://www.asme.org/terms/Terms_Use.cfm

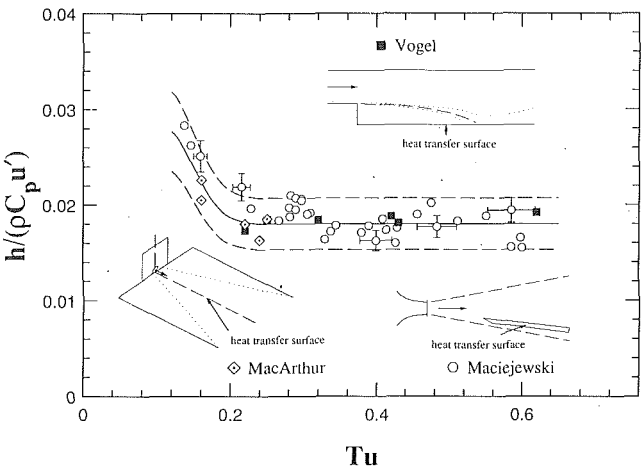

Fig. 5 Relationship between h and u' extended to other experiments with very high free-stream turbulence

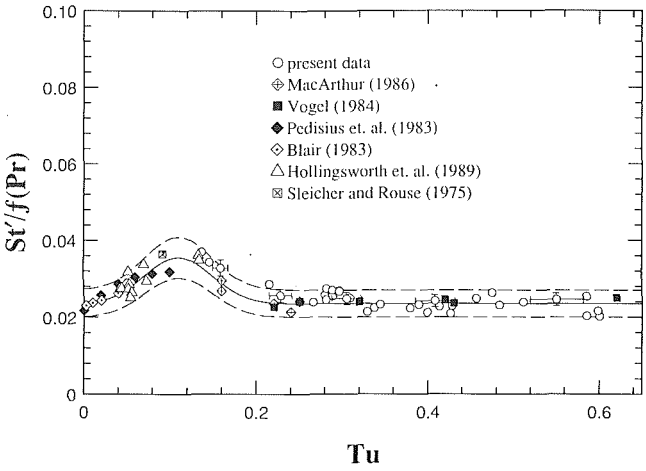

Fig. 6 A new correlation accounting for free-stream turbulence

Comparison to Data From Other Experiments

For the present experiments, the heat transfer coefficient, h, can be described as a linear function of the turbulent fluctuation in the free stream, u', independent of the free-stream mean velocity, U, and the length scale of the turbulence in the free stream, Λ. This simple relationship works better than any correlation proposed in the literature, bringing together, within ± 15 percent, the data for turbulence levels from 20 to 60 percent. In itself, this result may not seem unusual: The data all come from the same apparatus, using the same instrumentation, and it is not uncommon that an experimenter reports a tight correlation over the range of one set of experiments. However, two aspects of these findings suggested to us that a heat transfer parameter based on u' might be useful on a broader domain. The first is the simplicity of the relationship itself, particularly the absence of any "rig descriptors" in it. The second is that the data came from a set of rather widely different flow fields with a broad range of scales and intensities.

The possibility that some functional relationship between u' and h is a more general feature of turbulent boundary layer heat transfer will presently be explored through a set of comparisons to data from experiments conducted in other research facilities under a variety of conditions. The first question is the following: Can the functional relationship between u' and h for the present data be extended to other flows over flat surfaces in air with very high free-stream turbulence?

The heat transfer experiments of Vogel (1984) and MacArthur (1986) may reasonably be considered studies of flow over a flat plate in air in the presence of very high free-stream turbulence, and therefore offer a basis for comparison to the present experiments on the domain on which the experiments were conducted. Vogel studied a turbulent reattaching flow behind a backward-facing step, providing heat transfer data on a constant heat flux surface extending through the recirculation region, $Tu = 0.65$, the reattachment region, $Tu = 0.4$, and the recovery region, $0.2 < Tu < 0.3$. The approach velocity to the step was $U = 11$ m/s with a Reynolds number based on step height of 28,000. The flow field is highly three dimensional, inhomogeneous, and anisotropic. MacArthur studied the effect of a circular tangential turbulent wall jet on a flat plate constant heat flux heat transfer surface. The local free-stream turbulence levels for this experiment are on the domain $0.16 < Tu < 0.25$. The velocity at the exit of the jet was 59.1 m/s and the Reynolds number based on the jet diameter and exit velocity was 99,000. This flow field is highly three dimensional, inhomogeneous, and anisotropic. Figure 5 compares the present data to the data of Vogel and MacArthur. All three data sets fall within the scatter of the present experiment, within ± 15 percent given by the dashed lines in Fig. 5. Above $Tu = 0.2$, the parameter $h/\rho C_p u'$ is constant, suggesting that a single linear relationship between h and u' characterizes air flows over flat surfaces with very high free-stream turbulence.

If u' determines h for boundary layer flows with very high free-stream turbulence as suggested by Fig. 5, then it is at least possible that u' contributes to the determination of h in other physical situations as well. Can a functional relationship between u' and h be extended to flows over flat surfaces in air with negligible, low, and moderate levels of free-stream turbulence? Can a functional relationship between u' and h be extended to flows over curved surfaces with and without free-stream turbulence? Can a functional relationship between u' and h be extended to flows in other fluids with and without free-stream turbulence?

The relationship between h and u' for the case of very high free-stream turbulence in air has lead Maciejewski and Moffat (1990) to develop a correlation describing the effects of free-stream turbulence on boundary layer heat transfer on the domain $\mathrm{Re}_\theta > 1000$, $0.71 < \mathrm{Pr} < 100$, and $0 < Tu < 0.65$. In order to extend the use of the parameter $h/\rho C_p u'$ to flows with negligible levels of free-stream turbulence, Maciejewski and Moffat introduce a new Stanton number, St', defined by

$$\mathrm{St}' \equiv h/\rho C_p u'_{\max}$$

where $u'_{\max}$ is the maximum standard deviation in the streamwise component of velocity in the wall-affected region, i.e., the region near the surface that exhibits "law-of-the-wall" behavior in the mean velocity profile, regardless of the mechanism by which the turbulent fluctuations were produced. [In the case of turbulence produced in a turbulent boundary layer at high Reynolds number with no free-stream turbulence, $u'_{\max}$ occurs near $y^+ = 15$ and has a value approximately equal to 11 percent of the free-stream mean velocity. In the case of boundary layer flow with very high free-stream turbulence, $u'_{\max} = u'$. Consequently, St' will be constant for the experiments of Vogel and MacArthur, as well as for the present data.] In our 1990 paper we argue that St' is a very weak function of Reynolds number and that variation in St' due to differences in Reynolds number can be neglected. We propose the following correlation:

$$\mathrm{St}'/f(\mathrm{Pr}) = 0.024 + 0.012 \exp - [(Tu - 0.11)/0.055]^2$$

where the function $f(\mathrm{Pr})$ accounts for differences in Pr, with $f(\mathrm{Pr}) = \mathrm{Pr}^{-0.6}$ for $\mathrm{Pr} > 3$ and $f(\mathrm{Pr}) = 0.75$ for $\mathrm{Pr} = 0.71$. At present, we are not concerned with the analyses employed in this correlation, which are presented in Maciejewski and Moffat,

Downloaded 13 Dec 2010 to 193.140.21.150. Redistribution subject to ASME license or copyright; see http://www.asme.org/terms/Terms_Use.cfm

but the usefulness of the parameter $St'/f(Pr)$ to collapse turbulent heat transfer data.

Figure 6 presents heat transfer data, in terms of the parameter $St'/f(Pr)$ versus Tu, measured in a variety of different physical situations. The solid line in Fig. 6 represents the correlation of Maciejewski and Moffat, and the dashed lines represent ±15 percent error bands about the correlation. In order to impress the reader with the diversity of the physical situations represented by the data in Fig. 6, each of the experiments will be described briefly.

The present experiments and the experiments of Vogel and MacArthur are described above.

Blair and Pedisius et al. each studied the effects of free-stream turbulence on a flat-plate heat transfer surface in a closed-loop wind tunnel downstream of a set of rectangular grids. Blair's data cover the domain $0 < Tu < 0.06$. In his experiments, the boundary layer was fully turbulent and two dimensional. The turbulence in the free stream was nearly isotropic and of scales on the order of the thickness of the boundary layer. The free-stream mean velocity was 30.3 m/s and the momentum thickness Reynolds number ranged from 1000 to 7000. The data of Pedisius et al. cover the domain $0 < Tu < 0.10$ over a comparable range of Reynolds numbers.

Hollingsworth et al. (1989) studied the effect of free-stream turbulence on both a constant-temperature flat-plate heat transfer surface and a constant-temperature heat transfer surface with concave curvature placed in a closed-loop water channel downstream of a set of rectangular grids. In the flat section the boundary layer was fully turbulent and two dimensional. The free-stream turbulence was nearly isotropic (except for the first measurement location downstream of the grids) and had scales on the order of the thickness of the boundary layer. The mean velocity was 15.5 m/s, the enthalpy thickness Reynolds number ranged from 200 to 400, and Tu ranged from 0.04 to 0.14. In the curved section the boundary layer was fully turbulent and quasi-two-dimensional. The turbulence in the free stream was nearly isotropic and of scales on the order of the thickness of the boundary layer. The wall potential velocity was 11.1 m/s, the enthalpy thickness Reynolds number ranged from 375 to 625, and Tu ranged from 0.04 to 0.06.

The single data point attributed to Sleicher and Rouse (1975) in Fig. 6 represents a correlation to turbulent flow in a pipe that fits experimental data to within ±10 percent on the domain $0.1 < Pr < 10^4$ and $10^4 < Re < 10^6$. According to Laufer (1954), pipe flow at $Re_D = 50{,}000$ has a maximum fluctuating velocity near the wall, u'_{max}, that is 9 percent of the centerline velocity, or 11 percent of the bulk mean velocity, U_b. In this case, U_b can be used to estimate u'_{max}, which in turn can be used to estimate St'.

The coherence of the data in Fig. 6 suggests that the parameter St' plays a fundamental role in characterizing turbulent boundary layer heat transfer. Despite the differences in flow geometry and Reynolds number found in the experiments included in Fig. 6, all the heat transfer data collapse onto a single correlation to within ±15 percent. This residual scatter in the data may be attributed to the geometry of the flow, the means by which the turbulence is produced, the scale of the free-stream turbulence, and the Reynolds number, as well as the higher order uncertainty associated with making comparisons between separate research facilities. It should be noted that the data presented in Fig. 6 are limited to flows with uniform temperature initial conditions and uniform temperature boundary conditions.

Discussion

Within the comparison of the data presented in Fig. 6, the flow geometry, velocity distribution, and fluid properties vary between experimental facilities. Despite this, to a good approximation,

$$St' = f(Pr, Tu)$$

This is an extremely simple form for a correlation on a problem with many variables. For a given Pr, the turbulence locally sets the heat transfer coefficient. Although the correlation describes data from flow behind a backward-facing step, flow with curvature, flow due to a wall jet, and flow over a flat plate, there is no parameter in the correlation describing flow geometry. The correlation carries information about the mean velocity field only through the parameter Tu. The primary aerodynamic influence on heat transfer is due to the turbulent fluctuations incorporated in the definition of St'.

The present development suggests that the near-wall turbulent fluctuations have always been the most important variable in the determining the surface heat transfer rate in turbulent boundary layers. For turbulent boundary layers with negligible free-stream turbulence, the free-stream mean velocity is highly correlated with the turbulent fluctuations produced near the wall. Once the free-stream mean velocity becomes uncorrelated with the turbulent fluctuations, as it is in the present experiments, Stanton number, as defined conventionally, ceases to be the proper parameter for describing turbulent boundary layer heat transfer.

According to Hancock and Bradshaw, increases in skin friction depend on both the intensity and the scale of free-stream turbulence. However, St' depends only on Tu. Taken together, these two findings suggest that free-stream turbulence transports momentum and heat by different mechanisms. It may be the case that discussions of the Reynolds analogy or Reynolds analogy factors only confuse the issue of modeling heat transfer in the presence of free-stream turbulence. Models and correlations for surface heat transfer and wall shear stress can and perhaps should be developed independently.

Conclusion

The correlations of Simonich and Bradshaw, Pedisius et al., and Blair each fail to describe the present data. For flows over flat surfaces in air with very high free-stream turbulence, $Tu > 0.2$, u' determines h. A new heat transfer parameter, St', characterizes turbulent boundary layer heat transfer with free-stream turbulence on the domain $0 < Tu < 0.65$ to within ±15 percent for high Reynolds number flows with uniform thermal boundary conditions.

Acknowledgments

This study was supported by the NASA Hot Section Technology Program as NASA NAG 3-522. The work was initiated under the technical administration of Dr. John Rhode and continued under Dr. Raymond Gaugler, both of the Lewis Research Laboratories.

References

Baskaran, V., Abdellatif, O. E., and Bradshaw, P., 1989, "Effects of Free-Stream Turbulence on Turbulent Boundary Layers With Convective Heat Transfer," *Turbulent Shear Flows 7*, Vol. 2, pp. 20–21.

Blair, M. F., 1983a, "Influence of Free-Stream Turbulence on Turbulent Boundary Layer Heat Transfer and Mean Profile Development, Part I—Experimental Data," ASME JOURNAL OF HEAT TRANSFER, Vol. 105, p. 33.

Blair, M. F., 1983b, "Influence of Free-Stream Turbulence on Turbulent Boundary Layer Heat Transfer and Mean Profile Development, Part II—Analysis of Results," ASME JOURNAL OF HEAT TRANSFER, Vol. 105, p. 41.

Hancock, P. E., and Bradshaw, P., 1983, "The Effect of Free-Stream Turbulence on Turbulent Boundary Layers," ASME *Journal of Fluids Engineering*, Vol. 105, p. 284.

Hollingsworth, D. K., Johnson, P. L., Moffat, R. J., and Johnston, J. P., 1989, "Observations of the Effects of High Free-Stream Turbulence Levels on the Heat Transfer to a Concavely Curved Turbulent Boundary Layer," Report No. HMT-41, Thermosciences Division of Mechanical Engineering, Stanford University, Stanford, CA.

Downloaded 13 Dec 2010 to 193.140.21.150. Redistribution subject to ASME license or copyright; see http://www.asme.org/terms/Terms_Use.cfm

Laufer, J., 1954, "The Structure of Turbulence in Fully Developed Pipe Flow," NACA Tech. Rep. No. 1174.

MacArthur, C. D., 1986, "Fluid Dynamics and Heat Transfer of the Circular Tangential Wall Jet," Ph.D. Thesis, University of Dayton, Dayton, OH.

MacMullin, R., Elrod, W., and Rivir, R., 1989, "Free-Stream Turbulence From a Circular Wall Jet on a Flat Plate Heat Transfer and Boundary Layer Flow," ASME *Journal of Turbomachinery*, Vol. 111, p. 78.

Maciejewski, P. K., and Moffat, R. J., 1990, "A Correlation for Boundary Layer Heat Transfer Accounting for Free Stream Turbulence," *Heat Transfer 1990*, Vol. 3, p. 303.

Pedisius, A. A., Kazimekas, P.-V.A., and Zukauskas, A. A., 1983, "Effect of Free-Stream Turbulence on Heat Transfer in the Turbulent Boundary Layer," *Soviet Research*, Vol. 15, No. 4, p. 1.

Simonich, J. C., and Bradshaw, P., 1978, "Effect of Free-Stream Turbulence on Heat Transfer Through a Turbulent Boundary Layer," ASME JOURNAL OF HEAT TRANSFER, Vol. 100, p. 673.

Sleicher, C. A., and Rouse, M. W., 1975, "A Convenient Correlation for Heat Transfer to Constant and Variable Property Fluids in Turbulent Pipe Flow," *Int. J. Heat Mass Transfer*, Vol. 18, p. 677.

Vogel, J. C., 1984, "Heat Transfer and Fluid Mechanics Measurements in the Turbulent Reattaching Flow Behind a Backward-Facing Step," Ph.D. Thesis, Stanford University, Stanford, CA.

Downloaded 13 Dec 2010 to 193.140.21.150. Redistribution subject to ASME license or copyright; see http://www.asme.org/terms/Terms_Use.cfm

Turbulent Heat Transport in a Boundary Layer Behind a Junction of a Streamlined Cylinder and a Wall

D. E. Wroblewski[1]
Visiting Assistant Research Engineer.

P. A. Eibeck
Assistant Professor.

Mechanical Engineering Department,
University of California,
Berkeley, CA 94027

Measurements of the turbulent velocity and temperature fields were made in a heated boundary layer 14 diameters downstream of a junction of a tapered cylinder and a wall ($Re_D = 24{,}700$). The boundary layer is strongly affected by the presence of large-scale unsteadiness arising from vortex shedding, which appears in the measurements as "turbulence" with a strong spectral component at the shedding frequency. The boundary layer exhibits three distinct spanwise regions: (1) the inner-wake region, $z/D < 0.8$, where vortex shedding effects are observed only in the spanwise component of the fluctuations; (2) the middle-wake region, $0.8 < z/D < 1.6$, where strong vortex shedding is seen in all three components of the fluctuations; and (3) the outer-wake region, $z/D > 1.6$, where the flow is approaching a two-dimensional boundary-layer flow. Cross-spectra of $\overline{v\theta}$ indicate that vortex shedding increases the turbulent heat flux in the middle-wake region. However, peak values of the Stanton number and the eddy diffusivity are observed in the inner-wake region, where the cross-spectra of turbulent heat flux do not exhibit a peak near the shedding frequency, but do show an increase compared to a two-dimensional boundary layer over a much broader frequency range.

1 Introduction

When a flat plate boundary layer encounters an obstacle, such as a cylinder or a streamlined cylinder, placed normal to the wall, a complex three-dimensional turbulent flow arises that can influence wall properties, such as skin friction and heat transfer, downstream of the obstacle. Figure 1 shows a simplified schematic of such a junction flow. The interaction between the boundary layer and the stagnation point flow at the leading edge of the obstacle can result in the formation of a horseshoe-vortex system, which may persist far downstream. The flow behind the obstacle may also be characterized by the interaction of the developing wake of the obstacle and the wall. In this sense, the flow may be considered as a combination of a wake flow, developing in a plane parallel to the wall, and a boundary-layer flow, developing in a plane perpendicular to the wall. Periodic vortex shedding from the obstacle may introduce large-scale unsteadiness that could also influence the structure of the downstream boundary layer.

The formation and development of the horseshoe vortex in flows around cylinders and streamlined cylinders have been studied rather extensively. However, most of the attention has been concentrated on the region near the leading edge and immediately around the cylinder. Belik (1973) studied the leading edge region in a turbulent flow and was able to predict the position of the upstream separation line. Baker (1979, 1980) and Goldstein and Karni (1984) also investigated the leading edge region and postulated the existence of multiple vortices formed at the junction. Measurements of secondary velocities downstream of the leading edge of a Rankine half-body by Moore and Forlini (1984) showed streamwise vorticity associated with the horseshoe vortex. Extensive mean-velocity and turbulence measurements were made by Shabaka and Bradshaw (1981), McMahon et al. (1982, 1983), Hsing and Teng (1984), and Mehta (1984) for semi-infinite obstacles. The flows had well-defined longitudinal vortices with maximum spanwise velocities equal to 10 to 15 percent of the free stream. Using finite-chord obstacles, Dickinson (1984) measured velocity profiles near the obstacle that did not reveal the expected horseshoe vortex.

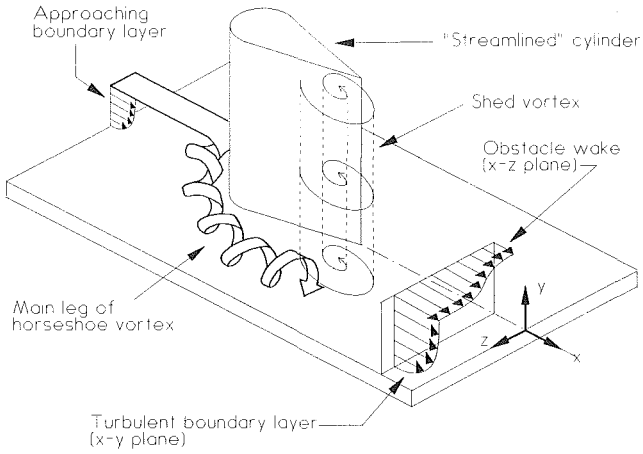

Fig. 1 Simplified schematic of flow near junction between "streamlined" cylinder and wall

The region downstream of the obstacle has received less attention. Merati (1988) measured mean velocity and turbulence quantities at the leading edge, near the junction, and three chord lengths downstream of a modified NACA 0020 airfoil and did observe a strong secondary flow dominated by a horseshoe vortex. Pierce and Harsh (1988) made measurements of surface pressure and velocity distributions around the base of a streamlined cylinder, which did not span the height of the wind tunnel. At the trailing edge of the obstacle (100 percent chord traverse plane), the secondary flow revealed a horseshoe vortex leg with an approximate size of $0.3D$ po-

[1]Current address: Department of Aerospace and Mechanical Engineering, Boston University, Boston, MA.

Contributed by the Heat Transfer Division for publication in the JOURNAL OF HEAT TRANSFER. Manuscript received by the Heat Transfer Division October 1991; revision received March 1992. Keywords: Forced Convection, Turbulence, Wakes. Associate Technical Editor: R. J. Simoneau.

Copyright © 1992 by ASME
Downloaded 13 Dec 2010 to 193.140.21.150. Redistribution subject to ASME license or copyright; see http://www.asme.org/terms/Terms_Use.cfm

sitioned roughly at $z/D=0.8$. Surface visualization of the flow downstream of a cylinder that spanned the height of a fully developed channel flow was performed by Ichimiya et al. (1988). Stable laminar twin vortices were observed behind the obstacle for low Reynolds numbers ($Re_D<750$), but these became irregular at higher Reynolds numbers.

Rood and Keller (1984) observed unsteady large-scale organized motions in the boundary layer 10 chord lengths downstream of a streamlined wing-body junction. The characteristic frequency of the structures was an order of magnitude smaller than the frequency of disturbances outside the boundary layer, which were attributed to vortex shedding at the trailing edge.

More recent studies have begun to concentrate on the flow much farther downstream. Measurements of the secondary velocity field by Eibeck (1990) revealed that the horseshoe vortex was not present behind the ciruclar cylinder or the streamlined cylinder at $x/D=4$. Farther downstream ($x/D=8$), the horseshoe vortex was observed near the wall for the streamlined cylinder, with the center approximately located at $y/D=0.1$ and $z/D=1.25$. However, no horseshoe vortex was observed for the circular cylinder at $x/D=8$. A much larger counterrotating swirling pair was seen behind both obstacles at both streamwise locations. The swirling pair seemed to have a length scale of approximately one-half the tunnel height and a rotational direction opposite to that of the horseshoe vortex.

Fisher and Eibeck (1990) studied heat transfer along the flat plate downstream of a streamlined cylinder and a circular cylinder up to $x/D=9.6$ using a liquid crystal technique. The heat transfer is increased by as much as 50 percent at a Reynolds number (Re_D) of 7.7×10^4 for the streamlined cylinder and by up to 32 percent at $Re_D=1.3\times10^5$ for the circular cylinder. Although it was concluded by Fisher and Eibeck that the horseshoe vortex led to the enhanced heat transfer, the absence of the horseshoe vortex in the velocity measurements of Eibeck (1990) suggests that another mechanism, possibly enhanced turbulent transport, must be involved.

The main purpose of the present study was to determine whether enhanced mixing due to turbulence was the mechanism for enhanced wall heat transfer observed by Fisher and Eibeck (1990) downstream of the junction between a streamlined cylinder and a wall. Detailed mean and turbulence measurements, including both cross-plane components of the turbulent heat fluxes, $\overline{v\theta}$ and $\overline{w\theta}$, were obtained. In addition to providing details of the heat transfer effects, the results indicated several interesting features of the boundary-layer region, including the role of large-scale unsteadiness due to vortex shedding. These aspects of the flow will also be highlighted in this paper.

The present study involves measurements at a streamwise location of $x/D=14$, where D is the root diameter of the streamlined cylinder (Fig. 2). This location corresponds to $x/L=6$, where L is the chord length. In a pure wake flow, this is well short of the streamwise location at which similarity within the wake is believed to occur for the turbulent stresses, $x/D>200$ (Tennekes and Lumley, 1972). Since most previous studies have concentrated on the similarity region, the upstream location under consideration in this study has not been well characterized even for the pure wake flow.

It is important to note that the use of the term streamlined to describe the cylinder is somewhat misleading, in that the circular shape of the leading edge extends to 105 deg from the stagnation point, suggesting that separation, and hence eddy shedding may still occur.

2 Experimental Procedure

The tests were performed in an open loop wind-tunnel facility at U.C. Berkeley, designed specifically for boundary-layer convection studies. Details of the facility and its qualification are contained in Wroblewski (1990) and Wroblewski and Eibeck (1991a). The tunnel consists of a centrifugal fan, a wide-angle diffuser, a series of screens and honeycomb to condition the flow, a two-dimensional contraction, a test sec-

Nomenclature

A, B = hot-wire calibration constants in Eq. (1)
c_p = specific heat, kJ/kg°C
D = root diameter of tapered cylinder, m
$\mathfrak{D}_{ij}$ = eddy-diffusivity tensor, m^2/s
E_{wi} = voltage measured across hot wire, V
E_{uu}, E_{vv}, E_{ww} = power spectra for $(u')^2$, $(v')^2$, and $(w')^2$, $m^2/s^2/Hz$
f = frequency of fluctuations, Hz
H = height of tapered cylinder, m
$\hat{j}$, $\hat{k}$ = unit vectors in the y and z directions
L = chord length of tapered cylinder, m
l/d = aspect ratio of hot or cold-wire sensor
m, n = exponents for hot-wire calibration, Eq. (1)
Pr_t = $([\overline{uv}(\partial\overline{T}/\partial y])/[\overline{v\theta}(\partial\overline{U}/\partial y)])$ = turbulent Prandtl number
q_w = wall heat flux, W/m^2
Re_D = $(U_\infty D/\nu)$ = Reynolds number based on diameter of obstacle
S = (fL/U_∞) = Strouhal number based on chord length
St = $q_w/[\rho c_p U_\infty(T_w-T_\infty)]$ = Stanton number
T = instantaneous temperature, °C
$\overline{T}$ = time-averaged temperature, °C
U_{eff} = effective cooling velocity of hot wire, m/s
U, V, W = instantaneous velocity components, m/s
$\overline{U}$, $\overline{V}$, $\overline{W}$ = time-averaged velocity components, m/s
u, v, w = fluctuating velocity components, m/s
u', v', w' = rms velocities, m/s
$\overline{u\theta}$ = longitudinal component of turbulent heat flux, m/s°C
$\overline{uv}$, $\overline{uw}$, $\overline{vw}$ = Reynolds shear stresses, $(m/s)^2$
$\overline{v\theta}$ = normal component of turbulent heat flux, m/s°C
$\overline{w\theta}$ = spanwise component of turbulent heat flux, m/s°C
x = streamwise distance in boundary layer, measured from trip, m
y = vertical distance measured from wall upward, m
z = spanwise distance in boundary layer, measured from centerline, m
δ_{2-D} = 0.99 momentum boundary-layer thickness for undisturbed two-dimensional boundary layer, m
ϵ_H = eddy diffusivity, Eq. (5), m^2/s
θ = temperature fluctuation, °C
θ' = rms temperature, °C
ν = molecular viscosity, m^2/s
ρ = density, kg/m^3
Ω_x = streamwise vorticity, s^{-1}

Subscripts

m = denotes a mean value between hot wire and air
wi = denotes condition at the hot-wire sensor
w = denotes condition at the wall
∞ = denotes condition in the free stream

Downloaded 13 Dec 2010 to 193.140.21.150. Redistribution subject to ASME license or copyright; see http://www.asme.org/terms/Terms_Use.cfm

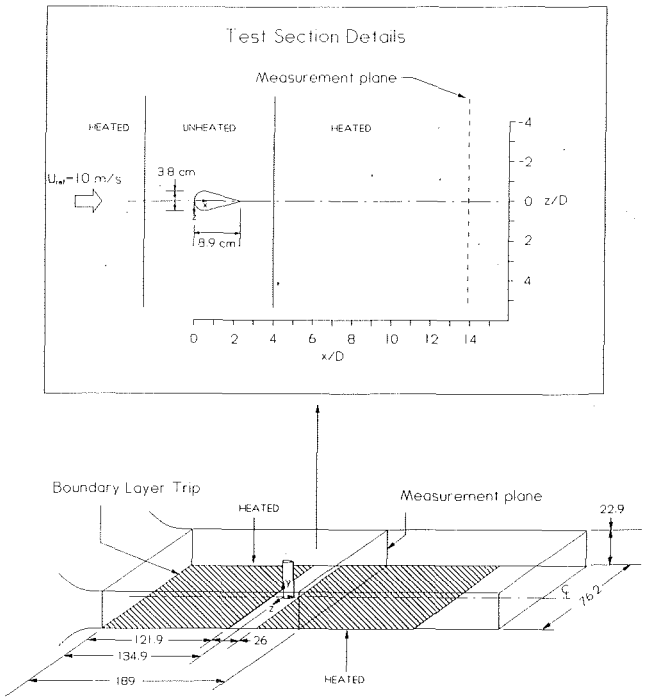

Fig. 2 Geometry of experimental test setup

tion, and a short exit section. The two-dimensional boundary layer was found to be very uniform across the test section, with less than 3 percent variation in the thickness (Wroblewski, 1990). It should be noted that this facility is not the same one used in previous horseshoe vortex studies at U.C. Berkeley (Eibeck, 1990; Fisher and Eibeck, 1990).

The test section is 76.2 cm in width and 22.9 cm high. The boundary layer is tripped by a 1.1-mm-high and 9.5-mm-wide phenolic strip located at the entrance to the working section. The thermal and momentum boundary layer develop initially over a heated entrance section, 121.9 cm long. The purpose of the upstream heating is to provide a more consistent match between the thermal and momentum boundary layers as they approach the obstacle. The entrance region is followed by a 26-cm-long unheated floor hatch, on which the streamlined cylinder rests. The leading edge of the cylinder is located 134.9 cm from the boundary-layer trip and at the center of the test section span.

The flow then continues over another heated section 156.9 cm long, over which data were taken across a plane located 189 cm from the boundary layer trip, which corresponds to 54.1 cm downstream of the leading edge of the cylinder.

The test-section floor heaters consist of etched foil heater elements, embedded within a flexible silicone rubber jacket. To provide a hydrodynamically smooth surface, 0.2-mm-thick stainless steel foil was attached to the upper surface of the heaters using double-sided adhesive tape. Type T thermocouples were laid between the heaters and the foil, in grooves cut in the adhesive liner. Details of the thermocouple locations and the qualification of the heat transfer surface can be found in Wroblewski (1990). When conduction and radiation losses are accounted for, the convective heat flux from the surface is 350 W/m^2.

The geometries of the test section and the cylinder are shown in Fig. 2. The streamlined cylinder has a chord length of 8.9 cm and its circular section is 3.8 cm in diameter. The diameter was chosen such that $\delta/D=0.67$, approximately the same as in Eibeck (1990) and Fisher and Eibeck (1990), where δ is the 0.99 momentum boundary-layer thickness at the leading edge of the obstacle. The obstacle extends to the full height of the tunnel, corresponding to an H/D of 6. The streamwise location at which the data were obtained was equivalent to $x/D=14$, where x is measured from the leading edge of the cylinder. The flow had a reference velocity of 10 m/s, measured in the free stream near the boundary-layer trip, which resulted in $\mathrm{Re}_D=24{,}700$.

Simultaneous velocity and temperature measurements were obtained using a pair of triple-wire heat-flux probes. Each probe consists of two constant-temperature hot wires, arranged in an X-wire configuration. In between and in a plane parallel to the X-wires, is a constant-current cold wire, used to measure temperature. On one of the probes (the uv probe), the sensors are oriented in a vertical direction, to measure U, V, and T. On the vw probe, the sensors are oriented horizontally to measure U, W, and T. The sensors are located 0.35 mm apart, which provided uncontaminated measurements, with only minor adverse spatial resolution effects.

All three sensors of the heat-flux probes are 2.5 μm diameter tungsten, with $l/d=280$. The wire ends are plated with 24 μm diameter copper plating, which extends the overall wire length to 3.3 mm for the X-wire sensors, and to 2.2 mm for the cold wire. An analytical technique was developed to compensate for the reduced frequency response of the constant-current cold wire, accounting for both end-conduction and wire-thermal-inertia effects. This technique, which compensates for both phase angle shift and amplitude attenuation, is described in detail by Wroblewski and Eibeck (1991a).

The heat-flux-probe X-wires were operated at an overheat ratio of approximately 0.8 by DISA 56C17/56C01 constant temperature anemometer (CTA) systems. Square-wave tests indicated a 3 dB cutoff frequency for the system of 6500 Hz. A DISA 56C20 temperature bridge used in conjunction with the 56C01 CTA module provided a constant-current (1 ma) system for the cold wires. DISA model 56NCN signal conditioners connected to the anemometer outputs provided adjustable gain, low-pass filtering, and high-pass filtering. The signal-conditioner outputs, unlinearized in the case of the hot wires, were digitized using a Data Translation 2828 high-speed data-acquisition board in a Data Translation CyClone JS 286 microcomputer. The A/D board featured simultaneous sample and hold, which allowed each channel to be sampled within 5 nanoseconds. Data were sampled at 6000 Hz per channel for 5.5 seconds. The relatively short sampling time, which was dictated by data storage limitations, was judged acceptable based on multiple sample tests, which were used for uncertainty analysis. Raw data were stored in extended memory buffers within the microcomputer, transferred to the hard disk for data reduction, and then archived on a Colorado Memory Systems DJ-10 streaming-tape backup-drive. The data were then reduced computationally, using the computer.

The measurements were obtained across the y–z plane in two steps. First, the uv probe was used to obtain measurements of $\overline{U}$, $\overline{V}$, $(u')^2$, $(v')^2$, $(\theta')^2$, $\overline{uv}$, $\overline{v\theta}$, and $\overline{u\theta}$ at all the desired y and z locations. Then, the uw probe was used to measure $\overline{U}$, $\overline{W}$, $(u')^2$, $(w')^2$, $(\theta')^2$, $\overline{uw}$, $\overline{w\theta}$, and $\overline{u\theta}$ at the same locations. Data were taken only on one side of the wake, assuming that the flow would be nearly symmetric around the spanwise centerline of the tunnel.

The hot-wire sensors, which form the X-wire component of the heat-flux probe, are calibrated by placing the probe in a separate laminar-jet calibration facility and varying the temperature and velocity of the jet. The data are fit to a calibration equation that is obtained from a modified form of the Collis and Williams (1959) equation,

$$U_{eff}=\left[A\left(\frac{T_m}{T}\right)^m \frac{T_m^{(1.76n-0.8)}}{(T_{wi}-T)}E_{wi}^2+BT_m^{1.76n}\right]^{1/n} \quad (1)$$

where E_{wi} is the voltage across the wire, T_{wi} is the wire temperature, T is the air temperature, $T_m=(T_{wi}+T)/2$, U_{eff} is the effective cooling velocity, and A, B, m, and n are the cali-

Downloaded 13 Dec 2010 to 193.140.21.150. Redistribution subject to ASME license or copyright; see http://www.asme.org/terms/Terms_Use.cfm

bration constants. In the standard Collis and Williams equation, the exponents n and m are specified to be 0.45 and 0.17, respectively. By allowing these exponents to be unknown constants that are specified in the calibration, a better fit of the data is provided.

The cold wire of the heat-flux probe is calibrated in the same laminar jet used for the hot-wire calibration by varying the temperature of the flow and assuming that the resistance of the sensor is linearly related to temperature.

The calibration procedure and the data-reduction techniques, including frequency-response compensation and cross-flow correction procedures, are described in detail by Wroblewski and Eibeck (1991a).

3 Results

Uncertainty estimates are provided on all figures presented. These were obtained following the approach described by Moffatt (1988).

Mean-Flow Characteristics. The secondary flow vectors, formed with $\overline{V}$ and $\overline{W}$, are shown in Fig. 3. The dominant feature of the secondary flow is the large swirling motion centered near $z/D=1.6$ and $y/D=1.5$. The vertical location of the center suggests that the vortex extends out to the centerline of the tunnel ($y/D=3$). This vortex, opposite in sense to the expected direction of the horseshoe vortex, has secondary velocities that are generally lower than that observed by Eibeck (1990). The lower velocities may be due to diffusion of vorticity, since the present data were obtained at a location farther downstream ($x/D=14$ compared to $x/D=8$).

The presence of the horseshoe vortex is also apparent from the secondary velocity vectors, and appears to be centered near $y/D=0.25$ and $z/D=0.6$. For comparison, Eibeck (1990) observed the center of the horseshoe vortex at $y/D=0.1$ and $z/D=1.25$ for a streamwise location of $x/D=8$. Note that the secondary velocities from the horseshoe vortex legs are generally less than 2 percent of the free-stream velocity. These values are approaching the level of uncertainty in the mean measurements.

The streamwise vorticity was calculated using the $\overline{V}$ and $\overline{W}$ results ($\Omega_x=\partial\overline{W}/\partial y-\partial\overline{V}/\partial z$). Because of the relatively small values of secondary velocities near the wall, the vorticity contours could not provide a clear picture of the horseshoe vortex location. They did seem to indicate a rather broad, flat region of peak vorticity at $y/D=0.17$ and ranging from $0.6<z/D<1.25$. If these results are indeed representative, and that may be doubtful given the uncertainty, then they may be indicating that the horseshoe vortex leg is elliptical in shape.

Mean streamwise velocity and temperature contours are shown in Fig. 4. Note that the temperature contours are normalized using the wall temperature that was measured at the same streamwise location in a two-dimensional boundary layer, $T_{w,2-d}$ (i.e., no obstacle present) and the free-stream temperature, T_∞. The velocity contours are nearly horizontal in the region near the wall, characteristic of a two-dimensional boundary-layer flow. A region of slightly lower velocity near the wall at $z/D=1.5$ corresponds to the location of the strongest upwash from the horseshoe vortex. This suggests that the relatively weak horseshoe vortex may be carrying low-momentum fluid away from the wall in this region.

Farther from the wall, the velocity contours follow the near-wall behavior only in the region near the spanwise edge of the measurement plane ($z/D=2.6$) where the flow appears to be returning to its two-dimensional character. In the remainder of the flow, the contours curve upward. If the flow outside the wall region behaved like a pure wake flow, these contour lines would eventually be vertical. The contours shown in Fig. 4(*a*) begin to curve upward, as expected, but then continue to curve back toward the outer edge, creating a bulge in the

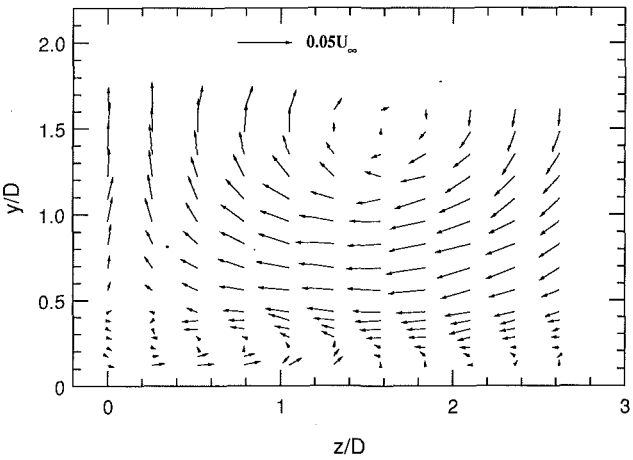

Fig. 3 Mean secondary velocity vectors $\overline{V}\hat{j}+\overline{W}\hat{k}$ at $x/D=14$ (uncertainty in $\overline{V}/U_\infty$ and $\overline{W}/U_\infty=\pm0.01$)

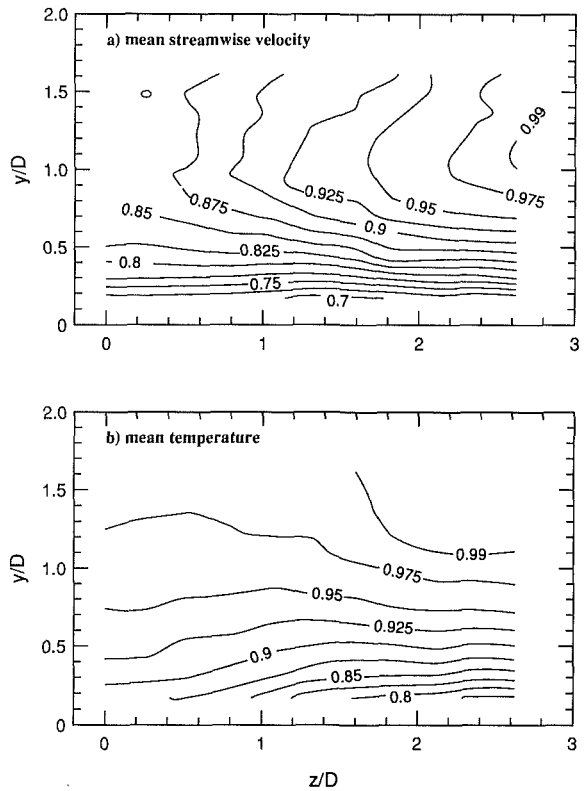

Fig. 4 Contours of mean streamwise velocity and mean temperature: (*a*) $\overline{U}/U_\infty$ (uncertainty = ±0.014); (*b*) $[(T_w)_{2-d}-\overline{T}]/[(T_w)_{2-d}-T_\infty]$ (uncertainty = ±0.06)

contours. This behavior may be attributable to the mean convective transport due to the secondary velocities associated with the large counterrotating vortex. The relatively strong lateral velocities in the region $0.6<z/D<2.4$ and $0.7<y/D<1.2$ (see Fig. 3) may be transporting higher momentum fluid from the edge of the wake region in toward the center.

The temperature profiles show a behavior that is different from the velocity contours. In the outer spanwise region of the flow, near the wake's edge, the contours are horizontal, like the velocity contours. But, as the center region is approached, they begin to curve downward near the wall and upward near the edge of the thermal layer. It should be noted, to avoid misinterpretation, that the end of the 0.99 contour in Fig. 4(*b*) near $y/D=1.6$ and $z/D=1.6$ marks the end of the

Downloaded 13 Dec 2010 to 193.140.21.150. Redistribution subject to ASME license or copyright; see http://www.asme.org/terms/Terms_Use.cfm

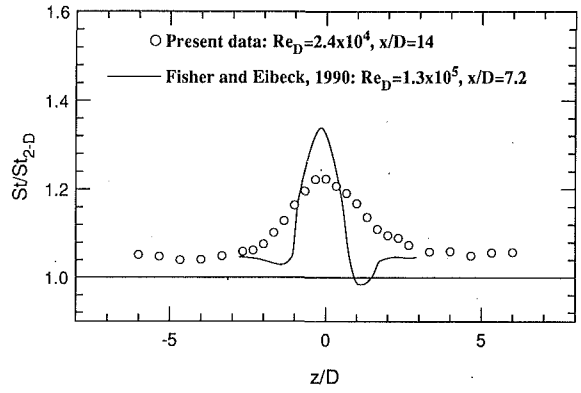

Fig. 5 Stanton number enhancement: $St = q_w/[U_\infty \rho c_p(T_w - T_\infty)]$ (uncertainty = ±0.09)

region for which measurements were obtained. The temperature in the region to the left of the endpoint of the 0.99 contour is less than 0.99. Measurements at the vertical centerline of the tunnel ($y/D = 3$), which are not shown in the figure, reveal that the 0.99 contour crosses $y/D = 3$ at a spanwise location of approximately $z/D = 0.7$. Even at $z/D = 1.0$ (for $y/D = 3$), the nondimensional temperature is still less than 0.995. This indicates that some heated fluid is still present at that vertical location for $z/D < 1$.

The behavior of the isotherms near the wall is probably an indication that enhanced turbulent mixing of heat is occurring in the region directly behind the obstacle, resulting in very strong near-wall temperature gradients. Similarly, the behavior farther from the wall (i.e., the presence of heated fluid as far out as the tunnel's centerline) may also be due to enhanced turbulent mixing, or it may be due to the secondary flow of the counterrotating vortex, which would tend to sweep higher temperature fluid away from the wall region, and carry it upward. The fact that heated fluid is present far from the wall only for $z/D < 1$ is consistent with either of the above explanations; in the former case, values of the eddy diffusivity, discussed below, are large for $z/D < 1$, and in the latter case, the strong upward vertical velocities from the large vortex extend out to approximately $z/D = 1$.

The difference in the behavior of the temperature and velocity contours as the upper edge of the measurement zone is approached is a result of the different boundary conditions for each case. The momentum boundary layer must asymptotically approach the wake flow, while the thermal boundary layer must approach the constant free-stream temperature, since only the wall is heated.

Stanton numbers, obtained from the thermocouples embedded within the heated floor sections, are shown in Fig. 5 as a function of spanwise location. The values are normalized on the Stanton numbers obtained at the same z location in a two-dimensional boundary layer (i.e., no obstacle). The peak enhancement is approximately 23 percent, near the spanwise centerline of the tunnel, which is consistent with the notion of enhanced mixing in this region, as indicated by the mean temperature contours in Fig. 4(*b*). Also shown in Fig. 5 are data from Fisher and Eibeck (1990) for a streamlined cylinder with $Re_D = 1.3 \times 10^5$ at $x/D = 7.2$. These show a higher and sharper peak enhancement, which may be a result of the stronger and more narrow wake present at the farther upstream location or may be a Reynolds number effect.

Farther out from the center, in the spanwise direction, the Stanton number enhancement does not approach unity—an approach to unity would indicate a return to the two-dimensional boundary-layer behavior—but instead approaches a value of 1.05. This behavior is also evident in the data of Fisher and Eibeck (1990), although their data do not extend to larger z/D values. Measurements in the free-stream wake (at $y/D = 3.0$) revealed that the velocity deficit was 1 percent of the free-stream velocity at approximately $z/d = 3.4$. This location corresponds to the point on Fig. 5 where the enhancement just reaches the asymptotic value of 1.05. Based on this, it seems unlikely that direct effects of the wake and its turbulence could be the cause of the outer region Stanton number enhancement. A more likely cause is the acceleration of the flow due to the growing wake, as well as the growing boundary layers, in the constant cross-sectional area tunnel.

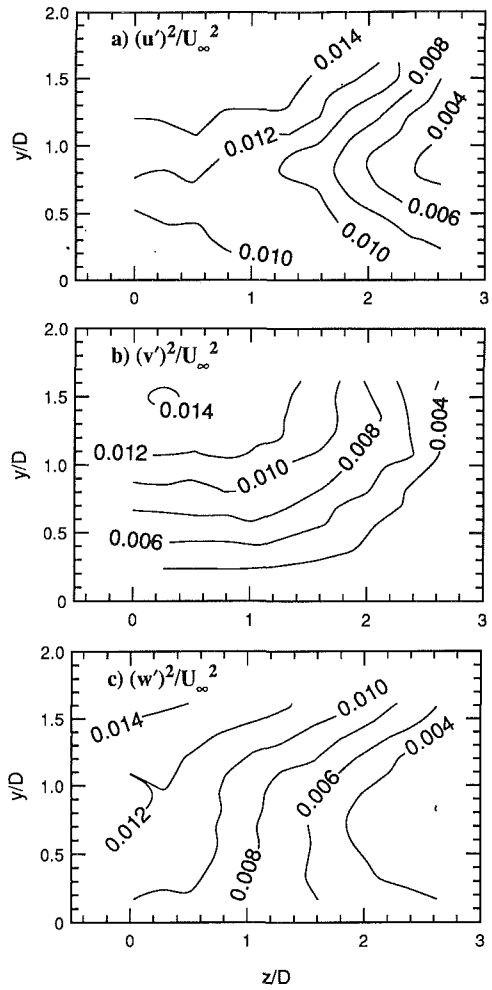

Fig. 6 Reynolds normal stresses: (*a*) $(u')^2/U_\infty^2$ (uncertainty = ±0.00014); (*b*) $(v')^2/U_\infty^2$ (uncertainty = ±0.00008); (*c*) $(w')^2/U_\infty^2$ (uncertainty = ±0.00007)

Reynolds Normal Stresses

Contours of the individual Reynolds normal stresses are plotted in Fig. 6. These results suggest that the flow can be divided into three spanwise regions: (1) the inner-wake region, $z/D < 0.8$; (2) the middle-wake region, $0.8 < z/D < 1.6$; and (3) the outer-wake region, $z/D > 1.6$. The inner-wake and middle-wake regions are dominated by the larger level of fluctuations characteristic of the wake turbulence, even near the wall. The wall acts to dampen these large fluctuations somewhat, especially $(v')^2$, accounting for the decreasing turbulence intensities closer to the wall. This wall effect is not as strong in the middle-wake region, where $(u')^2$ and $(w')^2$ values are nearly constant out to $y/D = 1.0$. In the outer-wake region, where the wake turbulence should be diminishing, the flow near the wall is characterized more by two-dimensional boundary-layer turbulence, with decreasing levels of fluctuations with increasing y/D. Farther from the wall, the turbulence intensities increase, as the asymptotic wake is approached.

Downloaded 13 Dec 2010 to 193.140.21.150. Redistribution subject to ASME license or copyright; see http://www.asme.org/terms/Terms_Use.cfm

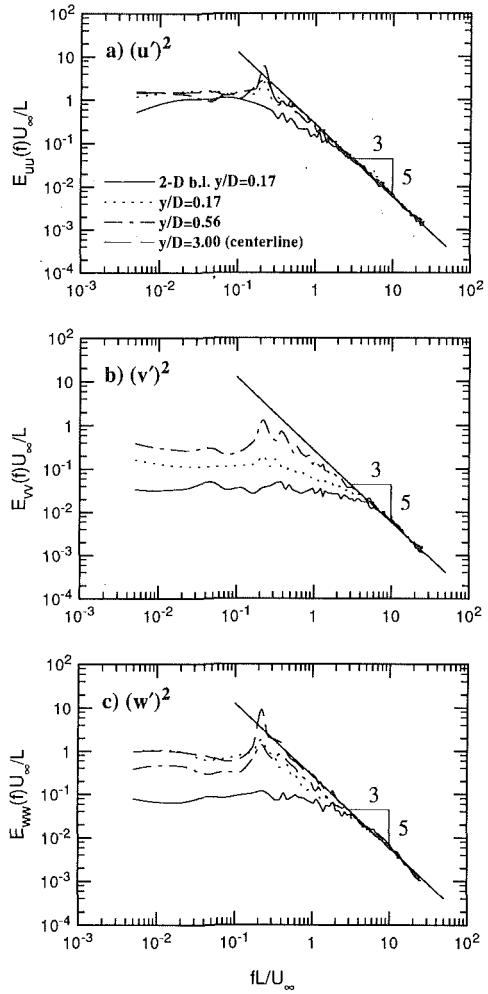

Fig. 7 Power spectra at $z/D = 1.31$ (middle-wake region) for: (*a*) $(u')^2$; (*b*) $(v')^2$; (*c*) $(w')^2$

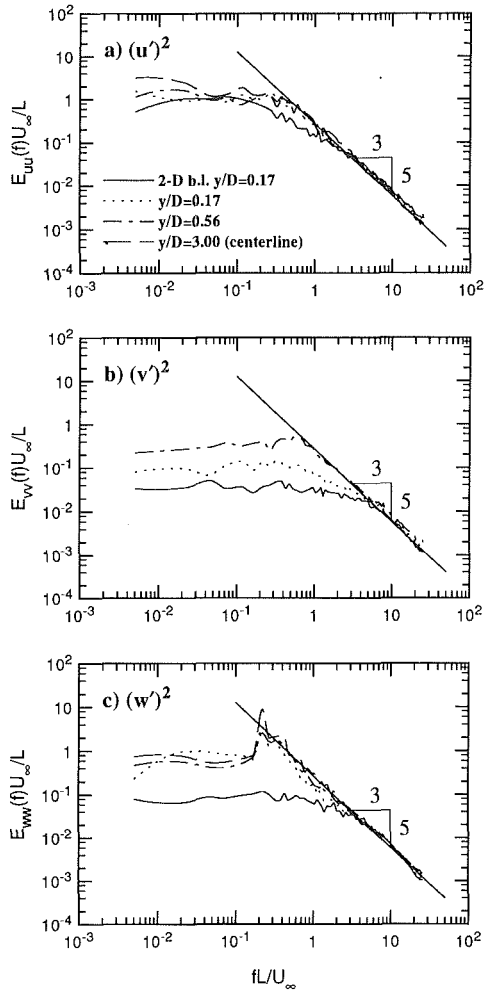

Fig. 8 Power spectra at $z/D = 0.52$ (inner-wake region) for: (*a*) $(u')^2$; (*b*) $(v')^2$; (*c*) $(w')^2$

To investigate further the structure of the turbulence, and to determine whether periodic large-scale motions were contributing to measured turbulence levels, spectra of $(u')^2$, $(v')^2$, and $(w')^2$ were obtained at several points within the flow. The spectra are defined such that, for example,

$$(u')^2 = \int_0^\infty E_{uu}(f)\,df \tag{2}$$

where f is the frequency in Hz. The spectra were obtained numerically by applying a fast Fourier transform to the entire measured time series. These were used to obtain broad band averages (approximately 25 to 50 points per decade). Because the total sampling time was limited, the spectra for frequencies less than approximately 10 Hz are questionable, since these represent averages over a limited number of event cycles. Fluctuations at these low frequencies account for only a small fraction of the total turbulent kinetic energy.

Figures 7, 8, and 9 show spectra for spanwise locations of $z/D = 1.31$, $z/D = 0.52$, and $z/D = 2.62$, which are located, respectively, in the middle, inner, and outer wake regions. Each figure contains spectra for $(u')^2$, $(v')^2$, and $(w')^2$ at two different vertical locations near the wall, $y/D = 0.17$ and $y/D = 0.56$. The $(u')^2$ and $(w')^2$ plots also contain spectra obtained at the vertical centerline ($y/D = 3$), outside the boundary-layer region.[2] Also shown are the spectra for a two-dimensional boundary layer at $y/D = 0.17$ (which corresponds to $y/\delta = 0.20$), obtained without the obstacle present. The results are shown using the Strouhal number ($S = fL/U_\infty$) as the abscissa. The chord length, L, of the streamlined cylinder, has been chosen as the characteristic length for the Strouhal number since the size of the shed vortices should depend more on the overall length of the obstacle than on the root diameter. The spectra are normalized such that the areas under the curves shown are equal to the appropriate Reynolds stress (e.g., $(u')^2$).

In the middle-wake region, Fig. 7, the spectra reveal a broad peak at $S = 0.2$ for all three components of the normal stresses, which is not seen in the spectra for the two-dimensional boundary layer. This indicates that there is some unsteadiness due to the vortex shedding that can still be observed at 14 diameters downstream. It is interesting to note that the $(v')^2$ spectra seem to reveal two peaks, with the second near $S = 0.4$.

It is questionable whether the unsteady motions suggested by these results are the same as the low-frequency phenomena observed by Rood and Keller (1984), since they did not observe the low-frequency peak in the spectrum outside of the boundary layer. The results here clearly indicate the same characteristic frequency is observed outside the boundary layer ($y/D = 3$) as is observed within.

The fact that the peaks are somewhat broad suggests that the energy contained within the shed vortices is gradually being redistributed into smaller-scale structures. This redistribution should be a function of streamwise location, with the limit being the elimination of the peak altogether, as is commonly

[2]Spectra at the vertical centerline are not available for $(v')^2$ because of a broken sensor on the *uv* probe.

Downloaded 13 Dec 2010 to 193.140.21.150. Redistribution subject to ASME license or copyright; see http://www.asme.org/terms/Terms_Use.cfm

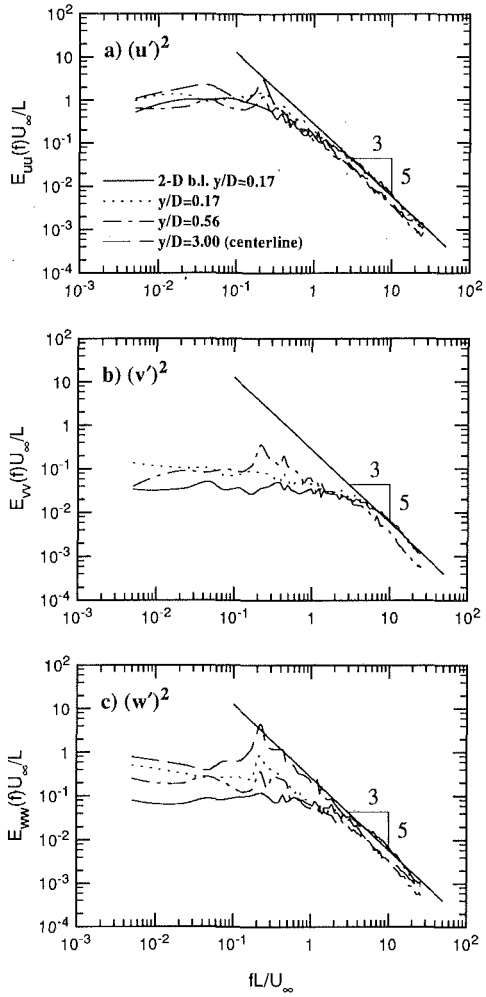

Fig. 9 Power spectra at $z/D=2.62$ (outer-wake region) for: (*a*) $(u')^2$; (*b*) $(v')^2$; (*c*) $(w')^2$

observed in pure wakes for $x/D>50$ (for example, see the spectra reported by Uberoi and Freymuth, 1969).

The vortex-shedding peaks are generally larger at the vertical centerline ($y/D=3$), and decrease somewhat as the wall is approached. This effect may be due to the interaction with the boundary layer, but is most likely a result of the damping effect of the wall on larger scale fluctuations. The wall-damping effect is most evident in the $(v')^2$ spectra, for which there is significantly less power in a broad range of low and midrange frequencies (including the vortex-shedding frequency) for $y/D=0.17$ compared to $y/D=0.56$.

Aside from the peak near the vortex-shedding frequency, the spectra reveal other interesting aspects of the turbulence structure. At high frequencies, the spectra for all y/D locations and all three components of the fluctuations approach the same curve as the two-dimensional boundary layer, at $y/D=0.17$, with the expected inertial subrange slope of $-5/3$. Thus, the flow seems to be characterized by a highly anisotropic structure at lower frequencies, as a result of vortex shedding and wall damping, and an isotropic structure at higher frequencies that is the same for all vertical locations within the boundary layer. The behavior of the high-frequency spectra as a function of the distance from the wall is unlike a pure two-dimensional boundary layer, which normally contains less energy at the higher frequencies for locations farther from the wall (Klebanoff, 1955).

The spectra for $(u')^2$, with the exception of the vortex-shedding peak, seem to be similar to the two-dimensional boundary-layer spectra at low and midrange frequencies. This is in strong contrast to $(w')^2$ and $(v')^2$, which contain significantly more power at low frequencies than the two-dimensional boundary layer.

In the inner-wake region, Fig. 8, the vortex-shedding peak is seen only in $(w')^2$, the spanwise component of the normal stresses. The $(w')^2$ spectra at both locations within the boundary layer are quite similar to the centerline-wake spectra ($y/D=3$), exhibiting significantly higher energy than in the two-dimensional boundary layer. This suggests that the wall has little effect on the spanwise fluctuations in this region. The $(u')^2$ and $(v')^2$ spectra, despite the absence of the shedding peak, contain more power than the two-dimensional boundary-layer spectra, for frequencies in the range $S=0.2$ to 1. This suggests that the energy due to vortex shedding in the streamwise and vertical fluctuations may be redistributed into smaller scale structures, which are seen as broader spectrum turbulence. In contrast, the spanwise fluctuations seem to maintain a strong vortex-shedding structure. At higher frequencies, the spectra all seem to approach the same curve, which is similar to the behavior seen in Fig. 7 for the middle-wake region.

In the outer wake region, Fig. 9, the contributions to the normal stresses due to vortex shedding are weaker. The low and midrange frequency spectra, aside from the peak near $S=0.2$, seem to be closer to the two-dimensional boundary-layer spectra than for the other regions. At high frequencies, the behavior is different than in the inner and middle wake regions in that the spectra for $y/D=0.56$ fall below that of the two-dimensional boundary layer at $y/D=0.17$ (closer to the wall). The reduced power at higher frequencies for locations farther from the wall is more characteristic of boundary layers. Thus, the spectra do seem to confirm the fact that the outer-wake region is beginning to approach a boundary-layer turbulence structure.

Turbulent Heat Fluxes. It is useful to define cross-plane transport vectors for the heat fluxes, $\overline{v\theta}\hat{j}+\overline{w\theta}\hat{k}$, and for the streamwise momentum flux, $\overline{uv}\hat{j}+\overline{uw}\hat{k}$ (Wroblewski and Eibeck, 1991b), where $\hat{j}$ and $\hat{k}$ are the unit vectors in the y and z directions, respectively. These transport vectors are plotted in Fig. 10, along with the contours of mean streamwise velocity and temperature.

In the middle-wake region, the magnitudes of both the heat and momentum-flux vectors show a local maximum. In this region, $\overline{v\theta}$ is nearly twice as large as values in a two-dimensional boundary layer at comparable distances from the wall, and peak values of $\overline{w\theta}$ are approximately 30 percent of the values of the vertical component of heat flux.

In the inner-wake region, the heat flux is predominantly in the vertical direction, with values of $\overline{v\theta}$ that are almost constant with vertical distance from the wall. This indicates significant transport of heat away from the wall in the inner-wake region, consistent with the notion of enhanced turbulent mixing suggested by the mean temperature profiles (Fig. 4*b*).

The heat-flux vectors appear to be nearly perpendicular to the mean isotherms for most of the flow. A major exception to this is in the middle-wake region away from the wall ($z/D\approx 1$ and $y/D\approx 0.5$). In this area of the flow, both the spanwise temperature gradients and the spanwise component of heat flux are positive, indicating countergradient heat transport. It is possible that this could be due to experimental uncertainty, since the values of the spanwise gradients are fairly small in this region.

The alignment of the heat-flux vectors and the isotherms for most of the flow implies an isotropic transport mechanism (Wroblewski and Eibeck, 1991b). So, a deviation from this behavior in the middle-wake region suggests a nonisotropic mechanism of heat transport, and in particular, one that appears to favor spanwise transport over vertical transport.

Momentum-flux vectors are not as closely aligned with the

Downloaded 13 Dec 2010 to 193.140.21.150. Redistribution subject to ASME license or copyright; see http://www.asme.org/terms/Terms_Use.cfm

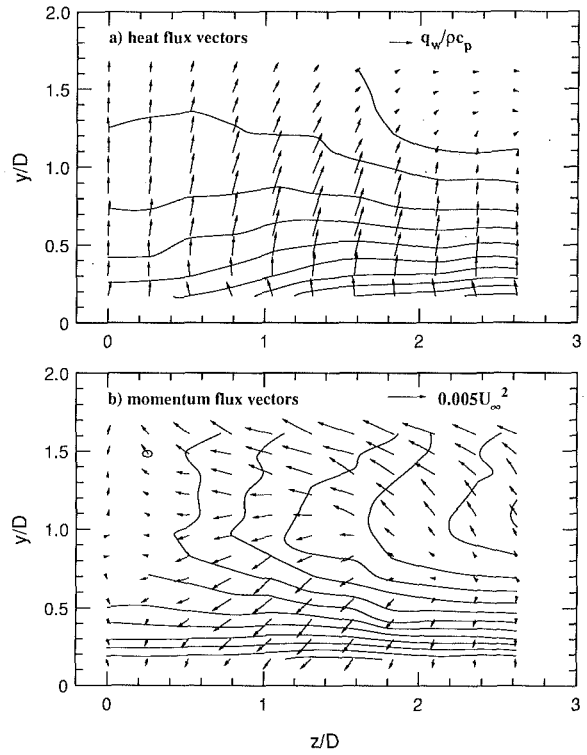

Fig. 10 Turbulent transport vectors: (*a*) heat transport, $\overline{v\theta}\hat{j}+\overline{w\theta}\hat{k}$, with mean isotherms; (*b*) momentum transport $\overline{uv}\hat{j}+\overline{uw}\hat{k}$, with mean streamwise velocity contours

mean streamwise velocity contours as the heat-flux vectors and isotherms, suggesting that the momentum transport is not isotropic. In particular, near the wall in the middle-wake region the velocity contours are nearly horizontal but the momentum fluxes show a strong spanwise component ($\overline{uw}$). The nonisotropic behavior of the turbulent momentum transport, as well as the apparent countergradient heat transport in the middle-wake region, may both be due to vortex-shedding effects, which were shown to be strongest for the spanwise component of the fluctuations in this region.

To investigate whether the increased heat-flux values in the middle wake region were due to the unsteadiness resulting from vortex shedding, cross-spectra of $\overline{v\theta}$ were obtained, where the cross-spectrum, $E_{v\theta}$, is defined such that

$$\overline{v\theta}=\int_0^\infty E_{v\theta}(f)\,df \tag{3}$$

The cross-spectrum was obtained numerically by subtracting the spectrum of $(v-\theta)^2$ from the spectrum of $(v+\theta)^2$ (Freymuth and Uberoi, 1971). Because of the uncertainy associated with subtracting two small numbers, the cross-spectra calculated by this method tend to be somewhat rough in appearance at higher frequencies. The spectra are normalized so that the areas under the curves shown are equal to $\overline{v\theta}$.

Figure 11 shows the cross-spectra of $\overline{v\theta}$ at the same locations for which the $(u')^2$, $(v')^2$, and $(w')^2$ spectra were shown previously, along with those for the two-dimensional boundary layer. In the middle-wake region ($z/D=1.31$), which was identified as the strong vortex-shedding region, there is a peak in the cross-spectra at the shedding frequency, at both $y/D=0.17$ and $y/D=0.56$. The peak is larger at $y/D=0.56$, which corresponds to the location of the peak magnitudes of $\overline{v\theta}$ and $\overline{w\theta}$ seen in Fig. 10. This suggests that these peak values of heat flux may arise as a result of unsteadiness due to vortex shedding. It is also interesting to note that the cross-spectra for the middle-wake region show the same double peak characteristic seen in the $(v')^2$ spectra in this region.

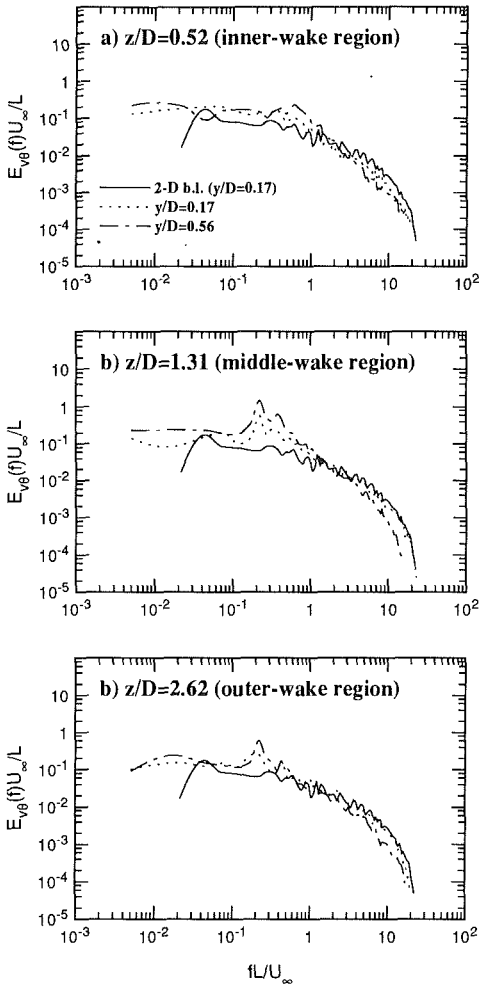

Fig. 11 Cross-spectra of vertical component of turbulent heat flux at: (*a*) $z/D=0.52$; (*b*) $z/D=1.31$; (*c*) *c*) $z/D=2.62$

In the inner-wake region, $z/D=0.52$, there is no contribution to the flux from vortex shedding, even at the location farther from the wall, $y/D=0.56$. However, for $y/D=0.56$, the low and midrange frequency cross-spectra, up to about $S=1$, are generally higher than in a two-dimensional boundary layer.

In the outer-wake region, $z/D=2.62$, there is a peak at the vortex shedding frequency, though smaller than the one observed in the spectra for the middle-wake region.

Eddy Diffusivity. In the most general sense, the eddy diffusivity can be expressed as a second-order tensor, $\mathfrak{D}_{ij}$ (Hinze, 1975), such that

$$\overline{u_i\theta}=\mathfrak{D}_{ij}\frac{\partial\overline{T}}{\partial x_j} \tag{4}$$

Here, index notation has been used for brevity (i.e., $\overline{u_2\theta}=\overline{v\theta}$, $\overline{u_1u_2}=\overline{uv}$, $x_2=y$, etc.).

As described in Wroblewski and Eibeck (1991b), the alignment of the cross-plane heat-transport vector and the mean-temperature-gradient vector implies that the eddy-diffusivity tensor reduces to a single scalar value times the identity tensor. This isotropic eddy diffusivity can be defined using the vector magnitudes as follows:

$$\epsilon_H=\frac{[(\overline{v\theta})^2+(\overline{w\theta})^2]^{1/2}}{[(\partial\overline{T}/\partial y)^2+(\partial\overline{T}/\partial z)^2]^{1/2}} \tag{5}$$

Defining the diffusivity in this sense reduces the possibility of extreme or negative values due to high uncertainties in regions where either $\overline{v\theta}$ or $\overline{w\theta}$ are small. Although it has been shown

Downloaded 13 Dec 2010 to 193.140.21.150. Redistribution subject to ASME license or copyright; see http://www.asme.org/terms/Terms_Use.cfm

that there might be deviations from the isotropic behavior of the heat flux in the middle-wake region, the isotropic eddy diffusivity will still be used to obtain a general view of the turbulent mixing.

The isotropic eddy diffusivity is plotted in Fig. 12 as a function of y/δ_{2-D}, where δ_{2-D} is the 99 percent boundary-layer thickness for the two-dimensional boundary layer (3.4 cm). Profiles are shown for six different spanwise positions (two for each of the three main regions of interest) as well as for the undisturbed two-dimensional boundary layer.

In the outer wake region, the eddy diffusivity follows a pattern similar to that of a two-dimensional boundary layer, but at an increased level. Even at $z/D=2.62$, ϵ_H values are twice as large as those in a two-dimensional boundary layer. (This can be seen more clearly on the inset that shows detail of the region near the wall.) Eddy diffusivity generally increases with decreasing z/D, until approximately $z/D=1.31$, near the center of the middle-wake region. From that point to $z/D=0$, the ϵ_H profiles are nearly identical, with maximum values that are an order of magnitude higher than those in a two-dimensional boundary layer. Close to the wall (see the inset in Fig. 12), ϵ_H has its largest values at $z/D\approx 0.52$, approximately 25 percent larger than ϵ_H at $z/D=0$. It is also interesting to note that, in the region of the peak heat-flux values (near $z/D=1.05$ and $y/D=0.7$), the eddy diffusivity is only slightly higher than at similar y locations in the inner-wake region. (Downward arrows mark the appropriate data points on Fig. 12.)

The significant increase in eddy diffusivity over a two-dimensional boundary layer suggests that increased turbulence mixing is the dominant mechanism for the enhanced wall heat transfer. The general trend of larger values near the inner-wake region and lower values near the outer wake region is consistent with the spanwise profiles of Stanton number shown in Fig. 5, as well as the isotherms shown in Fig. 4(*b*). It is somewhat inconsistent that the peak in ϵ_H occurs near $z/D=0.5$ (for the measurements at the y location nearest the wall) while the peak in Stanton number enhancement occurs at $z/D=0$. Measurements closer to the wall, which are difficult to obtain due to the probe's size, would be required to investigate this apparent discrepancy. In addition, the presence of enhanced Stanton numbers for $z/D>3$ suggests that another effect, such as the acceleration of the flow, may also provide a minor role in the increased wall heat transfer.

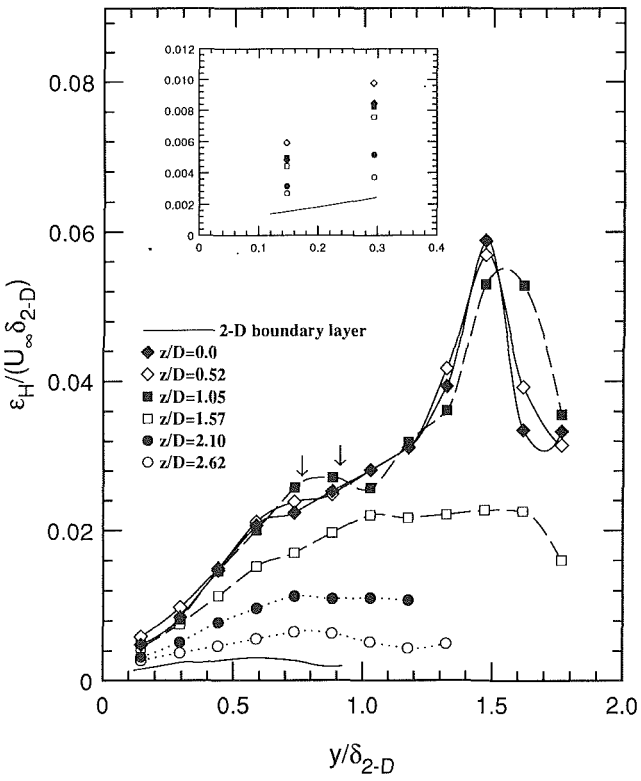

Fig. 12 Isotropic eddy diffusivity, $\epsilon_H/(U_\infty\delta_{2-d})$, where $\epsilon_H=[(\overline{v\theta})^2+(\overline{w\theta}^2]^{1/2}/[(\partial\overline{T}/\partial y)^2+(\partial\overline{T}/\partial z)^2]^{1/2}$ (uncertainty = ± 0.0003 at $\epsilon_H/(U_\infty\delta_{2-d})=0.002$ and ± 0.008 at $\epsilon_H/(U_\infty\delta_{2-d})=0.05$)

4 Summary/Conclusions

The boundary layer downstream of a junction between a wall and a streamlined cylinder is no doubt a complex one. In addition, some results indicate that the flow in the wake of the obstacle is interacting with the flow in the tunnel, leading to further complications. Despite this, some interesting features of the boundary-layer region can be distinguished.

The boundary-layer transport is affected by the presence of large-scale unsteadiness arising from vortex shedding. This unsteadiness appears in the measurements as "turbulence" with a strong spectral component at the shedding frequency, although it may be arguable whether this should be referred to as turbulence or as large-scale unsteadiness. The fact that the shedding peaks appear to be fairly broad suggests that the shed vortices are beginning to redistribute their energy into the broader-scale structures that will eventually (i.e., farther downstream) be seen as the low-frequency wake turbulence. Because of this redistribution, it is unlikely that the use of ensemble averaging would be a suitable method of separating the turbulence from the vortex-shedding unsteadiness.

The boundary-layer flow can be divided into three main spanwise regions: (1) the inner-wake region, $z/D<0.8$; (2) the middle-wake region, $0.8<z/D<1.6$; and (3) the outer-wake region, $z/D>1.6$. In general, the spectra indicate that all three regions exhibit a nonisotropic turbulent structure at low frequencies, which is strongly affected by vortex shedding and the damping effect of the wall, and an isotropic high-frequency structure that is similar to two-dimensional boundary-layer turbulence.

The inner-wake region ($z/D<0.8$) seems to be characterized by spanwise velocity fluctuations, w', with a strong spectral peak at the vortex-shedding frequency. The vertical and streamwise fluctuations do not show such a dominant spectral peak, but do show a generally increased level of turbulence, compared to a two-dimensional boundary layer, across a broad range of low and midrange frequencies. This general increase results in higher eddy diffusivities (i.e., increased turbulent mixing of heat) and a corresponding higher wall heat transfer rate.

The middle-wake region ($0.8<z/D<1.6$) is characterized by strong vortex-shedding effects in all three directions, with the strongest spectral peak observed in the spanwise direction, $(w')^2$. The strong vortex shedding appears to lead to increased values of turbulent heat flux (both $\overline{v\theta}$ and $\overline{w\theta}$) and of the Reynolds shear stresses ($\overline{uv}$ and $\overline{uw}$). It may also lead to the nonisotropic behavior of the momentum and heat transport, which suggest greater transport in the spanwise than in the normal direction. Despite the fact that the unsteadiness resulting from vortex shedding leads to increased heat-flux values in this region, it does not lead to increased wall heat transfer, nor does it lead to any substantial increase in eddy diffusivity compared to the inner-wake region, where a vortex-shedding peak is absent in the vertical and streamwise fluctuations.

The outer-wake region exhibits mean temperature and mean velocity profiles that approach two-dimensional boundary-layer behavior. The spectra suggest that the turbulent structure in this region is more characteristic of a boundary layer, but with a modest vortex-shedding effect. This results in elevated levels of eddy diffusivities and corresponding increases in wall heat transfer compared to the two-dimensional boundary layer.

The relatively weak horseshoe vortex, whose presence in the

Downloaded 13 Dec 2010 to 193.140.21.150. Redistribution subject to ASME license or copyright; see http://www.asme.org/terms/Terms_Use.cfm

flow is observed even at $x/D = 14$, does not seem to affect greatly the mean streamwise velocity or temperature profiles, and therefore, it is unlikely that it contributes to the enhanced wall heat transfer. Instead, the increase in turbulence mixing brought about by the wake of the cylinder, as evidenced by the substantially higher eddy diffusivities, is the dominant mechanism for the enhanced heat transfer.

Acknowledgments

Funding for this work was provided by the Department of Energy Office of Basic Energy Science under contract number DE-FG03-87ER13780, and monitored by Dr. Oscar Manley.

References

Baker, C. J., 1979, "The Laminar Horseshoe Vortex," *J. Fluid Mech.*, Vol. 95, Pt. 2, pp. 347–368.

Baker, C. J., 1980, "The Turbulent Horseshoe Vortex," *Journal of Wind Engineering and Industrial Aerodynamics*, Vol. 6, pp. 9–23.

Belik, L., 1973, "The Secondary Flow About Circular Cylinders Mounted Normal to a Flat Plate," *Aeronautical Quarterly*, Vol. 26, pp. 47–54.

Collis, D. C., and Williams, M. J., 1959, "Two-Dimensional Convection From Heated Wires at Low Reynolds Numbers," *J. Fluid Mech.*, Vol. 6, pp. 357–384.

Dickinson, S. C., 1984, "Flow Visualization and Velocity Measurements in the Separated Region of an Appendage-Flat Plate Junction," *Proceedings of the Ninth Biennial Symposium on Turbulence*, University of Missouri—Rolla, Rolla, MO.

Eibeck, P. A., 1990, "An Experimental Study of the Flow Downstream of a Circular and Tapered Cylinder," ASME *Journal of Fluids Engineering*, Vol. 112, pp. 393–401.

Fisher, E. M., and Eibeck, P. A., 1990, "The Influence of a Horseshoe Vortex on Local Convective Heat Transfer," ASME JOURNAL OF HEAT TRANSFER, Vol. 112, pp. 329–335.

Freymuth, P., and Uberoi, M. S., 1971, "Structure of Temperature Fluctuations in the Turbulent Wake Behind a Heated Cylinder," *Physics of Fluids*, Vol. 14, No. 12, pp. 2574–2580.

Goldstein, R. J., and Karni, J., 1984, "The Effect of a Wall Boundary Layer on Local Mass Transfer From a Cylinder in Crossflow," ASME JOURNAL OF HEAT TRANSFER, Vol. 106, pp. 260–267.

Hinze, J. O., 1975, *Turbulence*, 2nd ed., McGraw-Hill, New York, pp. 22–26.

Hsing, T., and Teng, H., 1984, "Experimental Study of the Behavior of 3-D Turbulent Boundary in a Simplified Wing/Body Junction," AIAA Report No. 84-1529.

Ichimiya, K., Akino, N., Kunugi, T., and Mitsushiro, K., 1988, "Fundamental Study of Heat Transfer and Flow Situation Around a Spacer (in the Case of a Cylindrical Rod as a Spacer)," *Int. J. Heat Mass Transfer*, Vol. 31, No. 11, pp. 2215–2225.

Klebanoff, P. S., 1955, "Characteristics of Turbulence in a Boundary Layer With Zero Pressure Gradient," NACA Report No. 1247.

McMahon, H., Hubbartt, J., and Kubendran, L., 1982, "Mean Velocities and Reynolds Stresses in a Juncture Flow," NASA Contractor Report No. 3605, NASA-Langley Research Center, Hampton, VA.

McMahon, H., Hubbartt, J., and Kubendran, L. 1983, "Mean Velocities and Reynolds Stresses Upstream of a Simulated Wing Fuselage Junction," NASA Contractor Report No. 3695, NASA-Langely Research Center, Hampton, VA.

Mehta, R. D., 1984, "Effect of Wing Nose Shape on the Flow in a Wing/Body Junction," *Aeronautical Journal*, Vol. 88, No. 880, pp. 456–460.

Merati, P., McMahon, H. M., and Yoo, K. M., 1988, "Experimental Modeling of a Turbulent Flow in the Junction and Wake of an Appendage Flat Plate," AIAA/ASME/SIAM/APS 1st National Fluid Dynamics Congress, Cincinnati, OH, pp. 1255–1264.

Moffat, R. J., 1988, "Describing Uncertainty in Experimental Results," *Exp. Thermal Fluid Sci.*, Vol. 1, pp. 3–17.

Moore, J., and Forlini, T. J., 1984, "A Horseshoe Vortex in a Duct," ASME *Journal of Engineering for Gas Turbines and Power*, Vol. 106, pp. 668–676.

Pierce, F. J., and Harsh, M. D., 1988, "The Mean Flow Structure Around and Within a Turbulent Junction or Horseshoe Vortex—Part II. The Separated and Junction Vortex Flow," ASME *Journal of Fluids Engineering*, Vol. 110, pp. 415–423.

Rood, E. P., and Keller, J. E., 1984, "Evidence of Large Scale Time Dependent Flow in Wing-Wall Interaction Wake," *Unsteady Turbulent Boundary Layers and Friction*, ASME FED-Vol. 12, pp. 39–44.

Shabaka, I. M. M. A., and Bradshaw, P., 1981, "Turbulent Flow Measurements in an Idealized Wing/Body Junction," *AIAA Journal*, Vol. 19, No. 12, pp. 131–132.

Tennekes, H., and Lumley, J. L., 1972, *A First Course in Turbulence*, The MIT Press, Cambridge, MA, pp. 114–115.

Uberoi, M. S., and Freymuth, P., 1969, "Spectra of Turbulence in Wakes Behind Circular Cylinders," *Physics of Fluids*, Vol. 12, No. 7, pp. 1359–1363.

Wroblewski, D. E., 1990, "An Experimental Investigation of Turbulent Heat Transport in a Boundary Layer With an Embedded Streamwise Vortex," Ph.D. Thesis, University of California, Berkeley, Mechanical Engineering Department.

Wroblewski, D. E., and Eibeck, P. A., 1991a, "A Frequency Response Compensation Technique for Cold Wires and Its Application to a Heat Flux Probe," *Exp. Thermal Fluid Sciences*, Vol. 4, pp. 452–463.

Wroblewski, D. E., and Eibeck, P. A., 1991b, "Measurements of Turbulent Heat Transport in a Boundary Layer With an Embedded Streamwise Vortex," *Int. J. Heat Mass Transfer*, Vol. 34, No. 7, pp. 1617–1631.

Downloaded 13 Dec 2010 to 193.140.21.150. Redistribution subject to ASME license or copyright; see http://www.asme.org/terms/Terms_Use.cfm

Effect of Uneven Wall Temperature on Local Heat Transfer in a Rotating Square Channel With Smooth Walls and Radial Outward Flow

J.-C. Han
Professor.
Fellow ASME

Y. M. Zhang
Research Associate.
Mem. ASME

Turbine Heat Transfer Laboratory,
Department of Mechanical Engineering,
Texas A&M University,
College Station, Texas 77843-3123

The influence of uneven wall temperature on the local heat transfer coefficient in a rotating square channel with smooth walls and radial outward flow was investigated for Reynolds numbers from 2500 to 25,000 and rotation numbers from 0 to 0.352. The square channel, composed of six isolated copper sections, has a length-to-hydraulic diameter ratio of 12. The mean rotating radius to the channel hydraulic diameter ratio is kept at a constant value of 30. Three cases of thermal boundary conditions were studied: (A) four walls uniform temperature, (B) four walls uniform heat flux, and (C) leading and trailing walls hot and two side walls cold. The results show that the heat transfer coefficients on the leading surface are much lower than that of the trailing surface due to rotation. For case A of four walls uniform temperature, the leading surface heat transfer coefficient decreases and then increases with increasing rotation numbers, and the trailing surface heat transfer coefficient increases monotonically with rotation numbers. The decreased (or increased) heat transfer coefficients on the leading (or trailing) surface are due to the cross-stream and centrifugal buoyancy-induced flows from rotations. However, the trailing surface heat transfer coefficients, as well as those for the side walls, for case B are higher than for case A and the leading surface heat transfer coefficients for cases B and C are significantly higher than for case A. The results suggest that the local uneven wall temperature creates the local buoyancy forces, which change the effect of the rotation. Therefore, the local heat transfer coefficients on the leading, trailing, and side surfaces are altered by the uneven wall temperature.

Introduction

The trend in advanced aeroengine design for high thermal efficiency and high power density is toward high entry gas temperature (1400–1500°C), which is far above the allowable metal temperature. Therefore, highly sophisticated cooling technologies such as film cooling, impingement cooling, and augmented convection cooling must be employed to maintain the structural integrity of blades and vanes used in advanced gas turbine engines. This investigation considers the local heat transfer characteristics in turbine coolant passages with rotation. Since heat is transferred from both the pressure and suction surfaces, rib turbulators (turbulence promoters) are often cast on two opposite walls of the cooling passages (i.e., inner walls of the pressure-trailing and suction-leading surface) to enhance heat transfer to the cooling air. A typical coolant passage can be modeled as a single pass or multipass rectangular channel with four smooth walls or with two opposite rib-roughened walls. This paper focuses on the effect of surface uneven temperature on the local heat transfer coefficient in a rotating, square channel with four smooth walls and radial outward flow.

Most of the available data/correlations in the literature on internal turbine blade cooling are from tests performed with nonrotating flow condition (e.g., Han, 1984, 1988; Han et al., 1992a). Heat transfer data are difficult and expensive to obtain under rotation; therefore, only limited amounts of data are available in the open literature. Mori et al. (1971) studied the mean convective heat transfer in a rotating radial circular pipe. Clifford et al. (1984) reported the local and mean transfer in a triangular-sectioned duct rotating in the orthogonal mode. Morris et al. (1988) and Morris and Ghavani-Nasr (1991) studied the effect of rotation on the heat transfer characteristics of circular, triangular, rectangular, and square-sectioned coolant passages of gas turbine rotor blades. Guidez (1989) presented the study of convective heat transfer in a rotating coolant channel. Taslim et al. (1991a, 1991b) studied heat transfer coefficients in a rotating channel with ribbed walls. Wagner et al. (1986, 1991a, 1991b, 1992) investigated the local heat transfer in rotating serpentine passages with smooth walls and two opposite ribbed walls. With the exception of Taslim et al. (1991a, 1991b), Wagner et al. (1986, 1992) and Clifford et al. (1984), all of the abovementioned work was conducted with smooth wall models, and with the exception of Wagner (1991b, 1992), the aforementioned studies were tested for straight channels. Some investigators found that large increases and decreases in trailing and leading surface heat transfer occur under certain conditions of rotation, while other investigators found lesser effects. Some inconsistencies exist between investigators due to differences in measurement techniques, models, and test conditions.

Wagner et al. (1991a, 1991b) was the most systematic investigation of the effects of Coriolis and buoyancy forces on local heat transfer coefficient distributions of a two-pass square channel with smooth walls. In summary, the difference in heat transfer between rotating and nonrotating flow conditions is primarily due to secondary flows associated with Coriolis acceleration (due to rotation) and the centrifugal buoyancy (due

Contributed by the Heat Transfer Division for publication in the JOURNAL OF HEAT TRANSFER. Manuscript received by the Heat Transfer Division January 1992; revision received May 1992. Keywords: Forced Convection, Rotating Flows, Turbines. Associate Technical Editor: R. J. Simoneau.

Copyright © 1992 by ASME
Downloaded 13 Dec 2010 to 193.140.21.150. Redistribution subject to ASME license or copyright; see http://www.asme.org/terms/Terms_Use.cfm

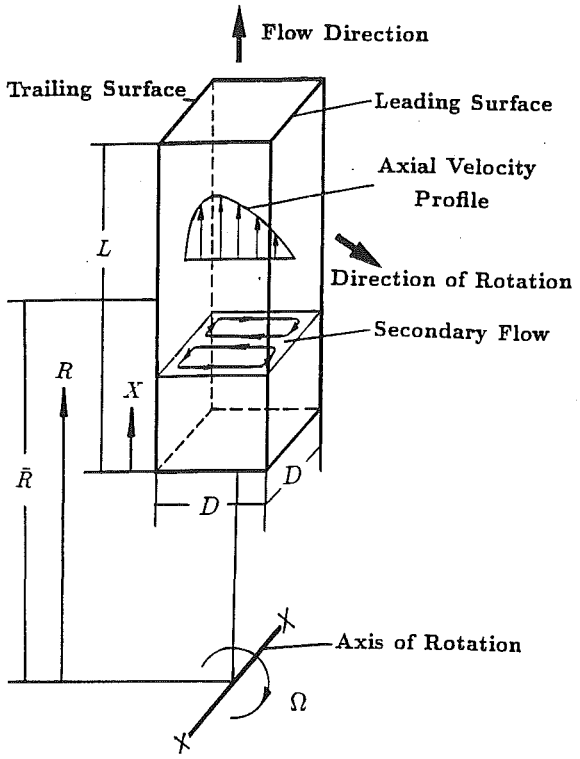

Fig. 1 Conceptual view of rotating coolant flow distribution

to large wall-to-coolant temperature differences). The rotating trailing surface heat transfer coefficient can be increased up to 3.5 times the nonrotating fully developed circular tube values, but the leading surface heat transfer coefficient can be decreased to 40 percent of the fully developed circular tube values. The local heat transfer coefficient on the trailing (pressure) surface of the first coolant passage (radial outward flow) increases with increasing rotational speed and wall-to-coolant temperature difference. This is because the rotation induces destabilization of the thinner boundary layer on the trailing surface (Johnston et al., 1972, see Fig. 1) and buoyancy causes near-wall turbulence on the trailing surface of the first coolant passage. However, the local heat transfer coefficient on the leading surface of the first coolant passage decreases with increasing rotational speed but increases with wall-to-coolant temperature differences. This is because the rotation causes stabilization of a thicker boundary layer (see Fig. 1). The cross-stream flows also induce heated, near-wall fluid from the trailing and sidewall surfaces to accumulate near the leading side of the coolant passage. This results in reduced heat transfer on the leading surface. Meanwhile, buoyancy causes the near-wall counterflow interaction with the mainstream on the leading surface of the first coolant passage, and tends to enhance heat transfer.

The studies mentioned above were limited to uniform wall temperature (Wagner et al., 1991a, 1991b) of the square channel. However, the heat flux or temperature of the leading surface is quite different from that of the trailing surface and sidewalls in advanced gas turbine blades (Han et al., 1992a) It is speculated that different wall thermal conditions may create different cross-stream secondary flow and buoyancy-induced near-wall turbulence under rotation. Consequently, it may alter the leading and trailing surface heat transfer coefficient distributions of the coolant passages. Figure 2 depicts a conceptual view of the effect of bulk buoyancy force on the coolant flow profile for the case of uniform wall temperature (both leading and trailing surface hot), and of local buoyancy force for the case of uniform wall heat flux (leading hotter than trailing, i.e., uneven wall temperature). This bulk or local buoyancy force, due to even or uneven wall temperature, may be responsible for shifting the coolant flow profile and changing the heat transfer coefficients on the leading and trailing surfaces of the square channel with rotation.

The objective of this study is to investigate the effect of wall heating condition on the local heat transfer coefficient in a rotating square channel with smooth walls and radial outward flow. Three surface heating conditions were tested: (A) four walls uniform temperature (a baseline test to compare the data of Wagner et al., 1991a), (B) four walls uniform heat flux (the absolute temperature ratios of leading surface to side wall and trailing surface to side wall are 1.05 and 0.95, respectively, another baseline test to compare the data of four walls uniform temperature), and (C) leading and trailing heated to the same temperature but with two side walls unheated (the absolute temperature ratio of leading or trailing surface to side wall is 1.10). The results, based on other surface heating conditions, are referred to by Han et al. (1992b).

Experimental Facility

Figure 3 shows a schematic of the rotating rig. The hollow rotating shaft is driven by a 25-hp a-c motor with a toothed

Nomenclature

A = heat transfer surface area
D = hydraulic diameter; square channel width or height
h = heat transfer coefficient
K = thermal conductivity of coolant
L = heated channel length
Nu = Nusselt number = hD/K
Nu_o = Nusselt number in fully developed tube flow
Pr = Prandtl number
q_{net} = net heat transfer rate, W
q'' = net heat transfer flux, W/m^2
R = rotating radius
$\bar{R}$ = mean rotating radius
Re = Reynolds number = $\rho DV/\mu$
Ro = rotation number = $\Omega D/V$
T_b = local bulk mean coolant temperature, °C or K
T_{bi} = inlet bulk mean coolant temperature, °C or K
T_w = local wall temperature, °C or K
T_{wA} = local wall temperature of side A surface, °C or K
T_{wB} = local wall temperature of side B surface, °C or K
T_{wL} = local wall temperature of leading surface, °C or K
T_{wT} = local wall temperature of trailing surface, °C or K
V = mean coolant velocity
X = axial distance from heated channel inlet
$\Delta\rho/\rho$ = coolant-to-wall density ratio based on local bulk mean coolant temperature = $(\rho_b-\rho_w)/\rho_b = (T_w-T_b)/T_w$
$(\Delta\rho/\rho)_i$ = coolant-to-wall density ratio based on inlet bulk mean coolant temperature = $(\rho_{bi}-\rho_w)/\rho_{bi} = (T_w-T_{bi})/T_w$
μ = coolant dynamic viscosity
ρ = coolant density
ρ_b = coolant density based on local bulk mean coolant temperature
ρ_{bi} = coolant density based on inlet bulk mean coolant temperature
ρ_w = coolant density based on local wall temperature
Ω = rotational speed, rpm

Downloaded 13 Dec 2010 to 193.140.21.150. Redistribution subject to ASME license or copyright; see http://www.asme.org/terms/Terms_Use.cfm

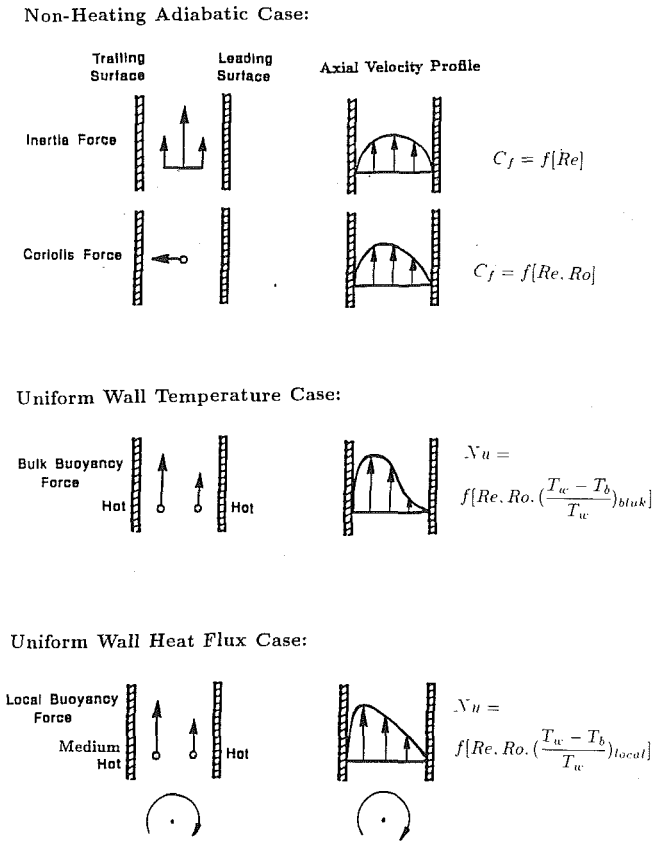

Fig. 2 *Conceptual view of effect of inertia, Coriolis, and buoyancy forces on axial velocity or temperature profile*

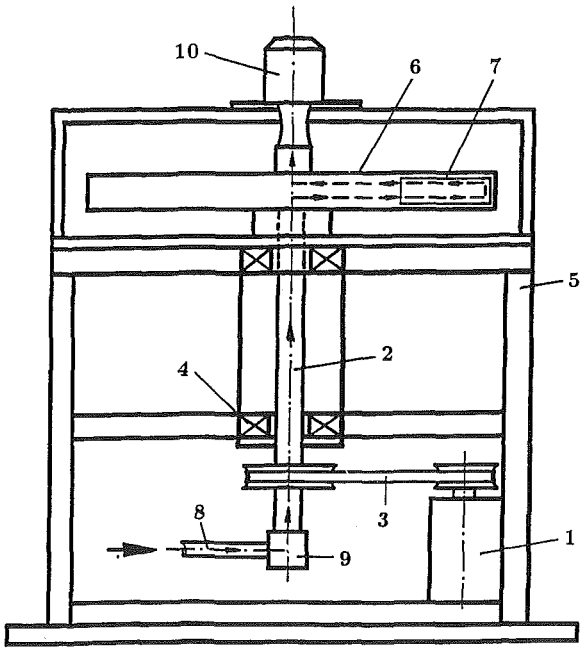

1. Electric Motor with Controller
2. Rotating Shaft
3. Belt Drive Pully System
4. Bearing Support System
5. Steel Table
6. Rotating Arm
7. Test Section
8. Compressor Air
9. Rotary Seal
10. Slip Ring

Fig. 3 Schematic of the rotating rig

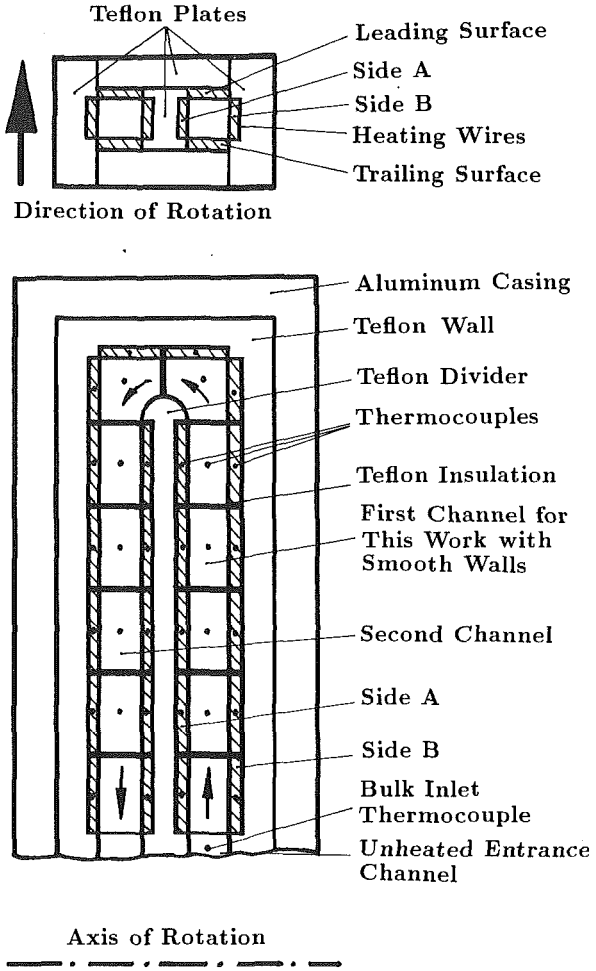

Fig. 4 *Schematic of the heat transfer test model*

belt drive pulley system through a frequency-controlled motor controller with a maximum rotating speed of 3400 rpm. The rotating shaft and supporting bearing system are vertically mounted on a rigid table made of heavy steel structure. The rotating arm is perpendicularly connected to the rotating shaft. The test model, a two-pass square channel with a sharp 180 deg turn (see Fig. 4 for details), is inserted to the end portion of one side of the rotating arm. The ratio of the mean rotating arm radius to the channel hydraulic diameter ($\bar{R}/D$) is 30. The regulated compressor air is routed through an orifice meter where the coolant flow rate was measured to the entrance (bottom) of the rotating shaft through a rotary seal. The coolant flows through the hollow rotating shaft, the hollow rotating arm, and the test model (two-pass channel) and is exhausted into the atmosphere at the exit (top) of the rotating shaft. The model pressure is about one atmosphere. The slip ring systems are attached to the exit portion of the rotating shaft. A 100 contact slip ring is used to transfer outputs from thermocouples attached to the rotating channel to a 100 point data logger interfaced to an IBM computer. A second 32 contact slip ring is used to transfer outputs from heaters attached to the rotating channels to a 32 point variac connected with digital multimeters. The local surface temperature and heat flux can be measured through these slip ring systems. The rotating speed is measured by a digital photo tachometer.

To obtain the true regionally averaged heat transfer coefficients for turbine cooling design, it is better to have a test section that can determine the regionally averaged heat transfer coefficients in the duct streamwise flow direction. The two-pass square duct is divided into twelve short copper sections,

Downloaded 13 Dec 2010 to 193.140.21.150. Redistribution subject to ASME license or copyright; see http://www.asme.org/terms/Terms_Use.cfm

as shown in Fig. 4. Each copper section is composed of four copper plates and has an inner cross section of 1.27 cm by 1.27 cm (1/2 in. by 1/2 in.). Thin Teflon strips are machined along the periphery contact surface between copper sections as insulation to prevent possible heat conduction. The square test duct length-to-hydraulic diameter ratio (L/D) is 12. The local wall temperature of the test duct is measured by 48 copper constantan thermocouples distributed along the length and across the circumference of the copper duct. The inlet air temperature was measured by a thermocouple at the inlet central plane of the heated duct. There is an unheated Teflon entrance duct (not shown in Fig. 4) that has the same cross section and length as that of the test duct. This entrance duct serves to establish hydrodynamically fully developed flow at the entrance to the test duct. The inlet velocity profiles were not measured.

Figure 4 also shows the cross section of the test duct. The resistance heaters are uniformly cemented between the copper plate backface grooves and the Teflon wall to insure good contact. Each of the four duct walls has its own heater with each heater independently controlled by a variac transformer. Each heater provides a controllable heat flux for each duct wall. The side walls are isolated from the leading and trailing walls to eliminate heat conduction. The entire heated test duct is insulated by Teflon material. Note that the test model was originally designed for a two-pass square channel with smooth or ribbed walls. However, only the first pass smooth wall results are presented in this paper. The objective is systematically to investigate the effect of varying wall heating condition on the leading and trailing surface heat transfer coefficients in a rotating square duct with smooth walls and radial outward flow.

Data Reduction

The local heat transfer coefficient was calculated from the local net heat transfer rate per unit surface area to the cooling air, the local wall temperature on each copper plate, and the local bulk mean air temperature as:

$$h = (q_{\text{net}})/[A(T_w - T_b)] \tag{1}$$

Equation (1) was used for the local leading, trailing, and side surface heat transfer coefficient calculations. The local net heat transfer rate (q_{net}) was the electrical power generated from the heaters minus the heat loss outside the test duct. The electrical power generated from the heater was determined from the measured heater resistance and voltage on each wall of the test duct. The effect of the local wall temperature variation on the local heater resistance was estimated to be less than 2 percent but was included in the data reduction. The effect of axial wall conduction between copper sections on the local net heat transfer rate was less than 2 percent but was also included in the data analysis. Loss tests were performed to determine the total heat loss from each of the test model walls for a no-flow condition (with rotation but without coolant flow). The loss calibration was performed by supplying power to the test model for steady state. This was done for several different power inputs to obtain the relation between the total heat loss from each surface and the corresponding surface temperature. The heat loss calibration was performed for three different surface heating conditions (cases A, B, and C) and for three rotation speeds (0, 400, and 800 rpm), respectively.

The local wall temperatures used in Eq. (1) were read from the thermocouple output of each copper plate. The local bulk mean air temperature used in Eq. (1) was calculated from the local net heat input to the coolant flow through each set of heated surfaces. The local bulk mean temperature was determined by marching along the test duct and calculating temperature rise due to the local net heat input to the coolant. The calculation was started at the inlet of the heated test duct

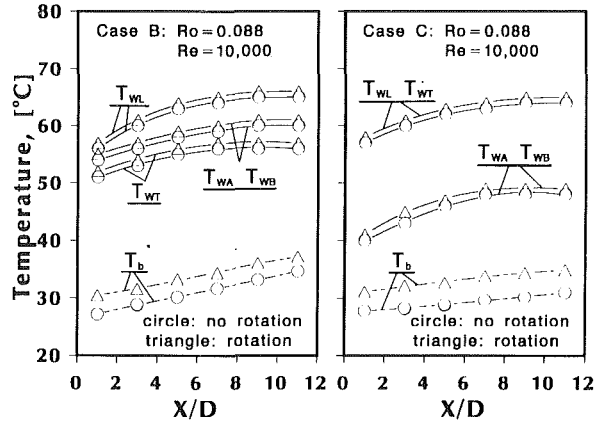

Fig. 5 Variation of surface and coolant temperature with axial location for cases *B* and *C*

where the coolant temperature was measured by a single thermocouple (about 30°C). The local bulk mean air temperature for each heated surface was determined by averaging the inlet and exit calculated bulk mean air temperatures for each set of four heated walls. Figure 5 shows the typical variations of local wall to bulk mean air temperature along the test duct for two different surface heating conditions (cases B and C) at rotation numbers of 0.0 and 0.088 (0.0 and 800 rpm at Re = 10,000). The local heat transfer coefficient calculated from Eq. (1) was converted to the dimensionless Nusselt number for a given flow Reynolds number. The properties in the Nusselt and Reynolds number were evaluated at the average of the inlet and outlet bulk mean coolant temperatures. To reduce the influence of flow Reynolds number on the heat transfer coefficient with rotation, the local Nusselt number of the present study was normalized by the Nusselt number for fully developed turbulent flow in smooth circular tubes with no rotation correlated by Dittus-Boelter/McAdams (Rohsenow and Choi, 1961) as:

$$\text{Nu}/\text{Nu}_0 = (hD/K)/[0.023\ \text{Re}^{0.8}\text{Pr}^{0.4}] \tag{2}$$

with Pr = 0.72. The uncertainty of the local heat transfer coefficient is affected by the local wall-to-coolant temperature difference and the net heat input to the coolant flow from each heated copper plate. The uncertainty of the local heat transfer coefficient increases when decreasing the wall-to-coolant temperature difference ($T_w - T_b$) and the net heat input. The uncertainty also increases for low heat inputs such as low Reynolds numbers and on the leading surfaces. Based on the method described by Kline and McClintock (1953), the typical uncertainty in the Nusselt number was estimated to be less than 8 percent for Reynolds numbers larger than 10,000. The maximum certainty, however, could be up to 20–25 percent for the lowest heat transfer coefficient on the leading surface of the test duct at the lowest Reynolds number tested.

Experimental Results and Discussion

The Nusselt number is a function of Reynolds and Prandtl numbers for fully developed turbulent forced convection in nonrotating channels. As previously discussed (e.g., Wagner et al., 1991a), the classical forced convection mechanism present in the channel is influenced by the presence of Coriolis forces (rotation number) and centrifugal buoyancy (wall-to-coolant temperature difference, $\Delta\rho/\rho$). The net results of these parameters due to rotation in the known forced convection heat transfer correlation may be written as:

$$\text{Nu} = f(\overline{R}/D,\ X/D,\ \text{Re},\ \text{Pr},\ \text{Ro},\ \Delta\rho/\rho) \tag{3}$$

where Pr = 0.72 and $\overline{R}/D$ = 30 for the present study. The tests were performed for four Reynolds numbers (Re = 2500,

Downloaded 13 Dec 2010 to 193.140.21.150. Redistribution subject to ASME license or copyright; see http://www.asme.org/terms/Terms_Use.cfm

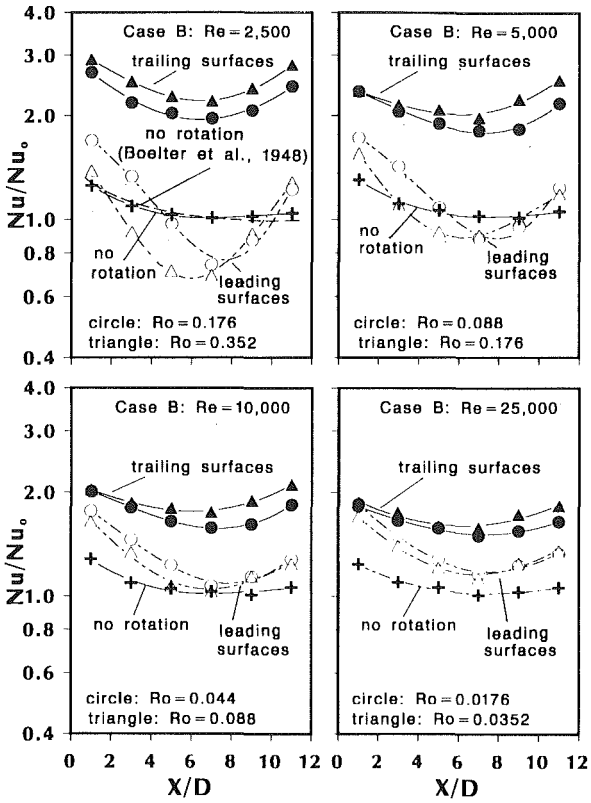

Fig. 6 Effect of rotation number on Nusselt number ratio variation for case *B* at selected Reynolds numbers

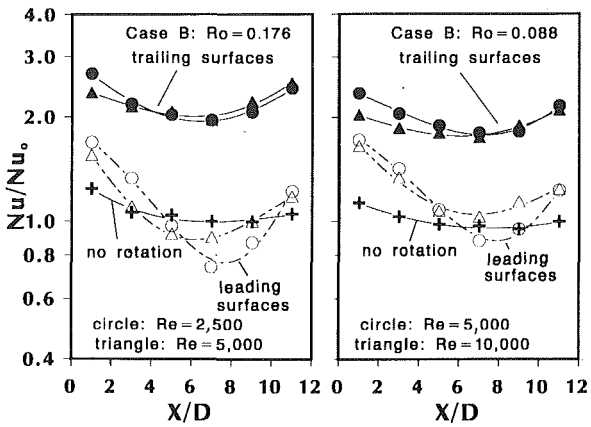

Fig. 7 Effect of Reynolds number on Nusselt number ratio variation for case *B* at selected rotation numbers

5000, 10,000 and 25,000) and three rotational speeds (Ω = 0, 400, and 800 rpm). Seven rotation numbers (Ro = 0.0, 0.0176, 0.0352, 0.044, 0.088, 0.176, and 0.352) were obtained. Three surface heating conditions were tested: (*A*) four walls uniform temperature (T_w = 60–65°C and $(\Delta\rho/\rho)_i$ = 0.1), (*B*) four walls uniform heat flux (T_w = 60–65°C, 50–55°C, 55–60°C, respectively, for leading, trailing, and sidewalls, and $(\Delta\rho/\rho)_i$ = 0.1, 0.07, 0.08, respectively, for leading, trailing, and sidewalls), and (*C*) leading and trailing hot but with sidewalls cold (T_w = 60–65°C and $(\Delta\rho/\rho)_i$ = 0.1 for both leading and trailing, and T_w = 50°C and $(\Delta\rho/\rho)_i$ = 0.06 for side walls). Coolant inlet temperature (T_{bi}) was about 30°C for cases *A*, *B*, and *C*. The results of all tests were evaluated on a local basis (i.e., on the leading and trailing surfaces along the *X/D* streamwise direction) by varying each parameter while holding the remaining parameters constant. The effect of each parameter on the local heat transfer coefficients is presented in the following order: effect of rotation number, effect of Reynolds number, effect of uneven wall temperature (i.e., effect of each surface's $(\Delta\rho/\rho)_i$), correlating data, and comparison with the previous investigators' results.

Effect of Rotation Number. The regionally averaged heat transfer results are presented as the axial distributions of a normalized Nusselt number ratio (Nu/Nu_o versus *X/D*). Figure 6 shows the effect of the rotation number on the leading and trailing surface Nusselt number ratio distributions with Re = 2500, 5000, 10,000 and 25,000, respectively, for case *B* of four walls uniform heat flux. The results for these corresponding nonrotation tests (Re = 2500, 5000, 10,000, and 25,000) are also shown for comparison. Note that the nonrotating heat transfer ratios on the leading and trailing surfaces are close to each other within 5 percent for the four Reynolds numbers studied. Therefore, a single curve along the axial location is presented (see Fig. 6, legend +). The nonrotating heat transfer ratio decreases monotonically from 1.5 near the thermal entrance of the first passage to about 1.0 near the downstream (*X/D* = 9) and then increases slightly near *X/D* = 11 because of flow entering the sharp 180 deg turn. The nonrotating results agree with the previous study of local heat transfer ratios in the entry region of a circular tube with fully developed flow condition (Boelter et al., 1948).

With a Reynolds number of 2500 and Ro = 0.352, the heat transfer ratio at the trailing surfaces increases by two to three times compared to the heat transfer ratio from the nonrotating condition. The heat transfer ratio on the leading surface decreases sharply from the entrance to about 60 percent of the nonrotating value at *X/D* = 6 and then increases rapidly at the larger *X/D* location. This means that the trailing surface heat transfer coefficients can be three to four times higher than that of the leading surface due to a rotation number of 0.352 and Re = 2500. However, as seen from Fig. 6, the difference of the heat transfer coefficients between that trailing and leading surfaces decreases with increasing Reynolds number from 2500 to 25,000 (i.e., with decreasing rotation number from 0.352 to 0.0352). It is seen that the Nusselt number ratio on the leading surface can be higher, instead of lower, than that of the nonrotating value for Reynolds number greater that 10,000 (i.e., for rotation number less than 0.088).

Effect of Reynolds Number. Figure 7 shows the effect of Reynolds number on the leading and trailing surface Nusselt number ratio for two different rotating numbers, for case *B* of four walls uniform heat flux. The rotation number can be viewed as the measurement of the relative strength of the Coriolis to inertia force (i.e., cross-stream to streamwise). The same rotation number (Ro = $\Omega D/V$) can be obtained by using larger or smaller values of Ω and *V*. The comparisons are based on: (1) Ro = 0.176 for Re = 2500 and 5000 and (2) Ro = 0.088 for Re = 5000 and 10,000. The same rotation number implies that the effect of rotation on the local heat transfer of the coolant passage should be the same regardless of the Reynolds number. However, the results show that the Nusselt number ratio near the inlet of the channel on both the lending and trailing surfaces (i.e., $X/D<6$) decrease slightly with an increasing Reynolds number for a given rotation number. The reverse is true near the end of the channel on both the leading and trailing surfaces (i.e., $X/D>6$).

Effect of Uneven Wall Temperature. Figure 8 shows the effect of uneven wall temperature on the leading and trailing surface Nusselt number ratio for cases *A*, *B*, and *C*. Note that the test results for the nonrotating Nusselt number ratios on the leading and trailing surface for the three cases of surface heating conditions are about the same within 5 percent. Therefore, the nonrotating Nusselt number ratios are presented as

Downloaded 13 Dec 2010 to 193.140.21.150. Redistribution subject to ASME license or copyright; see http://www.asme.org/terms/Terms_Use.cfm

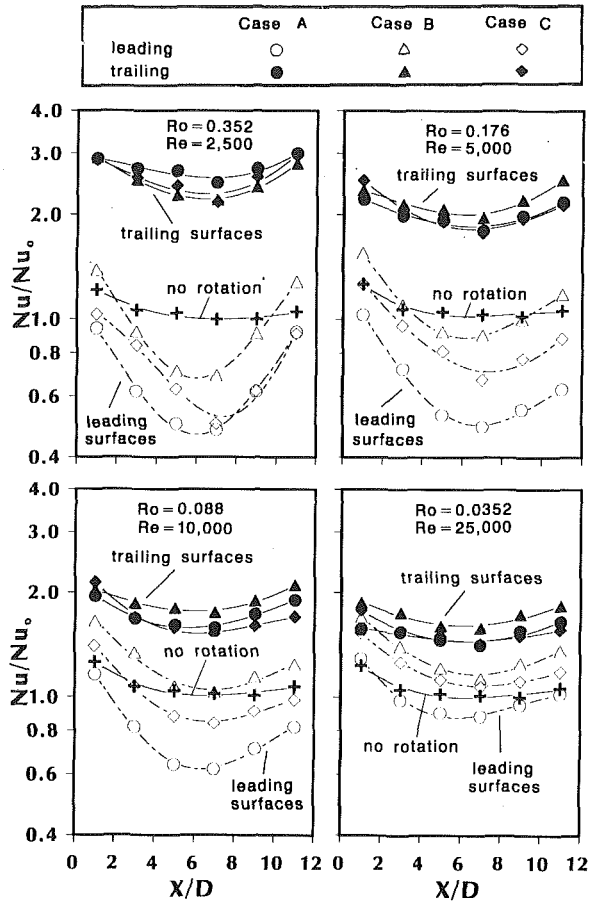

Fig. 8 Effect of surface heating condition on Nusselt number ratio variation for cases *A*, *B* and *C* at selected rotation and Reynolds numbers

a single curve and included in Fig. 8 for comparison (read legend +).

For case A of four walls uniform temperature (T_w = 60–65°C and $(\Delta\rho/\rho)_i = 0.1$), as previously discussed by Wagner et al. (1991a) and Han et al. (1992b), the difference of the heat transfer coefficients between the rotating and nonrotating conditions on the leading and trailing surfaces is attributed to both the increasing strength of the secondary cross-stream flow vortices due to the Coriolis force and the centrifugal buoyancy. The higher trailing surface heat transfer coefficients are because (1) the coolant impingement (due to rotation) on the trailing surface creates a thinner boundary layer, and (2) the coolant profile distortion (due to rotation) produces a stronger centrifugal buoyancy-induced wall turbulence near the destabilized trailing surface thin boundary layer. The decrease in heat transfer coefficients near the inlet of the channel on the leading surfaces is due to a thicker stabilized boundary layer, and the subsequent increase in heat transfer coefficients near the end of the channel is attributed to the stronger centrifugal buoyancy-induced, destabilized wall turbulence boundary layer. These are the typical combined effects of Coriolis and buoyancy forces due to rotation on the leading and trailing surfaces of a square channel with four walls uniform temperature and with radially outward flow.

For case B of four walls uniform heat flux, the results show that the trailing surface Nusselt number ratio is slightly higher than that of case A except for the one with the larger rotation number (Ro = 0.352). However, the results show that the leading surface Nusselt number ratio for case B is 20–80 percent higher than that of case A. For case C of leading and trailing hot but two side walls cold, the trailing surface heat transfer ratio is about the same as case A. Again, the leading surface heat transfer ratio for case C is 10–40 percent higher than case A for all studied rotation numbers.

For case B of four walls uniform heat flux (q'' = 1005, 1682, 2916, and 6172 W/m^2 for Ro = 0.352, 0.176, 0.088, and 0.0352, respectively), the trailing surface temperature (T_w = 50–55°C and $(\Delta\rho/\rho)_i = 0.07$) being lower than the leading (T_w = 60–65°C and $(\Delta\rho/\rho)_i = 0.1$) and side wall ($T_w$ = 55–60°C and $(\Delta\rho/\rho)_i = 0.08$) surface can result in more cooler fluid near the trailing surface. It is conjectured that this cooler fluid is accelerated due to centrifugal buoyancy and a thinner boundary layer (steeper velocity or temperature slope) is created near the trailing surface. Meanwhile, the secondary cross-stream flow carries the cooler fluid from trailing and side walls back to the leading surface due to the Coriolis force. This cooler fluid causes a steeper temperature profile (compared to case A of four walls uniform temperature) near the leading surface due to the centrifugal buoyancy force. Therefore, Fig. 8 shows that the trailing surface heat transfer coefficients for case B are slightly higher than case A and the leading surface heat transfer coefficients for case B are not as low as case A due to rotation. The difference in the heat transfer coefficients between the trailing and leading surface becomes smaller for case B. Similarly, for case C of hot trailing and leading surfaces (T_w = 60–65°C $(\Delta\rho/\rho)_i = 0.1$) but two cold side surfaces (T_w = 50°C and $(\Delta\rho/\rho)_i = 0.06$), the secondary cross-stream flow carries the cooler fluid from the side walls back to the leading surface due to rotation. Therefore, Fig. 8 shows that the trailing surface heat transfer coefficients for case C are slightly lower than case A and the leading surface heat transfer coefficients for case C are higher than case A.

Figure 2 sketches the conceptual view of the effects of inertia force (Reynolds number), Coriolis force (rotation number), bulk buoyancy force (for case A of uniform wall temperature), and local buoyancy force (for case B of uniform wall heat flux, i.e., uneven wall temperature) on the coolant flow or temperature profile, and the associated heat transfer coefficient. It is speculated that for case A of four walls uniform temperature, Coriolis force turns the coolant flow to the trailing surface and the bulk buoyancy force further keeps the coolant flow closer to the trailing surface. Therefore, the trailing surface heat transfer coefficient is much higher than the leading surface due to rotation. For case B (four walls uniform heat flux) of trailing colder than leading, however, the uneven wall temperature superimposed on the coolant flow profile creates cooler fluid near the trailing surface. Also the cross-stream moves this cooler fluid from trailing and side walls back to the leading surface and creates more centrifugal buoyancy effect (compared to case A) near the leading surface due to rotation. This implies that the uneven wall temperature (i.e., the unequal local buoyancy force) keeps the cooler fluid closer to both the trailing and leading surfaces and produces a greater velocity/temperature gradient (compared to case A) near both the trailing and leading surfaces, respectively. Therefore, the colder trailing surface and hotter leading surface eventually enhances the effect of rotation on the trailing, but reduces the effect of rotation on the leading heat transfer coefficients. Therefore, the trailing surface heat transfer coefficients for case B are slightly higher than case A and the leading surface heat transfer coefficients for case B are much higher than case A.

Correlating Data and Comparison With Previous Results As discussed above, the convective heat transfer coefficients on the leading and trailing surface of a rotating channel with radial outward flow can be affected by the Coriolis force (rotation number) and the surface heating condition (bulk or local buoyancy force). Figure 9 shows the variation of Nusselt number ratio with rotation number at selected axial locations for the three studied surface heating conditions. The experimental results from Wagner et al. (1991a) for the case of

Downloaded 13 Dec 2010 to 193.140.21.150. Redistribution subject to ASME license or copyright; see http://www.asme.org/terms/Terms_Use.cfm

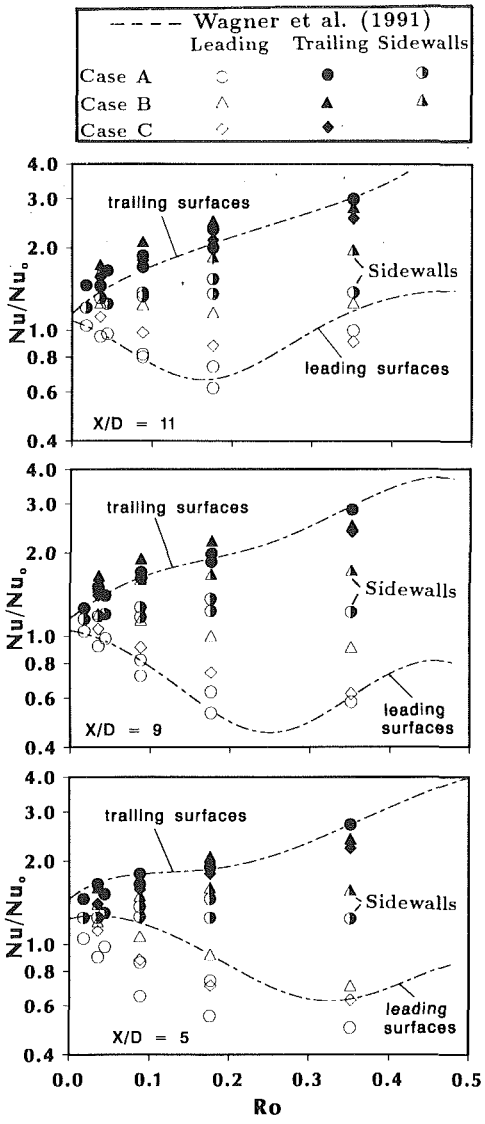

Fig. 9 Effect of rotation number on Nusselt number ratio variation at selected axial locations for cases *A*, *B*, and *C* and comparison with the previous results

uniform wall temperature are also included for comparison. Note that the Wagner et al. results are based on the following conditions and axial locations: Ro calculated at Re = 25,000 and varying rotational speed, $(\Delta\rho/\rho)_i = 0.13$, $\overline{R}/D = 49$, and $X/D = 4.7$, 8.5, and 12.4, respectively. The present data for the case of uniform wall temperature (case A) are based on: Ro calculated at Ω = 800 rpm and 400 rpm and varying Re between 2500 and 25,000, $(\Delta\rho/\rho)_i = 0.10$, $\overline{R}/D = 30$, and $X/D = 5$, 9, and 11, respectively. The results show that the present Nusselt number ratio on the trailing and leading surface for the case A of four walls uniform temperature (see Fig. 9, circular symbols) agrees with those of Wagner et al. except that $X/D = 5$. This confirms that the trailing surface Nusselt number ratio increases with an increasing rotation number, whereas the leading surface Nusselt number ratio decreases and then increases with an increasing rotation number for the case of uniform wall temperature condition. At $X/D = 5$, the leading surface Nusselt number ratios of this study are much lower than that of Wagner et al. The difference may be caused by the flow inlet condition used in each study: a fully developed flow entrance for this study versus a sharp developing flow entrance for Wagner et al. The fully developed flow profile with a thicker boundary layer can be more easily affected by the Coriolis force than the developing accelerating flow with a thinner boundary layer. The flow pattern at the test section entrance in the present study may have stronger cross-stream flow and thicker boundary layer on the leading surface. Therefore, the leading surface Nusselt number ratios of this study are much lower. Note that there are two sets of Ro for the case A of four walls uniform temperature in this study: (1) Ro = 0.0352, 0.088, 0.176, and 0.352 (based on Ω = 800 rpm and Re = 25,000, 10,000, 5,000 and 2500), and (2) Ro = 0.0176, 0.044, 0.088, and 0.176 (based on Ω = 400 rpm and Re = 25,000, 10,000, 5000, and 2500). It is interesting to see that the data generated from these two sets of Ro correlate to each other fairly well. This proves that the rotation number is indeed an important parameter in rotating heat transfer and can be obtained by using larger or smaller values of Ω and V.

As previously discussed, the uneven surface temperatures on both the leading and trailing surfaces create unequal local buoyancy forces that alter the heat transfer coefficients. Figure 9 shows that, as a result, the trailing surface Nusselt number ratios for case B are 10–20 percent higher than that for case A (except at Ro = 0.352), whereas the leading surface Nusselt number ratios for case B (triangular symbols) are 40–80 percent higher than that for case A. The trailing surface Nusselt number ratios for case C are about the same as case A, but the leading surface Nusselt number ratios for case C (diamond symbols) are 20–40 percent higher than that for case A. It is clear that the local buoyancy force interacts with the Coriolis force and enhances the effect of the rotation number on the trailing surface heat transfer coefficients but reduces the effect of the rotation number on the leading surface heat transfer coefficients. Figure 9 also shows that the heat transfer ratios from two side walls (see Fig. 4, side walls A and B) are about the same for case A for all X/D locations shown and about 20–30 percent higher than the nonrotating results (i.e., $\mathrm{Nu}/\mathrm{Nu}_o$ = 1.2–1.3). The results also show that the heat transfer ratios from two side walls are about the same for case B but about 20–50 percent higher than that for case A.

A buoyancy parameter $(\Delta\rho/\rho)(R/D)(\mathrm{Ro})^2$ was used by Wagner et al. (1991) to consider the combined effects of Coriolis and buoyancy forces on heat transfer. The buoyancy parameter includes the effects of axial coolant-to-wall density ratio ($\Delta\rho/\rho = (T_w - T_b)/T_w$, related to buoyancy force), secondary cross-stream flow (Coriolis force, R_o), and rotating radius to hydraulic diameter ratio (R/D, related to buoyancy force). Figure 10 shows the variation of the Nusselt number ratio with the buoyancy parameter at selected axial locations for the three studied surface heating conditions. The experimental results from Wagner et al. (1991) for the case of uniform wall temperature are also included for comparison. The shaded area shown in Fig. 10 represents the data from Wagner from two sets of mean rotating radius ($\overline{R}/D$ = 49 and 33) and Ro between 0.0 and 0.48. Note that the $\overline{R}/D$ ratio of the present study is 30 and R_o between 0.0 and 0.352. They indicated that the Nusselt number ratio variation for a given buoyancy parameter is primarily due to the range of studied rotation numbers. The results show that the present Nusselt number ratios on the trailing and leading surface for the case of uniform wall temperature (case A) are in the range of their data variation (except that the leading surface Nusselt number ratios are much lower at $X/D = 5$ as discussed above). Again, the results show that the effect of uneven surface temperature is (1) to increase the leading surface heat transfer coefficients for cases B and C at a given buoyancy parameter condition, (2) to increase the trailing surface heat transfer coefficients for case B except for the larger buoyancy parameter of 0.4 and for $X/D = 5$, and (3) to increase the side wall heat transfer coefficients for case B (compared to case A).

Figure 11 shows the variation of the channel-averaged Nusselt number ratio with rotation number for cases A, B, and C. The channel-averaged Nusselt number ($\overline{\mathrm{Nu}}$) on the leading

Downloaded 13 Dec 2010 to 193.140.21.150. Redistribution subject to ASME license or copyright; see http://www.asme.org/terms/Terms_Use.cfm

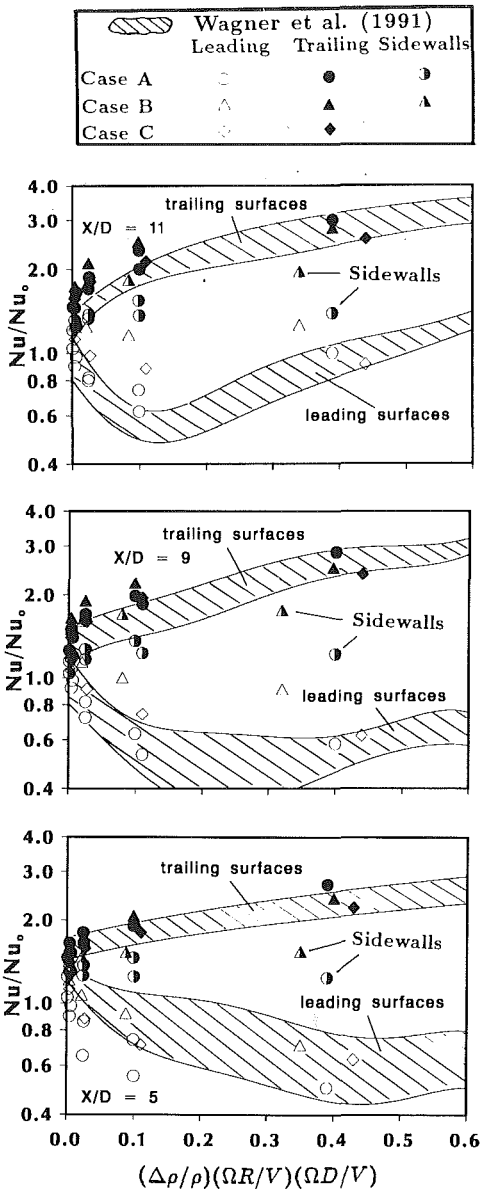

Fig. 10 Effect of buoyancy parameter on Nusselt number ratio variation at selected axial locations for cases *A*, *B*, and *C* and comparison with the previous results

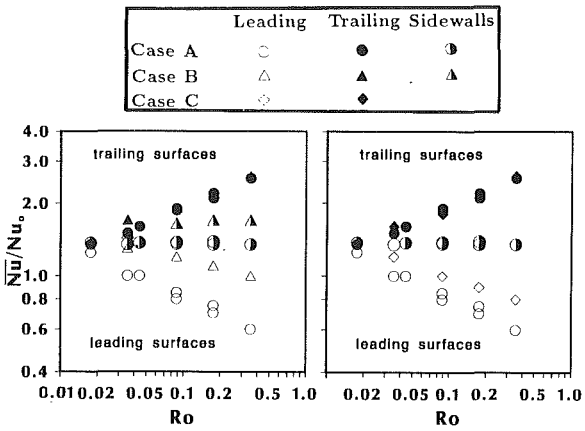

Fig. 11 Effect of rotation number on channel-averaged Nusselt number ratio variation for cases *A*, *B*, and *C*

surface (or trailing surface, side walls) is the average value of the entire leading surface (or trailing surface, side walls) local Nusselt number (Nu) from $X/D = 1$ to $X/D = 11$. Again, the data are from two sets of rotation numbers for case A: (1) Ro = 0.352, 0.176, 0.088, and 0.0352 (based on Ω = 800 rpm and Re = 2500, 5000, 10,000, and 25,000) and (2) Ro = 0.176, 0.088, 0.044, and 0.0176 (based on Ω = 400 rpm and Re = 2500, 5000, 10,000, and 25,000). The results show that for case A of uniform wall temperature, the channel-averaged Nusselt number ratio on the trailing surface increases from 1.3 to 2.5 when the rotation number changes from 0.0176 to 0.352, whereas the corresponding channel-averaged Nusselt number ratio on the leading surface decreases from 1.2 to 0.6, and the channel-average Nusselt number ratio from side walls are about the same equal to 1.2–1.3 over the range of rotation numbers studied. Again, the effect of uneven wall temperature is (1) to increase the leading surface average heat transfer coefficients for cases B and C (compared to case A) and (2) to increase the side wall heat transfer coefficients for case B (compared to case A).

Concluding Remarks

The influence of nonuniform wall temperature on the local heat transfer coefficients in a rotating square channel with smooth walls and radial outward flow has been studied for rotating numbers from 0.0 to 0.352 and Reynolds numbers from 2500 to 25,000. The main findings are:

1 The general trend of the effect of rotation on heat transfer is that the trailing surface Nusselt number ratio increases but the leading surface Nusselt number ratio decreases and then increases with increasing rotation numbers (or buoyancy parameters). The increased (or decreased) heat transfer coefficients on the trailing or leading surface are due to the cross-stream and centrifugal buoyancy-induced flows from rotation. The local trailing surface Nusselt number ratio can be as high as 2.5–3.0, whereas the local leading surface Nusselt number ratio can be as low as 0.4 for case A of four walls uniform temperature at $(\Delta\rho/\rho)_i = 0.10$ and Ro = 0.352. This confirms the previous investigators' results (Wagner et al., 1991a).

2 The uneven wall temperature for cases B and C creates unequal buoyancy forces between the leading and trailing surface. It is conjectured that the unequal local buoyancy forces are to keep the cooler fluid closer to both the leading and trailing surfaces and alter the effect of rotation on the local leading and trailing heat transfer coefficients compared to case A of four walls uniform temperature.

3 The trailing surface heat transfer coefficients for uneven surface temperature (case B) are slightly higher than those for uniform surface temperature (case A). The leading surface heat transfer coefficients for uneven surface temperature (cases B and C) are much higher than those for uniform surface temperature (case A). This implies that the difference between the leading and trailing heat transfer coefficient with uneven wall temperature becomes smaller compared to the uniform wall temperature case.

4 The trailing surface Nusselt number ratios for uniform wall heat flux (i.e., uneven surface temperature conditions (case B)) are 10–20 percent higher than those for uniform surface temperature (case A) at a given buoyancy parameter (or rotation number), whereas the leading surface Nusselt number ratios for cases B and C are 40–80 percent higher and 20–40 percent, respectively, than those for uniform surface temperature (case A) at a given buoyancy parameter (or rotation number).

5 The side wall Nusselt number ratios for case A are about 20–30 percent higher than the nonrotating results, whereas the side wall Nusselt number ratios for case B are about 20–50 percent higher than those for case A.

6 It should be noted that the present results are based on the rotating channel with a long length entrance and a low rotating radius to the channel diameter ratio ($\bar{R}/D = 30$).

Downloaded 13 Dec 2010 to 193.140.21.150. Redistribution subject to ASME license or copyright; see http://www.asme.org/terms/Terms_Use.cfm

However, in modern aircraft gas turbine engines, the typical coolant channel has a sharp entrance and a higher rotating radius to the channel diameter ratio.

Acknowledgments

The investigation was supported by the Texas Higher Education Coordinating Board (Energy Research in Application Programs, TEES 70730) and by the NASA Center for Space Power (RF2500020).

References

Boelter, L. M. K., Young, G., and Iverson, H. W., 1948, "An Investigation of Aircraft Heaters—Distribution of Heat Transfer Rate in the Entrance Section of a Circular Tube," NACA TN 1451, Washington, DC.

Clifford, R. J., Morris, W. D., and Harasgama, S. P., 1984, "An Experimental Study of Local and Mean Heat Transfer in a Triangular-Sectioned Duct Rotating in the Orthogonal Mode," ASME *Journal of Engineering for Gas Turbines and Power*, Vol. 106, pp. 661–667.

Guidez, J., 1989, "Study of the Convective Heat Transfer in Rotating Coolant Channels," ASME *Journal of Turbomachinery*, Vol. 111, pp. 43–50.

Han, J. C., 1984, "Heat Transfer and Friction in Channels With Two Opposite Rib-Roughened Walls," ASME JOURNAL OF HEAT TRANSFER, Vol. 106, pp. 774–781.

Han, J. C., 1988, "Heat Transfer and Friction Characteristics in Rectangular Channels With Rib Turbulators," ASME JOURNAL OF HEAT TRANSFER, Vol. 110, pp. 321–328.

Han, J. C., Zhang, Y. M., and Lee, C. P., 1992a, "Influence of Surface Heat Flux Ratio on Heat Transfer Augmentation in Square Channels With Parallel, Crossed, and V-Shaped Angled Ribs," ASME *Journal of Turbomachinery*, Vol. 114, No. 4, pp. 872–880.

Han, J. C., Zhang, Y. M., and Lee, C. P., 1992b, "Influence of Surface Heating Condition on Local Heat Transfer in a Rotating Square Channel With Smooth Walls and Radial Outward Flow," ASME Paper No. 92-GT-188, accepted for publication in the ASME *Journal of Turbomachinery*.

Harasgama, S. P., and Morris, W. D., 1988, "The Influence of Rotation on the Heat Transfer Characteristics of Circular, Triangular, and Square-Sectioned Coolant Passages of Gas Turbine Rotor Blades," ASME *Journal of Turbomachinery*, Vol. 110, pp. 44–50.

Johnston, J. P., Halleen, R. M., and Lezius, D. K., 1972, "Effects of Spanwise Rotation on the Structure of Two-Dimensional Fully Developed Turbulent Channel Flow," *Journal of Fluid Mechanics*, Vol. 56, Part 3, pp. 533–557.

Kline, S. J., and McClintock, F. A., 1953, "Describing Uncertainties in Single-Sample Experiments," *Mechanical Engineering*, Jan., pp. 3–8.

Mori, Y., Fukada, T., and Nakayama, W., 1971, "Convective Heat Transfer in a Rotating Radial Circular Pipe (2nd Report)," *International Journal of Heat and Mass Transfer*, Vol. 14, pp. 1807–1824.

Morris, W. D., Harasgama, S. P., and Salemi, R., 1988, "Measurements of Turbulent Heat Transfer on the Leading and Trailing Surfaces of a Square Duct Rotating About an Orthogonal Axis," ASME Paper No. 88-GT-114.

Morris, W. D., and Ghavami-Nasr, G., 1991, "Heat Transfer Measurements in Rectangular Channels with Orthogonal Mode Rotation," ASME *Journal of Turbomachinery*, Vol. 113, pp. 339–345.

Morris, W. D., and Salemi, R., 1991, "An Attempt to Experimentally Uncouple the Effect of Coriolis and Buoyancy Forces on Heat Transfer in Smooth Circular Tubes Which Rotate in the Orthogonal Mode," ASME Paper No. 91-FT-17.

Rohsenow, W. M., and Choi, H., 1961, *Heat, Mass and Momentum Transfer*, Prentice-Hall, New Jersey, pp. 192–193.

Taslim, M. E., Rahman, A., and Spring, S. D., 1991a, "An Experimental Investigation of Heat Transfer Coefficients in a Spanwise Rotating Channel With Two Opposite Rib-Roughened Walls," ASME *Journal of Turbomachinery*, Vol. 113, pp. 74–82.

Taslim, M. E., Bondi, L. A., and Kercher, D. M., 1991b, "An Experimental Investigation of Heat Transfer in an Orthogonally Rotating Channel Roughened With 45 deg Criss-Cross Ribs on Two Opposite Walls," ASME *Journal of Turbomachinery*, Vol. 113, pp. 346–353.

Wagner, J. H., Kim, J. C., and Johnson, B. V., 1986, "Rotating Heat Transfer Experiments With Turbine Airfoil Internal Passages," ASME Paper No. 86-GT-133.

Wagner, J. H., Johnson, B. V., and Hajek, T. J., 1991a, "Heat Transfer in Rotating Passages With Smooth Walls, and Radial Outward Flow," ASME *Journal of Turbomachinery*, Vol. 113, pp. 42–51.

Wagner, J. H., Johnson, B. V., and Kopper, F. C., 1991b, "Heat Transfer in Rotating Serpentine Passages With Smooth Walls," ASME *Journal of Turbomachinery*, Vol. 113, pp. 321–330.

Wagner, J. H., Johnson, B. V., Graziani, R. A., and Yeh, F. C., 1992, "Heat Transfer in Rotating Serpentine Passages With Trips Normal to the Flow," ASME *Journal of Turbomachinery*, Vol. 114, No. 4.

Downloaded 13 Dec 2010 to 193.140.21.150. Redistribution subject to ASME license or copyright; see http://www.asme.org/terms/Terms_Use.cfm

E. Y. Kwack
Member of Technical Staff.
Mem. ASME

P. Shakkottai
Member of Technical Staff.

T. S. Luchik
Member of Technical Staff.

K. M. Aaron
Member of Technical Staff.

G. Fabris
Member of Technical Staff.
Mem. ASME

L. H. Back
Group Supervisor.
Fellow ASME

Jet Propulsion Laboratory,
California Institute of Technology,
Pasadena, CA 91109

Hot Wire/Film Behavior in Low-Temperature Gases

Commercially available hot wires/films were used to measure the velocities of evaporated hydrogen or helium gas during cryogenic mixing experiments. Hot wires were found to be too delicate to use in this harsh environment. Hot films were rugged enough to use at cryogenic temperatures even though they failed after a number of thermal cycles. Since the hot films have small aspect ratios, 13.4 and 20, they are quite sensitive to the thermal loading, T_w/T_g, even with a correction for the conduction end loss. In general, although the increase of the Nusselt number with Reynolds number at low temperatures was similar to that at room temperature, there was also a pronounced variation with T_w/T_g over the large range of 1.2 to 12 investigated.

1 Introduction

In order to gain insight on the mixing processes resulting from an accidental spill of liquid oxygen (LO_2) into liquid hydrogen (LH_2), the Jet Propulsion Laboratory (JPL) has conducted inert cryogenic mixing experiments. The mixture properties are of great importance since these govern the explosive yield of the resulting detonation. In JPL's experiments, three combinations of fluids have been studied: (1) a jet of liquid nitrogen (LN_2) into a deep pool of liquid helium (LHe); (2) a jet of liquid oxygen (LO_2) into a pool of LHe; and (3) a jet of LN_2 into a pool of liquid hydrogen (LH_2). Results of these studies have been reported by Luchik et al. (1989, 1990a, 1990b, 1990c). In general the jet fluid impinges on the pool fluid, cools down as it penetrates the pool, and eventually freezes while the pool fluid boils at the mixing zone interface. The evaporating gas is also warmed slightly by the jet fluid.

One parameter of key importance in this mixing process is the rate of evaporation of the pool fluid. If the velocity and density (or temperature and pressure) of the gas are measured, the evaporation rate can be obtained. Measurements at a location where the gas is near the saturation temperature of the pool liquid, and at a location where the gas is significantly warmed ($T \geq 50$ K) have been made. Measurement at the location where the gas temperature was near the pool fluid saturation temperature was difficult because of the presence of frozen jet fluid particles carried by the gas. Although the latter measurement in the warmed gas is easier, it is also less accurate due to heat transfer effects in this unsteady process. Both of these measurements have been made using hot wires/films and thermocouples or cryodiodes at the mouth of the dewar and in the stack of the primary enclosure, which is mainly an exhaust for the fuel or the simulant boiled off during a mixing experiment.

Hot wires/films have been widely used for velocity measurements in fluid flow. The use and applications of hot wire/film anemometers have been well reviewed in the literature (e.g., Hinze, 1975; Perry, 1982; Fingerson and Freymuth, 1983). If the hot wires/films are carefully calibrated, velocity measurements are highly precise and accurate. Since the temperatures of the gaseous fuel or simulant vary from their boiling points to room temperature during the mixing experiments, hot wires/films require calibration over a large temperature range. As may be expected, numerous measurements have been made for air (e.g., Andrews et al., 1972). However, there are only a few measurements reported in the literature for other gases, especially for hydrogen gas, and still fewer at low temperatures.

In this investigation, several different types of cylindrical hot wires/films manufactured by TSI were used for various gases such as hydrogen, helium, and nitrogen over a wide range of temperatures from 30 to 300 K. The general behavior of hot wires/films was investigated at low temperatures. Since hot films have very small aspect ratios (13.4 and 20) and gas temperature varied from room temperature to 30 K, thermal loading effects were also examined.

2 Experimental Setup Procedure

2.1 Flow System and Experimental Procedures. The hot films/wires were calibrated for hydrogen and helium at various temperatures, since they would experience thermal as well as velocity transients during a cryogenic mixing experiment. This was accomplished by using a calibration chamber constructed of aluminum in conjunction with a bridge circuit as shown in Fig. 1. A portion of the test gas supplied from K-bottles passed through a cooling coil submerged in liquid nitrogen (the first cooler in Fig. 1), the portion depending on the bypass valve setting. The test gas can be chilled down to 95 K by the first cooler. For calibration below 100 K, a second cooling coil,

Contributed by the Heat Transfer Division for publication in the JOURNAL OF HEAT TRANSFER. Manuscript received by the Heat Transfer Division March 1991; revision received June 1992. Keywords: Cryogenics, Forced Convection, Instrumentation. Associate Technical Editor: J. H. Kim.

Copyright © 1992 by ASME
Downloaded 13 Dec 2010 to 193.140.21.150. Redistribution subject to ASME license or copyright; see http://www.asme.org/terms/Terms_Use.cfm

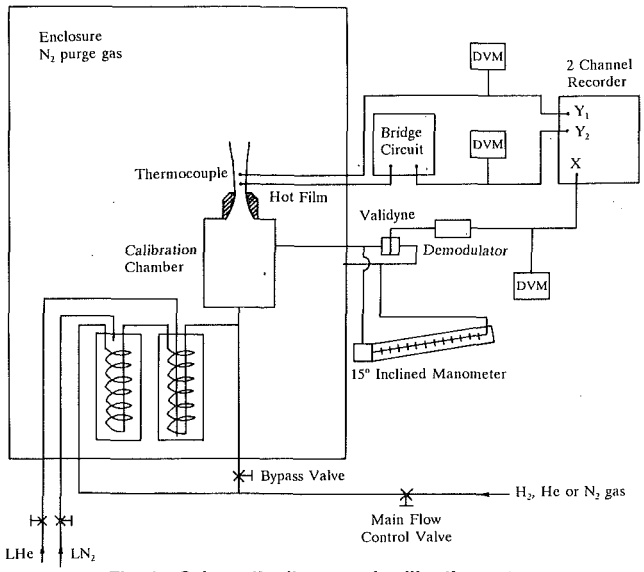

Fig. 1 Schematic diagram of calibration setup

located downstream of the first liquid nitrogen cooler, was submerged in liquid helium. In this case, the test gas can be chilled down to about 30 K. Since hot films were planned to be calibrated in hydrogen gas, the calibration chamber and the coolers were located in an enclosure used for the cryogenic mixing experiments (Luchik et al., 1989) and the enclosure was purged with nitrogen gas because of safety considerations. Nitrogen purge gas also prevents the formation of ice around the cold test gas jet. However, solid nitrogen forms around a hydrogen or helium jet when the jet temperature is below 40 K. When the cold gas flow is shut off, solid nitrogen melts and evaporates very rapidly.

The chilled test gas then entered the calibration chamber (10.2 cm i.d. and 10.2 cm long), which has flow straighteners (porous metal sponge, screen, and metal honeycomb) and exited through a small nozzle. The sizes of nozzle used in the measurements were 0.635 and 1.27 cm i.d. depending on the size of the hot film and on the range of velocity of interest. A hot film/wire was located in the center of the jet about 0.5 cm from the nozzle exit. The temperature of the test gas was measured in the jet with a type-E thermocouple, which had a 76.2 μm size junction. The output signals of the bridge circuit and thermocouple were fed into the y axis of a two-channel plotter. The static pressure difference between the calibration chamber and the jet (which is the same as the pressure in the enclosure) was measured using validyne pressure transducers. The pressure transducers were calibrated using a 15 deg inclined water manometer located outside the enclosure to minimize the zero shift due to temperature changes in the enclosure. The temperature inside the enclosure can be very low because of the vaporized cold cryogen. A tygon tube was used for transmitting the pressure from the calibration chamber to the pressure transducer to reduce heat conduction. The pressure signal was fed to the x axis of the two-channel plotter. The static pressure difference was used to calculate the velocity by using the Bernoulli equation. The physical properties of gases including density and viscosity was obtained from McCarty et al. (1981) and Sychev et al. (1987a, 1987b).

Initial efforts were made to obtain the hot film/wire results at various temperatures controlled by a suitable setting of the bypass valve. After a steady jet flow was established, the data were collected using digital volt meters, and then the jet velocity was varied by the main flow control valve. It was observed that the bypass valve needed to be adjusted to keep the temperature in the jet constant when the jet velocities changed. This technique proved to be very time consuming. Alternatively, the temperature of the test gas was allowed to change during the rather rapid closing of the main flow control valve to reduce the jet velocity down to zero, which usually took one minute. During this process, the outputs of the bridge circuit and the thermocouple were plotted on the x-y_1 y_2 recorder versus output of the pressure transducer. After the lowest gas temperature was obtained, data were collected and the cryogens for each cooler were shut off. Then, the test gas

Nomenclature

A = cross-sectional area, m^2
C_o = defined in Eq. (5)
c_p = specific heat at constant pressure, J/kgK
d = diameter of wire/film, m
D_o = defined in Eq. (6)
h = heat transfer coefficient, W/m^2K
I = current, amp
k_g = thermal conductivity of gas, w/mK
k_w = thermal conductivity of hot wire/film, w/mK
Kn = Knudsen number $= \lambda/d$
l = length of heat transfer section of wire/film, m
M = Mach number
Nu = Nusselt number $= hd/k_g$
P_g = heat generation in wire/film, w
Pr = Prandtl number $= \mu c_p/k_g$
q = power law exponent in Eq. (9)
r = recovery factor $= (T_{aw}-T_g)/(T_t-T_g)$
R = electric resistance of hot wire/film
Re = Reynolds number $= \rho u d/\mu$
s = power law exponent in Eq. (9)
T = temperature, K
T_{aw} = adiabatic wall temperature $= T_g + ru^2/2c_p$, K
T_t = total temperature $= T_g + u^2/2c_p$, K
u = velocity of gas, m/s
x = axial coordinate of wire/film, m
α = accommodation coefficient, Eq. (11)
α_ρ = thermal coefficient of electrical resistance of wire/film $= (R_{100}-R_0)/100KR_0$, K^{-1}
γ = specific heat ratio
Δ = temperature jump distance, m
ϵ = total energy for a molecule, J
θ = $T-T_g$, K
θ' = ratio of the temperature jump distance to the mean free path of a molecule
λ = mean free path of a molecule, m
μ = viscosity of gas
ρ = density of gas, kg/m^3
ρ_{rg} = electrical resistance of wire/film per unit length at $T=T_g$, ohm/m
ρ_{ro} = electrical resistance of wire/film per unit length at $T=0°C$, ohm/m
ϕ = Eq. (9)

Subscripts

c = accommodation
f = film
g = gas
i = incident
m = measured
min = minimum
r = reflected
w = wall or fully equibrated
∞ = infinite

Downloaded 13 Dec 2010 to 193.140.21.150. Redistribution subject to ASME license or copyright; see http://www.asme.org/terms/Terms_Use.cfm

slowly warmed up. When the test gas temperature reached the next intended temperature, data were collected as before in a one minute scan during the closing of the flow control valve. Temperature changes during data collection depended on the test gas temperature. During a run, more temperature changes were observed for a colder test gas, but normally the temperature changes were less than 5 K. Some data were also collected during the cool-down period. In this case, the temperature changes during data collection were larger, and the maximum variation was about 10 K.

2.2 Hot Wires/Films. Several different types of hot films/wires manufactured by TSI were used in the cryogenic mixing experiments. Initially, a hot wire (TSI 1210-T1.5) was used in the warmer ($T \geq 50$ K), milder location (stack) for quick response while a wedge-type film (TSI 1233) was located in the harsh particulate-laden region near the mixing zone (mouth of the dewar) since it is rugged. However, the hot wire proved to be too delicate in most cases and the wedge probe, although structurally more rigid than the cylindrical films, could not respond fast enough to the temperature changes during the experiments due to the high thermal capacitance of the film substrate (Nelson and Borgos, 1983). Therefore, cylindrical hot films (TSI 1211-10, 1211-20, and 1210-60) were used in the experiments. Although the hot films themselves have proven to be robust at low temperatures ($T < 100$ K), the junction between the film and the support does break down after repeated thermal cycling, rendering the film useless.

In this paper, only the results of the hot wires and the cylindrical hot films will be discussed. Even though the hot wires were too delicate for the current application, they could be used in low-temperature gas flow without particles so that the hot-wire results were included. Table 1 summarizes the dimensional data, the operating temperature of the wires/films (assuming uniform temperature along the entire length of the wires/films), thermal coefficient of electrical resistance α_ρ, and thermal conductivity at the operating temperature. The thermal coefficient of electrical resistance was calculated from TSI calibrations of the wire/film resistance at the melting and boiling points of water. The hot wire TSI 1210-T1.5 is made of tungsten, which is coated with a very thin layer of platinum to minimize surface oxidation. Since the layer of platinum is extremely thin and the thermal conductivity of platinum is the same order of magnitude as tungsten, the thermal conductivity of the wire was estimated using the properties of tungsten. The cylindrical hot films are manufactured by depositing a thin film of platinum onto a cylindrical quartz substrate and the probes are overcoated with a protective layer of alumina. The exact thicknesses of the substrate and coatings of these hot films are difficult to measure and are expected to vary from probe to probe. Pitts and McCaffrey (1986) assumed the thicknesses of platinum and protective alumina to be 0.1 and 0.8 μm, respectively, for TSI 1211-20 after consulting with TSI. The same assumptions were made for the present work. The thermal conductivities of platinum, tungsten, and quartz were obtained from the *Thermophysical Properties of Matter*, TPRC Data Series (Touloukian et al., 1970a, 1970b).

2.3 Data Treatment. The heat generation P_g, in a hot wire/film was estimated from the observed voltage drop across the bridge circuit, while the velocities of the gas were calculated using measured values of pressure drop and temperature. The Reynolds number and measured Nusselt number, Nu_m, were calculated as

$$\mathrm{Re} = \rho u d/\mu, \tag{1}$$

$$\mathrm{Nu}_m = hd/k_g = P_g/[\pi k_g l(T_w - T_g)] \tag{2}$$

where all the gas properties were taken at the "film" temperature, T_f, which is the arithmetic mean of the wall and gas temperatures. Since the aspect ratios of the hot films are not very large, the heat transfer coefficients were corrected for end-loss effects to obtain Nu_∞, which has been discussed in the literature (Hinze, 1975; Koch and Gartshore, 1972; Fingerson and Freymuth, 1983; Pitts and McCaffrey, 1986). The heat loss by conduction at the ends of the sensing area to the pronged support (end loss) was estimated from the temperature profile in the hot film obtained by solving the following differential equation with the assumptions that the temperature at both ends of the sensing area is the same as the gas temperature, the thermal conductivity of the hot film is independent of temperature, the radial temperature variation is negligible, and the heat transfer coefficient is invariable along the film;

$$\begin{aligned} d^2\theta/dx^2 - C_o\theta + D_o &= 0 \\ \theta &= 0 \quad \text{at} \quad x = \pm l/2 \\ d\theta/d_x &= 0 \quad \text{at} \quad x = 0 \end{aligned} \tag{3}$$

where

$$\theta = T - T_g \tag{4}$$

$$C_o = \pi dh/Ak_w - I^2\rho_{ro}\alpha_\rho/Ak_w \tag{5}$$

$$D_o = I^2\rho_{rg}/Ak_w \tag{6}$$

The same derivations are shown in Pitts and McCaffrey's paper (1986). However, an error appears in D_o where $\rho_r(0)$, which is the same as ρ_{ro} in the current paper, should be ρ_{rg}. The integration of solution of Eq. (3) yields the mean wall temperature along the probe

$$\bar{\theta} = T_w - T_g = D_o[1 - 2\tanh(lC_o^{1/2}/2)/lC_o^{1/2}]/C_o \tag{7}$$

Since the values of T_w, T_g, and D_o were known, C_o was calculated using a numerical method (Newton's method). From Eq. (5), the heat transfer coefficient, h_∞ was calculated and then Nu_∞ was calculated. Clearly the boundary condition $\theta = 0$ at $x = \pm l/2$ is an approximation, and the actual temperature at the end of the sensing area does exceed the gas temperature, more so for smaller l/d ratios. Therefore, calculated end losses are expected to exceed the actual values since the temperature gradient is somewhat smaller at the ends for the actual case.

Since the hot wire is very thin (3.8 μm), the Nusselt number was also corrected for thermal slip or noncontinuum effects. Andrews et al. (1972) showed that for an ideal gas, the Nusselt number (Nu_c) for the gas, in the absence of rarefied effects, could be related by

$$\mathrm{Nu}_c = \mathrm{Nu}_\infty/(1 - \phi \mathrm{Kn}\mathrm{Nu}_\infty) \tag{8}$$

where

$$\phi = \theta'[(2T_w/T_g)/(1 + T_w/T_g)]^{0.5+s-q} \tag{9}$$

and θ' is the ratio of the temperature jump distance, Δ, to the mean free path of a molecule, λ. The temperature jump distance can be expressed (Kennard, 1938) by

$$\Delta = ((2-\alpha)/\alpha)(2\gamma/(\gamma+1))\lambda/\mathrm{Pr} \tag{10}$$

where α is the accommodation coefficient, defined as

$$\alpha = (\epsilon_i - \epsilon_r)/(\epsilon_i - \epsilon_w) \tag{11}$$

where ϵ is the total energy for a molecule and the subscripts i, r, and w refer to incident, reflected, and fully equilibrated values at the sensor wall temperature, respectively. Since α is sensitive to the surface condition of the sensor and is very

Table 1 Hot wires/films

Type	Model	d,μm	ℓ,cm	ℓ/d	T_w, K	α_ρ, K^{-1}	k_w, w/mK
wire	TSI 1210-T1.5	3.81	0.125	333	373.5	0.00379	166
film	TSI 1211-10	25.4	0.0508	20	375.1	0.00211	5.81
film	TSI 1211-20	50.8	0.102	20	354.1 414.5	0.00248 0.00237	3.78 3.55
film	TSI 1210-60	152.	0.203	13.4	190.6	0.00239	2.51

Downloaded 13 Dec 2010 to 193.140.21.150. Redistribution subject to ASME license or copyright; see http://www.asme.org/terms/Terms_Use.cfm

Table 2 Estimation of endloss and noncontinuum effects

	$d\mu m$	ℓ/d	T_∞ K	k_∞ w/mk	Gas	T_g K	u m/s	Re	$\frac{h_\infty}{h}$	$\frac{h_c}{h_\infty}$	$\frac{h_c}{h}$
TSI 1210-60	152	13.4	190.6	2.51	H_2	110	10	50	0.837	1.004	0.840
						110	33	166	0.875	1.005	0.879
						29	5	43	0.826	1.002	0.828
						29	12	98	0.860	1.003	0.863
TSI 1211-20	50.8	20	354.1	3.78	H_2	242	15	7	0.866	1.009	0.874
						242	56	24	0.894	1.015	0.907
						47	7	5	0.877	1.007	0.883
						47	19	15	0.902	1.010	0.911
TSI 1211-10	25.4	20	375.1	5.81	H_2	290	48	10	0.852	1.029	0.877
						290	208	45	0.887	1.051	0.932
						120	31	10	0.843	1.019	0.859
						120	131	45	0.885	1.034	0.915
TSI 1210-T1.5	3.81	333	373.5	166	He	197	11	0.4	0.904	1.068	0.965
						197	76	2.6	0.925	1.113	1.030
						127	13.6	0.55	0.915	1.065	0.974
						127	91.3	3.86	0.940	1.118	1.051

difficult to measure, the value of α used in this paper is assumed to be 1. The values of s and q in Eq. (9) are the power law exponents, where viscosity and thermal conductivity of the gas are proportional to the absolute temperature T_w raised to the powers s and q, respectively. The values of s were 0.68–0.69 for H_2 and N_2, and 0.77 for He gas. The values of q were 0.68 for N_2, 0.80 for He and 0.78–0.93 for H_2 gas. The Knudsen number Kn was estimated at T_f.

An indication of the magnitude of the end-loss and noncontinuum effects is shown in Table 2, in particular for the hot films of various sizes in hydrogen, and the hot wire in helium over a range of gas temperatures, velocities, and Reynolds numbers. The heat transfer coefficient ratio, h_∞/h, gives the reduction due to heat loss to the film supports, and the ratio, h_c/h_∞, the increase due to noncontinuum effects. The last column in Table 2 gives the ratio h_c/h, which is the net correction to the data, i.e., the product, $(h_\infty/h)\ (h_c/h_\infty)$.

The maximum heat transfer rates by radiation and by natural convection were estimated to be 0.02 and 0.01 percent of the heat transfer rate by forced convection so that they were neglected in the current estimations. The maximum possible error in temperature measurements were less than ± 1.8 K at a gas temperature $T_g = 29$ K and ±0.4 K at $T_g = 290$ K. The actual temperature difference for heat transfer is $T_w - T_{aw}$, instead of $T_w - T_g$, which is used. T_{aw} is the adiabatic wall temperature. T_{aw} is higher than T_g by 1.25 K at the highest gas velocity of 208 m/s (M = 0.16, H_2 gas at 290 K), whereas the difference, $T_{aw} - T_g$, is only 10^{-3} K at the H_2 gas velocity of 5 m/s at $T_g = 29$ K (M = 0.011). In these calculations a recovery factor r of 0.84 was used. Based on these temperature errors, including uncertainty in the bridge output measurements, the maximum percent error in the estimation of heat transfer coefficients occurred in the case of H_2 gas at 290 K and Re = 45. The error was ± 1.9 percent. However, the errors were from ± 0.3 to ± 0.5 percent for most cases. Errors in velocity estimation vary from ± 0.04 to 1.1 percent depending on Reynolds number.

3 Results

Room temperature results for the TSI 1210-10 hot film with $T_w = 375.1$ K in nitrogen, hydrogen, and helium are shown in Fig. 2. The Nusselt number Nu_c of nitrogen gas increases linearly with increase of flow rate or Reynolds number in the log-log plot and has a slope of 0.45 up to a Reynolds number of about 40. Beyond this Reynolds number, the Nusselt number again increases linearly but with a higher slope of 0.52. These values of slope were obtained using curve fitting with 99 percent confidence and the change of slope can also be seen by plotting Nu_c versus $Re^{0.45}$ (not shown here). Presumably, eddies shed from the rear of the hot film at Reynolds number of about 40 and the change in the velocity distribution, which occurs abruptly, gives rise to the change in slope. The detailed measurements by Collis and Williams (1959) show that eddy shedding occurs at a Reynolds number of 44. The slopes reported by Collis and Williams were 0.45 and 0.51 before and after eddy shedding occurs.

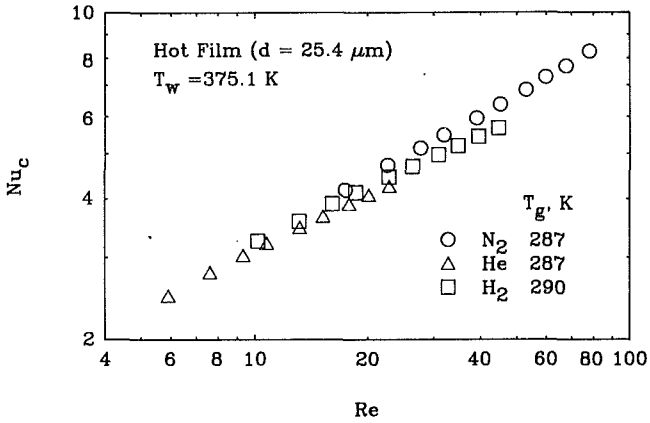

Fig. 2 Experimental data of a hot film (TSI 1211-10) for N_2, H_2, and He gases at room temperature

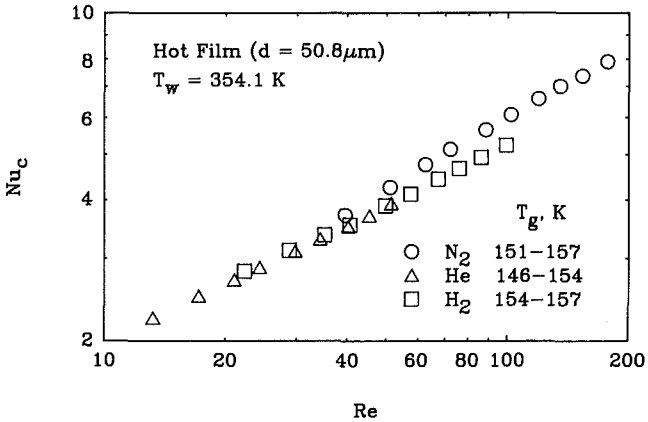

Fig. 3 Experimental data of a hot film (TSI 1211-20) for N_2, H_2, and He gases at $T_g = 146$–157 K

Nusselt numbers for hydrogen and helium gases are somewhat lower than those for nitrogen gas in the measured Reynolds number range (Fig. 2). Since the molecular weights of hydrogen and helium gas are very small, these differences may be due to accommodation effects (Kennard, 1938; Pitts and McCaffrey, 1986). A value of $\alpha = 1$ was assumed. All the data except one point for hydrogen gas were taken before eddy shedding occurs. The average slopes for helium and hydrogen gases are 0.39 and 0.38, respectively, which are lower than that of nitrogen gas, 0.45. The slope for helium gas is close to the value given by Pitts and McCaffrey (1986) even though the range of Reynolds number of the current data (6 to 23) is higher than that of the results of Pitts and McCaffrey (1 to 2.5).

In general, similar behavior was observed at low temperatures. Figure 3 shows the experimental results for the three different gases at low temperatures near 150 K. The hot film used was TSI 1211-20 with $T_w = 354.1$ K. The slope for nitrogen gas is 0.51, which is the same as the value obtained by Collis and Williams (1959). One point at a Reynolds number of 39.4 was not included to estimate the slope. Eddy shedding occurs at a Reynolds number of about 40 for hydrogen gas, which is the same as for nitrogen gas. The slope increases from 0.38 to 0.43 after eddy shedding occurs. It is interesting to note that the percentage increase of slope for hydrogen gas is the same as that of nitrogen gas, about a 13 percent increase for both gases.

Downloaded 13 Dec 2010 to 193.140.21.150. Redistribution subject to ASME license or copyright; see http://www.asme.org/terms/Terms_Use.cfm

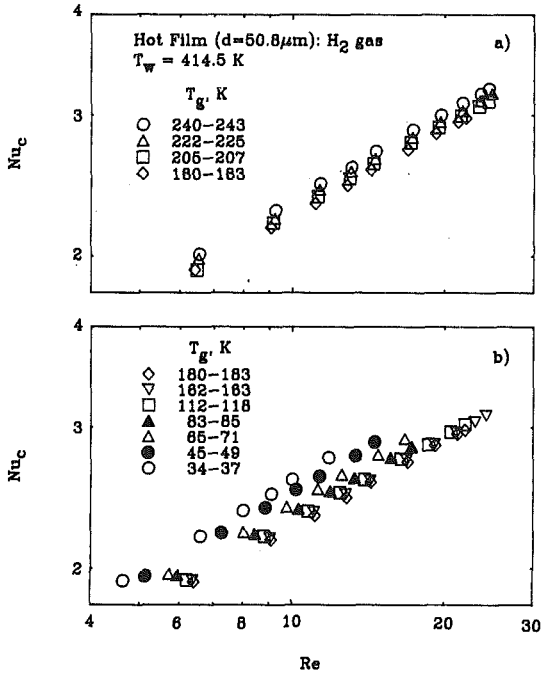

Fig. 4 Experimental data of a hot film (TSI 1211-20) for H_2 gas at various gas temperatures (T_g = 34–243 K)

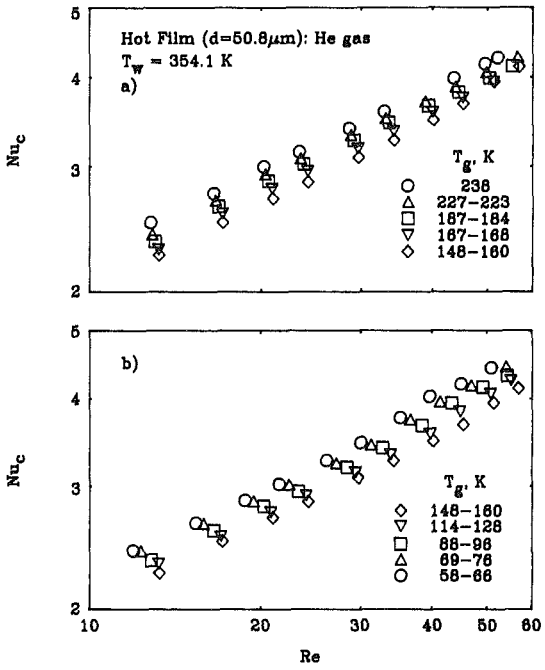

Fig. 5 Experimental data of a hot film (TSI 1211-20) for He gas at various gas temperatures (T_g = 58–238 K)

Figure 4 shows the experimental results for hydrogen gas over a wide range of temperatures. A hot film TSI 1211-20 was used and the operating temperature of the film was 414.5 K. The hydrogen gas temperature was varied from 34 to 243 K. As the gas temperature decreases down to 180 K, Nu_c gradually decreases and reaches a minimum (Fig. 4*a*). As the gas temperature decreases further, Nu_c increases at a fixed Re (Fig. 4*b*). For comparison, the results for gas temperatures of 180 to 183 K are shown in both Figs. 4(*a*) and 4(*b*) using the same symbols. The slope of the Nu_c–Re relation remains constant and seems to increase slightly at very low temperatures. The thermal loading, T_w/T_g, was varied from 1.7 to 2.3 in Fig.

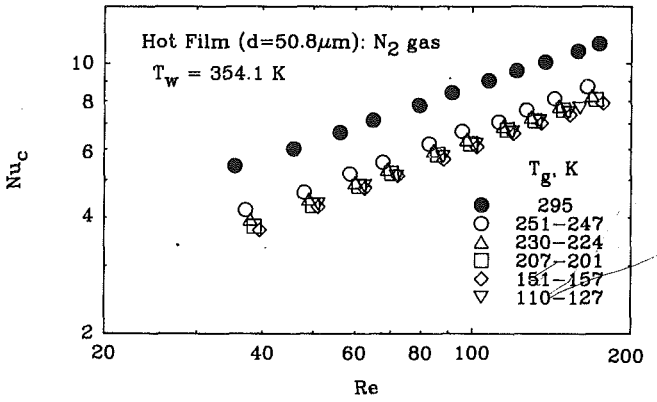

Fig. 6 Experimental data of a hot film (TSI 1211-20) for N_2 gas at various gas temperatures (T_g = 110–295 K)

4(*a*) and from 2.3 to 12.2 in Fig. 4(*b*). Nu_c reaches the minimum values at the thermal loading, $T_w/T_g \simeq 2.3$. This thermal loading effect may be attributable to the small aspect ratio, even though the conduction end loss was corrected. It will be discussed later.

Similar behavior was observed for helium and nitrogen gases. Figure 5 shows Nu_c versus Re for the helium gas in the temperature range from 58 to 238 K. The hot film was the same type as in Fig. 4 (TSI 1211-20), but the wall temperature was 354.1 K. Again, Nu_c initially decreases with decrease of the helium gas temperature, reaches minimum values at a gas temperature of about 154 K (Fig. 5*a*) and increases with a further decrease of the gas temperature (Fig. 5*b*). When Nu_c reaches the minimum, the value of the thermal loading is again about 2.3, the same as the value for hydrogen gas. Nitrogen gas was tested using the same hot film with the same wall temperature as used for helium gas. The results are shown in Fig. 6. Since only the first cooler (liquid nitrogen bath) was used, the minimum temperature of the test gas was 110 K. The minimum values of Nu_c were attained at a temperature near 150 K (T_w/T_g = 2.3). Nu_c seems to be higher at T_g = 110–127 K than the minimum near 150 K.

This thermal loading effect was confirmed by the results of other sizes of hot films (TSI 1211-10 and TSI 1210-60), especially, the TSI 1210-60 hot film tested in hydrogen gas flow at a low operating temperature, 190.6 K. As shown in Fig. 7, Nu_c reaches the minimum values at 80 K, which corresponds to the thermal loading value of 2.4.

To understand the temperature loading effects, Nu_c was normalized by the minimum value of Nu_c, $Nu_{c,min}$, which was estimated based on the measurements, and was plotted versus the thermal loading, T_w/T_g. Figure 8 shows these results for hydrogen gas. The values of Nu_c and gas temperature are plotted at a fixed Reynolds number, which was in the middle of the experimental range. The normalized Nu_c decreases sharply with increase of the thermal loading, reaches a minimum at T_w/T_g = 2.3, and gradually increases. The measured maximum value of the thermal loading was 12.2 for hydrogen gas. The effects of the wall temperature and the aspect ratio of the hot films on this relationship seem negligible in the measured ranges, 191 K < T_w < 414.5 K and 13.4 < l/d < 20. In addition, the same relationship is observed after eddy shedding occurs (for example, data points at Re = 75 and 100 in Fig. 8).

The same relation (curve) seems to be applicable for the results of helium and nitrogen gases with the same hot films. In Fig. 9, the results for helium gas are shown. The solid line represents the results for hydrogen gas from Fig. 8. The two data points at T_w/T_g = 6 are somewhat higher, but the overall results for helium gas with hot films are very close to those of

Downloaded 13 Dec 2010 to 193.140.21.150. Redistribution subject to ASME license or copyright; see http://www.asme.org/terms/Terms_Use.cfm

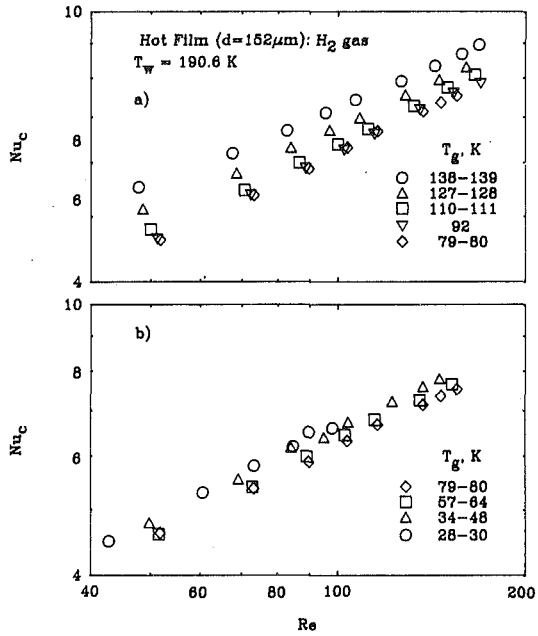

Fig. 7 Experimental data of a hot film (TSI 1210-60) for H_2 gas at various gas temperatures ($T_g = 28$–139K)

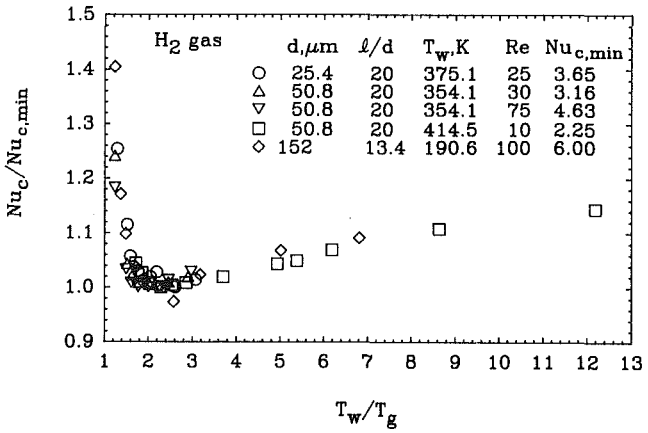

Fig. 8 Dimensionless Nu_c versus T_w/T_g for H_2 gas

hydrogen. The results for nitrogen gas also agree well with those of hydrogen and helium gases (not shown). However, the nitrogen data are limited to values of T_w/T_g below 3.6.

If $(T_f/T_g)^m$ is used to correlate the thermal loading effects as Collis and Williams (1959) did, i.e., $Nu_m(T_f/T_g)^m = f(Re)$, the value of m is positive for the thermal loading up to 2.3 and becomes negative when the thermal loading is larger then 2.3 for the present results. Koch and Gartshore (1972) also obtained a positive value of 0.67 for m for the thermal loading range up to about 1.9. They used a 5 μm hot wire having an aspect ratio of 230 with air at ambient temperature. They did not correct the results for conduction endloss. However, Collis and Williams suggested a negative value, $m = -0.17$, for the thermal loading from 1.1 to 2.0. They used hot wires having large values of l/d from 2950 to 8660 without correction for conduction end loss. Koch and Gartshore compared their results with those of Collis and Williams and found that this difference was attributable to aspect ratio effects. The thermal loading effect seems to be smaller for a hot wire with a large aspect ratio, 333. The present results with the hot wire were corrected for conduction end loss, and only vary within ± 3 percent when T_w/T_g changes from 1.7 to 3.0 (Fig. 9). More measurements for a wide range of T_w/T_g are required to confirm the smaller thermal loading effects at the larger aspect ratio. Of note is that the radial temperature variation in the hot films was neglected, which may be worthwhile to investigate subsequently.

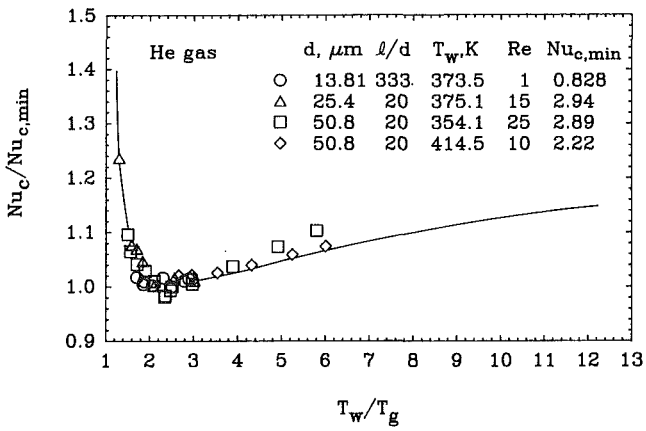

Fig. 9 Dimensionless Nu_c versus T_w/T_g for He gas

4 Concluding Remarks

Commercially available hot wires/films were used to measure the rate of evaporation of the pool fluid (LHe or LH_2) during mixing with a jet fluid (LN_2 or LO_2). Hot wires are found to be too delicate to use in this kind of harsh environment. Cylindrical hot films have quite fast time response and are rugged enough to use at cyrogenic temperatures even though the epoxy that affixes the film to the film support does break down after repeated thermal cycling. Since they have short aspect ratios, 13.4 and 20, they are quite sensitive to the thermal loading, T_w/T_g. In general, Nu_c decreases with increase of T_w/T_g up to about 2.3 and increases with further increase of T_w/T_g. However, cylindrical hot films provide quite accurate measurements of the velocity of the evaporated gas. The velocity of the gas was estimated using the following simple relation:

$$u = [C_1 + C_2 E^2/(T_w - T_g)^a]^b \quad (12)$$

over the range of T_w/T_g from 2.3 to 12 where E is the anemometer output in volts. The values of C_1, C_2, a, and b for each hot film were determined by nonlinear curve fitting with calibration data. The total amounts of LHe boil-off during the mixing tests were calculated by integrating the evaporation rate over the duration of the experiments. These integrated values were then compared to displacement measurements of liquid helium inside the dewar. The results reported in a recent paper (Luchik et al., 1990b) agree well, having a mean deviation of ± 4 percent. The amounts of He boil-off during the mixing tests were from 199 to 948 g.

Acknowledgments

The work described in this paper was carried out in the Applied Mechanics Technologies Section of the Jet Propulsion Laboratory, California Institute of Technology, under a contract with the National Aeronautics and Space Administration.

References

Andrews, G. E., Bradley, D., and Hundy, G. F., 1972, "Hot Wire Anemometry Calibrations for Measurements of Small Gas Velocities," *Int. J. Heat Mass Transfer*, Vol. 15, pp. 1765–1786.

Collis, D. C., and Williams, M. J., 1959, "Two-Dimensional Convection From Heated Wires at Low Reynolds Numbers," *J. Fluid Mech.*, Vol. 6, pp. 357–384.

Fingerson, L. M., and Freymuth, P., 1983, "Thermal Anemometers," in: *Fluid Mechanics Measurements*, R. J. Goldstein, ed., McGraw-Hill, New York, pp. 579–596.

Downloaded 13 Dec 2010 to 193.140.21.150. Redistribution subject to ASME license or copyright; see http://www.asme.org/terms/Terms_Use.cfm

Hinze, J. O., 1975, *Turbulence*, McGraw-Hill, New York.

Kennard, E. H., 1938, *Kinetic Theory of Gases*, McGraw-Hill, New York.

Koch, F. A., and Gartshore, I. S., 1972, "Temperature Effects on Hot Wire Anemometer Calibration," *J. Phys. E: Sci. Instrum.*, Vol. 5, pp. 58–61.

Luchik, T. S., Aaron, K. M., Fabris, G., Clayton, R. M., and Back, L. H., 1989, "Cryogenic Mixing Processes in the Simulation of LO_2/LH_2 Explosion Hazards: Experimental Facility and Initial Results With LN_2/LHe," JPL D-6394, Jet Propulsion Laboratory, Pasadena, CA.

Luchik, T. S., Aaron, K. M., Kwack, E. Y., Shakkottai, P., Clayton, R. M., and Back, L. H., 1990a, "Cryogenic Mixing Processes in the Simulation of LO_2/LH_2 Explosion Hazards: Results With LH_2/LHe and LO_2/LHe," JPL D-6987, Jet Propulsion Laboratory, Pasadena, CA.

Luchik, T. S., Aaron, K. M., Kwack, E. Y., Shakkottai, P., and Back, L. H., 1990b, "Cryogenic Mixing With Phase Change in the Simulation of LO_2/LH_2 Explosion Hazards," *Proc. of 9th Int. Heat Transfer Conf.*, Jerusalem, Israel, Vol. 1, Hemisphere Publishing Corp., New York, pp. 365–382.

Luchik, T. S., Aaron, K. M., Kwack, E. Y., Shakkottai, P., and Back, L. H., 1990c, "Mixing of Liquid Cryogens in the Simulation of Liquid Hydrogen/Liquid Oxygen Explosion Hazards," presented at the 24th DOD Explosives Safety Seminar, St. Louis, MO.

McCarty, R. D., Hord, J., and Roder, H. M., 1981, *Selected Properties of Hydrogen* (*NBS Monograph 168*), U. S. Government Printing Office, Washington, DC.

Nelson, E. W., and Borgos, J. A., 1983, "Dynamic Response of Conical and Wedge Type Hot Films: Comparison of Experimental and Theoretical Results," *TSI Quarterly*, Vol. 9, No. 1.

Perry, A. E., 1982, *Hot-Wire Anemometry*, Oxford University Press, London.

Pitts, W. M., and McCaffrey, B. J., 1986, "Response Behavior of Hot Wires and Films to Flows of Different Gases," *J. Fluid Mech.*, Vol. 169, pp. 465–512.

Sychev, V. V., Vasserman, A. A., Kozlov, A. D., Spiriddonov, G. A., and Tsymarny, V. A., 1987a, *Thermodynamic Properties of Helium*, Hemisphere Publishing Corp., New York.

Sychev, V. V., Vasserman, A. A., Kozlov, A. D., Spiriddonov, G. A., and Tsymarny, V. A., 1987b, *Thermodynamic Properties of Nitrogen*, Hemisphere Publishing Corp., New York.

Touloukian, Y. S., Powell, R. W., Ho, C. Y., and Klemens, P. G., 1970a, *Thermophysical Properties of Matter*, The TPRC Data Series, Vol. 1, IFI/Plenum, New York.

Touloukian, Y. S., Powell, R. W., Ho, C. Y., and Klemens, P. G., 1970b, *Thermophysical Properties of Matter*, The TPRC Data Series, Vol. 2, IFI/Plenum, New York.

Downloaded 13 Dec 2010 to 193.140.21.150. Redistribution subject to ASME license or copyright; see http://www.asme.org/terms/Terms_Use.cfm

Heat and Momentum Transport in Self-Sustained Oscillatory Viscous Flows

D. Majumdar
Graduate Student.

C. H. Amon
Assistant Professor.
Mem. ASME

Department of Mechanical Engineering,
Carnegie Mellon University,
Pittsburgh, PA 15213

Heat and momentum transport in self-sustained oscillatory viscous flows is investigated by direct numerical simulation using the spectral element method. Above a critical Reynolds number, these flows bifurcate to a time-periodic, self-sustained oscillatory state. Traveling waves are observed, even at moderately low Reynolds numbers, inducing self-sustained oscillations that result in very well-mixed flows, which, in turn, lead to convective heat transfer augmentation. These oscillatory states are investigated and correlations between the time- and space-averaged Nusselt and Reynolds numbers are obtained. The transport phenomena of heat and momentum due to the oscillatory components of the flow are analyzed by looking at the phase portraits of velocity and temperature, investigating the behavior of the terms involving their fluctuations, as well as considering the correlation coefficients between the fluctuating components. Results are presented for laminar and transitional incompressible flows in communicating channels, composed of interrupted surfaces, leading to relatively thin thermal boundary layers that further contribute to heat transfer augmentation.

I Introduction

In recent years, an increasing amount of research has been performed examining the extent to which complex geometries affect self-sustained oscillatory flows. The focus of these investigations has been on the exploitation of such flow behavior for purposes of transport augmentation. Above a critical value of the Reynolds number, the initial steady *primary flow* becomes unstable to small disturbances. However, nonlinear effects may stabilize the flow at some fixed amplitude. If this happens, the flow is said to have undergone a bifurcation from steady state to a time-periodic, self-sustained oscillatory regime. These self-sustained oscillatory flows are induced and sustained by spatially periodic geometric inhomogeneities and are characterized by supercritical bifurcation and narrowband excitation (Amon and Patera, 1989). For a certain range of Reynolds number, the two-dimensional oscillatory flow is stable to any three-dimensional disturbances. The present work pertains to this particular range of Reynolds number. The effect of three dimensionality is to be considered to determine the range of validity of the two-dimensional calculations.

Improvement in the heat transfer performance is achieved when the flow bifurcates to the unsteady, self-sustained oscillatory state (Amon and Mikic, 1990), particularly in small-scale systems that operate at moderate Reynolds numbers, such as compact heat transfer surfaces, blood oxygenators, and cooling of micro-electronic components. Such significant enhancement in heat transfer is attributed to the fact that the flow gets very well mixed in the oscillatory regime. Ghaddar et al. (1986) investigated numerically these nonlinear, self-sustained oscillations while studying two-dimensional incompressible flows in periodic grooved channels. By performing an analysis of the dependence of the oscillation amplitude on the degree of criticality, they showed that these oscillations are the result of a primary Hopf bifurcation. Amon and Patera (1989) extended this investigation to three-dimensional flows. They found a secondary narrowband instability, when the Reynolds number was increased, leading to a second flow bifurcation and a three-dimensional quasi-periodic, self-sustained flow. Greiner et al. (1991) performed experiments on similar oscillatory flows in triangular grooved channels showing a significant improvement in heat transfer–pumping power performance relative to a flat channel.

It is believed (Lin, 1955) that the Reynolds stress, $\rho\overline{u'v'}$, which contributes significantly to momentum diffusion, converts energy from the mean flow to the fluctuating flow and sustains it. Not much, however, is known about the behavior of the oscillatory components of temperature in the context of transitional, self-sustained oscillatory flows. Specifically, the role that the Reynolds heat flux, $\rho c_p\overline{u'T'}$ or $\rho c_p\overline{v'T'}$, plays in the heat transport phenomenon in these well-organized oscillatory flows has not been investigated. Much work has been done over the years on the structure and generation of Reynolds stresses and Reynolds heat fluxes near the wall for random-fluctuating turbulent flows in simple geometries. Perry and Hoffman (1976) compared various sampled results for Reynolds stresses and heat fluxes in an experimental study of heat transfer from a flat plate. Subramanian and Antonia (1981) also looked at the distributions of the velocity and temperature fluctuations experimentally, but the measurements were taken in the turbulent boundary layer of a smooth flat plate. Kim and Moin (1987) discussed correlations between the streamwise velocity and temperature fields, while performing a direct numerical simulation of turbulent straight channel flow. It should be noted that turbulent flow in simple geometries was the focus of attention for all these papers. However, no previous work has been reported on the *equivalent* Reynolds heat flux and its interplay with the Reynolds stress, both involving the unsteady components of velocity and temperature in self-sustained oscillatory flows in complex geometries, which is the objective of the present paper. In the context of discussing self-sustained oscillatory viscous flows, we choose a particular geometry, known as communicating channels, to present our numerical results.

The fact that higher heat transfer coefficients are attainable in the entrance region of internal flows has motivated the design of heat exchangers having flow passages that consist of a succession of entrance regions. The walls of such passages are interrupted periodically along the streamwise direction, and

Contributed by the Heat Transfer Division and presented at the 28th National Heat Transfer Conference, Minneapolis, Minnesota, July 28–31, 1991. Manuscript received by the Heat Transfer Division July 1991; revision received March 1992. Keywords: Augmentation and Enhancement, Forced Convection, Transient and Unsteady Heat Transfer. Associate Technical Editor: R. J. Simoneau.

Copyright © 1992 by ASME
Downloaded 13 Dec 2010 to 193.140.21.150. Redistribution subject to ASME license or copyright; see http://www.asme.org/terms/Terms_Use.cfm

such arrangements are called communicating channels. Each interruption enables the velocity and temperature distributions to become more cross-sectionally homogeneous, and a new boundary layer starts when the passage wall is resumed downstream of the interruption. The relatively thin boundary layers that are obtained by the use of interrupted surfaces in communicating channels is one important factor in the high heat transfer effectiveness of such surfaces. Research reported in the literature on steady laminar and turbulent flows through in-line colinear plate arrays shows significant heat transfer augmentation compared to the compatible basic geometry (Sparrow and Liu, 1979). It has been shown (Amon and Mikic, 1990) that additional improvement in the heat transfer performance is achieved when the flow undergoes transition to unsteady, self-sustained oscillatory flow. However, the geometric parameters must be chosen such that the normally damped Tollmien–Schlichting waves present in plane channel steady flow can be excited and sustained. Sekulic (1989) investigated experimentally the global (macro) fluid performances of these communicating-channels flows and found a satisfactory agreement with the numerically predicted (Amon and Mikic, 1990) flow patterns in these types of geometries. A combined numerical and experimental study of the flow patterns and thermal phenomena was also performed in these self-sustained oscillatory flows (Amon et al., 1992), and good agreement was obtained on the flow conditions for the onset of hydrodynamic instabilities. The purpose of the present work is to study the effect of the oscillatory components of the velocity and temperature on the transport phenomena of heat and momentum in the context of self-sustained oscillatory flows in communicating channels.

II Problem Description

The flow in the communicating channels (Fig. 1) is simulated numerically by solving the unsteady Navier–Stokes and energy equations for Newtonian, incompressible, two-dimensional flows. Natural convection, viscous dissipation, and variation of thermal properties are neglected in the formulation of the problem. The velocity boundary conditions are Dirichlet on rigid walls and periodic fully developed in the streamwise direction. The thermal boundary conditions are uniform flux on the interrupted plates with adiabatic top and bottom walls. Details of the mathematical formulation are presented by Amon et al. (1992).

The numerical approach to be followed here is that of direct simulation, in which steady and supercritical states are computed using initial value solvers. The discretization in time is done using a three-step splitting scheme (Orszag and Kells, 1980), in which three fractional steps are introduced within one time step. In the first step, the convective terms of the Navier–Stokes equation are treated explicitly using a third-order Adams–Bashforth scheme; a Poisson equation for pressure is solved at the second step along with the imposition of the incompressibility condition. Finally, at the third step, viscous terms are handled implicitly to avoid unreasonably time-step restrictions due to the high resolution of spectral approximations near the boundary of the elements. In addition, boundary conditions are imposed at this last step. For two-dimensional simulations, the spatial discretization proceeds using the spectral element method proposed by Patera (1984). It is a high-order weighted-residual technique, where the computational domain is broken up into general quadrangular elements, and the geometry, pressure, and velocity in each element are represented as a tensor product of high-order Lagrangian interpolants through Chebyshev collocation points. The convective terms are treated using explicit collocation operators, while the elliptic contributions are handled with variational projection operators. The numerical calculations are performed employing 51 spectral elements using a 7×7 Chebyshev collocation grid in the x and y directions of each element. A typical run of 10,000 time steps of size equal to 8.4×10^{-3} units of nondimensional time takes about 2600 CPU seconds on Cray Y-MP/832.

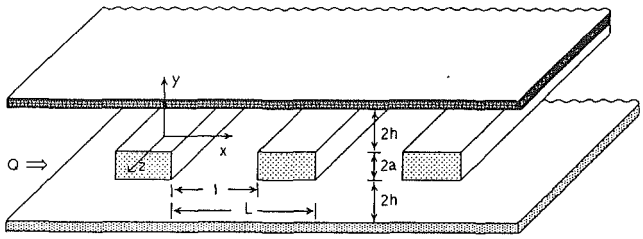

Fig. 1 Communicating-channels geometry characterized by L = periodicity length, l = separation between the interrupted plates, $2a$ = separation between the channels, and $2h$ = height of each channel

III Results and Discussion

This section presents a discussion of the numerical results obtained for the flow field and heat transfer characteristics in the periodic communicating channels of Fig. 1. This geometry corresponds to a nondimensionalized periodicity length of $L/h = 8$, length of the communicating region between the channels $l/h = 3$, and separation between the channels, $2a/h = 1$. The corresponding spectral element mesh is shown in Fig. 2, where more elements are packed in the communicating region to accurately resolve the vortical structures. Starting from arbitrary initial conditions, the nonlinear Navier–Stokes and energy equations were integrated and the results were confirmed to be convergent in both time and space.

The steady-state field is shown in Fig. 3(*a*) in the form of

Nomenclature

a = half-separation distance between the channels (Fig. 1)
h = half-channel height
k = thermal conductivity
l = separation between the interrupted plates (Fig. 1)
L = periodicity length (Fig. 1)
Nu = Nusselt number
Pr = Prandtl number $= \nu/\alpha$
q'' = heat flux per unit area
rms = root mean square
Re = Reynolds number $= Vh/\nu$
t = time
T = temperature, nondimensionalized by $q''h/k$
$\overline{T}$ = time-averaged temperature
T' = fluctuating component of the temperature
$\overline{TS}$ = Tollmien–Schlichting
$\overline{\Delta T}$ = time- and space-averaged temperature difference between wall temperature and mean fluid temperature
u, v = dimensionless velocity components in the x and y directions, respectively
u', v' = fluctuating components of the x and y velocities
$\overline{U}$ = time-averaged x velocity
V = cross-channel average velocity
$-\overline{u'v'}$ = *oscillatory* shear stress
$-\overline{v'T'}$ = *oscillatory* heat flux
α = molecular thermal diffusivity
α_{tr} = transitional thermal diffusivity
β = nondimensional streamwise wavenumber
ν = kinematic viscosity
τ = period of oscillatory velocity

Downloaded 13 Dec 2010 to 193.140.21.150. Redistribution subject to ASME license or copyright; see http://www.asme.org/terms/Terms_Use.cfm

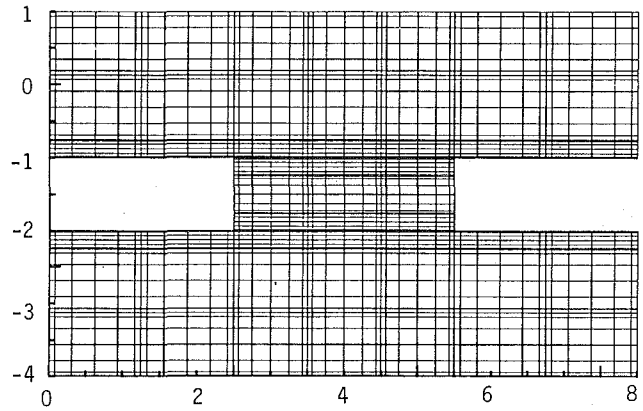

Fig. 2 Computational domain and corresponding spectral element mesh

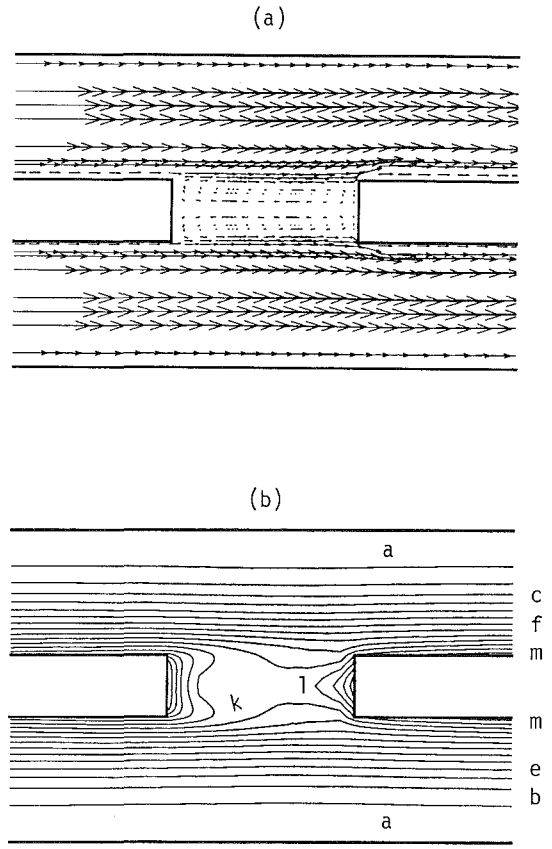

Fig. 3 (*a*) Velocity-vector field and (*b*) isotherm plot, for a steady state Re = 175; isotherm levels equally spaced from $a = T_{min}$ to $m = T_{max}$

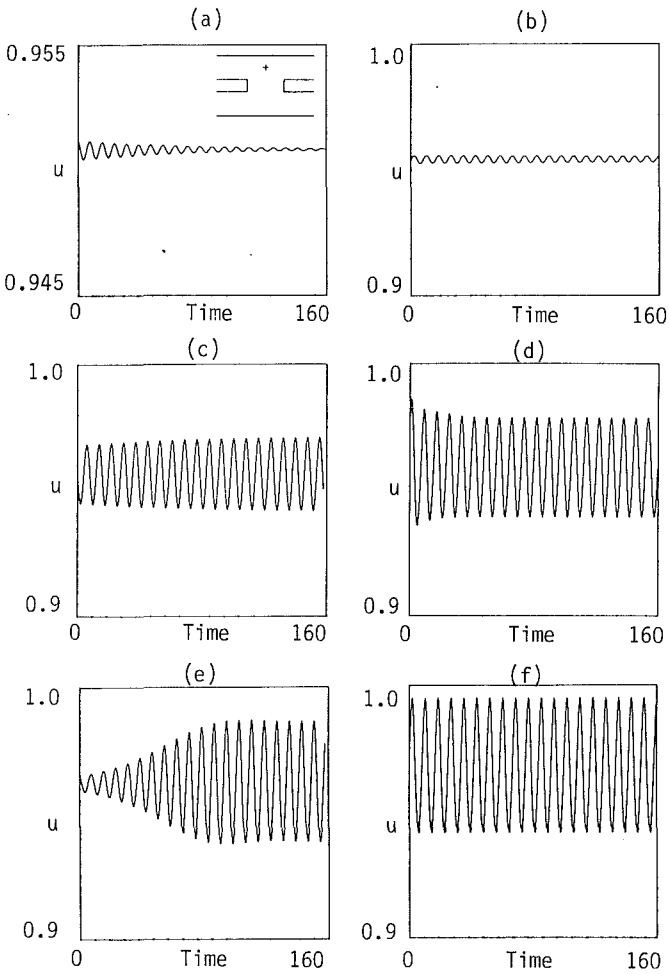

Fig. 4 Streamwise u velocity as a function of time at ($x/h = 4.0$, $y/h = 0.125$) for (*a*) Re = 175, (*b*) Re = 200, (*c*) Re = 225, (*d*) Re = 250, (*e*) Re = 300, and (*f*) Re = 400

velocity vectors for a Reynolds number Re = 175, where the flow direction is from left to right. Two counterrotating vortices are seen to be aligned and confined in the communicating region due to strong viscous effects. Figure 3(*b*) displays the isotherm plot for Re = 175, which indicates that there is almost no material communication between the communicating region and the main channel flows for this Reynolds number. This is evident from the parallel isotherms present in the main channels, which is a consequence of the flow being a typical laminar fully developed plane channel flow. The fact that these cases correspond to steady state is highlighted in the time-history plot of the streamwise velocity corresponding to Re = 175 at a characteristic point in the domain (Fig. 4*a*). It can be seen that the amplitude of the velocity is becoming almost invariant with time. However, if one looks at the plot for Re = 200, it can be seen that the velocity is converging asymptotically to a steady-periodic state with fixed amplitude, which indicates that the critical value of the Reynolds number is somewhere between 175 and 200.

The velocity-history plots corresponding to higher values of the Reynolds number, e.g., 225, 250, 300, and 400 (Fig. 4) indicate that these flows are time-periodic, self-sustained, and oscillatory in nature, and that the primary bifurcation has already taken place. It should also be noted that amplitudes increase with the Reynolds number and, thus, the flow becomes better mixed as the Reynolds number is increased. Incidentally, these oscillatory flows contain one well-defined frequency, which can be determined from these time-history plots or by their Fourier-spectrum analyses. This frequency corresponds to the least-stable channel mode compatible with the given geometry, known as the Tollmien–Schlichting (TS) frequency. The TS mode corresponds to a nondimensional wavenumber $\beta = 2\pi mh/L$, where m is the number of waves that spans the periodicity length L. As can be seen from the velocity fields in Fig. 5, there are two waves that occupy the periodicity length yielding a value of $\beta = 1.5708$. The TS nondimensional angular frequency corresponding to this value of β and a Reynolds number of 400 is 0.761, which agrees well with the value of 0.721 obtained for the corresponding communicating-channel flows at the same Reynolds number.

Figure 5 shows the evolution of the flow structure in terms of the instantaneous velocity vectors in a sequence of six time frames within one flow cycle ($0 \le t \le \tau$, τ = time period of a flow cycle) for a Reynolds number of 400. The wavy character

Downloaded 13 Dec 2010 to 193.140.21.150. Redistribution subject to ASME license or copyright; see http://www.asme.org/terms/Terms_Use.cfm

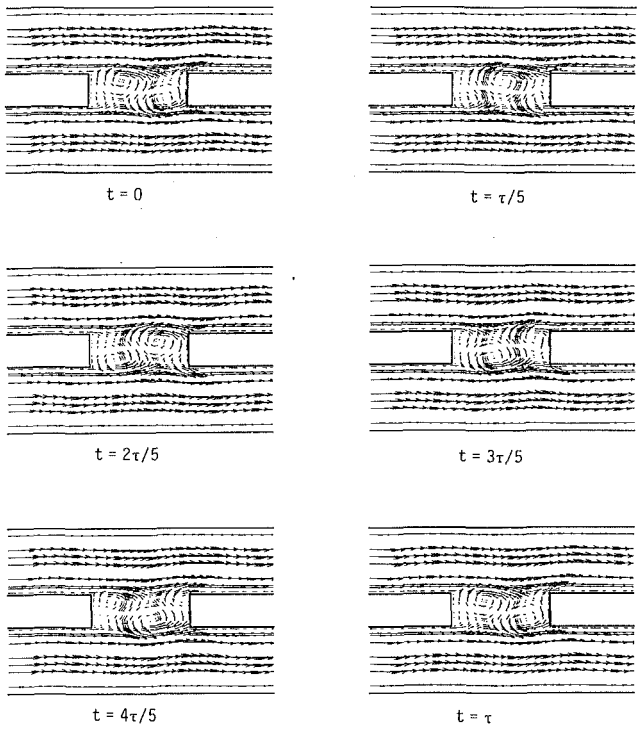

Fig. 5 Instantaneous velocity-vector fields in a sequence of six time frames within one flow cycle ($0 \le t \le \tau$) for Re = 400

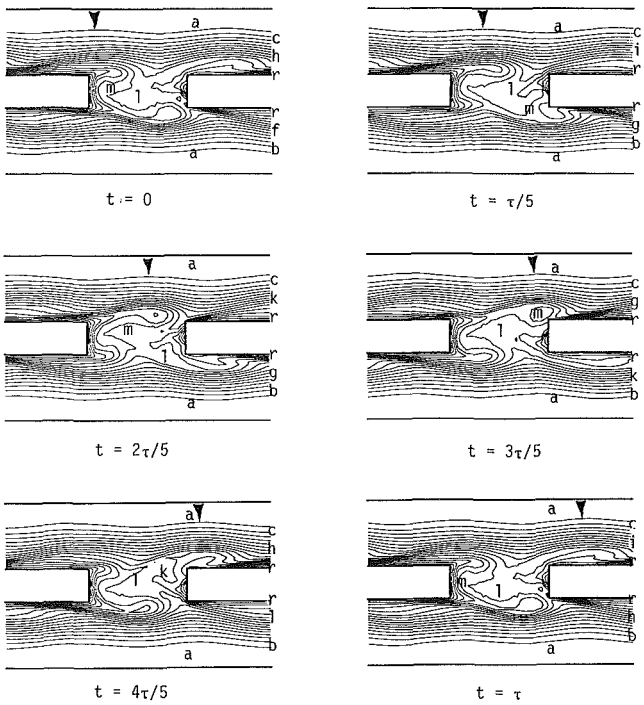

Fig. 6 Instantaneous temperature fields corresponding to the same time instants of the velocity fields of Fig. 5; isotherm levels equally spaced from $a = T_{min}$ to $r = T_{max}$

of these flow fields compared to the relatively flat profiles of Fig. 3 indicates that the flow has undergone bifurcation from a steady, time-independent state to a time-periodic flow. The flow structures clearly demonstrate that the waves are traveling waves and Tollmien–Schlichting-like in nature as mentioned in the previous paragraph. The sharper shear layers associated

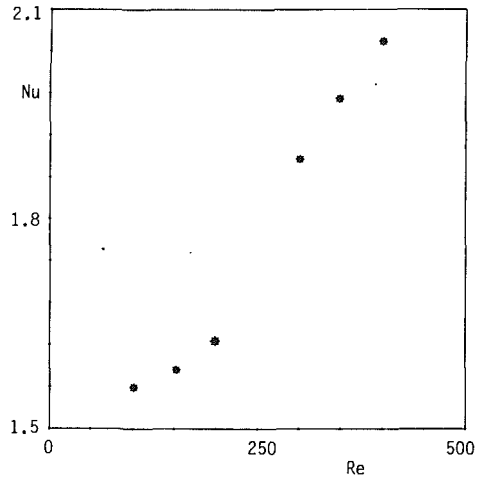

Fig. 7 Time- and space-averaged Nusselt number versus Reynolds number ($175 < Re_{cr} < 200$)

with these flows compared to those of Fig. 3 are also noticeable. It is clear that for these supercritical flows, the viscous forces are not strong enough to keep the vortices confined to the communicating region. The vortices are ejected alternately to the upper and lower channels, producing mixing between the flow in the communicating region and the bulk flows, thereby augmenting the heat transfer in the transverse direction, which is indeed the predominant direction of heat transfer.

At $t = 0$ (Fig. 5), there are two counterrotating vortices of almost equal strength confined in the communicating region. As time passes, the clockwise rotating vortex that is confined in the lower-left corner of the region gains in strength and moves downstream, dissipating rotational kinetic energy. At $t = 2\tau/5$, the clockwise rotating vortex has moved farther downstream and a counterclockwise recirculation zone is formed in the lower-left corner of the communicating region. A similar pattern is repeated for the rest of the cycle, with the vortices alternatively ejecting to the upper and lower channels. It is noteworthy that the vortex dynamics are synchronized with the wavy characteristics of the flow, which corresponds to in-phase traveling Tollmien–Schlichting waves in both channels. Pressure fields interact between the channels, driving the flow up or down the communicating region.

Figure 6 shows instantaneous isotherm plots in a sequence of six time frames corresponding to the same flow cycle and Reynolds number as in Fig. 5 and for a Prandtl number Pr = 1. These plots portray the effect of the flow structure on the resulting thermal boundary layers and depict how the layers thicken and become thin again as the flow turns at the *trailing* edge of the interrupted wall. The channel isotherms look similar to the wavy flow as seen in the velocity-vector plots, indicating a two-wave solution but with a more pronounced waviness. In this sense, the temporal sequence of isotherms is a thermal visualization of the Tollmien–Schlichting waves, which can be followed up in time through the flow cycle, as indicated by the arrows corresponding to the crests in Fig. 6. In the communicating region of the domain, the temperature distribution is affected by the recirculating flow and associated boundary layers. If one looks at a typical temperature field plot, say, at $t = 2\tau/5$ in Fig. 6, it can be seen that cold fluid is forced from the lower channel into the communicating region, which is in conformity with the corresponding velocity vector field shown in Fig. 5, where fluid is seen to be entrained from the lower channel and delivered to the communicating region. The thin thermal boundary layers associated with the flows in this geometry and responsible for heat transfer augmentation are also noticeable.

Downloaded 13 Dec 2010 to 193.140.21.150. Redistribution subject to ASME license or copyright; see http://www.asme.org/terms/Terms_Use.cfm

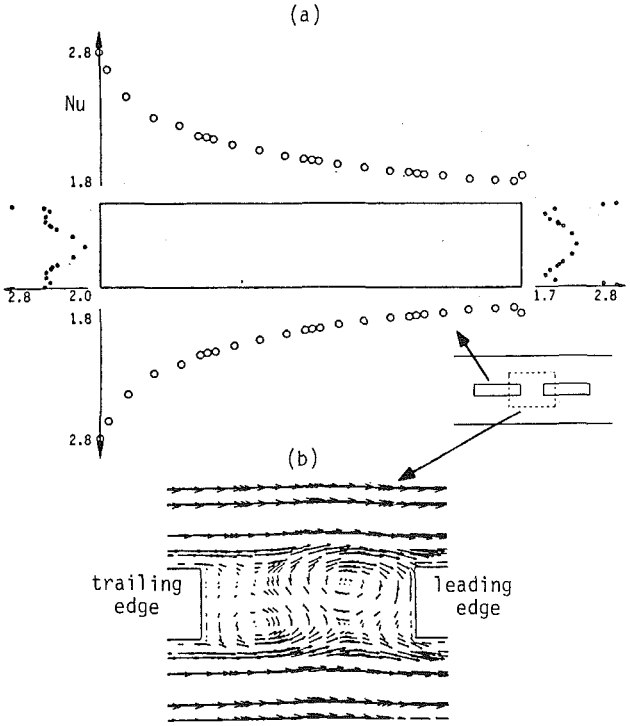

Fig. 8 (*a*) Time-averaged local Nusselt number distribution along a heated interrupted plate for Re = 400 and (*b*) magnified velocity-vector field in the communicating region corresponding to $t = 2\tau/5$ in Fig. 5

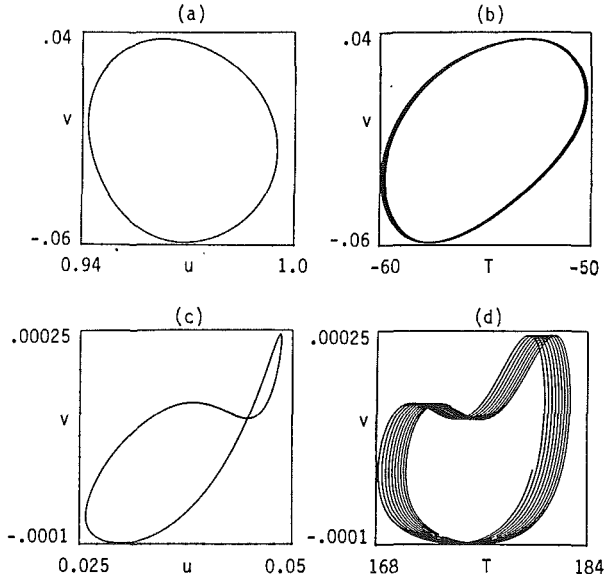

Fig. 9 Phase portraits of (*a*) *u*-*v*, (*b*) *T*-*v* at a point near the center of the upper main channel, (*c*) *u*-*v*, and (*d*) *T*-*v* at a point near the interrupted wall

In order to get an overall measure of the transport characteristics of these flows, we define a Nusselt number as

$$\mathrm{Nu} = \frac{q'' h}{k\overline{\Delta T}} \tag{1}$$

where $\overline{\Delta T}$ is the temperature difference between the heated wall temperature, T, and the bulk mixed-mean temperature, T_b, averaged in time and space, defined as

$$\overline{\Delta T} = \int_{\partial D_H} \langle T - T_b \rangle dl \Big/ \int_{\partial D_H} dl,$$

where

$$T_b = \frac{\int_{-h}^{h} \langle u(x=0, y, t) T(x=0, y, t) \rangle dy}{\int_{-h}^{h} \langle u(x=0, y, t) \rangle dy} \tag{2}$$

∂D_H is the heated wall and $\langle\ \rangle$ refers to a time average.

Figure 7 shows a plot of the time- and space-averaged Nusselt number as a function of Reynolds number. The fully developed value of the Nusselt number for plane channel flow without interrupted plates is 1.35 for the entire range of laminar Reynolds numbers. It can be seen from Fig. 7 that even for the steady flow (Re = 100), there is an increase in the Nusselt number over the plane channel fully developed value. As the Reynolds number is increased above the critical value, the Nusselt number increases even further. Let us try to explain this behavior by comparing the rate of increase of the Nusselt number, over Reynolds numbers ranging from 100 to 200, with the rate of increase corresponding to the Reynolds number range of 300 to 400 in Fig. 7. The slope increases abruptly from the lower to the higher range of the Reynolds number in the region near the critical Reynolds number. In the range of lower Reynolds numbers, the flow regime corresponds to steady state, and so, any increase in Nusselt number over the fully developed plane channel value can be solely attributed to the successive formation of the boundary layers. However, in the higher Reynolds number range, the flow becomes time-dependent and oscillatory in nature. This, together with the successive resumption of the boundary layers, leads to a higher heat transfer augmentation rate with a further rate of increase in the Nusselt number. In fact, a comparison between the Nusselt number for the communicating-channel, self-sustained, oscillatory flow (Fig. 7) and the corresponding value for the laminar channel flow at the same Reynolds number, Re = 400, indicates as much as 53 percent enhancement in heat transfer. The increase in the Nusselt number for a given Reynolds number can be attributed to a decrease in the stability of the flow with corresponding contributions from the velocity and temperature fluctuations as shown below.

Time-averaged local Nusselt numbers along the heated wall have been plotted in Fig. 8(*a*) for a Reynolds number Re = 400. The plots corresponding to the top and the bottom walls, which are parallel to the flow direction, indicate a close relationship between the development of the thermal boundary layer and the heat transfer. As the thickness of the boundary layer increases with the distance from the leading edge, the thermal resistance increases and, therefore, the Nusselt number decreases as one moves downstream. However, at the right-hand corners of the top and bottom walls, the Nusselt number shoots up due to the sudden acceleration of the flow as it approaches the corner. Let us now consider the Nusselt number distributions at the two sides, i.e., the leading and the trailing edges of the interrupted walls. At the trailing edge, the value of the Nusselt number at the midpoint of the vertical wall is larger than those of its surroundings, whereas at the leading edge, the Nusselt number reaches a local minimum at the midpoint of the wall. To explain these different behaviors, let us analyze the vortex-dynamics structure in a typical velocity-vector plot. Figure 8(*b*) is a blowup of the communicating region-flow field at $t = 2\tau/5$ in Fig. 5. It indicates that there are two counter-rotating vortices in the communicating region; the upper one rotates clockwise and the lower one rotates counterclockwise. Near the trailing edge, the flow approaches the midpoint region of the vertical wall from the right to the left, creating basically a local stagnation flow, which essentially accelerates the flow around the midpoint yielding a higher Nusselt number. Near the leading edge, however, the flows from the top and bottom

Downloaded 13 Dec 2010 to 193.140.21.150. Redistribution subject to ASME license or copyright; see http://www.asme.org/terms/Terms_Use.cfm

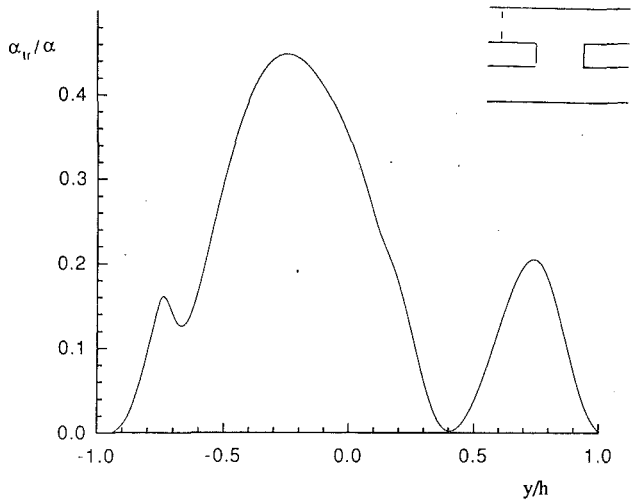

Fig. 10 Distribution of α_{tr}/α along the transverse direction at a streamwise location $x/h = 0.75$ for Re = 400

parts of the communicating region are diverted away from the wall, thus creating a local *reversed* stagnation flow, and hence the Nusselt number decreases and reaches a minimum at the midpoint of the wall.

Figure 9(*a–d*) shows phase portraits of v versus u and v versus T for Re = 400 at two characteristic points in the computational domain near the center of the channel and near the wall, respectively. The phase portrait of v versus u (Fig. 9*c*) indicates that the trajectories cross over, whereas the other phase portraits display a simpler closed loop. The orbits converge upon sharply defined, narrow-banded limit cycles clearly indicating that the flow is in a time-periodic regime. The folds in the T–v phase portraits are due to slowly disappearing transients. The fact that the temperatures and velocities are approaching a limit cycle indicates that they are indeed periodic in time and this time-dependent flow is well organized. It has been found that ordered supercritical oscillatory flows require less pumping power than turbulent flows to achieve the same transport rates, because these laminar self-sustained oscillations yield less viscous dissipation than random chaotic turbulent fluctuations, and thereby require less pumping power to reach the same transport rates (Karniadakis et al., 1988; Amon and Mikic, 1990; Greiner et al., 1991). Similar heat transfer/pumping power performance is thus expected for these self-sustained oscillatory flows in the communicating-channels geometry.

In order to quantify the contribution of the fluctuating components of the velocity and temperature to the heat transfer normal to the direction of the mean flow in these oscillatory flows, we compute an equivalent *transitional* diffusivity for heat, α_{tr}, defined as $|-\overline{v'T'}/(\partial\overline{T}/\partial y)|$ similarly as done in turbulent flows. To evaluate numerically α_{tr} for these oscillatory flows, it suffices to average over one cycle as the flow is time periodic. Figure 10 shows the distribution of the ratio of the *transitional* thermal diffusivity, α_{tr}, and the molecular thermal diffusivity, α, as a function of the nondimensionalized transverse coordinate, y/h, at a particular streamwise location ($x/h = 0.75$). It is seen that very close to the walls $\alpha_{tr} \ll \alpha$, while α_{tr} increases to be of the same order of magnitude as α as one approaches the center region of the channel, indicating that the oscillatory heat transport contribution is comparable to the molecular heat diffusion in this region. In particular, the fact that the maximum ratio tends to be in the *lower* part of the channel illustrates the influence of the vortices and the associated oscillatory components of the flow in the communicating region nearby.

To gain insight into the behavior of the oscillatory fluxes

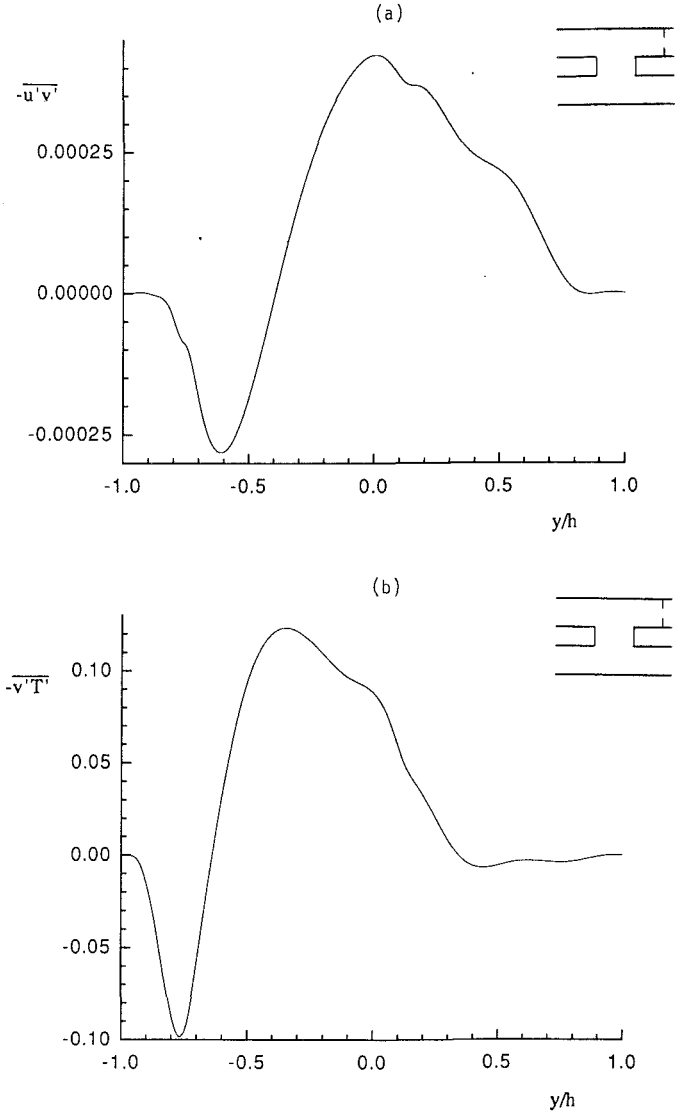

Fig. 11 Distributions of (*a*) oscillatory shear stress, $-\overline{u'v'}$, and (*b*) oscillatory heat flux, $-\overline{v'T'}$, along the transverse direction at $x/h = 7.375$ for Re = 400

of momentum and heat, we plot in Fig. 11 the distributions of $-\overline{u'v'}$ and $-\overline{v'T'}$, along the transverse direction in the upper channel at a typical streamwise location ($x/h = 7.375$). The oscillatory shear stress, $-\overline{u'v'}$, is mostly positive except in the region near the interrupted wall (Fig. 11*a*). Since the mean velocity gradient is positive in this region, the dominant part of the energy production due to the fluctuating components, i.e., $-\overline{u'v'}(\partial\overline{U}/\partial y)$ is negative. Similar negative energy production is observed near the other wall, where $-\overline{u'v'}$ is positive, but the mean velocity gradient is negative. Accordingly, energy is transferred from the oscillatory components to the mean flow in these regions. However, in the bulk flow region near the interrupted plates, $-\overline{u'v'}$ is positive yielding a positive production, which is indicative of energy transfer from the mean flow to the oscillatory components. Therefore, the oscillatory velocity components are damped near the walls, but are sustained in the lower central region close to the interrupted plates, which is commensurate with the fact that most of the energy production occurs near the interfaces of the main channels and the communicating region. It is interesting to note here that the mechanism of sustaining the oscillatory flow differs from that of a fully turbulent channel flow. In the latter, the Reynolds stresses as well as the

Downloaded 13 Dec 2010 to 193.140.21.150. Redistribution subject to ASME license or copyright; see http://www.asme.org/terms/Terms_Use.cfm

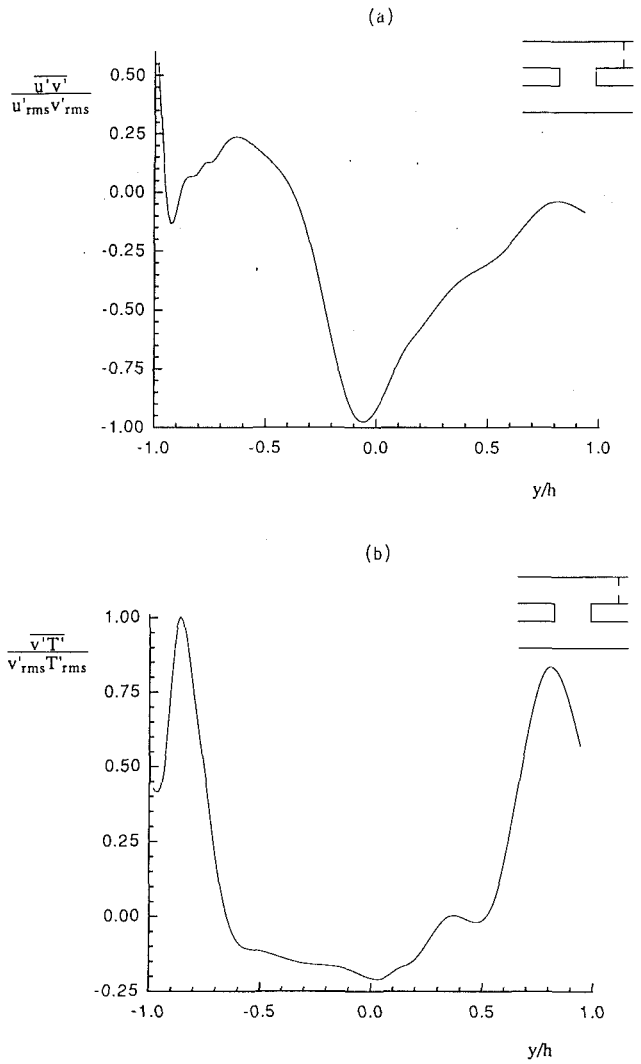

Fig. 12 Correlation coefficient for the oscillatory fluctuations of (*a*) u', v' and (*b*) v', T' along the transverse direction at $x/h = 7.375$ for Re = 400

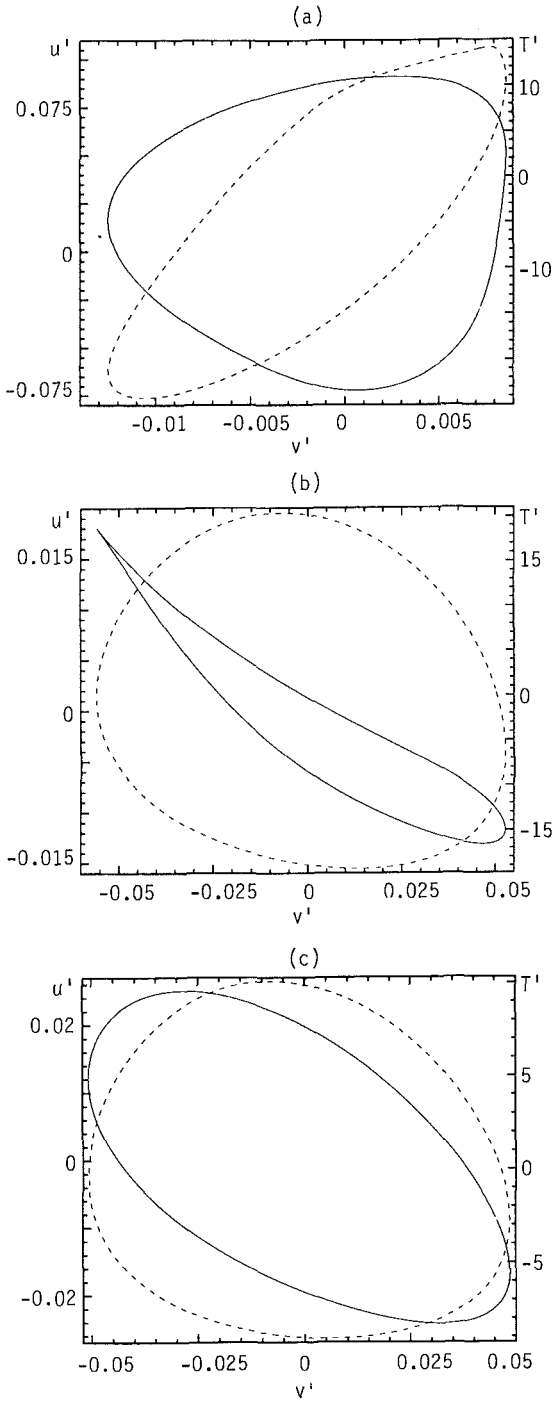

Fig. 13 Phase portraits of $u' - v'$ (solid line) and $T' - v'$ (dashed line) at a streamwise location $x/h = 7.375$ for (*a*) $y/h = -0.8125$, (*b*) $y/h = -0.0937$, and (*c*) $y/h = 0.1836$ for Re = 400

production of turbulent energy attain maximum values in the near-wall regions, which is attributed to the turbulent *bursting* process (Wei and Willmarth, 1989). The behavior of the oscillatory heat flux, $-v'T'$, shown in Fig. 11(*b*), is similar to that of $-u'v'$ in regards to being negative only in the region close to the interrupted wall, which is also the heated wall. Since the mean temperature gradient is negative throughout the transverse direction, the term responsible for the production of the temperature fluctuations, $-v'T'(\partial\overline{T}/\partial y)$, has a positive contribution only near the heated wall, indicating the generation of temperature fluctuations in that region.

The distributions of the correlation coefficients for the fluctuating quantities, u', v', and v', T' are shown in Figs. 12(*a*) and 12(*b*), respectively. For u' and v', a strong peak is observed near the interrupted wall, whereas the other wall indicates the presence of a weak peak. A strong positive correlation exists between v' and T' near the walls, whereas in the bulk flow region, they exhibit a mild negative correlation. The correlation coefficient between the velocity and temperature fluctuations at a fixed point is a good indicator of the degree of contribution to the mean heat transport, which is maximum when the coefficient is one.

The above is also demonstrated in the phase portraits (Figs. 13*a–c*) of u' versus v' and T' versus v' at several positions across the channel at the same typical streamwise location. For example, the phase portraits at $(x/h, y/h) = (7.375, -0.8125)$, shown in Fig. 13(*a*), indicate that u' and v' are weakly correlated, whereas T' and v' exhibit a moderate positive correlation. This is commensurate with the value of the correlation coefficients of 0.15 and 0.55 obtained from Figs. 12(*a*) and 12(*b*), respectively. Similarly, Fig. 13(*b*) shows a strong negative correlation between u' and v', whereas a weak correlation seems to exist between T' and v', which is consistent with the correlation coefficients of -0.75 and -0.15, respectively, obtained from Fig. 12. Therefore, the phase plane plots are indeed in good agreement with the correlation coefficients at those points.

Downloaded 13 Dec 2010 to 193.140.21.150. Redistribution subject to ASME license or copyright; see http://www.asme.org/terms/Terms_Use.cfm

IV Conclusion

A numerical investigation was performed to study the structure of the self-sustained oscillatory viscous flow and its transport characteristics in communicating channels. The transition from steady to time-dependent oscillatory flow occurs at a critical Reynolds number between 175 and 200. The frequency of the oscillatory flow agrees well with that of the Tollmien–Schlichting mode of the compatible plane-channel geometry having the same nondimensional wavenumber. Two flow mechanisms have been identified as responsible for heat transfer augmentation: the decrease in thermal resistance due to the thinner boundary layers on the interrupted plates and the mixing induced by the time-dependent oscillations.

Phase-plane plots show that these self-sustained oscillatory flows are indeed ordered in nature. The relative contribution of the temperature and velocity fluctuations on transport of heat increases as one nears the communicating region from within the interior of the main channels. Distributions of the *oscillatory* shear stress and heat flux components indicate that the velocity oscillations are sustained in the central region of the channel, and damped near the walls, whereas temperature fluctuations are mainly generated near the heated wall.

Acknowledgments

The authors are grateful to the National Science Foundation for the financial support of this work under grants Nos. CTS-8908808, EDC-8943164, and INT-9123807.

References

Amon, C. H., and Patera, A. T., 1989, "Numerical Calculation of Stable Three-Dimensional Tertiary States in Grooved-Channel Flow," *Phys. Fluids A*, Vol. 1, No. 12, pp. 2005–2009.

Amon, C. H., and Mikic, B. B., 1990, "Numerical Prediction of Convective Heat Transfer in Self-Sustained Oscillatory Flows," *J. Thermophys. Heat Transf.*, Vol. 4, pp. 239–246.

Amon, C. H., Herman, C. V., Majumdar, D., Mayinger, F., Mikic, B. B., and Sekulic, D., 1992, "Numerical and Experimental Studies of Oscillatory Flows in Communicating Channels," *Int. J. Heat Mass Transfer*, Vol. 35, No. 11, pp. 3115–3129.

Ghaddar, N. K., Korczak, K. Z., Mikic, B. B., and Patera, A. T., 1986, "Numerical Investigation of Incompressible Flow in Grooved Channels. Part 2. Resonance and Oscillatory Heat-Transfer Enhancement," *J. Fluid Mech.*, Vol. 168, pp. 541–567.

Greiner, M., Chen, R. F., and Wirtz, R. A., 1991, "Enhanced Heat Transfer/Pressure Drop Measured From a Flat Surface in a Grooved Channel," ASME JOURNAL OF HEAT TRANSFER, Vol. 113, pp. 498–501.

Karniadakis, G. E., Mikic, B. B., and Patera, A. T., 1988, "Minimum Dissipation Transport Enhancement by Flow Destabilization: Reynolds Analogy Revisited," *J. Fluid Mech.*, Vol. 192, pp. 365–391.

Kim, J., and Moin, P., 1987, "Transport of Passive Scalars in a Turbulent Flow," *Proc. 6th Symposium on Turbulent Shear Flows*, Toulouse, France.

Lin, C. C., 1955, *The Theory of Hydrodynamic Stability*, Cambridge University Press, United Kingdom.

Orszag, S. A., and Kells, L. C., 1980, "Transition to Turbulence in Plane Poiseuille and Plane Couette Flows," *J. Fluid Mech.*, Vol. 96, pp. 159–205.

Patera, A. T., 1984, "A Spectral Element Method for Fluid Dynamics: Laminar Flow in a Channel Expansion," *J. Comp. Phys.*, Vol. 54, pp. 468–477.

Perry, A. E., and Hoffman, P. H., 1976, "An Experimental Study of Turbulent Convective Heat Transfer From a Flat Plate," *J. Fluid Mech.*, Vol. 77, pp. 355–368.

Sekulic, D. P., 1989, "Flow Through Communicating Channels Compact Heat Transfer Geometry," *Int. Comm. Heat Mass Transfer*, Vol. 16, pp. 667–679.

Sparrow, E. M., and Liu, C. H., 1979, "Heat Transfer, Pressure Drop and Performance Relationships for In-Line, Staggered, and Continuous Plate Heat Exchangers," *Int. J. Heat Mass Transfer*, Vol. 22, pp. 1613–1625.

Subramanian, C. S., and Antonia, R. A., 1981, "Effect of Reynolds Number on a Slightly Heated Turbulent Boundary Layer," *Int. J. Heat Mass Transfer*, Vol. 24, No. 11, pp. 1833–1846.

Wei, T., and Willmarth, W. W., 1989, "Reynolds-Number Effects on the Structure of a Turbulent Channel Flow," *J. Fluid Mech.*, Vol. 204, pp. 57–95.

Downloaded 13 Dec 2010 to 193.140.21.150. Redistribution subject to ASME license or copyright; see http://www.asme.org/terms/Terms_Use.cfm

Effect of Nozzle Configuration on Transport in the Stagnation Zone of Axisymmetric, Impinging Free-Surface Liquid Jets: Part 1—Turbulent Flow Structure

J. Stevens[1]

Y. Pan

B. W. Webb

Heat Transfer Laboratory,
Department of Mechanical Engineering,
Brigham Young University,
Provo, UT 84602

This study characterized the mean and fluctuating parts of the radial component of the local velocity in the stagnation region of an impinging, free-surface liquid jet striking a smooth flat plate. Four different nozzle exit conditions were studied, including fully developed pipe flow, a contoured nozzle, and turbulence-damped and -undamped sharp-edged orifices. Liquid jet Reynolds numbers in the range 30,000 to 55,000 were investigated. Velocities were measured using laser-Doppler velocimetry. Mean velocities were found to vary nearly linearly with radial location, with the slope of the line being a function of distance from the impingement plate. Dimensionless mean velocity gradients, of relevance to the heat transfer, were found to be a strong function of nozzle type, but roughly independent of jet Reynolds number for a given nozzle type. Turbulence levels were also found to be strongly influenced by the nozzle exit condition. Local heat transfer data corresponding to the flow structure measurements presented here are reported in Part 2 of this study.

Introduction

Impinging jets are characterized by unusually high transfer coefficients near the stagnation region. For this reason, they have found wide application in a variety of industries. They are used in the glass and metal industries for cooling, and in the paper and textile industries for drying. There has also been recent interest in using impinging jets to dissipate the high heat fluxes found in electronic equipment such as VLSI circuits (Kiper, 1984; Yamamoto et al., 1987; Jiji and Dagan, 1987).

Submerged, impinging jets have received substantially more attention in the literature than have impinging free liquid jets. However, there are significant differences between the two cases. In the case of a free liquid jet, a free surface is formed after the jet leaves the nozzle, and due to the usual large difference in kinematic viscosity between the liquid and the surrounding gas, shear and entrainment at the jet boundary are generally negligible. In addition, gravity can play a more significant role for the free liquid jet, so that the jet configuration with respect to gravity is often more important than for the submerged case.

While the flow and heat transfer for submerged jets, in general, and for air jets in particular, have been studied extensively in the literature for the cases of both impinging and nonimpinging jets, free-surface liquid jets have only recently received research attention. There has been considerable prior work focusing on the local and average heat transfer characteristics. Recent reviews discuss the work in this area (Faggiani and Grassi, 1990a, 1990b). Studies that have the influence of flow structure on transport as their main or secondary focus are reviewed briefly here.

Nakoryakov et al. (1978) discussed the flow field of an impinging liquid jet in an experimental and theoretical study on the mass transfer and friction factor under such a jet. Olsson and Turkdogan (1966) investigated experimentally the radial flow field of an impinging liquid jet. The stagnation point velocity gradient has been shown by many previous analytical and experimental investigations to be an important parameter in stagnation heat transfer (Sibulkin, 1952; Burmeister, 1983; Shadlesky, 1983; Vader et al., 1991; Donaldson and Snedeker, 1971; Donaldson et al., 1971). Recent studies on planar free-surface liquid jets discuss the effect of jet exit velocity profile on the heat transfer (Zumbrunnen et al., 1989; Wolf et al., 1990; Vader et al., 1991). The magnitude of the heat transfer coefficient was found to be influenced by the stagnation line velocity gradient so that a narrower jet provided higher heat transfer coefficients. It was also concluded that free-stream turbulence intensity plays a significant role in determining the magnitude of the heat transfer coefficient. Stevens and Webb (1992) recently reported experimental measurements of the free surface flow structure of impinging liquid jets. Azuma and Hoshino (1983) present measurements of a thin liquid layer issuing from a circular nozzle placed very close to the impingement surface.

None of the aforementioned investigations report direct measurements of the flow structure in the stagnation zone of free-surface liquid jets, and the corresponding heat transfer behavior. Yet several related factors, including the jet exit velocity profile, stagnation region radial velocity gradient, and free-stream turbulence, have been proposed to be of importance in governing the heat transfer under an impinging jet (Stevens and Webb, 1991; Vader et al., 1991; Wolf et al., 1990; Zumbrunnen et al., 1989). All of these factors are influenced by the type of nozzle used to form the jet discharge. The objective of this research was to determine the effect of nozzle shape on the turbulent flow field and local heat transfer to an axisymmetric, free-surface liquid jet impinging normally against a flat surface. Inasmuch as the heat and mass transfer beneath an impinging jet depend on the nature of the flow field, a full understanding of the flow is prerequisite to understanding the associated transport phenomena. To this end, Part 1 of this study reports the local velocity and turbulence measurements made in the stagnation region of impinging jets formed by various nozzle configurations. Part 2 presents local heat transfer results for duplicated experimental conditions.

[1]Present address: Department of Mechanical Engineering, Mississippi State University, State College, MS.

Contributed by the Heat Transfer Division for publication in the JOURNAL OF HEAT TRANSFER. Manuscript received by the Heat Transfer Division January 1992; revision received June 1991. Keywords: Forced Convection, Jets. Associate Technical Editor: Y. Bayazitoglu.

Copyright © 1992 by ASME
Downloaded 13 Dec 2010 to 193.140.21.150. Redistribution subject to ASME license or copyright; see http://www.asme.org/terms/Terms_Use.cfm

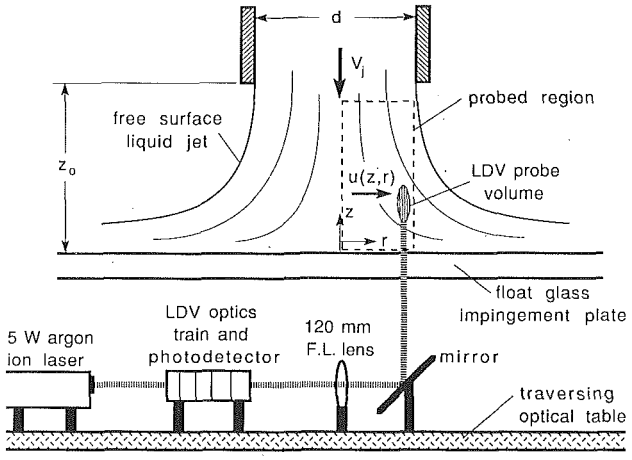

Fig. 1 Schematic of the apparatus for measurement of flow structure in the stagnation zone of the free-surface liquid jet

Experimental Apparatus

For the flow field characterization (Part 1 of study), laser-Doppler velocimetry was used to make detailed local velocity measurements throughout the impingement region of the impinging liquid jet. Figure 1 illustrates the geometric nomenclature used in this paper, as well as the method by which measurements were made in the interior of the jet stagnation zone.

Liquid velocities were measured with a TSI laser-Doppler velocimeter using a Spectra-Physics 5 watt argon-ion laser. The optics were configured for backscatter operation. A tenth-wave, front surface mirror was used to reflect the laser beams through a glass impingement plate from below, such that the measurement volume was positioned inside the liquid jet. The mirror was attached rigidly to the same traversing table upon which the LDV system was mounted. The measurement volume was moved relative to the stationary experiment setup by moving the entire LDV system on a three-axis traversing table with ± 0.1 mm resolution in each direction. The location of the impingement plate was determined for referencing the measurements by lowering the diagnostic volume successively until the Doppler signal frequency matched the shift frequency, indicating zero velocity.

Only one component of the velocity was measured in this study, using the 488 nm (blue) line of the laser. A lens of focal distance 120 mm was used at the end of the optics train. Beam expansion was used, resulting in a calculated measurement volume size of 156×28 μm on the major and minor ellipsoid axes, respectively. Coarse measurements indicated, however, that for the laser power settings and flow situations of this study, the actual length of the major axis was more nearly 300 μm for this configuration. The optical train included a field stop system with an aperture of 0.20 mm to minimize the collection of stray light.

Photodetector output was processed by a TSI model 1980B signal processor operating in continuous data collection mode. Typical sampling times were between 5 and 30 seconds, with the LDV data rate varying between 100 and 1000 samples/s. Stationary turbulence statistics were assured by taking several measurements under identical flow conditions with data records in the range 500 to 10,000 instantaneous velocity points, and comparing the computed mean and rms velocities for each record. It was found that very little change in these statistics resulted for measurements of greater than 2000 points. Therefore, a minimum of 2000 instantaneous points were collected and used in the velocity statistics. While the inverse velocity-weighted averaging presented by McLaughlin and Tiederman (1973) is recommended to eliminate the velocity bias present in LDV turbulence measurements, this processing procedure is accurate only for one-dimensional flow situations. The radial velocity component measurements in the jet stagnation zone presented here have a significant *axial* velocity component as well, which was not measured, prohibiting the adoption of the inverse velocity-weighted data processing. The ensemble averaging used for the results presented here yields small error for high data density situations (such as that which prevailed in these experiments) except for high turbulence levels. Frequency shifting at either 1or 2 MHz was employed to improve the signal data rate, effectively eliminating the fringe bias and assisting in the experimental determination of the impingement plate location.

The impinging jet was formed in a closed-loop system containing a pump, flow meters, a nozzle and associated nozzle plenum, and apparatus for collecting spent water and directing it back to the pump. The pump was a Teel model 2PO19 with maximum capacity of 53 lpm at 0.069 MPa and 7.6 lpm at 1.1 MPa. A bypass circuit was included in order to allow the pump to operate at optimal conditions while maintaining the jet at the desired flow rate. The flow meters were King Instrument Co. K72 series rotameters with a combined measurement range of 0.38 to 45.6 lpm and uncertainty of 0.38 lpm for flow rates greater than 3.8 lpm. The average jet exit velocity was calculated from the flow meter readings and the known nozzle diameter. Flow rates used in the study resulted in an approximate Reynolds number range of 30,000–55,000.

Measurements were made with four nozzle configurations, as illustrated in Fig. 2. One nozzle consisted of a straight pipe of sufficient length ($l = 30d$) so that the flow was fully developed at the nozzle exit. The other three nozzle configurations were composed of an orifice machined in a flat plate, which formed the outlet to a nozzle plenum chamber. One sharp-edged orifice plate and one contoured orifice plate were constructed for study (see Fig. 2). The contoured orifice had a radius of curvature equal to the thickness of the plate (7.8 mm). A small nozzle plenum of square cross section 57 mm on a side, and 76 mm long, was placed upstream of the selected orifice plate. Liquid flowing through the 19-mm-dia inlet of this nozzle plenum was fed by the supply tube coming from the pump/bypass circuit, and impinged on a plexiglass disk with an array of 6.4-mm-dia holes drilled around its circumference.The purpose of the disk was to decelerate the liquid flow entering the small nozzle plenum.

In order to evaluate the effects of turbulence, measurements with the sharp-edged orifice were made with and without turbulence-damping screens placed in the nozzle plenum chamber

Nomenclature

ν = fluid kinematic viscosity
d = nozzle diameter
l = fully developed nozzle length
Q = volume flow rate
r = radial coordinate measured from the stagnation point
Re = Reynolds number = $4Q/\pi d\nu$
u = local mean velocity in the radial direction
u' = local rms fluctuation in the radial direction
V_j = average jet exit velocity = $4Q/\pi d^2$
z = coordinate measured normal to the impingement plate
z_o = nozzle-to-plate spacing

Downloaded 13 Dec 2010 to 193.140.21.150. Redistribution subject to ASME license or copyright; see http://www.asme.org/terms/Terms_Use.cfm

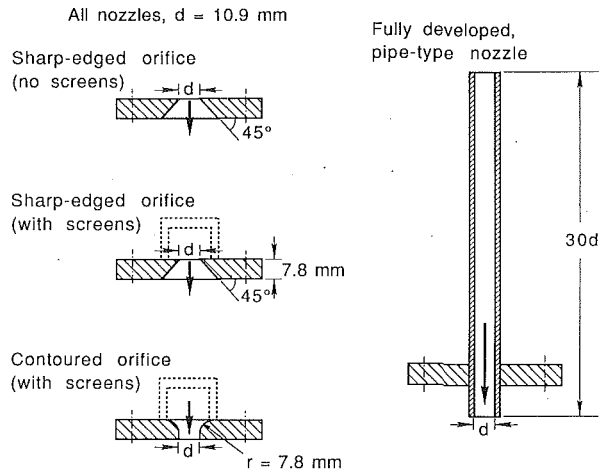

Fig. 2 Nozzle configurations used in the flow and heat transfer studies

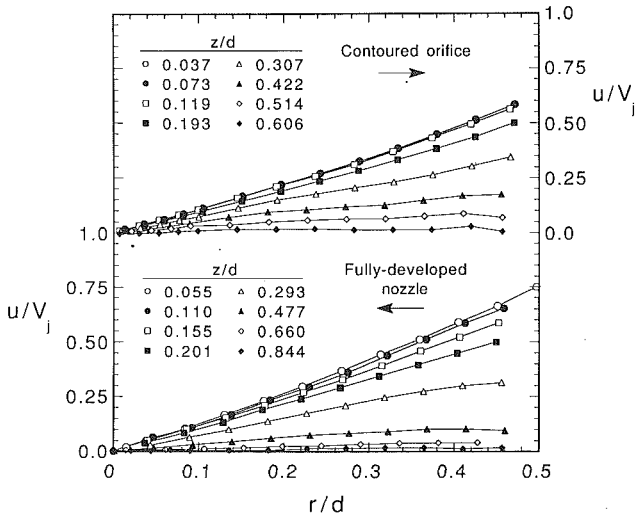

Fig. 3 Mean radial velocity profiles in the stagnation zone for the contoured orifice and fully developed nozzle, Re = 39,800

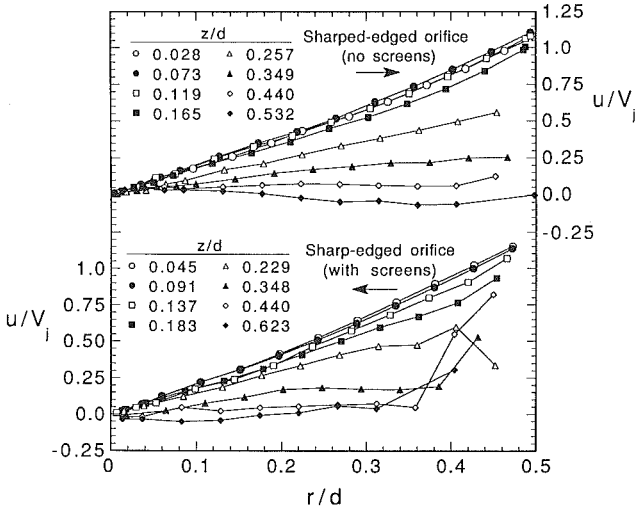

Fig. 4 Mean radial velocity profiles in the stagnation zone for the sharp-edged orifice with and without turbulence-damping screens in the plenum chamber, Re = 39,800

on the downstream side of the plexiglass disk with drilled-hole array described in the foregoing paragraph. The screens consisted of 0.36-mm-dia wire spaced at 12 wires per cm for an overall open area of approximately 30 percent. Two concentric cylinders of screen, each topped with a flat sheet of screen, were placed in the nozzle plenum around the orifice. Thus, the four nozzle configurations for which measurements were made consisted of: (1) fully developed pipe flow, (2) sharp-edged orifice with damping screens present in the plenum chamber, (3) sharp-edged orifice without damping, and (4) a contoured orifice. All nozzles were 10.9 mm in diameter. The same nozzle plenum and orifice plates as well as fully developed nozzle were also used in the heat transfer measurements reported in the companion paper.

For each flow and nozzle configuration, a square matrix of local velocity and turbulence measurements were taken in a plane perpendicular to the impingement surface and intersecting the stagnation streamline of the jet as shown in Fig. 1. For each radial traverse, the measurement volume was initially positioned slightly to one side of the stagnation streamline, then moved radially across that streamline out to $r/d \approx 0.5$. The stagnation streamline was then determined for each radial scan by interpolating between discrete measurement locations to locate the point where the measured velocity was exactly zero. There was very little error in this interpolation to detemine the stagnation streamline because of the fine spatial resolution in the velocity data collected. A single nozzle-to-plate spacing of $z_o/d = 1$ was used in both flow structure and heat transfer results.

An uncertainty analysis following the procedure of Kline and McClintock (1953) was performed. The maximum uncertainty in the average jet velocity (measured with calibrated flowmeters of 5 percent) is estimated to be 7 percent. Uncertainty in the local mean velocity measurements (measured with the LDV) is estimated to be less than 2 percent. Uncertainty in radial and axial locations is estimated to be ± 0.1 mm.

Experimental Results

Mean Radial Velocity In order to illustrate a representative sample of the data, measured mean radial velocities for a single Reynolds number (Re = 39,800) are shown in Figs. 3 and 4. These data are representative of measurements made at other Reynolds numbers (Stevens, 1991). Figure 3 illustrates the velocity measurements for the pipe-type nozzle and contoured orifice, while Fig. 4 shows the same type of measurements for the sharp-edged orifice with and without damping screens in the plenum chamber. Data for all of the nozzle configurations share some common features. As expected, the mean radial velocity vanishes at increasing distance from the impingement plate, z/d. The measurements identify the distance from the impingement plate where the plate ceases to influence the flow of the pre-impingement jet, since the radial velocities are nearly zero at approximately $z/d = 0.5$. While this may be a function of the nozzle-to-plate spacing, z_o/d, these measurements suggest that at higher z/d, the plate's influence appears to be negligible.

In all of the data of Figs. 3 and 4, the maximum velocity occurs at the closet measurement location, suggesting that none of the measurements penetrated the hydrodynamic boundary layer. Despite the extremely small diagnostic volume characteristic of the LDV system used, the measurements were made outside the boundary layer, in what may be termed the free-stream region. The boundary layer thickness was estimated from heat transfer measurements to be on the order of tens of micrometers.

It is interesting to note that all profiles exhibit a near-linear u/V_j behavior with radius. The slope of these profiles decreases with increasing z/d. Thus, the (free-stream) mean radial velocity in the stagnation zone of axisymmetric, free-surface liquid jets may be described quite accurately by an expression of the form $u(z, r) = f(z)r$, where $f(z)$ exhibits straight-line

Downloaded 13 Dec 2010 to 193.140.21.150. Redistribution subject to ASME license or copyright; see http://www.asme.org/terms/Terms_Use.cfm

behavior. This is in contrast with the infinite stagnation flow result, which, from the potential flow solution of the free-stream region, yields $u = Cr$, where C is the constant radial velocity gradient outside the boundary layer. The implication is that analytical studies that use the infinite jet stagnation relation, $u = Cr$, for the free-stream velocity as the matching condition at the boundary layer edge for finite free-surface liquid jets may be in error.

The fully developed nozzle data (lower panel, Fig. 3) exhibits differences from each of the other types of nozzle. While the measured velocities corresponding to the fully developed nozzle were always positive (directed radially outward), all orifice-type flows exhibited slight negative velocities at large z/d (far from the impingement plate). This simply means that the flow close to the orifice exit has a small component of velocity directed radially inward. Such negative velocities were never observed for fully developed pipe flows, even for z/d greater than unity (Stevens, 1991). These negative velocities are clearly an inward-directed, radial velocity component resulting from the flow negotiating the 90 deg corner in the orifice-type nozzles. Despite the negative measured velocities, no significant necking was visible in the jet flows exiting these nozzles, supported by the fact that LDV measurements were possible at r/d as high as 0.45. The contoured orifice (upper panel, Fig. 3) also contained these negative velocities, although they were generally of slightly smaller magnitude than those of the sharp-edged orifice.

Mean Radial Velocity Gradient. The velocity gradient at the impingement plate is a quantity of critical interest in heat transfer considerations of jet impingement transport. Near the impingement plate (small z/d), the mean radial velocities have been observed to vary almost linearly with radial position. In addition, the radial velocity component always vanishes at the stagnation streamline so that the radial velocity profile, u/V_j versus r/d, can be described by a single number (namely, the slope of the profile) for a given nozzle type, Reynolds number, and z/d location. In other words, in the description of the mean radial velocity, $u(z, r) = f(z)r$, where $f(z)$ is a constant for a given z, Re, and nozzle type, and represents the slope of the u versus r profile. Since the profiles are nearly linear, this slope represents the radial velocity gradients, $d(u/V_j)/d(r/d)$, at the given vertical distance, z/d, from the impingement plate, z/d, and at any radial location. Figure 5 illustrates the variation of mean radial velocity gradient with distance from the impingement plate for all nozzle types and Reynolds numbers considered. These gradients were determined by a least-squares fit of the mean velocity data out to $r/d = 0.3$. There are clearly differences in both the magnitude and the functional dependence of the velocity gradient on z/d for all nozzle types investigated. Additionally, the inward directed radial velocity component at larger z/d for the orifice-type nozzles is manifest by slight negative values of $d(u/V_j)/d(r/d)$ in Fig. 5.

One very important observation emerges from the data of Fig. 5. For a given nozzle type the dimensionless gradient is virtually independent of jet Reynolds number for small z/d. Indeed, measurements for fully developed pipe-type nozzles reveal the dimensionless velocity gradient, $d(u/V_j)/d(r/d)$, to be independent of both nozzle diameter and Reynolds number in the broad ranges $2.1 \leq d \leq 23.0$ mm and $2000 \leq \text{Re} \leq 60{,}000$ (Stevens, 1991). This suggests that, for a given nozzle geometry, the dimensionless velocity gradient is not a strong function of nozzle diameter or Reynolds number. Such information will be shown to be valuable in the development of a correlation between flow structure and local heat transfer, carried out in Part 2 of this study.

Inasmuch as this study is to be correlated with the heat transfer at the impingement plate, the behavior of the velocity gradient close to the plate is of particular interest. The infinite jet similarity solution reveals that the heat transfer is proportional to the velocity gradient (Sibulkin, 1952; Burmeister, 1983). There is a striking disparity in the magnitude of the gradient at small z/d among the different orifice-type nozzle configurations, as well as between the orifice-type nozzles and the fully developed nozzle. The gradient of the contoured orifice at small z/d is significantly below that of the fully developed nozzle, while the sharp-edged orifice gradient is well above the others for both damped and undamped plenums. Presumably, the axial velocity profile at the jet exit differs for each of the nozzle styles, and is responsible for the various gradient profile magnitudes and shapes. This is supported by the results of Wolf et al. (1990) for planar jets. However, without detailed knowledge of the various jet exit velocity profiles, quantitative conclusions about the cause of different gradient magnitudes are not possible. Nevertheless, the local heat transfer results presented in the companion paper to follow will exhibit a clear dependence on the velocity gradient.

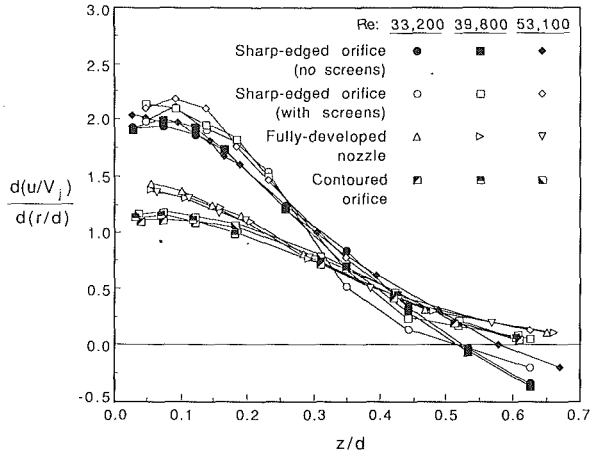

Fig. 5 Mean radial velocity gradient as a function of distance from the impingement plate for the four nozzle configurations studied

Figure 5 also illustrates that the addition of the turbulence-damping screens in the plenum chamber of the sharp-edged orifice does little to affect the mean radial velocity gradient. The difference in $d(u/V_j)/d(r/d)$ near $z/d = 0$ is approximately 8 percent for the sharp-edged orifice with and without screens. As will be shown later, the difference in turbulence levels for the two sharp-edged orifice configurations is striking.

Turbulence Level. Figures 6 and 7 show the dimensionless rms turbulence (u'/V_j) for the same configurations as shown in Figs. 3 and 4. The data reveal that the local rms turbulence profiles are approximately constant for $r/d < 0.3$ at all z/d. Since this is so, a simple radial averaging can be performed in order to examine the variation of turbulence level with z/d. This is done in Fig. 8, which illustrates spatially averaged (for $r/d < 0.3$) rms turbulence, $\overline{u'/V_j}$, as a function of z/d. Figure 8 reveals a pronounced difference in the variation in average rms turbulence with z/d between the various nozzle types. The pipe-type nozzle exhibits high turbulence near the plate followed by relatively constant turbulence for $z/d > 0.15$. By contrast, the turbulence for the contoured orifice is nearly constant (and low, 2 percent or less) at all z/d, the turbulence for the damped sharp-edged orifice increases nearly monotonically with z/d, and the turbulence for the undamped sharp-edged orifice has a maximum at $z/d \approx 0.4$. It should also be noted that the average rms turbulence levels are nearly independent of jet Reynolds number over the range investigated here. In light of these different variations of turbulence with z/d, any ordering of the turbulence levels assumes a degree of arbitrariness. The general levels of rms turbulence may be ranked from highest to lowest as follows: sharp-edged orifice without screens, sharp-edged orifice with screens, fully developed nozzle, and contoured orifice.

Downloaded 13 Dec 2010 to 193.140.21.150. Redistribution subject to ASME license or copyright; see http://www.asme.org/terms/Terms_Use.cfm

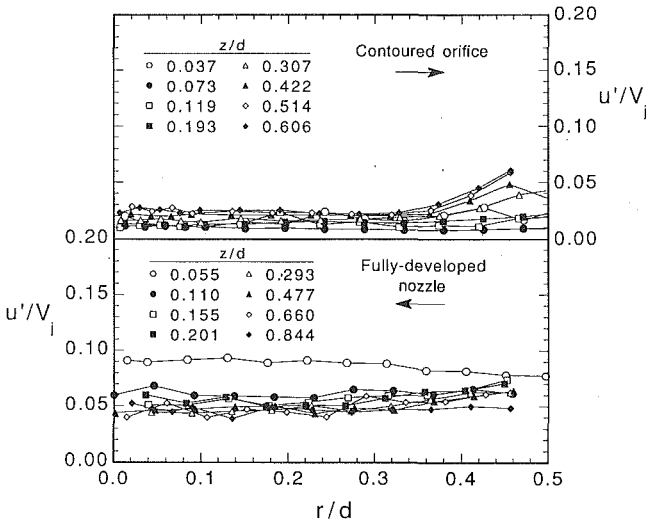

Fig. 6 Profiles of the radial rms turbulence level (u'/V_j) for the contoured orifice and fully developed nozzle, Re = 39,800

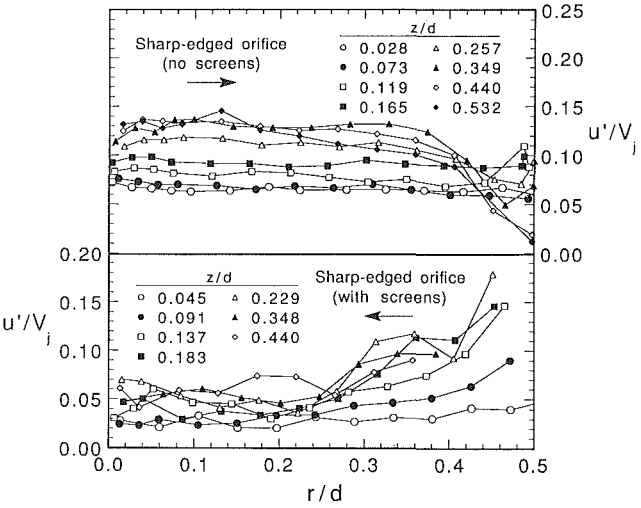

Fig. 7 Profiles of the radial rms turbulence level (u'/V_j) for the sharp-edged orifice with and without turbulence-damping screens in the plenum chamber, Re = 39,800

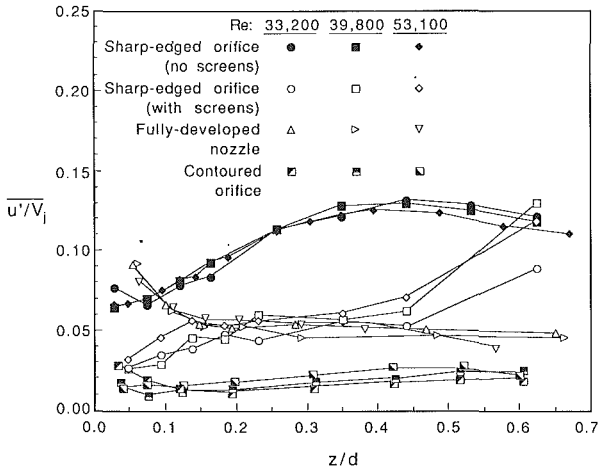

Fig. 8 Profiles of the average rms turbulence level as a function of z/d for all nozzle types at the three Reynolds numbers investigated

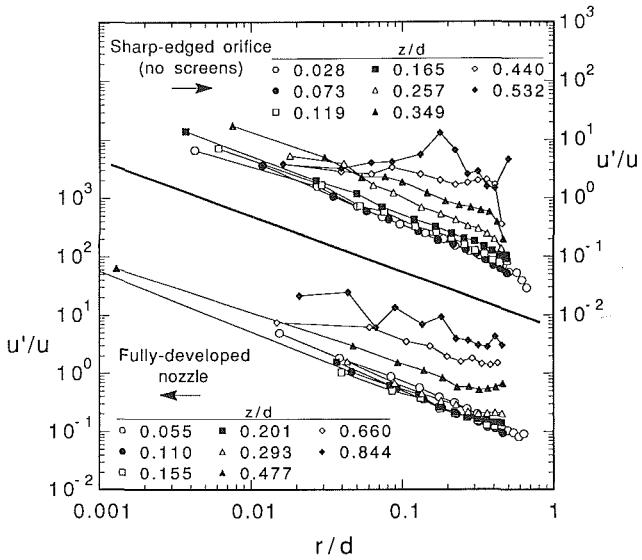

Fig. 9 Radial profiles of the radial turbulence intensity (u'/u) for the fully developed nozzle and sharp-edged orifice without damping screens, Re = 39,800

It should be noted that the sharp-edged orifice turbulence data shown in Figs. 7 and 8 reveal significant differences in u'/V_j for the configurations with and without damping screens in the plenum chamber. Levels of rms turbulence without the damping screens are two to three times higher than corresponding values with damping screens at similar measurement locations. Thus, although the addition of the damping screens to the sharp-edged orifice yielded small differences in the mean velocity gradient (see Fig. 5), significant differences in the levels of turbulence arise. Such differences provide the opportunity to compare the effect of turbulence (albeit radial component) on the local heat transfer for the same approximate gradient. This will be pursued in more detail in Part 2 of the study.

Turbulence intensity (u'/u) profiles are shown in Fig. 9 for the fully developed nozzle and sharp-edged orifice without damping screens. Since the turbulence intensity tends to infinity as r/d approaches zero, the logarithmic scales are the natural way to present the data. The data for the two nozzle configurations illustrate a nearly straight-line behavior in u'/u for small z/d. The decay in turbulence intensity with radial position is identical for the two nozzle configurations shown, and the same observation is made for the remaining two nozzle types studied (Stevens, 1991). The turbulence intensity decreases roughly with $(r/d)^{-1}$. Since u varies linearly with r/d, this further illustrates that u' is nearly independent of r/d for a given z/d, as was seen in Figs. 6 and 7.

It is signficant to note that the flow rate and diameters of the damped sharp-edged orifice and the undamped sharp-edged orifice were identical, and that the turublence level for the undamped case was nearly a factor of three higher than that of the damped case (see Figs. 6–8). Again, the observation is made that the addition of the turbulence-damping screen in the sharp-edged orifice results in only a minor change in the mean radial velocity gradient (see Fig. 5), but is accompanied by significant differences in the turbulence level. This conclusion relative to the turbulent flow structure will be critical in the examination of the local heat transfer data in Part 2 of this study.

Conclusions

The flow structure under axisymmetric free-surface liquid jets has been characterized using laser-Doppler velocimetry. The measurements of four different flow configurations permit the comparison of the flow fields generated by a pipe-type

Downloaded 13 Dec 2010 to 193.140.21.150. Redistribution subject to ASME license or copyright; see http://www.asme.org/terms/Terms_Use.cfm

nozzle, sharp-edged orifices with and without turbulence damping, and a contoured orifice. Distinctly different mean radial velocity gradient and turbulence behavior was observed for each of the nozzle types. Close to the plate, the magnitude of the radial velocity gradient was highest for the sharp-edged orifices, followed by the pipe-type nozzle, and finally by the contoured orifice. The turbulence was a strong function of the distance from the impingement plate. It was found that the addition of the turbulence-damping screens to the plenum chamber of the sharp-edged orifice resulted in only minor changes in the mean radial velocity structure and associated velocity gradients, but yielded substantial differences in the turbulent fluctuations of the radial velocity component.

Acknowledgments

This work was supported by the National Science Foundation under grant No. CBT-8552493.

References

Adrian, R. J., Fingerson, L. M., and Kaufman, S. L., 1988, "Laser Velocimetry Theory, Application and Techniques," TSI LDV Short Course Notes, Minneapolis, MN.

Azuma, T., and Hoshino, T., 1983, "LDV Measurement in Radial Flow of Thin Liquid Film," *Proceedings Osaka Symposium on Flow Measuring Techniques: The Application of LDV*, Association for the Study of Flow Measurements, Osaka, Japan, pp. 1–15.

Burmeister, L. C., 1983, *Convective Heat Transfer*, Wiley, New York.

Donaldson, C. D., Snedeker, R. S., and Margolis, D. P., 1971, "A Study of Free Jet Impingement. Part 2. Free Jet Turbulent Structure and Impingement Heat Transfer," *Journal of Fluid Mechanics*, Vol. 45, pp. 477–512.

Donaldson, C. D., and Snedeker, R. S., 1971, "A Study of Free Jet Impingement. Part 1. Mean Properties of Free and Impinging Jets," *Journal of Fluid Mechanics*, Vol. 45, pp. 281–319.

Faggiani, S., and Grassi, W., 1990a, "Impinging Liquid Jets on Heated Surfaces," *Proceedings of the Ninth International Heat Transfer Conference*, Vol. 1, pp. 275–285.

Faggiani, S., and Grassi, W., 1990b, "Round Liquid Jet Impingement Heat Transfer: Local Nusselt Numbers in the Region With Non Zero Pressure Gradient," *Proceedings of the Ninth International Heat Transfer Conference*, Vol. 4, pp. 197–202.

Jiji, L. M., and Dagan, Z., 1987, "Experimental Investigation of Single Phase Multi-jet Impingement Cooling of an Array of Micro-electronic Heat Sources," *Proceedings of the International Symposium on Cooling Technology for Electronic Equipment*, Pacific Institute for Thermal Engineering, HI, pp. 265–283.

Kiper, A. M., 1984, "Impinging Water Jet Cooling of VLSI Circuits," *International Communications in Heat and Mass Transfer*, Vol. 11, pp. 517–526.

Kline, S. J., and McClintock, F. A., 1953, "Describing Uncertainties in Single-Sample Experiments," *Mechanical Engineering*, Jan., pp. 3–12.

McLaughlin, D. K., Tiederman, W. K., 1973, "Biasing Correction for Individual Realization of Laser Anemometer Measurements in Turbulent Flows," *Physics of Fluids*, Vol. 16, pp. 2082–2088.

Nakoryakov, V. E., Pokusaev, B. G., and Troyan, E. N. 1978, "Impingement of an Axisymmetric Liquid Jet on a Barrier," *International Journal of Heat and Mass Transfer*, Vol. 21, pp. 1175–1184.

Olsson, R. G., and Turkdogan, E. T., 1966, "Radial Spread of a Liquid Stream on a Horizontal Plate," *Nature*, Vol. 211, pp. 813–816.

Shadlesky, D. S., 1983, "Stagnation Point Heat Transfer for Jet Impingement to a Plane Surface," *AIAA Journal*, Vol. 21, No. 8, pp. 1214–1215.

Sibulkin, M., 1952, "Heat Transfer Near the Forward Stagnation Point of a Body of Revolution," *Journal of the Aeronautical Sciences*, Vol. 9, pp. 570–571.

Stevens, J., 1991, "Measurements of Local Fluid Velocities in an Axisymmetric, Free Liquid Jet Impinging on a Flat Plate," Ph.D. Dissertation, Brigham Young University, Provo, UT.

Stevens, J., and Webb, B. W., 1991, "Local Heat Transfer Coefficients Under an Axisymmetric, Single-Phase Liquid Jet," ASME JOURNAL OF HEAT TRANSFER, Vol. 113, pp. 71–78.

Stevens, J., and Webb, B. W., 1992, "Measurements of the Free Surface Flow Structure Under an Impinging, Free Liquid Jet," ASME JOURNAL OF HEAT TRANSFER, Vol. 114, pp. 79–84.

Vader, D. T., Incropera, F. P., and Viskanta, R., 1991, "Local Convective Heat Transfer From a Heat Surface to an Impinging Planar Jet of Water," *International Journal of Heat and Mass Transfer*, Vol. 34, No. 3, pp. 611–623.

Wolf, D. H., Viskanta, R., and Incropera, F. P., 1990, "Local Convective Heat Transfer From a Heated Surface to a Planar Jet of Water With a Non-uniform Velocity Profile," ASME JOURNAL OF HEAT TRANSFER, Vol. 112, pp. 899–905.

Yamamoto, H., Udagawa, Y., and Suzuki, M., 1987, "Cooling System for FACOM M-780 Large-Scale Computer," *Proceedings of the International Symposium on Cooling Technology for Electronic Equipment*, pp. 96–109.

Zumbrunnen, D. A., Incropera, F. P., and Viskanta, R., 1989, "Convective Heat Transfer Distributions on a Plate Cooled by Planar Water Jets," ASME JOURNAL OF HEAT TRANSFER, Vol. 111, pp. 889–896.

Downloaded 13 Dec 2010 to 193.140.21.150. Redistribution subject to ASME license or copyright; see http://www.asme.org/terms/Terms_Use.cfm

Effect of Nozzle Configuration on Transport in the Stagnation Zone of Axisymmetric, Impinging Free-Surface Liquid Jets: Part 2—Local Heat Transfer

Y. Pan

J. Stevens[1]

B. W. Webb

Heat Transfer Laboratory,
Department of Mechanical Engineering,
Brigham Young University,
Provo, UT 84602

This is the second of a two-part study on the flow structure and heat transfer characteristics of turbulent, free-surface liquid jets. Part 2 deals with the effect of selected nozzle configurations on the local heat transfer in the stagnation zone. Infrared techniques have been used to characterize the local heat transfer for the four nozzle configurations whose mean and turbulent flow structure was detailed in Part 1. The results show that for identical jet Reynolds numbers, significant differences exist in the magnitudes of the local Nusselt number for the nozzle types studied. Differences of approximately 40 percent were observed. Local heat transfer results reveal that for already turbulent jets, the mean radial velocity gradient appears to be more influential in determining the heat transfer than incremental changes in the level of turbulence (as measured by the radial component of the fluctuations). An empirical correlation of the experimental data supports this conclusion, and reveals that the stagnation Nusselt number is affected independently by the jet Reynolds number and the dimensionless mean radial velocity gradient.

Introduction

This is the second part of an investigation of the relation between heat transfer and hydrodynamic conditions of a single, axisymmeteric, free-surface liquid jet impinging normally on a flat plate with uniform heat flux. Heat transfer to axisymmetric liquid jets has been studied experimentally in the past (Faggiani and Grassi, 1990a, 1990b; Ma et al., 1990; Stevens and Webb, 1991; Liu et al., 1991; Lienhard et al., 1991). However, the nozzle geometries employed in these studies were diverse. Different nozzle geometries are expected to produce different nozzle exit hydrodynamic conditions, and therefore yield different heat transfer behavior. The first part of this research has investigated the dependence of the hydrodynamic conditions on nozzle shape. This paper, Part 2 of the study, reports on the heat transfer characteristics of different nozzle geometries, and then explores the correlation between heat transfer and hydrodynamic conditions (presented in the companion paper).

Experimental Method and Apparatus

An experimental facility was designed to allow detailed local heat transfer measurements for nozzle configurations duplicating those for which flow structure data were collected in Part 1. Infrared radiometry was used for the experimental determination of the local temperature of a uniform heat flux surface. This option was chosen because it can provide considerably higher spatial resolution of temperature than thermocouples without mechanical probing and its associated thermal disturbance of the system. The infrared imaging system used was the Model 600 IR Imaging Radiometer, which yields a resolution of about 0.3 mm per pixel as demonstrated in a recent study (Lytle and Webb, 1991). The facility included a test chamber, power supply, the infrared imaging system, and data processing system, as illustrated in Fig. 1.

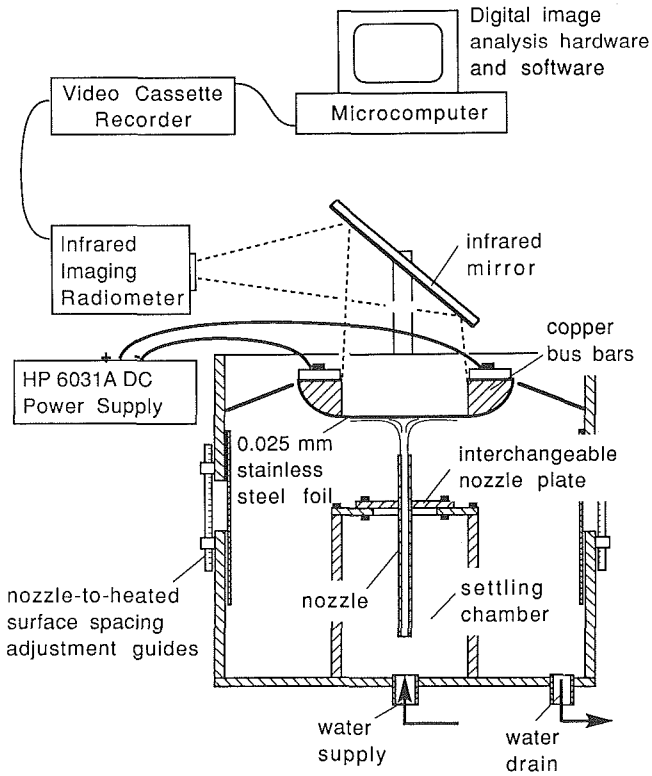

Fig. 1 Schematic diagram of experimental apparatus for heat transfer measurements

Since the flow and heat transfer are likely to be a function of both the nozzle geometry and the upstream plenum configuration, they are described in detail here. The liquid delivery system consisted of an upper box and a lower box, which were made of plexiglass. A fluid settling chamber was housed inside

[1] Present address, Department of Mechanical Engineering, Mississippi State University, State College, MS.

Contributed by the Heat Transfer Division for publication in the JOURNAL OF HEAT TRANSFER. Manuscript received by the Heat Transfer Division December 1991; revision received June 1992. Keywords: Forced Convection, Jets. Associate Technical Editor: F. P. Incropera.

Copyright © 1992 by ASME
Downloaded 13 Dec 2010 to 193.140.21.150. Redistribution subject to ASME license or copyright; see http://www.asme.org/terms/Terms_Use.cfm

the lower box. The walls of the settling chamber were made of plexiglass of 12.7 mm thickness to withstand the fluid pressure. The chamber had an internal cross-sectional area of 185 mm by 185 mm, and a height of 280 mm, with an inlet pipe diameter of 38 mm. A smaller nozzle plenum (not shown in Fig. 1) was housed inside the larger settling chamber. This plenum was of square cross section 57 mm on a side, was 76 mm long, and was the same nozzle plenum used in the flow structure measurements. Liquid flowing from the large fluid settling chamber through the 19-mm-dia inlet of the small nozzle plenum impinged on a plexiglass disk with an array of 6.4-mm-dia holes drilled around its circumference. The purpose of the disk was to decelerate the liquid flow entering the small nozzle plenum. Interchangeable orifice plates were attached to the end of the plenum opposite the 19-mm-dia inlet. The smaller nozzle plenum was used to house the concentric screens described in Part 1 of this study, which were employed to alter the turbulence characteristics of the sharp-edged orifice plate. The screens were positioned in the small nozzle plenum on the downstream side of the plexiglass disk with drilled-hole array described in the foregoing. The same nozzle plenum and orifice plates (see Fig. 2, Part 1) were used in both the flow structure measurements of Part 1 and the heat transfer data to be reported here. The nozzle plenum was not used for the fully developed pipe-type nozzle, which was fed directly from the settling chamber, since the pipe-type nozzle was sufficiently long to eliminate any dependence on the fluid delivery configuration.

The impingement plate used for the heat transfer study, a 0.0254-mm-thick stainless steel foil, was installed in the upper box of the test chamber shown in Fig. 1. Each end of the foil was clamped tightly by a contoured copper bus bar, whose ends were made to slide in rectangular slots on two opposite walls of the upper box. Each end of the bus bars was connected to a screw bar, such that the foil tension could be adjusted. In this way, the stainless steel foil provided a tight, flat impingement surface. No further adjustment for the deformation of the foil during operation of water jets was necessary, since the threaded rod arrangement allowed the foil to be placed under sufficient tension so as to preclude any dimpling or deflection.

Water from a laboratory supply was used as the impingement fluid. The temperature of the supply water was very stable over time; after running for more than half an hour a temperature variance of $\pm 0.1°C$ could be obtained. Water passed through a flow meter (the same flowmeter as used in the flow structure measurements), entered the plenum from the bottom, passed through a nozzle on the top of the plenum, and impinged on the lower surface of the stainless steel foil. Thin plexiglass plates and rubber sheets were used to prevent water from splattering on the upper surface of the impingement plate, thereby contaminating the optical temperature measurements. The spent liquid was collected in the bottom of the test chamber and drained.

The HP 6031A System Power Supply units were applied to provide 20V d-c power to heat the stainless steel foil. Two units connected in parallel supplied up to 180 amp of current. The electrical resistance of the stainless steel foil was only slightly higher than the resistance of the connecting wires and bus bars, so the voltage drop and heat dissipation outside the foil could be significant. In order to minimize electrical resistance, heavy copper wires were used to connect the power supply units and the copper bus bars. The copper bus bars were designed to clamp the foil firmly with a large contact area, thus minimizing the electrical contact resistance. With these considerations, more than 70 percent of the power dissipation occurred in the foil. As will be described later, however, power dissipation for heat transfer calculations was measured directly at the foil surface.

The local temperature of the heated stainless steel foil was measured by an infrared scanner on its upper surface, while it was cooled with the water jet on the lower surface. The scanned surface of the heated foil was painted with flat black lacquer paint to (1) increase the emission signal in the infrared, and (2) reduce the signal contamination from reflection of background radiation. The temperature of the jet-exposed lower surface was required for the calculation of the local heat transfer coefficient. A finite-difference analysis of the plate revealed the lateral heat conduction in the foil to be negligible. Additionally, the one-dimensional heat conduction equation with generation was solved across the foil thickness to determine the difference in measured and liquid-side foil temperature. The analysis revealed that the maximum temperature difference between upper and lower surfaces of the heated foil was 0.13°C, which may be compared to the minimum temperature difference between jet and heated surface of 6°C. Estimates also revealed there to be negligible temperature drop across the paint layer. The heat dissipation from the upper surface by means of radiation and natural convection was calculated to be less than 0.08 percent of the Ohmic heat generated in the foil, so it was assumed that the upper surface was adiabatic and all of the energy generated in the foil was dissipated through the lower surface by means of the liquid jet impingement.

Four nozzle types were investigated in this study. The physical nozzle/plenum apparatus were the same as those described in Part 1 where the turbulent flow structure was outlined. All nozzles had the same diameter, $d = 10.9$ mm. As shown in Fig. 2 of Part 1, they included the fully developed pipe-type nozzle, the contoured orifice, and the sharp-edged orifice with and without damping screens in the plenum chamber. A more complete description of the nozzles used may be found in the companion paper, Part 1. As explained previously, a single nozzle-to-plate spacing of $z_o/d = 1$ was used in both the flow

Nomenclature

d = nozzle diameter
G = dimensionless radial velocity gradient in the stagnation region = $d(u/V_j)/d(r/d)$
h = local heat transfer coefficient
k = thermal conductivity
l = fully developed nozzle length
Nu = local Nusselt number based on nozzle diameter = hd/k
Nu_o = stagnation point Nusselt number
Pr = fluid Prandtl number
Q = volume flow rate
q = heat flux through the impingement plate
r = radial coordinate measured from the stagnation point
Re = jet Reynolds number = $4Q/\pi d\nu$
t = stainless steel foil heater thickness
T_o = measured temperature at the upper surface of the heated foil
T_s = local heated surface temperature
T_∞ = liquid jet temperature
u = radial component of velocity
u' = local rms fluctuation in the radial direction
V_j = average jet exit velocity
z = axial coordinate measured from the impingement plate
z_o = nozzle-to-plate spacing
ν = fluid kinematic viscosity

Downloaded 13 Dec 2010 to 193.140.21.150. Redistribution subject to ASME license or copyright; see http://www.asme.org/terms/Terms_Use.cfm

structure and local heat transfer studies. This spacing was selected because the flow structure facet of the work featured the jet impinging vertically downward, while the heat transfer portion used an upward-directed configuration. The nozzle-to-plate spacing used ensured that gravitational effects influenced the jets by less than 2 percent.

For each of the four nozzle configurations studied, heat transfer experiments were conducted at the same flow rates covering the range from 0.19 to 0.50 l/s, corresponding to the Reynolds number range of $16{,}500 \leq \mathrm{Re} \leq 43{,}500$. The same physical plenum was used in the heat transfer and flow field studies in order to insure that any influence of plenum conditions would be identical between the two types of measurements.

To characterize the heat transfer, Nusselt numbers were calculated from experimental temperature data. The local Nusselt number is defined as

$$\mathrm{Nu} = \frac{qd}{k\Delta T} \tag{1}$$

where $\Delta T = T_s - T_\infty$, T_s being the local surface temperature of the foil and T_∞ the water jet temperature at the nozzle exit.

Since the energy dissipation through the upper surface of the stainless steel foil was negligible compared to the heat generation in the foil, it was assumed that the upper surface was adiabatic. Hence, the applied heat flux was the Ohmic heat flux generated in the foil, and was calculated from electrical power considerations:

$$q = \frac{VI}{LW} \tag{2}$$

The current drawn by the heater foil, I, was measured by the power supply digital readout. The length and width of the heater foil over which the electrical power given by VI was dissipated were L and W, respectively. Since the voltage drop across the power supply lines and the bus bars was considerable, it was necessary to measure directly the voltage drop along the foil. For this purpose, small voltage taps were spot-welded a known spacing, $L = 79$ mm, along one edge of the foil, and wired to a multimeter. Very thin unpainted lines were masked on the scanned side of the foil. The drastic difference in emissivity (and hence, IR scanner signal) was used to determine the pixel resolution and the distance from the stagnation point.

The temperatures T_s and T_∞ were measured using thermal infrared radiometry. The thermal infrared imaging camera collects thermal emission (and reflection) from the upper surface of the stainless steel foil in the 8–12 μm spectral range. The two-dimensional infrared radiometer used is capable of scanning the entire plate, thus characterizing the local variation in heat transfer. The radiometer was calibrated by measuring the unheated foil temperature with a liquid jet of known temperature (measured in the settling chamber with a mercury-in-glass thermometer to 0.1°C) impinging on its underside. The jet temperature was varied over a range of temperatures that spanned those anticipated in the heat transfer experiments, 10°C–80°C, and a calibration curve was developed between measured and actual foil temperature.

Once the imaging camera had been calibrated, the impingement heat transfer study was undertaken. The determination of the heat transfer coefficient requires knowledge of both the liquid jet and the heated surface temperatures. The liquid jet temperature, T_∞, was measured by recording the thermal image of the plate with the impinging water, but *without* imposed electrical heating in the foil. The heat transfer coefficient is sufficiently high to ensure that the water temperature measured at the opposite surface of the unheated foil was in fact the same as that at the nozzle exit. The measurement of the local surface temperature, T_s, was conducted the same way as that of T_∞ but *with* heating imposed in the foil. Surface temperature data were recorded only after the temperature field of the stainless steel foil displayed by the thermal infrared camera was stable. Measurements of both T_s and T_∞ were corrected using the calibration function whose development was described in the foregoing.

The two-dimensional infrared image of the heated plate, detected by the thermal imaging camera, was recorded onto videotape using a conventional video cassette recorder. From the video tape, using a commercial image processing system, the infrared image data were extracted and the calibrated local temperatures were computed. Local Nusselt numbers were calculated from the measured temperature and power dissipation according to Eq. (1). Average Nusselt number data are reported elsewhere (Stevens, 1991).

Following the method of Kline and McClintock (1953), experimental uncertainties were estimated. Uncertainty in jet Reynolds number was dominated by the measurement of liquid flow rate, and was estimated at 7 percent. Experimental errors associated with the Nusselt number were limited primarily by the temperature measurement, which was influenced by the accuracy of the infrared imaging sensors, the digitization of the emission data, and the resolution of the calibration thermometer. The resulting uncertainty in Nu was evaluated at 5 percent or less. Both of these uncertainty measurements were based on 95 percent confidence levels.

Experimental Results

Stagnation Region Nusselt Numbers. Figures 2 and 3 present the local Nusselt number as a function of dimensionless radial position, r/d, in the near-stagnation zone for the contoured and fully developed nozzles, and sharp-edged orifice with and without screens, respectively. The data are shown for all Reynolds numbers investigated. Consider the results for the fully developed nozzle, given in Fig. 2(*b*). There exists a region of constant Nusselt number defined generally by $r/d \leq 0.5$. The local Nusselt number drops sharply to approximately 60 percent of its stagnation point value by $r/d = 2$. As expected, the Nusselt number increases with Reynolds number, the functional relationship of which will be described in a subsequent section. These observations are similar to those documented by Stevens and Webb (1991) for fully developed pipe type nozzles. The local heat transfer behavior of the contoured orifice (Fig. 2*a*) is similar to that of the fully developed nozzle. However, the magnitudes of Nu are somewhat lower for the same jet Reynolds number. More quantitative comparisons of all nozzles in this respect will be presented. Note also the off-stagnation-point maximum in local Nusselt number at $r/d \approx 0.5$. The increase, however, is only slight, amounting to 5–6 percent. This off-centerline maximum is also observed in the fully developed nozzle data, although its presence is less pronounced. This has not been observed in prior work, largely because of the limitations on the spatial resolution of the local temperature in previous work.

The sharp-edged orifice local Nusselt number data are shown in Fig. 3. The same qualitative characteristics found in other free-surface liquid jets are seen; high, relatively uniform local Nusselt number distributions are found in the stagnation zone, with a decrease in Nu in the radial jet region. The same off-stagnation maximum in Nu is observed in the sharp-edged orifice data. As with the fully developed nozzle and contoured orifice profiles of Fig. 2, the off-stagnation peak is only 5–6 percent higher than the stagnation point value. The off-stagnation peak may be the result of locally higher turbulence there, or the locally increased velocity gradient observed in the mean flow structure data for all nozzles in Figs. 3 and 4 of Part 1 of this study. Of more importance are the relative magnitudes of the local Nusselt number for the nozzle types investigated. Comparison of Figs. 2 and 3 reveals that the sharp-edged orifice

Downloaded 13 Dec 2010 to 193.140.21.150. Redistribution subject to ASME license or copyright; see http://www.asme.org/terms/Terms_Use.cfm

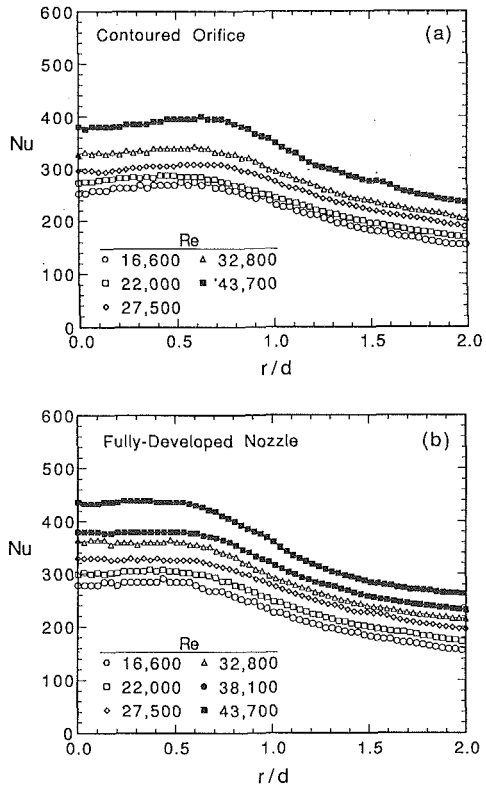

Fig. 2 Radial profiles of the local Nusselt number: (*a*) contoured orifice, and (*b*) fully developed nozzle

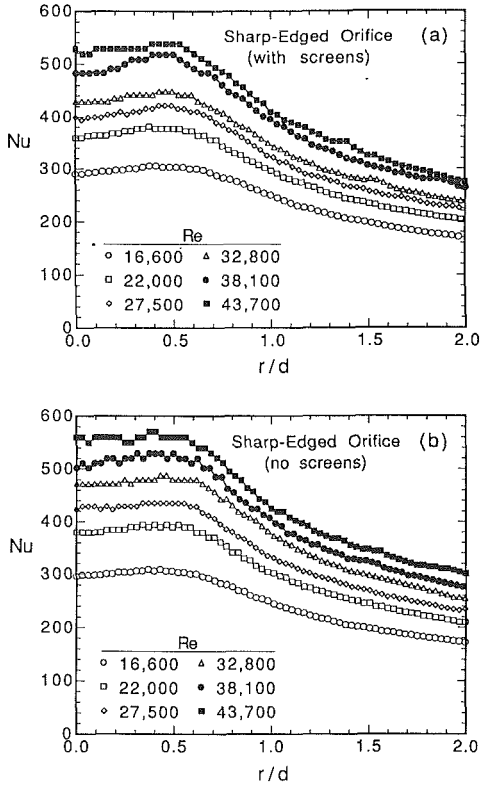

Fig. 3 Radial profiles of the local Nusselt number for the sharp-edged orifice: (*a*) with damping screens, and (*b*) without damping screens in the upstream nozzle plenum

yields significantly higher heat transfer characteristics than either the fully developed nozzle or contoured orifice.

Effect of Nozzle Configuration on Nusselt Number. The relative magnitudes of the local Nusselt number for the four nozzle configurations studied is documented in Fig. 4. The local heat transfer behavior is presented as a function of r/d for fixed jet Reynolds numbers Re = 22,000 and 43,700. Despite sharing the same general profile shape (Nu versus r/d), the four configurations yield distinctly different magnitudes in Nu. From highest to lowest Nusselt number, the data reveal the following ranking: sharp-edged orifice without screens, sharp-edged orifice with screens, fully developed pipe nozzle, and contoured orifice. This ranking matches the mean radial velocity gradient magnitudes found for the four configurations seen in Fig. 5 of Part 1. The difference in stagnation Nusselt numbers among the nozzle configurations studied is roughly 40 percent at both Reynolds numbers shown. Within a few percent, the ratios of stagnation Nusselt number for the four different nozzle types considered were found to be nearly independent of Re over the Reynolds number range studied. Recall that the measured mean radial velocity gradients were nearly independent of Reynolds number as well. It should be emphasized that these differences in the magnitudes of Nu are observed for the same flow rate (Re) through the different nozzles. The differences in Nu are significant and point to the careful characterization of nozzle type in any study.

Also of interest in Fig. 4 is the comparison of heat transfer for the sharp-edged orifice with and without damping screens. Recall that the general levels of rms turbulence for the no-screen case were approximately three times higher than the corresponding data with damping screens in the plenum. Further, the stagnation point mean radial velocity gradient for the two cases varied by only 8 percent (the screened configuration being higher). The data of Fig. 4 reveal that the sharp-edged orifice without damping screens yields stagnation heat transfer coefficients only 7–8 percent higher than the orifice with

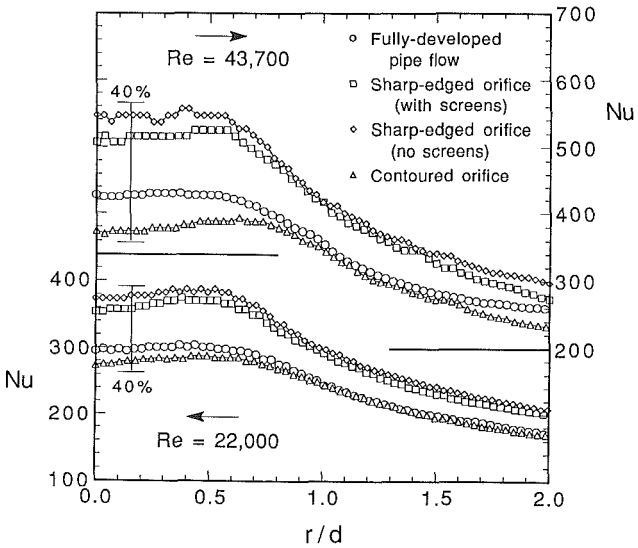

Fig. 4 Comparison of the local Nusselt number for the four nozzle configurations at Re = 22,000 and Re = 43,700

screens. This suggests that the effect of changes in jet turbulence level, as gaged by the fluctuations in radial velocity component, is less significant than changes in the mean radial velocity gradient in determining the heat transfer from a turbulent, free-surface liquid jet. This will be further explored and quantified in a section to follow.

It should be emphasized that the differences in Nu for the different nozzle geometries are for a nozzle-to-plate spacing of one diameter. One might expect that the relative differences in Nu would vanish as the nozzle exit were located at greater distances from the impingement plate (jet stability considerations aside). The increased spacing would provide more dis-

Downloaded 13 Dec 2010 to 193.140.21.150. Redistribution subject to ASME license or copyright; see http://www.asme.org/terms/Terms_Use.cfm

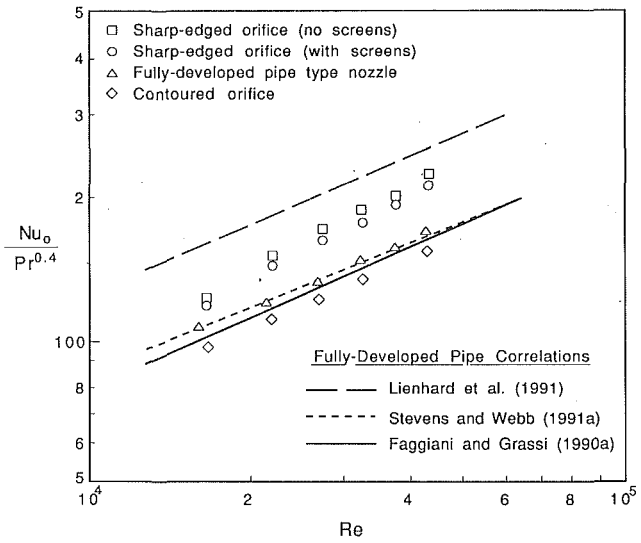

Fig. 5 Stagnation Nusselt number as a function of Reynolds number for the four nozzle configurations studied

tance for hydrodynamic development, and differences in the velocity profiles would vanish. Stevens and Webb (1992) have studied the pre-impingement development free-surface liquid jet from fully developed pipe flow. The free-surface velocity of the pre-impingement liquid jet was found to reach 90 percent of the average jet velocity just 2–3 diameters from the nozzle exit. The development length of other nozzle configurations, however, would be expected to be different.

Figure 5 illustrates the stagnation Nusselt number dependence on Reynolds number for the four nozzle configurations investigated. Although a single Prandtl number was used in this study, the 0.4 exponent on the Prandtl number was adopted arbitrarily based on results for different Prandtl number fluids in previous work (Ma et al., 1990). As was seen in Fig. 4, there are clear differences in the magnitude of the stagnation heat transfer coefficient for the four nozzle types. Differences of 40–50 percent are observed in $Nu_o/Pr^{0.4}$ for the same Reynolds number between the sharp-edged orifice without damping screens and the contoured orifice. Three prior correlations for fully developed pipe-type nozzles are also shown in the figure (Lienhard et al., 1991; Faggiani and Grassi, 1990a; Stevens and Webb, 1991). The correlations of Faggiani and Grassi (1990a) and Stevens and Webb (1991), and the fully developed nozzle data of this study, all of which focused on relatively low nozzle-to-plate spacings, agree to within ±4 percent. The correlation of Lienhard et al. (1991), however, is higher than the Nu_o data for all nozzle configurations studied. The focus of that study was the effect of jet splattering on heat transfer, and the Reynolds numbers and nozzle-to-plate spacings investigated were higher than those employed here. The implication is that jet conditions that result in splattering yield substantially higher heat transfer, possibly due to a combination of significantly higher turbulence, jet destabilization, and/or altered velocity gradient. Interestingly, if the heat transfer solution for the laminar infinite stagnation flow of White (1974) is evaluated using the velocity gradients of this study (measured experimentally for *turbulent* finite liquid jet flow and reported in Part 1 of this study), the predicted heat transfer coefficient results are within a few percent of the measured turbulent flow stagnation heat transfer coefficients. This agreement may only be fortuitous. On the other hand, it may suggest that the mean velocity gradient in turbulent liquid jets (which is undoubtedly affected by the turbulence level in the jet) adequately describes the combined effect of gradient and turbulence. This, however, cannot be conclusively confirmed.

Correlated Flow Structure and Heat Transfer. In order to assess the effects of the different velocity gradients, and levels of turbulence quantitatively, all data were correlated using a multivariate least-squares analysis for the stagnation Nusselt number, $Nu_o = f(Re, u'/V_j, G)$. The mean radial velocity gradient, $G = d(u/V_j)/d(r/d)$, was extrapolated to $z/d \rightarrow 0$, and the rms turbulence data were taken from corresponding vertical distances from the impingement plate from the data of Part 1 of the study. The resulting correlation of the heat transfer and flow structure data is:

$$Nu_o = 1.115 Re^{0.53} G^{0.63} (u'/V_j)^{-0.022} \quad (3)$$

Although based on only four independent variations in nozzle configuration, the results of Eq. (3) are noteworthy. The dependence of the average Nusselt number on $Re^{0.5}$, as suggested by the infinite stagnation flow solution (White, 1974), is evident. In the regression, the dependence of Nu_o on the turbulence level is seen to be negligible; over the 1 to 15 percent range of rms turbulence encountered in the flow structure experiments, $(u'/V_j)^{-0.022}$ changes by only 6 percent, and then in a direction opposite to the expected trend. This suggests that Nu_o and any independent effect of u'/V_j (independent of Re or G) are effectively uncorrelated. That is, once a threshold level of turbulence has been exceeded, the effect of further incremental changes in turbulence on the heat transfer may be adequately represented by the velocity gradient and Reynolds number, which would themselves be related to the turbulence level. This possibility is suggested by the aforementioned agreement between the measured results of this study and the laminar flow analysis of White (1974), evaluated using the measured turbulent flow velocity gradient. The small effect of incremental changes in turbulence level has been seen clearly in Fig. 4 by comparing heat transfer results for the sharp-edged orifice with and without turbulence damping screens in the upstream plenum. The rms turbulence levels without damping screens were nearly three times higher than those with the damping screens, yet the corresponding stagnation heat transfer coefficients for the two cases differ by only 7 percent. The results indicated by Eq. (3) for liquid jet impingement are in direct contrast with the results for air jets, where the free-stream turbulence level independently exerts a more significant influence on the stagnation heat transfer (Kestin and Wood, 1971; Hoogendoorn, 1977; Kataoka and Mizushina, 1974). Indeed, if the rms turbulence levels measured from this study could be used interchangeably with the free-stream turbulence in the correlation of Hoogendoorn (1977), one would expect a difference in Nu_o of 20–40 percent for the sharp-edged orifice data with and without screens. Again, the free-surface liquid jet data suggest that the minor effect of turbulence level may indicate that beyond a threshold level of turbulence (presumably reached by all nozzle types studied), the effect of further increases in turbulence level is minimal. The idea of a threshold turbulence level may also apply to prior studies for free-surface *planar* liquid jet impingement, and is not inconsistent with explanation of observed heat transfer augmentation in terms of vortex amplification in turbulent stagnation flows (Vader et al., 1991; Wolf et al., 1990; Zumbrunnen et al., 1989). Thus, of the three factors in the boundary layer that influence impingement region heat transfer [dimensionless jet velocity (Re), dimensionless velocity gradient (G), and free-stream turbulence level (u'/V_j)], the Reynolds number and velocity gradient appear to be of primary importance for already turbulent, free-surface liquid jets. Further, the Reynolds number and velocity gradient act independently in governing the transport.

In light of the negligible independent effect of changes in turbulence level shown by the correlation of Eq. (3), the u'/V_j term may be dropped from the relationship, yielding

$$Nu_o = 0.50 Re^{0.53} G^{0.58} Pr^{0.4} \quad (4)$$

This correlation represents all of the experimental data with a maximum error of 4 percent. The correlation of Eq. (4) is

Downloaded 13 Dec 2010 to 193.140.21.150. Redistribution subject to ASME license or copyright; see http://www.asme.org/terms/Terms_Use.cfm

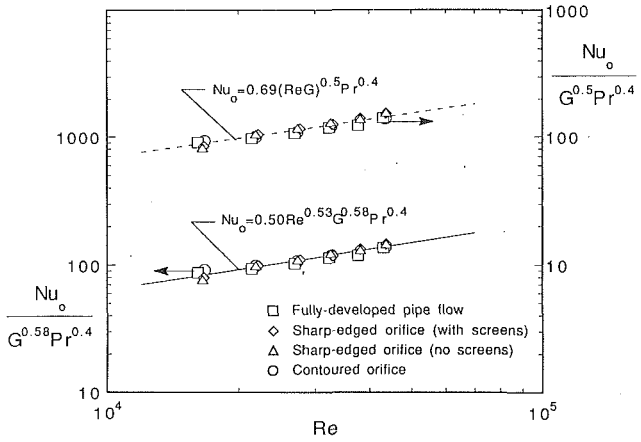

Fig. 6 Correlation of stagnation Nusselt number results

illustrated in Fig. 6 along with the experimental data from all tests. Based on the experimental measurements of the mean flow structure in the stagnation zone, a theoretical foundation for a stagnation Nusselt number dependence on $(ReG)^{0.5}$ has been shown (Stevens, 1991). If this dependence is required in the correlation of the experimental heat transfer data, Eq. (4) becomes

$$Nu_o = 0.69(ReG)^{0.5}Pr^{0.4} \tag{5}$$

This expression, which indicates that the heat transfer coefficient under a free-surface liquid jet depends equally on the jet Reynolds number and the velocity gradient, is also shown in Fig. 6. Again, the maximum deviation between Eq. (5) and the experimental data is small, 4 percent. Equation (5) explains to some degree the variance in published correlations for heat transfer characteristics of axisymmetric, free-surface liquid jets. Care must be taken to describe completely the issuing jet configuration and, even then, the effect of nozzle geometry on velocity gradient is not obvious.

It should be noted that the free-stream turbulence in this study is characterized by only the radial component of the fluctuating velocity. While the radial and axial components may be expected to scale similarly in the free stream, they may assume large differences in magnitude near the wall (Bird et al., 1960). More specific to this study, Tran and Taulbee (1989) predicted numerically (for planar stagnation flows) significantly larger axial velocity fluctuations than the corresponding velocity component parallel to the impingement surface. It seems likely that the axial component of the fluctuating velocity may have a greater influence on the stagnation region heat transfer. Thus, it may be conjectured that while significant differences in u' have been observed among the various nozzles, even greater differences in v' might prevail. Thus, while u' has been used to characterize the turbulence level for the nozzle configurations, levels of v' are likely higher, and are probably the more appropriate figure of merit. However, axial component mean and fluctuating velocity data could not be gathered in this study.

While Eq. (5) cannot be used in thermal design without knowledge of the stagnation point velocity gradient, G, it provides insight into the dependence of heat transfer on the hydrodynamic conditions in the stagnation region. The nozzle configurations whose flow structure was studied in Part 1 provide insight as to the magnitude of the velocity gradients for several different nozzle configurations. Further, the functional dependence of Nu_o on the velocity gradient may suggest directions for customized hydrodynamic tailoring to achieve enhanced heat transfer coefficient, and anticipated quantitative results.

Conclusions

The effect of selected nozzle configurations on heat transfer coefficients of single, axisymmetric turbulent water jets has been studied. For all Reynolds numbers studied the sharp-edged orifice without turbulence-damping screens provided the highest heat transfer coefficients, followed by the sharp-edged orifice with screens, the fully developed pipe-type nozzle, and finally, the contoured orifice. Differences in Nusselt number among the nozzle configurations were approximately 40 percent.

The dependence of heat transfer on nozzle configurations was found to be the result of hydrodynamic conditions, i.e., velocity gradient and turbulence level. In the impingement region, the heat transfer coefficient appears to be strongly influenced by the velocity gradient. The experimental data presented here for $z_o/d = 1$ and $16{,}500 \leq Re \leq 43{,}500$ show that the level of turbulence (as measured by fluctuations of the radial velocity component) independently plays only a secondary role in the stagnation zone heat transfer for liquid jets, which are already turbulent. For these experimental conditions, an empirical correlation of the heat transfer data suggests that the stagnation Nusselt number depends equally and independently on jet Reynolds number and mean radial velocity gradient. The results of this study were determined for a single nozzle-to-plate spacing of one nozzle diameter. Undoubtedly, different transport characteristics would emerge for other spacings.

Acknowledgments

This work was supported by the National Science Foundation under grant No. CBT-8552493.

References

Bird, R. B., Stewart, W. E., and Lightfoot, E. N., 1960, *Transport Phenomena*, Wiley, New York.

Faggiani, S., and Grassi, W., 1990a, "Round Liquid Jet Impingement Heat Transfer: Local Nusselt Numbers in the Region With Non Zero Pressure Gradient," *Proceedings International Heat Transfer Conference*, Vol. 4, G. Hetsroni, ed., Hemisphere Publ. Co., Washington, DC, pp. 197–202.

Faggiani, S., and Grassi, W., 1990b, "Impinging Liquid Jets on Heated Surfaces," *Proceedings International Heat Transfer Conference*, Vol. 1, G. Hetsroni, ed., Hemisphere Publ. Co., Washington, DC, pp. 275–285.

Hoogendoorn, C. J., 1977, "The Effect of Turbulence on Heat Transfer at a Stagnation Point," *International Journal of Heat and Mass Transfer*, Vol. 20, pp. 1333–1338.

Kataoka, K., and Mizushina, T., 1974, "Local Enhancement of the Rate of Heat Transfer in an Impinging Round Jet by Free Stream Turbulence," *Proceedings of the 5th International Heat Transfer Conference*, Vol. 2, pp. 305–309.

Kestin, J., and Wood, R., 1971, "The Influence of Turbulence on Mass Transfer From Cylinders," ASME JOURNAL OF HEAT TRANSFER, Vol. 93, pp. 321–327.

Kline, S. J., and McClintock, F. A., 1953, "Describing Uncertainties in Single-Sample Experiments," *Mechanical Engineering*, Jan., pp. 3–12.

Lienhard, J. H., V, Liu, X., and Gabour, L. A., 1991, "Splattering and Heat Transfer During Impingement of a Turbulent Liquid Jet," in: *Convective Heat Transfer and Transport Process—1991*, A. G. Lavine, M. K. Jensen, and M. A. Ebadian, eds., ASME, New York, pp. 51–60.

Liu, X., Lienhard, J. H., V, and Lombara, J. S., 1991, "Convective Heat Transfer by Impingement of Circular Liquid Jets," ASME JOURNAL OF HEAT TRANSFER, Vol. 113, pp. 571–582.

Lytle, D., and Webb, B. W., 1991, "Secondary Heat Transfer Maxima for Air Jet Impingement at Low Nozzle-to-Plate Spacings," in: *Proceedings Second World Conference on Experimental Heat Transfer, Fluid Mechanics, and Thermodynamics*, J. F. Keffer, R. K. Shah, and E. N. Gánic, eds., New York, pp. 776–783.

Ma, C. F., Sun, H., Auracher, H., and Gomi, T., 1990, "Local Convective Heat Transfer From Vertical Heated Surfaces to Impinging Circular Jets of Large Prandtl Number Liquids," *Proceedings 9th International Heat Transfer Conference*, Vol. 2, Hemisphere Publ. Co., Washington, DC, pp. 441–446.

Stevens, J. W., 1991, "Measurements of Local Fluid Velocities in an Axisymmetric, Free Liquid Jet Impinging on a Flat Plate," Ph.D. Dissertation, Brigham Young University, Provo, UT.

Stevens, J., and Webb, B. W., 1991, "Local Heat Transfer Coefficients Under an Axisymmetric, Single-Phase Liquid Jet," ASME JOURNAL OF HEAT TRANSFER, Vol. 113, pp. 71–78.

Stevens, J., and Webb, B. W., 1992, "Measurements of the Free Surface

Downloaded 13 Dec 2010 to 193.140.21.150. Redistribution subject to ASME license or copyright; see http://www.asme.org/terms/Terms_Use.cfm

Flow Structure Under an Impinging, Free Liquid Jet," ASME JOURNAL OF HEAT TRANSFER, Vol. 114, pp. 79–84.

Stevens, J., Pan, Y., and Webb, B. W., 1992, "Effect of Nozzle Configuration on Transport in the Stagnation Zone of Axisymmetric, Impinging Free-Surface Liquid Jets: Part 1—Turbulent Flow Structure," ASME JOURNAL OF HEAT TRANSFER (this issue).

Tran, L. T., and Taulbee, D. B., 1989, "Prediction of Stagnation Point Heat Transfer With Free Stream Turbulence," *Proc. 1989 National Heat Transfer Conference*, ASME Vol. HTD-107, New York, pp. 27–34.

Vader, D. T., Incropera, F. P., and Viskanta, R., 1991, "Local Convective Heat Transfer From a Heated Surface to an Impinging, Planar Jet of Water," *International Journal of Heat and Mass Transfer*, Vol. 34, pp. 611–623.

Wang, X. S., Dagan, Z., and Jiji, L. M., 1989, "Heat Transfer Between a Circular Free Impinging Jet and a Solid Surface With Nonuniform Wall Temperature or Wall Heat Flux—1. Solution for the Stagnation Region," *International Journal of Heat and Mass Transfer*, Vol. 32, pp. 1351–1360.

White, F. M., 1974, *Viscous Fluid Flow*, McGraw-Hill, New York.

Wolf, D. H., Viskanta, R., and Incropera, F. P., 1990, "Local Convective Heat Transfer From a Heated Surface to a Planar Jet of Water With a Nonuniform Velocity Profile," ASME JOURNAL OF HEAT TRANSFER, Vol. 112, pp. 899–905.

Zumbrunnen, D. A., Incropera, F. P., and Viskanta, R., 1989, "Convective Heat Transfer Distributions on a Plate Cooled by Planar Water Jets," ASME JOURNAL OF HEAT TRANSFER, Vol. 111, pp. 889–896.

Downloaded 13 Dec 2010 to 193.140.21.150. Redistribution subject to ASME license or copyright; see http://www.asme.org/terms/Terms_Use.cfm

Analysis of a Screen Heat Exchanger

G. F. Jones
Associate Professor,
Department of Mechanical Engineering,
Villanova University,
Villanova, PA 19085
Mem. ASME

F. C. Prenger
Staff Member,
Advanced Engineering Technology,
Los Alamos National Laboratory,
Los Alamos, NM 87545
Mem. ASME

Heat transfer in a fluid-to-fluid screen heat exchanger is analyzed from first principles. The screens are treated as an ensemble of pin fins and an empirical heat transfer coefficient accounts for convection heat transfer at the fin surface. Pressure drop and simultaneous axial conduction in the screen matrix and the wall separating the fluid streams are modeled. Expressions are obtained that relate dimensionless length ratios to exchanger effectiveness and pressure drop. The "mesh ratio," defined as the ratio of fin diameter (d) to spacing (s), prevails throughout the results. The key findings are: (1) the existence of an optimal ratio of fin length (a) to fin diameter that maximizes thermal performance (arising from the competition between the fin-length dependent heat transfer coefficient and fin surface area), (2) increasing a/d greater than optimal increases exchanger length and reduces pressure drop; for a/d less than optimal heat transfer is depressed and pressure drop increased, and (3) the pressure drop is linear with overall Ntu and varies as d^{-2}, $(1+d/s)^6$, and approximately the square of the mass flow rate per width of exchanger. An exact solution for axial conduction is presented that is valid in the limit of large Ntu and equal fluid capacity rates. Axial conduction is seen to decrease with increasing Ntu and mass flow rates and reduced fin a/d ratio. Predictions from the model are validated by comparing with published effectiveness and pressure-drop data.

Introduction

In an earlier paper the performance of a gas-to-plate screen heat exchanger (Jones and Prenger, 1990) was analyzed. A screen heat exchanger has the advantage of large heat transfer surface area and heat transfer coefficient and relatively small axial conduction (Lins and Elkan, 1975; Vonk, 1968). The latter feature is critical for good thermal performance when the exchanger is operated at cyrogenic temperatures. Several other concepts for cryogenic heat exchangers have been considered in the past. Among these are perforated plates (Flemming, 1969; Barclay and Sarangi, 1984), channels of rectangular and circular cross sections (Barclay and Sarangi, 1984), and poor-conducting circular tubes with intermittent bands of high-conductivity plating (Kroeger, 1967a).

In this note, we extend and apply the developments of the earlier paper to a fluid-to-fluid exchanger. Heat transfer is calculated from first principles by treating the screen as an ensemble of pin fins and by invoking an empirical correlation for the heat transfer coefficient. Pressure drop is modeled and the effect of axial conduction in both the matrix and adjoining wall is addressed. We produce a number of formulas for exchanger dimensions, pressure drop, and ineffectiveness and briefly discuss a procedure for their application.

Analysis

1 Geometry and Assumptions. The geometry is shown in Fig. 1. A large number of rectangular screens of height a and width b are separated by an equal number of poorly conducting spacers of uniform thickness t_{sp} and positioned in two parallel fluid-filled channels. The channels are connected by an impermeable common wall as shown. The faster-flowing fluid is designated by the subscript max and the other by the subscript min. Heat is transferred between the two fluids by convection at the surface of the screens and conduction in the screen wires. The casing of the exchanger is insulated. Each screen is composed of very fine mesh of circular wires, the wires having diameter d and spacing s. The wires normal to the common wall are pin fins of length a while the transverse wires provide support for the fin wires. Conduction occurs only in the wires over the thickness t_w of the common wall. The fluid streams enter at temperature T_i and exit at temperature T_o for each channel.

We assume steady-state conditions and that thermophysical properties for each fluid stream and the screen material in each fluid stream are constant. The fluid in each stream is taken to be cross-sectionally isothermal at each location in the direction of flow; a consequence of mixing caused by lateral motion of the gas as it passes through staggered screens. The alternate approach in Flemming (1969), which assumes a constant heat transfer rate along the fin wires, produces fin efficiencies to within 3 percent of those here. Thus, there is little to choose between the two approaches. The fins are treated as quasi-two-dimensional with the principal temperature distribution along the fin length. The temperature distribution in the fins in the direction of fluid flow is imposed by the fluid.

2 Heat Transfer. The steady-state, constant-property energy equation is solved to obtain the total heat transfer rate Q for an ensemble of convecting fins (Incropera and DeWitt, 1990). The usual fin parameter, m, appears in this expression.

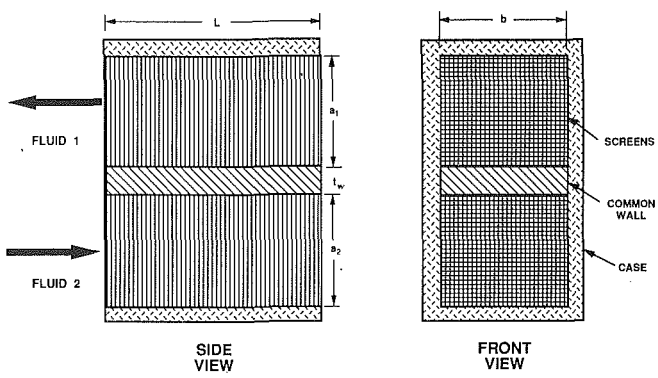

Fig. 1 Geometry

Contributed by the Heat Transfer Division for publication in the JOURNAL OF HEAT TRANSFER. Manuscript received by the Heat Transfer Division January 1991, revision received April 1992. Keywords: Conduction, Cryogenics, Heat Exchangers. Associate Technical Editor: W. A. Fiveland.

Copyright © 1992 by ASME
Downloaded 13 Dec 2010 to 193.140.21.150. Redistribution subject to ASME license or copyright; see http://www.asme.org/terms/Terms_Use.cfm

Substituting for the heat transfer coefficient in m and defining an overall heat transfer coefficient U_{tot} as $Q/[bL(T_{max}-T_{min})]$, we can write

$$1/U_{tot} = 1/U_{min} + 1/U_{max} + 1/U_w, \quad (1a)$$

where

$$U_i d = \{2/(1-\alpha)\}^{(2p-3)/(2-p)} \Gamma^{(1-p)/(2-p)} \cdot \{k_s (4\, c\, \mathrm{Pr}^q\, k_f/k_s)^{1/(2-p)} M^{p/(2-p)} F\}_i, \; i = \min, \max \quad (1b)$$

and

$$U_w d = \{(1-\alpha)/2\}\, k_s d/t_w. \quad (1c)$$

M is a dimensionless mass flow rate per width $\dot{m}/(\mu b)$ [M is equivalent to a Reynolds number based on mean velocity in an empty channel and channel height a] and L is the exchanger length. The variable f^* in the parameter Γ in Eq. (1b) is a dimensionless number between 0 and 1 that accounts for reduced heat transfer surface area for a fin wire due to flow blockage from a cross wire. f^* of 0 corresponds to no blockage and 1 to maximum blockage (i.e., a cross wire completely eliminates surface area $\pi d \times d$ of a fin wire where the two overlap). As shown below f^* has little effect on exchanger performance and so a nominal value of f^* (say 0.5) can be taken without much loss of accuracy.

In Eqs. (1) we have assumed a heat transfer coefficient from Qvale and Smith (1969)

$$hd/k_f = c\{4(1+t_{sp}/d)/R\}^{(p-1)} \{M d/a\}^p \mathrm{Pr}^q, \quad (2)$$

where c, p, and q have the values 1.1, 0.59, and 1/3, respectively. R is the ratio of the wetted surface area of a screen to the product ab and gives rise to the parameter f^* appearing in Eq. (1b) through the term Γ. Equation (2), which is based on data of Kays and London (1964), applies to flow over staggered tubes and rods, and randomly stacked screens or cross rods. Heat transfer coefficients from Eq. (2) compared well with data in independent tests (Kim and Qvale, 1971) and here are compared with data for in-line stacked screens from Kays and London (1964) and a correlation from Zukauskas (1987). The comparison shows that Eq. (2) overpredicts h for inline screens by about 20 percent (for d/s of 1.75) to 40 percent (for d/s of 0.71) but for staggered geometries is in reasonably good agreement (15 percent or better) with data as claimed by Qvale and Smith. The correlation of Zukauskas, which applies to an array of staggered circular tubes, $hd/k_f = 1.04\{M\,(d/a)(1+d/s)^2\}^{0.4}\,\mathrm{Pr}^{0.36}$, agrees with data to within 15 percent at low gas flow rates but at larger flow rates overpredicts h for small values of d/s and underpredicts for higher d/s values.

Appearing in Eqs. (1) is the term

$$F = \{(ma)_{opt}\}^{p/(p-2)} \tanh(ma)_{opt}, \quad (3)$$

for each channel where $(ma)_{opt}$ is determined from the solution of

$$(2/p-1)(ma)_{opt} - \sinh(ma)_{opt} \cosh(ma)_{opt} = 0. \quad (4)$$

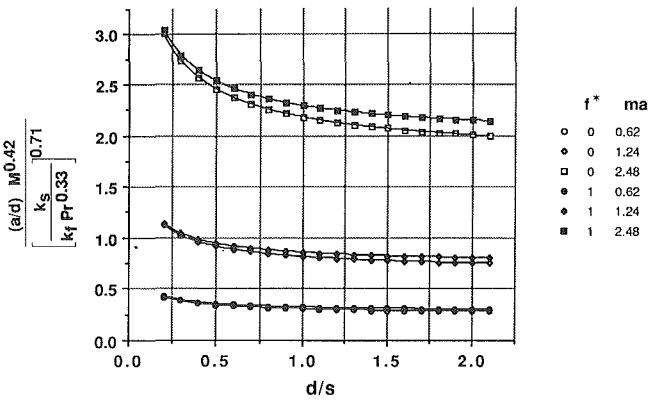

Fig. 2 Fin aspect ratio

$(ma)_{opt}$ is an optimal value for the product of the fin parameter m and fin height a. The existence of an optimal (ma) for each channel arises from two competing effects. For a constant $\dot{m}/b$ (i.e., constant M) increasing the channel height a decreases the flow speed and thus heat transfer coefficient [see Eq. (2)]. Simultaneously, the area for convection at the surface of the fins increases. Since the former effect tends to reduce U_{tot} and the latter tends to increase it, there exists an optimal fin height that maximizes fin heat transfer. For p of 0.59, $(ma)_{opt}$ of 1.24 is obtained from Eq. (4). This can be contrasted with (ma) of about 3 corresponding to the classical "infinitely long" fin.

The definition of m is combined with Eq. (2) to give an expression for fin aspect ratio, a/d

$$a/d = (c\,\mathrm{Pr}^q\, k_f/k_s)^{1/(p-2)} M^{p/(p-2)} [(ma)/2]^{2/(2-p)} \{2/\Gamma(1-\alpha)]\}^{(1-p)/(2-p)} \quad (5)$$

for each channel of the exchanger. For prescribed M, t_{sp}/d, thermophysical properties, f^*, and optimal (ma), fin aspect ratio depends upon only the "mesh ratio," d/s, which can be freely chosen. Guidelines for choice of mesh ratio are discussed below.

Equation (5) is presented in Fig. 2 to focus on the effects of f^*, (ma), and mesh ratio on fin aspect ratio. In Fig. 2, values for (ma) of optimal, twice optimal, and half optimal are shown while f^* ranges from 0 to 1. For optimal (ma) and smaller, a/d shows only weak sensitivity to mesh ratio (this is contrasted with strong pressure drop dependence on mesh ratio as discussed below). However, a/d is strongly dependent on (ma) as seen in Fig. 2. For (ma) less than optimal, a/d is smaller and the heat transfer coefficient larger than optimal but reduced fin surface area depresses thermal performance. For (ma) greater than optimal, a/d is larger, resulting in a smaller heat transfer coefficient, which, in turn, reduces thermal performance. In addition, a/d is also only weakly sensitive

Nomenclature

C_p = specific heat at constant pressure, J/g-K
C_r = $(\dot{m}C_p)_{min}/(\dot{m}C_p)_{max}$
e = heat exchanger effectiveness = $(T_{min,0}-T_{min,i})/(T_{max,i}-T_{min,i})$
h = convective heat transfer coefficient, W/m^2 K
i = heat exchanger ineffectiveness = $1-e$
k = thermal conductivity, W/m-K
m = fin parameter = $(2/d)(h\,d/k_s)^{1/2}$, m^{-1}
Ntu = number of transfer units = $UA/(\dot{m}C_p)_{min}$
Pr = Prandtl number = $\mu C_p/k_f$
T = temperature, K
t = thickness, m
U = overall heat transfer coefficient, W/m^2 K
α = porosity = 1 − ratio of volume of screens to volume of empty exchanger = $1-\pi/\{2(1+t_{sp}/d)(1+s/d)\}$
Γ = $1-f^*/[(1+s/d)\pi]$
μ = dynamic viscosity, g/cm-s
ρ = density, g/cm^3

Subscripts

f = fluid
i = fluid at inlet to exchanger
o = fluid at outlet from exchanger
opt = thermally optimal
s = screen
sp = spacer
tot = refers to entire exchanger
w = wall

Downloaded 13 Dec 2010 to 193.140.21.150. Redistribution subject to ASME license or copyright; see http://www.asme.org/terms/Terms_Use.cfm

to f^* for all $(m\,a)$ so that choosing f^* as a nominal value (say, 0.5) has little effect on the fin aspect ratio.

From the definition of $\mathrm{Ntu}(e, C_r)$ we obtain

$$\mathrm{Ntu}(e, C_r) = (L/d)\,(U_{\mathrm{tot}}\,d)/\{M_{\min}\,(\mu C_p)_{\min}\}. \quad (6)$$

C_r is the usual ratio of minimum to maximum fluid capacity rates and e is the heat exchanger effectiveness. Relationships between Ntu and terms e and C_r for different heat exchanger configurations are found in any elementary text on heat transfer (Incropera and DeWitt, 1990) although for cryogenic applications focus is typically on counterflow exchangers where $e = \mathrm{Ntu}/(\mathrm{Ntu}+1)$ for $C_r = 1$. The product $U_{\mathrm{tot}}\,d$ is from Eqs. (1). With

$$M_{\max} = M_{\min}\,(\mu C_p)_{\min}/(\mu C_p)_{\max}/C_r, \quad (7)$$

Eq. (6) relates e to C_r, L/d, mesh ratio, $M_{\min}$, t_w/d, t_{sp}/d, and thermophysical properties. We see through Eq. (6) that the effectiveness is increased by increasing L/d and $U_{\mathrm{tot}}\,d$. Also, by inspecting Eqs. (5) and (6), we note that both a/d and L/d are independent of any exchanger length dimension.

3 Pressure Drop. Because of the very large number of fin and cross wires in the exchanger, a conservative approach for pressure drop might be to model the exchanger as a packed bed (see, for instance the correlation of Gabor and Botterill, 1985). However, this approach produces friction factors that are much larger than those of Kays and London (1964) for staggered cross-rod geometries and Vonk (1968) for screens.

Friction factor data of Kays and London for $0.60 < \alpha < 0.83$ were fit to the following form:

$$f = 1.8\,\alpha\,\{2M\,(a/d)/[\Gamma(1-\alpha)]\}^{-0.11/\alpha}, \quad (8a)$$

where the term in curly braces is the Reynolds number defined by Kays and London. Alternately, a more-involved correlation from Tong and London (1956) could be used. Equation (8*a*) agrees with the data to within 15 percent over the range of Reynolds numbers from Kays and London. For porosity less than 0.6, Eq. (8*a*) underestimates f (for $\alpha = 0.5$, between 23 and 40 percent) while the trend is toward generally good agreement for porosity greater than 0.83. The pressure drop is related to f in the same way as given by Kays and London.

$$\Delta P = (\mu^2\rho^{-1}a^{-2})\,M^2(1+d/s)^6 f\,(L/d)\,\Gamma(1-\alpha) \quad (8b)$$

for each channel of the exchanger. With Eqs. (5), (6), and (7), Eqs. (8) relate ΔP to mesh ratio, e, C_r, $M_{\min}$, t_w/d, t_{sp}/d, thermophysical properties, and fin height, a. The term $\mu^2\rho^{-1}a^{-2}$ is a characteristic pressure drop per fin wire, which for cryogenic gases is on the order of 10^{-10} kPa. Recall that for optimal $(m\,a)$, a/d is constant [see Eq. (5)]. From this we see by inspecting Eq. (8*b*) that pressure drop is proportional to d^{-2}. ΔP is also very sensitive to M (to nearly the power 2) and mesh ratio as seen in Eq. (8*b*).

4 Effect of Conduction in the Direction of Fluid Flow. The object of any non-phase-change heat exchanger is to increase or decrease the temperature of a fluid in the direction of flow. Conduction in the direction of flow (axial conduction) always acts to oppose the temperature change, thus reducing exchanger effectiveness. Axial conduction is important in cryogenic heat exchangers because of the large thermal conductivities of most fluids and metals at reduced temperatures. In exchangers operating at room temperature, thermal conductivities are normally small enough that axial conduction can be neglected provided flow speeds are not small. Kroeger (1967b) considered axial conduction through just the common wall of cryogenic heat exchangers and obtained ineffectiveness results that for $C_r = 1$ and large Ntu were in general agreement of those from the simplified analysis of Kays and London (1964) (obtained by assuming equal axial temperature gradients in both fluids and the wall). For large Ntu and small conductance, the results of Bahnke and Howard (1964), who considered axial conduction in the matrix of a regenerator, likewise agreed with those from the simplified approach (see also Sarangi and Banal, 1987).

In the present treatment, we consider axial conduction in the common wall and the matrix to accommodate all designs including those that have matrix-to-wall conductance ratios of order unity.

Axial conduction in the matrix can be envisioned as occurring in the fluid as a consequence of the quasi-two-dimensional assumption. This approach requires knowledge of the spacer conductance and contact conductance between a spacer and screen that would be determined from laboratory tests (see, for example, Hermann and Radebaugh, 1986). The steady-state energy balances on the min and max fluid streams and common wall are

$$\epsilon\Omega_1 d^2T_{\min}/dy^2 - dT_{\min}/dy - (\beta/\epsilon)\,(T_{\min} - T_w) = 0, \quad (9a)$$

$$\epsilon\Omega_2 d^2T_{\max}/dy^2 + dT_{\max}/dy - (C_r/\epsilon)\,(T_{\max} - T_w) = 0, \quad (9b)$$

$$\epsilon\Omega_w d^2T_w/dy^2 + (1/\epsilon)[\beta T_{\min} + T_{\max} - (1+\beta)T_w] = 0, \quad (9c)$$

where y is the coordinate in the direction of min fluid flow made dimensionless by L. In Eqs. (9), $\beta = \mathrm{Ntu}_{\min}/\mathrm{Ntu}_{\max}$, $\epsilon = \beta/[(1+\beta)\ \mathrm{Ntu}_{\min}]$, $\Omega_1 = \Omega_{\min}\ (1+\beta)/\beta$, $\Omega_2 = \Omega_{\min}\ C_r[(1+\beta)/\beta]\,[(a\,k_{\mathrm{eff}})_{\max}/(a\,k_{\mathrm{eff}})_{\min}]$, and $\Omega_w = \Omega_w^*\,(1+\beta)/\beta$. The terms $\Omega_{\min}$ and Ω_w^* are dimensionless axial conductances for the min fluid and wall that control the effect of axial conduction,

$$\Omega_{\min} = \{(a/d)[k_{\mathrm{eff}}/(k_f \mathrm{Pr}\,M)]\}_{\min}[\mathrm{Ntu}/(L/d)], \quad (10a)$$

and

$$\Omega_w^* = (t_w/d)k_w\{[1/(k_f \mathrm{Pr}\,M)]\}_{\min}[\mathrm{Ntu}/(L/d)], \quad (10b)$$

where $k_{\mathrm{eff,min}}$ is the effective axial conductivity for the min fluid and k_w is the conductivity of the wall both in the direction of fluid flow. $\Omega_{\min}$ and Ω_w^* can range from near zero for cases where axial conduction is negligible to 10 and greater where axial conduction is severe. In Eqs. (10), we note that the ratio $\mathrm{Ntu}/(L/d)$ is independent of L/d and Ntu, which is evident from inspection of Eq. (6).

The boundary conditions are a specified inlet fluid temperature for each channel and zero fluid temperature gradients at each channel outlet. Wall temperature gradients are zero at both ends of the exchanger.

Equations (9) are solved analytically for $C_r = 1$ in the limit of large Ntu under the assumption of equal Ntu and equal k_{eff} for both streams. Details are presented in the appendix. A complete solution of Eqs. (9) for all C_r and Ntu can be found elsewhere (Jones and Whitman, 1992). The case for $C_r = 0$ was solved previously by Jones and Prenger (1990). Once the temperature distributions are obtained, the exchanger effectiveness is evaluated from the outlet fluid temperature for the min stream.

Ineffectiveness is plotted in Fig. 3 as a function of Ntu for $\Omega_{\min}$ of 0.5, 2.5, and 5.0 for $C_r = 1$, and $\Omega_{\min}$ of 0.5 and 5.0 for $C_r = 0.9$. On each graph, values of Ω_w^* range from 0 to 50. The trends indicate increased ineffectiveness with $\Omega_{\min}$ and Ω_w^* as expected. As Ntu increases, ineffectiveness decreases in all cases resulting from the increase in exchanger length [see Eq. (6)] (recall that $\Omega_{\min}$ and Ω_w^* are independent of Ntu and exchanger length). For Ω_w^* of one or less and $\Omega_{\min}$ of 0.5, results agree well with those of Kroeger (1967b), who considered only wall conduction, demonstrating the weak effects of matrix conduction for $\Omega_{\min}$ of 0.5. Consistent with the results of Kroeger, ineffectiveness values for imbalanced flow tend to be smaller than their balanced counterparts, an effect due to the asymptotic nature of the temperature distribution for the min fluid near the outlet.

Comparison With Data

Lins and Elkan (1975) obtained heat transfer and pressure drop data for a cryogenic counterflow heat exchanger 26.7 cm

Downloaded 13 Dec 2010 to 193.140.21.150. Redistribution subject to ASME license or copyright; see http://www.asme.org/terms/Terms_Use.cfm

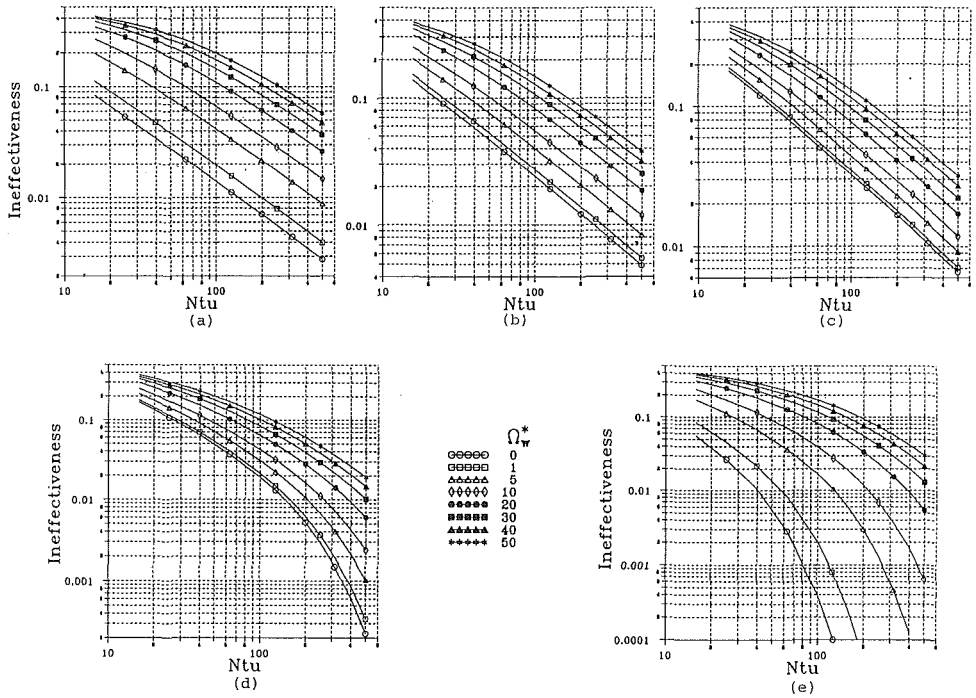

Fig. 3 Ineffectiveness: $C_r = 1$: (*a*) $\Omega_{min} = 0.5$; (*b*) $\Omega_{min} = 2.5$; (*c*) $\Omega_{min} = 5.0$. $C_r = 0.9$: (*d*) $\Omega_{min} = 5.0$; (*e*) $\Omega_{min} = 0.5$.

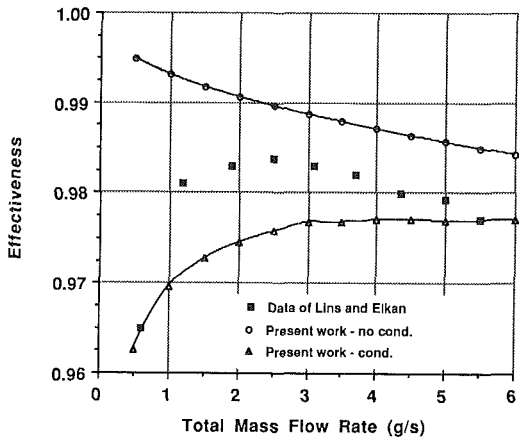

Fig. 4 Effectiveness versus mass flow rate

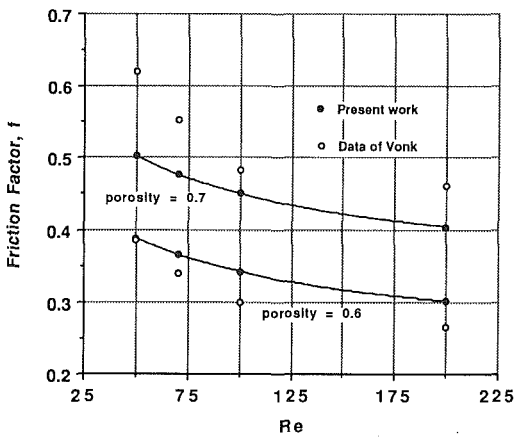

Fig. 5 Friction factor versus mass flow rate; Re is Reynolds number as defined by Vonk (1968)

in diameter and 11.4 cm long. The cross section of the ring-shaped exchanger consisted of 60 alternating hot and cold helium-flow passages. The passages were formed by plastic separating walls and were interconnected by wire screens of ETP copper. Generally, the exchanger is like 30 parallel modules similar to that shown in Fig. 1. The following data apply to this exchanger: $s/d = 1.23$ (assumed 60 mesh screen on average), $d = 0.01905$ cm, $a/d = 117$, $L/d = 599$, $b = 10.795$ cm, $f^* = 0.5$ (assumed), and $\mu = 35.8 \times 10^{-6}$ g/cm-s from which we calculate $\alpha = 0.65$ and $\Gamma = 0.93$.

Effectiveness predicted by Eq. (6) (no axial conduction) and Eq. (A1) (with axial conduction) are compared with the measured values of Lins and Elkan in Fig. 4. Accurate assessment of axial conduction of the Lins and Elkan exchanger is difficult because of construction uncertainties. For the purpose of estimation, we assumed axial conduction only in the plastic common wall of thermal conductivity 0.05 W/m-K and a matrix conductance equal to one-third of that for the wall. From Fig. 4, we see that agreement is generally good with the effectiveness from the model bracketing the data. For flow rates less than 2 g/s, the data show a considerable reduction in effectiveness with flow not predicted by Eq. (6). The results from Eq. (1*a*) clearly show that this discrepancy arises from the neglect of axial conduction in Eq. (6). Inspection of Eq. (10) shows that axial conductance, and thus ineffectiveness, increases with decreasing mass flow rate (the Ω parameters are inversely proportional to M). The effectiveness from Eq. (A1) exhibits a broad maximum at a greater mass flow rate than is evident from the data. By adjusting the assumed value of the dimensional wall conductance, it is possible to obtain better agreement between the two.

Friction factors calculated from Eq. (8*a*) are compared with the data of Vonk (1968) in Fig. 5. His exchanger is fundamentally similar to that of Lins and Elkan except that it is rectangular. In Fig. 5 Re is the Reynolds number based on flow in an open (unfilled) exchanger and wire diameter, and friction factor is defined as in Eq. (8*a*). In the calculations we assumed t_{sp}/d of 0.5 to estimate the number of screens in the exchanger. In Fig. 5, except for α of 0.7 at the lowest Reynolds number, calculated f values agree with the data to within 15

Downloaded 13 Dec 2010 to 193.140.21.150. Redistribution subject to ASME license or copyright; see http://www.asme.org/terms/Terms_Use.cfm

percent. Better agreement may be expected at larger Reynolds numbers. Reynolds numbers from the data of Vonk were below or at the lowest values for which Eq. (8*a*) is valid. Comparison of Eq. (8*a*) with f calculated from the pressure drop data of Lins and Elkan is not possible because of their extremely small values of Re.

Procedure

For known thermophysical properties and chosen $\dot{m}/b$, a is first estimated using Eq. (5). This is done by selecting a mesh ratio, d/s, and wire diameter, d, from commercially available candidates. Reducing d/s for a fixed d will decrease pressure drop [see Eq. (8*a*)] and height (see Fig. 2; for large d/s, a/d is insensitive to d/s). Reducing d for a fixed mesh ratio will decrease height [since a/d is a function of mesh ratio and not d; see Eq. (5)] and increase pressure drop [see Eqs. (8)].

The fin aspect ratio, a/d, should be based on optimal $(m\,a)$. Increasing $(m\,a)$ greater than optimal will increase exchanger height (see Fig. 2), reduce pressure drop [see Eqs. (8)], and increase exchanger length since the thermal performance of the exchanger per unit length is reduced [F and thus U_{tot} are reduced; see Eqs. (3) and (1)]. An $(m\,a)$ less than optimal is always undesirable from a performance standpoint since heat transfer per unit length of exchanger is reduced (as it was for $(m\,a)$ greater than optimal) and pressure drop is increased [see Eq. (8*b*)]. However, the reduction of exchanger height may be desirable from the standpoint of reduced volume or cost should these occur.

After prescribing e (or L/d), L/d (or e), and ΔP are determined next, from Eqs. (6) and (8). The ineffectiveness is found using Fig. 3 or alternately, the equations in the appendix. If ΔP, e, or L/d are unacceptable, d, $(m\,a)$, or k_s can be increased or e (or L/d) or $\dot{m}/b$ can be reduced and the procedure repeated.

Conclusions

We have analyzed a screen heat exchanger for cryogenic applications by treating the screen as an ensemble of pin fins. We find that an optimal fin aspect ratio (a/d) exists that maximizes thermal performance. Closed-form expressions for exchanger geometry and pressure drop (ΔP) versus exchanger effectiveness (e), flow rates, and thermophysical properties are obtained and verified by comparing with limited data, and a design procedure is described. The porosity appears consistently in all expressions that, for constant ratio of spacer thickness to fin diameter, d, are dependent upon only the mesh ratio, d/s. A closed-form expression for ineffectiveness was developed by considering simultaneous axial conduction in the matrix and common wall. Among our findings are:

1 Increasing the fin aspect ratio to greater than optimal increases the exchanger length and reduces ΔP, whereas an aspect ratio less than optimal is always undesirable from the perspective of heat transfer and pressure drop.
2 a/d decreases with increased mesh ratio, which for optimal and suboptimal conditions is a very weak effect.
3 Exchanger length and height are linear with fin diameter (all remaining variables fixed).
4 ΔP is linear with Ntu and proportional to: d^{-2}, approximately $(1+d/s)^6$, and nearly the square of mass flow rate per width of exchanger.
5 Ineffectiveness depends only on Ntu and two dimensionless axial conduction parameters corresponding to the matrix and wall. As Ntu increases, ineffectiveness decreases resulting from the increase in exchanger length.

References

Bahnke, G. D., and Howard, C. P., 1964, "The Effect of Longitudinal Heat Conduction on Periodic-Flow Heat Exchanger Performance," ASME *Journal of Engineering for Power*, Vol. 86, pp. 105–119.

Barclay, J. A., and Sarangi, S., 1984, "Selection of Regenerator Geometry for Magnetic Refrigerator Applications," in: *Cryogenic Processes and Equipment—1984*, P. J. Kerney, N. Chatterjee, D. B. Crawford, and M. El-Masri, eds., ASME, pp. 51–58.

Flemming, R. B., 1969, "A Compact Perforated Plate Heat Exchanger," *Advances in Cryogenic Engineering*, K. D. Timmerhaus, ed., Plenum Press, Vol. 14, pp. 197–204.

Gabor, J. D., and Botterill, J. S. M., 1985, "Heat Transfer in Fluidized and Packed Beds," in: *Handbook of Heat Transfer Applications*, W. M. Rohsenow, J. P. Hartnett, and E. N. Ganic, eds., McGraw-Hill, New York.

Herrmann, S., and Radebaugh, R., 1986, "Measurements of Efficiency and Refrigeration Power of Pulsed Tube Refrigerators," NBS Tech. Note TN-1301, National Institute of Standard and Technology, Boulder, CO.

Incropera, F. P., and DeWitt, D. P., 1990, *Introduction to Heat and Mass Transfer*, Wiley, New York.

Jones, G. F., and Prenger, F. C., 1990, "Analysis of a Gas-to-Plate Screen Heat Exchanger for Cryogenic Applications," ASME HTD-Vol. 167, pp. 1–9.

Jones, G. F., and Whitman, A. M., 1992, "Exact Solution for Axial Conduction in a Thick-Wall Matrix Heat Exchanger," submitted to *Int. J. Heat Mass Trans.*

Kays, W. M., and London, A. L., 1964, *Compact Heat Exchangers*, McGraw-Hill, New York.

Kim, J. C., and Qvale, E. B., 1971, "Analytical and Experimental Studies of Compact Wire-Screen Heat Exchangers," *Advances in Cryogenic Engineering*, K. D. Timmerhaus, ed., Plenum Press, Vol. 16, pp. 302–311.

Kroeger, P. G., 1967a, "Plated-Tube Heat Exchanger: Analytical Investigation of a New Surface Concept," *Advances in Cryogenic Engineering*, K. D. Timmerhaus, ed., Plenum Press, Vol. 12, pp. 340–351.

Kroeger, P. G., 1967b, "Performance Deterioration in High-Effectiveness Heat Exchangers Due to Axial Conduction Effects," *Advances in Cryogenic Engineering*, K. D. Timmerhaus, ed., Plenum Press, Vol. 12, pp. 363–372.

Lins, R. C., and Elkan, M. A., 1975, "Design and Fabrication of Compact, High Effectiveness Cryogenic Heat Exchangers Using Wire Mesh Surfaces," *Advances in Cryogenic Engineering*, K. D. Timmerhaus, ed., Plenum Press, Vol. 20, pp. 283–299.

Qvale, E. B., and Smith, J. L., 1969, "A Simple Correlation for the Heat Transfer Characteristics of a Family of Matrices Subjected to Complex Flow Conditions," *Cryogenics*, Vol. 9, pp. 62–63.

Sarangi, S., and Banal, H. S., 1987, "Effects of Axial Conduction in the Fluid on Cryogenic Regenerator Performance," *Cryogenics*, Vol. 27, pp. 505–509.

Tong, L. S., and London, A. L., 1956, "Heat Transfer and Flow-Friction Characteristics of Woven-Screen and Crossed-Rod Matrices," *Trans. ASME*, Vol. 79(10), pp. 1558–1570.

Vonk, G., 1968, "A New Type of Compact Heat Exchanger With a High Thermal Efficiency," *Advances in Cryogenic Engineering*, K. D. Timmerhaus, ed., Plenum Press, Vol. 13, pp. 582–589.

Zukauskas, A., 1987, "Convective Heat Transfer in Cross Flow," in: *Handbook of Single Phase Convective Heat Transfer*, R. Kakic, R. K. Shah, and W. Aung, eds., Wiley, New York.

APPENDIX

Solution of Eqs. (9) for $C_r = 1$ in the Limit of Large Ntu Under the Assumption of Equal Ntu and Equal k_{eff} for Both Streams

Using classical methods, Eqs. (9) have the following general solution:

$$\phi_{\min} = \epsilon(D - C/\beta) + Cy + A_1 \exp(s_1 y/\epsilon) + A_2 \exp(s_2 y/\epsilon) + A_3 \exp(s_3 y/\epsilon) + A_4 \exp(s_4 y/\epsilon), \quad \text{(A1)}$$

$$\phi_{\max} = \epsilon(D + C) + Cy + A_1 t_1 \exp(s_1 y/\epsilon) + A_2 t_2 \exp(s_2 y/\epsilon) + A_3 t_3 \exp(s_3 y/\epsilon) + A_4 t_4 \exp(s_4 y/\epsilon), \quad \text{(A2)}$$

$$\phi_w = \epsilon D + Cy + A_1 w_1 \exp(s_1 y/\epsilon) + A_2 w_2 \exp(s_2 y/\epsilon) + A_3 w_3 \exp(s_3 y/\epsilon) + A_4 w_4 \exp(s_4 y/\epsilon). \quad \text{(A3)}$$

where $\phi = (T - T_{\min,i})/(T_{\max,i} - T_{\min,i})$, A are constants, and

$$w_k = -(s_k^2 \Omega_1 - s_k - \beta)/\beta, \; t_k = -(s_k^2 \Omega_w - 1 - \beta) w_k - \beta, \; k = 1, \ldots, 4. \quad \text{(A5)}$$

The roots s_k are from a biquadratic characteristic equation, which when factored gives

$$s_{1,2} = -\{[2\Omega_1^2 + (1 + 2\Omega_1)\Omega_w] H/(\Omega_1^2 \Omega_w)\}^{1/2}, \quad \text{(A6)}$$

where

$$H = 1 \pm \{[1 + 4\Omega_1^2 \Omega_w (2 + 2\Omega_1 + \Omega_w)/[2\Omega_1^2 + (1 + 2\Omega_1)\Omega_w]^2\}^{1/2} \quad \text{(A7)}$$

Downloaded 13 Dec 2010 to 193.140.21.150. Redistribution subject to ASME license or copyright; see http://www.asme.org/terms/Terms_Use.cfm

Here, $s_3 = -s_1$, and $s_4 = -s_2$ yielding two positive roots (s_3 and s_4) and two negative roots (s_1 and s_2). There is also a repeated root at zero, which is included in Eqs. (A1)-(A3).

The coefficients are obtained by defining

$$A_1 = \epsilon A_{1L},\ A_2 = \epsilon A_{2L},\ A_3 = \epsilon A_{3R} \exp(-s_3/\epsilon),$$
$$A_4 = \epsilon A_{4R} \exp(-s_4/\epsilon). \quad \text{(A8)}$$

In the limit of large Ntu, we neglect terms of exponentially small order in applying the boundary conditions given in section 4 and get

$$A_{1L} = C(w_2 - t_2)/[s_1(t_2 w_1 - t_1 w_2)] \quad \text{(A9)}$$

$$A_{2L} = -C(w_1 - t_1)/[s_2(t_2 w_1 - t_1 w_2)] \quad \text{(A10)}$$

$$A_{3R} = C(w_4 - 1)/[s_3(w_3 - w_4)] \quad \text{(A11)}$$

$$A_{4R} = -C(w_3 - 1)/[s_4(w_3 - w_4)] \quad \text{(A12)}$$

$$D = C\{1/\beta + [(w_1 - t_1)s_1 - (w_2 - t_2)s_2]/[s_1 s_2(t_2 w_1 - t_1 w_2)]\} \quad \text{(A13)}$$

and

$$C = 1/(1 + \epsilon G), \quad \text{(A14)}$$

where

$$G = (1+\beta)/\beta + [(w_1 - t_1)s_1 - (w_2 - t_2)s_2]/[s_1 s_2(t_2 w_1 - t_1 w_2)] + [(w_4 - 1)t_3 s_4 - (w_3 - 1)t_4 s_3]/[s_4 s_3(w_3 - w_4)]. \quad \text{(A15)}$$

The effectiveness, $e = \phi_{\min,o} = \phi_{\min}(y = 1)$.

Downloaded 13 Dec 2010 to 193.140.21.150. Redistribution subject to ASME license or copyright; see http://www.asme.org/terms/Terms_Use.cfm

Prediction of Heat Transfer and Friction for the Louver Fin Geometry

A. Sahnoun

R. L. Webb

Department of Mechanical Engineering,
The Pennsylvania State University,
University Park, PA 16802

This paper is concerned with prediction of the air-side heat transfer coefficient of the louver fin geometry used in automotive radiators. An analytical model was developed to predict the heat transfer coefficient and friction factor of the louver fin geometry. The model is based on boundary layer and channel flow equations, and accounts for the "flow efficiency" in the array, as previously reported by Webb and Trauger. The model has no empirical constants. The model allows independent specifications of all of the geometric parameters of the louver fin. This includes the number of louvers over the flow depth, the louver width and length, and the louver angle. The model was validated by predicting the heat transfer coefficient and friction factor of 32 louver arrays tested by Davenport, which spanned hydraulic diameter based Reynolds numbers of 300–2800. At the highest Reynolds number, all of the heat transfer coefficients were predicted within a maximum error of −14 /+ 25 percent, and a mean error of ±8 percent. The high Reynolds number friction factors were predicted with a maximum error −22 /+ 26 percent, with a mean error of ±8 percent. The error ratios were slightly higher at the lowest Reynolds numbers.

Introduction

This paper is concerned with prediction of the heat transfer coefficient in the louver fin geometry used in a variety of automotive and aircraft air-cooled, heat exchanger applications. Figure 1 shows two automotive radiator construction types that use the louver fin geometry. Within the last eight years, significant advances have been made in understanding the heat transfer characteristics and mechanisms that exist within the louver fin array. The advances include published experimental data, empirical correlations, numerical solutions for the heat transfer coefficient, and detailed measurements of the flow structure.

Davenport (1983) developed an empirical power law correlation for his data on 32 cores of the type shown in Fig. 1(a), and Achaichia and Cowell (1988) provided a correlation for the Fig. 1(b) geometry. Numerical simulations have been reported by Kajino and Hiramatsu (1987), Achaichia and Cowell (1988), Aoki et al. (1989), and Ikuta et al. (1990). Aoki et al. (1989) used a constant heat flux boundary condition and measured the heat transfer coefficient on the individual louvers in the two-dimensional array illustrated in Fig. 2(a). Figure 2(b) shows that the Nusselt number (hL_p/k) may be correlated with the Reynolds number based on louver pitch (L_p) and the velocity over the louver ($u_c/\cos\theta$). The correlating line is 4 percent higher than that of the analytical solution for laminar flow over a flat plate with constant heat flux boundary condition.

Kajino and Hiramatsu (1987) performed flow visualization in the louver fin arrays, shown in Fig. 3. Both Figs. 3(a) and 3(b) have the same louver pitch (L_p) but different fin pitch (F_p). For small fin pitch (Fig. 3b), most of the flow is deflected by the louvers. For large fin pitch (Fig. 3a), nearly all of the flow bypasses the louvers. Our explanation of this phenomenon is that the flow divides between two possible channels. The first is through the louvers (boundary layer flow), and the second is in the axial passage between the fins (duct flow). The flow divides according to the hydraulic resistance of each path. For the large fin pitch of Fig. 3(a), most of the flow chooses the lower resistance duct flow path. However, the hydraulic resistance of the duct flow path is considerably increased in Fig. 3(b), so most of the flow chooses the boundary layer path through the louvers.

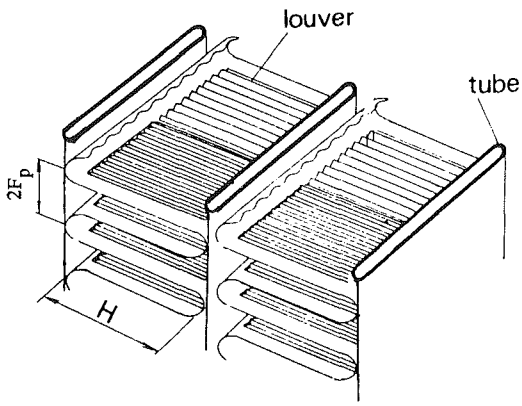

a) Corrugated fins

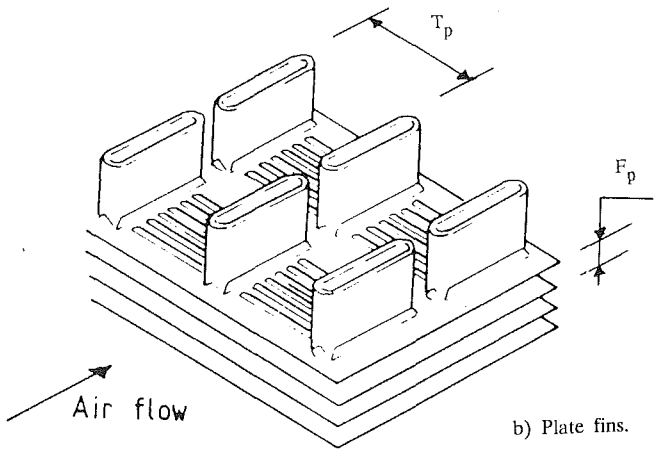

b) Plate fins.

Fig. 1 Automotive radiator core using louvered fins: (*a*) corrugated fins, and (*b*) plate fins

Contributed by the Heat Transfer Division for publication in the JOURNAL OF HEAT TRANSFER. Manuscript received by the Heat Transfer Division October 1991; revision received March 1992. Keywords: Finned Surfaces, Forced Convection, Heat Exchangers. Associate Technical Editor: W. A. Fiveland.

Copyright © 1992 by ASME
Downloaded 13 Dec 2010 to 193.140.21.150. Redistribution subject to ASME license or copyright; see http://www.asme.org/terms/Terms_Use.cfm

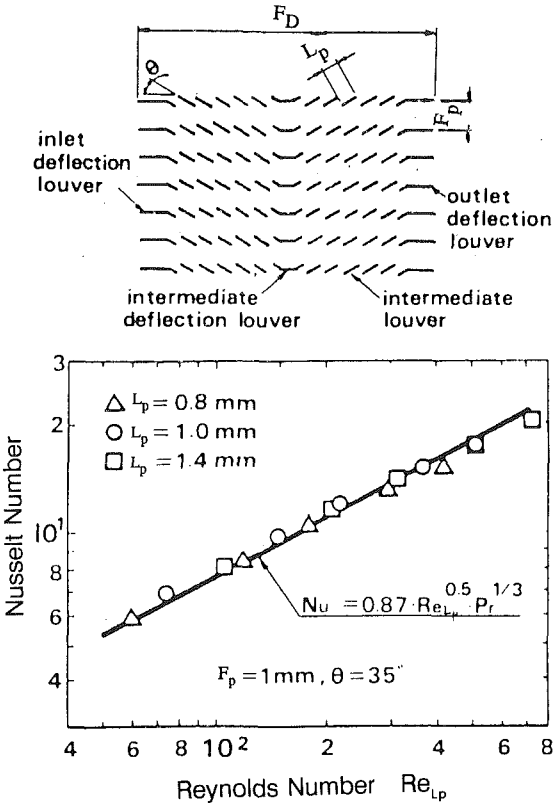

Fig. 2 Two-dimensional louver arrays tested by Aoki et al. (1989): (*a*) illustration of array tested, (*b*) correlation of average Nusselt number for three louver pitches

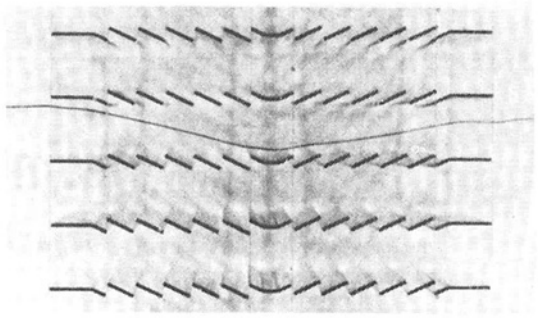

Fig. 3(*a*) Large fin pitch, F_p = 10 mm

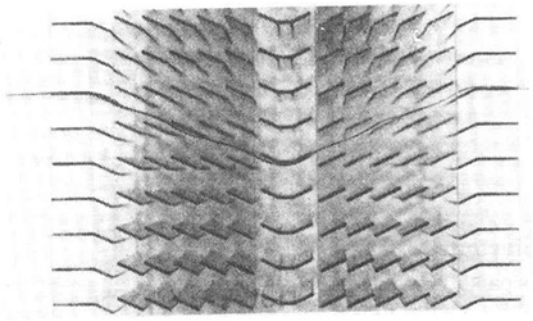

Fig. 3(*b*) Small fin pitch, F_p = 5 mm

Fig. 3 Observed streamlines in louver fin array from Kajino and Hiramatsu (1987): F_D = 160 mm, L_p = 10 mm, θ = 26 deg, Re_{Lp} = 500

Nomenclature

A_{D1} = area on which profile drag occurs, m^2
A = surface area defined on Fig. 8: A_e (end region), A_f (fin surface area), A_l (louvers), A_o (total air side), A_{S1} (nonlouvered inlet and exit fin regions), A_{S2} (internal flow redirection louver), m^2
A_r = end region aspect ratio
a = distance from fin base that is not louvered (Fig. 13), m
C_{D1} = drag coefficient on the louvers
D_1, D_2 = dimensions shown on Fig. 9, m
D_h = hydraulic diameter of fin array = $4A_cF_d/A_o$, m
D_{he} = hydraulic diameter of A_e, defined by Eq. (19), m
F_d = depth of fin array in flow direction, m
F_p = fin pitch, m
F_{th} = fin thickness, m
F_e = flow efficiency, Eq. (7)
F_e^* = flow efficiency for $Re_L > Re_L^*$, Eq. (8)
f = isothermal friction factor = $2\Delta pA_c/A_o\rho u_c^2$
f_e = friction factor of end regions, Eq. (23)
f_l = friction factor of the louvers, Eq. (22)
f_{S1}, f_{S2} = friction factor of the S_1 and S_2 regions
H = fin height, Fig. 1, m
h = heat transfer coefficient: h_e (end region), h_l (louvers), h_o (total air side), h_{S1} (nonlouvered inlet and exit fin regions), h_{S2} (internal flow redirection louver), W/m^2-K
j = heat transfer Colburn factor = $(h/u_cc_p)Pr^{2/3}$
k = thermal conductivity: k (of air), k_{fin} (fin material), k_w (tube), W/m-K
L_l = louver length, Fig. 8, m
L_p = louver pitch, Fig. 8, m
m = $(2h/k_Ft)^{1/2}$, m_e, m_* (defined by Eq. (17)), m^{-1}
N_l = number of full louvers over flow depth
Pr = air Prandtl number
Re = Reynolds number: $Re_{Dh}(D_hu_c/\nu)$, $Re_L(u_lL_p/\nu)$, Re_L^* (Eq. (8)), Re_{S1}, Re_{S2} (Eq. (11))
S_1 = nonlouvered inlet and exit fin regions, Fig. 8, m
S_2 = re-direction length, Fig. 8, m
T_D = tube depth, Fig. 8, m
T_p = tube pitch, Fig. 8, m
t_{th} = tube wall thickness, m
T_w = tube width, Fig. 8, m
UA = overall thermal conductance, K/W
u_{acc} = accelerated air flow, Eq. (6), and Fig. 9, m/s
u_c = minimum area flow velocity, Eq. (10), and Fig. 9, m/s
u_{fr} = frontal air velocity, m/s
u_l = flow velocity over the louvers, Eq. (9), m/s
x^+ = nondimensional duct length = $F_d/(Re_{Dh}D_h)$
α = air flow angle, Eq. (26), deg
Δp = pressure drop, Pa
η = surface efficiency = $(1 - \eta_f)A_f/A_o$
η_f = fin efficiency, $\eta_{f,*}$ (defined by Eq. (16))
θ = louver angle, Fig. 9, deg
ν = air kinematic viscosity, m^2/s
ρ = air density, kg/m^3
σ = contraction ratio of the fin array, Eq. (10)
τ = shear stress: τ_1 (on the louver), τ_{S1} (on S_1), τ_{S2} (on S_2), Pa

Downloaded 13 Dec 2010 to 193.140.21.150. Redistribution subject to ASME license or copyright; see http://www.asme.org/terms/Terms_Use.cfm

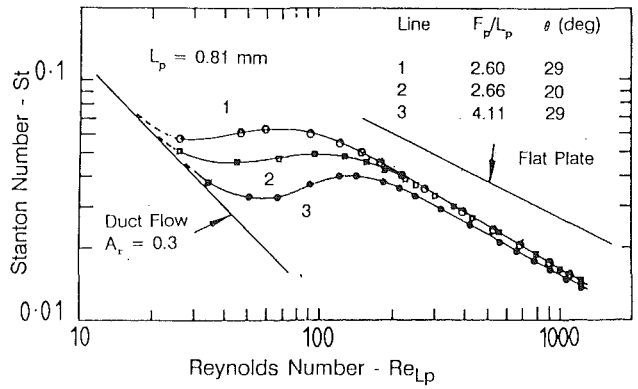

Fig. 4 Heat transfer characteristics of three louvered plate fin geometries having L_p = 0.81 mm reported by Achaichia and Cowell (1988)

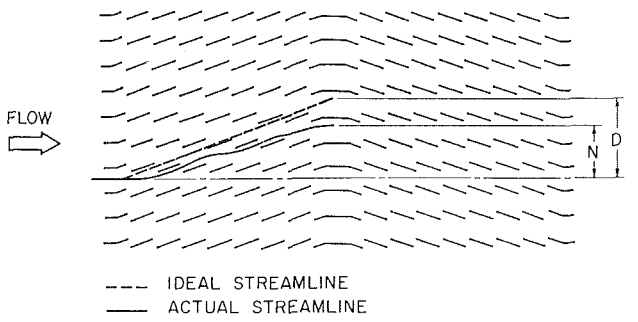

Fig. 5 Definition of method to define the "flow efficiency" proposed by Webb and Trauger (1991)

The concept of the "boundary layer" and the "duct flow" paths was initially proposed by Davenport (1980). Figure 4, taken from Achaichia and Cowell (1988), shows experimental St versus Re_{Lp} for three plate fin cores (Fig. 1*b*), which have different values of F_p/L_p, all with L_p = 0.81 mm. The solid lines show the asymptotes for laminar duct flow and boundary layer flow (the Pohlhausen solution). At high Re_{Lp}, the St is below, but parallel to the Pohlhausen solution. It is below the Pohlhausen solution because not all of the heat transfer surface consists of 0.81 mm louvers. The nonlouvered surface areas have a smaller heat transfer coefficient. The core having the largest F_p/L_p deviates first from the boundary layer type behavior as Re_{Lp} decreases. As the Re_{Lp} is reduced, the friction factor of the louvers increases, which causes more of the flow to choose the duct flow path. This causes the heat transfer coefficient to decrease.

Webb and Trauger (1991) performed flow visualization experiments on scaled up arrays to quantify the flow fraction that passes through the louvers. Figure 5 illustrates the louver array used in the experiments. If all of the flow passes through the louvers, it would follow the dashed line, and it would be displaced the lateral distance D shown on Fig. 5. The solid line illustrates a typical flow path, which is displaced a lateral distance N. They defined the term F_e, called the "flow efficiency," given by:

$$F_e = \frac{N}{D} = \frac{\text{Actual transverse distance}}{\text{Ideal transverse distance}} \tag{1}$$

From a mechanistic point of view, F_e is the fraction of the flow that passes through the louvers. If F_e = 1.0, all of the flow passes through the louvers, and if F_e = 0, none of the flow passes through the louvers. Figure 6 shows the measured F_e versus Re_{Lp} for six different arrays having $0.49 \le L_p/F_p \le 1.31$ and 20 deg louver angle. Empirical power law correlations were developed to predict $F_e(Re_{Dh}, L_p/F_p, \theta)$.

Four numerical analysis studies are reported in the literature,

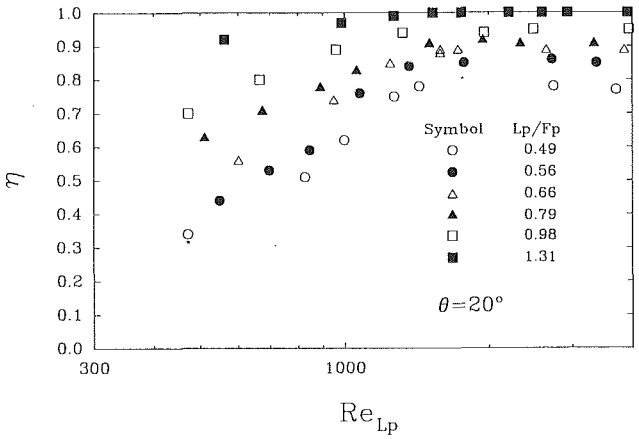

Fig. 6 Measured flow efficiency for θ = 20 deg reported by Webb and Trauger (1991)

including that of Aoki et al. (1989). Achaichia and Cowell (1988) assumed that the flow is fully developed in the periodic sense, and solved the flow field for the unit cell between two adjacent fins and of depth L_p. Aoki et al. (1989), Kajino and Hiramatsu (1987), and Ikuta et al. (1990) solved the problem for the full fin depth. Although numerical solutions are usually considered state of the art, those referenced contain three shortcomings: First, they consider only two-dimensional flow in the fin array. Thus, they neglect the nonlouvered end regions of the fin, and the base tube. Second, it is necessary to have the actual computer program to predict results for geometries of interest. Third, they do not provide an equation that allows one to understand how the various geometric factors interact to affect the result.

An analytical model that overcomes the above deficiencies is desirable. However, no such analytical models are reported in the literature. The present work offers an analytical model that is capable of predicting the air-side heat transfer coefficient and the friction factor for the actual heat exchanger configuration. The analytical model developed here somewhat parallels that of Joshi and Webb (1987) for the offset strip fin array. In the offset strip fin, all of the flow passes through an array that has θ = 0. The present louver fin array is more complex than the offset strip fin geometry. The flow efficiency parameter will be used to assist in describing this more complex flow.

Data are necessary to validate the analytical model. The only data set reported in the literature for the Fig. 1(*a*) geometry were provided by Davenport (1983) who tested an array of 32 single row cores. His cores were systematically selected so that the data span a range of F_p, L_p, L_1, and θ. Davenport measured the overall heat transfer coefficient (UA) and pressure drop in wind tunnel tests. He backed out the air side heat conductance ($\eta h_o A_o$) from the equation

$$\frac{1}{UA} = \frac{1}{\eta h_o A_o} + \frac{1}{h_i A_i} + \frac{t_{th}}{k_w A_w} \tag{2}$$

Heat Transfer Analytical Model

The Basis of the Model. Figure 7 shows the four different areas that are to be modeled. The terms A_1, A_{S1}, A_{S2}, and A_e represent the louvered areas, the plain leading and trailing areas, the plain middle area, and the end region area, respectively. These areas are defined by:

$$A_{S1} = 4L_1S_1$$

$$A_{S2} = 2L_1S_2$$

$$A_1 = 2L_1L_p(N_1 + 1)$$

$$A_e = 2F_d[(T_p - T_w - L_l) + (F_p - F_{th})]$$

Downloaded 13 Dec 2010 to 193.140.21.150. Redistribution subject to ASME license or copyright; see http://www.asme.org/terms/Terms_Use.cfm

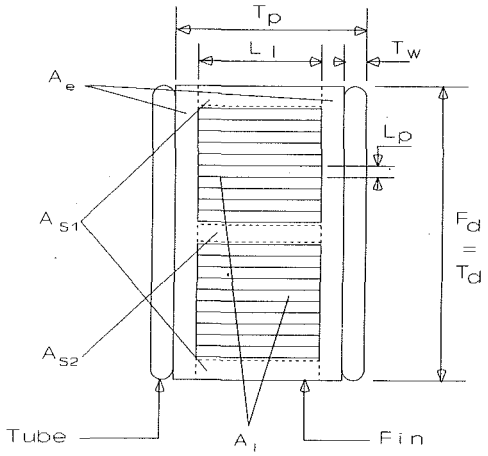

Fig. 7(*a*) Definition of the various fin regions used in model

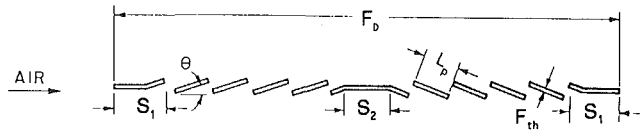

Fig. 7(*b*) Cross section of louver fin array depth

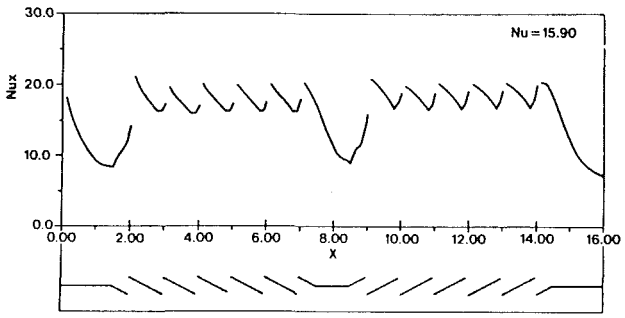

Fig. 8 Local Nusselt number in louver fin array numerically predicted by Kajino and Hiramatsu (1987) for F_p = 1.0, L_p = 1.0, θ = 26 deg, Re_{Lp} = 500

The composite heat transfer coefficient (h_o) is given by:

$$\eta h_o A_o = \eta_{f,l} h_l A_l + \eta_{f,S1} h_{S1} A_{S1} + \eta_{f,S2} h_{S2} A_{S2} + h_e A_e \qquad (3)$$

where the $1/\eta h_o A_o$ is the first term on the right-hand side of Eq. (2). The subscripts l, S_1, S_2, and e refer to the louvered areas, the plain leading and trailing areas, the plain middle area, and the end region area, respectively.

As shown in Fig. 7, the bent portions attached to the leading and the trailing edges, are included in the S_1 dimension. However, the redirection louver (the S_2 dimension) does not include the attached bent portions. The model assumes that the two bent portions of the redirection louver act as an extra louver in the array. This accounts for the (N_l + 1) term in the definition of A_l. This assumption was based on the numerical results of Kajino and Hiramatsu (1987) shown in Fig. 8. Figure 8 shows that the upstream bent portions of the redirection louver (in the middle of the array) and the bent portion of the exit S_1 louver performed like the interior louvers. However, the bent portions of the inlet louver (S_1) and the downstream bent portion of the redirection louver (S_2) provided lower performance.

Next, methods are developed to predict the individual coefficients, h_l, h_{S1}, h_{S2}, and h_e.

Interior Louvers (h_l). Based on the close agreement of the Pohlhausen flat plate solution with the experimental data for the fully louvered array (Fig. 2), the h_l is predicted using the

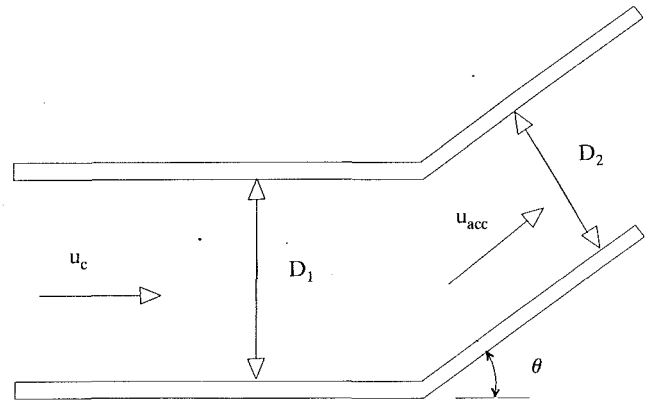

Fig. 9 Flow acceleration caused by the louver angle

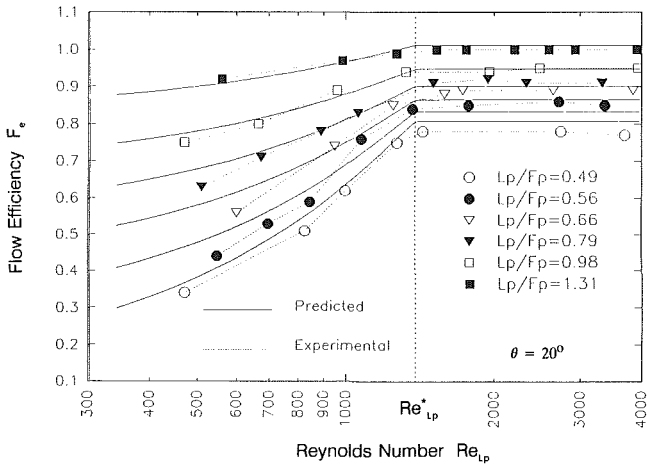

Fig. 10 Prediction of the θ = 20 deg data of Webb and Trauger (1991) using Eq. (7)

Pohlhausen solution for laminar boundary layer over a constant temperature flat plate,

$$h_l = \frac{0.664 k u_l \mathrm{Pr}^{1/3}}{\nu \mathrm{Re}_{Lp}^{0.5}} \qquad (4)$$

where

$$\mathrm{Re}_{Lp} = \frac{u_l L_p}{\nu} \qquad (5)$$

An appropriate air velocity over the louvers (u_l) is required to calculate the Reynolds number in Eq. (5). Two factors affect this velocity: (1) the acceleration of the flow due to the angular redirection caused by the louvers, and (2) the fraction of total air flow that passes over the louvers, or the flow efficiency (F_e). If the flow is deflected at the louver angle, Fig. 9 shows that the flow speed is increased from u_c to u_{acc}, because the flow area is reduced. Using the continuity equation between location 1 and location 2, one obtains

$$u_{acc} = u_c \frac{D_1}{D_2} = u_c \frac{F_p - F_{th}}{F_p \cos\theta - F_{th}} \qquad (6)$$

The actual flow speed over the louvers may be attenuated by the bypass flow associated with the flow efficiency. Webb and Trauger (1991) provided correlations to calculate the flow efficiency as a function of $\mathrm{Re}_L (= u_c L_p/\nu)$, the louver angle, and the L_p/F_p ratio. The present authors have tested the reported correlations and determined that the accuracy of the correlations was not satisfactory. A more accurate correlation was derived for the flow efficiency in the range $\mathrm{Re}_L < \mathrm{Re}_L^*$ using the data of Webb and Trauger (1991). The ability of the new correlation to predict F_e for the 20 deg louver angle data of Fig. 6 is shown in Fig. 10. The new correlation for the flow efficiency (F_e) is

Downloaded 13 Dec 2010 to 193.140.21.150. Redistribution subject to ASME license or copyright; see http://www.asme.org/terms/Terms_Use.cfm

$$F_e = F_e^* - 37.17 \times 10^{-6}(\mathrm{Re}_L^* - \mathrm{Re}_L)^{1.1}\left(\frac{L_p}{F_p}\right)^{-1.35}\left(\frac{2\theta}{\pi}\right)^{-0.610} \quad (7)$$

where F_e^*, Re_L^*, and Re_L are defined by:

$$F_e^* = 0.95\left(\frac{L_p}{F_p}\right)^{0.23} \quad \mathrm{Re}_L^* = 828\left(\frac{2\theta}{\pi}\right)^{-0.34} \quad \mathrm{Re}_L = \frac{u_c L_p}{\nu} \quad (8)$$

Equation (7) is used for $\mathrm{Re}_L < \mathrm{Re}_L^*$, and $F_e = F_e^*$ (Eq. (8)) is used for $\mathrm{Re}_L > \mathrm{Re}_L^*$. For $F_e = 0$, none of the flow goes over the louvers, and the flow passes in the "duct" region between the fins. When $F_e = 1$, all of the flow is parallel to the louvers, and $u_l = u_{\mathrm{acc}}$. The velocity over the louver (u_l) is related to the accelerated velocity u_{acc} by:

$$u_l = u_{\mathrm{acc}} \cdot F_e = u_c\left(F_e \frac{F_p - F_{th}}{F_p \cos(\theta) - F_{th}}\right) \quad (9)$$

where

$$u_c = \frac{u_{fr}}{\sigma} \quad \text{with} \quad \sigma = \frac{(T_p - T_w)(F_p - F_{th})}{(T_p F_{th})} \quad (10)$$

Inlet/Exit and Redirection Louvers (h_{S1} and h_{S2}). The speed of the flow over these regions is u_c [Eq. (10)]. The Pohlhausen solution [Eq. (4)] is used, with characteristic lengths S_1 and S_2, to predict the heat transfer coefficients h_{S1} and h_{S2}, respectively. The Re_{S1} and Re_{S2} are defined as

$$\mathrm{Re}_{S1} = \frac{u_c S_1}{\nu} \quad \text{and} \quad \mathrm{Re}_{S2} = \frac{u_c S_2}{\nu} \quad (11)$$

End Regions (h_e). These regions are shown by the dashed lines in Fig. 11. The air velocity is u_c. The analytical solution for constant wall temperature fully developed laminar flow in a rectangular channel is used to predict the heat transfer coefficient. Shah and London (1978) provided the following curve fit for such a flow.

$$\frac{h_e D_{he}}{k} = 7.541(1 - 2.610A_r + 4.970A_r^2 - 5.119A_r^3 + 2.702A_r^4 - 0.548A_r^5) \quad (12)$$

where A_r is the aspect ratio, which is defined to have $A_r \leq 1$. The aspect ratio of the end region is defined by

$$A_r = \frac{T_p - T_w - L_l}{F_p - F_{th}} \quad (13)$$

If the value of Eq. (13) is greater than one, the inverse of the value is used with Eq. (12). The hydraulic diameter (D_{he}) of the end region is

$$D_{he} = \frac{4A_{ce}}{P_e} = \frac{4(T_p - T_w - L_l)(F_p - F_{th})}{2(T_p - T_w - L_l + F_p - F_{th})} \quad (14)$$

Fin Efficiency. The fin efficiency of plane fins is typically calculated by

$$\eta_f = \frac{2}{mH}\tanh\left(\frac{mH}{2}\right) \quad (15)$$

Equation (15) is not precisely correct, because two different heat transfer coefficients exist over the fin length. Figure 11 shows that the end of the louver is a distance a from the fin base. The correct fin efficiency equation must account for heat transfer coefficient h_e in the end region (length a), and h_l in the louvered region and the S_1 and S_2 regions (length $H/2 - a$). We have derived the correct fin efficiency equation, which is

$$\eta_{f,*} = \frac{k_{\mathrm{fin}} F_{th}\left[\dfrac{1}{\dfrac{1}{m_e}\tanh(m_e a)} - \dfrac{1}{\dfrac{1}{m_e}\cosh(m_e a)\sinh(m_e a) + \dfrac{m_*}{m_e^2}\sinh^2(m_e a)\tanh(m_*(H/2-a))}\right]}{2(ah_e + (H/2-a)h_*)} \quad (16)$$

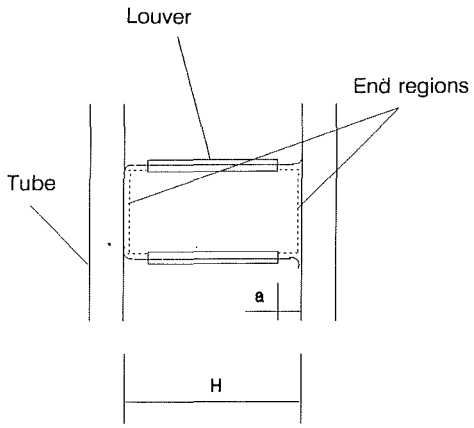

Fig. 11 End regions of the array

where

$$a = \frac{T_p - T_w - L_l}{2} \quad m_e = \sqrt{\frac{2h_e}{k_f F_{th}}} \quad m_* = \sqrt{\frac{2h_*}{k_f F_{th}}} \quad (17)$$

Equation (16) is used to calculate the fin efficiency for the interior louvers and for the S_1 and S_2 louvers. The value of h_* is assigned the value h_l, h_{S1}, or h_{S2} for calculation of the fin efficiencies $\eta_{f,l}$, $\eta_{f,S1}$, or $\eta_{f,S2}$, respectively. Equation (16) simplifies to Eq. (15) when $h_e = h_*$, and $a = H/2$ or $a = 0$.

Friction Analytical Model

The x-direction momentum equation for a unit cell that includes the volume between two fins, two tubes, and of the fin array depth (F_d) is:

$$\Delta p A_c = \Sigma F + (1 - F_e)(M_{\mathrm{in}} - M_{\mathrm{out}}) \quad (18)$$

where Δp is the pressure drop over depth F_d, and ΣF is the sum of the shear and pressure drag forces over the flow path acting on the various surface elements. The last term is the net axial momentum associated with the fraction of the air flow that bypasses the louvers. If $F_e = 1$, all the air passes over the louvers and the momentum term is zero. However, if $F_e = 0$, none of the air passes over the louvers, and a duct flow between the fins occurs. Equation (18) does not include entrance and exit losses, which are evaluated for the specific heat exchanger configuration of interest. The ΣF term is given by:

$$\Sigma F = \tau_l A_l + \tau_{s1} A_{s1} + \tau_{s2} A_{s2} + \tau_e A_e + \frac{1}{2} C_{Dl} \rho u_c^2 A_{Dl} \quad (19)$$

Dividing Eq. (19) by $0.5 A_o \rho u_c^2$ and using $f = \tau/(0.5\rho u_c^2)$ gives

$$\frac{\Sigma F}{\frac{1}{2} A_o \rho u_c^2} = f_l\left(\frac{u_l}{u_c}\right)^2 \frac{A_l}{A_o} + f_{s1}\frac{A_{s1}}{A_o} + f_{S2}\frac{A_{s2}}{A_o} + f_e\frac{A_e}{A_o} + C_{Dl}\frac{A_{Dl}}{A_o} \quad (20)$$

Substituting Eq. (20) into Eq. (18) and simplifying gives

$$f = f_l\left(\frac{u_l}{u_c}\right)^2 \frac{A_l}{A_o} + f_{s1}\frac{A_{s1}}{A_o} + f_{s2}\frac{A_{s2}}{A_o} + f_e\frac{A_e}{A_o} + C_{Dl}\frac{A_{Dl}}{A_o} + (1 - F_e) f_{\mathrm{app}} \quad (21)$$

Downloaded 13 Dec 2010 to 193.140.21.150. Redistribution subject to ASME license or copyright; see http://www.asme.org/terms/Terms_Use.cfm

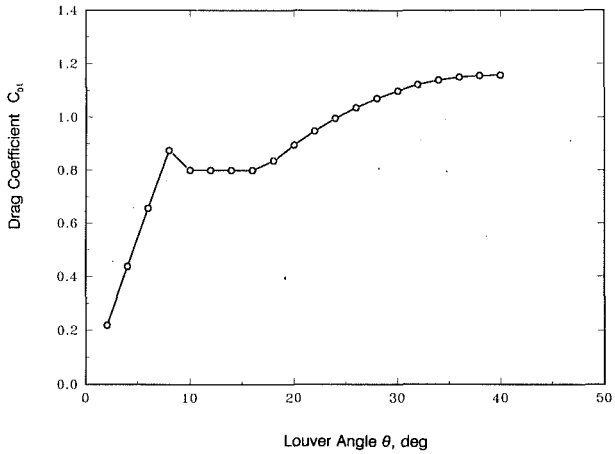

Fig. 12 Drag coefficient for an inclined flat plate versus θ

The equations to predict the individual f components of Eq. (21) are developed below.

The f Components. The predictions of the friction factor components f_l, f_{s1}, f_{s2}, and f_e are based on the same flow models used for the heat transfer coefficients. The friction factor on the louvers (f_l) is given by the flat plate Pohlhausen solution

$$f_l = \frac{1.328}{\mathrm{Re}_{Lp}^{0.5}} \tag{22}$$

where Re_{Lp} is as defined by Eq. (5).

The friction factor on the S_1 and S_2 louvers is also modeled by Eq. (22), except that the characteristic lengths are S_1 and S_2 and the velocity is u_c. The Re_{S1} and Re_{S2} are defined by Eq. (11).

As in the heat transfer case, the end regions are modeled with the equation for fully developed flow in a rectangular duct. Shah and London (1978) provide a 5th degree polynomial for this flow. The equation is

$$f_e = \frac{\nu}{u_c D_{he}} [24(1 - 1.3553A_r + 1.9467A_r^2 - 1.7012A_r^3 + 0.9567A_r^4 - 0.2537A_r^5)] \tag{23}$$

where D_{he} is as defined by Eq. (14).

Profile Drag C_D. The fin thickness of the louvers (F_{th}) causes profile drag, which is accounted for by the next-to-last term in Eq. (21). If the flow is parallel to the louvers, the projected area for profile drag within the flow depth is

$$A_{Dl} = N_l L_l F_{th} \tag{24}$$

When the flow efficiency (F_e) is less than one, the flow is not parallel to the louvers. Because the flow angle is less than the louver angle, the projected area for profile drag is increased and is given by

$$A_{Dl} = N_l L_l (F_{th} + L_p \sin(\theta - \alpha)) \tag{25}$$

where α and θ are the flow angle and the louver angle, respectively. The flow angle α is the angle between the solid flow line and the horizontal line shown in Fig. 5. Using the geometry of the figure and the definition of the flow efficiency, the flow angle is

$$\alpha = \tan^{-1}[F_e \tan(\theta)] \tag{26}$$

The drag coefficient C_{Dl} is determined using the equations published by Blevins (1984) for an inclined plate.

$$C_{Dl} = 2\pi \sin(\theta) \qquad \text{for } \theta < 8 \text{ deg} \tag{27}$$

Table 1 Geometries tested by Davenport (1983)

Geometries Tested by Davenport (1983)

H = 12.7 mm

		Geometric Parameters					Predicted/Experimental Ratio u_{fr} = 10.67 m/s		u_{fr} = 3.05 m/s	
#	Sym.	L_l	L_p	θ	N_l	F_p	$\eta h_o A_o$	f	$\eta h_o A_o$	f
1	α	9.5	3.0	8.37	8	1.65	0.95	0.99	1.29	0.99
2	β	9.5	3.0	10.26	8	1.65	0.96	0.90	1.12	0.88
14	ϕ	9.5	3.0	11.01	8	1.65	0.97	0.99	1.20	0.96
3	Γ	9.5	3.0	16.20	8	1.60	0.87	0.86	0.98	0.78
4	π	9.5	2.25	13.21	12	1.65	1.00	0.95	1.27	0.97
5	Σ	9.5	2.25	15.59	12	1.56	0.92	0.92	1.07	0.85
6	σ	9.5	2.25	18.51	12	1.56	0.95	0.92	1.11	0.90
13	∞	9.5	1.8	13.87	16	1.63	0.94	0.92	1.17	0.98
7	μ	9.5	1.8	18.14	16	1.65	1.02	0.95	1.18	0.97
8	τ	9.5	1.8	19.95	16	1.58	0.90	0.82	1.07	0.86
9	Φ	9.5	1.8	25.78	16	1.58	0.86	0.89	0.91	0.82
10	Θ	9.5	1.5	18.89	20	1.53	0.95	1.12	1.09	1.11
11	Ω	9.5	1.5	21.61	20	1.59	0.92	0.80	1.05	0.80
12	δ	9.5	1.5	31.72	20	1.59	0.87	0.83	1.02	0.83
15	ε	11.	2.25	22.78	12	1.68	0.87	0.89	0.97	0.82
16	$\cap$	11.	2.25	20.42	12	1.65	0.87	0.78	0.89	0.78
17	$\equiv$	10.	2.25	20.42	12	1.65	0.83	0.86	1.00	0.82
18	$\pm$	9.0	2.25	20.42	12	1.63	0.93	0.86	1.13	0.82
19	$\geq$	8.0	2.25	19.47	12	1.60	0.96	0.94	1.27	0.94

H = 7.8 mm

		Geometric Parameters					Predicted/Experimental Ratio u_{fr} = 10.67 m/s		u_{fr} = 3.05 m/s	
#	Sym.	L_l	L_p	θ	N_l	F_p	$\eta h_o A_o$	f	$\eta h_o A_o$	f
21	β	7.1	2.25	13.52	12	1.53	1.11	1.09	1.24	1.06
20	α	7.1	3.0	13.62	8	1.53	0.96	0.87	1.07	0.85
23	π	7.1	1.5	24.40	20	1.55	0.98	1.18	1.05	1.08
22	Γ	7.1	1.8	19.59	16	1.54	1.25	1.05	1.30	1.00
24	Σ	7.1	2.25	9.43	12	1.49	1.17	1.26	1.35	1.23
25	σ	7.1	2.25	16.08	12	1.51	1.11	1.11	1.19	1.00
26	μ	7.1	2.25	17.15	12	1.51	1.06	1.04	1.17	0.98
27	τ	7.1	2.25	15.59	12	1.23	1.15	1.07	1.36	1.04
28	Φ	7.1	2.25	13.62	12	1.00	1.09	1.00	1.20	0.83
29	θ	7.1	2.25	13.87	12	1.53	1.02	1.07	1.17	1.03
30	Ω	6.5	2.25	13.87	12	1.51	0.99	1.06	1.05	0.94
31	δ	6.0	2.25	17.05	12	1.53	0.96	1.06	1.07	0.97
32	∞	5.0	2.25	14.11	12	1.50	1.13	1.14	1.33	1.10

$$C_{Dl} = \frac{\cos(\theta)}{0.222 + \dfrac{0.283}{\sin(\theta)}} \qquad \text{for } \theta > 12 \text{ deg} \tag{28}$$

For 8 deg $< \theta <$ 12 deg, Blevins (1984) suggests that $C_{Dl} = 0.8$ be used. Figure 12 shows C_{Dl} as a function of θ.

The f_{app} Term. The f_{app} term in Eq. (21) accounts for friction and momentum of the developing flow associated with the flow fraction that bypasses the louvers. We have used the entrance length solution for a duct having aspect ratio 0.2. Shah and London (1987) provide data of $f_{app}\mathrm{Re}$ versus x^+ for this geometry. The data were curve-fitted by the equation

$$f_{app} = \frac{1}{\mathrm{Re}_{Dh}} \sqrt{328.24 + \frac{12.043}{x^+}} \tag{29}$$

Prediction of Experimental Data

Davenport (1983) obtained experimental data for 32 one-row, louver fin cores (Fig. 1*a*) having 0.0762-mm-thick copper fins. The geometric parameters of these cores are shown in Table 1. Davenport (1983) shows the results in the j and f versus Re_{Dh} format, which were linear on log–log format. The graphic data were enlarged and read to third digit accuracy. The experimental values were curve fitted with a power law function. The average errors of the curve fits ranged from 0.57 to 2.38 percent.

Downloaded 13 Dec 2010 to 193.140.21.150. Redistribution subject to ASME license or copyright; see http://www.asme.org/terms/Terms_Use.cfm

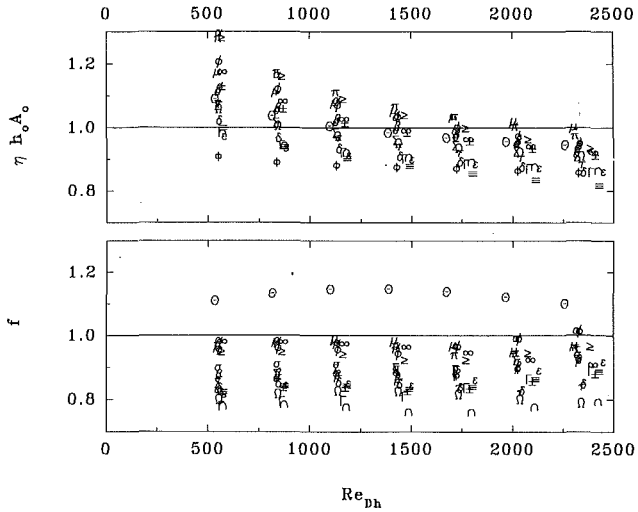

Fig. 13 Heat transfer and friction error plots for H = 12.7 mm

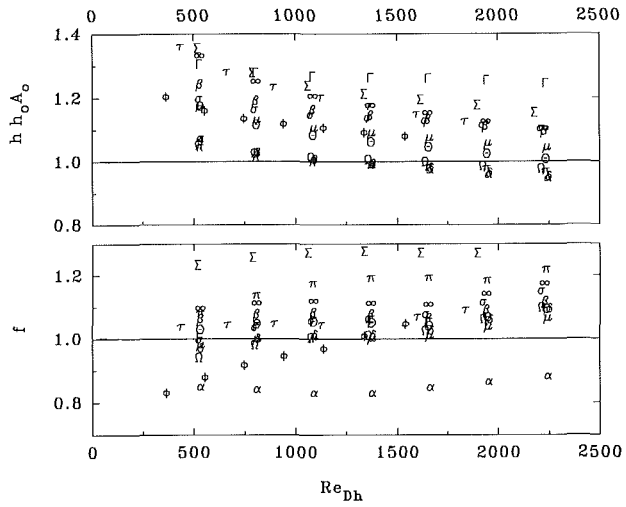

Fig. 14 Heat transfer and friction error plots for H = 7.8 mm

Table 1 shows that the data are for two fin heights, 12.7 and 7.8 mm. For each fin height, the cores were selected to provide systematic variation of fin pitch (F_p), louver pitch (L_p), louver angle (θ), and louver length (L_l). The data are ordered in Table 1 to show the systematic variation of the geometric parameters.

The $\eta h_o A_o$ and f-factors of Table 1 were predicted using Eqs. (3) and (21), respectively, with η_f given by Eq. (16). The predicted heat transfer data were compared against the Davenport data in the form $\eta h_o A_o$, using Eq. (15) for η_f as was used by Davenport. The surface efficiency (η) is defined in the Nomenclature. Figures 13 and 14 show the heat transfer and the friction error plots for the 32 cores listed in Table 1. Figures 13 and 14 are for 12.7 mm and 7.8 mm fin heights, respectively. The second column of Table 1 defines the symbols used on Figs. 13 and 14. The last four columns of Table 1 show tabled values of the error ratio (predicted/experimental) for u_{fr} of 10.67 and 3.05 m/s, respectively. The predictive ability of the model is summarized in Table 2, based on the predicted/experimental values given in Table 1. The subscripts p and e in Table 2 refer to predicted and experimental values, respectively.

Discussion

Careful evaluation of the data showed some moderate inconsistencies. However, none of the data were excluded from the comparison of predicted-to-experimental evaluation. For high Reynolds number, the flow efficiency (Eqs. (7) and (8)) is 0.95 or higher. Inspection of the heat transfer data in Table 1 shows that the H = 12.7 mm data are underpredicted by 8 percent, and the H = 7.8 mm are overpredicted 8 percent (mean value). Similar inspection of the friction data shows that the H = 12.7 mm data are underpredicted 8.5 percent, and the H = 7.8 mm are overpredicted 8 percent. We do not feel that the mean underprediction of the H = 12.7 mm heat transfer data and overprediction of the 7.8 mm data are caused by a systematic error in the model. Our careful examination of the data suggests that experimental errors are an important factor. For example, core 32 is overpredicted 13 percent and core 31 is underpredicted 4 percent. The only difference between these cores is the 0.5 mm different louver lengths. It appears that the data of core 32 are too low.

Table 2 Summary of ability to predict the experimental data

Summary of Ability to Predict the Experimental Data

	H = 12.7 mm u_{fr} (m/s)		H = 7.8 mm u_{fr} (m/s)	
	10.67	3.05	10.67	3.05
Min/Max				
$(\eta h_o A_o)_p/(\eta h_o A_o)_e$	0.86/1.02	0.91/1.29	0.96/1.25	1.05/1.36
f_p/f_e	0.88/1.12	0.78/1.11	0.87/1.26	0.83/1.23
Mean				
$(\eta h_o A_o)_p/(\eta h_o A_o)_e$	0.92	1.04	1.08	1.19
f_p/f_e	0.91	0.88	1.08	1.01

Approximately 75 percent of the H = 7.8 mm geometries have 7.1 mm louver height (L_l/H = 91 percent). Typical industrial values of L_l/H are 0.75–0.80. The fins were bonded to the tube by solder, which was precoated on the tubes. The distance from the fin base to the start of the louver was only 0.35 mm. It is possible that some solder wicked into these louvers, which would reduce both the heat transfer and friction characteristics, and account for the 8 percent mean overprediction of the H = 7.8 mm data. The model predicts the effect of louver angle quite well, for louver angles between 8 and 32 deg. The effect of louver length (L_l) is closely predicted (cores 15 to 19 and cores 29 to 32). We feel that a strictly analytical model that predicts both the heat transfer and friction data with a mean error ratio of ±8 percent is quite good.

As the Reynolds numbers attain low values, the flow efficiency starts to decline, especially for large fin pitch (F_p), which decreases the speed over the louvers. The predicted-to-experimental comparisons show that the heat transfer data are overpredicted at the lowest R_{Dh} values. If these data are predicted assuming F_e = 1, the overprediction is slightly increased.

Conclusions

An analytical model, which contains no empirical constants, has been developed to predict the heat transfer coefficient and friction factor of the Fig. 1(a) corrugated louver fin array. The model correctly predicts the effects of changes of louver angle, louver pitch, louver length, and fin pitch. The mean error ratios of the high Reynolds number heat transfer and friction data are ±8 percent. Slightly higher error ratios exist at the lowest Re_{Dh}.

Acknowledgments

This research was funded by the International Copper Association. We are grateful to Dr. C. J. Davenport, who provided additional detail on his test data.

Downloaded 13 Dec 2010 to 193.140.21.150. Redistribution subject to ASME license or copyright; see http://www.asme.org/terms/Terms_Use.cfm

References

Achaichia, A., and Cowell, T. A., 1988, "A Finite Difference Analysis of Fully Developed Periodic Laminar Flow in Inclined Louvre Arrays," *Proc. 2nd UK National Heat Transfer Conference*, Vol. 2, Glasgow, pp. 883–888.

Achaichia, A., and Cowell, T. A., 1988, "Heat Transfer and Pressure Drop Characteristics of Flat Tube and Louvered Plate Fin Surfaces," *Experimental Thermal and Fluid Science*, Vol. 1, pp. 147–157.

Aoki, H., Shinagawa, T., and Suga, K., 1989, "An Experimental Study of the Local Heat Transfer Characteristics in Automotive Louvered Fins," *Experimental Thermal and Fluid Science*, Vol. 1, pp. 293–300.

Blevins, R. D., 1984, *Applied Fluid Dynamic Drag*, Van Nostrand Reinhold, New York, p. 322.

Davenport, C. J., 1980, "Heat Transfer and Fluid Flow in the Louvered Triangular Ducts," Ph.D. Thesis, Lanchester Polytechnic Institute, United Kingdom.

Davenport, C. J., 1983, "Correlations for Heat Transfer and Flow Friction Characteristics of Louvered Fins," *Heat Transfer—Seattle 1983*, N. M. Farukhi, ed., AIChE Symp. Ser. Vol. 79, No. 225.

Ikuta, S., Sasaki, Y., Tanaka, K., Takaji, M., and Himeno, R., 1990, "Numerical Analysis of Heat Transfer Around Louver Assemblies," SAE Technical Paper Series 900081.

Joshi, H. M., and Webb, R. L., 1987, "Heat Transfer and Friction in the Offset Strip-Fin Array Geometry," *Int. J. Heat Mass Transfer*, Vol. 30, No. 1, pp. 69–84.

Kajino, M., and Hiramatsu, M., 1987, "Research and Development of Automotive Heat Exchangers," in: *Heat Transfer in High Technology and Power Engineering*, W. J. Yang and Y. Mori, eds., pp. 420–432, Hemisphere Publishing Corp.

Shah, R. K., and London, A. L., 1978, *Laminar Flow Forced Convection in Ducts*, p. 196, Academic Press, New York.

Webb, R. L., and Trauger, P., 1991, "Flow Structure in the Louvered Fin Heat Exchanger Geometry," *Experimental Thermal and Fluid Science*, Vol. 4, pp. 205–217.

Downloaded 13 Dec 2010 to 193.140.21.150. Redistribution subject to ASME license or copyright; see http://www.asme.org/terms/Terms_Use.cfm

T. Tsuji
Associate Professor.

Y. Nagano
Professor.
Mem. ASME

M. Tagawa
Associate Professor.

Department of Mechanical Engineering,
Nagoya Institute of Technology,
Gokiso-cho, Showa-ku,
Nagoya 466, Japan

Experiment on Spatio-Temporal Turbulent Structures of a Natural Convection Boundary Layer

The spatio-temporal structures of a turbulent natural convection boundary layer along a vertical flat plate in air have been examined using a thermocouple rake and a pair of hot-wire/cold-wire arrangements. The instantaneous temperature profile clearly indicates the evolution of a large-scale motion originating in the outer region of the boundary layer. However, the space–time correlation measurements did not suggest the existence of any quasi-coherent structures such as low-speed streaks and bursts. The convection (or advection) velocity and characteristic length scales of turbulence were also investigated. The convection velocity exceeds the local mean velocity in the near-wall and outermost regions. The microscale of the thermal field shows a strongly anisotropic structure, and the integral scale indicates a large-scale structure normal to the wall.

1 Introduction

The characteristics of a turbulent natural convection boundary layer along a vertical flat plate have been clarified to some extent through recent research (Miyamoto et al., 1982; Cheesewright and Ierokipiotis, 1982, 1984; Cheesewright and Mirzai, 1988; Tsuji and Nagano, 1988a, 1988b, 1989a). In our experiment on the streamwise development of a turbulent natural convection boundary layer (Tsuji and Nagano, 1988a), it has been found that: The mean velocity profile approaches a straight-line only in the region much nearer the wall ($y^+ < 1$); the heat transfer rate is almost constant in the streamwise direction, as expressed by the empirical equation $Nu_x = 0.120(Gr_xPr)^{1/3}$, whereas the wall shear stress increases. Moreover, from simultaneous measurements of two velocity components in the directions parallel and normal to the wall and temperature (Tsuji and Nagano, 1988b), it has been quantitatively clarified that: Reynolds shear stress near the wall is not necessarily negative but almost zero in spite of the positive velocity gradient; although the streamwise turbulent heat flux becomes slightly negative near the wall, the absolute value is far smaller than the corresponding value for forced convection (heated flow). Thus, the characteristics of this boundary layer differ markedly from those observed in ordinary turbulent boundary layers.

In view of these, the investigation of the turbulent structure is very important not only to comprehend the peculiar characteristics of a natural convection boundary layer but also to construct a universal model for turbulent buoyant flows. However, because of the difficulty in obtaining the measurements, systematic studies of the turbulent structure are very few in comparison with those of forced convection. Although space–time correlation measurements in the thermal field have been performed by Cheesewright and Doan (1978) and Cheesewright and Dastbaz (1983) using two thermocouples and flow-visualization experiments have been attempted by Kitamura et al. (1985), many details of the turbulent structure are still unknown.

In the present study, the turbulent structure of a natural convection boundary layer has been examined using a thermocouple rake and a pair of hot-wire/cold-wire arrangements. These measurements are new attempts in the study of natural convections. The spatio-temporal turbulent structures are discussed on the basis of measurements of instantaneous temperature profiles and of space–time correlations in the velocity and thermal fields.

2 Experimental Apparatus and Instrumentation

The apparatus used for the present study is the same as that earlier described in detail by Tsuji and Nagano (1988a). The flat surface generating flow was a copper plate 4 m high and 1 m wide. Uniform surface temperature $\overline{T}_w = 60°C$ was obtained by electrical heating from the back of the plate. The developed turbulent boundary layer existed in the range $Gr_x > 10^{10}$ (Tsuji and Nagano, 1988a). Two types of probe were used for the measurements. One was a thermocouple rake consisting of ten chromel-alumel thermocouples (wire diameter: 12.7 μm), as shown in Fig. 1(*a*). The distance between the head of the rake and the tenth thermocouple is about 120 mm. This probe was used to measure instantaneous temperature profiles in the streamwise, normal, and spanwise directions. The temperature calibration was conducted by submerging the thermocouple rake covered with an acrylate pipe in a water bath controlled within $\pm 0.02°C$. The uncertainty of temperature measurement with each thermocouple was estimated to be below $\pm 0.15°C$, including d-c amplification and analog-to-digital conversion. The other is a probe comprised of a pair of hot-wire/cold-wire arrangements, as shown in Fig. 1(*b*), which was used for simultaneous measurements of velocity and temperature at two points in the direction normal to the plate. Fixing one hot-wire/cold-wire arrangement at a measuring location in the boundary layer, we traversed another arrangement in the normal direction. Hot and cold wires are both 3.1-μm-dia tungsten wires, and the sensitive lengths were 1.5 mm ($\simeq 6\nu/u_\tau$) and 3.5 mm ($\simeq 14\nu/u_\tau$), respectively. The cold wire was located 2.5 mm ($\simeq 10\nu/u_\tau$) upstream of the hot wire so as not to induce interference with the velocity and thermal fields between the wires. Temperature compensation for the hot wire was made by the technique described by Hishida and Nagano (1978). To minimize measurement error caused by the spatial difference between thermal fields around the hot and cold wires, the temperature compensation of the hot wire was made by delaying temperature signals in the same manner as in the previous paper (Tsuji and Nagano, 1988a). A low-velocity wind tunnel (Tsuji and Nagano, 1989b) was used for the velocity calibration of the hot wires. Measurements with these probes were carried out

Contributed by the Heat Transfer Division and presented at the Joint AIAA/ASME Thermophysics and Heat Transfer Conference, Seattle, Washington, June 18–20, 1990. Manuscript received by the Heat Transfer Division August 1990; revision received May 1992. Keywords: Natural Convection, Turbulence. Associate Technical Editor: D. M. McEligot.

Copyright © 1992 by ASME
Downloaded 13 Dec 2010 to 193.140.21.150. Redistribution subject to ASME license or copyright; see http://www.asme.org/terms/Terms_Use.cfm

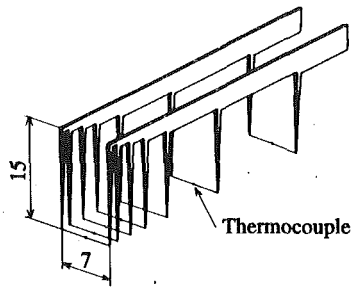

Fig. 1(*a*) Thermocouple rake

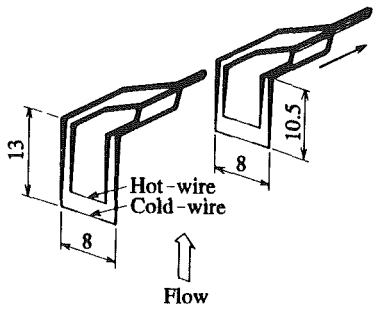

Fig. 1(*b*) Hot-wire/cold-wire arrangements

Fig. 1 *Probes for measurement (all dimensions in mm)*

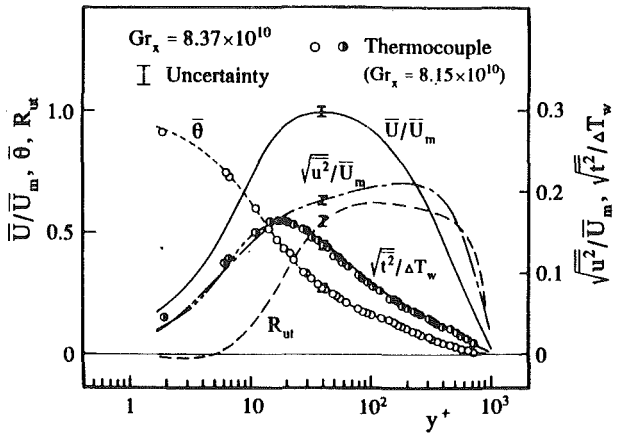

Fig. 2 Distributions of turbulent quantities

near the centerline of the plate at a location of 2.53 m downstream from the leading edge of the plate ($Gr_x \simeq 8 \times 10^{10}$). Velocity and temperature data for about 4 minutes per measurement were processed on a personal computer (NEC-PC9801) and on a computer system (FACOM-M780/20) after analog-to-digital conversion at a sampling frequency of 400 Hz.

Ambient fluid temperature $\overline{T}_\infty$ was about 16 ~ 17°C for all experiments; the variations of wall temperature and ambient temperature were at most ±0.2°C and ±0.3°C, respectively, for each experiment. Physical properties were evaluated at the film temperature ($=(\overline{T}_w + \overline{T}_\infty)/2$) except for the coefficient of volumetric expansion ($= 1/\overline{T}_\infty$).

In evaluating u_τ, the wall shear stress τ_w was estimated with the empirical equation, $\tau_w/\rho(g\beta\Delta T_w\nu)^{2/3} = 0.684\mathrm{Gr}_x^{1/11.9}$, obtained by Tsuji and Nagano (1988a). The above equation for wall shear stress is also well correlated with the data of Cheesewright and Mirzai (1988) using a fiber optic laser-Doppler anemometer and with the recent numerical prediction of Henkes and Hoogendoorn (1990).

3 Basic Turbulent Quantities in the Natural Convection Boundary Layer

The distributions of turbulent quantities of the velocity and thermal fields measured with a hot-wire/cold-wire arrangement are shown in Fig. 2 against dimensionless distance y^+ from the wall. The use of coordinate y^+ is effective to identify the difference of the characteristics between the natural con-

Nomenclature

E_u, E_t = spectrum functions of velocity and temperature fluctuations
f = frequency
Gr_x = Grashof number = $g\beta\Delta T_w x^3/\nu^2$
L_{tx}, L_{ty}, L_{tz} = integral scales of thermal field in x, y, and z directions
L_{uy} = integral scale of velocity field in y direction
Nu_x = Nusselt number
Pr = Prandtl number
R_u, R_t = space–time correlations of velocity and thermal fields
R_{ut} = cross-correlation between velocity and thermal fields = $\overline{ut}/(\sqrt{\overline{u^2}}\sqrt{\overline{t^2}})$
r_x, r_y, r_z = distances between two measuring points in x, y, and z directions
T = instantaneous fluid temperature
ΔT_w = fluid temperature difference = $\overline{T}_w - \overline{T}_\infty$
t = temperature fluctuation
U = instantaneous velocity in x direction
U_c = convection velocity
$\overline{U}_m$ = maximum velocity
u = velocity fluctuation in x direction
u_τ = friction velocity = $\sqrt{\tau_w/\rho}$
x, y, z = streamwise, normal, and spanwise directions (coordinates)
y^+ = dimensionless distance from wall = $u_\tau y/\nu$
$Z_{\min}$, $Z_{\max}$ = intervals corresponding to first minimum and first maximum of short-time averaged spatial correlation coefficient in z direction
β = volumetric expansion coefficient = $1/\overline{T}_\infty$
θ = dimensionless temperature = $(T - \overline{T}_\infty)/\Delta T_w$
λ_{tx}, λ_{ty}, λ_{tz} = microscales of thermal field in x, y, and z directions
λ_{uy} = microscale of velocity field in y direction
ν = kinematic viscosity
ρ = density
τ = time
τ_a = averaging time
τ_w = wall shear stress
$\Delta\tau$ = delay time
$\overline{(\ )}$ = time-averaged quantities
$\langle\ \rangle$ = ensemble-averaged quantities

Subscripts

w = wall condition
∞ = ambient condition

Superscript

$+$ = dimensionless quantities normalized by wall variables

Downloaded 13 Dec 2010 to 193.140.21.150. Redistribution subject to ASME license or copyright; see http://www.asme.org/terms/Terms_Use.cfm

vection and the usual turbulent boundary layers (Tsuji and Nagano, 1988a, 1988b). Measurement uncertainties at 95 percent coverage (ANSI/ASME, 1985; Moffat, 1988) were ± 0.13 in y^+, ± 0.015 in $\overline{U}/\overline{U}_m$, ± 0.009 in θ, ± 0.005 in $\sqrt{\overline{u^2}}/\overline{U}_m$, ± 0.003 in $\sqrt{\overline{t^2}}/\Delta T_w$, and ± 0.020 in R_{ut}, respectively. These intervals are indicated in the figure. Because the profiles obtained with hot-wire/cold-wire arrangements are almost the same as those reported previously (Tsuji and Nagano, 1988a), the data points are omitted for simplicity. The maximum velocity location is at $y^+ \simeq 40$ ($y \simeq 10$ mm). The intensities of temperature and velocity fluctuations reach their maxima at $y^+ \simeq 20$ in the inner layer (from the wall to the maximum velocity location) and at $y^+ \simeq 250$ in the outer layer (beyond the maximum velocity location), respectively. The cross-correlation coefficient R_{ut} between velocity and temperature fluctuations takes a constant value of about 0.65 over most of the outer layer, while it becomes slightly negative very near the wall. Also shown in Fig. 2 are mean and fluctuating temperature profiles measured with the thermocouple probe. Since the cutoff frequency of thermocouple is about 20 Hz, high-frequency components of temperature fluctuation may be eliminated in comparison with those obtained with a cold wire (cutoff frequency of about 250 Hz). However, there was no significant difference between the results obtained with different probes. This is due to little contribution of higher frequency components ($f > 30$ Hz) to a temperature variance, as shown below.

Figures 3(a) and 3(b) show typical frequency spectra of velocity and temperature fluctuations measured with a hot-wire/cold-wire arrangement. Spectra are normalized such that:

$$\int_0^\infty [fE_u(f)/\overline{u^2}]d(\ln f) = 1, \quad \int_0^\infty [fE_t(f)/\overline{t^2}]d(\ln f) = 1 \qquad (1)$$

The uncertainties were ± 7 percent in $fE_u(f)/\overline{u^2}$ and ± 6 percent in $fE_t(f)/\overline{t^2}$ (Bendat and Piersol, 1971). The bulk of the energies of both velocity and temperature fluctuations occurs in the frequency range of 0.1 to 50 Hz and it can be conjectured that fluid motions of several Hz mainly control the structure of the natural convection boundary layer. The velocity fluctuation has energetic, lower frequency components than the temperature fluctuation except the region very near the wall. The temperature fluctuation intensity at frequencies higher than 30 Hz is evidently very small and thus the fine thermocouple probe is useful for investigating the structure of the thermal field.

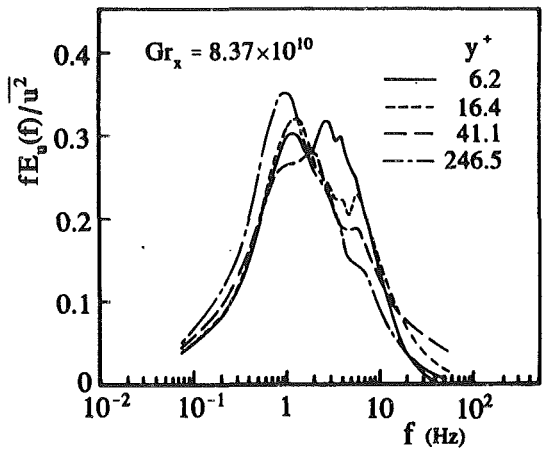

Fig. 3(a) Velocity fluctuation spectra

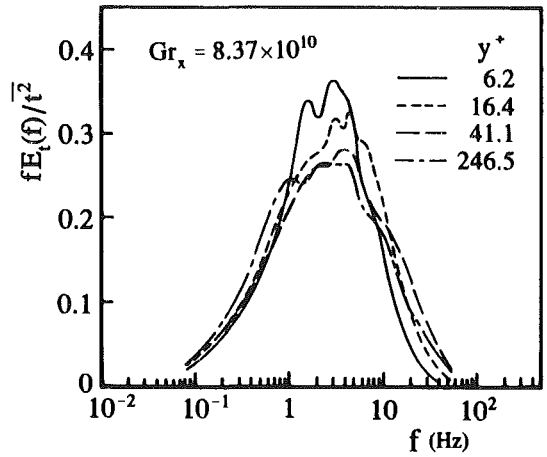

Fig. 3(b) Temperature fluctuation spectra

Fig. 3 Spectra of velocity and temperature fluctuations

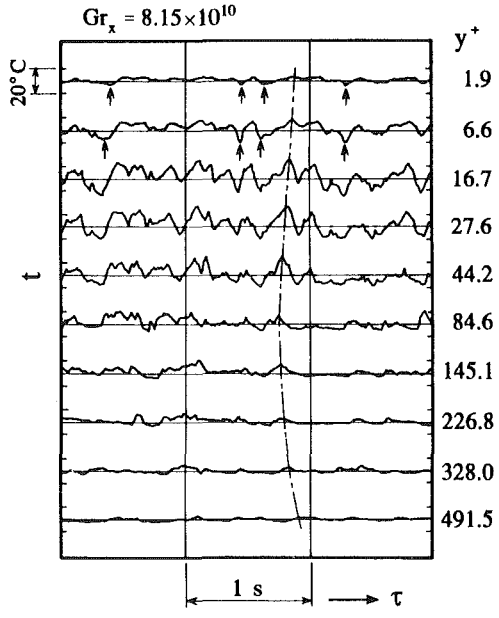

Fig. 4 Waveforms of temperature fluctuation in normal direction

4 Thermal and Velocity Fields in the Direction Normal to the Plate

4.1 Temporal Variation of Temperature Profile. Waveforms of instantaneous temperature in the boundary layer measured with the thermocouple probe are shown in Fig. 4. High- and low-temperature fluid motions encompassing the whole boundary layer region are observed, in particular, with the distinct invasions of low-temperature fluid in the wall vicinity (marked with arrows in the figure). Large-amplitude waveforms obviously indicate more rapid progress of the thermal field with time in the region of high-speed flow than in the near-wall and outermost regions, as shown by a chain line in the figure. However, the most rapid progress of waveform does not occur at the maximum velocity location but at a little farther out, as will be described later with respect to the space-time correlation for the thermal field.

An example of temporal variation of instantaneous temperature profile θ is shown in Fig. 5. This figure illustrates how the thermal field changes its state with time. In the boundary layer, many other profiles were observed in instantaneous temperatures. Therefore, we classified instantaneous temperature profiles into 1024 ($= 2^{10}$) kinds of events with the condition that the instantaneous temperature was higher or lower

Downloaded 13 Dec 2010 to 193.140.21.150. Redistribution subject to ASME license or copyright; see http://www.asme.org/terms/Terms_Use.cfm

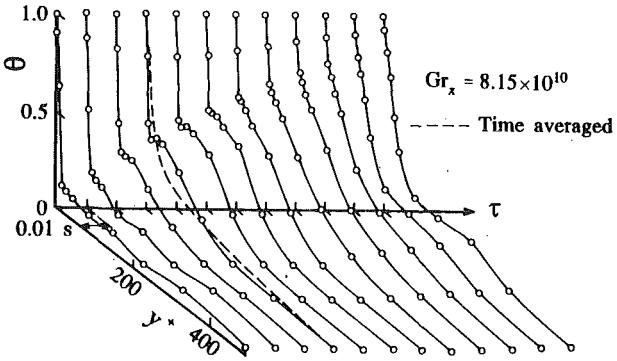

Fig. 5 Instantaneous temperature profiles

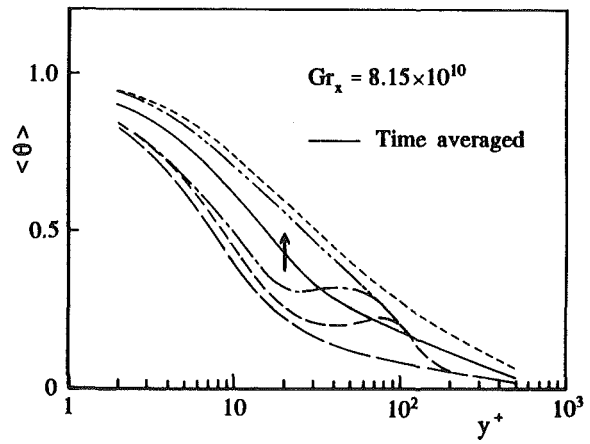

Fig. 6(*a*) Pattern increasing with time

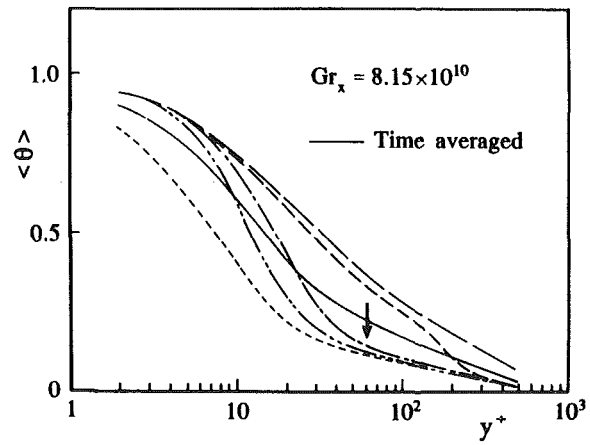

Fig. 6(*b*) Pattern decreasing with time

Fig. 6 Variation of temperature profiles

than the time-averaged one at each measuring point (ten points in all), and then we obtained a frequency distribution for the events. The typical patterns were specified with the events having a definite peak in the frequency distribution. The most distinct patterns recognized were those in which the instantaneous temperature became lower or higher than the time-averaged values over all measuring points, the time fraction of the respective pattern occurrence being about 10 ~ 15 percent of the whole measuring time. Figure 6(*a*) shows patterns that appeared most frequently when the temperature profile was initially lower than the time-averaged temperature and then increased with time. Here, $\langle\theta\rangle$ denotes a pattern recognized, ensemble-averaged temperature. The ensemble average was obtained by averaging more than four hundreds for each typical pattern. The fluctuating amplitude of $\langle\theta\rangle$ was mostly $\sqrt{\langle(\theta-\langle\theta\rangle)^2\rangle} \simeq 0.1$ and the uncertainty in $\langle\theta\rangle$ was estimated to be less than ±0.01. The temperature increase first occurs in the outer layer, and then evolves toward the inner layer. Figure 6(*b*) shows patterns that appeared when the temperature profile was initially higher than the mean temperature and then decreased with time. Again, the temperature begins to decrease in the outer region of the boundary layer. Although the periodic regularity in the change of these patterns, which occurred at a frequency of more than one hundred in 3 minutes, was not clearly identified, we found that the temperature profile varied consistently under the control of the thermal field in the outer layer. This corresponds to an observation of the most rapid progress of waveform in the outer layer as shown in Fig. 4, and may hold a significant key for elucidating the turbulent structure of the natural convection boundary layer.

4.2 Space-Time Correlations for the Thermal and Velocity Fields. Space-time correlation coefficients for the thermal and velocity fields were measured with two hot-wire/cold-wire arrangements. A space-time correlation coefficient R_t between two points in the thermal field is defined by the following equation:

$$R_t(r_y^+, \Delta\tau) = \frac{\overline{t(y^+, \tau)t(y^+ + r_y^+, \tau+\Delta\tau)}}{\sqrt{t^2(y^+, \tau)}\sqrt{t^2(y^+ + r_y^+, \tau+\Delta\tau)}} \quad (2)$$

The two-point, space-time correlation coefficient R_u in the velocity field is defined in the same manner. Spatial correlation coefficients for zero delay-time ($\Delta\tau = 0$) between two points in the thermal and velocity fields are shown in Figs. 7(*a*) and 7(*b*). The uncertainties were ±0.018 in R_t and ±0.025 in R_u, respectively. Dimensionless distance y^+ denotes the position of a fixed, near-wall-side hot-wire/cold-wire arrangement and r_y^+ is the distance between the two arrangements (the other being traversed). Obviously, there is an overall similarity between the correlations of the velocity and thermal fields. However, a marked difference really exists in the correlation between the near-wall and outer region structures of the velocity and thermal fields (see the results for $y^+ = 6.2$). Thus, with increasing r_y^+, the correlation coefficient for the thermal field decreases rapidly in the region up to about the maximum velocity location. Farther out, it remains almost constant independent of r_y^+. These facts are also confirmed by the spatial correlation-coefficient measurements obtained with the thermocouple rake. Cheesewright and Doan (1978) reported similar data for the thermal field and explained that such constancy in the spatial correlation coefficient in the natural convection boundary layer might be related to one of the intermittent bursts (Kline et al., 1967; Corino and Brodkey, 1969) and a large structure of the boundary layer might be controlled by this phenomenon. However, as shown in Fig. 7(*b*), no evidence to justify their conjecture has been obtained in the spatial correlation of the velocity field.

In natural convection in which a temperature is no longer a passive scalar, there may be some differences in the large-scale structures and the convection velocities of the velocity and thermal fields. Therefore, it is not sufficient to investigate the structure only through a spatial correlation value while ignoring the information on time. Thus, we have obtained the two-point, space-time correlation coefficients in the thermal and velocity fields (Figs. 8(*a*) and 8(*b*)). The delay time corresponding to the maximum correlation coefficient of temperature fluctuations moves in the negative direction with increasing r_y^+, as expected from temperature waveforms in Fig. 4. The maximum delay in the negative direction occurs at the location $r_y^+ = 82.1$ (slightly farther out than the velocity max-

Downloaded 13 Dec 2010 to 193.140.21.150. Redistribution subject to ASME license or copyright; see http://www.asme.org/terms/Terms_Use.cfm

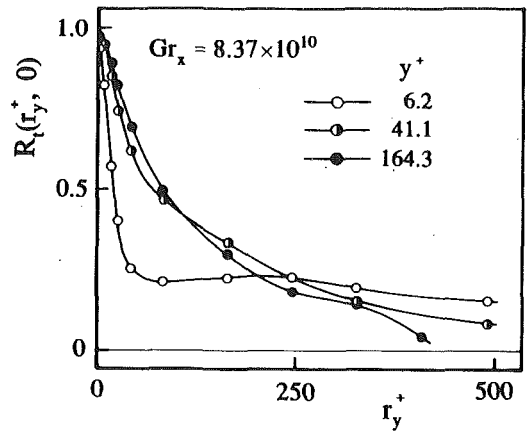

Fig. 7(*a*) Thermal field

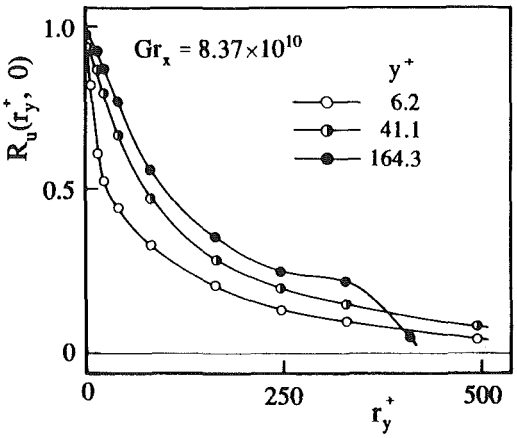

Fig. 7(*b*) Velocity field

Fig. 7 Spatial correlations normal to wall

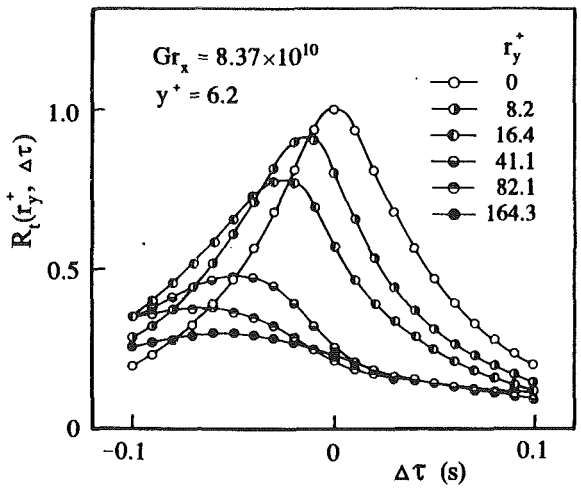

Fig. 8(*a*) Thermal field

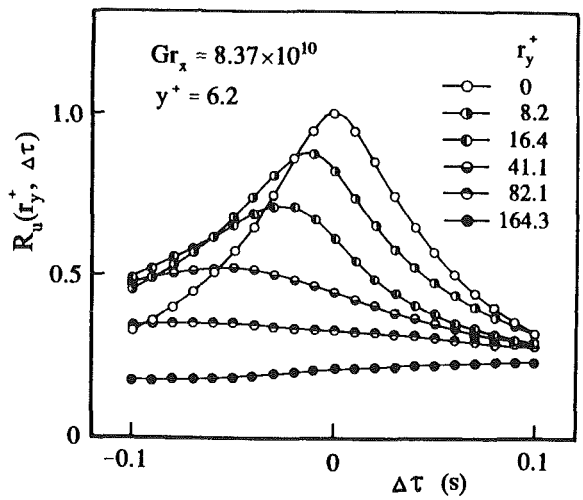

Fig. 8(*b*) Velocity field

Fig. 8 Space-time correlations normal to wall

imum). The maximum values of the correlation coefficient for the thermal field are almost the same as those for the velocity field in the range of r_y^+ up to about 40. However, in the same r_y^+ range, the correlation values of $\Delta\tau = 0$ for the thermal field, as shown in Fig. 7, decrease much more quickly than the corresponding velocity correlations, although they remain almost constant for $r_y^+ > 40$. As shown in Fig. 6, the structural change in the thermal field due to large-scale motion appears first in the outer layer and then evolves to the inner layer. The space-time correlation coefficients shown in Figs. 7 and 8 will be a reflection of this progress of the thermal field. It is not logically defensible to relate such a correlation coefficient behavior directly to the coherent structures (Kline and Robinson, 1990; Nagano and Hishida, 1990) as seen in the isothermal or forced convection turbulent boundary layer.

5 Thermal Field in the Streamwise Direction

Streamwise instantaneous temperature was measured by setting the thermocouple rake parallel to the wall in the vertical direction. Waveforms of temperature fluctuation near the wall ($y^+ = 6.2$) are shown in Fig. 9. The well-preserved thermal field is found to exist in the streamwise direction. Such a state was also observed at any y^+ location in the boundary layer. The space-time correlations (not shown) agreed comparatively well with those reported by Cheesewright and Doan (1978). Cheesewright and Dastbaz (1983) estimated the convection (or advection) velocity of the thermal field from the delay time at which a space-time correlation coefficient becomes maximum. The convection velocity U_c obtained in a similar manner is presented in Fig. 10, normalized with the local mean velocity $\overline{U}$

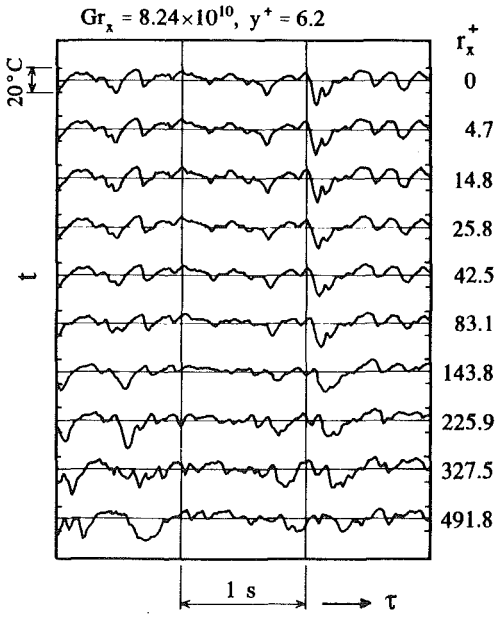

Fig. 9 Waveforms of temperature fluctuation in streamwise direction

Downloaded 13 Dec 2010 to 193.140.21.150. Redistribution subject to ASME license or copyright; see http://www.asme.org/terms/Terms_Use.cfm

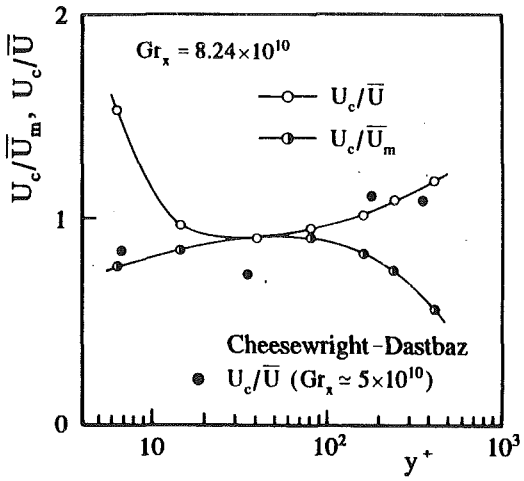

Fig. 10 Convection velocity

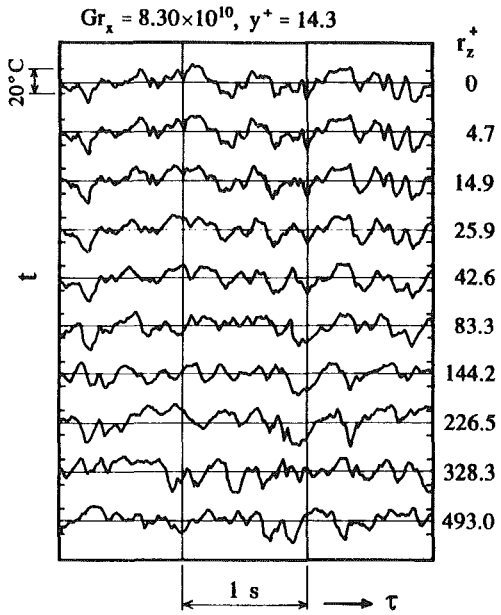

Fig. 11 Waveforms of temperature fluctuation in spanwise direction

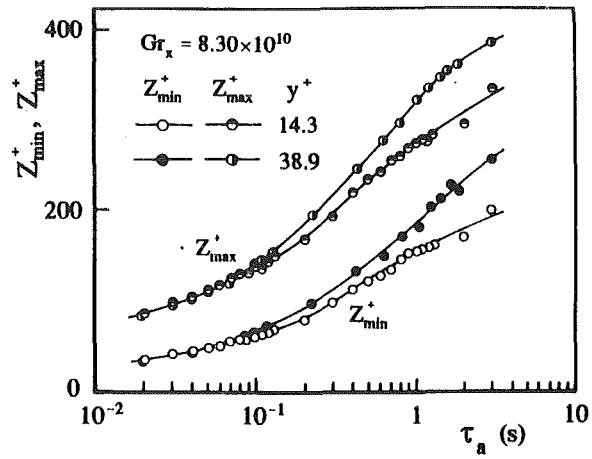

Fig. 12 Z^+_{min} and Z^+_{max} of short-time averaged correlation in spanwise direction

or the maximum velocity $\overline{U}_m$. The uncertainty was ± 0.03 in $U_c/\overline{U}_m$. The convection velocity depends on the distance r_x between two measuring points, but becomes almost constant for $r_x > 20$ mm, which is consistent with the result of Cheesewright and Dastbaz (1983) shown in the figure. Thus, in the present study, the convection velocity is defined by the relevant constant value for $r_x > 20$ mm (and may be regarded as the convection velocity of a large-scale turbulent eddy). As seen in Fig. 10, the convection velocity exceeds the local mean velocity near the wall and in the outermost region, while it becomes smaller than the mean velocity around the maximum velocity location. The measurements of Cheesewright and Dastbaz (1983) differ from the present result in the near-wall region (which may be attributed to their measurements of local mean velocity in the neighborhood of the wall). Also, in a forced convection boundary layer, it is known that the convection velocity becomes greater than the local mean velocity in the near-wall region (Antonia and Fulachier, 1989).

6 Thermal Field in the Spanwise Direction

Figure 11 shows temperature waveforms near the location where the intensity of temperature fluctuation reaches a maximum. The thermocouple rake is set in the spanwise direction with its head at the center of the plate ($r_z^+ = 0$). Kitamura et al. (1985) deduced the existence of a coherent streaky structure in the velocity field of a turbulent natural convection boundary layer in air (under uniform wall heat flux condition) from observation using a smoke-wire technique. However, no spanwise regularity in passing high- and low-temperature fluids is observed in the present waveforms of the thermal field. The spanwise spatial correlation coefficient decreases monotonically with increasing r_z^+ at any y^+ location in the boundary layer (not shown).

We have also investigated the short-time averaged spatial correlation. In ordinary turbulent boundary layers (Gupta et al., 1971), it has been established that there exists a deterministic interval z^+ at which the short-time averaged spatial correlation coefficient becomes minimum or maximum independent of an averaging time (sample length), which corresponds to a mean spanwise spacing of streaks. Figure 12 shows ensemble-averaged intervals Z^+_{min} and Z^+_{max}, at which the spatial correlation coefficient respectively becomes first minimum then maximum, as a function of averaging time τ_a. The uncertainties in Z^+_{min} and Z^+_{max} were estimated to be less than ± 14. Obviously, the intervals depend on the length of averaging time τ_a. From these results, it is quite inconclusive that a streaky structure exists in a turbulent natural convection boundary layer. Cheesewright and Dastbaz (1983) tried to identify a spanwise coherent structure with a short-time averaging method. They inferred the existence of streaky structure and suggested that the dimensionless wavelength and period, which were obtained from the space-time correlation measurement with a pair of thermocouples, became much greater than those in the forced convection boundary layer. The discrepancy between the present and their results may be attributed to the difference in the measuring technique and the criterion of detection. Therefore, additional experimental approaches would be needed to understand fully the spanwise structure in a natural convection boundary layer. It should be mentioned that in ordinary turbulent boundary layers, low-speed streaks associated with quasi-coherent structures never fail to exist near the wall (e.g., Kline and Robinson, 1990). These coherent structures, moreover, play a key role in determining the forced convective heat transfer as demonstrated by Nagano and Tagawa (1988), and Nagano and Hishida (1990).

7 Characteristic Length Scales of Turbulence Structure

Next, we investigate the spatial length scales to gain more insight into the structural difference in each direction. Microscale and integral scale, defined by the following equations

Downloaded 13 Dec 2010 to 193.140.21.150. Redistribution subject to ASME license or copyright; see http://www.asme.org/terms/Terms_Use.cfm

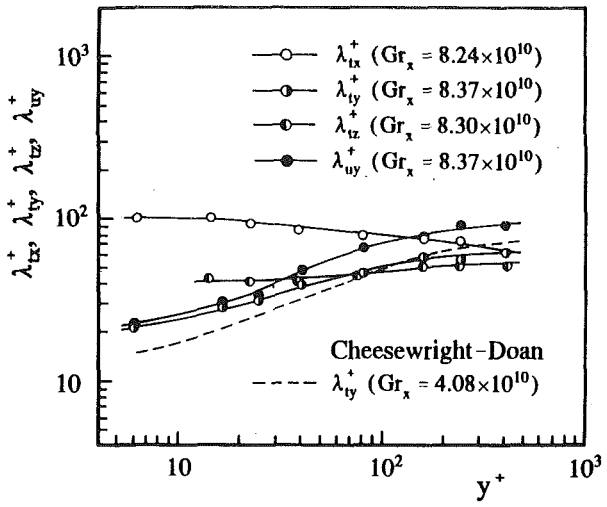

Fig. 13(*a*) Microscales

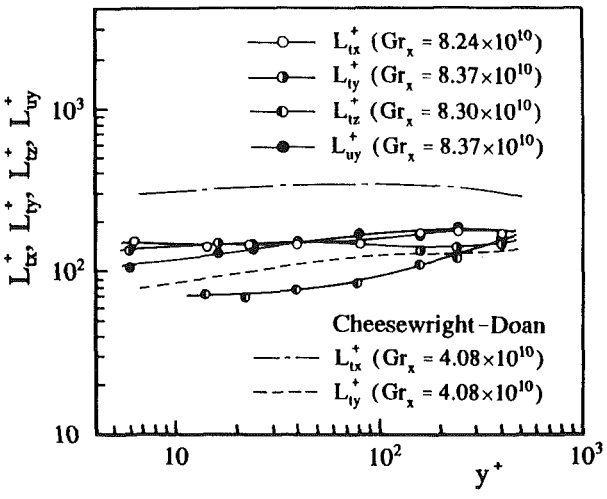

Fig. 13(*b*) Integral scales

Fig. 13 Characteristic length scales

(Hinze, 1975), are important characteristic length scales of the turbulence field:

$$\frac{1}{\lambda_{ty}^{+2}} = -\frac{1}{2}\left[\frac{\partial^2 R_t(r_y^+, 0)}{\partial r_y^{+2}}\right]_{r_y^+=0} \tag{3}$$

$$L_{ty}^+ = \int_0^\infty R_t(r_y^+, 0)dr_y^+ \tag{4}$$

Microscale is a characteristic length related to destruction rates of temperature and velocity fluctuations. Integral scale, on the other hand, is regarded as a characteristic length related to large-scale structures. Equations (3) and (4) express the scales of the thermal field in the direction normal to the plate (y direction). Scales in other directions and the relevant velocity-field scales are defined in the same manner. Figure 13(*a*) shows the microscale λ_{uy}^+ of the velocity field and the microscales λ_{tx}^+, λ_{ty}^+, and λ_{tz}^+ of the thermal field. The uncertainties were less than ± 7 percent in these dimensionless microscales. In the inner layer of the thermal field, the largest scale is λ_{tx}^+ in the x direction and the smallest is the scale λ_{ty}^+ in the y direction. This indicates that the destruction process of temperature fluctuation is strongly anisotropic in the near-wall region. Away from the wall, the scales λ_{ty}^+ and λ_{tz}^+ increase with y^+, while λ_{tx}^+ decreases. Ultimately, the scales in each direction become almost equal at the outer edge of the boundary layer. Also shown in Fig. 13(*a*) is the scale λ_{ty}^+ measured by Cheesewright and Doan (1978), which is almost in agreement with the present result. The increase of the scales λ_{uy}^+ and λ_{ty}^+ with y^+ suggests that the destruction rates of velocity and temperature fluctuations become smaller toward the outer edge of the boundary layer.

Integral scales L_{uy}^+, L_{tx}^+, L_{ty}^+ and L_{tz}^+ of the velocity and thermal fields are shown in Fig. 13(*b*). The uncertainties estimated in these dimensionless integral scales were less than ± 12 percent. The thermal-field integral scales L_{tx}^+ and L_{ty}^+ in the x and y directions take nearly constant and identical values throughout the boundary layer. Note that, however, the scale L_{ty}^+ near the wall is estimated from the definition Eq. (4) with the peculiar spatial correlation profile shown in Fig. 7(*a*). Therefore, the result of Fig. 13(*b*) does not necessarily imply the similarity of large-scale structures in the x and y directions across the boundary layer. However, the scale L_{ty}^+ of about 140 near the wall indicates that the foregoing temporal variation of the thermal field is caused by large-scale motions extending over the maximum velocity location ($y^+ \simeq 40$). It can be also seen from Fig. 13(*b*) that the scale L_{tz}^+ in the z direction is smaller than the other scales in the inner layer and approaches those of L_{tx}^+ and L_{ty}^+ with increasing y^+. The scale L_{uy}^+ of the velocity field is seen to increase slightly toward the outer edge of the boundary layer. The measurements of L_{tx}^+ and L_{ty}^+ by Cheesewright and Doan (1978) are also shown in Fig. 13(*b*) for comparison. The scale L_{ty}^+ agrees with the present results in the outer region, although somewhat smaller values are indicated in the near-wall region. On the other hand, their measurements of L_{tx}^+ are much greater than the present results in the entire boundary layer. They reported that L_{tx}^+ was about three times as large as L_{ty}^+. However, this conclusion seems incomplete since they adopted the maximum value of the space-time correlation only for obtaining the integral scale L_{tx}^+. When all the integral scales are consistently defined by Eq. (4), L_{tx}^+ becomes approximately equal to L_{ty}^+ as shown in Fig. 13(*b*). The fact that the scales of large-scale motions are nearly equal in the streamwise and normal directions is also characteristic of a natural convection boundary layer.

8 Conclusions

The multipoint simultaneous measurement of the thermal field with a thermocouple rake and two-point simultaneous measurement of the velocity and thermal fields with two hot-wire/cold-wire arrangements have been made to investigate the turbulent structure of a natural convection boundary layer in air along a vertical flat plate.

Results obtained may be summarized as follows:

1 Temperature profile changes under the control of the thermal field in the outer region of boundary layer.

2 The spatial correlation coefficient of the thermal field between the near-wall region and the rest of the boundary layer decreases sharply in the region up to the maximum velocity location and then becomes almost constant in the outer layer. However, such a spatial correlation does not appear in the velocity field. Therefore, it is not logical to connect directly the observed unique distribution of the thermal-field correlation with the possible existence of quasi-coherent structures like bursts, as done before.

3 The thermal field is well preserved in the streamwise direction. The convection velocity becomes greater than the local mean velocity in the near-wall and outermost regions and smaller around the maximum velocity location.

4 No periodic streaky structure as seen in a forced convection boundary layer can be recognized in the waveforms and spatial correlations of the thermal field in the spanwise direction.

5 Microscales of the thermal field show a strong aniso-

Downloaded 13 Dec 2010 to 193.140.21.150. Redistribution subject to ASME license or copyright; see http://www.asme.org/terms/Terms_Use.cfm

tropic structure in the near-wall region. Integral scales in the x and y directions take constant and almost equal values throughout the whole boundary layer region.

References

Antonia, R. A., and Fulachier, L., 1989, "Topology of a Turbulent Boundary Layer With and Without Wall Suction," *J. Fluid Mech.*, Vol. 198, pp. 429–451.

ANSI/ASME PTC 19.1, 1985, *Supplement to Performance Test Codes, Instruments and Apparatus, Part 1, Measurement Uncertainty*, ASME, New York.

Bendat, J. S., and Piersol, A. G., 1971, *Random Data: Analysis and Measurement Procedures*, Wiley, New York.

Cheesewright, R., and Doan, K. S., 1978, "Space-Time Correlation Measurements in a Turbulent Natural Convection Boundary Layer," *Int. J. Heat Mass Transfer*, Vol. 21, pp. 911–921.

Cheesewright, R., and Ierokipiotis, E., 1982, "Velocity Measurements in a Turbulent Natural Convection Boundary Layer," *Proc. 7th Int. Heat Transfer Conf.*, Munich, Vol. 2, pp. 305–309.

Cheesewright, R., and Dastbaz, E., 1983, "The Structure of Turbulent in a Natural Convection Boundary Layer," *Proc. 4th Turbulent Shear Flow Symp.*, Karlsruhe, pp. 17.25–17.30.

Cheesewright, R., and Ierokipiotis, E., 1984, "Measurements in a Turbulent Natural Convection Boundary Layer," *Proc. 1st U. K. National Conf. Heat Transfer*, Leeds, Vol. 2, pp. 849–856.

Cheesewright, R., and Mirzai, M. H., 1988, "The Correlation of Experimental Velocity and Temperature Data for a Turbulent Natural Convection Boundary Layer," *Proc. 2nd U. K. National Conf. Heat Transfer*, Glasgow, pp. 79–89.

Corino, E. R., and Brodkey, R. S., 1969, "A Visual Investigation of the Wall Region in Turbulent Flow," *J. Fluid Mech.*, Vol. 37, pp. 1–30.

Gupta, A. K., Laufer, J., and Kaplan, R. E., 1971, "Spatial Structure in the Viscous Sublayer," *J. Fluid Mech.*, Vol. 50, pp. 493–512.

Henkes, R. A. W. M., and Hoogendoorn, C. J., 1990, "Numerical Determination of All Functions for the Turbulent Natural Convection Boundary Layer," *Int. J. Heat Mass Transfer*, Vol. 33, pp. 1087–1097.

Hinze, J. O., 1975, *Turbulence*, 2nd ed., McGraw-Hill, New York, pp. 41–43.

Hishida, M., and Nagano, Y., 1978, "Simultaneous Measurements of Velocity and Temperature in Nonisothermal Flows," ASME JOURNAL OF HEAT TRANSFER, Vol. 100, pp. 340–345.

Kitamura, K., Koike, K., Fukuoka, I., and Saito, T., 1985, "Large Eddy Structure and Heat Transfer of Turbulent Natural Convection Along a Vertical Flat Plate," *Int. J. Heat Mass Transfer*, Vol. 28, pp. 837–850.

Kline, S. J., Reynolds, W. C., Schraub, F. A., and Runstadler, P. W., 1967, "The Structure of Turbulent Boundary Layer," *J. Fluid Mech.*, Vol. 30, pp. 741–773.

Kline, S. J., and Robinson, S. K., 1990, "Quasi-Coherent Structures in the Turbulent Boundary Layer: Part 1. Status Report on a Community-Wide Summary of the Data," *Near-Wall Turbulence*, S. J. Kline and N. H. Afgan, eds., Hemisphere, Washington, DC, pp. 200–217.

Miyamoto, M., Kajino, H., Kurima, J., and Takanami, I., 1982, "Development of Turbulence Characteristics in a Vertical Free Convection Boundary Layer," *Proc. 7th Int. Heat Transfer Conf.*, Munich, Vol. 2, pp. 323–328.

Moffat, R. J., 1988, "Describing the Uncertainties in Experimental Results," *Exp. Thermal Fluid Science*, Vol. 1, pp. 3–17.

Nagano, Y., and Tagawa, M., 1988, "Statistical Characteristics of Wall Turbulence With a Passive Scalar," *J. Fluid Mech.*, Vol. 196, pp. 157–185.

Nagano, Y., and Hishida, M., 1990, "Turbulent Heat Transfer Associated With Coherent Structures Near the Wall," *Near-Wall Turbulence*, S. J. Kline and N. H. Afgan, eds., Hemisphere, Washington, DC, pp. 568–581.

Tsuji, T., and Nagano, Y., 1988a, "Characteristics of a Turbulent Natural Convection Boundary Layer Along a Vertical Flat Plate," *Int. J. Heat Mass Transfer*, Vol. 31, pp. 1723–1734.

Tsuji, T., and Nagano, Y., 1988b, "Turbulence Measurements in a Natural Convection Boundary Layer Along a Vertical Flat Plate," *Int. J. Heat Mass Transfer*, Vol. 31, pp. 2101–2111.

Tsuji, T., and Nagano, Y., 1989a, "Velocity and Temperature Measurements in a Natural Convection Boundary Layer Along a Vertical Flat Plate," *Exp. Thermal Fluid Science*, Vol. 2, pp. 208–215.

Tsuji, T., and Nagano, Y., 1989b, "An Anemometry Technique for Turbulence Measurements at Low Velocities," *Exp. Fluids*, Vol. 7, pp. 547–559.

Downloaded 13 Dec 2010 to 193.140.21.150. Redistribution subject to ASME license or copyright; see http://www.asme.org/terms/Terms_Use.cfm

S. Lee
Research Assistant Professor.
Mem. ASME

M. M. Yovanovich
Professor.
Fellow ASME

Microelectronics Heat Transfer Laboratory,
Department of Mechanical Engineering,
University of Waterloo,
Waterloo, Ontario, Canada

Linearization of Natural Convection From a Vertical Plate With Arbitrary Heat-Flux Distributions

A simple model is developed to predict the heat transfer characteristics of a vertical plate with arbitrarily prescribed surface heat-flux variations under a buoyancy-driven flow. The analysis is based on the linearized approximations to the boundary layer form of the conservation equations. Explicit, closed-form solutions for the surface temperature of the plate and fluid temperature distributions are obtained for the full range of Prandtl numbers. Surface heat-flux variations of discontinuous as well as continuous types are examined, and the results are compared with air data obtained by using various solution methods including numerical simulations. It is shown that the present predictions are in excellent agreement with those of other methods that are capable of producing exact solutions.

Introduction

Natural convection heat transfer from a vertical plate has been a subject of numerous investigations in the past few decades. Plates with thermal conditions that allow similarity transformations have been examined by Ostrach (1953), Sparrow and Gregg (1956, 1958), and Jaluria and Gebhart (1977). They have considered steady-state, two-dimensional laminar boundary layer equations for a uniform wall temperature, a uniform surface heat flux, excess wall temperature variations of the power and exponential forms, and a line thermal source on an adiabatic plate. Yang (1960) reported that there are no other types of boundary condition that would make similarity solutions possible for steady natural convection heat transfer from a vertical plate.

Many more studies have followed in order to expand the number of available solutions for nonsimilar boundary conditions. An early attempt was made by Schetz (1962, 1963), who employed a collocation method to develop an approximate model for problems of discontinuous wall temperature type. In his study, the temperature and velocity profiles were assumed similar to those associated with unsteady one-dimensional conduction. Schetz and Eichhorn (1964) conducted an experiment with a Mach-Zehnder Interferometer, Hayday et al. (1967) and Sokovishin and Érman (1982) carried out numerical studies, and Smith (1970), Kelleher (1971), and Kao (1975) used series expansions to solve the same type of problems. Jaluria (1982, 1985), employing finite difference methods, investigated cases with a number of uniform heat-flux sources on an adiabatic plate in air. Several approximating techniques are also available for surfaces with continuous thermal conditions. An integral method was employed by Sparrow (1955) and Scherberg (1964), and a Görtler-type series expansion was used by Kelleher and Yang (1972). Kao and his coworkers (1977) developed local similarity and local nonsimilarity methods for problems with arbitrarily specified surface thermal conditions and presented comparisons of the results with numerical solutions. The boundary layer equations with nonuniform surface thermal conditions were again solved numerically by Yang et al. (1982). They obtained Merk-type series solutions, which resulted in values that are identical or very close to the numerical results of Kao et al. (1977) for a variety of surface conditions. Lee and Yovanovich (1989, 1991a), employing integral methods, and Park and Tien (1990), using modified similarity parameters, also developed approximate models for a vertical plate with changes in thermal conditions.

Except for numerical methods, such as finite difference, finite volume, and finite element methods, exact solution techniques for general cases of nonsimilar problems do not exist in the literature. For the cases with an arbitrary surface thermal variation, the boundary layer equations may be modified through variable transformations, but the resulting differential equations will remain partial with multiple independent space variables. Close-to-exact solutions to these partial differential equations can be found by means of direct numerical integrations, or approximate solutions may be obtained by solving the ordinary differential equations resulting from either the local similarity or local nonsimilarity method (Kao et al., 1977). As can be seen from comparisons with the numerical results presented by Kao et al. (1977), the local nonsimilarity method is capable of producing highly accurate solutions for most of the examples that were considered. It was found, however, that both local similarity and local nonsimilarity methods fail to predict the proper solutions for some cases.

Simple, general solutions are of a great value to those involved in practical applications where problems arise in such a way that the surface thermal condition is not known but is itself to be found. This interfacial condition established between the fluid and the solid has to be determined by solving the fluid side convection heat transfer problem and the solid side heat diffusion process in an iterative procedure. Such conjugate problems occur in many practical situations including the thermal modeling of printed circuit boards, and the iterative solution procedure necessitates that the convection model be simple and capable of dealing with arbitrary surface thermal conditions.

In this paper, a new approximate method is developed based on the linearization of the governing differential equations. The linearization is performed by introducing an effective boundary layer velocity, which is subsequently determined by relating the total thermal energy dissipated into the fluid to the effective kinetic energy of the fluid flow. The effective velocity determined in this manner becomes analogous to an externally induced free-stream velocity, thereby allowing the analysis to proceed in a way that is similar to forced convection analysis. The resulting model, consisting of a summation of simple power terms, is capable of predicting local laminar

Contributed by the Heat Transfer Division for publication in the JOURNAL OF HEAT TRANSFER. Manuscript received by the Heat Transfer Division August 1991; revision received April 1992. Keywords: Natural Convection. Associate Technical Editor: W. A. Sirignano.

Copyright © 1992 by ASME
Downloaded 13 Dec 2010 to 193.140.21.150. Redistribution subject to ASME license or copyright; see http://www.asme.org/terms/Terms_Use.cfm

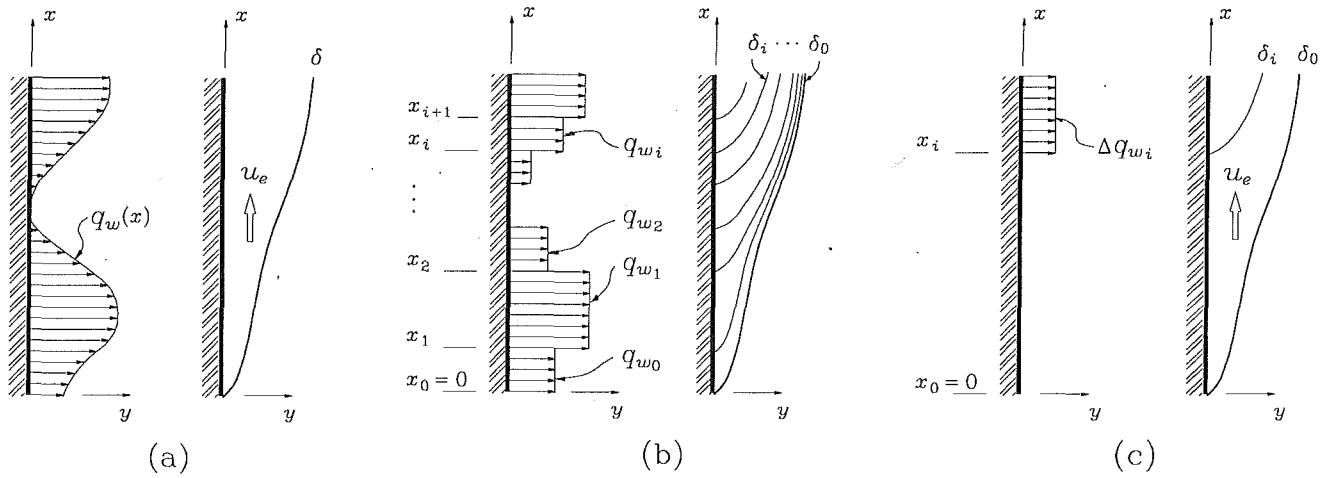

Fig. 1 Geometric configuration and coordinate system shown with schematic representations of surface heat-flux variation and development of boundary layers where surface heat flux is prescribed by (*a*) continuous variation; (*b*) step changes; (*c*) an isolated step change in the wake of a buoyancy-driven flow

natural convection heat transfer from a flat, vertical plate dissipating energy with arbitrarily prescribed surface heat-flux variations, including step discontinuities.

Problem Statement

The geometric configuration and coordinate system of the problem are depicted in Fig. 1(*a*), where a vertical plate is shown with an arbitrarily prescribed surface heat-flux variation. Also depicted in the right side of the figure is the development of the hydrodynamic boundary layer whose thickness is greatly exaggerated in the y direction. The plate is dissipating heat into an extensive, quiescent fluid, which is assumed to be maintained at uniform temperature.

The conservation of mass, momentum, and energy for two-dimensional, steady-state, laminar boundary layer flow yields a set of governing differential equations, expressed as

$$\frac{\partial u}{\partial x}+\frac{\partial v}{\partial y}=0 \tag{1}$$

$$u\frac{\partial u}{\partial x}+v\frac{\partial u}{\partial y}=\nu\frac{\partial^2 u}{\partial y^2}+g\beta T \tag{2}$$

$$u\frac{\partial T}{\partial x}+v\frac{\partial T}{\partial y}=\alpha\frac{\partial^2 T}{\partial y^2} \tag{3}$$

The boundary conditions associated with the above equations are

$$\text{at } y=0, \quad u=v=0, \quad -k\frac{\partial T}{\partial y}=q_w(x)$$

$$\text{at } y\to\infty, \quad u\to 0, \quad T\to 0$$

$$\text{at } x=0, \quad u=T=0 \tag{4}$$

where T denotes the temperature excess over the ambient fluid temperature. The usual assumptions and approximations, such as those of constant fluid properties, except the density in the derivation of the buoyant term, and negligible viscous heating are made in deriving these equations.

Without a loss of generality, the surface heat-flux variation $q_w(x)$ is discretized into a number of step changes as shown in Fig. 1(*b*) where only a few step changes are shown for brevity. The surface thermal condition given in Eq. (4) is replaced by

Nomenclature

b = exponent determined by Eq. (34)
C = coefficient given by Eq. (26)
C_1, C_2 = coefficients
f_u = function defined by Eq. (15)
g = gravitational acceleration
Gr_a^* = modified Grashof number $= g\beta q_a x_a^4/k\nu^2$
Gr_x^* = modified Grashof number $= g\beta q_{w_0} x^4/k\nu^2$
$\overline{\mathrm{Gr}}_x^*$ = modified Grashof number $= g\beta \bar{q}_w x^4/k\nu^2$
$\bar{h}$ = average heat transfer coefficient
k = thermal conductivity
Nu_x = Nusselt number $= q_{w_0}x/T_w k$
Pr = Prandtl number $= \nu/\alpha$
q = local heat flux
q^* = dimensionless heat flux $= q/q_{w_0}$
$\bar{q}$ = average heat flux defined by Eq. (32)
Q_w = heat dissipation defined by Eq. (30)
Re_x = Reynolds number $= u_e x/\nu$
t = variable defined by Eq. (9)
T = temperature excess over ambient fluid temperature
u = local velocity in x direction
u_e = effective velocity across the boundary layer
v = local velocity in y direction
x = coordinate along the plate
y = coordinate normal to the plate
α = thermal diffusivity of fluid
β = thermal expansion coefficient
δ = boundary layer thickness
Δq_{w_i} = heat-flux difference $= q_{w_i} - q_{w_{i-1}}$
ζ = dummy variable
η = similarity variable
θ = dimensionless temperature, Eq. (42)
ν = kinematic viscosity
ξ = dimensionless x coordinate $= x/x_1$
ϕ = dependent variable, u or T
χ = delay factor

Subscripts

a = arbitrary references
i = parameters at ith step
w = wall conditions
κ = parameters at κth step
0 = parameters at leading section

Downloaded 13 Dec 2010 to 193.140.21.150. Redistribution subject to ASME license or copyright; see http://www.asme.org/terms/Terms_Use.cfm

$$-k\left.\frac{\partial T}{\partial y}\right|_{y=0}=q_{w_i} \quad \text{for } x_i \le x < x_{i+1};\ i=0,\ 1,\ 2,\ \ldots \tag{5}$$

where $x_0 = 0$, and q_{w_i} is the average surface heat flux over the ith section between $x = x_i$ and x_{i+1}. Obviously, a finer discretization would yield a closer representation of the continuous variation, and in such cases, q_{w_i} may be approximated simply by the heat flux at the midlocation of the section. It is to be noted that local heat flux may be zero, representing an adiabatic surface, or it may become negative provided that the resulting fluid velocity is maintained positive everywhere in the boundary layer.

Also shown in Fig. 1(*b*) are the outer edges of the boundary layers developed by the onset of the step changes. The primary boundary layer developed by the initial step jump of q_{w_0} at the leading edge of the plate is denoted with a subscript 0. The inner sublayers are denoted with the subscript that corresponds to that of the matching step change.

Figure 1(*c*) shows an adiabatic plate with an isolated single step heat input beyond $x = x_i$. Shown in the right side is the growth of the corresponding sublayer within the wake of the primary boundary layer. The purpose of this figure is to describe the conceptual approach that is taken in the present analysis to determine the effects that an individual step change has on the overall upstream flow and local heat transfer. This is an important aspect of the analysis as it will be discussed in the later section.

Linearization of Equations

An exact solution to the above problem for $x > x_1$ does not exist. An approximate solution is sought in which the nonlinear convective terms appearing in the left side of the momentum and energy equations are linearized by introducing an effective velocity:

$$u\frac{\partial \phi}{\partial x}+v\frac{\partial \phi}{\partial y}\approx u_e(x)\frac{\partial \phi}{\partial x} \tag{6}$$

where ϕ represents the dependent variable, either u or T, and $u_e(x)$ is the unknown effective velocity. Note that the above approximation is applied to the differential equations and the effective velocity is defined to be uniform across the boundary layer.

The linearization requires finding the function $u_e(x)$ that properly describes the characteristics of the fluid flow in the x direction. By integrating the above equation from $y = 0$ to δ with $\phi = u$, the effective *hydrodynamic* velocity may be defined as

$$u_e(x)=\frac{\dfrac{d}{dx}\displaystyle\int_0^\delta u^2 dy}{\dfrac{d}{dx}\displaystyle\int_0^\delta u dy} \tag{7}$$

Equation (1) was used in simplifying the numerator of the above expression. Alternative definition of $u_e(x)$ can be obtained also by integrating Eq. (6) with $\phi = T$. This would lead to another definition for $u_e(x)$, which can be seen as the effective *thermal* velocity. These definitions are exact in the integral form of the governing equations, and it can be shown that they both possess the same functional expression. Since only the determination of the functional dependency of $u_e(x)$ becomes necessary in the present analysis, either definition may be used in determining $u_e(x)$.

A transient variable t such that

$$dt=\frac{dx}{u_e(x)} \tag{8}$$

is introduced to transform the linearized convective operator given by the right side of Eq. (6). Upon integration,

$$t=\int_0^x \frac{d\zeta}{u_e(\zeta)} \tag{9}$$

which can be viewed as the residence time of the flow from the leading edge of the plate to the downstream location x. With the use of the above newly defined variable, the original x–y plane is transformed into the t–y plane, and the momentum and energy equations become, respectively,

$$\frac{\partial u}{\partial t}=\nu\frac{\partial^2 u}{\partial y^2}+g\beta T \tag{10}$$

$$\frac{\partial T}{\partial t}=\alpha\frac{\partial^2 T}{\partial y^2} \tag{11}$$

Note that the continuity equation has been absorbed in the above transformed equations through $u_e(x)$. The thermal boundary condition given by Eq. (5) becomes

$$-k\left.\frac{\partial T}{\partial y}\right|_{y=0}=q_{w_i} \text{ for } t_i \le t < t_{i+1};\ i=0,\ 1,\ 2,\ \ldots \tag{12}$$

where t_i corresponds to x_i.

The most notable features that are different in the above transformed equations from the steady-state equations are the linearity of the dependent variables u and T, and the decoupling of the temperature field from the velocity field in the t–y plane. It is worthwhile to mention that the above equations will result in correct forms of the exact solutions once the proper expression of $u_e(x)$ is found according to the definition given by Eq. (7).

Analysis

The exact solutions to the linearized problem defined by Eqs. (10)–(12) with the rest of the boundary conditions given in Eq. (4) can be found by means of similarity transformations and the method of superposition (Lee, 1988). For $x_\kappa \le x < x_{\kappa+1}$, they are

$$T=\frac{2\sqrt{\alpha}}{k}\sum_{i=0}^{\kappa}\Delta q_{w_i}(t-t_i)^{1/2}\text{ierfc}\eta_i \tag{13}$$

$$u=\frac{4\sqrt{\alpha}q\beta}{k}\sum_{i=0}^{\kappa}\Delta q_{w_i}(t-t_i)^{3/2}f_u(\eta_i) \tag{14}$$

where

$$f_u(\eta)=\begin{cases}\eta i^2\text{erfc}\eta & \text{for Pr}=1\\ \dfrac{2}{1-\text{Pr}}\left(i^3\text{erfc}\eta-i^3\text{erfc}\dfrac{\eta}{\sqrt{\text{Pr}}}\right) & \text{for Pr}\neq 1\end{cases} \tag{15}$$

$$\eta_i=\frac{y}{2\sqrt{\alpha(t-t_i)}} \tag{16}$$

Here, and throughout the paper, $\Delta q_{w_i} = q_{w_i}$ when $i = 0$, and $t_0 = 0$.

The local surface temperature can be obtained by substituting $y = 0$ into Eq. (13):

$$T_w=\frac{2\sqrt{\alpha}}{k\sqrt{\pi}}\sum_{i=0}^{\kappa}\Delta q_{w_i}(t-t_i)^{1/2} \tag{17}$$

where ierfc $0 = 1/\sqrt{\pi}$ was used.

The only unknown in the above solutions is the transient variable $(t - t_i)$. Determination of $(t - t_i)$ in terms of the known steady-state variables is carried out in two stages as follows.

Downloaded 13 Dec 2010 to 193.140.21.150. Redistribution subject to ASME license or copyright; see http://www.asme.org/terms/Terms_Use.cfm

First, consider the case of uniform surface heat flux represented by the first term of the summation for $0 \le x < x_1$. Although exact similarity solutions are available (Sparrow and Gregg, 1956), an examination of this case will provide the basis upon which the current analysis can be extended to include general situations involving multistep changes.

Substituting the first term of Eq. (14) into Eq. (7) and evaluating the integrals with $\delta \to \infty$ leads to

$$u_e(x) = C_1 \frac{\sqrt{\alpha g \beta q_{w_0}}}{k} t^{3/2} \tag{18}$$

where the coefficient C_1 is a function of the Prandtl number. Determination of this coefficient is not necessary, and it is sufficient to note that it is a constant for a given fluid.

Equation (18) is differentiated after taking a 2/3 power of both sides. The resulting expression, after substituting Eq. (8) for dt and separating the variables, is

$$u_e du_e^{2/3} = \left(\frac{C_1\sqrt{\alpha g \beta q_{w_0}}}{k}\right)^{2/3} dx \tag{19}$$

Upon integration, this yields

$$u_e(x) = \left(\frac{C_1\sqrt{\alpha g \beta q_{w_0}}}{k}\right)^{2/5} \left(\frac{5x}{2}\right)^{3/5} \tag{20}$$

By substituting Eq. (20) into Eq. (9) for $u_e(x)$ and evaluating the integral, it can be shown that

$$t = \frac{5}{2}\frac{x}{u_e(x)} \tag{21}$$

With $u_e(x)$ from Eq. (20), the transient variable t can now be expressed in terms of the steady-state variables.

The surface temperature variation for the isoflux case is obtained from Eq. (17) with $\kappa = 0$:

$$T_w = \frac{2\sqrt{\alpha t} q_{w_0}}{\sqrt{\pi} k} \tag{22}$$

By substituting Eq. (21) for t into the above equation, the local Nusselt number can be expressed as

$$\mathrm{Nu}_x = C_2 \mathrm{Re}_x^{1/2} \tag{23}$$

where C_2 is another function of the Prandtl number, and Re_x denotes the Reynolds number defined as

$$\mathrm{Re}_x = \frac{u_e x}{\nu} \tag{24}$$

Note that the form of the above heat transfer expression is identical to that of the forced convection result. It reveals that $u_e(x)$ is analogous to the externally induced free-stream velocity in the forced convection study. By substituting Eq. (20) for u_e, Eq. (23) becomes

$$\mathrm{Nu}_x = C\mathrm{Gr}_x^{*1/5} \tag{25}$$

where C, consisting of C_1 and C_2, depends solely on Pr. This is again identical to the form of known results for laminar natural convection heat transfer from an isoflux surface. The Prandtl number function C can be determined by conserving the momentum and energy over the boundary layer (Lee, 1988) or simply by comparing the above heat transfer result with known data. Since the prime objective of the present study is to seek a simple solution that requires the least computational effort, the latter will be adopted to determine C. For example, by comparing Eq. (25) with the correlation equation proposed by Fujii and Fujii (1976), it is found that

$$C = \left(\frac{\mathrm{Pr}^2}{4 + 9\sqrt{\mathrm{Pr}} + 10\mathrm{Pr}}\right)^{1/5} \tag{26}$$

Also, with the use of Eqs. (20) and (21), the temperature solution for isoflux cases can be expressed as

$$T = \frac{\sqrt{\pi} x}{Ck\mathrm{Gr}_x^{*1/5}} q_{w_0} \,\mathrm{ierfc}\eta_0 \tag{27}$$

with

$$\eta_0 = \frac{C}{\sqrt{\pi}} \mathrm{Gr}_x^{*1/5} \frac{y}{x} \tag{28}$$

The method so far has demonstrated that the correct heat transfer relationship can be obtained for isoflux cases from the linearized differential equations. As the second stage of the analysis in determining $(t - t_i)$, the current analysis is extended for problems involving multiple step changes in surface heat flux as outlined in the following.

Recall that, in linearizing the differential equations, the effective velocity $u_e(x)$ was introduced as a parameter and, therefore, it needs to be determined based on information external to the equations. In the above example with an isoflux surface, this was accomplished by equating the integral forms of the equations. It resulted in Eq. (19), which was subsequently integrated to obtain Eq. (20) for $u_e(x)$.

Equation (20) can be rewritten to reveal the relationship between the effective kinetic energy of the fluid flow at an arbitrary location x and the total energy input into the fluid from the leading edge of the plate to the location of interest. It shows

$$u_e^2 \propto Q_w^{4/5} x^{2/5} \tag{29}$$

where

$$Q_w = \int_0^x q_w(\zeta) d\zeta \tag{30}$$

For the case of varying surface heat flux, an assumption is made such that the relationship between the effective kinetic energy and the total heat input is maintained as per Eq. (29). It follows that

$$u_e(x) = \left(\frac{C_1\sqrt{\alpha g \beta \bar{q}_w}}{k}\right)^{2/5} \left(\frac{5x}{2}\right)^{3/5} \tag{31}$$

where $\bar{q}_w$ is the average surface heat flux defined as

$$\bar{q}_w(x) = \frac{Q_w}{x} \tag{32}$$

As was previously indicated, the effective velocity defined by Eq. (31) is analogous to the induced free-stream velocity in the forced convection analysis. In the following, the effects that each isolated step jump in surface heat flux has on the overall temperature solution and the heat transfer characteristics of the plate will be determined.

Consider the flow over a vertical plate that experiences a single step jump in surface heat flux of Δq_{w_i} at some downstream location $x = x_i$. This is a classical problem that appears in the study of forced convection heat transfer from a flat plate that has an unheated starting length in the wake of a hydrodynamic boundary layer, as shown in Fig. 1(*c*). The primary hydrodynamic boundary layer growth denoted by δ_0 begins at the leading edge whereas the thermal boundary layer development begins at $x = x_i$. Through use of an integral boundary layer solution (Sparrow and Lin, 1965), it can be shown that the delay factor χ, which accounts for the unheated starting-length effect, can be obtained through the ratio of the thermal-to-hydrodynamic boundary layer thicknesses. It is found that

$$\chi = \left(1 - \frac{x_i}{x}\right)^b \tag{33}$$

with $b = 1/3$ for the externally induced laminar flow of a high Prandtl number fluid.

However, the above delay factor is obtained by regarding

Downloaded 13 Dec 2010 to 193.140.21.150. Redistribution subject to ASME license or copyright; see http://www.asme.org/terms/Terms_Use.cfm

the entire boundary layer flow over the heated section being externally induced, and the effect that the buoyant force due to the step heating over the surface has on the growth of the thermal boundary layer beyond $x = x_i$ is not accounted for in the derivation. This effect of buoyant force on the delay factor would depend on the Prandtl number. By recognizing that b is related to the Prandtl number as well as to the type of flow, it is seen that the effect can be incorporated by adjusting b. An examination of the limiting values of the Prandtl number revealed that b values are bounded. Furthermore, the wall temperature variations of various cases and comparisons of the heat transfer results with known data show that the final temperature solution depends weakly on b, and b rapidly approaches its limiting constant value as the Prandtl number becomes large ($\mathrm{Pr} > 10^2$) or small ($\mathrm{Pr} < 10^{-2}$). As a result, the following correlation equation is proposed:

$$b = 0.48 + 0.08\,\frac{0.2 - \mathrm{Pr}^{0.7}}{0.2 + \mathrm{Pr}^{0.7}} \tag{34}$$

This yields the value of 0.433 with Pr = 0.7.

Recall that the delay factor is proportional to the ratio of the thermal-to-hydrodynamic boundary layer thicknesses. Also, by noting from Eq. (16) that the growth of the boundary layer thickness varies with the square root of the transient variable, it can be written that

$$\chi = \frac{\sqrt{t - t_i}}{\sqrt{t}} \tag{35}$$

Upon equating Eqs. (33) and (35), one finds

$$t - t_i = t\left(1 - \frac{x_i}{x}\right)^{2b} \tag{36}$$

Here, the parameter t in the right side is related to the growth of the primary boundary layer. By substituting Eq. (21) for t with Eq. (31) for $u_e(x)$, the above equation becomes

$$t - t_i = \left(\frac{5}{2}\,\frac{kx}{C_1\sqrt{\alpha g\beta \bar{q}_w}}\right)^{2/5}\left(1 - \frac{x_i}{x}\right)^{2b} \tag{37}$$

With this equation for $t - t_i$, the parameters associated with the temperature solution given by Eq. (13) are completely determined. The final temperature solution is

$$T = \frac{\sqrt{\pi}x}{Ck\overline{\mathrm{Gr}}_x^{*1/5}} \sum_{i=0}^{\kappa} \Delta q_{w_i}\left(1 - \frac{x_i}{x}\right)^{b} \mathrm{ierfc}\,\eta_i \tag{38}$$

with

$$\eta_i = \frac{C}{\sqrt{\pi}}\,\overline{\mathrm{Gr}}_x^{*1/5}\,\frac{y}{x}\left(1 - \frac{x_i}{x}\right)^{-b} \tag{39}$$

where $\overline{\mathrm{Gr}}_x^*$ is the modified Grashof number based on the average surface heat flux $\bar{q}_w$. The complementary error function appearing in the solution can be evaluated by means of a numerical integration or by using a rational approximation (Abramowitz and Stegun, 1972) with a high degree of accuracy.

By substituting $\eta_i = 0$ into Eq. (38), the local wall temperature over the κth step for $x_\kappa \le x < x_{\kappa+1}$ can be obtained as

$$T_w(x) = \frac{x}{Ck\overline{\mathrm{Gr}}_x^{*1/5}} \sum_{i=0}^{\kappa} \Delta q_{w_i}\left(1 - \frac{x_i}{x}\right)^{b} \tag{40}$$

where C and b are given by Eqs. (26) and (34), respectively.

Comparisons and Discussions

Many simplifying approximations, such as the linearization of the governing differential equations and the assumption of a nonvariant proportionality relationship between the effective kinetic energy of the flow and the total heat dissipation, were introduced into the development of the model. Since the present solutions are based on a novel, approximate method, a major portion of this section will be devoted to comparisons with other data obtained by using various techniques. It is to be remembered that the intent of the study was to develop the simplest possible solutions that are sufficiently accurate for practical uses in predicting temperature distributions and surface heat transfer characteristics.

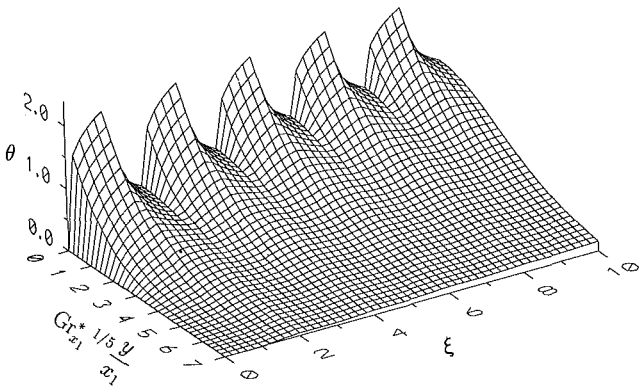

Fig. 2 Dimensionless temperature distribution due to alternating positive uniform and zero surface heat fluxes of equal size for Pr = 0.7

The present model successfully simulates the similarity solution of Jaluria and Gebhart (1977) who examined the case with a line thermal source on an adiabatic surface. For this case, a single step heat input of fixed Q is imposed over $x = 0$ to x_1 and the surface temperature variation given by Eq. (40) was evaluated as $x_1 \to 0$. In the limit, it can be shown that Eq. (40) reduces to

$$T_w(x) = \frac{bQ^{4/5}}{C(g\beta/k^4\nu^2)^{1/5}x^{3/5}} \tag{41}$$

which has the same form as the exact similarity solution.

To examine further the solutions for step changes in surface heat flux, a case in air (Pr = 0.7) with a number of strip heat sources mounted flush with the surface of an adiabatic plate is considered. The dimensionless temperature distribution in the fluid is presented in Fig. 2. All five sources shown in this figure have a uniform surface heat flux of equal strength and size, with nonsource spaces equal to the source size. The dimensionless temperature θ appearing in the figure is defined as

$$\theta = \frac{T}{q_{w_0}x_1/k\mathrm{Gr}_{x_1}^{*}} \tag{42}$$

and $\xi = x/x_1$.

In terms of dimensionless parameters, Eq. (40) can be rewritten as

$$\theta_w = \frac{\xi^{1/5}}{C\bar{q}_w^{*1/5}} \sum_{i=0}^{\kappa} \Delta q_{w_i}^{*}\left(1 - \frac{\xi_i}{\xi}\right)^{b} \tag{43}$$

where $\Delta q_{w_i}^* = \Delta q_{w_i}/q_{w_0}$ and $\bar{q}_w^* = \bar{q}_w/q_{w_0}$. This is evaluated for the previous case with five heat sources. As can be seen from Fig. 3, the results are in excellent agreement with the numerical data of STAN7. STAN7 is a finite difference code developed for solving the boundary layer momentum and energy equations for laminar and turbulent flows over a body of revolution, and it is an abridged version of program STAN5 (Crawford and Kays, 1976).

Figure 4 presents a similar situation with two heat sources, showing the effect of the source spacings on the wall temperature variations. One source is at the leading edge of the plate and the other is located downstream, as indicated by ξ_2 in the figure. Comparisons with the numerical data of Jaluria (1982) and STAN7 show good agreement, particularly in the trend of the local peak temperatures. Small deviations are observed

Downloaded 13 Dec 2010 to 193.140.21.150. Redistribution subject to ASME license or copyright; see http://www.asme.org/terms/Terms_Use.cfm

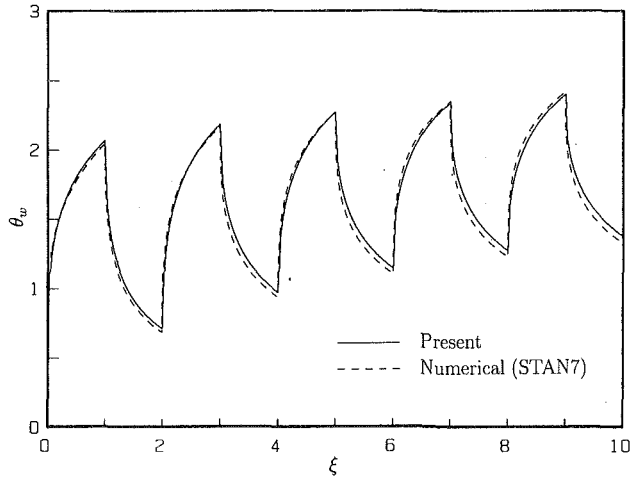

Fig. 3 Comparison of dimensionless wall temperature variation due to alternating positive uniform and zero surface heat fluxes of equal size for Pr = 0.7

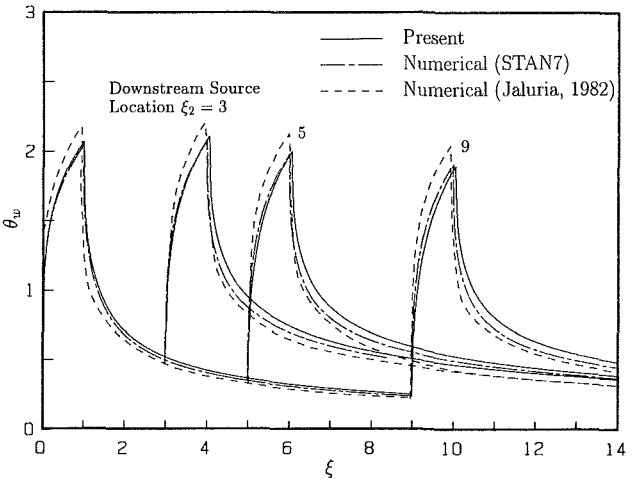

Fig. 4 Comparison of dimensionless wall temperature variations due to two identical thermal sources of uniform heat flux on an adiabatic plate with different source spacings for Pr = 0.7

in the numerical data of Jaluria who solved the boundary layer equations using finite difference methods. Jaluria's numerical prediction overestimates the peak temperature over the first source by approximately 5 percent when it is compared to the present solution. The present solution is identical, by choice, to the correlation equation of Fujii and Fujii (1976) for $\xi \leq 1$.

An examination of Fig. 4 also reveals the effects of the nonlinearity of natural convection. Although the two sources are identical, dissipating the same amount of heat into the fluid over the same width, the peak temperature over the downstream source can become lower than that of the upstream source. The wall temperature due solely to the first source decreases asymptotically to the ambient fluid temperature as ξ increases, and the fluid temperature excess within the boundary layer remains positive. The positive temperature excess results in a positive buoyant force, which, in turn, results in a perpetual increase in the overall downstream flow velocity as presented by Jaluria (1982). Despite the fact that the fluid flowing toward the downstream source is at a higher temperature than the ambient temperature, its increased flow velocity enhances the heat transfer from the second source and, therefore, the downstream source temperature becomes lower as the source spacing increases.

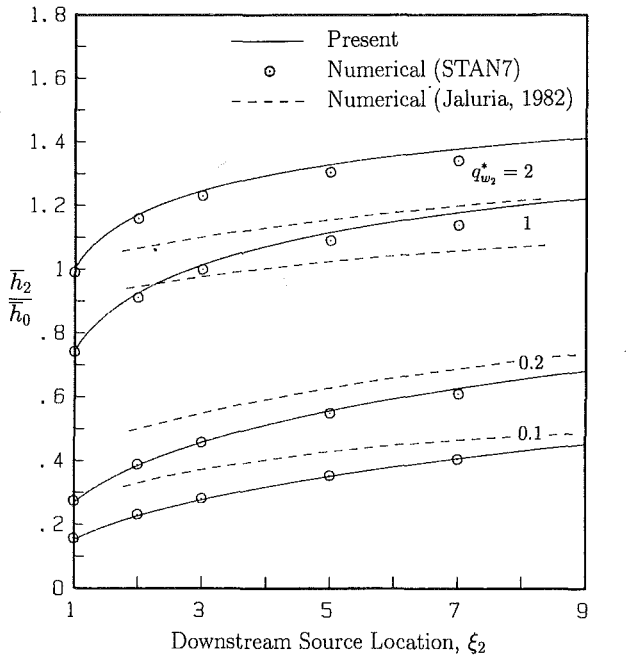

Fig. 5 Comparison of heat transfer coefficient with two thermal sources of uniform heat flux on an adiabatic plate showing the effects of flux ratios and source spacing for Pr = 0.7

For problems with two heat sources of uniform but different fluxes on an adiabatic plate, a ratio of the average heat transfer coefficient of the downstream to upstream sources can be defined as

$$\frac{\bar{h}_2}{\bar{h}_0} = q^*_{w_2} \frac{\int_{\xi_2}^{\xi_2+1} \frac{d\xi}{\theta_w}}{\int_0^1 \frac{d\xi}{\theta_w}} \tag{44}$$

The integral in the denominator can be evaluated to yield $5C/4$, and Eq. (43) can be used for θ_w in the numerical integration of the numerator. This ratio is evaluated as a function of ξ_2 for $q^*_{w_2} = 0.1$, 0.2, 1, and 2, and Pr = 0.7. The results are shown in Fig. 5, and compared again with the boundary layer solutions of Jaluria (1982) and STAN7.

When the surface heat flux of the downstream source is equal to that of the upstream source ($q^*_{w_2} = 1$) and the space between the two sources approaches zero ($\xi_2 \to 1$), the exact value of the above ratio of 0.741 can be found by using the uniform flux solution. As can be seen from Fig. 5, the present model and STAN7 correctly predict the value for this situation.

The rest of this section examines the case with continuous surface heat-flux variations. To generalize the solutions to account for any arbitrary variation of $q_w(x)$, which may include a sectionally continuous and varying function, the summation in the solutions may be replaced by a Stieltjes integral. For example, the surface temperature solution given by Eq. (40) can be generalized as

$$T_w(x) = \frac{x}{Ck\overline{\mathrm{Gr}}_x^{*1/5}} I_s \tag{45}$$

where

$$I_s = \int_{\zeta=0}^{x} \chi(\zeta, x) dq_w(\zeta) \tag{46}$$

with

$$\chi(\zeta, x) = \left(1 - \frac{\zeta}{x}\right)^b \tag{47}$$

Downloaded 13 Dec 2010 to 193.140.21.150. Redistribution subject to ASME license or copyright; see http://www.asme.org/terms/Terms_Use.cfm

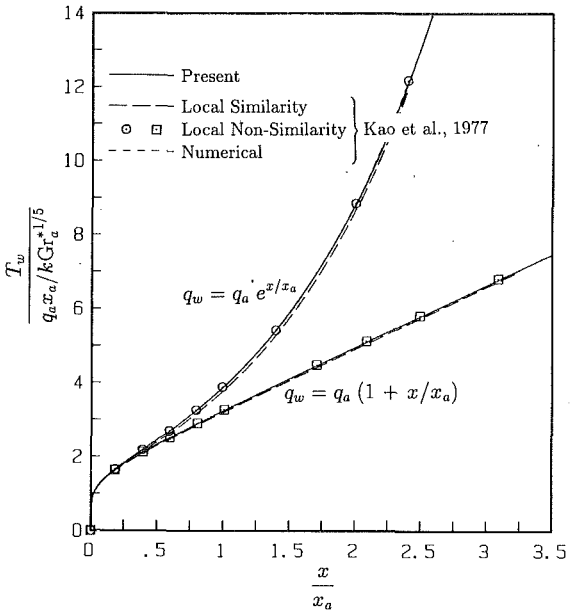

Fig. 6 Comparison of dimensionless wall temperature variations with exponentially and linearly increasing surface heat fluxes for Pr = 0.7

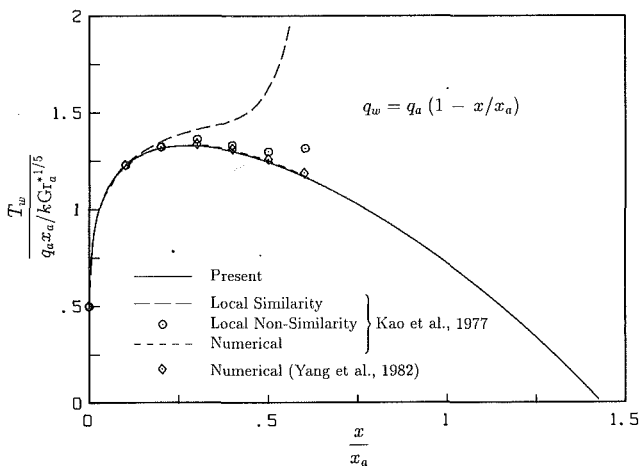

Fig. 7 Comparison of dimensionless wall temperature variations with linearly decreasing surface heat flux for Pr = 0.7

I_s, defined by Eq. (46), is the Stieltjes integral. It includes the ordinary Riemann integral, plus contributions that occur whenever $q_w(x)$ has a discontinuity:

$$I_s = \int_0^x \chi(\zeta, x)\,\frac{dq_w(\zeta)}{d\zeta}\,d\zeta + \sum \chi(\zeta_i, x)[q_w(\zeta_i^+) - q_w(\zeta_i^-)] \quad (48)$$

Here, the summation represents all jumps in q_w at $x = \zeta_i$.

While the above integral form of the solution is general, it is rarely the case where $q_w(x)$ is given such that the integration can be performed analytically. Numerical computations must be carried out by discretizing $q_w(x)$ distributions, and it becomes apparent that Eq. (40) can be used also for continuous $q_w(x)$ variations.

Surface heat fluxes in the form of a linearly increasing or decreasing function and exponentially increasing surface heat flux are selected as test cases. They are given by

$$\frac{q_w(x)}{q_a} = 1 \pm \frac{x}{x_a} \quad (49)$$

and

$$\frac{q_w(x)}{q_a} = e^{x/x_a} \quad (50)$$

where q_a and x_a are arbitrary heat-flux and length scales, respectively.

Figures 6 and 7 show comparisons of the present wall temperature predictions with the results obtained by using the local similarity, local nonsimilarity, and difference-differential numerical methods (Kao et al., 1977). Also included in Fig. 7 are the numerical data of Yang et al. (1982). The data of Kao et al. and those of Yang et al. are obtained by digitizing the plots presented in their papers and converting the variables to the present forms. Although Yang et al. (1982) also reported numerical solutions for the cases presented in Fig. 6, their results are virtually identical to the numerical data of Kao et al. (1977) and are not included in Fig. 6 for clarity. Figure 6 exhibits an excellent agreement among all methods with small differences between the local similarity solutions and others. As can be seen from Fig. 6, the present predictions are completely overlapping with and indistinguishable from the results of numerical and local nonsimilarity methods. Figure 7 reveals the possibility of diverging solutions that can result from both local similarity and local nonsimilarity methods, whereas the present solution continues to maintain the close agreement with the numerical solutions of Kao et al. (1977) and Yang et al. (1982), which are reported up to $x/x_a = 0.643$.

Summary and Conclusions

An approximate method of determining the temperature distributions in laminar free convection along a vertical plate with an arbitrarily specified surface heat flux has been described. This new technique is based on a transformation of the problem into a linearized form by introducing an effective velocity, which is determined by relating the effective kinetic energy of the fluid flow to the total heat dissipation into the fluid. The effective velocity determined in this manner is found to be analogous to an externally induced free-stream velocity. Therefore, by using the integral solution technique developed for forced convection problems, the delay factor that accounts for the effects of an incremental step change in surface heat flux upon the temperature field is obtained. The resulting model is a simple, explicit expression that only requires a summation of a finite number of algebraic terms for computing surface temperature distributions as a function of downstream location. The present solutions are shown to be in excellent agreement with other data obtained by employing various solution methods for different surface heat-flux variations.

The same methodology described herein for heat-flux specified problems can also be applied for temperature specified problems. Such a study has been carried out by the current authors (Lee and Yovanovich, 1991b) and an equally simple and accurate expression has been obtained for predicting heat-flux distributions of a vertical plate with an arbitrary temperature variation prescribed along the surface.

Acknowledgments

The authors would like to acknowledge the financial support of Bell Northern Research of Canada and the Manufacturing Research Corporation of Ontario during the course of this study. The support of the Natural Sciences and Engineering Research Council of Canada under operating grant A7455 to the second author is also acknowledged. The authors wish to express their appreciation to Professor W. M. Kays of Stanford University for providing STAN7.

References

Abramowitz, M., and Stegun, I. A., 1972, *Handbook of Mathematical Functions*, Dover Publications, New York.

Crawford, M. E., and Kays, W. M., 1976, "STAN5—A Program for Nu-

Downloaded 13 Dec 2010 to 193.140.21.150. Redistribution subject to ASME license or copyright; see http://www.asme.org/terms/Terms_Use.cfm

merical Computation of Two-Dimensional Internal and External Boundary Layer Flows," NASA CR-2742.

Fujii, T., and Fujii, M., 1976, "The Dependence of Local Nusselt Number on Prandtl Number In the Case of Free Convection Along a Vertical Surface With Uniform Heat Flux," *Int. J. Heat Mass Transfer*, Vol. 19, pp. 121–122.

Hayday, A. A., Bowlus, D. A., and McGraw, R. A., 1967, "Free Convection From a Vertical Flat Plate With Step Discontinuities in Surface Temperature," ASME JOURNAL OF HEAT TRANSFER, Vol. 89, No. 3, pp. 244–250.

Jaluria, Y., and Gebhart, B., 1977, "Buoyancy-Induced Flow Arising From a Line Thermal Source on an Adiabatic Vertical Surface," *Int. J. Heat Mass Transfer*, Vol. 20, pp. 153–157.

Jaluria, Y., 1982, "Buoyancy-Induced Flow Due to Isolated Thermal Sources on a Vertical Surface," ASME JOURNAL OF HEAT TRANSFER, Vol. 104, pp. 223–227.

Jaluria, Y., 1985, "Interaction of Natural Convection Wakes Arising From Thermal Sources on a Vertical Surface," ASME JOURNAL OF HEAT TRANSFER, Vol. 107, pp. 883–892.

Kao, T. T., 1975, "Laminar Free Convective Heat Transfer Response Along a Vertical Flat Plate With Step Jump in Surface Temperature," *Lett. Heat Mass Transfer*, Vol. 2, No. 5, pp. 419–428.

Kao, T. T., Domoto, G. A., and Elrod, H. G. Jr., 1977, "Free Convective Along a Nonisothermal Vertical Flat Plate," ASME JOURNAL OF HEAT TRANSFER, Vol. 99, pp. 72–78.

Kelleher, M., 1971, "Free Convection From a Vertical Plate With Discontinuous Wall Temperature," ASME JOURNAL OF HEAT TRANSFER, Vol. 93, pp. 349–356.

Kelleher, M., and Yang, K. T., 1972, "A Görtler-Type Series for Laminar Free Convection Along a Non-isothermal Vertical Plate," *The Quarterly Journal of Mechanics and Applied Mathematics*, Vol. 25, pp. 445–457.

Lee, S., 1988, "Laminar Natural Convection From a Vertical Plate With Variations in Thermal Boundary Conditions," Ph.D. Thesis, Department of Mechanical Engineering, University of Waterloo, Ontario, Canada.

Lee, S., and Yovanovich, M. M., 1989, "Natural Convection From a Vertical Plate With Step Changes in Surface Heat-Flux," *Heat Transfer in Convective Flows*, ASME HTD—Vol. 107, pp. 239–247.

Lee, S., and Yovanovich, M. M., 1991a, "Laminar Natural Convection From a Vertical Plate With a Step Change in Wall Temperature," ASME JOURNAL OF HEAT TRANSFER, Vol. 113, pp. 501–504.

Lee, S., and Yovanovich, M. M., 1991b, "Linearization Method for Buoyancy Induced Flow Over a Non-isothermal Vertical Plate," AIAA Paper No. 91-1308.

Ostrach, S., 1953, "An Analysis of Laminar Free-Convection Flow and Heat Transfer About a Flat Plate Parallel to the Direction of the Generating Body Force," NACA Report No. 1111.

Park, S. H., and Tien, C. L., 1990, "An Approximate Analysis for Convective Heat Transfer on Thermally Nonuniform Surfaces," ASME JOURNAL OF HEAT TRANSFER, Vol. 112, pp. 952–958.

Scherberg, M. G., 1964, "Natural Convection From Wall Sections of Arbitrary Temperature Distribution by an Integral Method," *Int. J. Heat Mass Transfer*, Vol. 7, pp. 501–516.

Schetz, J. A., 1962, "Natural Convection in the Vicinity of a Vertical Plate With a Step-Change in Wall Temperature," Ph.D. Thesis, Department of Mechanical Engineering, Princeton University, Princeton, NJ.

Schetz, J. A., 1963, "On the Approximate Solution of Viscous-Flow Problems," ASME *Journal of Applied Mechanics*, Vol. 85, pp. 263–268.

Schetz, J. A., and Eichhorn, R., 1964, "Natural Convection With Discontinuous Wall-Temperature Variations," *J. Fluid Mech.*, Vol. 18, Part 2, pp. 167–176.

Smith, R. K., 1970, "The Laminar Free-Convection Boundary Layer on a Vertical Heated Plate in the Neighbourhood of a Discontinuity in Plate Temperature," *J. Austral. Math. Soc.*, Vol. 11, No. 2, pp. 149–168.

Sokovishin, Y. A., and Érman, L. A., 1982, "Free-Convection Heat Transfer on a Vertical Surface With a Temperature Discontinuity," *J. Eng. Phys.*, Vol. 43, No. 2, pp. 858–861.

Sparrow, E. M., 1955, "Laminar Free Convection on a Vertical Plate With Prescribed Non-uniform Wall Heat Flux or Prescribed Non-uniform Wall Temperature," NACA TN-3508.

Sparrow, E. M., and Gregg, J. L., 1956, "Laminar Free Convection From a Vertical Plate With Uniform Surface Heat Flux," *Trans. ASME*, Vol. 78, pp. 435–440.

Sparrow, E. M., and Gregg, J. L., 1958, "Similar Solutions for Free Convection From a Nonisothermal Vertical Plate," *Trans. ASME*, Vol. 80, pp. 379–386.

Sparrow, E. M., and Lin, S. H., 1965, "Boundary Layers With Prescribed Heat Flux—Application to Simultaneous Convection and Radiation," *Int. J. Heat Mass Transfer*, Vol. 8, pp. 437–448.

Yang, J., Jeng, D. R., and De Witt, K. J., 1982, "Laminar Free Convection From a Vertical Plate With Nonuniform Surface Conditions," *Numerical Heat Transfer*, Vol. 5, pp. 165–184.

Yang, K. T., 1960, "Possible Similarity Solutions for Laminar Free Convection on Vertical Plates and Cylinders," ASME *Journal of Applied Mechanics*, Vol. 82, pp. 230–236.

Downloaded 13 Dec 2010 to 193.140.21.150. Redistribution subject to ASME license or copyright; see http://www.asme.org/terms/Terms_Use.cfm

Natural Convection Heat Transfer From an Isothermal Vertical Surface to a Stable Thermally Stratified Fluid

D. Angirasa
Department of Mechanical Engineering,
University of Colorado,
Boulder, CO 80309-0427
Assoc. Mem. ASME

J. Srinivasan
Department of Mechanical Engineering,
Indian Institute of Science,
Bangalore 560 012, India

Natural convection from an isothermal vertical surface to a thermally stratified fluid is studied numerically. A wide range of stratification levels is considered. It is shown that at high levels of ambient thermal stratification, a portion at the top of the plate absorbs heat, while a horizontal plume forms around a location where the plate temperature equals the ambient temperature. The plume is shown to be inherently unsteady, and its transient nature is investigated in detail. The effect of the temperature defect in striating the plume is discussed. Average Nusselt number data are presented for $Pr = 6.0$ and 0.7.

Introduction

Natural convection from a vertical surface in a constant-density medium has been widely studied. Gebhart et al. (1988) recently provided an overview of natural convection heat and mass transfer. In natural and industrial free convection heat transfer processes, the density of the medium is often stably stratified, with lighter fluid overlaying denser fluid. A fluid is stratified with temperature varying with height. It may also be due to a variation of the concentration of one or more species in the fluid. For stable thermal stratification, the temperature of the fluid almost always increases with height in a gravitational field (a notable exception is water between zero and 4°C).

Pioneering studies of natural convection heat transfer in stable thermally stratified media were done by Eichhorn and co-workers (Eichhorn, 1969; Eichhorn et al., 1975; Chen and Eichhorn, 1976, 1977). Eichhorn (1969) presented a series solution for the prediction of heat transfer from a vertical plate in a linearly stratified fluid. He considered three terms in the series expansion of the nonlinear partial differential equations. Fujii et al. (1974) considered nonlinear thermal stratification and showed that four terms are required to be solved. Yang et al. (1972) tried to obtain a similarity solution, and proved that similarity is possible for the physically unrealistic case of decreasing temperature with height. However, similarity solutions could be obtained for both wall and ambient temperature increasing with height. Jaluria and Gebhart (1974) obtained a similarity solution for the constant wall heat flux case, with the temperatures of both the plate and the ambient increasing with height. They also considered the effect of stratification on the stability of natural convection flows from vertical surfaces with constant heat flux, and compared their theoretical results with experiments in water.

Observing that neither the similarity arguments nor series expansions were making much headway, Chen and Eichhorn (1976, 1977) used the local nonsimilarity technique developed by Sparrow and co-workers (Sparrow et al., 1970; Sparrow and Yu, 1971; Minkowycz and Sparrow, 1974) for the case of an isothermal plate in a linearly stratified fluid. However, this method is not without its own share of problems when applied to the cases of high levels of stratification. Eichhorn and co-workers also presented excellent experimental results, from both measurements and flow visualizations. Venkatachala and Nath (1981) solved the boundary layer ordinary differential equations for natural convection (also considering suction and injection) using an implicit finite-difference scheme (see Venkatachala, 1978, for details of the numerical procedures). Their solutions agreed well with the local nonsimilarity solutions of Chen and Eichhorn (1976). Angirasa and Srinivasan (1989) considered boundary layer flows in a linear thermally stratified medium with an additional buoyant mechanism in the form of diffusion of a species. They solved boundary layer partial differential equations with an explicit finite-difference method, and have shown that boundary layer approximations break down in the case of opposing buoyant mechanisms (thermal buoyancy upwards, and the species buoyancy downward), and high levels of ambient thermal stratification.

The search for similarity solutions continued in recent years. Kulkarni et al. (1987) claimed to have found a new class of similarity solutions, but Henkes and Hoogendoorn (1989) have shown that Semenov (1984) had in fact obtained a more general class of similar solutions. The similarity solutions, however, have one major drawback. One can at least claim that they are valid only if the wall temperature is always higher than the ambient temperature at all heights of the surface. In search for a similarity solution, one commits oneself to a boundary layer type flow where none may exist at all.

In this paper, numerical simulations will be presented for natural convection from an isothermal plate immersed in a stable thermally stratified fluid for a wide range of stable thermal stratification levels. In the numerical simulations all the problems associated with the similarity, local nonsimilarity, and series solutions will disappear. Boundary layer approximations are discarded, and the full two-dimensional partial differential equations are solved using a finite-difference method.

Analysis of the Problem

Consider a flat vertical surface of height L at a uniform temperature t_w. The ambient temperature is $t_{\infty,o}$ at the bottom of the plate ($x = 0$) and increases linearly with height (x). The geometry and coordinate system are shown in Fig. 1. The equations governing the mass, momentum, and energy conservation that describe the laminar flow and temperature field adjacent to the plate are

$$\frac{\partial u}{\partial x} + \frac{\partial v}{\partial y} = 0 \tag{1}$$

$$\frac{\partial u}{\partial \tau} + u\frac{\partial u}{\partial x} + v\frac{\partial u}{\partial y} = -\frac{1}{\rho}\frac{\partial p}{\partial x} + \nu\left(\frac{\partial^2 u}{\partial x^2} + \frac{\partial^2 u}{\partial y^2}\right) + g\beta(t - t_{\infty,x}) \tag{2}$$

Contributed by the Heat Transfer Division for publication in the JOURNAL OF HEAT TRANSFER. Manuscript received by the Heat Transfer Division July 1991; revision received May 1992. Keywords: Flow Instability, Natural Convection, Stratified Flows. Associate Technical Editor: J. R. Lloyd.

Copyright © 1992 by ASME
Downloaded 13 Dec 2010 to 193.140.21.150. Redistribution subject to ASME license or copyright; see http://www.asme.org/terms/Terms_Use.cfm

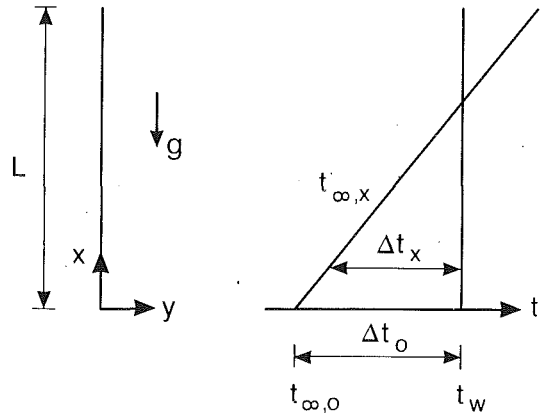

Fig. 1 Geometry and coordinate system

$$\frac{\partial v}{\partial \tau}+u\frac{\partial v}{\partial x}+v\frac{\partial v}{\partial y}=-\frac{1}{\rho}\frac{\partial p}{\partial y}+\nu\left(\frac{\partial^2 v}{\partial x^2}+\frac{\partial^2 v}{\partial y^2}\right) \quad (3)$$

$$\frac{\partial t}{\partial \tau}+u\frac{\partial t}{\partial x}+v\frac{\partial t}{\partial y}=\alpha\left(\frac{\partial^2 t}{\partial x^2}+\frac{\partial^2 t}{\partial y^2}\right) \quad (4)$$

In the above formulation the flow is assumed to be two dimensional, which is valid for larger depth compared to the height of the plate L. The flow is assumed to be incompressible and the usual Boussinesq approximation is made, which means that the density variation is important only for the buoyancy term. In the above equations, τ is the time; u and v are velocity components in the x and y directions, respectively. The volumetric expansion coefficient β is defined as $-(1/\rho)(\partial\rho/\partial t)_p$, where ρ is the density and p the pressure. α is thermal diffusivity and is equal to $k/\rho C_p$, where C_p is the specific heat and k the thermal conductivity of the fluid. ν is the fluid property, kinematic viscosity. The gravitational acceleration is represented by g.

Nondimensional Parameters and Equations. The characteristic length of the system is the plate height L. The characteristic velocity is $u_c=\sqrt{g\beta\Delta t_o L}$, where $\Delta t_o=(t_w-t_{\infty,o})$ is the maximum temperature potential. The following nondimensional variables are defined:

$X=x/L$, $Y=y/L$, $\tau^*=\tau u_c/L$, $U=u/u_c$, $V=v/u_c$, and

$$T=\frac{(t-t_{\infty,x})}{(t_w-t_{\infty,o})}=\frac{\Delta t_x}{\Delta t_o}. \quad (5)$$

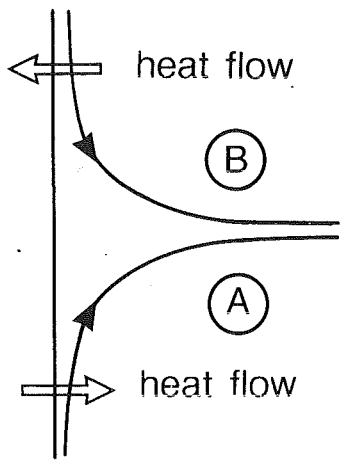

Fig. 2 Flow and heat transfer behavior at high levels of thermal stratification

The conservative Eqs. (1)–(4) can now be written in nondimensional form as follows:

$$\frac{\partial U}{\partial X}+\frac{\partial V}{\partial Y}=0 \quad (6)$$

$$\frac{\partial U}{\partial \tau^*}+U\frac{\partial U}{\partial X}+V\frac{\partial U}{\partial Y}=-\frac{\partial P}{\partial X}+\frac{1}{\sqrt{\mathrm{Gr}}}\left(\frac{\partial^2 U}{\partial X^2}+\frac{\partial^2 U}{\partial Y^2}\right)+T \quad (7)$$

$$\frac{\partial V}{\partial \tau^*}+U\frac{\partial V}{\partial X}+V\frac{\partial V}{\partial Y}=-\frac{\partial P}{\partial Y}+\frac{1}{\sqrt{\mathrm{Gr}}}\left(\frac{\partial^2 V}{\partial X^2}+\frac{\partial^2 V}{\partial Y^2}\right) \quad (8)$$

$$\frac{\partial T}{\partial \tau^*}+U\frac{\partial T}{\partial X}+V\frac{\partial T}{\partial Y}=\frac{1}{\mathrm{Pr}\sqrt{\mathrm{Gr}}}\left(\frac{\partial^2 T}{\partial X^2}+\frac{\partial^2 T}{\partial Y^2}+S'\right)-SU \quad (9)$$

In the above equations, $P=p/\rho u_c^2$, $\mathrm{Gr}=g\beta\Delta t_o L^3/\nu^2$, the Grashof number, $\mathrm{Pr}=\nu/\alpha$, the Prandtl number, and $S=(1/\Delta t_o)(dt_{\infty,x}/dX)$ is defined as the thermal stratification parameter. S' is the derivative of S (dS/dX), and accounts for the nonlinear effects of the stratification. In this work, we are concerned with linear thermal stratification for which $S'=0$.

If the thermal stratification level is high, the ambient temperature can exceed the plate temperature at some height. This type of situation is shown in Fig. 2. In region A, the plate temperature is higher than that of the ambient, while in region B, the ambient temperature exceeds the plate temperature. Hence, the flow is upward in the lower part while it is downward in the upper part. These two flows merge where the wall

Nomenclature

C_p = specific heat
g = gravitational acceleration
Gr = Grashof number
k = thermal conductivity of the fluid
L = height of the plate
$\overline{\mathrm{Nu}}$ = average Nusselt number
$\overline{\mathrm{Nu}}_{\mathrm{iso}}$ = average Nusselt number in an isothermal fluid
p = pressure
P = nondimensional pressure
Pr = Prandtl number
q_x'' = local wall heat flux
S = thermal stratification parameter = $(1/\Delta t_o)(dt_{\infty,x}/dX)$
S' = dS/dX
t = temperature
Δt_o = temperature potential at $x=0$, $(t_w-t_{\infty,o})$
Δt_x = excess temperature at x, $(t-t_{\infty,x})$
T = temperature excess ratio = $(t-t_{\infty,x})/(t_w-t_{\infty,o})$
u_c = convective velocity = $\sqrt{g\beta\Delta t_o L}$
u, v = velocity components
U, V = nondimensional velocity components
x, y = space coordinates
X, Y = nondimensional space coordinates
α = thermal diffusivity
β = volumetric coefficient of thermal expansion = $-(1/\rho)(\partial\rho/\partial t)_p$
ν = kinematic viscosity
ρ = density
τ = time
τ^* = nondimensional time
ψ = stream function
ω = vorticity

Subscripts

w = wall
∞ = location far away from the wall
∞,o = location away from the wall at $x=0$
∞,L = location away from the wall at $x=L$
∞,x = location away from the wall at x

Downloaded 13 Dec 2010 to 193.140.21.150. Redistribution subject to ASME license or copyright; see http://www.asme.org/terms/Terms_Use.cfm

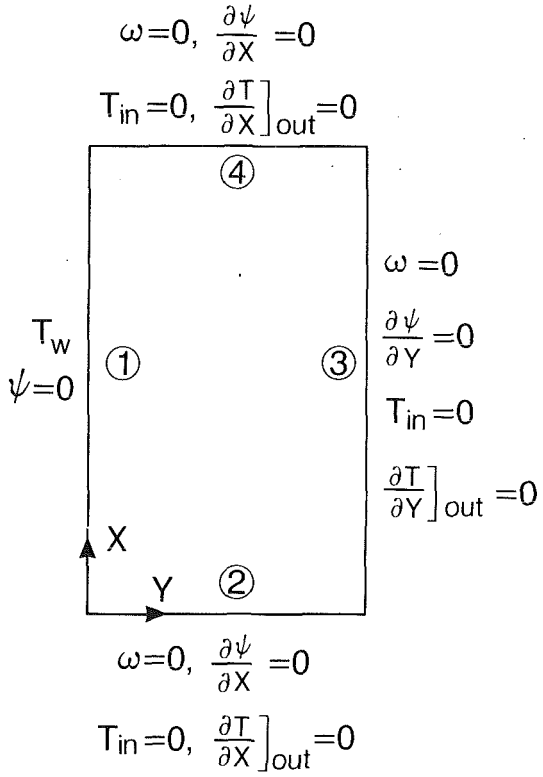

Fig. 3 Numerical boundary conditions

temperature is equal to the ambient temperature, and emerge as a horizontal plume.

For linear thermal stratification, the gradient $dt_{\infty,x}/dX$ is constant, which gives a constant value for S. In the definition of S, we can replace $dt_{\infty,x}/dX$ with $(t_{\infty,x}-t_{\infty,o})/X$. At a location of X where $(t_{\infty,x}-t_{\infty,o})$ equals $(t_w-t_{\infty,o})$, the temperature potential $(t_w-t_{\infty,x})$ is zero, i.e., the ambient temperature equals wall temperature. Since the height of the plate is normalized with L (maximum nondimensional height = 1), when $S>1$, the temperature of a portion of the plate at the top falls behind that of the ambient. If $\Delta t_x=0$ at the midheight of the plate ($X=0.5$), then we obtain $S=2$.

We define vorticity ω as $[(\partial U/\partial Y)-(\partial V/\partial X)]$, and reduce Eqs. (6)–(8) to a single, vorticity-transport equation as

$$\frac{\partial\omega}{\partial\tau^*}+U\frac{\partial\omega}{\partial X}+V\frac{\partial\omega}{\partial Y}=\frac{\partial T}{\partial Y}+\frac{1}{\sqrt{\mathrm{Gr}}}\left(\frac{\partial^2\omega}{\partial X^2}+\frac{\partial^2\omega}{\partial Y^2}\right) \tag{10}$$

We may define a stream function ψ such that

$$U=\frac{\partial\psi}{\partial Y} \quad \text{and} \quad V=-\frac{\partial\psi}{\partial X}. \tag{11}$$

From this it follows that

$$\omega=\nabla^2\psi. \tag{12}$$

Boundary Conditions. The physical boundary conditions are given as

$$\begin{aligned} y=0 \quad & u=0,\ v=0,\ t=t_w \\ y\to\infty \quad & u=0,\ t=t_{\infty,x} \\ y\to\infty \quad & x=0,\ t=t_{\infty,o} \ \text{ and } \ x=L,\ t=t_{\infty,L} \end{aligned} \tag{13}$$

In nondimensional form these are reduced to

$$\begin{aligned} Y=0 \quad & U=0,\ V=0,\ T=T_w \\ Y\to\infty \quad & U=0,\ T=0. \\ Y\to\infty \quad & X=0,\ T=0 \ \text{ and } \ X=1,\ T=0 \end{aligned}$$

T_w is evaluated as follows:

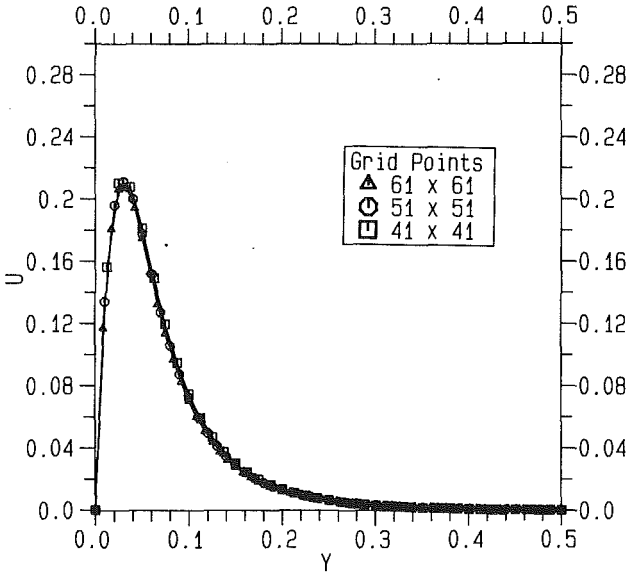

Fig. 4 Grid-independence demonstration: *U*-velocity profiles at $X=0.5$ for $\mathrm{Gr}=10^6$, $\mathrm{Pr}=6.0$, and $S=0.0$

$$T_w=\frac{t_w-t_{\infty,x}}{t_w-t_{\infty,o}}=\frac{\Delta t_o}{\Delta t_o}-\frac{t_{\infty,x}-t_{\infty,o}}{\Delta t_o}.$$

By the definition of S,

$$t_{\infty,x}-t_{\infty,o}=\Delta t_o S X.$$

Hence,

$$T_w=1-SX \tag{14}$$

Evaluation of Nusselt Number. When data are presented for natural convection heat transfer in stratified fluids, the effect of the thermal stratification parameter S on the average Nusselt number $\overline{\mathrm{Nu}}$ is shown. Larger values of S decrease the heat transfer rates, because the local temperature potential $(t_w-t_{\infty,x})$ falls. The average Nusselt number $\overline{\mathrm{Nu}}$ is evaluated as

$$\overline{\mathrm{Nu}}=\int_0^1\frac{q_x'' L}{k\,\Delta t_o}dX=\int_0^1\left(-\left.\frac{\partial T}{\partial Y}\right|_{Y=0}\right)dX \tag{15}$$

By this evaluation, $\overline{\mathrm{Nu}}$ will decrease with an increase of S. We note that in defining S, we have made use of the same constant reference temperature potential, $(t_w-t_{\infty,o})$. The above evaluation makes it easier to compare with $\overline{\mathrm{Nu}}_{\mathrm{iso}}$, the average Nusselt number in a constant density medium of temperature t_∞, since $\overline{\mathrm{Nu}}$ now gives the reduced value of $\overline{\mathrm{Nu}}_{\mathrm{iso}}$ as a function of S. For instance, $\overline{\mathrm{Nu}}/\overline{\mathrm{Nu}}_{\mathrm{iso}}=1$ for $S=0$, and equals zero for $S=2$. In the latter situation, the top half of the plate absorbs an equal amount of heat to the one lost be the bottom half, and the net heat transfer rate is zero (Fig. 2).

Numerical Procedures

The energy and vorticity-transport equations, Eqs. (9) and (10), are solved by the Alternating Direction Implicit (ADI) method described in the textbook by Roache (1982). Upwind-differencing is employed for convective terms for numerical stability. The Successive Over-Relaxation (SOR) method is utilized to solve the stream function equation, Eq. (12). Iterative convergence is obtained for stream function solution at each time step.

Steady-state solutions to Eqs. (9) and (10) could not be obtained for higher values of S. Where they are possible, steady state is assumed to have reached if the change in a dependent variable is less than 10^{-4}. The temperature field in the boundary layer region often converged at higher S, although the flow field remained unsteady.

Downloaded 13 Dec 2010 to 193.140.21.150. Redistribution subject to ASME license or copyright; see http://www.asme.org/terms/Terms_Use.cfm

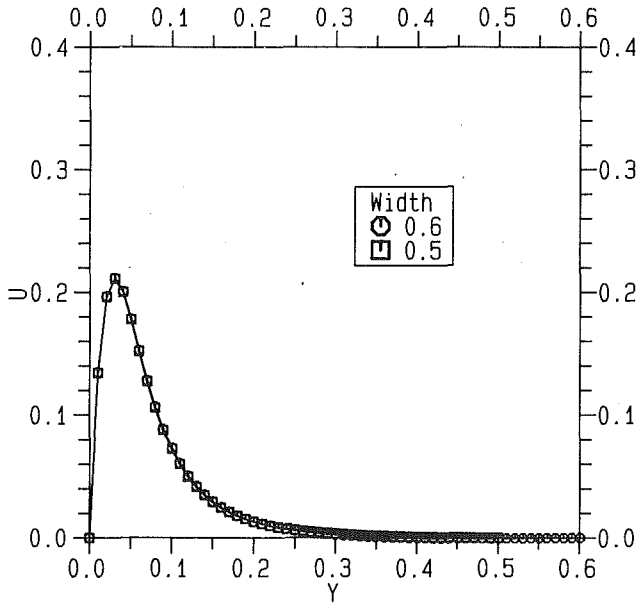

Fig. 5 Effect of computational width in *Y*-direction: *U*-velocity profiles at $X = 0.5$ for $Gr = 10^6$, $Pr = 6.0$ and $S = 0.0$

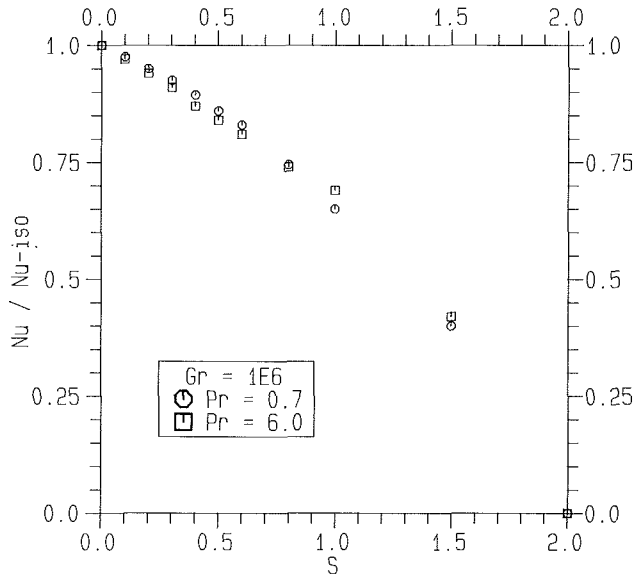

Fig. 6 Effect of *S* on average Nusselt number

Numerical boundary conditions are shown in Fig. 3. These have been obtained after careful numerical experiments. The boundary conditions on sides 2, 3, and 4 allow "free flow" of fluid in and out of the computational domain. Wall vorticities are evaluated from the values of the stream function at the adjacent grid points (Roache, 1982).

Uniform grid spacings are employed in both directions. Numerical results were first obtained to check for grid dependence. Figure 4 shows *U*-velocity profiles for three different sizes of the grid. For results presented in this paper, 51×51 grid points have been employed. The numerical errors are assessed as 1 percent for the flow field variables and temperature, and 2 percent for Nusselt number.

A small time step was required to obtain the details of the unsteady flows. Hence, a time step of $\Delta\tau^* = 0.005$ is chosen. On the other hand, if the time step is too small, say $\Delta\tau^* = 0.001$, the solution remained closer to the given initial condition even after 500 time steps.

For the numerical calculations of wall-bounded flows, we need to check that the computational domain normal to the wall is larger than the thickness of the boundary layer adjacent to the wall. We have varied the width in the *Y*-direction to check its influence on the solution. For instance, the *U*-velocity profiles for two widths are shown in Fig. 5. The solutions are identical. The width chosen for the present study is 0.5.

The average Nusselt number is calculated by the numerical integration of Eq. (15) using Simpson's rule. To account for the effect of the gradients at the end points of the wall, an open-ended formula was used (see, for instance, Press et al., 1986).

Table 1 Comparison of $\overline{Nu}$ with experimental data; $Gr = 10^6$ and $Pr = 6.0$

	Nu/Nu_{iso}	
S	Present (Numerical)	Chen and Eichhorn (1976) (Experiment)
0.0	1.0	1.0
0.5	0.84	0.85
0.6	0.81	0.82
0.8	0.74	0.76
1.0	0.69	0.7

Table 2 Comparison of $\overline{Nu}_{iso}$ with literature; $Gr = 10^6$, $Pr = 6.0$

	$\overline{Nu}_{iso}$
Present	30.1
Chen and Eichhorn (1976)	32.52
McAdams (1954)	29.2
Churchill and Chu (1975)	30.76

Results and Discussion

Numerical results are first compared to the experimental data of Chen and Eichhorn (1976) for different values of *S* (Table 1). For this comparison $Gr = 10^6$, $Pr = 6.0$, and *S* varying between 0.0 and 1.0. The computed values of $\overline{Nu}$ are found to be in good agreement with the experimental measurements. For higher values of *S* (≥ 1.0) there is a large scatter in experimental data. Our numerical results in this range of *S* compared well with the correlation obtained from the experimental data, $\overline{Nu}^*/\overline{Nu}_{iso} = 1.179\, S^{*1/4}$. Here $*$ refers to the definitions of $\overline{Nu}$ and *S* as given by Chen and Eichhorn (1976). For larger values of *S*, steady-state flows do not exist as will be discussed in a subsequent section, but thermal fields closer to the wall converged, resulting in a constant value of $\overline{Nu}$. Figure 6 presents $\overline{Nu}$ data for $Pr = 6.0$ and 0.7. Table 2 gives a comparison of $\overline{Nu}_{iso}$ with those of others.

To study the effect of thermal stratification on flow and heat transfer, computations were carried out for $Gr = 10^6$ and $Pr = 6.0$, with thermal stratification parameter *S* varying between 0.0 and 2.0. In Fig. 7, profiles of residual temperature at $X = 0.5$ are shown for $S < 1.0$. We note that away from the wall, there are regions in which the local temperature lags behind the ambient temperature. This is called the temperature defect in the flow, and its nature was well documented in the literature (see, for instance, Angirasa and Srinivasan, 1989). The temperature defect arises because fluid rising up in a thermally stratified environment will find itself in a warmer surrounding.

The wall temperature excess decreases with increasing *S*, which is expected because higher levels of thermal stratification enhance the local ambient temperature. As a consequence the local buoyancy force is depleted and the vertical velocity levels fall with increasing *S* as can be seen in Fig. 8. The flow reverses in the outer region of the boundary layer because of the temperature defect.

Figure 9 presents the stream function and isotherm contours for $S = 0.0$, 0.5, 1.0, and 1.5. The isotherms are drawn with

Downloaded 13 Dec 2010 to 193.140.21.150. Redistribution subject to ASME license or copyright; see http://www.asme.org/terms/Terms_Use.cfm

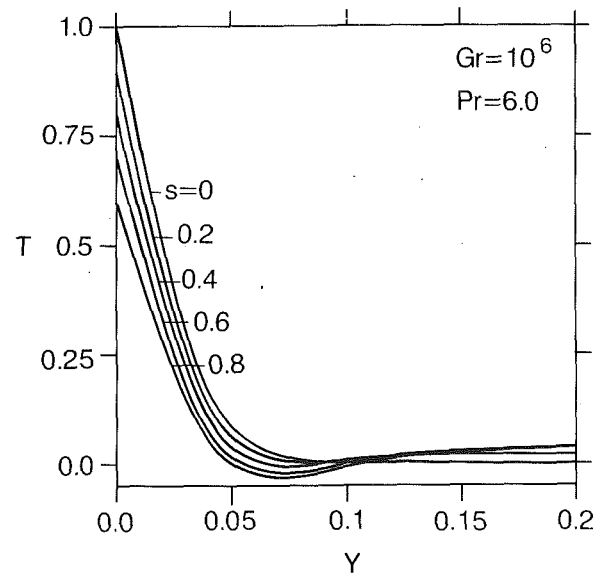

Fig. 7 Temperature profiles at $X=0.5$ for various values of S

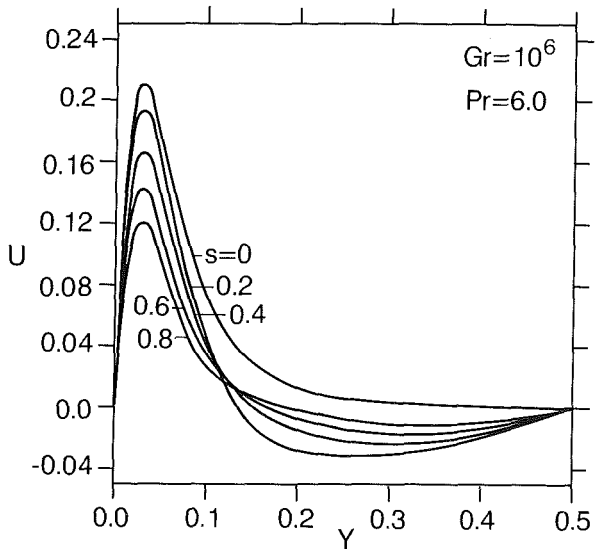

Fig. 8 U-velocity profiles at $X=0.5$ for different values of S

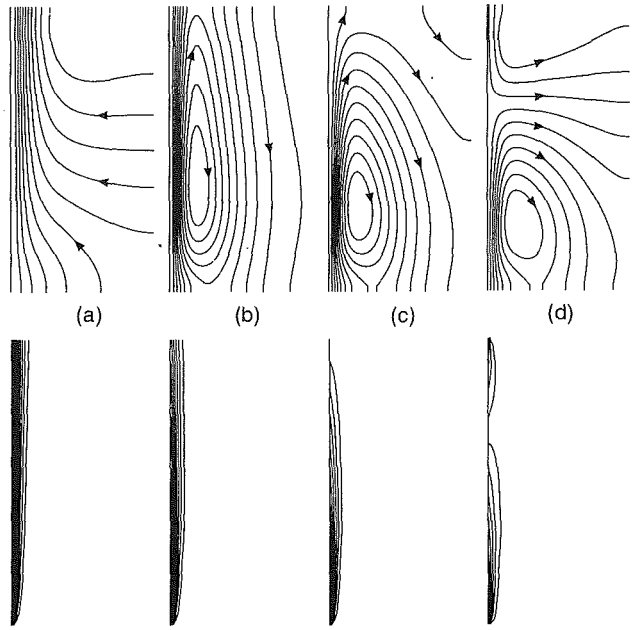

Fig. 9 Stream function (top) and isotherm (bottom) contours for $Gr=10^6$, $Pr=6.0$: $S=$ (*a*) 0.0; (*b*) 0.5; (*c*) 1.0; (*d*) 1.5

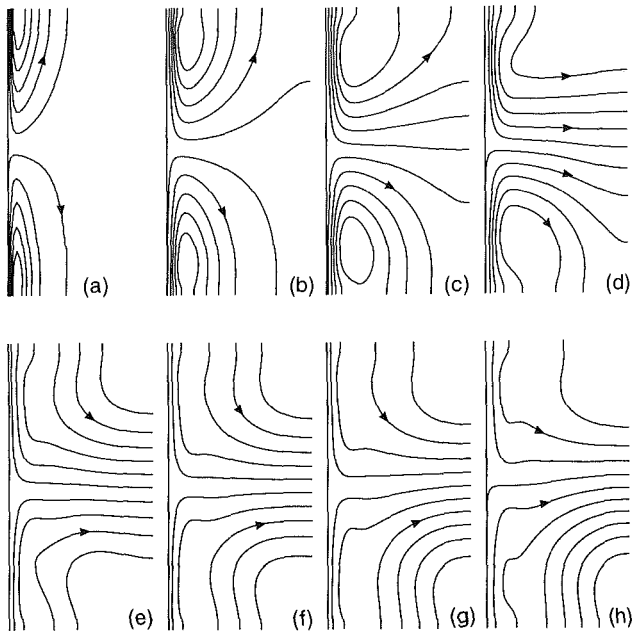

Fig. 10 Transient stream function contours for $S=2.0$, $Gr=10^6$, and $Pr=6.0$; $\tau^*=$ (*a*) 0.25; (*b*) 1.25; (*c*) 2.25; (*d*) 3.0; (*e*) 4.25; (*f*) 4.75; (*g*) 5.25; (*h*) 5.5

the residual temperature (i.e., local ambient temperature removed). For $S\geq 1$, steady flow solutions do not exist because a horizontal plume emerges from the wall at about a location where $t_w=t_{\infty,x}$. When $t_w=t_{\infty,x}$ occurs in the upper half of the wall (for $1.0<S<2.0$), the upward flow from the bottom has more momentum than the downward flow from the top. Hence, the plume emerging point is slightly offset to above the location where $t_w=t_{\infty,x}$. Although the plume is inherently unsteady (which we will discuss in detail), it is not unstable, i.e., while the plume "striates," the overall velocity field is left intact. But from numerical point of view, the flow field does not converge.

The classical problem of isothermal flat vertical plate in an unstratified fluid is represented by $S=0$ (Fig. 9*a*). For $S=0.5$, we observe a significant region of flow reversal and a drop in the temperature gradient along the wall. $S=1.0$ results in plume formation just above the top of the plate. In this region there is no heat transfer at the wall. The isotherms for this case show no temperature gradients at the top of the plate. For $S=1.5$, the horizontal plume formation is clearly demonstrated (Fig. 9*d*). For this case, a portion of the top half of the plate gains heat. The isotherm contours demarcate the two regions of heat transfer on the plate, with the bottom region losing heat while the top one gains it from the fluid. The net heat transfer from the plate is the difference between the heat lost at the bottom part and the heat gained from the top portion. For a higher value of S, the location of the plume shifts downward. In the case of $S=2$, $t_w=t_{\infty,x}$ at $X=0.5$, where the plume emerges. This will now be considered in detail.

Unsteady Plume Behavior. In this section we explore the unsteady nature of the horizontal plume, which originates at a location where $t_w=t_{\infty,x}$. The case we consider is $S=2$, which gives zero local temperature potential and plume location at

Downloaded 13 Dec 2010 to 193.140.21.150. Redistribution subject to ASME license or copyright; see http://www.asme.org/terms/Terms_Use.cfm

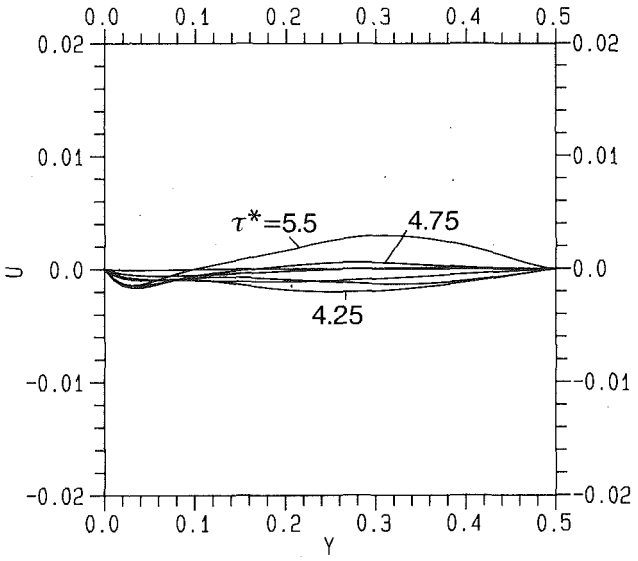

Fig. 11 Transient U-velocity profiles at $X=0.5$ for $S=2$, $Gr=10^6$, and $Pr=6.0$

$X=0.5$. In such a situation, the flow and heat transfer domains are as shown in Fig. 2. In Fig. 10, transient stream function contours are shown. Initially, the two halves of the flow field are symmetric. Once the plume emerges, the flow field will be unsteady (probably periodic). Fluid is drawn from the top (hot) and bottom (cold), and ejected by the side (Figs. 10*e–h*). Although the "hot" and the "cold" boundary layers grow over the same length of the plate, the flow ceases to be symmetric about the middle horizontal line because the temperature defects in the viscous boundary layers are preserved in the outflow. This means that the flow in the plume is less stably stratified than the ambient. The temperature defects in the boundary layers try to reverse the flow in the outer regions of the boundary layers (although the magnitude of this velocity is small, as we have seen in the velocity profiles in Fig. 8), which makes the plume experience small pulls of upward and downward buoyancies just a little away from its origin, i.e., where the temperature defects interact with each other. Eichhorn coined the word "striation" to describe the unsteady plume flow, which shows in the form of small furrows or ridges normal to the plume (see the fine photographs in Chen and Eichhorn, 1976). Gresho (1989) suggested that the striations be called "gravity waves." Striations of the type shown in Fig. 10 go on indefinitely.

The origin of the instabilities is the term SU in the energy equation, Eq. (9), which, in turn, is coupled to the vorticity-transport equation, Eq. (10), through the buoyancy term. The instabilities are physical, not numerical, in nature, and depend solely on the value of S. For instance, no physical instabilities are observed for $S<1$. These results agree with the flow visualizations of Chen and Eichhorn (1976).

To estimate the order of magnitude of the vertical velocities in the plume, the U-velocity profiles at $X=0.5$ (the location of the plume) are shown in Fig. 11. Comparing with the magnitude of U-velocities in Fig. 8, we note that the vertical velocities in the plume are less than an order of magnitude. If we take the time scale to be $\tau^*=1.0$, then we will get a length scale of 0.005 for the striations. This is a very small value compared to 1.0, the height of the plate, and 0.5, the length over which a boundary layer grows.

Figure 12 shows typical isotherm contours for $S=2.0$. The top half of the plate absorbs an amount of heat equal to the one lost by the bottom half. Hence the plate as a whole is thermally neutral. Maximum heat transfer occurs at the top and the bottom of the plate, but in opposite directions. At the midheight of the plate where the plume forms, temperature gradients normal to the wall vanish, indicating very little heat transfer in this region.

Fig. 12 Typical isotherm contours for $S=2.0$, $Gr=10^6$, and $Pr=6.0$

Conclusions

The present numerical study dispenses with the problems associated with the analytical treatment of natural convection from isothermal vertical surfaces in thermally stratified fluids. At higher levels of thermal stratification, horizontal plumes appear on the plate that are shown to be unsteady. The plume striates because of the effect of the temperature defects in the boundary layers, while the rest of the flow field remains intact. The length scale of the striations is found to be much smaller compared to the height of the plate. Increasing levels of thermal stratification reduce heat transfer rates and in the extreme case, the net heat transfer rate can be zero.

Downloaded 13 Dec 2010 to 193.140.21.150. Redistribution subject to ASME license or copyright; see http://www.asme.org/terms/Terms_Use.cfm

Acknowledgments

Many of the original ideas expressed in this paper are those of Professor Roger Eichhorn, with whom one of the authors (D.A.) held fruitful discussions. We acknowledge the help of Dr. M. S. Phanikumar in the development of the Fortran code.

References

Angirasa, D., and Srinivasan, J., 1989, "Natural Convection Flows Due to the Combined Buoyancy of Heat and Mass Diffusion in a Thermally Stratified Medium," ASME JOURNAL OF HEAT TRANSFER, Vol. 111, pp. 657–663.

Chen, C. C., and Eichhorn, R., 1976, "Natural Convection From a Vertical Surface to a Thermally Stratified Fluid," ASME JOURNAL OF HEAT TRANSFER, Vol. 98, pp. 446–451.

Chen, C. C., and Eichhorn, R., 1977, "Natural Convection From Simple Bodies Immersed in Thermally Stratified Fluids," Report No. UKY TR105-ME14-77, ORES Publications, College of Engineering, University of Kentucky, Lexington, KY.

Churchill, S. W., and Chu, H. H. S., 1975, "Correlating Equations for Laminar and Turbulent Free Convection From a Vertical Plate," *Int. J. Heat Mass Transfer*, Vol. 18, pp. 1323–1329.

Eichhorn, R., 1969, "Natural Convection in a Thermally Stratified Fluid," *Prog. Heat Mass Transfer*, Vol. 2, pp. 41–53.

Eichhorn, R., Lienhard, J. H., and Chen, C. C., 1974, "Natural Convection From Isothermal Spheres and Cylinders Immersed in a Stratified Fluid," *Proc. 5th Int. Heat Transfer Conf.*, Tokyo, NC 1.3, pp. 10–14.

Fujii, T., Takuechi, M., and Morioka, I., 1974, "Laminar Boundary Layer of Free Convection in a Temperature Stratified Environment," *Proc. 5th Int. Heat Transfer Conf.*, Tokyo, NC 2.2, pp. 44–48.

Gebhart, B., Jaluria, Y., Mahajan, R. L., and Sammakia, B., 1988, *Buoyancy-Induced Flows and Transport*, Hemisphere, Washington, DC.

Gresho, P. M., 1989, Personal Communication.

Henkes, R. A. W. M., and Hoogendoorn, C. J., 1989, "Laminar Natural Convection Boundary-Layer Flow Along a Heated Vertical Plate in a Stratified Environment," *Int. J. Heat Mass Transfer*, Vol. 32, pp. 147–155.

Jaluria, Y., and Gebhart, B., 1974, "Stability and Transition of Buoyancy-Induced Flows in a Stratified Medium," *J. Fluid Mechanics*, Vol. 65, Part 3, pp. 593–612.

Kulkarni, A. K., Jacobs, H. R., and Hwang, J. J., 1987, "Similarity Solution for Natural Convection Flow Over an Isothermal Vertical Wall Immersed in Thermally Stratified Medium," *Int. J. Heat Mass Transfer*, Vol. 30, pp. 691–698.

McAdams, W. H., 1954, *Heat Transmission*, 3rd ed., McGraw-Hill, New York.

Minkowycz, W. J., and Sparrow, E. M., 1974, "Local Nonsimilar Solutions for Natural Convection on a Vertical Cylinder," ASME JOURNAL OF HEAT TRANSFER, Vol. 96, pp. 178–183.

Press, W. H., Flannery, B. P., Teukolsky, S. A., and Vetterling, W. T., 1986, *Numerical Recipes*, Cambridge University Press, New York.

Roache, P. J., 1982, *Computational Fluid Dynamics*, rev. ed., Hermosa, Albuquerque, NM.

Semenov, V. I., 1984, "Similar Problems of Steady-State Laminar Free Convection on a Vertical Plate," *Heat Transfer—Soviet Research*, Vol. 16, pp. 69–85.

Sparrow, E. M., Quack, H., and Boerner, C. J., 1970, "Local Nonsimilarity Boundary-Layer Solutions," *AIAA J.*, Vol. 8, pp. 1936–1942.

Sparrow, E. M., and Yu, H. S., 1971, "Local Non-similarity Thermal Boundary Layer Solutions," ASME JOURNAL OF HEAT TRANSFER, Vol. 93, pp. 328–334.

Venkatachala, B. J., 1978, "A Numerical Study of Some Flow and Heat Transfer Problems in Laminar Boundary Layers," Ph.D. Thesis, Department of Applied Mathematics, Indian Institute of Science, Bangalore, India.

Venkatachala, B. J., and Nath, G., 1981, "Nonsimilar Laminar Natural Convection in a Thermally Stratified Fluid," *Int. J. Heat Mass Transfer*, Vol. 24, pp. 1848–1850.

Yang, K. T., Novotny, J. L., and Cheng, Y. S., 1972, "Laminar Free Convection From a Nonisothermal Plate Immersed in a Temperature Stratified Medium," *Int. J. Heat Mass Transfer*, Vol. 15, pp. 1097–1109.

Downloaded 13 Dec 2010 to 193.140.21.150. Redistribution subject to ASME license or copyright; see http://www.asme.org/terms/Terms_Use.cfm

Three-Dimensional Natural Convection in a Vertical Porous Layer With a Hexagonal Honeycomb Core

Y. Asako

H. Nakamura

Y. Yamaguchi

Department of Mechanical Engineering,
Tokyo Metropolitan University,
Tokyo, 192-03 Japan

M. Faghri

Department of Mechanical Engineering,
University of Rhode Island,
Kingston, RI 02881

Numerical solutions are obtained for a three-dimensional natural convection heat transfer problem in a vertical porous layer with a hexagonal honeycomb core. The porous layer is assumed to be long and wide such that the velocity and temperature fields repeat themselves in successive enclosures. The natural convection problem is solved for only one honeycomb enclosure with periodic thermal boundary conditions. The porous layer is assumed to be homogeneous and isotropic and the flow is obtained by using the Darcian model. The numerical methodology is based on an algebraic coordinate transformation technique, which maps the hexagonal cross section onto a rectangle. The transformed governing equations are solved with the SIMPLE algorithm. The calculations are performed for the Darcy-Rayleigh number in the range of 10 to 10^3 and for eight values of the aspect ratio (H/L = 0.25, 0.333, 0.5, 0.7, 1, 1.4, 2, and 5). Two types of thermal boundary condition for the honeycomb core wall are considered: conduction and adiabatic honeycomb core wall thermal boundary conditions. The results are presented in the form of average and local heat transfer coefficients and are compared with the corresponding values for two and three-dimensional rectangular enclosures.

Introduction

An air layer with a hexagonal honeycomb core is often used as a thermal insulating wall. Inside such a layer, the main mechanisms of heat transfer are natural convection and radiation. A number of studies for natural convection heat transfer in such an air layer has been investigated by Asako et al. (1989, 1990a, 1990b). If the air layer is filled with thermal insulation such as glass wool, both convective and radiative heat transfer rates will decrease. The convection in the layer can be treated as a flow in a porous medium.

The numerical methodology used in this study utilizes an algebraic coordinate transformation developed previously in a paper by Faghri et al. (1984), which maps an irregular cross section onto a rectangle. This method was extended to fully three-dimensional problems by Asako et al. (1989). In this paper, the flow is obtained by the Darcian model and the porous layer is assumed to be homogeneous and isotropic. The numerical solutions are obtained for both the adiabatic and conductive honeycomb core wall thermal boundary conditions and for the Darcy-Rayleigh number in the range of 10 to 10^3, and for the aspect ratio, H/L, in the range of 0.25 to 5. Unfortunately, no experimental results are available for comparison with the present work. However, the results of this work are compared with the corresponding values for two and three-dimensional rectangular enclosures.

Formulation

Description of the Problem. The problem to be considered in this study is schematically depicted in Fig. 1. It involves the determination of three-dimensional heat transfer for natural convection in a vertical porous layer with a hexagonal honeycomb core. If the porous layer is very long and wide in both the vertical and the horizontal directions, the velocity and temperature fields repeat themselves in successive enclosures except at the end boundaries of the layer. Then, it is possible to solve the natural convection problem in only one hexagonal honeycomb porous enclosure with an appropriate thermal

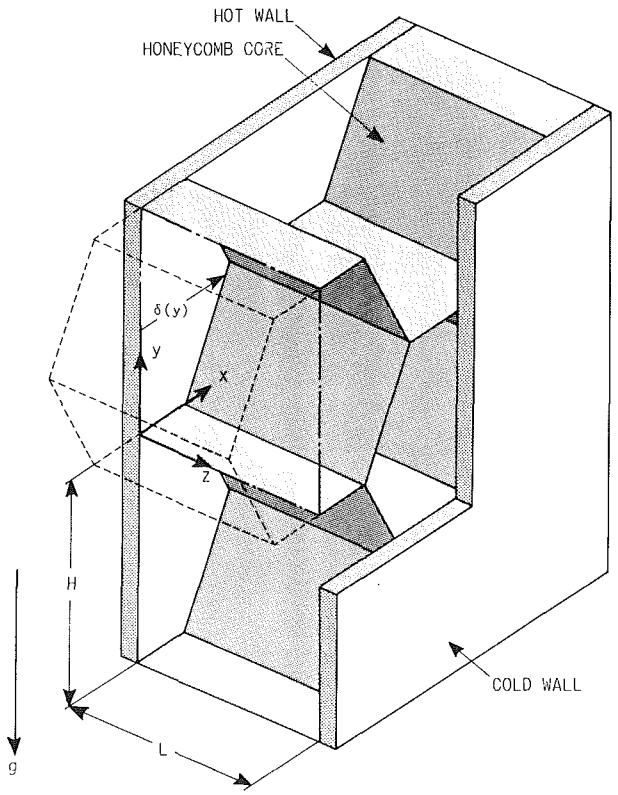

Fig. 1 Schematic diagram of a vertical porous layer with honeycomb core

Contributed by the Heat Transfer Division for publication in the JOURNAL OF HEAT TRANSFER. Manuscript received by the Heat Transfer Division September 1991; revision received April 1992. Keywords: Natural Convection, Numerical Methods, Porous Media. Associate Technical Editor: J. R. Lloyd.

Copyright © 1992 by ASME
Downloaded 13 Dec 2010 to 193.140.21.150. Redistribution subject to ASME license or copyright; see http://www.asme.org/terms/Terms_Use.cfm

boundary condition. As seen in Fig. 1, the two hexagonal end walls of the enclosure are kept at uniform temperatures t_H and t_C, respectively. The honeycomb core walls (the side walls) can be modeled as good conductors and thick, or thermally insulated. The geometry of the problem is specified by the height (H) and the length (L). The solution domain, with the assumption of symmetry, is confined to the right half of the honeycomb enclosure. The mathematical expression for the width of this honeycomb, $\delta(y)$, is given in an earlier paper by Asako et al. (1989).

Conservation Equations. The governing equations to be considered are the continuity and energy equations. The flow field is approximated by the Darcian model. Constant thermophysical properties are assumed except for the density in the buoyancy force term. The following dimensionless variables are used:

$$X=x/L, \quad Y=y/L, \quad Z=z/L,$$
$$U=u/(a/L), \quad V=v/(a/L), \quad W=w/(a/L), \quad (1)$$
$$P=pK/a\mu, \quad T=(t-t_m)/(t_H-t_C)$$

where t_m is the average temperature of the end walls and is expressed by $t_m = (t_H+t_C)/2$. Then, upon introduction of dimensionless variables and parameters, for steady natural convection in a porous medium, the governing equations take the following forms:

$$\partial U/\partial X+\partial V/\partial Y+\partial W/\partial Z=0 \quad (2)$$

$$U=-\partial P/\partial X \quad (3)$$

$$V=-\partial P/\partial Y+\mathrm{Ra}^*T \quad (4)$$

$$W=-\partial P/\partial Z \quad (5)$$

$$U(\partial T/\partial X)+V(\partial T/\partial Y)+W(\partial T/\partial Z)=\nabla^2 T \quad (6)$$

where (7)

$$\nabla^2=\partial^2/\partial X^2+\partial^2/\partial Y^2+\partial^2/\partial Z^2$$

To complete the formulation of the problem, it remains to discuss the boundary conditions. These are:

$$\text{at all walls: } \mathbf{V}\cdot\mathbf{N}=0$$

$$\text{at the symmetry plane } (X=0): \quad U=\partial V/\partial X=\partial W/\partial X=0 \quad (8)$$

where $\mathbf{V}$ and $\mathbf{N}$ are the velocity vector and the normal vector to the walls, respectively. That is, the nonpermeable boundary condition is assumed at the wall. The thermal boundary conditions on the hot and cold walls reduce to

$$\text{hot wall:} \quad T=0.5$$

$$\text{cold wall} \quad : \quad T=-0.5 \quad (9)$$

As mentioned earlier, two types of thermal boundary condition for the honeycomb core wall are considered. The first boundary condition is the so-called conductive condition. This condition exists when the honeycomb core walls are good conductors and thick. In this condition, the temperature of the side walls varies linearly in the Z direction. The mathematical expression for this condition is expressed as:

$$T=0.5-Z \quad (10)$$

The second boundary condition for the honeycomb core wall is that of the adiabatic condition. This condition exists when the side walls are thermally insulated and is expressed as:

$$\partial T/\partial N=0 \quad (11)$$

where N is the dimensionless coordinate directed along the outward normal to the walls.

Transformation of Equations. The first step of the solution methodology is to introduce a transformation of coordinates, which maps the hexagonal cross section onto a rectangle. This is documented in earlier papers by Asako et al. (1989), and only a brief description will be given here. The X, Y coordinates are transformed into the η, ξ coordinates by the relations

$$\eta=X[\delta(y)/L], \quad \xi=Y, \quad (12)$$

In terms of the new coordinates, the solution domain is bounded by $0<\eta<1$, $0<\xi<H/L$.

Numerical Solutions. The discretized procedure of the equations is based on the power-law scheme of Patankar (1981), and the discretized equations are solved by using a line-by-line method. The pressure and velocities are linked by the SIMPLE algorithm of Patankar (1980). Note that the SIMPLE algorithm for the pressure-velocity linkage for the Darcian model can be considered as an implicit method rather than a semi-implicit method. Because of this, a good convergence was obtained.

The computations were performed with $(16\times22\times22)$, $(16\times30\times30)$, and $(16\times40\times40)$ grids for $\mathrm{Ra}^*=10$, 10^2, and 10^3, respectively. The grid points were uniformly distributed in the η and ξ directions, but nonuniformly in the Z direction with higher concentrations near the hexagonal end walls.

Supplementary runs for $H/L=1$ and for the adiabatic side wall condition were performed to investigate the grid size effects. The comparison of the Nusselt number is listed in Table 1. The change in Nusselt number between the coarse mesh $(12\times16\times16)$ and the medium mesh $(16\times22\times22)$ is 0.03 percent for $\mathrm{Ra}^*=10$, between the medium mesh $(16\times22\times22)$ and the fine mesh $(16\times30\times30)$ it is 0.6 percent for $\mathrm{Ra}^*=10^2$, and between the fine mesh $(16\times30\times30)$ and the very fine mesh $(16\times40\times40)$ it is 2 percent for $\mathrm{Ra}^*=10^3$. Thus, $(16\times22\times22)$, $(16\times30\times30)$, and $(16\times40\times40)$ grid points, respectively, were selected for $\mathrm{Ra}^*=10$, 10^2, and 10^3 to maintain relatively moderate computing costs.

From an examination of the governing equations, Eqs. (2)–(6), it can be seen that there is only one flow parameter whose value has to be specified prior to the initiation of the numerical

Nomenclature

a = thermal diffusivity of porous layer
H = height of a hexagonal honeycomb enclosure
h, h_m = local and average heat transfer coefficients [Eq. (13)]
K = permeability
k = thermal conductivity
L = axial length of a hexagonal honeycomb enclosure
Nu, Nu_m = local and average Nusselt numbers [Eq. (14)]
Q = total heat transfer from a hot wall
q = heat flux on a hot wall
Ra^* = Darcy-Rayleigh number $=Kg\beta L(t_H-t_c)]/a\nu$
T = dimensionless temperature
t_c = cold wall temperature
t_H = hot wall temperature
β = coefficient of thermal expansion of fluid
$\delta(y)$ = half width of a hexagonal enclosure
η = transformed coordinate $= X/\{\delta(y)/L\}$
μ = viscosity of fluid
ν = kinematic viscosity of fluid
ξ = transformed coordinate $= Y$

Downloaded 13 Dec 2010 to 193.140.21.150. Redistribution subject to ASME license or copyright; see http://www.asme.org/terms/Terms_Use.cfm

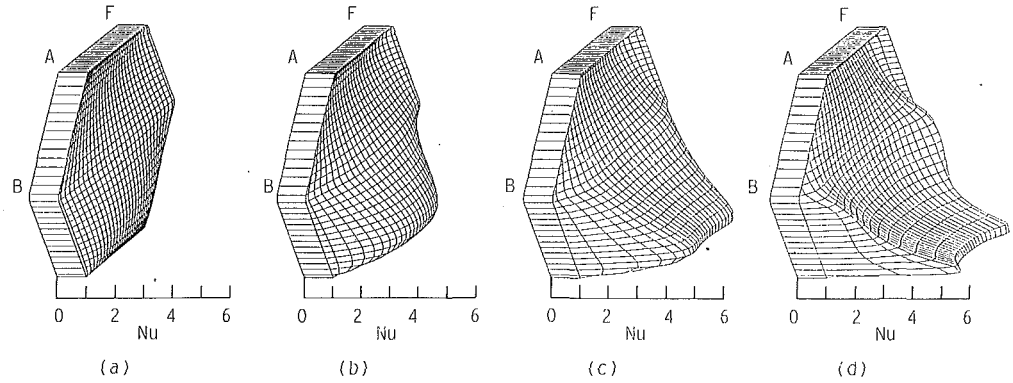

Fig. 2 Local Nusselt number on the hot wall for $Ra^* = 10^2$ and for the conductive side wall: (*a*) $H/L = 0.5$; (*b*) $H/L = 1$; (*c*) $H/L = 2$; (*d*) $H/L = 5$

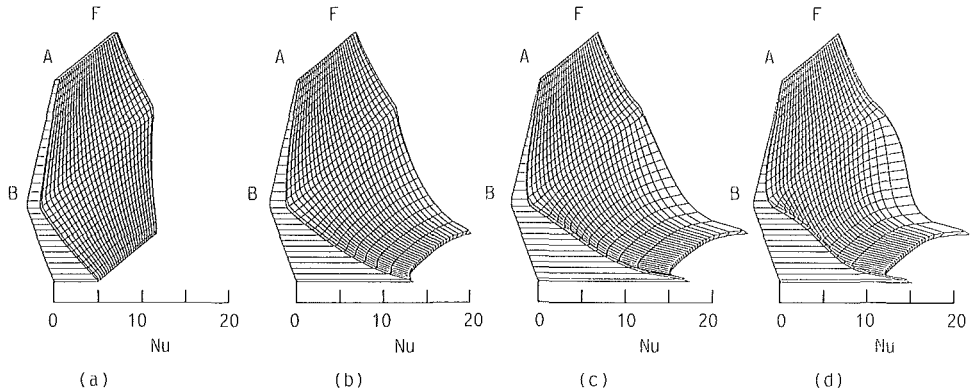

Fig. 3 Local Nusselt number on the hot wall for $Ra^* = 10^2$ and for the adiabatic side wall: (*a*) $H/L = 0.5$; (*b*) $H/L = 1$; (*c*) $H/L = 2$; (*d*) $H/L = 5$

Table 1 Effect of grid size on average Nusselt number for adiabatic sidewall and for $H/L = 1$

	Num			
Ra^*	12×16×16	16×22×22	16×30×30	16×40×40
10	1.0748	1.0751	1.0753	1.0754
10^2	3.012	3.047	3.064	3.072
10^3	12.084	12.922	13.386	13.650

solution. This is the Darcy-Rayleigh number, Ra^*. In this paper, the values chosen for the Darcy-Rayleigh number are in the range from 10 to 10^3. Aside from Ra^*, there are two geometric parameters that have to be specified. These are the height (H) and the length (L) of the enclosure. If L is used as a reference length, then H/L needs to be specified as the geometric parameter. The selected values for H/L were 0.25, 0.333, 0.5, 0.7, 1, 1.4, 2, and 5.

Nusselt Number. The local and average heat transfer coefficient and Nusselt number on the hot wall are defined as

$$h = q/(t_H - t_c) \qquad h_m = Q/[A_H(t_H - t_C)] \quad (13)$$

$$\mathrm{Nu} = hL/k = -(\partial T/\partial Z)_H \qquad \mathrm{Num} = h_m L/k$$

$$= -2\int_0^{H/L}\int_0^1 (\partial T/\partial Z)_H(\delta/L)\, d\eta d\xi/[(3/2)(H/L)^2\tan(\pi/6)] \quad (14)$$

where q is the local heat flux, A_H is the area of the hexagonal hot wall equal to $(3/2)\,H^2\tan(\pi/6)$, and Q is the total heat transfer rate from the hot wall.

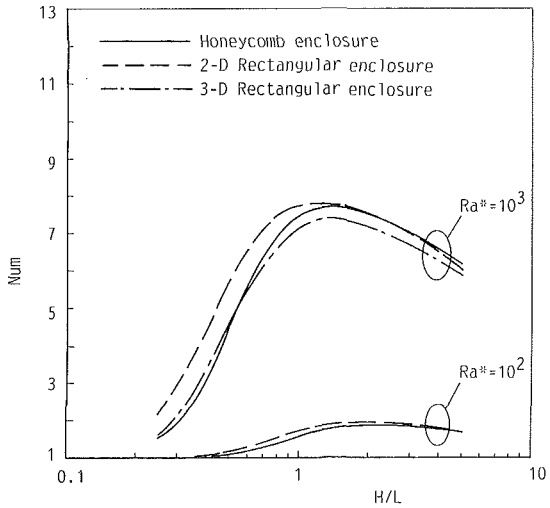

Fig. 4 Average Nusselt number, Nu_m, for the conductive side wall as a function of the aspect ratio, H/L

Results and Discussion

Local Nusselt Number. The local Nusselt numbers on the hot wall for conductive side wall boundary condition and for $Ra^* = 10^2$ are presented in Fig. 2 and the results for $Ra^* = 10^3$ are presented in Fig. 3. In each figure, the Nusselt numbers for the aspect ratios $H/L = 0.5$, 1, 2, and 5 are shown in Figs. (*a*), (*b*), (*c*), and (*d*), respectively. As seen from the figure, in the case of a low aspect ratio ($H/L = 0.5$ and 1), the local Nusselt number value takes the highest value on the symmetry line at the same elevation and its peak is located away from the bottom. The Nusselt number profile changes with increas-

Downloaded 13 Dec 2010 to 193.140.21.150. Redistribution subject to ASME license or copyright; see http://www.asme.org/terms/Terms_Use.cfm

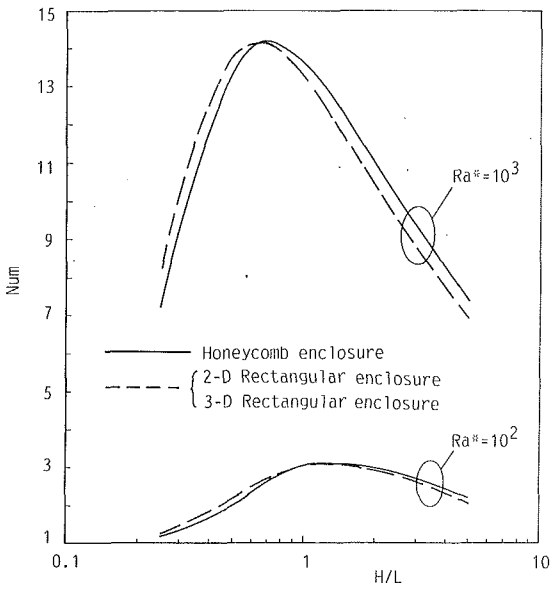

Fig. 5 Average Nusselt number, Nu_m, for the adiabatic side wall as a function of the aspect ratio, *H/L*

ing values of the aspect ratio. It has two peaks, which move to lower corners of the hot wall with increasing values of the aspect ratio.

The local Nusselt number on the hot wall for adiabatic side wall boundary condition and for $Ra^* = 10^2$ and for the aspect ratio in the range of 0.5 to 5 are also presented in Fig. 3. As seen from the figure, in the case of the adiabatic boundary condition, the local Nusselt number profile does not change with increasing values of the aspect ratio.

Average Nusselt Number. The average Nusselt number for the conductive and adiabatic side wall boundary conditions are plotted as a function of the aspect ratio, H/L, with the Darcy-Rayleigh number as a curve parameter in Figs. 4 and 5, respectively. For both cases, the average Nusselt number values for $Ra^* = 10$ are almost unity. Therefore, the results for $Ra^* = 10$ are not plotted. As seen from Figs. 4 and 5, the value of the aspect ratio where the Nusselt number takes the highest value is a function of Ra^* for both the conductive and adiabatic side wall boundary conditions. This trend is accentuated for the adiabatic side wall boundary condition.

From the comparison of Figs. 4 and 5, the average Nusselt numbers for the adiabatic boundary condition are higher than those for the conductive boundary condition. The fluid temperature for the conductive side wall that arrives at the hot wall is higher than that for the adiabatic wall because of the heat exchange on the side wall. This is why the Nusselt number for the conductive side wall boundary condition is lower than that for the adiabatic condition.

The dashed lines in the figures are the results for a two-dimensional rectangular enclosure of height H and horizontal length L and this enclosure has infinite length in the x direction. The full three-dimensional computation requires excessive computing time. Therefore, it would be helpful if the average Nusselt number could be predicted from the results of a two-dimensional model. To investigate this, supplementary two-dimensional computations were performed with (40×40) and (30×30) grid points for $Ra^* = 10^3$ and 10^2, respectively, for both boundary conditions. The grid point distribution is similar to the three-dimensional computations. That is, the grid points were distributed uniformly along the Y direction and nonuniformly along the Z direction with higher concentration of the grid points near the hexagonal end walls. As seen from Figs. 4 and 5, small differences between Nusselt numbers for the two-dimensional and the honeycomb enclosure can be seen for both boundary conditions.

Supplementary computations were also performed for three-dimensional rectangular enclosures with a square cross section in the X-Y plane for $Ra^* = 10^3$ to investigate the observed differences between Nusselt numbers for the two-dimensional rectangular and honeycomb enclosures. Computations were performed with $(16 \times 40 \times 40)$ grid points for both boundary conditions. The grid points were distributed uniformly along the Y direction and nonuniformly along the Z direction with a higher concentration of the grid points near the hexagonal end walls. The chain line in Fig. 4 for the conductive side wall condition is the result of these computations. The Nusselt number value for the three-dimensional rectangular enclosure takes a value close to one for the honeycomb enclosure at lower aspect ratios. This result indicates that the observed difference between Nusselt numbers is due to the difference between two-dimensional and three-dimensional modeling. On the contrary, as seen from Fig. 5 for the adiabatic condition, the Nusselt number value for the three-dimensional rectangular enclosure perfectly coincides with one for the two-dimensional rectangular enclosure. This result indicates that the observed difference between Nusselt numbers at lower aspect ratios is due to the hexagonal geometry in the adiabatic side wall condition. However, it is not clear why the Nusselt numbers for the two and three-dimensional rectangular enclosures are lower than the values for the honeycomb enclosure at higher aspect ratios.

Concluding Remarks

Three-dimensional natural convection heat transfer characteristics in a porous layer with hexagonal honeycomb core were obtained numerically by a coordinate transformation technique. The computations were performed for Darcy-Rayleigh numbers in the range of 10 to 10^3 and for five values of the aspect ratio. The main conclusions are:

(*a*) The value of the aspect ratio where the average Nusselt number takes the highest value is function of Ra^* for both the conductive and adiabatic side wall boundary conditions. This trend is accentuated for the adiabatic side wall boundary condition.

(*b*) The average Nusselt number can be predicted by a two-dimensional model depending on the aspect ratio and the Darcy-Rayleigh number value.

References

Asako, Y., Nakamura, H., and Faghri, M., 1989, "Three-Dimensional Laminar Natural Convection in a Honeycomb Enclosure With Hexagonal End Walls," *Numerical Heat Transfer*, Vol. 15, pp. 67-86.

Asako, Y., Nakamura, H., and Faghri, M., 1990a, "Three-Dimensional Laminar Natural Convection in a Vertical Air Slot With Hexagonal Honeycomb Core," ASME JOURNAL OF HEAT TRANSFER, Vol. 112, pp. 130-136.

Asako, Y., Nakamura, H., Chen, Z., and Faghri, M., 1990b, "Three-Dimensional Laminar Natural Convection in an Inclined Air Slot With a Hexagonal Honeycomb Core," *AIAA/ASME Thermophysics and Heat Transfer Conference*, ASME HTD-Vol. 140, pp. 19-24.

Faghri, M., Sparrow, E. M., and Prata, A. T., 1984, "Finite Difference Solutions of Convection-Diffusion Problems in Irregular Domains Using a Non-orthogonal Coordinate Transformation," *Numerical Heat Transfer*, Vol. 7, pp. 183-209.

Patankar, S. V., 1980, *Numerical Heat Transfer and Fluid Flow*, Hemisphere, Washington, DC.

Patankar, S.V., 1981, "A Calculation Procedure for Two-Dimensional Elliptic Situations," *Numerical Heat Transfer*, Vol. 4, pp. 409-425.

Downloaded 13 Dec 2010 to 193.140.21.150. Redistribution subject to ASME license or copyright; see http://www.asme.org/terms/Terms_Use.cfm

Reversed Flow Structure and Heat Transfer Measurements for Buoyancy-Assisted Convection in a Heated Vertical Duct

C. Gau

K. A. Yih

W. Aung

Institute of Aeronautics and Astronautics,
National Cheng Kung University,
Tainan, Taiwan 700

Buoyancy-assisted convection flow and heat transfer processes in a heated vertical channel are studied experimentally for situations where the buoyancy parameter Gr/Re^2 is relatively large. The channel wall is made of two parallel plates, with one wall heated uniformly and the opposite wall insulated. A uniform air flow is made to enter the channel from the bottom. The reversed flow is visualized, which occurs initially near the channel exit for the case when Gr/Re^2 is greater than a threshold value. The cold reversed flow enters the channel from the outside and forms a V-shaped recirculating flow region in the downstream part of the duct. This region gradually propagates upstream as the buoyancy parameter Gr/Re^2 increases. The counterflow motion, leading to mixing between the heated buoyant fluid and the V-shaped recirculation, is shown to be highly unstable and characterized by generation of eddies and vortices when the value of Gr/Re^2 is large. An increase in Re has the effect of pushing the reversed flow downstream and making the recirculating region wider. Temperature fluctuations are measured to provide insight into the complex phenomena being studied. The penetration depth of the reversed flow is measured and compared with prediction based on a simple model. Local and average Nusselt numbers are also measured and presented.

1 Introduction

Mixed convection heat transfer and flow in vertical channels has been studied extensively. However, most of the work in the past has been either analytical (Hanratty et al., 1958; Tao, 1960; Rao and Morris, 1967–68) or numerical analyses (Quintiere and Mueller, 1973; Yao, 1983; Habchi and Acharya, 1986; Aung and Worku, 1986, 1987). A limited number of experiments have also been performed to indicate that aiding or opposed buoyancy forces can have a significant effect on the flow and heat transfer in the channel (Scheele and Hanratty, 1962; Brown and Gauvin, 1965; Sherwin and Wallis, 1971; Zeldin and Schmidt, 1972; Chow et al., 1984; Wirtz and Mckinley, 1985; Incropera and Campbell, 1990). While the experimental data and the numerical predictions agree well, at large values of the buoyancy parameter Gr/Re^2, flow reversal can occur, which can have a significant effect on the entire channel flow structure and the heat transfer process. A review of literature indicates that only a few studies have reported on the occurrence of flow reversal (Aung and Worku, 1986; Ingham et al., 1988a, 1990; Morton et al., 1989).

By assuming a steady, two-dimensional, laminar flow, Ingham et al. (1988b) solved the coupled momentum and energy equations and obtained a numerical solution with flow reversal. Earlier, Aung and Worku (1986) made similar assumptions and obtained a fully developed solution with flow reversal. The assumptions made in these analyses concerning steady and laminar flow, however, represent idealized cases and may not be appropriate for the practical situation.

Gau et al. (1990) recently performed mixed convection experiments in finite vertical channels for both buoyancy-assisted and opposed flows. For opposed flow, the occurrence of flow reversal is visualized and is observed to initiate in the downstream region (at the bottom of the channel) and to extend gradually upstream when the buoyancy parameter Gr/Re^2 increases. However, due to the counterflow motion and the mixing between the mainstream and the reversed flow, the reversed flow can render the flow in its vicinity highly unstable and give rise to transition to turbulent flow. The heat transfer coefficient along the heated wall is also measured and is significantly higher than the results of laminar forced convection. It appears, therefore, that the experimental results are significantly different from the numerical prediction.

For the case of buoyancy-assisted flow, no oscillation or reversal of flow has been found for Gr/Re^2 up to 50 at $Re = 600$ (Gau et al., 1990). For a fully developed flow in a vertical tube, subject to different heating and cooling wall sections, however, steady recirculation regions of flow have been found both experimentally and numerically, which have a significant effect on the heat transfer and friction along the wall (Morton et al., 1989; Ingham et al., 1990). However, for the case of pure natural convection in a one-side-heated vertical channel, both numerical results (Chang and Lin, 1990) and experimental observation (Sparrow et al., 1984) indicate the appearance of flow reversal. Natural convection in these geometric configurations is very similar to the case of mixed convection with aiding buoyancy force at a relatively large Gr/Re^2 value. Therefore, flow reversal is expected to appear for the case of mixed convection flow. In the present experiments, the characteristic of the reversed flow structure and its effect on the entire flow and the heat transfer along the wall will be systematically studied.

In the current work, an experiment is designed to study and visualize the flow structure at relatively large values of the buoyancy parameter. The large value of Gr/Re^2 is achieved by reducing the entrance velocity of air, which decreases Re. An electrical resistance wire coated with oil is inserted into the channel to generate smoke for the purpose of flow visualization. A thermocouple probe is inserted into the channel at different locations to measure the temperature fluctuations. The penetration depth of the reversed flow is measured and

Contributed by the Heat Transfer Division for publication in the JOURNAL OF HEAT TRANSFER. Manuscript received by the Heat Transfer Division March 1991; revision received February 1992. Keywords: Electronic Equipment, Flow Visualization, Mixed Convection. Associate Technical Editor: F. P. Incropera.

Copyright © 1992 by ASME
Downloaded 13 Dec 2010 to 193.140.21.150. Redistribution subject to ASME license or copyright; see http://www.asme.org/terms/Terms_Use.cfm

compared with the prediction based on a simple model. Both local and average Nusselt numbers are also measured and compared with the predictions for the case of pure free/forced convection inside the channel and the case of mixed convection using an ad hoc model.

2 Experimental Apparatus and Procedures

The present measurements are performed in a vertical wind tunnel, which can provide a uniform air flow in the upward direction, as shown in Fig. 1. To ensure a uniform entering air flow in the upward direction, the wind tunnel is furnished with a settling chamber and a contraction section upstream (and also downstream) of the test section. The turbulence intensity of the uniform air flow at the outlet of the contraction is minimized and is less than 0.5 percent when the flow speed is higher than 5 m/s. The turbulence intensity, however, becomes relatively high when the flow velocity is very low. The turbulence intensity for the upward flow at 0.3 m/s is 2.1 percent and that at 1.2 m/s is 0.9 percent.

The flow velocity is measured with a TSI hot-wire anemometer. Since a Pitot tube cannot accurately measure the low velocities of interest here, the hot wire is calibrated in a specially designed system (Chen and Miau, 1987). During the calibration process, the hot wire is placed on a traversing mechanism located in a quiescent room. The traversing velocity of the probe, which corresponds to the velocity of the air flow past the wire, is controlled by a step motor of variable speed. By this means, a calibration curve for the air flow velocity past the wire and the corresponding compensation voltage across the wire can be obtained. To minimize the effect of buoyancy-induced flow around the heated wire when the wire is used to measure the upward air flow, the probe is made to traverse downward in the calibration process. The maximum uncertainty of the velocity measurement is 6 percent.

The vertical channel is made of plexiglass and has inside dimensions of 30 mm in gap width, 455 mm in height, and 300 mm in depth. The channel height of heated section is 360 mm. The heated wall is made of a 3-mm-thick aluminum plate that is cut into 22 sections each of 15 mm width. A 1.5-mm-thick balsa wood strip is inserted between the adjacent aluminum sections to reduce the axial heat conduction in the wall. The aluminum plate is heated on the back with a silicon rubber heater that is insulated on the outside with balsa wood of 1 cm thickness. A d-c power generator is used to provide the electric energy required for generating the desired uniform heat flux. For better insulation the entire channel is covered with foamed rubber having a thickness of 35 mm. Before the experiments, all the thermocouples are calibrated in a constant temperature bath and the measurement error is within ± 0.1°C. All the temperature signals acquired are sent to a PC/AT data system for management and plotting. The temperature data

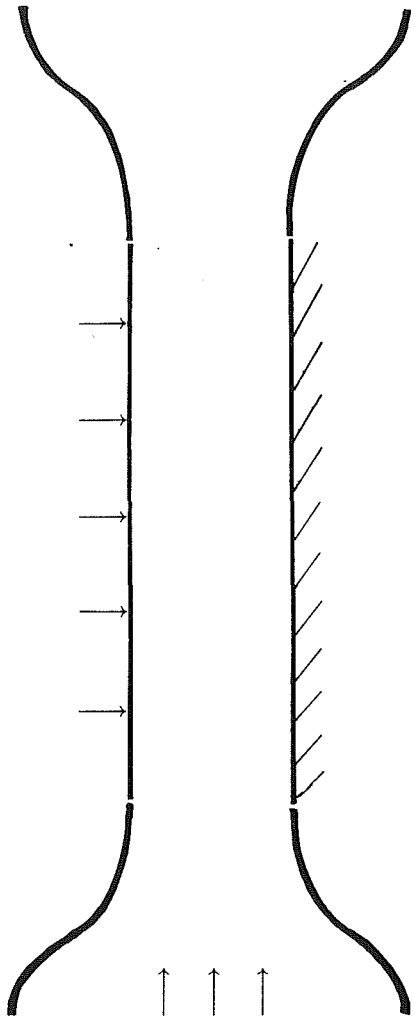

Fig. 1 Schematic diagram of the apparatus

are taken when the system reaches steady state, usually in 5 ~ 6 hours.

The total heat transfer rate on a single aluminum section can be calculated from the electric current and voltage across the heater, and the local heat transfer coefficient on a single strip is evaluated from the equation:

$$h = Q/[A(T_w - T_o)] \tag{1}$$

All the thermophysical properties of air are evaluated at the inlet temperature, except that the thermal conductivity of air

Nomenclature

A = area of a single aluminum strip
b = channel width
D_h = channel hydraulic diameter $= 2b$
g = gravitational acceleration
Gr = Grashof number $= g\beta q D_h^4/(k_f \nu^2)$
Gr_x = Grashof number $= g\beta q x^4/(k_f \nu^2)$
h = local heat transfer coefficient
$\bar{h}$ = average heat transfer coefficient
k_f = thermal conductivity of air
L = channel height of heated section
Nu = local Nusselt number $= hD_h/k_f$
$\overline{\mathrm{Nu}}$ = average Nusselt number $= \bar{h}D_h/k_f$
Pr = Prandtl number
q = heat flux $= Q/A$
Q = total heat transfer rate on a single strip
Re = Reynolds number $= u_o D_h/\nu$
T_f = film temperature $= (T_o + T_w)/2$
T = temperature
u_o = mean velocity at inlet
u = boundary layer velocity
u_r = reference velocity
x = streamwise coordinate
$\bar{x}$ = penetration depth $= L - x$
y = transverse coordinate
β = coefficient of expansion
δ = thermal or momentum boundary layer thickness
η = dimensionless distance $= y/\delta$
ν = kinematic viscosity

Subscripts

o = refers to inlet
w = refers to heated wall

Downloaded 13 Dec 2010 to 193.140.21.150. Redistribution subject to ASME license or copyright; see http://www.asme.org/terms/Terms_Use.cfm

is evaluated at the film temperature defined as the average of the wall and air temperatures at the entrance.

Following the procedures reported by Kline and McClintock (1953), the uncertainty analysis for the heat flux, the Nusselt number, the Reynolds number, the Grashof number and the buoyancy parameter Gr/Re^2 is performed. The maximum uncertainties estimated for q, Nu, Re, Gr, and Gr/Re^2 are 4, 8, 6, 12, and 24 percent, respectively.

During the experiment, both the radiation loss from the entire heated surface and the heat conduction loss for the last three aluminum strips are found to be relatively large. Relatively large heat conduction loss in the region near the channel exit is also found in the experiment by Wirtz and Mckinley (1985). In the current experiment, conduction loss is estimated by solving the two-dimensional conduction equation for the composite wall of the channel with convective heat transfer boundary condition. The heat transfer coefficient outside the channel is estimated, while the one inside is obtained from the current experimental measurement. Therefore, both the conduction and the radiation losses for each strip heater are calculated and can be accounted for during the data reduction process.

During the flow visualization experiments, a thin, electrically heated wire coated with oil is used to generate smoke. The smoke wire can be inserted through a small hole drilled on the insulated plate at a distance of approximately 1.5 cm from the entrance. A vertical sheet of light oriented perpendicular to the insulated plate is used for illumination. Flow patterns at the upstream, the central, and the downstream regions can be observed and recorded using this method.

3 Results and Discussion

3.1 Flow Visualization. When the vertical side wall is heated uniformly, the fluid near the heated wall moves more rapidly due to the aiding buoyancy force, while the fluid adjacent to the insulated wall moves slowly. When Gr/Re^2 is less than 80 with $Re = 650$, the flow in the entire channel is steady; no oscillation of flow is found. The flow velocity near the heated wall increases with increasing Gr/Re^2, while that near the insulated wall decreases. When $Gr/Re^2 = 120$ with $Re = 514$, the fluid in the downstream region near the heated wall moves so rapidly, due to the aiding buoyancy force, that the flow velocity near the insulated wall at a certain channel height may become zero. At a region farther downstream, flow reversal occurs, as shown in Fig. 2. The reversed flow is relatively cold, and enters the channel from the outside at the top of the channel and moves along the insulated wall in a direction opposed to the mainstream. The heated buoyant flow near the heated wall drives and entrains the reversed cold flow, so that part of it changes direction once again and moves downstream, thereby forming a V-shaped recirculation region along the insulated wall. This phenomenon is illustrated in Fig. 2.

Flow reversal is triggered when the buoyancy force becomes so large that local natural convection starts to dominate the flow process. In this event, the total mass flow rate furnished by the blower is less than the total mass flow rate driven by the buoyant heated flow along the heated vertical plate. Therefore, a minimum pressure is created inside the channel that sucks in the cold air from the outside. It is noted that the occurrence of flow reversal depends on such parameters as Gr/Re^2, Re, Pr, and the aspect ratio of the channel. In the current experiments of air flow through a given size of channel, there are only two parameters, i.e., Gr/Re^2 and Re, that can be varied. It is found that the increase of Gr/Re^2 can induce the flow reversal, while the increase of Re can suppress it.

To describe the relative importance of natural convection versus pure forced convection inside the channel at a given location, the parameter Gr_x/Re is selected. In the entrance

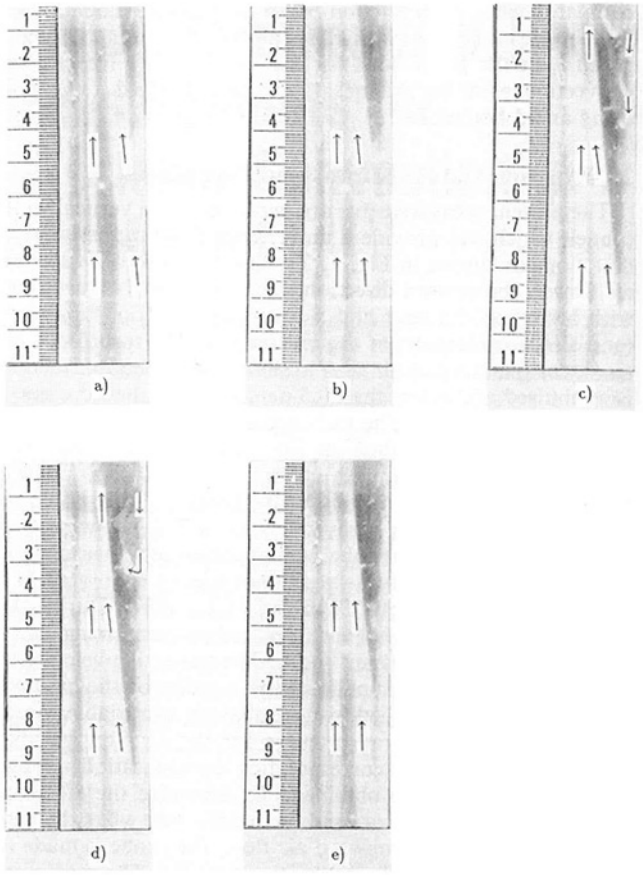

Fig. 2 Occurrence of the V-shaped recirculation flow for $Re = 514$, $Gr/Re^2 = 120$, at (*a*) $t = 0$, (*b*) $t = 1$, (*c*) $t = 2$, (*d*) $t = 3$, and (*e*) $t = 4$ (s)

region, the natural convection effect on the flow and heat transfer process is small, since the value of Gr_x/Re is relatively small and the physical process is dominated by forced convection. As the fluid moves downstream, it is heated gradually along with the increase of Gr_x/Re. The natural convection effect gradually becomes significant and starts to dominate the physical process in the downstream region when a critical value of Gr_x/Re is reached. Therefore, as the heat flux on the wall increases or the entrance flow velocity decreases, which corresponds to the increase of Gr_x/Re, the position at which natural convection begins to dominate moves upstream, causing the reversed flow to move upstream. The increase of the penetration depth of the V-shaped recirculation flow with increasing Gr/Re or Gr/Re^2 can be clearly observed in Figs. 2, 3, and 4.

Experiments have been performed to vary the buoyancy parameter Gr/Re^2 with Re being fixed or vice versa. In general, the buoyancy parameter Gr/Re^2 has the effect of causing the heated buoyant flow to move more rapidly, which leads to a deeper penetration of the reversed flow and a wider recirculating region, as shown in Figs. 4(*e*) and 5(*a*). However, the increase of Reynolds number has the opposite effect of pushing the reversed flow downstream. At this downstream location, the heated buoyant flow has become thinner and moved more rapidly that can make the recirculating region wider, as shown in Figs. 5(*a*) and 5(*b*).

An important finding in the present study is that the V-shaped recirculation flow is not steady, but instead grows and collapses in a periodic manner. The periodic behavior of recirculation flow is not reported in either the natural convection experiment with water (Sparrow et al., 1984) or the numerical analysis with air (Chang and Lin, 1990). This can be attributed to the relatively low Rayleigh number prescribed in their chan-

Downloaded 13 Dec 2010 to 193.140.21.150. Redistribution subject to ASME license or copyright; see http://www.asme.org/terms/Terms_Use.cfm

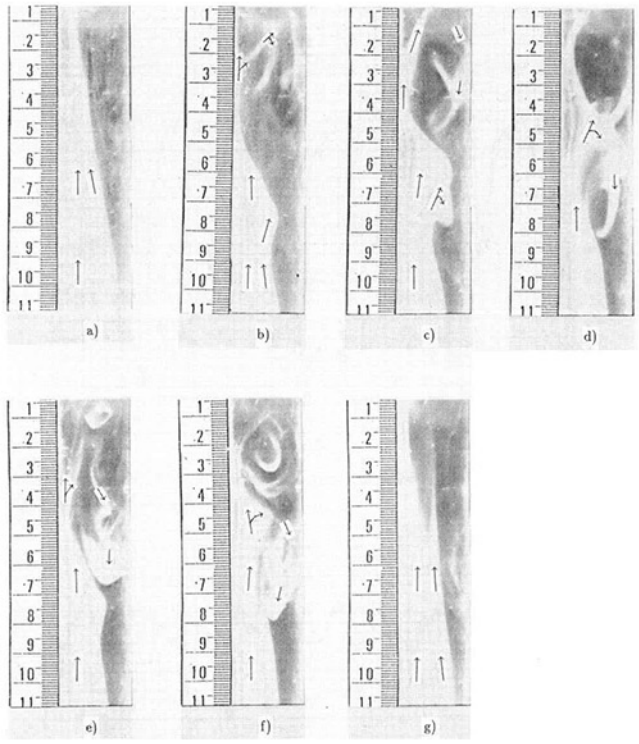

Fig. 3 Occurrence of the V-shaped recirculation flow for Re = 400, Gr/Re^2 = 210, at (*a*) $t = 0$, (*b*) $t = 1.5$, (*c*) $t = 1.7$, (*d*) $t = 1.8$, (*e*) $t = 2.0$, (*f*) $t = 2.2$, and (*g*) $t = 4.0$ (s)

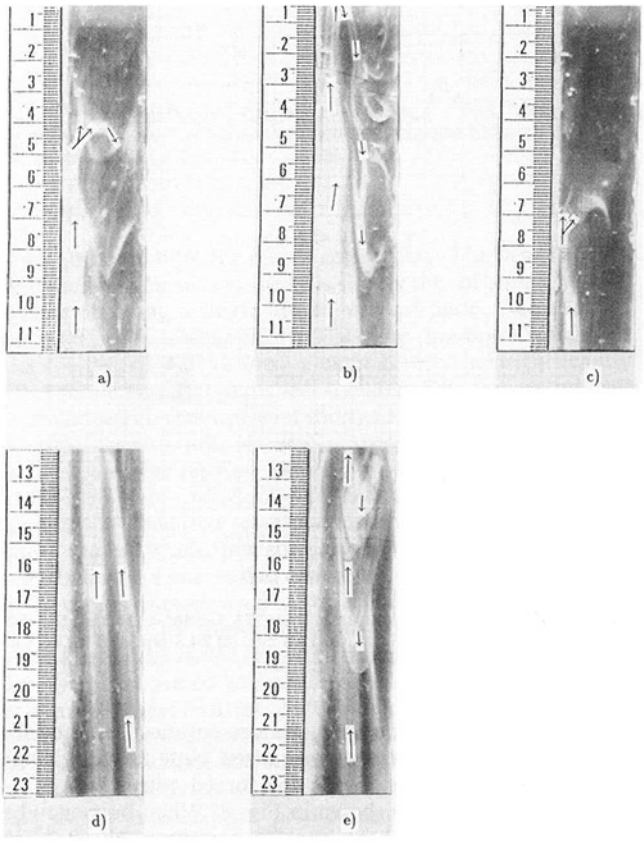

Fig. 4 Occurrence of the V-shaped recirculation flow for Re = 171, Gr/Re^2 = 1160: (*a*) generation of eddies and vortices, (*b*) generation of different eddies and vortices, (*c*) complete mixing of buoyant heated flow with the V-shaped recirculation flow, (*d*) V-shaped recirculation flow region close to the separation point, and (*e*) upstream motion of eddies and vortices

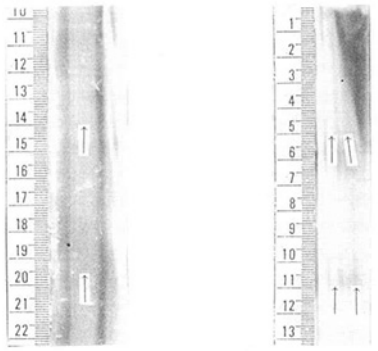

Fig. 5 Variation of the reversed flow structure with the Reynolds number: (*a*) at Re = 200, Gr/Re^2 = 100, smoke on the right-hand side indicates the thin, reversed flow region and (*b*) at Re = 600, Gr/Re^2 = 100, the V-shaped black region on the upper right corner represents the recirculation flow

nels. However, at Re = 10^6, an oscillatory behavior of wake flow outside of the channel is predicted (Chang and Lin, 1990). Therefore, it can be expected that in a higher aspect ratio channel, an oscillatory behavior of V-shaped recirculation flow can occur. For Gr/Re^2 = 120 and Re = 514, the tilted interface between the heated buoyant flow and the cold recirculation flow oscillates towards the right and left. This causes the separation point of the V-shaped recirculation flow to move up and down with a period of approximately 4 s, as shown in Fig. 2.

During the oscillation process, mixing of the heated buoyant flow with the cold reversed flow occurs, as can be clearly observed in Fig. 3 for Gr/Re^2 = 210 and Re = 400. The interface starts to become wavy and distorted, as shown in Figs. 3(*b*) and 3(*c*), and then the heated buoyant flow protrudes and breaks into the cold recirculation flow region as shown in Figs. 3(*d*), 3(*e*), and 3(*f*). This leads to the generation of unsteady eddies and vortices. The mechanism responsible for this is evidently the counterflow motion between the heated buoyant flow and the cold recirculation flow, giving rise to a Kelvin Helmhotz instability that makes the flow unstable, eventually leading to the generation of vortices. Finally, the buoyant heated flow which penetrates into the recirculation region is carried away by the recirculating flow.

For a large value of Gr/Re^2, the oscillation of the interface and the mixing of heated flow with cold recirculation flow become so intense that a number of small unsteady eddies and vortices are generated, as shown in Figs. 4(*a*) and 4(*b*). The mixing process can make the flow so highly unstable that a complete mixing of the heated flow with recirculation flow can occur, as shown in Fig. 4(*c*), where the buoyant smoke flow and the recirculation flow region could not be distinguished. At this stage, the flow in the upper (downstream) part of the channel has actually become turbulent. Therefore, it is expected that the heat transfer in the downstream region can be significantly enhanced. In addition, the eddies or vortices generated downstream in the cold recirculation may be carried upstream by the reversed flow and move into the heated buoyant flow region where the process is dominated by natural convection, as shown in Fig. 4(*e*). The current experiments show that the channel flow is highly unsteady, three dimensional, and becomes turbulent in the region which the reversed flow traverses. However, in the upstream region where the reversed flow does not reach, the flow is steady and laminar. No oscillation of flow is observed in the upstream region.

3.2 Temperature Fluctuations. A K type thermocouple

Downloaded 13 Dec 2010 to 193.140.21.150. Redistribution subject to ASME license or copyright; see http://www.asme.org/terms/Terms_Use.cfm

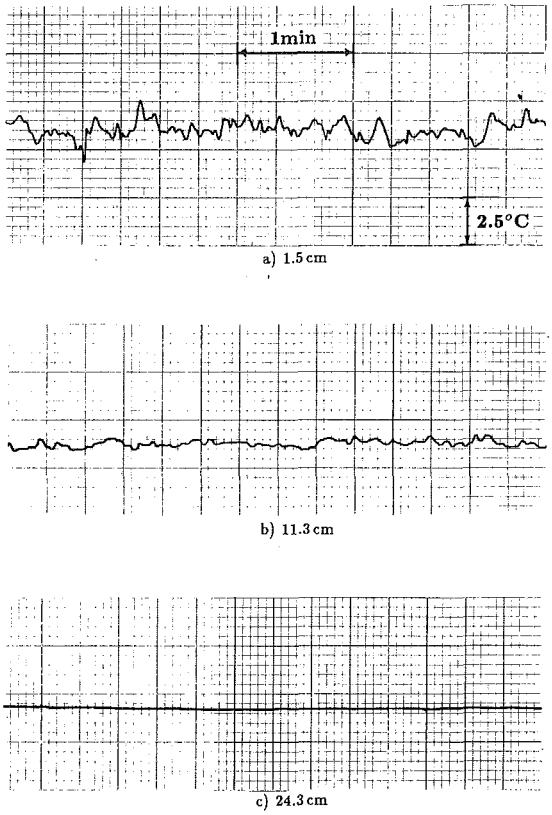

Fig. 6 Temperature fluctuations at Re = 400, $Gr/Re^2 = 210$ for the thermocouple located at (*a*) 1.5 cm, (*b*) 11.3 cm, and (*c*) 24.3 cm from the channel exit

probe having wire diameter of 0.1 mm is inserted into the center of the channel gap at different locations along the vertical wall. No temperature fluctuation is found for $Gr/Re^2 < 80$ and Re = 650. For $Gr/Re^2 = 90$ and Re = 610, small temperature fluctuations occur but only for the thermocouple located at 1.5 cm from from the channel exit. In the upstream region, temperature fluctuation is not found. With the increase of Gr/Re^2, temperature fluctuations become significant, as shown in Fig. 6. Concurrently, oscillation of temperature also is picked up by the thermocouple located at 11.3 cm, which is within the region of reversed flow. The oscillation at the latter location, however, is at a lower frequency. In the upstream region ahead of the V-shaped recirculation flow, no oscillation in temperature is found. It appears that the occurrence of temperature fluctuation is attributable to the oscillation of the interface between the heated buoyant flow and the V-shaped recirculating flow. As the buoyancy parameter Gr/Re^2 increases further, relatively large amplitude and higher frequency temperature fluctuations set in, as shown in Fig. 7. The significant temperature dip is caused by the cold flow outside the channel moving into the channel. For the thermocouple located at 24.3 cm from the exit, which is still within the region of reversed flow, the amplitude of temperature fluctuation is greatly reduced. In the upstream region where the reversed flow does not reach, no temperature fluctuation is found. It would appear that as the value of Gr/Re^2 increases, the oscillation of the interface becomes more intense with a concomitant increase in both the amplitude and frequency of temperature fluctuations. As the V-shaped recirculation region extends upstream, so does the region of temperature fluctuation. Therefore, it can be concluded that the increase of Gr/Re^2 can induce the temperature fluctuation, while the increase of Re can suppress it.

3.3 Heat Transfer. To avoid the Reynolds number effect

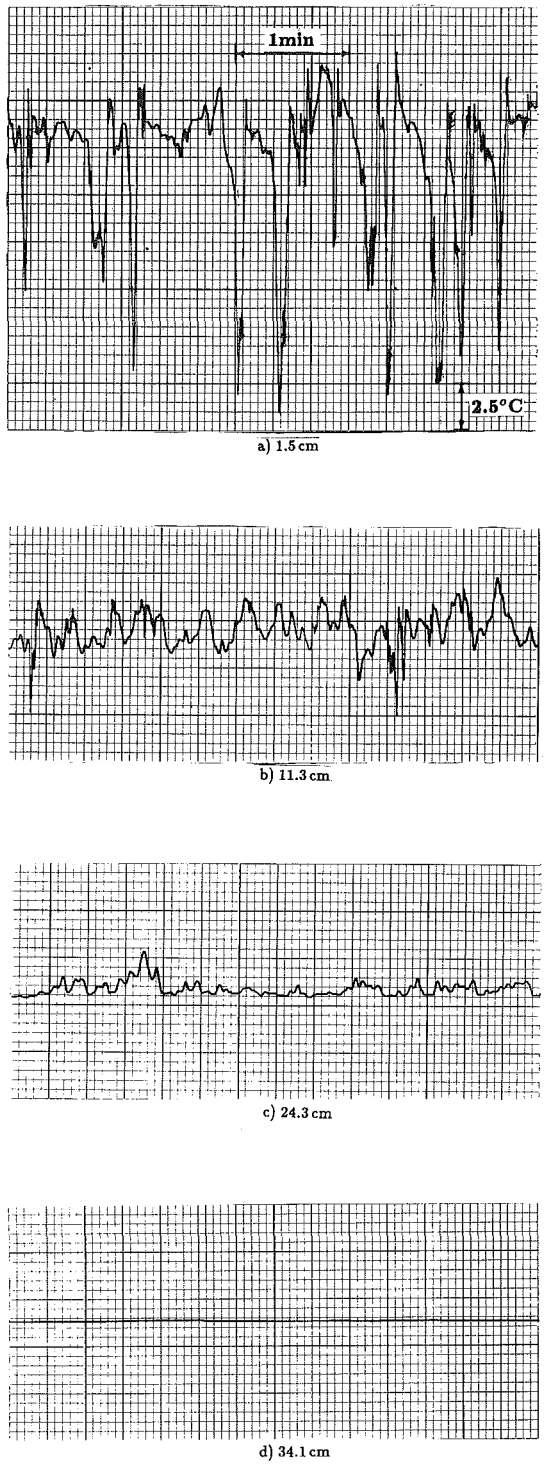

Fig. 7 Temperature fluctuations at Re = 171, $Gr/Re^2 = 1160$ for the thermocouple located at (*a*) 1.5 cm, (*b*) 11.3 cm, (*c*) 24.3 cm, and (*d*) 34.1 cm from the channel exit

on the local Nusselt number in the presentation, all the local Nusselt number results are normalized with $Re^{0.4}$. A single curve represents all the results for forced convection in the $Nu/Re^{0.4} \sim x/L$ plot, as shown in Fig. 8. When buoyancy becomes significant, the heat transfer parameter $Nu/Re^{0.4}$ increases with increasing Gr/Re^2. The results clearly indicate that buoyancy-assisted flow can enhance the heat transfer process. It is noted that in the region downstream of the separation point, the transport process is dominated by natural convection. Therefore, comparison is also made with the prediction

Downloaded 13 Dec 2010 to 193.140.21.150. Redistribution subject to ASME license or copyright; see http://www.asme.org/terms/Terms_Use.cfm

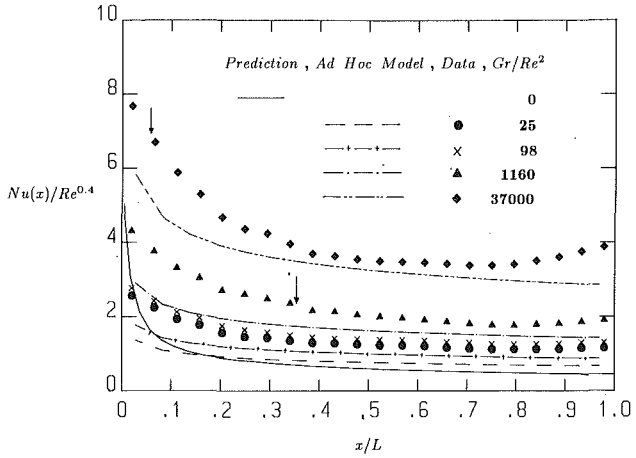

Fig. 8 Comparison of the local Nusselt number between the data and the prediction of an ad hoc model

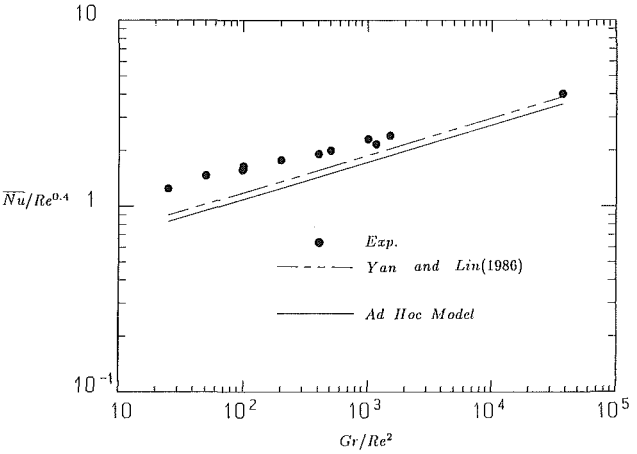

Fig. 9 Comparison of the average Nusselt number between the data and the prediction of an ad hoc model

of an ad hoc model for mixed convection. The heat transfer coefficient of the ad hoc model is simply that of a pure natural convection along a single heated vertical plate. One assumes that adding one additional vertical plate that is well insulated near the heated wall to form a channel does not significantly affect the vertical flat plate heat transfer. This assumption will be confirmed in a later presentation of average Nusselt number along the heated wall. Natural convection occurring inside a channel can drive air flow entering from the outside, and this air flow can enter the channel from both the entrance and the exit location when flow reversal occurs. One can thus purposely adjust and let the air flow entering the channel at the entrance location be the same as that for mixed convection. Therefore, the Reynolds number used in the calculation of buoyancy parameter Gr/Re^2 for the ad hoc model in each case corresponds to the one for the mixed convection experiment. It is expected, therefore, that the ad hoc model should give an accurate prediction of the heat transfer coefficient for the mixed convection in the region downstream of the separation point. The arrows in the figure indicate the occurrence of flow separation. For the cases when the V-shaped recirculation flow occurs, the data indeed approach the prediction of the ad hoc model in the region immediately downstream of the separation point where the process is dominated by natural convection. However, the local Nusselt number in the region close to the channel exit does not decrease with distance as would be the case for natural convection; instead, the heat transfer increases as the flow moves downstream toward the exit. Since all possible heat losses have been accounted for as described previously, it is concluded that the reversed flow is contributing to the increase of the local Nusselt number near the channel exit. In addition, the occurrence of the V-shaped recirculation flow makes the entire flow in the downstream region unstable with the attendant generation of eddies and vortices, and thus to enhance the heat transfer.

The average heat transfer coefficient over the entire heated plate is calculated by dividing the average heat flux by the mean temperature difference between the heated plate and the entrance air. The average Nusselt number, which is defined as $\bar{h}D_h/k_f$, is also normalized with $Re^{0.4}$ and the results are presented in Fig. 9. The average Nusselt number also increases with increasing Gr/Re^2 and becomes significantly different from the one for pure forced convection. For the purpose of comparison, the average Nusselt number correlation for the ad hoc model, which is simply the analytical results of a natural convection heat transfer along a vertical plate (Sparrow, 1955) divided by $Re^{0.4}$, can be written in terms of the nondimensional parameters defined in this report as follows:

$$\overline{Nu}/Re^{0.4} = 0.434(Gr/Re^2)^{0.2} \tag{2}$$

which is also presented in Fig. 9. In addition, the correlation obtained from numerical calculation of natural convection heat transfer in a finite vertical channel (Yan and Lin, 1986) is adopted, which is divided again by $Re^{0.4}$, and the result can be written as follows:

$$\overline{Nu}/Re^{0.4} = 0.476(Gr/Re^2)^{0.2} \tag{3}$$

However, Eq. (3) is valid only when $Gr < 10^3$ and flow reversal does not occur. In spite of this fact, the average Nusselt number correlations from both Eqs. (2) and (3) are very close, which confirms our earlier assumption that the insulated wall of the channel does not have a significant effect on the natural convection heat transfer along a vertical plate. It appears that the flat plate heat transfer equation can be used to predict the heat transfer inside a vertical channel with a sufficient accuracy. Figure 9 indicates that the agreement between the data and both the predictions is closer when the buoyancy parameter is large and the transport process in the channel is largely dominated by natural convection. However, the data are still higher due to the occurrence of the V-shaped recirculation flow.

3.4 Model Prediction for the Penetration Depth. The penetration depth for the reversed flow can be analyzed by means of a simple theoretical model. To simplify the analysis, the mixed convection process in the heated vertical channel is assumed to be steady and two dimensional. In addition, the Boussinesq approximation is employed. It should be noted that the bottom point of the V-shaped recirculation flow is the point of flow separation beyond or downstream of which the transport process is dominated by natural convection. This is the point where all the air flow generated by the blower is used completely to furnish the air required for the occurrence of pure natural convection flow in the downstream region of the channel. In addition, the flow and transport process in the entire channel is in the developing region. The heat transfer data in the region downstream of the separation point agree satisfactorily with the prediction of the ad hoc model. Therefore, the natural convection process in the channel at and beyond the separation point can be viewed as natural convection along a single heated vertical plate which starts developing from the entrance of the channel. Accordingly, the following equation can be written and used to predict the penetration depth,

$$u_o b = \int_o^\delta u dy \,|_{\text{at separation point}} \tag{4}$$

where u is the boundary layer velocity distribution of a natural

Downloaded 13 Dec 2010 to 193.140.21.150. Redistribution subject to ASME license or copyright; see http://www.asme.org/terms/Terms_Use.cfm

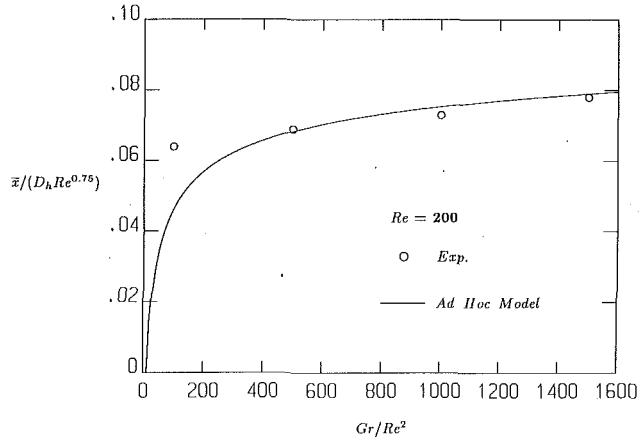

Fig. 10(*a*) Comparison of measured and predicted penetration depth at Re = 200

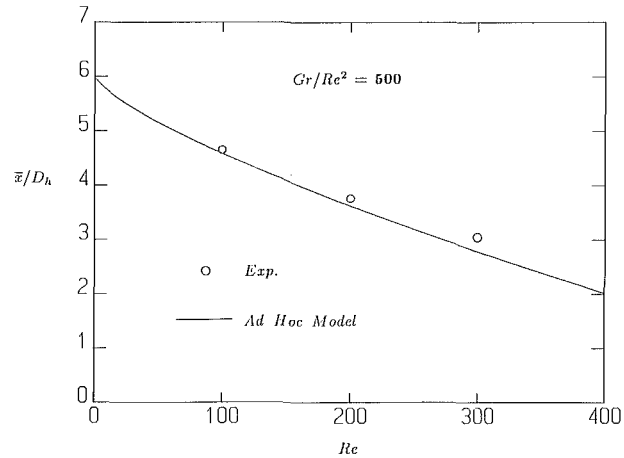

Fig. 10(*b*) Comparison of measured and predicted penetration depth at $Gr/Re^2 = 500$

convection flow along a vertical flat plate. By using the integral method and assuming third order polynomials for the velocity and the temperature distributions, the coupled momentum and energy equations for natural convection along a vertical plate can be readily solved (Sparrow, 1955). The velocity distribution obtained is as follows:

$$u = u_r \eta (1-\eta)^2 \tag{5}$$

where

$$u_r = (\nu/x)[6000 Gr_x^2/Pr(Pr+0.8)^2]^{1/5},$$

$$\eta = y/\delta$$

and

$$\delta = x[360(Pr+0.8)/Pr^2 Gr_x]^{1/5}.$$

By substituting Eq. (5) into Eq. (4), the separation point can be easily obtained as follows:

$$x/D_h = C(Re^5/Gr)^{1/4} \tag{6}$$

where

$$C = [36Pr^3(Pr+0.8)/10^4]^{1/4}$$

Rearranging Eq. (6), the penetration depth can be obtained as follows:

$$\bar{x}/(D_h Re^{0.75}) = L/(D_h Re^{0.75}) - C(Gr/Re^2)^{-0.25} \tag{7}$$

which can be plotted as shown in Figs. 10 and 11.

Since the model can be used only for the case when Gr/Re^2 is large and natural convection dominates the transport process, one needs to determine the regime for Re and Gr/Re^2

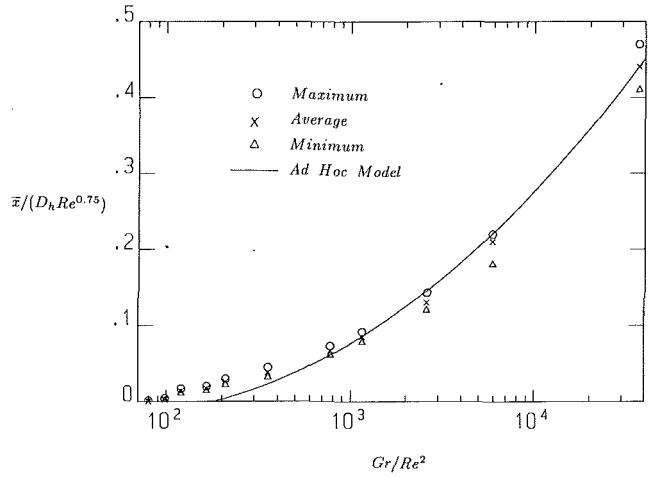

Fig. 11 Comparison of measured and predicted penetration depth for $40 < Re < 1200$, $80 < Gr/Re^2 < 37{,}000$

where the model can be used satisfactorily. Comparison of the penetration depth of the reversed flow between data and model prediction is made for Re = 200 at various Gr/Re^2, as shown in Fig. 10(*a*). However, in the experiment, the V-shaped recirculation flow is not steady and the penetration depth oscillates up and down. Therefore, only the average value of the penetration depth is used and presented for comparison. The discrepancy becomes large when Gr/Re^2 is small. This fact suggests that the model fails to predict the penetration depth as the buoyancy force inside the channel is relatively weak as compared with the inertia force. Comparison between data and prediction is made for $Gr/Re^2 = 500$ at various Re as shown in Fig. 10(*b*). As the Reynolds number increases and forced convection effect becomes significant, the model cannot accurately predict the penetration depth. It is found that for model prediction within 10 percent of the data, the range for Re used in the model should be less than 300 and Gr/Re^2 greater than 350. Comparison between data and the prediction for $40 < Re < 1200$ and $80 < Gr/Re^2 < 37{,}000$ is shown in Fig. 11. In addition, both the minimum and the maximum penetration depths are also measured and presented in the figure for the purpose of comparison. The deviation among the minimum, the average, and the maximum penetration depths increases when the value of Gr/Re^2 is large. However, the model can accurately predict the average penetration depth. At lower values of Gr/Re^2 and higher Re where channel flow is dominated by forced convection, the model underpredicts it.

4 Conclusions

Assisted convection flow with flow reversal has been visualized experimentally where the basic forced flow is directed vertically upward in a one-side-heated vertical channel. The reversed flow forms a V-shaped recirculating flow along the insulated wall, and occurs initially in the downstream region, but extends gradually upstream (downward) when the value of Gr/Re^2 increases. However, the increase of Re has the effect of pushing the reversed flow downstream and make the recirculating region wider. The counterflow motion and the mixing of the heated buoyant flow with the V-shaped recirculating flow renders the flow highly unstable and leads to generation of eddies and vortices, and fluctuations of temperature. In the region upstream of the reversed flow, the motion is steady, and no oscillation of temperature is found. The penetration depth of the V-shaped recirculation flow is measured and compared with the prediction based on a simple model. This model can accurately predict the penetration depth when the transport process inside the channel is largely dominated by natural convection.

Downloaded 13 Dec 2010 to 193.140.21.150. Redistribution subject to ASME license or copyright; see http://www.asme.org/terms/Terms_Use.cfm

Both local and average Nusselt numbers are measured and compared with the prediction for both the case of pure forced convection inside the channel and mixed convection using an ad hoc model. The buoyancy-assisted flow can significantly enhance the heat transfer. The Nusselt number results approach the prediction of the ad hoc model when the buoyancy parameter Gr/Re^2 is large. The local Nusselt number results indicate that the occurrence of the V-shaped recirculation can enhance the heat transfer process in the region close to the channel exit.

References

Aung, W., and Worku, G., 1986a, "Developing Flow and Flow Reversal in a Vertical Channel With Asymmetric Wall Temperatures," ASME JOURNAL OF HEAT TRANSFER, Vol. 108, pp. 299–304.

Aung, W., and Worku, G., 1986b, "Theory of Fully Developed, Combined Convection Including Flow Reversal," ASME JOURNAL OF HEAT TRANSFER, Vol. 108, pp. 485–488.

Aung, W., and Worku, G., 1987, "Mixed Convection in Ducts With Asymmetric Wall Heat Fluxes," ASME JOURNAL OF HEAT TRANSFER, Vol. 109, pp. 947–951.

Brown, C. K., and Gauvin, W. H., 1965, "Combined Free and Forced Convection, I. Heat Transfer in Aiding Flow," *The Canadian Journal of Chemical Engineering*, pp. 306–312.

Chang, T. S., and Lin, T. F., 1990, "On the Reversed Flow and Oscillating Wake in an Asymmetrically Heated Channel," *International Journal for Numerical Methods in Fluids*, Vol. 10, pp. 443–459.

Chen, T. L., and Miau, J. J., 1987, "The Making and Application for a Hot-Film Calibration," *Proceedings of 4th National Conference on Mechanical Engineering*, CSME, pp. 147–152.

Chow, L. C., Husain, S. R., and Campo, A., 1984, "Effects of Free Convection and Axial Conduction on Forced Convection Heat Transfer Inside a Vertical Channel at Low Peclet Numbers," ASME JOURNAL OF HEAT TRANSFER, Vol. 106, pp. 297–303.

Gau, C., Yih, K. A., and Aung, W., 1990, "Mixed Convection Heat Transfer in Vertically Heated Channels," AIAA Paper No. 90-1723.

Gau, C., Yih, K. A., and Aung, W., 1992, "Measurements of Heat Transfer and Flow Structure in Heated Vertical Channels With Buoyancy Assisted and Opposed Flows," AIAA *Journal of Thermophysics and Heat Transfer*, in press.

Habchi, S., and Acharya, S., 1986, "Laminar Mixed Convection in a Symmetrically or Asymmetrically Heated Vertical Channel," *Numerical Heat Transfer*, Vol. 9, pp. 605–618.

Hanratty, T. J., Rosen, E. M., and Kabel, R. L., 1958, "Effect of Heat Transfer on Flow Field at Low Reynolds Number in Vertical Tubes," *Industrial and Engineering Chemistry*, Vol. 50, pp. 815–820.

Incropera, F. P., and Campbell, J. S., 1990, "Effect of Orientation on Solidification for Mixed-Convection Flow in a Rectangular Channel," *Experimental Heat Transfer*, Vol. 3, pp. 377–396.

Ingham, D. B., Keen, D. J., and Heggs, P. J., 1988a, "Two Dimensional Combined Convection in Vertical Parallel Plate Ducts, Including Situations of Flow Reversal," *International Journal for Numerical Methods in Engineering*, Vol. 26, pp. 1645–1664.

Ingham, D. B., Keen, D. J., and Heggs, P. J., 1988b, "Flows in Vertical Channels With Asymmetric Wall Temperatures and Including Situations Where Reverse Flows Occur," ASME JOURNAL OF HEAT TRANSFER, Vol. 110, pp. 910–917.

Ingham, D. B., Keen, D. J., Heggs, P. J., and Morton, B. R., 1990, "Recirculating Pipe Flows," *Journal of Fluid Mechanics*, Vol. 213, pp. 443–464.

Kline, S. J., and McClintock, F. A., 1953, "Describing Uncertainties in Single-Sample Experiments," *Mechanical Engineering*, Jan., pp. 3–12.

Morton, B. R., Ingham, D. B., Keen, D. J., and Heggs, P. J., 1989, "Recirculating Combined Convection in Laminar Pipe Flow," ASME JOURNAL OF HEAT TRANSFER, Vol. 111, pp. 106–113.

Quintiere, J., and Mueller, W. K., 1973, "An Analysis of Laminar Free and Forced Convection Between Parallel Plates," ASME JOURNAL OF HEAT TRANSFER, Vol. 95, pp. 53–59.

Rao, T. L. S., and Morris, W. D., 1967–68, "Superimposed Laminar Forced and Free Convection Between Vertical Parallel Plates When One Plate is Uniformly Heated and the Other is Thermally Insulated," *Proceedings of Institution of Mechanical Engineers*, Vol. 182, Part 3H, pp. 347–381.

Scheele, G. F., and Hanratty, T. J., 1962, "Effect of Natural Convection on Stability of Flow in a Vertical Pipe," *Journal of Fluid Mechanics*, Vol. 14, pp. 244–255.

Sherwin, K., and Wallis, J. D., 1971, "Combined Natural and Forced Laminar Convection for Upflow Through Heated Vertical Annuli," *Proceedings of Institution of Mechanical Engineers*, pp. c112–c118.

Sparrow, E. M., 1955, "Laminar Free Convection on a Vertical Plate With Prescribed Non-uniform Wall Heat Flux or Prescribed Non-uniform Temperature," NACA TN 3508.

Sparrow, E. M., Chrysler, G. M., and Azevedo, L. F., 1984, "Observed Flow Reversals and Measured-Predicted Nusselt Numbers for Natural Convection in a One-Sided Heated Vertical Channel," ASME JOURNAL OF HEAT TRANSFER, Vol. 106, pp. 325–332.

Tao, L. N., 1960, "On Combined Free and Forced Convection in Channels," ASME JOURNAL OF HEAT TRANSFER, Vol. 82, pp. 233–238.

Wirtz, R. A., and Mckinley, P., 1985, "Buoyancy Effects on Downward Laminar Convection Between Parallel Plates," *Fundamentals of Forced and Mixed Convection*, ASME HTD-Vol. 42, pp. 105–112.

Yan, W. M., and Lin, T. F., 1986, "Natural Convection Heat Transfer in Vertical Open Channel Flows With Discrete Heating," *Proceedings of 3rd National Conference on Mechanical Engineering*, CSME, pp. 157–167.

Yao, L. S., 1983, "Free and Forced Convection in the Entry Region of a Heated Vertical Channel," *International Journal of Heat and Mass Transfer*, Vol. 26, pp. 65–72.

Zeldin, B., and Schmidt, F. W., 1972, "Developing Flow With Combined Forced-Free Convection in an Isothermal Vertical Tube," ASME JOURNAL OF HEAT TRANSFER, Vol. 94, pp. 211–223.

Downloaded 13 Dec 2010 to 193.140.21.150. Redistribution subject to ASME license or copyright; see http://www.asme.org/terms/Terms_Use.cfm

Effects of Buoyancy on Laminar Flow in Curved Elliptic Ducts

Z. F. Dong

M. A. Ebadian
Mem. ASME.

Department of Mechanical Engineering,
Florida International University,
Miami, FL 33199

This paper numerically investigates the effects of buoyancy on fully developed laminar flow in a curved duct with an elliptic cross section. The flow of Newtonian fluids is assumed steady in terms of Boussinesq approximation. The curved elliptic duct is subjected to thermal boundary conditions of axially uniform heat flux and peripherally uniform wall temperature. The numerically generated boundary-fitted coordinate system is applied to discretize the solution domain of the elliptic duct, and the Navier–Stokes equations and the energy equation, including the curvature ratio, are solved by use of the control volume-based finite difference method. The solution covers a wide range of curvature ratios, and Dean and Grashof numbers. The results presented are displayed graphically and in tabular form to illustrate the buoyancy effect. It is further shown that buoyancy acts to increase both the Nusselt number and the friction factor and changes the distribution of the velocity and the temperature. The results for the curved circular duct with and without buoyancy are compared with the data available in the open literature for all cases. Also compared with the published data are the results of laminar flow in a curved elliptic duct, and very good agreement is obtained.

Introduction

The study of viscous flow in a curved duct constitutes a problem of fundamental interest in the field of fluid mechanics and heat transfer. It serves as a basis for understanding some of the important phenomena occurring in flow through turbomachinery blade passages, aircraft intake diffusers, and heat exchangers. Recently, the flow of blood through human arteries has also been modeled as flow through a curved passage. A characteristic of flow in a curved duct is the presence of cross-steam recirculation in the twin counterrotating vortices known as "secondary flow," which are generated by the action of centrifugal force on the primary flow. Literature on flow and heat transfer in curved pipes is very extensive due to its technical importance in the scientific community. Some of the literature surveys and reviews of pertinent works in this field are documented by Berger et al. (1983) and Shah and Joshi (1987). In contrast to the number of published papers dealing with flow and heat transfer in curved ducts in circular and rectangular cross sections, the works relating to flow and heat transfer in a curved elliptic duct are rather limited in spite of its significance to practical applications.

For flow through a curved pipe with an elliptic cross section, relevant work has been published by Thomas and Walters (1965), Srivastava (1980), and Takami and Sudou (1984). In these analyses, a secondary flow is investigated by using Dean's formulation (1927, 1928) in which either the simplified forms of the momentum and continuity equations have been used, or the boundary-layer approximation approach has been used. Topakoglu and Ebadian (1985, 1987) investigated flow in curved elliptic pipes using the double expansion method of Topakoglu (1967). Their results are limited by the finite number of calculated terms of expansion. Recently, Dong and Ebadian (1991) numerically investigated flow in the curved elliptic duct based on complete Navier–Stokes equations for the laminar region. However, heat transfer in the curved elliptic duct was not considered in the above-mentioned paper. When the fluid in the curved elliptic duct is heated, the flow will be greatly affected by the buoyancy force in addition to centrifugal force. Therefore, because of both centrifugal and buoyancy forces, the secondary flow existing in the cross section of the duct is enhanced and the friction factor and heat transfer coefficient are increased.

The objective of this work, therefore, is to present numerical results for both hydrodynamically and thermally fully developed laminar flow in a curved duct with an elliptic cross section by considering the effects of buoyancy. Variations in the gravitational force are due mainly to the differences in density, which cause the fluid elements to travel in a vertical direction rather than in a horizontal direction as induced by centrifugal force. The Boussinesq hypothesis has been used to approximate the buoyancy term in the momentum equations. The thermal boundary conditions concerned in this work are assumed to be a constant wall heat flux axially and a constant wall temperature peripherally. The solutions are obtained by solving the coupled Navier–Stokes equations with the energy equation in which the effects of the curvature ratio are included. The numerically generated boundary-fitted coordinate system is used to overcome the difficulties of discretizing the solution domain. The buoyancy effects reported here are for a combination of a relatively wide range of axial pressure gradients, Grashof numbers, and Dean numbers. It is found that the flow, including the flow due to buoyancy, is very different from pure forced convection. It is shown that as a result of buoyancy, the distributions of velocity and temperature in the curved elliptic duct have been altered. In addition, the asymmetry of the secondary flow in mixed convection leads to an increase of friction, consequently increasing the average heat transfer coefficient. On the other hand, the smaller curvature ratio of the curved elliptic duct and the larger axial pressure gradient can enhance the heat transfer coefficient at the wall.

Problem Formulation

Consideration is given to the steady, hydrodynamically and thermally fully developed laminar flow of viscous fluid in a curved elliptic duct. The curved elliptic duct is subjected to the thermal boundary conditions of axial uniform wall heat flux and peripheral uniform wall temperature. The buoyancy term is governed by Boussinesq approximation, and the other thermal properties of the fluids are considered to be constant. It is assumed that viscous dissipation is negligible.

The curved elliptic duct is shown in Fig. 1, in which the toroidal coordinate system is used. The elliptical cross section considered here has a semimajor axis, a, and a semiminor axis,

Contributed by the Heat Transfer Division for publication in the JOURNAL OF HEAT TRANSFER. Manuscript received by the Heat Transfer Division June 1991; revision received June 1992. Keywords: Augmentation and Enhancement, Mixed Convection, Numerical Methods. Associate Technical Editor: F. P. Incropera.

Copyright © 1992 by ASME
Downloaded 13 Dec 2010 to 193.140.21.150. Redistribution subject to ASME license or copyright; see http://www.asme.org/terms/Terms_Use.cfm

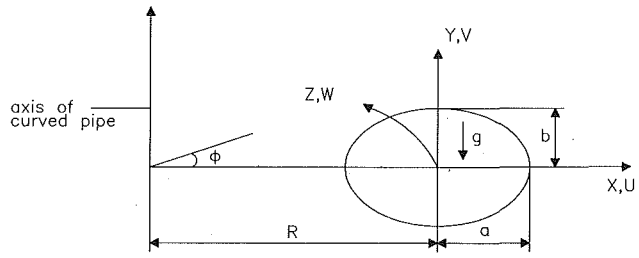

Fig. 1 Geometry and coordinates

b. The cross section is oriented in such a way that the major axis, X, is along the direction of the curvature of the curved duct, and the minor axis, Y, is along the direction of the axis of symmetry of the curved duct. Gravity is opposite to the Y direction. Therefore, the governing equations for the present problem are:

Continuity Equation:

$$\frac{\partial U}{\partial X}+\frac{\partial V}{\partial Y}+\frac{U}{R+X}=0 \tag{1}$$

Momentum Equation:

$$\rho\left(U\frac{\partial U}{\partial X}+V\frac{\partial U}{\partial Y}-\frac{W^2}{R+X}\right)=-\frac{\partial P}{\partial X}+\mu\left[\frac{\partial^2 U}{\partial X^2}+\frac{\partial^2 U}{\partial Y^2}+\frac{1}{R+X}\frac{\partial U}{\partial X}-\frac{U}{(R+X)^2}\right] \tag{2}$$

$$\rho\left(U\frac{\partial V}{\partial X}+V\frac{\partial V}{\partial Y}\right)=-\frac{\partial P}{\partial Y}-\rho g+\mu\left[\frac{\partial^2 V}{\partial X^2}+\frac{\partial^2 V}{\partial Y^2}+\frac{1}{R+X}\frac{\partial V}{\partial X}\right] \tag{3}$$

$$\rho\left(U\frac{\partial W}{\partial X}+V\frac{\partial W}{\partial Y}+\frac{UW}{R+X}\right)=-\frac{R}{(R+X)}\frac{\partial P}{\partial Z}+\mu\left[\frac{\partial^2 W}{\partial X^2}+\frac{\partial^2 W}{\partial Y^2}+\frac{1}{R+X}\frac{\partial W}{\partial X}-\frac{W}{(R+X)^2}\right] \tag{4}$$

Energy Equation:

$$\rho C_p\left[U\frac{\partial T}{\partial X}+V\frac{\partial T}{\partial Y}+W\frac{R}{R+X}\frac{\partial T}{\partial Z}\right]=k\left[\frac{\partial^2 T}{\partial X^2}+\frac{\partial^2 T}{\partial Y^2}+\frac{1}{R+X}\frac{\partial T}{\partial X}\right] \tag{5}$$

The buoyancy term, ρg, in Eq. (3) can be expressed as follows by Boussinesq approximation:

$$\rho g=\rho_{\text{ref}}[1-\beta(T-T_{\text{ref}})]g \tag{6}$$

where T_{ref} is a reference temperature, ρ_{ref} is the density of the fluid of the reference temperature, and β is the volumetric thermal expansion coefficient. Usually, the pressure at any point consists of two parts:

$$P=P_o(Z)+P'(X,\ Y). \tag{7}$$

Therefore, for fully developed flow, we have $dP/dZ=dP_o(Z)/dZ=\text{const}$, and $dP/dX=dP'/dX$, $dP/dY=dP'/dY$. P' is noted as P without prime for convenience in the following discussion. Substituting Eq. (6) into Eq. (3) and rewriting $(P+\rho_{\text{ref}}\ g\ Y)$ as P, Eq. (3) becomes:

$$\rho_{\text{ref}}\left(U\frac{\partial U}{\partial X}+V\frac{\partial V}{\partial Y}\right)=-\frac{\partial P}{\partial Y}+\rho_{\text{ref}}\beta g(T-T_{\text{ref}})+\mu\left[\frac{\partial^2 V}{\partial X^2}+\frac{\partial^2 V}{\partial Y^2}+\frac{1}{R+X}\frac{\partial V}{\partial X}\right] \tag{8}$$

Correspondingly, ρ in the other equations is replaced by ρ_{ref} according to the Boussinesq hypothesis.

By introducing the following dimensionless variables:

$$x=\frac{X}{D_h},\quad y=\frac{Y}{D_h},\quad z=\frac{Z}{D_h},\quad r=\frac{R}{D_h}$$

$$u=\frac{U}{\frac{\nu}{D_h}},\quad v=\frac{V}{\frac{\nu}{D_h}},\quad w=\frac{W}{\frac{\nu}{D_h}},\quad p=\frac{P}{\rho_{\text{ref}}\frac{\nu^2}{D_h^2}}$$

$$\theta=\frac{T_w-T}{\frac{\partial T}{\partial Z}D_h},\quad \text{Re}=\frac{W_m D_h}{\nu},\quad \text{De}=\text{Re}\ r^{-1/2}$$

$$\text{Gr}=\frac{g\beta\frac{\partial T}{\partial Z}D_h^4}{\nu^2},\quad \text{Pr}=\frac{\nu}{\alpha_T} \tag{9}$$

Nomenclature

a = semimajor axis of the curved elliptic duct, m
A = cross-sectional area of the curved elliptic duct, m^2
b = semiminor axis of the curved elliptic duct, m
C_p = specific heat, J kg^{-1} K^{-1}
De = Dean number = $\text{Re}(D_h/R)^{1/2}$
D_h = hydraulic diameter, m
f = friction factor
g = gravitational acceleration constant, m s^{-2}
Gr = Grashof number = $g\beta D_h^4(\partial T/\partial Z)/\nu^2$
h = heat transfer coefficient, W m^{-2} K^{-1}
$\bar{h}$ = average heat transfer coefficient, W m^{-2} K^{-1}
J = Jacobian transformation, Eq. (23)
k = thermal conductivity, W m^{-1} K^{-1}
Nu = Nusselt number = $h\ D_h/k$
P = pressure, Pa
Pr = Prandtl number = ν/α_T
p = dimensionless pressure = $P/(\rho_{\text{ref}}\nu^2/D_h^2)$
R = curvature radius of the duct centerline, m, Fig. 1
Re = Reynolds number = $D_h W_m/\nu = w_m$
r = dimensionless radius of the curvature = R/D_h
S = source term, Eq. (18)
T = temperature of fluid, K
$\overline{\left[\frac{\partial T}{\partial n}\right]_w}$ = dimensional wall temperature gradient average normal
$\overline{\left[\frac{\partial \theta}{\partial n}\right]_w}$ = dimensionless wall temperature gradient
T_w = wall temperature, K
U, V, W = dimensional velocity components in the X, Y, and Z directions, m s^{-1}
u, v, w = dimensionless velocity components = $(U, V, W)/(\nu/D_h)$
$\bar{U}$ = factor, Eq. (19)

Downloaded 13 Dec 2010 to 193.140.21.150. Redistribution subject to ASME license or copyright; see http://www.asme.org/terms/Terms_Use.cfm

the dimensionless governing equations can be obtained in the following form as:

$$\frac{\partial u}{\partial x}+\frac{\partial v}{\partial y}+\frac{u}{r+x}=0 \tag{10}$$

$$\frac{\partial(uu)}{\partial x}+\frac{\partial(uv)}{\partial y}-\frac{w^2}{r+x}=-\frac{\partial p}{\partial x}+\frac{\partial^2 u}{\partial x^2}+\frac{\partial^2 u}{\partial y^2}+\frac{1}{r+x}\frac{\partial u}{\partial x}-\frac{u}{(r+x)^2}-\frac{u^2}{r+x} \tag{11}$$

$$\frac{\partial(uv)}{\partial x}+\frac{\partial(vv)}{\partial y}=-\frac{\partial p}{\partial y}-\mathrm{Gr}\theta+\frac{\partial^2 v}{\partial x^2}+\frac{\partial^2 v}{\partial y^2}+\frac{1}{r+x}\frac{\partial v}{\partial x}-\frac{uv}{r+x} \tag{12}$$

$$\frac{\partial(uw)}{\partial x}+\frac{\partial(vw)}{\partial y}+\frac{uw}{r+x}=-\frac{r}{r+x}\frac{dp}{dz}+\frac{\partial^2 w}{\partial x^2}+\frac{\partial^2 w}{\partial y^2}+\frac{1}{r+x}\frac{\partial w}{\partial x}-\frac{w}{(r+x)^2}-\frac{uw}{r+x} \tag{13}$$

$$\frac{\partial(u\theta)}{\partial x}+\frac{\partial(v\theta)}{\partial y}=\frac{r}{r+x}w+\frac{1}{\mathrm{Pr}}\left[\frac{\partial^2\theta}{\partial x^2}+\frac{\partial\theta}{\partial y^2}+\frac{1}{r+x}\frac{\partial\theta}{\partial x}\right]-\frac{u\theta}{r+x} \tag{14}$$

In the present study, fluid flow is no longer symmetric about the x axis because of the buoyancy effects. Therefore, the entire flow area of the cross section must be used as a solution domain and the associated boundary conditions in dimensionless form are given as:

$$u=v=w=0 \quad \text{at the wall} \tag{15}$$

$$\theta=0 \quad \text{on the wall.} \tag{16}$$

Numerical Solution

Grid Generation. From a conceptual point of view, discretization of the solution domain for ellipse geometry in the Cartesian coordinate system, Fig. 1, is a difficult task. Therefore, a numerically generated boundary-fitted coordinate system is applied. Thus, the elliptic duct in the physical domain can be transformed into rectangular geometry in the computational domain. This is achieved by solving two coupled differential equations with two sets of coordinates (x, y) and (ξ, η) as suggested by Thompson et al. (1974) and Thomas and Middlecoff (1980). The resulting grid configurations in the physical and computational planes are shown in Figs. 2(*a*) and 2(*b*), respectively.

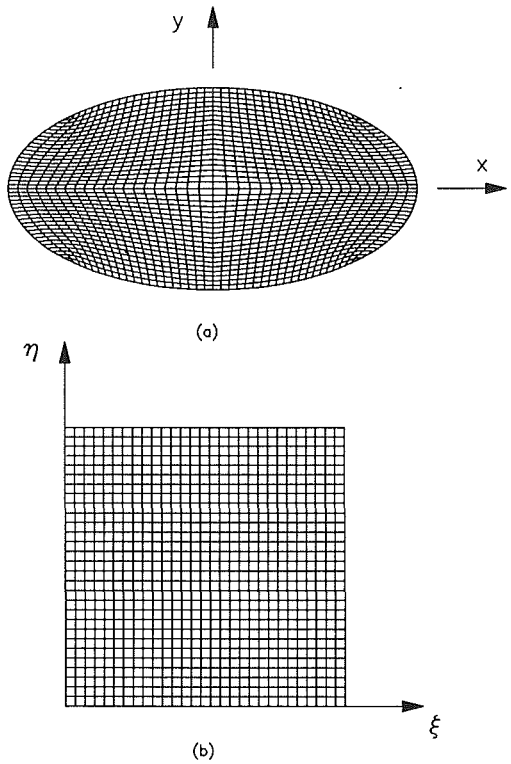

Fig. 2 Grid configuration: (*a*) physical domain; (*b*) computational domain

Transformation of the Governing Equations and the Method of Solution. Dimensionless governing Eqs. (10)–(14) can be expressed in the form of the following general conservation equation:

$$\frac{\partial(u\phi)}{\partial x}+\frac{\partial(v\phi)}{\partial y}=\frac{\partial}{\partial x}\left(\Gamma_\phi\frac{\partial\phi}{\partial x}\right)+\frac{\partial}{\partial y}\left[\Gamma_\phi\frac{\partial\phi}{\partial y}\right]+R_\phi(x, y). \tag{17}$$

For the general dependent variables, $\phi=1, u, v, w, \theta$, Eq. (17) refers to the continuity equation, the momentum equations in

Nomenclature (cont.)

$\overline{V}$ = factor, Eq. (19)
W_m = dimensional average axial velocity, m s^{-1}
w_m = dimensionless average axial velocity
X, Y = dimensional transversal coordinates, Figs. 1 and 2(*a*)
x, y = dimensionless transversal coordinates = $(X, Y)/D_h$
Z = dimensional axial coordinate, Fig. 1
z = dimensionless axial coordinate
α = coefficient, Eq. (20)
α^* = minor-axis to major-axis ratio of the elliptic duct = $2b/2a$
α_T = thermal diffusivity, m^2 s^{-1}
β = coefficient, Eq. (21); coefficient of volumetric expansion, K^{-1}
γ = coefficient, Eq. (22)
γ_c/γ_s = friction coefficient ratio, Fig. 4
Γ = coefficient, Eq. (18)
θ = dimensionless temperature = $(T_w-T)/(\partial T/\partial Z)\,D_h$
θ_b = dimensionless bulk temperature = $\int_A\theta w dA/\int_A w dA$
κ = modified Dean number = $2\mathrm{Re}(a/R)^{-1}$, Fig. 4
μ = dynamic viscosity, kg m^{-2} s^{-1}
ν = kinematic viscosity, m^2 s^{-1}
ξ, η = transversal coordinate in the computational plane, Fig. 2(*b*)
ρ = density, kg m^{-3}
ϕ = general dependent variable

Subscripts

c, s = values for curved and straight ducts, respectively
i, j = space subscripts of a grid point
ref = reference
w = wall

Downloaded 13 Dec 2010 to 193.140.21.150. Redistribution subject to ASME license or copyright; see http://www.asme.org/terms/Terms_Use.cfm

Table 1 Variables in the conservation equations

Equation	ϕ	Γ_ϕ	S_ϕ
Continuity	1	0	$-\frac{u}{r+x}$
u-momentum	u	1	$-\frac{1}{J}\left(\frac{\partial p}{\partial \xi}\frac{\partial y}{\partial \eta}-\frac{\partial p}{\partial \eta}\frac{\partial y}{\partial \xi}\right)+\frac{1}{r+x}\frac{1}{J}\left(\frac{\partial u}{\partial \xi}\frac{\partial y}{\partial \eta}-\frac{\partial u}{\partial \eta}\frac{\partial y}{\partial \xi}\right)-\frac{u}{(r+x)^2}+\frac{w^2}{r+x}-\frac{u^2}{r+x}$
v-momentum	v	1	$-\frac{1}{J}\left(-\frac{\partial p}{\partial \xi}\frac{\partial x}{\partial \eta}+\frac{\partial p}{\partial \eta}\frac{\partial x}{\partial \xi}\right)+\frac{1}{r+x}\frac{1}{J}\left(\frac{\partial v}{\partial \xi}\frac{\partial y}{\partial \eta}-\frac{\partial v}{\partial \eta}\frac{\partial y}{\partial \xi}\right)-\frac{uv}{(r+x)}-Gr\theta$
w-momentum	w	1	$-\frac{r}{r+x}\frac{\partial p}{\partial z}+\frac{1}{r+x}\frac{1}{J}\left(\frac{\partial w}{\partial \xi}\frac{\partial y}{\partial \eta}-\frac{\partial w}{\partial \eta}\frac{\partial y}{\partial \xi}\right)-\frac{w}{(r+x)^2}-\frac{2uw}{r+x}$
Energy	θ	$\frac{1}{Pr}$	$\frac{r}{r+x}w+\frac{1}{r+x}\frac{1}{J}\left[\frac{\partial \theta}{\partial \xi}\frac{\partial y}{\partial \eta}-\frac{\partial \theta}{\partial \eta}\frac{\partial y}{\partial \xi}\right]\frac{1}{Pr}-\frac{u\theta}{r+x}$

the x, y, z directions, and the energy equation, respectively. After some mathematical transformation, the corresponding equation in the computational plane of the general equation, Eq. (17), is written as:

$$\frac{\partial}{\partial \xi}(\overline{U}\phi)+\frac{\partial}{\partial \eta}(\overline{V}\phi)=\frac{\partial}{\partial \xi}\left[\frac{\Gamma_\phi}{J}\left(\alpha\frac{\partial \phi}{\partial \xi}-\beta\frac{\partial \phi}{\partial \eta}\right)\right]+\frac{\partial}{\partial \eta}\left[\frac{\Gamma_\phi}{J}\left(-\beta\frac{\partial \phi}{\partial \xi}+\gamma\frac{\partial \phi}{\partial \eta}\right)\right]+JS_\phi(\xi,\eta), \quad (18)$$

where $\overline{U}$ and $\overline{V}$ are defined as:

$$\overline{U}=u\frac{\partial y}{\partial \eta}-v\frac{\partial x}{\partial \eta}, \quad \overline{V}=v\frac{\partial x}{\partial \xi}-u\frac{\partial y}{\partial \xi}, \quad (19)$$

and

$$\alpha=\left(\frac{\partial x}{\partial \eta}\right)^2+\left(\frac{\partial y}{\partial \eta}\right)^2, \quad (20)$$

$$\beta=\frac{\partial x}{\partial \xi}\frac{\partial x}{\partial \eta}+\frac{\partial y}{\partial \xi}\frac{\partial y}{\partial \eta}, \quad (21)$$

$$\gamma=\left(\frac{\partial x}{\partial \xi}\right)^2+\left(\frac{\partial y}{\partial \xi}\right)^2, \quad (22)$$

$$J=\frac{\partial x}{\partial \xi}\frac{\partial y}{\partial \eta}-\frac{\partial x}{\partial \eta}\frac{\partial y}{\partial \xi}. \quad (23)$$

The general dependent variable, ϕ, the diffusion coefficient, Γ_ϕ, and the source term, S_ϕ, in the (ξ, η) coordinate system, are defined in Table 1 for each conservation equation.

In addition, the boundary condition for Eq. (18) is expressed as:

$$\phi=0 \quad \text{on the wall.} \quad (24)$$

The governing equation, Eq. (18), along with the boundary condition, Eq. (24), is approximated with finite difference equations by a control volume-based finite difference method for the dependent variables, u, v, w, and θ. The convection-diffusion terms are discretized by a power-law scheme (Patankar, 1980). A staggered grid system is employed for the velocity components, u and v, as well as $\overline{U}$ and $\overline{V}$, and solutions are obtained by an iterative scheme, which is a modified SIMPLE algorithm in the boundary-fitted coordinate system (Shyy et al., 1985). A brief description of the main steps of this numerical procedure follows.

For a given minor-axis to major-axis ratio, α^*, the curvature ratio, r, the axial pressure gradient, dp/dz, the Grashof number, Gr, and the Prandtl number, Pr, distributions of the velocity components, u, v, w, and distributions of the pressure and the temperature are initially guessed. The momentum equations for u and v are then solved to obtain new velocity distributions for u and v. Generally, this transverse velocity field, with the initially guessed pressure field, cannot satisfy the continuity equation. Thus, the pressure correction equation is solved and then u, v, and p are corrected accordingly. Furthermore, $\overline{U}$ and $\overline{V}$ are updated and the momentum equation for w and the energy equation are solved based on the corrected transversal velocity fields and the pressure field. Thus, one iteration cycle is completed. The iteration is repeated until the following convergence criterion is satisfied for all nodes:

$$\frac{\|\phi_{ij}^{k+1}-\phi_{ij}^{k}\|_\infty}{\|\phi_{ij}^{k+1}\|_\infty}\le 10^{-4}, \quad (25)$$

where ϕ refers to u, v, w, and θ. The subscript i, j represents the ξ, η coordinate, and the superscript k represents the kth iteration. It is necessary to use underrelaxation factors for the variables u, v, w, p, and θ, to reach a convergent solution. The existence of the buoyancy term and the nonorthogonality of the grids leads to using smaller underrelaxation factors in the calculation. The greater the Dean number or Grashof number, the smaller the relaxation number. The relaxation factors ranging from 0.15 to 0.3 have been used according to different computational cases.

Results and Discussion

Flow and Heat Transfer Characteristics. In this paper, the expression for the product of the friction factor and the Reynolds number, fRe, is obtained by considering the overall force balance for the differential axial length. fRe is given by the following formula (Cheng et al., 1976):

$$f\mathrm{Re}=-\frac{dp}{dz}\Big/2\,w_m. \quad (26)$$

The Nusselt number is defined by:

$$\mathrm{Nu}=\frac{\overline{h}\,D_h}{k}, \quad (27)$$

where $\overline{h}$ is the average Nusselt number on the boundary and can be obtained by:

$$\overline{h}=\frac{-k\overline{\left[\frac{\partial T}{\partial n}\right]_w}}{T_w-T_b}. \quad (28)$$

Substituting Eq. (28) into Eq. (27) and using the dimensionless variable, the result is:

$$\mathrm{Nu}=\frac{1}{\theta_b}\overline{\left[\frac{\partial \theta}{\partial n}\right]_w} \quad (29)$$

where $\overline{\left[\frac{\partial \theta}{\partial n}\right]_w}$, is the average dimensionless temperature gradient on the boundary.

Downloaded 13 Dec 2010 to 193.140.21.150. Redistribution subject to ASME license or copyright; see http://www.asme.org/terms/Terms_Use.cfm

Table 2 Independent grid size experiment ($Gr = 10^4$)

$\frac{dp}{dz}$	r	Pr	Grid	f_c/f_s	Nu
-8×10^4	10.	1	30x30	2.23	14.12
-8×10^4	10.	1	60x60	2.19	13.76
-8×10^4	10.	1	80x80	2.17	13.62
-2.5×10^4	10.	0.7	30x30	1.68	8.84
-2.5×10^4	10.	0.7	60x60	1.64	8.62
-2.5×10^4	10.	0.7	80x80	1.63	8.54
-8×10^4	100	5	60x60	1.74	22.79
-8×10^4	100	5	80x80	1.75	22.68

Table 3 Comparison of the results with those of Kalb and Seader (1972) ($Gr = 0.0$)

De	Pr	Nu		Deviation (%)
		Present Results	Kalb and Seader (1972)	
96.4	0.7	6.50	6.34	2.46
128.2	5	11.35	10.76	5.20
158.5	0.7	7.95	8.03	1.05
158.3	1	8.85	8.62	2.60
359.3	0.7	11.51	11.86	3.00

Numerical experiments have been conducted to choose independent grids. As shown in Table 2, the three grids of 30×30, 60×60, and 80×80 are used to calculate flow and heat transfer in the curved elliptic duct. It is indicated that the values of f_c/f_s and Nu obtained from the 60×60 grids deviated by less than 1 percent as compared with the corresponding values of f_c/f_s and Nu from the finer 80×80 grid. The CPU time required by the 60×60 grid is much less than that of the finer 80×80 grid. From the viewpoint of compromising computational time and numerical accuracy, the 60×60 gird is employed in most cases. The finer grid is used only for the cases with larger Grashof and Prandtl numbers. On the other hand, the present solution is tested for accuracy by solving the forced convection in the circular pipe and in the elliptic ducts for which published results are available. The results of convection without buoyancy in a circular pipe are compared with those of Kalb and Seader (1972), as shown in Table 3. The data of Kalb and Seader in that table are obtained from Eq. (23) in their paper. The discrepancy between the present results and the Kalb and Seader results is less than 6 percent. However, Eq. (23), provided by Kalb and Seader, has a standard deviation of 2.3 percent and a maximum deviation of 5 percent. The results of the reduction of the flow rate in the curved elliptic duct without buoyancy have been compared with those by Topakoglu and Ebadian (1985, 1987) in which the double expansion method is used to obtain an analytical solution. The dots shown in Fig. 3 are the result of the present computation and the solid line is the result by Topakoglu and Ebadian (1987). The nomenclature in Fig. 3 is identical to that used by Topakoglu and Ebadian (1987). According to this figure, Re is defined based on the flow rate in a straight pipe, and λ is the curvature defined as a/R. Q and Q_o are the flow rate in the curved duct and straight pipe, respectively. Inspection of this figure indicates good agreement between the present computation and the published analytical solution. Furthermore, flow in the curved circular duct with the buoyancy effect is numerically calculated by the present program for purposes of comparison with the results of Prusa and Yao (1982). This is shown in Fig. 4, and for the sake of comparison, the same definitions in Prusa and Yao (1982) are used in the calculation. γ_c/γ_s in Fig. 4 is the friction factor ratio between the curved circular duct and the straight circular duct. κ is defined as $2\,\mathrm{Re}(a/R)^{1/2}$. Here, the dots in Fig. 4 indicate the results obtained by the present method for the corresponding case of $\mathrm{Re}\cdot\mathrm{Ra} = 20{,}000$.

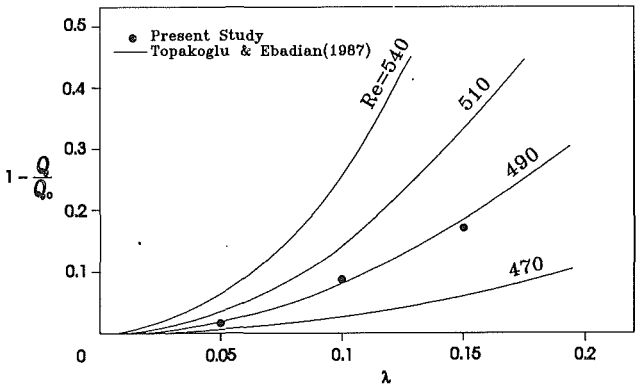

Fig. 3 Comparison of flow rate reduction with Topakoglu and Ebadian (1987)

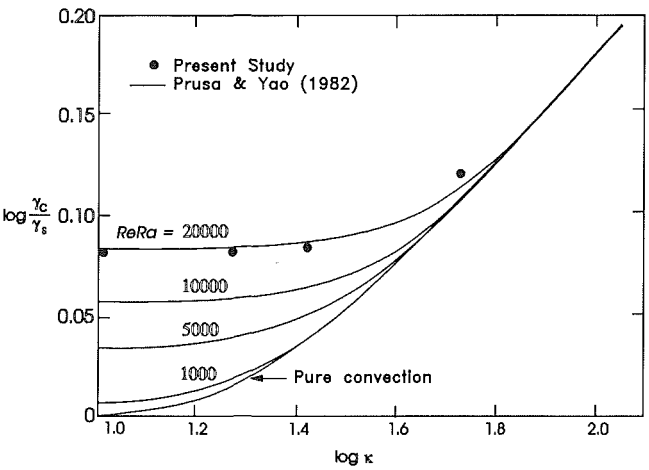

Fig. 4 Comparison of the friction factor ratio with Prusa and Yao (1982)

Inspection of this figure reveals very close agreement between the two studies at a low value of κ (low Dean number values), and a small deviation can be found in the case of a larger Dean number. The difference is due mainly to the fact that a different numerical scheme and different convergent criteria are used.

Effects of the Grashof Number. Figures 5(a) and 5(b) show how the Grashof number affects distribution of the axial velocity and the temperature on the major and minor axes of the curved elliptic duct for the cases of $dp/dz = -8\times10^4$, $r = 10$, $\mathrm{Pr} = 1$, $\alpha^* = 0.5$. It is shown that with a smaller Gr, velocity and temperature distributions are similar to the distributions of pure forced convection in the curved duct where there is a maximum velocity and temperature near the outer wall on the major axis, and velocity and temperature distributions on the minor axis are symmetric to the major axis. When the Grashof number increases, both the velocity and temperature distributions on the major axis have a second peak value near the inner wall of the duct. This is attributed to the buoyancy force, which induces considerable secondary flow in the cross section of the duct. When secondary flow due to buoyancy is larger than secondary flow due to centrifugal force, velocity and temperature distributions on the major axis tend to be symmetric to the minor axis. When secondary flow due to centrifugal force is greater than secondary flow due to buoyancy, velocity and temperature distributions on the minor axis tend to be symmetric to the major axis.

Figure 6(a) illustrates the effects of buoyancy on the secondary flow in the cross-sectional plane perpendicular to the axial flow direction of the curved elliptic duct, while Fig. 6(b) shows the corresponding secondary flow without natural convection due to buoyancy. These are obtained in the cases of $\alpha^* = 0.5$, $dp/dz = -8\times10^4$, $r = 10$, $\mathrm{Pr} = 1$, and $\mathrm{Gr} = 10^4$, Fig.

Downloaded 13 Dec 2010 to 193.140.21.150. Redistribution subject to ASME license or copyright; see http://www.asme.org/terms/Terms_Use.cfm

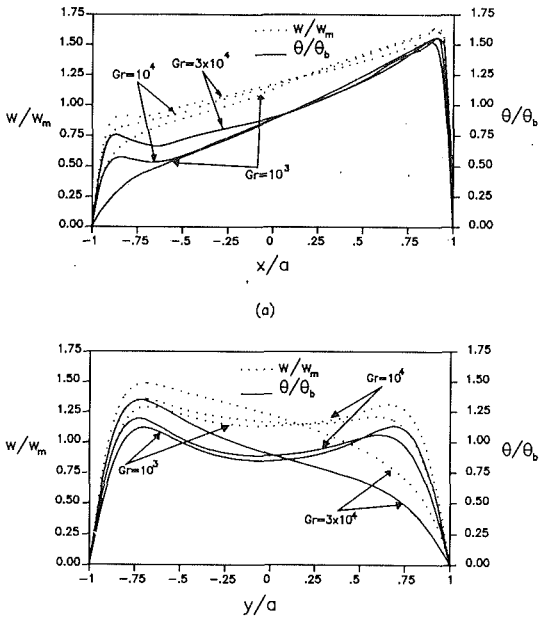

Fig. 5 The effects of Gr on distributions of axial velocity and temperature ($dp/dz = -8 \times 10^4$, $r = 10$, $\Pr = 1$, $\alpha^* = 0.5$): (*a*) on the major axis of ellipse; (*b*) on the minor axis of ellipse

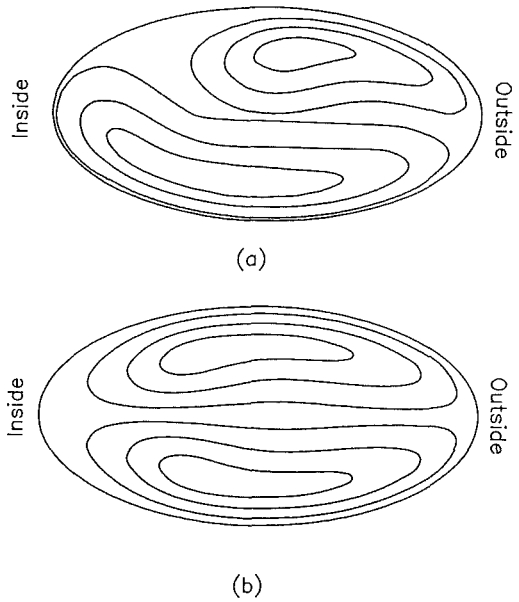

Fig. 6 Secondary flow pattern ($dp/dz = -8 \times 10^4$, $r = 10$, $\Pr = 1$, $\alpha^* = 0.5$): (*a*) with buoyancy influence ($Gr = 10^4$); (*b*) without buoyancy influence ($Gr = 0$)

$6(a)$ or $Gr = 0$, Fig. $6(b)$. By comparing these two figures, it is found that the symmetric construction of the two vortices in the forced convection is altered by the buoyancy flow. The two vortices rotate clockwise. The center of the upper vortex shifts toward the outside boundary, and the center of the bottom vortex shifts to the inside boundary. This is because the buoyancy force induces the secondary flow in a vertical direction, while centrifugal force leads to a horizontal flow. Therefore, the existence of buoyancy disturbs the symmetry structure of the secondary flow due to centrifugal force, as seen in Fig. $6(b)$. The resulting vortices are shown in Fig. $6(a)$. Also, the buoyancy effect on the temperature field can be seen in Figs. $7(a)$ and $7(b)$. Figure $7(a)$ illustrates the isotherms of θ/θ_b for the secondary flow induced by both centrifugal force and buoyancy force. Figure $7(b)$ shows the

Table 4 Results for variations of Gr; parameters: $dp/dz = -8 \times 10^4$, $r = 10$, $\Pr = 1$, $\alpha^* = 0.5$

Gr	De	fRe	Nu	f_c/f_s	Nu/Nu_s
0	349.2	36.23	13.36	2.15	2.93
5×10^3	347.5	36.40	13.51	2.16	2.96
10^4	342.7	36.91	13.76	2.19	3.02
3×10^4	324.0	39.04	14.89	2.32	3.27
10^5	290.1	43.60	17.08	2.59	3.75

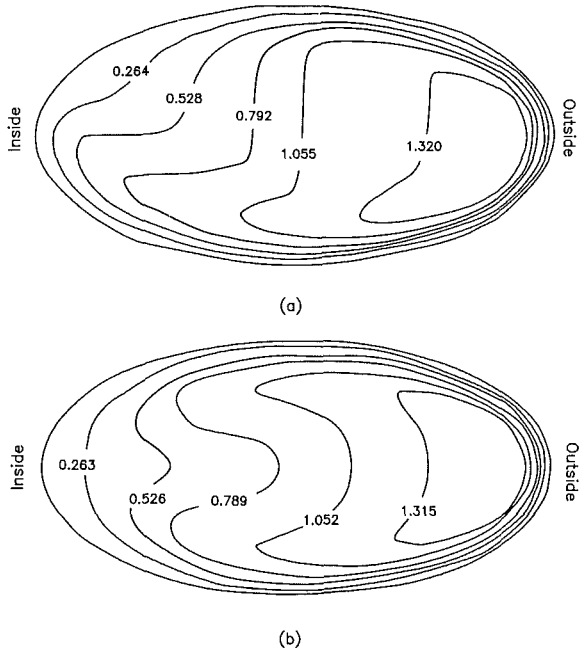

Fig. 7 Isotherms of θ/θ_b for flow in the curved elliptic duct ($dp/dz = 8 \times 10^4$, $r = 10$, $\Pr = 1$, $\alpha^* = 0.5$); (*a*) with buoyancy influence ($Gr = 10^4$); (*b*) without buoyancy influence ($Gr = 0$)

isotherms of θ/θ_b for the flow caused by centrifugal force alone. The isotherms in Fig. $7(a)$ are seriously affected by buoyancy and they are not symmetric to the major axis of ellipse. The shape of the isotherms in Fig. $7(a)$ is far different from the shape of the isotherms without buoyancy flow, Fig. $7(b)$. For purposes of further illustrating the effects of the Grashof number on flow and heat transfer, several computations have been done with variations of the Grashof number. The results are given in Table 4, where f_s and Nu_s are taken from the literature (Shah and London, 1978). It is seen from Table 4 that the Dean number decreases and the friction factor increases when the Grashof number increases. This is because buoyancy results in a decrease of axial velocity or flow rate and an increase of friction on the wall under the same axial pressure gradient. Therefore, the Dean number decreases as the Grashof number increases. On the other hand, the secondary flow in the cross section of the elliptic duct is intensified by the buoyancy force so that the Nusselt number is enhanced.

The local Nusselt number variation with a circumferential location is displayed in Fig. 8. It is seen that in the absence of buoyancy force ($Gr = 0$), the maximum Nusselt number is located around $\phi = 90$ deg, while the minimum value of the Nusselt number is located around $\phi = 270$ deg. That is because centrifugal force produces a stagnation-point flow in the region of $\phi = 90$ deg and a reverse stagnation-point flow in the region of $\phi = 270$ deg. Therefore, the average Nusselt number on the right half surface of the duct ($\phi = 0 \sim 180$) is larger than that of the left half surface ($\phi = 180 \sim 360$ deg). When the buoyancy force exists, the location of the maximum and minimum values

Downloaded 13 Dec 2010 to 193.140.21.150. Redistribution subject to ASME license or copyright; see http://www.asme.org/terms/Terms_Use.cfm

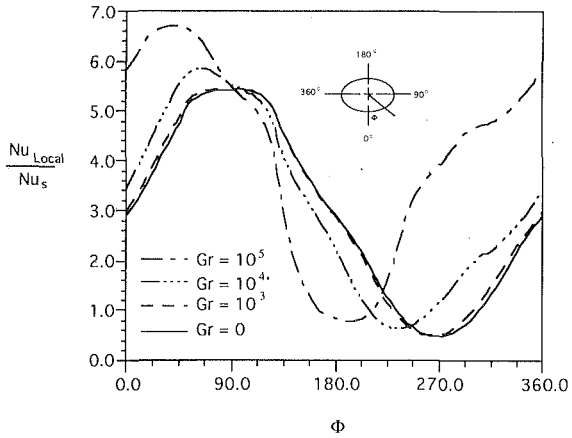

Fig. 8 Variation of the local peripheral Nusselt number

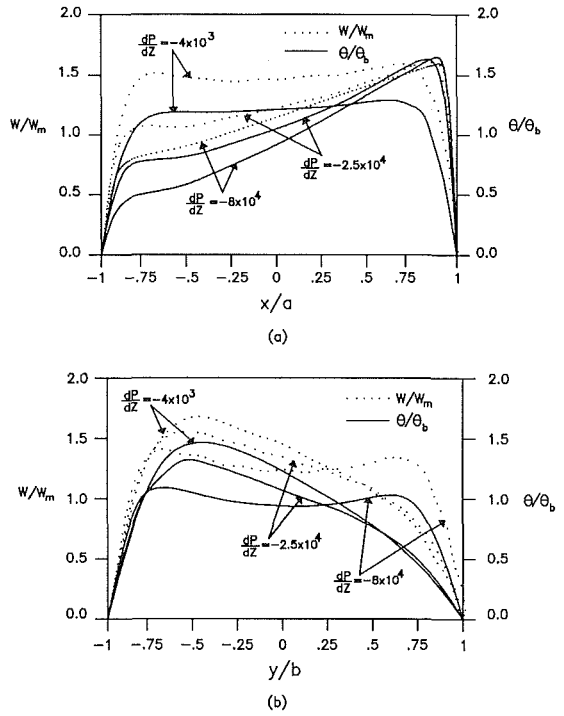

Fig. 9 Effects of *dp/dz* on the distributions of axial velocity and temperature ($r = 10$, $Gr = 10^4$, $Pr = 0.7$, $\alpha^* = 0.5$): (*a*) on the major axis of ellipse; (*b*) on the minor axis of ellipse

of the local Nusselt number shifts toward small ϕ values, as is seen in Fig. 8. Distribution of the local Nusselt number in the case of a small Gr number (e.g., 10^3) is similar to that of pure forced convection because of the dominant forced convection. However, the more important effects on the local Nusselt number distribution can be found in the case of larger Gr numbers (10^4, 10^5) where natural convection is dominant. The local Nusselt number on the bottom boundary of the duct becomes larger as the Grashof number increases. The average Nusselt number on the bottom boundary is larger than that on the upper boundary. The reason for this is that there is a greater temperature gradient on the bottom boundary.

Effects of the Axial Pressure Gradient. In order to see the effects of the axial pressure gradient on the velocity and the temperature fields when buoyancy exists, the dimensionless axial velocity (w/w_m) and the temperature profile (θ/θ_b) on the major axis of ellipse at $y = 0$, and the minor axis of ellipse at $x = 0$, are plotted in Figs. 9(a) and 9(b), respectively. This is achieved for the case of $\alpha^* = 0.5$, $Pr = 0.7$, $Gr = 10^4$, $r = 10$ with variations of the axial pressure gradients. It is seen from

Table 5 Results for variations of *dp/dz*; parameters: $Pr = 0.7$, $Gr = 10^4$, $r = 10$, $\alpha^* = 0.5$

$\frac{dp}{dz}$	De	fRe	Nu	f_c/f_s	Nu/Nu_s
$-4x10^3$	29.3	21.56	6.54	1.28	1.44
$-2.5x10^4$	143.2	27.60	8.62	1.64	1.89
$-8x10^4$	340.7	30.65	10.17	2.21	2.23

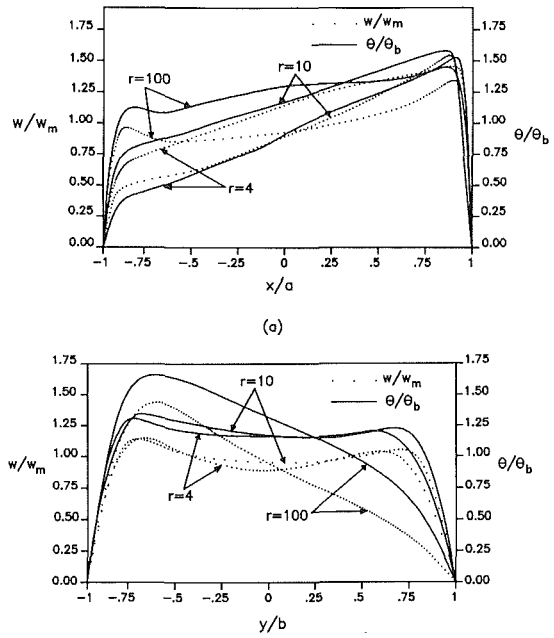

Fig. 10 Effects of r on the distributions of axial velocity and temperature ($dp/dz = -8 \times 10^4$, $Gr = 10^4$, $Pr = 1.0$, $\alpha^* = 0.5$): (*a*) on the major axis of ellipse; (*b*)on the minor axis of ellipse

these figures that the temperature and velocity distributions on the major axis of ellipse are nearly symmetric to $x = 0$ for a small axial pressure gradient. When the axial pressure gradient increases, the symmetry disappears and maximum velocity and temperature distributions occur near the outside boundary. However, for the axial velocity and temperature distributions on the minor axis of ellipse, the maximum temperature and velocity distribution appears near the bottom boundary in the case of a small axial pressure gradient. Symmetry of the axial velocity and the temperature distributions appears in the case of a large axial pressure gradient. This means that when the axial pressure gradient is larger, forced convection by centrifugal force is stronger than natural convection due to buoyancy and vice versa. The results for fRe and Nu variations with dp/dz are given in Table 5. It is obvious that the fRe, the Dean number, and the Nusselt number increase with an increase in the axial pressure gradient whether buoyancy exists or not.

Effects of the Curvature Ratio. Figures 10(a) and 10(b) illustrate the effects of curvature ratio, r, on the velocity and temperature distribution on the major and minor axes of the ellipse, respectively, with fixed parameters of $Gr = 10^4$, $dp/dz = -8 \times 10^4$, $Pr = 1.0$, and $\alpha^* = 0.5$. It is observed that on the major axis of the elliptic duct, the maximum velocity and temperature distribution located near the outside of the duct. The second peak values of the velocity and temperature distribution occur near the inside when $r = 100$. This is because centrifugal force is relatively smaller compared to the buoyancy

Downloaded 13 Dec 2010 to 193.140.21.150. Redistribution subject to ASME license or copyright; see http://www.asme.org/terms/Terms_Use.cfm

Table 6 Results for variations of r; parameters: $dp/dz = -8 \times 10^4$, Pr = 1, Gr = 10^4, $\alpha^* = 0.5$

r	De	fRe	Nu	f_c/f_s	Nu/Nu_s
4	462.2	43.27	15.12	2.57	3.32
10	342.7	36.91	13.76	2.19	3.02
100	135.1	30.43	11.28	1.81	2.48

Table 7 Results for variations of Pr; parameters: $dp/dz = -8 \times 10^4$, $r = 10$, $\alpha^* = 0.5$

Gr	Pr	De	fRe	Nu	f_c/f_s	Nu/Nu_s
10^4	1	342.7	36.91	13.76	2.19	3.02
	5	235.3	53.76	18.23	3.20	4.00
10^5	1	290.1	43.6	17.08	2.59	3.75
	5	216.1	58.54	28.95	3.48	6.35

force; natural convection dominates the flow, which in turn then leads to a tendency of symmetric velocity and temperature distribution to the minor axis of the duct. Velocity and temperature distributions on the minor axis of ellipse can be seen in Fig. 10(b). When the curvature ratio is smaller, e.g., $r = 4$ and 10, the secondary flow, due to this strong centrifugal force, leads to approximate symmetric distributions of velocity and temperature. However, when the curvature ratio is larger, such as $r = 100$, the secondary flow due to buoyancy is dominant, resulting in maximum velocity and temperature distribution near the bottom boundary. The effects of curvature ratio, r, on the friction factor and the Nusselt number are given in Table 6. It is seen from Figs. 10(a) and 10(b) and Table 6 that curvature ratio, r, is an important factor. Because centrifugal force decreases as the curvature ratio increases, the flow due to centrifugal force prevails on the flow induced by buoyancy only in the case of a small curvature ratio. Otherwise, the buoyancy flow is dominant. The friction factor and the Nusselt number always increase as the curvature ratio decreases.

Effects of the Prandtl Number. In Table 7, the effects of the Prandtl number on fluid flow and heat transfer are given with parameters of $dp/dz = -8 \times 10^4$, $r = 10$, and $\alpha^* = 0.5$ at Gr = 10^4 and Gr = 10^5. From the data shown in this table, it is seen that the Prandtl number has a significant influence on heat transfer in the fluid flow in a curved elliptic duct. When the Prandtl number increases, the Nusselt number increases. This is because convection is more important relative to conduction as the Prandtl number becomes larger. At a greater Pr, the transverse convection owing to secondary flow is dominant, which leads to a thin thermal boundary layer on the duct wall. Therefore, a greater Nusselt number can be attained with larger Prandtl numbers, as well as larger Grashof numbers.

Conclusion

Hydrodynamically and thermally fully developed steady laminar flow with a buoyancy effect in the curved elliptic duct is investigated by a control volume-based finite difference method via a numerically generated boundary-fitted coordinate system. The following major conclusions are obtained from the present analysis:

1 Velocity and temperature distribution is no longer symmetric to the horizontal major axis of the elliptic duct when buoyancy exists.
2 The friction factor and the Nusselt number increase as the Grashof number increases.
3 When buoyancy is present, the axial pressure gradient has a positive effect on flow and heat transfer in the curved elliptic duct; that is, the larger the axial pressure gradient, the greater the Dean number, the friction factor, and the Nusselt number.
4 It is found that the friction factor and the Nusselt number decrease as the curvature ratio increases.
5 The Prandtl number has a more significant effect on heat transfer in the curved elliptic duct, especially in the case of a larger Grashof number.

Acknowledgments

The results presented in this paper were obtained in the course of research sponsored by the National Science Foundation under Grant No. CTS-9017732.

References

Berger, S. A., Talbot, L., and Yao, L. S., 1983, "Flow in Curved Pipes," *Ann. Rev. Fluid Mech.*, Vol. 15, pp. 461–512.

Cheng, K. C., Lin, R. C., and Ou, J. W., 1976, "Fully Developed Laminar Flow in Curved Rectangular Channels," ASME *Journal of Fluids Engineering*, Vol. 98, pp. 41–48.

Dean, W. R., 1927, "Note on the Motion of Fluid in a Curved Pipe," *Phil. Mag.*, Vol. 20, pp. 208–223.

Dean, W. R., 1928, "The Streamline Motion of Fluid in a Curved Pipe," *Phil. Mag.*, Vol. 30, pp. 673–695.

Dong, Z. F., and Ebadian, M. A., 1991, "Numerical Analysis of Laminar Flow in Curved Elliptic Ducts," ASME *Journal of Fluids Engineering*, Vol. 113, pp. 555–562.

Kalb, C. E., and Seader, J. D., 1972, "Heat and Mass Transfer Phenomena for Viscous Flow in Curved Circular Tubes," *Int. J. Heat Mass Transfer*, Vol. 15, pp. 801–817.

Patankar, S. V., 1980, *Numerical Heat Transfer and Fluid Flow*, Hemisphere, Washington, DC.

Prusa, J., and Yao, L. S., 1982, "Numerical Solution for Fully Developed Flow in Heated Curved Tubes," *J. Fluid Mech.*, Vol. 123, pp. 503–522.

Shah, R. K., and London, A. L., 1978, "Laminar Flow Forced Convection in Ducts," *Supplement I to Advances in Heat Transfer*, Academic Press, New York.

Shah, R. K., and Joshi, S. D., 1987, "Convective Heat Transfer in Curved Duct," in: *Handbook of Single-Phase Convective Heat Transfer*, S. Kakac et al., eds., Wiley Interscience, New York.

Shyy, W., Tong, S. S., and Correa, S. M., 1985, "Numerical Recirculating Flow Calculation Using a Body-Fitted Coordinate System," *Numer. Heat Transfer*, Vol. 8, pp. 99–113.

Srivastava, R. S., 1980, "On the Motion of a Fluid in a Curved Pipe of Elliptical Cross-Section," *J. of Applied Mathematics and Physics (ZAMP)*, Vol. 31, pp. 297–303.

Takami, T., and Sudou, K., 1984, "Flow Through Curved Pipe With Elliptic Cross Sections," *Bull. JSME*, Vol. 27, pp. 1176–1181.

Thomas, P. D., and Middlecoff, J. F., 1980, "Direct Control of Grid Point Distribution in Meshes Generated by Elliptic Equation," *AIAA J.*, Vol. 18, pp. 652–656.

Thomas, R. M., and Walters, K., 1965, "On the Flow of an Elastico-Viscous Liquid in a Curved Pipe of Elliptic Cross-Section Under a Pressure-Gradient," *J. Fluid Mech.*, Vol. 21, Part 1, pp. 173–182.

Thompson, J. F., Thames, F., and Mastin, C., 1974, "Automatic Numerical Generation of Body-Fitted Curvilinear Coordinate System for Field Containing Any Number of Arbitrary Two-Dimensional Bodies," *J. Comp. Phys.*, Vol. 24, pp. 299–319.

Topakoglu, H. C., 1967, "Steady Laminar Flows of an Incompressible Viscous Fluid in Curved Pipes," *J. Math. Mech.*, Vol. 16, pp. 1321–1337.

Topakoglu, H. C., and Ebadian, M. A., 1985, "On the Steady Laminar Flow of an Incompressible Viscous Fluid in a Curved Pipe of Elliptical Cross-Section," *J. Fluid Mech.*, Vol. 158, pp. 329–340.

Topakoglu, H. C., and Ebadian, M. A., 1987, "Viscous Laminar Flow in a Curved Pipe of Elliptical Cross-Section," *J. Fluid Mech.*, Vol. 184, pp. 571–580.

Downloaded 13 Dec 2010 to 193.140.21.150. Redistribution subject to ASME license or copyright; see http://www.asme.org/terms/Terms_Use.cfm

Holographic Interferometry Temperature Measurements in Liquids for Pool Fires Supported on Water

A. Ito

K. Saito

T. Inamura

Department of Mechanical Engineering,
University of Kentucky,
Lexington, KY 40506-0046

This study provides detailed temperature and physical structure measurements for liquid pool fires supported on water within both the liquid fuel layer and the supporting water sublayer from ignition to the onset of the boiling water sublayer, WSB. Understanding the mechanism of WSB is important to predict the so-called "boilover phenomenon," which is associated with an intense spattering of water and fuel droplets. The in-depth physical structure and temperature profiles were obtained using a holographic interferometer for n-decane supported on water in rectangular Pyrex containers with large aspect ratios to provide two-dimensional conditions. The experiments demonstrated that: maximum temperature was achieved 0.1–0.15 cm below the fuel surface due to the combined effect of evaporation heat loss at the fuel surface and in-depth radiation absorption. As a result, Rayleigh convection was generated in the fuel near the fuel surface, and the total heat transfer rate to the fuel–water interface increased by approximately 30 percent. Hence, the water at the fuel–water interface was superheated, so that sporadic spattering of water and fuel droplets (boilover) resulted. To check the applicability of those results to a larger pool fire system and to different fuels, a rectangular container (10 cm long × 5 cm wide × 9 cm high) was designed and eight different liquid hydrocarbon fuels were tested; for all fuels the occurrence of Rayleigh convection was confirmed using fine thermocouples and a streak shadowgraph technique.

Introduction

Crude oil is a complex mixture of hydrocarbons and contains high boiling point fractions whose boiling point is greater than that of water. When these fuels are burned on water, the heat is transferred by both conduction from the high-temperature vaporizing fuel surface and radiation from the flame to induce boiling in the water layer below the fuel. The onset of WSB changes the combustion process; the fuel layer is stirred by the passage of water vapor bubbles traveling to the surface. In pool fires of 0.6 m and greater diameters, churning of the fuel surface causes fuel droplets to be injected into the flame enhancing the burning, while in pool fires of 5 cm diameter, the churning effect decreased the burning rate (Arai et al., 1990) due to the smaller heat feed back rate to the fuel surface by radiation.

Based on previous results (Inamura et al., 1992), we developed a one-dimensional model to predict the onset of WSB, which is composed of an unsteady heat term, a conduction term, and an in-depth radiation absorption term. Previous studies (Arai et al., 1990; Bruzustowski and Twardus, 1982; Evans et al., 1988, 1989; Inamura et al., 1992) also demonstrated that burning is an efficient means of removing spilled crude oil from the ocean surface. In the process of developing the model we made several assumptions; this study was directed to test the validity of neglecting the convection term. To achieve this, the temperature and physical structures in the liquid phase from ignition through WSB should be understood in detail. Thus, a holographic interferometer connected to a photographic recording system was applied to detect a sudden and sensitive temperature change occurring in a distributed area. For this measurement, a small-scale pool fire system was designed, because the flame is stable (laminar), fuel surface waves due to gravity are negligible, and the boiling of the water sublayer begins nearly uniformly over the entire fuel–water interface.

To check the applicability of the results to larger scale pool fires and to different fuels, we designed a rectangular Pyrex container (10 cm long × 5 cm wide × 9 cm high) and employed eight different liquid hydrocarbon fuels. Since the current holographic interferometry technique is not appropriate for the larger pool fire system due to the three-dimensional temperature structure in the liquid, fine thermocouples and a streak shadowgraph technique were employed, and the occurrence of Rayleigh convection was confirmed in all the fuels.

Experimental Methods

Rectangular-shaped Pyrex containers were designed (Fig. 1*a*) and a 35-mm motor-driven camera with a telephoto lens was used to record the holographic interferograms using a shutter speed of 1/500, which was fast enough to "freeze" the diffraction image. Interferograms were taken at 1 to 0.1 s intervals depending on the phenomena of our interest (the moderate process was taken at 1 s intervals and the rapid transient process was taken at 0.1 s intervals). The optical system used for the holographic interferometry was the same as in previous studies (Ito and Kashiwagi, 1988), and includes a 5 mW He-Ne laser as the light source (Fig. 1*b*). The diffraction image was enhanced by enhancing the reference light so that a real time method (Ito et al., 1991), could apply. To obtain conditions of uniform and short path length, and two dimensionality of the system, rectangular Pyrex containers with large aspect ratios (the container widths are 0.5 and 1.0 cm and length is 4 cm) were used (Fig. 1*a*). All the tests were conducted with an

Contributed by the Heat Transfer Division and presented at the 3rd ASME-JSME Joint Thermal Engineering Conference, Reno, Nevada, March 19-22, 1991. Manuscript received by the Heat Transfer Division June 1991; revision received March 1992. Keywords: Combustion, Fire/Flames, Measurement Techniques. Associate Technical Editor: J. R. Lloyd.

Copyright © 1992 by ASME
Downloaded 13 Dec 2010 to 193.140.21.150. Redistribution subject to ASME license or copyright; see http://www.asme.org/terms/Terms_Use.cfm

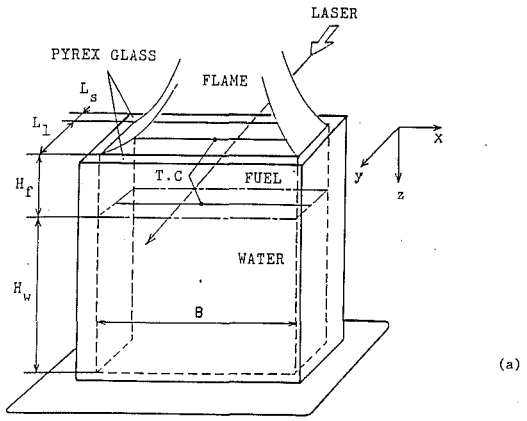

(a)

Container	L_1 (cm)	L_s (cm)	B (cm)	H_f (cm)	H_w (cm)
A	0.5	0.2	4	0.6	3
B	1	0.2	4	0.6	3
C	5	0.3	10	1	8

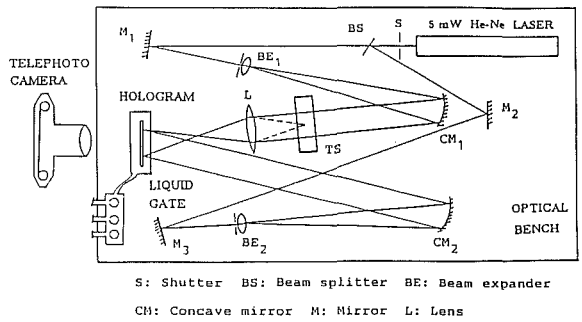

(b)

Fig. 1 (*a*) Pyrex pool fires apparatus and dimensions; (*b*) optical system used for holographic interferometry

initial fuel layer thickness of 0.6 cm and a water layer thickness of 3.0 cm to satisfy the "thermally thick" condition.

Assuming the laser beam emitted along the y direction (normal to the x-z plane in Fig. 1*a*) moves straight, and the temperature variation along its path is negligible (this assumption is justified from the experiment and is explained later), the relationship between fringe number, N, and temperature, T, can be described as follows:

$$L_1 \int_{T_0}^{T} (dn_1/dT)dT + 2L_s \int_{T_0}^{T} (dn_s/dT)dT = N\lambda \qquad (1)$$

where N = 1, 2, 3, ..., L_1 = the inner width of tray, dn/dT = thermo-optic coefficient of material (n_1 = refractive index of liquid and n_s = refractive index of Pyrex), L_s = thickness of Pyrex wall, λ = wavelength of the light, and T_0 = the initial liquid temperature. Detailed derivation of Eq. (1) was given previously (Ito et al., 1992). The second term of the left-hand side in Eq. (1) can be neglected with less than 2 percent error because of the weak thermal dependence of the refractive index of Pyrex (Ito et al., 1990). The reference temperature for the interferogram was obtained by a 50 μm wire diameter chromel-alumel thermocouple placed 0.2 mm below the fuel surface and at the fuel-water interface. The spatial resolution for the interferogram is estimated to be 30 μm (Ito et al., 1990).

Thermo-optic coefficients for n-decane and water as a function of temperature between 2°C and 90°C were measured using an Abbe refractometer with a He-Ne laser as the light source (λ = 632.8 nm). The derivative with respect to temperature of the refractive index for both the fuel and water was represented by linear expressions as: $-dn_f/dT = (4.5 + 0.0034T) \times 10^{-4}$ and $-dn_w/dT = (3.6 + 0.256T) \times 10^{-5}$, respectively, where n_f = refractive index of n-decane, n_w = refractive index of water, and T = temperature in °C. Special care was taken to prevent evaporation of the liquid during measurement (Ito et al., 1990).

At the early stage of combustion, the liquid loses heat to the Pyrex free-board, while with continued combustion, the increased free-board area is heated by the flame, and hence the heat is transferred back to the liquid. These effects can create a temperature gradient (dT/dy) along the laser beam, causing errors when temperatures are determined from the interferograms. To estimate this effect, four chromel-alumel thermocouples with 50 μm wire diameter were placed in the liquid and walls of the Pyrex B container (inner and outer) along the y direction 0.3 cm from the liquid surface. The thermocouple wires were horizontal to the fuel surface to minimize the conduction loss. Radiation loss is negligible due to relatively low temperature in the liquids. Response time of the thermocouple (50 μm wire diameter and 80 μm bead diameter) is sufficiently fast to detect the fluctuation of liquid convection that was determined by the combination of video camera and holographic interferometry to be at most a few Hertz. The results showed that at the beginning stages (t < 30 s), the maximum temperature in the liquid was achieved at 0.2 cm from the wall surface along the y direction, causing at most a 12 K difference from the average temperature. At later stages (t > 30 s), the temperature profiles became rather uniform along the y direction (the temperature) difference between the center and the edge is less than 4 K). The temperature distribution in the Pyrex walls does not affect the results as explained earlier, and the other errors (e.g., error due to refraction of the laser beam) involved in our holographic interferometry system were previously shown to be at most 3 percent (Ito et al., 1990).

To understand the onset mechanism of Rayleigh convection, which may be attributed to the local instability of the liquid temperature, the two-dimensional temperature structure of the liquid in the x-y plane is important. However, holographic interferometry can only provide the average temperatures along the path length. To estimate temperature distributions in the x-y plane, we designed a rectangular Pyrex container (10 cm long × 5 cm wide × 9 cm high) (Fig. 1*a*) and placed 12 chromel-alumel thermocouples of 50 μm diameter in the liquid (the locations of the thermocouples are shown in Fig. 4). For the Pyrex container, whose path length is relatively long compared to the containers A and B, a streak shadowgraph backlighted with a 150 W tungsten lamp was applied to check the occurrence of the liquid-phase convection qualitatively.

Results and Discussion

When an ignition source was applied to the fuel surface, a surface-tension-driven flow was observed that disappeared after the whole surface was ignited. After several trials, the onset time of WSB was determined from the interferograms, as 205 ± 11 s for L_1 = 0.5 cm, 240 ± 12 s for L_1 = 1.0 cm and 310 ± 15 s for L_1 = 5.0 cm. Recent measurements (Bouhafid et al., 1988; Venkatesh et al., 1992) suggest that a steep gas-phase temperature gradient was formed in the vicinity of the liquid surface near the rim where the flame is anchored, while the temperature gradient becomes less steep toward the center. Our pool fire experiments using several different pan diameters confirmed that the flame shape near the rim was not significantly changed with the container size (up to 30 cm in diameter). This indicates that the liquid surface area that is under the significant influence of the steep gas-phase temperature gradient does not increase with increasing pan diameter. Therefore, the average heat flux from the gas phase to the liquid surface is expected to decrease with increasing open fuel sur-

Downloaded 13 Dec 2010 to 193.140.21.150. Redistribution subject to ASME license or copyright; see http://www.asme.org/terms/Terms_Use.cfm

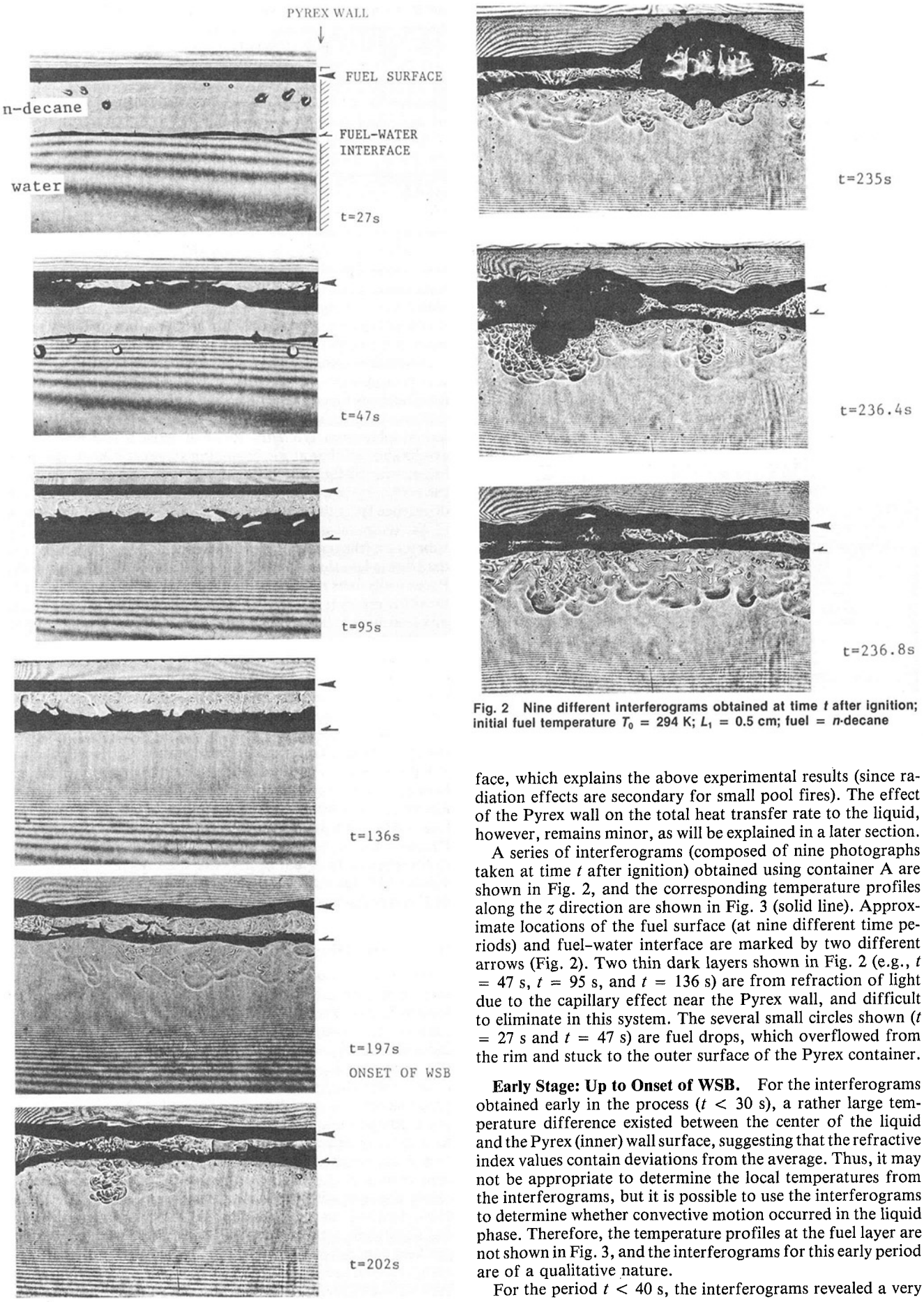

Fig. 2 Nine different interferograms obtained at time t after ignition; initial fuel temperature T_0 = 294 K; L_1 = 0.5 cm; fuel = n-decane

face, which explains the above experimental results (since radiation effects are secondary for small pool fires). The effect of the Pyrex wall on the total heat transfer rate to the liquid, however, remains minor, as will be explained in a later section.

A series of interferograms (composed of nine photographs taken at time t after ignition) obtained using container A are shown in Fig. 2, and the corresponding temperature profiles along the z direction are shown in Fig. 3 (solid line). Approximate locations of the fuel surface (at nine different time periods) and fuel-water interface are marked by two different arrows (Fig. 2). Two thin dark layers shown in Fig. 2 (e.g., t = 47 s, t = 95 s, and t = 136 s) are from refraction of light due to the capillary effect near the Pyrex wall, and difficult to eliminate in this system. The several small circles shown (t = 27 s and t = 47 s) are fuel drops, which overflowed from the rim and stuck to the outer surface of the Pyrex container.

Early Stage: Up to Onset of WSB. For the interferograms obtained early in the process (t < 30 s), a rather large temperature difference existed between the center of the liquid and the Pyrex (inner) wall surface, suggesting that the refractive index values contain deviations from the average. Thus, it may not be appropriate to determine the local temperatures from the interferograms, but it is possible to use the interferograms to determine whether convective motion occurred in the liquid phase. Therefore, the temperature profiles at the fuel layer are not shown in Fig. 3, and the interferograms for this early period are of a qualitative nature.

For the period t < 40 s, the interferograms revealed a very

Downloaded 13 Dec 2010 to 193.140.21.150. Redistribution subject to ASME license or copyright; see http://www.asme.org/terms/Terms_Use.cfm

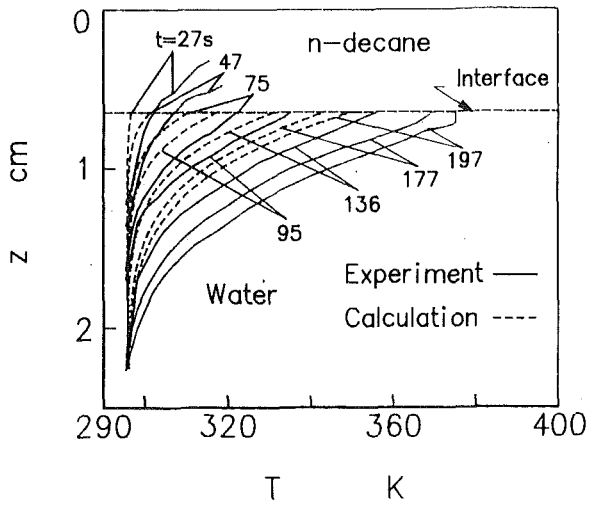

Fig. 3 Measured and calculated temperature profiles in the water along the z direction

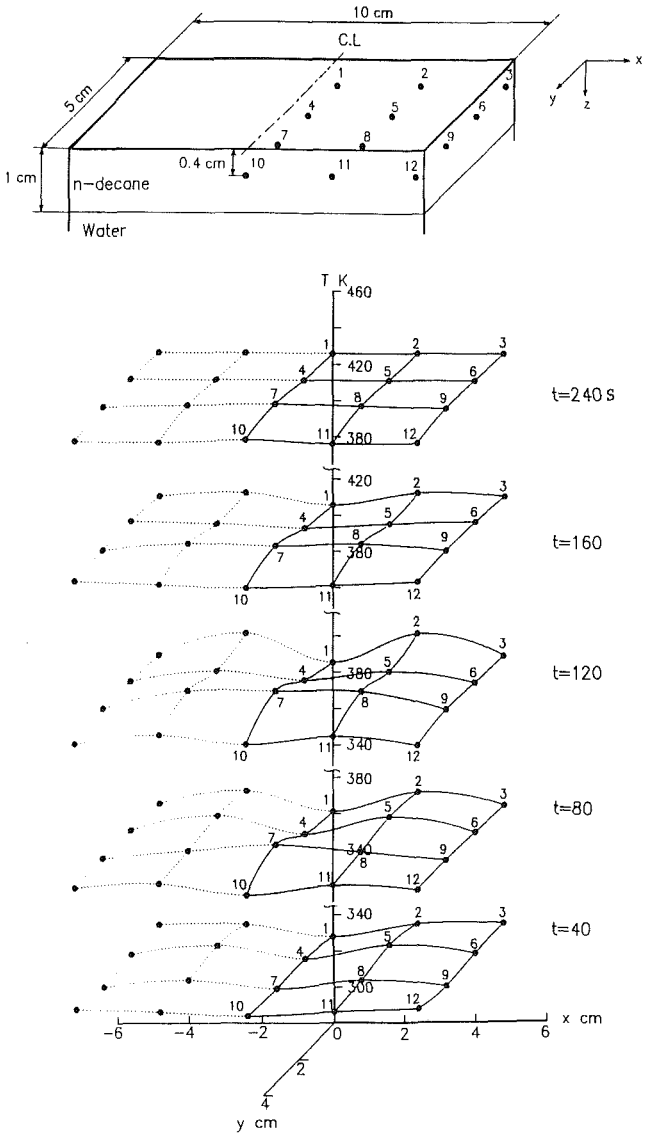

Fig. 4 Instantaneous temperature profiles measured with 50-μm-dia chromel-alumel thermocouples along the x-y plane (solid lines indicate measurement data; dotted lines indicate mirror image assuming the symmetry of the temperature structure). Numbers shown in figure indicate the location of the thermocouple beads (fuel = n-decane; T_0 = 290 K, H_f = 1 cm).

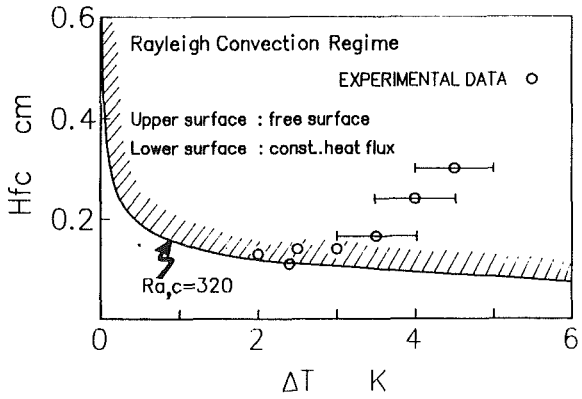

Fig. 5 Fuel layer thickness as a function of temperature difference formed in the fuel layer; Rayleigh convection regime is indicated with slashed lines

steep temperature gradient only at the vicinity of the fuel surface (approximately 2 mm thickness) and a very gradual temperature change occurred in the water layer (see Fig. 2 at t = 27 s). The dark layer near the fuel surface indicates that the temperature gradient (dT/dy) is too large to be resolved. Irregularity in the refractive index of the fuel layer occurred at t = 40 s and continued to grow until flame extinction. A detailed scrutiny of the interferograms found that the convective motion (corresponding to the irregularity of the refractive index) was initiated 0.1 to 0.15 cm below the fuel surface. A discontinuous white layer shown between the two dark layers at t = 47 s indicates the convective motion where the temperature gradient is small due to the mixing effect by the convection motion.

Instantaneous thermocouple-temperature data obtained at 12 different locations 0.4 cm below the fuel surface are shown in Fig. 4 as a function of five different times (t = 40, 80, 120, 160, and 240 s) after ignition. No temperature fluctuation was observed before Rayleigh convection occurred, while after Rayleigh convection occurred, the temperature plane fluctuated approximately with 1 Hz. At t = 40 s, the temperature gradients, dT/dx and dT/dy, are rather small, indicating a flat temperature structure in the x-y plane. By comparison, at t = 80 s and 120 s, the temperature structure at the x-y plane are wavy, indicating the occurrence of Rayleigh convection in a local area. With the progress of combustion (t = 160 s), the temperature gradients (dT/dx and dT/dy) decreased, indicating the growth of Rayleigh convection along the z direction, and therefore the liquid temperature becomes rather uniform due to the increased mixing effect. Finally at t = 240 s, the temperature gradients (dT/dx and dT/dy) diminished completely. The holographic interferometry detected the occurrence of Rayleigh convection instantaneously (approximately at t = 40 s), while the thermocouple detected it approximately at t = 60 s due to the location of the thermocouple (0.4 cm below the fuel surface).

A previous analysis (Inamura et al., 1992) predicted the existence of Rayleigh convection in the fuel layer due to in-depth radiation absorption. To understand the nature of Rayleigh convection in the fuel layer, a critical Rayleigh number over which convection could be generated is calculated using $\mathrm{Ra},c = \mathrm{Pr}\,(H_{fc}^3 g\beta\Delta T/\nu^2)$. Here Pr = Prandtl number for n-decane (15.3), H_{fc} = vertical distance between the fuel surface and the location of the maximum temperature in the liquid, g = acceleration due to gravity, β = thermal coefficient of volumetric expansion for n-decane (9.9×10^{-4} K^{-1}), ΔT = temperature difference between the fuel surface and a few mm below the fuel surface where the maximum temperature was achieved, and ν = kinematic viscosity of n-decane (1.27×10^{-6} m^2/s). Ra,c = 320 is shown using H_{fc}-ΔT coordinates (Fig.

Downloaded 13 Dec 2010 to 193.140.21.150. Redistribution subject to ASME license or copyright; see http://www.asme.org/terms/Terms_Use.cfm

5) and the calculated data points from the interferograms are on or above this curve, indicating that the condition is within the Rayleigh convection regime.

At the onset of WSB (see Fig. 2 at $t = 197$ s), the entire fuel layer is stirred by a strong convective motion; the fuel surface and the fuel-water interface are physically distorted. The distortion may be attributed to a dynamic effect of the superheated water sublayer due to sudden vapor expansion. The temperature at the fuel-water interface was determined from the interferograms to be at least 376 K. The actual temperature may be higher than this because of the effect of deflection of light along the y direction, the temperature difference along the y direction, and the edge effect. The strong convective motion generated in the water layer causes uniform temperature profiles in the fuel and the water layers near the fuel-water interface (see Fig. 2 at $t = 197$ s). This result is consistent with our previous thermocouple temperature measurements for n-decane on water in 5-cm and 10-cm dia pans (Arai et al., 1990).

To check the occurrence of Rayleigh convection for other fuels, holographic interferometry and streak shadowgraph techniques were applied to eight different fuels (pentane, heptane, octane, nonane, benzene, toluene, ethylbenzene, and kerosene) using containers B and C, whose dimensions are shown in Fig. 1. HI measures the density or temperature directly and is accurate for a relatively small container, while streak shadowgraph measures the derivative of the density gradient and is accurate for a relatively large container. For all the fuels, the occurrence of Rayleigh convection, which was always initiated near the center of fuel surface (but not at or near the wall surface), was confirmed. Interestingly, for toluene and ethylbenzene but not for other fuels, Rayleigh convection existed for a while, then it was diminished and finally disappeared (this type of convection will be called "weak Rayleigh convection"). For these two fuels, it was observed that soot formed in the flame deposited on the fuel surface. Because of this soot layer, the radiation absorption is enhanced at the fuel surface, therefore eliminating in-depth radiation absorption. For other fuels, however, soot deposition was not observed, causing the in-depth radiation penetration and generation of Rayleigh convection (this type of convection will be called "strong Rayleigh convection"). The reason for the observed soot deposition for the particular fuels was thought to be thermophoretic effect, because the soot formation region for these two fuels (where the temperature is approximately 1500 K) is close to the fuel surface (where the temperature is at the saturation temperature), while other fuels form soot in further downstream regions.

The saturation temperature of the fuel surface determined by both interferograms and a 50 μm chromel-alumel thermocouple remained at 425 K, which is 18 K below the boiling point (443 K). This is mainly due to the heat loss by evaporation at the fuel surface, while the heat gain by diffusion of high-temperature combustible gas into the fuel surface remains minor (Williams, 1985). The saturation temperature, $T_{sat} = 425$ K, is reasonable compared to the previous thermocouple temperature measurements for 5 and 10-cm-dia pools (Arai et al., 1990).

The temperature profiles in the fuel and water layers were previously obtained by numerically solving the following equation (Inamura et al., 1991) and assuming that the heat transfer occurs only along the z direction:

$$\rho c(\partial T/\partial t) = \partial(\kappa \partial T/\partial z)/\partial z + q\mu \exp(-\mu z) \qquad (2)$$

where ρ = density of liquid, c = specific heat of liquid, t = time after ignition, κ = thermal conductivity of liquid, q = average radiative heat flux (absorbed and transmitted) at the fuel surface, and μ = effective average radiation absorption coefficient.

Equation (2) is solved numerically using the Crank-Nicolson scheme and Gauss-Seidel method. The employed time step is 0.01-0.1 s, and three different mesh spacings (0.01, 0.02,and 0.05 mm) were used. There is a difference between the 0.02 mm and 0.05 mm spacings, but no difference between the 0.01 and 0.02 spacings. Therefore the 0.01 mm spacing was employed for our calculation. The temperature at the fuel-water interface is matched with an accuracy of better than 0.05 K. The values, μ and q, were experimentally determined (Inamura et al., 1991) to calculate the temperature profiles in the liquid. The obtained temperature profiles were plotted along the z direction for seven different time periods after ignition and the onset of WSB was estimated as 320 s for the container B (the calculation results are shown in Fig. 3 with broken lines). The calculation predicted a time for the onset of WSB approximately 1.4 times longer than that measured through the experiment. The difference is mainly due to the neglect of the Rayleigh convection effect, which enhances the heat transfer rate in the fuel layer, causing earlier onset of WSB.

The heat transfer from the Pyrex wall to the liquid along the x direction can be seen in Fig. 2 for container A (however, both HI and thermocouple temperature measurements were not made along the y direction due to the long path length for HI and insufficient space for the thermocouple implementation). The figure shows slightly bending isothermal lines in water toward Pyrex wall for $t = 27$ s and 47 s, while the isothermal lines for $t = 95$ s are parallel to the open fuel surface, suggesting that the heat transfer rate from the Pyrex wall to the liquid is minor. Accurate estimation of heat transfer from the Pyrex wall to the liquid both along the x and y directions was made for containers B and C from the thermocouple temperature measurements (see Fig. 4). It was found that the heat transfer rate from the Pyrex wall to the liquid was at most 5 percent of total heat feedback to the fuel surface. Calculation of onset of WSB was made by assuming the additional 5 percent heat was used to heat up the fuel-water interface; the calculation resulted in a time for the onset of WSB approximately 1.3 times longer than the experiment. Therefore, Rayleigh convection is responsible for the remaining difference (approximately 30 percent; for details, see Ito et al., 1992) between the calculation and the experiment.

Later Stage: After the Onset of WSB. Temperature and physical structures in the fuel and the water layers are significantly different before and after the onset of WSB. After WSB a strong convective column descending from the water layer is shown (Fig. 2 at $t = 202$ s), which indicates active boiling of the water sublayer. At $t = 235$ s, an egg-shaped dark circle appeared between the fuel layer and the fuel-water interface, pushing the fuel surface toward the flame. This indicates a superheated water vapor bubble trapped between the two layers and is the driving force to cause spattering of water and fuel droplets (boilover). The video film, which was taken at a time corresponding to the above event, recorded evidence of droplet injection from the fuel surface to the flame. The droplet emitted brightly and made a crackling sound when it burned.

Formation and growth processes of the superheated water vapor bubble are somehow related to the intensity of the boiling, but intense boiling does not always inject droplets from the fuel surface. In the interferograms at $t = 236.4$ s, several small round dark circles (initiation of vapor bubbles) are shown between the two dark layers and in the water sublayer. However, momentarily ($t = 236.8$ s) they disappeared without injecting any droplets from the surface; the superheated vapor energy must have been released to the fuel layer. The degree of the superheat of the water sublayer is also an important factor to estimate the intensity of boilover and is likely to depend on the open surface area and the ratio of the perimeter to the open surface area. The larger the open surface area and the smaller the ratio, the higher the temperature at the fuel-

Downloaded 13 Dec 2010 to 193.140.21.150. Redistribution subject to ASME license or copyright; see http://www.asme.org/terms/Terms_Use.cfm

water interface. Thus, the intensity of the boilover could increase with increasing the pool diameter. This interpretation is consistent with previous experimental results for up to 1.2 m diameter (Evans et al., 1986, 1988; Arai et al., 1990). However, experiments on much larger diameters report no boilover (Koseki et al., 1991); thus further studies are needed.

Summary and Conclusions

To understand the temperature structure in the liquid fuel of pool fires supported on water, three different sizes of rectangular Pyrex container were designed and eight different fuels were tested using three different techniques, a holographic interferometry, fine thermocouples and a streak shadowgraph.

The following conclusions are deduced:

1 The occurrence of Rayleigh convection was confirmed for all the fuels tested, of which toluene and ethylbenzene generated a weak Rayleigh convection due to the deposition of the soot layers at the fuel surface. Other fuels generated a strong Rayleigh convection.

2 For *n*-decane and water in a pool fire system, the maximum temperature was achieved 0.1–0.15 cm below the fuel surface, possibly due to in-depth radiation absorption. The effect of the in-depth radiation caused Rayleigh convection in the fuel layer, and generated a mixing motion by which the heat transfer rate was increased approximately 30 percent along the z direction.

3 The fuel surface remained at saturation temperature (425 K), while the temperature of the fuel–water interface at the onset of WSB was superheated to above 376 K. The superheated water layer is dynamically unstable, and sporadic spattering of water and fuel droplets occurred.

Acknowledgments

We wish to acknowledge A. Goto of Kyushu University for his assistance on experiments and E. Tennyson of the Minerals Management Service, USDI, for organizing this research program. Special thanks go to Dave Evans of National Institute of Standards and Technology for his many valuable comments and guidance as a technical officer for Grant #60NANB9D0960.

References

Arai, M., Saito, K., and Altenkirch, R. A., 1990, "A Study of Boilover in Liquid Pool Fires Supported on Water—Part I: Effects of a Water Sublayer on Pool Fires," *Combustion Science and Technology*, Vol. 71, pp. 25–40.

Bouhafid, A., Vantelon, J. P., Joulain, P., and Fernandez-Pello, A. C., 1988, "On the Flame Structure at the Base of a Pool Fire," *Twenty-Second International Symposium on Combustion*, The Combustion Institute, pp. 1291–1298.

Bruzustowski, T. A., and Twardus, E. M., 1982, "A Study of the Burning of a Slick of Crude Oil on Water," *Nineteenth Symposium (International) on Combustion*, The Combustion Institute, pp. 847–854.

Evans, D., Baum, H., McCaffrey, B., Mulholland, G., Harkleroad, M., and Manders, W., 1986, "Combustion of Oil on Water," Report NBSIR 86-3420, National Bureau of Standards, Gaithersburg, MD 20899.

Evans, D., Mulholland, G., Gross, D., Baum, H., and Saito, K., 1988, "Environmental Effects of Oil Spill Combustion," Report NISTIR 88-3822, National Institute of Standards and Technology, Gaithersburg, MD 20899.

Evans, D., Mulholland, G., Gross, D., Baum, H., and Saito, K., 1989, "Burning, Smoke Production, and Smoke Dispersion From Oil Spill Combustion," Report NISTIR 89-4091, National Institute of Standards and Technology, Gaithersburg, MD 20899.

Inamura, T., Saito, K., and Tagavi, K. A., 1992, "A Study of Boilover in Liquid Pool Fires Supported on Water—Part II: Effect of In-Depth Absorption," *Combustion Science and Technology*, Vol. 86, pp. 105–120.

Ito, A., and Kashiwagi, T., 1988, "Measurement Technique for Determining the Temperature Distribution in a Transparent Solid Using Holographic Interferometry," *Applied Optics*, Vol. 26, pp. 954–958.

Ito, A., Choudhury, S. K., and Fukano, T., 1990, "A Techniques for Measuring an Unsteady Temperature Distribution in a Liquid Using Holographic Interferometry," *Transactions of JSME*, Series B, Vol. 56, pp. 194–199.

Ito, A., Masuda, D., and Saito, K., 1991, "A Study of Flame Spread Over Alcohols Using Holographic Interferometry," *Combustion and Flame*, Vol. 83, pp. 375–389.

Ito, A., Goto, A., and Saito, K., 1992, "Heat Transfer Mechanism in Liquid Phase of Pool Fires Supported on Water: From Ignition to the Onset of Water Sublayer Boiling," *Combustion and Flame*, submitted.

Koseki, H., Mulholland, G., and Jin, T., 1991, "Experimental Study of Water Boiling Phenomena in Crude Oil Fires," presented at the 3rd International Symposium on Fire Safety Science, July 8–12, Edinburgh, United Kingdom.

Venkatesh, S., Ito, A., and Saito, K., 1992, "Flame Structure, Air Entrainment and Anchoring Mechanisms Near the Base of a (Small-Scale) Pool Fire," Dept. of Mechanical Engineering Report, University of Kentucky, Lexington, KY.

Williams, F. A., 1985, *Combustion Theory*, 2nd ed., Benjamin/Cummings, United Kingdom.

Downloaded 13 Dec 2010 to 193.140.21.150. Redistribution subject to ASME license or copyright; see http://www.asme.org/terms/Terms_Use.cfm

Radiative Properties of Interacting Particles

M. A. Al-Nimr

V. S. Arpaci

Department of Mechanical Engineering
and Applied Mechanics,
The University of Michigan,
Ann Arbor, MI 48109

Two statistical models for the radial distribution function are proposed. In terms of these models, analytical expressions for the radiation efficiency factors of random homogeneous systems are derived. The Planck and Rosseland mean absorption coefficients are evaluated and the ratio of dependent over independent mean absorption coefficients is given. The role of the far-field and the near-field effects on radiation is investigated. The near-field effect on the scattered radiation is found to be negligible compared to the far-field effect. The effect of particle interaction is demonstrated by a simple transport problem.

1 Introduction

Thermal radiation from particulate-laden media plays an important role in industrial applications as well as in atmospheric and extraterrestrial problems. Examples are fluidized and packed beds, oil and gas-fired furnaces, pulverized coal combustion, radiative burners, solid propellant rockets, gas turbine combustors, internal combustion engines, natural fires, typical porous insulation systems, microsphere and cryogenic insulation, paint layers, laser coating, clouds, fog, aerosols, atmospheric and interstellar dust. The radiation in these applications depends on the spectral coefficients, which can be obtained from the classical Lorenz-Mie (LM) theory for isotropic and homogeneous spherical particles (Bohren and Huffman, 1983; Born and Wolf, 1986) or from its limit, the Rayleigh approximation (Hottel and Sarofim, 1967) or the Penndorf extension (Penndorf, 1960, 1962).

In the literature independent scattering and absorption are commonly used assumptions where the interaction of each particle with the incident wave is unaffected by the presence of other particles. The radiative properties of a system are then obtained by algebraically adding the properties of each isolated particle. However, the assumption of isolated particles fails when the internal field of each particle is enhanced by the radiation scattered from other particles and by the interference of the scattered radiation. The first effect, or the near-field mechanism (Kumar and Tien, 1990), increases the radiation absorbed as well as the radiation scattered by each particle due to the enhancement in the internal field of each particle. The second effect, or the far-field mechanism, influences the shape and the amount of the scattered radiation. This gives rise to coherent, incoherent, and multiple scattering, and, in cases where the particles are regularly spaced, to diffraction. However, for small and randomly distributed particles, the diffraction or reinforcement of scattered radiation becomes negligible even in the direction of the incident wave. The only appreciable contribution is then that of the coherent addition due to phase difference of the far-field scattered radiation. Among the experimental studies on the second mechanism are Churchill et al. (1960); Hottel et al. (1971); Chan and Tien (1974); van de Hulst (1981); Brewster and Tien (1982); Yamada et al. (1987); Drolen et al. (1987); White and Kumar (1990); and those on the theoretical aspects are Kerker (1969); Jones (1979a, 1979b); Ishimaru and Kuga (1982); Cartigny et al. (1987); Tien and Drolen (1987); Drolen and Tien (1987a, 1987b); White and Kumar (1990). Both of the foregoing mechanisms have been numerically investigated by Jones (1979a, 1979b); Hunka and Mie (1981); Drolen and Tien (1987a, 1987b) for systems involving a small number of particles. In terms of a distribution function for local particle density relative to average particle density, Cartigny et al. (1986); Tien and Drolen (1987); Tien (1988); Ma et al. (1990); Kumar and Tien (1990) studied these mechanisms for large number of particles.

The first objective of the present study is to examine the literature on models for radial distribution function and to develop two new models, one incorporating the effect of volume fraction into the amplitude of impulse model and the other describing the asymptotic behavior of the Percus-Yevick model near a reference particle. These models provide an order of magnitude improvement over the literature on the statistical models. The second and major objective is to develop the Planck and Rosseland mean absorption coefficients for particulate systems. The study consists of seven sections: following this introduction, Section 2 reviews the literature. Section 3 introduces two new models for the radial distribution function, evaluates the correction factors in terms of these models, and develops expressions for the efficiency factors of interacting Penndorf particles. Section 4 derives the Planck and Rosseland mean absorption coefficients. Section 5 develops a criterion under which the interaction among particles can be neglected. Section 6 investigates the modification introduced by the dependency effect through the radiation properties by considering a simple transport problem, and Section 7 concludes the study.

2 Background

A homogeneous system of randomly positioned, uniformly distributed small spherical particles with a moderate refractive index dispersed in a dielectric medium is known to satisfy the condition for Rayleigh-Debye scattering: $2\alpha|m-1|<<1$, where α is the size parameter, m the complex refractive index. This condition neglects the phase shift across a particle and assumes a constant internal field for each particle. For a dense particulate system, the scattering and absorption properties of the system are not described by the independent theory. Two new mechanisms need to be taken into account: perturbation of the internal field of each particle by the presence of other particles, and the coherent addition of the far-field scattered radiation. The first mechanism has been modeled by modifying the internal electrical field of each particle with a complex correction factor ξ (Kumar and Tien, 1990):

$$E(r_l)=\xi\,\frac{3}{\epsilon+2}\,E_{\text{inc}}(r_l), \tag{1}$$

where l is a particle in the system and the subscript inc stands for the incident wave. With this factor, the internal field becomes

$$E(r)=\xi E_M(r), \quad X=\xi X_{\text{M}}, \tag{2}$$

where the subscript M refers to the Mie theory and X is the scattering matrix. In terms of this matrix, the scattering and

Contributed by the Heat Transfer Division for publication in the JOURNAL OF HEAT TRANSFER. Manuscript received by the Heat Transfer Division July 1991; revision received April 1992. Keywords: Combustion, Radiation, Radiation Interactions. Technical Editor: R. Viskanta.

Copyright © 1992 by ASME
Downloaded 13 Dec 2010 to 193.140.21.150. Redistribution subject to ASME license or copyright; see http://www.asme.org/terms/Terms_Use.cfm

extinction cross sections are (Bohren and Huffman, 1983; Born and Wolf, 1986):

$$C_{sN}=\frac{1}{k^2}\,\mathrm{Re}\left[\sum_l\sum_j\int_{4\pi}X_j\cdot\overline{X}_l e^{[ik(e_z-e_r)\cdot(r_j-r_l)]}d\Omega\right] \quad (3)$$

$$C_{eN}=\frac{4\pi}{k^2}\,\mathrm{Re}\left[\sum_j X_j\cdot e_x|_{\theta=0}\right], \quad (4)$$

$k=2\pi/\lambda$ being the propagation constant, and $\overline{X}$ the conjugate of X. Here, Eqs. (3) and (4) are written in terms of the X-polarized scattering matrix. For unpolarized radiation, the cross sections are the average of X-polarized and Y-polarized cases. For identical particles, insertion of Eq. (2) into Eqs. (3) and (4) yields:

$$C_{sD}=\frac{1}{k^2}\,\mathrm{Re}\left[\sum_l\sum_j\int_{4\pi}|\xi|^2|X_M|^2 e^{[ik(e_z-e_r)\cdot(r_j-r_l)]}d\Omega\right]. \quad (5)$$

The assumption that all particles have the same correction factor ξ is reasonable for a system involving a large number of particles where the angular position of each sphere is random in space. The averaging of this factor over a solid angle and introducing a pair distribution function as a weighting function eliminate the need for particle location. Thus, Eqs. (5) and (6) become:

$$C_{sD}=|\xi|^2\gamma C_{sM} \quad (7)$$

$$C_{eD}=\frac{4\pi}{k^2}\,\mathrm{Re}[\xi X_M\cdot e_x|_{\theta=0}], \quad (8)$$

where

$$C_{sM}=\int_{4\pi}\frac{|X_M|^2}{k^2}\,d\Omega, \quad (9)$$

γ being the far-field correction factor defined in terms of a form factor $F(\theta)$ and a phase function $\Phi_M(\theta)$ (Debye, 1925). For $\alpha<<1$,

$$\gamma=\frac{1}{4\pi}\int_0^{2\pi}\int_0^{\pi}F(\theta)\Phi_M(\theta)\sin(\theta)d\theta d\phi, \quad (10)$$

$$F(\theta)=\frac{1}{N}\sum_l\sum_j e^{[ik(e_z-e_r)\cdot(r_j-r_l)]} \quad (11)$$

$$\Phi_M=\frac{3}{4}(1+\cos^2\theta). \quad (12)$$

The form factor accounts for the amplitudes of all the waves scattered by all N particles in a scattering volume. For a homogeneous, continuous, isotropic, and infinite distribution of particles, the form factor is averaged over all orientation of particles and the double sum is replaced by an integral giving (Cartigny et al., 1986)

$$F(\theta)=1+24f_v\int_0^{\infty}R^2[G(R)-1]\frac{\sin(\beta R)}{\beta R}\,dR, \quad (13)$$

where $\beta=4\alpha\sin(\theta/2)$ and $G(R)$ is a particle distribution function. In terms of Eqs. (7) and (8), the efficiency factors are given by Kumar and Tien (1990),

$$Q_{sD}=|\xi|^2\gamma Q_{sM}, \quad (14)$$

$$Q_{eD}=\frac{4}{\alpha^2}\,\mathrm{Re}[\xi S_M(0)], \quad (15)$$

where

$$S_M(0)=0.5(X_M\cdot e_x|_{\theta=0}+Y_M\cdot e_y|_{\theta=0}), \quad (16)$$

$S_M(0)$ being the averaged forward scattering matrix evaluated by the Mie theory. Again, following Kumar and Tien, the complex correction factor ξ is written as:

$$\xi=\left[1-\frac{i(\epsilon-1)}{3(\epsilon+2)}\alpha^3 A\right]^{-1}, \quad (17)$$

where

$$A=24f_v\int_0^{\infty}R^2[A_1(\alpha R)+A_2(\alpha R)A_3(\alpha R)]G(R)e^{2i\alpha R}\,dR, \quad (18)$$

and

Nomenclature

A = complex number, Eq. (21)
C = cross section
C_1 = first radiation constant
C_2 = second radiation constant
D = diameter of the particle
E = electrical field vector
$E_{b\lambda}$ = emissive power of black body
f_v = solid volume fraction
$F(\theta)$ = form factor
G = radial distribution function
h = Planck's constant or constant related to the modeling of $G(R)$
i = complex unit
I = "the imaginary part of"
k = absorptive index, Boltzmann's constant, propagation constant $=2\pi/\lambda$
K = absorption coefficient
m = complex refractive index $=n+ik$
n = refractive index
N = particle number density
P = normalized size distribution function
q = radiative flux
Q = efficiency factor
r = radial vector
R = dimensionless radial distance $=r/D$
Re = "real part of"
S = averaged scattered matrix
T = temperature
X = scattering matrix, x-polarized
Y = scattering matrix, y-polarized
α = size parameter $=\pi D/\lambda$
β = $4\alpha\sin(\theta/2)$
γ = function defined in the definition of the form factor
Γ = Gamma function
$\mathcal{E}$ = photon energy
ϵ = relative dielectric constant, or m^2
θ = dimensionless temperature or polar angle
λ = wavelength
ν = frequency
Ξ = Reiman Zeta function
ρ = particle number density
τ = optical depth
Φ = scattering phase function
χ = parameter defined in liquid model

Subscripts

a = absorption
b = black body
D = dependent effect
e = extinction
inc = incident radiation
M = Mie theory for one particle
N = N particles
P = Planck mean absorption coefficient
R = Rosseland mean absorption coefficient
s = scattering

Superscripts

$^-$ = "complex conjugate of" or dimensional parameter
P = Penndorf
R = Rayleigh

Downloaded 13 Dec 2010 to 193.140.21.150. Redistribution subject to ASME license or copyright; see http://www.asme.org/terms/Terms_Use.cfm

$$A_1(\alpha R)=\frac{i\sin(2\alpha R)}{(2\alpha R)^2},$$

$$A_2(\alpha R)=\frac{i}{2\alpha R}\left(\frac{3}{(2\alpha R)^2}-1\right)+\frac{3}{(2\alpha R)^2},$$

$$A_3(\alpha R)=\frac{\sin(2\alpha R)}{2\alpha R}+3\,\frac{\cos(2\alpha R)}{(2\alpha R)^2}-3\,\frac{\sin(2\alpha R)}{(2\alpha R)^3}.$$

The previous statistical models lead to a nonlinear integral equation for $G(R)$ that needs to be solved numerically. Approximate analytical models are also available in the literature. Because of their relevance to the models developed in the next section, two of these models are cited here. They are the gas model (Kumar and Tien, 1990):

$$G(R)=\begin{cases}0 & \text{if } R<1\\ 1 & \text{if } R>1\end{cases}$$

and the modified liquid model (Tien and Drolen, 1987):

$$G(R)=\begin{cases}0 & R<1,\ 1<R<\chi\\ 1 & R>\chi\\ \lim\limits_{\sigma\to 0}\int_{1-\epsilon}^{1+\epsilon}R^2G(R)dR=\left[\frac{1}{3}-\frac{1}{4\pi\sqrt{2}}\right]\end{cases}$$

where $\chi=1+0.5\exp(-f_v/0.15)$. The special case of this model for $\chi=1$ is the packed sphere model. For the gas model, ξ and γ are:

$$\xi=\left[1-\frac{(\epsilon-1)}{(\epsilon+2)}f_v(1+1.6\alpha^2)\right]^{-1} \tag{19}$$

$$\gamma=1-8\,f_v(1-0.8\alpha^2) \tag{20}$$

and, for the liquid model, they are

$$\xi=\left[1-\frac{(\epsilon-1)}{(\epsilon+2)}f_v(1+1.6\alpha^2(\chi^2-0.554))\right]^{-1} \tag{21}$$

$$\gamma=1-8\,f_v[(\chi^3-0.831)-\alpha^2(0.8\chi^5-1.108)] \tag{22}$$

3 Proposed Models

Experimental results and the statistical models show that the radial distribution function $G(R)$ has a sharp peak near $r=D$ (the particle diameter) and an oscillatory behavior at moderate to high volume fractions (Reed and Gubbins, 1973). For a system of particles, where the particles exhibit short-range potentials, the PY model (Percus and Yevick, 1958; Percus, 1962; Reed and Gubbins, 1973) appears to be most realistic. A solution of this model is given by Wertheim (1963) and Thiele (1963). However, the explicit form of $G(R)$ over the entire domain is not available. A closed-form solution for $1\le R\le 2$ provided by Wertheim (1963) is valid up to $f_v=0.4$. For $R\ge 2$, $G(R)$ can be approximated by the gas model, $G(R)=1$.

Now, consider $G(R)$ based on the PY model:

$$G(R)=\begin{cases}0 & R<1,\\ \dfrac{[A_1e^{a_1(R-1)}+e^{a_2(R-1)}[A_2\cos(a_3(R-1))-A_3\sin(a_3(R-1))]]}{[(1-f_v)R]} & 1\le R\le 2\\ 1 & R>2\end{cases}$$

where

$$A_1=\frac{1}{3}\,[H_0+H_1+H_2],\quad A_2=2\left[\frac{H_0}{3}-\frac{H_1+H_2}{6}\right],$$

$$A_3=2\,\frac{H_1-H_2}{2\sqrt{3}}a_1=\frac{2f_v}{1-f_v}[-1+y_++y_-],$$

$$a_2=\frac{-2f_v}{1-f_v}[1+0.5(y_++y_-)],\quad a_3=\frac{\sqrt{3}f_v}{1-f_v}[y_+-y_-,$$

$$H_0=1+0.5f_v,\quad H_1=-C[y_-^2(1-3f_v-4f_v^2)+y_+(1-2.5f_v^2)],$$

$$H_2=C[y_+^2(1-3f_v-4f_v^2)+y_-(1-2.5f_v^2)]$$

$$C=(4f_v)^{-1}\left(Z^2+\frac{1}{8}\right)^{-0.5},\quad Z=\frac{3+3f_v-f_v^2}{4f_v^2},$$

$$y_\pm=\left[Z\pm\left(Z^2+\frac{1}{8}\right)^{0.5}\right]^{1/3}.$$

Insertion of the foregoing $G(R)$ into $F(\theta)$ or ξ leads to rather lengthy and cumbersome manipulations. However, these manipulations can be simplified by noting that $G(R)-1\approx 0$ for $R>2$ and $0\le\theta\le 2\pi$, which for the Rayleigh limit ($\alpha<<1$) suggests $\sin\beta R/\beta R\sim 1$. Then, Eq. (13) is reduced to

$$F=1+24f_v\int_0^2R^2[G(R)-1]dR. \tag{23}$$

In terms of the exact behavior of $G(R)$, the form factor is

$$F(\theta)=1-64f_v+24f_v[B_1e^{a_1}+e^{a_2}[B_2\cos(a_3)+B_3\sin(a_3)+B_4\sin(a_3)+B_5\cos(a_3)]+B_6], \tag{24}$$

where

$$B_1=2L_1/a_1-L_1/a_1^2,\quad B_2=L_2[2a_2/b_1-b_2/b_1^2],$$

$$B_3=L_2[2a_3/b_1-2a_2a_3/b_1^2],\quad B_4=L_3[2a_2/b_1-b_2/b_1^2],$$

$$B_5=-L_3[2a_3/b_1-2a_2a_3/b_1^2],$$

$$B_6=[2L_1/a_1^2-L_1/a_1+L_2b_2/b_1^2-L_2a_2/b_1-2L_3a_2a_3/b_1^2+L_3a_3/b_1],$$

and

$$b_1=a_2^2+a_3^2,\quad b_2=a_2^2-a_3^2,$$

$$L_1=A_1/(1-f_v)^2,\quad L_2=2A_2/(1-f_v)^2,\quad L_3=-2A_3/(1-f_v)^2.$$

The first model proposed in this study is the impulse model. This model incorporates the effect of volume fraction into the amplitude of the packed sphere model. This impulse model assumes that the number density of particles in the spherical shell of outer radius $(D+b)$ and the inner radius (D) is concentrated on the spherical shell of diameter D and thickness 2σ. Thus,

$$\lim_{\sigma\to 0}\int_{D-\sigma}^{D+\sigma}4\pi r^2\rho(r)dr=\frac{2}{3}(H-1)\pi[(D+b)^3-D^3]\rho_0, \tag{25}$$

where D is the diameter of the particle, b is a radial distance determined by the intersection of the tangent of the peak at $R=1$ with $G(R)=1$, ρ is the particle number density, and ρ_o is the average particle number density. In Eq. (25) the value of 1 is subtracted from $G(1)=H$, where H is the height of the peak, since the model involves a superposition with the gas model. Then, after rearranging Eq. (25) as

Downloaded 13 Dec 2010 to 193.140.21.150. Redistribution subject to ASME license or copyright; see http://www.asme.org/terms/Terms_Use.cfm

$$\lim_{\epsilon\to 0}\int_{1-\epsilon}^{1+\epsilon} R^2G(R)dR=\frac{b}{2D}\,(H-1)\left[1+\frac{b}{D}\right], \qquad (26)$$

where $(b/D)^3\approx 0$, the impulse model may be written as:

$$G(R)=\begin{cases} 0 & R<1,\ 1<R<\chi \\ 1 & R>\chi \\ \lim\limits_{\epsilon\to 0}\int_{1-\epsilon}^{1+\epsilon} R^2G(R)dR=\dfrac{H-1}{2}\chi[\chi-1] \end{cases} \qquad (27)$$

where

$$H=(0.5f_v^3-1.5f_v+1)/(f_v-1)^4=G(1),$$
$$\chi=(1-F)/E=b/D+1,$$
$$F=(-4f_v^3+3f_v+1)/(f_v-1)^4,\quad E=-4.5(f_v-f_v^3)/(f_v-1)^4.$$

The value of H is obtained following Thiele (1963) and χ is obtained following Thiele (1963) or the liquid and packed-sphere models. At $R=1$, because of its continuity up to the third derivatives, $G(R)$ is used to get $G(1)$ and $dG(1)/dR$. Then, the intersection of an assumed linear profile with $G(R)=1$ provides χ.

The second model proposed in this study is the linear model. For this model, first consider the radial distribution function approximated by Thiele (1963) in the shell $0\le R\le 1$,

$$G(R)=a+bR+cR^3$$

where

$$a=(2f_v+1)^2/(f_v-1)^4,\quad b=-(6f_v+6f_v^2+1.5f_v^3)/(f_v-1)^4,$$
$$c=0.5f_v(2f_v+1)^2/(f_v-1)^4.$$

Then, $G(1)$ and $dG(1)/dR$ obtained from the first shell provide the asymptote of $G(R)$ and the proposed linear model:

$$G(R)=\begin{cases} 0 & 0<R<1 \\ F+ER & 1<R<\chi_1 \\ 1 & R>\chi_1 \end{cases}$$

where χ_1 is the value of χ obtained by the intersection of the linear profile with $G=1$. Figure 1 compares the proposed linear model with the PY model.

At higher volume fractions, all the statistical models give inaccurate results because they are truncations in volume fraction. To improve accuracy at higher volume fractions, two self-consistent approximations have already been proposed (Rowlinson, 1965; Watts and Henderson, 1969). These approximations relate the pair distribution function and the direct correlation function by an appropriate equation of state. Following Watts and Henderson (1969), and after some lengthy manipulations, the pair distribution function may be written in terms of the hard sphere potential function as:

$$G(R)=G_{PY}(R)+\Phi(f_v)[e^{(G_{PY}(R)-1)}-G_{PY})(R)] \qquad (28)$$

$$\Phi(f_v)=0.47272-1.38186f_v+0.99002f_v^2-0.30688\exp\left(\frac{-6.37893f_v}{1.4142-1.9099f_v}\right) \qquad (29)$$

Now, Eqs. (28) and (29) may be used to modify the constants of the linear model. Inserting the linear model for $G(R)$ (without the modification of Eq. (28)) into Eqs. (18) and (17) yields, following further lengthy manipulations,

$$A=24f_v\left[\frac{\overline{\beta}_1}{\alpha^4}+\frac{i\overline{\beta}_2}{\alpha^3}+\frac{\overline{\beta}_3}{\alpha^2}+\frac{\overline{\beta}_4}{\alpha}\right] \qquad (30)$$

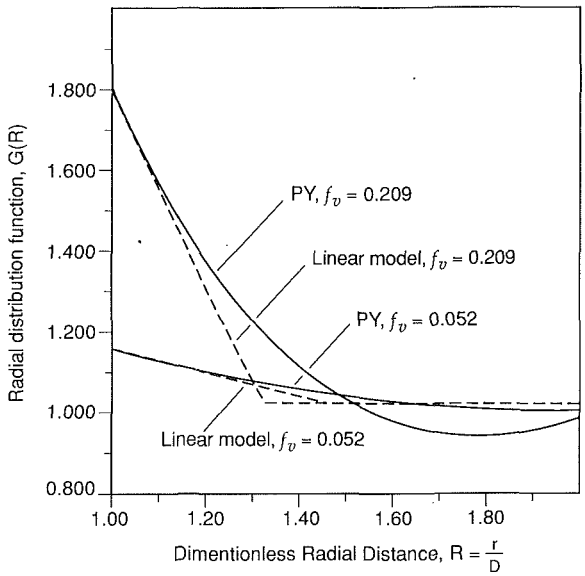

Fig. 1 The radial distribution function, linear, and PY model

$$\xi=\left(1+8f_v\frac{\epsilon-1}{\epsilon+1}\left(\frac{i\overline{\beta}_1}{\alpha}-\overline{\beta}_2+i\overline{\beta}_3\alpha-\overline{\beta}_4\alpha^2\right)+\ \ldots\ \right], \qquad (31)$$

where

$$\overline{\beta}_1=\frac{3E\ln(\chi_1)}{32},\quad \overline{\beta}_2=\frac{3E(\chi_1-1)-1}{8},$$
$$\overline{\beta}_3=\frac{3E(1-\chi_1^2)}{8},\quad \overline{\beta}_4=\left[\frac{F(\chi_1^2-1)}{5}+\frac{E(1-\chi_1^3)}{5}\right].$$

Here, it is assumed that $|\overline{\beta}_1/\alpha|<1$. Thus, the dependent absorption efficiency factor yields:

$$Q_{aD}=\beta_1+\beta_2\alpha+\beta_3\alpha^2+\beta_4\alpha^3, \qquad (32)$$

where

$$\beta_1=32(C_1^2-C_2^2)f_v\overline{\beta}_1,\quad \beta_2=(4C_2-64C_1C_2f_v\overline{\beta}_2),$$
$$\beta_3=32(C_1^2-C_2^2)f_v\overline{\beta}_3,$$
$$\beta_4=-64C_1C_2f_v\overline{\beta}_4,\quad C_1=L_6/4,\quad C_2=L_3/4,$$

and L_3 and L_6 are defined next.

In terms of Eqs. (14) and (15), expressions for the efficiency factors of Rayleigh particles are provided in the literature. However, the only restriction in these equations is the Rayleigh–Debye condition. For a small absorption index and a near-unity refractive index, this condition is satisfied up to size parameters within the Penndorf limit. Neglecting the terms of order α^7 or greater in Q_{sD}, and the terms of order α^5 or greater in Q_{eD}, Eqs. (14) and (15) are reduced to:

$$Q_{sD}^P=Q_{sD}^R[1+2\alpha^2(0.6L_1-2N_1\alpha)/L_2] \qquad (33)$$

$$Q_{eD}^P=\xi_R[L_3\alpha+L_4\alpha^3+L_5\alpha^4]+\xi_I[L_6\alpha+L_7\alpha^3+L_8\alpha^4], \qquad (34)$$

where the subscripts R and I denote the real and imaginary parts, respectively, and superscripts R and P denote the Rayleigh and Penndorf limits, and

$$L_1=N_o-4,\quad L_2=(N_2+2)^2+N_1^2,\quad L_3=12N_1/L_2,$$
$$L_4=14.4N_1[(N_2-2)(N_2+2)+N_1^2]/(5L_2^2)+2N_1/15-10N_1/[3((2N_2+3)^2+4N_1^2)],$$
$$L_5=8[M^2-9N_1^2]/(3L_2^2),\quad L_6=4M/L_2,$$

Downloaded 13 Dec 2010 to 193.140.21.150. Redistribution subject to ASME license or copyright; see http://www.asme.org/terms/Terms_Use.cfm

$$L_7 = 2.4(M^2 - 9N_1^2)/(L_2^2) +$$
$$2(N_2 - 1)/15 + 2[(N_2 - 1)(2N_2 + 3) + 2N_1^2]/[3(2N_2 + 3)^2 + 4N_1^2],$$
$$L_8 = -16N_1M/L_2^2, \quad M = [(N_2 - 1)(N_2 + 2) + N_1^2,]$$
$$N_o = N_1^2 + N_2^2, \quad N_1 = 2n\kappa, \quad N_2 = n^2 - \kappa^2.$$

Note that in the case of independent particles ($\xi_R = 1$, $\xi_I = 0$), when the terms of order greater than α are neglected in Eq. (34), the extinction efficiency factor based on the Rayleigh limit becomes (Selamet and Arpaci, 1989),

$$Q_{eD}^R = 12N_1\alpha/L_2. \tag{35}$$

To evaluate the form factor, insert $G(R)$ into Eq. (23):

$$F = 1 - 8f_v + 24f_v\left[\frac{F-1}{3}(\chi_1^3 - 1) + \frac{E}{4}(\chi_1^4 - 1)\right], \tag{36}$$

where terms of order α^2 or greater are neglected. Again note that as $f_v \to 0$, and $E \to 0$, $(F, \chi_1, \chi_2) \to 1$, then $F(\theta)$ approaches the form factor of the gas model. For a constant form factor, in view of Eq. (10), it is clear that $\gamma = F$. Then,

$$\gamma = 1 - 8f_v + 24f_v\left[\frac{F-1}{3}(\chi_1^3 - 1) + \frac{E}{4}(\chi_1^4 - 1)\right]. \tag{37}$$

For a small size parameter, γ is a measure for the ratio of dependent to independent scattering. Figure 2 represents this ratio for the impulse ($\chi = 1$) and linear models, as well as for gas and the PY models. Note that the impulse model doubles and the proposed linear model triples the range of the validity of this ratio against f_v. The relation between the efficiency factor and the monochromatic absorption coefficient is

$$\frac{K_{a\lambda}}{(1/D)} = 1.5f_vQ_a \tag{38}$$

The next section is devoted to the evaluation of the Planck mean and Rosseland mean of the absorption coefficient.

4 Planck and Rosseland Mean Absorption Coefficients

By definition,

$$K_P = \frac{\int_0^\infty K_{a\lambda}E_{b\lambda}d_\lambda}{\int_0^\infty E_{b\lambda}d_\lambda}, \tag{39}$$

$$K_R = \frac{\int_0^\infty \frac{\partial E_{b\lambda}}{\partial T}d\lambda}{\int_0^\infty \frac{1}{K_{a\lambda}}\frac{\partial E_{b\lambda}}{\partial T}d\lambda}, \tag{40}$$

where

$$E_{b\lambda} = \frac{\overline{C}_1}{\lambda^5[e^{[\overline{c}_2/(\lambda T)]} - 1]} \tag{41}$$

Insertion of Eq. (38) into Eqs. (39) and (40) yields the Planck and Rosseland mean absorption coefficients. In terms of the gas, modified liquid, and impulse models these coefficients are reduced to

$$\frac{K_P}{(1/D)} = \frac{1.5f_v[V_1(\pi DT/\overline{C}_2) + V_2(\pi DT/\overline{C}_2)^3 + V_3(\pi DT/\overline{C}_2)^4 + \ldots]}{(\Gamma(4)\Xi(4))} \tag{42}$$

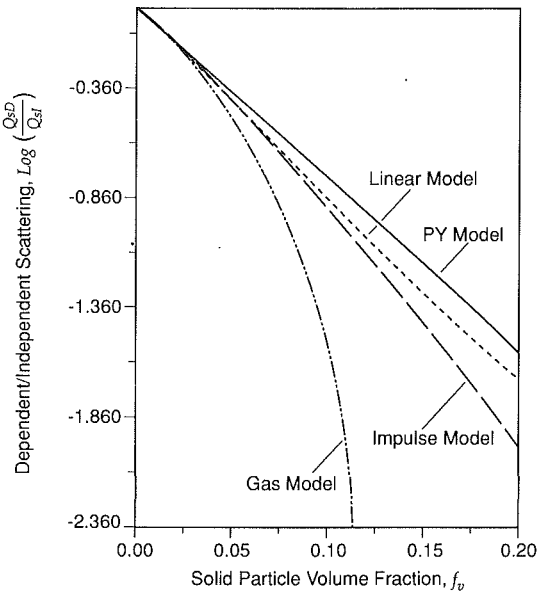

Fig. 2 The ratio of dependent to independent scattering efficiency versus volume fraction of solid particles

$$\frac{K_R}{(1/D)} = \frac{[1.5f_v\Gamma(4)\Xi(4)]}{[W_1(\overline{C}_2/(\pi DT)) - W_2(\pi DT/\overline{C}_2) - W_3(\pi DT/\overline{C})^2 + \ldots]}, \tag{43}$$

where

$$V_1 = E_1\Gamma(5)\Xi(5), \quad V_2 = E_2\Gamma(7)\Xi(7), \quad V_3 = E_4\Gamma(8)\Xi(8),$$
$$W_1 = (\Gamma(4)\Xi(3)/E_1), \quad W_2 = (E_2\Gamma(6)\Xi(5)/E_1^2,$$
$$W_3 = (E_4\Gamma(7)\Xi(6)/E_1^2),$$

Γ is the gamma function, Ξ is the Riemann Zeta function, and

$$E_1 + 4[H_1H_2 + H_3H_4], \quad E_2 = 4[H_1H_5 + H_3H_6],$$
$$E_3 = (8/3)[H_1^2 + H_3^2]H_4, \quad E_4 = E_3 - (8/3)[H_2^2 + H_4^2](1 - h_o)H_7,$$
$$H_1 = L_6/4, \quad H_2 = H_3f_v/J, \quad H_3 = L_3/4, \quad H_4 = (1 - H_1f_v)/J,$$
$$H_5 = -H_2JJ + (H_3f_vh)/J, \quad H_6 = -H_4JJ - (H_1f_vh)/J,$$
$$H_7 = 1 - 3(1 + 2N_2)/(N_1^2 + (2 + N_2)^2),$$
$$J = 1 + (H_1f_v)^2 - 2(H_1f_v) + (H_3f_v)^2,$$
$$JJ = [2(H_1f_v)^2h - 2H_1f_vh + 2(H_3f_v)^2h]/J,$$

h and h_o being related to the modeling of $G/(R)$. For the gas model, $h_o = 1 - 8f_v$, $h = 1.6$; for the liquid model, $h_o = 1 - 8f_v(\chi^3 - 0.8310)$, $h = 1.6(\chi^2 - 0.5541)$; for the impulse model, $h_o = 1 - 8f_v(\chi^3 - 3Y(H-1))$, $h = 1.6(\chi^2 - 2Y(H-1))$.

In terms of the linear model, the Planck and Rosseland mean adsorption coefficients are

$$K_P/(1/D) = 1.5f_v[P_1 + P_2(\pi DT/\overline{C}^2) + P_3(\pi DT/\overline{C}_2)^2 + P_4(\pi DT/\overline{C}_2)^3 + \ldots]/\Gamma(4)\Xi(4)) \tag{44}$$

$$K_R/(1/D) = [1.5f_v\Gamma(5)\Xi(4)]/[Q_1(\overline{C}_2/(\pi DT)) - Q_2(\overline{C}_2/(\pi DT))^2 - Q_3 - Q_4(\pi DT/\overline{C}_2 - \ldots], \tag{45}$$

where

Downloaded 13 Dec 2010 to 193.140.21.150. Redistribution subject to ASME license or copyright; see http://www.asme.org/terms/Terms_Use.cfm

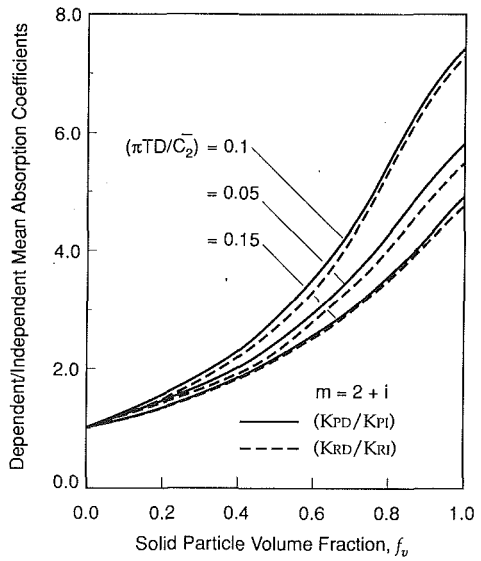

Fig. 3 The ratio of dependent to independent mean absorption coefficients

$$P_1=\beta_1\Gamma(4)\Xi(4),\quad P_2=\beta_2\Gamma(5)\Xi(5),$$
$$P_3=\beta_3\Gamma(6)\Xi(6),\quad P_4=\beta_4\Gamma(7)\Xi(7),$$
$$Q_1=\Gamma(4)\Xi(3)/\beta_2,\quad Q_2=\beta_1\Gamma(3)\Xi(2)/\beta_2^2,$$
$$Q_3=\beta_3\Gamma(5)\Xi(4)/\beta_2^2,\quad Q_4=\beta_4\Gamma(6)\Xi(5)/\beta_2^2.$$

In a typical combustion process, thermal radiation is limited to the range of $1\ \mu m<\lambda<10\mu m$. In the development of Planck and Rosseland mean absorption coefficients, it is then assumed that the diameter of the particle is small enough so that the size parameter α_{max} defined in terms of λ_{min} satisfies the Rayleigh limit. The physical significance of the dimensionless number $(\pi DT/\bar{C}_2)$ has been already recognized (Selamet and Arpaci, 1989). Note that as $f_v\to 0$, $\chi\to 1$, $E\to 0$, $(\beta_1, \beta_3, \beta_4)\to 0$, and $\beta_2\to 4C_2$. Then

$$\frac{K_P}{1/D}=68.979f_v\frac{2n\kappa}{[(n^2-\kappa^2+2)^2+4n^2\kappa^2]}\left(\frac{\pi DT}{\bar{C}_2}\right) \tag{46}$$

$$\frac{K_R}{1/D}=64.828f_v\frac{2n\kappa}{[(n^2-\kappa^2+2)^2+4n^2\kappa^2]}\left(\frac{\pi DT}{\bar{C}_2}\right) \tag{47}$$

which correspond to the Rayleigh limit. Figure 3 represents the ratio of dependent to independent mean absorption properties for the Rayleigh limit against the volume fraction.

Now, recall the definition of the emissivity:

$$\epsilon=1-\frac{\int_0^\infty E_{b\lambda}e^{-K_a\lambda^s}d\lambda}{\sigma T^4}. \tag{48}$$

Insertion of the first two terms of the spectral absorption coefficient followed by an integration yields:

$$\epsilon=1-\left[\frac{15}{\pi^4}e^{-1.5f_v\beta_1 s/D}\Gamma(4)\Xi\left(4,\ -1.5f_v\beta_2\frac{T_s}{\bar{C}_2}\right)\right] \tag{49}$$

It is clear from this equation that for systems of high volume fraction, and with the appreciable effect of interaction, $\epsilon\approx 1$. The next section is devoted to a criterion under which the interaction among particles can be neglected.

5 A Criterion for Independent Particles

For randomly distributed particles, the scattering efficiency is reduced because the interference among the scattered radiation is destructive and the absorption is modified due to the enhancement of the internal field of each particle by the radiation scattered from surrounding particles. The dependent absorption is then incorporated by multiple scattering, which is predicted from systems of optical thickness larger than 0.1 (Bayvel and Jones, 1981). Thus, the dependent scattering is expected to precede the dependent absorption. This is due to the fact that interference occurs even at relatively large interparticle spacing if the radiation scatters in an appropriate angular distribution. From the expressions for the dependent cross sections defined in Eqs. (14) and (15), the appearance of ξ in the absorption cross sections and $|\xi|^2\gamma$ in the scattering cross sections suggests that for independent absorption $\xi\le 1.05$ and for independent scattering $|\xi|^2\gamma\ge 0.95$, where the value of 0.05 is assumed following Tien and Drolen (1987). For dependent scattering, the restriction imposed by ξ is less severe than that imposed by γ and is excluded. Now, an expansion of ξ gives

$$\xi=H_4+H_6\alpha^2+\ \ldots\ +i(H_2+H_5\alpha^2+\ \ldots\ ) \tag{50}$$

from which a criterion for negligible dependent absorption may be obtained by applying the limitations suggested above. Thus, approximately,

$$f_v\le\frac{0.05}{\mathrm{Re}\left[\dfrac{\epsilon-1}{\epsilon+2}\right](1+h\alpha^2)}, \tag{51}$$

where Re denotes the "real part" and h is a constant related to the modeling of $G(R)$: $h=1.6$ for the gas model, $h=1.6(\chi^2-0.554)$ for the modified liquid model and $h=1.6[\chi^2-2Y(H-1)]$ for the impulse model. The criterion for the linear model leads to

$$f_v\le\frac{0.05}{\mathrm{Re}\left[\dfrac{\epsilon-1}{\epsilon+2}\right][1-3E(\chi_1-1)]}, \tag{52}$$

In the combustion literature, the values most commonly used for the complex refractive index remain between $1.5-0.5i$ (Dalzell and Sarofim, 1969) and $2-i$ (Janzen, 1979). For these values,

$$0.34\le\mathrm{Re}\left[\frac{\epsilon-1}{\epsilon+2}\right]\le 0.63.$$

This suggests an averaged value of $\mathrm{Re}[(\epsilon-1)/(\epsilon+2)]\approx 0.5$, and the dependent absorption interaction then requires $f_v>0.1$ for all models. In general, the dependent scattering efficiency factor is simultaneously affected by the near-field and far-field mechanisms. However, an examination of both mechanisms on the scattering efficiency reveals that the scattering efficiency is mostly affected by the far-field mechanism (Fig. 4). The criterion for independent scattering may then be given by setting $\gamma\approx 0.95$, which yields

$$f_v\le\frac{0.006}{h_1-h_2\alpha^2}. \tag{53}$$

where $h_1=1$, $h_2=0.8$ for the gas model, $h_1=\chi^3-0.831$, $h_2=0.8\chi^5-1.108$ for the modified liquid model,

$$h_1=1+24\,f_v\left[\frac{(F-1)(\chi_1^3-1)}{3}+\frac{E(\chi_1^4-1)}{4}\right],$$

$h_2=0$ for the linear model and $h_1=1-8f_v[\chi^3-3Y(H-1)]$, $h^2=8f_v[0.8\chi^5-4Y(H-1)]$ for the impulse model. Within the Rayleigh limit, the above criterion predicts scattering interaction for $f_v>0.006$, which is in agreement with the regime map provided by Tien and Drolen (1987). It is clear from Eq. (53) that the scattering interaction is very sensitive to modeling of $G(R)$. As α approaches zero, $G(R)$ has no effect on the enhanced absorption, but the scattering continues to be affected. This is due to the fact that as α approaches 0, the chance for a scattered beam striking another particle becomes

Downloaded 13 Dec 2010 to 193.140.21.150. Redistribution subject to ASME license or copyright; see http://www.asme.org/terms/Terms_Use.cfm

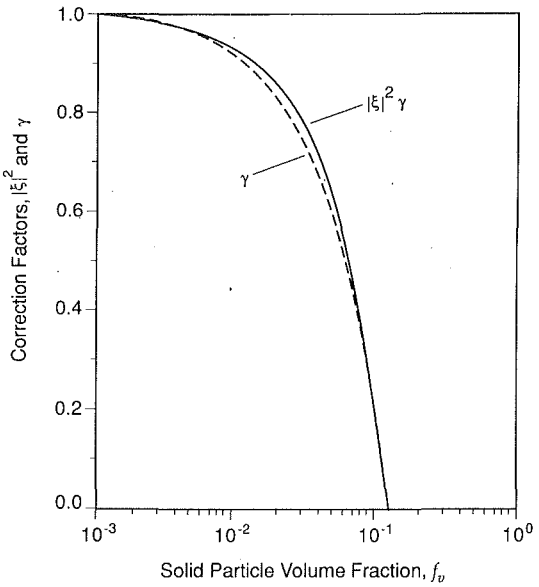

Fig. 4 The effect of far-field and near-field mechanisms on the ratio of dependent to independent scattering efficiency

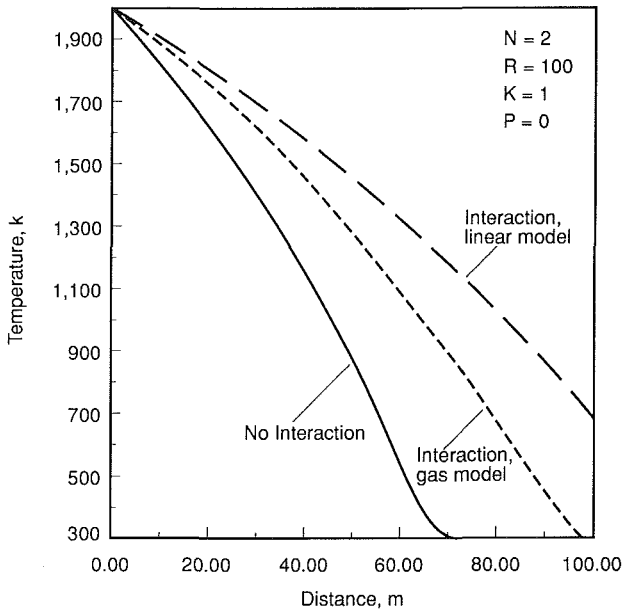

Fig. 5 The temperature distribution ahead of the flame

remote, and the interference of this scattered beam with other beams is not affected by the size parameter. Clearly, since absorption is controlled by the near-field mechanism, a particle is affected mostly by a few neighboring particles. On the other hand, the scattering efficiency is affected by particles in the far and near fields, and is sensitive to the radial distribution function over the entire domain.

As clearly demonstrated by Fig. 2, the different models proposed for $G(R)$ lead to wide variations in the dependent scattering efficiency. The sensitivity of this efficiency to modeling of the pair distribution function requires a criterion that describes the validity range of each model. Also, the modeling of the potential function in each model depends on the type and range of the forces among particles. Most of the models (hard-sphere potential, 6-12 potential, etc,...) for a system of particles like the one under consideration assume that the range of the potential force is roughly 2D (Friedman, 1985; Chandler, 1987). Assuming that the interparticle spacing $R \geq 2$, the corresponding volume fraction is evaluated from an empirical formula (Tien and Drolen, 1987): For example, $R = 0.95/f_v^{1/3} - 1$, which yields $f_v \leq 0.03$ as the upper limit for the gas model. The proposed linear model is valid up to f_v at which the fluctuations in $G(R)$ can be neglected. The following example illustrate the importance of particle interaction.

6 An Example

The temperature distribution ahead of a moving flame in a stagnant particulate system has important applications in ignition of solid fuels induced by radiation and in heat loss from a flame front. Assume this flame front at temperature T_f is propagating steadily with constant velocity V in a semi-infinite medium. For a typical situation, $Q_a \sim 0.001$, $\bar{x}/D \sim 10^5$ and the interaction of particles is significant when $f_v > 0.1$, where $\bar{x}$ is the penetration distance. Then, from the definition of the optical thickness.

$$\tau = \frac{3Q_a \bar{x} f_v}{2D} \sim 15, \tag{54}$$

and the particulate system behaves as a thick gas. The governing equation, after neglecting the effect of boundaries on thick gas in a thin layer next to boundaries (Arpaci and Larsen, 1969), is:

$$[\theta - \theta_\infty] + [R[a_1\theta^2 - a_2\theta - a_3\theta^3 - a_4\theta^4] + P]\frac{d\theta}{dx} = 0 \tag{55}$$

where

$$R = \frac{16\sigma \bar{C}_2^3}{3\rho c V D^3}, \quad P = \frac{k}{\rho c V D}, \quad \theta = \frac{TD}{\bar{C}_2}, \quad x = \frac{\bar{x}}{D}.$$

Here ρ is the density, c is the specific heat, k is the thermal conductivity and σ is the Stefan-Boltzmann constant,

$$a_1 = \frac{0.1851045}{\pi\beta_2 f_v}, \quad a_2 = \frac{0.084434\beta_1}{\pi^2\beta_2^2 f_v},$$

$$a_3 = \frac{0.6667\beta_3}{\beta_2^2 f_v}, \quad a_4 = \frac{3.1935\beta_4\pi}{\beta_2^2 f_v},$$

where β's were defined previously. Note that Eq. (55) already satisfies the boundary condition at infinity, $\theta = \theta_\infty$. The integration of this equation yields, with the boundary condition $\theta(0) = \theta_f$,

$$S_1(\theta_f^4 - \theta^4) + S_2(\theta_f^3 - \theta^3) + S_3(\theta_f^2 - \theta^2) + S_4(\theta_f - \theta) + S_5 \ln\left[\frac{(\theta_f - \theta)}{(\theta - \theta_\infty)}\right] = -\frac{x}{R} \tag{56}$$

where

$$S_1 = 0.25a_4, \quad S_2 = \frac{(a_3 + a_4\theta_\infty)}{3}, \quad S_3 = 0.05(-a_1 + a_3\theta_\infty + a_4\theta_\infty^2),$$

$$S_4 = (-a_1\theta_\infty + a_2 + a_3\theta_\infty^2 + a_4\theta_\infty^3),$$

$$S_5 = (-a_1\theta_\infty^2 - P/R + a_2\theta_\infty + a_3\theta_\infty^3 + a_4\theta_\infty^4).)$$

Figure 5 shows the temperature distribution ahead of the flame. Clearly, for a dense particulate system, the effect of the flame penetrates farther into the domain as the volume fraction increases. This is due to decrease in scattered radiation and increase in the mean absorption coefficient as a result of the enhancement of internal field from the scattered radiation. Also, the peak in the linear model increases the flame penetration because more particles are now enhancing the internal field of each particle.

7 Concluding Remarks

Two models are proposed describing the essential behavior

Downloaded 13 Dec 2010 to 193.140.21.150. Redistribution subject to ASME license or copyright; see http://www.asme.org/terms/Terms_Use.cfm

of the pair distribution function. The proposed models extend the validity of the gas model from $f_v = 0.05$ to $f_v = 0.25$. The correction factors that describe the interaction effects based on the proposed as well as available models for the distribution function are evaluated. The near-field mechanism increases the radiation absorbed as well as the radiation scattered by each particle due to the enhancement in the internal field of each particle, where the far-field mechanism reduces the scattered radiation due to the destructive interference. It is found that the effect of the near-field mechanism on the scattering efficiency factor is negligible compared to that of the far-field mechanism. On the other hand, the dependent absorption efficiency factor is affected by the near-field mechanism only. The efficiency factors of interacting particles that have size parameters larger than Rayleigh particles and up to the size of Penndorf particles are derived under the assumption of Rayleigh–Debye scattering. The thermal properties, such as the emissivity and the Planck and Rosseland mean absorption coefficients, are derived. A criterion is proposed under which the particulate system behaves independently. It is found that the effect of interaction on scattering precedes the effect of interaction on absorption. The dependent absorption is incorporated with multiple scattering and both are predicted at $f_v > 0.1$. The effect of the far-field mechanism on the modeling of the radial distribution function is investigated. The effect of particle interaction is demonstrated in terms of a simple transport problem.

References

Arpaci, V. S., and Larsen, P. S., 1969, "A Thick Gas Model Near Boundaries," *AIAA Journal*, Vol. 7, pp. 602–606.

Bayvel, L. P., and Jones, A. R., 1981, "Electromagnetic Scattering and Its Applications," *Applied Science*, London, pp. 5–6.

Bohren, C. F., and Huffman, D. R., 1983, *Absorption and Scattering of Light by Small Particles*, Wiley, New York.

Born, M., and Wolf, E., 1986, *Principles of Optics*, 6th ed., Pergamon Press, Oxford, United Kingdom.

Brewster, M. Q., and Tien, C. L., 1982, "Radiative Transfer in Packed/Fluidized Beds: Dependent Versus Independent Scattering," ASME JOURNAL OF HEAT TRANSFER, Vol. 104, pp. 573–579.

Cartigny, J. D., Yamada, Y., and Tien, C. L., 1986, "Radiative Transfer With Dependent Scattering by Particles: Part 1—Theoretical Investigation," ASME JOURNAL OF HEAT TRANSFER, Vol. 108, pp. 608–613.

Chan, C. K., and Tien, C. L., 1974, "Radiative Transfer in Packed Spheres," ASME JOURNAL OF HEAT TRANSFER, Vol. 96, pp. 52–58.

Chandler, D., 1987, *Introduction to Modern Statistical Mechanics*, Oxford University Press, United Kingdom, pp. 202–206.

Churchill, S. W., Clark, G. C., and Sliepcevich, C. M., 1960, "Light Scattering by Very Dense Monodispersions of Latex Particles," *Discussions, Faraday Society*, Vol. 30, pp. 192–199.

Dalzell, W. H., and Sarofim, A. F., 1969, "Optical Constants of Soot and Their Application to Heat Flux Calculations," ASME JOURNAL OF HEAT TRANSFER, Vol. 91, pp. 100–104.

Debye, P., 1925, "Note on the Scattering of X-Rays," *Journal of Mathematical Physics*, Vol. 4, p. 133.

Drolen, B. L., and Tien, C. L., 1987a, "Independent and Dependent Scattering in Packed-Sphere Systems," *Journal of Thermophysics*, Vol. 1, pp. 63–68.

Drolen, B. L., and Tien, C. L., 1987b, "Absorption and Scattering of Agglomerated Soot Particles," *Journal of Quantitative Spectroscopy and Radiative Transfer*, Vol. 37, pp. 433–448.

Drolen, B. L., Kumar, S., and Tien, C. L., 1987, "Experiments on Dependent Scattering of Radiation," AIAA Paper No. TP-87-210.

Friedman, H., 1985, *A Course in Statistical Mechanics*, Prentice-Hall, Inc., Englewood Cliffs, NJ, pp. 83–85.

Gingrich, N. S., 1943, "The Diffraction of X-Rays by Liquid Elements," *Reviews of Modern Physics*, Vol. 15, pp. 90–110.

Hottel, H. C., and Sarofim, A. F., 1967, *Radiative Transfer*, McGraw-Hill, New York, Chap. 12.

Hottel, H. C., Sarofim, A. F., Dalzell, W. H., and Vasalos, I. A., 1971, "Optical Properties of Coatings, Effect of Pigment Concentration," *AIAA Journal*, Vol. 9, pp. 1895–1898.

Hunka, J. F., and Mei, K. K., 1981, "Electromagnetic Scattering by Two Bodies of Revolution," *Electromagnetic*, Vol. 1, pp. 329–347.

Ishimaru, A., and Kuga, Y., 1982, "Attenuation Constant of a Coherent Field in a Dense Distribution of Particles," *Journal Optical Society of America*, Vol. 72, pp. 1317–1320.

Janzen, J., 1979, "The Refractive Index of Colloidal Carbon," *Journal of Colloid and Interface Science*, Vol. 69, pp. 436–447.

Jones, A. R., 1979a, "Electromagnetic Wave Scattering by Assemblies of Particles in the Rayleigh Approximation," *Proceedings Royal Society of London A*, Vol. 366, pp. 111–127.

Jones, A. R., 1979b, "Scattering Efficiency Factors for Agglomerates of Small Spheres," *Journal of Physics D: Applied Physics*, Vol. 12, pp. 1661–1672.

Kerker, M., 1969, *The Scattering of Light and Other Electromagnetic Radiation*, Academic Press, New York.

Kumar, S., and Tien, C. L., 1990, "Dependent Absorption and Extinction of Radiation by Small Particles," ASME JOURNAL OF HEAT TRANSFER, Vol. 112, pp. 178–185.

Ma, Y., Varadan, V. K., and Varadan, V. V., 1990, "Enhanced Absorption Due to Dependent Scattering," ASME JOURNAL OF HEAT TRANSFER, Vol. 113, pp. 403–407.

Penndorf, R. B., 1960, "Scattering Coefficients for Absorbing and Nonabsorbing Aerosols," Technical Report RAD-TR-60-27; AFCRL-TN-60-667, Avco Corp., Wilmington, MA.

Penndorf, R. B., 1962, "Scattering and Extinction Coefficients for Small Absorbing and Nonabsorbing Aerosols," *Journal Optical Society of America*, Vol. 52, pp. 896–904.

Percus, J. K., and Yevick, G. J., 1958, "Analysis of Classical Statistical Mechanics by Means of Collective Coordinates," *Physical Review*, Vol. 110, pp. 1–13.

Percus, J. K., 1962, "Approximation Methods in Classical Statistical Mechanics," *Physical Review Letters*, Vol. 8, No. 11, pp. 462–463.

Reed, T. M., and Gubbins, K. E., 1973, *Applied Statistical Mechanics*, McGraw-Hill, New York, pp. 225–248.

Rowlinson, J. S., 1965, "Self-Consistent Approximations for Molecular Distribution Functions," *Reports on Progress in Physics*, Vol. 28, pp. 217–227.

Selamet, A., and Arpaci, V., 1989, "Rayleigh Limit-Penndorf Extension," *International Journal of Heat and Mass Transfer*, Vol. 32, pp. 1809–1820.

Thiele, E., 1963, "Equation of State for Hard Spheres," *Journal of Chemical Physics*, Vol. 39, pp. 474–479.

Tien, C. L., and Drolen, B. L., 1987, "Thermal Radiation in Particulate Media With Dependent and Independent Scattering," *Annual Review of Numerical Fluid Mechanics and Heat Transfer*, Vol. 1, pp. 1–32.

Tien, C. L., 1988, "Thermal Radiation in Packed and Fluidized Beds," ASME JOURNAL OF HEAT TRANSFER, Vol. 110, pp. 1230–1242.

van de Hulst, H. C., 1981, *Light Scattering by Small Particles*, Dover, New York.

Watts, R. O., and Henderson, D., 1969, "Pair Distribution Function for Fluid Hard Spheres," *Molecular Physics*, Vol. 16, pp. 217–223.

Wertheim, M. S., 1963, "Exact Solution of the Percus–Yevick Integral Equation for Hard Spheres," *Physical Review Letters*, Vol. 10, pp. 321–322.

White, S. M., and Kumar, S., 1990, "Interference Effect on Scattering by Parallel Fibers at Normal Incidence," *Journal of Thermophysics*, Vol. 4, pp. 305–310.

Yamada, Y., Cartigny, J. D., and Tien, C. L., 1987, "Radiative Transfer With Dependent Scattering by Particles: Part 2," ASME JOURNAL OF HEAT TRANSFER, Vol. 108, pp. 615–619.

Downloaded 13 Dec 2010 to 193.140.21.150. Redistribution subject to ASME license or copyright; see http://www.asme.org/terms/Terms_Use.cfm

B. I. Choi

Z. M. Zhang

M. I. Flik

Department of Mechanical Engineering,
Massachusetts Institute of Technology,
Cambridge, MA 02139

T. Siegrist

AT&T Bell Laboratories,
Murray Hill, NJ 07974

Radiative Properties of Y-Ba-Cu-O Films With Variable Oxygen Content

The room-temperature radiative properties of $YBa_2Cu_3O_{7-\delta}$ superconducting films with varying oxygen content ($\delta = 0$ to 1) on a $LaAlO_3$ substrate are investigated. The fitting of reflectance spectra using thin-film optics and the Drude–Lorentz model function with multiple oscillators determines the optical constants. The film with high oxygen content ($\delta = 0$) has a metallic optical behavior. A decrease in the oxygen content causes a removal of free carriers, and the film with low oxygen content ($\delta = 1$) acts like a dielectric with a very weak free-electron contribution. Knowledge of the optical constants of oxygen-deficient $YBa_2Cu_3O_{7-\delta}$ films facilitates accurate substrate temperature measurement and control during the film deposition process.

1 Introduction

The application of high-temperature superconductors in electronic devices requires films with excellent electronic properties. To obtain high-quality superconducting films, the substrate temperature must be kept between 650°C and 800°C during the deposition process (Norton et al., 1989; Ramesh et al., 1991; Westerheim et al., 1991). If the temperature deviates from the optimum by only 10 K during deposition, the film properties are degraded significantly (Blank et al., 1990). Flik et al. (1992) showed that the substrate temperature is governed by thermal radiation heat transfer and changes as the film grows. They determined the change of the emittance with film thickness using thin-film optics. A possible method for the in-situ measurement and control of the substrate temperature is based on a pyrometer with an adaptive calibration of the substrate emittance.

The adaptive calibration requires the optical constants of the growing film. From the phase diagram, the growing film has an oxygen content close to 6 per unit cell (Morris et al., 1990). The unit cell of the $YBa_2Cu_3O_{7-\delta}$ superconductor is shown in Fig. 1. Depending on the temperature and the oxygen partial pressure, some or all of the oxygen atoms in the bottom and top planes are missing and the resulting properties are different from those of a fully oxidized superconductor. The optical constants of $YBa_2Cu_3O_{7-\delta}$ *films* whose oxygen content 7-δ varies from 6 to 7 must be investigated to facilitate the pyrometric measurement of the substrate temperature.

The optical properties of *ceramic* $YBa_2Cu_3O_{7-\delta}$ with oxygen content 7-δ between 6 and 7 were investigated by Thomsen et al. (1988) and Tajima et al. (1988). Since the test samples were multicrystalline ceramics, the optical properties of epitaxial films cannot be inferred from these studies. Recently Yasuoka et al. (1991) fabricated oxygen-deficient $YBa_2Cu_3O_{7-\delta}$ films by annealing films in vacuum and investigated absorption spectra in the wavelength range from 0.2 to 6.7 μm. They estimated the oxygen content of the annealed films by measuring the lattice parameters using x-ray diffraction. The correlation between lattice parameters and oxygen contents is not well established. The reported values of the lattice parameter vary among different sources for the same oxygen content. The estimation of the oxygen content based on the lattice parameters can have an error of ± 0.1. Studies of the film refractive index as a function of oxygen content are not available at present. This lack of data results from the difficulty of characterizing the oxygen content in films. There is no well-established technique for the measurement of oxygen content of films.

In the present work, $YBa_2Cu_3O_{7-\delta}$ films of known oxygen content are prepared by allowing them to achieve oxygen-pressure equilibrium with an $YBa_2Cu_3O_{7-\delta}$ pellet of known oxygen content. For the first time the oxygen content of films is changed in a controllable manner. The normal reflectance and normal transmittance are measured at room temperature for wavelengths from 1 to 100 μm using a Fourier-transform infrared spectrometer. The measured spectra are used to extract the optical constants of the film by applying thin-film optics and fitting measured reflectance data to a Drude–Lorentz model. The optical properties of $YBa_2Cu_3O_{7-\delta}$ superconductors are highly anisotropic due to the orthorhombic crystal structure shown in Fig. 1. Since the investigated $YBa_2Cu_3O_{7-\delta}$ film is epitaxial with the *c*-axis normal to the substrate, the measured normal-incidence spectra show the optical properties of the *ab*-plane.

Although the analysis of radiation heat transfer for the film deposition and the pyrometric temperature measurement require high-temperature optical properties, the room-temperature properties are investigated in order to identify the influence of the oxygen content, which in turn depends on temperature and gas environment. There is a separate influence of the temperature on the optical constants for a given oxygen

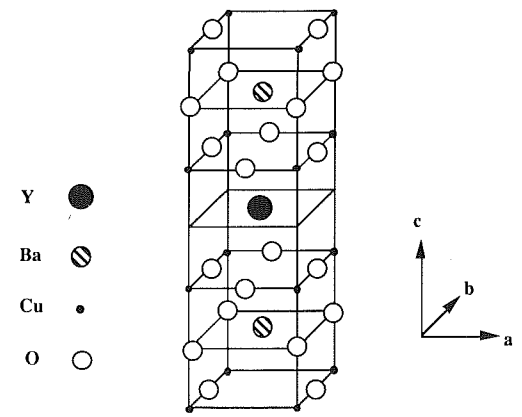

Fig. 1 Structure of the $YBa_2Cu_3O_7$ superconductor unit cell (Zhang et al., 1988)

Contributed by the Heat Transfer Division for publication in the JOURNAL OF HEAT TRANSFER. Manuscript received by the Heat Transfer Division July 1991; revision received February 1992. Keywords: Materials Processing and Manufacturing Processes, Radiation, Thermophysical Properties. Associate Technical Editor: R. O. Buckius.

Copyright © 1992 by ASME
Downloaded 13 Dec 2010 to 193.140.21.150. Redistribution subject to ASME license or copyright; see http://www.asme.org/terms/Terms_Use.cfm

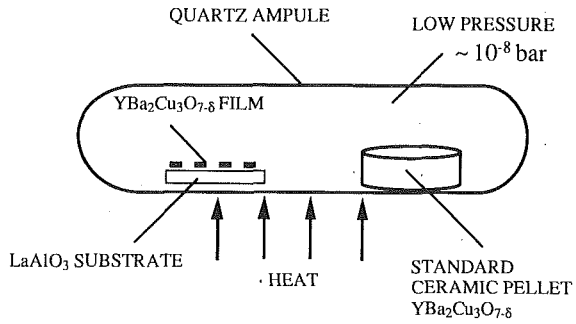

Fig. 2 Annealing of an $YBa_2Cu_3O_{7-\delta}$ film in order to change oxygen content

content, which is the subject of a future study. Once the high-temperature optical constants are known, the adaptively calibrated pyrometer can accurately measure the substrate temperature at any film thickness. This work also provides data for the design of devices that require $YBa_2Cu_3O_{7-\delta}$ films with tailored oxygen content.

2 Experiments

2.1 Sample Preparation. The oxygen content of the film is changed by allowing it to reach oxygen-pressure equilibrium with a ceramic pellet whose oxygen content is known precisely. As shown in Fig. 2, a film and a pellet are encapsulated in a quartz ampule, which is evacuated to a pressure lower than 10^{-8} bar. Since at temperatures above 400°C equilibrium with ambient oxygen pressure occurs rapidly (Gallagher et al., 1987), the oxygen pressure in the ampule is determined by the vapor pressure of the ceramic. Since the film mass is negligible compared to that of the ceramic, the oxygen content of the film adjusts according to the oxygen pressure in the ampule. The same film is used repeatedly to obtain different oxygen contents. In annealing, the ampule is heated rapidly from room temperature to 200°C and then at a rate of 1.5 K per minute up to the temperature above which oxygen diffusion out of the pellet is activated. This temperature varies depending on the oxygen content. It is 460°C for oxygen content $7\text{-}\delta = 6.8$, 510°C for $7\text{-}\delta = 6.6$, 560°C for $7\text{-}\delta = 6.4$, and 900°C for $7\text{-}\delta = 6.0$ (Gallagher et al., 1987). The ampule remains 15 min at that temperature to allow equilibrium between the film and pellet to be achieved and is cooled to room temperature at a rate of about 1.5 Ks^{-1}.

The ceramic oxygen content is determined by mixing appropriate ratios of $YBa_2Cu_3O_7$ and $YBa_2Cu_3O_6$ standard ceramics. The $YBa_2Cu_3O_7$ ceramic is prepared by a conventional method. Weighed quantities of $Ba(NO_3)_2$, Y_2O_3, and CuO are mixed by grinding and calcined to form the correct phase. The mixed powder is heated to 560°C in 3 h from room temperature and then in 4 h to 630°C. It stays at this temperature for 2 h and is heated to 950°C in 6 h and stays at this temperature for 10 h. After cooling to room temperature, the molten ceramic is ground by hand and the powder is pressed to form a pellet. The pellet is baked at 950°C for 24 h to ensure homogeneity. Complete oxygenation is achieved by annealing the pellet in oxygen for 5 h at 450°C, followed by slow cooling in oxygen. Annealing at 650°C in flowing N_2 gas produces $YBa_2Cu_3O_6$. Powder x-ray diffraction patterns show no impurity phases.

The $YBa_2Cu_3O_7$ film used for the investigation is deposited in a single-target, off-axis sputtering system. The film has a thickness of 0.28 μm and is deposited on a $LaAlO_3$ substrate 454 μm thick. The properties of films deposited in this system are a critical temperature (at zero resistance) of 88 K, and critical current densities of 2.8×10^7 A cm^{-2} at 4.2 K and 2.8×10^6 A cm^{-2} at 77 K (Westerheim et al., 1991).

2.2 Measurement. A Biorad FTS-60A Fourier-transform infrared (FT-IR) spectrometer is employed to measure the reflectance and transmittance for the wavelength region from 1 to 100 μm. A gold mirror is used as the reference for the reflectance measurements. The spectral reflectance is obtained by dividing the spectral response of the sample by the spectral response of the mirror. The reflectance of the gold mirror is estimated to be 0.99 for all wavelengths (Toscano and Cravalho, 1976), which is used as a correction factor for the raw data. To avoid reflections from the sample holder to the back of the sample, a black tape with a reflectance of less than 0.01 is placed beneath the sample. A more detailed description of the experimental setup for the reflectance and transmittance measurements was given by Zhang et al. (1991).

Nomenclature

d = thickness, m
e = charge of an electron $= 1.602\times10^{-19}$ C
i = $(-1)^{1/2}$
m_e = electron mass $= 9.110\times10^{-31}$ kg
$\bar{n}$ = complex refractive index $= n + i\kappa$
n = real part of refractive index
n_e = free carrier number density, m^{-3}
r = complex Fresnel coefficient for reflection
R_a = reflectance of film for incidence from air
R_b = reflectance of film for incidence from substrate
R_S = reflectance of substrate
R_{FS} = reflectance of film–substrate composite
S_j = oscillator strength of jth phonon
t = complex Fresnel coefficient for transmission
T_F = transmittance of film for incidence from air
T_p = transmittance along path inside substrate
T_S = transmittance of substrate
β = constant, Eq. (7), s
γ_e = oscillator width of midinfrared band, rad s^{-1}
γ_j = oscillator width of jth phonon, rad s^{-1}
δ_F = complex phase angle, rad
ϵ = dielectric function
ϵ_0 = electric permittivity of free space $= 8.85\times10^{-12}$ $C^2N^{-1}m^{-2}$
ϵ_∞ = high-frequency dielectric constant
κ = imaginary part of refractive index
λ = wavelength, m
ρ_S = reflectivity of substrate
σ = electric conductivity, $\Omega^{-1}m^{-1}$
τ = scattering time, s
φ = phase shift, rad
φ_c = corrected phase shift $= \varphi + \beta\omega$, rad
ω = frequency, rad s^{-1}
ω_e = center frequency of midinfrared band, rad s^{-1}
ω_p = plasma frequency, rad s^{-1}
ω_{pe} = plasma frequency of midinfrared band, rad s^{-1}
ω_j = oscillator frequency of jth phonon, rad s^{-1}

Subscripts

0 = air
a = interface between air and film
b = interface between film and substrate
F = film
S = substrate

Downloaded 13 Dec 2010 to 193.140.21.150. Redistribution subject to ASME license or copyright; see http://www.asme.org/terms/Terms_Use.cfm

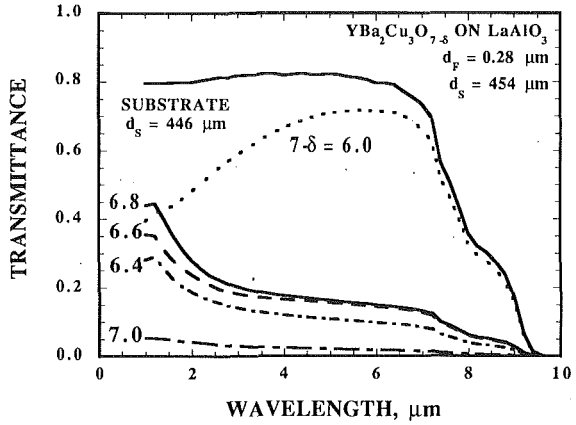

Fig. 3 Transmittance of a $LaAlO_3$ substrate and an $YBa_2Cu_3O_{7-\delta}$ film with varying oxygen content on a $LaAlO_3$ substrate

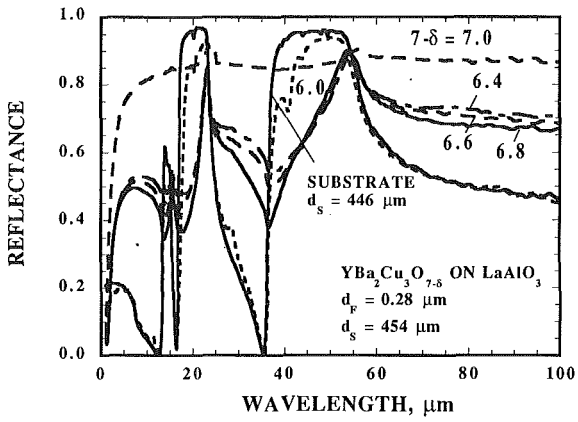

Fig. 4 Reflectance of a $LaAlO_3$ substrate and an $YBa_2Cu_3O_{7-\delta}$ film with varying oxygen content on a $LaAlO_3$ substrate

The photometric accuracy in the transmittance measurements is better than 1 percent for the near-infrared region, from 1 to 3 μm, and midinfrared region, from 2.5 to 25 μm, and 2 percent for the far-infrared region, from 20 to 100 μm. The agreement in the overlapping spectral regions is better than 2 percent. The photometric accuracy in the reflectance measurements is estimated to be better than 3 percent for all wavelengths considering the uncertainty in the estimated reflectance of the gold mirror.

The measured transmittance and reflectance of the film-substrate composite are shown in Figs. 3 and 4 and are compared to those of a bare $LaAlO_3$ substrate. To investigate whether the optical properties of $LaAlO_3$ change significantly with annealing, the bare substrate is annealed with the same conditions as those used in preparing the $YBa_2Cu_3O_6$ film, and the reflectance and transmittance are measured before and after the annealing. The results show only a 2 percent difference, which is within the photometric uncertainty of the FT-IR spectrometer. It is concluded that the optical properties of $LaAlO_3$ do not change with the annealing.

As the oxygen content decreases from 7 to 6, the transmittance of the film-substrate composite increases. The transmittance of the $YBa_2Cu_3O_6$ film on the substrate is very close to that of the bare substrate for 6 $\mu m < \lambda < 10$ μm. For wavelengths less than 6 μm, the $YBa_2Cu_3O_6$ film reduces the transmittance of the substrate. This cannot be caused by diffuse scattering at the film surface, because the film appears specular to the human eye and must have a surface roughness of 0.1 μm or less. Although the transmittance in Fig. 3 increases from 7-δ = 7.0 to 7-δ = 6.0, there is no monotonic change in the radiative properties between 7-δ = 6.4 and 7-δ = 6.8. Other properties of high-temperature superconductors such as transition temperature and d-c resistivity also do not change monotonically with the oxygen content (Cava et al., 1987). The reflectance data in Fig. 4 exhibit the same behavior. Since the $YBa_2Cu_3O_7$ film has a large absorption coefficient, the strong features of the $LaAlO_3$ substrate almost disappear in the reflectance. The films with oxygen contents between 7-δ = 6.4 and 7-δ = 6.8 show the substrate features. The penetration depths in these films are larger than the film thickness. The $YBa_2Cu_3O_6$ film on the substrate has a reflectance almost identical to that of the bare substrate. This film exhibits two strong phonon structures at wavelengths of 30 μm and 40 μm.

3 Analysis

To extract the complex refractive index from the measured data, thin-film optics is used in combination with a Drude-Lorentz dispersion relation.

3.1 Substrate. Since the refractive index of the $LaAlO_3$ substrate was not available, it is calculated from the measured data. The normal transmittance, T_S, and normal reflectance, R_S, of the substrate are given by Siegel and Howell (1981),

$$T_S = \frac{T_p(1-\rho_S)^2}{1-\rho_S^2 T_p^2} \tag{1}$$

$$R_S = \rho_S\left[1 + \frac{T_p^2(1-\rho_S)^2}{1-\rho_S^2 T_p^2}\right], \tag{2}$$

where T_p is the transmittance along the path inside the substrate and ρ_S is the reflectivity at the air-substrate interface. They are

$$T_p = \exp\left(-\frac{4\pi\kappa_S d_S}{\lambda}\right) \tag{3}$$

$$\rho_S = \frac{(n_S-1)^2+\kappa_S^2}{(n_S+1)^2+\kappa_S^2}, \tag{4}$$

where d_S is the thickness of the substrate and n_S and κ_S are the real and imaginary parts of the refractive index, which is a function of frequency, ω. Using the measured transmittance and reflectance values in the transparent spectral region from 1 to 9.5 μm, Eqs. (1)-(4) can be solved for n_S and κ_S using the Newton-Raphson method (Press et al., 1986).

For wavelengths longer than 9.7 μm, the substrate is opaque and the Kramers-Kronig transformation is applied (Wooten, 1972). The phase shift, φ, is the phase angle difference between the reflected wave and the incident wave, which is related to the complex refractive index by

$$\sqrt{\rho_S}\exp(i\varphi) = \frac{n_S + i\kappa_S - 1}{n_S + i\kappa_S + 1}. \tag{5}$$

The phase shift φ at a frequency ω is expressed as an integral of the reflectivity by

$$\varphi(\omega) = \frac{\omega}{\pi}\int_0^\infty d\omega' \, \frac{\ln\rho_S(\omega')}{\omega^2-\omega'^2}. \tag{6}$$

Since measured reflectivity data are available for only a limited spectral range from 9.7 to 100 μm, the reflectivity outside the measured range is extrapolated as follows: For $\lambda > 100$ μm, the reflectivity is extrapolated as a constant value equal to the measured value at $\lambda = 100$ μm. This is a good approximation because the measured value of 0.46 at $\lambda = 100$ μm is close to the reflectivity of 0.45 at 1 MHz, which is calculated from the dielectric constant reported by Lee et al. (1990). For the wavelength region $\lambda < 1$ μm, the reflectivity is extrapolated as a constant value equal to the reflectivity, ρ_S, at $\lambda = 1$ μm, which

Downloaded 13 Dec 2010 to 193.140.21.150. Redistribution subject to ASME license or copyright; see http://www.asme.org/terms/Terms_Use.cfm

is calculated from n_S and κ_S determined from the reflectance and transmittance measurements. Since the reflectivity inaccuracy for $\lambda < 1$ μm produces an error in the phase shift for $10\ \mu m \le \lambda \le 100\ \mu m$, which is approximately proportional to the frequency, a correction term, $\beta\omega$, is added to the phase shift,

$$\varphi_c = \varphi + \beta\omega. \tag{7}$$

The constant, $\beta = 4.791 \times 10^{-16}$ s, is determined such that the corrected phase shift, φ_c, is equal to that obtained from Eq. (5) using calculated n_S and κ_S at $\lambda = 9.5$ μm. The optical constants for $10\ \mu m \le \lambda \le 100\ \mu m$ are calculated from the measured ρ_S and the corrected phase angle using Eq. (5),

$$n_S = \frac{1-\rho_S}{1-2\sqrt{\rho_S}\cos\varphi_c + \rho_S} \tag{8}$$

$$\kappa_S = \frac{2\sqrt{\rho_S}\sin\varphi_c}{1-2\sqrt{\rho_S}\cos\varphi_c + \rho_S}. \tag{9}$$

3.2 Film–Substrate Composite. Once the optical constants of the substrate are known, thin-film optics relations and a Drude–Lorentz model function are used to find the film optical constants from the reflectance measurements. The reflectance of the film–substrate composite was given by Flik et al. (1992),

$$R_{FS} = R_a + \frac{\rho_S T_p^2 T_F^2}{1-\rho_S T_p^2 R_b} \tag{10}$$

$$R_a = \left| \frac{r_a + r_b e^{2i\delta_F}}{1 + r_a r_b e^{2i\delta_F}} \right|^2 \tag{11}$$

$$R_b = \left| \frac{r_b + r_a e^{2i\delta_F}}{1 + r_a r_b e^{2i\delta_F}} \right|^2, \tag{12}$$

where R_a is the normal reflectance of the film for radiation incident from the air, and R_b the normal reflectance of the film for incidence from the substrate. The transmittance of the film into the substrate, T_F, is

$$T_F = \frac{n_S}{n_0} \left| \frac{t_a t_b e^{i\delta_F}}{1 + r_a r_b e^{2i\delta_F}} \right|^2 \tag{13}$$

and the complex Fresnel coefficients for normal incidence are

$$r_a = \frac{\bar{n}_0 - \bar{n}_F}{\bar{n}_0 + \bar{n}_F} \tag{14}$$

$$t_a = \frac{2\bar{n}_0}{\bar{n}_0 + \bar{n}_F} \tag{15}$$

$$r_b = \frac{\bar{n}_F - \bar{n}_S}{\bar{n}_F + \bar{n}_S} \tag{16}$$

$$t_b = \frac{2\bar{n}_F}{\bar{n}_F + \bar{n}_S}. \tag{17}$$

The complex phase angle is

$$\delta_F = \frac{2\pi}{\lambda} \bar{n}_F d_F. \tag{18}$$

The measured reflectances are fitted using the Drude–Lorentz model. The dielectric function of $YBa_2Cu_3O_{7-\delta}$ can be expressed as (Timusk and Tanner, 1989)

$$\epsilon(\omega) = \epsilon_\infty + \sum_{j=1}^{6} \frac{S_j \omega_j^2}{\omega_j^2 - \omega^2 - i\omega\gamma} + \frac{\omega_{pe}^2}{\omega_e^2 - \omega^2 - i\omega\gamma_e} + \frac{i\sigma(\omega)}{\omega\epsilon_0}. \tag{19}$$

The first term on the right-hand side, ϵ_∞, is the high-frequency dielectric constant, which is approximately equal to 4 (Zimmermann et al., 1991). The second term is a superposition of the contributions of six phonons, with oscillator frequencies ω_j, strengths S_j, and widths γ_j. The third term is a midinfrared band, representing the electronic absorption caused by the transition of electrons between energy levels, which has a center frequency ω_e, plasma frequency ω_{pe}, and width γ_e. The last term is the contribution of free electrons, where ϵ_0 is the electric permittivity of free space, and $\sigma(\omega)$ is the frequency-dependent complex electric conductivity. The frequency-dependent conductivity can be expressed as a function of frequency by the Drude model,

$$\sigma(\omega) = \frac{\epsilon_0 \omega_p^2}{1/\tau - i\omega}, \tag{20}$$

where $1/\tau$ is the scattering rate and ω_p is the plasma frequency, which is given by $\omega_p = (n_e e^2/\epsilon_0 m_e)^{1/2}$, where n_e is the electron number density, e is the electron charge, and m_e is the electron mass. As in the work of Kamaras et al. (1990), the two adjustable parameters of the Drude term are the plasma frequency and the scattering rate. The real part, $n_F(\omega)$, and the imaginary part, $\kappa_F(\omega)$, of the film refractive index are determined by

$$[n_F(\omega) + i\kappa_F(\omega)]^2 = \epsilon(\omega). \tag{21}$$

The reflectance of the $YBa_2Cu_3O_7$ film can be fitted only with the Drude term and midinfrared absorption band in agreement with the results of Renk et al. (1990). The fitting of the reflectance of the $YBa_2Cu_3O_6$ film requires the Drude and the phonon contributions, while for films with intermediate oxygen constants, Drude term, midinfrared band, and phonon contributions serve to fit the reflectance data.

The fitting proceeds as follows: For the set of parameters in Eq. (19), the optical constants of $YBa_2Cu_3O_{7-\delta}$ films are determined from Eqs. (19)–(21) and the reflectance of the film–substrate composite is computed from Eq. (10). Comparing the calculated reflectance to the measured reflectance, the fitting parameters are adjusted such that the two reflectances agree within 5 percent. The sensitivity of the fitting has been investigated and uncertainties of the parameters are shown in Table 1. Since each term in Eq. (19) contributes to the reflectance in a distinct manner, its magnitude is determined from the fitting without ambiguity. A phonon contribution affects the reflectance only in a narrow spectral region around the resonance frequency and its magnitude and width can be determined independently of other phonons. The overall reflectance level is not influenced by changes in a phonon parameter but it is sensitive to the Drude parameters. The midinfrared band affects the reflectance only in the midinfrared region but not in the far-infrared region. Since these three mechanisms have their own unique behavior, they are not interchangeable.

4 Results

Figure 5 compares the measured reflectances of $YBa_2Cu_3O_{7-\delta}$ films of varying oxygen content with the fitted reflectances. The values of the fitting parameters in Eq. (19) are given in Table 1, and the values for the $YBa_2Cu_3O_6$ bulk sample obtained by Bauer et al. (1989) are also provided for comparison. For the $YBa_2Cu_3O_7$ film, the fitting does not predict the small features at 25 μm and 55 μm due to neglect of the phonon contribution. For $7-\delta = 6.6$ and 6.0, fitted and measured reflectances are in excellent agreement in the entire investigated wavelength region. The fitted reflectances of all films with varying oxygen content agree with the experimental data within 5 percent.

The real and imaginary parts of the refractive index of the $YBa_2Cu_3O_6$ film are compared in Figs. 6 and 7 to the data obtained by Bauer et al. (1989). They performed polarized reflectance measurements on a highly c-axis oriented (more than 95 percent) multicrystalline ceramic $YBa_2Cu_3O_6$ sample and performed a fitting resulting in the depicted phonon structure. The inclusion of the Drude term provides a slightly better

Downloaded 13 Dec 2010 to 193.140.21.150. Redistribution subject to ASME license or copyright; see http://www.asme.org/terms/Terms_Use.cfm

Table 1 Fitting parameters for $YBa_2Cu_3O_{7-\delta}$ films

OXYGEN CONTENT	7.0	6.8	6.6	6.4	6.0	Bauer et al. (1989)
PHONON PARAMETERS						
ω_1 (cm^{-1})		105	105	105	105	
S_1		0.8	0.8	0.8	0.7±0.3	
γ_1 (cm^{-1})		5	5	5	5±1	
ω_2 (cm^{-1})		114	114	114	114	116
S_2		0.8	0.8	0.8	1±0.5	2.1
γ_2 (cm^{-1})		5.5	5.5	5.5	6±1	3.9
ω_3 (cm^{-1})		179	179	179	188	188
S_3		3.6	3.6	3.6	0.6±0.3	1.9
γ_3 (cm^{-1})		5.0	5.0	5.0	7±0.5	5.5
ω_4 (cm^{-1})		246	246	246	246	246
S_4		0.016	0.016	0.016	0.5±0.2	1.4
γ_4 (cm^{-1})		28	28	28	20±5	3.9
ω_5 (cm^{-1})		351	351	351	351	351
S_5		0.56	0.56	0.56	0.7±0.2	2.5
γ_5 (cm^{-1})		17	17	17	17±3	17.2
ω_6 (cm^{-1})		595	595	595	595	595
S_6		0.05	0.05	0.05	0.3±0.1	0.4
γ_6 (cm^{-1})		23	23	23	23±5	14
FREE-CARRIER PARAMETERS						
ω_p (cm^{-1})	9600±200	4100±200	4150	4200	800	
$1/\tau$ (cm^{-1})	660±60	660±60	540	450	550	
MID-INFRARED BAND PARAMETERS						
ω_e (cm^{-1})	1800	1800	1800	1800		
ω_{pe} (cm^{-1})	24150±4000	10800±2000	10800	10800		
γ_e (cm^{-1})	7500±600	6000±1000	5000	5000		

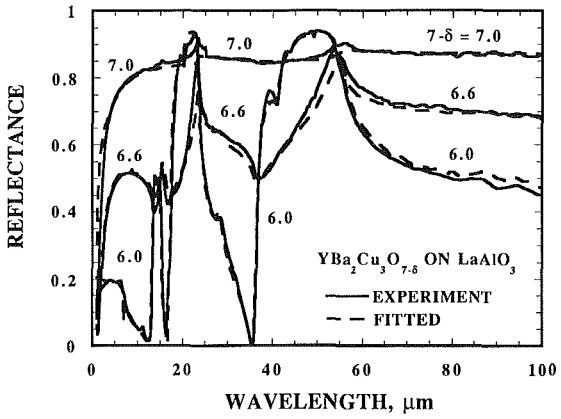

Fig. 5 Comparison between the fitted reflectances and experimental data

agreement between the fitted and measured reflectance at wavelength $\lambda = 20$ μm, but the influence of the Drude term on the reflectance in the whole spectral range is very small due to its low plasma frequency. Both the film and oriented ceramic sample have the same resonance frequencies except at $\lambda = 95$ μm. Bauer et al. (1989) also predicted a phonon at this wavelength from lattice-dynamic calculations, but they could not observe it experimentally. In contrast, the present reflectance data of the $YBa_2Cu_3O_6$ film clearly exhibit a phonon feature at $\lambda = 95$ μm. Compared to the results of Bauer et al. (1989), the phonons of the film are weaker and wider. These discrepancies can be explained by the different microstructures of the two samples.

The extracted optical constants are shown in Figs. 8 and 9.

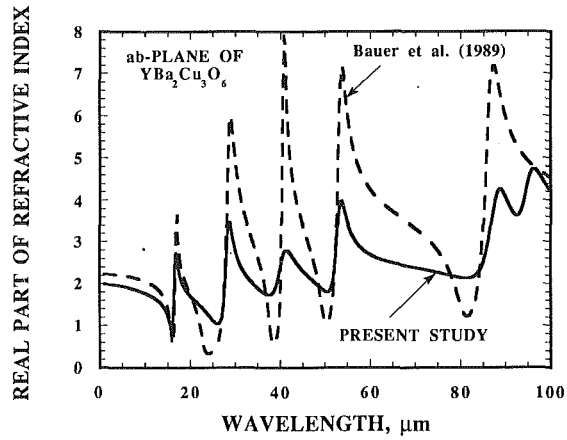

Fig. 6 Comparison of the real part of the refractive index of an $YBa_2Cu_3O_6$ film with that of a multicrystalline ceramic sample

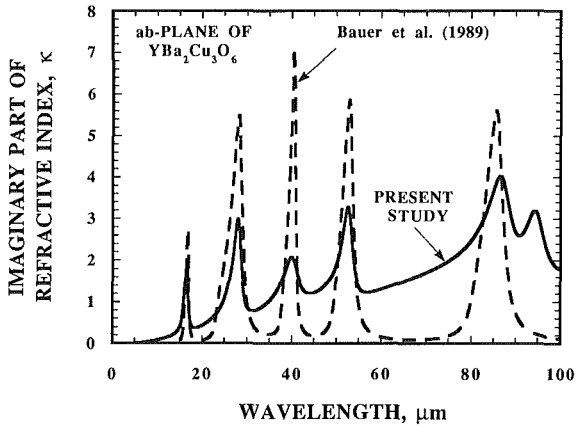

Fig. 7 Comparison of the imaginary part of the refractive index of an $YBa_2Cu_3O_6$ film with that of a multicrystalline ceramic sample

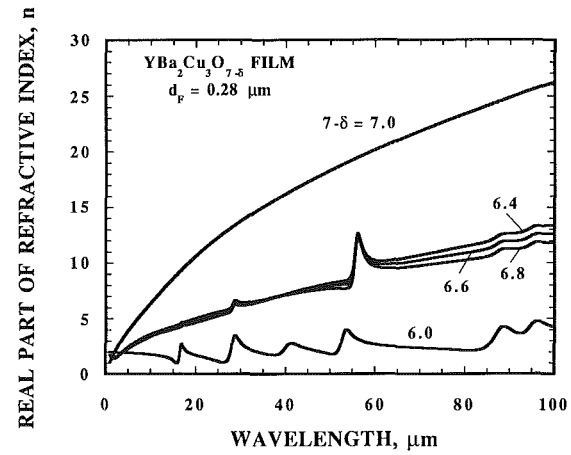

Fig. 8 Real part of the refractive index of $YBa_2Cu_3O_{7-\delta}$ films with varying oxygen content

The $YBa_2Cu_3O_7$ film shows metallic behavior with n and κ increasing and approaching each other as wavelength increases. As the oxygen content of the film decreases, the phonon features become visible, which are screened for $7-\delta = 7.0$ by the strong contribution of the free carriers. At $7-\delta = 6.0$, the free carrier contribution is very weak. The refractive indices of films with intermediate oxygen contents between $7-\delta = 6.4$ and 6.8 are nearly the same and do no change monotonically with oxygen content. The optical constants of an $YBa_2Cu_3O_{7-\delta}$ film

Downloaded 13 Dec 2010 to 193.140.21.150. Redistribution subject to ASME license or copyright; see http://www.asme.org/terms/Terms_Use.cfm

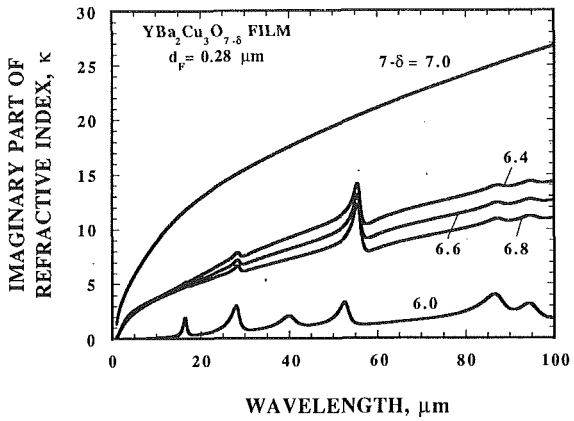

Fig. 9 Imaginary part of the refractive index of $YBa_2Cu_3O_{7-\delta}$ films with varying oxygen content

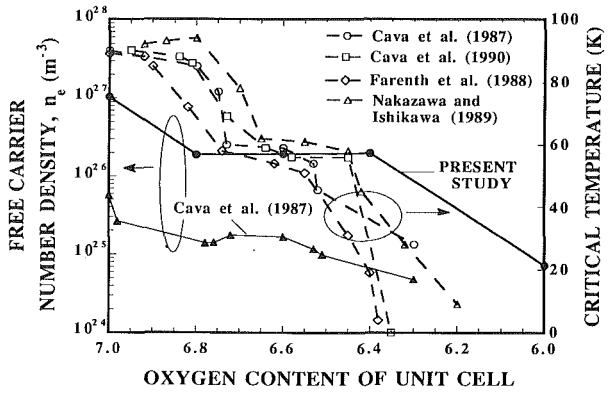

Fig. 10 Free-carrier number density and critical temperature for varying oxygen content

exhibit a sharp change when the oxygen content changes from $7\text{-}\delta = 7.0$ to 6.8 and from $7\text{-}\delta = 6.4$ to 6.0. The optical features outside the measurement spectral range may influence the optical properties near the limit of the measurement spectral range. This is the case for an $YBa_2Cu_3O_6$ film with an absorption band in the visible range (Yasuoka et al., 1991). Since the present study does not include this band of the $YBa_2Cu_3O_6$ film for the fitting, the fitted results underpredict the imaginary part of refractive index of the $YBa_2Cu_3O_6$ film near $\lambda = 1$ μm.

Since the oxygen atoms provide the charge carriers, the free-carrier number density would be expected to be linearly dependent on the oxygen content. Figure 10 shows that this is not true. The free-carrier number density is calculated by $n_e = \omega_p^2 \epsilon_0 m_e / e^2$, assuming that the effective mass of the free carriers is equal to the electron rest mass independent of the oxygen content. The plasma frequencies, ω_p, of films with varying oxygen content are obtained by fitting and compiled in Table 1. The fitted plasma frequencies for $7\text{-}\delta = 6.8$, 6.6, and 6.4 have 5 percent uncertainty, resulting in a 10 percent uncertainty in the calculated free-carrier number density. The calculated free-carrier number density of the $YBa_2Cu_3O_7$ film is 1.0×10^{27} m^{-3}. If the film has an oxygen content $7\text{-}\delta = 6.8$, the free-carrier number density decreases to 1.9×10^{26} m^{-3}. The number density is almost constant for an oxygen content between 6.4 and 6.8. For the $YBa_2Cu_3O_6$ film, the number density is calculated as 7.0×10^{24} m^{-3}, which is eight orders of magnitude larger than that of pure silicon at room temperature (Wolf and Tauber, 1986).

The free-carrier number densities are also calculated based on the d-c conductivity, σ, reported by Cava et al. (1987) from the equation $n_e = m_e \sigma / (e^2 \tau)$. The scattering rates, $1/\tau$, are assumed to be those obtained in the present study. The sample used for the d-c conductivity measurement was multicrystalline, and the scattering rates obtained from the epitaxial film in this study may not be the same. However, a qualitative comparison should be possible. The number density obtained from the d-c conductivity also does not change monotonically with the oxygen content. Figure 10 also shows the critical temperatures of $YBa_2Cu_3O_{7-\delta}$ bulk samples with varying oxygen contents, which were measured by several groups (Cava et al., 1987, 1990; Farenth et al., 1988; Nakazawa and Ishikawa, 1989). It is generally observed that the $YBa_2Cu_3O_{7-\delta}$ superconductor has two distinct phases that are superconducting at 90 K and 60 K. Since the reflectance spectra of the $YBa_2Cu_3O_{7-\delta}$ film with oxygen contents between $7\text{-}\delta = 7.0$ and 6.8 are not resolved, the plateau feature of the 90 K phase cannot be observed. However, the results of the present study clearly show the 60 K phase in the samples with oxygen contents between $7\text{-}\delta = 6.8$ and 6.4, where the free-carrier number density is constant. This region corresponds to an orthorhombic II phase in the crystal structure, where the lattice constants are such that $a < b < c/3$. In an orthorhombic I phase, the lattice constants are such that $a < b \approx c/3$ and in a tetragonal phase, $a = b < c/3$. Across the phase boundaries, a drastic change in the free-carrier number density is observed.

The nonlinear variation of the calculated free-carrier number density with oxygen content can be explained with the charge reservoir model proposed by Cava (1990). Analyzing the local charge distribution in the crystal structure, he observed that the amount of positive charge in the chemical bonds of the Cu atoms of the superconducting Cu–O planes shows a nonlinear behavior similar to that of the carrier number density variation with oxygen content. The superconducting Cu–O planes are the third layers from the bottom and top of the unit crystal cell of Fig. 1, and these layers are responsible for the electrical properties of $YBa_2Cu_3O_{7-\delta}$ superconductors. With increasing oxygen deficiency, oxygen atoms in the chain Cu–O layer, the top and bottom layer of Fig. 1, are removed. The electrons that were originally attached to these oxygen atoms are transferred to the Cu–O planes, resulting in a decrease in the hole population of the Cu–O planes. The amount of electrons moving to the Cu–O planes depends on the oxygen deficiency. For small deficiencies, the electrons formerly bonded to the oxygen are not transferred to the Cu–O planes but remain in electronic states of the Cu–O chains. For oxygen deficiencies up to $7\text{-}\delta = 6.55$, the electrons are gradually transferred to the Cu–O planes, yielding a plateau for an oxygen content between 6.4 and 6.8. The electrons produced by oxygen removal are stored in the reservoir of the chain Cu–O layers up to a critical value of $7\text{-}\delta = 6.55$. Finally, for the oxygen content smaller than $7\text{-}\delta = 6.55$, further negative charge is abruptly transferred to the planes and the carrier density decreases significantly. Cava (1990) proposed that the chain Cu–O layers act as charge reservoirs, controlling the amount of free carriers in the superconducting Cu–O planes.

5 Conclusions

1 The optical properties of an $YBa_2Cu_3O_7$ film can be modeled with free electrons and an electronic midinfrared absorption band. This film shows metallic behavior.

2 An $YBa_2Cu_3O_6$ film has dielectric characteristics and its optical behavior can be modeled with phonon oscillators representing bound charges and with a weak free-electron contribution. The phonons of the film have the same resonance frequencies as those of a multicrystalline ceramic sample, but are weaker.

3 For the films with intermediate oxygen contents, the optical properties result from the superposition of both free carrier and phonon contributions. They have almost identical optical characteristics for oxygen contents from $7\text{-}\delta = 6.8$ to

Downloaded 13 Dec 2010 to 193.140.21.150. Redistribution subject to ASME license or copyright; see http://www.asme.org/terms/Terms_Use.cfm

6.4. In this range of oxygen content, the films exhibit metallic features with smaller plasma frequencies than that of the $YBa_2Cu_3O_7$ film. The oxygen content affects the optical constants through the free-carrier number density.

4 Free-carrier number densities calculated from the fitted plasma frequencies agree qualitatively with those of ceramic samples and show a plateau behavior similar to the oxygen-content dependence of the critical temperature. The reflectance spectra can be used to characterize the oxygen content of $YBa_2Cu_3O_{7-\delta}$ films.

Acknowledgments

The authors are grateful to Dr. A. C. Anderson of Lincoln Laboratory for the preparation of the film employed in this study and for his valuable comments. The technical assistance of Y. L. Xie is acknowledged. The authors thank K. E. Goodson and C. G. Malone for their critical review. This work was conducted under the auspices of the Consortium for Superconducting Electronics with support from the Defense Advanced Research Projects Agency, contract No. MDA972-90-C-0021.

References

Bauer, M., Ferreira, I. B., Genzel, L., Cardona. M., Murugaraj, P., and Maier, J. 1989, "Far-Infrared Study of Optical Phonons in an $YBa_2Cu_3O_6$ Crystal," *Solid State Commun.*, Vol. 72, pp. 551–554.

Blank, D. H. A., Adelerhof, D. J., Flokstra, J., and Rogalla, H., 1990, "Preparation of YBaCuO Thin Films on Various Substrates by Laser Ablation: Influence of the Substrate Temperature," *Physica C*, Vol. 167, pp. 423–432.

Cava, R. J., Batlogg, B., Chen, C. H., Rietman, E. A., Zahurk, S. M., and Werder, D., 1987, "Single-Phase 60 K Bulk Superconductor in Annealed $Ba_2YCu_3O_{7-\delta}$ ($0.3<\delta<0.4$) With Correlated Oxygen Vacancies in the Cu–O Chains," *Phys. Rev. B*, Vol. 36, pp. 5719–5722.

Cava, R. J., 1990, "Structural Chemistry and the Local Charge Picture of Copper Oxide Superconductors," *Science*, Vol. 247, pp. 656–662.

Cava, R. J., Hewat, A. W., Hewat, E. A., Batlogg, B., Marezio, M., Rabe, K. M., Krajewski, J. J., Peck, W. F., Jr., and Rupp, L. W., Jr., 1990, "Structural Anomalies, Oxygen Ordering and Superconductivity in Oxygen Deficient $YBa_2Cu_3O_x$," *Physica C*, Vol. 165, pp. 381–384.

Farenth, W. E., Bordia, R. K., McCarron, E. M., III, Crawford, M. K., and Flippen, R. B., 1988, "Influence of Oxygen Stoichiometry on the Structure and Superconducting Transition Temperature of $YBa_2Cu_3O_x$," *Solid State Commun.*, Vol. 66, pp. 953–959.

Flik, M. I., Choi, B. I., Anderson, A. C., and Westerheim, A. C., 1992, "Thermal Analysis and Control for Sputtering Deposition of High-T_c Superconducting Films," ASME JOURNAL OF HEAT TRANSFER, Vol. 114, pp. 255–263.

Gallagher, P. K., O'Bryan, H. M., Sunshine, S. A., and Murphy, D. W., 1987, "Oxygen Stoichiometry in $Ba_2YCu_3O_x$," *Mat. Res. Bull.*, Vol. 22, pp. 995–1006.

Kamaras, K., Herr, S. L., Porter, C. D., Tache, N., Tanner, D. B., Etemad, S., Venkatesan, T., Chase, E., Inam, A., Wu, X. D., Hegde, M. S., and Dutta, B., 1990, "In a Clean High-T_c Superconductor You Do Not See the Gap," *Phys. Rev. Lett.*, Vol. 64, pp. 84–87.

Lee, A. E., Platt, C. E., Burch, J. F., and Simon, R. W., 1990, "Epitaxially Grown Sputtered $LaAlO_3$ Films," *Appl. Phys. Lett.*, Vol. 57, pp. 2019–2021.

Morris, D. E., Markelz, A. G., Fayn, B., and Nickel, J. H., 1990, "Conversion of 124 Into 123 + CuO, and 124, 123, and 247 Phase Regions in the Y–Ba–Cu–O System," *Physica C*, Vol. 168, pp. 153–156.

Nakazawa, Y., and Ishikawa, M., 1989, "Effects of Oxygen Stoichiometry and Oxygen Ordering in $Ba_2YCu_3O_y$ ($6\leq y\leq 7$)," *Physica C*, Vol. 158, pp. 381–384.

Norton, M. G.; Tietz, L. A., Summerfelt, S. R., Carter, C. B., 1989, "Observation of the Early Stages of Growth of Superconducting Thin Films by Transmission Electron Microscopy," *Appl. Phys. Lett.*, Vol. 55, pp. 2348–2350.

Press, W. H., Flannery, B. P., Teukolsky, S. A., and Vetterling, W. T., 1986, *Numerical Recipes*, Cambridge University Press, New York, Chap. 9.

Ramesh, R., Inam, A., Hwang, D. M., Sands, T. D., Chang, C. C., and Hart, D. L., 1991, "Surface Roughness Problem in *c*-Axis Oriented Y–Ba–Cu–O Superconducting Thin Films," *Appl. Phys. Lett.*, Vol. 58, pp. 1557–1559.

Renk, K. F., Eschrig, H., Hofmann, U., Keller, J., Schützmann, J., and Ose, W., 1990, "Dynamical Conductivity of High-T_c Superconductors," *Physica C*, Vol. 165, pp. 1–7.

Siegel, R., and Howell, J. R., 1981, *Thermal Radiation Heat Transfer*, 2nd ed., McGraw-Hill, New York, Chap. 19.

Tajima, S., Nakahashi, T., Uchida, S., and Tanaka, S., 1988, "Correlation Between Plasma Frequency and Superconducting Transition Temperature in $YBa_2Cu_3O_y$," *Physica C*, Vol. 156, pp. 90–96.

Timusk, T., and Tanner, D. B., 1989, "Infrared Properties of High-T_c Superconductors," in: *Physical Properties of High-Temperature Superconductors I*, D. M. Ginsberg, ed., World Scientific Publishing Company, Singapore, pp. 339–407.

Thomsen, C., Liu, R., Bauer, M., Wittlin, A., Genzel, L., Cardona, M., Schönherr, E., Bauhofer, W., and König, W., 1988, "Systematic Raman and Infrared Studies of the Superconductor $YBa_2Cu_3O_{7-\delta}$ as a Function of Oxygen Concentration ($0\leq x\leq 1$)," *Solid State Commun.*, Vol. 65, pp. 55–58.

Toscano, W. M., and Cravalho, E. G., 1976, "Thermal Radiation Properties of the Noble Metals at Cryogenic Temperatures," ASME JOURNAL OF HEAT TRANSFER, Vol. 98, pp. 438–445.

Westerheim, A. C., Yu-Jahnes, L. S., and Anderson, A. C., 1991, "Off-Axis Magnetron Sputtering of YBCO Films: The Influence of Atomic Oxygen," *IEEE Trans. Magn.*, Vol. 27, pp. 1001–1005.

Wolf, S., and Tauber, R. N., 1986, *Silicon Processing for the VLSI Era, Vol. 1—Process Technology*, Lattice Press, Sunset Beach, CA, p. 647.

Wooten, F., 1972, *Optical Properties of Solids*, Academic Press, New York, Chap. 6.

Yasuoka, T., Mazaki, H., Terashima, T., and Bando, Y., 1991, "Optical Absorption Spectra of Single-Crystal $YBa_2Cu_3O_y$ Films," *Physica C*, Vol. 175, pp. 192–196.

Zhang, K., Bunker, G. B., Zhang, G., Zhao, Z. X., Chen, L. Q., and Huang, Y. Z., 1988, "Extended X-Ray Absorption Fine-Structure Experiment on the High-T_c Superconductor $YBa_2Cu_3O_{7-\delta}$," *Phys. Rev. B*, Vol. 37, pp. 3375–3380.

Zhang, Z. M., Choi, B. I., Le, T. A., Flik, M. I., Siegal, M. P., and Phillips, J. M., 1991, "Infrared Refractive Index of Thin $YBa_2Cu_3O_7$ Superconducting Films," *Thin-Film Heat Transfer—Properties and Processing*, M. K. Alam et al., eds., ASME HTD-Vol. 184, pp. 1–8; to appear in ASME JOURNAL OF HEAT TRANSFER.

Zimmermann, W., Brandt, E. H., Bauer, M., Seider, E., and Genzel, L., 1991, "Optical Conductivity of BCS Superconductors With Arbitrary Purity," *Physica C*, Vol. 183, pp. 99–104.

Downloaded 13 Dec 2010 to 193.140.21.150. Redistribution subject to ASME license or copyright; see http://www.asme.org/terms/Terms_Use.cfm

Evaporation of Single Drops of *n*-Pentane/*n*-Hexane Mixtures in Water

H. Shimaoka[1]
Graduate Student.

Y. H. Mori
Professor.
Mem. ASME

Department of Mechanical Engineering,
Keio University,
3-14-1 Hiyoshi, Kohoku-ku,
Yokohama 223, Japan

The evaporation of isolated drops (2.1–3.0 mm diameter) of nonazeotropic n-pentane/n-hexane mixtures in the medium of water was observed under pressures of 0.11–0.46 MPa and temperature differences up to 27 K. The mole fractions of n-pentane, x, in the mixtures were set at 0.9, 0.5, 0.1, and 0, to be completed by the condition x = 1 set in a preceding work (Shimaoka and Mori, 1990). Experimental results are presented in terms of the instantaneous rise velocity of, and an expression of instantaneous heat transfer to, each drop evaporating and thereby transforming into a liquid/vapor two-phase bubble and finally into a vapor bubble. The dependencies of the heat transfer characteristics on the pressure, the temperature difference, and x are discussed.

Introduction

This paper compiles results of a work performed as a part of our ongoing experimental program on direct-contact evaporation of single liquid drops in an immiscible liquid medium. The program aims at investigating the physics of the phenomena involved and at the same time at obtaining information of practical importance that is applicable to mathematical modeling of spray-column, direct-contact evaporators. (Typical examples of the evaporator modeling are given by Smith et al., 1982; Çoban and Boehm, 1989; Mori, 1991; and Tadrist et al., 1991.) Since evaporation should transform each drop immediately into a "two-phase bubble"—which consists of a growing vapor phase and a reducing liquid phase—and finally into a single-phase vapor bubble, while rising in the medium, the variations of the rise motion of, and of the heat transfer to, each two-phase bubble with the progress of evaporation are the information of primary importance for the modeling.

After establishing appropriate experimental techniques (Shimizu and Mori, 1988a) in the first step in the abovementioned program, our effort was addressed to studying the evaporation of small-diameter drops of *n*-pentane and R 113 in water (Shimizu and Mori, 1988b) and then that of larger *n*-pentane drops (Shimaoka and Mori, 1990). As a whole, the experiments with *n*-pentane drops in water have covered the range 1.4–6.5 mm in initial drop diameter and 0.11–0.49 MPa in system pressure. Some correlations describing the characteristics of heat transfer in the above range have been prepared.

Besides dealing with evaporation of single-component drops, an investigation of evaporation of nonazeotropic mixture drops was commenced. The only work reported so far on this aspect is limited, however, to the case of rather small drops of a blend of 10-mole-percent R 114 and 90-mole-percent R 113 (Shimizu et al., 1989). The blend has some advantages as a test fluid for laboratory experiments, but no opportunity for using it (or any other CFC blends as well) in an industrial evaporator will be found because of the CFC restrictions. In view of an appreciable difference in heat transfer characteristics between *n*-pentane drops and R 113 drops both evaporating in water (Shimizu and Mori, 1988b), it is reasonable to assume that the heat transfer characteristics controlling the evaporation of drops of such alkane blends as those considered for practical use elsewhere (Mines et al., 1983; Goswami et al., 1987) may differ considerably from those observed with the R 114/R 113 blend.

In the above-stated context, we set up the present work to observe the evaporation of *n*-pentane/*n*-hexane mixture drops in water. The work covered the full range of mixture compositions [but with the aid of the previous work dealing with pure *n*-pentane drops (Shimaoka and Mori, 1990)], 2.1–3.0 mm in initial drop diameter, 0.11–0.46 MPa in system pressure, and 2.6–27 K in initial temperature difference. The motion of, and the heat transfer to, each two-phase bubble are described, the dependencies of the latter on the composition, the pressure, and the temperature difference being particularly stressed.

Experimental

Throughout our experimental program briefly surveyed in the preceding section, we have used essentially the same apparatus and procedure, but with minor modifications made at some phases of the program. In the present work, we used exactly the same versions of the apparatus and procedure that we had once used in dealing with R 114/R 113 mixture drops. Therefore, readers can consult the paper of Shimizu et al. (1989) to find sufficient details of the apparatus and procedure and also of the data processing, while the major portion of the apparatus is described in a greater detail in an earlier paper (Shimizu and Mori, 1988a). For this reason, the description in this section is cut short, except for the evaluation of the thermodynamic properties of the *n*-pentane/*n*-hexane mixtures and that of the uncertainties of the data processed.

Apparatus and Procedure. The major portion of the apparatus consisted of a cylindrical polycarbonate column of 77 mm i.d., in which a test fluid, water, was to be confined, and a rectangular, polycarbonate-made water jacket set concentrically with the inner cylindrical column. The jacket served as a constant-temperature water bath and also contributed to minimizing the optical distortion of the images of bubbles or drops inside the cylindrical column. The column was equipped with a high-pressure syringe assembly with which *n*-pentane/*n*-hexane mixture drops could be released into the column at its bottom irrespective of the pressure set in the column, an electric discharge device for inducing nucleation inside each drop, and a dilatometer, which was to indicate the change in volume of a two-phase bubble in the course of evaporation of each mixture drop. The volume–time and position–time records obtained dilatometrically and photographically, respec-

[1]Current address: Kōei-sha, Ltd., 33-5 Ōyaguchi-kitamachi, Itabashi-ku, Tokyo, 173, Japan.

Contributed by the Heat Transfer Division for publication in the JOURNAL OF HEAT TRANSFER. Manuscript received by the Heat Transfer Division October 1991; revision received March 1992. Keywords: Direct-Contact Heat Transfer, Evaporation, Sprays/Droplets. Associate Technical Editor: L. C. Witte.

Copyright © 1992 by ASME
Downloaded 13 Dec 2010 to 193.140.21.150. Redistribution subject to ASME license or copyright; see http://www.asme.org/terms/Terms_Use.cfm

tively, with each two-phase bubble constituted the primary data set from which the information on the motion of, and the heat transfer to, the bubble was to be extracted.

For the purpose of saving time in the experiments, the temperature difference between the continuous phase of water and evaporating two-phase bubbles was adjusted by changing the pressure in the column, while the water temperature was held constant, instead of changing the water temperature under a constant pressure in the column. This scheme of the experiments caused some ambiguity, as discussed later, in evaluating separately the pressure dependence and the temperature-difference dependence of the heat transfer characteristics.

Fluid Samples and Their Properties. Water used as the continuous phase in the test column was taken from a commercial purification apparatus, which was comprised of a reverse-osmosis device and an ion-exchange device as well as an all-glass distillation unit. *n*-Pentane and *n*-hexane were of 99.0 and 96.0 wt % certified purities, respectively. They were so blended as to yield three different mixtures in which x, the mole fraction of *n*-pentane, was 0.9, 0.5, and 0.1, respectively. The *n*-hexane was also preserved, undiluted, to be used as the fourth sample ($x=0$).

The physical properties of water were evaluated by use of curve-fitting correlations that Shimizu (1989) prepared based on the data given in *JSME Steam Tables* (1980) and *JSME Data Book* (1983). The properties of the *n*-pentane/*n*-hexane mixtures over the range of the present experiments were once calculated, using a computer program developed by Deeds (1979). Applying regression analyses to the numerical output thus obtained, we prepared a correlation for each of the properties (x_V, x_L, v_V, v_L, h_V, h_L) relevant to each of the three x values (0.9, 0.5, and 0.1) in the form of a polynomial function of temperature and pressure. A complete list of the correlations is given by Shimaoka (1990). Here we only illustrate in Fig. 1 the isobaric vapor–liquid equilibria (VLE) given by the correlations, as compared with those predicted by Deeds' program directly. In processing each data set, we used exclusively the correlations, instead of Deeds' program, to save the enormously long computation time otherwise required.

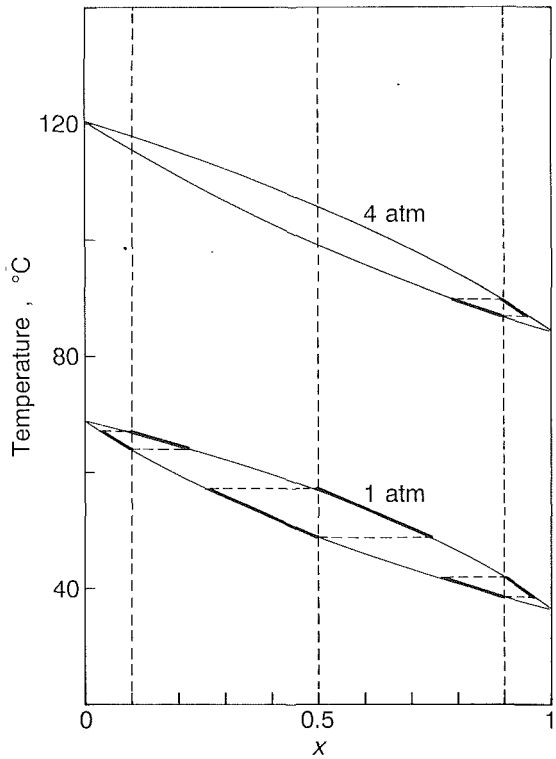

Fig. 1 Isobaric VLE for the *n*-pentane/*n*-hexane mixtures as predicted by Deeds' program (fine solid lines) and by polynomial correlations used in this study (bold solid lines)

No convincing means was available to examine the accuracy of Deeds' program, which had been used in prior works dealing with hydrocarbon mixtures (Mines et al., 1983; Goswami et

Nomenclature

C = constant defined by Eq. (5)
D = diameter of sphere volume, equivalent to two-phase bubble
D_0 = initial drop diameter
g = acceleration due to gravity
h = specific enthalpy
H_d = sum of enthalpies of *n*-pentane and *n*-hexane in two-phase bubble
H_t = sum of enthalpies of *n*-pentane, *n*-hexane, and water in two-phase bubble
n = number of moles of *n*-pentane/*n*-hexane mixture in liquid or vapor state in two-phase bubble
N = total number of moles of *n*-pentane/*n*-hexane mixture in two phase bubble
Nu = Nusselt number defined as $\alpha D/\lambda_c$
p_∞, p^*_∞ = pressure in the continuous phase and its value at the location where drop evaporation starts
Pe = Péclet number defined as UD/κ_c
Re = Reynolds number defined as UD/λ_c
t = time
t_v = time required for complete evaporation of drop
T_{if} = temperature at evaporating interface in two-phase bubble
T_s = temperature of two-phase bubble assumed to be instantaneously in thermal equilibrium
T = undisturbed temperature in the continuous phase
ΔT = $T_\infty - T_s$
ΔT^*, $\Delta T^\dagger$ = initial and final values of ΔT
U = rise velocity of two-phase bubble
v = specific volume
V = volume of two-phase bubble
x = mole fraction of *n*-pentane in *n*-pentane/*n*-hexane mixture to form drops or, when accompanied with subscript L or V, mole fraction of *n*-pentane in liquid or vapor phase in partially vaporized mixture
α = heat transfer coefficient based on surface area of sphere volume—equivalent to two-phase bubble
κ = thermal diffusivity
λ = thermal conductivity
ν = kinematic viscosity
ξ = evaporation ratio defined as n_v/N
ρ = mass density
$\Delta\rho$ = difference between ρ_c and average mass density of two-phase bubble

Subscripts

c = continuous-phase substance
L = *n*-pentane/*n*-hexane mixture in liquid state
V = *n*-pentane/*n*-hexane mixture in vapor state

Downloaded 13 Dec 2010 to 193.140.21.150. Redistribution subject to ASME license or copyright; see http://www.asme.org/terms/Terms_Use.cfm

al., 1987). The only check we made was the comparison of the predictions by Deeds' program of the properties at $x \to 0$ or $x \to 1$ with relevant data given in *TRC Tables* (1989). There was no significant discrepancy noted between them.

The use of the approximate correlations we prepared, instead of direct use of Deeds' program, is more or less an error source, which is taken into account in evaluating the uncertainties of the final results of the data processing.

Data Processing. In the same way as previously (Shimizu and Mori, 1988b; Shimizu et al., 1989), discrete position(z)-time(t) and volume(V)-time(t) data obtained photographically and dilatometrically, respectively, in each experimental run were transformed into continuous z-t and V-t relations with the aid of curve-fitting procedures. The former relation was utilized to calculate the instantaneous velocity of bubble rise, U ($=dz/dt$). The latter relation was utilized to deduce the instantaneous heat transfer coefficient α as described below.

In deducing α, we assume an instantaneous thermal equilibrium being established in each bubble. That is, the bubble is assumed to be composed of a ternary *n*-pentane/*n*-hexane/water vapor mixture and a binary *n*-pentane/*n*-hexane liquid mixture, both being in equilibrium at a temperature T_s, which should vary with the progress of evaporation indicated by $\xi \equiv n_V/N$; where n_V is the sum of the numbers of moles of *n*-pentane and *n*-hexane in the vapor phase, and N is that inside the whole bubble. Being consistent with the multiple definitions of α that we indicated in dealing with evaporation of single-component drops (Shimaoka and Mori, 1990), we can define α in the present case in the following two ways:

$$\alpha_3 = \frac{dH_d/dt}{\pi D^2 \Delta T}, \tag{1}$$

$$\alpha_4 = \frac{dH_l/dt}{\pi D^2 \Delta T}; \tag{2}$$

where H_d is the sum of enthalpies of *n*-pentane and *n*-hexane in the bubble, and H_l means H_d plus the enthalpy of water in the bubble; $D=(6V/\pi)^{1/3}$; and $\Delta T = T_\infty - T_s$. The calculation scheme for obtaining t-ξ and t-T_s-H_d (or H_l) relations, into which the correlations for x_V, x_L, v_V, v_L, h_V, and h_L as well as V-t relation need to be incorporated, is given by Shimizu et al. (1989) and Shimaoka (1990); in the former for "R 114" and "R 113" should be read "*n*-pentane" and "*n*-hexane," respectively. It should be stressed that α_4 is relevant to the total heat transfer, from the continuous phase to each bubble, causing the vaporization of *n*-pentane, *n*-hexane, and also water, while α_3 accounts for only a part of the heat transfer contributing to the vaporization of *n*-pentane and *n*-hexane.[2]

In practice we evaluated U and α_i ($i=3$ or 4) as well as ξ every 10 ms in the course of evaporation of each drop. (10 ms is less than one-hundredth of the whole evaporation time, t_v.) Then we deduced, in the same way as before (Shimizu and Mori, 1988b; Shimizu et al., 1989; Shimoaka and Mori, 1990), Pe and Nu_i ($i=3$ or 4) defined as

$$\mathrm{Pe} = UD/\kappa_c, \tag{3}$$

$$\mathrm{Nu}_i = \alpha_i D/\lambda_c. \tag{4}$$

Later we use $\mathrm{Nu}_i/\mathrm{Pe}^{1/2}$ as a quantity representing the instantaneous heat transfer characteristics. We also use, as a measure of the heat-transfer characteristics averaged over the whole process of evaporation of each drop, a constant C_i defined as

$$C_i = \int_0^{t_v} D\,\mathrm{Nu}_i\,\Delta T\,dt \Big/ \int_0^{t_v} D\,\mathrm{Pe}^{1/2}\,\Delta T\,dt. \tag{5}$$

Evaluation of the Uncertainties. The error sources relevant to the evaluation of C_i lie in the readings of the displacement of a water meniscus in the dilatometer tube, the determination of t_v based on the curve-fitting to the dilatometer readings, and the polynomial correlations for VLE and some other physical properties of the *n*-pentane/*n*-hexane mixtures. The possible errors in the dilatometer readings and in t_v can be estimated empirically. The error in each property value we used in the data processing is assumed to be approximated by the discrepancy of the very value from the corresponding value compared by direct use of Deeds' program. The uncertainty in C_i is estimated by considering the propagation of the abovementioned element errors. The uncertainty at ~95 percent coverage thus estimated is within ±7.0 percent for $x=0.9$, ±5.5 percent for $x=0.5$, and ±14 percent for $x=0.1$.

Results and Discussion

It should be noted that in the present experiments, each drop was evaporated in a uniform temperature field established in a water column. The effective temperature driving force for evaporation, ΔT, must have decreased monotonically from the initial value, ΔT^*, to the final value, $\Delta T^\dagger$, through the whole process of evaporation of the drop because of an enrichment of *n*-hexane in the yet-to-be vaporized liquid phase with a progress of evaporation. The magnitude of the difference between ΔT^* and $\Delta T^\dagger$ is never equal to but is approximated by the difference between the dew-point and the bubble-point temperatures plotted on an appropriate isobaric VLE diagram such as the one given in Fig. 1. (The difference between ΔT^* and $\Delta T^\dagger$ is always slightly smaller than the difference between the isobaric dew-point and bubble-point temperatures, because of a decrease in the hydrostatic head and an increase in the water-vapor pressure in the course of evaporation of each drop.)

The variable ΔT condition set in our experiments is not consistent with a nearly constant ΔT condition assumed to be established in a counterflow evaporator incorporated in a Lorenz-cycle power station. This means that the raw data on the time and the height required for evaporation of drops in our experiments are of little usefulness as they are. Thus, we show, in the following, the experimental results arranged into the form of U versus ξ, $\mathrm{Nu}_i/\mathrm{Pe}^{1/2}$ versus ξ, and C_i versus ΔT^* relations, which are suitable for inspecting the fundamental aspects of the drop evaporation process and will possibly be a basis to modeling the evaporator performance on a line similar to those taken by, for example, Smith et al. (1982), Çoban and Boehm (1989), Mori (1991), and Tadrist et al. (1991).

Velocity of Bubble Rise. All of the data on the instantaneous velocities of rise, U, of individual bubbles, each evolved from a drop of a mixture ($x=0.9$, 0.5, or 0.1), are plotted in Fig. 2(a) against the instantaneous, volume-equivalent spherical diameters of the very bubbles, D. Each solid curve represents the history of evaporation of one drop. These data were used to calculate Pe and then $\mathrm{Nu}/\mathrm{Pe}^{1/2}$ shown later. The data must reflect, however, some effect of the column wall. The rise velocities of individual bubbles to be attained in a medium of a practically infinite extent can be estimated by multiplying the U data by an appropriate, empirically determined correction factor. The velocities thus standardized with the aid of Tsuge and Hibino's correction factor (1973) are plotted in Fig. 2(b). Here each U-D curve is drawn, for the sake of clarity, only in the range above 2 percent evaporation

[2] The notations α_3 and α_4 are so selected as to be consistent with the nomenclature used in our preceding paper (Shimaoka and Mori, 1990). The other two definitions of the heat transfer coefficient, α_1 and α_2, also listed in the paper are not used here. α_1 based on the assumption of water-vapor-free two-phase bubbles would show an anomalous temperature-difference dependency as explained by Shimizu and Mori (1988b). α_2 based on the assumption of a water-vapor-free core and an infinitesimally thin water-vapor-saturated shell in each two-phase bubble cannot be determined in case of evaporation of mixture drops, since there is no way to specify x_V in the shell at each stage of evaporation.

Downloaded 13 Dec 2010 to 193.140.21.150. Redistribution subject to ASME license or copyright; see http://www.asme.org/terms/Terms_Use.cfm

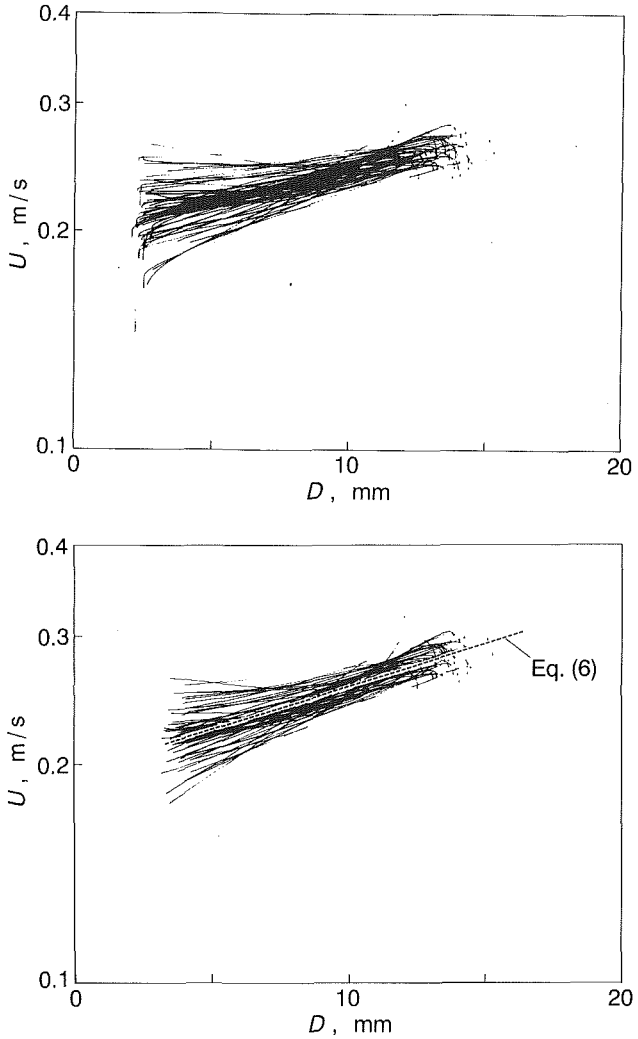

Fig. 2 Instantaneous rise velocity versus instantaneous diameter for individual bubbles of the mixtures ($x = 0.9$, 0.5, 0.1): (a) collection of all data obtained in the present experiments; (b) data limited to the range above 2 percent evaporation and corrected to eliminate wall effect

wherein the bubble motion is considered to be nearly quasi-steady.

Unexpectedly we find the bunch of U–D curves drawn in Fig. 2(b) exhibits some positive shift in U from the corresponding one observed with n-pentane bubbles by ourselves (Shimaoka and Mori, 1990), while we note no systematic dependency of the curves on x in the range of the present experiments ($0.1 \leq x \leq 0.9$). The curves in Fig. 2(b) may roughly be represented by a simple correlation such as[3]

$$U/[\mathrm{m/s}] = 0.195\, e^{27D/[\mathrm{m}]}. \tag{6}$$

This correlation differs only slightly from the one we fitted to the U–D curves observed with n-pentane bubbles (Shimaoka and Mori, 1990) both in the lead constant and in the power of e. The U–D curves for n-hexane bubbles (not shown in Figs. 2(a) and 2(b)) mostly fall in the band bordered by Eq. (6) and the lower limit of the scatter of the curves for the mixture bubbles. The reason the mixture bubbles showed rise velocities slightly higher, on the average, than those of n-pentane bubbles and also those of n-hexane bubbles of the same size has not been clarified yet.

Equation (6) is no more than a crude curve-fitting correlation, which is incoherent from a mechanistic viewpoint. It takes no account of the change in effective mass density of each two-phase bubble with the progress of evaporation; in fact, the density is dependent not only on D but also on the initial drop diameter D_0, the system pressure p_∞, and x. Expecting to remedy this defect, we examined the use of a dimensionless $\hat{U}$–$\hat{D}$ correlation recommended by Churchill (1989) for the case of steady bubble motion, where $\hat{U} \equiv U(\rho_c^2/\eta_c g \Delta\rho)^{1/3}$ and $\hat{D} \equiv D(\rho_c g \Delta\rho/\eta_c^2)^{1/3}$. However, the result was discouraging; the scatter of the curves as observed in Fig. 2(b) was little reduced by the replacement of the U–D coordinates with the $\hat{U}$–$\hat{D}$ coordinates. Thus, despite its apparent defect, Eq. (6) is still our compromise between ease of use and accuracy. It would be rather conservative to assume ±15 percent accuracy in using Eq. (6) to predict rise velocities of n-pentane/n-hexane mixture bubbles ($0.1 \leq x \leq 0.9$) in a sufficiently extended medium of water under the pressures up to 0.46 MPa and at temperatures up to 90°C.

Heat Transfer Characteristics. Before inspecting the results presented hereafter, one should note that α_i compiled with D and λ_c into Nu_i is not a film heat transfer coefficient in the continuous-phase side but an (effective) overall heat transfer coefficient. The modulus $\mathrm{Nu}_i/\mathrm{Pe}^{1/2}$ would be nearly constant irrespective of ξ if the resistance to heat flow is concentrated in the continuous-phase side. However, this is not the case. The vapor phase in each bubble must serve as a good insulator whenever it breaks immediate contact of the yet-to-be-vaporized liquid phase with the continuous phase, water, over a finite part of the bubble surface. The yet-to-be-vaporized liquid phase itself provides a finite resistance against the heat flow to the liquid/vapor interface inside the bubble, the actual evaporation site (Mori and Ehara, 1992a, 1992b). The resistance can be related in part to a composition distribution inevitably established in the liquid phase in case of evaporation of a mixture drop. It follows that $\mathrm{Nu}_i/\mathrm{Pe}^{1/2}$ varies with ξ, responding to a change in the two-phase structure in the bubble, which in turn must be dependent more or less on the buoying and growing motions of the bubble.[4] The variation of $\mathrm{Nu}_i/\mathrm{Pe}^{1/2}$ with ξ can thus be different, depending on operational parameters such as p_∞, ΔT, x, etc. This point is discussed later, based on the experimental results.

The constant C_i calculated by Eq. (5) for each evaporation process is assumed to be a measure of heat transfer performance of the whole process. It gives such a representative level of $\mathrm{Nu}_i/\mathrm{Pe}^{1/2}$ in the process that if $\mathrm{Nu}_i/\mathrm{Pe}^{1/2}$ were held constant at C_i throughout the process, the same evaporation time t_v as the one actually measured would result (Shimizu and Mori, 1988b).

Typical examples of the $\mathrm{Nu}_3/\mathrm{Pe}^{1/2}$ versus ξ relation are illustrated in Figs. 3(a) and 3(b). (No example of $\mathrm{Nu}_4/\mathrm{Pe}^{1/2}$ versus ξ relation is given, because we find little difference between $\mathrm{Nu}_4/\mathrm{Pe}^{1/2}$ versus ξ and $\mathrm{Nu}_3/\mathrm{Pe}^{1/2}$ versus ξ relations, except that the former is elevated nearly evenly from the latter.) All of the results for C_3 and C_4 calculated from the data are plotted in Figs. 4(a) and 4(b). Also plotted for comparison are the results obtained with medium-sized (2.0–3.8 mm diameter) n-pentane drops in our previous work (Shimaoka and Mori, 1990).

As indicated in the table inset in Fig. 4(a) or 4(b), the experiments with mixtures ($x = 0.9$, 0.5, and 0.1) and with n-hexane ($x = 0$) were made exclusively under low-to-medium pressures ($p_\infty \simeq 0.11$–0.25 MPa) except for the only class of experiments performed with the n-hexane-lean mixture ($x = 0.9$) at a somewhat higher pressure level ($p_\infty \simeq 0.32$–0.46 MPa).

[3] Here the U–D correlation is written in the style recommended by Mayhew (1989) for avoiding dimensional inconsistency.

[4] The growing motion can directly affect by itself the heat transfer coefficient in the continuous-phase side. However, the magnitude of a resultant change in the heat transfer coefficient is predicted to be sufficiently small in the range of bubble-growth rates of our present interest (Shimizu and Mori, 1989). Thus, the direct effect of the growing motion is no more considered in this paper.

Downloaded 13 Dec 2010 to 193.140.21.150. Redistribution subject to ASME license or copyright; see http://www.asme.org/terms/Terms_Use.cfm

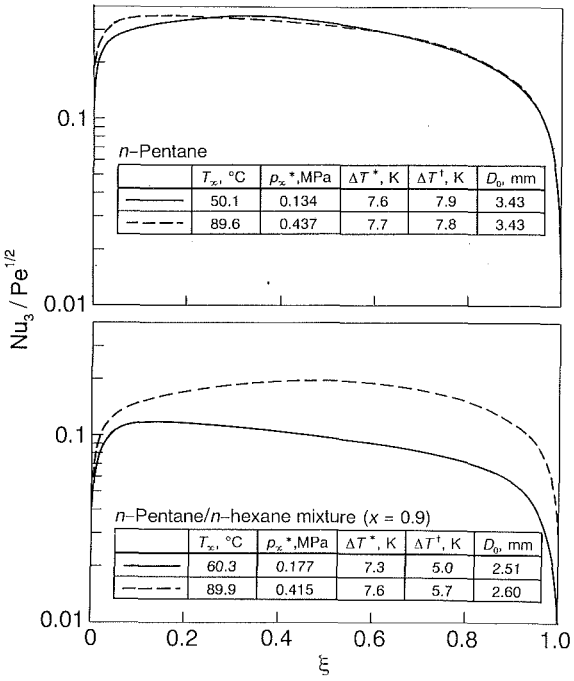

	T_∞, °C	p_∞*, MPa	ΔT^*, K	$\Delta T^\dagger$, K	D_0, mm
n-Pentane	50.1	0.134	7.6	7.9	3.43
n-Pentane	89.6	0.437	7.7	7.8	3.43
n-Pentane/n-hexane mixture (x = 0.9)	60.3	0.177	7.3	5.0	2.51
n-Pentane/n-hexane mixture (x = 0.9)	89.9	0.415	7.6	5.7	2.60

Fig. 3(*a*) Dependency on p_∞

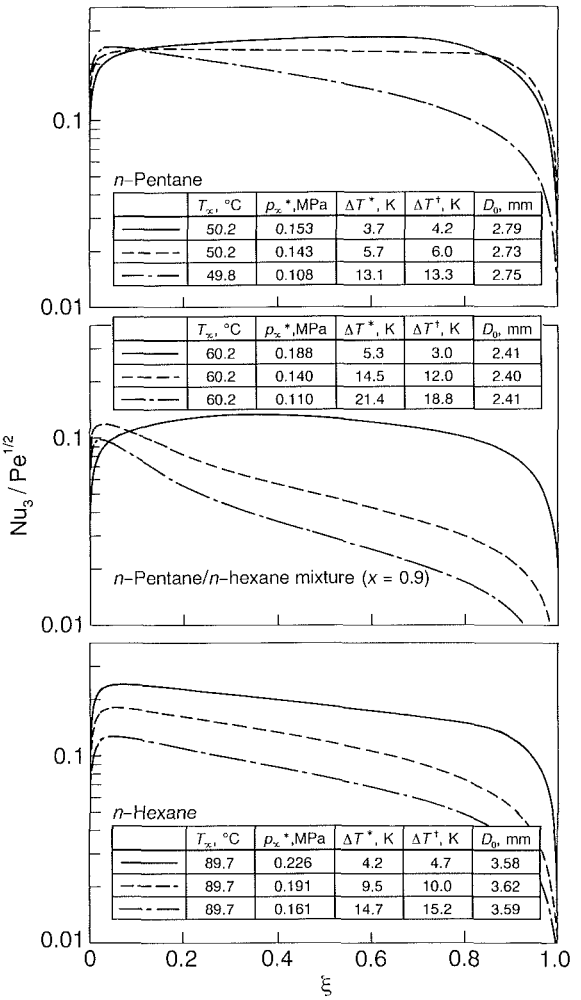

	T_∞, °C	p_∞*, MPa	ΔT^*, K	$\Delta T^\dagger$, K	D_0, mm
n-Pentane	50.2	0.153	3.7	4.2	2.79
n-Pentane	50.2	0.143	5.7	6.0	2.73
n-Pentane	49.8	0.108	13.1	13.3	2.75
n-Pentane/n-hexane mixture (x = 0.9)	60.2	0.188	5.3	3.0	2.41
n-Pentane/n-hexane mixture (x = 0.9)	60.2	0.140	14.5	12.0	2.40
n-Pentane/n-hexane mixture (x = 0.9)	60.2	0.110	21.4	18.8	2.41
n-Hexane	89.7	0.226	4.2	4.7	3.58
n-Hexane	89.7	0.191	9.5	10.0	3.62
n-Hexane	89.7	0.161	14.7	15.2	3.59

Fig. 3(*b*) Dependency on ΔT^*

Fig. 3 Typical examples of the variation of $Nu_3/Pe^{1/2}$ with evaporation ratio ξ. The curves for pure *n*-pentane drops are selected from the experimental results obtained in the preceding work (Shimaoka and Mori, 1990).

This limitation of the experiments resulted from the necessity to keep T_∞ safely below the thermodurability limit of the apparatus. Thus, we can observe the pressure dependency of $Nu_i/Pe^{1/2}$ or C_i only for the mixture of $x=0.9$. The dependency is clearly positive, as can be seen in Figs. 3(*a*), 4(*a*), and 4(*b*), which is in contrast to the insensitivity of $Nu_i/Pe^{1/2}$ or C_i to p_∞ for *n*-pentane drops ($x=1$). No reasonable interpretation of the above finding has been found yet. Nevertheless, it seems reasonable to assume that p_∞ dependency similar to the one observed with the mixture of $x=0.9$ exists for any mixture falling in the range $0.1 \le x \le 0.9$, considering the fact that the C_i–ΔT^* relation depends, at least at the lower level of p_∞ (0.11–0.25 MPa), no more than slightly on x in the abovementioned range (see Figs. 4(*a*) and 4(*b*)).

The most striking fact noticed in Figs. 4(*a*) and 4(*b*) is a sharp decrease, with an increase in ΔT^*, of C_i for any mixture and also for *n*-hexane. This clearly contrasts with our previous findings with pure *n*-pentane drops: i.e., C_i is almost independent of ΔT^* whenever D_0 is rather small (<2 mm), and negatively dependent on ΔT^* but in a degree increasing only gradually with an increase in D_0 from 2 to 6.5 mm (Shimizu and Mori, 1988b; Shimaoka and Mori, 1990). The apparent ΔT^* dependency of C_i for the mixtures observed in Figs. 4(*a*) and 4(*b*) may be exaggerated a little, because an increase of ΔT^* for each mixture was achieved, as described in the "Experimental" section, by reducing p_∞, which must have served by itself to decrease C_i to some extent as long as C_i has a positive p_∞ dependency as discussed above. However, even if we subtract the possible contribution of a reducing p_∞ to the lowering C_i, we still observe a significant decrease of C_i with an increase in ΔT^*. The decrease of C_i with an increase in ΔT^* thus recognized is primarily ascribed, as exemplified in Fig. 3(*b*), to a tendency that a decrease in $Nu_i/Pe^{1/2}$ with an increasing ξ in each evaporation process becomes sharper with an increase in ΔT^*. Thus we need to explain this tendency.

The most common explanation of heat transfer deterioration observed in the evaporation of a nonazeotropic mixture may be to indicate a diffusional resistance appearing in the yet-to-be-vaporized liquid phase (Tsotsas and Schlünder, 1987). This explanation still holds at least in part in the present case. A preferential evaporation of *n*-pentane from the mixture-liquid phase in each two-phase bubble must cause a progressive decrease in x_L, the mole fraction of *n*-pentane in the mixture-liquid phase, in the vicinity of the liquid/vapor interface so far as some diffusional resistance in the liquid phase controls the rate of transport of *n*-pentane molecules to the interface. Such a localized decrease in x_L at the interface results in a rise of the temperature at the interface, T_{if}, exceeding the nominal saturation temperature, T_s. This leads to a reduction of the actual temperature difference, $T_\infty - T_{if}$, below the nominal temperature difference, $\Delta T \equiv T_\infty - T_s$, and thereby to a lowering of the heat transfer coefficient α_i based on ΔT. This effect must become increasingly significant as the bulk–interface difference in x_L expands and as ΔT decreases, and hence it appears to account for the decrease in $Nu_i/Pe^{1/2}$ with an increasing ξ in each evaporation process. On the contrary, we encounter a difficulty explaining the experimental finding that the magnitude of the decrease in $Nu_i/Pe^{1/2}$ (and hence in C_i) is enlarged, not reduced, with an increase in ΔT^*. The finding conflicts with our expectation that an increase in ΔT^* will "dilute" the effect of the discrepancy between T_{if} and T_s. A hypothetical explanation of this "conflict" is given below.

It is reasonably assumed that the heat transfer to a two-phase bubble during each evaporation process is substantially influenced by some secondary motions of the bubble itself. The secondary motions are, as recognized with single-phase bubbles or drops (Clift et al., 1978), a rocking from side to side, which causes a zigzag or helical trajectory of the bubble, and a shape oscillation. These motions must add a secondary flow to the continuous-phase liquid passing by the bubble, and

Downloaded 13 Dec 2010 to 193.140.21.150. Redistribution subject to ASME license or copyright; see http://www.asme.org/terms/Terms_Use.cfm

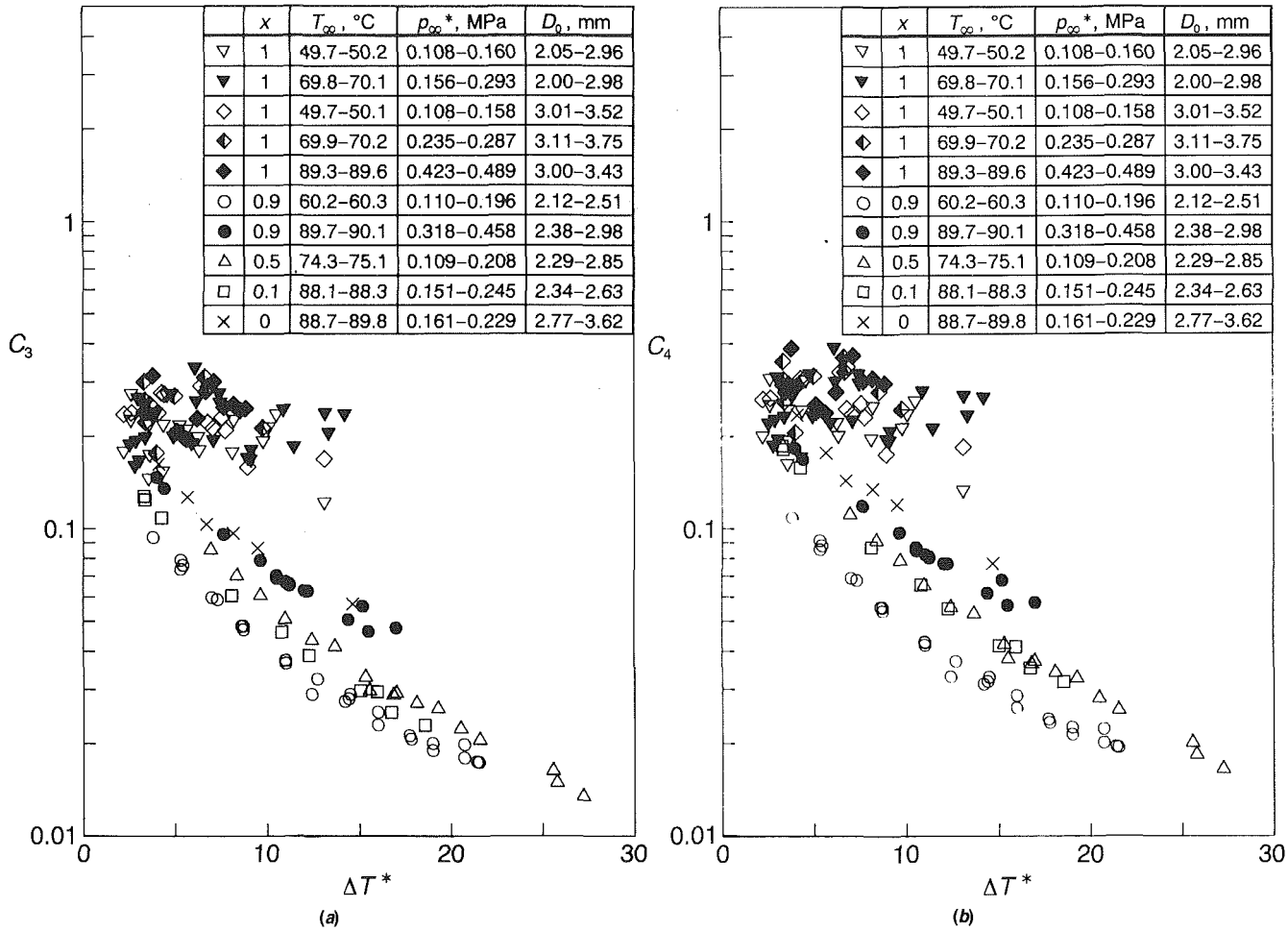

Fig. 4 Temperature-difference dependencies of C_3 and C_4. A part of the results obtained with *n*-pentane drops in the preceding work (Shimaoka and Mori, 1990) is included for comparison.

at the same time cause a sloshing of the yet-to-be vaporized liquid inside the bubble, thus promoting the spreading of the liquid over the bubble surface as well as the mixing in the liquid. In other words, the secondary motions must promote the convective heat transfer in the continuous-phase side, extend the effective heat transfer area (the liquid/liquid interface) over the surface, and reduce the diffusional resistance in the yet-to-be-vaporized liquid.

It should be noted that the secondary motions under consideration are periodic by nature, and their frequencies are primarily dependent on Re at each instant as long as the chemical compounds constituting the bubble/medium system of interest are specified. It follows that as ΔT^* increases and thereby the evaporation time, t_v, is shortened, the extent of possible contribution of the time-dependent secondary motions will be increasingly reduced. This mechanism of heat transfer degradation with an increase in ΔT^* can exist whether the dispersed-phase substance is a pure compound or a mixture, but it may play a more pronounced role in the case of a mixture accompanied with a diffusional resistance in the yet-to-be-vaporized liquid phase. Unfortunately we have found no means to investigate quantitatively whether the role of the mechanism described above is truly enough to explain the negative ΔT^* dependency of C_i observed with *n*-pentane/*n*-hexane mixtures in the experiments.

A separate explanation is needed for the negative ΔT^* dependency of C_i observed with *n*-hexane ($x=0$), which is much stronger than that for *n*-pentane ($x=1$) and almost comparable with those for the mixtures ($x=0.9$, 0.5, and 0.1). Here we point out a possible overestimation, in our data processing scheme, of the water vapor pressure in each two-phase bubble, which, if any, leads to an overestimation of the instantaneous temperature difference, ΔT, and consequently an underestimation of $\mathrm{Nu}_i/\mathrm{Pe}^{1/2}$. As described in the "Experimental" section, our data processing scheme assumes an instantaneous equilibrium inside each two-phase bubble, i.e., a complete mixing of saturated common vapors of the hydrocarbon (or hydrocarbon mixture) in use and water in the bubble. However, the mixing of the vapors at any stage of evaporation presumably becomes increasingly incomplete, as ΔT^* increases and thereby so does the rate of evaporation. The more incomplete the mixing is, the lower will be the water vapor pressure over the hydrocarbon liquid/vapor interface, and thus the greater should be the excess of the temperature at the interface above T_s. It follows that the "effective" temperature difference is always smaller than the nominal temperature difference, ΔT, and the discrepancy between them tends to increase, as T_∞, or to be more exact, T_s, and thereby the saturated-vapor pressure of water achievable inside bubbles increase and as ΔT^* increases. Based on the above consideration, we can presume that the values of C_i for *n*-hexane are evaluated excessively lower, compared to those obtained with *n*-pentane or the mixtures at lower levels of T_∞, to a degree increasing with an increase in ΔT^*.

Downloaded 13 Dec 2010 to 193.140.21.150. Redistribution subject to ASME license or copyright; see http://www.asme.org/terms/Terms_Use.cfm

Concluding Remarks

The evaporation of, and the heat transfer to, single drops of *n*-pentane/*n*-hexane mixtures in water have been studied experimentally. A slight variation is found in the rise motion of drops, each taking the form of a two-phase bubble in the course of evaporation, as the compostion of the drop-forming liquid changes from pure *n*-pentane to pure *n*-hexane. Considerable deterioration of heat transfer is noted with the mixtures and even with pure *n*-hexane, as compared to the heat transfer characteristics observed with pure *n*-pentane, so far as the heat transfer characteristics are evaluated on a formally common basis. As discussed in the text, the deterioration is presumably apparent rather than substantial in part. It should be stressed, however, that the heat transfer characteristics as evaluated here are just those to be used or considered in predicting, with the aid of some model of multibubble systems, the performance of spray-column-type evaporators.

On the whole, the magnitudes of the heat transfer deterioration observed with the *n*-pentane/*n*-hexane mixtures are considerably larger than, and quite different in the temperature-difference dependency from, those we observed previously with an R 114 (10 percent)/R 113 (90 percent) mixture (Shimizu et al., 1989). These differences may be ascribed in part to the smaller drop size used in the previous study with the R 114/R 113 mixture, but for the rest to differences in physical properties between the *n*-pentane/*n*-hexane and the R 114/R 113 systems. These points are not yet clarified.

Acknowledgments

We wish to express our gratitude to N. Ehara and T. Tagaya, former students in the Department of Mechanical Engineering, Keio University, for their assistance in the experimental and computational works.

References

Churchill, S. W., 1989, "A Theoretical Structure and Correlating Equation for the Motion of Single Bubbles," *Chemical Engineering and Processing*, Vol. 26, pp. 269–279.

Clift, R., Grace, J. R., and Weber, M. E., 1978, *Bubbles, Drops, and Particles*, Academic Press, New York, pp. 185–189.

Çoban, T., and Boehm, R., 1989, "Performance of a Three-Phase, Spray-Column, Direct-Contact Heat Exchanger," ASME JOURNAL OF HEAT TRANSFER, Vol. 111, pp. 166–172.

Deeds, R. S., 1979, "THERPP—A Thermodynamic Properties Program," Tree-1081.

Goswami, D. Y., Sharpe, L., Jr., Hingorani, S., Demuth, O. J., and Mines, G., 1987, "Analysis of Tray Thermal Efficiencies of Direct Contact Heat Exchangers for Vaporizing Hydrocarbon Mixtures," *Proceedings of 1987 ASME-JSME Thermal Engineering Joint Conference*, Vol. 3, pp. 3–11.

JSME Data Book: The Thermophysical Properties of Fluids, 1983, Japan Soc. Mech. Engrs., Tokyo.

JSME Steam Tables, 1980, Japan Soc. Mech. Engrs., Tokyo.

Mayhew, Y. R., 1989, "Use of Physical Quantities, Units, Mathematics, and Nomenclature in Heat Transfer Publications," *Experimental Heat Transfer*, Vol. 2, pp. 149–172.

Mines, G. L., Demuth, O. J., and Wiggins, D. J., 1983, "Thermal and Hydraulic Performance Tests of a Sieve-Tray Direct-Contact Heat Exchanger Vaporizing Pure and Mixed-Hydrocarbon Rankine-Cycle Working Fluids," Report EGG-2253, EG&G Idaho, Inc., Idaho Falls, ID.

Mori, Y. H., 1991, "An Analytic Model of Direct-Contact Heat Transfer in Spray-Column Evaporators," *AIChE Journal*, Vol. 37, pp. 539–546.

Mori, Y. H., and Ehara, N., 1992a, "Direct-Contact Heat Transfer to a Spherical Liquid/Vapor Two-Phase Bubble Trailing a Wake," *Wärme- und Stoffübertragung*, Vol. 27, pp. 337–345.

Mori, Y. H., and Ehara, N., 1992b, "Direct-Contact Heat Transfer to a Spherical-Cap Liquid/Vapor Two-Phase Bubble," *International Journal of Heat and Mass Transfer*, Vol. 35, pp. 63–72.

Shimaoka, H., 1990, "Heat Transfer to Single-Component Drops and Two-Component Mixture Drops Evaporating in an Immiscible Liquid" [in Japanese], M. Eng. thesis, Keio University, Yokohama, Japan.

Shimaoka, H., and Mori, Y. H., 1990, "Evaporation of Single Liquid Drops in an Immiscible Liquid: Experiments With *n*-Pentane Drops in Water and Preparation of New Heat Transfer Correlations," *Experimental Heat Transfer*, Vol. 3, pp. 159–172.

Shimizu, Y., and Mori, Y. H., 1988a, "Evaporation of Single Liquid Drops in an Immiscible Liquid at Elevated Pressures: Equipment and Preliminary Results," *Experiments in Fluids*, Vol. 6, pp. 73–79.

Shimizu, Y., and Mori, Y. H., 1988b, "Evaporation of Single Liquid Drops in an Immiscible Liquid at Elevated Pressures: Experimental Study With *n*-Pentane and R 113 Drops in Water," *International Journal of Heat and Mass Transfer*, Vol. 31, pp. 1843–1851.

Shimizu, Y., 1989, "Characteristics of Heat Transfer to Liquid Drops Evaporating in an Immiscible Liquid" [in Japanese], D. Eng. thesis, Keio University, Yokohama, Japan.

Shimizu, Y., and Mori, Y. H., 1989, "Direct Contact Heat Transfer to Bubbles With Simultaneous Translation and Growth," *Numerical Heat Transfer*, Part A, Vol. 15, pp. 509–524.

Shimizu, Y., Shimaoka, H., and Mori, Y. H., 1989, "Heat Transfer to Single Drops of a Nonazeotropic Fluorocarbon Mixture Evaporating in Water," *JSME International Journal*, Series II, Vol. 32, pp. 630–638.

Smith, R. C., Rohsenow, W. M., and Kazimi, M. S., 1982, "Volumetric Heat-Transfer Coefficients for Direct-Contact Evaporation," ASME JOURNAL OF HEAT TRANSFER, Vol. 104, pp. 264–270.

TRC Thermodynamic Tables—Hydrocarbons, 1989, Thermodynamics Research Center, Texas A&M University, College Station, TX.

Tadrist, L., Sun, L., Santini, R., and Pantaloni, J., 1991, "Heat Transfer With Vaporization of a Liquid by Direct Contact in Another Immiscible Liquid: Experimental and Numerical Study," ASME JOURNAL OF HEAT TRANSFER, Vol. 113, pp. 705–713.

Tsotsas, E., and Schlünder, E. U., 1987, "Heat Transfer During Evaporation and Condensation of Binary Mixtures," *Chemical Engineering and Processing*, Vol. 21, pp. 209–215.

Tsuge, H., and Hibino, S., 1973, "Effect of Wall Proximity on the Rising Velocity of Gas Bubbles in Various Liquids" [in Japanese], *Kagaku Kōgaku*, Vol. 37, pp. 1125–1130.

Downloaded 13 Dec 2010 to 193.140.21.150. Redistribution subject to ASME license or copyright; see http://www.asme.org/terms/Terms_Use.cfm

Unifying the Controlling Mechanisms for the Critical Heat Flux and Quenching: The Ability of Liquid to Contact the Hot Surface

C. Unal

V. Daw

R. A. Nelson

Los Alamos National Laboratory,
Nuclear Technology and
Engineering Division,
Engineering and Safety Analysis Group,
Los Alamos, NM 87545

We investigated the hypothesis that the critical heat flux (CHF) occurs when some point on a heated surface reaches a temperature high enough that liquid can no longer maintain contact at that point, resulting in a gradual but continuous increase in the overall surface temperature for most power-controlled systems. This hypothesis unifies the occurrence of the CHF with the quenching of hot surfaces by relating them to the same concept: the ability of a liquid to contact a hot surface, generally defined as some fraction of the liquid's homogeneous nucleation temperature, depending on the contact angle. The proposed hypothesis about the occurrence of the CHF is investigated through a study of the boiling mechanism of the second transition region of nucleate pool boiling of water on copper. An idealized two-dimensional transient conduction heat transfer model was developed to investigate the heat transfer mechanism. The initial macrolayer thickness on the dry portion of the heater, in the second transition region, was found to be bounded between 0 and 11 μm. The radius of the dry patch varied from 15 to 23 mm (60 and 92 percent of the heater radius, respectively) for initial macrolayer thicknesses of 0 and 11 μm, respectively. The results indicated that the critical liquid–solid contact temperature at the onset of CHF (the surface temperature at the center of the dry patch) must be lower than the homogeneous nucleation temperature of the liquid for the pool boiling of water on a clean horizontal surface. The liquid–solid contact temperature was dependent on the initial dry patch liquid macrolayer thickness, varying from 180°C to 157°C for initial macrolayer thicknesses of 0 and 11 μm, respectively. Independent assessment of these values shows good agreement with extrapolated contact temperature data at the onset of film boiling. This indicates that the mechanism for the occurrence of the CHF could be similar to the mechanism generally accepted for the quenching of the hot surfaces. Further study of this mechanism to understand better the observed trends in other experimental results show qualitative agreement with those results. These include a significant decrease in the radius of the dry patch to 4 mm (16 percent of the heater radius) when the thermal conductivity of the heater was decreased to that corresponding to nickel. When the thickness of a copper heater was decreased from 10 mm (representing an infinitely thick medium) to 0.1 mm, a dry patch radius of 2.25 mm (9 percent of the heater radius) was found to be sufficient for the temperature at the center of the dry patch to reach the critical contact temperature. These comparisons are felt to provide some understanding as to why the second transition region has been observed only in limited cases.

I Introduction

Of the three boiling heat transfer regimes (nucleate, transition, and film boiling), nucleate boiling is the regime most important for industrial applications. Although this has resulted in the study of nucleate boiling phenomena for at least five decades, prediction still remains principally an empirical art. The nucleate boiling region on a classical boiling curve of heat flux versus wall superheat (q versus ΔT_{sat}) starts with incipient boiling and extends until the first boiling crisis, critical heat flux (CHF). The vapor transport mechanisms between incipient boiling and the CHF point change considerably. Typical regions classified by Gaertner (1965) from his experimental study are (*a*) incipient boiling, (*b*) discrete bubble region, (*c*) first transition region, (*d*) vapor mushroom region, (*e*) second transition region, and (*f*) CHF. The pool nucleate boiling portion of the boiling curve obtained by Gaertner for a polished copper surface is shown in Fig. 1, with sketches of the boiling phenomena.

Of these subregions within nucleate boiling, the CHF point has been given a significant amount of study. Studies of the CHF phenomena mainly fall into three categories (Hsu and Graham, 1976): empirical correlations, bubble interaction models, and hydrodynamic instability models. For the empirical models (Kutateladze, 1951; Sterman, 1953; Borishansky, 1965), the CHF is expressed in terms of dimensionless groups, and either a statistical fit or a fit based on some simple model is obtained. Bubble interaction models (Rohsenow and Griffith, 1956; Chang and Snyder, 1960) consider the CHF to be limited by the removal rate of bubbles, which carry away the heat in the form of evaporation. This theory was based on critical bubble spacing near the heated surface. The hydrodynamic model, based on the instability of a wave at the liquid/

Contributed by the Heat Transfer Division for publication in the JOURNAL OF HEAT TRANSFER. Manuscript received by the Heat Transfer Division September 1991; revision received April 1992. Keywords: Boiling, High-Temperature Phenomena. Associate Technical Editor: L. C. Witte.

Copyright © 1992 by ASME
Downloaded 13 Dec 2010 to 193.140.21.150. Redistribution subject to ASME license or copyright; see http://www.asme.org/terms/Terms_Use.cfm

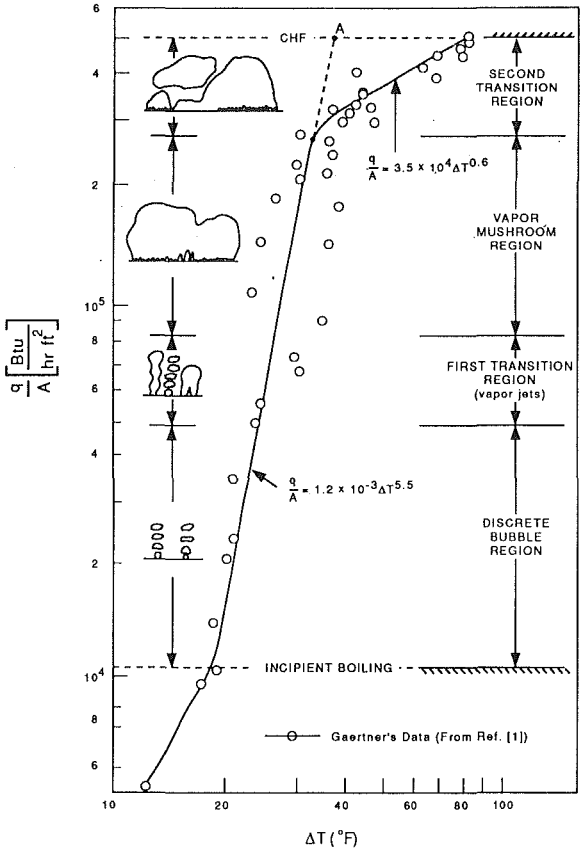

Fig. 1 Gaertner's heat transfer data for water boiling on a polished thick flat horizontal copper plate

vapor interface, first was proposed by Chang (1957), but was completed by Zuber (1958, 1959) and Zuber et al. (1961). This approach assumes that near the CHF point, the heating surface is covered by rising vapor columns in the form of vapor jets, with countercurrent liquid jets flowing downward to replenish the evaporation loss. When the relative velocity is high enough, an instability (Kelvin–Helmholtz) occurs, and the vapor jets collapse. This collapse produces the CHF condition by preventing the escape of the vapor and, because the surface is vapor covered, by preventing the return of liquid to the surface.

Although Zuber's instability theory is significant and superior to the others, it neither explains nor predicts the experimental data obtained for finite flat plates of various sizes, geometries, and surface conditions. Lienhard and Dhir (1973) modified Zuber's theory to account for both size and geometry effect and gave several empirical relationships for finite bodies. However, the predicted values of CHF by these equations still did not predict the experimental data when the characteristic length was smaller than the most dangerous wavelength as reported by Egan and Westwater (1985).

The most important experimental observation to challenge Zuber's hydrodynamic theory was the detection of a thin liquid macrolayer with many vapor stems on the heated surface (Kirby and Westwater, 1965; Yu and Mesler, 1977). Haramura and Katto (1983) postulated that CHF will occur if the heat flux is high enough to evaporate the macrolayer before departure of the vapor mushroom bubble. This picture, then, is for a macrolayer *uniformly* distributed over the heater surface. This model does not contradict Zuber's hydrodynamic instability model but instead extends the physics for a more complete description of the phenomenon. Katto's multistep CHF model considers steady-state conditions. Pasamehmetoglu et al. (1990) showed that it can be extended to explain transient CHF phenomena. One may consider this type of theory to be a fourth category of CHF modeling and call it a surface-controlled theory. We will define a surface-controlled theory as one that relates the occurrence of CHF to the drying of a liquid layer from the heater surface prior to vapor bubble departure. Resupply of the liquid layer at bubble departure, liquid layer drying times, and their associated mechanisms are unspecified.

None of the models we have discussed above consider the dry patches observed by Gaertner (1965) in the second transition region leading up to the CHF point. It is important to note that it is the much poorer heat transfer provided by the dry patches, as opposed to the macrolayer-covered surface, which is believed to create the change in slope of the boiling curve at this point (see Fig. 1). Kirby and Westwater (1965) and Van Ouwerkerk (1972) also indicated that dry spots sometimes appear in the liquid film at high heat fluxes near the CHF point. In fact, the occurrence of dry patches and patchwise boiling has been observed previously by Corty and Foust (1955), Carne (1965), and Torikai and Yamazaki (1967). A detailed summary of findings from these studies regarding dry patch formation is given in the following section.

As the time- and area-averaged surface temperature represented on the boiling curve in the second transition region

Nomenclature

c = specific heat capacity
h = heat-transfer coefficient
h_{fg} = latent heat of vaporization
H = heater thickness
k = thermal conductivity
LP = integer defining the heat flux boundary condition
N/A = nucleation site density
r = space coordinate
Q_o = heat generation
q = heat flux
t = time
T = temperature
z = space coordinate
ΔT_{BL} = wall superheat at the bottom left corner of the heater at the end of the lifetime of the vapor mushroom (see Fig. 3*b*)
ΔT_{BR} = wall superheat at the bottom right corner of the heater at the end of the lifetime of the vapor mushroom (see Fig. 3*b*)
ΔT_{TL} = wall superheat at the top left corner of the heater at the end of the lifetime of the vapor mushroom (see Fig. 3*b*)
ΔT_{TR} = wall superheat at the top right corner of the heater at the end of the lifetime of the vapor mushroom (see Fig. 3*b*)
β_a = advancing contact angle
δ = macrolayer thickness
ΔT_{sat} = $T - T_{sat}$
ξ = volumetric ratio of the accompanying liquid to the moving bubble
ρ = density
τ = lifetime of the vapor mushroom (hovering period)
$n\tau$ = number of hovering periods
$\langle\ \rangle$ = time-dependent, surface-averaged

Subscripts

av = surface-time average
CHF = critical heat flux
d = dry patch
h = heater
hn = homogeneous nucleation
l = liquid
rew = rewetting
s = stem
sat = saturation
v = vapor
1 = dry patch region
2 = two-phase macrolayer region

Downloaded 13 Dec 2010 to 193.140.21.150. Redistribution subject to ASME license or copyright; see http://www.asme.org/terms/Terms_Use.cfm

increases, the number and size of the patches increase (Kirby and Westwater, 1965; Van Ouwerkerk, 1972). Vapor mushrooms still exist above the heater surface and are still responsible for the transport of vapor from the surface. During the life of a mushroom bubble before its departure from the surface, these dry spots appear and grow in size. After bubble departure, liquid washes across the dry area and rewets the surface. This transient process of bubble growth and departure is repeated over and over for any given point on the boiling curve and produces the "steady-state" data represented by the boiling curve. It seems obvious that local-instantaneous surface temperatures within these dry patches will increase as a function of time and toward the innermost regions of the dry patch as the patch grows during each bubble's lifetime.

As the heat flux increases to higher levels on the boiling curve, the local-instantaneous surface temperature at the center of the largest dry patch will eventually increase to a point where rewetting of the surface is no longer possible. Although it has been indicated by several researchers that these dry patches are important to the understanding of the boiling crisis, it has not received much attention because of both experimental difficulties in determining dry patch behavior and computational difficulties in solving any model constructed to address the phenonema. We believe these dry patches provide the key to understanding the mechanism that produces the CHF.

We believe that the formation of the dry patches is a result of the evaporation of thinner regions of the local liquid macrolayer. The thickness of the liquid macrolayer must vary from one point to another on the heater surface and show some nonuniform statistical distribution. This might be considered a simple extension of Katto's CHF theory, which assumes a uniform macrolayer thickness. However, it is not the evaporation of the liquid macrolayer and the corresponding occurrence of these dry patches themselves that causes CHF. Instead, the temperature at the center of the dry patch first must reach some critical value above which liquid–solid contact is no longer possible.

Once this "hot-spot" condition occurs at a local point within the dry patch on the heater surface, the further response of the surface depends on the heater/boiling system's stability as defined by Hesse (1973) and the test procedure used if the system is power-controlled. Conceptually for "ideal" temperature-controlled systems, all increasingly higher temperatures are stable and data can be obtained. Depending on the system's thermal resistance, power-controlled systems also may have stable transition boiling regions that the experimenter can realize if he "gently moves" the system into transition boiling by decreasing the heat flux as the temperature rises. If the experimenter does not decrease the power or the system is simply unstable in the transition boiling regime, the hot spot begins to grow, further deteriorating the heat removal and increasing the average wall temperature for each bubble in a transient process until the next stable film boiling point is reached.

Conceptually, this hypothesis is very exciting because it unifies the occurrence of the CHF with the quenching of hot surfaces by relating them both to the same governing mechanism, i.e., the ability of liquid to contact a hot surface, generally defined in terms of the liquid's homogeneous nucleation temperature. Although quenching of hot surfaces (the second boiling crisis) will not be discussed here, it is generally accepted that quenching is controlled by this process (Nelson, 1986; Nelson and Pasamehmetoglu, 1992). Recently, Ramilison and Lienhard (1987) indicated that the liquid–solid contact temperature at the onset of the film boiling is contact-angle dependent: It approaches the homogeneous nucleation temperature of the fluid when the contact angle goes to zero (highly wetting fluids) and decreases with increasing contact angle.

Thus, the objectives of this paper become the following: (1) to propose and discuss the hypothesis that CHF is controlled by the occurrence of a hot spot on a heated surface where (on a transient-local basis) the critical rewetting temperature is reached; (2) to provide estimations of the hot-spot critical temperature, hot-spot size, and other hot-spot characteristics; (3) to compare the estimates of critical temperatures to data; and (4) to provide an explanation as to why the second-transition region is seen only on occasion. Our calculations of the hot spot are built around Gaertner's observation of the second-transition region. Therefore, we feel we must be able to explain why this region is seen only on occasion, yet mechanisms from these observations can control other situations. Being able to provide insight for this point is necessary but not sufficient to prove the hypothesis.

II Background on the Size and Formation of Dry Patches

Although we arrived at the idea of a hot-spot-controlled CHF independently, we soon found that, in fact, it had been advanced previously by others. Research in the area of "hot spot" or "dry patch" CHF has involved work in three main areas: (1) thin horizontal boiling surfaces—size, formation, and growth of dry patches investigated but no work done on the contact temperature; (2) thick horizontal boiling surfaces—formation of dry patches observed; and (3) wires—spatial distribution of dry patches along the length of a wire, with much "CHF hot spot temperature" work done. Dry patch formation on horizontal flat boiling surfaces and horizontal wires could show slightly different characteristics because of the hydrodynamics of the vapor mushrooms. In this paper, emphasis is given to the formation of dry patches on horizontal flat boiling surfaces. Therefore, the following subsections will discuss the first two of these three areas in more detail. Detailed information regarding wires is discussed by Unal et al. (1991).

(A) Thin Horizontal Surfaces. Kirby and Westwater (1965) conducted pool boiling experiments with carbon tetrachloride and methanol on a horizontal glass surface plated with an extremely thin conducting material. Near the CHF, they observed irregular vapor masses, rather than individual bubbles, hovering above a thin liquid layer. A sketch of the vapor masses observed in this study is shown in Fig. 2(*a*). Their description of the vapor masses was similar to that of Gaertner. Under these vapor masses, a bubble would nucleate at a site, expand into the vapor mass, then suddenly burst, leaving only a small wake as a clue to its disappearance. As illustrated in Fig. 2(*a*), irregular vapor masses were sometimes followed immediately by the appearance of a dry spot on the heater surface (dark spots). These dry spots were measured to be as large as 1.8 mm in diameter and sometimes grew to merge with neighboring ones, as indicated in Fig. 2(*a*). The typical lifetime of a dry spot was measured to be 10 ms, after which liquid again washed across the area and wet the solid. As Kirby and Westwater's heater had almost no thermal mass, the rapid growth of the dry areas could result in the CHF.

Van Ouwerkerk (1972) experimentally studied the occurrence of dry areas using *n*-heptane on a 20-mm-thick, round Pyrex plate with a diameter of 0.2 m. The plate was heated by passing an electric current through a transparent electroconductive layer (gold sandwiched between two layers of bismuth oxide), which was deposited on the plate. Van Ouwerkerk reported a vapor structure similar to that described by Kirby and Westwater: a thin layer of liquid lying under a vapor mass. New bubbles nucleate and coalesce in this liquid layer. Dry spots occurred under each of these bubbles under the large vapor mass. Evaporation of the liquid film caused these dry spots to grow and to merge with neighboring ones to form larger dry areas. In the next hovering period, the solid was

Downloaded 13 Dec 2010 to 193.140.21.150. Redistribution subject to ASME license or copyright; see http://www.asme.org/terms/Terms_Use.cfm

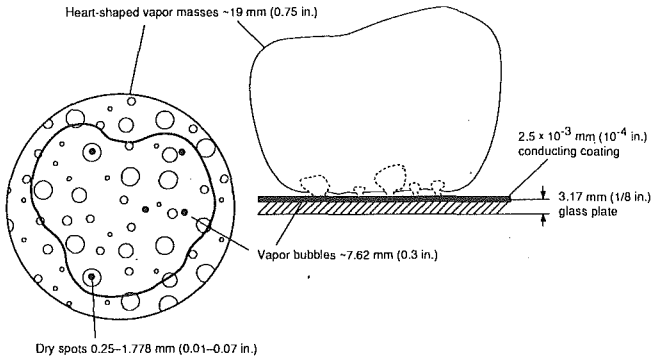

Fig. 2(*a*) Sketch of vapor structure and dry spots observed by Kirby and Westwater (1965) on a flat horizontal plate

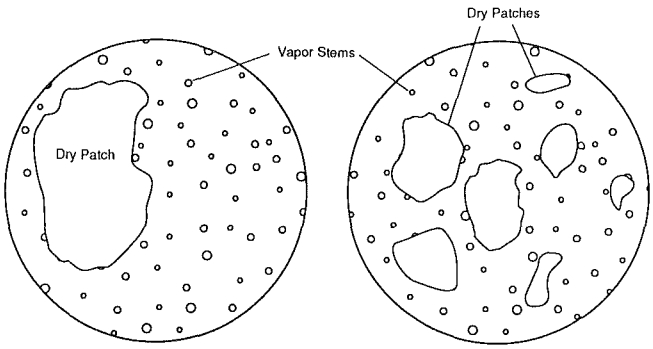

Fig. 2(*b*) Sketch of the top view of vapor structure and vapor patches in the second transition region

normally wetted when liquid rushed to the surface. If the heat flux was sufficiently high, at some point on the heated surface a dry area was not wetted and started growing, leading to burnout. Van Ouwerkerk also observed that the formation and disappearance of dry areas continued at other points while the critical one continued to grow. It is interesting to note that at atmospheric pressures, the dry areas formed a square grid at 10-mm intervals. The maximum size and lifetime of dry areas did not change significantly when the heat flux varied from 80 to 100 percent of the burnout value. However, the frequency of their occurrence did increase with increasing heat flux.

(B) Thick Horizontal Surfaces. One of the earliest papers reporting information on patchwise boiling using organic fluids was published by Corty and Foust (1955). They observed that stable patchwise boiling on a thick, rectangular, horizontal copper plate was possible. The wall superheats in these liquid patches were at typical nucleate boiling values, whereas the bare spots were at much higher superheats.

Carne (1965) studied pool boiling of organic fluids and water at atmospheric pressures on horizontal steel elements with various diameters. He visually observed that a small vapor patch instantaneously occurred at some random location on the heater surface. He postulated that the fluid local to the patch passes through a transition boiling state where the mode of heat transfer changes from nucleate to film boiling.

The existence of an unexpected region beyond the vapor mushroom region was first reported by Gaertner and Westwater (1960) when they studied the nucleation characteristics of nickel salt solution on a thick horizontal copper block 50 mm in diameter. The boiling curve indicated that the heat transfer coefficient was decreased when the heat flux was above 317,000 Btu/(h•ft^2). Gaertner initially postulated that the occurrence of the second transition region was a result of either the unique properties of the nickel salt solution or geometry, orientation, and heater surface effects. Finally, he stated that at high heat fluxes, the formation of dry patches large in comparison with individual bubbles could be responsible for the decrease in heat transfer rate.

Later Gaertner (1965) repeated this experiment for water with similar-sized heaters made of copper and platinum. The second transition region again was observed. Gaertner speculated that the reason these vapor patches were not seen on small wires, thin strips, and small tubes was that the heat capacity for these heaters is small. It was also difficult to distinguish vapor patches from a vapor mushroom on the horizontal copper plate. Thus, no information on the size and the formation of these vapor patches was reported. The sketch shown in Fig. 1 (similar to that given by Gaertner) for the vapor structure in the second transition region implies that a significant amount of the surface area can be covered by vapor patches. This sketch also implies that the patch appears over only part of the heater surface. An imagined top view of the heater is illustrated in Fig. 2(*b*). As shown in the figure, the patches can occur in different sizes at several different locations on the heater surface. The locations of these patches could be stationary or nonstationary for each bubble cycle (hovering period). More definite information on this is not currently available.

III The Heat Transfer Model for the Second Transition Region of Nucleate Boiling

The term "steady-state," as used in boiling heat transfer, really means that the total time over which process averaging is done is large enough to include a sufficient number of periods of the controlling phenomena to produce a time-averaged quantity that is constant from one time window to the next; i.e., the quantities typically used to represent the process are stationary. Heat flux (energy transferred to the fluid from the surface per unit area and time) and surface temperature are such quantities. If one were to consider the steady-state process in terms of a time period shorter than that which produces stationary quantities, it would become apparent that the controlling physical phenomena involved in the boiling process are really transient, even in a "steady-state" situation. The steady-state data available in the literature allow us to develop detailed, microscopic transient physical models of the boiling process. This is done by making time and space averages of calculated quantities to compare with data. We have applied this approach in our study of the second transition region of nucleate boiling.

The key to the development of a dry patch model in the second transition region is the solution of the transient two-dimensional conduction problem in a heater under various boundary conditions (see Fig. 3). Figure 3 is an idealized representation of any single dry spot or patch in Fig. 2(*b*). The coordinate system is located at the "center" of the patch. The boundary between the dry-patch region and the two-phase macrolayer region is assumed circular. This approximation is probably more accurate for small spots and patches than large ones; however, no information is available on either large or small patches to justify a more complex solution of an irregular boundary.

The wetted portion of the heater in Fig. 3, denoted as a two-phase macrolayer region, includes the macrolayer with numerous vapor stems. Single stems involve relatively small dimensions (on the order of several hundred microns) when compared to the dimensions of the dry patch (on the order of centimeters). This size (scale) consideration allows the rate of heat transfer in the two-phase macrolayer region to be represented by a surface-averaged, time-dependent heat-transfer coefficient, h_2. The major difficulty in developing the model is the construction of a realistic representation of the "dry" portion of the surface. Remember that this part of the heater

Downloaded 13 Dec 2010 to 193.140.21.150. Redistribution subject to ASME license or copyright; see http://www.asme.org/terms/Terms_Use.cfm

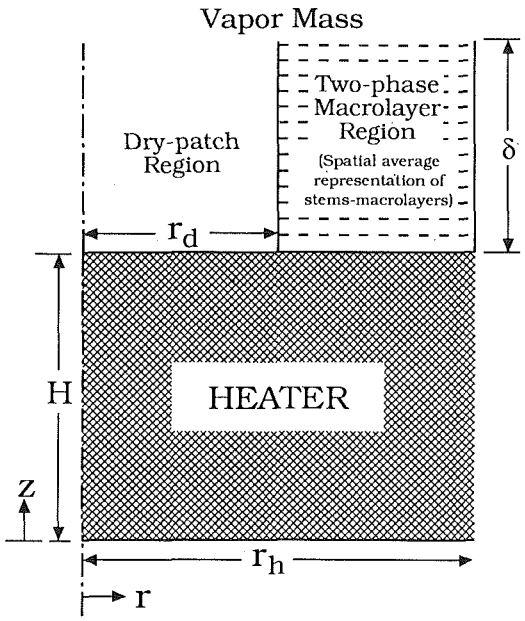

Fig. 3 Sketch of the proposed heat transfer model for the second transition region of the nucleate boiling

is actually dry only for some fraction of the lifetime of the vapor bubble. A realistic estimate of when during the vapor mushroom's lifetime a dry patch appears and how it appears and grows must be made. During the time that dry patches occur, the rate of heat transfer from the dry portion of the heater is represented by a surface-averaged, time-dependent heat transfer coefficient, h_1. The determination of h_1 and h_2 will be discussed in greater detail in Sections III.F and III.G. This problem is numerically solved in a manner similar to the method used by Pasamehmetoglu et al. (1991), Chappidi et al. (1991), and Pasamehmetoglu et al. (1992).

(A) Heater Conservation Equation. For the dry patch model shown in Fig. 3, the two-dimensional heat conduction equation in cylindrical coordinates is given for the heater by

$$\rho_h c_h \frac{\partial T}{\partial t} = k_h \left(\frac{\partial^2 T}{\partial r^2} + \frac{1}{r}\frac{\partial T}{\partial r} + \frac{\partial^2 T}{\partial z^2} \right) + LP \times Q_0, \tag{1}$$

where LP is an integer quantity representing the problem type and is equal to 1 for internal heat generation and 0 for the boundary condition of constant heat flux or temperature at the lower end of the heater. In this study, the constant heat flux boundary condition at the bottom of the heater is used for all calculations except for the thin copper heater, where the internal heat generation option was used.

(B) Heater Boundary Conditions. Symmetric radial boundary conditions are used at $r = 0$ and $r = r_h$ for all z. Thus, the radial temperature gradient becomes zero at those boundaries:

$$\frac{\partial T}{\partial r} = 0. \tag{2}$$

At $z = 0$ for all r, the heat flux is specified as the surface- and time-averaged (STA) experimental heat flux if a thick heater is considered (in this case, this is the CHF value):

$$-k_h \left.\frac{\partial T}{\partial z}\right|_{z=0} = q_{\mathrm{CHF}} \text{ for } LP = 0. \tag{3}$$

For thin heaters, the internal heat generation option, $LP = 1$, is used. In this case, the bottom of the heater is considered to be perfectly insulated.

$$\left.\frac{\partial T}{\partial z}\right|_{z=0} = 0 \text{ for } LP = 1. \tag{4}$$

At $z = H$, the boundary conditions are the surface-averaged, time-dependent heat transfer coefficients for both the dry patch and macrolayer regions and are given by

$$-k_h \left.\frac{\partial T}{\partial z}\right|_{z=H} = \langle h_1 \rangle (T(H, r, t) - T_{\mathrm{sat}}) \text{ for } 0 < r < r_d, \tag{5}$$

where

$$\langle h_1 \rangle = \begin{cases} \langle h_1 \rangle(t) & \text{for } 0 < t < t_d \\ 0 & \text{for } t_d < t < \tau \end{cases} \tag{6}$$

and

$$-k_h \left.\frac{\partial T}{\partial z}\right|_{z=H} = \langle h_2 \rangle (T(H, r, t) - T_{\mathrm{sat}})$$

$$\text{for } r_d \le r \le r_h \text{ and } 0 < t < \tau. \tag{7}$$

Determination of $\langle h_2 \rangle$ and $\langle h_1 \rangle$ are discussed in Sections III.F and III.G, respectively. Note that although the spatial averaging brackets, $\langle\ \rangle$, are shown in Eqs. (5)–(7), they will be dropped for convenience in the remainder of the paper.

(C) Heater Initial Conditions. The importance of the initial temperature distribution in the heater is dependent on whether single or multiple bubble lifetimes produce the hot spots. It will be shown later that thin isothermal and non-isothermal heaters produce a dry spot within the first bubble's lifetime. Thus, a realistic estimate of the initial temperature distribution in the heater is required. On the other hand, thick isothermal heaters required multiple bubble lifetimes for heating of the hotspots, indicating the bubble's position must be nearly stationary on the heater surface. For this case, the stationary temperature solution is independent of the initial temperature estimate as long as the initial estimate is reasonable. Although we feel it is important to realize the different perspectives of these two limiting conditions, we use our best estimate of the initial temperature distribution in the heater before dry spot appearance for both types of calculations.

To calculate an initial temperature distribution that would represent the heater before the appearance of a dry spot, no dry region was assumed. Thus, h_2 was assigned to the whole upper surface of the heater, and some initial temperature distribution was estimated. The governing equation for the heater was solved numerically until convergence between two consecutive hovering periods was obtained. This calculated heater temperature distribution (found to be a function of z only) at the end of this converged hovering period was used as the "initial temperature condition" within the heater for the general problem formulation of the heat transfer characteristics in the second transition region.

(D) Closure Relationships. The mushroom bubble hovering period, τ, was calculated from the relationship suggested by Haramura and Katto (1983) given by

$$\tau = \left[\frac{3}{4\pi}\right]^{\frac{1}{5}} \left[\frac{4(\xi\rho_1 + \rho_v)}{g(\rho_1 - \rho_v)}\right]^{\frac{3}{5}} \left[\frac{A_h q}{\rho_v h_{fg}}\right]^{\frac{1}{5}} \tag{8}$$

where ξ is assumed to be 11/16. After the vapor mushroom departs, the model assumes that fresh saturated liquid wets the surface. The interfacial surface temperatures between the heater and liquid at the instant of rewet are calculated through the instantaneous contact temperature relationship given by Carslaw and Jaeger (1959).

(E) Solution Method and Accuracy. The governing equations were solved using an explicit finite-difference scheme. With small time steps, the explicit finite-difference solution

Downloaded 13 Dec 2010 to 193.140.21.150. Redistribution subject to ASME license or copyright; see http://www.asme.org/terms/Terms_Use.cfm

yields accurate results. The time-step size was selected based on standard Courant-limit stability considerations.

The validity of the numerical model was checked in two ways. First, the model was used to predict known solutions for various problems. Second, the stability of the stationary solution was verified by changing the initial thermal conditions in the heater (see Section III.C) such that convergence was obtained from different starting points. Convergence occurs when the STA wall heat flux and temperature between two consecutive hovering periods are unchanged. These starting points included both points above and below the stationary heat temperature distribution.

The calculations were done using a CRAY XMP that has a round-off error of 0.3 (10^{-14}). This implies round-off beginning with the 14th digit of a real number. With double precision, this round-off error becomes smaller (29 digits of precision). To check the propagation of round-off error, a typical problem was run to convergence to the stationary solution in the standard single-precision mode. The problem then was restarted using both single- and double-precision versions of the computer code and run for a single bubble lifetime. This restarted calculation indicated that the surface temperatures differed only in the ninth digit at the end of the bubble's life for the single-precision calculation. This propagation error resulting from round-off is very small because of the stationary nature of the calculation, indicating that the calculation is far more accurate than the model itself.

Dry patch calculations began by inputting both the experimental wall heat flux as a lower ($z = 0$) boundary condition and dry patch size into the model. For a thick copper boiling surface, a minimal change in the STA wall temperature was observed over a single bubble lifetime because of the capacity of the copper to store heat energy. Thus, a number of bubble lifetimes were calculated. For multiple bubble lifetimes, the dry patch boundary, r_d, is envisioned as representing the "average boundary" location because this boundary might move somewhat from bubble to bubble. The calculation is started from the initial temperature distribution in the heater described in Section III.C, but for succeeding bubbles, the instantaneous temperature distribution at the end of the previous hovering period becomes the initial heater temperature distribution for the next hovering period. The transient calculation was terminated when the convergence criterion was satisfied. If the converged STA wall temperature and heat flux do not agree with the measured values, the size of the dry patch is varied and the calculation is repeated until agreement between the calculated and measured information is achieved.

(F) Calculation of the Surface-Averaged, Time-Dependent Heat Transfer Coefficient, h_2, Representing the Macrolayer Region (Wetted Region). The two-phase macrolayer region, shown in Fig. 3, is characterized by numerous vapor stems and a liquid macrolayer. The evaporation of the liquid macrolayer is the main mechanism for transporting energy from the heater. This process is very efficient; thus, the STA wall superheat in the macrolayer region is expected to be lower than the measured STA wall superheat in the second transition region. At the CHF, the STA wall superheat for the macrolayer region can be estimated by the wall-heat-flux/wall-superheat relationship suggested by Gaertner (1965) for the vapor mushroom region, as shown in Fig. 1 (point A). At point A, the STA wall superheat is 20.3°C, whereas the measured STA wall superheat, which is really the CHF, is 43.4°C. The overall heat transfer in the wetted region is represented by a time-dependent, surface-averaged heat-transfer coefficient, h_2, that is used in the proposed model.

This coefficient, h_2, can be obtained from the model and method developed by Pasamehmetoglu and Nelson (see Chappidi et al., 1991, and Unal et al., 1991) valid at point A of Fig. 1. Here, only the main features of the model are summarized. A sketch of the model would be similar to that shown in Fig. 3, except the "two-phase macrolayer region" would be replaced by a single-phase liquid macrolayer and the "dry patch region" replaced by a totally dry vapor stem. This stem calculation represents a single vapor-stem and the associated macrolayer configuration. The stem and heater sizes are those required to represent an average vapor stem. The single-stem model numerically solves Eq. (1) for the heater, the same equation with $LP = 0$ within the liquid macrolayer, and the appropriate transport properties using an explicit scheme. The boundary conditions and major assumptions used in the stem model are summarized by Pasamehmetoglu et al. (1991) or Unal et al. (1991). Dividing the instantaneous surface-averaged heat flux by the corresponding instantaneous surface-averaged wall superheat for this stem calculation yields the time-dependent, surface-averaged, heat transfer coefficient, h_2, for the hovering period in which convergence to a stationary solution is obtained.

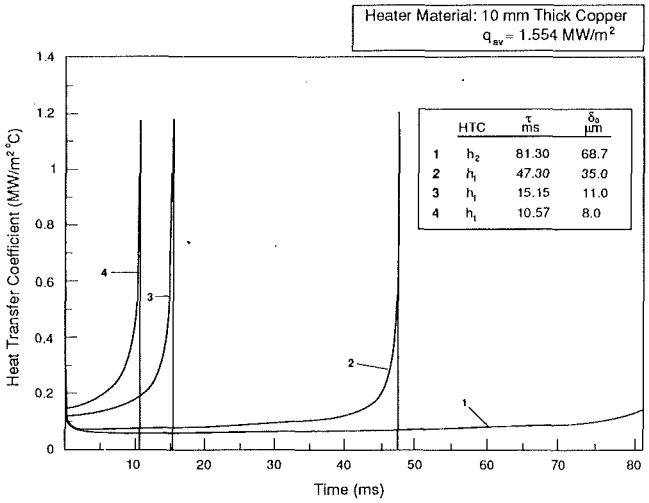

Fig. 4 Instantaneous surface-averaged heat transfer coefficient representing dry patch and two-phase macrolayer regions for 10-mm-thick copper plate

To obtain h_2, a stem calculation was performed for a copper heater representing Gaertner's heater. The stem and other calculations presented in this paper were performed for a CHF of 1.554 MW/m^2, the value reported by Gaertner. Details of the input parameters defining the finite-difference node sizes and the calculated output parameters for the stem calculation are available from Unal et al. (1991). The result is shown in Fig. 4 with the symbol 1. The heat transfer coefficient h_2 is relatively high at the beginning of the new hovering period. This is because when fresh saturated liquid wets the surface, the surface temperature, calculated through the instantaneous contact temperature relationship, decreases. Conduction within the heater then transports significant energy early in the bubble's lifetime to reheat the surface and liquid. The increase in the surface heat flux and a decrease in wall temperature result in a significant increase in h_2. Later, in the window between 5 and 90 percent of the hovering period, h_2 gradually increases. At the end of the hovering period, the heat transfer coefficient increases at a relatively faster rate. In this period, the liquid macrolayer thickness becomes relatively thin, causing the conduction through the liquid macrolayer to increase significantly. While not shown here, the surface-averaged, time-dependent heat transfer coefficient h_2 is calculated in a similar manner for both the 10-mm-thick nickel and 0.1-mm-thick copper heaters, which are discussed as part of the Results Section.

(G) Calculation of the Surface-Averaged, Time-Dependent, Heat Transfer Coefficient, h_1, Representing the Dry Patch Region. The determination of the surface-averaged, time-

Downloaded 13 Dec 2010 to 193.140.21.150. Redistribution subject to ASME license or copyright; see http://www.asme.org/terms/Terms_Use.cfm

dependent heat transfer coefficient for the dry region, h_1, uses the same approach and model used in determining h_2. The only difference is in the specification of the initial liquid macrolayer thickness and the initial heater temperature distribution. With a specified initial macrolayer thickness and heater temperature distribution, the governing equations are solved only for a time period, t_d, necessary to evaporate the macrolayer completely.

The difficult part is the selection of the initial macrolayer thickness that will dry out and cause the dry patch. Several different alternatives were tried in order to estimate this thickness realistically. In the first approach, we asked the question, "What initial macrolayer thickness would evaporate in a hovering period at the heat flux level (0.906 MW/m^2) corresponding to the beginning of the second transition region?" The answer to this question can be obtained by making a stem calculation with an initially guessed macrolayer thickness at a heat flux of 0.906 MW/m^2. The initial macrolayer thickness that would evaporate in a hovering period (73 ms at 0.906 MW/m^2) was found to be 35 μm. This value represents an upper limit for the surface-averaged initial macrolayer thickness that might exist on the part of the heater where the dry patches occur.

We also chose two other initial thicknesses for the macrolayer in the evaluation of h_1, 11 and 8 μm. The initial thickness of 11 μm was selected based on Haramura's (1989) recent study. He obtained transient surface-averaged heat flux measurements with simultaneously taken high-speed photographs on a constant-temperature surface (horizontal tube) heated by electric current. He postulated that the heated surface begins to dry when the heat flux begins to decrease while a coalesced bubble covers the surface. Therefore, heat added in the interval between the time when the coalesced bubbles are formed and the time when the heat flux begins to decrease might equal the latent heat of the liquid layer. Using this argument, he calculated an 11-μm initial macrolayer thickness for a stainless-steel rod heater 0.69 mm in diameter. We realize that Haramura's geometry is different than ours; however, it is the only information of this type available to us and does not contradict the maximum possible thickness of 35 μm. The third value of 8 μm is simply an intermediate value. Thus, at this point, we can say that the initial minimum macrolayer thickness occurring in the dry patch region theoretically could vary between 0 and 35 μm.

The time required to evaporate the macrolayer (drying time), t_d, can be estimated from a heat-balance equation using the STA heat flux. The drying times were estimated to be 47.7, 14.99, and 10.9 ms for initial thicknesses of 35, 11, and 8 μm at an STA heat flux of 1.554 MW/m^2. Because of the explicit nature of the finite-difference solution, the numerical solution was not stable when the macrolayer thickness was close to a value corresponding to the two axial node sizes in the macrolayer. (This is simply a result of our current numerics and has no real physical or numerical meaning.) Therefore, care was taken to prevent this numerical instability by increasing the number of axial nodes in the macrolayer and assuming that the macrolayer was completely evaporated when the thickness of the macrolayer calculated at the last time step was less than 1.5 μm. This resulted in a minor adjustment of the drying times that were found to be 47.3, 15.15, and 10.57 ms for initial thicknesses of 35, 11, and 8 μm, respectively.

The calculated instantaneous heat transfer coefficients h_1 for initial thicknesses of 35, 11, and 8 μm are given in Fig. 4 for a 10-mm-thick copper heater. As the initial macrolayer thickness decreases, the instantaneous heat transfer coefficient increases.

IV Results and Discussion

This section discusses several aspects of the dry-patch second transition region problem. First, the necessary surface dry patch areas corresponding to different drying times are determined if homogeneous nucleation is used as the criterion for liquid-solid contact at the center of the dry patch. Second, the bounds on the initial dry patch macrolayer thickness are refined. Third, an improved estimate of the critical liquid-solid contact temperature is made and compared to available data. Finally, the effects of heater material and thickness on dry patch size are studied.

(A) Surface Areas and Drying Times Required for the Temperature at the Center of the Dry Patch to Reach the Homogeneous Nucleation Temperature of the Fluid. The homogeneous nucleation temperature of water at atmospheric pressure was calculated by the equation suggested by Lienhard (1982) to be 345°C. Ramilison and Lienhard (1987) indicated that the liquid-solid contact temperature at the onset of film boiling could be as high as the homogeneous nucleation temperature of the fluid if the advancing contact angle is low (approaching 0 deg, highly wetting fluid). Although the contact angle of water on a clean copper surface was reported to be 90 deg by Liaw (1988), we nevertheless *initially* investigated the possibility of having the local point at the center of the dry patch reach the homogeneous nucleation temperature of the fluid as a bounding case. In doing this, we asked the following questions:

(*a*) What dry patch area is possible?
(*b*) How quickly should the liquid macrolayer be evaporated in order to obtain the homogeneous nucleation temperature at the center of a dry patch?

To calculate the maximum possible dry patch area, an "infinitely large" copper heater with a radius of 300 mm was considered in the first calculation (Run 1). On the heater surface, the dry patch was assumed to appear instantly with a given size. (The drying time of the liquid macrolayer in this region was assumed to be 0.0 ms.) The heat transfer coefficient, h_2, representing numerous vapor stems on the wetted portion of the heater and shown in Fig. 4, was used for the boundary condition. The dry patch radius required for the center temperature (T_{TL}) of the dry patch to exceed the homogeneous nucleation temperature of the liquid was calculated to be 44.4 mm. The other calculated parameters, such as heater superheats at four locations "in" the heater, are listed in Table 1.

The calculated maximum dry patch radius (44.4 mm) is much larger than the heater size used by Gaertner (25.4 mm) and implies that the temperature at the center of dry patches at the occurrence of CHF in Gaertner's experiments must have been less than the homogeneous nucleation temperature of the liquid.

To answer the second question, a heater with a radius of 25 mm (the same size as Gaertner's heater) was considered. In this calculation (Run 2), we assumed that the whole heater surface was covered by the dry patch region (no wetted region existed). As a boundary condition on the heater surface, the heat transfer coefficient h_1, obtained with an initial macrolayer thickness of 35 μm, was used. The drying time and its corresponding h_1 were varied until the temperature at the center of the heater exceeded the homogeneous nucleation temperature of the water. As shown in Fig. 4, this simple time scaling of the drying time to reflect different initial dry patch macrolayer thicknesses does produce some error for thinner initial

Table 1 Calculated STA wall heat flux and surface temperatures

Run No.	Material	t_d (ms)	H (mm)	δ_d (μm)	r_d (mm)	r_h (mm)	r_d/r_h	T_{av} (°C)	q_{av} (MW/m^2)	ΔT_{BL} (°C)	ΔT_{BR} (°C)	ΔT_{TL} (°C)	ΔT_{TR} (°C)
1	Copper	0.0	10.0	0.0	44.4	300	0.148	23.8	1.540	266.0	60.2	246.0	22.1
2	Copper	7.0	10.0	~5.0	25.0	25	1.000	228.8	1.553	269.1	267.5	235.5	230.2
3	Copper	47.3	10.0	35.0	25.0	25	1.000	27.0	1.553	66.2	66.2	33.0	32.0
4	Copper	15.0	10.0	11.0	23.0	25	0.920	44.2	1.550	86.1	82.2	57.0	34.0
5	Copper	10.57	10.0	8.0	20.9	25	0.836	42.5	1.548	87.0	79.2	59.0	29.4
6	Copper	0.0	10.0	0.0	15.0	25	0.600	43.8	1.543	100.0	76.5	80.0	27.0
7	Nickel	0.0	10.0	0.0	4.0	25	0.160	27.0	1.520	225.0	219.0	80.5	26.1
8	Copper	0.0	0.1	0.0	2.25	25	0.090	21.3	1.554	82.0	19.3	82.0	19.4

Downloaded 13 Dec 2010 to 193.140.21.150. Redistribution subject to ASME license or copyright; see http://www.asme.org/terms/Terms_Use.cfm

dry patches. However, a conservative heat transfer coefficient does result, and it saves going through the iterative process of generating the true h_1 required. Subject to this approximation, the necessary drying time was found to be 7 ms (a small fraction of the mushroom lifetime, 81.3 ms), indicating almost instantaneous occurrence of the dry patch over the whole heater surface. The calculated wall superheats at the "four corners" of the heater and STA wall heat flux are listed in Table 1.

The above analysis indicates that the liquid–solid contact temperature at the occurrence of CHF should be well below the homogeneous nucleation temperature of the water in order to predict Gaertner's CHF data obtained on a thick copper heater with a radius of 25 mm. The requirement of relatively lower temperatures for liquid–solid contact to occur will result in relatively smaller dry patch sizes, as discussed below. The analysis also shows the importance of knowing when the dry patches occur.

(B) The Thickness of the Initial Macrolayer in the Dry Region of the Heater. In Section III.G, the upper bound of the initial macrolayer thickness in the dry patch region of Gaertner's heater was estimated to be 35 μm. This number was calculated at the beginning of the second transition region. Using h_1 calculated for the initial macrolayer thickness of 35 μm in the dry-patch region and h_2 for the macrolayer region, the size of the dry patch was varied to match the measured STA wall superheat at a CHF of 1.554 MW/m^2 in Run 3. The calculated STA wall superheats and heat fluxes with other parameters are listed in Table 1.

Even though the dry-patch radius was selected to be 25 mm, the heat transfer coefficient used in the dry-patch region, h_1, and the drying time, t_d, were high enough to keep calculated STA wall superheat, 27°C, less than measured value, 43°C. This is consistent with the results of Run 2 and again reflects the effectiveness of the latent heat in thin liquid layers to cool a surface. It implies that either a larger dry-patch size or a thinner liquid is needed to match the measured STA wall temperature.

Next, the initial thickness suggested by Haramura (1989), 11 μm, was assumed to exist before dry-patch occurrence. It should be remembered that Haramura considers the surface-area-averaged initial macrolayer thickness. In our model, we specify a thickness for local macrolayers in the dry patch region which should be less than Haramura's average. In Run 4, using h_2 and the h_1 calculated with an initial thickness of 11 μm, a dry patch radius of 23 mm was found to be necessary to obtain a reasonable comparison between the calculated STA wall superheat and the measured value. The calculated STA wall heat flux and superheat for Run 4 are given in Table 1. The calculated and measured STA wall heat fluxes and temperatures are in good agreement. The radius of the dry patch is 23 mm (92 percent of the heater radius). Although Gaertner did not report any information on the size of the dry patch, from his sketch, the radius of the dry patch is expected to be less than 23 mm. In light of this information, the initial thickness of 11 μm could only be an upper limit. Thus, we conclude that more realistic bounds on the initial thickness of the macrolayer at the location where the dry patch CHF occurs would be between 0 and 11 μm.

The answers associated with Runs 2, 3, and 4 also are important when considering Haramura and Katto's CHF model (1983). Because of its thermal properties, a flat thick copper plate shows no significant thermal response resulting from drying of the macrolayer at or just slightly before bubble departure: certainly nothing of a catastrophic nature such as CHF.

(C) The Critical Temperature for Liquid–Solid Contact at the Onset of the First Boiling Crisis. Above, we estimated a possible upper bound for the macrolayer thickness in the dry patch region. Using this maximum value, the wall surface temperature at the center of the dry patch (T_{TL}) was calculated to be 157°C at the end of the converged hovering period (see Run 4 in Table 1). This local-instantaneous temperature was considered to be the critical liquid–solid contact temperature for CHF to occur, because the calculation used an input heat flux that was observed as CHF in Gaertner's experiments. The reader must allow a slight contradiction here. We are allowing liquid–solid contact in the calculation by placing an initial liquid thickness of 11 μm on the dry patch, yet we call the resulting temperature at the center of the patch the "critical liquid–solid contact temperature," where liquid–solid contact is not possible. One might think of this calculation as being performed just a few W/m^2 below the CHF and the resulting critical temperature as just a fraction of a degree below the true critical temperature. In the spirit of the calculation, we think this terminology is acceptable. However, 157°C represents a lower bound for the critical liquid–solid (rewetting) contact temperature because it was calculated using a maximum possible macrolayer thickness. Based on Gaertner's observation, the dry patch radius is expected to be smaller than 23 mm. Although this is certainly a debatable view, we feel that if Gaertner had observed 92 percent (based on diameter) of the heater dry at the CHF, he would have been much more emphatic about it. This is only possible if a smaller initial macrolayer thickness and, correspondingly, a shorter drying time were used for the dry patch region of the heater. Of course, one can expect that the critical rewetting temperature might increase with decreasing dry patch lifetime.

To investigate further the possible range for the rewetting temperatures (superheats) at which no liquid–solid contact can occur, two additional cases were considered as follows:

(*a*) An initial thickness of 8 μm existed in the dry patch liquid macrolayer.

(*b*) The dry patch was assumed to occur instantaneously (drying time was zero, implying that no heat transfer occurred in the dry patch region).

Case (*b*) represents the other bounding case, i.e., 11 μm is the maximum thickness, and instantaneous dryout is the minimum thickness. Case (*a*) is simply an intermediate value for initial thickness. Again, the calculated STA wall superheats were matched with the measured superheat by varying the size of the dry patch at the CHF point.

The results obtained for a δ_d of 8 μm in Run 5 are summarized in Table 1; the radial wall superheats at the end of the converged hovering period at six different axial elevations are plotted as function of the heater radius in Fig. 5. When the δ_d (and thus the drying time, t_d) was decreased, the predicted dry patch radius decreased to 20.9 mm (83.6 percent of the heater radius), indicated by a vertical line in the figure. The calculated wall superheat at the center of the dry patch increased to 59°C. The instantaneous surface temperatures at the top of the heater are fairly constant up to the heater radius of 18 mm. Then it gradually decreases to typical values calculated for the macrolayer region. The radial variations in temperature at the bottom of the heater are relatively small, about 5°C. The radial temperature profile a few millimeters beneath the surface becomes practically flat.

The heater temperature distributions for δ_d of zero, Run 6, are given in Fig. 6, and the calculated STA wall heat flux and superheat are listed in Table 1. As shown in Fig. 6, the radial temperature profile becomes much steeper since no heat transfer was assumed to occur at the dry patch. The surface superheats in the macrolayer region are further decreased to about 27°C. The superheat at the center of the dry patch for this case is calculated as 80°C. The predicted radius of the dry patch becomes 15 mm (60 percent of the heater radius) as indicated in Fig. 6.

A quick summary of our results shows that the initial thickness of liquid macrolayers causing dry patch formation should vary between 0 and 11 μm. We found that the corresponding

Downloaded 13 Dec 2010 to 193.140.21.150. Redistribution subject to ASME license or copyright; see http://www.asme.org/terms/Terms_Use.cfm

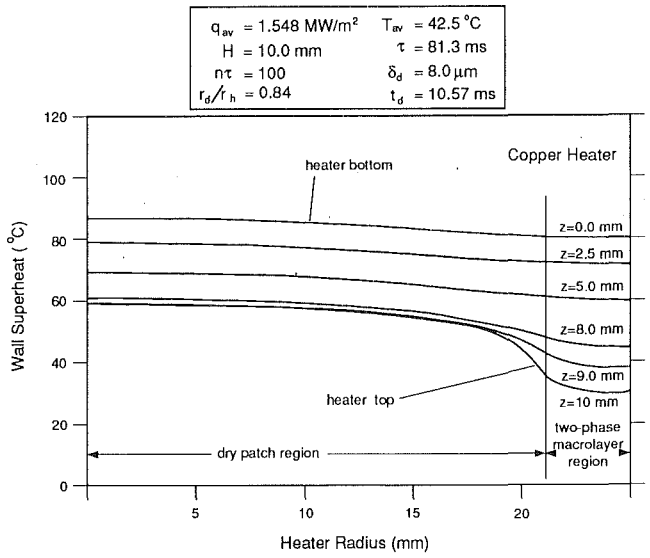

Fig. 5 Calculated heater temperature distribution for 10-mm-thick copper plate using a heat transfer coefficient in the dry patch region that is obtained with an initial thickness of 8 μm

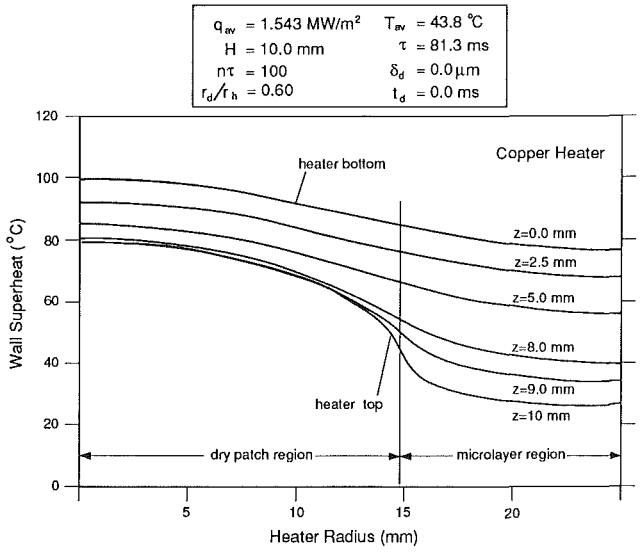

Fig. 6 Calculated heater temperature distribution for 10-mm-thick copper plate using a heat transfer coefficient in the dry patch region that is obtained with an initial thickness of 0 μm

dry patch radii resulting from these thicknesses were 15 and 23 mm, respectively. As noted earlier, our judgment, based on the Gaertner's dry patch description, is that the dry patch radius of 23 mm is too large. Therefore, 11 μm is too thick. Consideration of an arbitrary 8-μm thickness yields a dry patch radius of 20.9 mm. We believe that this dry patch radius is more reasonable, and therefore, the initial dry patch macrolayer thickness more likely varies between 0 and 8 μm. The calculated wall superheats at the center of the dry patch (local-instantaneous temperature) at which liquid-solid contact is no longer possible are 80°C and 59°C for macrolayer thicknesses of 0 and 8 μm, respectively. In practice, whether one believes that 20.9 mm is a better representation of the dry patch size than 23 mm has little effect on the calculated minimum temperature. If 11 μm is retained as the maximum thickness, the calculated critical superheat only decreases 2°C to 57°C.

Are these calculated rewetting temperatures realistic or reasonable? Unfortunately, we do not have any direct experimental data to support the findings of the analysis we discussed

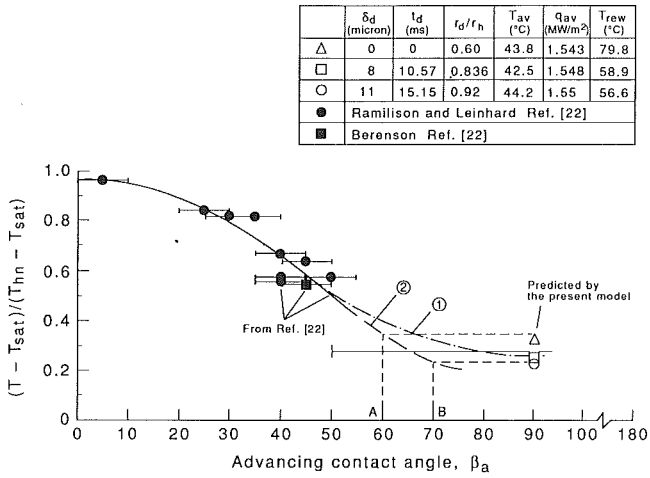

Fig. 7 Calculated liquid-solid contact (rewetting) temperature at the onset of CHF

above. However, Ramilison and Lienhard (1987) reported some limited information for contact temperature data at the onset of the transition-film boiling region as a function of contact angle, which we will use to provide some assessment of our results. Their data are shown in Fig. 7 with the solid circles and rectangles. Figure 7 shows the fraction of the limiting liquid superheat at which the first contact occurs as a function of the advancing contact angle. The limit of the contact temperature as the advancing contact angle approaches zero (perfectly wetting fluid) is the homogeneous nucleation temperature of the liquid. An increase in the contact angle makes liquid-solid contact more difficult.

To assess our estimated contact temperatures against the data in Fig. 7, we also must estimate a contact angle for water on copper. Liaw (1988) reported that the contact angle was measured to be 90 deg for water on a clean copper surface. In Gaertner's study, the surface was cleaned before each test; thus, it is reasonable to assume that the contact angle in Gaertner's study was about 90 deg. However, it should be noted that Liaw measured static contact angle, whereas the contact angle of the rewet process at the beginning of each hovering period is dynamic in nature. Nevertheless, differences between dynamic and static contact angle will be considered as part of the uncertainty of contact angle as noted below.

Liaw and Dhir (1989) also indicated that the contact angle of water on copper surfaces falls below the value of 90 deg if the heater surface oxidizes. In Gaertner's nucleate boiling experiments, the water was degassed; however, it is still possible that some air could have remained in the water, resulting in the oxidation of the copper surface during the experiments. In light of this statement, Liaw and Dhir's experimental observation, and considering the differences between static and dynamic conditions, the contact angle of water in Gaertner's experiments could have uncertainties as high as 50 percent, varying between 50 and 90 deg. In fact, for industrial applications, the contact angle of water is generally assumed to vary between 50 and 90 deg. Therefore, in Fig. 7, we indicate a contact angle of 90 deg, with an uncertainty band of −50 percent.

In Fig. 7, our calculated rewetting temperatures are compared with Ramilison and Lienhard's data and are indicated at a 90 deg contact angle point. It should be remembered that the local-instantaneous temperature at the center of the dry patch was relatively high, indicating that the surface was dry at the end of a hovering period. Thus, the liquid-solid contact at the beginning of the following hovering period can be characterized by the advancing contact angle. The calculated liquid-solid contact temperatures at the CHF do show reasonable

Downloaded 13 Dec 2010 to 193.140.21.150. Redistribution subject to ASME license or copyright; see http://www.asme.org/terms/Terms_Use.cfm

agreement with the contact temperature at the onset of the liquid–solid contact in film boiling, if the Ramilison and Lienhard data are extrapolated by the line numbered with 1. If the calculated contact temperatures were plotted on their extrapolated curve (curve 2), the contact angle of water is estimated to vary between 60 and 70 deg (points A and B in Fig. 7). These values are in the expected range of the contact angle of water as discussed above. This indicates that the calculated contact temperatures at the onset of CHF are in good agreement with extrapolated contact temperatures at the onset of film boiling. Thus, the hypothesis we propose for the controlling mechanism of the CHF—that the local-instantaneous temperature at the center of a dry patch reaches a point where rewetting of the surface is no longer possible, causing a runaway condition—seems quite reasonable.

(D) The Effect of the Thermal Conductivity and Thickness of the Heater on Dry Patch Size. Several researchers have reported that the thermophysical properties and the thickness of the heating surface may affect the boiling heat transfer coefficient. In most of the boiling tests that used either a thin heater or nonisothermal materials such as nickel, a second transition region did not exist, and the results showed a sharp decrease in wall heat flux after the CHF. Because of these experimental observations, we investigate below the effect of the thermal conductivity and heater thickness on dry patch characteristics.

To investigate the effect of thermal conductivity, a nickel heater with the same dimensions as the copper heater studied earlier (10 mm thick and 25 mm in diameter) was selected for Run 7. To produce the maximum bounding temperature, the dry patch with a given size was assumed to occur instantaneously (t_d = 0 s). The dry patch radius necessary to obtain the same contact temperature at the center of the dry patch as the value calculated for the copper heater was found to be 4 mm (16 percent of the heater radius). The STA wall heat flux and superheat are listed in Table 1.

It is clear that the dry patch is much smaller for the nickel heater than for the copper heater. It would be difficult to detect patches this small visually in experimental studies, and their effect on the boiling curve to create a second transition region should be minimal. For nonisothermal materials, the heat transfer becomes conduction-controlled and the local-instantaneous wall temperature at the center of the relatively small dry patch reaches the critical rewetting temperature in relatively short times (a single hovering period), leading to CHF at relatively lower heat fluxes.

To investigate the thickness effect, a similar bounding calculation was performed for a copper heater with a thickness of 0.1 mm and with no heat transfer on the dry patch region (Run 8). A dry patch radius of 2.25 mm (9 percent of the heater radius) was enough for the temperature at the center of the dry patch to reach the rewetting temperature of 80°C. Dry patches with radii of 1–2 mm have been observed by Kirby and Westwater and Van Ouwerkerk, although their heater thicknesses were much smaller than 0.1 mm. In our calculation, further decreases in heater thickness would result in dry patch sizes smaller than 2.25 mm. Here, we only intend to demonstrate the importance of the heater thickness in determining the dry patch size. The other calculated parameters are given in Table 1. As it was in the case of a nonisothermal heater material, we believe the nucleate boiling curve would not indicate a second transition region if the heater is very thin.

The results obtained above for nonisothermal and thin-isothermal materials did not require that the calculations be performed over several hovering periods and were obtained in a single hovering period. This indicates that the stationary dry patch assumption required by the thick copper heater is not necessary for these situations. Thus, as observed by Van Ouwerkerk and Kirby and Westwater, the location of small dry spots may vary for each hovering period. We believe the results of the consideration of nonisothermal and thin materials does provide some qualitative assessment of the model and indicates why second transition is seen so infrequently.

V Summary and Conclusions

The current model assumes that the formation of dry patches is a result of the evaporation of the local liquid macrolayers. The thickness of the liquid macrolayer is believed to vary from one point to another on the heater surface, showing some statistical distribution. The thinner macrolayer regions dry out first, forming dry patches. The current idealized model considers a dry patch with a given size to have a circular shape. Currently, no radial growth of the dry patch is considered.

The occurrence of these patches alone is not sufficient to cause CHF. The temperature at the center of the dry patch first must reach a critical value above which liquid–solid contact is no longer possible. Once this condition occurs at a local point on the heater surface for most power-controlled systems, the hot spot starts growing, causing the dry patch finally to cover the entire heater surface, as the surface moves through transition boiling into film boiling. We believe that the occurrence of such a hot spot on the surface is the real cause of the CHF. This hypothesis unifies the CHF with the quenching of hot surfaces by relating them both to the same governing mechanism, i.e., the ability of liquid to contact a hot surface.

The boiling phenomenon in the second transition region of saturated pool nucleate boiling on a horizontal surface is used to study the hypothesis. A two-dimensional, transient-conduction model is used to represent the heater and its boiling surface. The wetted portion of the heater, denoted as having a time-dependent, surface-averaged heat transfer coefficient h_2, is characterized by a macrolayer having numerous vapor stems. The heat transfer coefficient h_2 was obtained from the model developed by Pasamehmetoglu and Nelson. Another time-dependent, surface-averaged heat transfer coefficient, h_1, describes the dry patch behavior, which is related to the thinner macrolayer initial thickness.

Using the information provided by Gaertner for the second transition region, the initial thinner macrolayer thickness on the dry portion of the heater was found to be bounded between 0 and 11 μm for a copper heater with infinite thickness. The corresponding dry patch radius varied from 15 to 23 mm, respectively. The liquid–solid contact temperature was found to vary from 180°C to 157°C for these bounding initial macrolayer thicknesses, respectively. These temperatures are much lower than the homogeneous nucleation temperature for water. The calculated contact temperatures were in reasonable agreement with the extrapolated contact temperature data for the onset of film boiling.

We also found that the formation of the dry patch must occur over a number of hovering periods on a thick isothermal heater. The calculated minimum dry patch radius of 15 mm represents a significantly large area and has not been reported quantitatively by any researchers either experimentally or analytically. Although it is possible that several dry patches of different sizes could occur on the surface, we think that, because the calculated dry-patch size is high when compared with Gaertner's heater size, the dry patch or patches on thick copper heater occur at a pseudostationary location. Therefore, the model considers a stationary dry patch.

To study the effects of thin heaters and heaters of different nonisothermal materials, we calculated the sizes of the dry patches associated with these changes. The radius of the dry patch for a thick nickel heater of the same diameter was small, 4 mm, using the same liquid–solid contact temperature obtained for the copper heater. When the thickness of the copper heater was decreased to 0.1 mm, the required dry patch radius was found to be 2.25 mm in order for the temperature at the

Downloaded 13 Dec 2010 to 193.140.21.150. Redistribution subject to ASME license or copyright; see http://www.asme.org/terms/Terms_Use.cfm

center of the dry patch to reach the same critical contact temperature. These dry patch sizes were obtained in a single-vapor-mushroom lifetime and thus did not require the dry patch to be stationary. Both the small dry patch size and its occurrence within a single-vapor-mushroom lifetime are believed to provide some explanation of why the second transition region has not been observed in these experimental situations.

The results obtained from the above analytical study are presented in the hope of furthering understanding of the mechanism governing the CHF. We suggest as a first step that future experiments easily could investigate the dry-patch characteristics implied for thick copper (i.e., pseudostationary, reasonably sized dry patches) to either discredit or further refine this hypothesis.

References

Borishansky, V. M., 1965, "An Equation Generalizing Experimental Data on the Cessation of Bubble Boiling in Large Volume of Liquid," *Zh. Tekh. Fiz.*, Vol. 26, No. 7, pp. 452–456.

Carne, M., 1965, "Some Effects of Test Section Geometry in Saturated Pool Boiling on the Critical Heat Flux for Some Organic Liquids and Liquid Mixtures," *Chem. Engr. Prog. Symp. Ser.*, Vol. 61, No. 59, p. 281.

Carslaw, H. S., and Jaeger, J. C., 1959, *Conduction of Heat in Solids*, 2nd ed., Oxford University Press, London.

Chang, Y. P., 1957, "A Theoretical Analysis of Heat Transfer in Natural Convection and in Boiling," *Trans. ASME*, Vol. 79, pp. 1501–1513.

Chang, Y. P., and Snyder, N. W., 1960, "Heat Transfer in Saturated Boiling," *Chem. Engr. Prog. Symp. Ser.*, Vol. 56, No. 30, pp. 25–38.

Chappidi, P., Unal, C., Pasamehmetoglu, K., and Nelson, R. A., 1991, "Saturated Pool Boiling Mechanisms at High Heat Fluxes; A Superposition Method for Averaging the Local-Instantaneous Variation in Wall Temperatures and Heat Flux With a Statistical Distribution of Active Cavities," ASME HTD-Vol. 159, pp. 119–130; Los Alamos National Laboratory document LA-UR-90-4385 (1990).

Corty, C., and Foust, A. S., 1955, "Surface Variables in Nucleate Boiling," *Chem. Engr. Prog. Symp. Ser.*, Vol. 51, No. 17, pp. 1–12.

Egan, P. J., Jr., and Westwater, J. W., 1985, "Effect of Horizontal Plate Diameter on Boiling Heat Transfer From Copper to Nitrogen," *J. Thermal Engineering*, Vol. 4, No. 1.

Gaertner, R. F., and Westwater, J. W., 1960, "Population of Active Sites in Nucleate Boiling Heat Transfer," *Chem. Engr. Prog. Symp. Ser.*, Vol. 56, No. 30, pp. 39–48.

Gaertner, R. F., 1965, "Photographic Study of Nucleate Pool Boiling on a Horizontal Surface," ASME JOURNAL OF HEAT TRANSFER, Vol. 87, pp. 17–29.

Haramura, Y., 1989, "Characteristics of Pool Boiling Heat Transfer in the Vicinity of the Critical Heat Flux (Relations Between Bubble Motion and Heat Flux Fluctuations)," *Journal of the JSME*, Vol. 53, 1986–87, p. 490; translated by Scripta Technica.

Haramura, Y., and Katto, Y., 1983, "A New Hydrodynamic Model of Critical Heat Flux, Applicable Widely to Both Pool and Forced Convection Boiling on Submerged Bodies in Saturated Liquids," *Int. J. Heat Mass Transfer*, Vol. 26, No. 3, pp. 389–399.

Hesse, G., 1973, "Heat Transfer in Nucleate Boiling, Maximum Heat Flux and Transition Boiling," *Int. J. Heat Mass Transfer*, Vol. 16, pp. 1611–1627.

Hsu, Y. Y., and Graham, R. W., 1976, *Transport Processes in Boiling and Two-Phase Systems*, McGraw-Hill, New York.

Kirby, D. B., and Westwater, J. W., 1965, "Bubble and Vapor Behavior on a Heated Horizontal Plate During Pool Boiling Near-Burnout," *Chem. Engr. Prog. Symp. Ser.*, Vol. 61, No. 57.

Kutateladze, S. S., 1951, "A Hydrodynamic Theory of Changes in Boiling Process Under Free Convection," *Izv. Akademia Nauk Otdelarie Tekh.*, Vol. 4, pp. 529–536; AEC-TR-1441, 1954.

Liaw, S. P., 1988, "Experimental and Analytical Study of Nucleate and Transition Boiling on Vertical Surfaces," Ph.D. thesis, Mechanical Engineering Department, University of California, Los Angeles.

Liaw, S. P., and Dhir, V. K., 1989, "Void Fraction Measurements During Saturated Pool Boiling of Water on Partially Wetted Vertical Surfaces," ASME JOURNAL OF HEAT TRANSFER, Vol. 111, pp. 731–738.

Lienhard, J. H., and Dhir, V. K., 1973, "Hydrodynamic Prediction of Peak Pool-Boiling Heat Fluxes From Finite Bodies," ASME JOURNAL OF HEAT TRANSFER, Vol. 95, pp. 152–157.

Lienhard, J. H., 1982, "Corresponding States Correlations for the Spinodal and Homogeneous Nucleation Temperature," ASME JOURNAL OF HEAT TRANSFER, Vol. 104, No. 23, pp. 379–381.

Nelson, R. A., 1986, "Mechanisms of Quenching Surfaces," in: *Handbook of Heat and Mass Transfer*, N. P. Cheremisinoff, ed., Vol. 1, Chap. 35, Gulf Publishing Company, Houston, TX, pp. 1103–1153.

Nelson, R. A., and Pasamehmetoglu, K. O., 1992, "Quenching Phenomena," in: *Post-Dryout Heat Transfer*, G. F. Hewitt, J. M. Delhaye, and N. Zuber, eds., CRC Press, Inc., Boca Raton, FL, pp. 39–183.

Pasamehmetoglu, K. O., Nelson, R. A., and Gunnerson, F. S., 1990, "Critical Heat Flux Modeling in Pool Boiling for Steady-State and Power Transients," ASME JOURNAL OF HEAT TRANSFER, Vol. 112, pp. 1048–1057.

Pasamehmetoglu, K. O., Chappidi, P. R., and Nelson, R. A., 1992, "Pool Boiling Mechanisms in Saturated Liquids at High Heat Fluxes Near Critical Heat Flux," Los Alamos National Laboratory report, in press.

Pasamehmetoglu, K. O., Chappidi, P. R., Unal, C., and Nelson, R. A., 1991, "Saturated Pool Nucleate Boiling Mechanism at High Heat Fluxes," Los Alamos National Laboratory report LA-UR-91-3684; *Int. J. Heat Mass Transfer*, in press.

Ramilison, J. M., and Lienhard, J. H., 1987, "Transition Boiling Heat Transfer and Film Transition Regime," ASME JOURNAL OF HEAT TRANSFER, Vol. 109, pp. 746–752.

Rohsenow, W., and Griffith, P., 1956, "Correlation of Maximum Heat Flux Data for Boiling of Saturated Liquid," *Chem. Engr. Prog. Symp. Ser.*, Vol. 52, No. 18.

Sterman, L. S., 1953, "Theory of Heat Transfers in Boiling Liquids," *Zh. Tekh. Fiz.*, Vol. 23, No. 2, pp. 341–351; CTS-62, 1955.

Torikai, K., and Yamazaki, T., 1967, "Dry State in a Contact Area of a Boiling Bubble on a Heating Surface," *Bulletin of JSME*, Vol. 10, No. 38.

Unal, C., Daw, V., and Nelson, R. A., 1991, "Unifying the Controlling Mechanisms for the Critical Heat Flux and Quenching: The Ability of Liquid to Contact the Hot Surface," Los Alamos National Laboratory report LA-UR-91-933.

Van Ouwerkerk, H. J., 1972, "Burnout in Pool Boiling the Stability of Boiling Mechanism," *Int. J. Mass Heat Transfer*, Vol. 15, pp. 25–34.

Yu, C. L., and Mesler, R. B., 1977, "Study of Nucleate Boiling Near the Peak Heat Flux Through Measurements of Transient Surface Temperature," *Int. J. Heat Mass Transfer*, Vol. 20, pp. 827–840.

Zuber, N., 1958, "Stability of Boiling Heat Transfer," *Trans. ASME*, Vol. 80, pp. 711–720.

Zuber, N., 1959, "Hydrodynamic Aspects of Boiling Heat Transfer," Ph.D. Thesis, University of California, Los Angeles.

Zuber, N., Tribus, M., and Westwater, J. W., 1961, "The Hydrodynamic Crisis in Pool Boiling of Saturated and Subcooled Liquids," *2nd Int. Heat Transfer Conference*, Denver, CO, paper 27.

Downloaded 13 Dec 2010 to 193.140.21.150. Redistribution subject to ASME license or copyright; see http://www.asme.org/terms/Terms_Use.cfm

Modeling of Transient Stratified Flow in Vertical Tube Assemblies

P. F. Peterson
Department of Nuclear Engineering,
University of California,
Berkeley, CA 94720
Mem. ASME

A. Akbarzadeh
Department of Mechanical Engineering,
Royal Melbourne Institute of Technology,
Melbourne, Australia

This study considers a case of uniform flow into the bottom of a rectangular vertical tube array, with outflow from a point sink in one bottom corner. Experimental results show that, upon a step change to a higher density, a clearly defined density interface forms, and buoyancy forces cause channeling of the dense fluid. The tube array geometry permits an analytic solution, which agrees well with the experiments. Standard control-volume numerical methods, however, predict a diffuse, thick, and viscous density interface, in contrast to the thin interface seen in the experiment. This viscous effect can be attributed to numerical diffusion, and a Lagrangian interface tracking procedure is shown to reduce the diffusion effect greatly.

Introduction

When the temperature of a fluid entering a flow system is subjected to a rapid change, transient stratified flow can result, with a subsequent strong impact on mixing processes and vessel thermal stresses. Transient stratification examples include the activation of emergency core cooling systems in light water reactors, where the cold injected water can stratify along the bottom of the cold legs (Theofanous and Iyer, 1987; Nourbakhsh and Theofanous, 1986). In heavy water reactors, the rapid change of water temperature that occurs upon power shutdown can create stratified moderator flow. Even when scaling would predict a thin density interface, the numerical diffusion in the control-volume modeling normally applied to such flows spreads the interface considerably, and for coarser control volumes gives physically unreasonable results.

To illustrate the potential impact of numerical diffusion on the numerical modeling of stratified flows, this study presents experimental, scaling, analytical, and numerical modeling of flow in a rectangular vertical-tube array. For the case of an inlet flow uniformly distributed across the bottom of the tube array and a point sink in the right bottom corner, a step increase in the density of the entering fluid results in a transient stratification process, creating a density interface as illustrated in Fig. 1(*a*). As the density interface rises, buoyancy forces cause channeling of the dense fluid toward the sink, while the upper light fluid layer first recirculates in a single large cell, and eventually becomes stagnant.

Early studies of stratified flow have considered two-dimensional flow of a stably stratified fluid in a channel toward a line sink, as shown in Fig. 1(*b*). Huber (1960) obtained an analytic solution for the case of two fluid layers of different densities flowing toward a line sink. Based on inviscid flow equations balancing inertia and gravity forces, he demonstrated that a critical flow rate exists where the lighter fluid ceases to flow and becomes stagnant. Debler (1959) performed experiments for the case of a linear density gradient in the vertical direction at $x = -\infty$, confirming the analytic prediction of Yih (1958) that stagnation and isolation of the upper lighter fluid occurs for Richardson numbers above a critical value.

Buoyancy forces generate vorticity at the density interface, creating slip between the upper and lower fluids. With higher Reynolds numbers, convection provides the primary mechanism for the transport of the vorticity generated by buoyancy at the interface. This vorticity remains concentrated in the density interface and is removed from the system by convection to the point sink. Unlike the potential flow case considered by Huber (1960), here the vertical tube array provides an additional distributed source of vorticity, which modifies flow patterns from the potential flow solution.

To address the problem of transient flow stratification in vertical tube arrays, volume averaging and scaling arguments are applied here to derive governing conservation equations based on a nonisotropic distributed flow resistance generated by the tube bank. A simplified analytical solution is provided for the steady-state flow case. Numerical results are presented for the transient flow case, showing that numerical diffusion effects create a diffuse, thick and viscous density interface, unlike the thin density interface observed experimentally. Lagrangian tracking of the density interface is shown to improve the quality of the numerical solution significantly.

Volume Averaging

In porous media like fuel bundles, compact heat exchangers, regenerators, and fibrous insulation, many of the mechanisms that govern the flow occur on scales much smaller than the tube pitch or pore size. Large eddy simulation of turbulent flow in tube bundles is possible for two-dimensional flow through small arrays of tubes (Pruitt et al., 1990), but for large tube banks it is computationally difficult to resolve flow details on these small scales. These computational difficulties can be addressed using volume averaging and semi-empirical closure relationships, such as friction and form loss coefficients. Tra-

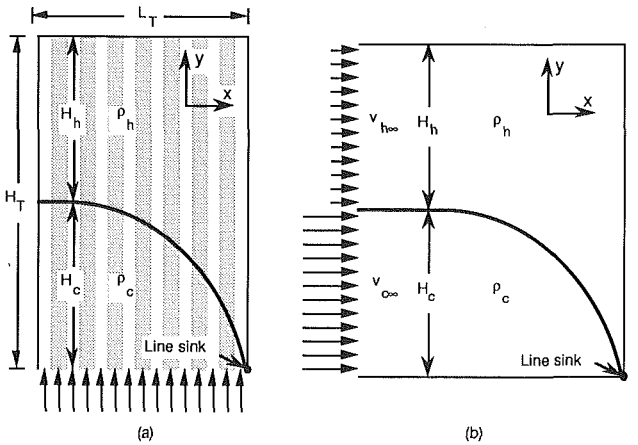

Fig. 1 Stratified flow to a line sink: (*a*) a uniform bottom inlet flow to tube array considered here and (*b*) potential flow from $x = -\infty$ as studied by Debler (1959) and Huber (1960)

Contributed by the Heat Transfer Division for publication in the JOURNAL OF HEAT TRANSFER. Manuscript received by the Heat Transfer Division August 1991; revision received March 1992. Keywords: Mixed Convection, Stratified Flows, Transient and Unsteady Heat Transfer. Associate Technical Editor: J. H. Kim.

Copyright © 1992 by ASME
Downloaded 13 Dec 2010 to 193.140.21.150. Redistribution subject to ASME license or copyright; see http://www.asme.org/terms/Terms_Use.cfm

ditional analysis of flow and heat transport in porous media uses Darcian or slug-flow models and neglects non-Darcian effects due to inertia forces. A more fundamental basis for studying such flows can come from volume-averaging techniques (Vafai and Tien, 1981; Slattery, 1968). For porous media it becomes useful to define a *local volume average* of a quantity Ψ as

$$\langle \Psi \rangle = \frac{1}{V} \int_{V_f} \Psi dV \tag{1}$$

where V is a volume around the point of interest, sufficiently large relative to the tube spacing or pore size to permit averaging, and V_f is the fluid volume inside the volume V. With the "volume average of a divergence" theorem (Whitaker, 1969; Slattery, 1978), the local volume averages of the mass, momentum, and energy conservation equations for incompressible, transient flow through a porous medium can be established respectively as

$$\nabla \cdot \langle \mathbf{v} \rangle = 0 \tag{2}$$

$$\rho_f \langle (\mathbf{v} \cdot \nabla)\mathbf{v} \rangle = -\nabla \langle p \rangle + \mu_f \nabla^2 \langle \mathbf{v} \rangle + \mathbf{F} + \rho_f \mathbf{g} \tag{3}$$

$$\rho_f c_f \langle \mathbf{v} \rangle \cdot \nabla \langle T \rangle = -\nabla \cdot \chi + q \tag{4}$$

where $\mathbf{v}$ is the flow velocity vector, ρ_f the fluid density, p the fluid pressure, μ_f the fluid viscosity, $\mathbf{F}$ the distributed drag force due to frictional resistance, $\mathbf{g}$ gravity, c_f the fluid specific heat, T the fluid temperature, and q a source term. The effective heat flux vector, χ, is a complex function of the fluid and solid matrix thermal conductivity, solid matrix geometry, and local velocity and temperature fields.

Because the detailed velocity distribution is not known, here the volume average of the convective momentum terms is approximated with the convection of the volume-averaged momentum, that is, the left-hand side of Eq. (3) is written

$$\rho_f \langle (\mathbf{v} \cdot \nabla)\mathbf{v} \rangle = \rho_f (\langle \mathbf{v} \rangle \cdot \nabla) \frac{\langle \mathbf{v} \rangle}{\phi} \tag{5}$$

introducing the volume porosity ϕ, which corrects the volume-averaged velocity $\langle \mathbf{v} \rangle$ to the average local velocity in the void space,

$$\phi = \frac{V_f}{V} = 1 - \frac{\pi D_t^2}{4 S_t^2 \sin 60} \quad \text{(triangular array)}$$

$$= 1 - \frac{\pi D_t^2}{4 S_{tx} S_{tz}} \quad \text{(rectangular array)} \tag{6}$$

for tubes of diameter D_t with pitch S_t.

The distributed drag force term $\mathbf{F}$ is given by

$$\mathbf{F} = \int_{A_{sf}} S \cdot dA \tag{7}$$

where S is the fluid stress tensor and A_{sf} is the surface area inside the volume. For flow in a tube bank the flow resistance is anisotropic, and the distributed drag force term can be expressed in terms of a flow resistance tensor, as discussed by Butterworth (1978). For horizontal turbulent flow perpendicular to tube banks, the distributed drag force component can be characterized by

$$F_x = \frac{\rho_f k_x N_t A_x^2}{L_T} \frac{u|u|}{2} \tag{8}$$

where

$$A_x = S_{tz}/(S_{tz} - D_t) \tag{9}$$

is the ratio of the minimum perpendicular flow area to the total flow area, u the perpendicular component of the volume average velocity $\langle \mathbf{v} \rangle$, and N_t the number of tube banks along the perpendicular distance L_T. Each bank of tubes creates a pressure drop, which can be given by the form loss coefficient k_x, taking values ranging from 0.15 to 2 as provided in graphic form by Zukauskas (1972).

For turbulent flow parallel to channels, the distributed drag force component F_y can be characterized by a friction factor f_y

$$F_y = \frac{\rho_f f_y}{\phi^2 D_h} \frac{v|v|}{2} \tag{10}$$

where the volume porosity ϕ corrects the parallel velocity component v of the volume-averaged velocity $\langle \mathbf{v} \rangle$ to the average local velocity. The hydraulic diameter is given as

$$D_h = 4 \frac{S_t^2 \sin 60 - \frac{1}{4}\pi D_t^2}{\pi D_t} \quad \text{(triangular array)}$$

$$= 4 \frac{S_{tx} S_{tz} - \frac{1}{4}\pi D_t^2}{\pi D_t} \quad \text{(rectangular array)} \tag{11}$$

In general, the perpendicular form loss coefficient k_x and friction factor f_y vary weakly with the Reynolds number and with

Nomenclature

A = area
A_x = ratio of minimum radial area over total area, Eq. (9)
c = specific heat
D_t = tube outside diameter
D_h = hydraulic diameter, Eq. (11)
f_y = vertical friction factor
F = distributed drag force, Eqs. (8) and (10)
g = gravitational constant
H_T = tube array height
H_n = outlet sink height
k = thermal conductivity
k_x = horizontal form loss coefficient
K = nondimensional loss coefficients, Eqs. (23) and (24)
L_T = horizontal tube array length
N_t = number of tube bank rows over L_T
p = pressure
Pr = Prandtl number, Eq. (25)
q = source term
Q = volume flow rate
Re = Reynolds number, Eq. (21)
Ri = Richardson number, Eq. (22)
S = stress tensor
S_t = tube pitch
t = time
T = temperature
u = volume-averaged horizontal velocity
v = volume-averaged vertical velocity
$\mathbf{v}$ = velocity vector
V = volume
V_o = bottom average inlet velocity
β = coefficient of thermal expansion
μ = dynamic viscosity
ρ = density
ϕ = volume porosity, Eq. (6)
χ = heat flux vector
Ψ = conserved quantity
ψ = stream function, Eq. (36)
ω = vorticity, Eq. (37)

Subscripts

c = cold, density interface
f = fluid
h = hot
t = tube
T = tube array
x = horizontal direction
y = vertical direction
z = horizontal direction

Superscripts

* = nondimensional quantity
n = time step

Downloaded 13 Dec 2010 to 193.140.21.150. Redistribution subject to ASME license or copyright; see http://www.asme.org/terms/Terms_Use.cfm

the flow orientation. Here the effects of flow velocity and orientation are neglected, and constant values of k_x and f_y applied.

Scaling

To derive scaling parameters to characterize stratified flow in tube banks, the volume-averaged continuity, Navier–Stokes, and energy equations, Eqs. (2)–(4), can be nondimensionalized using the following characteristic quantities:

$$u^* = u/V_0 \quad v^* = v/V_0 \quad p^* = (p-p_o)/\rho_f V_o^2$$
$$y^* = y/L_T \quad x^* = x/L_T \quad t^* = tV_o/L_T \tag{12}$$
$$T^* = \frac{(T-T_c)}{(T_h-T_c)} \quad q^* = \frac{qL_T}{\rho_f c_f (T_h-T_c) V_o}$$

where starred quantities are nondimensional, x and y are the perpendicular and axial coordinates, u and v the radial and vertical components of the volume-averaged velocity $\langle \mathbf{v} \rangle$, t time, L_T the horizontal tank dimension, V_o the average upward velocity of water at the tank bottom, and T_h and T_c the initial hot and cold liquid temperatures. Mass continuity can be written from Eq. (1),

$$\frac{\partial u}{\partial x} + \frac{\partial v}{\partial y} = 0 \tag{13}$$

The Navier–Stokes equations, from Eqs. (2), (5), (8), and (10), become

$$\frac{\rho_f}{\phi}\left(\frac{\partial u}{\partial t} + u\frac{\partial u}{\partial x} + v\frac{\partial u}{\partial y}\right) = -\frac{\partial p}{\partial x} + \mu\left[\frac{\partial^2 u}{\partial x^2} + \frac{\partial^2 u}{\partial y^2}\right] - \frac{\rho_f k_x N_t A_x^2}{L_T}\frac{u|u|}{2} \tag{14}$$

$$\frac{\rho_f}{\phi}\left(\frac{\partial v}{\partial t} + u\frac{\partial v}{\partial x} + v\frac{\partial v}{\partial y}\right) = -\frac{\partial p}{\partial y} - \rho_f \beta (T-T_c) g + \mu\left[\frac{\partial^2 v}{\partial x^2} + \frac{\partial^2 v}{\partial y^2}\right] - \frac{\rho_f f_y}{\phi^2 D_h}\frac{v|v|}{2} \tag{15}$$

The Boussinesq approximation for buoyancy is introduced in the y-direction momentum equation. The inertia terms are divided by the volume porosity to correct the area-averaged velocity to the local average velocity. The energy equation, from Eq. (3), becomes

$$\rho_f c_f\left(\frac{\partial T}{\partial t} + u\frac{\partial T}{\partial x} + v\frac{\partial T}{\partial y}\right) = k_{\text{eff}}\left[\frac{\partial^2 T}{\partial x^2} + \frac{\partial^2 T}{\partial y^2}\right] + q \tag{16}$$

Substitution of the nondimensional terms provides

$$\frac{\partial u^*}{\partial x^*} + \frac{\partial v^*}{\partial y^*} = 0 \tag{17}$$

$$\frac{\partial u^*}{\partial t^*} + u^*\frac{\partial u^*}{\partial x^*} + v^*\frac{\partial u^*}{\partial y^*} = -\phi\frac{\partial p^*}{\partial x^*} + \frac{1}{\text{Re}_T}\left[\frac{\partial^2 u^*}{\partial x^{*2}} + \frac{\partial^2 u^*}{\partial y^{*2}}\right] - K_x\frac{u^*|u^*|}{2} \tag{18}$$

$$\frac{\partial v^*}{\partial t^*} + u^*\frac{\partial v^*}{\partial r^*} + v^*\frac{\partial v^*}{\partial z^*} = -\phi\frac{\partial p^*}{\partial z^*} - \text{Ri}T^* + \frac{1}{\text{Re}_T}\left[\frac{\partial^2 v^*}{\partial x^{*2}} + \frac{\partial^2 v^*}{\partial y^{*2}}\right] - K_y\frac{v^*|v^*|}{2} \tag{19}$$

$$\frac{\partial T^*}{\partial t^*} + u^*\frac{\partial T^*}{\partial x} + v^*\frac{\partial T^*}{\partial y^*} = \frac{1}{\text{Pr}_{\text{eff}}\text{Re}_T}\left[\frac{\partial^2 T^*}{\partial x^{*2}} + \frac{\partial^2 T^*}{\partial y^{*2}}\right] = q^* \tag{20}$$

which forms three groups of nondimensional parameters:

Reynolds Number:

$$\text{Re}_T = \frac{\rho_f L_T V_o}{\phi \mu_f} \tag{21}$$

Richardson Number:

$$\text{Ri} = \frac{\phi L_T \beta (T_h - T_c) g}{V_o^2} \tag{22}$$

Friction Factors:

$$K_y = f_y L_T/\phi D_h \tag{23}$$
$$K_x = k_x N_t \phi A_x^2 \tag{24}$$

Prandtl Number:

$$\text{Pr}_{\text{eff}} = \frac{\rho_f c_f \phi \mu}{k_{\text{eff}}} \tag{25}$$

These nondimensional governing equations can be simplified by noting that the Reynolds number based on the array dimension L_T is normally large (Re = 10^3 to 10^4 in the experiments here), making the viscous diffusion negligible. Elimination of the viscous terms from the momentum equations, Eqs. (18), (19) and energy equation, Eq. (20), gives Euler-type equations. Viscosity impacts the flow only through the distributed resistance K. The elimination of diffusion terms has important implications for the thickness of the density interface. Because no convection occurs normal to the interface and diffusion is small, vorticity generated by buoyancy forces remains at the interface, giving a slip condition. The interface remains thin, relative to the length scale of the tube array, L_T.

Steady-State Analytic Solution

A simple analytic model for the steady-state density-interface location can be developed by considering the balance between horizontal friction pressure drop and buoyancy forces, while neglecting inertia and vertical friction pressure drop. The momentum equations, Eqs. (14) and (15), then reduce to the simpler forms

$$\frac{\partial p}{\partial y} = -\rho_f \beta (T - T_c) g \tag{26}$$

$$\frac{\partial p}{\partial x} = -\frac{\rho_f k_x N_t}{L_T}\left(\frac{S_{tz}}{S_{tz} - D_t}\right)^2 \frac{u|u|}{2} \tag{27}$$

Under steady-state conditions the light, upper layer of fluid is stagnant while the denser, lower layer of fluid flows beneath. Defining the height of the interface between the light and dense fluids as $H_c(x)$ as illustrated in Fig. 1(*a*), the pressure distribution in the vertical direction is the hydrostatic head as given by Eq. (26),

$$p(y) = \rho_f g (H_T - y) \quad H_T > y > H_c \tag{28}$$
$$p(y) = \rho_f g[(H_T - H_c) + (1 + \beta\Delta T)(H_c - y)] \quad H_c > y > 0 \tag{29}$$

where H_T is the total height of the fluid and $\beta\Delta T$ gives the density difference between the upper and lower fluid layers.

For stagnant conditions in the upper fluid layer, the horizontal velocity u is zero. This in turn, through Eq. (27), requires that the horizontal pressure gradient be zero,

$$\frac{\partial p}{\partial x} = 0 \quad H_T > y > H_c \tag{30}$$

Thus the liquid level H_T must be constant, even if the upper layer has a free surface at H_T. For H_T = const, Eq. (29) can be differentiated with x to give the horizontal pressure gradient in the lower fluid layer,

$$\frac{\partial p}{\partial x} = \rho_f g \beta \Delta T \frac{dH_c}{dx} \quad H_c > y > 0 \tag{31}$$

Downloaded 13 Dec 2010 to 193.140.21.150. Redistribution subject to ASME license or copyright; see http://www.asme.org/terms/Terms_Use.cfm

For a uniform bottom inlet flow with velocity V_o, mass conservation requires that

$$V_o x = \int_0^{H_T} u \, dy \tag{32}$$

The horizontal velocity u can be expressed in terms of the pressure gradient through Eq. (27). The pressure gradient is known through Eqs. (30) and (31). Integration gives the differential equation

$$\left(\frac{V_o S_{tz}}{S_{tz} - D_t}\right)^2 x^2 dx = \left(\frac{2L_T g\beta\Delta T}{k_x N_t}\right) H_c^2 dH_c \tag{33}$$

Applying the boundary condition $H_c = 0$ at $x = L_T$, an analytic expression for the height of the density interface is obtained,

$$\frac{H_c}{L_T} = \left(\frac{S_{tz}}{S_{tz} - D_t}\right)^{2/3} \left(\frac{V_o^2 k_x N_t}{2L_T g\beta\Delta T}\right)^{1/3} \left(1 - \left(\frac{x}{L_T}\right)^3\right)^{1/3} \tag{34}$$

The maximum steady-state height of the interface occurs at $x = 0$,

$$\frac{H_{c,\max}}{L_T} = \left(\frac{S_{tz}}{S_{tz} - D_t}\right)^{2/3} \left(\frac{V_o^2 k_x N_t}{2L_T g\beta\Delta T}\right)^{1/3} = \left(\frac{S_{tz}}{S_{tz} - D_t}\right)^{2/3} \left(\frac{\phi}{\mathrm{Ri}}\right)^{1/3} \left(\frac{k_x N_t}{2}\right)^{1/3} \tag{35}$$

The dependence of the interface height on the cube root of the Richardson number and the prediction of the maximum interface height match well with experimental observations, as seen in the results section.

Numerical Formulation

To determine the details of the transient flow distribution, a finite-difference solution of the combined vorticity transport and Poisson equations was employed. The stream function ψ gives volume-averaged velocities

$$u = \frac{\partial \psi}{\partial y} \quad v = -\frac{\partial \psi}{\partial x} \tag{36}$$

which satisfy mass conservation. The stream function can then be coupled with the definition of vorticity to obtain Poisson's equation,

$$\omega = \frac{\partial u}{\partial y} - \frac{\partial v}{\partial x} = \frac{\partial^2 \psi}{\partial y^2} + \frac{\partial^2 \psi}{\partial x^2} \tag{37}$$

The vorticity transport equation can be derived by considering the momentum conservation equations, Eqs. (14) and (15). When cross-differentiated and subtracted, and the definition for vorticity, Eq. (37), is inserted, the result is

$$\frac{\partial \omega}{\partial t} + u\frac{\partial \omega}{\partial x} + v\frac{\partial \omega}{\partial y} = \frac{\partial}{\partial x}\left(\frac{f_y}{\phi D_h}\frac{v|v|}{2}\right) - \frac{\partial}{\partial y}\left(\frac{k_x N_t \phi A_x^2}{R_T}\frac{u|u|}{2}\right) - \phi g \frac{\partial}{\partial x}(\beta T) \tag{38}$$

Scaling also shows that the diffusive terms are negligible in the energy equation, Eq. (16), and with no heat source it becomes

$$\frac{\partial T}{\partial t} + u\frac{\partial T}{\partial x} + v\frac{\partial T}{\partial y} = 0 \tag{39}$$

Because the diffusive terms have been eliminated based on scaling arguments, vorticity and heat are transported only by convection. The boundary conditions for these equations are simple, since with no diffusive terms only the inlet boundary needs to be specified,

$$\omega = 0 \qquad \text{at } y = 0 \tag{40}$$

$$T = T(t) \quad \text{at } y = 0 \tag{41}$$

The flow entering the bottom of the tank is irrotational, and thus the only vorticity in the flow is generated by the distributed tube bank frictional resistance and buoyancy at the hot/cold fluid interface.

The boundary conditions for the Poisson equation come from the normal velocities,

$$v = 0 \qquad \frac{\partial \psi}{\partial x} = 0 \qquad \text{at } 0 < x < L_T,\ y = H_T \tag{42}$$

$$v = V_o \qquad \frac{\partial \psi}{\partial x} = -V_o \qquad \text{at } 0 < x < L_T,\ y = 0 \tag{43}$$

$$u = V_o \frac{L_T}{H_n} \qquad \frac{\partial \psi}{\partial y} = V_o \frac{L_T}{H_n} \qquad \text{at } x = L_T,\ 0 < y < H_n \tag{44}$$

$$u = 0 \qquad \frac{\partial \psi}{\partial y} = 0 \qquad \text{at } x = L_T,\ H_n < y < H_T \tag{45}$$

$$u = 0 \qquad \frac{\partial \psi}{\partial y} = 0 \qquad \text{at } x = 0,\ 0 < y < H_T \tag{46}$$

where H_n is the outlet sink height and H_T the tank height.

The initial condition of interest is a fully developed isothermal flow through the tube array. At $t = 0$ the inlet temperature (or concentration) is subjected to a step change, creating a translating density interface.

The Poisson and vorticity transport equations, Eqs. (37) and (38), were converted to control-volume form (conservative upwind finite difference) on a uniform 11 × 21 rectangular grid and solved numerically subject to the boundary conditions, Eqs. (40) and (42)–(46). The vorticity transport equation was written in an explicit form. The Poisson equation was written in an implicit form and solved by successive overrelaxation.

Two methods were compared for solving the energy equation, Eq. (39). First, the equation was written in control-volume form and solved explicitly. The second technique tracked the density interface in a Lagrangian manner, using the scheme discussed in the next section. The control-volume solution suffered from large numerical diffusion effects, giving physically unreasonable results. Lagrangian tracking of the density interface performed much better.

The solution scheme involved advancing the vorticity and energy equation solutions explicitly one time step, based on the initial velocity distribution. The Poisson equation was then solved to provide a new velocity distribution for the subsequent time step.

Particle Tracking

Both fluid particles and the hot/cold water interface were tracked in a Lagrangian manner. The tracking of "plumes" generated by multiple particles injected at the fluid inlet provided visualization of shear effects at the density interface. The new location of a particle was found from the old location, using an interpolated value for the horizontal and vertical velocities, u_{ave} and v_{ave}, based on linear interpolation from the neighboring finite-difference nodes,

$$x^{n+1} = x^n + \frac{u_{\mathrm{ave}} \Delta t}{\phi} \tag{47}$$

$$y^{n+1} = y^n + \frac{v_{\mathrm{ave}} \Delta t}{\phi} \tag{48}$$

where the volume porosity ϕ is introduced to correct the volume-averaged velocity to the local average velocity between the tubes. Equations (47) and (48) result from considering the time required to displace the liquid in a volume V with area

Downloaded 13 Dec 2010 to 193.140.21.150. Redistribution subject to ASME license or copyright; see http://www.asme.org/terms/Terms_Use.cfm

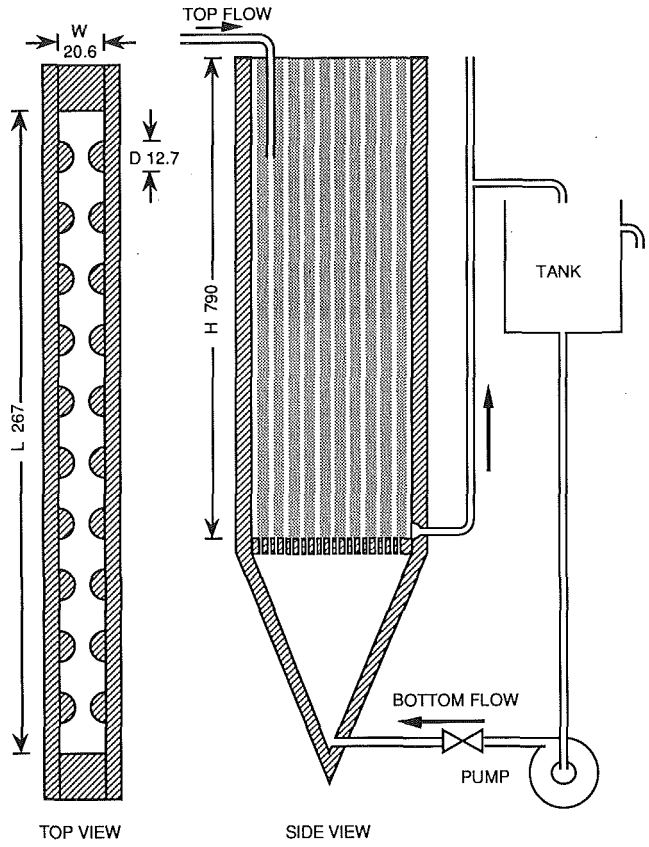

Fig. 2 Schematic of the experimental apparatus (dimensions in mm)

A and length L. The quantity of liquid to be displaced is $V_f = \phi V = \phi AL$. The time required to displace the liquid depends on the volume flow rate, $Q = vA$,

$$t = \frac{\phi AL}{vA} \tag{49}$$

The liquid front velocity, and the velocity a particle attached to the front would have, is then given by

$$v_{\text{eff}} = \frac{L}{t} = \frac{v}{\phi} \tag{50}$$

Because points fixed to the density interface are eventually convected out through the sink, after each time step linear interpolation is used to shift the location of the interface points, such that the points remain evenly distributed along the length of the interface. The temperature distribution required for solution of the vorticity transport equation, Eq. (38), is then found from the known interface location. To do this the Lagrangian interface information is transferred to a finite-difference grid. For grid cells near the interface, the temperature value is calculated as a weighted fraction based on the fraction of the cell occupied by colder fluid. It should be noted, however, that the Lagrangian interface tracking method can fail if the interface becomes unstable or if large amounts of mixing occur.

Experiment Description

The experiment illustrated in Fig. 2 confirmed the validity of assumptions regarding the thickness and shape of the density interface used in the analytical and numerical modeling. The apparatus consisted of two clear 6.3-mm-thick acrylic plates with heights $H_T = 790$ mm and lengths $L_T = 267$ mm. Spacer bars separated the plates by $S_{tz} = 20.6$ mm. Ten vertical $D_t = 12.7$-mm-dia half-round acrylic rods were glued to each plate with a uniform pitch of $S_{tx} = 25.4$ mm. To provide a uniform flow distribution across the bottom of the channel assembly, 27 uniform 3.2-mm-dia holes were drilled in the bottom spacer bar. At the lowest flow rates and highest density differences (worst case) horizontal pressure drop was 25 percent of the pressure drop through the 27 injection holes, resulting in some nonuniformity of the inlet flow. However, for most of the runs horizontal pressure drop was much smaller, and the flow distribution very nearly uniform. A single outlet port was provided in the lower right corner. A tank and pump circulated water at flow rates ranging from 15 to 150 cm^3/s. Salt was added to the water to obtain specific gravity values ranging from 1.007 to 1.055. Potassium permanganate dye mixed in the salt water permitted visualization of the flow.

The experimental procedure consisted of initially filling the channel assembly with tap water and the tank with a salt water mixture, keeping the pump outlet valve closed. After starting the pump and opening the valve, a steady-state stratified flow was rapidly achieved. To counteract the entrainment of clear water that occurred at the density interface, a slow makeup flow of clean tap water, ranging from 1 to 4 cm^3/s, was provided from the top of the device. The makeup flow provided gradual dilution of the salt water density, allowing measurements at different specific gravity values. The makeup flow rate was measured by collecting overflow from the tank over a period of 1 to 2 minutes and measuring the quantity collected with a 500 cm^3 graduated cylinder, providing a flow rate measurement of ± 2 percent accuracy. Likewise, the total flow rate was measured by collecting recirculated water in a container for a 10 to 60 second period and measuring the total quantity collected using a graduated cylinder, providing a flow rate measurement of ± 5 percent accuracy. The specific gravity of the salt-water mixture was measured with a hygrometer with an accuracy of ± 5 percent.

Results

Figure 3 shows two photographic examples of the steady-state stratified flow that occurs in vertical tube arrays. Superimposed on the photographs are the interface height distributions predicted by Eq. (34) for $k_x = 0.5$ (Re = 500; Zukauskas, 1972). For both case (*a*), with a flow rate of 143 cm^3/s, and case (*b*), with a flow rate of 90 cm^3/s, the horizontal velocities in the lower region differ by only 2 percent, since the ratio $u_a/u_b = Q_a H_{cb}/Q_b H_{ca} = 1.02$. Thus the horizontal Reynolds numbers, and form loss coefficients k_x, are also approximately equal. However, for the higher flow rate of case (*a*), the analytic solution of Eq. (35) overpredicts the maximum interface height by 9 percent, while for the lower flow rate of case (*b*) it underpredicts by 22 percent. These errors result from the assumption in the analytic model that vertical pressure drop is small compared to horizontal pressure drop. Vertical pressure drops scale as $H_c V_o^2$ for a given geometry. Horizontal pressure drop occurs due to the hydrostatic gradient, and scales as $H_c(1 - SG)$. The ratio of vertical to horizontal pressure drop then scales as $V_o^2/(1 - SG) \propto 1/\text{Fr} \propto (H_c/L_T)^{1/3}$ noting the relationship between Richardson number and the interface height H_c given by Eq. (35). Thus vertical pressure drop would be expected to become significant as H_c becomes large. Vertical pressure drop causes channeling of flow in the lower region and thus decreases H_c, as is seen later in Fig. 5. Figure 4 shows numerical results corresponding to the photographs in Fig. 3. The numerical scheme comes closer to predicting the correct interface heights, also overpredicting by 9 percent in case (*a*), but underpredicting by only 8 percent in case (*b*).

Table 1 provides data from other experimental runs. All of the experimental runs displayed a clearly defined interface between the light and heavy fluids. Injection of dye in the upper stagnant region confirmed that the light fluid was essentially motionless. Figure 5 shows a comparison between the

Downloaded 13 Dec 2010 to 193.140.21.150. Redistribution subject to ASME license or copyright; see http://www.asme.org/terms/Terms_Use.cfm

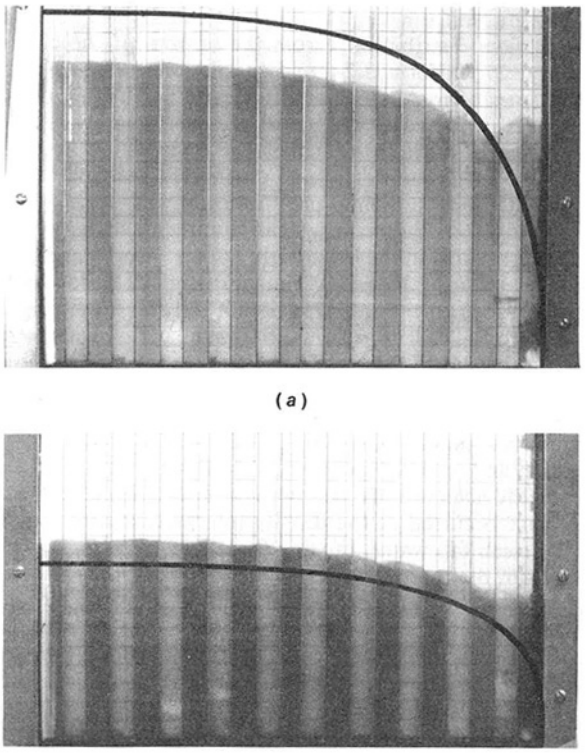

Fig. 3 Experimental observations of steady-state stratified flow, and analytical profile predicted by Eq. (34): (*a*) Q = 143 cm^3/s, *S.G.* = 1.015, and (*b*) Q = 90 cm^3/s, *S.G.* = 1.050

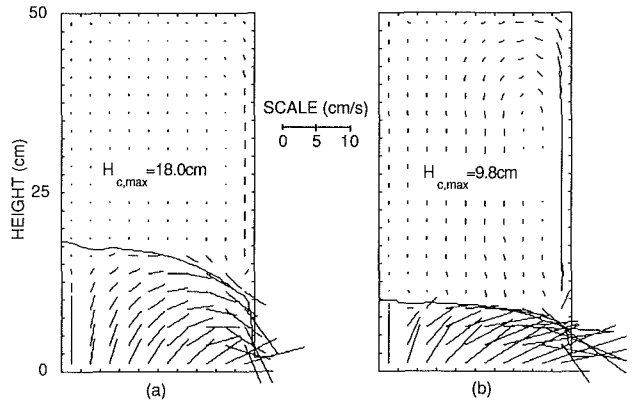

Fig. 4 Numerical calculations for steady-state (t = 2000 s) stratified flow: (*a*) Q = 143 cm^3/s, *S.G.* = 1.015, and (*b*) Q = 90 cm^3/s, *S.G.* = 1.050

experimentally measured maximum interface height $H_{c,\max}$ and that predicted by the analytical model, Eq. (35). The agreement for these steady-state conditions is good.

Transient effects and stratification control the initial mixing behavior and temperature distribution. Here numerical methods are useful to provide detailed information on the transient flow patterns and recirculation. For numerical solutions, coarse grids are commonly desired and employed in reactor system simulation. However, for control-volume formulations, coarse grids can cause large numerical diffusion effects, giving physically unreasonable results. When the density interface is tracked in a Lagrangian manner, numerical diffusion effects are reduced, as seen in Fig. 6. The figure compares transient results for Lagrangian and control-volume solutions. The velocity vectors show the magnitude and direction of the fluid

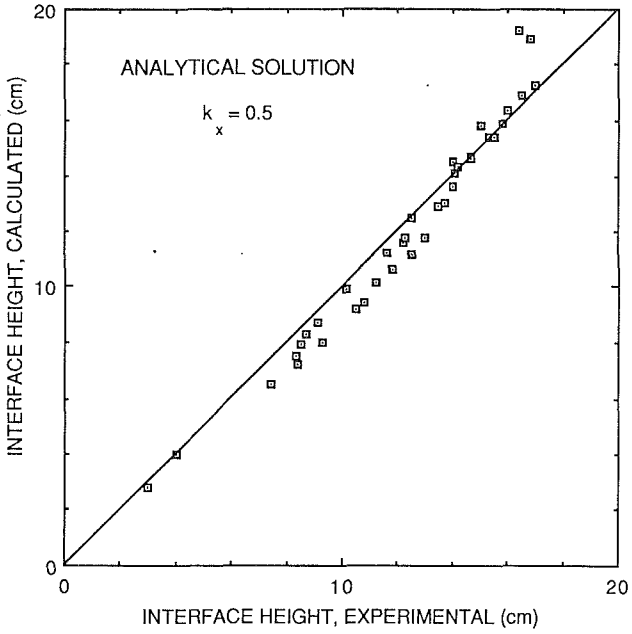

Fig. 5 Comparison of measured maximum interface heights with the analytical solution, Eq. (35)

Table 1 Summary of experimental results

Run	Q_{top} cm^3/s	Q_{bottom} cm^3/s	specific gravity	$H_{c,max}$ (exp) cm	$H_{c,max}$† Eq.(35) cm
1§	4.0	90	1.050	10.8	9.44
2	4.0	107	1.015	15.0	15.83
3	4.0	152	1.010	17.7	22.89
4	4.0	131	1.055	12.3	11.75
5	4.0	123	1.048	13.0	11.79
6	4.0	130	1.041	13.5	12.89
7	4.0	137	1.035	14.1	14.07
8	4.0	133	1.029	14.7	14.69
9	4.0	133	1.025	15.3	15.43
10	4.0	133	1.023	15.8	15.87
11	4.0	133	1.021	16.0	16.36
12	4.0	133	1.019	16.5	16.91
13§	4.0	143	1.015	16.4	19.20
14	4.0	130	1.040	13.7	13.00
15	2.0	130	1.035	14.0	13.59
16	2.0	130	1.030	14.2	14.30
17	2.2	130	1.028	14.7	14.64
18	2.1	130	1.024	15.5	15.41
19	2.1	130	1.022	15.8	15.86
20	2.1	130	1.017	17.0	17.28
21	4.0	130	1.013	16.8	18.90
22	4.0	127	1.060	12.5	11.18
23	4.0	122	1.050	12.2	11.56
24	4.0	118	1.060	11.8	10.64
25	4.0	110	1.060	11.2	10.16
26	4.0	95	1.060	10.5	9.21
27	4.0	77	1.060	9.3	8.01
28	4.0	56	1.060	7.4	6.48
29	4.0	27	1.060	4.0	3.98
30	4.0	16	1.060	3.0	2.81
31	4.0	64	1.056	8.4	7.24
32	4.0	64	1.050	8.3	7.52
33	5.5	64	1.042	8.5	7.97
34	5.0	64	1.037	8.7	8.32
35	5.0	64	1.032	9.1	8.73
36	5.0	64	1.022	10.1	9.89
37	5.0	64	1.015	11.6	11.24
38	5.0	64	1.011	12.5	12.46
39	5.0	64	1.007	14.0	14.49

§ Shown in Figs. 1 and 2.
† For k_x=0.5

flow. Isodensity profiles for 0.1, 0.5, and 0.9 give the density distribution. Numerical diffusion, primarily in the streamwise direction, spreads the isodensity profiles for the control-vol-

Downloaded 13 Dec 2010 to 193.140.21.150. Redistribution subject to ASME license or copyright; see http://www.asme.org/terms/Terms_Use.cfm

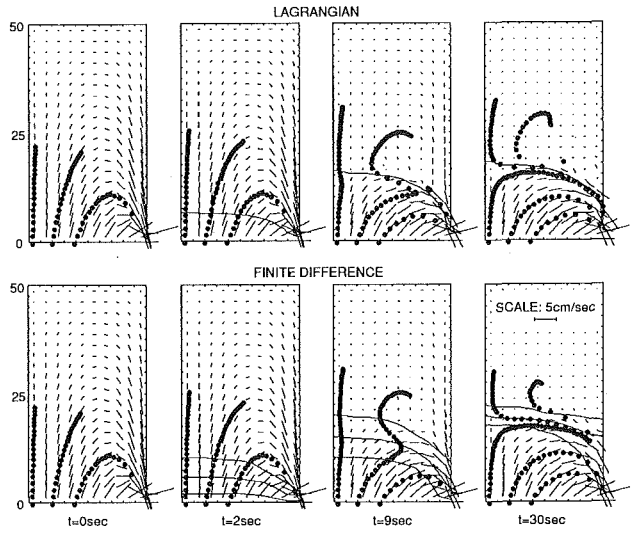

Fig. 6 Comparison of transient numerical results for 143 mm³/s, *S.G.* = 1.015, k_x = 0.5, f_y = 0.02 for (*a*) Lagrangian and (*b*) control-volume solutions for density distribution, with isodensity profiles for 0.1, 0.5, and 0.9

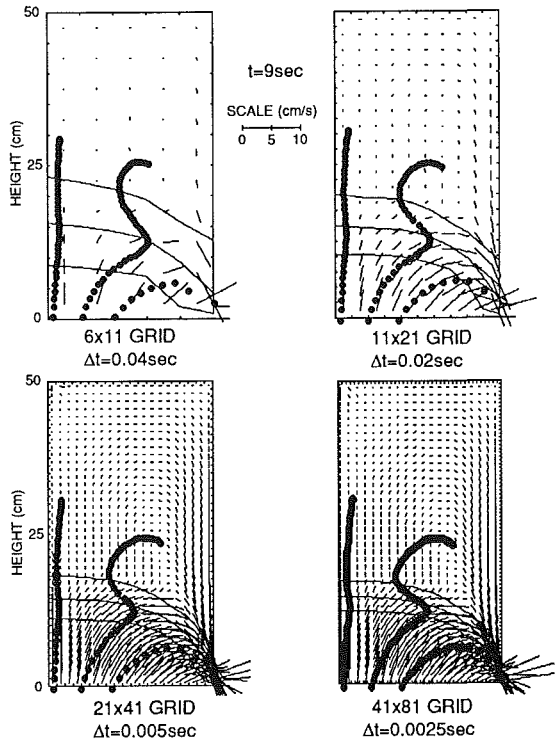

Fig. 7 Comparison of grid size effect on transient numerical results at t = 9 s for Q = 143 cm³/s, *S.G.* = 1.015, k_x = 0.5, f_y = 0.02 for control-volume solutions for the density distribution, with isodensity profiles for 0.1, 0.5, and 0.9.

ume solutions, while for the Lagrangian technique only a single isodensity line is required. To aid visualization of the flow, three "plumes" are added, consisting of circles that are convected with the flow. The artificial viscosity of the control-volume solution is apparent in the comparison of the plume shapes, while the Lagrangian solution gives the desired slip at the interface.

Even with the Lagrangian density solution, the vorticity transport equation is still subject to some numerical diffusion, and vorticity is transported away from the density interface. Some of this vorticity diffuses upward, resulting in a small, nonphysical counterclockwise rotation of the upper fluid layer in the final steady-state solution, as seen in Fig. 4.

For control-volume solutions, grid size has important effects on the numerical diffusion, as seen in Fig. 7. This comparison shows that for the coarsest grids, the interface rapidly spreads over one third of the experiment height, in strong contrast to the sharp interface that should be found for solutions to the Euler equation. Even for the finest grid spacing, significant interface spreading occurs. The finest grid spacing cannot match the slip obtained with the coarser Lagrangian solution in Fig. 3. The numerical diffusion effects arising from the control-volume approach provide a strong argument for care in the analysis of transient stratified flows.

Conclusions

Although commonly applied in reactor and other simulations, control volume and other upwind finite-difference numerical formulations can introduce significant numerical diffusion and error, particularly for transient problems. Here the problem of transient stratification of flow through a vertical tube array was studied. Experiments showed that a clearly defined interface forms between the light and heavy fluids. A simple analytic expression was proposed and provided good agreement with steady-state experimental measurements and the expectation of a thin density interface obtained through scaling. Numerical results were presented for both steady-state and transient cases, and a Lagrangian interface tracking procedure was shown to provide the best results.

Acknowledgments

Summer fellowship support for P. F. Peterson under the Savannah River Laboratory Faculty Research Participation Program is appreciated.

References

Butterworth, D., 1978, "The Development of a Model for Three-Dimensional Flow in Tube Bundles," *International Journal of Heat and Mass Transfer*, Vol. 21, pp. 253–256.

Debler, W. R., 1959, "Stratified Flow Into a Line Sink," *Journal of the Engineering Mechanics Division, Proceedings of the ASCE*, Vol. 85, pp. 51–65.

Huber, D. G., 1960, "Irrotational Motion of Two Fluid Strata Towards a Line Sink," *Journal of the Engineering Mechanics Division, Proceedings of the ASCE*, Vol. 86, pp. 71–86.

Hunt, M. L., and Tien, C. L., 1988, "Effects of Thermal Dispersion on Forced Convection in Fibrous Media," *International Journal of Heat and Mass Transfer*, Vol. 31, pp. 301–309.

Nourbakhsh, H. P., and Theofanous, T. G., 1986, "A Criterion for Predicting Thermal Stratification Due to High-Pressure Injection in a Circulating Reactor Loop," *Nuclear Science and Engineering*, Vol. 94, pp. 77–79.

Pruitt, J. M., Hassan, Y. A., and Steininger, D. A., 1990, "Large Eddy Simulation of Turbulent Flow in a Tube Bundle," *Thermal Hydraulics of Advanced Heat Exchangers*, ASME NE-Vol. 5, pp. 1–6.

Slattery, J. C., 1968, "Two-Phase Flow Through Porous Media," *AIChE Journal*, Vol. 14, pp. 50–56.

Slattery, J. C., 1978, *Momentum, Energy and Mass Transfer in Continua*, Kreiger Press, New York.

Theofanous, T. G., and Iyer, K., 1987, "Mixing Phenomena of Interest to SBLOCAs," *Nuclear Engineering and Design*, Vol. 102, pp. 91–103.

Vafai, K., and Tien, C. L., 1981, "Boundary and Inertia Effects on Flow and Heat Transfer in Porous Media," *International Journal of Heat and Mass Transfer*, Vol. 24, pp. 195–203.

Whitaker, S., 1969, "Advances in Theory of Fluid Motion in Porous Media," *Ind. Engg. Chem.*, Vol. 61, pp. 14–28.

Yih, C.-S., 1958, "On the Flow of a Stratified Fluid," *Proceedings 3rd U.S. National Congress of Applied Mechanics*, Providence, RI, June 11–14, pp. 857–861.

Zukauskas, A., 1972, "Heat Transfer From Tubes in Crossflow," *Advances in Heat Transfer*, J. P. Hartnett and T. F. Irvine, eds., Academic Press, New York, Vol. 8, pp. 93–161.

Downloaded 13 Dec 2010 to 193.140.21.150. Redistribution subject to ASME license or copyright; see http://www.asme.org/terms/Terms_Use.cfm

I. Pop
Faculty of Mathematics,
University of Cluj,
R-3400 Cluj, CP 253, Romania

D. B. Ingham
Department of Applied Mathematical Studies,
The University of Leeds,
Leeds, LS2, 9JT, United Kingdom

P. Cheng
Department of Mechanical Engineering,
University of Hawaii at Manoa,
Honolulu, HI, 96822

Transient Natural Convection in a Horizontal Concentric Annulus Filled With a Porous Medium

The method of matched asymptotic expansions is applied to study the problem of transient natural convection in a horizontal concentric porous annulus with inner and outer cylinders maintained at uniform temperatures. Asymptotic solutions for the inner layer, the outer layer, and the core are obtained for small times. A uniformly valid solution for stream function, tangential velocity, and temperature, which is valid for the whole domain, is constructed.

Introduction

The problem of natural convection between horizontal concentric cylinders or spheres filled with porous media has received increased attention in recent years due to its application in thermal insulation, geothermal activities, chemical and nuclear engineering, etc. Caltagirone (1976) gave an extensive analysis of steady natural convection in a porous annulus between horizontal concentric cylinders, but since then there have been several publications on this problem. Two-dimensional results for the average and local heat transfer rates have been presented by Brailovskaya et al. (1978). Another important paper by Burns and Tien (1979) used the finite difference method and the regular perturbation method to study natural convection in porous media enclosed by concentric spheres and horizontal cylinders. Further numerical work on this problem has been performed by Vasseur et al. (1984a, 1984b) who considered the problem of natural convection in a porous annulus with uniformly distributed energy sources. Both the case of isothermal and constant heat flux boundary conditions are considered. Bau (1984a, 1984b) and Himasekhar and Bau (1986, 1988) have reported analytical results for the thermal convection in a porous medium confined between two horizontal eccentric cylinders based on a regular perturbation expansion in terms of the Rayleigh number. In particular, the Nusselt number is expressed as a power series of the Rayleigh number for various eccentricities. Their results have, however, a limited radius of convergence and various nonlinear transformations are employed in order to extend the range of utility of the series. Recently, Kimura and Pop (1991, 1992) have investigated conjugate problems on natural convection in porous media enclosed by horizontal concentric cylinders. Numerical results by a finite-difference technique were presented for a large variation in the parameters entering the problems.

The literature survey conducted above demonstrates that our knowledge on this problem is limited to the steady-state case only. The importance of a fundamental study of transient natural convection in a porous medium bounded by two horizontal concentric cylinders is evident, considering that practical insulation systems do not operate in the steady state. In fact, there is no actual flow situation, natural or artificial, that does not involve some unsteadiness.

In this paper, we present some features associated with the development of the natural convection flow in a fluid-saturated porous medium between two horizontal concentric cylinders from a state of rest when the unsteady flow is caused by step changes in the wall temperature of the inner and outer cylinders. Formulation of the problem is based on Darcy's law, which is valid when the particle Reynolds number is very small and the ratio of particle diameter to the inner cylinder diameter is small so that the boundary friction effect can be neglected. Short-time solutions of the governing equations are obtained through an elegant use of the method of matched asymptotic expansions, similar to those employed by Sano (1986). The problem is first divided into the inner boundary layer (adjacent to the inner cylinder), the outer boundary layer (adjacent to the outer cylinder), and a core region. An analytical solution is obtained for each region.

Basic Equations

The problem under consideration is that of two-dimensional unsteady natural convection in a porous medium bounded by two infinitely long horizontal concentric circular cylinders. The porous medium is isotropic, homogeneous, and saturated with an incompressible fluid. Initially, the fluid is at rest and at a uniform and constant temperature T_f. Transient flow in the porous annulus is initiated as a result of a step change in the surface temperature of the inner or outer cylinder to T_i' and T_o', respectively. The saturated porous medium will be treated as a continuum, with the solid and fluid phases in thermal equilibrium. The physical properties of the saturating fluid, except the fluid density that gives rise to the buoyancy force, are taken as constant. Finally, the fluid motion is assumed slow enough for the inertial force to be small compared to the buoyancy, and the diffusion of vorticity from the boundaries to be negligible. With these assumptions the governing equations can be written in polar coordinates, (r', θ^*) as (Vasseur et al., 1984a, 1984b)

$$\nabla'^2\psi' = -\frac{\rho g \beta K}{\mu}\left(\frac{\partial T'}{\partial r'}\sin\theta^* + \frac{\partial T'}{\partial \theta^*}\frac{\cos\theta^*}{r'}\right) \tag{1}$$

$$\sigma\frac{\partial T'}{\partial t'} + \frac{1}{r'}\frac{\partial(T', \psi')}{\partial(r', \theta^*)} = \alpha\nabla'^2 T' \tag{2}$$

where t' is the time, g is the gravitational acceleration, ψ', T', ρ, μ, and α are the stream function, temperature, density, viscosity, and thermal diffusivity of the porous medium, K is the permeability of the porous medium, β is the thermal expansion coefficient of the fluid, and σ is the ratio of composite material heat capacity to fluid heat capacity. The stream function ψ' is related to the velocity components (u', v') in (r', θ^*) coordinates by the usual relations

$$(u', v') = \left(\frac{1}{r'}\frac{\partial\psi'}{\partial\theta^*}, -\frac{\partial\psi'}{\partial r'}\right).$$

The initial and boundary conditions of the problem are

Contributed by the Heat Transfer Division for publication in the JOURNAL OF HEAT TRANSFER. Manuscript received by the Heat Transfer Division December 1991; revision received May 1992. Keywords: Natural Convection, Porous Media, Transient and Unsteady Heat Transfer. Technical Editor: R. Viskanta.

Copyright © 1992 by ASME
Downloaded 13 Dec 2010 to 193.140.21.150. Redistribution subject to ASME license or copyright; see http://www.asme.org/terms/Terms_Use.cfm

$$t' < 0: \ \psi' = 0, \quad T' = T'_f \tag{3a}$$

$$t' \geq 0: \begin{cases} \psi' = 0, \ T' = T'_i & r' = R_i \\ \psi' = 0, \ T' = T'_o & r' = R_o \end{cases} \tag{3b}$$

where R_i and R_o are the radii of the inner and outer cylinders, respectively, and we assume that $T'_i \neq T'_o$.

We now define the following dimensionless variables:

$$t = t'/(\sigma t_o), \quad r = r'/R_i, \quad R = R_o/R_i,$$
$$\psi = \psi'/UR_i; \ T = (T' - T'_f)/\Delta T$$
$$T_i = (T'_i - T'_f)/\Delta T, \quad T_o = (T'_o - T'_f)/\Delta T = T_i - 1 \tag{4}$$

where t_o, $U = \rho g \beta K \Delta T/\mu$ and $\Delta T = T'_i - T'_o$ are characteristic time, speed, and temperature difference, respectively. Then Eqs. (1) and (2), and boundary conditions (3) become

$$\nabla^2 \psi = -\frac{\partial T}{\partial r} \sin \theta^* - \frac{\partial T}{\partial \theta^*} \frac{\sin \theta^*}{r} \tag{5}$$

$$\frac{\partial T}{\partial t} + \frac{\epsilon}{r} \frac{\partial (T, \psi)}{\partial (r, \theta^*)} = \alpha^* \epsilon^2 \nabla^2 T \tag{6}$$

$$t < 0: \quad \psi = T = 0 \tag{7a}$$

$$t \geq 0: \begin{cases} \psi = 0, & T = T_i \quad \text{at } r = 1 \\ \psi = 0, & T = T_o \quad \text{at } r = R \end{cases} \tag{7b}$$

where

$$\epsilon = \frac{U t_o}{R_i}, \quad \alpha^* = \frac{\alpha}{U^2 t_o} = (\epsilon \mathrm{Ra})^{-1} \tag{8}$$

with $\mathrm{Ra} = \rho g \beta K \Delta T R_i/(\mu \alpha)$ being the Rayleigh number.

Solutions to Eqs. (5)–(7) are sought for $\alpha^* = \mathbf{O}(1)$ as perturbation expansions in powers of the small parameter $|\epsilon| \ll 1$. The flow field in the porous annulus will now be divided into three regions: an inner layer near the inner cylinder, an outer layer near the outer cylinder, and a core between the two layers. The inner and outer layers are to be matched in the overlapping core domain.

Equations in the Core Region

In the core region the asymptotic expansions for the stream function ψ and temperature T are assumed to be of the form

$$\psi = \psi_0^{(c)}(t, r, \theta) + |\epsilon| \psi_0^{(c)}(t, r, \theta) + \epsilon^2 \psi_2^{(c)}(t, r, \theta) + \text{h.o.t.} \tag{9a}$$

$$T = T_0^{(c)}(t, r, \theta) + |\epsilon| T_0^{(c)}(t, r, \theta) + \epsilon^2 T_2^{(c)}(t, r, \theta) + \text{h.o.t.} \tag{9b}$$

where θ denotes θ^* when $\Delta T > 0$ and $(\pi - \theta^*)$ when $\Delta T < 0$. Substituting Eq. (9) into Eqs. (5) and (6) and equating coefficients of like powers of $|\epsilon|$, we obtain an infinite set of partial differential equations. The first several set of equations are

$$\nabla^2 \psi_0^{(c)} = -\frac{\partial T_0^{(c)}}{\partial r} \sin \theta - \frac{\partial T_0^{(c)}}{\partial \theta} \frac{\cos \theta}{r}, \quad \frac{\partial T_0^{(c)}}{\partial t} = 0; \tag{10a, b}$$

$$\nabla^2 \psi_1^{(c)} = -\frac{\partial T_1^{(c)}}{\partial r} \sin \theta - \frac{\partial T_1^{(c)}}{\partial \theta} \frac{\cos \theta}{r}, \frac{\partial T_1^{(c)}}{\partial t} = -\frac{1}{r} \frac{\partial T_0 (T_0^{(c)}, \psi_0^{(c)})}{\partial (r, \theta)} \tag{11a, b}$$

$$\nabla^2 \psi_2^{(c)} = -\frac{\partial T_2^{(c)}}{\partial r} \sin \theta - \frac{\partial T_2^{(c)}}{\partial \theta} \frac{\cos \theta}{r} \tag{12a}$$

$$\frac{\partial T_2^{(c)}}{\partial t} = -\frac{1}{r} \left\{ \frac{\partial (T_0^{(c)}, \psi_1^{(c)})}{\partial (r, \theta)} + \frac{\partial (T_1^{(c)}, \psi_0^{(c)})}{\partial (r, \theta)} \right\} + \alpha^* \nabla^2 T_0^{(c)}. \tag{12b}$$

The solution of Eqs. (10b), (11b), and (12b) subject to the initial condition (7a) is $T_n^{(c)} \equiv 0$ for all n. Thus, the equation for $\psi_n^{(c)}$ is found to be governed by the Laplace equation $\nabla^2 \psi_n^{(c)} = 0$ (for all n) suggesting that in the core region the flow is inviscid and irrotational to all orders of $|\epsilon|$. It can be shown that the general solution for $\psi_n^{(c)}$ is given by

$$\psi_n^{(c)} = \sum_{k=1}^{\infty} \left\{ A_{nk}(t) r^k + B_{nk}(t) r^{-k} \right\} \sin k\theta, \ n = 0, 1, 2, \ldots \tag{13}$$

Nomenclature

A_{nk}, B_{nk} = constants, Eq. (13)
$C_1^{(i)}$, $C_1^{(0)}$, $C_2^{(i)}$, $C_2^{(0)}$ = constants, Eqs. (34 e–h)
$f_0, f_1, \ldots, f_7$ = functions, Eqs. (34i–n), (37), and (39)
g = acceleration due to gravity
k = effective thermal conductivity
K = porous medium permeability
Nu = Nusselt number
q = heat transfer rate
r = radial coordinate, Eq. (4)
r_i = inner coordinate $= (r-1)/|\epsilon|$
r_o = outer coordinate $= (R-r)/|\epsilon|$
R = radius ratio, Eq. (4)
Ra = Rayleigh number for a porous medium
R_i = radius of the inner cylinder
R_o = radius of the outer cylinder
t = time, Eq. (4)
t^* = time, Eq. (34a)
t_o = characteristic time
T = dimensionless temperature, Eq. (4)
T_f = initial temperature
T_i = inner cylinder temperature, Eq. (4)
T_o = outer cylinder temperature, Eq. (4)
u, v = velocity components along (r, θ^*) coordinates
U = characteristic speed
α = effective thermal diffusivity
α^* = parameter, Eq. (8)
β = coefficient of thermal expansion
ϵ = parameter, Eq. (8)
η = similarity variable
θ^* = angular coordinate
μ = fluid viscosity
ξ = similarity variable
ρ = density
σ = ratio of heat capacity of the saturated porous medium to that of the fluid
ψ = stream function

Subscripts

c = composite
w = value at the wall

Superscripts

$'$ = dimensional variables
c = core region
i = inner boundary layer
0 = outer boundary layer
$\bar{}$ = average quantity

Downloaded 13 Dec 2010 to 193.140.21.150. Redistribution subject to ASME license or copyright; see http://www.asme.org/terms/Terms_Use.cfm

where A_{nk} and B_{nk} are integral constants to be determined through matching with the boundary layer solutions.

Equations in the Boundary Layers

The asymptotic expansions for ψ and T in the inner boundary layer are assumed to be of the form

$$\psi = |\epsilon| \left[\psi_0^{(i)}(t, r_i, \theta) + |\epsilon|\ \psi_1^{(i)}(t, r_i, \theta) + \epsilon^2 \psi_2^{(i)}(t, r_i, \theta) + \text{h.o.t.} \right] \quad (14a)$$

$$T = T_0^{(i)}(t, r_i, \theta) + |\epsilon|\ T_1^{(i)}(t, r_i, \theta) + \epsilon^2 T_2^{(i)}(t, r_i, \theta) + \text{h.o.t.} \quad (14b)$$

where the radial coordinate is stretched as $r_i = (r-1)/|\epsilon|$. Thus Eqs. (5) and (6) result in the following set of equations in the inner boundary layer:

$$\psi_{0,r_i r_i}^{(i)} = -T_{0,r_i}^{(i)} \sin\theta,\ T_{0,t}^{(i)} - \alpha^* T_{0,r_i r_i}^{(i)} = 0 \quad (15a, b)$$

$$\psi_{1,r_i r_i}^{(i)} = -T_{1,r_i}^{(i)} \sin\theta - T_{0,\theta}^{(i)} \cos\theta - \psi_{0,r_i}^{(i)} \quad (16a)$$

$$T_{1,t}^{(i)} - \alpha^* T_{1,r_i r_i}^{(i)} = \alpha^* T_{0,r_i}^{(i)} + T_{0,\theta}^{(i)} \psi T_{0,r_i}^{(i)} - T_{0,r_i}^{(i)} \psi_{0,\theta}^{(i)} \quad (16b)$$

$$\psi_{2,r_i r_i}^{(i)} = -T_{2,r_i}^{(i)} \sin\theta - T_{1,\theta}^{(i)} \cos\theta - \psi_{1,r_i}^{(i)} - \psi_{0,\theta\theta}^{(i)} + r_i \left(\psi_{0,r_i}^{(i)} + T_{0,\theta}^{(i)} \cos\theta \right) \quad (17a)$$

$$T_{2,t}^{(i)} - \alpha^* T_{2,r_i r_i}^{(i)} = \alpha^* \left(T_{1,r_i}^{(i)} - r_i T_{o,r_i}^{(i)} + T_{0,\theta\theta}^{(i)} \right) + T_{1,\theta}^{(i)} \psi_{0,r_i}^{(i)} - T_{0,r_i}^{(i)} \psi_{1,\theta}^{(i)} + T_{0,\theta}^{(i)} \psi_{1,r_i}^{(i)} - T_{1,r_i}^{(i)} \psi_{o,\theta}^{(i)} + r_i \left(T_{o,r_i}^{(i)} \psi_{o,\theta}^{(i)} - T_{o,\theta}^{(i)} \psi_{o,r_i}^{(i)} \right) \quad (17b)$$

Similarly, the asymptotic expansions for ψ and T in the outer boundary layer can be assumed to be of the form

$$\psi = |\epsilon| \left[\psi_o^{(0)}(t, r_o, \theta) + |\epsilon| \psi_1^{(0)}(t, r_o, \theta) + \epsilon^2 \psi_2^{(o)}(t, r_o, \theta) + \text{h.o.t.} \right] \quad (18a)$$

$$T = T_o^{(0)}(t, r_o, \theta) + |\epsilon| T_1^{(0)}(t, r_o, \theta) + \epsilon^2 T_2^{(0)}(t, r_o, \theta) + \text{h.o.t.} \quad (18b)$$

where the radial coordinate is stretched as $r_o = (R-r)/|\epsilon|$. Thus Eqs. (5) and (6) result in the following sets of equations in the outer boundary layer:

$$\psi_{o,r_o r_o}^{(o)} = T_{o,r_o}^{(o)} \sin\theta,\ T_{o,t}^{(o)} - \alpha^* T_{o,r_o r_o}^{(o)} = 0 \quad (19a, b)$$

$$\psi_{1,r_o r_o}^{(o)} = T_{1,r_o}^{(o)} \sin\theta + R^{-1} \left[\psi_{o,r_o}^{(o)} - T_{o,\theta}^{(o)} \cos\theta \right] \quad (20a)$$

$$T_{1,t}^{(o)} - \alpha^* T_{1,r_o r_o}^{(o)} = \mathrm{R}^{-1} \left[T_{o,r_o}^{(o)} \psi_{o,\theta}^{(o)} - T_{o,\theta}^{(o)} \psi_{o,r_o}^{(o)} - \alpha^* T_{o,r_o}^{(o)} \right] \quad (20b)$$

$$\psi_{2,r_o r_o}^{(o)} = T_{2,r_o}^{(o)} \sin\theta + R^{-1} \left[\psi_{1,r_o}^{(o)} - T_{1,\theta}^{(o)} \cos\theta \right] + R^{-2} \left[r_o \left(\psi_{o,r_o}^{(o)} - T_{o,\theta}^{(o)} \cos\theta \right) - \psi_{o,\theta\theta}^{(o)} \right] \quad (21a)$$

$$T_{2,t}^{(0)} - \alpha^* T_{2,r_o r_o}^{(o)} = \alpha^* \left[R^{-2} \left(-r_o T_{o,r_o}^{(o)} + T_{o,\theta\theta}^{(o)} \right) - R^{-1} T_{1,r_o}^{(o)} \right] + R^{-2} r_o \left(T_{o,r_o}^{(o)} \psi_{o,\theta}^{(o)} - T_{o,\theta}^{(o)} \psi_{o,r_o}^{(o)} \right) + R^{-1} \left(T_{o,r_o}^{(o)} \psi_{1,\theta}^{(o)} + T_{1,r_o}^{(o)} \psi_{o\theta}^{(o)} - T_{1,\theta}^{(o)} \psi_{o,r_o}^{(o)} - T_{1,\theta}^{(o)} \psi_{1,r_o}^{(o)} \right) \quad (21b)$$

The inner and outer boundary layer expansions given by Eqs. (14) and (18) are required to satisfy the boundary conditions on the inner and outer cylinders, respectively. In addition, they must match with the core region expansion (9), which requires that

$$|\epsilon| \lim_{r_i \to \infty} \left(\psi_o^{(i)} + |\epsilon| \psi_1^{(i)} + \epsilon^2 \psi_2^{(i)} + \text{h.o.t.} \right) = \lim_{(r-1)\to 0} \left(\psi_0^{(c)} + |\epsilon| \psi_1^{(c)} + \epsilon^2 \psi_2^{(c)} + \text{h.o.t.} \right) \quad (22a)$$

$$|\epsilon| \lim_{r_o \to 0} \left(\psi_o^{(o)} + |\epsilon| \psi_1^{(o)} + \epsilon^2 \psi_2^{(o)} + \text{h.o.t.} \right) = \lim_{(R-r)\to 0} \left(\psi_0^{(c)} + |\epsilon| \psi_1^{(c)} + \epsilon^2 \psi_2^{(c)} + \text{h.o.t.} \right) \quad (22b)$$

$$\lim_{r_i \to \infty} T_n^{(i)} = \lim_{r_o \to \infty} T_n^{(o)} \to 0 \text{ for all } n \quad (22c)$$

The leading order temperature distributions for the inner and outer boundary layers can be obtained from Eqs. (15*b*) and (19*b*) with the corresponding boundary and matching conditions obtained from Eqs. (7*b*) and (22*c*), which give

$$T_o^{(i)} = T_i \operatorname{erfc}(\eta), \quad T_o^{(o)} = T_o \operatorname{erfc}(\xi) \quad (23a, b)$$

where

$$\eta = r_i / 2(\alpha^* t)^{1/2}, \quad \xi = r_o / 2(\alpha^* t)^{1/2} \quad (24a, b)$$

are the similarity variables and $\operatorname{erfc}(x)$ denotes the complementary error function.

The solutions to Eqs. (15*a*) and (19*a*) are

$$\psi_o^{(i)} = 2(\alpha^* t)^{1/2} T_i \left[-\eta \operatorname{erfc}(\eta) + \frac{1}{\sqrt{\pi}} e^{-\eta^2} + C_0^{(i)} \eta - \frac{1}{\sqrt{\pi}} \sin\theta \right] \quad (25a)$$

$$\psi_o^{(o)} = 2(\alpha^* t)^{1/2} T_o \left[\xi \operatorname{erfc}(\xi) - \frac{1}{\sqrt{\pi}} e^{-\xi^2} + C_o^{(o)} \xi + \frac{1}{\sqrt{\pi}} \sin\theta \right] \quad (25b)$$

where $C_o^{(i)}$ and $C_o^{(o)}$ are constants to be determined by matching with the core region solution. For this purpose, we note that for $\eta \to \infty$ and $\xi \to \infty$, Eqs. (25) become

$$\psi_o^{(i)} \sim 2(\alpha^* t)^{1/2} T_i \left[C_o^{(i)} \eta - \frac{1}{\sqrt{\pi}} \right] \sin\theta \quad (26a)$$

$$\psi_o^{(o)} \sim 2(\alpha^* t)^{1/2} T_o \left[C_o^{(o)} \xi + \frac{1}{\sqrt{\pi}} \right] \sin\theta \quad (26b)$$

The matching condition between the inner and outer boundary layers for $r^* \to 0$ and $r^o \to 0$ with $\psi_o^{(c)}$ should behave as

$$\psi_o^{(c)} \sim T_i \left[C_o^{(i)} \frac{r^*}{|\epsilon|} - \frac{2}{\sqrt{\pi}} (\alpha^* t)^{1/2} + \ldots \right] \sin\theta \quad (27a)$$

$$\psi_o^{(c)} \sim T_o \left[C_o^{(o)} \frac{r^o}{|\epsilon|} + \frac{2}{\sqrt{\pi}} (\alpha^* t)^{1/2} + \ldots \right] \sin\theta \quad (27b)$$

Downloaded 13 Dec 2010 to 193.140.21.150. Redistribution subject to ASME license or copyright; see http://www.asme.org/terms/Terms_Use.cfm

where $r^* = r - 1$ and $r^o = R - r$. On the other hand, the general solution for $\psi_o^{(c)}$ given by Eq. (13) with $n = 0$ and $k = 1$, is

$$\psi_o^{(c)} = \left[A_{01}(t) r + B_{01}(t) r^{-1} \right] \sin\theta \tag{28}$$

From the above equation, we have for $r^* \to 0$

$$\psi_o^{(c)} \sim \left[A_{01} + B_{01} + (A_{01} - B_{01}) r^* + \ldots \right] \sin\theta \tag{29a}$$

and for $r^o \to 0$

$$\psi_o^{(c)} \sim \left[R A_{01} + R^{-1} B_{01} - (A_{01} - R^{-2} B_{01}) r^o + \ldots \right] \sin\theta \tag{29b}$$

A comparison of Eqs. (27) and (29) shows that

$$A_{01} = B_{01} = 0 \quad \text{and} \quad C_o^{(i)} = C_o^{(o)} = 0 \tag{30}$$

Solutions to higher-order approximations can be obtained in a similar manner. Using the matching technique described by Van Dyke (1975), we obtain, after some algebra, the following solutions:

(*i*) *For the inner boundary layer:*

$$T = T_i \operatorname{erfc}(\eta) - t^{*1/2} T_i \eta \operatorname{erfc}(\eta) + t^* T_i \left[\eta^2 \operatorname{erfc}(\eta) + \frac{1}{2\sqrt{\pi}} \eta\, e^{-\eta^2} \right] - t^* |\mathrm{Ra}| T_i^2 f_o(\eta) \cos\theta + t^{*3/2} |\mathrm{Ra}| T_i^2 \left[f_4(\eta) + \frac{16}{5\pi} C_1^{(i)} \eta e^{-\eta^2} \right] \cos\theta + \ldots \tag{31a}$$

$$\psi = 2t^{*1/2} T_i \left[-\eta \operatorname{erfc}(\eta) + \frac{1}{\sqrt{\pi}} e^{-\eta^2} - \frac{1}{\sqrt{\pi}} \right] \sin\theta + t^* T_i \left[f_1(\eta) + \frac{8}{\sqrt{\pi}} C_1^{(i)} \eta \right] \sin\theta - t^{*3/2} T_i \left[f_3(\eta) + \frac{8}{\sqrt{\pi}} C_1^{(i)} \eta^2 + C_2^{(i)} \eta \right] \sin\theta + t^{*3/2} |\mathrm{Ra}| T_i^2 f_2(\eta) \sin\theta \cos\theta + \ldots \tag{31b}$$

(*ii*) *For the core region:*

$$T = 0 \tag{32a}$$

$$\psi = \frac{2t^{*1/2}}{\sqrt{\pi}\,(R^2-1)} \left[(T_i + RT_o) r - R(T_o + RT_i) r^{-1} \right] \sin\theta + \frac{t^*}{2(1-R^2)} \left[(T_o - T_i) r + (R^2 T_i - T_o) r^{-1} \right] \sin\theta + \frac{t^{*3/2}}{6\sqrt{\pi}\, R(1-R^2)} \left[(T_o + RT_i) r - (T_o + R^3 T_i) r^{-1} \right] \sin\theta + \frac{2|\mathrm{Ra}| t^{*3/2}}{3\sqrt{\pi}(R^4-1)} \left[\frac{4\sqrt{2}-9}{2} + \frac{8}{3\pi} \right] \times \left[(T_i^2 + RT_o^2) r^2 - R(T_o^2 + R^3 T_i^2) r^{-2} \right] \sin\theta \cos\theta + \ldots \tag{32b}$$

(*iii*) *For the outer boundary layer:*

$$T = T_o \operatorname{erfc}(\xi) + t^{*1/2} R^{-1} T_o \xi \operatorname{erfc}(\xi) + t^* R^{-2} T_o \left[\xi^2 \operatorname{erfc}(\xi) + \frac{1}{2\sqrt{\pi}} \xi\, e^{-\xi^2} \right] - t^* |\mathrm{Ra}| R^{-1} T_o^2 f_o(\xi) \cos\theta + t^{*3/2} |\mathrm{Ra}| R^{-2} T_o^2 \left[-f_4(\xi) + \frac{16}{5\pi} C_1^{(0)} \xi e^{-\xi^2} \right] \cos\theta + \ldots \tag{33a}$$

$$\psi = 2t^{*1/2} T_0 \left[\xi \operatorname{erfc}(\xi) - \frac{1}{\sqrt{\pi}} e^{-\xi^2} + \frac{1}{\sqrt{\pi}} \right] \sin\theta + t^* R^{-1} T_0 \left[f_1(\xi) - \frac{8}{\sqrt{\pi}} C_1^{(0)} \xi \right] \sin\theta + t^{*3/2} R^{-2} T_0^2 \left[f_3(\xi) - \frac{8}{\sqrt{\pi}} C_1^{(0)} \xi^2 - C_2^{(0)} \xi \right] \sin\theta - t^{*3/2} |\mathrm{Ra}| R^{-1} T_0^2 f_2(\xi) \sin\theta \cos\theta + \ldots \tag{33b}$$

In the above equations we have adopted the notations:

$$t^* = \alpha t' / (\sigma R_i^2), \quad \psi = \psi' / (\alpha \mathrm{Ra}), \quad \eta = \frac{r-1}{2t^{*1/2}}, \quad \xi = \frac{R-r}{2t^{*1/2}} \tag{34a-d}$$

$$C_1^{(i)} = \frac{1 + R(T_o/T_i)}{R^2 - 1}, \quad C_1^{(0)} = \frac{R(R + T_i/T_0)}{R^2 - 1} \tag{34e, f}$$

$$C_2^{(i)} = \frac{1 + R^2 - 2\,T_o/T_i}{1 - R^2}, \quad C_2^{(0)} = \frac{1 + R^2 - 2R^2\,T_i/T_o}{1 - R^2} \tag{34g, h}$$

$$f_0(x) = \left(\frac{1}{2} + x^2 \right) \operatorname{erfc}^2(x) - \frac{1}{\sqrt{\pi}} x e^{-x^2} \operatorname{erfc}(x) + \frac{4}{3\pi} e^{-x^2} - \left(\frac{1}{2} + \frac{4}{3\pi} \right) \left[(1 + 2x^2) \operatorname{erfc}(x) - \frac{2}{\sqrt{\pi}} x e^{-x^2} \right] \tag{34i}$$

$$f_1(x) = \left(3x^2 + \frac{1}{2} \right) \operatorname{erfc}(x) - \frac{3}{\sqrt{\pi}} x e^{-x^2} + \frac{4}{\sqrt{\pi}} x - \frac{1}{2} \tag{34j}$$

$$f_2(x) = \left(x + \frac{2}{3} x^2 \right) \operatorname{erfc}^2(x) - \frac{1}{3\sqrt{\pi}} \left[4 + (7 + 4x^2) e^{-x^2} \right] \operatorname{erfc} x + \frac{8}{3\sqrt{2\pi}} \operatorname{erfc}(\sqrt{2}x) + \frac{2}{3\pi} x e^{-2x^2} - \frac{2}{3\sqrt{\pi}} \left(\frac{4\sqrt{2}-9}{2} + \frac{8}{3\pi} \right) + \left(1 + \frac{8}{3\pi} \right) \left[\frac{2}{3\sqrt{\pi}} (1 + x^2) e^{-x^2} - \left(x + \frac{2}{3} x^3 \right) \operatorname{erfc}(x) \right] \tag{34k}$$

$$f_3(x) = \left(x + \frac{16}{3} x^3 \right) \operatorname{erfc}(x) + \frac{2}{3\sqrt{\pi}} \left(\frac{1}{4} - 8x^2 \right) e^{-x^2} + \frac{8}{\sqrt{\pi}} x^2 - \frac{1}{6\sqrt{\pi}} \tag{34l}$$

$$f_4(x) = \frac{3}{8} \left[(3x + 2x^3) \operatorname{erfc}(x) - \frac{2}{\sqrt{\pi}} (1 + x^2) e^{-x^2} \right] + \frac{4}{3} x^3 \operatorname{erfc}^2(x) + \frac{1}{3\sqrt{\pi}} \left[(5 + 2x^2) e^{-x^2} - 2 \right] \operatorname{erfc}(x) - \frac{2}{\pi} x e^{-2x^2} + \frac{68}{15\pi} x e^{-x^2} - \frac{1}{4\sqrt{\pi}} e^{-x^2} - \left(1 + \frac{8}{3\pi} \right) \left[\left(\frac{x}{2} + x^3 \right) \operatorname{erfc}(x) - \frac{1}{\sqrt{\pi}} x^2 e^{-x^2} \right] \tag{34m}$$

Results and Discussion

In this section we present composite solutions that are uniformly valid throughout the whole flow field. A uniformly valid stream function can be obtained using

$$\psi_c(t^*, \eta, \xi, r, \theta) = \psi^{(i)}(t^*, \eta, \theta) + \psi^{(o)}(t^*, \xi, \theta) + \psi^{(c)}(t^*, r, \theta) - (\text{the part common to the three expansions}) \tag{35}$$

which gives

$$\psi_c = 2t^{*1/2} T_i \left[-\eta \operatorname{erfc}(\eta) + \frac{1}{\sqrt{\pi}} e^{-\eta^2} \right] \sin\theta + 2t^{*1/2} T_o \left[\xi \operatorname{erfc}(\eta) - \frac{1}{\sqrt{\pi}} e^{-\xi^2} \right] \sin\theta$$

Downloaded 13 Dec 2010 to 193.140.21.150. Redistribution subject to ASME license or copyright; see http://www.asme.org/terms/Terms_Use.cfm

$$+\frac{2t^{*1/2}}{\sqrt{\eta}\,(R^2-1)}[(T_i+RT_o)r-R(T_o+RT_i)r^{-1}]\sin\theta$$
$$+t^*T_i\left[\left(3\eta^2+\frac{1}{2}\right)\operatorname{erfc}(\eta)-\frac{3}{\sqrt{\pi}}\eta e^{-\eta^2}\right]\sin\theta$$
$$+t^*R^{-1}T_o\left[\left(3\xi^2+\frac{1}{2}\right)\operatorname{erfc}(\xi)-\frac{3}{\sqrt{\pi}}\xi e^{-\xi^2}\right]\sin\theta$$
$$+\frac{t^*}{2(1-R^2)}[T_o-T_i)r+(R^3T_i-T_o)r^{-1}]\sin\theta$$
$$-t^{*3/2}T_if_5(\eta)\sin\theta+t^{*3/2}R^{-2}T_of_5(\xi)\sin\theta$$
$$+\frac{t^{*3/2}}{6\sqrt{\pi}R(1-R^2)}[(T_o-RT_i)r+(T_o+R^3T_i)r^{-1}]\sin\theta$$
$$+t^{*3/2}|\mathrm{Ra}|T_i^2f_6(\eta)\sin\theta\cos\theta$$
$$-t^{*3/2}|\mathrm{Ra}|R^{-1}T_o^2f_6(\xi)\sin\theta\cos\theta$$
$$+\frac{2|\mathrm{Ra}|t^{*3/2}}{3\sqrt{\pi}\,(R^4-1)}\left[\frac{4\sqrt{2}-9}{2}+\frac{8}{3\pi}\right]$$
$$\times[(T_i^2+RT_0^2)r^2-R(T_0^2+R^3T_i^2)r^{-2}]\sin\theta\cos\theta \quad (36)$$

where

$$f_5(x)=f_3(x)+\frac{1}{6\sqrt{\pi}}, \quad (37a)$$

$$f_6(x)=f_2(x)+\frac{2}{3\sqrt{\pi}}\left(\frac{4\sqrt{2}-9}{2}+\frac{8}{3\pi}\right) \quad (37b)$$

The composite tangential velocity is

$$V_c=T_i\operatorname{erfc}(\eta)\sin\theta+T_o\operatorname{erfc}(\xi)\sin\theta$$
$$-\frac{2t^{*1/2}}{\sqrt{\pi}\,(R^2-1)}[(T_i+RT_o)+R(T_o+RT_i)r^{-2}]\sin\theta$$
$$-t^{*1/2}T_i\left[3\eta\operatorname{erfc}(\eta)-\frac{2}{\sqrt{\pi}}e^{-\eta^2}\right]\sin\theta$$
$$+t^{*1/2}R^{-1}T_o\left[3\xi\operatorname{erfc}(\xi)-\frac{2}{\sqrt{\pi}}e^{-\xi^2}\right]\sin\theta$$
$$-\frac{t^*}{2(1-R^2)}[(T_o-T_i)-(R^2T_i-T_o)r^{-2}]\sin\theta$$
$$+t^*T_if_7(\eta)\sin\theta+t^*R^{-2}T_of_7(\xi)\sin\theta$$
$$-\frac{t^{*3/2}}{6\sqrt{\pi}R(1-R^2)}[(T_o+RT_i)+(T_o+R^3T_i)r^{-2}]\sin\theta$$
$$-t^*|\mathrm{Ra}|T_i^2f_o(\eta)\sin\theta\cos\theta-t^*|\mathrm{Ra}|R^{-1}T_o^2f_o(\xi)\sin\theta\cos\theta$$
$$-\frac{4|\mathrm{Ra}|t^{*3/2}}{3\sqrt{\pi}\,(R^4-1)}\left(\frac{4\sqrt{2}-9}{2}+\frac{8}{3\pi}\right)$$
$$\times[(T_i^2+RT_o^2)r+R(T_o^2+R^3T_i^2)r^{-3}]\sin\theta\cos\theta \quad (38)$$

where

$$f_7(x)=\left(\frac{1}{2}+8x^2\right)\operatorname{erfc}(x)-\frac{13}{2\sqrt{\pi}}xe^{-x^2} \quad (39)$$

The expression for the composite temperature is also given by

$$T_c=T_i\operatorname{erfc}(\eta)+T_o\operatorname{erfc}(\xi)-t^{*1/2}T_i\eta\operatorname{erfc}(\eta)$$
$$+t^{*1/2}R^{-1}T_o\xi\operatorname{erfc}(\xi)+t^*T_i\left[\eta^2\operatorname{erfc}(\eta)+\frac{1}{2\sqrt{\pi}}\eta e^{-\eta^2}\right]$$
$$+t^*R^{-2}T_o\left[\xi^2\operatorname{erfc}(\xi)+\frac{1}{2\sqrt{\pi}}\xi e^{-\xi^2}\right]$$

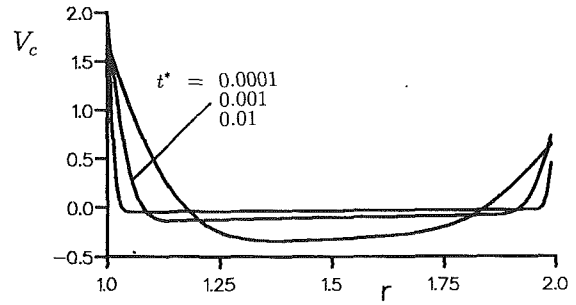

Fig. (1a) $R=2$, $\theta=\pi/2$, $T_i=2.0$

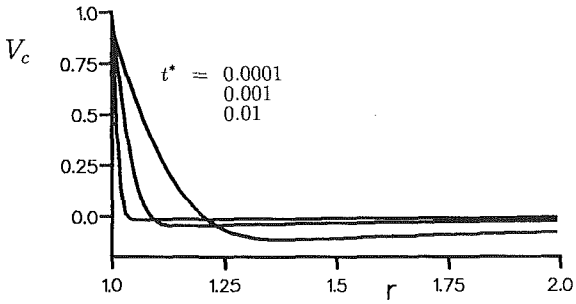

Fig. 1(b) $R=2$, $\theta=\pi/2$, $T_i=1.0$

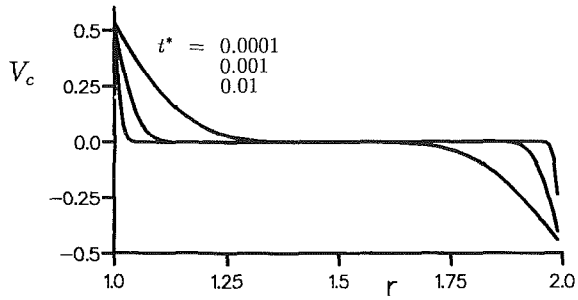

Fig. 1(c) $R=2$, $\theta=\pi/2$, $T_i=0.5$

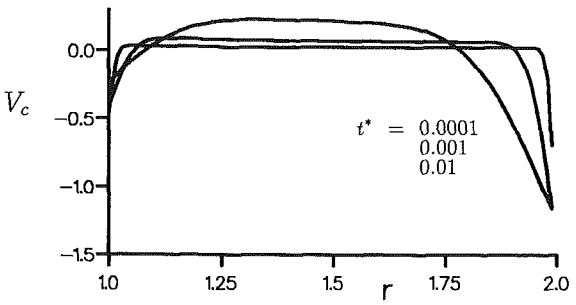

Fig. 1(d) $R=2$, $\theta=\pi/2$, $T_i=-0.5$

Fig. 1 Tangential velocity profiles for $t^*=0.0001$, 0.001 and 0.01

$$-t^*|\mathrm{Ra}|T_i^2f_o(\eta)\cos\theta-t^*|\mathrm{Ra}|R^{-1}T_o^2f_o(\xi)\cos\theta$$
$$+t^{*3/2}|\mathrm{Ra}|T_i^2\left[f_4(\eta)+\frac{16}{5\pi}C_1^{(i)}\eta e^{-\eta^2}\right]\cos\theta$$
$$+t^{*3/2}|\mathrm{Ra}|R^{-2}T_o^2\left[-f_4(\xi)+\frac{16}{5\pi}C_1^{(0)}\xi e^{-\xi^2}\right]\cos\theta+\ldots \quad (40)$$

It is observed from expressions (38) and (40) that the effects of the impulsive changes in the temperatures of the cylinders are felt in the core region after a time of $\mathbf{O}(t^{*1/2})$ whereas in the corresponding nonporous flow it takes much longer for the flow in the core region to be affected, namely $\mathbf{O}(t^{*3/2})$.

Downloaded 13 Dec 2010 to 193.140.21.150. Redistribution subject to ASME license or copyright; see http://www.asme.org/terms/Terms_Use.cfm

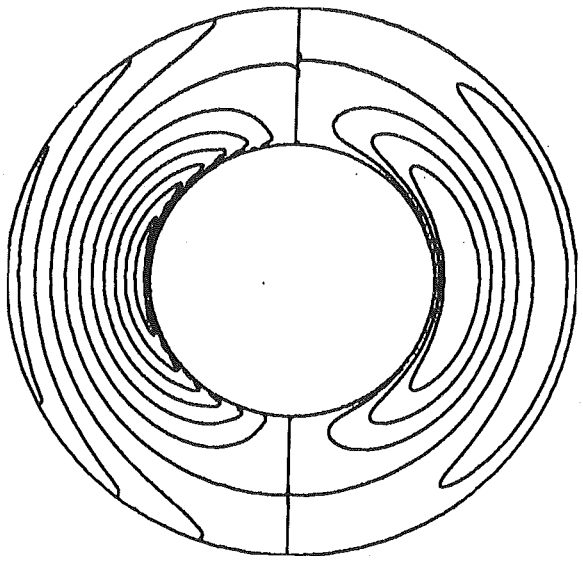

(i) (ii)

Fig. 2(*a*) $R=2$, $|\mathrm{Ra}|=10$, $T_i=2$; (i) $t^*\to 0$; (ii) $t^*=0.01$

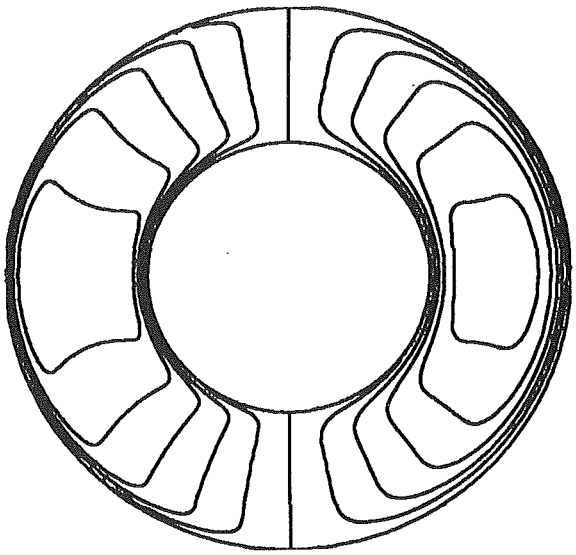

(i) (ii)

Fig. 2(*c*) $R=2$, $|\mathrm{Ra}|=10$, $T_i=0.5$; (i) $t^*=0.001$; (ii) $t^*=0.01$

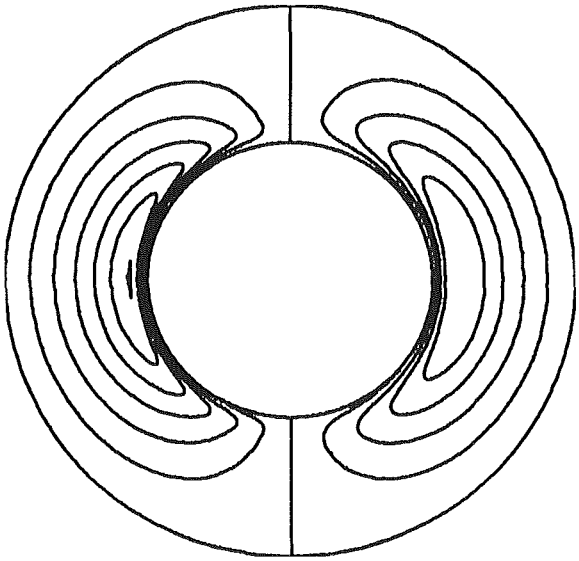

(i) (ii)

Fig. 2(*b*) $R=2$, $|\mathrm{Ra}|=10$, $T_i=1$; (i) $t^*=0.001$; (ii) $t^*=0.01$

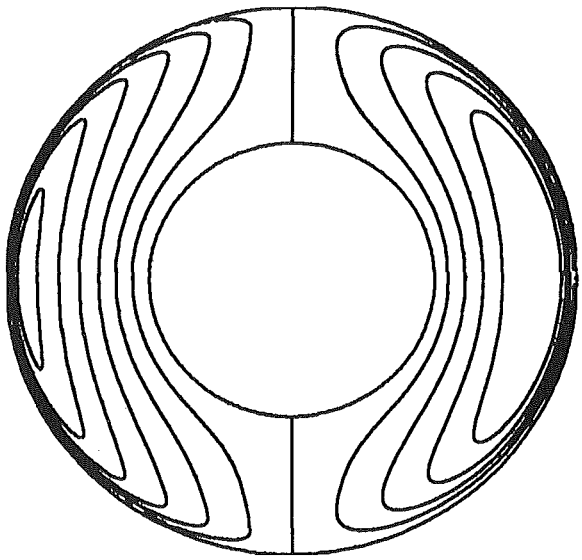

(i) (ii)

Fig. 2(*d*) $R=2$, $|\mathrm{Ra}|=10$, $T_i=0$; (i) $t^*=0.001$; (ii) $=0.01$

Fig. 2 Streamline patterns

This is not surprising since the viscous effects in the boundary layers in the nonporous flow are more efficient at damping out any changes that occur than the effects of thermal diffusion. Further, it is important to observe that the Rayleigh number has no effect on the flow until the third term in the asymptotic expansion, and that in all the results presented in this paper the assumption that $\alpha^*=\mathbf{O}(1)$ is satisfied.

Figure 1 shows the variation of the tangential velocity as a function of the radial distance at $\theta=\pi/2$ for $R=2$ and at various values of t^* for $T_i=2$, 1, 0.5, and -0.5 ($T_o=T_i-1$). It is of interest to note that, up to the order of approximation obtained here, the tangential velocity distribution at $\theta=\pi/2$ is independent of the value of the Rayleigh number. For $T_i>1$ both the inner and outer cylinders are heated and therefore the fluid rises near these boundaries. Because of the continuity equation there must be a corresponding downflow in the core of the region.

Figures 2(*a–d*) show the streamlines for $\mathrm{Ra}=10$, for various values of t^* and $T_i=2$, 1, 0.5, and 0, respectively. Since as $t^*\to 0$ the solution is independent of the Rayleigh number, the solution in Fig. 2*a*(*i*) is valid for all values of Ra. Further, for $T_i=2$, as $t^*\to 0$, the upflow in the boundary layers is confined to a very thin region and is therefore not seen in Fig. 2(*a*), but as t^* increases, the thickness of these boundary layers

Downloaded 13 Dec 2010 to 193.140.21.150. Redistribution subject to ASME license or copyright; see http://www.asme.org/terms/Terms_Use.cfm

increases; see Fig. 2(*a*). Therefore two cells in the form of crescents are formed and they rotate in opposite directions. As t^* increases the strengths of these recirculation regions grow; the larger the value of Ra, the quicker the symmetry of the flow about $\theta = \pi/2$ is broken. Further, as $t^* \to 0$, we observe from Eq. (32*b*) that there is a circular streamline of radius r_c

$$r_c = \sqrt{\left[\frac{(1+R)T_i - 1}{(1+R)T_i - R}\right]} R \tag{41}$$

which separates the two cells, and r_c varies from R to $\sqrt{R}$ as T_i increases from 1 to infinity.

When the inner cylindrical surface is impulsively changed but the outer surface is maintained at the original temperature of the porous media ($T_i = 1$) then the corresponding streamlines with Ra = 10 are given in Fig. 2(*b*) for $t^* = 0.001$ and 0.01. The fluid near the inner surface now rises and, from continuity, the flow returns via both the core region and the boundary-layer on the outer cylinder. Hence the flow develops only a single-cell structure, the center of which moves outward as t^* increases and is stronger the larger the value of Ra.

When $0 < T_i < 1$ and $-1 < T_o < 0$, the flow will rise near the inner surface and fall near the outer surface and a single cell will occur with boundary layers being generated impulsively on both the inner and outer surfaces. The streamlines with Ra = 10 and $t^* = 0.001$ and 0.01 are shown in Fig. 2(*c*); these agree with the flow picture that we would expect. This is confirmed by the tangential velocity profiles given in Fig. 1. It is interesting to note that for $R = 2$ the leading order core tangential velocity is given by

$$V_c = -\frac{2}{3}\frac{t^{*1/2}}{\sqrt{\pi}}\left[(3T_i - 2) + \frac{2}{r^2}(3T_i - 1)\right] \sin\theta \tag{42}$$

This is zero when

$$r^2 = -\frac{2(3T_i - 1)}{(3T_i - 2)} \tag{43}$$

Thus there is a unique point at which the leading core velocity for $R = 2$ is zero if $4/9 < T_i < 5/9$. When $T_i = 1/2$, the leading order core velocity is zero at $r = \sqrt{2}$ and this is clearly illustrated in Figs. 1(*c*) and 2(*c*).

Figure 2(*d*) shows the streamlines for Ra = 10, $T_i = 0$ ($T_o = -1$) when $t^* = 0.001$ and 0.01. The impulsive cooling of the outer cylinder causes the flow to fall near this surface and from continuity the flow returns by means of the core region and the inner boundary layer. However, the inner boundary layer is only playing a passive role in the dynamics of the flow in much the same way the outer boundary layer plays when $T_i = 1$ and $T_o = 0$.

The situation when both the inner and outer surfaces are impulsively cooled (i.e., $T_i < 0$ and $T_o < -1$) is very similar to the case when $T_i > 1$. The fluid falls near both the inner and outer surface and from continuity rises in the core region. Thus the streamline pattern consists of two cells of the crescent type. As $t^* \to 0$ the streamline separating the two cells is of radius r_c, which varies from 1 to $\sqrt{R}$ as T_i decreases from 0 to minus infinity. Clearly the outer cell must be much stronger in strength than the inner one.

The local Nusselt numbers for the inner and outer cylinders are given by

$$\mathrm{Nu}^i/T_i = \frac{1}{t^{*1/2}\sqrt{\pi}} + \frac{1}{2} - \frac{t^{*1/2}}{4\sqrt{\pi}} + t^{*1/2}\,|\mathrm{Ra}|\,\frac{T_i}{\sqrt{\pi}}\left(\frac{8}{3\pi} - \frac{1}{2}\right)\cos\theta + t^*\,|\mathrm{Ra}|\,T_i\left[-\frac{5}{16} + \frac{2}{5\pi}(1 - 4_1 C^{(i)})\right]\cos\theta \tag{44a}$$

and

$$\mathrm{Nu}^o/T_o = \frac{1}{t^{*1/2}\sqrt{\pi}} - \frac{1}{2}R^{-1} - \frac{1}{4\sqrt{\pi}}t^{*1/2}R^2 - t^{*1/2}\,|\mathrm{Ra}|\,R^{-1}\frac{T_o}{\sqrt{\pi}}\left(\frac{8}{3\pi} - \frac{1}{2}\right)\cos\theta + t^*\,|\mathrm{Ra}|\,R^{-2}T_o\left[\frac{5}{16} - \frac{2}{5\pi}(1 + 4C_1^{(o)})\right]\cos\theta \tag{44b}$$

where $\mathrm{Nu}^i = q_w^i R_i/k\Delta T$ and $\mathrm{Nu}^o = q_w^o R_i/k\Delta T$ with $q_w^i = -k\left(r'\frac{\partial T'}{\partial r'}\right)_{r'=R_i}$ and $q_w^o = k\left(r'\frac{\partial T'}{\partial r'}\right)_{r'=R_o}$. The average Nusselt numbers can be obtained from

$$\overline{\mathrm{Nu}}^i = \frac{1}{\pi}\int_o^\pi \mathrm{Nu}^i d\theta \text{ and } \overline{\mathrm{Nu}}^o = \frac{1}{\pi}\int_o^\pi \mathrm{Nu}^o d\theta \tag{45}$$

which give

$$\overline{\mathrm{Nu}}^i/T_i = \frac{1}{t^{*1/2}\sqrt{\pi}} + \frac{1}{2} - \frac{t^{*1/2}}{4\sqrt{\pi}} \tag{46a}$$

$$\overline{\mathrm{Nu}}^o/T_o = \frac{1}{t^{*1/2}\sqrt{\pi}} - \frac{1}{2}R^{-1} - \frac{1}{4\sqrt{\pi}}t^{*1/2}R^{-2} \tag{46b}$$

It is observed that the Nusselt number is infinite at time $t^* = 0$. The leading term of the expansions gives the ratio of Nusselt number to the local temperature to be the same on both the inner and outer cylinder while the second term shows that the first term underestimates (overestimates) the Nusselt numbers of the inner (outer) cylinders. Further, the Rayleigh number has no effect on the predicted average Nusselt numbers as obtained from the first three terms of the expansions.

Conclusions

An analytical study for the small time transient natural convection in a horizontal concentric porous annulus with inner and outer cylinders maintained at constant temperatures is presented in this paper. The strength of the work is the analytical part in which a very compact solution is obtained, using the method of matched asymptotic expansions, for the temperature and flow fields. It is found that the present short time solution is significantly different from the steady-state solution. For example, at relatively high Rayleigh numbers the core is stratified and not isothermal.

The paper demonstrates that the flow consists of three distinct regions: an inner boundary layer adjacent to the inner surface, an outer boundary layer adjacent to the outer surface, and a core region between the two boundary layers.

Acknowledgments

The authors would like to thank Faris Oghanna for his assistance in producing some of the figures.

References

Bau, H. H., 1984, "Thermal Convection in a Horizontal, Eccentric Annulus Containing a Saturated Porous Medium—An Extended Perturbation Expansion," *Int. J. Heat Mass Transfer*, Vol. 27, pp. 2277-2287.

Bau, H. H., 1984b, "Low Rayleigh Number Thermal Convection in a Saturated Porous Medium Bounded by Two Horizontal, Eccentric Cylinders," ASME JOURNAL OF HEAT TRANSFER, Vol. 106, pp. 166-175.

Brailovskaya, V. A., Petrazhitsky, G. B., and Polezhev, V. J., 1978, "Natural Convection and Heat Transfer in Porous Interlayers Between Horizontal Coaxial Cylinders," *J. of Appl. Mech. Tech. Phys.*, Vol. 19, pp. 781-785.

Burns, J. P., and Tien, C. L., 1979, "Natural Convection in Porous Media Bounded by Concentric Spheres and Horizontal Cylinders," *Int. J. Heat Mass Transfer*, Vol. 22, pp. 929-939.

Downloaded 13 Dec 2010 to 193.140.21.150. Redistribution subject to ASME license or copyright; see http://www.asme.org/terms/Terms_Use.cfm

Caltagirone, J. P., 1976, "Thermoconvective Instabilities in a Porous Medium Bounded by Two Concentric Horizontal Cylinders," *J. Fluid Mech.*, Vol. 76, pp. 337–362.

Himasekhar, K., and Bau, H. H., 1986, "Large Rayleigh Number Convection in a Horizontal Eccentric Annulus Containing Saturated Porous Media," *Int. J. Heat Mass Transfer*, Vol. 29, pp. 703–712.

Himasekhar, K., and Bau, H. H., 1988, "Two Dimensional Bifurcation Phenomena in Thermal Convection in Horizontal, Concentric Annuli Containing Saturated Porous Media," *J. Fluid Mech.*, Vol. 187, pp. 267–300.

Kimura, S., and Pop, I., 1991, "Non-Darcian Effects on Conjugate Natural Convection Between Horizontal Concentric Cylinders Filled With a Porous Medium," *Fluid Dynamics Res.*, Vol. 7, pp. 241–254.

Kimura, S., and Pop, I., 1992, "Conjugate Natural Convection Between Horizontal Concentric Cylinders Fill With a Porous Medium," *Wärme- und Stoffübertragung*, Vol. 27, pp. 85–91.

Sano, T., 1986, "Transient Natural Convection Between Horizontal Concentric Cylinders," *Fluid Dynamics Res.*, Vol. 1, pp. 33–47.

Van Dyke, M., 1975, *Perturbation Methods in Fluid Mechanics*, Parabolic Press, Stanford, CA.

Vasseur, P., Nguyen, T. H., Robillard, L., and Thi, V. K. T., 1984a, "Natural Convection Between Horizontal Concentric Cylinders Filled With a Porous Layer With Internal Heat Generation," *Int. J. Heat Mass Transfer*, Vol. 27, pp. 337–349.

Vasseur, P., Nguyen, T. H., Caltagirone, T. H., and Shekar, B. C., 1984b, "Convection in a Horizontal Annular Porous Layer With Nonlinear Density Effects," *Chem. Eng. Comm.*, Vol. 26, pp. 55–71.

Downloaded 13 Dec 2010 to 193.140.21.150. Redistribution subject to ASME license or copyright; see http://www.asme.org/terms/Terms_Use.cfm

A Two-Wavelength Holographic Interferometry Study on the Solidification of a Binary Alloy Around a Horizontal Pipe

T. L. Spatz

D. Poulikakos

Mechanical Engineering Department,
University of Illinois at Chicago,
Chicago, IL 60680

An experimental study on the transient outward solidification of a transparent binary alloy from an internally cooled horizontal pipe is reported in this paper. Two-wavelength holographic interferometry was used to visualize the density field in the liquid phase and to measure the local heat and mass transfer rates at the mush/liquid interface at characteristic times, Stefan numbers, and initial concentrations. The presence of double diffusive convection in the liquid phase greatly affected the local Nusselt and Sherwood numbers. The dependence of the pipe wall temperature, the solidified volume fraction, and the shape of the solid/mush and mush/liquid interfaces on the Stefan number, time, and initial concentration were also determined. The flow field in the liquid phase was visualized with the help of shadowgraphs. Interface photographs presented in this paper demonstrate the effect of the initial concentration on the structure of the mush/liquid interface, which varies from rather smooth to highly dendritic.

1 Introduction

Solidification processes can be grouped into two major categories: solidification of pure substances and solidification of alloys (or mixtures). The solidification of a pure substance is usually characterized by a sharp solid/liquid interface. The solidification of an alloy, on the other hand, is characterized by a mixed-phase region, which separates the liquid region from the solid region. The mixed-phase region, commonly termed "the mushy zone," is a combination of liquid solute and solid crystals (Viskanta, 1988).

Solidification of alloys has a wide range of applications. One pivotal application that initiated theoretical research in this area is the formation of sea ice. Several applications of current interest lie in the area of casting and coating of metallic and nonmetallic alloys. Some of the more obscure applications range from thermal energy storage to the processing of mixtures in the food industry and to the modeling of molten magma. Research in all these areas has been accelerated recently with advances in computational and experimental technologies. Representative studies on alloy solidification are reviewed in the following paragraphs.

Incropera and co-workers have published a series of interesting studies on the solidification of binary alloys in enclosed spaces in recent years. To this end, Bennon and Incropera (1987a) developed a continuum model for momentum heat and species transport during solidification in a binary alloy. The numerical solution of their model does not require tracking of the solid/mush and mush/liquid interfaces. The equilibrium phase diagram is assumed to be valid and it defines the solidus and liquidus boundaries. Bennon and Incropera (1987b, 1988) utilized the abovementioned model to solve numerically the problem of solidification of a binary alloy in a rectangular mold. Neilson et al. (1990) presented a numerical simulation of solidification of an aqueous salt solution in a horizontal annulus cooled through its inner cylinder. Their results on the flow field in the liquid phase agreed qualitatively with the findings in the experiments of Christenson and Incropera (1989a). Incropera et al. (1989) and Engel and Incropera (1989) investigated numerically and experimentally the effect of surface tension on the buoyancy-driven convection during solidification of a binary alloy with a free surface in a rectangular cavity. Comparisons with experiments showed encouraging qualitative agreement but also clear quantitative discrepancies. Christenson and Incropera (1989b) as well as Christenson et al. (1989) reported theoretical and experimental results on the freezing of an aqueous ammonium chloride solution in a rectangular cavity. For the theoretical work in all studies discussed so far, the model of Bennon and Incropera (1987a) was utilized. A reassessment of this model was recently published by Prescott and Incropera (1991). In this paper, the authors evaluate the two main different approaches (mixture theory and volumetric averaging) utilized in the past to obtain the conservation equations in the mushy region. They demonstrate that both the volumetric averaging approach (Beckermann, 1987; Beckermann and Viskanta, 1988; Ni and Beckermann, 1990; Viskanta, 1990) and the mixture theory approach (Bennon and Incropera, 1987a; Voller et al., 1989; Kececioglu and Rubinsky, 1989) yield consistent macroscopic conservation equations for the mushy zone.

Poulikakos (1988) and Poulikakos and Cao (1989) numerically solved the problem of the growth of a solid from a thin wire in a binary alloy both when the effect of mass transfer on the solidification process is negligible and when it is not. They accounted for the presence of the mushy zone separating the solid from the liquid region, but they neglected the effect of buoyancy driven flow on the freezing process. Cao and Poulikakos (1992) reported an experimental study on the freezing of a binary mixture of water and ammonium chloride in an inclined rectangular mold. It was shown that the inclination angle seriously affects the double diffusion in the liquid phase as well as the solidification rate. This work extended the findings of Cao and Poulikakos (1990) on solidification of a binary alloy in a rectangular cavity cooled through its top surface.

The numerical modeling of freezing of binary solutions using a fixed grid methodology and accounting for the mushy zone as well as for the presence of convection in the system was investigated by Voller and Prakash (1987) as well as by Voller

Contributed by the Heat Transfer Division for publication in the JOURNAL OF HEAT TRANSFER. Manuscript received by the Heat Transfer Division September 1991; revision received February 1992. Keywords: Double Diffusion Systems, Measurement Techniques, Phase-Change Phenomena. Associate Technical Editor: F. P. Incropera.

Copyright © 1992 by ASME
Downloaded 13 Dec 2010 to 193.140.21.150. Redistribution subject to ASME license or copyright; see http://www.asme.org/terms/Terms_Use.cfm

et al. (1989). Numerical simulations of convection in the two-phase zone of a binary alloy were carried out by Yu and Zhou (1991). An improved version of the continuum model, which considers the mushy zone to be a porous medium, was utilized. Calculated velocity profiles gave an indication of the magnitude of the flow in the mushy zone. The dendritic structure of the mush/liquid interface as well as the effect of various parameters on the freezing process of binary mixtures of water and salts in a cavity cooled from below was investigated by Webb and Viskanta (1986) as well as by Fang et al. (1984a, 1984b). Huppert and Worster (1985) assumed a linear relationship between temperature and composition along the liquidus line and reported temperature and concentration profiles in transient binary solidification experiments. They also presented interface growth rates for different initial concentrations and cooling temperatures. Szekely and Jassal (1978) used an optical Schlieren technique to report interface growth rates for both the liquid/mush and mush/solid interfaces.

A recent three-part study on the solidification of an alloy cooled from above was presented by Kerr et al. (1990a, 1990b, 1990c). In part one (Kerr et al., 1990a), a theoretical model based on equilibrium thermodynamics was developed where the properties in the mushy layer were functions of the local solid fraction. In part two (Kerr et al., 1990b) the nonequilibrium effects were explored. An empirical kinetic growth law was shown to predict rather accurately the growth of the mushy layer and the supersaturation of the rejected solute. Part three (Kerr et al., 1990c) investigated the late time compositionally zoned solid formed when an alloy is cooled from above. The model for complete solidification presented by Kerr et al. (1990a, 1990b, 1990c) is an extension of the studies performed by Arndt (1986) and Turner et al. (1986) related to the solidification of Komatiite lavas. Finally, several studies have been published in the literature on alloy solidification with direct relation to casting processes as exemplified by the work of Copley et al. (1970), McDonald and Hunt (1969, 1970) and Muehlabuer et al. (1973).

The present basic study is focused on the transient solidification of an aqueous water and ammonium chloride mixture around a cold pipe. The study is breaking new ground, for it utilizes a two-wavelength holographic interferometry technique to measure the local heat and mass transport coefficients at the mush/liquid interface. These coefficients are reported with the help of the local Nusselt and Sherwood numbers, respectively. The effect of the Stefan number and the initial concentration of the mixture on the growth and the structure of the solid/mush and the mush/liquid interfaces is also studied. Shadowgraphs reveal the presence of a complex flow field in the liquid region and indicate that flow exists inside the mushy region. Key results on the dependence of the pipe wall temperature and the amount of solid and mush produced on time, on the initial concentration, and on the Stefan number are also reported in this paper.

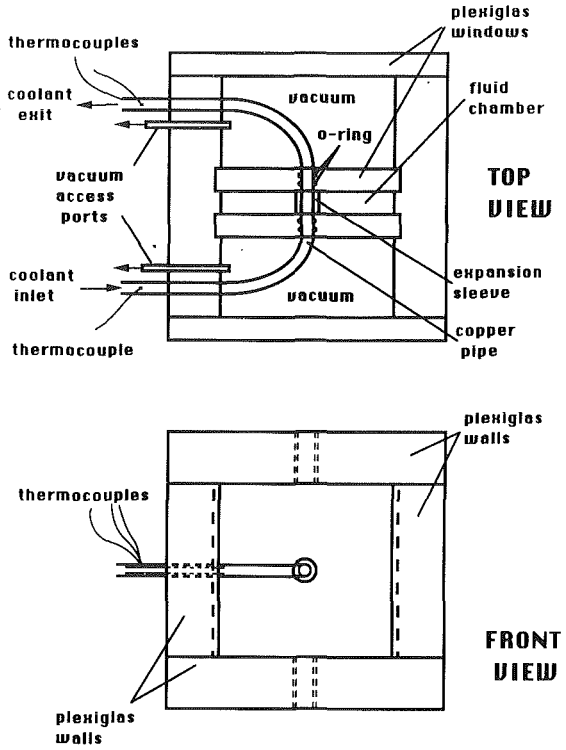

Fig. 1 Schematic of the experimental test section for alloy solidification: top view and front view

2 Experimental Setup and Test Section

The test section is basically a rectangular enclosure that is divided into three chambers: the central fluid-solidification chamber and two outer vacuum chambers. A schematic of the test section, with top and front view, is shown in Fig. 1. The two side walls, the top wall, and the bottom wall of the enclosure are made from 3.175 cm (1 1/4 in.) thick clear acrylic pieces. The bottom and top pieces each have a drilled and tapped hole in the center for filling and overflow purposes. One of the side walls has all the necessary holes for the vacuum access to the outer chambers and the coolant pipe entrance and exit in the outer chambers. The dimensions of the inner chamber containing the alloy are 10.16 × 10.16 cm (4 × 4 in.) square and 1.2 cm (0.47 in.) long. The two outer chambers have the same dimensions as the inner chamber except that they are 7.62 cm (3 in.) long each.

The four windows of the enclosure are made from 1.27 cm (1/2 in.) thick clear acrylic pieces. The two inner windows separate the alloy chamber from the two vacuum chambers. A hole exists at the center of each window to allow for the coolant pipe. The hole at the center of these two windows is

Nomenclature

b = fringe thickness
C = concentration, wt%
C_e = eutectic concentration, wt%
C_i = initial concentration, wt%
C_p = specific heat of ice, kJ/kgK
d = pipe diameter, m
D = mixture species diffusivity
h = heat transfer coefficient
h_m = mass transfer coefficient
k = conductivity, W/mk
L = latent heat of fusion of water, kJ/kg
M = fringe order
ΔM = change in fringe order due to diffraction errors
n = index of refraction
Nu = Nusselt number
s = direction perpendicular to mush/liquid interface
Sh = Sherwood number
Ste = Stefan number
T = temperature, °C
T_∞ = initial temperature (prior to cooling), °C
T_e = eutectic temperature, °C
T_{ieq} = liquidus temperature corresponding to the initial concentration, °C
T_{w120} = pipe wall temperature after 120 minutes of cooling, °C
W = length of the pipe
θ = angle, Fig. 15
λ = wavelength

Subscripts

Ar = denoting argon
HeNe = denoting helium–neon
j = denoting a wavelength
k = denoting a wavelength
∞ = initial state (prior to cooling)

Downloaded 13 Dec 2010 to 193.140.21.150. Redistribution subject to ASME license or copyright; see http://www.asme.org/terms/Terms_Use.cfm

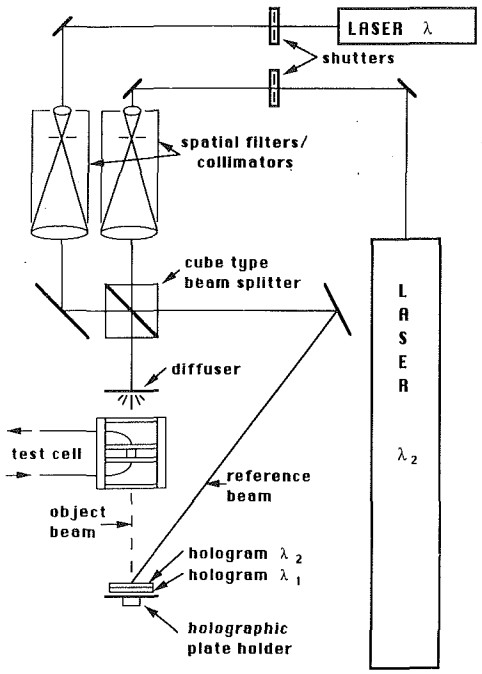

Fig. 2 Schematic of the experimental setup for the fabrication of the holograms

slightly larger than 0.635 cm (1/4 in.) in diameter. Each window has two slots cut inside the central hole to fit two O-rings, which seal the hole from leaking between the fluid and vacuum chambers. The 0.635 cm (1/4 in.) copper tubing coolant pipe has an additional copper sleeve to increase the pipe diameter in the fluid chamber to a total diameter of 0.9525 cm (3/8 in.). The copper tubing piece used was about 45.72 cm (18 in.) long with the sleeve silver soldered to its center. After the inner windows were put in place on both sides of the sleeve, the tubing itself was bent 90 deg to exit through the side walls of the outer vacuum chambers (Fig. 1). Even if slight condensation occurs on the outer surface of these walls in the vicinity of the pipe, it has no effect whatsoever on the holography measurements, which are performed through the front and rear windows.

There is one thermocouple embedded in the diameter expansion sleeve to measure the pipe surface temperature. This thermocouple is embedded in such a way that its bead is at the outer surface of the copper-tubing sleeve and the wire leads travel through the inside of the pipe until they exit the enclosure. There are also two thermocouples outside the enclosure, which are embedded in the pipe in such a way that the bead of each thermocouple is immersed in the coolant flowing through the pipe. They are used to measure the coolant temperature before it enters and after it leaves the enclosure.

A Hewlett-Packard data acquisition and personal computer system was used to record all thermocouple readings, usually at 10 s intervals. The coolant flowing through the pipe is a mixture of 50 percent ethylene glycol and 50 percent distilled water. It was cooled and pumped through the enclosure by a Brinkman RC20 recirculating bath refrigerator.

The optical equipment used to perform the two-wavelength holographic interferometry experiments will be discussed next. The schematic of the two-wavelength setup is shown in Fig. 2. The two lasers used were a 15-mW HeNe laser and a 2-W maximum output water-cooled argon ion laser. Each laser was shuttered separately to control exposure times. In this optical setup, each wavelength was spatially filtered and collimated separately. It is worth mentioning that an attempt was made to send both beams through the same spatial filter and collimator assembly. The problems of different beam diameters and different collimator focal lengths for each wavelength forced the abandonment of that design. The focusing optics for the spatial filters were 4 mm focal length reverse magnifying lenses. The collimators were three element collimators. Two different pinhole diameters were used: a 12 μm diameter for the HeNe beam and an 8 μm diameter for the argon beam. A 50 mm cube-type beam splitter was used to separate both beams into an object and a reference beam.

Two holographic plates were used for each experiment, as illustrated in Fig. 2. Most holographic plates are sensitive to a specific range of wavelengths depending on the material of the emulsion. An attempt was made to record all four exposures, two from each wavelength, on an Agfa-Gevaert 10E75 holographic plate. Although the images can be reconstructed, the plate becomes clouded and the resolution suffers dramatically. For this reason, the sandwich hologram approach was adopted. The front plate was an Agfa-Gevaert 10E56, which was very sensitive to the argon beam and virtually insensitive to the HeNe beam, and the second plate was an Agfa-Gevaert 10E75, which was very sensitive to the HeNe beam and virtually insensitive to the argon beam. The exposure times for both holographic plates were found by trial and error. Both holographic plates were developed using the same procedure as described by Spatz and Poulikakos (1991).

After developing the two holograms, each one is reconstructed separately (Spatz, 1991). The reconstruction is aided by the use of a "filler plate." The filler plate is an unexposed holographic plate that has undergone the developing process to yield a transparent imageless glass plate with the same thickness as a hologram. The plate that was closest to the enclosure during exposures was the 10E56 holographic plate sensitive to the argon wavelength. To reconstruct the image of this hologram, the filler plate is placed behind the developed 10E56 plate in the plate holder. The reference beam from the argon laser illuminates the plate while the object beam is blocked. The virtual image is then photographed with a 35 mm camera using Kodak T-max 100 film. To reconstruct the image of the 10E75 holographic plate, sensitive to the HeNe wavelength, the filler plate is placed *in front* of the 10E75 plate in the plate holder. The 10E75 holographic plate is illuminated with the reference beam from the HeNe laser while the object beam is blocked (Fig. 2). The virtual image is photographed with a 35 mm camera using Kodak T-max 100 film. Large prints of the reconstructed holograms are made for data processing.

The procedure for running the experiments is as follows: First, the test section is filled completely with the alloy. After some time passes and all fluid motion in the test section resulting from the filling process dies out, the coolant is circulated through the pipe. Note that the coolant has already been chilled down to a predetermined temperature with the help of the circulator refrigerator. Next, the data are recorded as the solidification phenomenon progresses. The experiment is terminated after about 120 min.

Before leaving this section, a brief description of the shadowgraph technique used for flow visualization will be presented. The shadowgraph visualization is performed by passing a plane wave of laser light through the enclosure and onto a ground glass or paper screen placed after the enclosure. This is quite easy to achieve with the optics tables setup for holography (Fig. 2) by simply removing the diffuser and blocking the reference beam. A piece of paper is placed on the enclosure window opposite to the side where the beam enters, the holographic plate holder is removed, and a 35 mm camera is set up to record the image on the paper. The shadowgraphs are performed strictly for flow visualization purposes with no quantitative information obtained.

3 Procedure for Holographic Interferometry Data Processing

A major difficulty with using holographic interferometry to

Downloaded 13 Dec 2010 to 193.140.21.150. Redistribution subject to ASME license or copyright; see http://www.asme.org/terms/Terms_Use.cfm

study an alloy is that the density of the solution, and consequently the refractive index, is a function of both temperature and concentration (Vest, 1979). To resolve this problem, a second wavelength was introduced. It can be shown (Ecker, 1988; Spatz, 1991) that the temperature and concentration gradients at the mush/liquid interface can be calculated from the following relations:

$$\frac{dT}{ds}=\frac{\frac{\lambda_k}{W}\left(\frac{dM}{ds}\right)_k\left(\frac{\partial n}{\partial C}\right)_j-\frac{\lambda_j}{W}\left(\frac{dM}{ds}\right)_j\left(\frac{\partial n}{\partial C}\right)_k}{\left(\frac{\partial n}{\partial T}\right)_k\left(\frac{\partial n}{\partial C}\right)_j-\left(\frac{\partial n}{\partial T}\right)_j\left(\frac{\partial n}{\partial C}\right)_k} \tag{1}$$

$$\frac{dC}{ds}=\left\{\frac{\lambda_j}{W}\left(\frac{dM}{ds}\right)_j-\left(\frac{\partial n}{\partial T}\right)_j\times\left[\frac{\frac{\lambda_k}{W}\left(\frac{dM}{ds}\right)_k\left(\frac{\partial n}{\partial C}\right)_j-\frac{\lambda_j}{W}\left(\frac{dM}{ds}\right)_j\left(\frac{\partial n}{\partial C}\right)_k}{\left(\frac{\partial n}{\partial T}\right)_k\left(\frac{\partial n}{\partial C}\right)_j-\left(\frac{\partial n}{\partial T}\right)_j\left(\frac{\partial n}{\partial C}\right)_k}\right]\right\}\frac{1}{\left(\frac{\partial n}{\partial C}\right)_j} \tag{2}$$

In the above equations M denotes the fringe order, λ the wavelength, s the direction perpendicular to the mush/liquid interface, T the temperature, C the concentration, W the length of the pipe, and n the index of refraction. The subscripts j and k stand for the two different wavelengths.

It is worth noting that in Eqs. (1) and (2) the fringe order gradients $(dM/ds)_j$ and $(dM/ds)_k$ are obtained from the reconstructed holograms as the two wavelengths λ_j, λ_k as well as the pipe length are known. However, in order to calculate the temperature and concentration gradients, the dependence of the index of refraction on temperature and on concentration for the two wavelengths of interest is necessary to yield $(\partial n/\partial T)_j$, $(\partial n/\partial T)_k$, $(\partial n/\partial C)_j$, $(\partial n/\partial C)_k$. After a thorough search, we were unable to locate this information in the open literature. Therefore, a series of side measurements was performed to obtain the dependence of n on C and T for the wavelengths of a HeNe laser and an argon laser. The details of these measurements are included in Spatz (1991). The final result for the temperature and concentration ranges of interest is summarized in the following two relationships:

$$n_{\mathrm{HeNe}}(C,\ T)=1.3332-(6.8276\times10^{-5})T(^\circ\mathrm{C})+(1.6764\times10^{-3})C(\mathrm{wt\%}) \tag{3}$$

$$n_{\mathrm{Ar}}(C,\ T)=1.3373-(7.1010\times10^{-5})T(^\circ\mathrm{C})+(1.7345\times10^{-3})C(\mathrm{wt\%}) \tag{4}$$

The standard deviation for the helium–neon refractive index equation is 2.80×10^{-4}, and the standard deviation for the argon refractive index equation is 2.29×10^{-4}. An additional indication of the accuracy of Eqs. (3) and (4) is that in the limit of zero concentration (pure water) at 20°C the results for the index of refraction for HeNe from Eq. (12) differs from that published by Hauf and Grigull (1970) by only three hundredths of one percent.

The temperature and concentration gradients obtained from Eqs. (1) and (2) will be presented in dimensionless form by means of the local Nusselt and the local Sherwood number. The local Nusselt number at any point around the liquid/mush interface is defined as

$$\mathrm{Nu}=\frac{hd}{k}=\left[\frac{d\left(\frac{dT}{ds}\right)}{T_\infty-T_{i_{eq}}}\right] \tag{5}$$

Table 1 Properties of ammonium chloride mixtures used in this study

c_p	= 1.99 kJ/kg·K
L	= 333.6 kJ/kg
T_e	= −15.25°C
C_e	= 0.197 wt%
C_i	= 0.05 wt%: $T_{eq}=-3.189$°C
C_i	= 0.10 wt%: $T_{eq}=-6.894$°C
C_i	= 0.25 wt%: $T_{eq}=12$°C

The local Sherwood number at any point around the liquid/mush interface is defined as

$$\mathrm{Sh}=\frac{h_m d}{D}=\left[\frac{d\left(\frac{dC}{ds}\right)}{C_e-C_i}\right] \tag{6}$$

A word of caution regarding the definition of Nu and Sh (Eqs. (5) and (6)) is necessary. In this study these numbers are meant to serve as dimensionless local temperature and concentration gradients, respectively. The heat and mass transfer coefficients in Eqs. (5) and (6) do not account for the energy crossing the permeable mush/liquid interface through convection. Therefore, these heat and mass transfer coefficients can only provide the user with estimates of the total heat and mass transfer rates at a location of the mush/liquid interface when the convection across this interface is not significant. This may be expected to be true at late stages in the solidification process. In addition, the pipe diameter (d) was utilized as a length scale in Eqs. (5) and (6) because it is the only tangible length scale in our experimental study and because it is representative of the domain of interest, at least in an order of magnitude sense. Utilizing a larger diameter that would have accounted for the presence of the solid and mushy regions around the pipe would have been physically more appropriate. However, the nonsymmetric, noncylindrical, and transient nature of the solidified region made such choice prohibitingly inconvenient.

Another dimensionless group that will aid the presentation of the results is the Stefan number:

$$\mathrm{Ste}=\frac{C_p(T_e-T_{w_{120}})}{L} \tag{7}$$

In the above Eqs. (5)–(7) h is the local heat transfer coefficient at the mush/liquid interface, h_m is the local mass transfer coefficient at the same interface, D is the species diffusivity of the mixture, k is the thermal conductivity of the mixture, T_∞ is the initial temperature of the mixture prior to the cooling process, $T_{i_{eq}}$ is the equilibrium (liquidus) temperature corresponding to the initial concentration, C_p is the specific heat of ice, T_e is the eutectic temperature, $T_{w_{120}}$ is the pipe wall temperature after 120 min from the beginning of the experiment (well after the pipe wall temperature has reached a practically constant value), and L the latent heat of fusion of water. The values of the various properties, temperatures, and concentrations used in this study are reported in Table 1.

The error associated with the local Nusselt number and Sherwood number measurements will be discussed before closing this section. There are three major contributors to the error to be considered: the error associated with the refractive index measurements, the error associated with diffraction effects, and the error associated with fringe measurements.

With reference to the refractive index measurements, the standard deviation of the refractive index linear equations from the measured data has already been reported as 2.84×10^{-4} for the HeNe equation and 2.29×10^{-4} for the argon equation.

The diffraction error is due to the fact that the mush/liquid interface acts as a surface. This error is inversely proportional

Downloaded 13 Dec 2010 to 193.140.21.150. Redistribution subject to ASME license or copyright; see http://www.asme.org/terms/Terms_Use.cfm

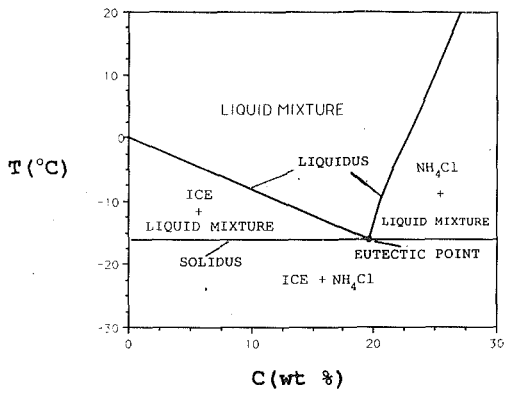

Fig. 3 Equilibrium phase diagram for solutions of aqueous ammonium chloride

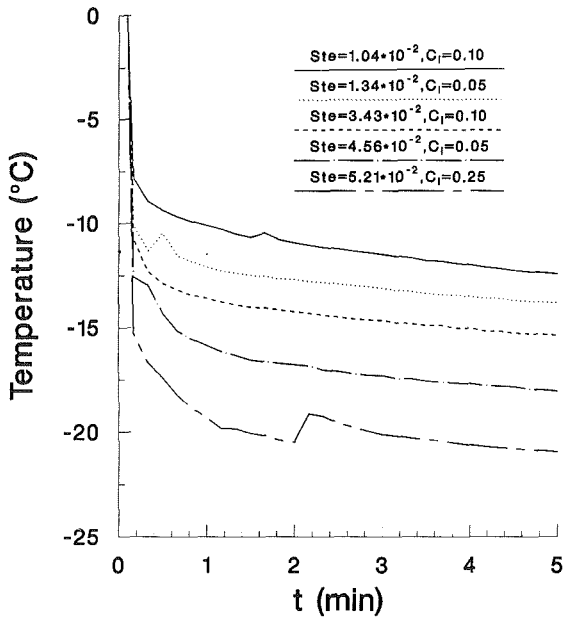

Fig. 4 Variation of the pipe wall temperature at early times

to the square of the fringe thickness. The change in the fringe order caused by the diffraction error is given by Hauf and Grigull (1970) as

$$\Delta M = \frac{n_\infty \lambda W}{12 b^2} \tag{8}$$

where b is the fringe thickness and the remaining symbols were defined earlier. Note that T_∞ and C_i have no effect on the accuracy of the results for Nu and Sh. T_∞ and C_i were not used in Eqs. (1) and (2) for the evaluation of the temperature and concentration gradients. The diffraction error in the argon holograms ranged between a maximum of about 14 percent at the highest fringe density (near 270°) and a minimum of about 2 percent at the lowest fringe density (near θ = 90 deg). Similarly, the HeNe diffraction error ranged from 1 to 10 percent.

Regarding the fringe measurement error, a serious attempt was made to measure the exact same location and thickness (ds) on both holograms. Each fringe measurement was taken three times and the difference between the maximum and the minimum result was always less than 5 percent of the maximum result. The arithmetic mean of the three measurements was utilized in the data processing.

4 Results and Discussion

The discussion of results will be placed into proper perspective by the presentation of the equilibrium phase diagram shown in Fig. 3. Note that because of the presence of flow in the liquid phase and in the mushy zone, the solidification phenomenon of interest is a nonequilibrium phenomenon. However, the equilibrium phase diagram will serve as a guide for the qualitative behavior of the different regions observed during the solidification process.

The equilibrium phase diagram of a eutectic water and ammonium chloride binary alloy shown in Fig. 3 features a liquidus line separating the liquid region from the mixed phase region (mushy zone) and a solidus line separating the mixed phase region from the solid region. It is worth noting that part of the solidus line in the hypoeutectic region coincides with the ordinate axis and represents the fact that the species concentration in the solid matrix of the mushy zone is zero and this matrix consists of pure ice. Indeed, the molecules of the NH_4Cl do not fit easily into the crystalline lattice of ice and they are rejected in the liquid phase saturating the mushy region. In the hypereutectic region, on the other hand, NH_4Cl crystallizes out of the mixture in the mushy zone. As a result, the solid matrix of the mushy zone in this region consists of crystals of NH_4Cl and it is saturated by a liquid mixture of concentration lower than the initial concentration.

The temperature history of the pipe wall temperature for the first five minutes of the solidification process is presented in Fig. 4 for representative Stefan numbers and initial concentrations. In all cases, the wall temperature initially decreases rapidly and later, after the solid formation, it approaches a plateau. Increasing the Stefan number implies lower pipe wall temperatures for the same initial concentration. The three lower curves for Stefan numbers of 3.43×10^{-2}, 4.56×10^{-2}, and 5.2×10^{-2} correspond to identical experiments, with the only difference between experiments being the initial concentration of the mixture. Comparing the abovementioned three temperature histories, we realize that the initial concentration C_i = 0.10 yields the highest pipe wall temperature. This result can be explained with the help of the equilibrium phase diagram of Fig. 3. First we note that the initial concentrations of 0.10 and 0.05 are both in the hypoeutectic region. Therefore, it is expected that the structure of the solid and the mushy regions during the solidification process for these two initial concentrations is similar. Next, Fig. 3 shows that the liquids temperature for C_i = 0.05 is higher than that for C_i = 0.10 and that the mushy region surrounding the pipe for C_i = 0.05 is likely to be thicker than the mushy region surrounding the pipe for C_i = 0.10. Hence, a better thermal "insulation" for the pipe is provided by the mushy zone for C_i = 0.05. As a result the "cold" pipe encounters more "thermal communication" with the "warmer" liquid phase for C_i = 0.10 and its temperature remains at a higher level. The lowest pipe wall temperature corresponds to the hypereutectic concentration C_i = 0.25. Note again that based on Fig. 3 this initial concentration features the thickest mushy region.

An interesting finding in Fig. 4 is the "jumps" observed on the pipe temperature curves. These jumps mark the onset of solidification on the pipe surface. Similar jumps have been observed in experiments on the freezing of pure substances (Hermann et al., 1984; Spatz and Poulikakos, 1991). Perhaps the presence of these jumps will be better understood if explained in connection with the freezing of a pure substance, say water. To this end, imagine that a horizontal pipe through which a coolant is circulated is immersed in a bath of water, initially at room temperature. Imagine further that the pipe wall temperature is measured to be considerably lower than the freezing point of water. Naturally, convection sets in the bath and the water in the vicinity of the pipe cools down gradually, until ice nucleation occurs at the pipe surface, after

Downloaded 13 Dec 2010 to 193.140.21.150. Redistribution subject to ASME license or copyright; see http://www.asme.org/terms/Terms_Use.cfm

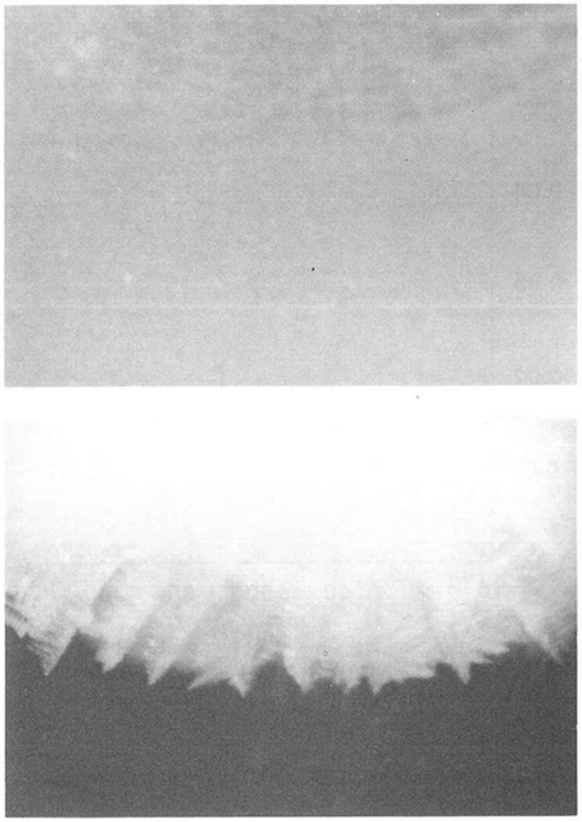

Fig. 5 Interface photographs for $C_i = 0.05$: (*a*) solid/mush interface, (*b*) mush/liquid interface

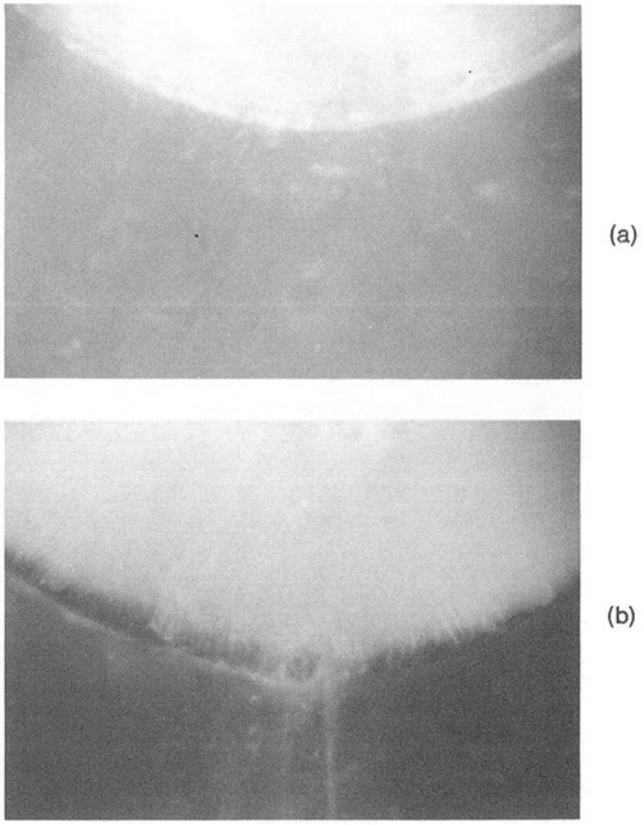

Fig. 6 Interface photographs for $C_i = 0.25$: (*a*) solid/mush interface, (*b*) mush/liquid interface

some subcooling of the water. At the instance of ice nucleation, the pipe surface is temporarily in contact with the "warm" ice/water interface, which is at the temperature of 0°C. As a result, the temperature of the pipe wall, which was below the freezing point of water prior to ice nucleation, will temporarily rise and result in the jumps shown in Fig. 4. The latent heat of fusion released upon solidification also contributes to the observed temperature jumps. The same "scenario" occurs in the solidification of the binary mixture of the present study. The pipe wall temperature at the instance of nucleation of the mushy zone on the pipe surface (Fig. 4) is considerably lower than the liquidus temperature of the mush/liquid interface (Fig. 3) in contact with the pipe surface. As a result the "warming" effect of the mush/liquid interface combined with the latent heat of fusion released upon solidification create the above mentioned temperature jumps. The appearance of the jumps is dependent upon the initial concentration.

The initial concentration of $C_i = 0.25$ has the most pronounced jump in surface temperature occurring at about 2 min. This jump occurs after the pipe surface temperature is well below the eutectic temperature and, we speculate, indicates nucleation of the solid and not the mush region around the pipe. The onset of the mushy region for the initial concentration of $C_i = 0.25$ (in the hypereutectic region) is not noticeable because, as we observed, the mushy zone in this case is a fragile, loosely interwoven, dendritic structure. This allows for convection at the pipe wall surface for a longer period of time before nucleation of the pure solid-phase region begins. To illustrate the difference in the porosity of the mushy zone for the different initial concentrations, photographs of the mush/liquid interface will be presented later in this section.

The two Stefan numbers corresponding to the initial concentration of $C_i = 0.05$ (Ste $= 1.34 \times 10^{-2}$ and Ste $= 4.56 \times 10^{-2}$) also exhibit noticeable jumps in the pipe surface temperature. These jumps occur at an earlier time and higher temperature than the jump for the initial concentration of $C_i = 0.25$ and mark the "nucleation" time of the mushy zone on the pipe. The initial concentration of $C_i = 0.10$ (Ste $= 1.04 \times 10^{-2}$ and Ste $= 3.43 \times 10^{-2}$) features the least noticeable jumps.

The structure of the mushy layer is revealed with the aid of close-up photographs. Figure 5 represents photographs of the solid/mush interface (Fig. 5*a*) and the mush/liquid interface (Fig. 5*b*) for the initial concentration of $C_i = 0.05$. The structure of mushy zone in Fig. 5 is rather dense, tightly packed, with a smooth mush/liquid interface (Fig. 5*b*). The solid/mush interface is also smooth as Fig. 5(*b*) illustrates. Similar photographs for the initial concentration of $C_i = 0.10$ exhibited analogous behavior and are not presented here, for brevity. Figure 6 illustrates that there is a drastic difference in the mushy layer and the mush/liquid interface for initial concentrations above the eutectic concentration (in the hypereutectic region). The mushy zone is now more porous and has a visibly dendritic structure. Clearly, the mush/liquid interface of Fig. 6(*b*) is rough and infested by dendrites. The solid/mush interface for $C_i = 0.25$ is not well defined, as Fig. 6(*a*) indicates. Note also that the solid in the mushy zone of Fig. 6(*b*) ($C_i = 0.25$) is composed of crystallized ammonium chloride while the solid in the mushy zone of Fig. 5(*b*) ($C_i = 0.05$) is composed of ice crystals.

Results on the growth of the solid and mushy regions are reported in Figs. 7 and 8. The interfaces presented in these figures are traced from photographs. Figure 7 represents the growth of the solid/mush and mush/liquid interfaces at three times for the three initial concentrations of $C_i = 0.05$, $C_i = 0.10$, and $C_i = 0.25$. Due to the dendritic structure of the mush/liquid interface for $C_i = 0.25$, an "average" interface is traced. The mush thickness is larger under the pipe than it is on the top of the pipe, for the initial concentrations of $C_i = 0.05$ and $C_i = 0.10$. The reason for this asymmetry is that

Downloaded 13 Dec 2010 to 193.140.21.150. Redistribution subject to ASME license or copyright; see http://www.asme.org/terms/Terms_Use.cfm

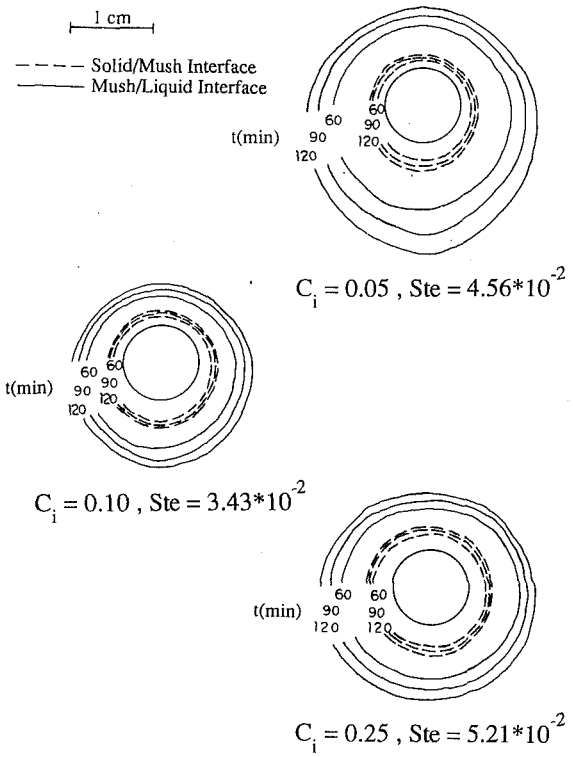

Fig. 7 The advancement of the solid/mush and mush/liquid interfaces for representative values of Stefan number and initial concentration

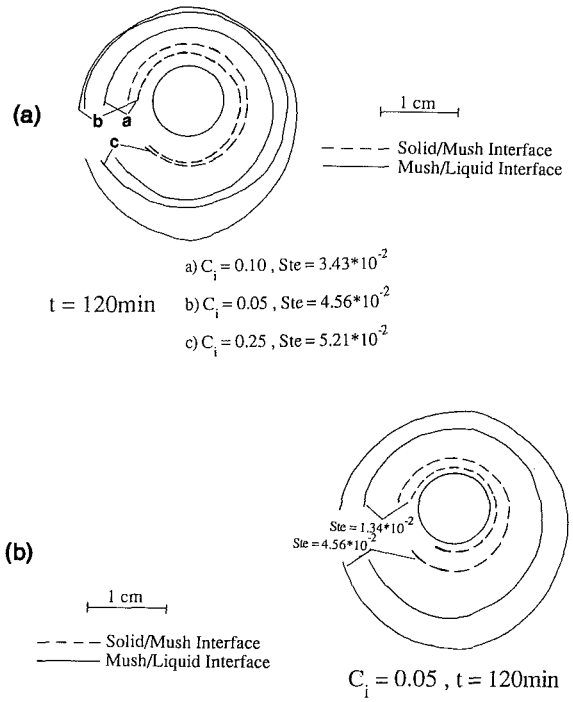

Fig. 8 (*a*) Interface profiles at t = 120 min for representative initial concentrations; (*b*) dependence of the interface profiles on the Stefan number at t = 120 min for C_i = 0.05

the buoyancy-driven flow in the liquid is directed downward for concentrations in the hypoeutectic region. The impact of this flow is more significant in the upper (upstream) half of the mush/liquid interface than in the lower half of this interface, which is protected by the upper half. As a result, a retardation in the growth of the mushy zone is caused at the top of the pipe. The interface sketches for the initial concentration of C_i = 0.25 are somewhat more symmetric because the thermally and solutally driven flows are directed both upward and downward. The presentation of the shadowgraphs of the flow field later in this section will substantiate these statements. In qualitative agreement with the equilibrium phase diagram, the initial concentration of C_i = 0.10 features the thinnest mushy regions. In addition, our results indicate that the mush/liquid interface grows faster than the solid/mush interface, in all cases.

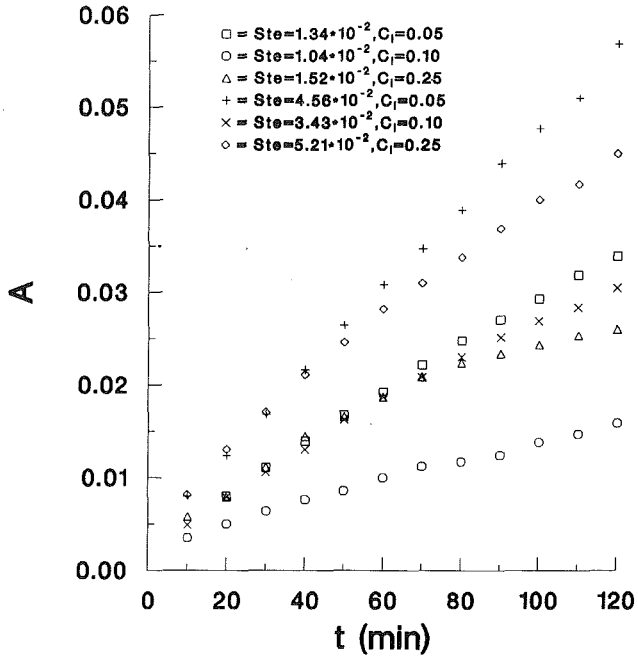

Fig. 9 Time history of mush plus solid (parameter *A*) production

The effect of the initial concentration on the solidification process is shown clearly in Fig. 8(*a*). The three Stefan numbers in this figure correspond to the same coolant temperature. Therefore, the differences observed in the solidification process are due to the effect of the initial concentration. Clearly, the initial concentration of C_i = 0.10 features the smallest solid and mush production. In addition, the initial concentration of C_i = 0.25 exhibits the largest accumulation of pure solid around the pipe. This is in agreement with the pipe surface temperature results of Fig. 4 where this concentration corresponded to the lowest pipe surface temperature. This low surface temperature led to a large accumulation of solid NH_4Cl around the pipe. The concentration of C_i = 0.05, on the other hand, features the thickest mushy zone. Figure 8(*b*) demonstrates the effect of the Stefan number on the interface shapes. Reducing the Stefan number reduces the amount of solid and mush formed proportionately. The general shape of the interfaces remain similar for both Stefan numbers presented in Fig. 8(*b*).

Figure 9 illustrates the variation of the mush plus solid volume produced around the pipe as a function of time. The nondimensional volume parameter A in Fig. 9 is defined as the sum of the mush plus solid volume divided by the enclosure inner chamber volume ($(V_{mush} + V_{solid})/V_{encl}$). The data corresponding to the initial concentrations of C_i = 0.05 and C_i = 0.10 exhibit approximately a linear increase in parameter A with time. The initial concentration of C_i = 0.25 also exhibits a linear dependence of A on time for t < 60 min. At late times, however, the growth of A tapers off. The trend at late times is consistent for both Ste = 1.52×10^{-2} and Ste = 5.21×10^{-2}.

The initial concentration of C_i = 0.10 yields about half the value of parameter A as does the initial concentration C_i = 0.05. This is evident by comparing the values of A for Ste

Downloaded 13 Dec 2010 to 193.140.21.150. Redistribution subject to ASME license or copyright; see http://www.asme.org/terms/Terms_Use.cfm

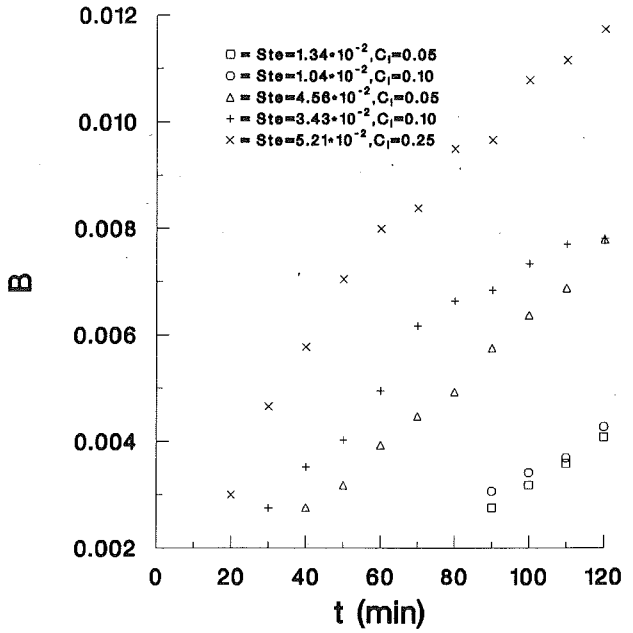

Fig. 10 Time history of solid (parameter B) production

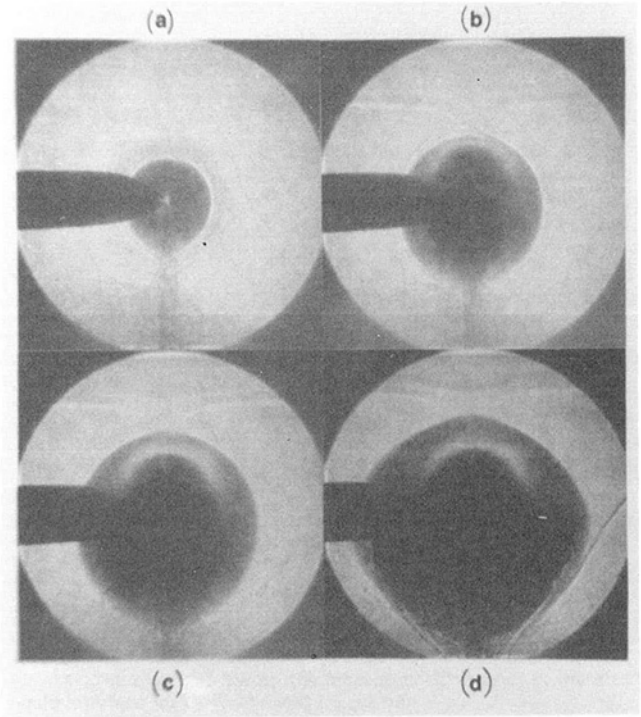

Fig. 11 Shadowgraph photographs for the initial concentration of C_i = 0.05 at times of (*a*) 20 min, (*b*) 60 min, (*c*) 100 min, and (*d*) 120 min

$= 3.43 \times 10^{-2}$ and Ste $= 4.56 \times 10^{-2}$ at $t = 120$ min in Fig. 9. The equilibrium phase diagram (Fig. 3) indicates this trend. Since mush starts to form at a higher temperature for $C_i = 0.05$, one would expect more mush to be formed.

It is worth mentioning that based on the equilibrium phase diagram alone, one would anticipate that the initial concentration of $C_i = 0.25$ yields the largest volume growth rate, since, of the three initial concentrations under investigation, it corresponds to the highest liquidus temperature. Figure 9 proves that this is not the case. The porous nature of the mushy zone for the $C_i = 0.25$ case allows convective flow to penetrate deeper into the mush and retard the growth of dendrites. In addition, the mushy zone in this case appeared to be fragile. At times, fragments of dendrites were separated from the mush/liquid interface and fell to the bottom of the cavity.

The variation in the solid volume produced around the pipe as a function of time is presented in Fig. 10. The parameter B is defined as the ratio of the solid volume to the enclosure inner chamber volume (V_{solid}/V_{encl}). Clearly the initial concentration of $C_i = 0.25$ exhibits the highest solid growth. It is also apparent in Fig. 10 that $C_i = 0.25$ has the earliest solid nucleation time. The data for the initial concentrations of $C_i = 0.05$ and $C_i = 0.10$ show that there is a tendency for the initial concentration of $C_i = 0.10$ to yield a larger production of pure solid than the concentration of $C_i = 0.05$. This difference becomes negligible in the small Stefan number cases. To explain this finding physically, one may consider the equilibrium phase diagram of Fig. 3. The mushy zone separating the solid from the liquid regions is much thicker in the case of $C_i = 0.05$ than in the case of $C_i = 0.10$. The presence of this thick mushy zone reduces the effectiveness of the cooling process and the production of the pure solid region. Reducing the Stefan number has the effect of increasing the nucleation time and reducing the solid production rate.

To visualize the flow in the liquid region as well as to aid the interpretation of the holographic interferometry measurements, a series of shadowgraph flow visualization experiments was performed. Figure 11 represents shadowgraphs for the initial concentrations $C_i = 0.05$ at the times of 20, 60, 100, and 120 min. The initial concentration of $C_i = 0.05$ is well to the left of the eutectic concentration ($C_e = 0.197$) on the equilibrium phase diagram (Fig. 3). This implies that as solidification occurs, ice crystallizes out of the liquid, and a fluid with a higher concentration than the initial concentration is rejected from the mushy layer. Therefore both the thermal and the solutal buoyancy drive the flow downward around the pipe. Our observations indicated that the first visible convection cell formation occurs at about $t = 20$ min. There are two large cells forming in the bottom half of the enclosure, which extend from the bottom of the enclosure to slightly above the pipe where they are bounded by a density interface. The cell motion is primarily driven by the downward-moving plume under the pipe (Fig. 11). This cold and heavy fluid then spreads out along the bottom of the enclosure were it is warmed by the enclosure walls and the surrounding fluid. The fluid being displaced by this cold heavy fluid is drawn horizontally toward the pipe to help feed the cold plume.

As the solidification progresses, the density interface bounding the two large convection cells gradually moves upward (Fig. 11*b*, *c*). Also of interest in Fig. 11(*b*) is the shadow at the mush–liquid interface on top of the pipe just to the right of center. This shadow indicates that there is a stronger flow on the right side of the pipe than on the left side. As will be shown later, the asymmetry of the transient flow field affected the heat and mass transport processes.

Figure 11(*d*) is the most interesting shadowgraph of this set. At this point in the solidification process, a large volume of mush has formed around the pipe, as also indicated by the interface sketches of Fig. 7, and high-concentration, heavy fluid has accumulated at the bottom of the cavity. This fluid is continuously pushed toward the corners of the cavity by the main bicellular flow field discussed earlier. As a result, a **V**-shaped sharp density interface develops, separating the corner regions from the rest of the fluid. The bicellular flow field is now squeezed between the **V**-shaped interface and the horizontal interface on top of the pipe. The shadowgraphs for $C_i = 0.10$ exhibited similar behavior to what was discussed in connection with Fig. 11 and are not included here, for brevity.

Figure 12 represents shadowgraphs for the initial concentration for $C_i = 0.25$ at times of 20, 50, 90, and 110 min. The initial concentration of $C_i = 0.25$ is to right of the eutectic concentration ($C_e = 0.197$) on the equilibrium phase diagram.

Downloaded 13 Dec 2010 to 193.140.21.150. Redistribution subject to ASME license or copyright; see http://www.asme.org/terms/Terms_Use.cfm

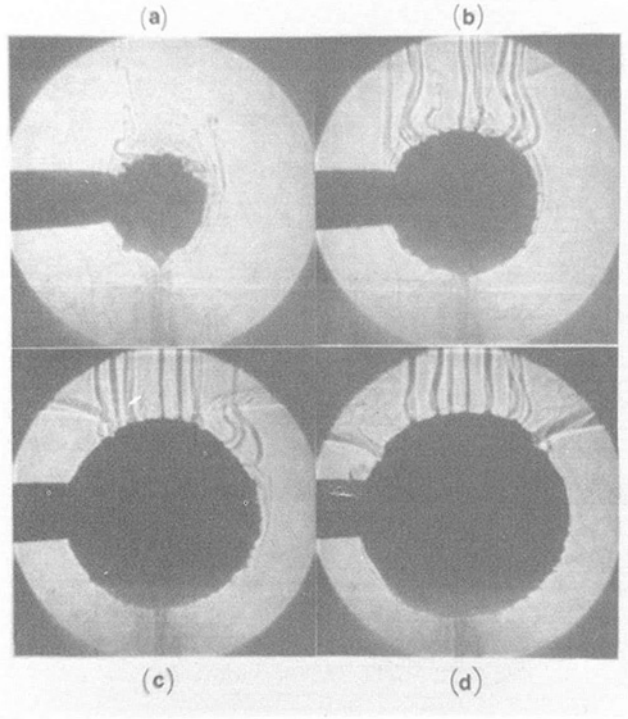

Fig. 12 Shadowgraph photographs for the initial concentration of C_i = 0.25 at times of (*a*) 20 min, (*b*) 50 min, (*c*) 90 min, and (*d*) 110

This implies that as solidification occurs, NH_4Cl crystallizes out of the liquid and a fluid with a lower concentration is rejected from the mushy layer. Therefore, the solutal buoyancy directs the flow upward while the thermally driven flow is still directed downward. This is observed in all four shadowgraphs of Fig. 12. The thermally driven plume at the bottom of the pipe is thinner than the downward plumes of the previous shadowgraphs, and unlike the previous shadowgraphs, there are no convection cells formed at the time t = 20 min (Fig. 12*a*). The first indication of diffusive interfaces is seen at about t = 50 min near the top of Fig. 12(*b*). The upward solutally driven flow starts slowly with meandering mushroom shaped plumes (Fig. 12*a*) and builds to become continuous streams flowing upward emanating across the entire top surface of the mush/liquid interface (Fig. 12*d*). The flow visualization results of Fig. 12 agree qualitatively with the findings of Christenson and Incropera (1989*a*) for the problem of solidification of an aqueous solution of sodium carbonate in a horizontal annulus. They also observed similar flow structures consisting of regions separated by sharp diffusive interfaces.

Before we begin the presentation of the results of the local Nusselt and Sherwood numbers obtained with holographic interferometry, representative photographs of holograms are shown. Figure 13, for example, presents photographs of a hologram of the top part of the pipe for C_i = 0.10 taken at t = 120 min constructed with either the HeNe laser (Fig. 13*a*) or the argon laser (Fig. 13*b*). Each fringe is a line of constant density. Note the thickening of the fringes on the right side of the hologram at the mush/liquid interface caused by the interface of the flow field in the mush and in the liquid regions. Note also the waviness of the fringes on top of the pipe. The transient flow field is rather unstable at times and not perfectly symmetric about the vertical axis of symmetry. The same is true for the temperature and concentration fields represented by the fringes in the holograms.

Figure 14 is the photograph of a hologram for C_i = 0.25 taken at t = 90 min. The difference between the smooth mush/liquid interface of Fig. 13 and the highly dendritic interface of Fig. 14 is indeed striking. Because of the highly dendritic

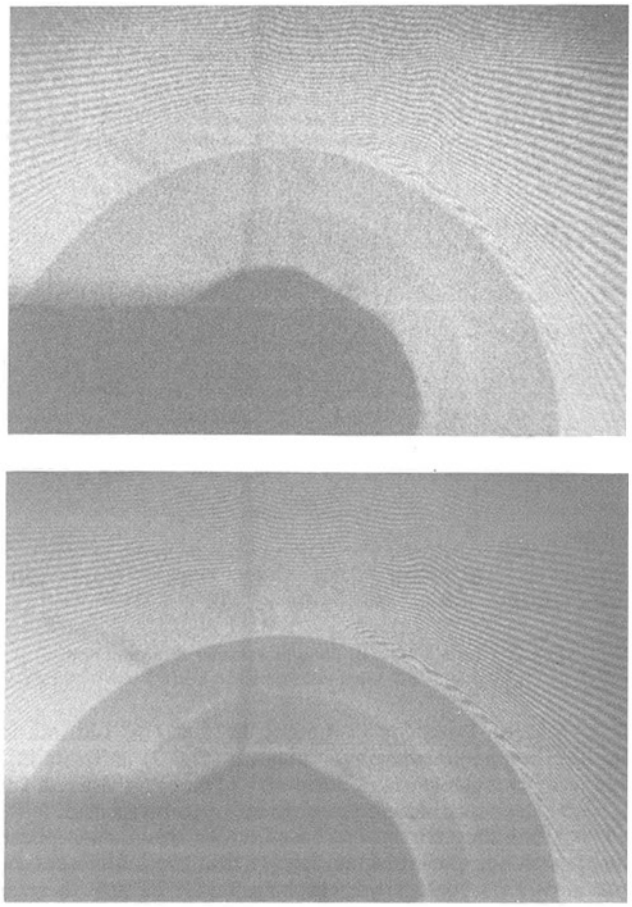

Fig. 13 Hologram photographs for Ste = 3.43 × 10^{-2} and C_i = 0.10 at t = 120 min; (*a*) HeNe hologram and (*b*) argon hologram

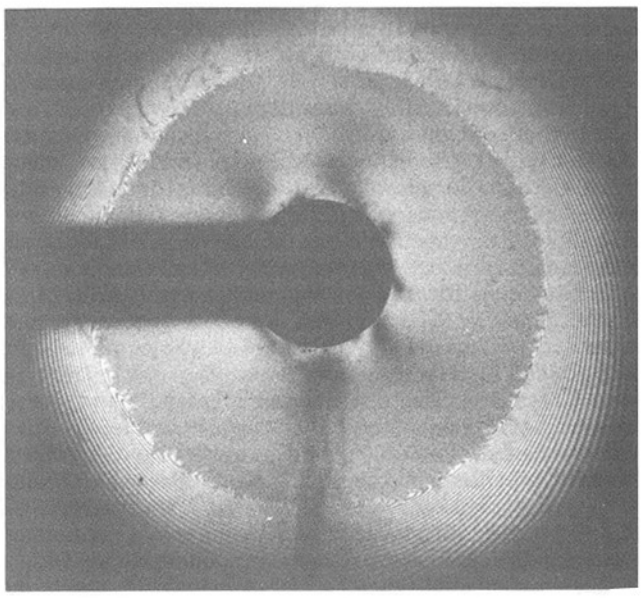

Fig. 14 Argon hologram photograph for Ste = 5.21 × 10^{-2} and C_i = 0.25 at t = 90 min

and irregular nature of the interfaces for initial concentrations higher than the eutectic, no accurate measurements of the temperature and concentration gradients were possible. However, important qualitative information can be gathered from the hologram of Fig. 14. For example, the fringe spacing between dendrites is sparse. This is evidence that the dendritic structure restricts fluid motion along the mush/liquid inter-

Downloaded 13 Dec 2010 to 193.140.21.150. Redistribution subject to ASME license or copyright; see http://www.asme.org/terms/Terms_Use.cfm

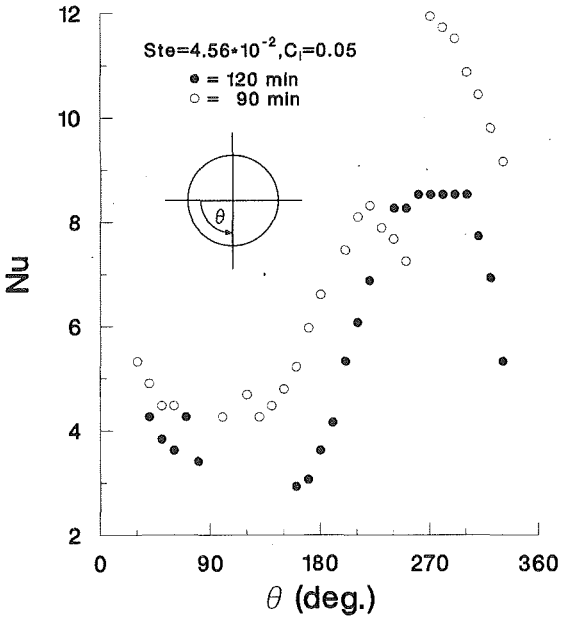

Fig. 15 The local Nusselt number at the mush/liquid interface for Ste = 4.56 × 10^{-2} and C_i = 0.05

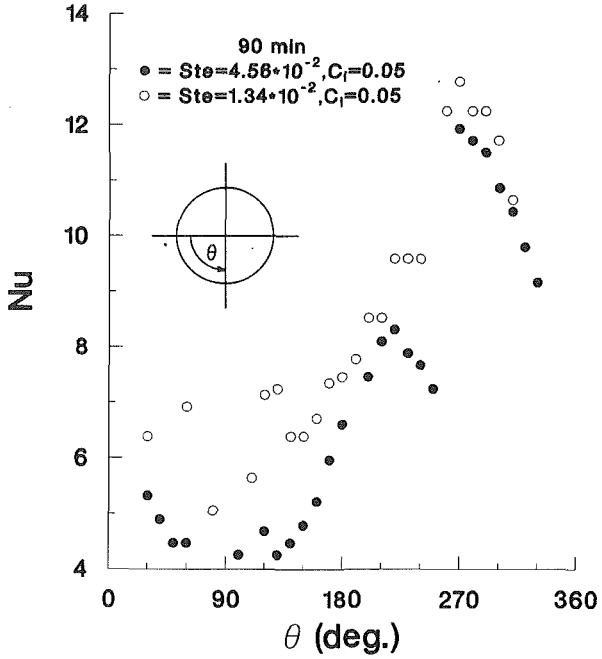

Fig. 17 The effect of Ste on the local Nusselt number at the mush/liquid interface for C_i = 0.05 and t = 90 min

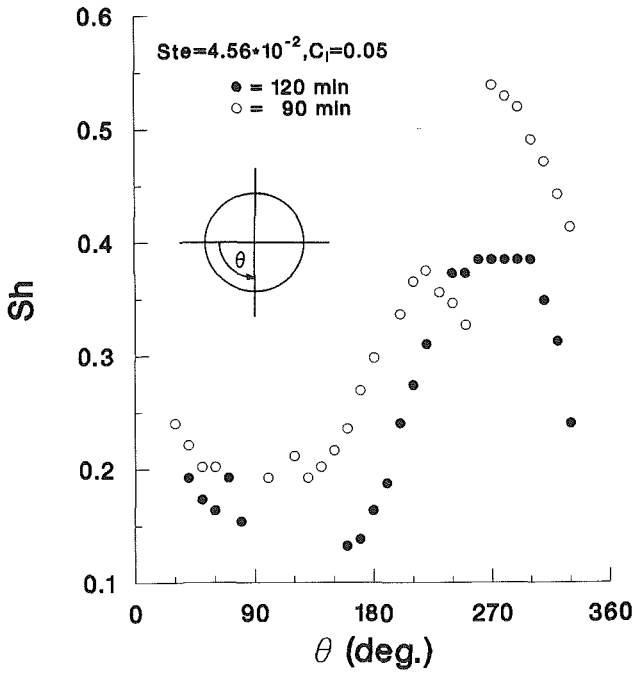

Fig. 16 The local Sherwood number at the mush/liquid interface for Ste = 4.56 × 10^{-2} and C_i = 0.05

face. In addition, the wavelike shape of the fringes on top of the pipe is clearly caused by the plumes emanating from the mushy zone and moving upward as discussed in connection with Fig. 12.

One main goal of this study is to present for the first time measurements of local Nusselt and Sherwood numbers around the mush/liquid interface using holographic interferometry. Such measurements are reported for Nusselt numbers in Fig. 15 and for Sherwood numbers in Fig. 16 for Ste = 4.56 × 10^{-2} and C_i = 0.05. The variation of Nusselt and Sherwood numbers with (θ) resembles a bell-shaped curve with the exception of the dropoff near θ = 220 deg for the 90 min sample. In general, the Nusselt and Sherwood numbers increase from their minimum near the bottom of the cylinder (θ = 90 deg) to a maximum value near the top of the cylinder (θ = 270 deg) and thereafter decrease. The fact that the heat and mass transfer reach a maximum in the vicinity of θ = 270 deg is evident in Fig. 13 by the high fringe density at the top of the solidifying interface, where relatively warm fluid near the initial concentration is drawn towards the mush/liquid interface. The minimum heat and mass transfer occurs in the vicinity of θ = 90 deg. This is due to the fact that this point resembles the "backward" stagnation point for flow over a cylinder. Also, note that the surrounding fluid at the bottom of the solidifying interface is colder and has a higher concentration, closer to the liquidus temperature and concentration, compared to the fluid coming into contact with the upper part of the interface. The dropoff in the heat and mass transfer near θ = 220 deg, for the 90 min sample, is a result of the thickening of the fringes in this region of the mush/liquid interface along the lines of what was discussed earlier in the connection with Fig. 13. As time increases from t = 90 min to t = 120 min, the local Nusselt and Sherwood numbers generally decrease. Note that an obvious qualitative similarity exists between the results for the Nusselt number and the results for the Sherwood number (Figs. 15 and 16) despite the distinct differences in the magnitudes of these numbers. The same similarity between Nu and the corresponding Sh will be observed in the remainder of this section. Since in all the cases for which the measurements for Nu and Sh were obtained the thermal buoyancy and the concentration buoyancy were "aiding" one another, the abovementioned similarity can be attributed to the heat and mass transfer analogy, which, as is well known, exists in convective flows.

For the same time and initial concentration, the values of Nu and Sh appear to increase as the Stefan number decreases as illustrated in Figs. 17 and 18 where the variations of Nu and Sh with position (θ) for two different Stefan numbers at t = 90 min are presented. An increase in Ste for the same initial concentration is equivalent to reducing the pipe wall temperature. It appears that the buoyancy-driven flow at late times is weaker for larger values of Ste. Through increased mixing, for larger values of Ste, the cooling effect of the pipe "propagates" faster in the enclosure. As a result, the tem-

Downloaded 13 Dec 2010 to 193.140.21.150. Redistribution subject to ASME license or copyright; see http://www.asme.org/terms/Terms_Use.cfm

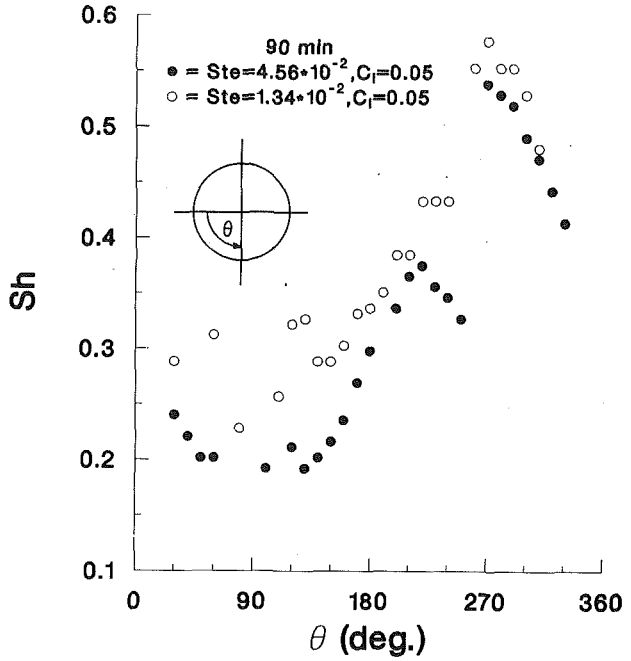

Fig. 18 The effect of Ste on the local Sherwood number at the mush/liquid interface for C_i = 0.05 and t = 90 min

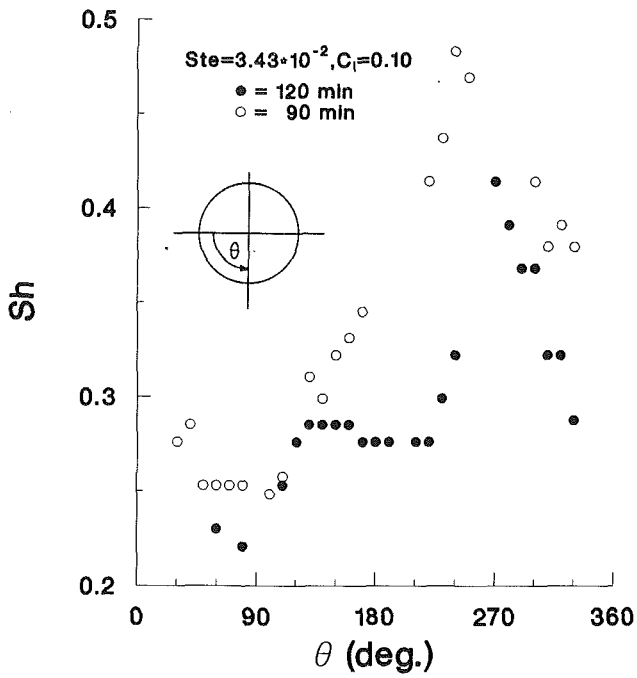

Fig. 20 The local Sherwood number at the mush/liquid interface for Ste = 3.43 × 10^{-2} and C_i = 0.10

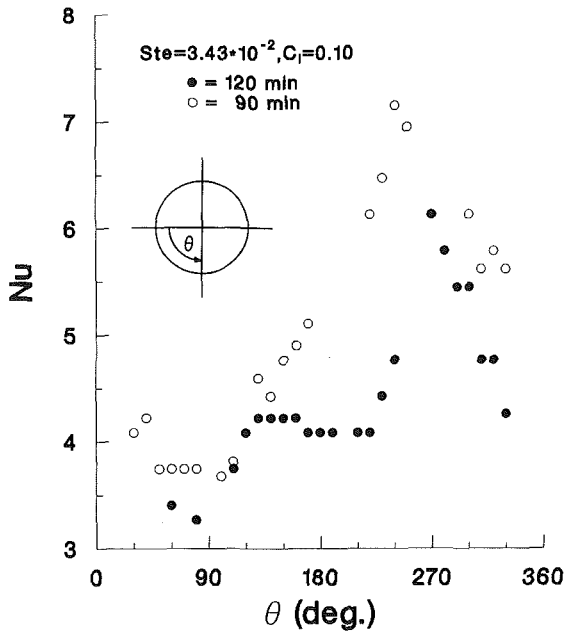

Fig. 19 The local Nusselt number at the mush/liquid interface for Ste = 3.43 × 10^{-2} and C_i = 0.10

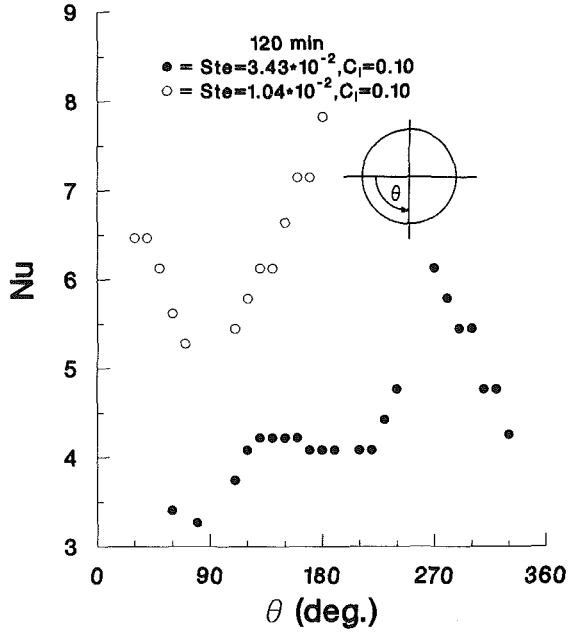

Fig. 21 The effect of Ste on the local Nusselt number at the mush/liquid interface for C_i = 0.10 and t = 120 min

perature and concentration gradients at late times decrease. This explains the result of the lower Nu and Sh with increased values of Ste at late times. It should be noted that all the holograpic intereferometry measurements were performed at rather late times (t > 90 min). At earlier times high fringe densities did not allow for reliable fringe interpretation.

Figures 19–22 represent similar results for the initial concentration of C_i = 0.10. The dependence of Nu and Sh on position (θ) remains qualitatively the same. The interesting feature of the data obtained for C_i = 0.10 is that there is a much stronger dependence of Nu and Sh on Ste. This is apparent by comparing Figs. 21 and 22 with Figs. 17 and 18. For a comparable change in the Stefan number the initial concentration of C_i = 0.10 shows a much larger change in Nu and Sh than the initial concentration of C_i = 0.05. It should be mentioned that reliable data for Ste = 1.04 × 10^{-2}, in Figs. 21 and 22, and for positions θ > 180 deg were not obtainable due to a very high fringe density, in excess of 14 fringes per mm.

An interesting feature of Figs. 19–22 is the plateau-shaped data around θ = 180 deg for Ste = 3.43 × 10^{-2}. This plateau is again due to the thickening of the fringes at this location caused by the temporal interaction between the double diffusion flow in the liquid region and the mush/liquid interface.

5 Conclusions

In this paper, the main results of an experimental study on

Downloaded 13 Dec 2010 to 193.140.21.150. Redistribution subject to ASME license or copyright; see http://www.asme.org/terms/Terms_Use.cfm

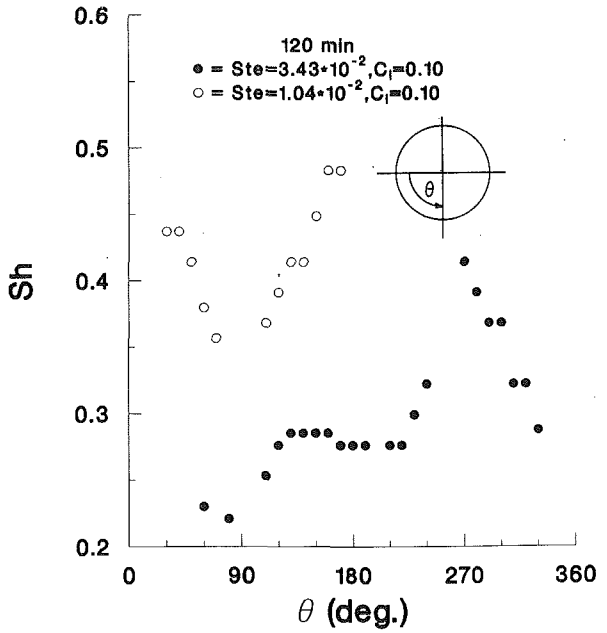

Fig. 22 The effect of Ste on the local Sherwood number at the mush/liquid interface for C_i = 0.10 and t = 120 min

the transient freezing of a binary alloy around a horizontal pipe in a rectangular enclosure were reported. Aqueous solutions of ammonium chloride and water were used to simulate a binary alloy. A two-wavelength holographic interferometry technique along with shadowgraph photographs were used to visualize the density field in the liquid phase and to determine the local Nusselt and Sherwood numbers at the solidifying interface. It was found that the initial concentration of the alloy affected both the flow field and the composition of the mushy zone. For example, for the initial concentration of C_i = 0.25 (above the eutectic point) the solutal buoyancy directed the flow in the system upward after emanating through the mushy zone while the thermal buoyancy directed the flow downward. As a result, a complex, possibly three-dimensional flow field was created in the system. Quantitative measurements for Nu and Sh in this case were not possible.

The results for the local Nusselt and Sherwood numbers reported are the first results of their kind published in the open literature on solidification (to the best of our knowledge). Here, the interaction between the double diffusion flow field in the liquid and the mushy regions clearly affected the heat and mass transfer rates at the mush/liquid interface. In some cases, this effect was unpredictable as the Nu versus θ and Sh versus θ distributions departed visibly from their usual "bell" shape. In general, increasing the value of the Stefan number decreased the values of Nu and Sh at late times. For the same initial concentration and Stefan number both Nu and Sh decreased with time.

The pipe surface temperature decreased rapidly at first, experienced a discontinuity, and kept decreasing thereafter until it became practically constant. The temperature discontinuity (rise) for initial concentrations below the eutectic concentration occurred at temperatures above the eutectic temperature, indicating the onset of mush formation around the pipe. The temperature discontinuity for initial concentrations above the eutectic concentration occurred at a temperature value well below the eutectic temperature, indicating the onset of formation of solid around the pipe.

The mush-plus-solid volume production increased almost linearly with time for initial concentrations below the eutectic concentration. Initial concentrations above the eutectic concentration exhibited a tapering off of the mush-plus-solid production at later times. This was primarily due to the difference in the structure of the mushy layer: at concentrations above the eutectic, the mushy zone was observed to be loosely interwoven, dendritic, and fragile.

In closing, in addition to the fact that the present experimental results shed light on the complex problem of alloy solidification around the pipe, they can be used to test the accuracy of future numerical models of alloy solidification, since experimental results on the local transport coefficients at the mush/liquid interface are indeed scarce in the literature.

Acknowledgments

Support for this work provided by NSF through grant No. ENG-84-51144 is gratefully acknowledged.

References

Arndt, N. T., 1986, "Differentiation of Komatiite Flows," *J. Petrol.*, Vol. 27, pp. 279–301.

Beckermann, C., 1987, "Melting and Solidification of Binary Mixtures With Double-Diffusive Convection in the Melt," Ph.D. Thesis, Purdue University, West Lafayette, IN.

Beckermann, C., and Viskanta, R., 1988, "Double-Diffusive Convection During Dendritic Solidification of a Binary Mixture," *Physico Chem. Hydrodyn.*, Vol. 10, pp. 195–213.

Bejan, A., 1984, *Convection Heat Transfer*, Wiley.

Bennon, W. D., and Incropera, F. P., 1987a, "A Continuum Model for Momentum, Heat and Species Transport in Binary Solid-Liquid Phase Change Systems—I: Model Formulation,'" *Int. J. Heat Mass Transfer*, Vol. 30(10), pp. 2161–2170.

Bennon, W. D., and Incropera, F. P., 1987b, "A Continuum Model for Momentum, Heat and Species Transport in Binary Solid-Liquid Phase Change System—II. Applications to Solidification in a Rectangular Cavity," *Int. J. Heat Mass Transfer*, Vol. 30(10), pp. 2171–2187.

Bennon, W. D., and Incropera, F. P., 1988, "Numerical Analysis of Binary Solid-Liquid Phase Change Using a Continuum Model," *Numer. Heat Transfer*, Vol. 13(3), pp. 277–296.

Cao, W.-Z., and Poulikakos, D., 1990, "Solidification of an Alloy in a Cavity Cooled Through Its Top Surface," *Int. J. Heat Mass Transfer*, Vol. 33(3), pp. 427–434.

Cao, W.-Z., and Poulikakos, D., 1992, "Transient Solidification of a Binary Mixture in an Inclined Rectangular Cavity," *AIAA Journal of Thermophysics and Heat Transfer*, Vol. 6(2), pp. 326–332.

Christenson, M. S., Bennon, W. D., and Incropera, F. P., 1989, "Solidification of an Aqueous Ammonium Chloride Solution in a Rectangular Cavity—II. Comparison of Predicted and Measured Results," *Int. J. Heat Mass Transfer*, Vol. 32(1), pp. 69–79.

Christenson, M. S., and Incropera, F. P., 1989a, "Experiments on Solidification of an Aqueous Sodium Carbonate Solution in a Horizontal Cylinder Annulus," ASME JOURNAL OF HEAT TRANSFER, Vol. 111, pp. 998–1005.

Christenson, M. S., and Incropera, F. P., 1989b, "Solidification of an Aqueous Ammonium Chloride Solution in a Rectangular Cavity—I. Experimental Study," *Int. J. Heat Mass Transfer*, Vol. 32(1), pp. 47–68.

Copley, S. M., Giamei, A. F., Johnson, S. M., and Hornbecker, M. F., 1970, "The Origin of Freckles in Undirectionally Solidified Castings," *Met. Trans.*, Vol. 1(8), pp. 2193–2204.

Ecker, A., 1988, "A Two-Wavelength Holographic Measurement of Temperature and Concentration During Alloy Solidification," *J. Thermophysics*, Vol. 2(3), pp. 193–196.

Engel, A. H. H., and Incropera, F. B., 1989, "Solidification of a Binary Mixture in a Square Cavity With a Free Surface," *Warme- und Stoffubertrajung*, Vol. 24(15), pp. 279–288.

Fang, L. J., Cheung, F. B., Linehan, J. H., and Pederson, D. R., 1984a, "Selective Freezing of a Dilute Salt Solution on a Cold Ice Surface," ASME JOURNAL OF HEAT TRANSFER, Vol. 106(2), pp. 385–393.

Fang, L. J., Cheung, F. B., Pederson, D. R., and Linehan, J. H., 1984b, "An Experimental Study of Natural Convection Melting of Ice in Salt Solutions," ASME Paper No. 84-WA/HT-55.

Hauf, W., and Grigull, U., 1970, "Optical Methods in Heat Transfer," *Advances in Heat Transfer*, Vol. 6, pp. 133–367.

Hermann, J., Leidenfrost, W., and Viskanta, R., 1984, "Effect of Natural Convection on Freezing of Water Around and Isothermal Horizontal Cylinder," *Int. Commun. Heat Mass Transfer*, Vol. 11, pp. 301–310.

Huppert, H. E., and Worster, M. G., 1985, "Dynamic Solidification of a Binary Melt," *Nature*, Vol. 314, pp. 703–707.

Incropera, F. P., Engel, A. H. H., and Bennon, W. D., 1989, "Numerical Analysis of Binary, Solid–Liquid Phase Change With Buoyancy and Surface Tension Driven Convection," *Numer. Heat Transfer*, Vol. 16(1), pp. 407–427.

Kececioglu, I., and Rubinsky, B., 1989, "A Continuum Model for the Prop-

Downloaded 13 Dec 2010 to 193.140.21.150. Redistribution subject to ASME license or copyright; see http://www.asme.org/terms/Terms_Use.cfm

agation of Discrete Phase-Change Fronts in Porous Media in the Presence of Coupled Heat Flow, Fluid Flow and Species Transport Processes," *Int. J. Heat Mass Transfer*, Vol. 32, p. 1111–1130.

Kerr, R. C., Woods, A. W., Worster, M. G., and Huppert, H. E., 1990a, "Solidification of an Alloy Cooled From Above. Part 1. Equilibrium Growth," *J. Fluid Mech.*, Vol. 216, pp 323–342.

Kerr, R. C., Woods, A. W., Worster, M. G., and Huppert, H. E., 1990b, "Solidification of an Alloy Cooled From Above. Part 2. Non-equilibrium Interfacial Kinetics," *J. Fluid Mech.*, Vol. 217, pp. 331–348.

Kerr, R. C., Woods, A. W., Worster, M. G., and Huppert, H. E., 1990c, "Solidification of an Alloy Cooled From Above. Part 3. Compositional Stratification With the Solid," *J. Fluid Mech.*, Vol. 218, pp. 337–354.

McDonald, R. J., and Hunt, J. D., 1969, "Fluid Motion Through the Partially Solid Regions of a Casting and Its Importance in Understanding A Type Segregation," *Trans. Metall. Soc. AIMI.*, Vol. 245, pp. 1993–1997.

McDonald, R. J., and Hunt, J. D., 1970, "Convective Fluid Motion With the Interdendritic Liquid of a Casting," *Met. Trans.*, Vol. 1, pp. 1787–1788.

Muehlabuer, J. C., Hatcher, J. D., Lyons, D. W., and Suderland, J. E., 1973, "Transient Heat Transfer Analysis of Alloy Solidification," ASME JOURNAL OF HEAT TRANSFER, Vol. 95(3), pp. 324–331.

Neilson, D. G., and Incropera, F. P., and Bennon, W. D., 1990, "Numerical Simulation of Solidification in a Horizontal Cylinder Annulus Charged With an Aqueous Salt Solution," *Int. J. Heat Mass Transfer*, Vol. 33(2), pp. 367–380.

Ni, J., and Beckermann, C., 1990, "A Two Phase Model for Mass, Momentum Heat and Species Transport During Solidification," presented at the AIAA/ASME Joint Thermophysics and Heat Transfer Conference, Seattle, WA.

Poulikakos, D., 1988, "On the Growth of a Solid From a Line Heat Sink in a Binary Alloy," *Numer. Heat Transfer*, Vol. 14(1), pp. 113–126.

Poulikakos, D., and Cao, W.-Z., 1989, "Solidification of a Binary Alloy From a Cold Wire or Pipe: Modelling of the Mixed Phase Region," *Numer. Heat Transfer*, Vol. 15(A), pp. 197–219.

Prescott, P. J., and Incropera, F. P., 1991, "Modelling of Dendritic Solidification Systems: Reassessment of the Continuum Momentum Equation," *Int. J. Heat Mass Transfer*, Vol. 34(9), pp. 2351–2359.

Spatz, T. L., 1991, "A Holographic Interferometry Study on the Freezing of an Alloy Around a Pipe in the Presence of a Mixed Phase Region," Ph.D. Thesis, University of Illinois at Chicago.

Spatz, T. L., and Poulikakos, D., 1991, "Holographic Interferometry Experiments on the Growth of Ice From a Horizontal Pipe," *Int. J. Heat Mass Transfer*, Vol. 35(7), pp. 1847–1860.

Szekely, J., and Jassal, A. S., 1978, "An Experimental and Analytical Study of the Solidification of a Binary Dendritic System," *Met. Trans. B.*, Vol. 9B(5), pp. 389–398.

Turner, J. S., Huppert, H. E., and Sparks, R. S. J., 1986, "Komatiites II. Experimental and Theoretical Investigations of Post-implacement Cooling and Crystallization," *J. Petrol.*, Vol. 27, pp. 397–437.

Vest, C. M., 1979, *Holographic Interferometry*, Wiley, New York.

Viskanta, R., 1988, "Heat Transfer During Melting and Solidification of Metals," ASME JOURNAL OF HEAT TRANSFER, Vol. 110, pp. 1205–1219.

Viskanta, R., 1990, "Mathematical Modelling of Transport Processes During Solidification of Binary Systems," *JSME Int. Series II*, Vol. 33, pp. 409–423.

Voller, V. R., and Prakash, C., 1987, "A Fixed Grid Numerical Modelling Methodology for Convection–Diffusion Mushy Region Phase-Change Problems," *Int. J. Heat and Mass Transfer*, Vol. 30(8), pp. 1709–1719.

Voller, V. R., Brent, A. D., and Prakash, C., 1989, "The Modeling of Heat, Mass and Solute Transport in Solidification Systems," *Int. J. Heat Mass Transfer*, Vol. 32(9), pp. 1719–1731.

Webb, B. W., and Viskanta, R., 1986, "An Experimental and Analytical Study of Solidification of a Binary Mixture," *Heat Transfer 1986: Proceedings of the Eighth International Heat Transfer Conference*, San Francisco, Aug., C. L. Tien, V. P. Carey, and J. K. Ferrell, eds., Vol. 4, pp. 1739–1744, Hemisphere, Washington, DC.

Yu, Q., and Zhou, Y., 1991, "Numerical Simulation of Convection in the Two-Phase Zone of a Binary Alloy," *Int. J. Heat Mass Transfer*, Vol. 34(3), pp. 843–852.

Downloaded 13 Dec 2010 to 193.140.21.150. Redistribution subject to ASME license or copyright; see http://www.asme.org/terms/Terms_Use.cfm

Condensation in a Porous Region Bounded by a Cold Vertical Surface

J. N. Chung

O. A. Plumb

W. C. Lee

Department of Mechanical and Materials Engineering, Washington State University, Pullman, WA 99164-2920

The problem of condensation in a porous medium near a cold vertical surface is investigated numerically and experimentally. Numerical solutions to the mathematical model, which assumes that a distinct two-phase zone exists between the liquid and the vapor phases, compare favorably with the experimental results. Experiments were performed for steam condensing in packed beds of glass beads of three different sizes. In the numerical model, the effect of the vapor flow in the two-phase zone is included. The interfacial velocity was determined through the matching of shear stress and a total mass balance. The predicted interfacial velocities are around one to two orders of magnitude smaller than the Darcy velocity. The calculated liquid film thicknesses are on the order of the diameter of the glass beads. The results, presented in dimensionless format, are applicable to transport processes in geothermal reservoirs, steam-driven enhanced petroleum recovery, and a number of industrial applications.

Introduction

Evaporation and condensation in porous media occur in geothermal reservoirs, in heat pipes, during thermally enhanced petroleum recovery, with in-situ processing of oil shale and tar sands, in underground nuclear waste repositories, and in porous enhanced heat transfer surfaces. Despite the long list of important applications, a basic understanding of the transport mechanisms of momentum, heat, and mass in porous media during change of phase remains incomplete.

The problem of condensation heat transfer has been given extensive attention since the pioneering work by Nusselt (1916) for vapor condensation on a vertical plate in a continuous medium. Udell (1983, 1985) developed a one-dimensional model to study the vapor and liquid transport in a porous medium with evaporation and condensation taking place respectively at each side of the two-phase boundary. For condensation on cold plates in porous media, Cheng (1981) and Cheng and Chui (1984) found similarity solutions for steady and unsteady film condensation assuming Darcy flow in a constant-porosity medium. Kaviany (1986) carried out an analytical modeling and White and Tien (1987a, 1987b) performed both analytical and experimental work on the condensation of vapor on a vertical plate in a porous medium. In their analytical approach, a more realistic model, which takes into account the no-slip boundary condition on the wall instead of the Darcy flow model, was developed. All the abovementioned porous media investigations were based on the assumption that a distinct interface exists between a pure vapor phase and a liquid film next to the cold wall. Plumb (1984) was the first to demonstrate analytically that capillary transport can play a significant role for most porous media and should be included. In his model the liquid film is separated from the vapor by a two-phase capillary fringe. He found that capillary effects can decrease the liquid film thickness and hence increase the heat transfer and condensation rates on a vertical isothermal surface. Shekarriz and Plumb (1986) used a one-dimensional model to study the influence of capillary porous fins on filmwise condensation. In their model, the liquid film and the vapor saturated region are separated by a two-phase zone. Again, they concluded that porous fins could enhance transfer and condensation under conditions of practical interest.

Contributed by the Heat Transfer Division for publication in the JOURNAL OF HEAT TRANSFER. Manuscript received by the Heat Transfer Division July 1991; revision received April 1992. Keywords: Condensation, Porous Media, Thermocapillary Flows. Technical Editor: R. Viskanta.

Recently, Majumdar and Tien (1990) endorsed the three-zone model of Plumb (1984) and further introduced refinements for the two-phase zone and the liquid film. In their model the effect of vapor flow in the two-phase zone that was assumed to be isothermal was neglected.

In this paper, we continue the development of the three-zone model. Vapor flow is included in the two-phase model and more realistic conditions are introduced for the interface. Some experimental results are included to assess the validity of the current mathematical model.

In the current model, the liquid film and the two-phase zone are coupled through the continuity of velocity and shear stress at the interface. The governing equations for both regions are solved simultaneously. In model 1 of Majumdar and Tien (1990), the shear stress on the liquid film was assumed to be zero at the interface, which decoupled the liquid zone from the two-phase region. Model 1 is therefore appropriate for systems where the porous matrix plays a minor role. In their model 2, the Darcy velocity was assumed at the interface and the two-phase region was also decoupled from the liquid film. For a thin liquid film, the velocity is usually much smaller than the Darcy velocity because of the no-slip condition imposed on the wall. Model 2 was found to overpredict the experimental data by more than two orders of magnitude because of the unrealistic interface velocity. For their model 3, the liquid film was assumed to have a uniform Darcy velocity and a full analysis was performed for the two-phase portion. Because of the neglect of both the no-slip on the cold wall and the thin-film characteristics of the liquid film, model 3 also overpredicted the experimental data by two orders of magnitude. The current model actually integrates the three models of Majumdar and Tien (1990) and provides a unified model, which includes the important elements of both the liquid film and the two-phase portion. We also address the effects of the vapor flow on the two-phase transport, which was neglected in Majumdar and Tien (1990).

Mathematical Formulation

Heat and mass transfer with phase change in a porous medium next to a cold vertical flat plate is considered as shown in Fig. 1. The temperature and pressure of the porous system far away from the plate are maintained at T_∞ and P_∞, respectively, with saturated dry vapor. The plate temperature is

Copyright © 1992 by ASME
Downloaded 13 Dec 2010 to 193.140.21.150. Redistribution subject to ASME license or copyright; see http://www.asme.org/terms/Terms_Use.cfm

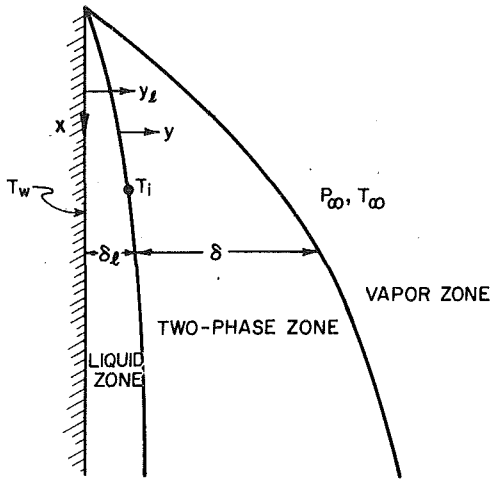

Fig. 1 Schematic of the mathematical model

at $T_w (T_w < T_\infty)$. Condensation of vapor is expected to take place on the cold vertical wall and inside the porous medium in the vicinity of the wall. As indicated in Fig. 1, we presume the existence of three regions, a liquid-saturated region nearest the surface, a vapor-saturated region far from the surface, and a two-phase region in between.

Governing Equations

Liquid-Saturated Region. In the liquid-saturated region near the cold surface the governing equations are given by

$$\frac{\partial U_l}{\partial x}+\frac{\partial V_l}{\partial y_l}=0 \quad \text{continuity} \tag{1}$$

$$\nu_l \frac{\partial^2 U_l}{\partial y_l^2}-\frac{\nu_l}{\kappa} U_l+\frac{(\rho_l-\rho_v)}{\rho_l} g=0 \quad \text{momentum} \tag{2}$$

$$\frac{d^2 T_l}{dy_l^2}=0 \quad \text{energy} \tag{3}$$

In the above, incompressible flow and constant properties are assumed. For the momentum equation, the thin-film assumption is made in addition to the Darcy flow assumption to allow the no-slip condition to be invoked at the solid surface. Conduction is considered dominant for the energy transport.

Two-Phase Zone. The model for the two-phase region assumes that condensation occurs only at the interface between the two-phase region and the liquid-saturated region (Udell, 1983, 1985).

$$\rho_l \frac{\partial u_l}{\partial x}+\rho_l \frac{\partial v_l}{\partial y}=0 \quad \text{liquid continuity} \tag{4}$$

$$\rho_v \frac{\partial v_v}{\partial y}=0 \quad \text{vapor continuity} \tag{5}$$

It is further assumed in Eq. (5) that there is no driving force for vapor flow in the x-direction. Equations (4) and (5) can be combined to obtain

$$\rho_l \frac{\partial u_l}{\partial x}+\rho_l \frac{\partial v_l}{\partial y}+\rho_v \frac{\partial v_v}{\partial y}=0 \quad \text{total continuity} \tag{6}$$

Equations (4) and (5) are solved together using phenomenological relationships between the velocities and the liquid saturation of the porous medium. For the x-component velocity, u_l, in many previous models it was suggested that

$$u_l=\kappa_{rl} u_D \quad x\text{-liquid momentum} \tag{7}$$

where κ_{rl} is the relative permeability of the liquid phase. u_D, the Darcy velocity, results solely from gravity,

$$u_D=\frac{\kappa(\rho_l-\rho_v)g}{\mu_l} \tag{8}$$

Equation (7) is also based on the assumption that the liquid phase pressure in the x direction is negligible, i.e.,

$$\frac{\partial P_l}{\partial x}\simeq 0. \tag{9}$$

The horizontal components of the liquid vapor velocities are given by

$$v_l=\frac{-\kappa\kappa_{rl}}{\mu_l}\frac{\partial P_l}{\partial y}, \quad y\text{-liquid momentum} \tag{10}$$

and

Nomenclature

C_p = specific heat at constant pressure
D = diameter of glass beads in porous medium
f = nondimensional capillary pressure
g = gravitational acceleration constant
h = heat transfer coefficient
h_{fg} = latent heat of evaporation
Ja = Jakob number = $C_{pl}(T_\infty - T_w)/h_{fg}$
K = thermal conductivity
L = length of the cold plate
$\dot{m}_v''$ = mass flux of vapor
$\dot{m}_{v,o}''$ = strength of mass flux of vapor
Nu_x = Nusselt number = hx/k_{eff}
P = pressure
R = dimensionless group = $\sigma(\kappa\phi)^{1/2}/\mu_l\alpha_{\mathrm{eff}}$
$\overline{R}$ = gas constant
S = liquid saturation
S_e = scaled liquid saturation
S_{IR} = irreducible saturation
T = temperature
u = x-component velocity in the two-phase zone
u_D = Darcy velocity
U = x-component velocity in the liquid film
v = y-component velocity in the two-phase zone
V = y-component velocity in the liquid film
x = coordinate along the cold plate
y = coordinate perpendicular to the cold plate starting from the interface between liquid and two-phase zone
y_l = coordinate perpendicular to the cold plate starting from the cold plate
α = thermal diffusivity
β = ratio of actual velocity to the Darcy velocity
δ = two-phase zone thickness
δ_l = liquid filter thickness
η = similarity variable
κ = permeability
κ_{rl} = relative permeability of liquid phase
κ_{rv} = relative permeability of vapor
μ = dynamic viscosity
ν = kinematic viscosity = μ/ρ
ρ = density
σ = vapor–liquid interface tension constant
ϕ = porosity

Subscripts

c = capillary
eff = effective porous bed quantity
i = at the interface between the liquid film and the two-phase zone
l = liquid phase
o = reference state
sat = saturation
tp = two-phase region
v = vapor phase
w = at the cold wall
x = at a local point x on the cold plate
∞ = condition in the pure vapor zone

Downloaded 13 Dec 2010 to 193.140.21.150. Redistribution subject to ASME license or copyright; see http://www.asme.org/terms/Terms_Use.cfm

$$v_v = \frac{-\kappa\kappa_{rv}}{\mu_v}\frac{\partial P_v}{\partial y} \quad y\text{-vapor momentum} \tag{11}$$

In all of the above equations, the Reynolds number for the porous medium is assumed small to allow the neglect of inertia effects. κ_{rv} is the relative permeability for the vapor phase. Additional relationships required for the model are given as follows:

$$P_c = P_v - P_l \quad \text{capillary pressure} \tag{12}$$

$$P_v = \rho_v \overline{R} T \quad \text{vapor phase is assumed as an ideal gas} \tag{13}$$

$$P_{\text{Sat}} = P_v \exp\left(\frac{P_c}{\rho_l \overline{R} T}\right) \quad \text{Kelvin equation} \tag{14}$$

$$P_{\text{Sat}} = P_o e^{(1/T_o - 1/T)h_{fg}/\overline{R}} \quad \text{Clapeyron equation} \tag{15}$$

Based on the above equations, we obtain

$$T = \frac{T_o\left[1 + \dfrac{P_c}{h_{fg}\rho_l}\right]}{1 - T_o\left(\dfrac{\overline{R}}{h_{fg}}\right)\ln\left(\dfrac{P_v}{P_o}\right)} \tag{16}$$

Equation (16), which constrains the two phases to thermodynamic equilibrium, replaces the energy equation for temperature estimates in the two-phase region. The relationships between relative permeability and the liquid saturation were reported by Fatt and Klikoff (1959) as follows:

$$\kappa_{rl} = S_e^3 \tag{17}$$

$$\kappa_{rv} = (1 - S_e^3) \tag{18}$$

$$S_e = \frac{S - S_{IR}}{1 - S_{IR}} \tag{19}$$

S_{IR} is defined as the saturation of immobile water or irreducible saturation. The relative permeabilities given in Eqs. (17) and (18) were chosen based on an extensive survey of literature and the comparison of numerical results with those of the experiment. In the literature, many different models have been suggested. They indicated that the relative permeabilities depend primarily on the phase saturation but also on viscosity ratio of the two phases, wetting characteristics, interfacial tension and saturation history. Schiedigger (1974) suggested $\kappa_{rl} = S_e^3$ and $\kappa_{rv} = 1 - S_e$. Bau and Torrance (1982) found that $\kappa_{rl} = S$ and $\kappa_{rv} = 1 - S$ were satisfactory for their water boiling experiments in low-permeability porous materials. Recently, Verma et al. (1985) did an extensive literature survey on relative permeabilities and performed an experiment to determine the relative permeabilities for steam and water concurrent flow in a porous medium. They concluded that Eq. (17), which has been suggested independently by many investigators for the liquid as the wetting phase, provided the best argument with their results. For the vapor on nonwetting phase, they found that $\kappa_{rv} = (1 - S_e)^3$ suggested by Brooks and Corey (1964) predicts values that are too small as compared to their experimental results. Verma et al. (1985) suggested the following equation for a steam–water system:

$$\kappa_{rv} = 1.2984 - 1.9832S_e + 0.7432S_e^2 \tag{20}$$

Both Eqs. (18) and (20) have been tested in the numerical model and they yield similar results, which agree reasonably well with the experimental measurements. $\kappa_{rv} = (1 - S_e)^3$ was also tested and yielded unsatisfactory results. Equation (18) also satisfies the argument that the sum for κ_{rl} and κ_{rv} should be approximately unity.

Leverett (1941) has shown that capillary pressure versus saturation data can be expressed in the following nondimensional form:

$$f(S_e) = \frac{P_c}{\sigma}\left(\frac{\kappa}{\phi}\right)^{1/2} \tag{21}$$

The following polynomial has been fit to the data by Udell (1983):

$$f(S_e) = 1.417(1 - S_e) - 2.120(1 - S_e)^2 + 1.263(1 - S_e)^3 \tag{22}$$

Boundary and Interfacial Conditions

$$U_l = 0 \quad y_l = 0 \tag{23}$$

$$T = T_w \quad y_l = 0 \tag{24}$$

$$U_l = u_i \quad y_l = \delta_l \tag{25}$$

$$T = T_i \quad y_l = \delta_l \tag{26}$$

$$S_e = S_{e,i} \quad y_l = \delta_l \tag{27}$$

It is noted that the liquid saturation at the interface for the two-phase region is not set to be equal to unity in the current model. This is based on the requirement that the total mass balance must be maintained for the condensate as shown later in Eq. (46). Also some portion of the interfacial area must be occupied by the vapor phase to allow its condensation to take place. Further support comes from the calculated saturation profile in the two-phase zone where evaporation and condensation take place at the left and the right boundaries, respectively (Udell, 1985). The calculated liquid saturations at the condensation and evaporation boundary are 0.78 and 0.09, respectively. Liquid saturation less than unity at the interface results in the interfacial velocity being smaller than the Darcy velocity, i.e., $u_i = S_{e,i}^3 u_D$. Majumdar and Tien (1990) also pointed out that u_i will be smaller than u_D for systems where the liquid films are relatively thin. When the film is thin, the effect of diffusion is also important at the interface according to Eq. (2). In the current study, u_i was found to be at least one order of magnitude smaller than the u_D as a result of the thinning of the liquid film by the two-phase region. Therefore u_i or $S_{e,i}$ is not known a priori in the current model; rather, it will be determined based on total mass and momentum balance detailed at a later point.

The interface temperature is an unknown constant, which will be determined as a result of the solution. The rest of the boundary conditions are

$$S_e = 0 \qquad y \to \infty \tag{28}$$

The above boundary condition is adequate because there is no evaporation at this side of the two-phase boundary in the current study.

$$T = T_\infty \qquad y \to \infty \tag{29}$$

T_∞ is the saturation temperature corresponding to P_∞, which is the pressure imposed on the system.

Method of Solution

Two-Phase Zone. First the saturation equation is established in terms of the continuity equation. The following equation is obtained by substituting Eq. (7) and (10) into Eq. (4):

$$\frac{\partial}{\partial x}\left[\frac{\kappa\kappa_{rl}(\rho_l - \rho_v)g}{\mu_l}\right] + \frac{\partial}{\partial y}\left[-\frac{\kappa\kappa_{rl}}{\mu_l}\frac{\partial P_l}{\partial y}\right] = 0 \tag{30}$$

Assuming that $\rho_l \gg \rho_v$ and constant properties

$$\rho_l g\frac{\partial \kappa_{rl}}{\partial x} - \frac{\partial}{\partial y}\left(\kappa_{rl}\frac{\partial P_l}{\partial y}\right) = 0 \tag{31}$$

Since κ_{rl}, κ_{rv}, and P_c are functions of S_e, Eq. (31) may be rearranged as the following:

$$\rho_l g\frac{\partial}{\partial x}\kappa_{rl} = \frac{\partial \kappa_{rl}}{\partial y}\frac{\partial P_v}{\partial y} + \kappa_{rl}\frac{\partial^2 P_v}{\partial y^2} - \frac{\partial}{\partial y}\left(\kappa_{rl}\frac{\partial P_c}{\partial S_e}\frac{\partial S_e}{\partial y}\right) \tag{32}$$

Equation (32) may be further arranged in terms of S_e using Eqs. (17)–(22),

Downloaded 13 Dec 2010 to 193.140.21.150. Redistribution subject to ASME license or copyright; see http://www.asme.org/terms/Terms_Use.cfm

$$3\rho_l g S_e^2 \frac{\partial S_e}{\partial x} = \left(3S_e^2 \frac{\partial S_e}{\partial y}\right)\frac{\partial P_v}{\partial y} + (S_e^3)\frac{\partial^2 P_v}{\partial y^2} - \left[3S_e^2\left(\frac{\partial S_e}{\partial y}\right)\frac{\sigma}{(\kappa/\phi)^{1/2}}\frac{\partial f}{\partial S_e} + S_e^3\frac{\partial}{\partial y}\left(\frac{\sigma}{(\kappa/\phi)^{1/2}}\frac{\partial f}{\partial S_e}\right)\right]\frac{\partial S_e}{\partial y} - \frac{S_e^3\sigma}{(\kappa/\phi)^{1/2}}\frac{\partial f}{\partial S_e}\frac{\partial^2 S_e}{\partial y^2} \quad (33)$$

Equation (33) is further transformed to a similarity formulation by the variable η introduced by Majumdar and Tien (1990) as

$$\eta = \frac{y}{(Ax)^{1/2}}, \qquad A = \frac{\sigma}{\rho_l g\left(\frac{\kappa}{\phi}\right)^{1/2}} \quad (34)$$

In terms of the similarity variable η, Eq. (33) becomes

$$\frac{3\eta}{2}\frac{dS_e}{d\eta} = -\frac{\left(\frac{\kappa}{\phi}\right)^{1/2}}{\sigma}\left(3\frac{dS_e}{d\eta}\frac{dP_v}{d\eta} + S_e\frac{d^2P_v}{d\eta^2}\right) + (3f' + S_e f'')\left(\frac{dS_e}{d\eta}\right)^2 + S_e f'\frac{d^2S_e}{d\eta^2} \quad (35)$$

The corresponding boundary conditions are

$$S_e = S_{e,i} \qquad \eta = 0$$
$$S_e = 0 \qquad \eta \to \infty \quad (36)$$

Before we proceed to obtain the solutions of Eqs. (35) and (36), $dP_v/d\eta$ and $d^2P_v/d\eta^2$ must be explicitly provided for; this is the primary difference between our model and that presented by Majumdar and Tien (1990) where the vapor flow was neglected in the modeling.

According to Eq. (5), the vapor mass flux in the two-phase region is a function only of x. With the similarity relationship indicated in Eq. (35), we may write this relationship as,

$$\dot{m}_v'' = \rho_v v_v = \frac{-\rho_v \kappa K_{rv}}{\mu_v}\frac{\partial P_v}{\partial y} = \frac{\dot{m}_{v,o}''}{x^{1/2}} \quad (37)$$

where $\dot{m}_{v,o}''$ is a constant, which we will term the strength of the vapor flow. Therefore we have the following for $dP_v/d\eta$ and $d^2P_v/d\eta^2$,

$$\frac{dP_v}{d\eta} = -\frac{\dot{m}_{v,o}''\mu_v}{\rho_v \kappa K_{rv}} \quad (38)$$

$$\frac{d^2P_v}{d\eta^2} = \frac{\dot{m}_{v,o}''\mu_v}{\rho_v \kappa K_{rv}^2}\frac{\partial K_{rv}}{\partial \eta} \quad (39)$$

In Eqs. (38) and (39), K_{rv} as given in Eq. (18) is a function of S_e only. f' and f'' in Eq. (35) are obtained directly from Eq. (22) as,

$$f' = -1.417 + 4.24(1 - S_e) - 3.789(1 - S_e)^2 \quad (40)$$

$$f'' = -4.24 + 7.578(1 - S_e) \quad (41)$$

With any given value of $\dot{m}_{v,o}''$, Eq. (35), the saturation equation, with boundary conditions, Eq. (36), and auxiliary Eqs. (38)–(41), can be solved by an appropriate numerical technique. However, some caution must be exercised since it is highly nonlinear.

Liquid Saturated Region. In the liquid saturated region, Eq. (2) is solved exactly, subject to the following boundary conditions:

$$U_l = 0 \qquad y_l = 0$$
$$U_l = u_i \qquad y_l = \delta_l \quad (42)$$

Thus the velocity at the interface between the liquid-saturated and the two-phase zone is not known a priori and will be determined by matching conditions at the interface. The closed-form solution is

$$U_l = \frac{(u_i - u_D) + u_D \cos h\left(\frac{\delta_l}{k'}\right)}{\sin h\left(\frac{\delta_l}{k'}\right)} \sin h\left(\frac{y_l}{k'}\right) - u_D \cos h\left(\frac{y_l}{k'}\right) + u_D \quad (43)$$

where $k' = (\kappa)^{1/2}$.

The solution of the energy equation, Eq. (3) is

$$T_l = \frac{(T_i - T_w)}{\delta_l} y_l + T_w \quad (44)$$

T_i, T_w, and δ_l are the interface temperature, condenser surface temperatures, and liquid film thickness, respectively; T_i is determined by Eq. (16). δ_l is found from the matching conditions at the interface.

Solution Procedure. The saturation equation, Eq. (35), is first solved with a specified vapor flow strength $\dot{m}_{v,o}''$ and a guessed $S_{e,i}$ by a finite difference method. Iteration was required because of the nonlinear terms. The rate of convergence depends on the vapor flow strength $\dot{m}_{v,o}''$ and the parameter $(\kappa/\phi)^{1/2}/\sigma$.

Once the saturation profile is determined for the two-phase zero, we proceed with the search for the interfacial velocity u_i and the liquid film thickness δ_l. The matching conditions are based on the continuity of shear stress and conservation of the total mass.

$$\mu_l \left.\frac{\partial U_l}{\partial y_l}\right|_{y_l=\delta_l} = \mu_{tp}\left.\frac{\partial u_l}{\partial y}\right|_{y=0} \qquad \text{at } x = L$$

continuity of shear stress (45)

$$\int_0^L \dot{m}_v'' dx = \int_0^\infty \rho_l \kappa_{rl} u_D dy + \int_0^{\delta_l} \rho_l U_l dy_l$$

conservation of total mass (46)

It should be emphasized that Eq. (45) is very similar to the interfacial condition adopted in Model 1 of Majumdar and Tien (1990), where they assumed a no-shear interface condition for the liquid film. Equation (46) represents the total conservation of liquid condensate. In the above equation, L is the length of the cold surface. μ_{tp} is the dynamic viscosity of the two-phase zone and its value is correlated with the liquid saturation at the interface. Using Eqs. (7) and (43), Eq. (45) may be re-arranged to give

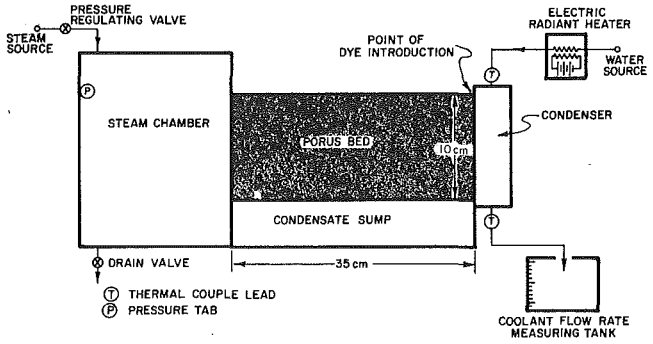

Fig. 2 Schematic of the experimental apparatus

Downloaded 13 Dec 2010 to 193.140.21.150. Redistribution subject to ASME license or copyright; see http://www.asme.org/terms/Terms_Use.cfm

$$u_i = \frac{-u_D(\cos h(\delta_l/k') - 1)\left(\dfrac{\cos h(\delta_l/k')}{\sin h(\delta_l/k')} + u_D \sin h(\delta_l/k') + 3k'\left(\dfrac{\mu_{lp}}{u_l}\right)u_D S_e^2\left(\dfrac{\partial S_e}{\partial y}\right)\right|_{y=0}}{\dfrac{\cos h(\delta_l/k')}{\sin h(\delta_l/k')}} \quad (47)$$

Applying Eqs. (17) and (43), Eq. (46) results in the following form:

$$u_i = \frac{\displaystyle\int_0^L \dot{m}_v'' dx - \int_0^\infty \rho_l S_e^3 dy - \rho_l k'\left[\frac{u_D(\cos h(\delta_l/k') - 1)^2}{\sin h(\delta_l/k')} - u_D \sin h(\delta_l/k') + u_D(\delta_l/k')\right]}{\rho_l k'\left(\dfrac{(\cos h(\delta_l/k') - 1)}{\sin h(\delta_l/k')}\right)} \quad (48)$$

Equations (47) and (48) provide the two equations for the unknowns u_i and δ_l. Iterations were required to obtain u_i and δ_l with $\partial S_e/\partial y|_{y=0}$ extracted from the solution of the saturation equation. At this point it is necessary to check the u_i obtained to determine whether it agrees with the original assumption with regard to $S_{e,i}$, i.e., $u_i = S_{e,i}^3 u_D$. If not, a revised guess for $S_{e,i}$ is made and the double iteration process is repeated. When both loops converge, the values for $S_{e,i}$, u_i, δ_l, and the saturation profile are all determined. It should be noted that Eqs. (45) and (46) are written for the trailing edge of the condenser plate ($x = L$) and u_i should be a function of x. In our numerical experiments, it was concluded that u_i is relatively independent of x for each case; therefore u_i is assumed constant in this analysis because of the similarity nature of the two-phase zone.

After δ_l is determined, the wall temperature is found from the following energy continuity equation:

$$T_w = T_i + \left\{\frac{\delta_l}{K_{\text{eff}}}\dot{m}_v''(x=L)h_{fg} - \delta_l\left.\frac{\partial T}{\partial y}\right|_{y=0,x=L}\right\} \quad (49)$$

where h_{fg} is the latent heat of condensation. The thermal conductivity is assumed equal to K_{eff}, the effective thermal conductivity in a liquid-saturated porous medium at the interface.

Experimental Study

Apparatus. Experiments on condensation of steam in porous media were conducted using the test facility shown in Fig. 2. The test apparatus contains a constant pressure steam chamber, a porous bed of glass beads, and a condenser that provides a vertical flat cold surface. The pressure in the steam chamber is regulated by adjusting the inlet steam pressure and the drain valve. The porous bed is enclosed on each side by double plexiglass layers with an air gap for insulation. Additional fiber glass insulation was wrapped around the porous bed section. The extra effort on the insulation was intended to make the porous bed as close to a two-dimensional environment as possible. The bottom portion of the porous bed section was fitted with a screen, which prevented the glass beads from falling through but allowed the draining of condensate, which forms the two-phase zone in the porous bed. The condenser was also thoroughly insulated. The cooling water flowed through the copper condenser in a labyrinth fashion to create as uniform a surface temperature as possible.

Procedure. Experiments were conducted using glass beads 350, 920, and 1545 μm in diameter. Measured values of the saturated permeability were 7.5×10^{-11} m^2, 3.5×10^{-10} m^2, and 1.2×10^{-9} m^2, respectively. The methods that determine those permeabilities and the size variations for each size group are detailed by Plumb et al. (1990).

The beads were washed and dried before they were placed in the test section to eliminate the introduction of impurities to the test section. At the start of each experiment, the steam pressure in the chamber was elevated above the intended pressure for the experiment to flush out the noncondensable gases. The pressure was lowered to 1.2 atm and kept constant during the entire experiment. The system was allowed to run at steady state for approximately thirty minutes before taking the data. The condensation rates were measured through the coolant temperature increase across the condenser and the coolant mass flow rate. The temperature difference was measured using a differential thermocouple and a potentiometer accurate to ± 0.025°C. The flow rates were determined by measuring the amount of coolant flow gathered in five minutes. The coolant flow rates were adjusted so that the temperature increase was not more than 2°C. A larger temperature increase would invalidate isothermal condenser surface assumption. The uncertainties associated with the measured condensation rates mainly result from the small heat loss through the plexiglass walls and the mean temperature of the coolant fluid exiting from the condenser.

Some flow visualization was attempted in order to measure the extent of the two-phase region. This was achieved by injecting a liquid dye on top of the bed where it meets the condenser surface, as shown in Fig. 2.

Results and Discussion

In this section, we first present both numerical and experimental condensation results in terms of the appropriate dimensionless parameters. Condensation heat transfer rate versus the potential is shown in Figs. 3–5 for the three glass bead sizes of 350 μm, 900 μm, and 1500 μm. The condensation heat transfer rate is represented by $\text{Nu}_x/\text{Ra}_x^{1/2}$, where $\text{Nu}_x = hx/$

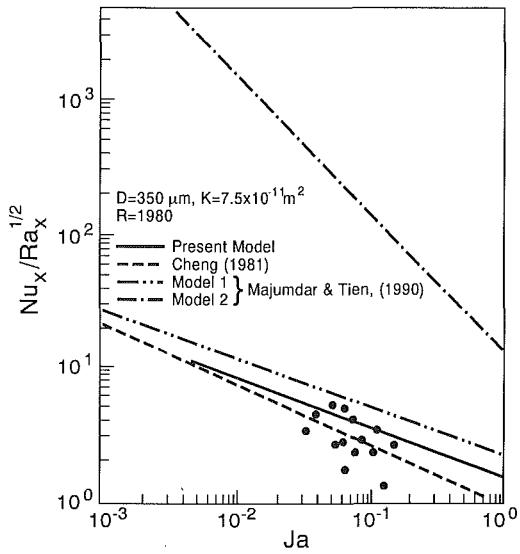

Fig. 3 Condensation heat transfer results for 350 μm glass beads

Downloaded 13 Dec 2010 to 193.140.21.150. Redistribution subject to ASME license or copyright; see http://www.asme.org/terms/Terms_Use.cfm

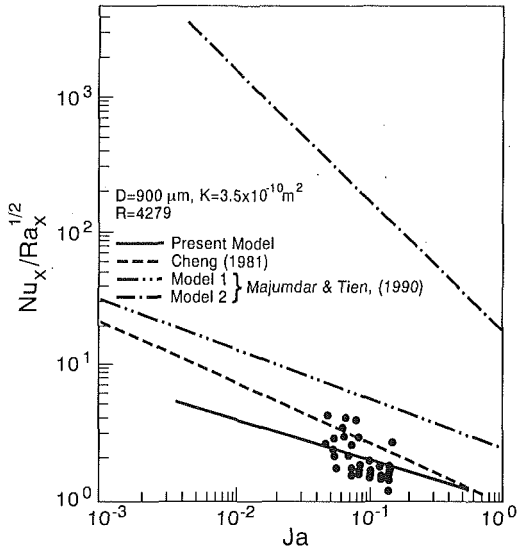

Fig. 4 Condensation heat transfer results for 900 μm glass beads

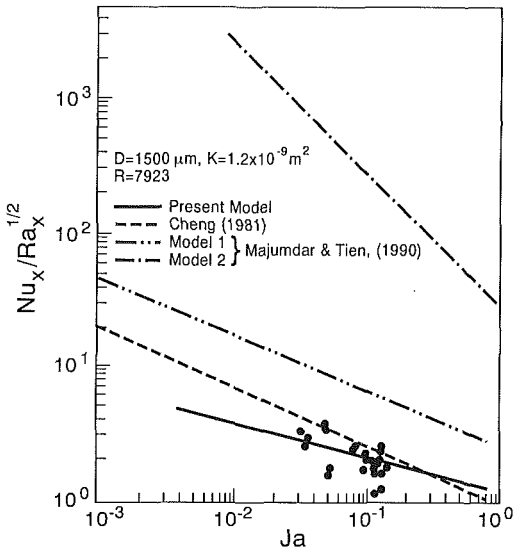

Fig. 5 Condensation heat transfer results for 1500 μm glass beads

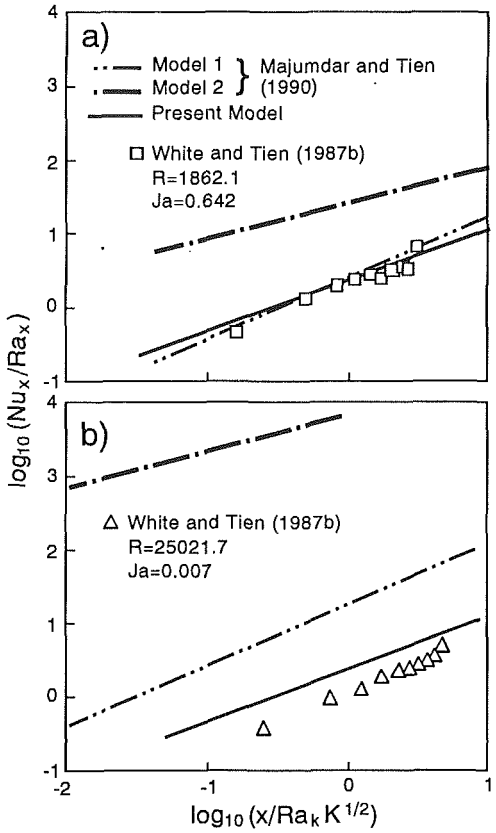

Fig. 6 Comparison with White and Tien (1987b)

K_{eff} and $\text{Ra}_x = \kappa x(\rho_l - \rho_v)g/\mu_l\alpha_{\text{eff}}$. The potential is expressed through the Jakob number, $\text{Ja} = C_{pl}(T_\infty - T_w)/h_{fg}$. These are the same parameters used successfully by previous investigators (Cheng, 1981; Majumdar and Tien, 1990) and they seem to be adequate for this study because logarithmic relationships have been obtained, as shown in Figs. 3-5. The experimental results were obtained for a limited range of the Ja, which corresponds to the steam inlet temperature of 100°C and the condenser temperature varying between 15°C and 75°C. For the experimental data, the degree of scattering decreases with increasing glass bead size. This is attributed to the measuring technique for the heat transfer, which results in a greater uncertainty when condensation rates are lower. Predictions by Cheng (1981) and Majumdar and Tien (1990) are also shown in the figures. Cheng (1981) did not include the two-phase zone in his model where the pure vapor is assumed to be in direct contact with the liquid film. As a result of the similarity solution obtained for the liquid film, Cheng's curve is unique for all three bead sizes. Majumdar and Tien (1990) addressed the existence of the two-phase zone but neglected the effects of vapor flow. Their results depend on the parameter $R = \sigma(\kappa\phi)^{1/2}/\mu_l\alpha_{\text{eff}}$, which characterizes the surface tension effects in the two-phase zone. The corresponding values of R are 1980, 4279, and 7923 for glass beads of 350,920, and 1545 μm in diameter, respectively. In general, both model 1 and model 2 of Majumdar and Tien (1990) overpredicted the experimental results, but model 1 did a much better job than model 2. This is mainly because a full-strength Darcy velocity was assumed at the interface, while in the current model the interfacial velocity was found to be one to two orders of magnitude smaller than the Darcy velocity based on the assumption that the liquid saturation at the interface is less than unity and its value is determined through a momentum and mass balance shown in Eqs. (45) and (46). Since the two-phase zone was decoupled from the liquid film in model 1 of Majumdar and Tien (1990), it would perform relatively better for systems with a lower R value, where the porous matrix plays a minor role. As shown in the comparison, model 1 did relatively well for the 350 μm case (R = 1980), but gets worse as the R value is increased to 4279 and 7923 for the 900 μm and 1500 μm beads, respectively. A similar conclusion was also made by Majumdar and Tien (1990) for the comparison of their model 1 with the experimental results of White and Tien (1987b). For completeness, comparisons are also made between the predictions of the current model and the same experimental results of White and Tien (1987b) in Figs. 6(a) and 6(b). It may be summarized that both the current model and model 1 of Majumdar and Tien (1990) perform very well for the aluminum foam metal, which has a very low R value of 1862. For the polyurethane with an R value of 25,021, the porous matrix and the two-phase zone are becoming important. The current model slightly overpredicted while model 1 overpredicted by more than one order of magnitude. The slight overprediction could be due to the fact that the porous sample used by White and Tien (1987b) is only 1.6 cm in thickness and 1.6 cm in width such that there may not be enough room for the two-phase zone to become fully developed. Cheng (1981) also assumed the Darcy velocity at the interface but predicted much lower condensation rates as compared to those of Majumdar and Tien (1990). The lower

Downloaded 13 Dec 2010 to 193.140.21.150. Redistribution subject to ASME license or copyright; see http://www.asme.org/terms/Terms_Use.cfm

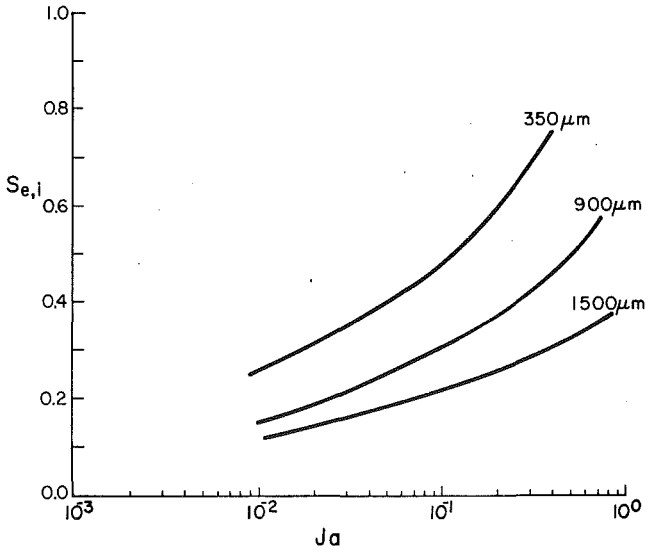

Fig. 7 Liquid saturation of the two-phase zone at the interface

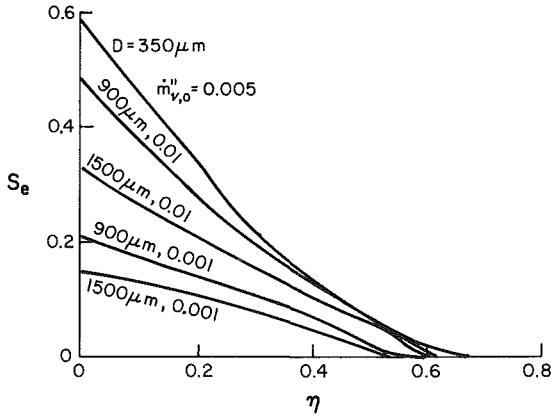

Fig. 8 Typical saturation profiles in the two-phase zone

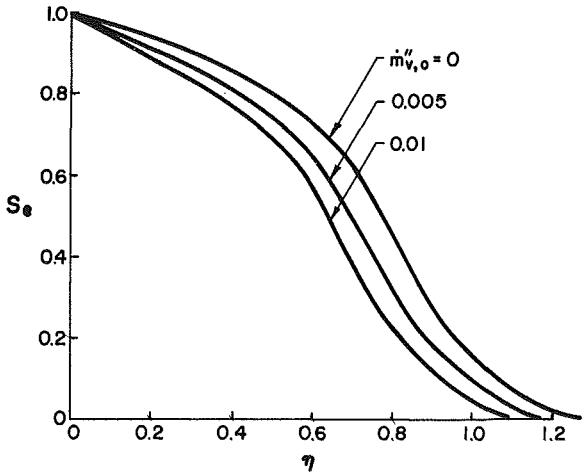

Fig. 9 Saturation profiles in the two-phase zone

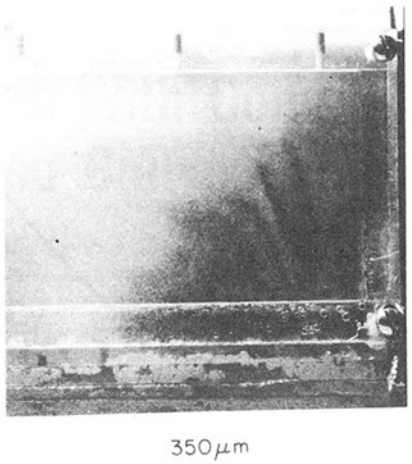

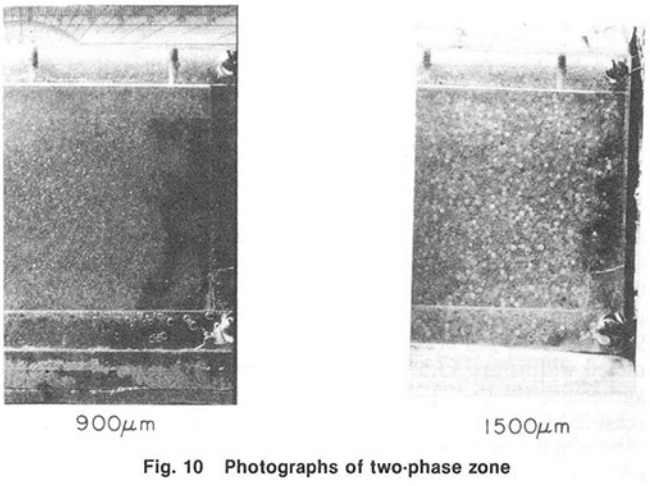

Fig. 10 Photographs of two-phase zone

rates are mainly resulted from much thicker liquid films because of the lack of a two-phase fringe, which thins the liquid film by drawing liquid away from the interface. The current model also predicted three different curves for the three bead sizes because of the nonsimilar governing equations for the liquid film, which is also the case for Majumdar and Tien (1990). The current model did relatively well for glass beads of 900 μm and 1500 μm in diameter and slightly overpredicted the 350 μm glass beads.

Figure 7 plots the liquid saturation of the two-phase zone at the interface, $S_{e,i}$. As shown in the figure, a common trend is that the liquid saturation increases monotonically with increasing Ja and with the decreasing bead size. As a result, the interfacial velocity becomes slower as Ja is decreased and the bead size is increased.

Figure 8 shows some typical liquid saturation profiles in the two-phase region. The profiles are, in general, linear near the interface between the liquid film and the two-phase region. The slopes are flattened as the pure vapor zone is approached. It is interesting to note that the dimensionless two-phase zone sizes for all the cases investigated are around 0.6.

Figure 9 is designed to show explicitly the effect of vapor flow on the saturation profile in the two-phase zone. For all three cases, the liquid saturation at the interface is assumed to be unity. The vapor flow effect is obscured in Fig. 8 where the saturation at the interface varies with the strength of the vapor flow. In Fig. 9 the strength of vapor flow, $\dot{m}''_{v,o}$, ranges from zero to 0.01. The saturation pattern is basically unaffected, but the size of the two-phase region is reduced for increasing vapor flow.

We also tried to measure the size of the two-phase zone by injecting red liquid dye as shown in Fig. 2. It was expected that the dye would be carried by the liquid back flow in the flow-phase zone. In general, we found that the measured sizes of the two-phase zone range between 70 and 80 percent of the predicted values. The discrepancy is probably due to the fact that the dye becomes too diluted to be recognized or the flow

Downloaded 13 Dec 2010 to 193.140.21.150. Redistribution subject to ASME license or copyright; see http://www.asme.org/terms/Terms_Use.cfm

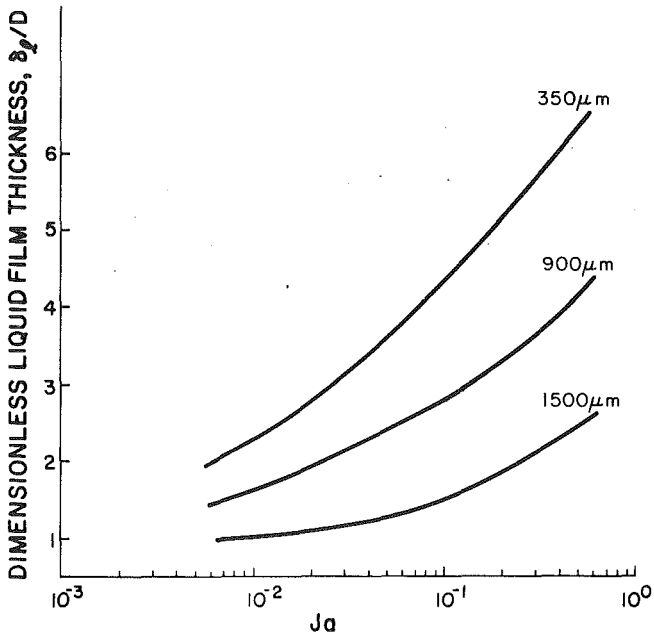

Fig. 11 Liquid film thickness

is too weak to carry the dye. Figure 10 shows the photographic results for the size and shape of the two-phase zone. The widths of the two-phase zone at the bottom of the porous bed measured from the photographs are 10.5, 6.5, and 3.1 cm for 350, 900, and 1500 μm beads, respectively. The corresponding predicted widths are 13.5, 8.7, and 5.6 cm based on Fig. 8. The agreement between the experimental and predicted results is reasonably good. Also the shapes of the two-phase zone as shown in the photographs are very close to the boundary layer pattern predicted by the mathematical model.

The liquid-film thickness, nondimensionalized by the diameter of the glass beads, is shown in Fig. 11 as a function of the Jakob number. For all three bead sizes, the trends are similar in that the dimensionless thickness increases exponentially with the dimensionless condensation potential, the Jakob number. This is expected because of the semilogarithmic scale. For the range of Jakob number investigated, the liquid film thickness is on the order of one to five glass bead diameters. Liquid-film thicknesses predicted by Cheng (1981) are at least 20 times thicker than those shown in Fig. 10. As a result of the extremely thin liquid films and the presence of a solid condenser surface, the transport properties, especially the permeability, were properly adjusted based on the model of White and Tien (1987a). They suggested that the porosity is unity at the wall and both the porosity and the permeability decay exponentially from the wall to their free-stream values in one to two diameters. Also owing to the thin liquid films, we included the second-order diffusion term in the liquid-film momentum Eq. (2) such that the no-slip boundary condition (42) can be applied, which was also suggested by White and Tien (1987a).

Conclusions

A mathematical model and some experimental results for the condensation heat and mass transfer in a porous medium bounded by a cold vertical surface are presented in this paper. The mathematical model is based on a three-zone approach, where the two-phase mixture separates the liquid film and the pure vapor core. The effect of the vapor flow is included in the modeling of the two-phase zone. A key step in the mathematical modeling, which deviates from previous analyses, is that the interfacial velocity is determined through the matching of momentum and the total mass balance instead of assuming the Darcy velocity. The predicted results of the present model compare reasonably well with the experimental measurements. The current model slightly overpredicts the condensation heat transfer for the 350 μm size glass beads. The interfacial velocities obtained are about one to two orders of magnitude smaller than the corresponding Darcy velocities. The liquid-film thickness as predicted by the present model is on the order of the glass bead diameter, which in turn requires the inclusion of the second-order diffusion term in the momentum equation and special accommodation for the porous transport properties such as the porosity and the permeability due to the presence of a solid wall.

Acknowledgments

The authors would like to acknowledge the support of the National Science Foundation under grant No. CBT-84-18497.

References

Bau, H. H., and Torrance, K. E., 1982, "Boiling in Low-Permeability Porous Materials," *International Journal of Heat and Mass Transfer*, Vol. 25, pp. 45–55.

Bear, J., 1972, *Dynamics of Fluids in Porous Media*, America Elsevier Pub. Co., New York.

Brooks, R. H., and Corey, A. T., 1964, "Hydraulic Properties of Porous Media," Colorado State University, Hydro. paper No. 3.

Cheng, P., 1981, "Film Condensation Along an Inclined Surface in a Porous Medium," *International Journal of Heat and Mass Transfer*, Vol. 24, pp. 983–990.

Cheng, P., and Chui, D. K., 1984, "Transient Film Condensation on a Vertical Surface in a Porous Medium," *International Journal of Heat and Mass Transfer*, Vol. 27, pp. 795–798.

Fatt, I., and Klikoff, W. A., 1959, "Effect of Fractional Wettability on Multiphase Flow Through Porous Media," AIME Technical Note 2043; *AIME Transactions*, Vol. 216, pp. 246–257.

Kaviany, M., 1986, "Boundary Layer Treatment of Film Condensation in the Presence of a Solid Matrix," *International Journal of Heat and Mass Transfer*, Vol. 29, pp. 951–954.

Leverett, M. C., 1941, "Capillary Behavior in Porous Solids," *AIME Transactions*, Vol. 142, pp. 152–169.

Majumdar, A., and Tien, C. L., 1990, "Effects of Surface Tension on Film Condensation in a Porous Medium," ASME JOURNAL OF HEAT TRANSFER, Vol. 112, pp. 751–757.

Nilson, R. H., and Romero, L. A., 1980, "Self-Similar Condensing Flows in Porous Media," *International Journal of Heat and Mass Transfer*, Vol. 23, pp. 1461–1470.

Nussett, W., 1916, "Die Oberflachen-kondensation des Wasserdampfes," *VDI Zeitung*, Vol. 60, pp. 541–546, 569–575.

Plumb, O. A., 1984, "Capillary Effects on Film Condensation in Porous Media," presented at the 19th AIAA Thermophysics Conference, Snowmass, CO.

Plumb, O. A., Burnett, D. B., and Shekarriz, A., 1990, "An Experimental Investigation of Film Condensation in a Porous Bed," ASME JOURNAL OF HEAT TRANSFER, Vol. 112, pp. 235–239.

Schiedigger, A. E., 1974, *The Physics of Flow Through Porous Media*, 3rd ed., University of Toronto Press, Toronto, Canada.

Shekarriz, A., and Plumb, O. A., 1986, "A Theoretical Study of Filmwise Condensation Using Porous Fins," ASME Paper No. 86-HT-31.

Udell, K. S., 1983, "Heat Transfer in Porous Media Heated From Above With Evaporation, Condensation, and Capillary Effects," ASME JOURNAL OF HEAT TRANSFER, Vol. 105, pp. 485–492.

Udell, K. S., 1985, "Heat Transfer in Porous Media Considering Phase Change and Capillarity—The Heat Pipe Effect," *International Journal of Heat and Mass Transfer*, Vol. 28, pp. 485–495.

Verma, A. K., Pruess, K., Tsang, C. F., and Witherspoon, P. A., 1985, "A Study of Two-Phase Concurrent Flow of Steam and Water in an Unconsolidated Porous Medium," *Heat Transfer in Porous Media and Particulate Flows*, L. S. Yao, ed., ASME HTD-Vol. 46.

White, S. M., and Tien, C. L., 1987a, "Analysis of Laminar Film Condensation in a Porous Medium," *Proceedings of the 1987 ASME-JSME Thermal Engineering Joint Conference*, Vol. 2, pp. 401–406.

White, S. M., and Tien, C. L., 1987b, "An Experimental Investigation of Film Condensation in Porous Structures," *Proceedings of the 6th International Heat Pipe Conference*, Grenoble, France.

Downloaded 13 Dec 2010 to 193.140.21.150. Redistribution subject to ASME license or copyright; see http://www.asme.org/terms/Terms_Use.cfm

Y. Cao

A. Faghri

Department of Mechanical and Materials Engineering,
Wright State University,
Dayton, OH 45435

A Study of Thermal Energy Storage Systems With Conjugate Turbulent Forced Convection

A phase-change energy storage module with a turbulent transport fluid is studied. The forced convection due to the turbulent transport fluid is solved with the k–ϵ model and coupled with the phase-change solution in the phase-change material (PCM). The numerical method is first compared with previous investigations, then conjugate computations for the energy storage module with different cases are conducted. A correlation for the energy storage capacity is derived and its empirical constants are determined by the numerical data. The correlation provides a reference for the module design and parameter optimization.

Introduction

The study of phase-change thermal energy storage systems is important due to applications in space-based power plants and solar energy utilization (Viskanta, 1983). Another application of phase-change energy storage is space-based heat-sink systems. Since phase-change materials (PCMs) have a large latent heat, it is an efficient way to absorb the waste heat energy in a short time when systems receive heat input and release it to space over a long period of time.

Thermal energy systems usually consist of a number of PCM modules with various possible configurations. Figure 1 presents a typical module, which consists of a hollow cylinder of phase-change material with a transfer fluid pumped through the interior tube for the purpose of heat energy exchange. The study of these PCM modules is essential to understand the characteristics of the PCM energy storage system. The problem by nature involves time-dependent phase-change heat transfer combined with conjugate forced convection.

Sparrow and Hsu (1981) numerically solved the conjugate phase-change/convection problem for two-dimensional freezing on the outside of a coolant-carrying tube with a constant heat transfer coefficient h for the coolant flow. Shamsundar (1982) presented an analytical closed-form solution for the same problem by neglecting the heat capacities and axial conduction effects in the PCM. The analytical results compared favorably with the numerical solution of Sparrow and Hsu (1981) for the case with Stefan number St = 0. In both of the above investigations, the thickness of the PCM outside the circular tube was considered to be infinite, the PCM was initially at its freezing temperature, and only the heat conduction in the solid region was considered.

More recently, the PCM module similar to that in Fig. 1 was studied by Solomon et al. (1986), Stovall and Arimilli (1988), and Yimer and Adami (1989). The studies were focused on the diffusion-controlled heat transfer in the PCM, with the heat transfer between the transfer fluid and the PCM calculated using empirical correlations for the heat transfer coefficient. Since the temperature field of the transfer fluid continues to change as the phase-change interface progresses, the use of a steady-state fully developed empirical heat transfer correlation and the assumption of a constant fluid temperature may result in a significant error in the evaluation of the system performance. To account for the temperature change in the transfer fluid along the axial direction, the technique adopted by Sparrow and Hsu (1981) and by Shamsundar (1982) can be used, in which the solution for the PCM is coupled by an energy balance over the transfer fluid by assuming a heat transfer coefficient between the transfer fluid and the PCM. In this technique, the heat transfer coefficient must be calculated using empirical correlations or other numerical solutions based on the steady-state constant heat rate or constant surface temperature condition. However, for transfer fluids with low Prandtl numbers, the heat transfer coefficient at the PCM–transfer fluid interface changes significantly along the axial direction, and the boundary condition there is neither steady-state constant heat rate nor constant surface temperature. Also, axial conduction in the transfer fluid cannot be neglected for low-Pr fluids. In addition, all the results presented in the previous studies, except those of Shamsundar (1982) for St = 0, are only some specific cases and general trends for the module performance, and no explicit relation for performance parameters related to the module design was given. This will surely limit the application of the previous studies.

In this paper, the conservation equations for turbulent flow were solved by applying the k–ϵ model, which was coupled with the heat conduction in the PCM. The numerical model was examined by comparing solutions for different cases with those of Shamsundar (1982) and Sparrow and Hsu (1981). Correlations for important parameters such as the energy storage capacity were derived. The constants in the correlation were determined by the numerical data generated from the conjugate numerical computation. To the authors' knowledge, this is the first effort to obtain such correlations for the PCM energy storage system design.

Mathematical Formulation

Conservation Equations for the Transfer Fluid. In energy

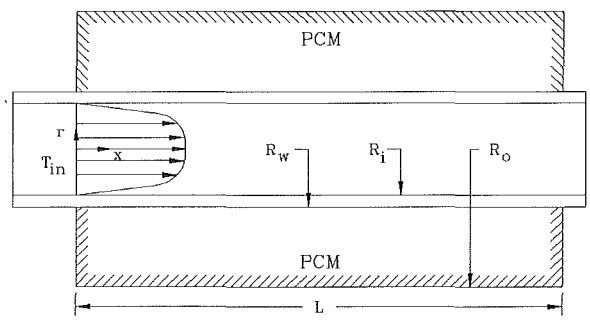

Fig. 1 Schematic of PCM energy storage module

Contributed by the Heat Transfer Division and presented at the ASME Winter Annual Meeting, Atlanta, Georgia, December 1–6, 1991. Manuscript received by the Heat Transfer Division March 1991; revision received June 1992. Keywords: Conjugate Heat Transfer, Phase-Change Phenomena, Thermal Energy Storage. Associate Technical Editor: J. H. Kim.

Copyright © 1992 by ASME
Downloaded 13 Dec 2010 to 193.140.21.150. Redistribution subject to ASME license or copyright; see http://www.asme.org/terms/Terms_Use.cfm

storage systems, large amounts of heat must be transferred between the PCM and the transfer fluid. Under this operating condition, the flow rate of the transfer fluid must be high, and the flow is turbulent in most cases. In this study, the incompressible Reynolds equations and the standard k–ϵ model were applied to the transport fluid. The turbulent time-averaged continuity, momentum, and energy equations in a two-dimensional cylindrical coordinate system can be written as:

$$\frac{1}{r}\frac{\partial}{\partial r}(rV)+\frac{\partial U}{\partial x}=0 \tag{1}$$

$$\frac{\partial(\rho V)}{\partial t}+\frac{\partial}{\partial x}(\rho VU)+\frac{1}{r}\frac{\partial}{\partial r}(\rho rV^2)=-\frac{\partial p}{\partial r}+\frac{1}{r}\frac{\partial}{\partial r}\left(r\mu_{\text{eff}}\frac{\partial V}{\partial r}\right)+\frac{\partial}{\partial x}\left(\mu_{\text{eff}}\frac{\partial V}{\partial x}\right)+S_v \tag{2}$$

$$\frac{\partial(\rho U)}{\partial t}+\frac{\partial}{\partial x}(\rho U^2)+\frac{1}{r}\frac{\partial}{\partial r}(\rho rUV)=-\frac{\partial p}{\partial x}+\frac{1}{r}\frac{\partial}{\partial r}\left(r\mu_{\text{eff}}\frac{\partial U}{\partial r}\right)+\frac{\partial}{\partial x}\left(\mu_{\text{eff}}\frac{\partial U}{\partial x}\right)+S_u \tag{3}$$

$$\frac{\partial T}{\partial t}+\frac{\partial}{\partial x}(UT)+\frac{1}{r}\frac{\partial}{\partial r}(rVT)=\frac{1}{r}\frac{\partial}{\partial r}\left(r\Gamma_{\text{eff}}\frac{\partial T}{\partial r}\right)+\frac{\partial}{\partial x}\left(\Gamma_{\text{eff}}\frac{\partial T}{\partial x}\right) \tag{4}$$

where

$$S_v=-\frac{\mu V}{r^2}+\frac{\partial}{\partial x}\left(\mu_t\frac{\partial U}{\partial r}\right)+\frac{1}{r}\frac{\partial}{\partial r}\left(r\mu_t\frac{\partial V}{\partial r}\right)-\frac{1}{r}\frac{\partial}{\partial r}\left(\frac{2}{3}rk\rho\right)$$

$$S_u=\frac{\partial}{\partial x}\left(\mu_t\frac{\partial U}{\partial x}\right)+\frac{1}{r}\frac{\partial}{\partial r}\left(r\mu_t\frac{\partial V}{\partial x}\right)-\frac{\partial}{\partial x}\left(\frac{2}{3}k\rho\right)$$

$$\mu_{\text{eff}}=\mu+\mu_t$$

$$\Gamma_{\text{eff}}=\alpha+\frac{\mu_t/\rho}{\text{Pr}_t}$$

$\mu_t = \rho C_\mu k^2/\epsilon$ is the turbulent eddy viscosity, k is the kinetic energy of turbulence, and ϵ is the dissipation rate of turbulence.

The differential equations conserving the transport of k and ϵ are

$$\frac{\partial}{\partial t}(\rho k)=-\nabla\cdot(\rho\mathbf{V}k+\mathbf{q}^k)+S_k \tag{5}$$

$$\frac{\partial}{\partial t}(\rho\epsilon)=-\nabla\cdot(\rho\mathbf{V}\epsilon+\mathbf{q}^\epsilon)+S_\epsilon \tag{6}$$

where

$$S_k=G-\rho\epsilon$$

$$S_\epsilon=\frac{\epsilon}{k}(C_1G-C_2\rho\epsilon)$$

$$\mathbf{q}^k=-\Gamma_k\nabla k,\quad \Gamma_k=\frac{\mu_t}{\sigma_k}$$

$$\mathbf{q}^\epsilon=-\Gamma_\epsilon\nabla\epsilon,\quad \Gamma_\epsilon=\frac{\mu_t}{\sigma_\epsilon}$$

$$G=\mu_t\left[2\left[\left(\frac{\partial U}{\partial x}\right)^2+\left(\frac{\partial V}{\partial r}\right)^2+\left(\frac{V}{r}\right)^2\right]+\left(\frac{\partial U}{\partial r}+\frac{\partial V}{\partial x}\right)^2\right]$$

The standard turbulence model constants are (Launder and Spalding, 1974):

$$C_\mu=0.09,\quad C_1=1.44,\quad C_2=1.92,\quad \sigma_k=1.0,\quad \sigma_\epsilon=1.3 \tag{7}$$

Boundary Conditions for the Transfer Fluid:

Inlet plane: $x = 0$

$$0<r<R_i:\quad U=U_{in},\quad T=T_{in} \tag{8}$$

Outlet plane: $x = L$

$$0<r<R_i:\quad \frac{\partial U}{\partial x}=0,\quad \frac{\partial V}{\partial x}=0,\quad \frac{\partial T}{\partial x}=0 \tag{9}$$

For the turbulent flow and heat transfer near the fluid–wall interface, the wall functions are applied (Launder and Spalding, 1974; Djilali et al., 1989).

Wall shear stress:

$$\frac{U_p}{U_\tau}=\frac{1}{\kappa}\ln(y_p^+E) \tag{10}$$

where

$$U_\tau=\sqrt{\tau_w/\rho},\quad y_p^+=\frac{y_pU_\tau}{\nu},\quad E=9.0.$$

This expression is used to evaluate the near-wall diffusion terms in the momentum equations.

Nomenclature

c = specific heat, J/(kg-K)
c_m = specific heat of mushy phase = $(c_s+c_l)/2$, J/(kg-K)
c_p = specific heat of PCM, J/(kg-K)
C_1, C_2, C_μ = turbulence model constants
C = coefficient in Eq. (14), J/(kg-K)
C', C'' = correlation constants
D = diameter of the circular cylinder = $2R_i$, m
E = constant in near-wall description of velocity profile
g_l, g_s = integrals in Eq. (19)
G = source term in Eqs. (5) and (6)
H = latent heat, J/kg
h = heat transfer coefficient, W/(m^2-K)
k = kinetic energy of turbulence, m^2/s^2
K = thermal conductivity, W/(m-K)
L = length of PCM module, m
M = total mass of the PCM module, kg
Nu_f = Nusselt number = $2R_ih/K_f$
p = pressure, N/m^2
Pr_f = fluid Prandtl number = ν/α
Pr_t = turbulent fluid Prandtl number
Q = heat energy, J
Q_t = total energy stored or energy storage capacity, J
Q_m = energy storage density = Q_t/M, J/kg
q_{fw} = heat flux at the wall–PCM interface, W/m^2
R = phase-change interface radius, m
R_i = inside radius of the pipe, m
R_o = outside radius of the PCM module, m
R_w = radius of the wall–PCM interface, m
Re_f = fluid Reynolds number = U_mD/ν
S = term in Eq. (14), J/kg
S^2 = characteristic area of the annular PCM = $\pi(R_o^2-R_i^2)L/(R_o-R_i)$, m^2

Downloaded 13 Dec 2010 to 193.140.21.150. Redistribution subject to ASME license or copyright; see http://www.asme.org/terms/Terms_Use.cfm

Turbulent Kinetic Energy: The turbulent kinetic energy k is neither convected nor diffused into the control volume across the wall. A zero normal velocity assures the former, while setting the boundary condition $\partial k/\partial y|_w = 0$ guarantees the latter. Also,

$$\bar{\epsilon} = \frac{C_\mu^{3/4} k^{3/2}}{\kappa y_p} \ln (E y_p^+) \tag{11}$$

is used to evaluate the dissipation term $-\rho\epsilon$ in Eq. (5).

Dissipation Rate: At a node p adjacent to the wall in the transport fluid, ϵ is evaluated under the local equilibrium condition as

$$\epsilon = C_\mu^{3/4} \frac{k_p^{3/2}}{\kappa y_p} \tag{12}$$

Temperature: Given a heat flux q_{fw}, the interface temperature can be obtained from

$$\frac{(T_{fw} - T_p)\rho c_f C_\mu^{1/4} k_p^{1/2}}{q_{fw}} = \mathrm{Pr}_t \left[\frac{1}{\kappa} \ln (E y_p^+) + P \right] \tag{13}$$

where

$$P = 9.0 \left(\frac{\mathrm{Pr}_f}{\mathrm{Pr}_t} - 1 \right) \left(\frac{\mathrm{Pr}_t}{\mathrm{Pr}_f} \right)^{0.25}$$

and q_{fw} should be coupled with the PCM solution.

Conservation Equations for the PCM. The phase-change model applied is the efficient temperature-based fixed-grid formulation that was developed by Cao and Faghri (1990). This model has the advantage of eliminating the time step and grid size limitations that are normally encountered in other fixed-grid methods.

$$\frac{\partial(\rho C T)}{\partial t} = \frac{1}{r}\frac{\partial}{\partial r}\left(Kr \frac{\partial T}{\partial r} \right) + \frac{\partial}{\partial x}\left(K \frac{\partial T}{\partial x} \right) - \frac{\partial(\rho S)}{\partial t} \tag{14}$$

where

$$C(T) = \begin{cases} c_s & (T < T_m - \delta T) \\ c_m + \dfrac{H}{2\delta T} & (T_m - \delta T \le T \le T_m + \delta T) \\ c_l & (T > T_m + \delta T) \end{cases}$$

$$S(T) = \begin{cases} c_s(\delta T - T_m) & (T < T_m - \delta T) \\ -\left(c_m + \dfrac{H}{2\delta T} \right) T_m + c_m \delta T + \dfrac{H}{2} & (T_m - \delta T \le T \le T_m + \delta T) \\ -c_l T_m + c_s \delta T + H & (T > T_m + \delta T) \end{cases}$$

$$K(T) = \begin{cases} K_s & (T < T_m - \delta T \\ K_s + (K_l - K_s)(T - T_m + \delta T)/2\delta T & (T_m - \delta T \le T \le T_m + \delta T) \\ K_l & (T > T_m + \delta T) \end{cases}$$

Equation (14) is also applicable to heat transfer in the container wall with $C = c_w$, $K = K_w$, and $S = 0$. In addition, the possibility of natural convection occurring in the PCM was neglected due to the primary space application concerned. The initial condition for the system and boundary conditions for the PCM and pipe wall are as follows:

Initial Conditions: $t = 0$

Entire domain: $0 \le x \le L$, $0 \le r \le R_o$

Nomenclature (cont.)

St = Stefan number $= c_p(T_{in} - T_m)/H$ for melting or $c_p(T_m - T_{in})/H$ for freezing
T = temperature, K
T_{fm} = fluid mixed-mean temperature, K
T_m = melting or freezing temperature, K
t = time, s
U_{in} = inlet velocity, m/s
U_m = mean velocity in the pipe, m/s
U_p = velocity at node p, m/s
U, V = time-averaged turbulent velocities, m/s
V_p = total PCM volume of the module $= \pi(R_o^2 - R_i^2)L$, m^3
$\mathbf{V}$ = velocity vector
x, r = coordinate directions
y_p = distance from the wall to the adjacent node p, m
α = molecular thermal diffusivity, m^2/s
Γ = diffusion coefficient
δ_w = thickness of container wall, m
$2\delta T^o$ = phase-change temperature range or mushy phase range, K
ϵ = dissipation rate of turbulence, m^2/s^3
κ = von Karman constant
μ = molecular viscosity, kg/(m-s)
μ_t = turbulent viscosity, kg/(m-s)
ν = kinematic viscosity, m^2/s
ρ = density, kg/m^3
$\sigma_k, \sigma_\epsilon$ = turbulence model constant
τ = Fourier number $= \alpha_p t/S^2$, or shear stress, N/m^2

Subscripts

eff = effective
f = transfer fluid
fw = fluid–wall interface
i = initial condition
in = inlet
s = solid PCM, or sensible heat energy
l = liquid PCM or latent heat
m = mushy phase or mean value
p = PCM or grid point near fluid–wall interface in the transfer fluid
t = turbulent
w = container wall

Downloaded 13 Dec 2010 to 193.140.21.150. Redistribution subject to ASME license or copyright; see http://www.asme.org/terms/Terms_Use.cfm

$$T = T_i \tag{15}$$

Boundary Conditions: $t > 0$

Outer Wall: $0 \le x \le L$, $r = R_o$

$$\frac{\partial T}{\partial r} = 0 \tag{16}$$

At both ends: $x = 0$ and L, $R_i \le r \le R_o$

$$\frac{\partial T}{\partial x} = 0 \tag{17}$$

PCM-wall interface: $0 \le x \le L$, $R = R_w$

$$K_p \frac{\partial T}{\partial r}\bigg|_{r=R_w^+} = K_w \frac{\partial T}{\partial r}\bigg|_{r=R_w^-}$$

Fluid-wall interface: $0 \le x \le L$, $r = R_i$

$$T = T_{fw} \tag{18}$$

The transient conjugate analysis of Cao and Faghri (1991) for laminar flow showed that the velocity reached the steady state very quickly from the initial zero velocity, while the temperature counterpart continued to change as the phase-change front moved in the PCM. Therefore, the velocity transient period can be ignored without losing generality in the numerical modeling. Also, for most engineering problems the inlet velocity can be assumed to be in the fully developed turbulent state because of the connecting pipeline between the PCM system and the pump. These assumptions simplified the model and reduced computation time significantly.

The key module parameters used to evaluate the performance of a thermal energy storage system are the energy storage capacity or total energy stored/extracted, Q_t (J), and the energy storage density $Q_m = Q_t/M$ (J/kg), where M is the total mass of the PCM module.

The total energy stored Q_t consists of two parts, i.e., the latent heat energy and the sensible heat energy:

$$Q_t = Q_l + Q_s = \rho H \pi \int_0^L (R^2(x, t) - R_i^2)dx + 2\pi\rho \int_{R_i}^{R_o}\int_0^L c_p(T - T_i)rdrdx = \rho H \pi g_l + 2\pi\rho g_s \tag{19}$$

where $g_l = \int_0^L (R^2(x, t) - R_i^2)dx$, $g_s = \int_{R_i}^{R_o}\int_0^L c_p(T - T_i)\, rdrdx$, $R(x, t)$ is the radius of the melting interface at time t, and T_i is the initial temperature of the PCM system.

Numerical Procedure and Fluid-Wall Interface Treatment

The problem specified in the last section was solved by applying the control-volume finite-difference approach described by Patankar (1980, 1988). The discretization equations were obtained by applying the conservation laws over a finite size control volume surrounding the grid node and integrating over the control volume. The SIMPLE algorithm was used to solve the velocity and pressure for the transport fluid. Since the fluid is incompressible, they are decoupled from the temperature solution. For the temperature solution, Cao and Faghri (1991) applied the harmonic mean of the thermal conductivity at the fluid-PCM interface for the laminar flow such as (for a uniform grid size)

$$K_p \frac{\partial T}{\partial r}\bigg|_{r=R_i^+} = K_f \frac{\partial T}{\partial r}\bigg|_{r=R_i^-} = \frac{2K_pK_f}{K_f + K_p}\frac{\partial T}{\partial r}\bigg|_{r=R_i} \tag{20}$$

and solved the transport fluid and PCM as a single-domain problem.

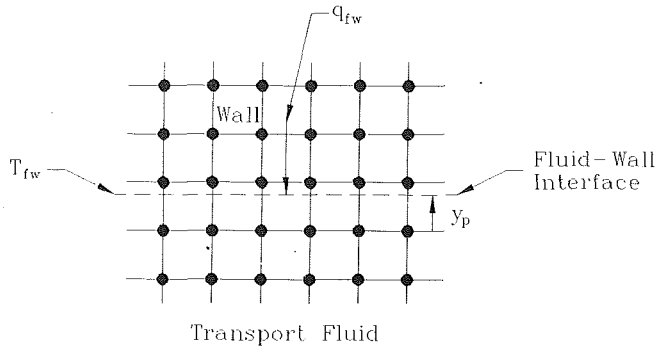

Fig. 2 Schematic of grid arrangement around the fluid-wall interface

For the present problem, however, the transport fluid is turbulent so this approach is not applicable. The reason is that the temperature gradient in the transfer fluid is very steep at the fluid-wall interface. In this numerical model, the transfer fluid and PCM-wall regions were solved separately and coupled via the wall function. Figure 2 represents the grid arrangement around the fluid-wall interface. The two-domain problem was solved sequentially and iteratively. During the iterations at each time step, the PCM-wall region was first solved with the T_{fw} from the previous iteration as a boundary condition. The q_{fw} was then estimated by the relation:

$$q_{fw} = K_w \frac{\partial T}{\partial r} \tag{21}$$

using the temperatures at the grids in the pipe wall close to the interface. This q_{fw} was then applied in the turbulent wall function, Eq. (13), to solve for the temperature in the transfer fluid. The interface temperature T_{fw} was recalculated from the transfer fluid solution and used as a boundary condition for the PCM-wall region in the next iteration. The whole iteration procedure was repeated until a converged solution was obtained for each time step. The converged results were assumed to be reached when the maximum relative change of temperature between the consecutive iterations was less than 5×10^{-5}. Different grid sizes for the same problem were tested and it was demonstrated that the numerical solutions were essentially independent of the grid size used. A change from 25×29 to 50×56, for example, resulted in changes in the energy storage capacity and the outlet transport fluid temperature of about 2 and 1 percent, respectively. The grid size and time step are given in the next section for the case presented.

Results and Discussion

The computer codes for both the turbulent model of the transport fluid and the phase-change model of the PCM in a cylindrical coordinate system have been checked against two correlations and a numerical solution in the literature, respectively, to validate the numerical accuracy. Figure 3 shows the comparison of the present numerical solution and the experimental correlations for the fully developed turbulent forced convection Nusselt number with Pr = 0.706. Both correlations shown in the figure were considered to have a high degree of accuracy in representing a large variety of turbulent experimental data (Kays and Crawford, 1980; Bhatti and Shah, 1987). As can be seen, the agreement between the numerical solution and the correlations is good. Figure 4 compares the present numerical phase-change radius with the one-dimensional numerical result of Lunardini (1981). The geometry of the phase-change system studied was a circular cylinder surrounded by an infinite, homogeneous medium. The agreement between the two numerical solutions is very good. More information concerning the PCM model verification can be found in the paper by Cao and Faghri (1990).

Downloaded 13 Dec 2010 to 193.140.21.150. Redistribution subject to ASME license or copyright; see http://www.asme.org/terms/Terms_Use.cfm

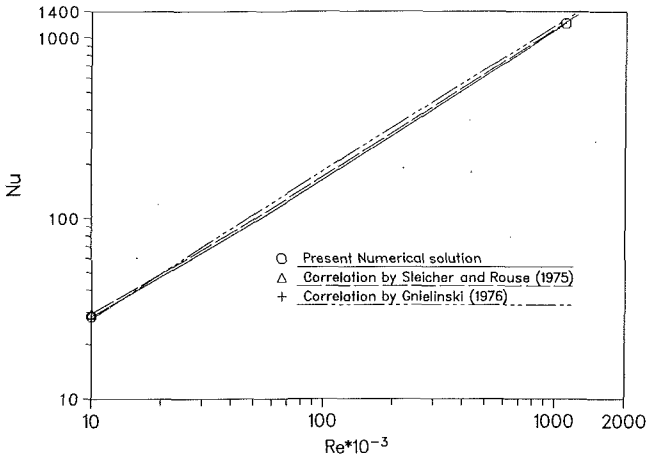

Fig. 3 Comparison of numerical solution and the experimental correlations for fully developed turbulent Nusselt number with Pr = 0.706

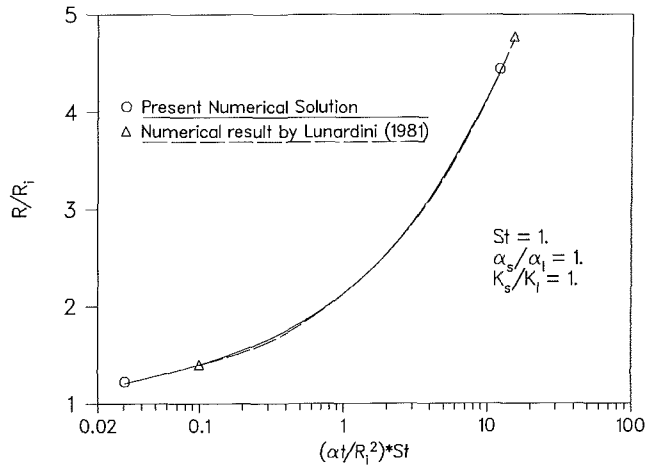

Fig. 4 Comparision of phase-change radius of a cylinder surrounded by an infinite PCM medium

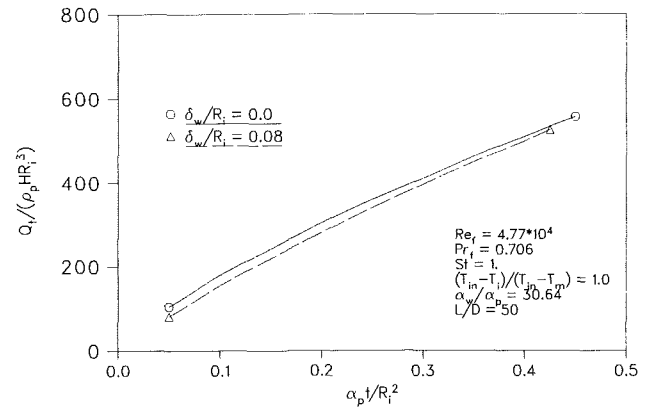

Fig. 5 The effect of the pipe wall on the energy storage capacity

The effect of the pipe wall on the performance of the energy storage module was examined by running cases with a wall of zero thickness, $\delta_w/R_i = 0.0$, and with a fairly thick wall, $\delta_w/R_i = 0.08$. The total energies extracted from the PCM for the two cases are plotted in Fig. 5. In the early period, the total energy extracted from the PCM with a thick wall was slightly less than that with a wall of zero thickness. Over time, however, the total energies extracted for the two cases are almost the same. Since the pipe wall has a much higher thermal conductivity than that of the PCM, which provides a significant heat path between the transfer fluid and the PCM, the influence

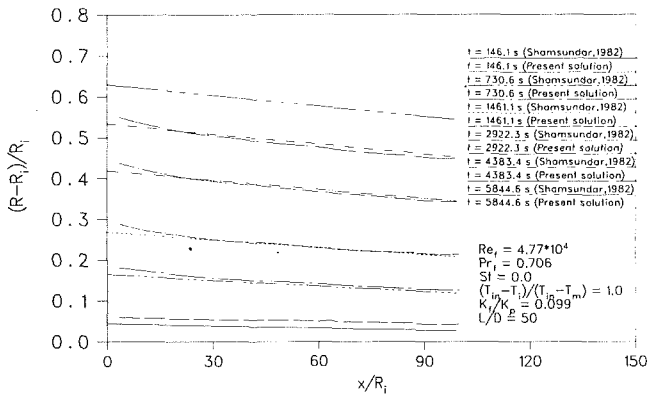

Fig. 6 Comparisons of phase-change fronts at different times for the conjugate one-region phase-change problem (St = 0.0)

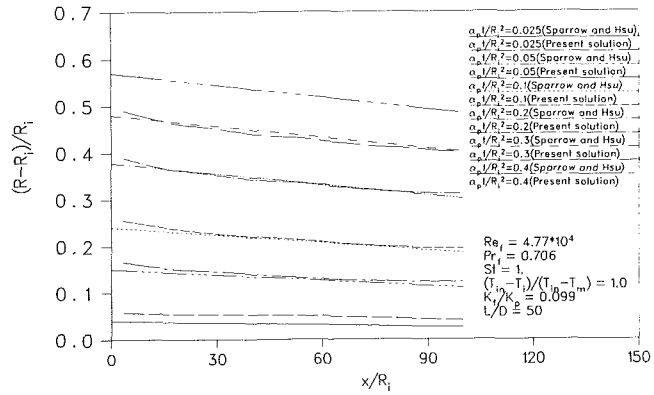

Fig. 7 Comparisons of phase-change fronts at different times for the conjugate one-region problem (St = 1.0)

of the container wall on the heat transfer in the PCM is very small. The same conclusion was also drawn by Cao and Faghri (1991) with laminar transfer fluids. For this reason, the thickness of the container wall is considered to be negligibly small in the following analysis for simplicity.

Before proceeding to the analysis of the energy storage module in Fig. 1, the numerical method is examined by simulating the one-region conjugate phase-change problem presented by Sparrow and Hsu (1981). Figure 6 compares the present solutions for the thickness of the frozen layer with the closed-form solution by Shamsundar (1982) using the Newton–Raphson/Secant method. The agreement between the two solutions is very good except at the very early operation time in which the transient behavior of the transfer fluid is very important, which was not taken into account in the closed-form solution of Shamsundar (1982). In the analysis of Shamsundar (1982), the sensible heat and axial conduction in the PCM were neglected, and the initial system temperature was assumed to be at the freezing temperature. The transfer fluid temperature was obtained by making an energy balance over the PCM and the transfer fluid with an assumed heat transfer coefficient. The solution is a function of Biot number, hR_i/K, and Stanton number, $h/\rho U_m c_f$. The case in which the comparison was made corresponds to $hR_i/K = 5.0$ and $h/\rho U_m c_f = 0.003$. In the present computation, the operational parameters such as Re_f and K_f/K_p were determined based on these Biot and Stanton numbers, in which the heat transfer coefficient h was obtained via the correlation by Gnielinski (1976) for a given Prandtl number. It can be seen from the comparison that little error was introduced by using a constant h for the gaseous transfer fluid with relatively high Prandtl number except in the region very close to the entrance. Figure 7 compares the present solution and the numerical solution by Sparrow and Hsu (1981)

Downloaded 13 Dec 2010 to 193.140.21.150. Redistribution subject to ASME license or copyright; see http://www.asme.org/terms/Terms_Use.cfm

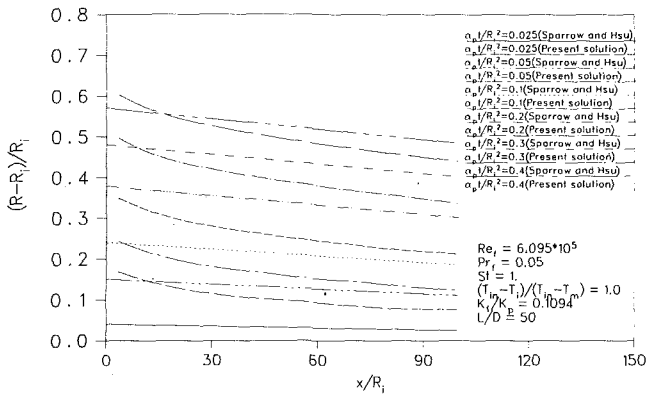

Fig. 8 Comparisons of phase-change fronts at different times for the conjugate one-region problem with lower Prandtl number

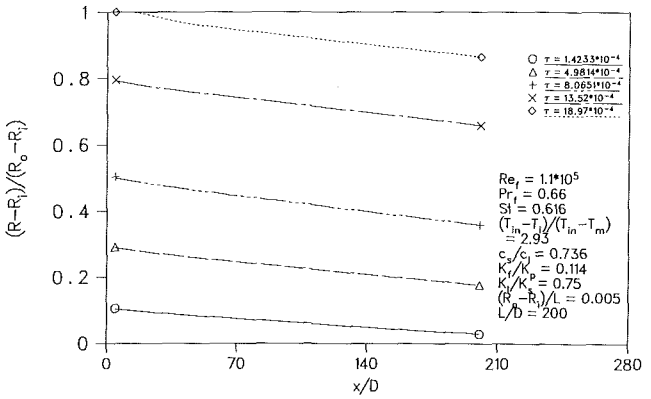

Fig. 9 Melting front locations at different time periods

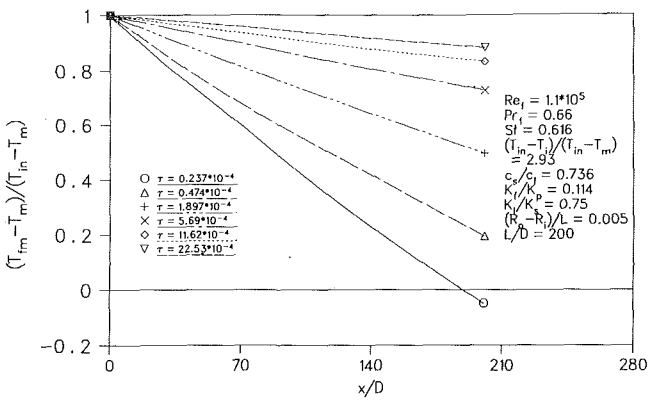

Fig. 10 Mixed-mean fluid temperature along axial direction at different time periods for the melting problem

for St = 1, with the other parameters being the same. The comparison was also made with the gaseous transfer fluid and the same trend was observed. Figure 8 compares the present solution and the numerical results by Sparrow and Hsu (1981) for the same case but with a relatively low Prandtl number, Pr = 0.05. For the present numerical result, the operational parameters Re_f and K_f/K_p were calculated based on Biot number $hR_i/K = 5$, Stanton number $h/\rho U_m c_f = 0.003$, and Pr = 0.05 using the correlation by Notter and Sleicher (Bhatti and Shah, 1987) for the constant heat rate. The difference between the two solutions is significant. For transfer fluids with low Prandtl numbers, the heat transfer coefficient changes significantly in the axial direction, and the axial conduction and developing flow effects are dominant along the pipe length. The present numerical results show that the fully developed flow was not reached even at the outlet of the pipe flow, $x/R_i = 100$. As a result, a significant error may be introduced by employing a steady-state fully developed heat transfer coefficient and neglecting the axial conduction in the transfer fluid. In this case, the more comprehensive method adopted by the present study is needed to obtain accurate solutions. Another aspect that needs to be mentioned is that the technique adopted by Sparrow and Hsu (1981) and by Shamsundar (1982) deals with the phase change on the outside of a coolant-carrying tube surrounded by an infinite PCM with the initial temperature being the freezing temperature. In this case, only the heat conduction in the solid region needs to be considered and the sensible heat may only play a minor role when the thickness of the frozen layer is relatively small ($(R-R_i)/R_i<0.7$). For the energy storage module presented in Fig. 1, however, the initial temperature may be much lower or higher than the phase-change temperature, and in many cases, the sensible heat can constitute more than 50 percent of the total energy storage capacity. Obviously, the problem by nature is a two-region problem in which both the solid and liquid regions need to be considered.

The numerical computation for the thermal energy storage module shown in Fig. 1 was first made with a melting problem. The phase-change material studied is LiH, which is considered to be one of the most promising candidates for the space-based energy storage system. The system was initially at a temperature T_i lower than the melting temperature T_m = 962 K of the PCM. The grid size used in the calculation was 51 (axial) × [20 (radial fluid) + 50 (radial PCM)] and a time step Δt = 8 min. The phase-change temperature range was taken to be δT = 0.5 to simulate phase change at a single temperature. It has been shown by Cao and Faghri (1990) that a moderately small δT is enough to simulate the phase-change problem occurring at a single temperature.

Figure 9 shows melting front locations along the axial direction for different time periods. The melting interface moves in the radial direction with time. However, the interface moves faster upstream due to the temperature drop of the transport fluid along the axial direction. Although the melting interface curves are sloped along the axial direction, the curves are still relatively flat owing to the high flow rate and the strong turbulent heat transfer between the transport fluid and the PCM. Figure 10 shows the mixed-mean transport fluid temperature along the axial direction at different times, which is defined as

$$T_{fm}=\frac{2}{R_i^2 U_m}\int_0^{R_i} UTrdr. \tag{22}$$

The fluid temperature is initially at the starting system temperature T_i, which is lower than T_m. As operation began, the outlet temperature rose very quickly. After the initial sharp increase, the outlet temperature maintained a continuous but very slow increasing trend for the rest of the operational period. Figure 11 shows the radial temperature distribution at an axial location of x/D = 100 for different time periods. Two different regions (the PCM and the transport fluid) are also indicated in the figure, noting that the pipe wall between the transport fluid and the PCM has been assumed to be negligibly small. The phase-change front at different times is the intersection of $(T-T_m)/(T_{in}-T_m) = 0$ and the corresponding temperature curves. The largest radial temperature drop in the transport fluid occurs at the fluid-PCM interface due to the turbulent nature of the transport fluid.

The numerical computation for the energy storage module was then made with a freezing problem. The phase-change material considered is octadecane with an initial temperature T_i higher than its freezing temperature T_m = 301.2 K. Figures 12–14 show the freezing fronts along the axial direction, mixed-mean transport fluid temperature along the axial direction, and the radial temperature distribution at x/D = 25 for dif-

Downloaded 13 Dec 2010 to 193.140.21.150. Redistribution subject to ASME license or copyright; see http://www.asme.org/terms/Terms_Use.cfm

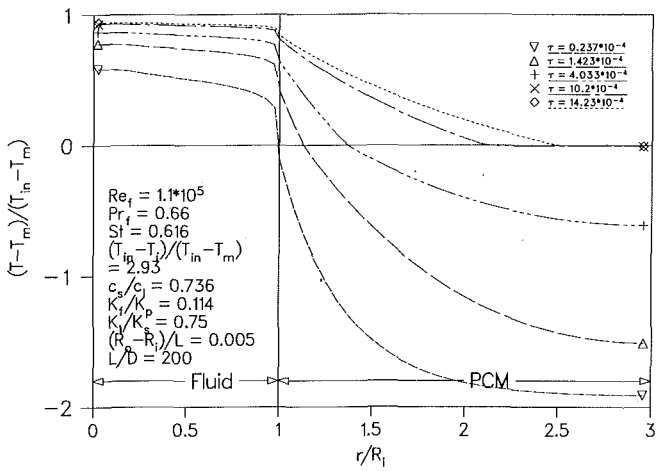

Fig. 11 Radial temperature distribution at $x/D = 100$ for different time periods for the melting problem

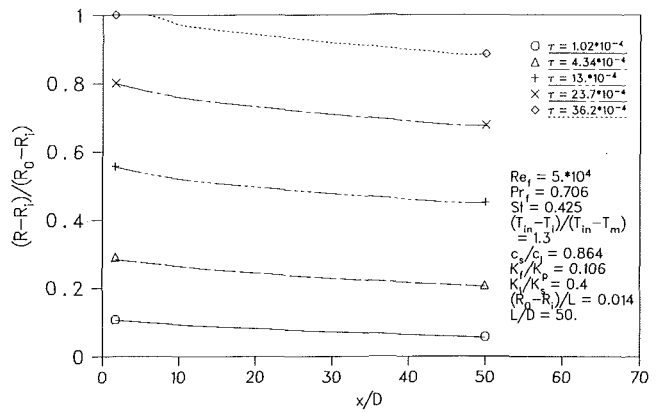

Fig. 12 Freezing fronts along axial direction at different time periods

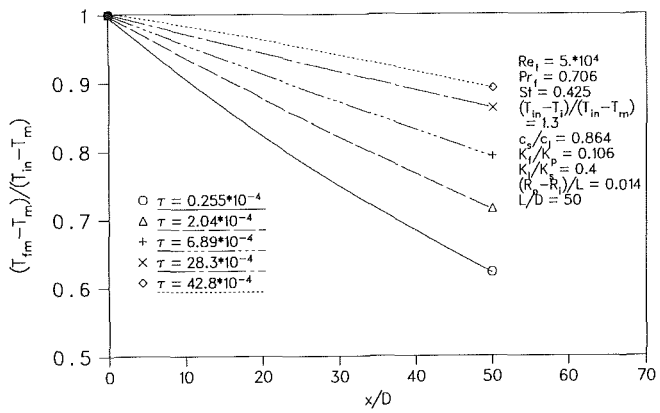

Fig. 13 Mixed-mean fluid temperature along axial direction at different time periods for the freezing problem

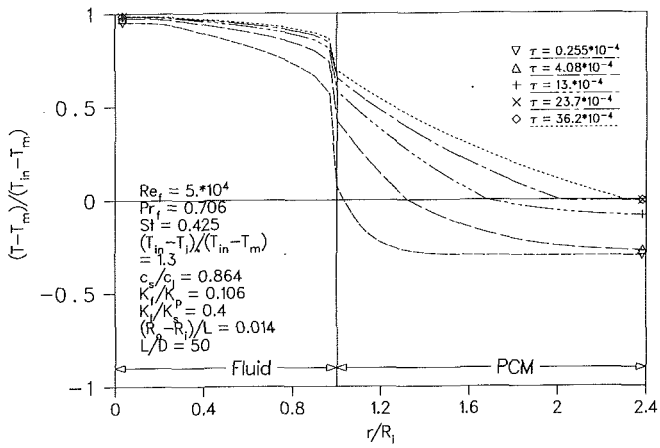

Fig. 14 Radial temperature distribution at $x/D = 25$ and different time periods for the freezing problem

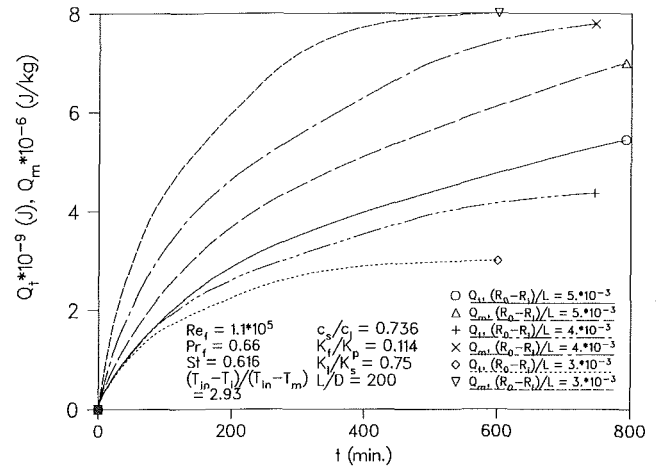

Fig. 15 Energy storage capacity and density with different geometry parameters for the melting problem

ferent time periods. The general trends of the three graphs are similar to those of the melting problem presented earlier. It should be pointed out that in Figs. 13 and 14, the temperature distributions are presented in dimensionless form. While the trends of the dimensionless temperature distributions are similar for freezing and melting, the trends are opposite for the dimensional temperature profiles. This is due to the fact that the phase-change temperature is higher than the inlet temperature for freezing and lower for melting.

Figure 15 shows the energy storage capacity and density at different times for the melting problem described earlier with different values of the geometry parameter $(R_o - R_i)/L$. Both the storage capacity and the density are time dependent. At very early times, the energy storage capacities for the three PCM modules with different $(R_o - R_i)/L$ are almost the same. For longer times, the storage capacity of the module with smaller PCM thickness $R_o - R_i$ is lower than those with larger thicknesses. At about 400 min, the PCM encapsulated in the module with $(R_o - R_i)/L = 3 \times 10^{-3}$ was almost completely melted, while the heat storage capacities of the other two modules continue to increase since the phase change still takes place in the PCM. For the energy storage density, the module with small $R_o - R_i$ has a higher value in most cases due to the smaller total PCM in the module. For the module design, optimization is required, and sometimes a tradeoff is needed among different module parameters. It should be pointed out that the results shown in Fig. 15 only involve variation of a single parameter $(R_o - R_i)/L$. In the real design process, many parameters need to be considered simultaneously. It is important to obtain some explicit expressions of Q_t and Q_m of the purpose of design and optimization. Since any purely analytical expressions are not available, an attempt to obtain some semi-empirical relations was made in this paper.

In order to evaluate the integrals g_l and g_s in Eq. (19) and to obtain a correlation frame for Q_t, consider a simplified quasi-stationary model as described below. A hollow PCM cylinder of inner radius R_i is initially solid at its melting temperature. At the surface $r = R_i$, heat is input via convective heat transfer with a film coefficient h from a transfer fluid at ambient temperature T_{in}. In this case, a uniform phase-change front $R(t)$ exists, separating liquid PCM ($r < R(t)$) from solid

Downloaded 13 Dec 2010 to 193.140.21.150. Redistribution subject to ASME license or copyright; see http://www.asme.org/terms/Terms_Use.cfm

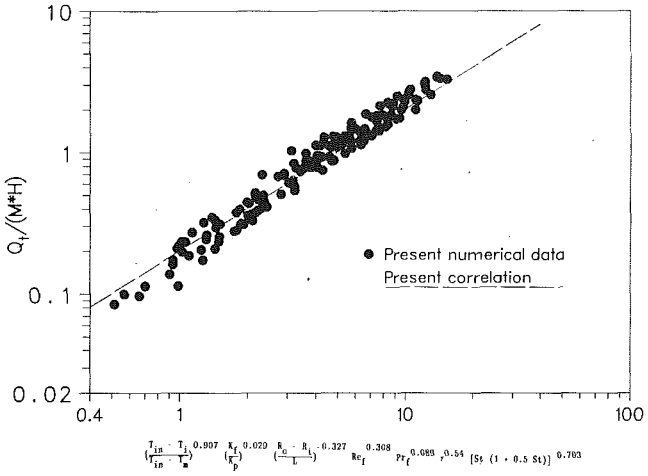

Fig. 16 Comparison of numerical data and the proposed correlation

($r > R(t)$). In the liquid region there is a radially symmetric, time-dependent temperature function $T(r, t)$, satisfying the heat equation

$$\frac{\partial T}{\partial t} = \frac{\alpha}{r}\frac{\partial}{\partial r}\left(r\frac{\partial T}{\partial r}\right) \tag{23}$$

with boundary conditions

$$T(R(t), t) = T_m \tag{24}$$

$$\rho H \frac{dR}{dt} = -K_p \frac{\partial T}{\partial r}(R(t), t) \tag{25}$$

At the inner radius, R_i,

$$K_p \frac{\partial}{\partial r}[T(R_i, t)] = h[T(R_i, t) - T_{in}] \tag{26}$$

An analytical approximation to $T(r, t)$ and $R(t)$ can be obtained based on the quasi-stationary approximation approach (Solomon et al., 1986; London and Seban, 1943), by replacing the heat equation, Eq. (23), with the steady-state equation $\frac{\partial}{\partial r}\left(r\frac{\partial T}{\partial r}\right) = 0$, while retaining the remaining conditions (24)–(26). The solution for the above problem is

$$h\left[\frac{K_p t(T_{in}-T_m)}{\rho H} + \frac{R^2 - R_i^2}{4} - \frac{R^2 \ln(R/R_i)}{2}\right] = \frac{K_p}{2R_i}(R^2 - R_i^2) \tag{27}$$

Since the magnitude of R_i is usually on the order of 10 mm, the term

$$\frac{R^2 - R_i^2}{4} - \frac{R^2 \ln(R/R_i)}{2}$$

is much smaller than the first term,

$$\frac{K_p t(T_{in}-T_m)}{\rho H}$$

and can usually be neglected. Therefore,

$$R^2 - R_i^2 = \frac{2R_i h t(T_{in}-T_m)}{\rho H}$$

or

$$R^2 - R_i^2 = S^2 \frac{K_f}{K_p} \mathrm{Nu}_f \,\mathrm{St}\, \tau \tag{28}$$

where the characteristic area of the annular PCM is $S^2 = V_p/(R_o - R_i)$, V_p is the total PCM volume of the module, the Nusselt number for the transfer fluid is $\mathrm{Nu}_f = 2R_i h/K_f$, the Stefan number is $\mathrm{St} = c_p(T_{in} - T_m)/H$, and the Fourier number for the PCM is $\tau = t\alpha_p/S^2$.

With the expression for $R^2 - R_i^2$ above and a constant specific heat, we can evaluate the integrals in Q_t:

$$g_l = \int_0^L (R^2 - R_i^2)\,dx = (R^2 - R_i^2)L$$

$$g_s = \int_{R_i}^{R_o}\int_0^L c_p(T - T_m)\,dr\,dx = c_p \frac{(T_{in}-T_m)}{2} L\,(R^2 - R_i^2)/2$$

In the above integration, we have assumed that the liquid PCM has an average temperature of $(T_{in} + T_m)/2$. Therefore,

$$Q_t = \rho H \pi g_l + 2\pi\rho g_s$$

$$= \rho\pi L(R^2 - R_i^2)\left[H + \frac{c_p}{2}(T_{in} - T_m)\right]$$

$$= \rho\pi LHS^2 \frac{K_f}{K_p}\mathrm{Nu}_f \tau \mathrm{St}\left(1 + \frac{1}{2}\mathrm{St}\right)$$

$$= \rho HL \frac{L(R_o^2 - R_i^2)\pi}{R_o - R_i}\,\pi \frac{K_f}{K_p}\mathrm{Nu}_f \tau \mathrm{St}\left(1 + \frac{1}{2}\mathrm{St}\right)$$

or

$$\frac{Q_t}{\rho HL(R_o^2 - R_i^2)\pi} = \pi\left(\frac{R_o - R_i}{L}\right)^{-1}\frac{K_f}{K_p}\mathrm{Nu}_f \tau \mathrm{St}\left(1 + \frac{1}{2}\mathrm{St}\right) \tag{29}$$

The dimensionless energy storage capacity $Q_t/\rho HL(R_o^2 - R_i^2)\,\pi = Q_t/MH$ is the ratio of the total energy stored at time t to the total latent energy avialable for the PCM module.

Similarly, the dimensionless energy storage density can be written as

$$\frac{Q_m}{H} = \pi\left(\frac{R_o - R_i}{L}\right)^{-1}\left(\frac{K_f}{K_p}\right)\mathrm{Nu}_f \tau \mathrm{St}\left(1 + \frac{1}{2}\mathrm{St}\right) \tag{30}$$

It should be pointed out that the above expressions have been obtained based on a very simplified model. The purpose of the derivation is to obtain an expression frame for the correlation. The above parameters such as $R(t)$ and h could only be considered as average or effective parameters. The whole expression must be modified and the final version be determined by the conjugate numerical data.

In the simplified model, the initial temperature T_i of the PCM was assumed to be the melting temperature T_m, which is not the case in general for engineering applications. Therefore, a correction factor

$$C'\left(\frac{T_{in}-T_i}{T_{in}-T_m}\right)^a$$

was included in the expression. With additional exponent modifications for the rest of the dimensionless numbers, the correlation can be written as

$$\frac{Q_t}{MH} = C''\left(\frac{T_{in}-T_i}{T_{in}-T_m}\right)^a\left(\frac{K_f}{K_p}\right)^b\left(\frac{R_o - R_i}{L}\right)^c \mathrm{Re}_f^d \mathrm{Pr}_f^e \tau^f [\mathrm{St}(1 + 0.5\mathrm{St})]^g \tag{31}$$

where the constants C'', a, b, c, d, e, f, and g are to be determined by the numerical solutions. In the above expression, we have expressed the effective Nusselt number Nu_f as $\mathrm{Nu}_f \sim \mathrm{Re}_f^d \mathrm{Pr}_f^e$, which is generally acceptable for engineering applications.

Numerical computations for the PCM energy storage module with different parameters were made extensively, and about

Downloaded 13 Dec 2010 to 193.140.21.150. Redistribution subject to ASME license or copyright; see http://www.asme.org/terms/Terms_Use.cfm

150 numerical data points, most for high-temperature energy storage systems, were taken from the numerical solutions. These numerical data were used in conjunction with a regression analysis to determine the constants in Eq. (31). The expression thus obtained is

$$\frac{Q_t}{HM}=0.203\left(\frac{T_{in}-T_i}{T_{in}-T_m}\right)^{0.907}\left(\frac{K_f}{K_p}\right)^{0.029}\left(\frac{R_o-R_i}{L}\right)^{-0.327}$$
$$\mathrm{Re}_f^{0.308}\,\mathrm{Pr}_f^{0.089}\tau^{0.54}[\mathrm{St}(1+0.5\,\mathrm{St})]^{0.703} \quad (32)$$

Figure 16 shows the comparison of the numerical data and the correlations, Eq. (32). For most of the data points, the differences between the numerical data and the correlation are within 25 percent.

The correlation is applicable within

$$0.20<\frac{Q_t}{MH}<3.0$$

which covers the most useful operating ranges.

Other parameters covered by the numerical data are

$$0.05\le\frac{K_f}{K_p}\le 0.72;\quad 1.05\le\left(\frac{T_{in}-T_i}{T_{in}-T_m}\right)\le 3.78;$$
$$0.0014\le\left(\frac{R_o-R_i}{L}\right)\le 0.02\quad 0.1\le\mathrm{St}\le 1.34$$
$$0.1\le\mathrm{Pr}_f\le 1.0\quad 5\times10^4\le\mathrm{Re}_f\le 1.1\times10^6$$

The expression for energy storage density Q_m, following the result for Q_t, can be written as

$$\frac{Q_m}{H}=0.203\left(\frac{T_{in}-T_i}{T_{in}-T_m}\right)^{0.907}\left(\frac{K_f}{K_p}\right)^{0.029}\left(\frac{R_o-R_i}{L}\right)^{-0.327}\mathrm{Re}_f^{0.308}$$
$$\mathrm{Pr}_f^{0.089}\,\tau^{0.54}\,[\mathrm{St}(1+0.5\mathrm{St})]^{0.703} \quad (33)$$

which is applicable within the same parameter ranges covered by the numerical data. For phase-change materials with different values of properties between the liquid and the solid phases, such as thermal conductivity and specific heat, the parameters in Eqs. (32) and (33) can be evaluated based on the averaged values over the two phases. Although most of the numerical data used to obtain Eqs. (32) and (33) were taken from the melting solutions of high-temperature storage modules, Eqs. (32) and (33) are equally applicable to freezing problems of high-temperature storage modules with St = $c_p(T_m-T_{in})/H$.

Conclusions

A numerical procedure solving the transport fluid and the PCM as a conjugate problem was presented. It has been shown that for one-region conjugate phase-change problems with the initial temperature close to the freezing temperature and gaseous transfer fluids, the closed-form solution of Shamsundar (1982) and the numerical solution of Sparrow and Hsu (1981) provided an efficient way to predict system performance. For two-region conjugate phase-change problems or PCM modules with lower Prandtl number transfer fluids, the present method was needed to obtain accurate solutions. The performance of the energy storage module in Fig. 1 was simulated systematically for different parameters, and correlations for energy storage capacity and energy storage density were obtained using the conjugate numerical data. These correlations provide guidance for module design and optimization.

References

Bhatti, M. S., and Shah, R. K., 1987, "Turbulent and Transition Flow Convective Heat Transfer in Ducts," in: *Handbook of Single-Phase Convective Heat Transfer*, S. Kakac et al., eds.

Cao, Y., and Faghri, A., 1990, "A Temperature Transforming Model With a Fixed Grid Numerical Methodology for Phase-Change Problems Including Natural Convection," ASME JOURNAL OF HEAT TRANSFER, Vol. 112, pp. 812–816.

Cao, Y., and Faghri, A., 1991, "Performance Characteristics of a Thermal Energy Storage Module: A Transient PCM/Forced Convection Conjugate Analysis," *Int. J. Heat Mass Transfer*, Vol. 34, No. 1, pp. 93–101.

Djilali, N., Gartshore, I., and Salcudean, M., 1989, "Calculation of Convective Heat Transfer in Recirculating Turbulent Flow Using Various Near-Wall Turbulence Models," *Numerical Heat Transfer*, Part A, Vol. 16, pp. 189–212.

Ganic, E. N., Hartnett, J. P., and Rohsenow, W. M., 1985, "Basic Concepts of Heat Transfer," *Handbook of Heat Transfer Fundamentals*, W. M. Rhosenow et al., eds., pp. 15–25.

Gnielinski, V., 1976, "New Equations for Heat and Mass Transfer in Turbulent Pipe and Channel Flow," *Int. Chem. Eng.*, Vol. 16, pp. 359–368.

Kays, W. M., and Crawford, M. E., 1980, *Convective Heat and Mass Transfer*, 2nd ed., McGraw-Hill, New York.

Launder, B. E., and Spalding, D. B., 1974, "The Numerical Computation of Turbulent Flow," *Comp. Meth. Appl. Mech. Eng.*, Vol. 3, pp. 263–289.

London, A. L., and Seban, R. A., 1943, *Transactions of the ASME*, Vol. 65, p. 771.

Lunardini, V. J., 1981, "Phase Change Around a Circular Cylinder," ASME JOURNAL OF HEAT TRANSFER, Vol. 103, pp. 589–600.

Patankar, S. V., 1980, *Numerical Heat Transfer and Fluid Flow*, McGraw-Hill, New York.

Patankar, S. V., 1988, "Elliptic Systems: Finite-Difference Method I," in: *Handbook of Numerical Heat Transfer*, W. J. Minkowycz et al., eds., pp. 215–290.

Shamsundar, N., 1982, "Formulae for Freezing Outside a Circular Tube With Axial Variation of Coolant Temperature," *Int. J. Heat Mass Transfer*, Vol. 25, No. 10, pp. 1614–1616.

Sleicher, C. A., and Rouse, M. W., 1975, "A Convenient Correlation for Heat Transfer to Constant and Variable Property Fluids in Turbulent Pipe Flow," *Int. J. Heat Mass Transfer*, Vol. 18, pp. 667–683.

Solomon, A. D., Morris, M. D., Martin, J., and Olszewski, M., 1986, "The Development of a Simulation Code for a Latent Heat Thermal Energy Storage System in a Space Station," Technical Report ORNL-6213.

Sparrow, E. M., and Hsu, C. F., 1981, "Analysis of Two-Dimensional Freezing on the Outside of a Coolant-Carrying Tube," *Int. J. Heat Mass Transfer*, Vol. 24, Vol. 8, pp. 1345–1357.

Stovall, T. K., and Arimilli, R. V., 1988, "Transient Thermal Analysis of Three Fast-Changing Latent Heat Storage Configurations for a Space-Based Power System," *Proc. 23rd Intersociety Energy Conversion Engineering Conference*, pp. 171–177.

Viskanta, R., 1983, "Phase-Change Heat Transfer," in: *Solar Heat Storage: Latent Heat Material*, G. A. Lane, ed., Vol. 1, pp. 153–222.

Yimer, B., and Adami, M., 1989, "Parametric Study and Optimization of Phase Change Thermal Storage Systems," *Proc. 1989 ASME National Heat Transfer Conf.*, HTD-Vol. 109, pp. 1–8.

Downloaded 13 Dec 2010 to 193.140.21.150. Redistribution subject to ASME license or copyright; see http://www.asme.org/terms/Terms_Use.cfm

Closed-Form Analytical Solutions of High-Temperature Heat Pipe Startup and Frozen Startup Limitation

Y. Cao

A. Faghri

Department of Mechanical and Materials Engineering, Wright State University, Dayton, OH 45435

Previous numerical and experimental studies indicate that the high-temperature heat pipe startup process is characterized by a moving hot zone with relatively sharp fronts. Based on the above observation, a flat-front model for an approximate analytical solution is proposed. A closed-form solution related to the temperature distribution in the hot zone and the hot zone length as a function of time are obtained. The analytical results agree well with the corresponding experimental data, and provide a quick prediction method for the heat pipe startup performance. Finally, a heat pipe limitation related to the frozen startup process is identified, and an explicit criterion for the high-temperature heat pipe startup is derived. The frozen startup limit identified in this paper provides a fundamental guidance for high-temperature heat pipe design.

Introduction

In the preceding paper by Cao and Faghri (1992), the heat pipe startup process was described and a comprehensive numerical model for the heat pipe startup from the frozen state was proposed. The numerical simulation covered the entire heat pipe startup process and compared well with the experimental data. Although the numerical simulation has the advantage of being robust and able to solve the problem in a general way, developing the computer model is time consuming and the computer time is costly. On the other hand, a simple approximate analytical solution, although its applicability may be limited, can provide a tangible relation among the important system parameters, and can aid in understanding the physical phenomena occurring in the problem.

Cotter (1967) was the first to attack the heat pipe startup problem analytically. In his analysis, Cotter proposed a lumped one-dimensional model and introduced an effective thermal conductivity in the axial direction of the heat pipe. The results were presented graphically, but no complete closed-form analytical relation concerning the heat pipe startup process was given. Also, the analytical solution was not compared with experimental data.

Sockol and Forman (1970) studied a high-temperature heat pipe with lithium as the working fluid. They observed that at sufficiently high heat inputs, the heat pipe wall temperature rose to some intermediate level and remained almost constant as a steep temperature front moved down the length of the pipe. After the uniform hot zone reached the condenser end of the heat pipe, the temperature increased to its steady-state value. Based on the above observation, the Cotter model was reassessed and modified. Sockol and Forman assumed that the wall temperature in the hot zone was uniform, and the cold zone remained at the initial temperature T_a. By making an energy balance over the evaporator and condenser sections, two lumped first-order differential equations for the evaporator and condenser walls were obtained. To evaluate the vapor flow rate in the heat pipe, a one-dimensional approximate vapor flow model was considered, and it was assumed that the vapor velocity becomes sonic at the end of the hot zone. The hot zone temperatures were obtained by solving the four coupled equations numerically. Four numerical hot zone temperatures were compared with some measured experimental data, and were 50 to 80°C higher than the measured values. Considering the 30°C discrepancy attributable to the temperature measurement, the numerical value thus obtained was considered to be in good agreement with the experimental data.

Ponnappan (1989) studied the startup of a 2-m-long gas-loaded, sodium heat pipe. Energy balances were made for the lumped control volumes enclosing the hot and cold zones of the heat pipe wall, with the assumption that the hot and cold zone temperatures were uniform. Two sets of lumped first-order differential equations corresponding to the thawing stage and transporting stage for each of the control volumes were given along with the initial and boundary conditions. The four governing differential equations and the initial conditions were solved by numerical integration using the fourth-order Runge–Kutta method. The numerical results for the hot zone temperature and hot zone length were plotted as a function of the initial noncondensible gas pressure. Most of experimental data fell within the bands close to the actual initial noncondensible gas pressure in the experiment.

A literature survey concerning the approximate solution for the heat pipe startup process revealed that a closed-form solution is not available. In this paper, a simple analytical closed-form solution is obtained based on the flat-front startup model and compared with experimental startup data. In addition, a heat pipe limit related to frozen startup is identified, and an explicit criterion for the frozen startup limit of high-temperature heat pipes is derived.

Analytical Solution

Based on the experimental study and visual observation of a lithium heat pipe, Sockol and Forman (1970) pointed out that at sufficiently high heat inputs the heat pipe wall temperature was seen to rise to some intermediate level and remain almost constant as a steep temperature front moved down the pipe. When the hot zone filled the pipe, the temperature gradually increased to a steady-state value. The same trends were also observed from the experimental data by Faghri et al.

Contributed by the Heat Transfer Division and presented at the ASME National Heat Transfer Conference, San Diego, California, August 9–12, 1992. Manuscript received by the Heat Transfer Division January 1992; revision received May 1992. Keywords: Heat Pipes and Thermosyphons, Transient and Unsteady Heat Transfer. Associate Technical Editor: T. W. Simon.

Copyright © 1992 by ASME

Downloaded 13 Dec 2010 to 193.140.21.150. Redistribution subject to ASME license or copyright; see http://www.asme.org/terms/Terms_Use.cfm

(1991a), Ponnappan (1989), as well as the numerical predictions by Cao and Faghri (1992). The numerical solution by Cao and Faghri (1992) showed that the vapor hot zone moving fronts were steeper than those of the wall temperature, and were located nearly in the middle of the slope region of the wall temperature distributions. In order to analyze the heat pipe startup process, a flat-front startup model is proposed based on the above experimental facts. At time t and $t + \delta t$, the heat pipe wall temperature distributions are schematically shown by the two solid curves in Fig. 1. The wall temperature distributions were approximated by the two dashed curves with linear distributions, where flat fronts are located in the middle of the slope regions of the solid curves. The temperatures of the flat fronts were assumed to be at the continuum–rarefied transition temperature, T_{tr}, based on the assumption that the vapor temperature at the continuum–rarefied interface is almost equal to T_{tr}. The hot zone wall temperature at the evaporator end cap is denoted by T_h. The hot zone lengths at t and $t + \delta t$ are denoted by l and $l + \delta l$ in the figure. Both T_h and l are functions of time. The value of T_{tr} is constant for a specific heat pipe, and can be found from Fig. 2 in the paper by Cao and Faghri (1992) or by solving the following equation given in the same paper:

$$\ln\left(T_{tr}\rho_v R/p_{rf}\right)+\frac{h_{fg}}{R}\left(\frac{1}{T_{tr}}-\frac{1}{T_{rf}}\right)=0 \tag{1}$$

where

$$\rho_v=\frac{1.051\kappa}{\sqrt{2}\pi\sigma^2 RD\mathrm{Kn}}$$

The average hot zone wall temperature based on a linear assumption is

$$T_{aw}=0.5(T_h+T_{tr}) \tag{2}$$

An energy balance over the time interval t and $t + \delta t$ in terms of average hot zone temperature T_{aw} for the hot zone wall and wick of the heat pipe results in

$$\begin{aligned}C(l+\delta l)(T_{aw}|_{t+\delta t}-T_a)-Cl(T_{aw}|_t-T_a)&\\ =Q(t)\delta t-2\pi q_c R_o(l-L_e-L_a)\delta t&\\ =Q(t)\delta t-h(T_{aw}|_t-T_a)2\pi R_o(l-L_e-L_a)\delta t&\end{aligned} \tag{3}$$

where C is the heat capacity per unit length of the heat pipe, which includes the heat capacities of the wall and wick, and has units of J/m·K. The radial temperature difference in the wick and wall as well as the heat capacity of the vapor in the heat pipe have been neglected. Since the heat capacity of the vapor is at least five orders of magnitude smaller than that of the container, and the heat pipe wall and wick are usually very thin, neglecting the vapor heat capacity and the radial temperature difference in the wick and wall is reasonable. T_a is the initial heat pipe temperature, $Q(t)$ is the heat input at the evaporator, q_c is the heat flux at the condenser surface, and h is the corresponding heat transfer coefficient between the heat pipe wall and the ambient, which is related to q_c.

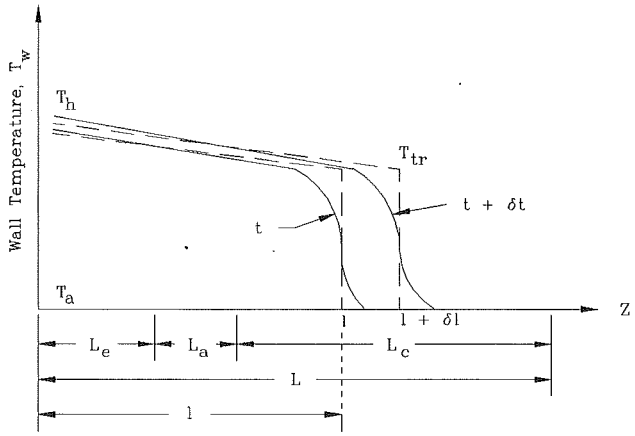

Fig. 1 Description of the flat-front startup model

Equation (3) can be written in differential form as:

$$\begin{aligned}C\frac{d}{dt}\left[l(T_{aw}-T_a)\right]=&-2\pi\, hR_o l(T_{aw}-T_a)+Q(t)\\ &+2\pi hR_o(T_{aw}-T_a)(L_e+L_a)\end{aligned} \tag{4}$$

For noncircular heat pipes, $2\pi R_o$ should be replaced by the circumferential length W. Let

$$h^*=2\pi R_o h,\quad Q^*(t)=Q(t)+h^*(T_{aw}-T_a)(L_e+L_a) \tag{5}$$

we have

$$C\frac{d}{dt}\left[l(T_{aw}-T_a)\right]+h^*\left[l(T_{aw}-T_a)\right]=Q^*(t) \tag{6}$$

Equation (6) has a general solution assuming h^* is constant:

Nomenclature

A = area, m^2
A_w' = cross-sectional area of the working fluid in the wick, m^2
C = heat capacity per unit length of heat pipe, J/m·K
c = specific heat, J/(kg-K)
c_1 = integration constant in Eq. (7)
c_{me} = average effective specific heat of the wick over the liquid wick and the solid wick, J/(kg-K)
c_p = specific heat at constant pressure, J/(kg-K)
D = vapor core diameter, m
FSL = frozen startup limit
H = latent heat due to melting or freezing, J/kg
h = convective heat transfer coefficient, W/(m^2-K)
h^* = term defined in Eq. (5)
h_{fg} = latent heat of vaporization, J/kg
Kn = Knudsen number = 0.01 for transition from rarefied to continuum vapor flow
l = length of the hot zone region, or the location of the liquid-solid interface in the wick, m
L = total length of the heat pipe, m
L_a = length of the adiabatic section, m
L_c = length of the condenser section, m
L_e = length of the evaporator section, m
$\dot{M}_{cl}$ = mass flow rate condensed on the liquid-wick surface in Fig. 9, kg/s
$\dot{M}_{cs}$ = mass flow rate condensed on the solid-wick surface in Fig. 9, kg/s
$\dot{M}_e$ = total mass flow rate in Fig. 9, kg/s
M_t = working fluid inventory, kg
p = pressure, N/m^2
Q = heat input at active evaporators, W
Q^* = term in Eq. (5)
Q_o = heat output at condenser, W
Q_{cl} = heat dissipation from heat pipe in the region $z \le l$ and axial conduction into the region $z > l$, W
Q_{cs} = heat absorption rate at solid-wick region corresponding to $\dot{M}_{cs}$, W
q = heat flux, W/m^2
R = gas constant, J/(kg-K)
R_o = outer pipe wall radius, m

Downloaded 13 Dec 2010 to 193.140.21.150. Redistribution subject to ASME license or copyright; see http://www.asme.org/terms/Terms_Use.cfm

$$l(T_{aw}-T_a)=\exp(-h^*t/C)\int_{t_i}^{t}\frac{Q^*(t)}{C}\exp(h^*t/C)dt + c_1\exp(-h^*t/C) \quad (7)$$

where t_i is the initial time from which the solution is to be considered, and c_1 is a constant to be determined by the initial condition. In the adiabatic section, $L_e < l < (L_e+L_a)$, the term h^* in Eq. (6) is zero. Therefore, from Eq. (6), we have

$$l(T_{aw}-T_a)=\frac{1}{C}\int_0^t Q(t)dt \quad (8a)$$

or

$$l=Qt/[C(T_{aw}-T_a)] \quad (8b)$$

when Q is constant.

At the evaporator, heat is applied in the region $0 \le z \le L_e$, and the temperature in this whole region increases. Therefore, the hot zone length l should be equal to L_e before the temperature at the exit of the evaporator reaches the transition temperature T_{tr} and the hot zone begins to move into the adiabatic section. For $l = L_e$, a lumped energy balance over the evaporator section is needed. The relation between the startup time and the average hot zone temperature, based on the flat-front startup model for a constant heat input at the evaporator, is

$$t=CL_e(T_{aw}-T_a)/Q \quad (8c)$$

Equation (8c) can be used to calculate the time needed for the evaporator exit temperature to reach the transition temperature T_{tr}. Since the relations for $l < (L_e + L_a)$ have already been obtained (Eqs. (8b) and (8c)), Eq. (7) is used only for finding the solution for $l \ge (L_e+L_a)$. For this reason, the time when the hot zone reaches the condenser inlet is considered to be the initial time t_i for the solution of Eq. (7).

The constant, c_1, in Eq. (7) can be determined to be

$$c_1=(L_e+L_a)(T_{aw,i}-T_a)\exp(h^*t_i/C) \quad (9)$$

where $T_{aw,i}$ is the average hot zone wall temperature when the flat front reaches the condenser inlet. The corresponding time t_i can be obtained from Eq. (8a):

$$\int_0^{t_i}Q(t)dt=C(L_e+L_a)(T_{aw,i}-T_a) \quad (10a)$$

or from Eq. (8b):

$$t_i=C(L_e+L_a)(T_{aw,i}-T_a)/Q \quad (10b)$$

when Q is constant. Therefore, Eq. (7) can be written as

$$l(T_{aw}-T_a)=\exp(-h^*t/C)\int_{t_i}^{t}\frac{Q^*(t)}{C}\exp(h^*t/C)dt + (L_e+L_a)(T_{aw,i}-T_a)\exp[-h^*(t-t_i)/C] \quad (11a)$$

or

$$l=\frac{1}{(T_{aw}-T_a)}\exp(-h^*t/C)\int_{t_i}^{t}\frac{Q^*(t)}{C}\exp(h^*t/C)dt + \frac{(L_e+L_a)(T_{aw,i}-T_a)}{(T_{aw}-T_a)}\exp[-h^*(t-t_i)/C] \quad (11b)$$

In many cases, heat pipes start from the frozen state with a radiative boundary condition at the condenser:

$$q_c=\sigma\epsilon(T_{aw}^4-T_a^4) \quad (12)$$

Therefore,

$$h^*=2\pi R_o q_c/(T_{aw}-T_a)=2\pi R_o\sigma\epsilon(T_{aw}^2+T_a^2)(T_{aw}+T_a) \quad (13)$$

Since the average hot zone temperature, T_{aw}, is a weak function of time as shown experimentally by previous investigators, for a constant Q, Q^* can be treated as a constant in the integration, and Eq. (11b) is simplified to be

$$l=\left[\frac{Q}{(T_{aw}-T_a)h^*}+(L_e+L_a)\right]\left[1-\exp[-h^*(t-t_i)/C]\right] + \frac{(L_e+L_a)(T_{aw,i}-T_a)}{(T_{aw}-T_a)}\exp[-h^*(t-t_i)/C] \quad (14)$$

Equation (14) is applicable for $l \ge (L_e+L_a)$. For $L_e < l < (L_e+L_a)$ and $l = L_e$, Eqs. (8b) and (8c) should be used, respectively. These equations provide a simple tool to predict the location of the hot zone front during the heat pipe startup process. It follows from the above equations that the hot zone length is a function of time t and the average hot zone wall temperature T_{aw}. Since T_{aw} is directly related to the wall temperature distribution in the hot zone, the hot zone temperature distribution should be considered.

Temperature Distribution in the Hot Zone

In the last section, the heat pipe wall temperature was as-

Nomenclature (cont.)

R_v = vapor space radius, m
R_{vw} = average radius of heat pipe wick, m
R_w = wick-wall interface radius, m
R_{wo} = average radius of heat pipe wall, m
r = radial coordinate, m
T = temperature, K
T_a = ambient temperature, or the initial temperature of the frozen heat pipe, K
T_{av} = average hot zone vapor temperature, K
T_{aw} = average hot zone wall temperature, K
$T_{aw,i}$ = average hot zone wall temperature when the flat front reaches the condenser inlet, K
T_h = hot zone wall temperature at the evaporator end cap, K
T_m = melting temperature, K
T_{tr} = transition temperature, K
t = time, s
U_i = liquid-solid interfacial velocity in Fig. 9
V = volume, m^3
W = circumferential length of the heat pipe, m
z = axial coordinate, m
δ = wall or liquid-wick thickness, m
δ_l = thickness of the wick structure, m
δ_l' = thickness of the working fluid in the wick, m
ϵ = radiation emissivity
κ = Boltzmann constant, J/K
μ = dynamic viscosity of the vapor, kg/(m-s)
ρ = density, kg/m^3
σ = Stefan-Boltzmann constant, $W/(m^2\text{-}K^4)$, or collision diameter in Eq. (1), Å
φ = heat pipe wick porosity

Subscripts

a = abiabatic or ambient
c = condenser
e = evaporator
eff = effective
l = liquid or working fluid in the liquid state in the wick
m = mushy phase
me = average effective specific heat of wick over the liquid and solid working fluid
rf = reference
v = vapor
w = wall or wick
ws = wick structure material

Downloaded 13 Dec 2010 to 193.140.21.150. Redistribution subject to ASME license or copyright; see http://www.asme.org/terms/Terms_Use.cfm

sumed to be linear along the hot zone length with the transition temperature T_{tr} at the flat front, which is constant for a specific heat pipe. In order to compute the average hot zone temperature, $T_{aw} = 0.5\ (T_h + T_{tr})$, the hot zone temperature at the evaporator end cap T_h needs to be obtained. In other words, the total temperature drop $\Delta T = T_h - T_{tr}$ over the hot zone should be considered since $T_{aw} = 0.5\ (T_h + T_{tr}) = 0.5\ \Delta T + T_{tr}$. The temperature of the heat pipe wall in the hot zone is directly related to the vapor temperature in the heat pipe. This is especially true for the present flat startup model, since it was assumed that the temperature distribution is very similar to the vapor temperature distribution. By neglecting the radial heat conduction in the wick and wall, the temperature drop ΔT of the hot zone can be approximated to be that of the vapor temperature in the heat pipe.

Vapor flow in a heat pipe with mass injection or removal is a very complicated process, and often requires numerical computations, as was the case in the paper by Cao and Faghri (1992). Analytical solutions are available only for some one-dimensional and incompressible vapor flows (Faghri, 1989; Busse, 1967; Cotter, 1965). Since the objective of this paper is to derive an analytical solution for the heat pipe startup from the frozen state, a simple analytical solution for vapor flow in a heat pipe is considered.

Busse (1967) studied laminar incompressible vapor flow in a cylindrical heat pipe. The total pressure drop along the heat pipe length was given by

$$\Delta p = p(z=0) - p(z=L) = \frac{4\mu Q}{\pi \rho_v R_v^4 h_{fg}} (L_e + 2L_a + L_c) \quad (15)$$

where Q is the total heat input at the evaporator. Equation (15) indicates that the pressure drop due to the inertia force cancels out over the heat pipe, and the pressure drop is solely due to the frictional drag forces of a Poiseuille flow. The theory also indicates that the friction pressure drop resulting from deviation from the Poiseuille profile due to mass injection and removal at the evaporator and condenser cancels out over the entire heat pipe.

For heat pipes without an adiabatic section, $L_a = 0$, Eq. (15) reduces to

$$\Delta p = \frac{4\mu Q}{\pi \rho_v R_v^4 h_{fg}} (L_e + L_c) = \frac{4\mu QL}{\pi \rho_v R_v^4 h_{fg}} \quad (16)$$

where L is is the total heat pipe length.

The vapor flow in the hot zone region during the frozen startup closely resembles the vapor flow in a heat pipe with the length of the hot zone l equal to the total length of the heat pipe based on the flat startup model. For $z > l$, the heat pipe is inactive and the flat front is equivalent to the condenser end cap. During the heat pipe startup process, the heat pipe container temperature is increased due to the addition of heat energy from vapor condensation at the vapor–wick interface in the region $L_e < z < l$. Therefore, Eq. (16) is applied to the vapor flow in the hot zone region with l replacing L

$$\Delta p = \frac{4\mu Ql}{\pi \rho_v R_v^4 h_{fg}} \quad (17)$$

In order to obtain the temperature drop, ΔT, corresponding to the pressure drop Δp, the vapor is assumed to be in an equilibrium condition, and the Clausius-Clapeyron equation in differential form is applied

$$\frac{dp}{dT} = \frac{\rho_v h_{fg}}{T} \quad (18)$$

Integrating Eq. (18) within the finite intervals Δp and ΔT, we obtain

$$\Delta T = \left(\frac{T}{\rho_v h_{fg}}\right)_{av} \Delta p \quad (19)$$

where $(T/\rho_v h_{fg})_{av}$ is the average value over the integration interval. Therefore, combining Eqs. (17) and (19), we have

$$\Delta T = \frac{4T_{av}\mu Ql}{\pi \rho_v^2 R_v^4 h_{fg}^2} \quad (20)$$

The above equations have been obtained based on the incompressible assumption. To take the vapor compressibility and the density variation into account, the vapor density in Eq. (20) is taken to be the average density corresponding to the average temperature T_{av}. Applying the ideal gas law and the integrated form of the Clausius–Clapeyron equation, we have

$$\rho_v = \frac{1}{RT_{av}} p_{rf} \exp\left[-\frac{h_{fg}}{R}\left(\frac{1}{T_{av}} - \frac{1}{T_{rf}}\right)\right] \quad (21)$$

where p_{rf} and T_{rf} are the saturation reference pressure and temperature, respectively. According to the assumption of a linear hot zone temperature distribution and the neglection of the radial temperature drop across the wall and wick, we have

$$T_{av} = T_{aw} = 0.5\ (T_h + T_{tr}) = T_{tr} + 0.5\ \Delta T \quad (22)$$

Combining Eqs. (20)–(22) yields

$$\exp\left[-\frac{h_{fg}}{R}\left(\frac{1}{T_{tr} + 0.5\ \Delta T} - \frac{1}{T_{rf}}\right)\right] = \frac{R(T_{tr} + 0.5\ \Delta T)}{p_{rf}} \left[\frac{4(T_{tr} + 0.5\ \Delta T)\mu Ql}{\pi \Delta T R_v^4 h_{fg}^2}\right]^{0.5} \quad (23)$$

or

$$\frac{h_{fg}}{R}\left(\frac{1}{T_{rf}} - \frac{1}{T_{tr} + 0.5\ \Delta T}\right) - \ln\left[\frac{R(T_{tr} + 0.5\ \Delta T)}{p_{rf}}\left(\frac{4(T_{tr} + 0.5\ \Delta T)\mu Ql}{\pi \Delta T R_v^4 h_{fg}^2}\right)^{0.5}\right] = 0 \quad (24)$$

Equation (24) can be solved iteratively for ΔT by the Newton–Raphson/secant method (Pletcher et al., 1988). Therefore, T_{aw} in Eq. (14) can be calculated

$$T_{aw} = T_{tr} + 0.5\Delta T \quad (25)$$

and

$$T_h = T_{tr} + \Delta T \quad (26)$$

Analytical Results and Discussion

The analytical close-form solutions for the heat pipe startup from the frozen state are obtained from Eqs. (14) and (24)–(26) for $(L_e + L_a) \le l \le L$, Eqs. (8*b*) and (24)–(26) for $L_e < l < (L_e + L_a)$, and Eqs. (8*c*) and (24)–(26) for $l = L_e$. In each case, there are four equations corresponding to four variables: l, ΔT, T_{aw}, and T_h. From these equations, the linear hot zone temperature distribution as well as the hot zone length can be obtained as functions of time. In order to obtain the values of the four variables at different times, the equations can be solved sequentially. For an initial hot zone length l_i at an initial time t_i, the temperature drop over the hot zone can be obtained from Eq. (24), and the average hot zone wall temperature T_{aw} and the hot zone temperature at the evaporator end cap T_h can be obtained from Eqs. (25) and (26), respectively. Then, the hot zone length at time $t = t_i + \Delta t$, where Δt is the time step, can be calculated using Eq. (8*b*) or (14), depending on the location of the hot zone front. The values of ΔT, T_{aw}, and T_h can be calculated at time $t_i + \Delta t$ using the corresponding hot zone length obtained.

Figure 2 compares the analytical wall temperature with the experimental outer wall temperature data for case 13 of Faghri et al. (1991a, 1991b) and Buchko (1990). It should be mentioned that the analytical wall temperature is a lumped average temperature in the radial direction over the heat pipe wall and wick. The radial temperature difference over the wall and wick

Downloaded 13 Dec 2010 to 193.140.21.150. Redistribution subject to ASME license or copyright; see http://www.asme.org/terms/Terms_Use.cfm

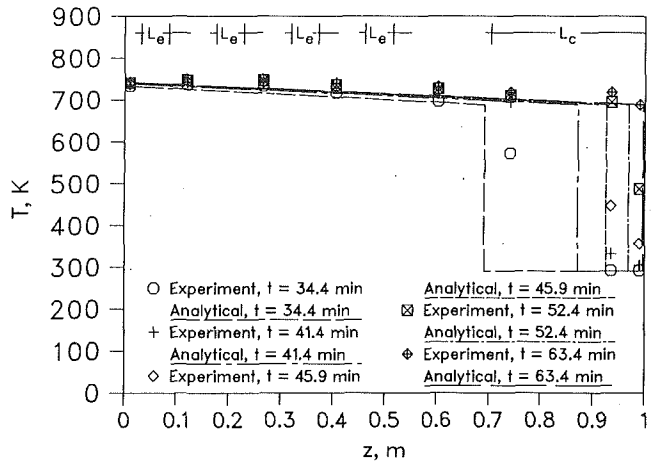

Fig. 2 The analytical wall temperature compared with the experimental data for Case 13*a* (Faghri et al., 1991)

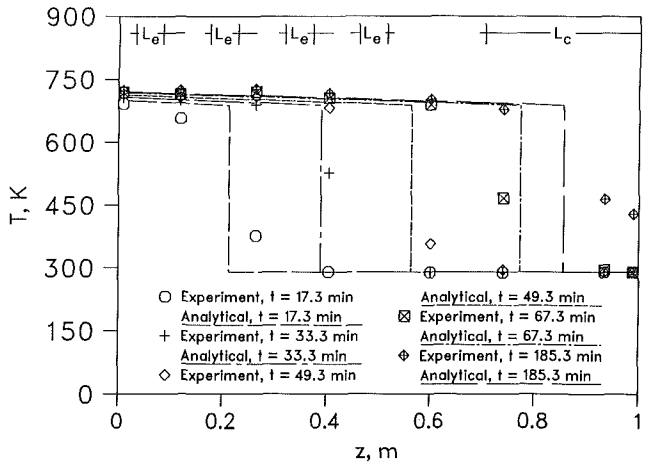

Fig. 3 The analytical wall temperature compared with the experimental data for Case 11*a* (Faghri et al., 1991)

regions is small due to the small thickness and high thermal conductivities of the wick and wall. The solution started from the inlet of the condenser, and Eq. (14) was used to calculate l from T_{aw}, which was obtained from Eqs. (24) and (25). The agreement between the analytical results and the experimental data is generally good. Figures 3 and 4 compare the analytical wall temperatures with the experimental data for case 11*a* (Faghri et al., 1991a) and the experimental data for the case of Q_o = 289.6 W (Ponnappan, 1989) with an effective emissivity of 0.32 at the condenser. In both cases, the solutions started from the exit of the active evaporator when the hot zone temperature reached the continuum-rarefied transition temperature T_{tr} there, and Eqs. (8*c*), (24), and (25) were used in calculating the starting time. Both Eq. (8*b*) and Eq. (14) were involved in the subsequent calculation of the hot zone length. The analytical results in both cases agree very well with the experimental data except the curves nearest the condenser end caps. The experimental data near the condenser end caps indicated that those regions may have been only partially activated. However, the wall temperatures there are still rather low. The corresponding vapor temperatures are below the continuum-rarefied transition temperature, indicating that the vapor flow is still in a rarefied state. It can be seen from Figs. 2–4 that the temperature drops over the hot zone are highly dependent on the vapor space radius due to the fourth power of R_v in the analytical solution. For the heat pipe of Faghri et al. (1991a), the vapor space radius is relatively large, R_v = 10.75 mm, and the temperature drops over the hot zone are relatively small. However, for the heat pipe of Ponnappan (1989), the vapor space radius is small, R_v = 6.35 mm, and the temperature drops over the hot zone are significant. The analytical closed-form solution predicted the temperature drops over the hot zones remarkably well.

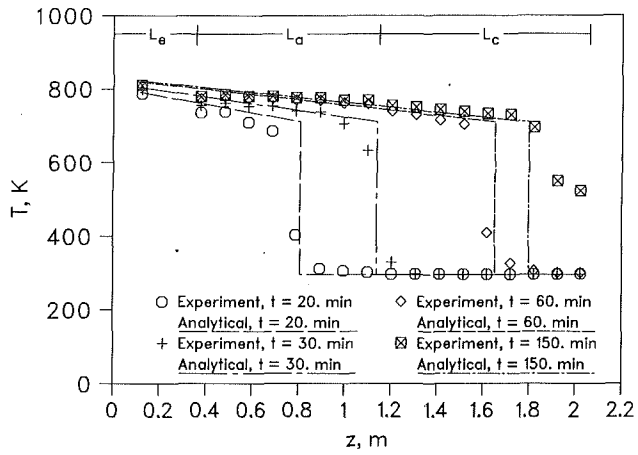

Fig. 4 The analytical wall temperature compared with the experimental data from Ponnappan (1989) for Q_o = 289.6 W

Since the analytical variables were obtained by solving the related equations sequentially, a time step Δt was involved in the calculation. The analytical results were calculated with different time steps, and it was found that the analytical results are insensitive to the time step used. A change of time step from Δt = 10.9 s to Δt = 5.41 s, for example, resulted in a change in the analytical solutions of less than 0.05 percent. This means that with a relatively small time step, the potential uncertainties related to the time step can be avoided.

For the comparison in Fig. 2, the solution started from the inlet of the condenser, and a calculated heat capacity of C = 905 J/(m · K) from the thermal properties and dimensions of the wall and wick was used in the computation without involving the additional heat capacity of the system. For the comparisons in Figs. 3 and 4, however, the solutions started from the exit of the active evaporator, and the additional heat capacities due to the electrical resistance heaters and radiation shields were involved (Cao and Faghri, 1992). For the analytical results in Fig. 3, an estimated additional heat capacity of 677 J/(m · K) was added in the evaporator and adiabatic sections. For the analytical results in Fig. 4, however, a calculated heat capacity C = 1100 J/(m · K) was used without taking into account the exact additional heat capacities due to the lack of detailed information. As a result, the hot zone fronts move somewhat faster than the corresponding transient experimental data.

Figure 5 shows the analytical outer wall temperature compared with the experimental data and the numerical solution by Cao and Faghri (1992) for case 11*a* of Faghri et al. (1991a). The flat fronts of the analytical results intercept the numerical curves almost in the middle of the slope regions, and compare well with the numerical solutions and the experimental data.

Figures 6–8 show the analytical transient profiles of the average hot zone wall temperature T_{aw}, the hot zone temperature at the evaporator end cap T_h, and the hot zone length l for cases 13*a* and 11*a* of Faghri et al. (1991a) and the case Q_o = 289.6 W of Ponnappan (1989), respectively. Although the hot zone temperature at the evaporator end cap may change substantially with time, the change in the average hot zone temperature with time is relatively small.

Frozen-Startup Limitation

The heat pipe performance limitations are generally de-

Downloaded 13 Dec 2010 to 193.140.21.150. Redistribution subject to ASME license or copyright; see http://www.asme.org/terms/Terms_Use.cfm

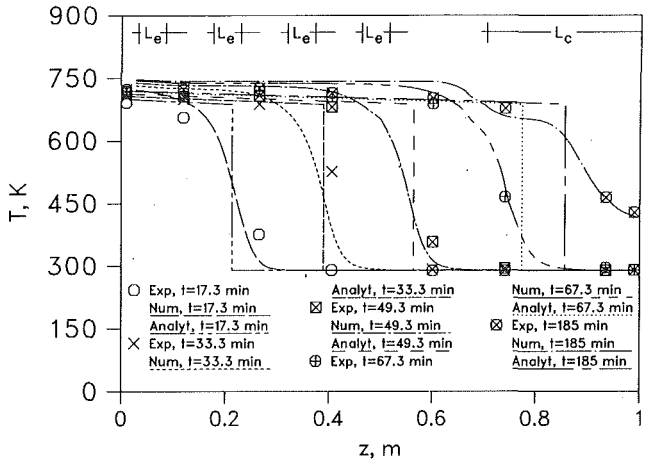

Fig. 5 The analytical wall temperature compared with the experimental data and numerical solution for Case 11*a* (Faghri et al., 1991)

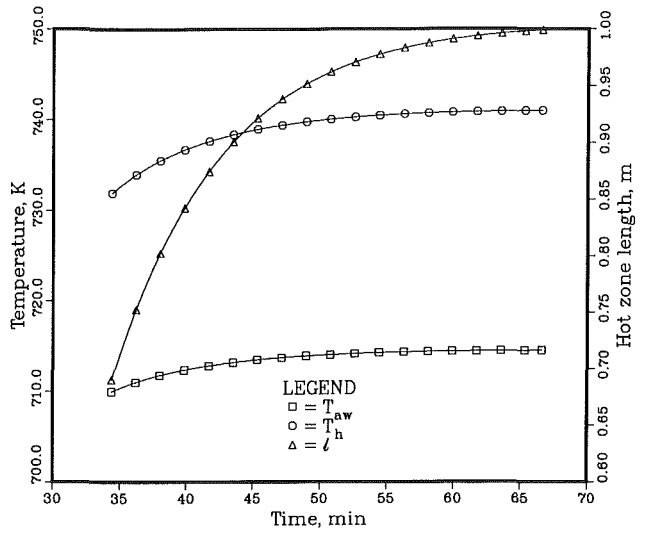

Fig. 6 Transient profiles of T_{aw}, T_h, and l for Case 13*a* (Faghri et al., 1991)

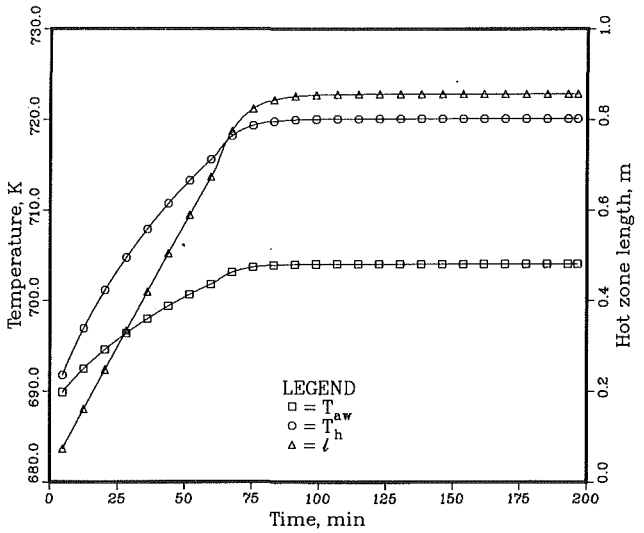

Fig. 7 Transient profiles of T_{aw}, T_h, and l for Case 11*a* (Faghri et al., 1991)

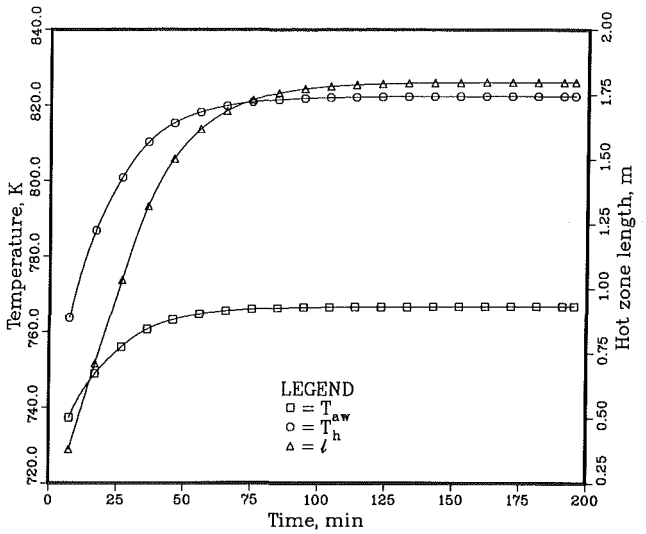

Fig. 8 Transient profiles of T_{aw}, T_h, and l for the case with Q_o = 289.6 W (Ponnappan, 1989)

scribed to be the sonic, boiling, and capillary limits (Chi, 1976; Dunn and Reay, 1982). In most cases, heat pipe designs are based on these limits. When the vapor velocity in the heat pipe reaches sonic or supersonic values, this working condition is called the sonic limit. The sonic limit does not necessarily represent an operational failure. During the high-temperature heat pipe startup process, sonic or supersonic vapor flow will always be encountered due to the low vapor density. In most cases, the sonic or supersonic vapor flow is temporary and will disappear when the heat pipe working temperature rises to a sufficiently high level.

If the radial heat flux or the heat pipe wall temperature becomes excessively high, boiling of the working fluid in the wick may severely affect the circulation of the working fluid and lead to the boiling limit. The boiling limit rarely happens for a high-temperature heat pipe with liquid metal working fluids, due to the high thermal conductivity of the liquid metal and the thin wick structure.

For a given heat pipe capillary wick structure and working fluid combination, the ability of the capillary structure to circulate the working fluid is limited, which is called the capillary limit. The capillary limit consideration is usually based on the steady-state and fully started condition, and is related to the heat pipe effective length when designing a heat pipe. During the startup process from the frozen state, the active length is less than the total length, and the distance the liquid has to travel in the wick is less than that required for steady-state operation. Therefore, the capillary limit will not occur during the startup process if the heat input at the evaporator is not very high and is not applied suddenly, i.e., the heat input condition does not exceed the design limit. However, when a heat pipe starts with the working fluid frozen and heat is applied only in the evaporator region, startup may be disrupted due to freezing out of the working fluid from the evaporation zone to the adiabatic or condensation zone. In this case, a frozen-startup limit, which is different from the normal operation limits, needs to be considered.

Figure 9 schematically shows the heat pipe startup process from the frozen state. The heat input flux q_e is applied at the evaporator and evaporation takes place at the wick–vapor interface. The vapor flows down the heat pipe and condenses on the wick surface, releasing its latent heat. Meanwhile, a liquid–solid interface in the wick moves down the heat pipe with a velocity U_i due to the vapor condensation on the wick surface. Since the wick is very thin and the effective thermal conductivity of the wick is large, the radial temperature difference in the wick can be neglected. The evaporated working fluid is accumulated at the adiabatic inlet with a total mass

Downloaded 13 Dec 2010 to 193.140.21.150. Redistribution subject to ASME license or copyright; see http://www.asme.org/terms/Terms_Use.cfm

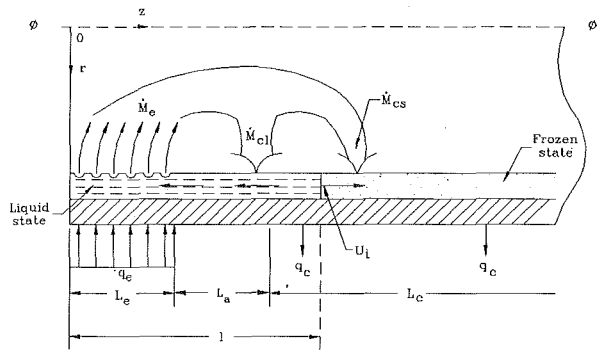

Fig. 9 Description of the frozen-startup limit

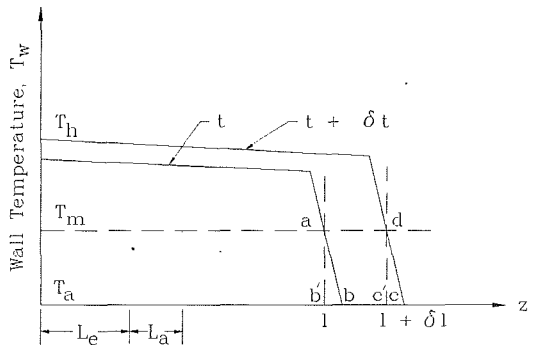

Fig. 10 Description of the criterion of frozen-startup limit

flow rate $\dot{M}_e$ as shown in the figure. The total vapor mass flow rate $\dot{M}_e$ is split into $\dot{M}_{cl}$ and $\dot{M}_{cs}$, which condense on the wick surface where the liquid phase of the working fluid is present and on the wick surface where the working fluid is solid, respectively. The mass flow rate that condenses on the liquid-wick surface, $\dot{M}_{cl}$, helps to supply liquid condensate back to the evaporator section by the capillary pumping action in the liquid working fluid region. The mass flow rate that condenses on the solid-wick region, $\dot{M}_{cs}$, is virtually frozen out and cannot flow back to the evaporator section. However, the movement of the liquid–solid interface in the wick down the heat pipe will increase the mass of the liquid working fluid, and may compensate the mass loss due to the freezing out of the vapor on the frozen solid-wick surface. A mass balance over the liquid working fluid in the liquid-wick region requires that

$$\varphi\rho_l A_w' U_i \geq \dot{M}_e - \dot{M}_{cl} = \dot{M}_{cs} \tag{27}$$

where φ is the porosity of the wick, ρ_l is the liquid density of the working fluid, and A_w' is the cross-sectional area of the working fluid in the wick. Equation (27) indicates that the amount of liquid mass increase in the wick due to the liquid–solid interface movement should be greater than that of the mass loss from the liquid-wick region due to the vapor freezing out on the solid-wick interface. When Eq. (27) is not satisfied, the mass of liquid working fluid in the liquid-wick region begins to decrease. As a result, liquid depletion at the evaporator may occur due to the insufficient liquid supply to the evaporator. Since this requirement is directly related to the heat pipe frozen startup, Eq. (27) is referred to as the frozen startup limit in this paper.

Equation (27) can also be expressed as

$$h_{fg}\varphi\rho_l A_w' \frac{dl}{dt} \geq Q_e - Q_{cl} - \int_{V_l} \rho c \frac{\partial T}{\partial t}\, dV \tag{28}$$

where l is the location of the liquid–solid interface measured from the evaporator end cap, h_{fg} is the evaporation/condensation latent heat, Q_e is the total heat input rate related to q_e at the evaporator, Q_{cl} is the sum of the axial conduction rate into the region $z > l$ and the heat dissipation rate from the heat pipe related to q_c in the region $z \leq l$, and V_l is the volume of heat pipe wall and wick in the region $z \leq l$.

For high-temperature heat pipe startup from the frozen state, an explicit approximate relation for the startup limit can be derived. As demonstrated by Cao and Faghri (1992), startup is characterized by a hot zone with a relatively steep front moving toward the condenser end cap. At time t, the wall temperature distribution is shown schematically in Fig. 10. The location of the melting front in the wick is at $z = l$. At time $t + \delta t$, the corresponding melting front moves to $l + \delta l$. The melting temperature T_m is also indicated in the figure, which intercepts the two curves at points a and d. Assuming the heat pipe has a heat capacity C per unit length (including both wall and wick and having units of the J/m·K), the heat energy received by the part of the slope region whose temperature is below T_m during the time interval δt is

$$Q_{cs}\,\delta t = C \cdot A_{a-b-c-d} \tag{29}$$

where $A_{a-b-c-d}$ is the area enclosed by the curves connecting points a, b, c, and d. Since

$$A_{a-b-c-d} \approx A_{a-b'-c'-d} = (T_m - T_a)\delta l \tag{30}$$

we have

$$Q_{cs}\delta t = C(T_m - T_a)\delta l \tag{31}$$

The corresponding mass of vapor that condensed on the frozen part of the wick during the time interval δt, neglecting the axial conduction, is

$$\delta M_{cs} = \dot{M}_{cs}\delta t = Q_{cs}\delta t / h_{fg} = C(T_m - T_a)\delta l / h_{fg} \tag{32}$$

The corresponding mass condensation rate is

$$\dot{M}_{cs} = \delta M_{cs}/\delta t = \frac{C(T_m - T_a)}{h_{fg}} \frac{\delta l}{\delta t} \tag{33}$$

Assuming the melting front velocity in Fig. 9 is U_i, the corresponding rate of increase of the liquid mass is $\varphi\rho_l A_w' U_i$ and the time rate of change in the hot zone length is:

$$\frac{\delta l}{\partial t} = U_i \tag{34}$$

According to Eq. (27) and Eqs. (33) and (34), we have

$$\varphi\rho_l A_w' U_i \geq C(T_m - T_a)U_i / h_{fg} \tag{35}$$

Rearranging the above equation gives

$$\frac{\varphi\rho_l A_w' h_{fg}}{C(T_m - T_a)} \geq 1 \tag{36}$$

Equation (36) is an approximate expression of the frozen startup limit for high-temperature heat pipes and is applicable to circular and noncircular cross-sectional heat pipes. For convenience, the term on the left-hand side of Eq. (36) is referred to as FSL, which stands for frozen startup limit.

For a conventional circular heat pipe,

$$A_w' = 2\pi R_v \delta_l' \tag{37}$$

where R_v is the radius of the vapor space and δ_l' is the thickness of the working fluid in the wick structure. Also, in this case,

$$C(T_m - T_a) \approx (2\pi R_v \delta_l' c_{me}\rho_{\text{eff}} + 2\pi R_o \delta_w c_w \rho_w)(T_m - T_a) + 2\pi R_v \delta_l' H\rho_l\varphi \tag{38}$$

where c_{me} is the average effective specific heat of the wick over the liquid wick and solid wick, ρ_{eff} is the effective density of the porous wick, δ_w is the thickness of the wall, and H is the latent heat due to melting of the working fluid in the wick. Consequently, Eq. (36) can be written as

$$\text{FSL} = \frac{\varphi\rho_l R_v \delta_l' h_{fg}}{(R_v\delta_l' c_{me}\rho_{\text{eff}} + R_o\delta_w c_w\rho_w)(T_m - T_a) + R_v\delta_l' H\rho_l\varphi} \geq 1 \tag{39}$$

Downloaded 13 Dec 2010 to 193.140.21.150. Redistribution subject to ASME license or copyright; see http://www.asme.org/terms/Terms_Use.cfm

For a thick wall or wick, R_o and R_v in Eq. (39) should be replaced by the average radius of the wall R_{wo} or the average radius of the wick R_{vw}.

$$R_{wo}=0.5(R_w+R_o) \tag{40}$$

or

$$R_{vw}=0.5(R_v+R_w) \tag{41}$$

It should be pointed out that for normal operation, δ_l' may not be necessarily equal to the wick structure thickness δ_l.

The criterion for the frozen startup limit was first applied to the heat pipe studied by Faghri et al. (1991a). The minimum working fluid inventory in the heat pipe was $M_t = 30$ g. The working fluid thickness in the wick structure was estimated to be

$$\delta_l'=\frac{M_t}{2\pi R_v L\rho_l\varphi}\approx 0.81 \text{ mm} \tag{42}$$

Substituting Eq. (42) and other geometric parameters and thermal properties into Eq. (39) yields

$$\text{FSL}\approx 1.46>1 \tag{43}$$

Equation (43) indicates that the heat pipe design satisfied the criterion for frozen startup, and the heat pipe would not encounter the frozen startup limit during normal operation. This is indeed the case for the operation of this heat pipe. The heat pipe started from the frozen state many times without encountering any difficulties (Faghri et al., 1991a). However, it is important to note that the value of FSL is very close to 1. This means that the frozen startup limitation identified in this paper is indeed a potential factor that may affect the heat pipe startup process from the frozen state.

For the heat pipe studied by Ponnappan (1989), the working fluid inventory in the screen and grooves was $M_t = 67.52$ g. The average porosity of the wick structure was taken to be $\varphi = 0.6$. Since the wick structure is relatively thick, the average radius of the wick structure R_{vw} (Eq. 41) was used

$$R_{vw}=0.5(R_v+R_w)=0.0079 \text{ m}$$

Therefore,

$$\delta_l'=\frac{M_t}{2\pi R_{vw}L\rho_l\varphi}=1.31 \text{ mm} \tag{44}$$

Substituting Eq. (44) into Eq. (39) together with other geometric parameters and thermal properties yields

$$\text{FSL}\approx 1.82>1$$

In the above computation, the working fluid in the wick has been assumed to be uniformly distributed along the heat pipe length, which is the case for normal heat pipe operation. However, the actual thickness of working fluid in the wick structure may sometimes deviate largely from the value based on the assumption of a uniform distribution. This is especially true for the heat pipe shutdown process, where the wall temperature in the condenser section may be much lower than that in the evaporator section. As a result, a large amount of vapor may be frozen in the condenser region close to the condenser end cap. In this case, the actual thickness of the working fluid in the wick structure δ_l' in the evaporator is very small, and the frozen startup criterion described above will not be satisfied. An attempt to restart the heat pipe will not be successful, such as the experimental study described by Merrigan et al. (1986).

From Eqs. (36) and (39), it can be seen that a larger working fluid inventory and larger evaporation/condensation latent heat aid in the startup process from the frozen state, while a larger heat pipe heat capacity and higher melting temperature of working fluid have an opposite effect. Like other working limit criteria, the frozen startup criterion presented in this paper provides a fundamantal guidance for the heat pipe design to avoid difficulties during startup from the frozen state.

Conclusions

A closed-form solution based on the flat-front startup model for heat pipe startup from the frozen state was derived. The analytical solutions were compared with both experimental and numerical solutions with good agreement. The closed-form solution obtained in this chapter provides a quick prediction method for the heat pipe startup process and is very useful for practical engineering purposes. A heat pipe limitation related to frozen startup was identified and an explicit criterion for the high temperature startup was obtained. The frozen startup limitation identified in this chapter provides a fundamental guidance for the heat pipe design.

Acknowledgments

Funding for this work was provided by a joint effort of the NASA Lewis Research Center and the Thermal Energy Group of the Aero Propulsion Laboratory of the U.S. Air Force under contract No. F33615-89-C-2820.

References

Buchko, M. T., 1990, "Experimental Investigation of Low and High Temperature Heat Pipes With Multiple Heat Sources and Sinks," Master's Thesis, Wright State University, Dayton, OH.

Busse, C. A., 1967, "Pressure Drop in the Vapor Phase of Long Heat Pipes," *Thermionic Conversion Specialist Conference*, Palo Alto, CA, pp. 391–398.

Cao, Y., and Faghri, A., 1992, "A Numerical Analysis of High Temperature Heat Pipe Startup From the Frozen State," to appear in ASME JOURNAL OF HEAT TRANSFER.

Chi, S. W., 1976, *Heat Pipe Theory and Practice*, Hemisphere, Washington, DC.

Cotter, T. P., 1965, *Theory of Heat Pipes*, LA-3246-MS.

Cotter, T. P., 1967, "Heat Pipe Start-Up Dynamics," presented at the Thermionics Conversion Specialist Conference, Palo Alto, CA, Oct. 30–Nov. 1.

Dunn, P. D., and Reay, D. A., 1982, *Heat Pipes*, 3rd ed., Pergamon Press, Oxford, United Kingdom.

Faghri, A., 1989, "Performance Characteristics of Concentric Annular Heat Pipes: Part II—Vapor Flow Analysis," ASME JOURNAL OF HEAT TRANSFER, Vol. 111, pp. 851–857.

Faghri, A., Buchko, M., and Cao, Y., 1991a, "A Study of High Temperature Heat Pipes With Multiple Heat Sources and Sinks: Part I— Experimental Methodology and Frozen Startup Profiles," ASME JOURNAL OF HEAT TRANSFER, Vol. 113, pp. 1003–1009.

Faghri, A., Buchko, M., and Cao, Y., 1991b, "A Study of High Temperature Heat Pipes With Multiple Heat Sources and Sinks: Part II—Analysis of Continuum Transient and Steady State Experimental Data With Numerical Predictions," ASME JOURNAL OF HEAT TRANSFER, Vol. 113, pp. 1010–1016.

Merrigan, M. A., Keddy, E. S., and Sena, J. T., 1986, "Transient Performance Investigation of a Space Power System Heat Pipe," *Proc. AIAA/ASME 4th Joint Thermophysics and Heat Transfer Conf.*, AIAA-86-1237, Boston, MA, June 2–4.

Pletcher, R. H., Minkowycz, W. J., Sparrow, E. M., and Schneider, G. E., 1988, "Overview of Basic Numerical Methods," in: *Handbook of Numerical Heat Transfer*, Wiley, New York.

Ponnappan, R., 1989, "Studies on the Startup Transients and Performance of a Gas-Loaded Sodium Heat Pipe," Technical Report, WRDC-TR-89-2046, Universal Energy Systems, Inc., Dayton, OH.

Sockol, P. M., and Forman, R., 1970, "Re-examination of Heat Pipe Startup," *Proc. 9th IEEE Thermionic Conversion*, pp. 571–573.

Downloaded 13 Dec 2010 to 193.140.21.150. Redistribution subject to ASME license or copyright; see http://www.asme.org/terms/Terms_Use.cfm

Freezing Flow in a Subcooled Permeable Medium

S. K. Griffiths
Sandia National Laboratories,
Livermore, CA 94551-0969

R. H. Nilson
S-CUBED,
A Division of Maxwell Laboratories,
La Jolla, CA 92038-1620

Analytical similarity solutions are derived for the problem of transient one-dimensional flow and freezing of a liquid in an initially dry permeable half-space. The structure of the flow consists of three regions: a liquid zone in which the temperature decreases to the freezing temperature, a central two-phase zone where the temperature is at the freezing point, and a leading gas-filled region in which the temperature is nearly undisturbed. The propagation velocity of this intrusion is determined as a function of the subcooling, latent heat, and other process parameters. As the inlet temperature approaches the freezing temperature, the governing equations admit a pair of solutions having propagation velocities that sometimes differ by more than an order of magnitude.

Introduction

The freezing of liquids within permeable materials is important in a number of natural processes and engineering systems. Previous mathematical investigations have generally addressed situations in which fluid motions are either absent or induced by buoyancy forces, resulting in heat transfer processes controlled by conduction or natural convection (Viskanta, 1985; Chellaiah and Viskanta, 1989). Previous studies involving forced convection deal mainly with the two-dimensional growth of the frozen zone surrounding a cooling pipe embedded in a saturated medium to achieve soil stabilization or prevent water encroachment (Goldstein and Reid, 1978; Frivik and Comini, 1982). There have also been a number of experimental studies aimed at the characterization of partially frozen soils, including the determination of their hydraulic conductivity (Black and Miller, 1990). In contrast to those earlier studies, our interest lies in the transient freezing of a one-dimensional pressure-driven flow.

The present paper addresses the freezing flow of a liquid that invades a dry permeable medium having an initial temperature less than the freezing temperature of the liquid. Freezing will occur at the leading edge of the flow when the fluid first contacts the subcooled matrix. The frozen phase will begin to accumulate in the relatively stagnant interstices of the matrix, leaving the remainder of the porosity to accommodate forward motion of the liquid. Moreover, for moderate amounts of subcooling, the local accumulation of frozen phase should nowhere be so great as to entirely obstruct the flow. Over time, the continuing inflow of heat by conduction and convection will gradually melt the frozen liquid that had solidified earlier, resulting in a traveling wavelike structure having three distinct regions: a liquid-filled inflow zone, a central zone containing frozen liquid as well as mobile liquid, and a thermal precursor zone containing only indigenous gas, as illustrated schematically in Fig. 1. For later reference, note that the subscripts 1, 2, and 3 will be used to designate a particular region of the flow, while the subscripts I and II will refer to the interfaces between regions.

The goal of our analysis is to describe such a freezing flow in a fundamental manner that retains only the essential features of the problem. The following simplifications are consistent with this goal: (1) one-dimensional flow, (2) incompressible liquid, (3) distinct freezing temperature, (4) local thermal equilibrium between fluid and solid phases, (5) capillary and gravity forces small compared to pressure and viscous forces, (6) indigenous gas completely and uniformly displaced by invading liquid, (7) viscosity and heat capacity of indigenous gas small compared to those of invading liquid, (8) kinetic energy, viscous dissipation, and flow work small compared to convection and conduction, (9) no density change on freezing, (10) linear relative permeability functions. The first seven of these are so familiar as to require no commentary; the eighth is almost certain to be satisfied for liquid flows in permeable media (Garg and Pritchett, 1977), and the last two can be easily relaxed by the reader, as explained at the appropriate points in the analysis. No further simplifications will be made.

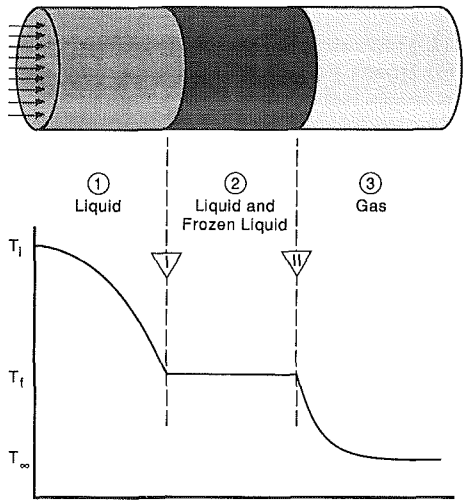

Fig. 1 Schematic of flow structure and temperature profile

The essential processes included in the model are energy transport by conduction and convection, freezing controlled by temperature and latent heat, and a flow velocity that depends upon the applied pressure, penetration depth, and effective permeability. All of these processes are coupled because the effective permeability depends upon the amount of freezing.

Mathematical Model

Under the condition stated above, conservation of mass and energy may be written in the following form, which is applicable in regions containing mobile liquid in possible combination with frozen liquid that is attached to the surface of the solid matrix:

Contributed by the Heat Transfer Division for publication in the JOURNAL OF HEAT TRANSFER. Manuscript received by the Heat Transfer Division March 1991; revision received June 1992. Keywords: Phase-Change Phenomena, Porous Media. Associate Technical Editor: F. P. Incropera.

Copyright © 1992 by ASME
Downloaded 13 Dec 2010 to 193.140.21.150. Redistribution subject to ASME license or copyright; see http://www.asme.org/terms/Terms_Use.cfm

$$\frac{\partial}{\partial t}(\rho_f \phi f + \rho_l \phi(1-f)) + \frac{\partial}{\partial x}(\rho_l \phi(1-f)u) = 0 \quad (1)$$

$$\frac{\partial}{\partial t}(\rho_f \phi f e_f + \rho_l \phi(1-f)e_l + \rho_m(1-\phi)e_m) + \frac{\partial}{\partial x}(\rho_l \phi(1-f)e_l u) = \frac{\partial}{\partial x}\left(\kappa \frac{\partial T}{\partial x}\right) \quad (2)$$

Here, x and t are position and time, ϕ is the porosity, f is the fraction of porosity occupied by frozen liquid, u is the interstitial velocity of the flowing liquid, T is the temperature, and κ is the thermal conductivity, while ρ and e are density and internal energy, with subscripts l, f, and m referring to liquid, frozen liquid, and matrix, respectively.

These conservation equations resemble those normally used to describe evaporating and condensing flows of steam in permeable media (Morrison, 1973; Cheng, 1978; Faust and Mercer, 1979). As in those applications, the capacitance term of the continuity equation reflects the fact that the material of interest may exist in either of two phases, here, either unfrozen or frozen liquid. However, in contrast to earlier liquid/vapor applications, it is only our liquid phase that is mobile, so the liquid is the only phase that contributes to the advective fluxes of mass and energy. Similarly, the energy equation includes the internal energy stored within the frozen liquid, unfrozen liquid, and the solid matrix, but the advective energy flux is associated with the mobile liquid alone. Also, the advective energy flux is written in terms of internal energy, rather than enthalpy, because flow work is generally negligible for liquid flows in permeable media (Garg and Pritchett, 1977) and this affords some simplification of our notation.

The liquid velocity is controlled by the balance between pressure forces and viscous drag in accordance with Darcy's law

$$u\phi(1-f) = \tilde{u} = -k_r \frac{k}{\mu}\frac{\partial P}{\partial x} \quad (3)$$

in which P is the pressure, k is the permeability, and μ is the liquid viscosity. The interstitial velocity, u, is the actual velocity of the fluid, which exceeds the apparent or Darcy velocity, $\tilde{u}$, by the reciprocal of the available porosity. A relative permeability function, k_r, has been introduced to account for the reduction in permeability due to freezing. Our sample calculations utilize a simple linear relationship, $k_r = 1 - f$, based on analogy to flows involving two immiscible fluids (Scheidegger, 1974). This choice places our mobile liquid in the role of the nonwetting phase, since the frozen liquid should first appear within the relatively stagnant interstices normally occupied by a wetting phase.

No equations need be solved for the motion of the indigenous air displaced by the invading liquid, because the specific heat of a gas is too small to influence the energy transport and the gas viscosity is too small to cause a significant pressure rise ahead of the invading liquid. These features could, however, be added to the model while still permitting an exact solution. Also, we note that the gas/liquid displacement interface is stable against Saffman–Taylor viscous fingering (Homsy, 1987), but gravity-driven fingering (Glass et al., 1989) could occur if the flow were vertically down and gravitational forces were comparable to pressure and viscous forces.

Analysis

A few preliminary observations allow us to anticipate the three-region flow structure depicted in Fig. 1. Each of these observations is a consequence of the stated transport equations and the assumptions itemized earlier. First, with $\rho_l = \rho_f$, the quantity within the time derivative of the continuity equation is a constant, which requires that the volumetric flow rate of the liquid, $\rho_l u\phi(1-f)$, be uniform along the flow at any given instant. Second, since the liquid possesses a distinct freezing temperature, the partially frozen region must have a uniform temperature and, hence, a uniform value of the specific energy of the liquid, e_l. These two conditions imply that the advective energy flux, $\rho_l u\phi(1-f)e_l$, must be uniform. Thus, the spatial derivative of the advective energy flux is identically zero in the isothermal region, as is the conductive heat flux. It follows from the energy equation, Eq. (2) that there can be no time variation of the frozen fraction, f, anywhere within the partially frozen region. Although it does not necessarily follow

Nomenclature

c = specific heat = de/dT
D^* = diffusivity ratio = α_t/α_l
e = internal energy
f = fraction of porosity containing frozen liquid
k = permeability
k_r = relative permeability = $1 - f$
L = penetration depth
L = penetration velocity
$\mathcal{L}$ = energy of fusion = $e_l - e_f$
P = pressure
P^* = normalized pressure = $(P-P_\infty)/(P_i-P_\infty)$
Pe = Peclet number = $uL/\alpha_t = \lambda^2/D^*$
T = temperature
T_f = freezing temperature
T^* = normalized temperature = $(T-T_\infty)/(T_i-T_\infty)$
t = time
u = intersticial fluid velocity
$\tilde{u}$ = Darcy mean velocity
u^* = normalized fluid velocity = u/L
x = spatial coordinate
α_l = hydraulic diffusivity = $k(P_i-P_\infty)/\mu\phi$
α_t = thermal diffusivity of wet medium = $\kappa_1/(\rho_l c_l \phi + \rho_m c_m(1-\phi))$
α_3^* = ratio of dry to wet diffusivity = α_3/α_t
β = modified Peclet number = $u_1^*(\rho c)_l^* \lambda/(2D^*)^{1/2}$
ΔT^* = normalized temperature difference = $\rho_m c_m(1-\phi)(T_f - T_\infty)/\rho_l \phi \mathcal{L}$
η = scaled similarity variable = $\theta\lambda/(2D^*)^{1/2}$
$\hat{\eta}$ = scaled similarity variable = $\eta/(\alpha_3)^{1/2}$
θ = similarity variable = $x/L(t) = x/(\lambda(2\alpha_l t)^{1/2}$
κ = thermal conductivity
κ_3^* = ratio of dry to wet conductivity = κ_3/κ_1
λ = normalized penetration depth = $L/(2\alpha_l t)^{1/2}$
μ = liquid viscosity
ρ = density
$(\rho c)_l^*$ = $\rho_l c_l \phi/(\rho_l c_l \phi + \rho_m c_m(1-\phi))$
$(\rho c)_3^*$ = $\rho_m c_m(1-\phi)/(\rho_l c_l \phi + \rho_m c_m(1-\phi))$
ϕ = porosity

Subscripts

1 = inlet superheated region
2 = central partially frozen region
3 = subcooled region ahead of intrusion
∞ = ambient or far field
I = interface between regions 1 and 2
II = interface between regions 2 and 3
i = inlet boundary
f = frozen phase
l = liquid phase
m = matrix material

Downloaded 13 Dec 2010 to 193.140.21.150. Redistribution subject to ASME license or copyright; see http://www.asme.org/terms/Terms_Use.cfm

that f must also be spatially uniform, this must be the case when self-similar solutions exist. The existence of such solutions is now demonstrated by analytical construction.

The governing equations, Eqs. (1) and (2), together with constant boundary conditions (T_i, P_i) and uniform initial conditions (T_∞, P_∞), can be satisfied by similarity solutions in which the normalized dependent variables

$$T^* = \frac{T - T_\infty}{T_i - T_\infty},\ P^* = \frac{P - P_\infty}{P_i - P_\infty},\ u^* = \frac{u}{\dot{L}} \tag{4}$$

are expressed as analytical functions of the similarity variable

$$\theta = \frac{x}{L(t)} \text{ where } L(t) = \lambda(2\alpha_l t)^{1/2} \tag{5}$$

Here, L is the penetration depth of the liquid, $\dot{L}$ is the penetration velocity, $\alpha_l = k(P_i - P_\infty)/\mu\phi$ is the hydraulic diffusivity, and λ is an unknown eigenvalue, which represents the velocity of a freezing flow relative to that of an equivalent single-phase liquid flow. Thus, by definition, $\theta = 1$ at the leading edge of the intrusion, and $\lambda = 1$ when there is no freezing.

Under this similarity transformation, the energy equation yields the following ordinary differential equation for the temperature of the entry region:

$$2(\eta - \beta)\frac{\partial T^*}{\partial \eta} + \frac{\partial^2 T^*}{\partial \eta^2} = 0 \tag{6}$$

in which $\eta = \theta\lambda(2D^*)^{1/2}$, $\beta = u_1^*(\rho c)_l^*\lambda/(2D^*)^{1/2}$, and u_1^* is the fluid velocity, which must be uniform over the entry region because $\rho_l u \phi(1-f)$ is everywhere uniform, the liquid is incompressible, and $f = 0$ throughout the entry region. The two dimensionless parameters arising here are defined as follows:

$$D^* = \frac{\alpha_t}{\alpha_l} \text{ and } (\rho c)_l^* = \frac{\rho_l c_l \phi}{\rho_l c_l \phi + \rho_m c_m (1-\phi)} \tag{7}$$

where α_t is the thermal diffusivity of the liquid saturated medium and the c's are specific heats. The solution to Eq. (7) is

$$T^* = 1 + (T_f^* - 1)F(\eta)/F(\eta_I) \tag{8}$$

in which $F(\eta) = \text{erf}(\eta - \beta) + \text{erf}(\beta)$, T_f^* is the normalized freezing temperature, and the subscript I refers to the trailing interface shown in Fig. 1. Similarly, the temperature distribution of the air-filled precursor is simply a conduction profile, since convective transport by the gas is negligible.

$$T = T_f^* \,\text{erfc}(\hat{\eta})/\text{erfc}(\hat{\eta}_{II}) \tag{9}$$

Here, $\hat{\eta} = \eta/(\alpha_3^*)^{1/2}$, $\alpha_3^* = \alpha_3/\alpha_l$ is the ratio of dry to wet thermal diffusivity, and the subscript II refers to the leading interface where $\theta = 1$.

Jump conditions must be satisfied at the interfaces where melting and freezing occur. Since pressure is continuous in the absence of inertia, and temperature is continuous in the presence of conduction, it is only the amount of frozen liquid which changes abruptly. Recalling the subscript notation of Fig. 1, the interface balances of mass and energy may be written in the concatenated forms

$$u_1^* = u_2^*(1-f) = 1 \tag{10}$$

$$\frac{1}{\theta_1}\frac{\partial T^*}{\partial \theta}\bigg|_{\theta_1} = \frac{\kappa_3^*}{\theta_{II}}\frac{\partial T^*}{\partial \theta}\bigg|_{\theta_{II}^+} = -\frac{f\lambda^2}{D^*}\frac{T_f^*}{\Delta T^*}(\rho c)_3^* \tag{11}$$

in which κ_3^* and $(\rho c)_3^*$ are ratios of dry to wet thermal properties and $f \equiv f_2$ is the frozen fraction in the central two-phase region. The first of these requires that the inflow velocity be identical to the velocity of the leading edge and, further, that the liquid velocity be greater in the central region where some of the pore space is occupied by frozen liquid. These relationships can be readily modified, if desired, to account for a density contrast between frozen and unfrozen liquid. The second of the above equations indicates that local heat conduction must account for the latent heat effects. The parameter that arises is a normalized temperature difference or Stefan number

$$\Delta T^* = \frac{\rho_m c_m (1-\phi)(T_f - T_\infty)}{\rho_l \phi \mathcal{L}} \tag{12}$$

in which $\mathcal{L} = e_l - e_f$ is the energy of fusion. These energy balances also ensure that the rates of freezing and melting have the ratio required to maintain self-similarity.

The liquid velocity must be spatially uniform in regions 1 and 2, because the liquid is incompressible and the frozen fraction is uniform within each of these regions. This implies that the pressure gradient is uniform in each. Darcy's law can therefore be combined with the continuity requirements of Eq. (10) to yield

$$u_1^* = \frac{1}{\lambda^2}\left(\frac{1 - P_I^*}{\theta_I}\right) = u_2^*(1-f) = \frac{k_r}{\lambda^2}\left(\frac{P_I^*}{1-\theta_I}\right) = 1 \tag{13}$$

from which the interface pressure P_I^* is eliminated to reveal a simple relationship between the three primary unknowns:

$$\lambda^2 = \frac{k_r}{1 - \theta_I(1-k_r)} = \frac{1-f}{1 - f\theta_I} \tag{14}$$

As expected, λ is unity in the absence of freezing, and the velocity decreases when f is larger and/or the breadth of the partially frozen zone is greater. It is noted that any alternative relative permeability model may be introduced into Eq. (14) to replace the current choice of $k_r = 1 - f$.

To determine the unknown values of λ, θ_I, and f, Eq. (14) is solved in conjunction with the following pair of transcendental equations:

$$\lambda f = \left(\frac{2D^*\alpha_3^*}{\pi}\right)^{1/2}\frac{\Delta T^*}{\exp(\hat{\eta}_{II}^2)\text{erfc}(\hat{\eta}_{II})} \tag{15}$$

$$\theta_I = \frac{1 - T_f^*}{T_f^*}\frac{\exp(\hat{\eta}_{II}^2)\text{erfc}(\hat{\eta}_{II})}{F(\eta_I)\exp((\eta_I - \beta)^2)}(\kappa\rho c)_3^{*\,-1/2} \tag{16}$$

which are the jump balances of energy at the freezing and melting boundaries, Eqs. (11), with the temperature gradients now replaced by derivatives of the analytical profiles given earlier in Eqs. (8) and (9).

Results

Solutions are now presented for various values of the three primary parameters (D^*, ΔT^*, and T_f^*) while holding fixed the conductivity ratio and specific heat ratio at the typical values, $\kappa_3^* = 1/5$ and $(\rho c)_3^* = 1/2$. These are the only independent parameters, since $\alpha_3^* = \kappa_3^*/(\rho c)_3^*$, $(\rho c)_l^* = 1 - (\rho c)_3^*$, and the corresponding values of f, λ, and θ_I are constrained by Eqs. (14)–(16).

The changing character of the temperature profile is illustrated in Fig. 2, where ΔT^* is varied while D^* and T_f^* are held constant at 0.01 and 0.4, respectively. For clarity of discussion, the profiles are labeled with values of the frozen fraction, but the corresponding values of ΔT^* are also included in the legend. The temperature is uniform at T_f^* within the central region where liquid and frozen liquid are both present. The right edge of this thermal plateau is coincident with the leading edge of the liquid intrusion, which always lies at $\theta = 1$. The left edge of the plateau moves forward with increasing f, collapsing the plateau into a single point as the frozen fraction approaches unity. The remaining discontinuity of the temperature gradient is caused by the difference in thermal properties of wet and dry media.

The temperature gradients at the edges of the plateau become steep when the Peclet number, $\text{Pe} = uL/\alpha_t = \lambda^2/D^*$, is large. This is seen in Fig. 2 for cases having a small frozen fraction and, hence, a relatively large velocity, λ. In the limit of very

Downloaded 13 Dec 2010 to 193.140.21.150. Redistribution subject to ASME license or copyright; see http://www.asme.org/terms/Terms_Use.cfm

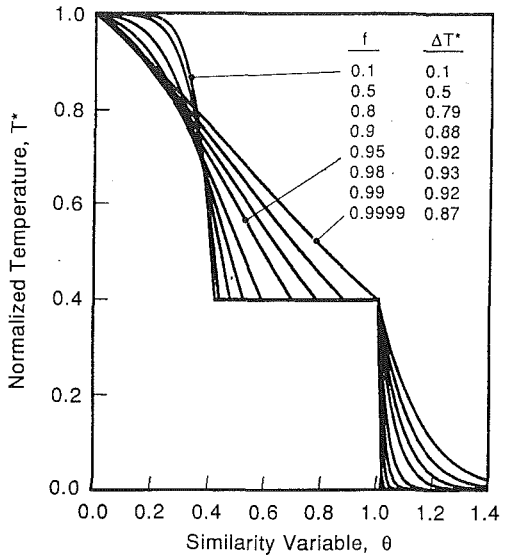

Fig. 2 Temperature profiles for various values of the normalized temperature difference, ΔT^*, with $D^* = 0.01$ and $T_f^* = 0.4$

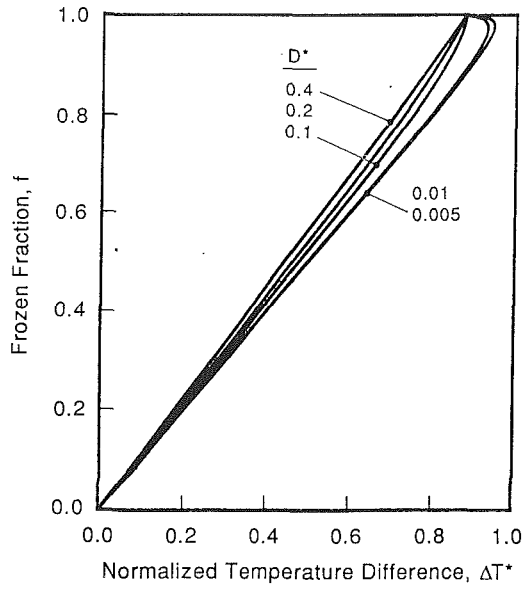

Fig. 3 Frozen fraction versus normalized temperature difference

large Peclet number, the conduction terms can be deleted from the energy equation, leaving a hyperbolic form that posseses discontinuous solutions having three temperature plateaus: an inlet region with $T^* = 1$, a partially frozen region at T_f^*, and the undisturbed far field with $T^* = 0$. The corresponding interfacial energy balances can be derived either by applying the large Pe limit to Eqs. (15) and (16), with $\eta_I < \beta$, or by writing interfacial balances, which include temperature jumps rather than conduction fluxes

$$f = \Delta T^* \text{ and } \theta_I = \frac{(\rho c)_l^* (1 - T_f^*)}{(\rho c)_f^* (1 - T_f^*) + (1 - (\rho c)_l^*)}. \quad (17)$$

The velocity of the intrusion then follows from Eq. (14). The first of these balance equations simply reveals the source of the scaling. The second, however, curiously implies that a very broad plateau may be buffered at the freezing temperature, even when the frozen fraction f is vanishingly small. These asymptotic results are applicable when the frozen fraction is relatively small, but are eventually violated when the flow velocity is reduced by clogging of the pores.

The relationship between f and ΔT^* is depicted in Fig. 3 for several choices of the diffusivity ratio, D^*. The curve labeled $D^* = 0.01$ corresponds to the family of solutions shown previously in Fig. 2. The amount of frozen liquid generally increases as the amount of subcooling increases or, equivalently, as the latent heat of freezing decreases. For the most part, these results are remarkably consistent with the large Peclet estimate, $f = \Delta T^*$, except that the frozen fraction reaches unity at a critical temperature difference, which is less than unity, and there are multiple solutions in this neighborhood.

The quantity of greatest interest is the normalized intrusion velocity, λ, which is shown in Fig. 4 as a function of ΔT^* for the same choices of D^*. The velocity generally decreases with increasing ΔT^* because the frozen fraction is then larger and, for that reason, the flow resistance is greater. In keeping with the previous figure, there are sometimes multiple solutions in the vicinity of the end member, which has a frozen fraction of unity. Moreover, it is seen that the intrusion velocity at this critical state is proportional to $(D^*)^{1/2}$ suggesting that the process has become conduction limited.

The nature of these conduction-limited end-member solutions can be understood by considering a severely subcooled situation with $\Delta T^* \gg 1$. One might expect to see a fully frozen

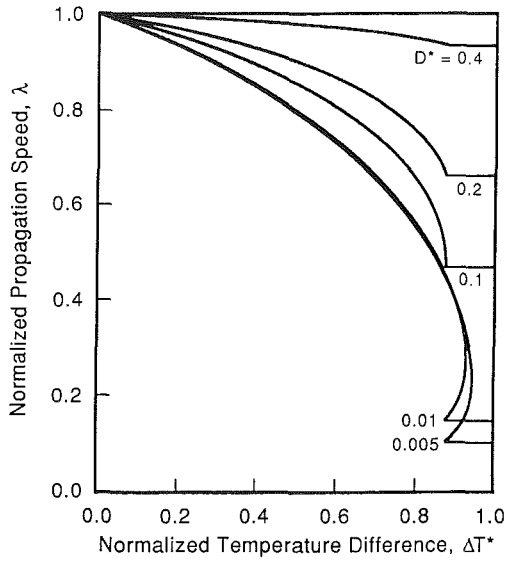

Fig. 4 Normalized propagation velocity versus normalized temperature difference

region of broad extent. However, if a blockage should form at the leading edge, there can be no liquid motion anywhere within the medium, leaving conduction as the only heat transfer mechanism. Since the inlet temperature is warmer than freezing, heat conduction will gradually melt a blockage, from the trailing edge forward, permitting fluid motion as soon as the melting is complete. However, the advancing fluid will immediately encounter the highly subcooled medium and freeze again unless heat is continuously supplied by conduction. Thus, under highly subcooled conditions, the liquid intrusion cannot advance any faster than a conduction wave, as suggested by the end-member speeds, which are indicated in Fig. 4 as applicable for all large values of ΔT^*.

These critical or end-member solutions have a number of interesting and somewhat unexpected properties. First, it is surprising that the breadth of the frozen zone is smallest under highly subcooled conditions. Second, it is remarkable that the frozen fraction always reaches unity at precisely the point where the width of the frozen region shrinks to zero. However, by inspection of Eq. (14) we see that this must occur in order

Downloaded 13 Dec 2010 to 193.140.21.150. Redistribution subject to ASME license or copyright; see http://www.asme.org/terms/Terms_Use.cfm

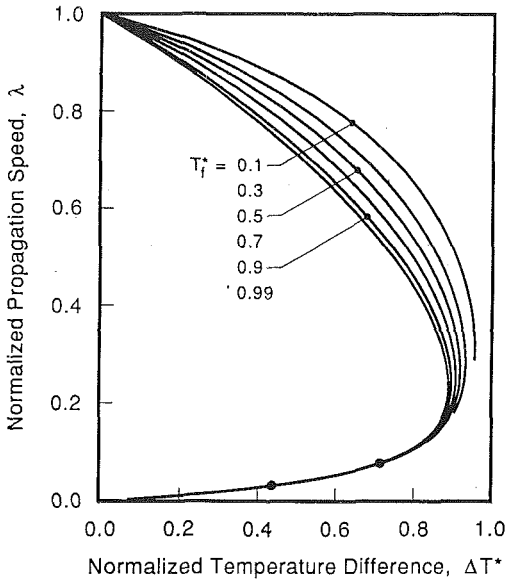

Fig. 5 Multiple solutions have vastly different speeds as $T_f^* \to 1$ with $D^* = 0.01$

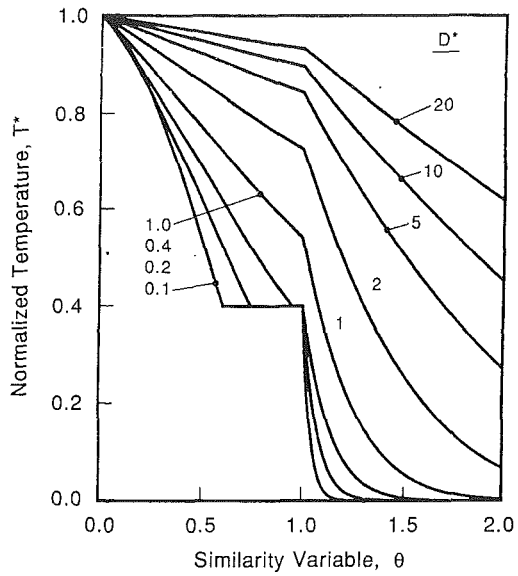

Fig. 6 Temperature profiles for various values of the normalized thermal diffusivity, D^*, with $f \to 0$ and $T_f^* = 0.4$

that the associated propagation velocity be physically plausible, rather than zero or infinity. Third, it is apparent in Figs. 3 and 4 that the critical temperature difference is independent of D^*. This might have been anticipated from the energy jump condition (15), which indicates that ΔT^* depends upon D^* only through the ratio λ^2/D^*, which is a constant for the end-member solutions, because their velocity, λ, is controlled by conduction and is, therefore, proportional to $(D^*)^{1/2}$. Finally, it is particularly surprising that multiple solutions are sometimes associated with near-critical temperature differences.

The multiplicity of solutions becomes more pronounced when the inlet temperature is closer to freezing, as seen in Fig. 5 where the bold dots mark the terminal points for $T_f^* = 0.7$ and 0.9. In the limit as $T_f^* \to 1$, two nontrivial solutions exist for all ΔT^* within the interval $0 < \Delta T^* \lesssim 0.9$, one having a relatively small frozen fraction and a large velocity, the other nearly frozen with a small velocity. These two solutions offer different balances between the rates of forward heat conduction and latent heat rejection, even though the related parameter $\Delta T^* \sim \Delta T/\mathcal{L}$ is the same for both. On the upper branch, a steep temperature gradient balances the relatively large rate of latent heat rejection associated with a large propagation velocity. On the lower branch, a smaller rate of heat conduction balances a smaller rate of latent heat rejection, since the product $\lambda f \mathcal{L}$ is much smaller.

Solutions on the lower branch of Fig. 5 can be understood in terms of the interfacial energy balance equations, which apply in the limit of small Peclet number

$$\lambda f = \Delta T^* \left(\frac{2D^* \alpha_3^*}{\pi}\right)^{1/2} \text{ and } \lambda \theta_1^2 = \frac{1 - T_f^*}{T_f^*} \left(\frac{\pi D^*}{2(\kappa\rho c)_3^*}\right)^{1/2}. \quad (18)$$

A careful examination of Fig. 5 reveals that the limiting family of solutions for $T_f^* \to 1$ is identical to the locus of end-member solutions, which each have $f = \theta_1 = 1$ for various T_f^*. Thus, upon replacing f and θ_1 with unity, the first of the small Peclet equations confirms that the velocity should increase with ΔT^*, in direct contrast to the large Peclet equations, Eqs. (17), which apply to the other branch. Similarly, the second of the above equations confirms that small values of the Peclet number, $Pe = \lambda^2/D^*$, are attainable when T_f^* is near unity, since the freezing front may then lie far behind the conduction front. Finally, λ may be eliminated between the pair of equations to deduce the end-member values of ΔT^*.

None of the partially frozen solutions can exist when the thermal diffusivity, D^*, is large enough to preheat the medium ahead of the flow. The gradual disappearance of the freezing flows is illustrated in Fig. 6 by a sequence of temperature profiles for increasing D^*. The central plateau is broadest when D^* is small and conduction is negligible. The plateau shrinks as D^* increases, disappearing entirely for D^* of order one. For greater D^*, the cold matrix is sufficiently preheated by conduction that the incoming liquid never encounters a subfreezing temperature, as illustrated by the temperature profiles having $T^* > T_f^*$ at $\theta = 1$. Although the thermal wave is free to outrun the liquid intrusion whenever $D^* \gtrsim 1$, the liquid intrusion can only lead when the temperature difference is subcritical and, hence, the frozen fraction is greater than zero.

Summary

Exact similarity solutions were derived for a fundamental problem of freezing flow in a subcooled permeable medium, which is initially dry. The flow structure consists of a liquid-filled inflow region, a partially frozen zone, and an air-filled precursor zone. The fluid velocity is uniform within both the entry region and the partially frozen zone, changing abruptly at their interface.

Although the frozen liquid is immobile, the partially frozen region migrates forward in time, because the trailing edge is melting while the leading edge is freezing. The penetration depth grows like the square root of time, as in the absence of freezing, but the velocity is reduced when some of the porosity is occupied by frozen liquid. Under highly subcooled conditions the frozen fraction reaches unity at the leading edge, thereby obstructing the flow and requiring that the penetration rate be no greater than that of heat conduction.

Multiple solutions are sometimes encountered in the vicinity of the fully frozen end members. This multiplicity spreads as the inflow temperature is reduced, such that two solutions having vastly differing velocities and frozen fractions may exist over a broad range of parameters.

Acknowledgments

The authors would like to thank an anonymous reviewer for providing us an elegant closed-form solution to Eq. (6). This work was supported by the U.S. Department of Energy under contract No. DE-AC04-76P00789.

Downloaded 13 Dec 2010 to 193.140.21.150. Redistribution subject to ASME license or copyright; see http://www.asme.org/terms/Terms_Use.cfm

References

Black, P. B., and Miller, R. D., 1990, "Hydraulic Conductivity and Unfrozen Water Content of Air-Free Frozen Silt," *Water Resources Research*, Vol. 26, No. 2, pp. 323–329.

Cheng, P., 1978, "Heat Transfer in Geothermal Systems," *Advances in Heat Transfer*, Vol. 14, pp. 1–106.

Chellaiah, S., and Viskanta, R., 1989, "Freezing of Water-Saturated Porous Media in the Presence of Natural Convection: Experiments and Analysis," ASME JOURNAL OF HEAT TRANSFER, Vol. 111, pp. 425–431.

Faust, C. F., and Mercer, J. W., 1979, "Geothermal Reservoir Simulation: 1. Mathematical Models for Liquid- and Vapor-Dominated Hydrothermal Systems," *Water Resources Research*, Vol. 15, No. 1, pp. 23–46.

Frivik, P. E., and Comini, G., 1982, "Seepage and Heat Flow in Soil Freezing," ASME JOURNAL OF HEAT TRANSFER, Vol. 104, pp. 323–328.

Garg, S. K., and Pritchett, J. W., 1977, "On Pressure Work, Viscous Dissipation, and the Energy Balance Relation for Geothermal Reservoirs," *Advances in Water Resources*, Vol. 1, No. 1, pp. 41–47.

Glass, R. J., Parlange, J.-Y., and Steenhuis, T. S., 1989, "Wetting Front Instability, 1. Theoretical Discussion and Dimensional Analysis," *Water Resources Research*, Vol. 25, No. 6, pp. 1195–1207.

Goldstein, M. E., and Reid, R. L., 1978, "Effect of Fluid Flow on Freezing and Thawing of Saturated Porous Media," *Proceedings of the Royal Society of London*, Series A, Vol. 364, pp. 45–73.

Homsy, G. M., 1987, "Viscous Fingering in Porous Media," *Annual Review of Fluid Mechanics*, Vol. 19, pp. 271–311.

Morrison, F. A., 1973, "Transient Multiphase Multicomponent Flow in Porous Media," *Int. J. Heat Mass Transfer*, Vol. 16, pp. 2331–2342.

Scheidegger, A. H., 1974, *The Physics of Flow Through Porous Media*, University of Toronto Press, Toronto, Canada.

Viskanta, R., 1985, "Natural Convection in Melting and Solidification," in: *Natural Convection Fundamentals and Applications*, S. Kakac, W. Aung, and R. Viskanta, eds., Hemisphere, Washington, DC, pp. 845–877.

Downloaded 13 Dec 2010 to 193.140.21.150. Redistribution subject to ASME license or copyright; see http://www.asme.org/terms/Terms_Use.cfm

Journal of Heat Transfer

Technical Notes

This section contains shorter technical papers. These shorter papers will be subjected to the same review process as that for full papers.

Experimental Evidence for the Temperature Waves Around a Rapidly Propagating Crack Tip

D. Y. Tzou[1]

Nomenclature

A = amplitude of the eigenfunction for temperature, °C
C = thermal wave speed, m/s
M = thermal Mach number defined as v/C
r = radial distance measured from the crack tip, mm
T = temperature, °C
v = crack speed, m/s
x_i = moving coordinates centered at the propagating crack tip, i = 1, 2 mm
θ = polar angle measured from crack surface, deg

Introduction

The wave behavior in heat conduction may become pronounced when the time-rate change of temperature in material continua is high. Typical examples include the thermal shock formation around a fast-moving heat source (Tzou, 1989a, 1989b, 1990c) and a rapidly propagating crack tip (Tzou, 1990a, 1990b). Especially when material failure is involved in a short-time transient, as demonstrated by Tzou (1989c, 1992a), the thermally induced crack may be initiated in a shorter period of time than that required for the diffusion behavior to be retrieved. The wave behavior in heat conduction, therefore, must be incorporated for a more informative analysis. A categorized, detailed review on the research of thermal wave theory is provided in a recent annual review article by Tzou (1992b) and will not be repeated here.

Development of the thermal wave theory has been made in two major directions. While an irreversible, nonequilibrium thermodynamic basis enhances the theoretical foundation (Jou et al, 1988; Tzou, 1992c), experimental evidence is needed for further promotion of engineering applications. The present work compares the wave solutions obtained by Tzou (1990a, 1990b) to the recent experimental results obtained by Zehnder and Rosakis (1991). The phenomenon under examination is the temperature rise induced by a rapidly propagating crack tip in 4340 steel. For a crack speed of 900 m/s, the crack surface is heated to a temperature of 450°C. The temperature results from local heating due to intensified plasticity developed in the vicinity of the propagating crack tip. Coincidences between the theory and the experiment include (1) parallel isotherm pattern in the near-tip region, (2) diminution of the temperature gradient in the radial direction measured from the crack tip, and (3) transition of isotherms to a hyperbola-like pattern at a higher crack speed of 980 m/s.

[1]Associate Professor, Department of Mechanical Engineering, The University of New Mexico, Albuquerque, NM 87131; Mem. ASME.

Contributed by the Heat Transfer Division of the THE AMERICAN SOCIETY OF MECHANICAL ENGINEERS. Manuscript received by the Heat Transfer Division May 1991; revision received April 1992. Keywords: Conduction, Thermophysical Properties. Associate Technical Editor: W. A. Sirignano.

Experimental Results

Recently, Zehnder and Rosakis (1991) performed a novel experiment determining the temperature distribution in the neighborhood of a rapidly propagating crack tip in 4340 steel. The experiment was made in a wedge-loaded compact tension specimen and the load level is sufficiently high to maintain a dynamic crack propagation. The crack speed covered in their experiment ranges from 900 to 1700 m/s but only the results for 900 and 980 m/s were reported in their paper. A total of eight infrared detectors were used in measuring the temperature rise. They are symmetrically placed in the direction perpendicular to that of crack propagation. Each measurement area is 160 μm × 160 μm and the sensitivity in detecting the temperature rise is 20°C. The rise time for temperature is in the range of 1 to 2 μs and a high rate increase of temperature is evident. Other details for the experimental procedure are clearly described in their work and will not be repeated here. Their results showed a temperature increase of 450°C over the ambient in the local area surrounding the crack tip. Depending on the material type, the local temperature may reach as high as several hundreds to a thousand degrees Celsius in dynamic crack propagation (Rice and Levy, 1969; Weichert and Schönert, 1974, 1978; Kuang and Atluri, 1985; Sung and Achenbach, 1987).

For a crack speed of 900 m/s, Fig. 1 shows the temperature contour pattern surrounding the crack tip. A local area of 3 mm × 1.5 mm in the neighborhood of the crack tip is selected in their presentation. A distinct feature is the parallel isotherms behind the crack tip. Also, due to equal spacing between the isochromatic lines, the temperature gradient in the r-direction, $T_{,r}$, seems to be a constant in the near-tip region. This behavior becomes more obvious by examining the parallel isotherms right above the crack tip. At the same crack speed, Fig. 2 shows the isotherm pattern made in a larger area surrounding the crack tip, 80 mm × 1.5 mm. The isotherms are parabola-like and have widely opened tails. For a slightly higher crack speed of 980 m/s, the isotherm pattern is shown in Fig. 3, where the same enlarged area of 80 mm × 1.5 mm is used. Note that a slight increase of the crack speed results in isotherms with much narrower tails, as evidenced by the isochromatic lines of 325°C in Figs. 2 and 3. In these figures, temperature rise over the ambient is presented. At the instant shown, the crack tip is located at $x_1 \simeq -0.5$ mm and $x_2 \simeq 0.6$ mm (Fig. 1) and $x_1 \simeq 0$ mm and $x_2 \simeq 0.6$ mm (Figs. 2 and 3).

Temperature-Wave Solutions

In the vicinity of a rapidly propagating crack tip, the asymp-

Copyright © 1992 by ASME
Downloaded 13 Dec 2010 to 193.140.21.150. Redistribution subject to ASME license or copyright; see http://www.asme.org/terms/Terms_Use.cfm

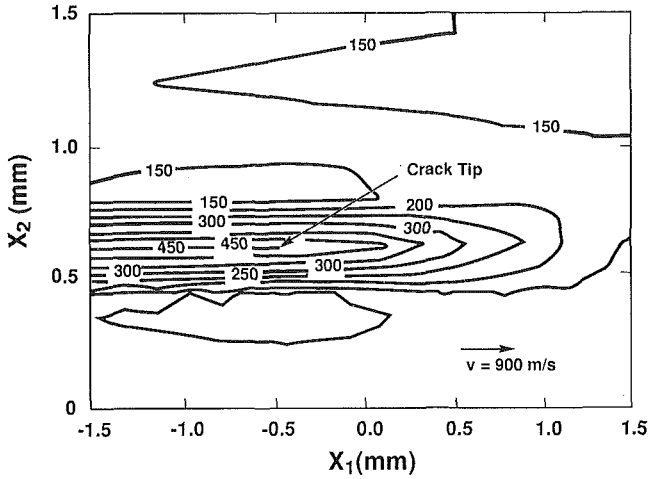

Fig. 1 Experimental results for the parallel isotherms behind the propagating crack tip; v = 900 m/s; reproduced from the paper by Zehnder and Rosakis (1991)

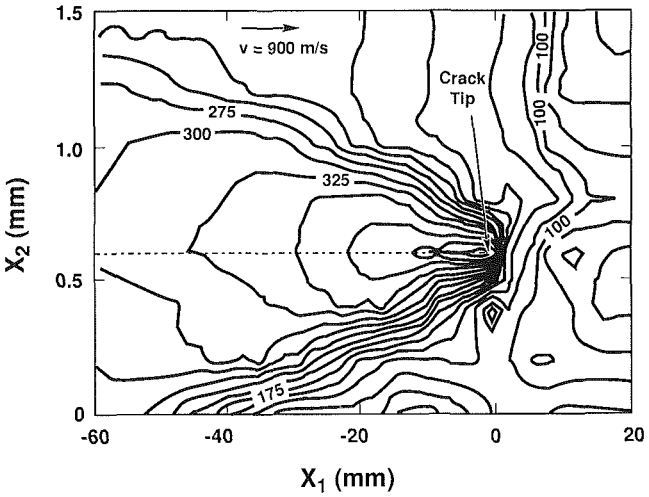

Fig. 2 Experimental results for the isotherms in a larger area surrounding the crack tip; v = 900 m/s; reproduced from the paper by Zehnder and Rosakis (1991)

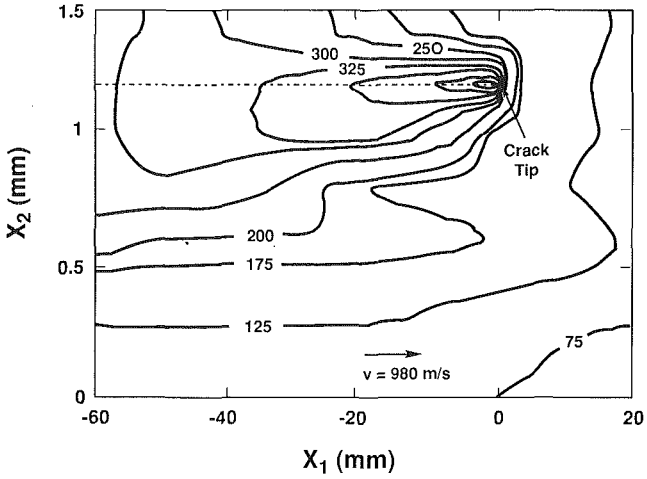

Fig. 3 Experimental results for the isotherms surrounding the crack tip; v = 980 m/s; reproduced from the paper by Zehnder and Rosakis (1991)

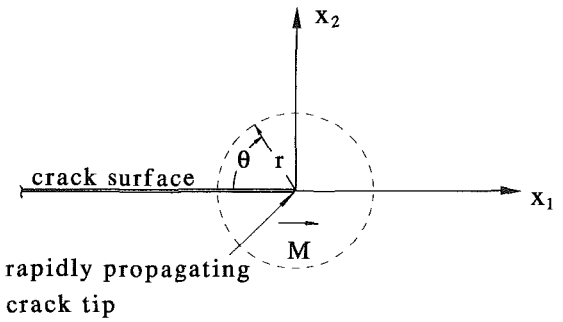

Fig. 4 Material coordinates convecting with the crack tip: Cartesian coordinates (x_1, x_2) and polar coordinates (r, θ)

totic solutions for the temperature waves have been obtained by Tzou (1990a). A thermal Mach number defined as M = v/C, with v being the crack speed and C the thermal wave speed, was introduced to characterize the near-tip temperature. The results are summarized as follows:

The subsonic range with $M<1$:

$$T(r,\theta)=A\sqrt{r}[(1-\mathrm{M}^2\sin^2\theta)^{1/2}-\cos\theta]^{1/2},\ \text{for } 0<\theta<\pi. \quad (1)$$

The transonic stage with $M=1$:

$$T(r,\theta)=\begin{cases} Ar\sin\theta, & 0<\theta<\pi/2 \quad \text{(heat-affected zone)} \\ 0, & \pi/2<\theta<\pi \quad \text{(thermally undisturbed zone).} \end{cases} \quad (2)$$

The supersonic range with $M>1$:

$$T(r,\theta)=\begin{cases} Ar^2(\mathrm{M}^2-1)^{1/2}\sin^2\theta, & 0<\theta<\sin^{-1}(1/\mathrm{M}) \quad \text{(heat-affected zone)} \\ 0, & \sin^{-1}(1/\mathrm{M})<\theta<\pi \quad \text{(thermally undisturbed zone).} \end{cases} \quad (3)$$

Three individual expressions result from the intrinsic transition of the temperature wave equation from elliptic, parabolic, to hyperbolic type in the respective range of the thermal Mach number. The coefficient A is the amplitude of the eigenfunctions resulting from the asymptotic analysis employing the hypovariable transformations. Respectively, its unit changes from $°C/\sqrt{m}$, °C/m, to C/m^2 when the thermal Mach number transits from the subsonic, transonic, to the supersonic ranges. The polar coordinates (r, θ) used for describing the state of the affairs in the near-tip region are defined in Fig. 4. They relate to the Cartesian coordinates by

$$x_1=-r\cos\theta, \quad x_2=r\sin\theta. \quad (4)$$

Due to symmetry of the problem, Eqs. (1)–(3) only present the temperature distributions in the upper-half plane. In the supersonic range with M > 1, Eq. (3), $\sin^{-1}(1/\mathrm{M})$ is the thermal shock angle defining the location of the thermal shock wave. The shock wave separates the heat-affected zone ($0<\theta<\sin^{-1}(1/\mathrm{M})$) from the thermally undisturbed zone ($\sin^{-1}(1/\mathrm{M})<\theta<\pi$) due to the finite speed of heat propagation. At the transonic stage with M = 1, the thermal shock angle reduces to $\pi/2$, as depicted by Eq. (2). The temperature in the thermally undisturbed zone is assumed zero without loss in generality.

Downloaded 13 Dec 2010 to 193.140.21.150. Redistribution subject to ASME license or copyright; see http://www.asme.org/terms/Terms_Use.cfm

Comparisons

Temperature rise in the experiment by Zehner and Rosakis results from energy dissipation due to intensified plasticity developed in front of the propagating crack tip. The temperature field thereby relies heavily on the way in which plastic energy is generated and dissipated. Because the near-tip stresses are highly localized, the intensity of the energy dissipation rapidly decreases when approaching the wake region. As a result, the temperature distribution behind the crack tip is dominated by heat conduction. According to Fig. 1, the energy dissipation developed in front of the crack tip renders a constant temperature of 450°C at the crack surface.

In the absence of modeling the energy dissipation in the analytical solutions, the wake region behind the crack tip is where a fair comparison should be made. If the wave behavior in heat conduction becomes pronounced, the thermal wave model should predict similar isotherm patterns.

(a) The Parallel Isotherms. Geometric configurations of isotherms can be obtained by equating the temperatures in Eqs. (1)–(3) to constants. With the assistance Eq. (4), the results are:

The subsonic range with $M<1$

$$(1-M^2)x_2^2+2\cdot\text{const}\cdot x_1=\text{cons}^2. \tag{5}$$

The transonic stage with $M=1$:

$$x_2=\text{cons for } \theta<\theta<\pi/2 \text{ (the heat-affected zone).} \tag{6}$$

The supersonic range with $M>1$:

$$-\sqrt{M^2-1}\,x_1x_2=\text{const for } 0<\theta<\sin-1(1/M) \text{ (the heat-affected zone).} \tag{7}$$

Note that the origins of (x_1,x_2) coordinates are shifted to the crack tip as shown by Fig. 4. In the subsonic range with $M<1$, Eq. (5) depicts a family of parabolas for the isotherms. The isotherms predicted by the classical diffusion model which assumes the thermal wave speed infinity ($C\to\infty$), fall into this category. When the value of C approaches infinity, the thermal Mach number reduces to zero ($M=0$) and Eq. (5) becomes

$$x_2^2+2\cdot\text{const}\cdot x_1=\text{const}^2. \tag{8}$$

In transition to the transonic stage, Eq. (6) depicts a family of isotherms parallel to the crack surface. In view of Fig. 1, such a special feature is well-captured in the thermal wave model. Since the crack tip is advancing into a heated area of 450°C, moreover, agreement between the theory and experiment implies a value of 900 m/s for the thermal wave speed in 4340 steel at an elevated temperature of 450°C. It is approximately five times slower than the speed of normal stress wave.

(b) Temperature Gradient at the Crack Tip. In Fig. 1, the parallel isotherms with equal spacing and temperature decrements away from the crack tip imply a finite value for the temperature gradient $T_{,r}$ at the crack tip. From the coordinate system in Fig. 4, more precisely, the use of the chain rule results in

$$\frac{\partial T}{\partial r}=\frac{\partial T}{\partial x_2}\frac{\partial x_2}{\partial r}=A\sin\theta, \text{ with } A\equiv T_{,2}. \tag{9}$$

Noticing that an added constant B is also allowed in the analytical solution (2), i.e.,

$$T(r,\theta)=Ar\sin\theta+B \quad \text{for} \quad 0<\theta<\pi, \tag{10}$$

the experimental results shown in Fig. 1 give

$$A=-1687.5\ ^\circ\text{C/mm}, \quad B=450\ ^\circ\text{C}. \tag{11}$$

Obviously, the temperature gradient in the x_2 direction determines the value of A while the temperature at the crack surface determines the value of B. Rather than a finite value of $T_{,r}$ at the crack tip, the diffusion model predicts a $1/\sqrt{r}$-type of singularity at the crack tip (Tzou, 1991a, 1991b). For the present problem, this is readily seen by the r derivative of Eq. (1) with $M=0$:

$$T_{,r}=\left(\frac{A}{2}\right)\cdot\frac{1}{\sqrt{r}}\cdot\sqrt{1-\cos\theta} \quad \text{for} \quad 0<\theta<\pi. \tag{12}$$

As shown by Eq. (1), the temperature possessing a $1/\sqrt{r}$-type of singularity in $T_{,r}$ will present a family of isotherms represented by

$$r[(1-M^2\sin^2\theta)^{1/2}-\cos\theta]=\text{const}. \tag{13}$$

Including the diffusion model with $M=0$, it is a family of *closed* curves concurrent in the neighborhood of the crack tip (Tzou, 1991a, 1991b). According to the experimental result shown in Fig. 1, obviously, this is not the case, and Eqs. (6) and (9)–(11) provide strong support for the activation of thermal wave behavior in the wake region. For the present problem, the wave behavior is pronounced due to the high-rate change of temperature induced by the rapid speed of crack propagation.

When the crack speed exceeds the thermal wave speed, the thermal Mach number transits into the supersonic range ($M>1$). In this case, the isotherms represented by Eq. (7) evolve into a family of hyperbolas. Comparing the isotherm patterns shown in Figs. 2 and 3, especially the ones with $T=325$°C, the tail region of the isotherm does show a clear trend of narrowing down. As summarized in Fig. 5, this salient feature is nicely preserved in the thermal wave theory when the value of M is greater than one. Since such an intrinsic transition of the isotherm pattern occurs in a slight increase of the crack speed (from 900 to 980 m/s), more refined experimental data in this region are needed for better resolutions. In passing, note that a perfectly symmetric pattern of isotherms is difficult to achieve in experiments. Although a Mode-I situation is attempted in the experiment by Zehnder and Rosakis, formation of the local shear lips due to intensified plasticity can hardly be controlled. As a result, a slight asymmetry of the shear-lip formation interrupts the symmetric conditions imposed globally. This is especially the case for dynamic crack propagation involving a rapid crack speed and a small scale observation.

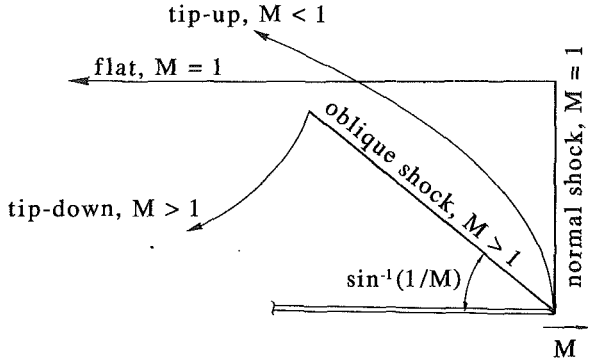

Fig. 5 Intrinsic transition of the isotherm pattern from the subsonic, transonic, to the supersonic ranges

Conclusion

While the theoretical foundation for the thermal wave theory is continuously being sought (Tzou, 1992a), experimental evidence is necessary to promote the engineering applications. The wave theory of heat conduction is no longer narrow and restricted to the environment with low temperature. Indeed, in an earlier paper by Tzou (1989a), a temperature-rate criterion was derived for the dominance of wave behavior over diffusion. The novel experimental result obtained by Zehnder and Rosakis seems to support such a rate-dependent condition for the activation of thermal wave behavior.

Downloaded 13 Dec 2010 to 193.140.21.150. Redistribution subject to ASME license or copyright; see http://www.asme.org/terms/Terms_Use.cfm

Weichert and Schöner (1974, 1978) made an attempt to employ the diffusion theory in studying the temperature rise induced by a rapidly propagating crack tip. The emphasis is placed on the onset of interchange between isothermal and adiabatic heating with the crack speed. Although parallel isotherms in the wake region also result from their analysis, the geometric shape of the heat-production zone and the heat-generation rate play an important role. Rectangles, triangles, and circles were assumed in their analyses to simulate the heat-production zone. Besides, no crack-surface condition is modeled and the resulting singular behavior of the temperature gradient at the crack tip is absent. Evidently, their approach is more appropriate for the temperature field established in front of the crack tip where the effect of heat generation dominates. The present analysis employing the thermal wave model, on the other hand, brings attention to the wave behavior in heat conduction. It has been shown that even in the absence of a refined structure of the mechanism of energy dissipation, the model successfully preserves several unique features in the experimental observations. Of course, a more refined analysis incorporating both the effects of thermal wave and heat production is eventually needed for a complete description.

Acknowledgments

This work was accomplished in the course of the research sponsored by the National Science Foundation under Grant No. MSS-9200993 with the University of New Mexico.

References

Jou, D., Casas-Vázquez, J., and Lebon, G., 1988, "Extended Irreversible Thermodynamics," *Report of Progress in Physics*, Vol. 51, pp. 1105–1179.

Kuang, Z.-B., and Atluri, S., 1985, "Temperature Field Due to a Moving Heat Source: A Moving Mesh Finite Element Analysis," ASME *Journal of Applied Mechanics*, Vol. 52, pp. 274–280.

Rice, J. R., and Levy, N., 1969, "Local Heating by Plastic Deformation at a Crack Tip," in: *The Physics of Strength and Plasticity*, A. S. Argon, ed., MIT Press, pp. 277–292.

Sung, J. C., and Achenbach, J. D., 1987, "Temperature at a Propagating Crack Tip in a Viscoplastic Material," *Journal of Thermal Stresses*, Vol. 10, pp. 243–262.

Tzou, D. Y., 1989a, "On the Thermal Shock Wave Induced by a Moving Heat Source," ASME JOURNAL OF HEAT TRANSFER, Vol. 111, pp. 232–238.

Tzou, D. Y., 1989b, "Shock Wave Formation Around a Moving Heat Source in a Solid With Finite Wave Speed," *International Journal of Heat and Mass Transfer*, Vol. 32, pp. 1979–1987.

Tzou, D. Y., 1989c, "The Effects of Thermal Shock Waves on the Crack Initiation Around a Moving Heat Source," *Journal of Engineering Fracture Mechanics*, Vol. 34, pp. 1109–1118.

Tzou, D. Y., 1990a, "Thermal Shock Wave Induced by a Moving Crack," ASME JOURNAL OF HEAT TRANSFER, Vol. 112, pp. 21–27.

Tzou, D. Y., 1990b, "Thermal Shock Waves Induced by a Moving Crack—A Heat Flux Formulation," *International Journal of Heat and Mass Transfer*, Vol. 33, pp. 877–885.

Tzou, D. Y., 1990c, "Three-Dimensional Structures of the Thermal Shock Waves Around a Rapidly Moving Heat Source," *International Journal of Engineering Science*, Vol. 28, pp. 1003–1017.

Tzou, D. Y., 1991a, "The Singular Behavior of the Temperature Gradient in the Vicinity of a Macrocrack Tip," *International Journal of Heat and Mass Transfer*, Vol. 33, pp. 2625–2630.

Tzou, D. Y., 1991b, "The Effect of Thermal Conductivity on the Singular Behavior of the Near-Tip Temperature Gradient," ASME JOURNAL OF HEAT TRANSFER, Vol. 113, pp. 806–813.

Tzou, D. Y., 1992a, "Fracture Path Emanating From a Rapidly Moving Heat Source—The Effect of Thermal Shock Waves Under High Rate Response," *Journal of Engineering Fracture Mechanics*, Vol. 41, pp. 111–125.

Tzou, D. Y., 1992b, "Thermal Shock Phenomena in Solids Under High Rate Response," *Annual Review of Heat Transfer*, Chang-Lin Tien, ed., Vol. IV, Chap. 3, Hemisphere Publishing Co., Washington, DC.

Tzou, D. Y., 1992c, "An Engineering Assessment to the Relaxation Time in the Thermal Wave Theory," *International Journal of Heat and Mass Transfer*, accepted for publication.

Weichert, R., and Schönert, K., 1974, "On the Temperature Rise at the Tip of a Fast Running Crack," *Journal of the Mechanics and Physics of Solids*, Vol. 22, pp. 127–133.

Weichert, R., and Schönert, K., 1978, "Heat Generation at the Tip of a Moving Crack," *Journal of the Mechanics and Physics of Solids*, Vol. 26, pp. 151–161.

Zehnder, A. T., and Rosakis, A. J., 1991, "On the Temperature Distribution at the Vicinity of Dynamically Propagating Cracks," *Journal of the Mechanics and Physics of Solids*, Vol. 39, pp. 385–415.

The Effect of Interstitial Fluid on Thermal Constriction Resistance

A. K. Das[1] and S. S. Sadhal[1]

Nomenclature

A_λ, B_λ = constants, Eqs. (9)–(11)
h = metric coefficient
I = values of integrals, Eq. (14)
k = thermal conductivity
L = length of a gap surface, Eq. (13)
n = outward normal
q_0 = heat flux at infinity
$\Re_c$ = constriction resistance, Eq. (12)
T = temperature fields
$\overline{T}$ = average interface temperatures, Eq. (13)
t_1, t_2 = gap depths, Fig. 2
t = total gap thickness $= t_1 + t_2$
w = gap half-width, Fig. 2
x, z = rectangular coordinates, Fig. 2
κ = contact area fraction, gap distribution parameter
λ = dummy integration variable, eigenvalue
ξ, η = bipolar coordinates, Fig. 2
ψ_c = nondimensional resistance, Eq. (15)

Subscripts

1, 2, 3 = medium 1, 2, 3
12, 23, 13 = media interfaces

1 Introduction

While a number of studies have been carried out on the analysis of thermal constriction resistance between two solids in contact (a brief review appears in Das and Sadhal, 1990), many investigators have focused attention on cases in which the fluid that might be present in the interstitial regions, or gaps, is a high-resistivity material such as air, or in space where there is simply vacuum. But, in several other situations, the gaps could be occupied by some contact grease or other conducting fluid. This brings about the complexity that the noncontacting regions cannot be simply regarded as adiabatic, but require full interfacial coupling between the solids and the fluid in the interstitial region. An attempt has been made to analyze such cases for an array of gaps filled with a conducting interfacial fluid at the surfaces of contact of two semi-infinite solids.

There have been several studies made on the gap conductance at the contact interface. Extensive reviews have been done by Yovanovich (1986), Snaith et al. (1986), Madhusudana and Fletcher (1986), and Fletcher (1988) on the general contact and gap conductance investigations. A review on gas conductance was done by Snaith et al. (1984) based on the engineering applications, and by Madhusudana and Fletcher (1981) on the various empirical, analytical, and statistical models for the determination of the "effective gas gap thickness." This quantity has been used extensively by several investigators to determine the gap conductance. For this effective thickness, Yovanovich et al. (1982) provided estimations based on a statistical model.

Most of the work in gap conductance has been experimental and/or empirical in nature. There are not many analytical

[1] Department of Mechanical Engineering, University of Southern California, Los Angeles, CA 90089-1453.

Contributed by the Heat Transfer Division and presented at the National Heat Transfer Conference, Minneapolis, Minnesota, July 28–31, 1991. Manuscript received by the Heat Transfer Division February 1991; revision received February 1992. Keywords: Conduction. Associate Technical Editor: L. S. Fletcher.

Downloaded 13 Dec 2010 to 193.140.21.150. Redistribution subject to ASME license or copyright; see http://www.asme.org/terms/Terms_Use.cfm

Weichert and Schöner (1974, 1978) made an attempt to employ the diffusion theory in studying the temperature rise induced by a rapidly propagating crack tip. The emphasis is placed on the onset of interchange between isothermal and adiabatic heating with the crack speed. Although parallel isotherms in the wake region also result from their analysis, the geometric shape of the heat-production zone and the heat-generation rate play an important role. Rectangles, triangles, and circles were assumed in their analyses to simulate the heat-production zone. Besides, no crack-surface condition is modeled and the resulting singular behavior of the temperature gradient at the crack tip is absent. Evidently, their approach is more appropriate for the temperature field established in front of the crack tip where the effect of heat generation dominates. The present analysis employing the thermal wave model, on the other hand, brings attention to the wave behavior in heat conduction. It has been shown that even in the absence of a refined structure of the mechanism of energy dissipation, the model successfully preserves several unique features in the experimental observations. Of course, a more refined analysis incorporating both the effects of thermal wave and heat production is eventually needed for a complete description.

Acknowledgments

This work was accomplished in the course of the research sponsored by the National Science Foundation under Grant No. MSS-9200993 with the University of New Mexico.

References

Jou, D., Casas-Vázquez, J., and Lebon, G., 1988, "Extended Irreversible Thermodynamics," *Report of Progress in Physics*, Vol. 51, pp. 1105–1179.

Kuang, Z.-B., and Atluri, S., 1985, "Temperature Field Due to a Moving Heat Source: A Moving Mesh Finite Element Analysis," ASME *Journal of Applied Mechanics*, Vol. 52, pp. 274–280.

Rice, J. R., and Levy, N., 1969, "Local Heating by Plastic Deformation at a Crack Tip," in: *The Physics of Strength and Plasticity*, A. S. Argon, ed., MIT Press, pp. 277–292.

Sung, J. C., and Achenbach, J. D., 1987, "Temperature at a Propagating Crack Tip in a Viscoplastic Material," *Journal of Thermal Stresses*, Vol. 10, pp. 243–262.

Tzou, D. Y., 1989a, "On the Thermal Shock Wave Induced by a Moving Heat Source," ASME JOURNAL OF HEAT TRANSFER, Vol. 111, pp. 232–238.

Tzou, D. Y., 1989b, "Shock Wave Formation Around a Moving Heat Source in a Solid With Finite Wave Speed," *International Journal of Heat and Mass Transfer*, Vol. 32, pp. 1979–1987.

Tzou, D. Y., 1989c, "The Effects of Thermal Shock Waves on the Crack Initiation Around a Moving Heat Source," *Journal of Engineering Fracture Mechanics*, Vol. 34, pp. 1109–1118.

Tzou, D. Y., 1990a, "Thermal Shock Wave Induced by a Moving Crack," ASME JOURNAL OF HEAT TRANSFER, Vol. 112, pp. 21–27.

Tzou, D. Y., 1990b, "Thermal Shock Waves Induced by a Moving Crack—A Heat Flux Formulation," *International Journal of Heat and Mass Transfer*, Vol. 33, pp. 877–885.

Tzou, D. Y., 1990c, "Three-Dimensional Structures of the Thermal Shock Waves Around a Rapidly Moving Heat Source," *International Journal of Engineering Science*, Vol. 28, pp. 1003–1017.

Tzou, D. Y., 1991a, "The Singular Behavior of the Temperature Gradient in the Vicinity of a Macrocrack Tip," *International Journal of Heat and Mass Transfer*, Vol. 33, pp. 2625–2630.

Tzou, D. Y., 1991b, "The Effect of Thermal Conductivity on the Singular Behavior of the Near-Tip Temperature Gradient," ASME JOURNAL OF HEAT TRANSFER, Vol. 113, pp. 806–813.

Tzou, D. Y., 1992a, "Fracture Path Emanating From a Rapidly Moving Heat Source—The Effect of Thermal Shock Waves Under High Rate Response," *Journal of Engineering Fracture Mechanics*, Vol. 41, pp. 111–125.

Tzou, D. Y., 1992b, "Thermal Shock Phenomena in Solids Under High Rate Response," *Annual Review of Heat Transfer*, Chang-Lin Tien, ed., Vol. IV, Chap. 3, Hemisphere Publishing Co., Washington, DC.

Tzou, D. Y., 1992c, "An Engineering Assessment to the Relaxation Time in the Thermal Wave Theory," *International Journal of Heat and Mass Transfer*, accepted for publication.

Weichert, R., and Schönert, K., 1974, "On the Temperature Rise at the Tip of a Fast Running Crack," *Journal of the Mechanics and Physics of Solids*, Vol. 22, pp. 127–133.

Weichert, R., and Schönert, K., 1978, "Heat Generation at the Tip of a Moving Crack," *Journal of the Mechanics and Physics of Solids*, Vol. 26, pp. 151–161.

Zehnder, A. T., and Rosakis, A. J., 1991, "On the Temperature Distribution at the Vicinity of Dynamically Propagating Cracks," *Journal of the Mechanics and Physics of Solids*, Vol. 39, pp. 385–415.

The Effect of Interstitial Fluid on Thermal Constriction Resistance

A. K. Das[1] and S. S. Sadhal[1]

Nomenclature

A_λ, B_λ = constants, Eqs. (9)–(11)
h = metric coefficient
I = values of integrals, Eq. (14)
k = thermal conductivity
L = length of a gap surface, Eq. (13)
n = outward normal
q_0 = heat flux at infinity
$\Re_c$ = constriction resistance, Eq. (12)
T = temperature fields
$\overline{T}$ = average interface temperatures, Eq. (13)
t_1, t_2 = gap depths, Fig. 2
t = total gap thickness $= t_1 + t_2$
w = gap half-width, Fig. 2
x, z = rectangular coordinates, Fig. 2
κ = contact area fraction, gap distribution parameter
λ = dummy integration variable, eigenvalue
ξ, η = bipolar coordinates, Fig. 2
ψ_c = nondimensional resistance, Eq. (15)

Subscripts

1, 2, 3 = medium 1, 2, 3
12, 23, 13 = media interfaces

1 Introduction

While a number of studies have been carried out on the analysis of thermal constriction resistance between two solids in contact (a brief review appears in Das and Sadhal, 1990), many investigators have focused attention on cases in which the fluid that might be present in the interstitial regions, or gaps, is a high-resistivity material such as air, or in space where there is simply vacuum. But, in several other situations, the gaps could be occupied by some contact grease or other conducting fluid. This brings about the complexity that the noncontacting regions cannot be simply regarded as adiabatic, but require full interfacial coupling between the solids and the fluid in the interstitial region. An attempt has been made to analyze such cases for an array of gaps filled with a conducting interfacial fluid at the surfaces of contact of two semi-infinite solids.

There have been several studies made on the gap conductance at the contact interface. Extensive reviews have been done by Yovanovich (1986), Snaith et al. (1986), Madhusudana and Fletcher (1986), and Fletcher (1988) on the general contact and gap conductance investigations. A review on gas conductance was done by Snaith et al. (1984) based on the engineering applications, and by Madhusudana and Fletcher (1981) on the various empirical, analytical, and statistical models for the determination of the "effective gas gap thickness." This quantity has been used extensively by several investigators to determine the gap conductance. For this effective thickness, Yovanovich et al. (1982) provided estimations based on a statistical model.

Most of the work in gap conductance has been experimental and/or empirical in nature. There are not many analytical

[1]Department of Mechanical Engineering, University of Southern California, Los Angeles, CA 90089-1453.

Contributed by the Heat Transfer Division and presented at the National Heat Transfer Conference, Minneapolis, Minnesota, July 28–31, 1991. Manuscript received by the Heat Transfer Division February 1991; revision received February 1992. Keywords: Conduction. Associate Technical Editor: L. S. Fletcher.

Copyright © 1992 by ASME
Downloaded 13 Dec 2010 to 193.140.21.150. Redistribution subject to ASME license or copyright; see http://www.asme.org/terms/Terms_Use.cfm

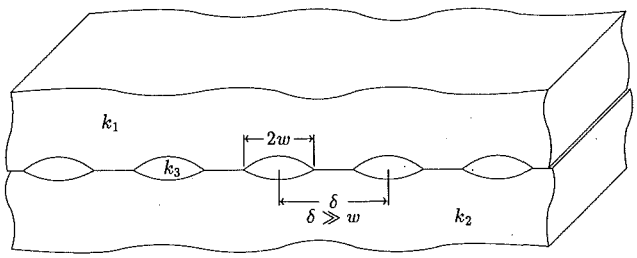

Fig. 1 An array of two-dimensional gaps and contacts at the interface of two semi-infinite solids in contact

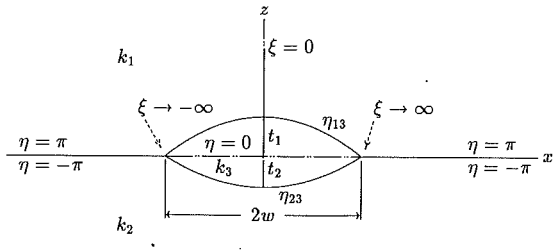

Fig. 2 One two-dimensional gap at the interface of two semi-infinite solids in contact

treatments of the problem available in literature. Analytical solutions, though limited by their simplifications, do provide an insight into the problem and help identify important parameters and their effects. Fenech and Rohsenow (1963) studied a simple cylindrical cell model with a uniform thickness gap. However, they satisfied only the average boundary conditions between the regions. They also provided models relating the uniform thickness to the actual surface characteristics. Many years later, Mentes et al. (1981) studied a similar cylindrical cell model for the contact of coated multilayer sheets. They introduced the effect of interstitial gases through an equivalent heat transfer coefficient for the interstitial medium and provided models to relate this coefficient to the physical and geometric properties of the gap of uniform thickness. A numerical study of the gap conductance was done by Madhusadana (1980), assuming the gap profile to be a cone-frustrum at the interface of two cylinders. In spite of all these studies, there is still a need for rigorous analytical treatment of the problem.

The general three-dimensional multicontact problem for nonadiabatic gaps of nonzero thickness is very complicated to handle analytically. Therefore, we first consider the two-dimensional idealization. Our model consists of two semi-infinite conducting solids in contact over spatially periodic "strips" (see Fig. 1). The gaps betwen these contacting strips are filled with a conducting fluid. The gaps are assumed to be circular in profile, while the contact strips are flat. There have been some studies made in the two-dimensional constriction problems in the past. Veziroglu and Chandra (1969) solved the problem of uniformly distributed two-dimensional symmetric and eccentric constrictions by the method of conformal mapping. Dundurs and Panek (1976) analyzed the problem of regularly spaced strip contacts between two sinusoidal wavy surfaces by the dual series method. However, they assumed purely adiabatic gaps of zero thickness, and satisfied the mixed boundary conditions on the "nominal plane of contact," rather than the actual surfaces; and thus simplified the problem to "flat" contacts and gaps. Later, Sadhal (1981) obtained a long-time approximate solution for the corresponding transient problem. He also assumed the gap to be adiabatic and planar in shape.

The analytical solution to the multicontact problem with interacting gaps and contacts, is not easy to handle directly. But, as a first-order approximation, we model the problem as consisting of one two-dimensional gap at the surface of contact of two semi-infinite conducting solids, the rest of the surface being in perfect contact, which also represents the case of a sparsely distributed gaps at the interface. This model forms the basis of our later work, which takes into account the gap interactions. We intend to employ the Corrective-Iterative technique applied by Tio and Sadhal (1991) by superimposing such one-gap solutions to handle the interaction of the gaps and contacts for densely populated cases.

2 Mathematical Analysis

The model for the present analysis is shown in Fig. 2. It depicts a gap occupied by a material of conductivity k_3 at the surface of contact of two solids of conductivities k_1 and k_2. A constant heat flux q_0 is imposed at infinity. The governing differential equations are:

$$k_i \nabla^2 T_i = 0, \qquad i = 1, 2, 3, \tag{1}$$

or, in rectangular coordinates,

$$\frac{\partial^2 T_i}{\partial x^2} + \frac{\partial^2 T_i}{\partial z^2} = 0, \qquad i = 1, 2, 3. \tag{2}$$

The boundary conditions are (Fig. 2):

1. Interface 12: $T_1 = T_2$; $k_1 \dfrac{\partial T_1}{\partial z} = k_2 \dfrac{\partial T_2}{\partial z}$, (3)

2. Interface 13: $T_1 = T_3$; $k_1 \dfrac{\partial T_1}{\partial n_{13}} = k_3 \dfrac{\partial T_3}{\partial n_{13}}$, (4)

3. Interface 23: $T_2 = T_3$; $k_2 \dfrac{\partial T_2}{\partial n_{23}} = k_3 \dfrac{\partial T_3}{\partial n_{23}}$, (5)

4. $z \to \infty$: $-k_1 \dfrac{\partial T_1}{\partial z} = q_0$; or, $T_1 = -\dfrac{q_0 z}{k_1}$, (6)

5. $z \to -\infty$: $-k_2 \dfrac{\partial T_2}{\partial z} = q_0$; or, $T_2 = -\dfrac{q_0 z}{k_2}$, (7)

An analytical solution of this mixed boundary value problem is not straightforward because of the complex geometry of the surface. However, the representation of the gap surfaces turns out to be very simple if we employ the bipolar coordinates (ξ, η), which are related to the rectangular coordinates (x, z) as (see Fig. 2):

$$x = \frac{w \sin \xi}{\cosh \xi + \cos \eta}, \qquad z = \frac{w \sin \eta}{\cosh \xi + \cos \eta}, \tag{8}$$

for $-\pi \le \eta \le \pi$ and $-\infty < \xi < \infty$, with metric coefficient $h = w/(\cosh \xi + \cos \eta)$, where w is the half-width of the gap. The thicknesses of the gap, t_1 and t_2, relate to the η coordinate as $t_1 = w|\tan 1/2\ \eta_{13}|$ and $t_2 = w|\tan 1/2\ \eta_{23}|$. The temperature fields in this coordinate system are given by (see Das and Sadhal, 1991, and Das, 1992),

$$T_1 = -\frac{q_0 w}{k_1} \frac{\sin \eta}{\cosh \xi + \cos \eta} + \frac{q_0 w}{k_1} \int_0^\infty \left[A_{1\lambda} \frac{\sinh \lambda(\pi - \eta)}{\sinh \lambda(\pi - \eta_{13})} + B_{1\lambda} \frac{\sinh \lambda(\eta - \eta_{13})}{\sinh \lambda(\pi - \eta_{13})} \right] \cos \lambda \xi \, d\lambda, \tag{9}$$

$$T_2 = -\frac{q_0 w}{k_2} \frac{\sin \eta}{\cosh \xi + \cos \eta} + \frac{q_0 w}{k_2} \int_0^\infty \left[A_{2\lambda} \frac{\sinh \lambda(\pi + \eta)}{\sinh \lambda(\pi + \eta_{23})} + \frac{k_2}{k_1} B_{1\lambda} \frac{\sinh \lambda(\eta_{23} - \eta)}{\sinh \lambda(\pi + \eta_{23})} \right] \cos \lambda \xi \, d\lambda, \tag{10}$$

Downloaded 13 Dec 2010 to 193.140.21.150. Redistribution subject to ASME license or copyright; see http://www.asme.org/terms/Terms_Use.cfm

$$T_3=\frac{q_0 w}{k_3}\int_0^\infty\left\{\frac{k_3}{k_1}\left[A_{1\lambda}-2\frac{\sinh\lambda\eta_{13}}{\sinh\lambda\pi}\right]\frac{\sinh\lambda(\eta-\eta_{23})}{\sinh\lambda(\eta_{13}-\eta_{23})}\right.$$
$$\left.+\frac{k_3}{k_2}\left[A_{2\lambda}-2\frac{\sinh\lambda\eta_{23}}{\sinh\lambda\pi}\right]\frac{\sinh\lambda(\eta_{13}-\eta)}{\sinh\lambda(\eta_{13}-\eta_{23})}\right\}\cos\lambda\xi\, d\lambda. \quad (11)$$

The thermal constriction resistance is defined as,

$$\mathcal{R}_c=\frac{\left[\begin{array}{c}\text{average temperature jump across the}\\ \text{interface over a unit cell of width } \delta\end{array}\right]}{\text{far field heat flux}}$$

$$=\frac{\overline{T}_{23}-\overline{T}_{13}}{\delta q_0}, \quad (12)$$

where $\overline{T}_{13}$ and $\overline{T}_{23}$ are the average temperatures at the gap surfaces η_{13} and η_{23}, and are given by

$$\overline{T}_{j3}=\frac{1}{L_{j3}}\int_{-\infty}^{\infty}T_j\frac{w}{\cosh\xi+\cos\eta}\bigg|_{\eta=\eta_{j3}}d\xi$$

$$=\frac{2q_0w^2}{\delta k_j L_{j3}}I_{j3}, \quad j=1,\ 2, \quad (13)$$

Here, $L_{j3}=2w\eta_{j3}/\sin\eta_{j3}$ are the arc lengths of the curved surfaces η_{j3} for $j=1,\ 2$ and

$$I_{j3}=\int_0^\infty\left\{\int_0^\infty\left[A_{j\lambda}-2\frac{\sinh\lambda\eta_{j3}}{\sinh\lambda\pi}\right]\cos\lambda\xi\, d\lambda\right\}$$
$$\times\frac{d\xi}{\cosh\xi+\cos\eta_{j3}}, \quad j=1,\ 2. \quad (14)$$

The nondimensional resistance is given by

$$\psi_c=\frac{k_1k_2}{k_1+k_2}\mathcal{R}_c$$
$$=\frac{w}{\delta}\frac{1}{1+k_2/k_1}\frac{\sin\eta_{13}}{\eta_{13}}\left[\frac{\eta_{13}}{\sin\eta_{13}}\frac{\sin\eta_{23}}{\eta_{23}}I_{23}-\frac{k_2}{k_1}I_{13}\right]. \quad (15)$$

The nondimensional parameters are identified as the conductivity ratios k_2/k_1 and k_3/k_1, the aspect ratios t_1/w and t_2/w, and the fractional contact are $\kappa=1-2w/\delta$, where w/δ is also the gap distribution parameter.

3 Results and Discussion

At the boundary η_{12}, where the two solids are in contact, the terms containing $A_{1\lambda}$ and $A_{2\lambda}$ vanish in Eq. (9)-(10), and $B_{1\lambda}$ remains the only contributing coefficient. It is obvious that, in general, $B_{1\lambda}\neq 0$, and hence, the surface η_{12} is not, in genereal, isothermal. It is interesting to check this surface temperature for the case of a symmetric gap, in which case $\eta_{13}=-\eta_{23}=\eta_0$. For this special case, it is found, after a lot of algebra, that

$$B_{1\lambda}=\frac{2C_\lambda}{D_\lambda}\frac{\sinh\lambda(\pi-\eta_0)}{\sinh\lambda\Delta\eta}\left[\left(\frac{k_3}{k_2}-\frac{k_3}{k_1}\right)(\cosh\lambda\Delta\eta-1)\right], \quad (16)$$

where C_λ and D_λ are given by Das and Sadhal (1990). Therefore, the surface η_{12} in contact between the two solids is isothermal only if the following two conditions are satisfied:

1. $\eta_{13}=-\eta_{23}=\eta_0$ (geometrical symmetry),
2. $k_1=k_2$ (identical solids), or $k_3=0$ (adiabatic gaps), or $\Delta\eta=0$ (zero gas thickness).

It should be noted here that the observation made by Cooper et al. (1969), that the contact surface must be isothermal for two symmetric semi-infinite bodies in contact with zero gap thickness and nonzero void conductance, is not a general observation and is just a part of the above result.

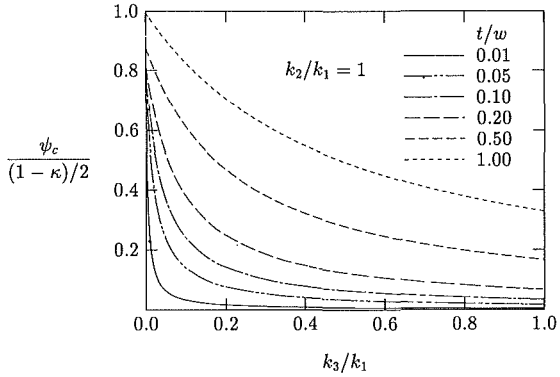

Fig. 3 Dimensionless resistance, ψ_c, as a function of gap conductivity ratio, k_3/k_1

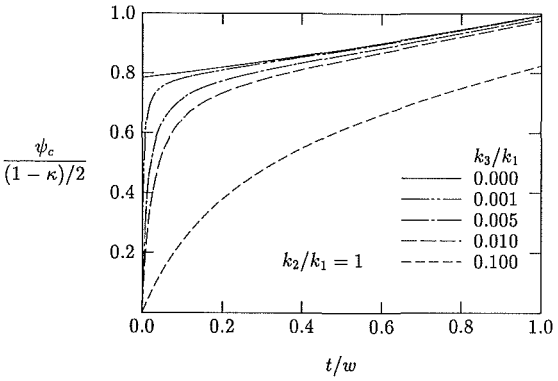

Fig. 4 Dimensionless resistance, ψ_c, as a function of gap thickness to gap half-width ratio, t/w

The nondimensional resistance ψ_c was computed as a function of the four governing nondimensional parameters, t_1/w, t_2/w, k_3/k_1 and k_2/k_1. The parameter w/δ or κ appears only as a simple multiple and scales the nondimensional resistance. The results are shown in Figs. 3 and 4. It was observed that it is mostly the sum of t_1 and t_2, that is the gap thickness, which governs the resistance, rather than their individual values. We, therefore, define a combined parameter, t/w, where $t=t_1+t_2$ is the gap thickness. This conclusion is based on the observed values of ψ_c for both symmetric and asymmetric values of t_1/w and t_2/w such that $t_1/w+t_2/w$ remains constant. Only for large values of $t/w>5$ and also large differences in t_1/w and t_2/w was a noticeable difference in the values of ψ_c observed for the asymmetric configuration. It was also observed that the dimensionless resitance ψ_c is a very weak function of the solid conductivity ratio k_2/k_1 for $k_2/k_1>1$. For $k_2/k_1<1$, the value of ψ_c is observed to drop, which is simply a manifestation of scaling the resistance $\mathcal{R}_c$ with the equivalent conductivity $k_1k_2/(k_1+k_2)$ for nondimensionalization.

A direct comparison of the present results with the experimental investigations is not possible due to the nature of the parameters used. However, the general trends and observations are compared with some of the experimental and/or numerical results wherever possible.

Figures 3 and 4 show the plots for ψ_c as a function of the parameters k_3/k_1 and t/w. As evident from the two figures, ψ_c is found to be a very strong function of these parameters, especially for small values. From Fig. 3, it can be readily concluded that as the gap sets thicker, the plot becomes flatter, showing the weakening effect of k_3/k_1 for large gaps. A similar conclusion can be deduced from Fig. 4 for larger values of k_3/k_1. For thin gaps, the resistance approaches zero at an extremely rapid rate. Similarly, for small k_3/k_1, ψ_c approaches the adiabatic value at a much faster rate than that for higher values. It is also observed (not shown in Fig. 4) that as $k_3/$

Downloaded 13 Dec 2010 to 193.140.21.150. Redistribution subject to ASME license or copyright; see http://www.asme.org/terms/Terms_Use.cfm

$k_1 \to 0$, the resistance approaches that of adiabatic case ($k_3/k_1 = 0$ in Fig. 4) for all values of t. Here, the plots are shown only for $k_3/k_1 \leq 1$ and $t/w \leq 1$. For larger k_3/k_1, ψ_c approaches zero monotonically, whereas for larger t/w, it approaches the adiabatic value.

Physically, what the results imply is that as soon as a conducting fluid is introduced in the gap, the resistance rapidly starts decreasing, and this effect is more pronounced if the gap is thin or when the fluid conductivity is small. For large fluid conductivity, the drop is significant at all gap thicknesses, but not as sharp. Madhusudana (1975) made a similar observation in his experimental analysis. In most of the experimental investigations, contact pressure is used as the parameter. A low contact pressure would generally result in small contact area and large gap area, and hence a small t/w. Madhusudana (1975) and Song et al. (1989) both reported the relatively significant improvement in gap conductance at low pressures (low t/w), which conforms to the results of the present study. Madhusudana's (1980) numerical study using the cone frustrum geometry reports the results in terms of the cone semi-angle β and the radius ratio a/b. These correspond respectively to the parameters t/w and κ of the present study. A large β (for fixed a/b) corresponds to a small t/w (with fixed κ) and a large a/b (for fixed β) to a large κ (for fixed t/w). Madhusudana's numerical results show a decrease in the resistance for increasing β and/or increasing a/b, which is also observed in the present study (for decreasing t/w and/or increasing κ, respectively). However, Madhusudana reports that the reduction in the resistance is less significant for large β (or small t/w), which is in contradiction to the observations of the present study. Physically also, it can be easily seen that if the gap is thin (large β), the effects of introducing a conducting fluid would be more significant, as predicted by the present study.

An attempt was made to quantify the distribution parameter δ/w in order to check the sparseness conditions. We define a distribution to be sparse if, for the one-gap model, the solid interface temperature, $T_{12,\delta}$, at a distance δ from the center of the gap is approximately 99 percent of the value ($T_{12,\infty}$) far away from the gap. It is observed that this ratio, $T_{12,\delta}/T_{12,\infty}$, is a strong function of t/w. In order to obtain $T_{12,\delta}/T_{12,\infty} = 0.99$, δ/w ranges from 6 to 10 for $t/w < 1$. However, it goes up to 50 as t/w approaches 5. For $T_{12,\delta}/T_{12,\infty} = 0.95$, the corresponding values of δ/w are 2.5 to 4 for $t/w < 1$, and up to 15 for $t/w \to 5$. It is also observed that the required δ/w is slightly lower for adiabatic gaps as compared to the nonadiabatic case. Hence, we see that the single gap model cannot be used for a general case, and must be improved to account for the gap interactions.

4 Conclusions

Thermal constriction resistance between two semi-infinite solids in contact has been studied for two-dimensional gaps. For sparsely distribution gaps, analysis for a single gap at the interface has been done. Analytical solutions obtained for this idealization show that for symmetric gaps, the interface areas, which are in perfect contact, are not, in general, isothermal. The isothermal condition prevails only in certain special cases of adiabatic or zero-thickness gaps, or when the two solids have the same conductivities.

The contact resistance is observed to be a strong function of the gap thickness and the conductivity of the interstitial fluid, especially at lower values of these quantities. The resistance increases very sharply as the gap conductivity approaches zero and the gap becomes thin. The results conform to the observations made by Yovanovich and Madhusudana in the experimental and numerical studies. Although the results are valid for sparsely distributed contacts, it is established that the conductivity of the interstitial fluid plays a very important role in contact resistance. A more general analysis of this problem, which includes the interaction of multiple gaps, is under investigation.

References

Cooper, M. G., Mikic, B. B., and Yovanovich, M. M., 1969, "Thermal Contact Conductance," *Int. J. Heat Mass Transfer*, Vol. 12, pp. 279–300.

Dundurs, J., and Panek, C., 1976, "Heat Conduction Between Bodies With Wavy Surfaces," *Int. J. Heat Mass Transfer*, Vol. 19, pp. 731–736.

Das, A. K., 1992, 'Thermal Contact Conductance—Effects of Clustering, Random Distribution and Interstitial Fluid," PhD thesis, University of Southern California, Los Angeles.

Das, A. K., and Sadhal, S. S., 1990, "The Effect of Clustering in Thermal Contact Resistance," *Proc. 9th Intn'l. Heat Transfer Conference*, Vol. 5, pp. 517–522.

Das, A. K., and Sadhal, S. S., 1991, 'Thermal Constriction Resistance: the Effect of Interstitial Fluid," ASME HTD-Vol. 173, pp. 35–39.

Fenech, H., and Rohsenow, W. M., 1963, "Prediction of Thermal Conductance of Metallic Surfaces in Contact," ASME JOURNAL OF HEAT TRANSFER, Vol. 85, pp. 15–24.

Fletcher, L. S., 1988, "Recent Developments in Contact Conductance Heat Transfer," ASME JOURNAL OF HEAT TRANSFER, Vol. 110, pp. 1059–1070.

Madhusudana, C. V., 1975, "The Effect of Interface Fluid on Thermal Contact Conductance," *Int. J. Heat Mass Transfer*, Vol. 18, pp. 989–991.

Madhusudana, C. V., 1980, "Heat Flow Through Conical Constriction," *AIAA Journal*, Vol. 18, No. 10, pp. 1261–1262.

Madhusudana, C. V., and Fletcher, L. S., 1981, "Gas Conductance Contribution to Contact Heat Transfer," AIAA Paper No. 81-1163.

Madhusudana, C. V., and Fletcher, L. S., 1986, "Contact Heat Transfer—the Last Decade," *AIAA Journal*, Vol. 24, No. 3, pp. 510–523.

Mentes, A., Sheffield, J. W., Veziroglu, T. N., Williams, A., and Samudrala, R., 1981, "Effect of Interface Gases on Contact Conductance," AIAA Paper No. 81-0214.

Sadhal, S. S., 1981, "Unsteady Heat Flow Between Solids With Partially Contacting Interface," ASME JOURNAL OF HEAT TRANSFER, Vol. 103, pp. 32–35.

Song, S., Yovanovich, M. M., and Nho, K., 1989, "Thermal Gap Conductance: Effect of Gas Pressure and Mechanical Load," AIAA Paper No. 89-0429.

Snaith, B., O'Callaghan, P. W., and Probert, S. D., 1984, "Use of Interstitial Materials for Thermal Contact Conductance Control," AIAA Paper No. 84-0145.

Snaith, B., Probert, S. D., and O'Callaghan, P. W., 1986, "Thermal Resistance of Pressed Contacts," *Applied Energy*, Vol. 22, pp. 31–84.

Tio, K.-K., and Sadhal, S.S., 1991, "Analysis of Thermal Constriction Resistance With Adiabatic Circular Gaps," *J. Thermophys. Heat Transfer*, Vol. 5, No. 4, pp. 550–559.

Veziroglu, T. N., and Chandra, S., 1969, "Thermal Conductance of Two-Dimensional Constrictions," *Progress in Astronautics and Aeronautics, Vol. 21: Thermal Design Principles of Spacecraft and Entry Bodies*, pp. 591–615.

Yovanovich, M. M., DeVaal, J. W., and Hegazy, A. H., 1982, "A Statistical Model to Predict Thermal Gap Conductance Between Conforming Rough Surfaces," AIAA Paper No. 82-0888.

Yovanovich, M. M., 1986, "Recent Developments in Thermal Contact, Gap and Joint Conductance Theories and Experiment," *Proc. 8th Int. Heat Transfer Conference*, pp. 35–45.

Nonlinear Steady-State Inverse Heat Conduction Problem With Space-Variable Boundary Conditions

J. Taler[1]

Theory

The purpose of this note is to present a technique for simply and accurately determining the space-variable heat transfer coefficient or boundary heat flux, given measurements of temperature at some interior points in the body. Suppose the steady-state temperature is known at m interior locations. The measured temperatures $\mathbf{y} = (y_1, \ldots, y_m)^T$ depend on the heat transfer coefficients (or other parameters) $\mathbf{x} = (x_1, \ldots, x_n)^T$ and can, therefore, be used for their determination. The object is to choose $\mathbf{x}$ such that computed temperatures $T(\mathbf{x}, \mathbf{r}_i)$ agree

[1]Professor, Department of Mechanical Engineering, Technical University of Cracow, 31-155 Kraków, Poland.

Contributed by the Heat Transfer Division of THE AMERICAN SOCIETY OF MECHANICAL ENGINEERS. Manuscript received by the Heat Transfer Division May 1991; revision received February 1992. Keywords: Conduction, Measurement Techniques, Numerical Methods. Associate Technical Editor: L. S. Fletcher.

Downloaded 13 Dec 2010 to 193.140.21.150. Redistribution subject to ASME license or copyright; see http://www.asme.org/terms/Terms_Use.cfm

$k_1 \to 0$, the resistance approaches that of adiabatic case ($k_3/k_1 = 0$ in Fig. 4) for all values of t. Here, the plots are shown only for $k_3/k_1 \leq 1$ and $t/w \leq 1$. For larger k_3/k_1, ψ_c approaches zero monotonically, whereas for larger t/w, it approaches the adiabatic value.

Physically, what the results imply is that as soon as a conducting fluid is introduced in the gap, the resistance rapidly starts decreasing, and this effect is more pronounced if the gap is thin or when the fluid conductivity is small. For large fluid conductivity, the drop is significant at all gap thicknesses, but not as sharp. Madhusudana (1975) made a similar observation in his experimental analysis. In most of the experimental investigations, contact pressure is used as the parameter. A low contact pressure would generally result in small contact area and large gap area, and hence a small t/w. Madhusudana (1975) and Song et al. (1989) both reported the relatively significant improvement in gap conductance at low pressures (low t/w), which conforms to the results of the present study. Madhusudana's (1980) numerical study using the cone frustrum geometry reports the results in terms of the cone semi-angle β and the radius ratio a/b. These correspond respectively to the parameters t/w and κ of the present study. A large β (for fixed a/b) corresponds to a small t/w (with fixed κ) and a large a/b (for fixed β) to a large κ (for fixed t/w). Madhusudana's numerical results show a decrease in the resistance for increasing β and/or increasing a/b, which is also observed in the present study (for decreasing t/w and/or increasing κ, respectively). However, Madhusudana reports that the reduction in the resistance is less significant for large β (or small t/w), which is in contradiction to the observations of the present study. Physically also, it can be easily seen that if the gap is thin (large β), the effects of introducing a conducting fluid would be more significant, as predicted by the present study.

An attempt was made to quantify the distribution parameter δ/w in order to check the sparseness conditions. We define a distribution to be sparse if, for the one-gap model, the solid interface temperature, $T_{12,\delta}$, at a distance δ from the center of the gap is approximately 99 percent of the value ($T_{12,\infty}$) far away from the gap. It is observed that this ratio, $T_{12,\delta}/T_{12,\infty}$, is a strong function of t/w. In order to obtain $T_{12,\delta}/T_{12,\infty} = 0.99$, δ/w ranges from 6 to 10 for $t/w < 1$. However, it goes up to 50 as t/w approaches 5. For $T_{12,\delta}/T_{12,\infty} = 0.95$, the corresponding values of δ/w are 2.5 to 4 for $t/w < 1$, and up to 15 for $t/w \to 5$. It is also observed that the required δ/w is slightly lower for adiabatic gaps as compared to the nonadiabatic case. Hence, we see that the single gap model cannot be used for a general case, and must be improved to account for the gap interactions.

4 Conclusions

Thermal constriction resistance between two semi-infinite solids in contact has been studied for two-dimensional gaps. For sparsely distribution gaps, analysis for a single gap at the interface has been done. Analytical solutions obtained for this idealization show that for symmetric gaps, the interface areas, which are in perfect contact, are not, in general, isothermal. The isothermal condition prevails only in certain special cases of adiabatic or zero-thickness gaps, or when the two solids have the same conductivities.

The contact resistance is observed to be a strong function of the gap thickness and the conductivity of the interstitial fluid, especially at lower values of these quantities. The resistance increases very sharply as the gap conductivity approaches zero and the gap becomes thin. The results conform to the observations made by Yovanovich and Madhusudana in the experimental and numerical studies. Although the results are valid for sparsely distributed contacts, it is established that the conductivity of the interstitial fluid plays a very important role in contact resistance. A more general analysis of this problem, which includes the interaction of multiple gaps, is under investigation.

References

Cooper, M. G., Mikic, B. B., and Yovanovich, M. M., 1969, "Thermal Contact Conductance," *Int. J. Heat Mass Transfer*, Vol. 12, pp. 279–300.

Dundurs, J., and Panek, C., 1976, "Heat Conduction Between Bodies With Wavy Surfaces," *Int. J. Heat Mass Transfer*, Vol. 19, pp. 731–736.

Das, A. K., 1992, 'Thermal Contact Conductance—Effects of Clustering, Random Distribution and Interstitial Fluid," PhD thesis, University of Southern California, Los Angeles.

Das, A. K., and Sadhal, S. S., 1990, "The Effect of Clustering in Thermal Contact Resistance," *Proc. 9th Intn'l. Heat Transfer Conference*, Vol. 5, pp. 517–522.

Das, A. K., and Sadhal, S. S., 1991, 'Thermal Constriction Resistance: the Effect of Interstitial Fluid," ASME HTD-Vol. 173, pp. 35–39.

Fenech, H., and Rohsenow, W. M., 1963, "Prediction of Thermal Conductance of Metallic Surfaces in Contact," ASME JOURNAL OF HEAT TRANSFER, Vol. 85, pp. 15–24.

Fletcher, L. S., 1988, "Recent Developments in Contact Conductance Heat Transfer," ASME JOURNAL OF HEAT TRANSFER, Vol. 110, pp. 1059–1070.

Madhusudana, C. V., 1975, "The Effect of Interface Fluid on Thermal Contact Conductance," *Int. J. Heat Mass Transfer*, Vol. 18, pp. 989–991.

Madhusudana, C. V., 1980, "Heat Flow Through Conical Constriction," *AIAA Journal*, Vol. 18, No. 10, pp. 1261–1262.

Madhusudana, C. V., and Fletcher, L. S., 1981, "Gas Conductance Contribution to Contact Heat Transfer," AIAA Paper No. 81-1163.

Madhusudana, C. V., and Fletcher, L. S., 1986, "Contact Heat Transfer—the Last Decade," *AIAA Journal*, Vol. 24, No. 3, pp. 510–523.

Mentes, A., Sheffield, J. W., Veziroglu, T. N., Williams, A., and Samudrala, R., 1981, "Effect of Interface Gases on Contact Conductance," AIAA Paper No. 81-0214.

Sadhal, S. S., 1981, "Unsteady Heat Flow Between Solids With Partially Contacting Interface," ASME JOURNAL OF HEAT TRANSFER, Vol. 103, pp. 32–35.

Song, S., Yovanovich, M. M., and Nho, K., 1989, "Thermal Gap Conductance: Effect of Gas Pressure and Mechanical Load," AIAA Paper No. 89-0429.

Snaith, B., O'Callaghan, P. W., and Probert, S. D., 1984, "Use of Interstitial Materials for Thermal Contact Conductance Control," AIAA Paper No. 84-0145.

Snaith, B., Probert, S. D., and O'Callaghan, P. W., 1986, "Thermal Resistance of Pressed Contacts," *Applied Energy*, Vol. 22, pp. 31–84.

Tio, K.-K., and Sadhal, S.S., 1991, "Analysis of Thermal Constriction Resistance With Adiabatic Circular Gaps," *J. Thermophys. Heat Transfer*, Vol. 5, No. 4, pp. 550–559.

Veziroglu, T. N., and Chandra, S., 1969, "Thermal Conductance of Two-Dimensional Constrictions," *Progress in Astronautics and Aeronautics, Vol. 21: Thermal Design Principles of Spacecraft and Entry Bodies*, pp. 591–615.

Yovanovich, M. M., DeVaal, J. W., and Hegazy, A. H., 1982, "A Statistical Model to Predict Thermal Gap Conductance Between Conforming Rough Surfaces," AIAA Paper No. 82-0888.

Yovanovich, M. M., 1986, "Recent Developments in Thermal Contact, Gap and Joint Conductance Theories and Experiment," *Proc. 8th Int. Heat Transfer Conference*, pp. 35–45.

Nonlinear Steady-State Inverse Heat Conduction Problem With Space-Variable Boundary Conditions

J. Taler[1]

Theory

The purpose of this note is to present a technique for simply and accurately determining the space-variable heat transfer coefficient or boundary heat flux, given measurements of temperature at some interior points in the body. Suppose the steady-state temperature is known at m interior locations. The measured temperatures $\mathbf{y} = (y_1, \ldots, y_m)^T$ depend on the heat transfer coefficients (or other parameters) $\mathbf{x} = (x_1, \ldots, x_n)^T$ and can, therefore, be used for their determination. The object is to choose $\mathbf{x}$ such that computed temperatures $T(\mathbf{x}, \mathbf{r}_i)$ agree

[1]Professor, Department of Mechanical Engineering, Technical University of Cracow, 31-155 Kraków, Poland.

Contributed by the Heat Transfer Division of THE AMERICAN SOCIETY OF MECHANICAL ENGINEERS. Manuscript received by the Heat Transfer Division May 1991; revision received February 1992. Keywords: Conduction, Measurement Techniques, Numerical Methods. Associate Technical Editor: L. S. Fletcher.

Copyright © 1992 by ASME

Downloaded 13 Dec 2010 to 193.140.21.150. Redistribution subject to ASME license or copyright; see http://www.asme.org/terms/Terms_Use.cfm

with certain limits with the experimentally measured temperatures y_i. This may be expressed as

$$T(\mathbf{x}, \mathbf{r}_i) - y_i \approx 0, \quad i = 1, \ldots, m. \tag{1}$$

The heat transfer coefficient components $\mathbf{x}$ or other independent variables are parameters of the problem that are to be manipulated in order to adjust the predicted temperatures $T(\mathbf{x}, \mathbf{r}_i)$ to the data. The extent of the fit or agreement is determined by the least-squares criteria. Then a standard procedure is to take more temperature measurements than the number of unknown heat transfer coefficients or parameters, so that $m > n$, and to find $\mathbf{x}$ so as to minimize the deviations $|T(\mathbf{x}, \mathbf{r}_i) - y_i|$; that is, we seek to minimize the functional g:

$$g(\mathbf{x}) = \sum_{i=1}^{m} [T(\mathbf{x}, \mathbf{r}_i) - y_i]^2. \tag{2}$$

The predicted temperatures T depend implicitly on the parameters $\mathbf{x} = (x_1, \ldots, x_n)^T$. Although the function (2) can be minimized by a general unconstrained method, in most circumstances the properties of (2) make it worthwhile to use methods designed specifically for the least-squares problem (Beck, 1988).

In this paper the Gauss-Newton method (Dahlquist and Björck, 1974) will be used. The over-determined set of m nonlinear algebraic equations (1) is first linearized by expanding the computed temperature $T(\mathbf{x}, \mathbf{r}_i)$ in a Taylor series about a known value of solution $\mathbf{x}^{(k)}$. Let $\mathbf{x}^{(k)} = (x_1^{(k)}, \ldots, x_n^{(k)})^T$ denote the current approximation of the solution. Assuming that the computed temperature is continuous in the parameters $\mathbf{x}$, the temperature can be expanded in a Taylor series about $\mathbf{x}^{(k)}$:

$$T_i^{(k+1)} = T_i^{(k)} + (x_1^{(k+1)} - x_1^{(k)}) \left.\frac{\partial T_i}{\partial x_1}\right|_{\mathbf{x}=\mathbf{x}^{(k)}} + \ldots + (x_n^{(k+1)} - x_n^{(k)}) \left.\frac{\partial T_i}{\partial x_n}\right|_{\mathbf{x}=\mathbf{x}^{(k)}}, \quad i = 1, \ldots, m. \tag{3}$$

Substituting Eq. (3) into each of the m equations represented by (1) and simplifying, we obtain

$$\sum_{j=1}^{n} \left.\frac{\partial T_i(x_1, \ldots, x_n)}{\partial x_j}\right|_{\mathbf{x}=\mathbf{x}^{(k)}} (x_j^{(k+1)} - x_j^{(k)}) + T_i(x_1^{(k)}, \ldots, x_n^{(k)}) - y_i \approx 0, \quad i = 1, \ldots, m; \quad j = 1, \ldots, n. \tag{4}$$

This set of linear equations can also be expressed in the matrix form

$$\mathbf{DT}(\mathbf{x}^{(k)})\mathbf{x}^{(k+1)} \approx \mathbf{DT}(\mathbf{x}^{(k)})\mathbf{x}^{(k)} - \mathbf{T}(\mathbf{x}^{(k)}) + \mathbf{y}, \tag{5}$$

where

$$\mathbf{DT}(\mathbf{x}^{(k)}) = \left[\begin{array}{ccc} \dfrac{\partial T_1}{\partial x_1} & \cdots & \dfrac{\partial T_1}{\partial x_n} \\ \vdots & & \vdots \\ \dfrac{\partial T_m}{\partial x_1} & \cdots & \dfrac{\partial T_m}{\partial x_n} \end{array}\right]_{\mathbf{x}=\mathbf{x}^{(k)}} \tag{6}$$

is the $m \times n$ Jacobi matrix of $\mathbf{T}(\mathbf{x}^{(k)})$. $\mathbf{y} = (y_1, \ldots, y_m)^T$ and $\mathbf{T}(\mathbf{x}^{(k)}) = (T_1^{(k)}, \ldots, T_m^{(k)})^T$ are the m vectors of the discrete temperature measurements and corresponding computed temperatures at the given sensor locations, respectively. The partial derivative functions in Eq. (6) are approximated by the forward differences

$$\frac{\partial T_i}{\partial x_j} \approx \frac{T_i(\mathbf{x}^{(k)} + \delta_j \mathbf{e}_j) - T(\mathbf{x}^{(k)})}{\delta_j}, \tag{7}$$

where the scalar δ_j is the jth finite-difference interval (a small value compared to $x_j^{(k)}$), and $\mathbf{e}_j$ is the jth column of the unit matrix. The iterative procedure is continued until the changes in $x_j^{(k)}$ are less than some small amount ϵ, i.e.,

Table 1 Selected data and results obtained for the horizontal evaporator tube

Case		I	II	III
Outside heat flux, q_o, W/m^2		61132	43383	26260
Measured temperatures, °C ; (Bonn et al.,1980)	y_1	26.4	21.7	16.8
	y_2	26.0	21.4	16.7
	y_3	23.9	19.9	15.9
	y_4	20.1	17.7	14.2
	y_5	17.3	15.7	13.2
	y_6	16.2	14.8	12.9
	y_7	16.0	14.6	12.9
Starting value of $Bi_j^{(1)}$, j = 1,...,5		0.06	0.04	0.04
$\delta_j^* = \delta_j r_{in}/k$, j = 1,...,5		0.0001		
Tolerance, ϵ		0.0001		
Number of iterations		11	11	6
Heat transfer coefficients, W/m^{2}K	h_1	- 183.8	- 178.3	185.4
	h_2	41.5	959.2	- 237.6
	h_3	5936.7	3641.5	3943.0
	h4	8319.5	6372.9	5101.7
	h_5	7914.4	6436.0	3441.1
Average heat transfer coefficient, $\bar{h}$, W/m^{2}K		3738.1	3065.6	2290.8
Singular values	σ_1	403.7	381.8	437.4
	σ_2	70.8	67.1	61.8
	σ_3	26.4	23.1	19.3
	σ_4	13.1	11.6	9.7
	σ_5	8.0	7.2	6.1
Sum of squares function, g, K^2		$5.65 \cdot 10^{-3}$	$1.5 \cdot 10^{-2}$	$2.28 \cdot 10^{-4}$
Condition number, σ_1/σ_5		50.5	53	71.7

$$\left|\frac{x_j^{(k+1)} - x_j^{(k)}}{x_j^{(k)}}\right| < \epsilon, \quad j = 1, \ldots, n. \tag{8}$$

The sequence $\{\mathbf{x}^{(k)}\}$ converges quadratically to a solution $\mathbf{x}^*$. The Gauss–Newton method requires the solution of the linear system (5) at each iteration step. A useful way of reducing the amount of computation per iteration is to keep one matrix $\mathbf{DT}^{(k)}$ for several iterations, for example, for five iterations.

Ill conditioning is a common feature of nonlinear least-squares problems derived from parameter estimation problems, because the underlying mathematical model is often ill-defined. Unnecessary exacerbation of the conditioning can be avoided by solving the linear overdetermined system of Eqs. (5) using the singular value decomposition of $\mathbf{DT}^{(k)}$ (Forsythe et al., 1977; Varah, 1973).

If the Jacobian matrix $\mathbf{DT}^{(k)}$ is well-conditioned, it is not necessary to use the SVD of $\mathbf{DT}^{(k)}$. In such a case the orthogonal factorization of $\mathbf{DT}^{(k)}$, for instance, the modified Gram–Schmidt (MGS) method, can be applied to solve the linear Eqs. (5).

Practical Examples

To evaluate the theory developed in the previous section, two sets of data were analyzed. One set of steady-state data, representing circumferential variations of horizontal tube temperature, was obtained by Bonn et al. (1980). The other set was obtained by Ishikawa et al. (1980) for a radiantly heated tube with temperature-dependent thermal conductivity.

Example 1 Horizontal Evaporator Tubes. To test the theory developed in the previous section, the circumferential wall temperature distributions obtained by Bonn et al. (1980) are used (Table 1). The test section was constructed from a copper tube with a thermal conductivity of 400 W/mK. The inside

Downloaded 13 Dec 2010 to 193.140.21.150. Redistribution subject to ASME license or copyright; see http://www.asme.org/terms/Terms_Use.cfm

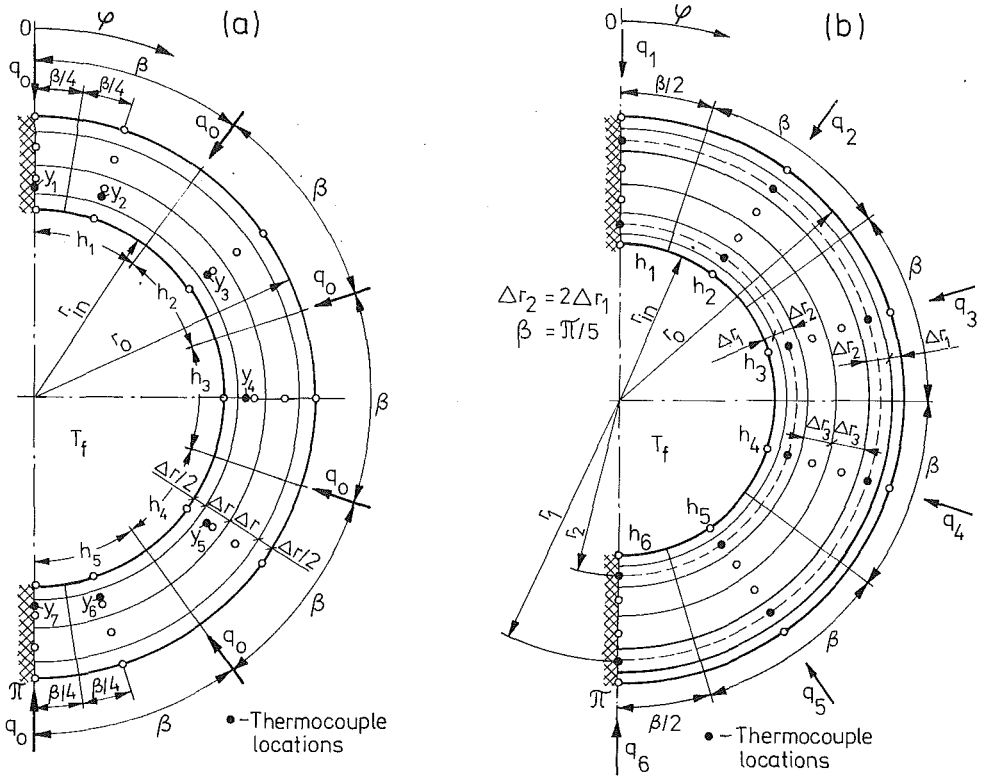

Fig. 1 Physical parameters and nodal network for heat balance analysis: (*a*) horizontal evaporator tube, (*b*) radiantly heated tube

tube radius and wall thickness were 0.007 m and 0.0022 m, respectively. The sheathed chromel-constantan thermocouples (0.0005 in diameter) were provided around the periphery of the measuring section to determine accurately the circumferential wall temperature profile. The hot junctions of the thermocouples were placed at the depth of 0.00055 m from the inside surface of the tube (Fig. 1). Heat was applied to the outside surface of the tube (electrical resistance heating). To determine the spatial variations of heat transfer coefficients $h(\varphi)$, the inside surface of the tube is divided into five segments, as shown in Fig. 1, assuming that the heat transfer coefficient is constant over each segment. Because of symmetry, only half of the tube is considered. The temperature distribution in the tube wall (the direct problem) is obtained using the heat balance method (Kreith and Black, 1980) in conjunction with the SOR method. The grid of finite control volumes is shown in Fig. 1. Introducing nondimensional heat transfer coefficients $Bi_j = x_j = h_j r_{in}/k$, the solution was obtained using the described method. To solve the linear Eqs. (5), the SVD method was used. The numerical results for the data given are shown in Table 1. The Jacobi matrix was calculated every four iterations.

Example 2 Radiantly Heated Tube. In this example, we consider measured data taken from an experiment conducted by Ishikawa et al. (1980) (Fig. 2). The test tube was radiantly heated on its circumference while being covered on its opposing semicircumference with ceramic wool and fire bricks. The austenitic steel tube (SUS 304 steel) with an outside diameter of 31.8 mm and a wall thickness of 6.5 mm was equipped with 20 thermocouples, measuring the circumferential temperature profile at intervals of 36 deg (Figs. 1 and 2). The outside and inside wall temperatures were measured at two radial locations: $r_1 = 15.4$ mm and $r_2 = 9.9$ mm, respectively. The thermal conductivity k of the tube material is temperature dependent:

$$k = 14.65 + 0.0144 \cdot T, \text{ W/mK}$$

where T is in °C. The fluid temperature T_f is assumed to be 100°C, because its value is not specified by Ishikawa et al.

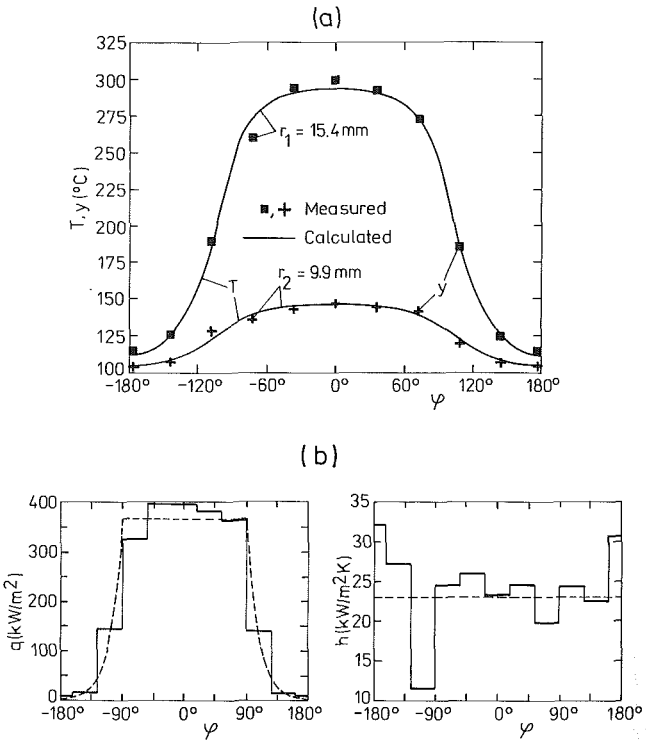

Fig. 2 Comparison of the results obtained using Gauss-Newton-SVD method with experimental data and space-marching predictions for radiantly heated tube: (*a*) comparison of the calculated temperatures with experimental data from Ishikawa et al. (1980) at $r_1 = 15.4$ mm and $r_2 = 9.9$ mm; (*b*) circumferential variation of predicted heat flux and heat transfer coefficient: ——— , space-marching technique; - - - - -, Gauss-Newton-SVD method

(1980). This value of the fluid temperature is added to the temperature differences given by Ishikawa et al. (1980). The temperatures obtained this way are then used as the experi-

Downloaded 13 Dec 2010 to 193.140.21.150. Redistribution subject to ASME license or copyright; see http://www.asme.org/terms/Terms_Use.cfm

mental data (Fig. 2). Two ways of estimating parameters are used. One is the Gauss–Newton method in combination with the SVD or MGS methods. Another method of solution uses the space-marching technique in combination with the heat balance method.

(i) Solution Using Gauss–Newton Method. The heat conduction in the tube is governed by

$$\frac{1}{r}\frac{\partial}{\partial r}\left[rk(T)\frac{\partial T}{\partial r}\right]+\frac{1}{r}\frac{\partial}{\partial \varphi}\left[\frac{k(T)}{r}\frac{\partial T}{\partial \varphi}\right]=0 \tag{9}$$

subject to the boundary condition on the inside surface

$$\left[k(T)\frac{\partial T}{\partial r}\right]\Bigg|_{r=r_{in}}=h(T|_{r=r_{\text{in}}}-T_f). \tag{10}$$

The heat flux distributions $q(\varphi)$ on the outside of the tube can be described fairly well by

$$\begin{aligned} q(\varphi)&=q_m, && 0\le\varphi\le\pi/2\\ q(\varphi)&=q_m\exp\left[\frac{1}{x_4}\left(1-\frac{2\varphi}{\pi}\right)\right], && \frac{\pi}{2}\le\varphi\le\pi, \end{aligned} \tag{11}$$

where T is the temperature, r and φ are radial and angular positions, respectively, h is heat transfer coefficient, k is thermal conductivity, T_f is the fluid temperature, q_m is measured heat flux, and x_4 is a constant. To simplify the analysis, the thermal conductivity is calculated at mean temperature of the whole cross section of the tube. A series solution for the direct heat conduction problem (Eqs. (9)–(11)) obtained by separation of variables is given by Taler (1992). In the estimation procedure, the quantities of interest are the dimensionless parameters:

$$x_1=\frac{q_m r_o}{kT_r},\quad x_2=Bi=\frac{hr_{in}}{k},\quad x_3=\frac{T_f}{T_r}\quad\text{and}\quad x_4$$

where r_{in} and r_o are inner and outer radii of the tube, respectively. Parameters $x_1, \ldots, x_4$ are determined from the solution of Eq. (1), which are written in the dimensionless form: $\theta(\mathbf{x}, r_i) - y_i/T_r \approx 0$, $i = 1, \ldots, m$, where $\theta = T/T_r$ and T_r is the reference temperature. Both the SVD and MGS methods are used to solve Eqs. (5).

The parameters are estimated using the measured temperature values given in Fig. 2 with $T_r = 300°C$, $\delta_j = 0.001$, $j = 1, \ldots, 4$ and $\epsilon = 0.001$. The estimated values of the parameters obtained by using the Gauss–Newton method in conjunction with the SVD method are: $\tilde{\bar{T}} = 185.12°C$, $k(\tilde{\bar{T}}) = 17.32$ W/mK, $\tilde{x}_1 = 1.1205$ ($\tilde{q}_m = 366247$ W/m^2), $\tilde{x}_2 = 12.4716$ ($\tilde{h} = 22984.2$ W/m^2 K), $\tilde{x}_3 = 0.3396$ ($\tilde{T}_f = 101.89°C$), $\tilde{x}_4 = 0.1866$ and $g = 344.95$ K^2. The singular values of the matrix $\mathbf{DT}(\mathbf{x}^*)$ are: $\sigma_1 = 1397.4$, $\sigma_2 = 316.9$, $\sigma_3 = 258.7$, and $\sigma_4 = 2.1$. The condition number is $\sigma_1/\sigma_4 = 665.4$. The predicted temperature distributions at $r_1 = 15.4$ mm and $r_2 = 9.9$ mm are compared with measured temperatures in Fig. 2. It is seen that the solution obtained by the method presented here is in very good agreement with experimental input data. For the same data the following estimates are obtained using the MGS method: $\tilde{\bar{T}} = 185.12°C$, $k(\tilde{\bar{T}}) = 17.32$ W/mK, $\tilde{x}_1 = 1.1197$ ($\tilde{q}_m = 365990$ W/m^2), $\tilde{x}_2 = 12.3503$ ($\tilde{h} = 22760.5$ W/m^2 K), $\tilde{x}_3 = 0.3392$ ($\tilde{T}_f = 101.75°C$), $\tilde{x}_4 = 0.1871$, and $g = 345.1$ K^2. The results are in very good agreement with those obtained by the SVD method.

(ii) Solution Using Space-Marching Technique. To investigate the accuracy of the present method, the same problem was solved using the space-marching technique (Müller-Steinhagen and Schlünder, 1984). The thermal conductivity of the tube is considered to be temperature dependent. Figure 1 shows the heat balance nodal network. By invoking the symmetry of the problem, it is necessary only to solve the temperature field for half the tube cross section. The nodal temperature values are computed by solving the system of nodal equations using the SOR method. The temperature-dependent thermal conductivity makes the problem nonlinear and the determination of the nodal temperatures requires iteration. Figure 2 shows the estimated heat transfer coefficient and the heat flux. As can be seen from the figure, the heat flux calculated by the space-marching technique compares well with the result obtained by minimizing the least-squares function (2) using the Gauss–Newton method.

Conclusions

An efficient technique for estimating the steady-state space-variable heat transfer coefficient or boundary heat flux has been developed using the Gauss–Newton linearization technique in combination with the singular value decomposition or Gram–Schmidt method for solving the overdetermined set of algebraic equations. To present a specific application of the methods presented, two illustrative examples using actual data were selected. The number of the parameters to be estimated is less than the number of the measured temperatures. The method in its present form has no inherent limitations as to the geometric complexity, the kinds of boundary conditions, or the material thermal conductivity. Transient heat conduction problems could also be treated using the basic approach given here.

References

Beck, J. V., 1988, "Combined Parameter and Function Estimation in Heat Transfer With Application to Contact Conductance," ASME JOURNAL OF HEAT TRANSFER, Vol. 110, pp. 1046–1058.

Bonn, W., Iwicki, J., Krebs, R., Steiner, D., and Schlünder, E. U., 1980, "Über die Auswirkungen der Ungleichverteilung des Wärmeübergangs am Rohrumfang bei der Verdampfung im durchströmten waagerechten Rohr," *Wärme- und Stoffübertragung*, Vol. 13, pp. 265–274.

Dahlquist, G., and Björck, A., 1974, *Numerical Methods*, Prentice-Hall, Englewood Cliffs, NJ.

Forsythe, G. E., Malcolm, M. A., and Moler, C. B., 1977, *Computer Methods for Mathematical Computations*, Prentice-Hall, Englewood Cliffs, NJ.

Ishikawa, H., Suhara, S., Abe, T., and Takahashi, T., 1980, "Thermal Conductivity of Scale Deposits in Supercritical Boilers," *Heat Transfer—Japanese Research*, Vol. 9, pp. 23–26.

Kreith, F., and Black, W. Z., 1980, *Basic Heat Transfer*, Harper and Row, New York.

Müller-Steinhagen, H., and Schlünder, E. U., 1984, "The Influence of the Circumferential Heat Conduction on the Perimeter-Averaged Heat Transfer Coefficient at Flow Boiling in Horizontal Tubes," *Chemical Engineering and Processing*, Vol. 18, pp. 303–316.

Taler, J., 1992, "A Method of Determining Local Heat Flux in Boiler Furnaces," *Int. J. Heat Mass Transfer*, Vol. 35, pp. 1625–1634.

Varah, J. M., 1973, "On the Numerical Solution of Ill-Conditioned Linear Systems With Applications to Ill-Posed Problems," *SIAM J. Numer. Anal.*, Vol. 10, pp. 257–267.

Effects of Axial and Radial-Gap Spacing on the Local Heat Transfer of a Shrouded Rotor-Stator System

M. K. Chyu[1] and D. J. Bizzak[1]

Nomenclature

- a = radial gap clearance between the shroud and rotor
- D = rotor diameter
- K = naphthalene-to-air mass transfer diffusivity
- R = rotor radius
- h = local heat transfer coefficient

[1]Department of Mechanical Engineering and Data Storage System Center, Carnegie Mellon University, Pittsburgh, PA 15213.

Contributed by the Heat Transfer Division of THE AMERICAN SOCIETY OF MECHANICAL ENGINEERS. Manuscript received by the Heat Transfer Division November 1990; revision received February 1992. Keywords: Forced Convection, Mass Transfer, Rotating Flows. Associate Technical Editor: J. H. Kim.

Downloaded 13 Dec 2010 to 193.140.21.150. Redistribution subject to ASME license or copyright; see http://www.asme.org/terms/Terms_Use.cfm

mental data (Fig. 2). Two ways of estimating parameters are used. One is the Gauss–Newton method in combination with the SVD or MGS methods. Another method of solution uses the space-marching technique in combination with the heat balance method.

(i) Solution Using Gauss–Newton Method. The heat conduction in the tube is governed by

$$\frac{1}{r}\frac{\partial}{\partial r}\left[rk(T)\frac{\partial T}{\partial r}\right]+\frac{1}{r}\frac{\partial}{\partial \varphi}\left[\frac{k(T)}{r}\frac{\partial T}{\partial \varphi}\right]=0 \tag{9}$$

subject to the boundary condition on the inside surface

$$\left[k(T)\frac{\partial T}{\partial r}\right]\Bigg|_{r=r_{in}}=h(T|_{r=r_{\text{in}}}-T_f). \tag{10}$$

The heat flux distributions $q(\varphi)$ on the outside of the tube can be described fairly well by

$$\begin{aligned} q(\varphi)&=q_m, && 0\le\varphi\le\pi/2\\ q(\varphi)&=q_m\exp\left[\frac{1}{x_4}\left(1-\frac{2\varphi}{\pi}\right)\right], && \frac{\pi}{2}\le\varphi\le\pi, \end{aligned} \tag{11}$$

where T is the temperature, r and φ are radial and angular positions, respectively, h is heat transfer coefficient, k is thermal conductivity, T_f is the fluid temperature, q_m is measured heat flux, and x_4 is a constant. To simplify the analysis, the thermal conductivity is calculated at mean temperature of the whole cross section of the tube. A series solution for the direct heat conduction problem (Eqs. (9)–(11)) obtained by separation of variables is given by Taler (1992). In the estimation procedure, the quantities of interest are the dimensionless parameters:

$$x_1=\frac{q_m r_o}{kT_r},\quad x_2=Bi=\frac{hr_{in}}{k},\quad x_3=\frac{T_f}{T_r}\quad\text{and}\quad x_4$$

where r_{in} and r_o are inner and outer radii of the tube, respectively. Parameters $x_1, \ldots, x_4$ are determined from the solution of Eq. (1), which are written in the dimensionless form: $\theta(\mathbf{x}, r_i) - y_i/T_r \approx 0$, $i = 1, \ldots, m$, where $\theta = T/T_r$ and T_r is the reference temperature. Both the SVD and MGS methods are used to solve Eqs. (5).

The parameters are estimated using the measured temperature values given in Fig. 2 with $T_r = 300°C$, $\delta_j = 0.001$, $j = 1, \ldots, 4$ and $\epsilon = 0.001$. The estimated values of the parameters obtained by using the Gauss–Newton method in conjunction with the SVD method are: $\tilde{\bar{T}} = 185.12°C$, $k(\tilde{\bar{T}}) = 17.32$ W/mK, $\tilde{x}_1 = 1.1205$ ($\tilde{q}_m = 366247$ W/m^2), $\tilde{x}_2 = 12.4716$ ($\tilde{h} = 22984.2$ W/m^2 K), $\tilde{x}_3 = 0.3396$ ($\tilde{T}_f = 101.89°C$), $\tilde{x}_4 = 0.1866$ and $g = 344.95$ K^2. The singular values of the matrix $\mathbf{DT}(\mathbf{x}^*)$ are: $\sigma_1 = 1397.4$, $\sigma_2 = 316.9$, $\sigma_3 = 258.7$, and $\sigma_4 = 2.1$. The condition number is $\sigma_1/\sigma_4 = 665.4$. The predicted temperature distributions at $r_1 = 15.4$ mm and $r_2 = 9.9$ mm are compared with measured temperatures in Fig. 2. It is seen that the solution obtained by the method presented here is in very good agreement with experimental input data. For the same data the following estimates are obtained using the MGS method: $\tilde{\bar{T}} = 185.12°C$, $k(\tilde{\bar{T}}) = 17.32$ W/mK, $\tilde{x}_1 = 1.1197$ ($\tilde{q}_m = 365990$ W/m^2), $\tilde{x}_2 = 12.3503$ ($\tilde{h} = 22760.5$ W/m^2 K), $\tilde{x}_3 = 0.3392$ ($\tilde{T}_f = 101.75°C$), $\tilde{x}_4 = 0.1871$, and $g = 345.1$ K^2. The results are in very good agreement with those obtained by the SVD method.

(ii) Solution Using Space-Marching Technique. To investigate the accuracy of the present method, the same problem was solved using the space-marching technique (Müller-Steinhagen and Schlünder, 1984). The thermal conductivity of the tube is considered to be temperature dependent. Figure 1 shows the heat balance nodal network. By invoking the symmetry of the problem, it is necessary only to solve the temperature field for half the tube cross section. The nodal temperature values are computed by solving the system of nodal equations using the SOR method. The temperature-dependent thermal conductivity makes the problem nonlinear and the determination of the nodal temperatures requires iteration. Figure 2 shows the estimated heat transfer coefficient and the heat flux. As can be seen from the figure, the heat flux calculated by the space-marching technique compares well with the result obtained by minimizing the least-squares function (2) using the Gauss–Newton method.

Conclusions

An efficient technique for estimating the steady-state space-variable heat transfer coefficient or boundary heat flux has been developed using the Gauss–Newton linearization technique in combination with the singular value decomposition or Gram–Schmidt method for solving the overdetermined set of algebraic equations. To present a specific application of the methods presented, two illustrative examples using actual data were selected. The number of the parameters to be estimated is less than the number of the measured temperatures. The method in its present form has no inherent limitations as to the geometric complexity, the kinds of boundary conditions, or the material thermal conductivity. Transient heat conduction problems could also be treated using the basic approach given here.

References

Beck, J. V., 1988, "Combined Parameter and Function Estimation in Heat Transfer With Application to Contact Conductance," ASME JOURNAL OF HEAT TRANSFER, Vol. 110, pp. 1046–1058.

Bonn, W., Iwicki, J., Krebs, R., Steiner, D., and Schlünder, E. U., 1980, "Über die Auswirkungen der Ungleichverteilung des Wärmeübergangs am Rohrumfang bei der Verdampfung im durchströmten waagerechten Rohr," *Wärme- und Stoffübertragung*, Vol. 13, pp. 265–274.

Dahlquist, G., and Björck, A., 1974, *Numerical Methods*, Prentice-Hall, Englewood Cliffs, NJ.

Forsythe, G. E., Malcolm, M. A., and Moler, C. B., 1977, *Computer Methods for Mathematical Computations*, Prentice-Hall, Englewood Cliffs, NJ.

Ishikawa, H., Suhara, S., Abe, T., and Takahashi, T., 1980, "Thermal Conductivity of Scale Deposits in Supercritical Boilers," *Heat Transfer—Japanese Research*, Vol. 9, pp. 23–26.

Kreith, F., and Black, W. Z., 1980, *Basic Heat Transfer*, Harper and Row, New York.

Müller-Steinhagen, H., and Schlünder, E. U., 1984, "The Influence of the Circumferential Heat Conduction on the Perimeter-Averaged Heat Transfer Coefficient at Flow Boiling in Horizontal Tubes," *Chemical Engineering and Processing*, Vol. 18, pp. 303–316.

Taler, J., 1992, "A Method of Determining Local Heat Flux in Boiler Furnaces," *Int. J. Heat Mass Transfer*, Vol. 35, pp. 1625–1634.

Varah, J. M., 1973, "On the Numerical Solution of Ill-Conditioned Linear Systems With Applications to Ill-Posed Problems," *SIAM J. Numer. Anal.*, Vol. 10, pp. 257–267.

Effects of Axial and Radial-Gap Spacing on the Local Heat Transfer of a Shrouded Rotor-Stator System

M. K. Chyu[1] and D. J. Bizzak[1]

Nomenclature

- a = radial gap clearance between the shroud and rotor
- D = rotor diameter
- K = naphthalene-to-air mass transfer diffusivity
- R = rotor radius
- h = local heat transfer coefficient

[1]Department of Mechanical Engineering and Data Storage System Center, Carnegie Mellon University, Pittsburgh, PA 15213.

Contributed by the Heat Transfer Division of THE AMERICAN SOCIETY OF MECHANICAL ENGINEERS. Manuscript received by the Heat Transfer Division November 1990; revision received February 1992. Keywords: Forced Convection, Mass Transfer, Rotating Flows. Associate Technical Editor: J. H. Kim.

Copyright © 1992 by ASME

Downloaded 13 Dec 2010 to 193.140.21.150. Redistribution subject to ASME license or copyright; see http://www.asme.org/terms/Terms_Use.cfm

h_m = local mass transfer coefficient
$\underline{Nu}$ = local Nusselt number $= hR/\nu$
$\overline{Nu}$ = area-averaged Nusselt number
r = local radial position on rotor surface
Re = rotational Reynolds number $= R^2\omega/\nu$
$\underline{Sh}$ = local Sherwood number $= h_m R/K$
$\overline{Sh}$ = area-averaged Sherwood number
z = axial gap between rotor and stator
ν = kinematic viscosity of air
ω = rotor rotation speed

Introduction

Unlike the free disk in which heat transfer is primarily affected by rotational speed, heat transfer in rotor-stator systems is influenced by the operating conditions as well as system geometry. In a rotor-stator system with no radial shroud, commonly referred to as an open rotor-stator, Kreith et al. (1959, 1963) and Metzger (1970) demonstrated that the presence of the stator influences heat transfer from the disk at axial gap spacings less than 10 percent of the disk diameter. These studies also examined the effects that forced coolant flow introduced at the hub of the system has on the average heat transfer rate. As an extension of these studies, more recent evaluations by Metzger et al. (1979, 1991) and Popiel and Boguslawski (1986) have examined the effects of varying the location and rate of forced coolant flow.

An important geometric effect in actual disk systems such as gas turbines or computer disk storage devices is the presence of a radial clearance shroud. Few studies have explicitly examined the effect that a radial clearance shroud has on heat transfer in a disk system. Metzger et al. (1991) performed local heat transfer measurements across a disk face using a radially shrouded rotor-stator system, but the purpose of these experiments was to investigate the influence that the radial location and rate of coolant flow have on local heat transfer. Chyu and Bizzak (1991) have recently examined the influence of axial flow through the radial clearance on the heat transfer from a pair of corotating disks.

The primary objective of this study is to examine the effects that radial gap clearance and axial-gap spacing have on local heat transfer in a shrouded rotor-stator system with freely induced radial coolant flow. The effects of axial-gap spacing (z/D) and radial-gap clearance (a/D) on the mass transfer in a shrouded system are examined in a series of tests in which these parameters and the rotational speed are varied. The test range covers $0.02 \le a/D \le 0.042$, $0.01 \le z/D \le 0.05$, and $4\times10^4 \le \mathrm{Re} \le 2.5\times10^5$. This is similar to the operating conditions of the uppermost disk in a modern 3.5-in computer disk drive without slider-arm obstruction. To avoid the complications and errors associated with conventional experimental heat transfer techniques employing resistance heaters and thermocouples, a mass transfer analog based on naphthalene ($C_{10}H_8$) sublimation is used. This technique permits greater spatial resolution during data collection and more accurate measurement of local transfer coefficients. The naphthalene mass transfer analogy has previously been used to study average heat transfer in rotating systems by Kreith et al. (1959, 1963), while the present technique to measure local mass-transfer distributions on planar surfaces has been documented in detail by Goldstein et al. (1985) and Chyu (1986).

Experimental Apparatus and Procedure

The arrangement of the equipment used in this study is shown schematically in Fig. 1. The apparatus consists of a plexiglass shroud, an aluminum rotor having a naphthalene surface, a d-c motor, and a variable speed motor controller. The shroud is constructed of 165 mm (6.5 in.) i.d. plexiglass tubing sealed at one end with plexiglass sheeting. To permit variation of the radial gap clearance, two aluminum disks are

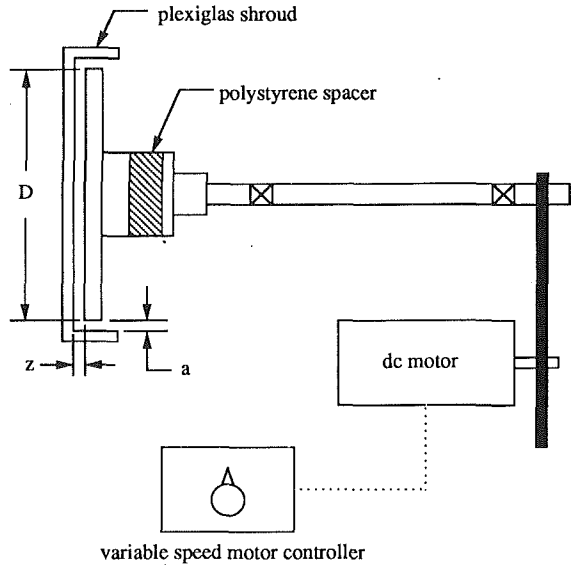

Fig. 1 Experimental equipment setup

used. One is 152 mm (6 in.) in diameter, and the diameter of the other is 159 mm (6.25 in.). The surfaces of both disks are machined to provide a cavity for naphthalene castings. The cavities on both disks are bounded by a 3.2 mm (1/8 in.) rim near the disk edge, which facilitates casting of a smooth naphthalene surface and also serves as a reference for determining tilt and vertical position of the disk during surface measurements.

In order to determine successfully the local variations in naphthalene surface sublimation depths, it is necessary to position the test specimen precisely and to use an accurate measurement device. To minimize human error, a computer-controlled data acquisition system is used. The depth gage in this system is composed of a linear variable differential transformer (LVDT) and a signal conditioner. This arrangement provides repeatable surface measurements accurate to within 2.5×10^{-3}mm (10^{-4} in.). The other components of the system are a digital multimeter, two stepper-motor positioners, a motor controller, and an IBM personal computer.

The duration of each test run is 2 hours. To ensure that frictional heating in the shaft bearings of the test apparatus does not cause heat-up of the naphthalene surface, a 25.4 mm (1.0 in.) polystyrene insulating spacer is used between the test specimen and the shaft-mounting plate. During the course of the test, the ambient air temperature is recorded at five-minute intervals using a mercury thermometer. In addition, a digital tachometer is used to record disk rotation speed. In general, observed variations in ambient air temperatures were less than 1°C, while disk speed was maintained within a 2 percent range by the motor controller.

Results and Discussion

An important phenomenon that is noted in post-test visual inspections of the naphthalene surface is the occurrence of periodic depressions in the form of swirls. These depressions, which are observed only in the high-speed disk cases at a local rotational Reynolds number of approximately 1.8×10^5, are attributable to the formation of stationary vortices. According to Owen and Rogers (1989), these vortices form in a transition region where flow is no longer laminar but not fully turbulent. These stationary vortices, however, are not observed in high-speed tests at the smallest axial-gap spacing ($z/D = 0.01$). This breakdown of the transition region vortices can be expected when boundary layer interactions between pumped flow on the rotor and inlet coolant flow on the stator occur.

Analytical solutions for laminar flow over a free disk indicate

Downloaded 13 Dec 2010 to 193.140.21.150. Redistribution subject to ASME license or copyright; see http://www.asme.org/terms/Terms_Use.cfm

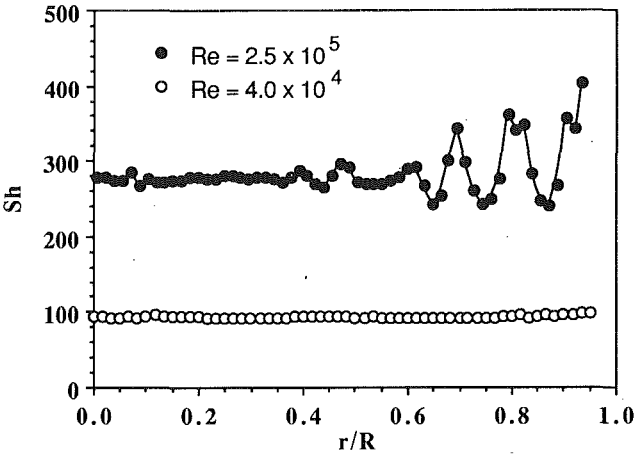

Fig. 2 Free disk local mass transfer distribution

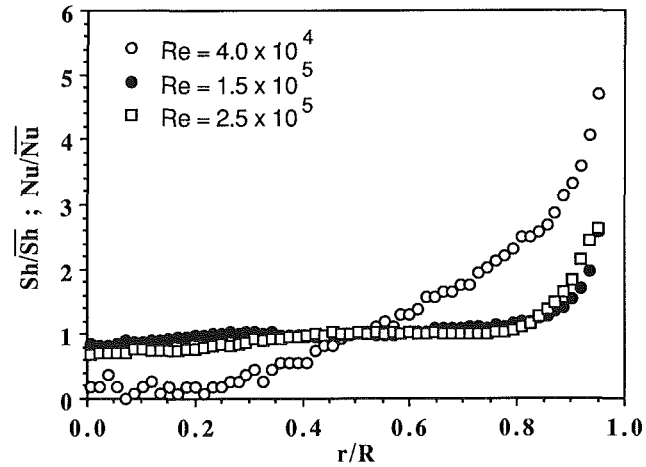

Fig. 3 Reynolds number effects on local mass/heat transfer: $a/D = 0.02$, $z/D = 0.01$

that heat transfer is uniform across the entire disk surface. As shown in Fig. 2, local Sherwood number profiles for the free disk cases obtained in the present study are generally consistent with this expectation. For the laminar flow case ($Re = 4.0 \times 10^4$), local Sherwood numbers vary less than 2 percent from the mean value. In the high-speed test ($Re = 2.5 \times 10^5$), however, a transition region characterized by random variations in the local Sherwood number near the disk edge occurs at a local rotational Reynolds number about 1.8×10^5, or $r/R \approx 0.7$. The corresponding area-averaged mass transfer results obtained by integrating the local data deviate less than 4 percent from theoretical predictions of the Sherwood number (Owen and Rogers, 1989).

The local Sherwood number profile for the rotor in a shrouded rotor-stator configuration are similar to those for free disks, except at the smallest axial gap spacing ($z/D = 0.01$). Figure 3 illustrates the effects of Reynolds number on the local mass transfer distribution on the rotor surface for this smallest axial spacing and radial clearance $a/D = 0.02$. To permit a meaningful evaluation of the local mass transfer distributions, the normalized Sherwood number ($Sh/\overline{Sh}$) is used here as the basis for comparison. Normalization of the results also serves to negate the difference between heat transfer and mass transfer (i.e., $Sh/\overline{Sh} = Nu/\overline{Nu}$). The values of $\overline{Sh}$ are 19.7, 59.3, and 104.0 for $Re = 4.0 \times 10^4$, 1.5×10^5, and 2.5×10^5, respectively. As shown in Fig. 3, the spatial variation in mass transfer appears to be most significant at the lowest Reynolds number. The local Sherwood number for all cases studied tends to increase near the edge of the disk. However, the magnitude

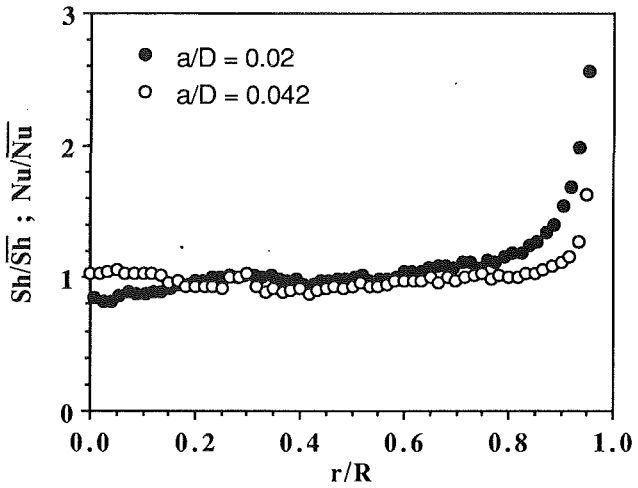

Fig. 4 Effect of radial gap clearance on local mass/heat transfer: $Re = 1.5 \times 10^5$, $z/D = 0.01$

of the increase in the mass transfer near the disk edge is influenced by the radial clearance. According to Fig. 4, the peak of the normalized Sherwood number for the 0.02 radial clearance case is nearly twice that of the 0.042 radial clearance test.

Based on the above results, it is speculated that the hydrodynamic behavior of a shrouded rotor-stator system can be at least partially attributable to boundary layer interactions inside the disk cavity. The boundary layer near a rotor is characterized by a pumped flow driven radially outward by the rotational force, while the boundary layer flows radially inward near the stator. For the present shrouded system with a radial gap, fresh air that is free of naphthalene (equivalent to coolant in heat transfer) entrains into the cavity through the radial gap and reaches near the stator outer edge. At relatively large axial spacings and high rotation rates, the entrained fresh "coolant" will reach the hub section and will then be pumped out of the cavity along the rotor surface. In these instances, the key parameter affecting mass transfer will be the radial clearance gap, which determines the fresh coolant entrainment rate. For small axial-gap spacings, however, wall shear can profoundly dissipate the radial flow momentum along the stator, causing a portion of the incoming coolant to reverse direction before reaching the hub and to merge with pumped flow along the rotor. This effect is expected to decrease the mass transfer toward the hub and increase the mass transfer near the disk outer edge.

Conclusions

Through this parametric investigation of a shrouded rotor-stator system, the effects of system geometry, in particular axial-gap spacing, radial clearance, and rotational Reynolds number, on heat transfer have been examined using a mass transfer analogy. The important findings of this study are summarized below.

While the local Sherwood number profiles at gap spacings of $z/D = 0.02$ and 0.05 are similar to those obtained for a free disk (i.e., uniform across the disk face), profiles at $z/D = 0.01$ exhibit a significant increase in mass transfer near the disk edge. The magnitude of this increase, as compared to the average mass transfer, is also found to be similarly related to both the rotational Reynolds number and the radial clearance gap.

This finding suggests that boundary layer interactions within the disk cavity determine the local mass transfer rates. It is speculated that the interactions between the boundary layers cause a portion of the incoming fresh coolant on the stator to reverse direction and merge with pumped flow along the rotor, causing an increase in mass transfer near the disk edge. This phenomenon is a function of the radial momentum of incoming

Downloaded 13 Dec 2010 to 193.140.21.150. Redistribution subject to ASME license or copyright; see http://www.asme.org/terms/Terms_Use.cfm

flow (Reynolds number dependence) and the amount of fresh coolant entrained into the boundary layer on the stator (radial clearance dependence).

Acknowledgments

This work is jointly supported by NASA Marshall Space Flight Center, an NSF equipment grant, and Data Storage System Center at Carnegie Mellon University.

References

Chyu, M. K., 1986, "Influence of Roughness Elements on Local Mass Transfer From a Flat Surface," Ph.D. Thesis, University of Minnesota, Minneapolis, MN.

Chyu, M. K., and Bizzak, D. J., 1992, "Surface Heat Transfer in a Hubbed Rotor-Stator and a Clamped Corotating Disk Assembly With and Without Axial Source Flow," *Advances in Information Storage System*, Vol. 4, ASME, pp. 383–394.

Goldstein, R. J., Chyu, M. K., and Hain, R. C., 1985, "Measurement of Local Mass Transfer on a Surface in the Region of the Base of a Protruding Cylinder With a Computer-Controlled Data Acquisition System," *Int. J. Heat Mass Transfer*, Vol. 28, pp. 977–985.

Kreith, F., Taylor, J. H., and Chong, J. P., 1959, "Heat and Mass Transfer From a Rotating Disk," ASME JOURNAL OF HEAT TRANSFER, Vol. 81, pp. 95–105.

Kreith, F., Doughman, E., and Kozlowski, H., 1963, "Mass and Heat Transfer From an Enclosed Rotating Disk With and Without Source Flow," ASME JOURNAL OF HEAT TRANSFER, Vol. 85, pp. 153–163.

Metzger, D. E., 1970, "Heat Transfer and Pumping on a Rotating Disk With Freely Induced and Forced Cooling," ASME *Journal of Engineering for Power*, Vol. 92, pp. 342–348.

Metzger, D. E., Mathis, W. J., and Grochowsky, L. D., 1979, "Jet Cooling at the Rim of a Rotating Disk," ASME *Journal of Engineering for Power*, Vol. 101, pp. 68–72.

Metzger, D. E., Bunker, R. S., and Bosch, G., 1991, "Transient Liquid Crystal Measurement of Local Heat Transfer on a Rotating Disk With Jet Impingement," ASME *Journal of Turbomachinery*, Vol. 113, pp. 52–59.

Owen, J. M., and Rogers, R. H., 1989, *Flow and Heat Transfer in Rotating-Disc Systems, Vol. 1—Rotor-Stator Systems*. Research Studies Press, Somerset, United Kingdom.

Popiel, C. O., and Boguslawski, L., 1986, "Local Heat Transfer From a Rotating Disk in an Impinging Round Jet," ASME JOURNAL OF HEAT TRANSFER, Vol. 108, pp. 357–364.

Measurement of the Free Convection Heat Transfer Coefficient for a Rough Horizontal Nonisothermal Cylinder in Ambient Air by Infrared Scanning

M. S. Farid[1] and C. K. Hsieh[1]

Nomenclature

- A = temperature vector
- B = heat flux vector
- a, b = coefficients in Eq. (1), or vector components in A and B
- C = correction for mirror reflection
- C_i = defined in Eq. (17) of Hsieh et al. (1989)
- F, G = coefficient matrices in Eq. (3)
- f, g = matrix elements in F, G, respectively
- Gr = Grashof number
- k = thermal conductivity
- Nu = Nusselt number
- q = heat flux
- R = radius of cylinder
- T = temperature
- w = uncertainty
- δ_{ij} = Kronecker delta
- ϵ = emissivity
- θ = angle measured from the lower stagnation point
- σ = Stefan–Boltzmann constant

Subscripts

- r = radiation
- s = ambient air
- w = wall
- w_o = lower stagnation point

Introduction

Free convection heat transfer coefficients have been measured by using optical techniques, heat flux gages, and analogies. In this paper, a new method of combining infrared scanning and the boundary element method is used to measure the convective coefficient for a rough circular cylinder suspended horizontally in ambient air. The flow is buoyancy driven and the cylinder is heated internally to a steady state with nonuniform temperature on its surface. It will be shown that the roughness on the surface has a decisive effect of enhancing the heat transfer by free convection. In this effort, a comparison will be made with a smooth cylinder with identical temperature distribution. The convective coefficient for the smooth cylinder is taken from a theoretical analysis by Koh and Price (1965). To the knowledge of the present authors, free convection from rough cylinders has rarely been studied in the literature. Only one reference (Morgan, 1973) has been found, and even that study was made for free convection from bare stranded electric conductors, a configuration bearing little resemblance to the surface roughness addressed in this study. The research presented in this paper thus provides a new direction for heat transfer enhancement. It also offers a new method for the measurement of the convective coefficient.

Test Apparatus

An AGA Thermovision System 680 was used for infrared scanning. It consisted of five components: the infrared scanning unit, the black-and-white image monitor, the color image monitor, the scan-line profile adapter, and the analog display unit; see Farid (1991). The test cylinder was made up of an opaque ceramic material and was heated by a cartridge heater inside a copper tubing that was placed at the center of the cylinder. The temperature of this tubing was measured by using four thermocouples half embedded in milled grooves on the outside surface of the tubing. The surface of the cylinder whose temperature was scanned was painted black using 3M Nextel velvet paint, which had a distinctive two-band reflection spectrum. A uniform reflectivity of 2 percent was found below 9 μm and a broad band of 4 percent was found above 10 μm. They were connected by a reflective peak of about 8 percent at 9.5 μm (Wong and Hsieh, 1983). Since the detector (indium antimonide) in the scanner is sensitive in the range from 2 to 5.6 (cutoff) μm, the surface can be treated as gray with good approximation.

The cylinder was suspended horizontally in a wooden chamber; see Fig. 1. The walls of the chamber facing the cylinder were lined with black-color papers. Rectangular ports with adjustable openings were cut at the top and bottom of the side walls for vents. The front of the chamber exposed to the scanner was covered with a large plastic film to form a tent, and the scanner was placed inside the tent throughout the course of the experiment. This arrangement isolated the ambient air inside the chamber from room-draft disturbance while providing limited air circulation to avert stratification. The ambient air temperature was measured by using 16 thermocouples (Farid, 1991). In tests, the cylinder was scanned in an axial

[1]Mechanical Engineering Department, University of Florida, Gainesville, FL 32611.

Contributed by the Heat Transfer Division of THE AMERICAN SOCIETY OF MECHANICAL ENGINEERS. Manuscript received by the Heat Transfer Division July 1991; revision received May 1992. Keywords: Augmentation and Enhancement, Measurement Techniques, Natural Convection. Associate Technical Editor: J. R. Lloyd.

Downloaded 13 Dec 2010 to 193.140.21.150. Redistribution subject to ASME license or copyright; see http://www.asme.org/terms/Terms_Use.cfm

flow (Reynolds number dependence) and the amount of fresh coolant entrained into the boundary layer on the stator (radial clearance dependence).

Acknowledgments

This work is jointly supported by NASA Marshall Space Flight Center, an NSF equipment grant, and Data Storage System Center at Carnegie Mellon University.

References

Chyu, M. K., 1986, "Influence of Roughness Elements on Local Mass Transfer From a Flat Surface," Ph.D. Thesis, University of Minnesota, Minneapolis, MN.

Chyu, M. K., and Bizzak, D. J., 1992, "Surface Heat Transfer in a Hubbed Rotor-Stator and a Clamped Corotating Disk Assembly With and Without Axial Source Flow," *Advances in Information Storage System*, Vol. 4, ASME, pp. 383–394.

Goldstein, R. J., Chyu, M. K., and Hain, R. C., 1985, "Measurement of Local Mass Transfer on a Surface in the Region of the Base of a Protruding Cylinder With a Computer-Controlled Data Acquisition System," *Int. J. Heat Mass Transfer*, Vol. 28, pp. 977–985.

Kreith, F., Taylor, J. H., and Chong, J. P., 1959, "Heat and Mass Transfer From a Rotating Disk," ASME JOURNAL OF HEAT TRANSFER, Vol. 81, pp. 95–105.

Kreith, F., Doughman, E., and Kozlowski, H., 1963, "Mass and Heat Transfer From an Enclosed Rotating Disk With and Without Source Flow," ASME JOURNAL OF HEAT TRANSFER, Vol. 85, pp. 153–163.

Metzger, D. E., 1970, "Heat Transfer and Pumping on a Rotating Disk With Freely Induced and Forced Cooling," ASME *Journal of Engineering for Power*, Vol. 92, pp. 342–348.

Metzger, D. E., Mathis, W. J., and Grochowsky, L. D., 1979, "Jet Cooling at the Rim of a Rotating Disk," ASME *Journal of Engineering for Power*, Vol. 101, pp. 68–72.

Metzger, D. E., Bunker, R. S., and Bosch, G., 1991, "Transient Liquid Crystal Measurement of Local Heat Transfer on a Rotating Disk With Jet Impingement," ASME *Journal of Turbomachinery*, Vol. 113, pp. 52–59.

Owen, J. M., and Rogers, R. H., 1989, *Flow and Heat Transfer in Rotating-Disc Systems, Vol. 1—Rotor-Stator Systems*. Research Studies Press, Somerset, United Kingdom.

Popiel, C. O., and Boguslawski, L., 1986, "Local Heat Transfer From a Rotating Disk in an Impinging Round Jet," ASME JOURNAL OF HEAT TRANSFER, Vol. 108, pp. 357–364.

Measurement of the Free Convection Heat Transfer Coefficient for a Rough Horizontal Nonisothermal Cylinder in Ambient Air by Infrared Scanning

M. S. Farid[1] and C. K. Hsieh[1]

Nomenclature

- A = temperature vector
- B = heat flux vector
- a, b = coefficients in Eq. (1), or vector components in A and B
- C = correction for mirror reflection
- C_i = defined in Eq. (17) of Hsieh et al. (1989)
- F, G = coefficient matrices in Eq. (3)
- f, g = matrix elements in F, G, respectively
- Gr = Grashof number
- k = thermal conductivity
- Nu = Nusselt number
- q = heat flux
- R = radius of cylinder
- T = temperature
- w = uncertainty
- δ_{ij} = Kronecker delta
- ϵ = emissivity
- θ = angle measured from the lower stagnation point
- σ = Stefan–Boltzmann constant

Subscripts

- r = radiation
- s = ambient air
- w = wall
- w_o = lower stagnation point

[1]Mechanical Engineering Department, University of Florida, Gainesville, FL 32611.

Contributed by the Heat Transfer Division of THE AMERICAN SOCIETY OF MECHANICAL ENGINEERS. Manuscript received by the Heat Transfer Division July 1991; revision received May 1992. Keywords: Augmentation and Enhancement, Measurement Techniques, Natural Convection. Associate Technical Editor: J. R. Lloyd.

Introduction

Free convection heat transfer coefficients have been measured by using optical techniques, heat flux gages, and analogies. In this paper, a new method of combining infrared scanning and the boundary element method is used to measure the convective coefficient for a rough circular cylinder suspended horizontally in ambient air. The flow is buoyancy driven and the cylinder is heated internally to a steady state with nonuniform temperature on its surface. It will be shown that the roughness on the surface has a decisive effect of enhancing the heat transfer by free convection. In this effort, a comparison will be made with a smooth cylinder with identical temperature distribution. The convective coefficient for the smooth cylinder is taken from a theoretical analysis by Koh and Price (1965). To the knowledge of the present authors, free convection from rough cylinders has rarely been studied in the literature. Only one reference (Morgan, 1973) has been found, and even that study was made for free convection from bare stranded electric conductors, a configuration bearing little resemblance to the surface roughness addressed in this study. The research presented in this paper thus provides a new direction for heat transfer enhancement. It also offers a new method for the measurement of the convective coefficient.

Test Apparatus

An AGA Thermovision System 680 was used for infrared scanning. It consisted of five components: the infrared scanning unit, the black-and-white image monitor, the color image monitor, the scan-line profile adapter, and the analog display unit; see Farid (1991). The test cylinder was made up of an opaque ceramic material and was heated by a cartridge heater inside a copper tubing that was placed at the center of the cylinder. The temperature of this tubing was measured by using four thermocouples half embedded in milled grooves on the outside surface of the tubing. The surface of the cylinder whose temperature was scanned was painted black using 3M Nextel velvet paint, which had a distinctive two-band reflection spectrum. A uniform reflectivity of 2 percent was found below 9 μm and a broad band of 4 percent was found above 10 μm. They were connected by a reflective peak of about 8 percent at 9.5 μm (Wong and Hsieh, 1983). Since the detector (indium antimonide) in the scanner is sensitive in the range from 2 to 5.6 (cutoff) μm, the surface can be treated as gray with good approximation.

The cylinder was suspended horizontally in a wooden chamber; see Fig. 1. The walls of the chamber facing the cylinder were lined with black-color papers. Rectangular ports with adjustable openings were cut at the top and bottom of the side walls for vents. The front of the chamber exposed to the scanner was covered with a large plastic film to form a tent, and the scanner was placed inside the tent throughout the course of the experiment. This arrangement isolated the ambient air inside the chamber from room-draft disturbance while providing limited air circulation to avert stratification. The ambient air temperature was measured by using 16 thermocouples (Farid, 1991). In tests, the cylinder was scanned in an axial

Copyright © 1992 by ASME
Downloaded 13 Dec 2010 to 193.140.21.150. Redistribution subject to ASME license or copyright; see http://www.asme.org/terms/Terms_Use.cfm

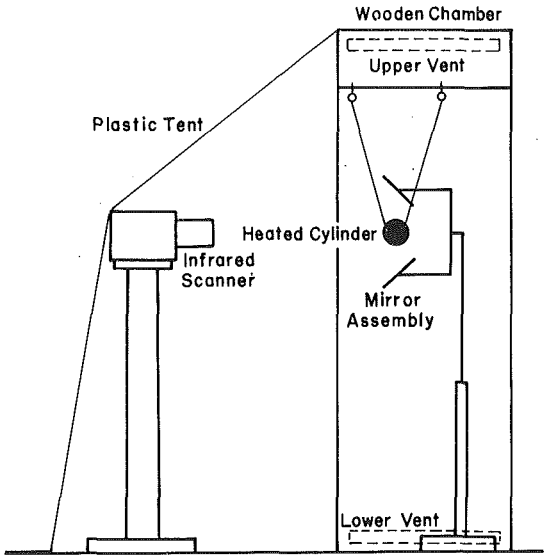

Fig. 1 System configuration

direction. The top and bottom of the cylinder that could not be reached directly by the scanner were viewed through the use of mirrors.

Analysis

Convection for smooth cylinder at nonuniform temperature has been analyzed in three studies: Chiang and Kaye (1962), Koh and Price (1965), and Lin and Chern (1981). Koh and Price's analysis is most general because they used an even fourth-degree polynomial with two adjustable coefficients to fit the surface temperature:

$$\frac{T_w - T_s}{T_{w_o} - T_s} = 1 + a\theta^2 + b\theta^4 \tag{1}$$

where all notations are defined in the nomenclature. They used this temperature to derive an analytic equation expressed in terms of the Nusselt number over the Grashof number to the one-fourth power as

$$\frac{\mathrm{Nu}}{\mathrm{Gr}^{0.25}} = 0.37023 + (0.75688a - 0.01609)\theta^2 + (0.92847b + 0.09471a^2 - 0.02885a - 0.00009)\theta^4 \tag{2}$$

where the characteristic lengths in these numbers are defined on the basis of the radius of the cylinder, and Pr = 0.7. In practice, the first equation is used to fit the surface temperature. The coefficients found in this equation are then used in the second equation to predict the Nusselt number. Wall temperature variation can thus be accounted for in their analysis, which is not possible with the other studies because they are based on fixed values of the coefficients.

For the free convection of interest in this study, the radiation heat loss from the surface was also important and must be accounted for. An effort has thus been made to estimate the radiative flux leaving the surface. For the present setup shown in Fig. 1, the cylinder can see itself through reflection in the mirrors; the radiative fluxes leaving the top and bottom of the cylinder are expected to be different from the rest of the surface. The analysis has been given in detail by Farid (1991).

The real variable boundary element method was used for determining the conductive heat flux in the cylinder wall. In this effort, the outer and inner boundaries of the cylinder were discretized into 32 elements and linear elements were used for the boundaries. The boundary-element equations were derived in a matrix form as

$$FA = GB \tag{3}$$

where

$$f_{ij} = (\hat{q}^b_{i,j-1} + \hat{q}^a_{i,j}) - \delta_{ij} C_i k \tag{4}$$

$$g_{ij} = \hat{T}^b_{i,j-1} + \hat{T}^a_{i,j} \tag{5}$$

$$a_j = T_j \tag{6}$$

$$b_j = q_j \tag{7}$$

The capped quantities above represented weighted integrals of a free-space Green's function and its normal derivative as defined by Hsieh et al. (1989). Clearly, Eq. (3) can be used to find T at a boundary node where q is given and vice versa. In the present analysis the temperatures at the inner and outer boundaries of the cylinder were measured by thermocouples and infrared scanning; they are thus fully specified. These temperatures can be used in Eq. (3) to evaluate the heat flux at the outer boundary of the cylinder. Then, once the radiation correction is accounted for at this boundary, the net heat flux for convection can be evaluated for the determination of the convective coefficient.

Calibration and Preliminary Measurements

Both position and temperature must be calibrated in infrared scanning. The position calibration was accomplished by using an aluminum checkerboard as described by Wong and Hsieh (1983). This board was placed at the focal point of the scanner and the images viewed on the monitors were used to correct for the distortion caused by the electronics. In practice, the position on the cylinder was identified by using aluminum foil markers affixed on the surface of the cylinder. These markers are highly reflective; they showed up clearly in infrared images.

Budget constraints precluded purchase of costly equipment for conversion of video signals. Temperatures were thus read off from the analog signals presented in the analog display unit. The scale divisions on the screen of this unit were quantified by using a copper plate that had a physical width that was wider than the line spread function of the scanner. One side of this plate was attached to a foil heater and the other side was instrumented with a thermocouple to measure temperature. This side of the plate was also painted black with the same paint used for the cylinder. The calibration procedure has been described by Wong and Hsieh (1983).

Prior to the measurement of the convective coefficient, the diffusion characteristic of the paint surface, the mirror reflectivity, and the cylinder thermal conductivity were determined experimentally. In these efforts, the cylinder was suspended in a vertical position so that its temperature became invariant over its circumference. The cylinder was scanned in a radial direction as described by Farid (1991).

Results and Discussion

The cylinder has a centerline-average roughness of 3.43 μm measured with a Brush surface analyzer. Two tests were made, and the mean temperatures of the surfaces were 330 K and 352 K. Local temperatures were collected and plotted in dimensionless form in Fig. 2. Here the temperature spread falls within a narrow band of 1.5 percent, except those at the top of the cylinder, where the spread appears to be larger. The curve fit with a fourth-degree even-function polynomial, which is necessary for comparison with Koh and Price's analysis for smooth cylinders, does not differ markedly from a tenth-degree fit, although the latter appears to be better statistically (Farid, 1991). The trends of the temperature curves give a clear indication of the poor convection at the top of the cylinder where the flow separates in a rising plume, a phenomenon related to the separation caused by interaction. Also for this reason the scatter of data at the top of the cylinder is large to the extent that they fail to show a zero temperature gradient as θ approaches 180 deg, the plane of symmetry.

Figure 3 compares the convection between a cylinder with

Downloaded 13 Dec 2010 to 193.140.21.150. Redistribution subject to ASME license or copyright; see http://www.asme.org/terms/Terms_Use.cfm

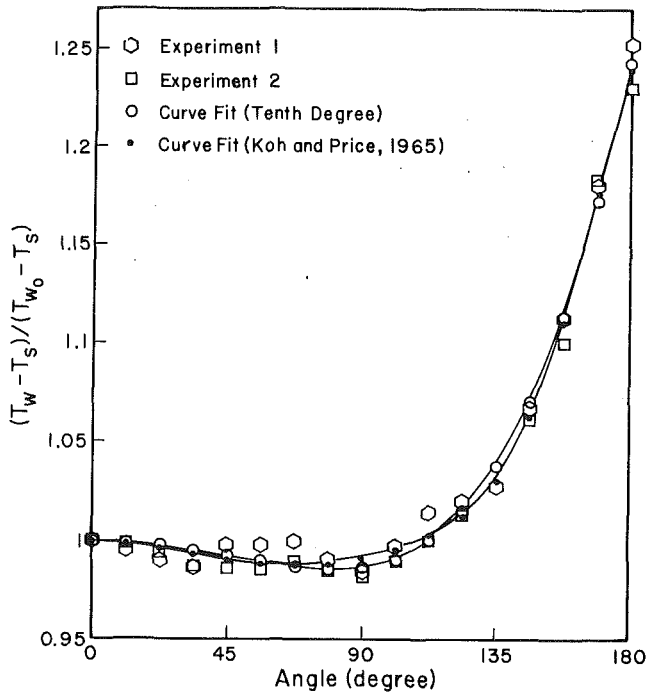

Fig. 2 Temperature distribution plots

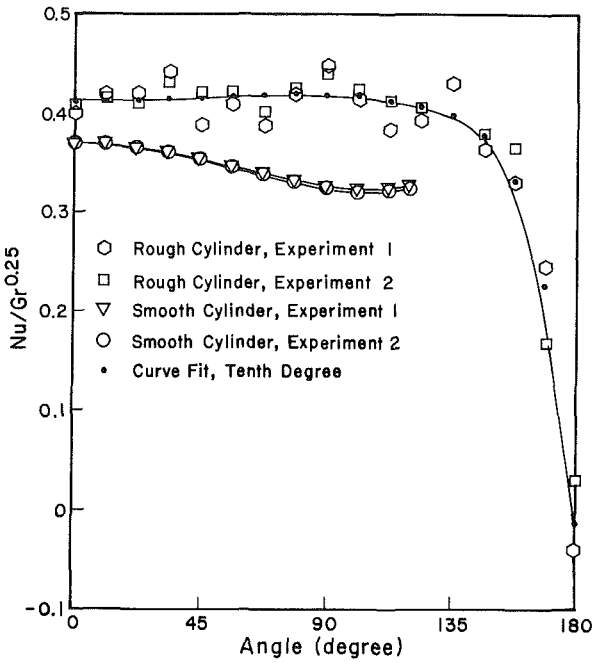

Fig. 3 $Nu/Gr^{0.25}$ curves

rough surface and a cylinder with smooth surface. The fourth-degree fit shown in Fig. 2 was used to generate the lower curves using Eq. (2). They are plotted up to 120 deg, the upper limit at which the boundary layer theory is valid in the analysis. Clearly, the convective coefficient, expressed in terms of the Nusselt number over the Grashof number to one-fourth power, is higher for the rough surface. Also the roughness tends to smooth out the effect due to temperature variation over the range of the angles where the comparison is possible.

The Grashof number tested ranges from 4.5×10^4 to 5.7×10^4. The experimental results for the rough cylinder given in Fig. 3 were fitted with the following equation:

$$\frac{\mathrm{Nu}}{\mathrm{Gr}^{0.25}} = 0.411289 + 0.003579\theta^2 + 0.001929\theta^4 - 0.001615\theta^6 + 0.000316\theta^8 - 2.236\times 10^{-5}\theta^{10} \quad (8)$$

Numerical integration yields a mean $Nu/Gr^{0.25}$ value of 0.382. In this study, all properties were evaluated on the basis of the mean wall temperature. The uncertainty for this study was evaluated by using the method proposed by Kline and McClintock (1953) for single-sample experiments. The uncertainty for the Nusselt number is

$$w_{\mathrm{Nu}} = \left[\left(\frac{\partial \mathrm{Nu}}{\partial T_w} w_{T_w} \right)^2 + \left(\frac{\partial \mathrm{Nu}}{\partial q_w} w_{q_w} \right)^2 \right]^{1/2} \quad (9)$$

where

$$\mathrm{Nu} = \frac{q_w - q_r}{T_w - T_s} \frac{R}{k} \quad (10)$$

and

$$q_r = \epsilon\sigma(T_w^4 - T_s^4)C \quad (11)$$

As for the present study, because of the careful calibration of temperature, the uncertainty of T_w is small estimated to be less than 1 percent, whereas for q_w, based on the uncertainty of the numerical solution, it is 1 percent. Using the maximum temperature spread at 112.5 deg in Fig. 2 (1.5 percent) and the numerical uncertainty (1 percent) in Eq. (9) yields an uncertainty for the Nusselt number that is better than 4 percent. It is noted that the spread of data for $Nu/Gr^{0.25}$ in Fig. 3 is larger than that for the temperature plot in Fig. 2. This can be ascribed to the appearance of $(T_w - T_s)$ in the Grashof number that appears in the denominator. Thus an upward spread of temperature in Fig. 2 leads to a downward spread of $Nu/Gr^{0.25}$ in Fig. 3 and vice versa, a trend that is not unexpected.

Concluding Remarks

There has been a notion in some quarters that the enhancement of convection due to surface roughness may be a result of surface emissivity. Such speculation is unfounded. In fact, a higher emissivity tends to increase the radiative heat loss, thus reducing the convection if the flux in the wall remains unchanged. For the present study, the temperature is quantified by calibrating the paint surface. The nonintrusive nature of the infrared scanning is particularly attractive in the present study.

References

Chiang, T., and Kaye, J., 1962, "On Laminar Free Convection From a Horizontal Cylinder," *Proceedings of the Fourth U.S. National Congress of Applied Mechanics*, Berkeley, CA, pp. 1213–1219.

Farid, M. S., 1991, "Infrared Scanning in Conjunction With Boundary Element Method to Determine Convective Heat Transfer Coefficients," Ph.D. Dissertation, University of Florida, Gainesville, FL.

Hsieh, C. K., Choi, C.-Y., and Liu, K. M., 1989, "A Domain-Extension Method for Quantitative Detection of Cavities by Infrared Scanning," *Journal of Nondestructive Evaluation*, Vol. 8, No. 3, pp. 195–211.

Kline, S. J., and McClintock, F. A., 1953, "Describing Uncertainties in Single-Sample Experiments," *Mechanical Engineering*, Vol. 75, pp. 3–9.

Koh, J. C. Y., and Price, J. F., 1965, "Laminar Free Convection From a Nonisothermal Cylinder," ASME JOURNAL OF HEAT TRANSFER, Vol. 87, pp. 237–242.

Lin, F. N., and Chern, S. Y., 1981, "Laminar Free Convection Boundary Layer Heat Transfer Over Non-isothermal Surface," ASME JOURNAL OF HEAT TRANSFER, Vol. 103, pp. 819–821.

Morgan, V. T., 1973, "The Heat Transfer From Bare Stranded Conductors by Natural and Forced Convection in Air," *International Journal of Heat and Mass Transfer*, Vol. 16, pp. 2023–2034.

Wong, E. T., and Hsieh, C. K., 1983, "Use of Infrared Scanners to Make Accurate Temperature and Position Measurements," ASME Paper No. 83-HT-85.

Downloaded 13 Dec 2010 to 193.140.21.150. Redistribution subject to ASME license or copyright; see http://www.asme.org/terms/Terms_Use.cfm

Measurements of Laminar Mixed Convection Adjacent to a Vertical Plate—Uniform Wall Heat Flux Case

H. I. Abu-Mulaweh,[1,3] B. F. Armaly,[2,3] and T. S. Chen[2,3]

Introduction

Buoyancy force can influence significantly the process of convective cooling of electronic components, heat exchangers, and fuel rods in nuclear reactors. This has motivated a large number of investigators to study the influence of the buoyancy force on forced convective flow and heat transfer, i.e., mixed convection. Reviews on the subject have been published by Chen and Armaly (1987) for external flows and by Aung (1987) for internal flows. It is clear from these reviews that additional measurements are needed to validate numerical models.

Mixed convection flow and heat transfer measurements have been reported by Ramachandran et al. (1985, 1987) and by Moharreri et al. (1988) for vertical, inclined, and horizontal plates with uniform wall temperature. Measured temperature and velocity distributions compared favorably with predictions when the local nonsimilarity solution method was used for solving the governing equations. The lack of similar measurements for mixed convection adjacent to surfaces with uniform wall heat flux has motivated the present study.

Apparatus and Procedure

The experimental study was carried out in an existing low-turbulence, open-circuit air tunnel that was oriented vertically with air flowing in the upward direction. Details of the air tunnel have been described by Ramachandran et al. (1985). The free-stream velocity in the tunnel could be varied between 0.3 and 3.0 m/s, with a free-stream turbulence intensity of less than 1 percent. The uniform heat flux surface was formed by using a single sheet (0.06 mm thick) of stainless steel foil (29.85 cm wide and 73.66 cm long) glued smoothly to a plexiglass plate (1.27 cm thick) using double-sided tape (0.05 mm thick). To minimize the heat loss by conduction from the back surface of the foil, insulation was added to the back of the plexiglass plate. This insulation consisted of two layers, balsa wood (1.27 cm thick) and styrofoam (5.08 cm thick). The surface temperature of the foil was measured with 30 copper-constantan thermocouples attached to the back side of the heated foil and distributed along the axial direction.

Electrical energy was added to the foil (test surface) by a d-c power supply, 8 V–100 A, which was connected to copper busbars that were firmly connected to both front and back ends of the foil. This arrangement provided a heated surface with a uniform heat flux. The input energy was determined by measuring the current and the voltage drop across the foil. The uncertainty associated with the energy input as determined from these measurements was less than 2 percent. Heat losses due to radiation from the heated foil and conduction from the back side through the insulation were determined through calibration. Air velocity measurements at any desired location were made by a backward scattering, laser-Doppler velocimeter (LDV), along with a three-dimensional traversing system. Glycerin smoke particles, resulting from the immersion of a 100 W heating element into a glycerin container, were mixed with the inlet air to provide the scattering particles for the LDV measurements and for the flow visualizations. Air temperature measurements were made by a cold-wire constant-current anemometer with boundary layer wire probe and a traversing system. Details of the measuring systems and their levels of accuracy have been described by Ramachandran et al. (1985) and by Moharreri et al. (1988). The temperature measuring probe was calibrated frequently to insure accurate measurements. The repeatability of making these measurements was within 1 percent.

Velocity and temperature profiles were measured simultaneously by adjusting the cold-wire probe to be about 2 mm behind the measuring volume of the LDV system. Rapid data acquisition and data reduction for measurements of both temperature and velocity were performed through a 12-bit analog to digital convertor and software on an IBM-AT personal computer. Measurements of the streamwise velocity component across the width of the tunnel, at various heights above the plate, displayed a wide two-dimensional flow region in the center of the tunnel's width (about 80 percent of the tunnel's width). All the reported velocity and temperature measurements were taken along the midplane of the plate's width, and only after the system had reached steady-state conditions. All fluid properties were evaluated at a film temperature $T_f = (T_w + T_\infty)/2$, where T_w is the local wall temperature.

Results and Discussion

A critical part of this experimental study is the proper calibration of the heated plate to account for the heat loss by conduction from the back side of the heated plate, and for the heat loss by radiation from the front face of the heated plate. This was accomplished by operating the vertical heated plate in the air tunnel without operating the suction fan that is located at the exit section of the tunnel, i.e., simulating the natural convection regime. The plate was heated to any desired level by controlling the energy input from the d-c power supply and waiting for 5–6 hours for steady state to be reached. For each steady-state level of heating, the energy input to the plate, the wall temperature distribution, and the free-stream temperature were recorded.

The conduction loss from the back side of the plate was determined by measuring the temperature drop across a known thickness of a balsa wood layer (heat flux meter) that was placed in the insulation structure. The measurements from several steady-state levels of plate heating indicate that the heat loss by conduction from the back side of the insulated plate can be approximated with reasonable accuracy as 11 percent of the total energy added to the plate. Radiation loss from the front side of the plate was estimated by assuming the heated surface to be gray with an emissivity of ϵ and by using the measured surface temperatures at the various axial locations, along with the measured free-stream air temperature. The measured free-stream temperature was constant along the length of the heated plate. The magnitude of the surface emissivity was determined by forcing the predicted wall temperature distribution to compare favorably with the measured wall temperatures for all the heating levels that were conducted in this calibration process. The comparison between the measured and predicted wall temperatures yielded an average emissivity value of $\epsilon = 0.055$. The difference between the measured and predicted temperature difference (wall temperature minus free stream temperature) under natural convection conditions using the above reported surface emissivity was less than 5 percent. The heat loss by radiation was calculated locally using the local wall temperature and the average emissivity, and for the cases examined could be approximated as being 10 percent of the total energy added to the heated plate. The small difference in the local radiative losses had very small effect on the uniformity of the wall heat flux. The convective flux for any heating level could then be easily determined for any steady-state condition by subtracting the conduction and the radiation heat losses, determined by the above methods, from the total

[1]Graduate student.
[2]Fellow ASME.
[3]Department of Mechanical and Aerospace Engineering and Engineering Mechanics, University of Missouri—Rolla, Rolla, MO 65401.

Contributed by the Heat Transfer Division of The American Society of Mechanical Engineers. Manuscript received by the Heat Transfer Division September 1991; revision received February 1992. Keywords: Measurement Techniques, Mixed Convection. Associate Technical Editor: F. P. Incropera.

Copyright © 1992 by ASME
Downloaded 13 Dec 2010 to 193.140.21.150. Redistribution subject to ASME license or copyright; see http://www.asme.org/terms/Terms_Use.cfm

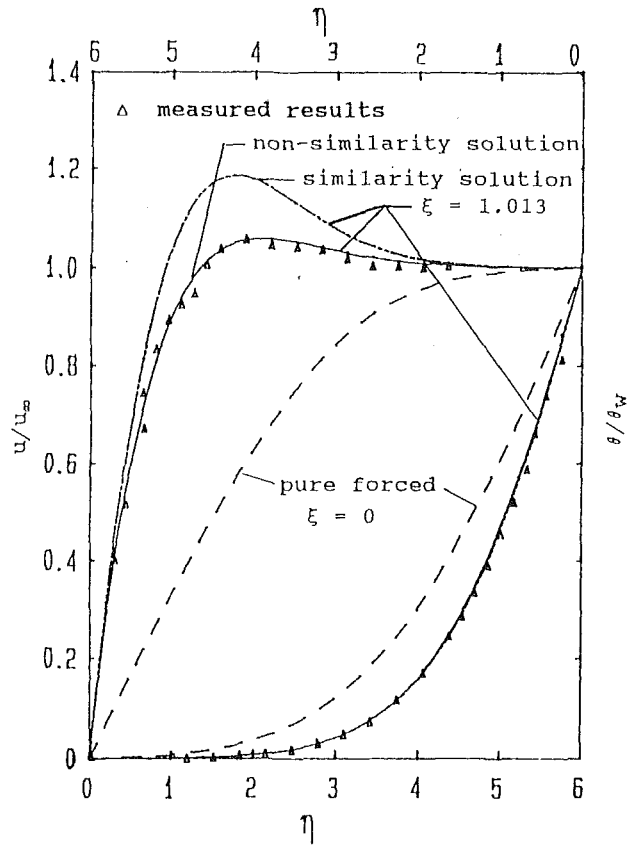

Fig. 1 Measured and predicted velocity and temperature distributions

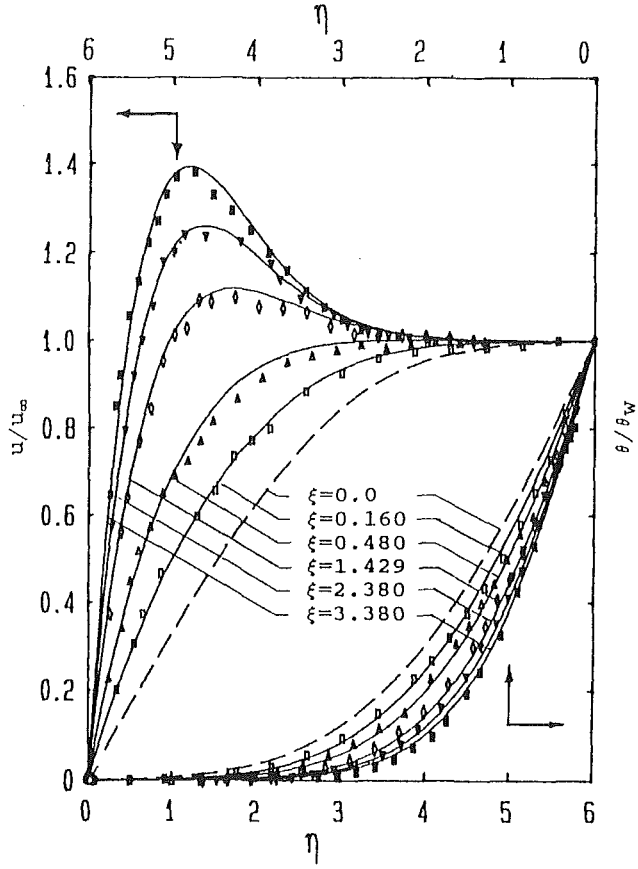

Fig. 2 Measured and predicted velocity and temperature distributions

energy input to the heated plate. This method was used to determine the convective component of the heat transfer from the heated plate in the mixed convection regime. The uncertainty associated with determining this convection component was 3 percent.

The predicted wall temperature for natural convection adjacent to a vertical surface with uniform heat flux was taken from Holman (1981), as:

$$T_w - T_\infty = q_w x/[0.60k(\mathrm{Gr}_x^* \mathrm{Pr})^{0.2}] \quad (1)$$

where T_w is the wall temperature, T_∞ is the free-stream temperature, q_w is the local surface heat flux, x is the axial location measured from the leading edge of the plate, Gr_x^* is the modified Grashof number ($g\beta q_w x^4/k\nu^2$), Pr is the Prandtl number, g is the gravitational acceleration, k is the thermal conductivity, β is the coefficient of thermal expansion, and ν is the kinematic viscosity.

The air tunnel was then operated to allow air to flow through the tunnel and adjacent to the unheated test surface. Flow visualizations were made to insure two-dimensional flow, and that a proper boundary layer develop over the unheated plate. Velocity distributions were measured at different locations and these measurements compared very favorably with the Blasius solution, i.e., deviations of less than 2 percent, thus validating the tunnel and its instrumentations. The test surface was then heated to an appropriate steady-state level to create a mixed convection regime. Input energy was measured and corrected for conduction and radiation heat losses, and other measurements such as wall temperatures, along with velocity and temperature distributions at different axial locations, were recorded for various steady-state heating levels. The reported measurements of velocity and temperature distributions were taken at an axial location greater than 5 cm from the leading edge. This was done to avoid the area where possible nonuniformity of wall heat flux could exist due to leading edge and axial heat conduction effects, and also to increase the buoyancy force to a level where mixed convection becomes important.

Predicted velocity and temperature distributions using the local similarity solution scheme as presented by Wilks (1973), and the local nonsimilarity solution scheme as presented by Armaly et al. (1987), were compared with measured data in Fig. 1 for buoyancy parameter of $\xi = 1.013$ (where $\xi = \mathrm{Gr}_x^*/\mathrm{Re}_x^{5/2}$, with $\mathrm{Re}_x = u_\infty x/\nu$ denoting the local Reynolds number, and u_∞ the free-stream velocity). The results are presented as u/u_∞ (where u is the local streamwise velocity) and as $\theta/\theta_w = (T - T_\infty)/(T_w - T_\infty)$ (where T is the local temperature) versus the dimensionless parameter $\eta = y[u_\infty/(\nu x)]^{1/2}$ (where y is the distance normal to the heated plate). The uncertainty in η is ± 0.04, in u/u_∞ it is ± 0.02, and in θ/θ_w it is ± 0.025. It is clear from the figure that local similarity results for the velocity distribution deviate significantly from the results predicted by the local nonsimilarity scheme, and the latter agrees favorably with measured results. Figure 1 also shows that the temperature distributions resulting from the similarity and the local nonsimilarity schemes compare favorably with measured data, reflecting the fact that the velocity is affected more by the buoyancy force than the temperature. Other measured velocity and temperature distributions are presented in Fig. 2, and they compare favorably with predicted local non-similarity results. The measured wall temperature also compares favorably (less than 4 percent deviation) with predicted values. The predicted results for the wall temperature under mixed convection conditions were generated from the correlation given by Armaly et al. (1987) for the Nusselt number for this geometry and boundary condition as:

$$\mathrm{Nu}_x \mathrm{Re}_x^{-1/2} = G_1(\mathrm{Pr})\{1 + [G_2(\mathrm{Pr})\xi^{0.2}/G_1(\mathrm{Pr})]^3\}^{1/3} \quad (2)$$

where:

Downloaded 13 Dec 2010 to 193.140.21.150. Redistribution subject to ASME license or copyright; see http://www.asme.org/terms/Terms_Use.cfm

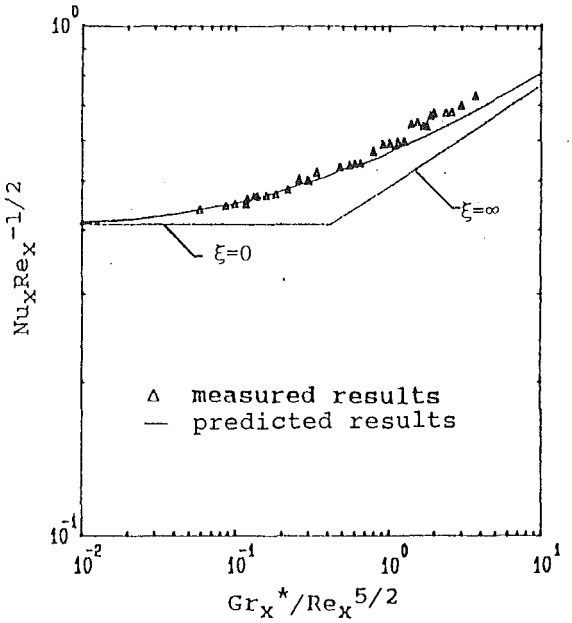

Fig. 3 Measured and predicted local Nusselt numbers

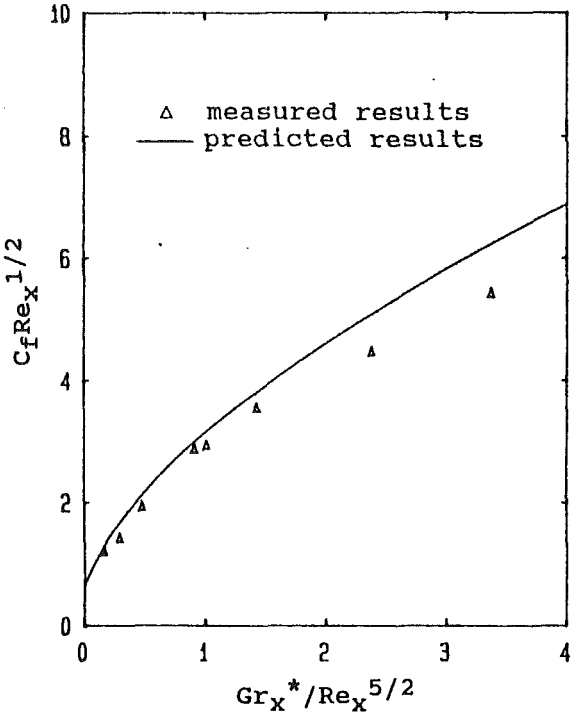

Fig. 4 Measured and predicted local friction coefficient

$$G_1(\mathrm{Pr}) = 0.464\mathrm{Pr}^{1/3}[1 + (0.0207/\mathrm{Pr})^{2/3}]^{-1/4} \quad (3a)$$

$$G_2(\mathrm{Pr}) = \mathrm{Pr}^{2/5}(4 + 9\mathrm{Pr}^{1/2} + 10\mathrm{Pr})^{-1/5} \quad (3b)$$

Thus

$$T_w - T_\infty = q_w x/[k(\mathrm{Re}_x^{1/2})G_1(\mathrm{Pr})\{1 + [G_2(\mathrm{Pr})\xi^{0.2}/G_1(\mathrm{Pr})]^3\}^{1/3}] \quad (4)$$

The measured wall temperature distribution and the deduced convective wall heat flux were utilized to calculate the local Nusselt number as defined by:

$$\mathrm{Nu}_x = q_w x/[k(T_w - T_\infty)] \quad (5)$$

Figure 3 illustrates the variation of the predicted and deduced local Nusselt number as a function of the buoyancy parameter. The uncertainty associated with deducing the Nusselt number is 5 percent and with ξ it is 6 percent. As expected, the mixed convection Nusselt number increases as the buoyancy parameter increases in this buoyancy-assisting flow. In addition, it is seen that measurements compare favorably with prediction (less than 6 percent deviations). The pure forced convection limit, $\xi = 0$, and the pure free convection limit, $\xi = \infty$, are also presented in the figure for comparison.

The measured velocity gradient at the wall was used to calculate the wall shear stress and the friction coefficient from the following relation:

$$C_f = \mu(\partial u/\partial y)_{y=0}/(\rho u_\infty^2/2) \quad (6)$$

The comparison of these results with predicted values in the form $C_f \mathrm{Re}_x^{1/2}$ (where μ is the dynamic viscosity and ρ is the density) indicates good agreement when the buoyancy force is small, but this agreement deteriorates as the buoyancy force increases, as shown in Fig. 4. The strong sensitivity of those results on the velocity gradient, and our inability to deduce accurately that quantity when the velocity profile near the wall becomes steep (i.e., for high buoyancy force), is the cause for the deterioration of the deduced results. The uncertainty associated with deducing the friction coefficient was estimated to be 8 percent.

Conclusion

Measured temperature and velocity distributions for mixed convection flow adjacent to a vertical heated plate with uniform wall heat flux compare very favorably with predictions that resulted from using the local nonsimilarity method for solving the governing equations. The local similarity method of solution resulted in a less favorable comparison. The Nusselt number and the friction coefficient that were deduced from measured data also compare favorably with predicted results. The trend of the results are the same as the ones observed for the uniform wall temperature case.

Acknowledgments

The present study was supported by the National Science Foundation under grant No. NSF CTS-8923010.

References

Armaly, B. F., Chen, T. S., and Ramachandran, N., 1987, "Correlations for Laminar Mixed Convection on Vertical, Inclined and Horizontal Flat Plates With Uniform Heat Flux," *International Journal of Heat and Mass Transfer*, Vol. 30, No. 2, pp. 405-408.

Aung, W., 1987, "Mixed Convection in Internal Flow," in: *Handbook of Single-Phase Convective Heat Transfer*, S. Kakac, R. K. Shah, and W. Aung, eds., Wiley, Chap. 15, pp. 1-51.

Chen, T. S., and Armaly, B. F., 1987, "Mixed Convection in External Flow," in: *Handbook of Single-Phase Convective Heat Transfer*, S. Kakac, R. K. Shah, and W. Aung, eds., Wiley, Chap. 14, pp. 1-35.

Holman, J. P., 1981, *Heat Transfer*, 5th ed., McGraw-Hill, New York, pp. 275-276.

Moharreri, S. S., Armaly, B. F., and Chen, T. S., 1988, "Measurements in the Transition Vortex Flow Regime of Mixed Convection Above a Horizontal Heated Plate," ASME JOURNAL OF HEAT TRANSFER, Vol. 110, pp. 358-365.

Ramachandran, N., Armaly, B. F., and Chen, T. S., 1985, "Measurements and Predictions of Laminar Mixed Convection Flows Adjacent to a Vertical Surface," ASME JOURNAL OF HEAT TRANSFER, Vol. 107, pp. 636-641.

Ramachandran, N., Armaly, B. F., and Chen, T. S., 1987, "Measurements of Laminar Mixed Convection Flow Adjacent to an Inclined Surface," ASME JOURNAL OF HEAT TRANSFER, Vol. 109, pp. 146-150.

Wilks, G., 1973, "Combined Forced and Free Convection Flow on Vertical Surfaces," *International Journal of Heat and Mass Transfer*, Vol. 16, pp. 1958-1964.

Downloaded 13 Dec 2010 to 193.140.21.150. Redistribution subject to ASME license or copyright; see http://www.asme.org/terms/Terms_Use.cfm

Identification of the Temperature Profile in an Absorbing, Emitting, and Isotropically Scattering Medium by Inverse Analysis

H. Y. Li[1] and M. N. Özişik[1]

Introduction

Radiative heat transfer is important in high-temperature devices such as combustion chambers and furnaces. A detailed review of radiative heat transfer in combustion systems has been given by Viskanta and Menguc (1987). In direct radiation problems, the equation of radiative transfer, the source term, the properties of the medium, and the boundary conditions are given, and the radiation intensity is to be determined. On the other hand, in inverse radiation problems, either the radiative properties, or the source term, or the boundary conditions are to be determined from the knowledge of the measured radiation data. Inverse radiation problems arise in a variety of applications, including among others, the remote sensing of atmosphere properties, the prediction of the temperature profile in a furnace or atmosphere. A considerable amount of work has been reported for determining the single scattering albedo, the phase function, or the optical thickness of a medium from various types of radiation measurements (Siewert, 1978; Ho and Özisik, 1989; Subramanian and Menguc, 1991).

In this work we use the conjugate gradient method of minimization to solve an inverse radiation problem for determining the temperature distribution in an absorbing, emitting, and isotropically scattering medium from the simulated exit radiation intensities.

Analysis

In the solution of the inverse radiation problem with finite-dimensional conjugate gradient method of minimization considered here, the analysis consists of the following basic steps: (1) the direct problem, (2) the sensitivity problem, and (3) the gradient equation. We describe below the procedure for each of these steps and then present an algorithm for the solution of the inverse problem.

(1) Direct Problem. We consider an absorbing, emitting, isotropically scattering, gray plane-parallel medium of optical thickness τ_o, and azimuthally symmetric radiation. The bounding surfaces at $\tau=0$, $\tau=\tau_o$ are transparent and there is no externally incident radiation. The equation of radiative transfer can be written as (Özişik, 1973)

$$\mu\frac{\partial I(\tau,\mu)}{\partial\tau}+I(\tau,\mu)=S(\tau)+\frac{\omega}{2}\int_{-1}^{1}I(\tau,\mu')d\mu' \qquad 0<\tau<\tau_o,\quad -1<\mu<1 \tag{1a}$$

$$S(\tau)=(1-\omega)\frac{\bar{n}^2\bar{\sigma}T^4(\tau)}{\pi} \tag{1b}$$

with boundary conditions

$$I(0,\mu)=0,\quad \mu>0 \tag{1c}$$

$$I(\tau_o,-\mu)=0,\quad \mu>0 \tag{1d}$$

where $I(\tau,\mu)$ is the radiation intensity, $T(\tau)$ is the temperature, $\bar{n}$ is the refractive index, $\bar{\sigma}$ is the Stefan-Boltzmann constant, ω is the single scattering albedo, τ is the optical variable, μ is the cosine of the angle between the direction of the radiation intensity and the positive τ axis. The source term involving the fourth power of the temperature is represented by a polynomial in the optical variable τ as

$$S(\tau)=\sum_{n=0}^{N}a_n\tau^n \tag{2}$$

When the source term $S(\tau)$, optical thickness τ_o, and single scattering albedo ω are all specified, the problem defined by Eqs. (1) becomes a direct problem for the determination of the radiation intensity. The problem becomes an inverse problem, if the source term $S(\tau)$ is unknown and to be estimated from the knowledge of the measured exit radiation intensities. We first present below the method of solution of the direct problem before describing the inverse analysis.

Using the P_N approximation, the solution of the direct problem given by Eqs. (1) for the radiation intensity $I(\tau,\mu)$ is expressed in the form (Benassi et al., 1983)

$$I(\tau,\mu)=\sum_{n=0}^{N}\frac{2n+1}{2}P_n(\mu)\sum_{j=1}^{J^*}[A_je^{-\tau/\xi_j}+(-1)^nB_je^{-(\tau_0-\tau)/\xi_j}]g_n(\xi_j)+I_p(\tau,\mu) \tag{3}$$

where $J^*=(N+1)/2$, N is an odd integer, P_n are the Legendre polynomials, and $I_p(\tau,\mu)$ denotes a particular solution of Eq. (1a) corresponding to the inhomogeneous source term $S(\tau)$. Here, $g_n(\xi)$ are the Chandrasekhar polynomials determined from the recurrence formula

$$(n+1)g_{n+1}(\xi)=h_n\xi g_n(\xi)-ng_{n-1}(\xi) \tag{4a}$$

for $n=1, 2, \ldots, N$, with $g_0(\xi)=1$ and $h_n=2n+1-\omega\delta_{0n}$, where δ_{0n} is the Kronecker delta. The eigenvalues ξ_j, $j=1, 2, \ldots, J^*$, are the J^* positive zeros of $g_{N+1}(\xi)$. However, by using the alternative expression given by

$$\frac{n(n-1)}{h_nh_{n-1}}g_{n-2}(\xi)+\frac{1}{h_n}\left[\frac{(n+1)^2}{h_{n+1}}+\frac{n^2}{h_{n-1}}\right]g_n(\xi)+\frac{(n+2)(n+1)}{h_{n+1}h_n}g_{n+2}(\xi)=\xi^2g_n(\xi) \tag{4b}$$

the squares of the J^* positive zeros of $g_{N+1}(\xi)$ are the J^* eigenvalues ξ^2 of the $J^*\times J^*$ tridiagonal matrix obtained from Eq. (4b), for $n=0, 2, \ldots, N-1$.

The particular solution of Eq. (1a) is (Siewert and Thomas, 1990)

$$I_p(\tau,\mu)=\sum_{n=0}^{N}\frac{2n+1}{2}P_n(\mu)\sum_{j=1}^{J^*}\frac{c_j}{\xi_j}\left[\int_0^{\tau}S(\tau')e^{-(\tau-\tau')/\xi_j}d\tau'+(-1)^n\int_{\tau}^{\tau_o}S(\tau')e^{-(\tau'-\tau)/\xi_j}d\tau'\right]g_n(\xi_j) \tag{5a}$$

where

$$c_j=\left[\sum_{n=1}^{J^*}g_{2n-2}^2(\xi_j)h_{2n-2}\right]^{-1} \tag{5b}$$

The constants A_j and B_j are determined by constraining the solution given by Eq. (3) to satisfy the Marshak boundary conditions for the problem to yield

$$\sum_{n=0}^{N}\frac{2n+1}{2}S_{\alpha,n}\sum_{j=0}^{J^*}[A_j+(-1)^nB_je^{-\tau_o/\xi_j}]g_n(\xi_j)=-\sum_{n=0}^{N}\frac{2n+1}{2}S_{\alpha,n}\sum_{j=1}^{J^*}\frac{c_j}{\xi_j}(-1)^ng_n(\xi_j)\int_0^{\tau_o}S(\tau')e^{-\tau'/\xi_j}d\tau' \tag{6a}$$

and

[1]Mechanical and Aerospace Engineering Department, North Carolina State University, Raleigh, NC 27695.

Contributed by the Heat Transfer Division of The American Society of Mechanical Engineers. Manuscript received by the Heat Transfer Division September 1991; revision received January 1992. Keywords: Radiation.

Copyright © 1992 by ASME
Downloaded 13 Dec 2010 to 193.140.21.150. Redistribution subject to ASME license or copyright; see http://www.asme.org/terms/Terms_Use.cfm

$$\sum_{n=0}^{N}\frac{2n+1}{2}S_{\alpha,n}\sum_{j=1}^{J^*}[(-1)^n A_j e^{-\tau_o/\xi_j} + B_j]g_n(\xi_j) = -\sum_{n=0}^{N}\frac{2n+1}{2}S_{\alpha,n} \sum_{j=1}^{J^*}\frac{c_j}{\xi_j}(-1)^n g_n(\xi_j)\int_0^{\tau_o} S(\tau')e^{-(\tau_o-\tau')/\xi_j}d\tau' \quad (6b)$$

for $\alpha = 0, 1, \ldots, (N-1)/2$, where

$$S_{\alpha,n} = \int_0^1 P_{2\alpha+1}(\mu)P_n(\mu)d\mu \quad (6c)$$

Once A_j and B_j are available, the radiation intensity can be calculation from Eq. (3). However, an improved expression for the intensity can be obtained by introducing Eq. (3) into the right-hand side of Eq. (1*a*) and solving the resulting expression for $I(\tau, \mu)$ as described by Benassi et al. (1983). Using the latter approach, the boundary intensities $I(0, -\mu)$ and $I(\tau_o, \mu)$ are determined from

$$I(0, -\mu) = \sum_{n=0}^{N}(-1)^n\frac{2n+1}{2}P_n(-\mu)\sum_{j=1}^{J^*}\frac{c_j}{\xi_j}g_n(\xi_j)\int_0^{\tau_o}S(\tau')e^{-\tau'/\xi_j}d\tau' - e^{-\tau_o/\mu}\sum_{n=0}^{N}\frac{2n+1}{2}P_n(-\mu)\sum_{j=1}^{J^*}\frac{c_j}{\xi_j}g_n(\xi_j) \times\int_0^{\tau_o}S(\tau')e^{-(\tau_o-\tau')/\xi_j}d\tau' + \frac{\omega}{2}\sum_{j=1}^{J^*}\xi_j\left[A_j\frac{1-e^{-\tau_o/\mu}e^{-\tau_o/\xi_j}}{\mu+\xi_j} + B_j\frac{e^{-\tau_o/\mu}-e^{-\tau_o/\xi_j}}{\mu-\xi_j}\right] \quad \mu>0 \quad (7a)$$

and

$$I(\tau_o, \mu) = \sum_{n=0}^{N}\frac{2n+1}{2}P_n(\mu)\sum_{j=1}^{J^*}\frac{c_j}{\xi_j}g_n(\xi_j)\int_0^{\tau_o}S(\tau')e^{-(\tau_o-\tau')/\xi_j}d\tau' - e^{-\tau_o/\mu}\sum_{n=0}^{N}\frac{2n+1}{2}(-1)^n P_n(\mu) \sum_{j=1}^{J^*}\frac{c_j}{\xi_j}g_n(\xi_j)\int_0^{\tau_o}S(\tau')e^{-\tau'/\xi_j}d\tau' + \frac{\omega}{2}\sum_{j=1}^{J^*}\xi_j\left[A_j\frac{e^{-\tau_o/\mu}-e^{-\tau_o/\xi_j}}{\mu-\xi_j} + B_j\frac{1-e^{-\tau_o/\mu}e^{-\tau_o/\xi_j}}{\mu+\xi_j}\right] \quad \mu>0 \quad (7b)$$

Before proceeding to the conjugate gradient method of minimization, we present below the development of the sensitivity problem and the gradient equation, which are needed in the inverse analysis.

(2) Sensitivity Problem. The problem defined by Eqs. (1) with the source term or the temperature unknown but measured exit intensities known is an inverse problem, which can be solved by minimizing the objective function, $J(\underline{q})$,

$$J(\underline{q}) = \int_{-1}^{0}[I(0, \mu; \underline{q}) - Y(\mu)]^2 d\mu + \int_0^1[I(\tau_o, \mu; \underline{q}) - Z(\mu)]^2 d\mu \quad (8)$$

where $Y(\mu)$ and $Z(\mu)$ are the measured exit radiation intensities at $\tau = 0$ and $\tau = \tau_o$, respectively; $I(0, \mu; \underline{q})$ and $I(\tau_o, \mu; \underline{q})$ are estimated exit radiation intensities at $\tau = 0$ and $\tau = \tau_o$, respectively, by using the estimated $\underline{q} = [a_0, a_1, \ldots, a_N]^T$. Thus the inverse radiation problem is reduced to an optimization problem in $(N+1)$-dimensional space.

The objective function $J(\underline{q})$ is minimized by differentiating it with respect to each of the unknown coefficients a_n. Then the resulting expression for $\partial J/\partial a_n$ contains the sensitivity coefficient $\partial I/\partial a_n$, which is determined from the solution of the sensitivity problem obtained by differentiating the direct problem, Eqs. (1), with respect to a_n:

$$\mu\frac{\partial}{\partial\tau}\left(\frac{\partial I(\tau, \mu)}{\partial a_n}\right) + \left(\frac{\partial I(\tau, \mu)}{\partial a_n}\right) = \tau^n + \frac{\omega}{2}\int_{-1}^{1}\left(\frac{\partial I(\tau, \mu')}{\partial a_n}\right)d\mu' \quad 0<\tau<\tau_o, \quad -1<\mu<1 \quad (9a)$$

$$\left(\frac{\partial I(0, \mu)}{\partial a_n}\right) = 0, \quad \mu>0 \quad (9b)$$

$$\left(\frac{\partial I(\tau_o, -\mu)}{\partial a_n}\right) = 0, \quad \mu>0 \quad (9c)$$

for $n = 0, 1, \ldots, N$. Here the row vector,

$$\Delta I = \left[\frac{\partial I}{\partial a_0}, \frac{\partial I}{\partial a_1}, \ldots, \frac{\partial I}{\partial a_N}\right] \quad (9d)$$

is the sensitivity coefficient vector. Since the solution procedure for this problem is the same as that for the direct problem with $S(\tau)$ replaced by τ^n, it will not be repeated here.

(3) The Gradient Equation. An expression for $\partial J/\partial a_n$ is obtained by differentiating J with respect to a_n:

$$\frac{\partial J}{\partial a_n} = \int_{-1}^{0}2[I(0, \mu; \underline{q}) - Y(\mu)]\frac{\partial I(0, \mu; \underline{q})}{\partial a_n}d\mu + \int_0^1 2[I(\tau_o, \mu; \underline{q}) - Z(\mu)]\frac{\partial I(\tau_o, \mu; \underline{q})}{\partial a_n}d\mu \quad (10a)$$

for $n = 0, 1, \ldots, N$, where the row vector

$$\Delta J = \left[\frac{\partial J}{\partial a_0}, \frac{\partial J}{\partial a_1}, \ldots, \frac{\partial J}{\partial a_N}\right] \quad (10b)$$

is the gradient of the objective function. The components $\partial J/\partial a_n$ are computed from Eq. (10*a*), since $\partial I/\partial a_n$, the exit intensities, and the measured data are available.

(4) The Conjugate Gradient Method of Minimization. To determine the unknown vector $\underline{q}$, we consider an iterative procedure (Alifanov, 1974; Huang and Özişik, 1992), and write

$$\underline{q}^{k+1} = \underline{q}^k - \beta^k\underline{d}^k \quad (11)$$

where β^k is the *step size* and $\underline{d}^k$ is the *direction of descent* at the kth iteration. Here, $\underline{d}_k$ is determined from

$$\underline{d}^k = \Delta J^T(\underline{q}^k) + \gamma^k\underline{d}^{k-1} \quad (12)$$

where the *conjugate coefficient* γ^k is computed from

$$\gamma^k = \frac{\Delta J(\underline{q}^k)\Delta J^T(\underline{q}^k)}{\Delta J(\underline{q}^{k-1})\Delta J^T(\underline{q}^{k-1})} \quad \text{with} \quad \gamma^0 = 0 \quad (13)$$

and the step size β^k in going from $\underline{q}^k$ to $\underline{q}^{k+1}$ is determined from the condition $\min_{\beta} J(\underline{q}^{k+1})$, which leads to the following expression for the determination of β^k:

Downloaded 13 Dec 2010 to 193.140.21.150. Redistribution subject to ASME license or copyright; see http://www.asme.org/terms/Terms_Use.cfm

$$\beta^k = \frac{\int_{-1}^{0} [I(0, \mu; \underline{q}^k) - Y(\mu)]\Delta I(0, \mu; \underline{q}^k)\underline{d}^k d\mu + \int_{0}^{1} [I(\tau_o, \mu; \underline{q}^k) - Z(\mu)]\Delta I(\tau_o, \mu; \underline{q}^k)\underline{d}^k d\mu}{\int_{-1}^{0} [\Delta I(0, \mu; \underline{q}^k)\underline{d}^k]^2 d\mu + \int_{0}^{1} [\Delta I(\tau_o, \mu; \underline{q}^k)\underline{d}^k]^2 d\mu} \quad (14)$$

Once $\underline{d}^k$ is calculated from Eq. (12) and β^k from Eq. (14), the iterative process defined by Eq. (11) can be used to determine $\underline{q}^{k+1}$ to satisfy a specified stopping criterion. If the problem involves no measurement errors, the condition

$$J(\underline{q}^{k+1}) < \delta^* \quad (15)$$

could be used for terminating the iterative process, where δ^* is a small positive number. However, the measure radiation intensities contain measurement errors, so computational experiments suggest the use of the following discrepancy principle for the stopping criteria (Alifanov, 1974):

$$J(\underline{q}^{k+1}) < 2\sigma^2 \quad (16)$$

where σ is the standard deviation of the measurement errors.

(5) Computational Algorithm. The iterative procedure for the conjugate gradient method can be summarized as follows: Assume $\underline{q}^k$ is known at the kth iteration.

1 Solve the sensitivity problem, Eqs. (9), and compute the sensitivity coefficient vector ΔI.

2 Solve the direct problem, Eqs. (1), and compute $I(0, \mu; a^k)$ and $I(\tau_o, \mu; a^k)$.

3 Knowing ΔI, $I(0, \mu; a^k)$ and the measured exit intensities $Y(\mu)$ and $Z(\mu)$, compute the gradient $\Delta J(a^k)$ from Eq. (10*a*).

4 Knowing $\Delta J(a^k)$, compute γ^k from Eq. (13); then compute d^k from Eq. (12).

5 Knowing ΔI, $I(0, \mu; a^k)$, $I(\tau_o, \mu; a^k)$, $Y(\mu)$, $Z(\mu)$, and d^k, compute β^k from Eq. (14).

6 Knowing β^k and d^k, compute a^{k+1} from Eq. (11).

7 Terminate the process if a specified stopping criterion (i.e., Eq. (15) or (16) is satisfied. Otherwise return to 2.

Results and Discussion

We present below some numerical results in order to examine the accuracy of the conjugate gradient method of minimization for estimating the spatial distribution of the unknown source term $S(\tau)$ or temperature $T(\tau)$ from the data of the exit radiation intensities. Three different spatial variations of $S(\tau)$ are considered, i.e., a polynomial of degree four, a polynomial of degree eight, and a sinusoidal variation. For combustion problems encountered in fires and furnaces, the temperatures are in general between 800 K and 1800 K (Grosshandler and Modak, 1981). Hence in the present work, the source terms are selected to lie in such a temperature range, the single scattering albedo is taken in the range 0.2 to 0.35 (Jamaluddin and Smith, 1988) and isotropic scattering is assumed. With these considerations, we have chosen the values of the single scattering albedo, the optical thickness and the refractive index to be 0.3, 1, and 1, respectively. In order to simulate the measured exit intensities, Y and Z, containing measurement errors, random errors of standard deviation σ are added to the exact exit intensities computed from the solution of the direct problem. Thus, we have

$$Y_{\text{measured}} = Y_{\text{exact}} + \sigma\zeta \quad (17a)$$

$$Z_{\text{measured}} = Z_{\text{exact}} + \sigma\zeta \quad (17b)$$

where the range of random variables ζ is chosen as $-2.576 < \zeta < 2.576$, which represents the 99 percent confidence bound for the measured intensities and the values of ζ are calculated by IMSL subroutine DRNNOR.

We examined the effects of the number of measurements on the accuracy of the estimation by using 10, 15, 20 simulated measurement data taken over the polar angle interval $0 \le \theta \le \pi/2$ for the cases with no measurement errors (i.e., $\sigma = 0$) and with measurement errors (i.e., $\sigma = 0.03$, $\sigma = 0.06$). With no measurement errors, no observable difference could be detected between the estimated and the exact values of the source term when the results were presented in graphic form. With measurement errors, the estimation of the source terms given in the forms of fourth and eighth-degree polynomials was not very sensitive to the number of measurements. However, in the case of the estimation of the source term in the sinusoidal form, increasing the number of measurement points from 10 to 20 improved the accuracy of the estimation. We also examined the effects of the optical thickness τ_o of the medium on the accuracy of the estimation for the cases of $\tau_o = 1$, 5, 10 by using 20 simulated measurement data. Estimations were very god for all the cases considered. It appears that the optical thickness of the medium does not affect the accuracy of the inverse analysis. As a result of these observations, we used 20 measurement points over the polar angle interval $0 \le \theta \le \pi/2$ for all the results presented in this work.

In Fig. 1, the source term is a polynomial of degree four in the optical variable

$$S(\tau) = 1 + 20\tau + 44\tau^2 - 128\tau^3 + 64\tau^4 \text{ W/cm}^2 \quad (18)$$

Simulated experimental data containing measurement errors of standard deviation $\sigma = 0.03$ and $\sigma = 0.06$ are used to estimate $S(\tau)$ with inverse analysis. Clearly, the agreement between the exact and the estimated results is excellent. Once the source term is available, the temperature distribution can be determined from the definition given by Eq. (1*b*).

In Fig. 2, the source term is a polynomial of degree eight in the optical variable

$$S(\tau) = 1 + 10\tau - 0.1\tau^2 + \tau^3 + \tau^4 - 10\tau^5 + 0.1\tau^6 + \tau^7 + \tau^8 \text{ W/cm}^2 \quad (19)$$

Simulated experimental data containing measurement errors of standard deviation $\sigma = 0.03$ and $\sigma = 0.06$ are used in the inverse analysis. The agreement between the exact and the estimated results is excellent.

Figure 3 is for a source term of sinusoidal variation given in the form

$$S(\tau) = 5 + 3\sin(2\pi\tau) \quad \text{W/cm}^2 \quad (20)$$

Simulated experimental data containing errors in standard de-

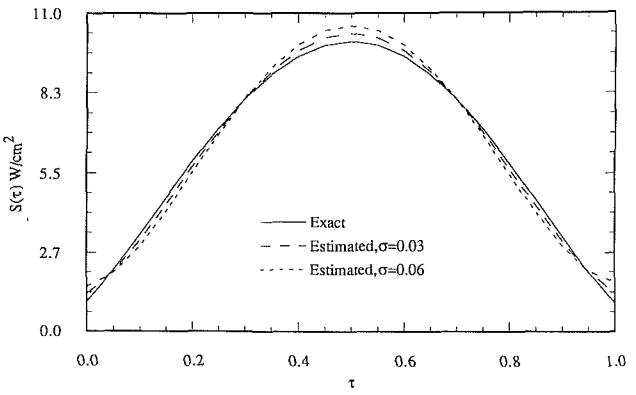

Fig. 1 Estimation of the source term $S(\tau) = 1 + 20\tau + 44\tau^2 - 128\tau^3 + 64\tau^4$ W/cm² with inverse analysis for the case $\omega = 0.3$, $\tau_o = 1$, $\bar{n} = 1$, using simulated measurement data with $\sigma = 0.03$ and $\sigma = 0.06$

Downloaded 13 Dec 2010 to 193.140.21.150. Redistribution subject to ASME license or copyright; see http://www.asme.org/terms/Terms_Use.cfm

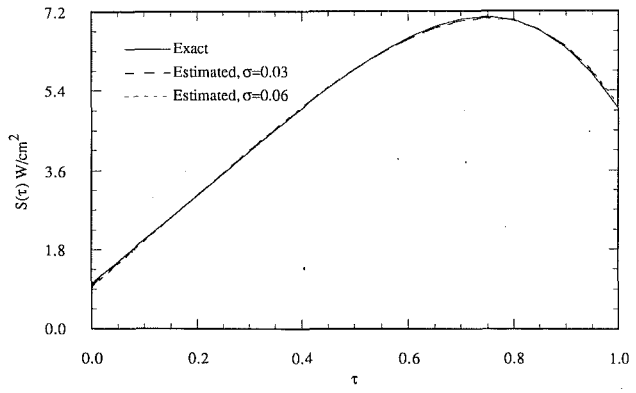

Fig. 2 Estimation of the source term $S(\tau) = 1 + 10\tau - 0.1\tau^2 + \tau^3 + \tau^4 - 10\tau^5 + 0.1\tau^6 + \tau^7 + \tau^8$ W/cm^2 with inverse analysis for the case $\omega = 0.3$, $\tau_o = 1$, $\bar{n} = 1$, using simulated measurement data with $\sigma = 0.03$ and $\sigma = 0.06$

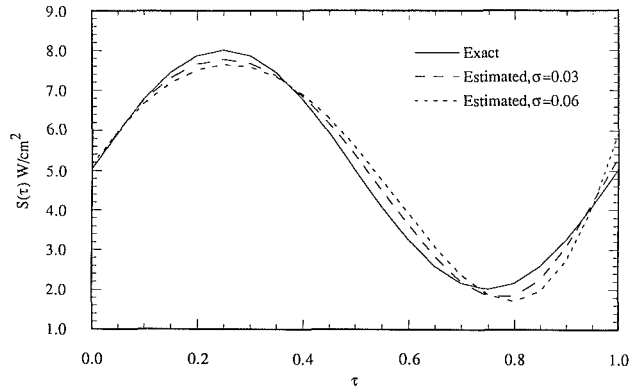

Fig. 3 Estimation of the source term $S(\tau) = 5 + 3 \sin(2\pi\tau)$ W/cm^2 with inverse analysis for the case $\omega = 0.3$, $\tau_o = 1$, $\bar{n} = 1$, using simulated measurement data with $\sigma = 0.03$ and $\sigma = 0.06$

viation $\sigma = 0.03$ and $\sigma = 0.06$ are used in the inverse analysis. Agreement between the exact and estimated values is good. For all the cases considered above, calculations are started with an initial guess $\underset{\sim}{q}^0 = \underset{\sim}{0}$. The CPU time required for each case varied from 2 to 10 seconds on an IBM RISC System/6000 computer.

References

Alifanov, O. M., 1974, "Solution of an Inverse Problem of Heat Conduction by Iteration Methods," *J. Engineering Physics*, Vol. 26, No. 4, pp. 471-476.

Benassi, M., Cotta, R. M., and Siewert, C. E., 1983, "The P_N Method for Radiative Transfer Problems With Reflective Boundary Conditions," *J. Quant. Spectrosc. Radiat. Transfer*, Vol. 30, No. 6, pp. 547-553.

Grosshandler, W. L., and Modak, A. T., 1981, "Radiation From Nonhomogeneous Combustion Products," *18th Symp. (Int.) on Combustion*, The Combustion Institute, Pittsburgh, PA, pp. 601-609.

Ho, C. H., and Özişik, M. N., 1989, "An Inverse Radiation Problem," *Int. J. Heat Mass Transfer*, Vol. 32, No. 2, pp. 335-341.

Huang, C. H., and Özişik, M. N., 1992, "Inverse Problem of Determining Unknown Wall Heat Flux in Laminar Flow Through a Parallel Plate Duct," *Numer. Heat Transfer*, Part A, Vol. 21, pp. 101-116.

Jamaluddin, A. S., and Smith, P. J., 1988, "Predicting Radiative Transfer in Axisymmetric Cylindrical Enclosures Using the Discrete Ordinates Method," *Combust. Sci. Tech.*, Vol.62, pp. 173-186.

Özişik, M. N., 1973, *Radiative Transfer*, Wiley, New York.

Siewert, C. E., 1978, "A New Approach to the Inverse Problem," *J. Math. Phys.*, Vol. 19, No. 12, pp. 2619-2621.

Siewert, C. E., and Thomas, J. R., 1990, "A Particular Solution for the P_N Method in Radiative Transfer," *J. Quant. Spectrosc. Radiat. Transfer*, Vol. 43, No. 6, pp. 433-436.

Subramanian, S., and Menguc, M. P., 1991, "Solution of the Inverse Radiation Problem for Inhomogeneous and Anisotropically Scattering Media Using a Monte Carlo Technique," *Int. J. Heat Mass Transfer*, Vol. 34, No. 1, pp. 253-266.

Viskanta, R., and Menguc, M. P., 1987, "Radiation Transfer in Combustion Systems," *Prog. Energy Combust. Sci.*, Vol. 13, pp. 97-160.

The Effect of Variable Viscosity on Forced Convection Over a Flat Plate Submersed in a Porous Medium

J. X. Ling[1] and A. Dybbs[2]

Nomenclature

A = const defined in Eq. (6)
a = const defined in Eq. (7)
C_p = specific heat of the convective fluid at constant pressure
f = dimensionless stream function defined in Eq. (11)
h = local heat transfer coefficient
K = permeability of the porous medium
k = thermal conductivity
Nu_x = local Nusselt number = hx/k
n = const defined in Eq. (6)
P = pressure
Pe_x = Peclet number = $(U_\infty x)/\alpha$
T = temperature
T_e = const defined in Eq. (7)
U_∞ = free-stream velocity
u = velocity in x direction
v = velocity in y direction
x = coordinate in the horizontal direction
y = coordinate in the vertical direction
α = equivalent thermal diffusivity
γ = const defined in Eq. (5)
η = dimensionless similarity variable defined in Eq. (10)
θ = dimensionless temperature profile defined in Eq. (11)
θ_e = dimensionless parameter defined in Eq. (14)
μ = viscosity of convective fluid
ν = kinematic viscosity of convective fluid
ψ = stream function ($u = \partial\psi/\partial y$, $v = -\partial\psi/\partial x$)

Introduction

The heat convection along a flat plate embedded in a porous medium is a classical topic because of its importance to applications, especially in petroleum and geothermal engineering. See Beckermann and Viskanta (1987), Bejan (1984), Cheng (1977a, 1977b), and Gary et al. (1982) for examples.

In most of these studies, the fluid viscosity is treated as a constant. However, it is well known that the viscosities of liquids change markedly with temperature. For instance, the viscosity of water decreases by about 240 percent when the temperature increases from 10°C (μ = 0.0131 g/cm•s) to 50°C (μ = 0.00548 g/cm•s). In this note, we will examine the effect of the variable viscosity on forced convection by presenting a similarity solution to the problem in which the viscosity of the fluid is taken as an inverse linear function of temperature.

Analysis

Consider the forced convection in a porous medium adjacent to a horizontal constant temperature surface with external flow $U_\infty(x)$. In formulating the problem, in addition to the assumptions made by Cheng (1977a, 1977b), we also assume that the viscosity of the fluid is an inverse linear function of temperature, which is a good approximation for liquids such as water and crude oil (Ling and Dybbs, 1987). Under these assumptions, the governing boundary layer equations for this problem are:

[1]Staff Scientist, Picker International, Inc., Cleveland, OH 44143; Mem. ASME.
[2]Professor, Department of Mechanical and Aerospace Engineering, Case Western Reserve University, Cleveland, OH 44106; Mem. ASME.

Contributed by the Heat Transfer Division of THE AMERICAN SOCIETY OF MECHANICAL ENGINEERS. Manuscript received by the Heat Transfer Division March 1991; revision received March 1992. Keywords: Forced Convection, Porous Media. Technical Editor: R. Viskanta.

Downloaded 13 Dec 2010 to 193.140.21.150. Redistribution subject to ASME license or copyright; see http://www.asme.org/terms/Terms_Use.cfm

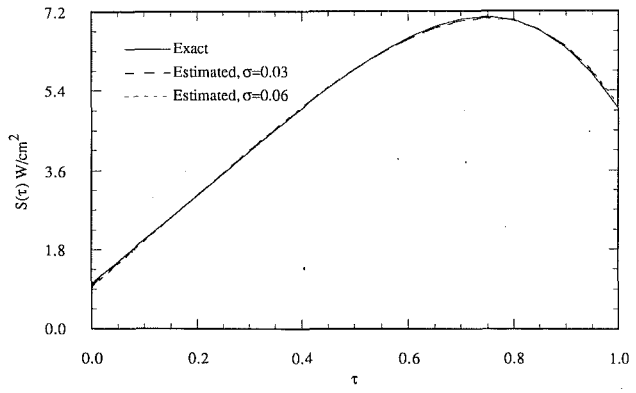

Fig. 2 Estimation of the source term $S(\tau) = 1 + 10\tau - 0.1\tau^2 + \tau^3 + \tau^4 - 10\tau^5 + 0.1\tau^6 + \tau^7 + \tau^8$ W/cm^2 with inverse analysis for the case $\omega = 0.3$, $\tau_o = 1$, $\bar{n} = 1$, using simulated measurement data with $\sigma = 0.03$ and $\sigma = 0.06$

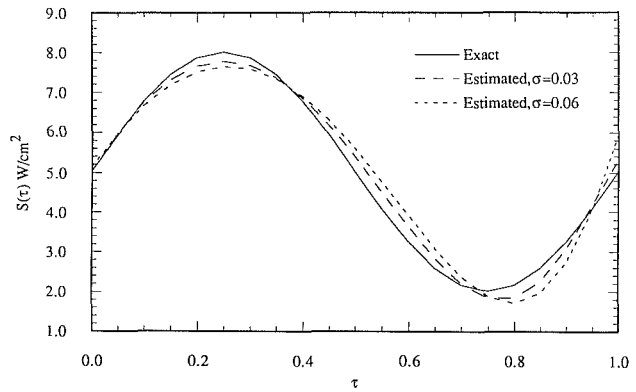

Fig. 3 Estimation of the source term $S(\tau) = 5 + 3 \sin(2\pi\tau)$ W/cm^2 with inverse analysis for the case $\omega = 0.3$, $\tau_o = 1$, $\bar{n} = 1$, using simulated measurement data with $\sigma = 0.03$ and $\sigma = 0.06$

viation $\sigma = 0.03$ and $\sigma = 0.06$ are used in the inverse analysis. Agreement between the exact and estimated values is good. For all the cases considered above, calculations are started with an initial guess $\underset{\sim}{q}^0 = \underset{\sim}{0}$. The CPU time required for each case varied from 2 to 10 seconds on an IBM RISC System/6000 computer.

References

Alifanov, O. M., 1974, "Solution of an Inverse Problem of Heat Conduction by Iteration Methods," *J. Engineering Physics*, Vol. 26, No. 4, pp. 471-476.

Benassi, M., Cotta, R. M., and Siewert, C. E., 1983, "The P_N Method for Radiative Transfer Problems With Reflective Boundary Conditions," *J. Quant. Spectrosc. Radiat. Transfer*, Vol. 30, No. 6, pp. 547-553.

Grosshandler, W. L., and Modak, A. T., 1981, "Radiation From Nonhomogeneous Combustion Products," *18th Symp. (Int.) on Combustion*, The Combustion Institute, Pittsburgh, PA, pp. 601-609.

Ho, C. H., and Özişik, M. N., 1989, "An Inverse Radiation Problem," *Int. J. Heat Mass Transfer*, Vol. 32, No. 2, pp. 335-341.

Huang, C. H., and Özişik, M. N., 1992, "Inverse Problem of Determining Unknown Wall Heat Flux in Laminar Flow Through a Parallel Plate Duct," *Numer. Heat Transfer*, Part A, Vol. 21, pp. 101-116.

Jamaluddin, A. S., and Smith, P. J., 1988, "Predicting Radiative Transfer in Axisymmetric Cylindrical Enclosures Using the Discrete Ordinates Method," *Combust. Sci. Tech.*, Vol.62, pp. 173-186.

Özişik, M. N., 1973, *Radiative Transfer*, Wiley, New York.

Siewert, C. E., 1978, "A New Approach to the Inverse Problem," *J. Math. Phys.*, Vol. 19, No. 12, pp. 2619-2621.

Siewert, C. E., and Thomas, J. R., 1990, "A Particular Solution for the P_N Method in Radiative Transfer," *J. Quant. Spectrosc. Radiat. Transfer*, Vol. 43, No. 6, pp. 433-436.

Subramanian, S., and Menguc, M. P., 1991, "Solution of the Inverse Radiation Problem for Inhomogeneous and Anisotropically Scattering Media Using a Monte Carlo Technique," *Int. J. Heat Mass Transfer*, Vol. 34, No. 1, pp. 253-266.

Viskanta, R., and Menguc, M. P., 1987, "Radiation Transfer in Combustion Systems," *Prog. Energy Combust. Sci.*, Vol. 13, pp. 97-160.

The Effect of Variable Viscosity on Forced Convection Over a Flat Plate Submersed in a Porous Medium

J. X. Ling[1] and A. Dybbs[2]

Nomenclature

A = const defined in Eq. (6)
a = const defined in Eq. (7)
C_p = specific heat of the convective fluid at constant pressure
f = dimensionless stream function defined in Eq. (11)
h = local heat transfer coefficient
K = permeability of the porous medium
k = thermal conductivity
Nu_x = local Nusselt number = hx/k
n = const defined in Eq. (6)
P = pressure
Pe_x = Peclet number = $(U_\infty x)/\alpha$
T = temperature
T_e = const defined in Eq. (7)
U_∞ = free-stream velocity
u = velocity in x direction
v = velocity in y direction
x = coordinate in the horizontal direction
y = coordinate in the vertical direction
α = equivalent thermal diffusivity
γ = const defined in Eq. (5)
η = dimensionless similarity variable defined in Eq. (10)
θ = dimensionless temperature profile defined in Eq. (11)
θ_e = dimensionless parameter defined in Eq. (14)
μ = viscosity of convective fluid
ν = kinematic viscosity of convective fluid
ψ = stream function ($u = \partial\psi/\partial y$, $v = -\partial\psi/\partial x$)

Introduction

The heat convection along a flat plate embedded in a porous medium is a classical topic because of its importance to applications, especially in petroleum and geothermal engineering. See Beckermann and Viskanta (1987), Bejan (1984), Cheng (1977a, 1977b), and Gary et al. (1982) for examples.

In most of these studies, the fluid viscosity is treated as a constant. However, it is well known that the viscosities of liquids change markedly with temperature. For instance, the viscosity of water decreases by about 240 percent when the temperature increases from 10°C (μ = 0.0131 g/cm•s) to 50°C (μ = 0.00548 g/cm•s). In this note, we will examine the effect of the variable viscosity on forced convection by presenting a similarity solution to the problem in which the viscosity of the fluid is taken as an inverse linear function of temperature.

Analysis

Consider the forced convection in a porous medium adjacent to a horizontal constant temperature surface with external flow $U_\infty(x)$. In formulating the problem, in addition to the assumptions made by Cheng (1977a, 1977b), we also assume that the viscosity of the fluid is an inverse linear function of temperature, which is a good approximation for liquids such as water and crude oil (Ling and Dybbs, 1987). Under these assumptions, the governing boundary layer equations for this problem are:

[1]Staff Scientist, Picker International, Inc., Cleveland, OH 44143; Mem. ASME.
[2]Professor, Department of Mechanical and Aerospace Engineering, Case Western Reserve University, Cleveland, OH 44106; Mem. ASME.

Contributed by the Heat Transfer Division of THE AMERICAN SOCIETY OF MECHANICAL ENGINEERS. Manuscript received by the Heat Transfer Division March 1991; revision received March 1992. Keywords: Forced Convection, Porous Media. Technical Editor: R. Viskanta.

Copyright © 1992 by ASME
Downloaded 13 Dec 2010 to 193.140.21.150. Redistribution subject to ASME license or copyright; see http://www.asme.org/terms/Terms_Use.cfm

$$\frac{\partial u}{\partial x}+\frac{\partial v}{\partial y}=0 \tag{1}$$

$$u=-\frac{K}{\mu}\frac{\partial P}{\partial x} \tag{2}$$

$$v=-\frac{K}{\mu}\frac{\partial P}{\partial y} \tag{3}$$

$$u\frac{\partial T}{\partial x}+v\frac{\partial T}{\partial y}=\alpha\frac{\partial^2 T}{\partial y^2} \tag{4}$$

$$\frac{1}{\mu}=\frac{1}{\mu_0}[1+\gamma(T-T_0)] \tag{5}$$

where u and v are the Darcy velocity components in the x and y directions, respectively; $\alpha = k_e/(\rho_\infty C_p)_f$ is the equivalent thermal diffusivity, $(\rho_\infty C_p)_f$ is the product of density and specific heat of the fluid, k_e is the effective thermal conductivity of the saturated porous medium. The subscripts "0" and "∞" refer to the conditions at the wall and at infinity.

The boundary conditions for this problem are:

$$y=0,\ T=T_0 \tag{6a}$$

$$y\to\infty,\ T=T_\infty,\ u=U_\infty(x)=Ax^n,\ v=0 \tag{6b}$$

For convenience, Eq. (5) can be rewritten as follows:

$$\frac{1}{\mu}=a(T-T_e) \tag{7}$$

where $a = \gamma/\mu_0$ is a constant; $T_e = T_0 - (1/\gamma)$ is a reference temperature.

By substituting Eq. (7) into Eqs. (2) and (3), eliminating P, integrating the resultant equation from $y = 0$ to ∞ with respect to y, and noting that $T = T_\infty$, $u = U_\infty$, $\partial^2 u/\partial y^2 = 0$ at $y \to \infty$, and introducing the stream function ψ, one obtains:

$$\frac{T-T_e}{T_\infty-T_e}=\frac{1}{U_\infty}\frac{\partial\psi}{\partial y} \tag{8}$$

$$\frac{\partial\psi}{\partial y}\frac{\partial T}{\partial x}-\frac{\partial\psi}{\partial x}\frac{\partial T}{\partial y}=\alpha\frac{\partial^2 T}{\partial y^2} \tag{9}$$

Introducing the similarity variable

$$\eta=\left(\frac{U_\infty x}{\alpha}\right)^{1/2}\frac{y}{x} \tag{10}$$

and similarity profiles

$$f(\eta)=\frac{\psi}{(\alpha U_\infty x)^{1/2}},\ \theta(\eta)=\frac{T-T_0}{T_\infty-T_0} \tag{11}$$

The problem statement then becomes

$$\frac{\theta+\theta_e}{1+\theta_e}=f' \tag{12}$$

$$\theta''+\frac{n+1}{2}f\theta'=0 \tag{13}$$

where

$$\theta_e=\frac{T_0-T_e}{T_\infty-T_0}=\frac{1}{\gamma(T_\infty-T_e)} \tag{14}$$

which depends on the wall temperature, the free-stream temperature, and the viscosity reference temperature T_e. If θ_e is large, in other words, if γ or $(T_\infty - T_0)$ is small, the effect of variable viscosity can then be neglected. If θ_e is small, which means either the fluid viscosity changes markedly with temperature or the temperature difference between the surface and the free stream is high, the effect of variable viscosity becomes very important.

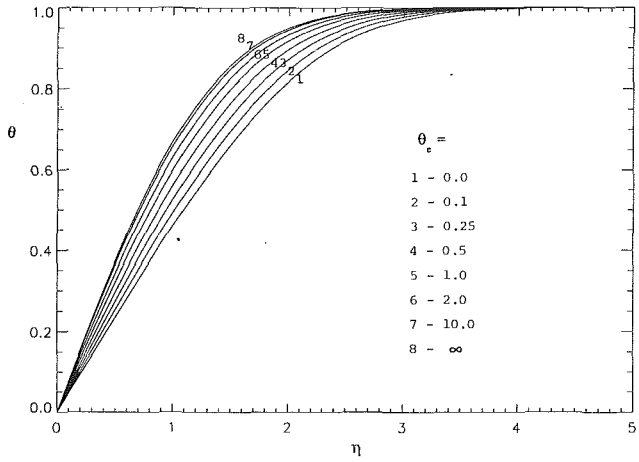

Fig. 1 Dimensionless temperature profiles, $n = 0$

The boundary conditions become:

$$\theta(0)=f(0)=0,\quad \theta(\infty)=f'(\infty)=1 \tag{15}$$

From Eqs. (12) and (13), it is apparent that similarity solutions exist for any value of n. Substituting Eq. (15) into Eq. (12) gives

$$f'(0)=\frac{\theta_e}{1+\theta_e} \tag{16}$$

Substituting Eq. (12) into Eq. (13), one obtains

$$f'''+\frac{n+1}{2}ff''=0 \tag{17}$$

with

$$f(0)=0,\quad f'(0)=\frac{\theta_e}{1+\theta_e},\quad f'(\infty)=1 \tag{18}$$

It is interesting to note that Eq. (17) is exactly the same as the classical Blasius equation if both n and θ_e are equal to zero.

Results and Discussion

1 Temperature Profiles. Equation (17), along with the boundary conditions (18), is integrated numerically using the Runge-Kutta method with a shooting technique to obtain the velocity and temperature profiles. Numerical computations are carried out for both $n = 0$ and $n = 1$ with the values of θ_e from 0 to 10.0. The temperature profiles for selected values of θ_e are shown in Figs. 1 and 2.

As can be seen from them, the thermal boundary thickness increases with decreasing values of θ_e. This is because for a given fluid, γ is fixed; smaller θ_e implies higher temperature difference between the wall and the free stream. Figure 1 also shows that for $\theta_e \gg 1$, the predicted temperature profile is close to Curve 8, which represents the analytical solution to the similar problem with constant viscosity as developed by Cheng (1977a) and Bejan (1984). This is expected since large θ_e implies that the effect of variable viscosity can be neglected.

2 Heat Transfer Results. The heat transfer rates are given by

$$\mathrm{Nu}_x=\theta'(0)(\mathrm{Pe}_x)^{1/2}$$

Downloaded 13 Dec 2010 to 193.140.21.150. Redistribution subject to ASME license or copyright; see http://www.asme.org/terms/Terms_Use.cfm

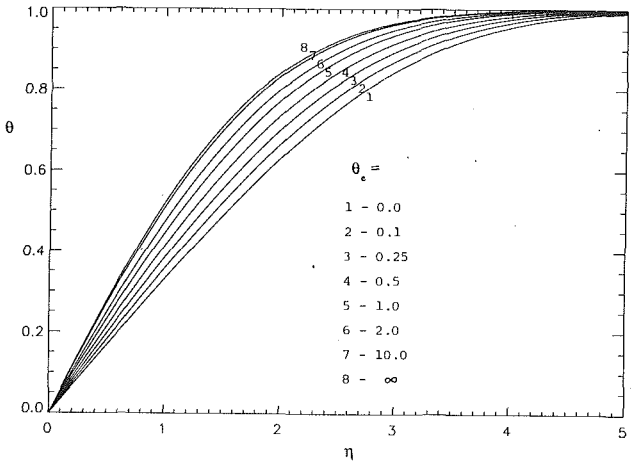

Fig. 2 Dimensionless temperature profiles, $n = 1$

Table 1 Values of $[\theta'(0)]$ for selected values of θ_e

θ_e	$n=0$	$n=1$
0.00	0.332	0.470
0.05	0.347	0.491
0.10	0.361	0.510
0.25	0.392	0.554
0.50	0.426	0.603
1.00	0.465	0.657
2.00	0.500	0.708
5.00	0.533	0.754
10.0	0.548	0.774
∞	0.564	0.798

The values of $\theta'(0)$ for $n = 0$ and $n = 1$ at selected values of θ_e are presented in Table 1.

As follows from Table 1, the variation of viscosity has significant influence on heat transfer. Nusselt number decreases with θ_e. For application of geothermal engineering, for example, if T_0 is 278 K (5°C), $(T_\infty - T_0)$ is 80 K (which is a fairly common situation), θ_e is then about 0.25 for water. The heat transfer results based on the constant viscosity assumption (corresponding to $\theta_e \to \infty$) are more than 40 percent higher than that of the present study for both $n = 0$ and $n = 1$. Therefore, when the viscosity of a working fluid is sensitive to the temperature variation or the temperature difference between the plate and the free stream is large, the effect of the variable viscosity has to be taken into account. For $n = 0$, if $\theta_e \to \infty$, $\theta'(0) = 0.564$, and which is exactly the same as presented by Bejan (1984) for the constant viscosity case. For both geothermal and petroleum flows, soil and sandstone are treated as porous media whose permeabilities are extremely small. In those cases, the Darcy's law model is a very good approximation, but the effect of the variable viscosity is important.

References

Beckermann, C., and Viskanta, R., 1987, "Forced Convection Boundary Layer Flow and Heat Transfer Along a Flat Plate Embedded in a Porous Medium," *International Journal of Heat and Mass Transfer*, Vol. 30, No. 7, pp. 1547-1551.

Bejan, A., 1984, *Convective Heat Transfer*, Chap. 10, Wiley, New York.

Cheng, P., 1977a, "Similarity Solutions for Mixed Convection From Horizontal Impermeable Surfaces in Saturated Porous Media," *International Journal of Heat and Mass Transfer*, Vol. 20, pp. 893-898.

Cheng, P., 1987b, "Combined Free and Forced Convection Flow About Inclined Surfaces in Porous Media," *International Journal of Heat and Mass Transfer*, Vol. 20, pp. 807-814.

Gary, J., Kassoy, D. R., Tadjeran, H., and Zebib, A., 1982, "The Effects of Significant Viscosity Variation on Convective Heat Transport in Water-Saturated Porous Media," *Journal of Fluid Mechanics*, Vol. 117, pp. 233-249.

Ling, J. X., and Dybbs, A., 1987, "Forced Convection Over a Flat Plate Submersed in a Porous Medium, Variable Viscosity Case," ASME Paper No. 87-WA/HT-23.

Analytical Solution of Steady Natural Convection in an Annular Porous Medium Evaluated With a Symbolic Algebra Code

A. Mojtabi[1] and M. C. Charrier-Mojtabi[2]

Nomenclature

g = gravitational acceleration
K = permeability of the porous medium
Nu^* = average Nusselt number
r_i, r_o = inner and outer cylinder radii
r = coordinate in radius direction scaled by $r_0 - r_i$
R = ratio of the outer to the inner radius
Ra^* = Rayleigh number of filtration $= g\beta K(T_i - T_o)(r_o - r_i)(\rho c)_f/(\lambda_{eq}\nu)$
T = dimensionless temperature $= (T' - T_o)/(T_i - T_o)$
T_i, T_o = inner and outer cylinder temperatures
β = thermal expansion coefficient of the fluid
θ = angular coordinate
λ_{eq} = equivalent thermal conductivity of the saturated porous medium
ν = kinematic viscosity of the fluid
$(\rho c)_f$ = heat capacity of the fluid
ψ = stream function

Introduction

Natural convection flows in a cylindrical annular porous medium have been studied extensively over the last twenty years.

The main results concern the two-dimensional steady state. Several techniques have been developed, such as the finite difference method (Caltagirone, 1976), the finite element method (Mojtabi et al., 1987), and the spectral method (Charrier-Mojtabi and Caltagirone, 1980; Rao et al., 1987; Himasekhar and Bau, 1988; Charrier-Mojtabi et al., 1991).

Caltagirone (1976) solved the problem using a regular perturbation method in powers of Ra, the Rayleigh number of filtration, up to order three. With the same method Himasekhar and Bau (1988) constructed an approximate solution: Terms up to $0(\mathrm{Ra}^{60})$ were computed. The dependent variables (ψ_i, T_i) with $T = \Sigma\ \mathrm{Ra}^i\ T_i(x, y)$ and $\psi = \Sigma\ \mathrm{Ra}^i\ \psi_i(x, y)$ have been expressed using the truncated Galerkin spectral representation.

In this paper, an analytical solution for unicellular natural convection flows that appear in a horizontal cylindrical annulus is presented. The solution is obtained using a regular perturbation method in powers of the dimensionless gap width ϵ. A symbolic algebra code (Mathematica) allows us to obtain the expanded solution at any order of ϵ. Then a correlation between the Nusselt number Nu^*, the Rayleigh number Ra^* (based on the gap width), and ϵ is deduced from this analytical solution. The results are compared to those previously obtained by numerical methods and the range of applicability of this new solution regarding parameter values (Ra^*, ϵ) is discussed.

Mathematical Formulation

Let us consider a saturated porous layer bounded by two horizontal coaxial cylinders. The inner and outer cylinders, of radius r_i and r_o, respectively, are maintained at constant and uniform temperatures, T_i and T_o, respectively, with $T_o < T_i$.

[1] Laboratoire de Modélisation en Mécanique des fluides, Université Paul Sabatier, Toulouse, France.

[2] Institut de Mécanique des Fluides, Avenue du Professeur Camille Soula, 31400 Toulouse, France.

Contributed by the Heat Transfer Division of THE AMERICAN SOCIETY OF MECHANICAL ENGINEERS. Manuscript received by the Heat Transfer Division October 1990; revision received February 1992. Keywords: Natural Convection, Numerical Methods, Porous Media. Technical Editor: R. Viskanta.

Downloaded 13 Dec 2010 to 193.140.21.150. Redistribution subject to ASME license or copyright; see http://www.asme.org/terms/Terms_Use.cfm

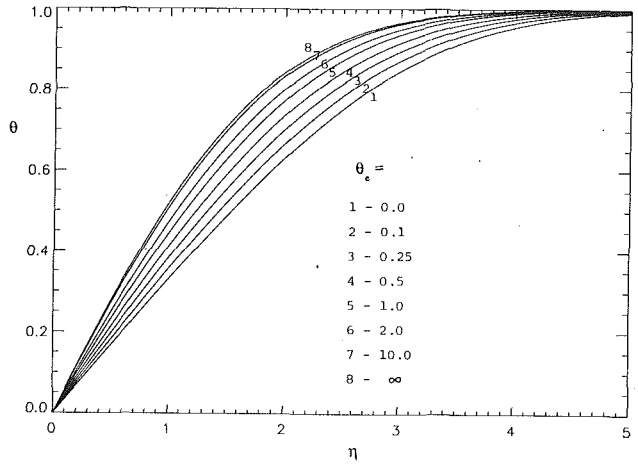

Fig. 2 Dimensionless temperature profiles, $n = 1$

Table 1 Values of $[\theta'(0)]$ for selected values of θ_e

θ_e	$n=0$	$n=1$
0.00	0.332	0.470
0.05	0.347	0.491
0.10	0.361	0.510
0.25	0.392	0.554
0.50	0.426	0.603
1.00	0.465	0.657
2.00	0.500	0.708
5.00	0.533	0.754
10.0	0.548	0.774
∞	0.564	0.798

The values of $\theta'(0)$ for $n = 0$ and $n = 1$ at selected values of θ_e are presented in Table 1.

As follows from Table 1, the variation of viscosity has significant influence on heat transfer. Nusselt number decreases with θ_e. For application of geothermal engineering, for example, if T_0 is 278 K (5°C), $(T_\infty - T_0)$ is 80 K (which is a fairly common situation), θ_e is then about 0.25 for water. The heat transfer results based on the constant viscosity assumption (corresponding to $\theta_e \to \infty$) are more than 40 percent higher than that of the present study for both $n = 0$ and $n = 1$. Therefore, when the viscosity of a working fluid is sensitive to the temperature variation or the temperature difference between the plate and the free stream is large, the effect of the variable viscosity has to be taken into account. For $n = 0$, if $\theta_e \to \infty$, $\theta'(0) = 0.564$, and which is exactly the same as presented by Bejan (1984) for the constant viscosity case. For both geothermal and petroleum flows, soil and sandstone are treated as porous media whose permeabilities are extremely small. In those cases, the Darcy's law model is a very good approximation, but the effect of the variable viscosity is important.

References

Beckermann, C., and Viskanta, R., 1987, "Forced Convection Boundary Layer Flow and Heat Transfer Along a Flat Plate Embedded in a Porous Medium," *International Journal of Heat and Mass Transfer*, Vol. 30, No. 7, pp. 1547-1551.

Bejan, A., 1984, *Convective Heat Transfer*, Chap. 10, Wiley, New York.

Cheng, P., 1977a, "Similarity Solutions for Mixed Convection From Horizontal Impermeable Surfaces in Saturated Porous Media," *International Journal of Heat and Mass Transfer*, Vol. 20, pp. 893-898.

Cheng, P., 1987b, "Combined Free and Forced Convection Flow About Inclined Surfaces in Porous Media," *International Journal of Heat and Mass Transfer*, Vol. 20, pp. 807-814.

Gary, J., Kassoy, D. R., Tadjeran, H., and Zebib, A., 1982, "The Effects of Significant Viscosity Variation on Convective Heat Transport in Water-Saturated Porous Media," *Journal of Fluid Mechanics*, Vol. 117, pp. 233-249.

Ling, J. X., and Dybbs, A., 1987, "Forced Convection Over a Flat Plate Submersed in a Porous Medium, Variable Viscosity Case," ASME Paper No. 87-WA/HT-23.

Analytical Solution of Steady Natural Convection in an Annular Porous Medium Evaluated With a Symbolic Algebra Code

A. Mojtabi[1] and M. C. Charrier-Mojtabi[2]

Nomenclature

g = gravitational acceleration
K = permeability of the porous medium
Nu^* = average Nusselt number
r_i, r_o = inner and outer cylinder radii
r = coordinate in radius direction scaled by $r_0 - r_i$
R = ratio of the outer to the inner radius
Ra^* = Rayleigh number of filtration $= g\beta K(T_i - T_o)(r_o - r_i)(\rho c)_f/(\lambda_{eq}\nu)$
T = dimensionless temperature $= (T' - T_o)/(T_i - T_o)$
T_i, T_o = inner and outer cylinder temperatures
β = thermal expansion coefficient of the fluid
θ = angular coordinate
λ_{eq} = equivalent thermal conductivity of the saturated porous medium
ν = kinematic viscosity of the fluid
$(\rho c)_f$ = heat capacity of the fluid
ψ = stream function

Introduction

Natural convection flows in a cylindrical annular porous medium have been studied extensively over the last twenty years.

The main results concern the two-dimensional steady state. Several techniques have been developed, such as the finite difference method (Caltagirone, 1976), the finite element method (Mojtabi et al., 1987), and the spectral method (Charrier-Mojtabi and Caltagirone, 1980; Rao et al., 1987; Himasekhar and Bau, 1988; Charrier-Mojtabi et al., 1991).

Caltagirone (1976) solved the problem using a regular perturbation method in powers of Ra, the Rayleigh number of filtration, up to order three. With the same method Himasekhar and Bau (1988) constructed an approximate solution: Terms up to $0(\mathrm{Ra}^{60})$ were computed. The dependent variables (ψ_i, T_i) with $T = \Sigma\ \mathrm{Ra}^i\ T_i(x, y)$ and $\psi = \Sigma\ \mathrm{Ra}^i\ \psi_i(x, y)$ have been expressed using the truncated Galerkin spectral representation.

In this paper, an analytical solution for unicellular natural convection flows that appear in a horizontal cylindrical annulus is presented. The solution is obtained using a regular perturbation method in powers of the dimensionless gap width ϵ. A symbolic algebra code (Mathematica) allows us to obtain the expanded solution at any order of ϵ. Then a correlation between the Nusselt number Nu^*, the Rayleigh number Ra^* (based on the gap width), and ϵ is deduced from this analytical solution. The results are compared to those previously obtained by numerical methods and the range of applicability of this new solution regarding parameter values (Ra^*, ϵ) is discussed.

Mathematical Formulation

Let us consider a saturated porous layer bounded by two horizontal coaxial cylinders. The inner and outer cylinders, of radius r_i and r_o, respectively, are maintained at constant and uniform temperatures, T_i and T_o, respectively, with $T_o < T_i$.

[1] Laboratoire de Modélisation en Mécanique des fluides, Université Paul Sabatier, Toulouse, France.

[2] Institut de Mécanique des Fluides, Avenue du Professeur Camille Soula, 31400 Toulouse, France.

Contributed by the Heat Transfer Division of THE AMERICAN SOCIETY OF MECHANICAL ENGINEERS. Manuscript received by the Heat Transfer Division October 1990; revision received February 1992. Keywords: Natural Convection, Numerical Methods, Porous Media. Technical Editor: R. Viskanta.

Copyright © 1992 by ASME
Downloaded 13 Dec 2010 to 193.140.21.150. Redistribution subject to ASME license or copyright; see http://www.asme.org/terms/Terms_Use.cfm

The gap width is $r_o - r_i$ and the radii ratio is $R = r_o/r_i$. The dimensionless gap width is then defined as $\epsilon = (r_o - r_i)/r_i = R - 1$.

In order to simplify the formulation, several classical assumptions have been made:

(*i*) The Boussinesq approximation and Darcy's law are assumed to be valid.

(*ii*) The inertia terms and viscous dissipations are neglected.

(*iii*) The fluid is assumed to be in thermal equilibrium with the porous matrix.

In dimensionless form, the governing equations, formulated in terms of stream function $\Psi(r, \theta)$ and temperature $T(r, \theta)$, are, for the steady two-dimensional state:

$$\nabla^2 \Psi = \mathrm{Ra}^* \left(\sin\theta \frac{\partial T}{\partial r} + \frac{\cos\theta}{r} \frac{\partial T}{\partial \theta} \right) \tag{1a}$$

$$\nabla^2 T = \frac{1}{r} \left(\frac{\partial \Psi}{\partial \theta} \frac{\partial T}{\partial r} - \frac{\partial \Psi}{\partial r} \frac{\partial T}{\partial \theta} \right) \tag{1b}$$

where $r = r'/(r_o - r_i)$ is the dimensionless radial coordinate and θ is the angular coordinate, $0 \le \theta \le \pi$. The Rayleigh number of filtration, Ra^*, is defined by:

$$\mathrm{Ra}^* = g \beta K (r_o - r_i)(T_0 - T_i)(\rho c)_f / (\nu \lambda_{eq})$$

and $\mathrm{Ra}^* = \epsilon\, \mathrm{Ra}_{ri}$ where Ra_{ri} is the Rayleigh number based on the radius of the inner cylinder, r_i. In this expression β, ν, ρ are, respectively, the thermal expansion coefficient, the kinematic viscosity, and the density of the saturating fluid. K is the permeability of the porous medium and λ_{eq} its equivalent thermal conductivity.

In order to express Eqs. (1*a*), (1*b*) in terms of relative gap width, ϵ, the new coordinate x, given by $x = r - 1/\epsilon$ is used so that the domain shifts from $1/\epsilon \le r \le 1 + 1/\epsilon$ to $0 \le x \le 1$ and θ remains unaltered. The resulting equations are:

$$\xi^2 \frac{\partial^2 \Psi}{\partial x^2} + \epsilon \xi \frac{\partial \Psi}{\partial x} + \epsilon^2 \frac{\partial^2 \Psi}{\partial \theta^2} = \mathrm{Ra}^* \left(\xi^2 \sin\theta \frac{\partial T}{\partial x} + \epsilon \xi \cos\theta \frac{\partial T}{\partial \theta} \right) \tag{2a}$$

$$\xi^2 \frac{\partial^2 T}{\partial x^2} + \epsilon \xi \frac{\partial T}{\partial x} + \epsilon^2 \frac{\partial^2 T}{\partial \theta^2} = \epsilon \xi \left(\frac{\partial \Psi}{\partial \theta} \frac{\partial T}{\partial x} - \frac{\partial \Psi}{\partial x} \frac{\partial T}{\partial \theta} \right) \tag{2b}$$

where $\xi = (1 + x\epsilon)$.

The boundary conditions are:

$$x = 0:\ \Psi = 0;\ T = 1\ \forall\theta \tag{3a}$$

$$x = 1:\ \Psi = 0;\ T = 0\ \forall\theta \tag{3b}$$

$$\theta = 0,\ \pi:\ \Psi = 0;\ \frac{\partial T}{\partial \theta} = 0\ \forall x \tag{3c}$$

The global Nusselt number, which corresponds to the ratio of the total heat transfer to the conductive heat transfer, is:

$$\mathrm{Nu}^* = -\frac{\ln(1+\epsilon)}{\pi\epsilon} \int_0^\pi \left. \frac{\partial T}{\partial x} \right|_{x=0} d\theta = -\frac{(1+\epsilon)\ln(1+\epsilon)}{\pi\epsilon} \int_0^\pi \left. \frac{\partial T}{\partial x} \right|_{x=1} d\theta \tag{4}$$

Solution Method

The solution is periodic in the azimuthal direction but not in the radial one; so the temperature T and the stream function Ψ are expanded as follows:

$$\Psi = \sum_{n=1}^{N} \sum_{i=0}^{I} \epsilon^i f_p^i(x) \sin(n\theta) \tag{5a}$$

$$T = \sum_{n=0}^{N} \sum_{i=0}^{I} \epsilon^i g_p^i(x) \cos(n\theta) \tag{5b}$$

Expansions (5*a*) and (5*b*) are inserted into Eqs. (2*a*), (2*b*); like terms in sin and cos and coefficients of like power of ϵ are equated.

We obtain a set of second-order linear differential equations:

$$f_p^{i\,\prime\prime}(x) = F(f_k^j, f_k^{j\,\prime\prime}, f_k^{j\,\prime}, g_m^l, g_m^{l\,\prime}, x) = F_p^i(x) \tag{6a}$$

$$g_p^{i\,\prime\prime}(x) = G(g_k^j, g_k^{j\,\prime}, g_k^{j\,\prime\prime}, f_m^l, f_m^{l\,\prime}, x) = G_p^i(x) \tag{6b}$$

with j and $l \le i$; k and $m \le p$. $F_p^i(x)$ and $G_p^i(x)$ are polynomial functions.

The appropriate boundary conditions for the functions $f^i{}_p(x)$, $g_p^i(x)$, and g_0^0 are:

$$x = 0:\quad f_p^i = g_p^i = 0 \quad \textit{and} \quad g_0^0 = 1$$

$$x = 1:\quad f_p^i = g_p^i = g_0^0 = 0\ \forall i,\ p$$

The analytical solution of Eqs. (6*a*), (6*b*), to any desired order, is given by:

$$f_p^i(x) = \mathfrak{F}_p^i(x) - x\,\mathfrak{F}_p^i(x=1) \tag{7a}$$

$$g_p^i(x) = \mathfrak{G}_p^i(x) - x\,\mathfrak{G}_p^i(x=1) \tag{7b}$$

where

$$\mathfrak{F}_p^i(x) = \int_0^x \left(\int_0^y (F_p^i(t)\,dt)\,dy \right)$$

and

$$\mathfrak{G}_p^i(x) = \int_0^x \left(\int_0^y (G_p^i(t)\,dt)\,dy \right) \tag{8}$$

The degree of the polynomial expressions $f_p^i(x)$ and $g_p^i(x)$ increases as the order of approximation, I, increases.

For $I = 1, 2$, we can calculate $f_p^i(x)$ and $g_p^i(x)$ without the need of any computer. For orders higher than $I = 2$, a symbolic algebra code has been used for the computations. If the central memory of the computer is sufficient the functions $f_p^i(x)$ and $g_p^i(x)$ could be obtained at any order. In the present paper the computations have been made on a Macintosh SE 30 with a central memory of 8 MEG, up to order $I = 6$.

For engineering applications, we are often concerned with the effect of fluid motion on the heat transfer between the two cylinders. This can be evaluated by calculating the mean Nusselt number averaged over the inner cylinder surface:

$$\mathrm{Nu}^* = -\ln(1+\epsilon) \sum_{i=0}^{\infty} \epsilon^{i-1} \frac{d g_0^i}{dx}(x=0) \tag{9}$$

Results and Discussion

The polynomial solutions presented in this paper describe the unicellular steady natural convection flows, numerically obtained by previous works.

It is found that Eqs. (5*a*), (5*b*) give a converging solution with increasing order N, for $\epsilon \le 2^{1/2} - 1$ and for $\mathrm{Ra}_{ri} \le 10{,}000$.

The values of the temperature at the point ($x = 1/2$, $\theta = 0$), maximum values of the streamfunction $\psi_{\max}$, and global Nusselt number Nu^* are compared for $\epsilon = 2^{1/16} - 1$ and $\epsilon = 2^{1/8} - 1$ to those obtained by the Galerkin method (Table 1). For $\epsilon = 2^{1/4} - 1$ and $\epsilon = 2^{1/2} - 1$, the comparisons concern the global Nusselt number and $\psi_{\max}$; our results are compared to those obtained by the Galerkin method (Charrier-Mojtabi and Caltagirone, 1980) and by finite difference method (Caltagirone, 1976) (Table 2). Good agreement is found for a large range of Rayleigh numbers.

We now focus on the Nusselt number Nu^*. Equation (9) gives the following correlation between Nu^*, ϵ, and Ra^*:

Downloaded 13 Dec 2010 to 193.140.21.150. Redistribution subject to ASME license or copyright; see http://www.asme.org/terms/Terms_Use.cfm

Table 1 Comparison of solutions (Nu^*, ψ_{max}, $T(1/2, 0)$) obtained with the symbolic code and Galerkin method for $\epsilon = 2^{1/16} - 1$ and $\epsilon = 2^{1/8} - 1$

$R = 2^{1/16}$	SYMBOLIC CODE			GALERKIN METHOD		
Ra_{ri}	Nu^*	ψ_{max}	$T(1/2,0)$	Nu^*	ψ_{max}	$T(1/2,0)$
10^3	1.0015	5.52	0.519	1.0015	5.53	0.519
$6\,10^3$	1.0530	32.84	0.638	1.0530	32.81	0.638
10^4	1.1362	53.71	0.711	1.1376	53.05	0.714
$R = 2^{1/8}$						
10^3	1.0251	11.23	0.589	1.0252	11.24	0.590
$2\,10^3$	1.0946	22.203	0.676	1.0946	21.89	0.679
$4\,10^3$	1.37	41.71	0.75	1.31	41.57	0.78

Table 2 Comparison of solutions (Nu^*, ψ_{max}) for different methods

$R = 2^{1/4}$	SYMBOLIC CODE		GALERKIN METHOD		A.D.I. METHOD	
Ra_{ri}	Nu^*	ψ_{max}	Nu^*	ψ_{max}	Nu^*	ψ_{max}
100	1.0045	2.33	1.0045	2.36	1.0045	2.35
200	1.0177	4.66	1.0177	4.70	1.0176	4.69
500	1.1020	11.53	1.1021	11.51	1.1017	11.50
1000	1.479	21.76	1.330	21.77	1.328	21.76
$R = 2^{1/2}$						
25	1.0	1.23	1.005	1.26	1.005	1.27
50	1.017	2.46	1.020	2.53	1.020	2.54
100	1.072	4.92	1.077	5.00	1.078	5.01
200	1.444	9.68	1.266	9.61	1.263	9.61

$$Nu^* = 1 + 4.216\times10^{-4}\,Ra^{*2}(\epsilon^2-\epsilon^3) - (2.579\times10^{-4} + 1.678\times10^{-7}\,Ra^{*2})Ra^{*2}\epsilon^4 + (1.187\times10^{-3} + 3.356\times10^{-7}\,Ra^{*2})Ra^{*2}\epsilon^5 - (1.845\times10^{-3} - 2.169\times10^{-7}\,Ra^{*2} - 9.737\times10^{-11}\,Ra^{*4})Ra^{*2}\,\epsilon^6 + 0(\epsilon^7) \quad (10)$$

The computed values of Nu^* given by Eq. (10) are listed in Table 3 at different orders of ϵ, for ϵ ranging from $2^{1/16}-1$ to $2^{1/2}-1$ and for Ra_{ri} ranging from 10 to 10,000. These results are compared to those obtained by Galerkin method (Charrier-Mojtabi and Caltagirone, 1980). It is shown that the limit of validity of this correlation decreases when one increases Ra^* and/or ϵ.

Another conclusion to be drawn from these comparisons is that correlation (10) may be truncated at order three in ϵ and that the following correlation:

$$Nu^* = 1 + \frac{17\,Ra^{*2}\,(\epsilon^2-\epsilon^3)}{40320} \quad (11)$$

is sufficient to describe the heat transfer for the studied cases. The standard deviation between the present correlation (11) and the numerical results for $\epsilon \le 0.1$ and $Ra_{ri} \le 2000$ is 0.5 parts per mil.

Table 3 Average Nusselt number Nu^* calculated as function of Ra_{ri} and ϵ; comparison with the Galerkin method

$Nu^* - 1 = f(Ra_{ri})$ for different values of ϵ.			
Ra_{ri}	Galerkin	Symbolic code: $o(\epsilon^7)$	Symbolic code: $o(\epsilon^3)$
$\epsilon = 2^{1/16} - 1$			
50	$387\,10^{-8}$	$387\,10^{-8}$	$405\,10^{-8}$
500	$155\,10^{-7}$	$155\,10^{-7}$	$162\,10^{-7}$
1000	$1547\,10^{-6}$	$1544\,10^{-6}$	$1619\,10^{-6}$
6000	$530\,10^{-4}$	$530\,10^{-4}$	$583\,10^{-4}$
10^4	$1376\,10^{-4}$	$1362\,10^{-4}$	$1619\,10^{-4}$
$\epsilon = 2^{1/8} - 1$			
50	$647\,10^{-7}$	$641\,10^{-7}$	$707\,10^{-7}$
500	$643\,10^{-5}$	$637\,10^{-5}$	$707\,10^{-5}$
1000	$252\,10^{-4}$	$251\,10^{-4}$	$283\,10^{-4}$
2000	$946\,10^{-4}$	$946\,10^{-4}$	$1132\,10^{-4}$
4000	$309\,10^{-3}$	$374\,10^{-3}$	$453\,10^{-3}$
$\epsilon = 2^{1/4} - 1$			
50	$112\,10^{-5}$	$108\,10^{-5}$	$135\,10^{-5}$
100	$446\,10^{-5}$	$432\,10^{-5}$	$540\,10^{-5}$
200	$177\,10^{-4}$	$171\,10^{-4}$	$216\,10^{-4}$
500	$102\,10^{-3}$	$102\,10^{-3}$	$135\,10^{-3}$
750	$208\,10^{-3}$	$230\,10^{-3}$	$304\,10^{-3}$
$\epsilon = 2^{1/2} - 1$			
50	$203\,10^{-4}$	$172\,10^{-4}$	$310\,10^{-4}$
75	$451\,10^{-4}$	$392\,10^{-4}$	$698\,10^{-4}$
100	$768\,10^{-4}$	$717\,10^{-4}$	$124\,10^{-4}$
150	$163\,10^{-3}$	18610^{-3}	$279\,10^{-3}$

To conclude, the use of a symbolic algebra code allows us to obtain polynomial coefficients in the temperature and the stream function series for the unicellular basic flows. This analytical solution could be introduced in a stability analysis of these flows. Another goal of this study was to give a useful correlation between the Nusselt number, the Rayleigh number, and the relative gap width ϵ for $\epsilon < 0.5$.

References

Caltagirone, J. P., 1976, "Thermoconvective Instabilities in a Porous Medium Bounded by Two Concentric Horizontal Cylinders," *J. Fluid Mech.*, Vol. 76, pp. 337–362.

Charrier-Mojtabi, M. C., and Caltagirone, J. P., 1980, "Numerical Simulation of Natural Convection in an Annular Porous Layer by Spectral Method," *Proc. 1st Int. Conf. of Numerical Methods for Nonlinear Problems*, Swansea, United Kingdom, pp. 821–828.

Charrier-Mojtabi, M. C., Mojtabi, A., Azaiez, M., and Labrosse, G., 1991, "Numerical and Experimental Study of Multicellular Free Convection Flows in an Annular Porous Layer," *Int. J. Heat Mass Transfer*, Vol. 34, No. 12, pp. 3061–3074.

Himasekhar, K., and Bau Haim, H., 1988, "Two-Dimensional Bifurcation Phenomena in Thermal Convection in Horizontal Concentric Annuli Containing Saturated Porous Media," *J. Fluid Mech.*, Vol. 187, pp. 267–300.

Mojtabi, A., Ouazzar, D., and Charrier-Mojtabi, M. C., 1987, "An Efficient Finite Element Code for 2D Steady State in Porous Annulus," *Proc. Int. Conf. Num. Methods for Thermal Problems*, Montreal, Vol. 5, Part 1, pp. 644–654.

Rao, Y. F., Fukuda, K., and Hasegawa, S., 1987, "Steady and Transient Analysis of Natural Convection in a Horizontal Porous Annulus With Galerkin Method," ASME JOURNAL OF HEAT TRANSFER, Vol. 109, pp. 919–927.

Downloaded 13 Dec 2010 to 193.140.21.150. Redistribution subject to ASME license or copyright; see http://www.asme.org/terms/Terms_Use.cfm

Thermocapillary Convection During Solid–Liquid Phase Change

T. E. Voth,[1,4] A. Liu,[2,4] and T. L. Bergman[3,4]

Nomenclature

Bo = dynamic Bond number = Ra/Ma
c = specific heat, concentration
Fo = Fourier number = $\alpha_\ell t/H^2$
H, L = PCM height and length
k = thermal conductivity
Ma = Marangoni number = $\partial\sigma/\partial T \cdot (T_h - T_f) \cdot H/\mu \cdot \alpha_\ell$
Pr = Prandtl number
Ra = Rayleigh number = $g\beta \cdot (T_h - T_f)H^3/\nu \cdot \alpha$
s = liquid layer thickness
Ste_ℓ = liquid Stefan number = $c_\ell \cdot (T_h - T_f)/\lambda$
Ste_s = solid Stefan number = $c_s \cdot (T_f - T_c)/\lambda$
t = time
T = temperature
u = horizontal velocity component
U = dimensionless surface velocity = uH/α_ℓ
x, y = horizontal and vertical coordinate directions
X = dimensionless free surface coordinate = $x/s(y=H)$
α = thermal diffusivity
β = thermal expansion coefficient
θ = dimensionless temperature = $(T - T_f)/(T_h - T_f)$
λ = latent heat of fusion
μ = dynamic viscosity
ν = kinematic viscosity
σ = surface tension

Subscripts

c = cold
f = fusion
h = hot

Introduction

Thermocapillary-induced convection (TC) is suspected to be relevant in various materials processing applications involving melting and solidification (Schwabe, 1981; Ostrach, 1982; Chen, 1987). Although an overwhelming number of studies have considered the fluid mechanics of TC, and a few numerical studies have investigated its effect upon solid–liquid phase change, no quantitative experimental phase-change results involving TC exist, although results of a qualitative experiment were reported by Schwabe and Scharmann (1981).

Observation of TC during solid–liquid phase change is difficult because of the small length and time scales involved, as well as the high melting temperature and opacity of materials of interest. Also restrictive are the complexities associated with solutocapillary forces established by contamination or oxidation along free liquid surfaces, which counteract and obfuscate TC (Keller and Bergman, 1990). A need persists to develop appropriate experimental methodologies in order to measure and observe TC and its influence upon solid–liquid phase change.

[1] Graduate Research Assistant; Assoc. Mem. ASME.
[2] Graduate Research Assistant.
[3] Associate Professor; Assoc. Mem. ASME.
[4] Department of Mechanical Engineering, The University of Texas at Austin, Austin, TX 78712.

Contributed by the Heat Transfer Division of The American Society of Mechanical Engineers. Manuscript received by the Heat Transfer Division July 1991; revision received January 1992. Keywords: Materials Processing and Manufacturing Processes, Phase-Change Phenomena, Thermocapillary Flows.

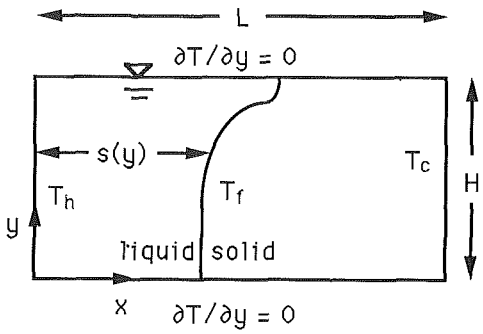

Fig. 1 Schematic of the physical system

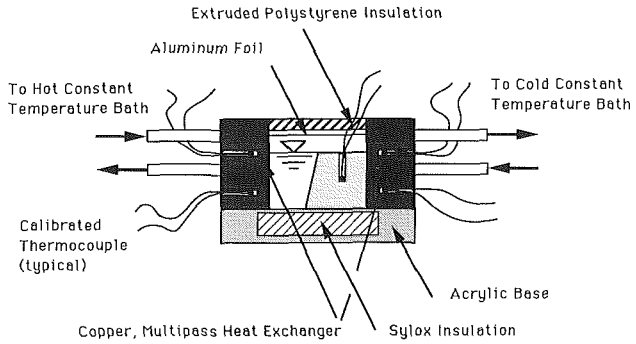

Fig. 2 Schematic of the test cell

Table 1 Thermophysical properties of silicone oil and ice

	k, W/m•K	ρ, kg/m³	c, kJ/kg•K	ν, m²/s	λ, kJ/kg	Pr
oil [a]	0.155	979	1.59	175×10^{-6}	-	1755
ice [b,c]	1.88	920	2.04	-	333.5	-

a. Dow Corning Data Sheets, 1991
b. Incropera and DeWitt, 1990
c. Weast, 1974

Experiments

A phase-change material (PCM) with a free liquid surface is contained within the enclosure of Fig. 1. Since the boundaries at $y = 0$ and H are insulated and $T_h > T_f$, a melt front propagates from left to right at a rate governed by the net heat transfer to the solid–liquid interface. Local melting is expected to be maximum at $y = H$ since warm fluid is advected at relatively high velocities to the solid–liquid interface by TC forces (Zehr et al., 1987). For a flat free surface, TC phenomena are embodied in the hydrodynamic boundary condition

$$\mu \partial u/\partial y|_{y=H} = \partial\sigma/\partial x|_{y=H} \quad (1)$$

where $\partial\sigma/\partial x$ may be expressed as $\partial\sigma/\partial T \cdot \partial T/\partial x$ (Levich and Krylov, 1969).

The experimental approach taken here avoids solutocapillary effects ($\partial\sigma/\partial c \cdot \partial c/\partial x$), which are dominant in nominally pure PCMs used in the heat transfer laboratory. Specifically, the solid is ice while silicone oil is the liquid (Table 1). As the ice melts, liquid water sinks to the bottom of the oil layer, where it is extracted and replaced with oil. This approach eliminates solutocapillary flow and allows TC influences to be observed, at the expense of matching the dimensionless parameters, such as Pr, of relevant materials that are processed under high-purity conditions.

The hybrid PCM was housed in the test cell of Fig. 2. The PCM height is maintained at either 10 or 20 mm while its width is fixed at 20 mm or 40 mm. Two 38-mm-high, 63-mm-deep

Copyright © 1992 by ASME
Downloaded 13 Dec 2010 to 193.140.21.150. Redistribution subject to ASME license or copyright; see http://www.asme.org/terms/Terms_Use.cfm

Table 2 Experimental conditions

Experiment	H, mm	L, mm	T_h, °C	T_c, °C	Ra x 10^{-3}	Ma	Bo	Ste_ℓ	Ste_s
A	20	40	10	-3.5	40	750	53.0	0.047	0.021
B	10	20	10	-1.65	5	400	12.5	0.047	0.010
C	20	40	10	0	40	750	53.0	0.047	0.0
D	10	40	10	0	5	400	12.5	0.047	0.0

copper heat exchangers were attached to one of two hollowed acrylic bases to control the thermal boundary conditions at $x=0$ and L. Acrylic windows (3.2 mm thick) were attached to the front and back of the heat exchangers to provide optical access.

To control conditions at $y=0$, a 19-mm-thick cavity (filled with Sylox) was milled into the base so that it spanned the bottom of the PCM. The thickness of the acrylic floor separating the Sylox and PCM was made small (3.2 mm) to minimize lateral conduction. Acrylic was selected as the base material since its thermal conductivity ($k=0.19$ W/m•K, Rohm and Hass, 1983) is similar to that of the silicone oil used, reducing conjugate effects at steady state. The PCM was covered with 198-mm-thick extruded styrofoam placed above a 5 to 15 mm air gap, and a sheet of aluminum foil was attached to the insulation to minimize radiative exchange. The entire test cell was insulated during experimentation. Even so, the experiments had to be performed in an environmental chamber maintained at approximately 3°C to minimize heat exchange with the laboratory and, in turn, obtain quantitative information.

The ice was prepared by freezing a layer of degassed water from $x=L$ until a desired thickness was obtained. The resulting solid–liquid interface was initially planar (as determined through inspection of enlarged photographs) to within ± 0.5 mm. The constant-temperature baths were set to their desired temperatures and the ice was allowed to reach thermal equilibrium (≈ 1 hour as indicated by several thermocouples cast into the ice), the heat exchangers were connected to the regulated baths, the silicone oil was poured into the volume previously occupied by the liquid water, and melting was initiated. Oil (at approximately 3°C) was added after extracting the melted water with a hypodermic needle to maintain the liquid surface at $y=H$.

Flow visualization was obtained with time exposure photographs (60 s) of neutrally buoyant, hollow glass spherical seeding, which was illuminated with a vertical sheet of HeNe laser light. The liquid surface temperature was monitored with an infrared camera (Inframetrics 600) equipped with special 3X telescopic and 6 in. close-up lenses (spatial resolution of ≈ 0.13 mm) operating in the 8–12 mm spectral range. Data (2D radiosity distributions of the oil surface) were acquired at steady state by removing the top insulation while simultaneously recording the image on videotape at 30 Hz. Frame averaging (over 16 frames) was used to reduce signal noise. Note that silicone oil is effectively opaque over the spectral range of the camera (Pline, 1989), and its high emissivity (≥ 0.90, Pline, 1989) provides a strong infrared signal with little reflected component. By critically considering the many errors associated with scanning detector imagers (Torres et al., 1990), the resulting temperature readings are estimated to be accurate to within $\theta \pm 0.07$ and $X \pm 0.02$. Errors associated with unavoidable heat exchange with the environment during imaging are more significant than those associated with equipment limitations.

The experimental conditions are shown in Table 2. Note that Bo indicates the relative strength of buoyancy to TC forces, and it has been suggested that TC is significant if $Bo < 1$ (Ostrach and Pradhan, 1978). In Experiments A and B, T_h and T_c were maintained above and below T_f, respectively. The ice was melted until steady state (estimated to be the time when no liquid water had accrued over, typically, a 3–4 hour time period). Experiments C and D were characterized by $s(t=0)=5$ mm and continuous melting. Two types of experimentation were performed in order to (*i*) measure the surface temperature of the oil without disturbing the transient system response due to removal of the top insulation (surface temperature are not reported for Experiments C and D) and (*ii*) measure indirectly the local heat transfer rates at the solid–liquid interface by observing the interface location at various times.

Results

Typical results are reported here. Also discussed are predictions (which include Eq. (1) or $u=0$ applied to $y=H$) generated by a numerical model described elsewhere (Bergman and Webb, 1990). In short, the model places two nonorthogonal meshes, one in the solid and one in the liquid, and solves simultaneously the Boussinesq forms of the quasi-steady continuity, momentum, and energy equations in the liquid, as well as the heat diffusion equation in the solid with a control-volume-based, finite difference technique. The interface location is advanced in response to the predicted net heat transfer rate at the solid–liquid interface and melt time step. Simulation of Experiments A and B showed that grid-independent solutions were obtained with a 38×38 mesh in both the solid and liquid, with dense grid packing near $y=H$, $x=s(y=H)$. Additional predictions are available elsewhere (Liu, 1992; Voth, 1992).

Steady-State Behavior. Figure 3 includes results for Experiments A and B. Note that the flow visualization shows the liquid domain (Figs. 3*a* and 3*c*), as well as reflections of illuminated seeding from the liquid free surface and the ice–oil interface. Close inspection of the flow visualization reveals TC-induced advection, with the streamlines propagating well into the upper right region of the oil layer.

Numerical predictions associated with Experiment A are presented in Fig. 3(*b*) (with TC and buoyancy effects included). The solid–liquid interface location was specified *a priori* using the experimental measurements and the liquid phase convection alone was predicted. The actual center of rotation is identified by a crosshair superposed upon the predicted streamlines. Comparison of the measured and predicted flow fields shows excellent agreement. The predicted surface temperature and velocity distributions are shown in Fig. 3(*a*). As evident, the predicted surface temperatures are moderately affected by the hydrodynamic boundary condition at $y=H$, and the TC and no-slip predictions bracket the experimental data in $0.8 \leq X \leq 1.0$. Deviation of experimental thermocapillary free surface temperatures from the predicted distribution is attributed to heat exchange at the free surface during surface temperature measurement (Liu, 1992; Voth, 1992).

The experimental results for Experiment B (Fig. 3*c*) are in good agreement with the predictions (Fig. 3*d*). Both the measured center of rotation and the streamline penetration near $x=s(y=H)$ are replicated by the simulations while the surface temperature distribution is considered to be in excellent agreement with the measurement. All told, the consistency between measurements and predictions suggests that the numerical model properly replicates the convective mechanisms in the liquid phase, but no conclusions can be drawn concerning heat transfer at the solid–liquid interface.

Melting. Figure 4 includes flow visualization and predictions for Experiments C (top two rows) and D (bottom two rows). Unlike in Fig. 3, the solid–liquid interface location is predicted and is dependent upon the highly variable local heat transfer rates at the solid–liquid interface (Bergman and Webb, 1990; Liu, 1992; Voth, 1992). The conduction solution and experimentally observed centers of rotation are indicated by arrows and crosshairs, respectively. Excellent agreement exists between the experimental results and the numerical predictions. Simulations that neglect TC underpredict the melting rates,

Downloaded 13 Dec 2010 to 193.140.21.150. Redistribution subject to ASME license or copyright; see http://www.asme.org/terms/Terms_Use.cfm

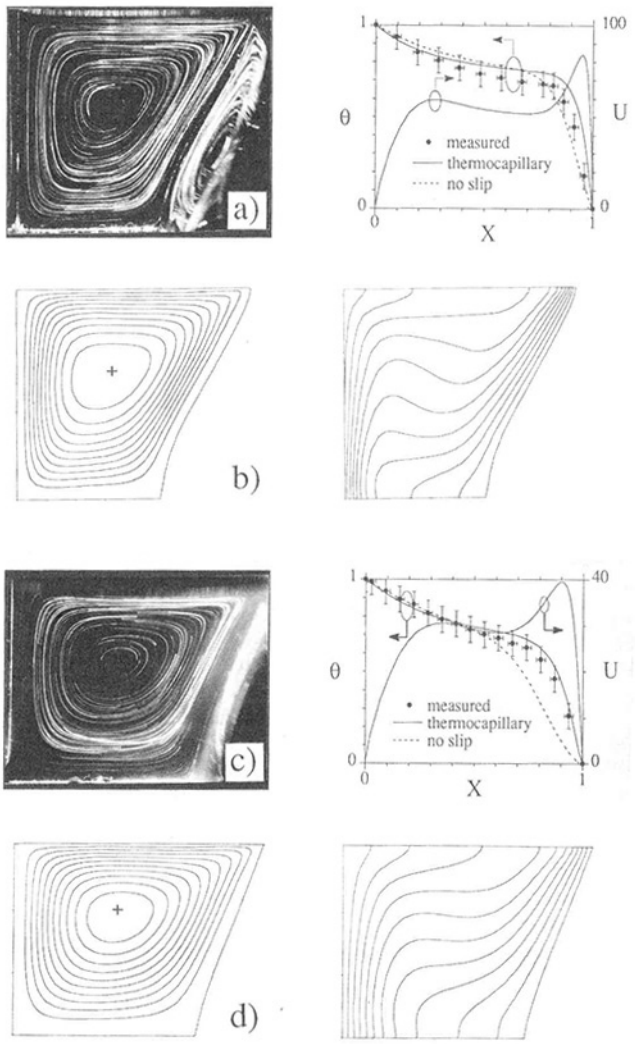

Fig. 3 Measured and predicted results including (*a*) the observed streamlines and surface temperature and velocity distributions of Experiment A, (*b*) the predicted streamlines and isotherms for Experiment A, (*c*) the observed streamlines and surface temperature and velocity distributions of Experiment B, and (*d*) the predicted streamlines and isotherms for Experiment B

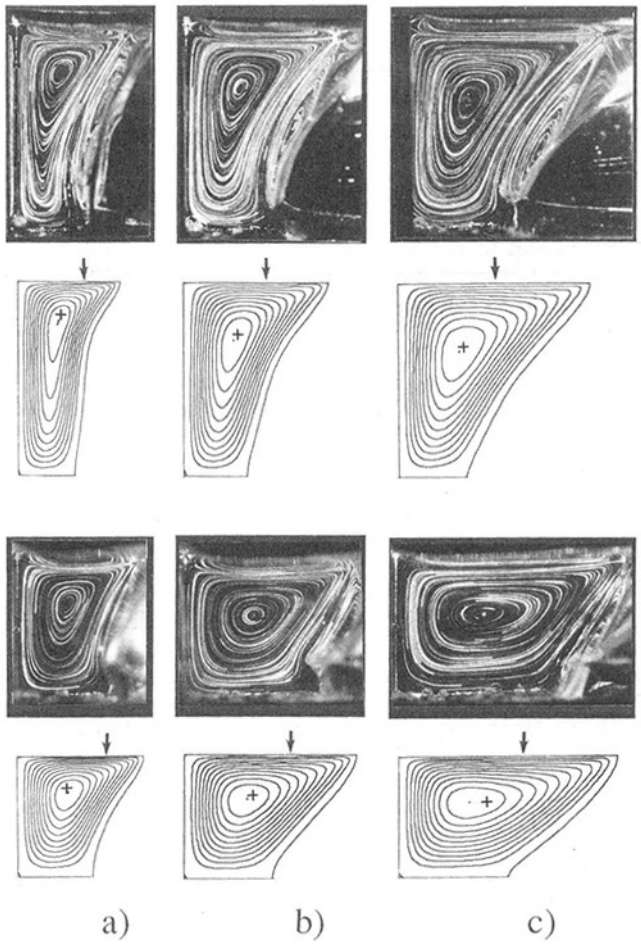

Fig. 4 Observed and predicted liquid phase domains and flow patterns for Experiment C (top two rows) at (*a*) Fo = 0.6, (*b*) Fo = 1.2, and (*c*) Fo = 2.0 and Experiment D (bottom two rows) at (*a*) Fo = 2.4, (*b*) Fo = 4.8, and (*c*) Fo = 7.8

showing directly the potential importance of TC during solid-liquid phase change (Liu, 1992; Voth, 1992).

Conclusions

This technical note has dealt with the effects of TC upon the solid-liquid phase change of pure PCMs. The experiments, which were designed specifically to minimize solutocapillary effects, have provided the first quantitative data concerning liquid phase hydrodynamics, liquid surface temperature distributions, and solid-liquid interface heat transfer rates in such problems. TC's impact is considered to be significant in terms of local phase change rates, even at the relatively high Bo considered here.

Acknowledgments

This research was sponsored by NSF Grant No. CBT-8552806. The authors are grateful for a software development grant from IBM, which made simulation of the system response possible.

References

Bergman, T. L., and Webb, B. W., 1990, "Simulation of Pure Metal Melting With Buoyancy and Surface Tension Forces in the Liquid Phase," *International Journal of Heat and Mass Transfer*, Vol. 33, pp. 139–149.

Chen, M. M., 1987, "Thermocapillary Convection in Materials Processing," in: *Interdisciplinary Issues in Materials Processing and Manufacturing*, S. K. Samanta et al., eds., Vol. 2, pp. 541–558.

Dow Corning, 1991, Data Sheets for Dow Corning 200 Fluid, received in personal communication, Dow Corning Corporation, Midland, MI.

Incropera, F. P., and DeWitt, D. P., 1990, *Fundamentals of Heat and Mass Transfer*, 3rd ed., Wiley, New York.

Keller, J. R., and Bergman, T. L., 1990, "Thermosolutal Inducement of No-Slip Free Surfaces in Combined Marangoni-Buoyancy Driven Cavity Flows," ASME Journal of Heat Transfer, Vol. 112, pp. 363–369.

Levich, V. G., and Krylov, V. S., 1969, "Surface-Tension-Driven Phenomena," *Annual Review of Fluid Mechanics*, Vol. 1, pp. 293–316.

Liu, A., 1992, "Solidification of Pure Materials With Buoyancy and Surface Tension Forces in the Liquid Phase," MS Thesis, University of Texas, Austin, TX.

Ostrach, S., and Pradhan, A., 1978, "Surface-Tension Induced Convection at Reduced Gravity," *AIAA Journal*, Vol. 6, pp. 419–424.

Ostrach, S., 1982, "Low-Gravity Fluid Flows," *Annual Review of Fluid Mechanics*, Vol. 14, pp. 313–345.

Pline, A. D., 1989, "Infrared Surface Temperature Measurements for the Surface Tension Driven Convection Experiment," NASA TM 101353.

Rohm and Haas Company, 1983, "Plexiglas Acrylic® Sheet General Information," Philadelphia, pp. 6–9.

Schwabe, D., 1981, "Marangoni Effects in Crystal Growth Melts," *PhysicoChemical Hydrodynamics*, Vol. 2, pp. 263–280.

Schwabe, D., and Scharmann, A., 1981, "Marangoni Convection in Open Boat and Crucible," *Journal of Crystal Growth*, Vol. 52, pp. 435–449.

Torres, J. H., Springer, T. A., Welch, A. J., and Pearce, J. A., 1990, "Limitations of a Thermal Camera in Measuring Surface Temperature of Laser-Irradiated Tissues," *Lasers in Surgery and Medicine*, Vol. 10, pp. 510–523.

Voth, T. E., 1992, "The Effect of Buoyancy and Surface Tension Driven Convection on Melting of a Pure Material," MS Thesis, University of Texas, Austin, TX.

Weast, R. C., 1974, *CRC Handbook of Chemistry and Physics*, 55th ed., CRC Press, Cleveland, OH.

Zehr, R. L., Chen, M. M., and Mazumder, J., 1987, "Thermocapillary Convection of a Differentially Heated Cavity at High Marangoni Numbers," ASME Paper No. 87-HT-29.

Downloaded 13 Dec 2010 to 193.140.21.150. Redistribution subject to ASME license or copyright; see http://www.asme.org/terms/Terms_Use.cfm